

## Durham E-Theses

---

# *Characterising fractured basement using the Lewisian Gneiss Complex, NW Scotland: Implications for fracture systems in the Clair Field basement*

PLESS, JENNIFER,CLAIRE

### How to cite:

---

PLESS, JENNIFER,CLAIRE (2012) *Characterising fractured basement using the Lewisian Gneiss Complex, NW Scotland: Implications for fracture systems in the Clair Field basement*, Durham theses, Durham University. Available at Durham E-Theses Online: <http://etheses.dur.ac.uk/3489/>

### Use policy

---

The full-text may be used and/or reproduced, and given to third parties in any format or medium, without prior permission or charge, for personal research or study, educational, or not-for-profit purposes provided that:

- a full bibliographic reference is made to the original source
- a [link](#) is made to the metadata record in Durham E-Theses
- the full-text is not changed in any way

The full-text must not be sold in any format or medium without the formal permission of the copyright holders.

Please consult the [full Durham E-Theses policy](#) for further details.

---

Academic Support Office, Durham University, University Office, Old Elvet, Durham DH1 3HP  
e-mail: [e-theses.admin@dur.ac.uk](mailto:e-theses.admin@dur.ac.uk) Tel: +44 0191 334 6107  
<http://etheses.dur.ac.uk>

DEPARTMENT OF EARTH SCIENCES, DURHAM UNIVERSITY

**Characterising fractured basement using the  
Lewisian Gneiss Complex, NW Scotland:  
Implications for fracture systems in the Clair Field  
basement**

---



A thesis submitted to Durham University for the degree of  
Doctor of Philosophy in the Faculty of Science

**Jennifer Claire Pless**

**201**





*To my grandparents:*

*Without your enthusiasm and garage full of rocks I would never have fallen in  
love with geology*



# Characterising fracture basement using the Lewisian Gneiss Complex, NW Scotland: Implications for fracture systems in the Clair Field basement

Jennifer C. Pless

---

1-, 2- and 3-dimensional fracture network characteristics of the mainland Lewisian Gneiss Complex (LGC) have been used to assess if the LGC is a suitable onshore analogue for the fracture networks within the offshore Clair basement. Faults that cut the Clair basement rocks are becoming increasingly recognised as important structural conduits that connect (oil & gas bearing) sedimentary packages across the main basement structure. The basement of the Clair field is poorly understood, with limited seismic and well datasets; so using an onshore fracture analogue, of the mainland LGC, will hopefully improve the understanding of the Clair basement fracture systems.

To determine the suitability of the mainland LGC as an analogue for the Clair basement four main research questions are asked in this thesis: What is the offshore Clair basement? What are the geological characteristics and attributes of the fracture networks in the mainland LGC? What are the dominant controls on these fracture network characteristics? How can the mainland Lewisian be used as an analogue for the Clair basement?

Onshore datasets (outcrop, terrestrial laser scans & NEXTMap® DEM) exhibit prominent NE-SW and/or NW-SE fault and fracture trends. The Clair basement seismic dataset exhibits comparable NE-SW & NW-SE trending faults, but the basement core samples exhibit a strongly aligned NNE-SSW fracture trend that is not so clearly represented in the onshore datasets. Fracture spacing distributions from the mainland LGC have strong power-law relationships over at least three orders of magnitude. Power-law relationships are also present from Clair basement datasets but the lack of large datasets means that these relationships are considered fairly weak.

Qualitative and Quantitative onshore and offshore analyses suggest that the mainland LGC is a suitable analogue for the Clair basement to some degree, but that their relationship is not a simple one. The results presented in this thesis do not provide a unique solution for the Clair basement fracture networks. Instead the onshore data provide model types that can be used in sensitivity models to ultimately assess which onshore dataset provides the best geological and statistical analogue for the Clair basement.

## Table of Contents

---

<b>Abstract .....</b>	<b>i</b>
<b>Table of Contents .....</b>	<b>ii</b>
<b>List of Figures .....</b>	<b>xii</b>
<b>List of Tables .....</b>	<b>xvii</b>
<b>List of Abbreviations .....</b>	<b>xix</b>
<b>Acknowledgements .....</b>	<b>xx</b>
<b>Declaration .....</b>	<b>xxi</b>

## Chapter 1

---

### Introduction and overview of fracture network characteristics

<b>1.1</b>	<b>Rationale for the project .....</b>	<b>1</b>
<b>1.2</b>	<b>Outline of the thesis .....</b>	<b>6</b>
<b>1.3</b>	<b>Introduction to deformation and reactivation processes in continental lithosphere .....</b>	<b>7</b>
1.3.1	<i>Fault Zone Structure .....</i>	<i>7</i>
1.3.1.1	Fault core .....	7
1.3.1.2	Fault damage zone .....	8
1.3.1.3	Protolith .....	11
1.3.2	<i>Fault zone products .....</i>	<i>11</i>
1.3.2.1	Fractures .....	11
1.3.2.2	Veins .....	14
1.3.2.3	Cataclasis .....	15
1.3.2.4	Pseudotachylites .....	16
1.3.2.5	Mylonites .....	16
1.3.3	<i>Kinematic indicators .....</i>	<i>18</i>
1.3.3.1	Displacement markers .....	18
1.3.3.2	Observation of fault planes .....	18
1.3.3.3	Secondary fractures .....	19

1.3.3.4	Vein infills .....	19
1.3.3.5	Viscous kinematic indicators .....	20
1.3.4	<i>Fault zone reactivation</i> .....	23
1.3.4.1	Estimating stress and strain trajectories from faults .....	26
1.3.4.2	Reactivation of pre-existing structures .....	26
1.3.5	<i>Fluid activity in faults</i> .....	28
<b>1.4</b>	<b>Fracture attribute characteristics</b> .....	<b>31</b>
1.4.1	<i>Orientation</i> .....	31
1.4.2	<i>Spacing</i> .....	34
1.4.3	<i>Aperture</i> .....	35
1.4.4	<i>Infill</i> .....	36
1.4.5	<i>Length</i> .....	37
1.4.6	<i>Geometry</i> .....	40
1.4.7	<i>Connectivity</i> .....	40
<b>1.5</b>	<b>Fracture population statistical analysis</b> .....	<b>42</b>
1.5.1	<i>Eigenvectors for fracture orientation analysis</i> .....	43
1.5.2	<i>Fracture population distribution plots</i> .....	44
1.5.2.1	Normal (or Gaussian) distribution .....	47
1.5.2.2	Log-normal distribution .....	47
1.5.2.3	Exponential distribution .....	47
1.5.2.4	Power-law distributions .....	48
1.5.2.4.1	Box-counting .....	50
1.5.2.4.2	Extrapolation of power-law distributions between scales .....	51
1.5.2.4.3	Extrapolation of power-law distributions between dimensions .....	54
1.5.2.4.4	Factors affecting power-law distributions .....	54
1.5.2.5	Reliability of statistical fracture distributions .....	55
1.5.3	<i>Coefficient of Variation (CV)</i> .....	55
<b>1.6</b>	<b>Data collection techniques and methodology</b> .....	<b>56</b>
1.6.1	<i>Field mapping and sample collection</i> .....	56
1.6.2	<i>Basement core logging</i> .....	57
1.6.3	<i>Onshore regional fault interpretation using NEXTMap® DEMs and aerial photographs</i> .....	58
1.6.4	<i>Offshore regional fault interpretation using a 3D seismic volume</i> .....	58

1.6.5	<i>1-dimensional line sampling</i> .....	58
1.6.6	<i>Optical microscopy</i> .....	59
1.6.7	<i>Terrestrial laser scanning (LiDAR)</i> .....	60
<b>1.7</b>	<b>Collaboration</b> .....	<b>61</b>

## Chapter 2

---

### Introduction to the geology of the NW Highlands and the Clair Field

<b>2.1</b>	<b>Introduction to the Lewisian Gneiss Complex</b> .....	<b>63</b>
2.1.1	<i>Regional setting</i> .....	66
2.1.2	<i>History of the Lewisian Complex</i> .....	67
2.1.3	<i>The Terrane Model</i> .....	67
2.1.4	<i>Regional geology of the mainland Lewisian Gneiss Complex</i> .....	72
2.1.4.1	Badcallian Gneisses .....	74
2.1.4.2	Inverian deformation .....	75
2.1.4.3	Scourie Dykes .....	75
2.1.4.4	The Loch Maree Group .....	77
2.1.4.5	Laxfordian deformation .....	77
2.1.5	<i>Post Lewisian Geology</i> .....	80
2.1.5.1	The Torridonian sedimentary sequence .....	80
2.1.5.1.1	Stoer Group .....	81
2.1.5.1.2	Sleat Group .....	84
2.1.5.1.3	Torridon Group .....	84
2.1.5.2	Cambro-Ordovician Sequence .....	86
2.1.5.3	Silurian-Devonian-Carboniferous .....	87
2.1.5.4	Permian-Triassic (Mesozoic) sediments .....	89
2.1.5.5	Tertiary rocks .....	92
2.1.5.6	Quaternary features .....	93
<b>2.2</b>	<b>The Clair Field</b> .....	<b>94</b>
2.2.1	<i>Location of the Clair Field</i> .....	94
2.2.2	<i>Clair Field development history and future</i> .....	96
2.2.2.1	Clair basement potential .....	97

2.2.2.2	Location of Clair basement wells .....	99
2.2.3	<i>Regional setting of the Clair Field</i> .....	99
2.2.3.1	Archaean basement .....	100
2.2.3.2	Devonian-Carboniferous succession .....	102
2.2.3.3	Late Cretaceous .....	104
2.2.3.4	Palaeocene to Eocene .....	105
2.2.3.5	Source rocks and oil migration history .....	107
2.2.4	<i>Clair Field tectonic history</i> .....	108
2.2.4.1	Hydrocarbon production from fractures in the Clair Field .....	110

## Chapter 3

---

### Mainland Lewisian Gneiss Complex fault and fracture analysis

<b>3.1</b>	<b>Introduction to the onshore fracture analysis</b> .....	<b>114</b>
<b>3.2</b>	<b>Regional lineament analysis</b> .....	<b>114</b>
3.2.1	<i>Method for production and interpretation of DEM maps of NW Scotland</i> .....	<b>118</b>
3.2.2	<i>Regional fault lineament orientation analysis</i> .....	<b>121</b>
3.2.3	<i>Regional fault lineament orientation: Discussion</i> .....	<b>127</b>
3.2.4	<i>Regional fault lineament spacing analysis</i> .....	<b>130</b>
3.2.4.1	Regional fault lineament spatial distributions .....	<b>130</b>
3.2.4.2	D-value .....	<b>139</b>
3.2.4.3	Coefficient of variation (CV) .....	<b>139</b>
3.2.4.4	Fault density (FD) .....	<b>140</b>
3.2.4.5	Regional fault lineament connectivity .....	<b>140</b>
3.2.5	<i>Regional fault lineament spatial analysis: Discussion</i> .....	<b>141</b>
<b>3.3</b>	<b>Fracture analysis from Lewisian outcrop data</b> .....	<b>147</b>
3.3.1	<i>Method for fracture logging and spatial analysis of fractures</i> .....	<b>149</b>
3.3.2	<i>Key Lewisian outcrop locations and lithological descriptions</i> .....	<b>149</b>
3.3.2.1	Alltan na Bradhan, Achmelvich & Clachtoll (Assynt Terrane) .....	<b>150</b>
3.3.2.2	Lochinver (Assynt Terrane) .....	<b>154</b>
3.3.2.3	Loch Assynt (Assynt Terrane) .....	<b>156</b>

3.3.2.4	Caolas Cumhann (Assynt Terrane) .....	157
3.3.2.5	Kinlochbervie (Rhiconich Terrane) .....	158
3.3.2.6	Traigh Allt Chailgeag & Rispond (Rhiconich Terrane) .....	162
3.3.2.7	Laxford Bridge (Rhiconich Terrane) .....	164
3.3.2.8	Oldshoremore (Rhiconich Terrane) .....	164
3.3.2.9	Rhiconich (Rhiconich Terrane) .....	165
3.3.2.10	Lithology Discussion .....	165
3.3.3	<i>Geological characterisation of onshore fracture sets</i> .....	166
3.3.3.1	‘Late Laxfordian’ faults .....	166
3.3.3.2	Stoer/Torridon Group age fractures .....	170
3.3.3.3	‘Later’ structures .....	172
3.3.3.4	Fault rock discussion .....	174
3.3.4	<i>Fracture orientation analysis from outcrop data</i> .....	175
3.3.4.1	Orientation analysis from outcrop data: Discussion .....	181
3.3.5	<i>Spacing analysis of fracture data from Lewisian Outcrop</i> .....	184
3.3.5.1	Fracture spatial distributions .....	185
3.3.5.2	D-value .....	190
3.3.5.3	CV .....	190
3.3.5.4	Fracture density .....	190
3.3.5.5	Fracture aperture versus length analysis .....	191
3.3.5.6	Fracture connectivity .....	193
3.3.5.7	Discussion of the Lewisian outcrop fracture spacing datasets .....	195
3.3.5.8	Comparison to previous fieldwork fracture studies in the mainland LGC .....	199
3.4	<b>Fault and fractures in the mainland Lewisian: Regional to outcrop synthesis</b> .....	201
3.5	<b>Mainland Lewisian summary</b> .....	203



## Chapter 4

---

### Clair Basement fault and fracture analysis

<b>4.1</b>	<b>Introduction to the offshore fracture analysis .....</b>	<b>207</b>
<b>4.2</b>	<b>Regional lineament analysis if seismic attribute maps .....</b>	<b>207</b>
4.2.1	<i>Method for production and interpretation of top basement seismic attribute maps .....</i>	<b>210</b>
4.2.2	<i>Regional fault lineament orientation analysis .....</i>	<b>212</b>
4.2.2.1	Clair basement .....	<b>213</b>
4.2.2.2	Clair sedimentary cover sequences .....	<b>219</b>
4.2.3	<i>Regional fault lineament orientation: Discussion .....</i>	<b>221</b>
4.2.4	<i>Regional fault lineament spacing analysis .....</i>	<b>223</b>
4.2.4.1	Regional fault lineament spatial distributions .....	<b>227</b>
4.2.4.2	D-value .....	<b>229</b>
4.2.4.3	Coefficient of variation (CV) .....	<b>229</b>
4.2.4.4	Fault Density (FD) .....	<b>229</b>
4.2.5	<i>Fault connectivity .....</i>	<b>229</b>
4.2.6	<i>Regional fault lineament spacing: Discussion .....</i>	<b>232</b>
<b>4.3</b>	<b>Fracture analysis from Clair basement well data .....</b>	<b>234</b>
4.3.1	<i>Method for core logging and spatial analysis of fractures .....</i>	<b>235</b>
4.3.2	<i>Clair Basement well locations and descriptions .....</i>	<b>238</b>
4.3.2.1	Well 206/7a-2 .....	<b>239</b>
4.3.2.1.1	Lithology .....	<b>239</b>
4.3.2.2	Well 206/8-8 .....	<b>243</b>
4.3.2.3	Well 206/8-2 .....	<b>244</b>
4.3.2.4	Well 206/12-1 .....	<b>245</b>
4.3.2.5	Well 206/9-2 .....	<b>246</b>
4.3.2.6	Well 206/8-15 .....	<b>246</b>
4.3.2.7	Lithology discussion .....	<b>247</b>
4.3.2.8	Fractures, veins and faults .....	<b>248</b>
4.3.2.8.1	Epidote/hematite and quartz fractures and veins .....	<b>250</b>
4.3.2.8.2	Carbonate-pyrite fills .....	<b>254</b>
4.3.2.8.3	Oil fills and 'open' fractures .....	<b>255</b>

4.3.2.9	Fault and fracture discussion .....	257
4.3.3	<i>Fracture orientation analysis from well datasets</i> .....	260
4.3.3.1	Orientation analysis from well data: Discussion .....	262
4.3.4	<i>Spacing analysis of fracture data from Clair basement well samples</i> ....	263
4.3.4.1	Fracture spatial distributions .....	263
4.3.4.2	D-value .....	271
4.3.4.3	CV .....	272
4.3.4.4	Fracture density (FD) .....	273
4.3.4.5	Fracture density versus Clair basement lithology .....	273
4.3.5	<i>Fracture aperture versus length analysis</i> .....	274
4.3.6	<i>Discussion of the Clair basement fracture spacing analysis</i> .....	277
4.4	<b>Faults and fractures in the Clair basement: Regional to well scale synthesis</b> .....	281
4.5	<b>Clair basement conclusions</b> .....	283

## Chapter 5

### Deterministic fracture network models form the Lewisian Gneiss Complex of the NW Scottish mainland

5.1	<b>Introduction to terrestrial laser scanning (ground-based LiDAR)</b> .....	285
5.2	<b>Rationale for the selection of scanned outcrops</b> .....	289
5.2.1	<i>Alltan na Bradhan (Canisp Shear Zone)</i> .....	292
5.2.2	<i>Kinlochbervie</i> .....	294
5.2.3	<i>Caolas Cumhann</i> .....	294
5.3	<b>3-dimensional fracture network model construction</b> .....	295
5.3.1	<i>Interpreting and creating fracture planes</i> .....	296
5.3.2	<i>Analysing the fracture networks</i> .....	298
5.4	<b>Results</b> .....	303
5.4.1	<i>3-dimensional fracture networks</i> .....	303
5.4.2	<i>Pseudo-well analysis</i> .....	308
5.4.2.1	Spacing distribution .....	308
5.4.2.2	D-value .....	311
5.4.2.3	CV .....	311

5.4.2.4	Fracture density analysis .....	312
5.4.2.5	Pseudo-well sampling discussion .....	312
5.4.3	<i>Fracture presence models</i> .....	314
5.4.3.1	Results .....	318
5.4.3.2	Discussion .....	318
5.4.4	<i>Fracture intersection models</i> .....	325
5.4.4.1	Results .....	329
5.4.4.2	Discussion .....	330
5.5	<b>Overall discussion</b> .....	333
5.6	<b>Conclusions</b> .....	337

## Chapter 6

---

### Data synthesis

6.1	<b>TLS modelling versus fieldwork and regional analysis</b> .....	340
6.1.1	<i>Orientation synthesis</i> .....	341
6.1.2	<i>Spatial synthesis</i> .....	347
6.2	<b>Onshore/Offshore synthesis</b> .....	356
6.2.1	<i>Comparison of lithologies</i> .....	356
6.2.2	<i>Comparison of fault rock characteristics</i> .....	359
6.2.3	<i>Synthesis of orientation data</i> .....	360
6.2.3.1	Regional orientation analysis .....	361
6.2.3.2	Well and outcrop (includes TLS) orientation analysis .....	362
6.2.3.3	Comparison of fracture network spatial characteristics .....	364
6.2.3.4	Regional fault data spatial synthesis .....	366
6.2.3.5	TLS model, fieldwork and well fracture data spatial synthesis .....	371
6.2.3.6	Regional and local scale synthesis .....	377

## Chapter 7

---

### Conclusions

7.1	<b>Impact</b> .....	388
7.2	<b>Recommendation for further work</b> .....	390

## **APPENDIX A**

**393**

- I: Summary of the tectonic, metamorphic, sedimentary and igneous history of the Clair basement and the mainland Lewisian Gneiss Complex.**

## **APPENDIX B**

**395**

- I: Workflow for creating fault surfaces from fault lineaments in Paradigm GoCAD® 2009.2.**
- II: Workflow for creating pseudo-wells through fault surface datasets in Paradigm GoCAD® 2009.2.**
- III: Regional fault spacing population distribution plots**
- IV: Thin section photo-micrographs from mainland LGC outcrop samples – photo-micrographs include lithological and fracture-fill images.**
- V: Stereonets from fracture datasets collected at outcrop.**
- VI: Fracture spatial population distribution plots from outcrop samples.**
- VII: Micro-fracture spatial analysis - thin section study. *Vernon, R.***

## **APPENDIX C**

**395**

- I: Examples of the seismic interpretation completed on the 3D seismic volume that covers the Clair Field.**
- II: Regional fault spacing population distribution plots from Clair basement**
- III: Descriptive core logs from Clair basement core samples.**
- IV: Fracture logs from Clair basement core samples.**
- V: Photo-logs of core from well 206/7a-2 and annotated photographs of pyrite overgrowth in core 206/12-1.**
- VI: Thin section photo-micrographs of core samples from the Clair basement – these photo-micro-graphs depict lithology and fracture-fill characteristics.**
- VII: Fracture spatial population distribution plots from Clair basement core samples.**

- I: Work-flow for converting RiScan® polyline picks into best-fit fracture planes
- II: Workflow for fracture presence analysis using S-Grids in Paradigm GoCad® 2009.2
- III: Video ‘flythrough’ of the terrestrial laser scan outcrop models
- IV: Dataset spreadsheets for the fracture presence and fracture intersection models

### List of Figures

---

Figure 1.1 – The principal components of an upper crustal fault zone .....	9
Figure 1.2 – Are faults barriers or conduits to fluid flow? .....	10
Figure 1.3 – Schematic illustration of a vertical crustal-scale fault zone .....	13
Figure 1.4 – Schematic diagrams of the three fundamental modes of fracturing .....	13
Figure 1.5 – Illustrations of mineral fibre growth in veins .....	15
Figure 1.6 – Examples of brittle kinematic markers .....	20
Figure 1.7 – Examples of viscous kinematic markers .....	22
Figure 1.8 – The two recognised types of reactivation .....	24
Figure 1.9 – The four main criteria considered reliable for recognising reactivation .....	25
Figure 1.10 – Plots of the criteria for reactivation .....	28
Figure 1.11 – Stress field criteria for fluid flow through fractures .....	29
Figure 1.12 – Examples of fluid flow mechanisms .....	30
Figure 1.13 – Examples of the different methods for analysing orientation .....	33
Figure 1.14 – Schematic illustration of fracture spacing .....	35
Figure 1.15 – Schematic diagrams illustrating the main fracture length biases .....	39
Figure 1.16 – Schematic illustrations of fracture connectivity analyses .....	41
Figure 1.17 – Stereonet illustrating eigenvector analysis .....	44
Figure 1.18 – Method used to analyse best-fit statistical distributions .....	46
Figure 1.19 – Population density functions .....	49
Figure 1.20 – Population distribution plots .....	50
Figure 1.21 – Illustration of the box-counting technique .....	52

<b>Figure 1.22</b> – Truncation and censoring in power-law distributions .....	<b>53</b>
<b>Figure 1.23</b> – Schematic diagrams illustrating the 1-dimensional sampling technique ..	<b>57</b>
<b>Figure 2.1</b> – Simplified map of the NW Highlands of Scotland .....	<b>63</b>
<b>Figure 2.2</b> – The distribution of the Lewisian Gneiss Complex across NW Scotland .....	<b>64</b>
<b>Figure 2.3</b> – Reconstruction of the North Atlantic Proterozoic belts .....	<b>65</b>
<b>Figure 2.4</b> – Sketch map of the LGC with the locations of the proposed terranes .....	<b>69</b>
<b>Figure 2.5</b> – Schematic block diagrams of brittle and ductile deformation in the LGC ...	<b>73</b>
<b>Figure 2.6</b> – Schematic models of shear zone networks and kinematics across the LGC	<b>79</b>
<b>Figure 2.7</b> – Geological map of the Northern Highlands including sediment .....	<b>82</b>
<b>Figure 2.8</b> – Restored section of the Stoer Group .....	<b>83</b>
<b>Figure 2.9</b> – Restored section of the Torridon Group .....	<b>86</b>
<b>Figure 2.10</b> – Illustrations of the Cambro-Ordovician succession .....	<b>88</b>
<b>Figure 2.11</b> – Map of Triassic sandstone locations within NW Scotland .....	<b>91</b>
<b>Figure 2.12</b> – Schematic cross-section of basement elevated in Mesozoic faults .....	<b>92</b>
<b>Figure 2.13</b> – The location and structure of the Clair Field .....	<b>95</b>
<b>Figure 2.14</b> – Schematic block diagram of the Clair Field basement structure .....	<b>95</b>
<b>Figure 2.15</b> – Clair Field outline including the location of basement wells .....	<b>98</b>
<b>Figure 2.16</b> – Map of the Faroe-Shetland Basin .....	<b>100</b>
<b>Figure 2.17</b> – Location of dated basement wells on the Rona Ridge .....	<b>102</b>
<b>Figure 2.18</b> – Location, stratigraphy and provenance of Devonian sediments .....	<b>104</b>
<b>Figure 2.19</b> – Tectonic reconstruction of the Palaeocene/Eocene N Atlantic .....	<b>106</b>
<b>Figure 2.20</b> – Hydrocarbon charge model for the Foinaven area .....	<b>107</b>
<b>Figure 3.1</b> – Schematic map of the three-fold classic subdivision of the mainland	
Lewisian .....	<b>113</b>
<b>Figure 3.2</b> – Maps illustrating the extent of the regional datasets .....	<b>115</b>
<b>Figure 3.3</b> – Schematic representation of the digital surface and terrane models .....	<b>116</b>
<b>Figure 3.4</b> – Examples of NEXTMap® surface analysis maps .....	<b>118</b>
<b>Figure 3.5</b> – Map of the mainland Lewisian fault lineaments .....	<b>119</b>
<b>Figure 3.6</b> – Map of fault lineaments in the mainland Lewisian and rose plots .....	<b>122</b>
<b>Figure 3.7</b> – Fault lineaments separated into their respective azimuth groups .....	<b>124</b>
<b>Figure 3.8</b> – Fault lineament distributions across the mainland Lewisian areas .....	<b>125</b>

<b>Figure 3.9</b> – Length density maps for the mainland Lewisian .....	<b>128</b>
<b>Figure 3.10</b> – Population distribution plots from pseudo-well analysis .....	<b>132</b>
<b>Figure 3.11</b> – Population distribution plots for the low resolution datasets .....	<b>137</b>
<b>Figure 3.12</b> – Density maps of lineament connectivity .....	<b>142</b>
<b>Figure 3.13</b> – Population distribution plots for individual lineament trends .....	<b>144</b>
<b>Figure 3.14</b> – Map of outcrop locations within the mainland LGC .....	<b>148</b>
<b>Figure 3.15</b> – Summary map of the Canisp Shear Zone .....	<b>151</b>
<b>Figure 3.16</b> – Stereonets showing foliation orientations from the Assynt Terrane .....	<b>153</b>
<b>Figure 3.17</b> – Diagrammatic cross-section of the Canisp Shear Zone .....	<b>154</b>
<b>Figure 3.18</b> – Annotated photograph showing Inverian deformation .....	<b>156</b>
<b>Figure 3.19</b> – Photographs of the lithologies present within the Rhiconich Terrane ....	<b>159</b>
<b>Figure 3.20</b> – Stereonets showing foliation orientations from the Rhiconich Terrane .	<b>161</b>
<b>Figure 3.21</b> – Details of the Rispond Shear Zone (map and outcrop photograph) .....	<b>163</b>
<b>Figure 3.22</b> – Examples of the three main fault sets present within the mainland LGC	<b>167</b>
<b>Figure 3.23</b> – Stereonets showing slickenline orientations from the mainland LGC ....	<b>169</b>
<b>Figure 3.24</b> - Examples of Stoer Group age fractures .....	<b>171</b>
<b>Figure 3.25</b> – Stereonets of fracture orientations within the Assynt Terrane .....	<b>177</b>
<b>Figure 3.26</b> - Stereonets of fracture orientations within the Rhiconich Terrane .....	<b>178</b>
<b>Figure 3.27</b> – Plots showing the relationship between C and K values .....	<b>180</b>
<b>Figure 3.28</b> – Photograph of a fracture surface from Kinlochbervie .....	<b>183</b>
<b>Figure 3.29</b> – Population distribution plots from outcrops in the Assynt Terrane .....	<b>186</b>
<b>Figure 3.30</b> - Population distribution plots from outcrops in the Rhiconich Terrane ....	<b>187</b>
<b>Figure 3.31</b> – Plot showing aperture versus length .....	<b>192</b>
<b>Figure 3.32</b> – 2-dimensional photo-mosaics showing fracture connectivity .....	<b>194</b>
<b>Figure 3.33</b> – Diagrams representing stress/strain and fracture development relationships .....	<b>197</b>
 <b>Figure 4.1</b> – Map of the Clair Field showing the main development areas .....	 <b>206</b>
<b>Figure 4.2</b> – Top basement seismic attribute maps for the Clair basement .....	<b>209</b>
<b>Figure 4.3</b> – Map of the Clair basement horizon showing all interpreted fault lineaments .....	<b>213</b>
<b>Figure 4.4</b> – Rose plot of the interpreted Clair basement fault lineaments .....	<b>215</b>
<b>Figure 4.5</b> – Top basement horizon coherence maps with fault lineaments .....	<b>216</b>

<b>Figure 4.6</b> – Length density maps for the Clair basement top horizon .....	<b>217</b>
<b>Figure 4.7</b> – Fault lineament interpretations for Clair sedimentary cover sediments ..	<b>220</b>
<b>Figure 4.8</b> – Horizon topography maps for each of the Clair Field horizons .....	<b>221</b>
<b>Figure 4.9</b> – Population distribution plots for pseudo-wells through the Clair basement seismic .....	<b>224</b>
<b>Figure 4.10</b> – Population distribution plots for individual fault lineament trends .....	<b>228</b>
<b>Figure 4.11</b> – Density maps of lineament connectivity from the Clair basement .....	<b>231</b>
<b>Figure 4.12</b> - Generalised lithological logs for vertical wells in the Clair basement .....	<b>236</b>
<b>Figure 4.13</b> – Generalised lithological log for well 206/7a-2 .....	<b>237</b>
 <b>Figure 4.14</b> – Outline of the Clair basement including the location of basement wells .....	<b>238</b>
<b>Figure 4.15</b> – Photographs of basement core samples from well 206/7a-2 .....	<b>240</b>
<b>Figure 4.16</b> – Fracture log for well 206/7a-2 .....	<b>249</b>
<b>Figure 4.17</b> – Examples of fracture modes seen within the Clair basement .....	<b>252</b>
<b>Figure 4.18</b> – Core sections of Basal Conglomerate providing evidence of vein age ....	<b>253</b>
<b>Figure 4.19</b> – Photograph of well 206/7a-2 highlighting the degraded nature of the core .....	<b>256</b>
<b>Figure 4.20</b> – Plot of Re-Os ages pyrite and bitumen ages from Clair basement core samples .....	<b>259</b>
<b>Figure 4.21</b> – Rose plots of fracture orientations from Clair basement core .....	<b>261</b>
<b>Figure 4.22</b> – Population distribution plots for all fractures sampled in the Clair basement .....	<b>264</b>
<b>Figure 4.23</b> – Population distribution plots for open fractures sampled in the Clair basement .....	<b>265</b>
<b>Figure 4.24</b> – Population distribution plots for individual spot cores from well 206/7a-2 .....	<b>266</b>
<b>Figure 4.25</b> – Population distribution plots for different mineralisation types .....	<b>269</b>
<b>Figure 4.26</b> – Plot of distance along core versus fracture density .....	<b>274</b>
<b>Figure 4.27</b> – Plot showing aperture versus length for Clair basement fractures .....	<b>275</b>
 <b>Figure 5.1</b> – Annotated laser scanner and illustration of how the scanner works .....	<b>287</b>
<b>Figure 5.2</b> – Examples of ‘cleaned’ TLS point clouds .....	<b>288</b>



<b>Figure 5.3 – Location map of the TLS outcrops .....</b>	<b>290</b>
<b>Figure 5.4 – Images of the TLS datasets collected from the three key outcrops .....</b>	<b>291</b>
<b>Figure 5.5 – Aerial photographs of the local areas surrounding the key outcrops .....</b>	<b>293</b>
<b>Figure 5.6 – Images outlining the process of interpreting fracture planes .....</b>	<b>297</b>
<b>Figure 5.7 – Outcrop surfaces in Paradigm GoCad 2009.2 including pseudo-wells .....</b>	<b>299</b>
<b>Figure 5.8 – 3D model fracture presence analysis workflow .....</b>	<b>300</b>
<b>Figure 5.9 – Fracture intersection analysis workflow using TLS datasets .....</b>	<b>302</b>
<b>Figure 5.10 – Resulting fracture network from Alltan na Bradhan .....</b>	<b>304</b>
<b>Figure 5.11 – Resulting fracture network from Kinlochbervie .....</b>	<b>305</b>
<b>Figure 5.12 – Resulting fracture network from Caolas Cumhann .....</b>	<b>306</b>
<b>Figure 5.13 – Population distribution plots from pseudo-wells through the TLS datasets .....</b>	<b>309</b>
<b>Figure 5.14 – 2-dimensional fracture presence models for the TLS outcrop at Alltan na Bradhan .....</b>	<b>315</b>
<b>Figure 5.15 - 2-dimensional fracture presence models for the TLS outcrop at Kinlochbervie .....</b>	<b>316</b>
<b>Figure 5.16 - 2-dimensional fracture presence models for the TLS outcrop at Caolas Cumhann .....</b>	<b>317</b>
<b>Figure 5.17 – Plot showing the variation in 2D fractal dimension across the three key outcrops .....</b>	<b>321</b>
<b>Figure 5.18 – Plot showing the estimation of damage zone width from Kinlochbervie .....</b>	<b>323</b>
<b>Figure 5.19 – Fracture intersection modelling from Alltan na Bradhan .....</b>	<b>326</b>
<b>Figure 5.20 – Fracture intersection modelling from Kinlochbervie .....</b>	<b>327</b>
<b>Figure 5.21 – Fracture intersection modelling from Caolas Cumhann .....</b>	<b>328</b>
<b>Figure 5.22 – Fracture geometries and conceptual fracture model .....</b>	<b>334</b>
<b>Figure 6.1 – Rose plots and stereonet from the Canisp Shear Zone .....</b>	<b>342</b>
<b>Figure 6.2 - Rose plots and stereonet from Kinlochbervie .....</b>	<b>343</b>
<b>Figure 6.3 – Rose plots and stereonet from Caolas Cumhann .....</b>	<b>344</b>
<b>Figure 6.4 – Rose plot of fracture data from north of Caolas Cumhann .....</b>	<b>346</b>
<b>Figure 6.5 – Power-law population distribution plot of all scales of fracture spacing data from the Canisp Shear Zone .....</b>	<b>348</b>

<b>Figure 6.6</b> – Power-law population distribution plot of all scales of fracture spacing data from Kinlochbervie .....	<b>349</b>
<b>Figure 6.7</b> – Power-law population distribution plot of all scales of fracture spacing data from Caolas Cumhann .....	<b>350</b>
<b>Figure 6.8</b> – Plot of fracture density versus CV value from mainland LGC datasets .....	<b>353</b>
<b>Figure 6.9</b> – Photographs of the mainland LGC and the Clair basement .....	<b>358</b>
<b>Figure 6.10</b> – Rose plots of regional fault lineament orientation data .....	<b>361</b>
<b>Figure 6.11</b> – Rose plots of fracture orientation data from outcrop and core .....	<b>362</b>
<b>Figure 6.12</b> – Power-law population distribution plot of spacing data from the Clair basement .....	<b>365</b>
<b>Figure 6.13</b> – Power-law population distribution plot of spacing data from regional onshore and offshore datasets .....	<b>367</b>
<b>Figure 6.14</b> – Exponential population distribution plot of spacing data from regional onshore and offshore datasets .....	<b>368</b>
<b>Figure 6.15</b> – Power-law population distribution plot of onshore meso- and macro-scale datasets and Clair basement macro-scale datasets .....	<b>372</b>
<b>Figure 6.16</b> – Plot of fracture density versus CV value for all onshore and offshore datasets .....	<b>375</b>
 <b>Figure 7.1</b> – A group of oil industry professionals on a Durham University-led fieldtrip	

## List of Tables

---

<b>Table 1.1</b> – Illustrates the textural classification of fault rocks .....	<b>17</b>
<b>Table 1.2</b> – Aperture width classification .....	<b>36</b>
 <b>Table 2.1</b> – Historical division of the LGC tectono-metamorphic stratigraphy .....	<b>67</b>
<b>Table 2.2</b> – Summarising the characteristics and protolith ages of the mainland LGC terranes .....	<b>70</b>
<b>Table 2.3</b> – Summary of the mainland Lewisian structural chronology .....	<b>72</b>
<b>Table 2.4</b> – Generalised summary of the geological evolution of northern Britain .....	<b>81</b>
<b>Table 2.5</b> – Stratigraphic subdivisions and reservoir properties of the Clair Group .....	<b>107</b>

<b>Table 3.1 – Power-law spatial attributes of faults from pseudo-wells in the mainland</b>	
LGC .....	<b>133</b>
<b>Table 3.2 – Exponential spatial attributes of faults from pseudo-wells in the mainland</b>	
LGC .....	<b>135</b>
<b>Table 3.3 – Low resolution spatial attributes of faults from pseudo-wells in the mainland</b>	
LGC .....	<b>138</b>
<b>Table 3.4 – C and K values for fractures and foliations from key outcrops across the</b>	
mainland LGC .....	<b>179</b>
<b>Table 3.5 – Spacing attributes measured and calculated from all 1-dimensional line</b>	
samples in Assynt Terrane outcrops .....	<b>188</b>
<b>Table 3.6 – Spacing attributes measured and calculated from all 1-dimensional line</b>	
samples in Rhiconich Terrane outcrops .....	<b>189</b>
 <b>Table 4.1 – Power-law spatial attributes of faults from pseudo-wells created in the Clair</b>	
top basement seismic horizon .....	<b>225</b>
<b>Table 4.2 – Exponential spatial attributes of faults from pseudo-wells created in the Clair</b>	
top basement seismic horizon .....	<b>226</b>
<b>Table 4.3 – Spacing attributes for all fractures measured in the Clair basement .....</b>	<b>267</b>
<b>Table 4.4 – Spacing attributes for fractures measured from 206/7a-2 .....</b>	<b>270</b>
 <b>Table 5.1 – Fracture spatial attributes from pseudo-wells across TLS models .....</b>	<b>310</b>
<b>Table 5.2 – 3D fractal dimensions for fracture presence models .....</b>	<b>320</b>
<b>Table 5.3 – 3D fractal dimensions for fracture intersection models .....</b>	<b>329</b>
 <b>Table 6.1 – Fracture spatial attributes for mainland LGC datasets .....</b>	<b>351</b>
<b>Table 6.2 – Regional lineament spatial attributes for onshore and offshore datasets .</b>	<b>369</b>
<b>Table 6.3 – Fracture spatial attributes for Clair basement and mainland LGC outcrop</b>	
samples .....	<b>374</b>
 <b>Table 7.1 - Comparing and contrasting the mainland LGC and the Clair basement .....</b>	<b>38</b>

## Glossary of Abbreviations and Acronyms

---

The following abbreviations and acronyms are used throughout this thesis:

<b>1-D</b>	<b>1-dimensional</b>
<b>2-D</b>	<b>2-dimensional</b>
<b>2.5D</b>	<b>2.5-dimensional</b>
<b>3-D</b>	<b>3-dimensional</b>
<b>BOPD</b>	<b>Barrels of Oil Per Day</b>
<b>CSZ</b>	<b>Canisp Shear Zone</b>
<b>FSB</b>	<b>Faroe-Shetland Basin</b>
<b>GPS</b>	<b>Global Positioning System</b>
<b>LGC</b>	<b>Lewisian Gneiss Complex</b>
<b>LiDAR</b>	<b>Light Detection And Ranging</b>
<b>LMG</b>	<b>Loch Maree Group</b>
<b>LSZ</b>	<b>Laxford Shear Zone</b>
<b>RSZ</b>	<b>Rispond Shear Zone</b>
<b>OBMI</b>	<b>Oil Based MicroImager</b>
<b>OOIP</b>	<b>Original Oil In Place</b>
<b>STB</b>	<b>Stock Tank Barrels</b>
<b>TIMS</b>	<b>Thermal Ionization Mass Spectrometry</b>
<b>TLS</b>	<b>Terrestrial Laser Scan</b>
<b>TTG</b>	<b>Tonalite-Trondjemite-Granodiorite</b>
<b>UBI</b>	<b>Ultrasonic Borehole Imager</b>
<b>UKCS</b>	<b>United Kingdom Continental Shelf</b>

## Acknowledgements

---

Firstly, I would like to say thank you my supervisors, Bob Holdsworth and Ken McCaffrey in Durham, Richard Jones from Geospatial Research Limited and Maarten Krabbendam from the BGS. Their support, advice and encouragement has kept me going and made this project a positive experience. I particularly want to thank my industry supervisor, Andy Conway, from ConocoPhillips (U.K.) Ltd. His invaluable guidance and oil industry insight has helped me develop my understanding of the industry perspective and has ultimately set me off on the path to a lifetime career. A special mention also to the Clair Joint Venture their financial support and willingness to listen to new ideas is what made this project possible.

I would also like to thank Catherine Sherwin and Will Dyott who were fantastic field assistants and made line sampling almost bearable. Their company and culinary skills made fieldwork far more enjoyable and having their input really helped me to focus on what I needed to achieve.

Thanks also to all my comrades in the department your banter and biscuit provisions have made my time at Durham most enjoyable. This particularly applies to Jon, Steve and Pete who have been with me from the start and have provided endless hours of vibrant discussions about the best way to bleed a radiator. I also wish to thank Karen, Paula, Gary and Dave and the rest of the administrative staff; your help has ensured the smooth running of my project.

Finally, and most importantly, I want to thank my friends and family without their support I would not have gotten this far. This is especially for true for Chris who has stuck with me through times of doubt and the occasional temper tantrum. He is not only my husband, he is my rock and has kept me grounded, making the last four years the most enjoyable of my whole life.

## **Declaration**

---

No part of this thesis has previously been submitted for a degree at this or any other university. The work described in this thesis is entirely that of the author, except where reference is made to previously published or unpublished work.

Jennifer C. Pless

Durham University

Department of Earth Sciences

April 2012

## **Copyright © by Jennifer C. Pless**

The copyright of this thesis rests with the author. No quotation or data from it should be published without the author's prior consent and any information derived from it should be acknowledged.

## **Chapter 1 – Introduction and overview of fracture network characteristics**

### **1.1 – Rationale for the project**

The Clair field is an oil and gas-bearing hydrocarbon field where the key role of fractures cutting basement gneisses is becoming increasingly recognised as the field develops. Well tests from the basement and from the overlying sediments suggest that there must be fluid pathways through the basement (Falt et al., 1992, Coney et al., 1993), connecting sedimentary packages across the main ridge structure (see *Chapter 2* for a structural overview of the Clair Field) and that fracture systems within the basement may, in addition, provide significant storage space for hydrocarbons.

Limited information can be gained from the well and seismic data from the Clair field because of the scarcity of basement-penetrating wells and core, together with the poor seismic imaging within the basement rocks (only the top basement horizon is reliably imaged). So in order to gain a better understanding of the fracture networks in 3-dimensions an onshore analogue needs to be utilised. The Lewisian Gneiss Complex (LGC) of NW mainland Scotland is being used as an analogue because of its geographic proximity to the Rona Ridge (where the Clair field is located), together with its apparent similarities in age, metamorphic grade and lithology based on comparisons with limited core samples taken from the Clair basement.

Using fracture analysis of 1-dimensional line sample techniques (Johnston et al., 1994) across basement well samples and outcrops in conjunction with 2-dimensional mapping of fault lineaments from seismic and onshore regional datasets it is possible to begin to assess the validity of the mainland LGC as a suitable analogue for the Clair basement and its associated fracture networks. Further, more detailed, analysis of specific structural settings within the mainland LGC has also been carried out using terrestrial laser scan datasets of three key outcrops. This provides deterministic fracture parameters that can be directly implemented into current Clair basement models to reduce the uncertainties created by the current stochastic process (Bergbauer and King, 2009) that is used to understand the basement fracture networks.

This project aims to answer a number of questions and fulfil a selection of objectives that explore the fracture network characteristics within the mainland LGC and

the Clair basement and to assess the validity of using the mainland LGC as an onshore analogue for the Clair basement. The four main scientific aims of this project and their objectives are outlined below.

(1) *What is the offshore Clair Field basement?*

The Clair field basement is known, from core samples, to be of an orthogneiss origin (Falt et al., 1992) with its closest affinities seemingly lying in the Lewisian Gneiss Complex (LGC) that outcrops across the NW Highlands of Scotland. It is accepted that the Scottish Highlands are a patchwork of different metamorphic terranes (Lewisian, Moine, Dalradian, etc.), with the Lewisian itself being potentially separated into several different autochthonous and allochthonous terranes which differ in lithology, metamorphic grade and age (e.g. Kinny and Friend, 1997, Friend et al., 2001, Kinny et al., 2005).

One of the main questions that this project will attempt to address is which Lewisian terrane is the most likely correlative of the Clair basement? To answer this question a combination of fieldwork, core logging and thin section analysis have been utilised to attempt to place the Clair basement within the terrane framework of the Scottish Highlands. Primary focus has been on the Assynt and Rhiconich Terranes within the Central and Northern regions of the mainland LGC (*Chapter 3*). These two terranes have been selected as they lie close to the Clair field and show significant lithological similarities. The various lithologies and fracture network parameters present within these two key terranes have been compared in detail to basement core materials from the Clair Field (*Chapter 4*) in order to establish the most appropriate onshore analogue(s) for the subsurface (Clair basement) fracture systems.



*(2) What are geological characteristics and attributes of the fracture systems developed in the onshore mainland Lewisian Gneiss Complex?*

Previous work has suggested that there are at least three main fracture sets, of varying kinematics and age, present within the mainland LGC (Beacom, 1999, Roberts and Holdsworth, 1999, Beacom et al., 2001 and references therein). This project aims to characterise these fracture sets, both qualitatively and quantitatively, using a variety of fieldwork- and computer-based analyses that provide the descriptive and statistical attributes needed to fully analyse fracture network characteristics across the mainland LGC.

Importantly, this project explores the scalability of the fractures sets; are the observed fracture patterns scale-invariant over a wide range of length scales (kilometres to less than a metre)? Are the fracture networks scale-invariant across different dimensions? To answer these questions, the fracture networks exposed in the mainland LGC have been mapped and quantified at several scales (regional, outcrop and thin section) and in different dimensions; 1-dimensional sampling of outcrop, well samples and regional datasets and 3-dimensional (or 2.5D) of terrestrial laser scan outcrop models.

Where possible, an equivalent set of analyses have been conducted using the available data from the Clair basement (seismic reflection data and core samples). By understanding in what way the fracture networks in the Clair basement are scalable and by comparing and contrasting these attributes to the mainland LGC, it potentially allows an assessment of the validity of the mainland LGC as an onshore analogue to be made.

*(3) What are the dominant controls on these fracture patterns?*

Previous work has invoked a range of possible controls that may affect the fracture network development in the mainland LGC (e.g. Beacom et al., 2001). These include lithology, metamorphic grade, intensity of pre-existing fabrics, proximity to major shear zones and proximity to major faults. This study aims to develop upon these previously recognised controls and in particular focus on the variations of fracture

network attributes (such as spacing distributions, density and connectivity) between different key structural settings within the mainland LGC. An important sub-task here is to establish if the fracture patterns vary between the Assynt and Rhiconich terranes, and if so, how and why?

To understand the fracture controls a combination of digital regional mapping (using NEXTMap® DEMs and aerial photographs), detailed field mapping and statistical analysis has been utilised. In addition to this, high-resolution terrestrial laser scanning (ground-based LiDAR) of key mainland outcrops has been utilised to create detailed 3-dimensional deterministic fracture network models. Three outcrops are used within the mainland LGC that have been determined to represent structural settings that have a profound effect on the characteristics on the fracture network within both the Assynt and Rhiconich terranes. The subsequent 3-dimensional virtual outcrop models have been used to interpret all of the viable fractures (see *Chapter 5*) at each location to create deterministic fracture network models that provide quantitative fracture attribute values that can be directly implemented into any ongoing Clair basement modelling.

*(4) How can the mainland Lewisian Gneiss Complex be best used as an onshore analogue for the Clair basement?*

By conducting similar regional and outcrop scale analyses with the available Clair basement datasets (seismic, core and image log fracture datasets) it is possible to compare and contrast the relatively sparse (and low resolution) age, orientation and spatial attributes of fracture networks from the Clair basement with the much more detailed fracture network analyses from the mainland LGC. Understanding how the fracture network in the mainland LGC varies due to changing structural settings (particularly proximity to shear zones and major faults), and understanding the likelihood of these structural settings within the Clair basement allows deterministic basement modelling of the Clair basement to be implemented. This ultimately improves the ability to understand the potential fluid storage capacity within the Clair basement and which areas within the basement are likely to provide the best pathways for fluid transport.

Although the above questions provide assistance towards the understanding of the Clair Field basement fracture network and the fracture networks in the mainland LGC it is also important to consider how these issues are applicable in a wider geological context. Crystalline basement rocks are becoming of increasing interest to commercial oil companies as other existing and new hydrocarbon fields are developed. For example, in Vietnam, fractured granite basement rocks of the Bach Ho (White Tiger) field in the Cuu Long basin produces almost 250,000 bopd (Du Hung and Van, 2003) and in 1984, the Zeit Bay field in the Gulf of Suez was producing 80,000 bopd (Salah and Alsharhan, 1998) from fractured Precambrian igneous and metamorphic basement rocks. Due to the crystalline nature of the basement rocks in these and other reservoir examples, primary porosity is almost non-existent so all the porosity and permeability is secondary and originates from fractures. Reservoirs containing fractured crystalline rocks are also of interest for their fluid transport properties and for the storage of radioactive materials and other wastes such as carbon dioxide (e.g. Herzog, 2001, Dockrill and Shipton, 2010, Nguyen and Le, 2010).

All of the aims and objectives described above will be explored in detail throughout this thesis. The outline of each thesis chapter is given in the following section.

## 1.2 – Outline of the Thesis

- **Chapter 1** – The processes and products of fault zone deformation in the lithosphere are discussed, together with key fault and fracture attributes. Fracture population analysis methods are also reviewed.
- **Chapter 2** – Introduces the regional geological setting of the Lewisian Gneiss Complex (and associated geological units) in the northwest Scottish Highlands and of the Clair Field in the Faroe-Shetland Basin by means of a literature review.
- **Chapter 3** – Explores the lithology, fault rock characteristics and fracture network characteristics within the onshore, Scottish mainland Lewisian Gneiss Complex from regional and fieldwork datasets gathered across the Assynt and Rhiconich Terranes. This chapter includes a synthesis of the similarities and differences between the regional and outcrop scale datasets.
- **Chapter 4** – Investigates the lithology, fault rock characteristics and network characteristics from seismic and core sample datasets from the offshore Clair Field basement using comparable techniques to the onshore study. This offshore study also includes a synthesis of the variations in fracture network characteristics between the regional- and core sample-scale datasets.
- **Chapter 5** – Presents a deterministic fracture network characterisation from key mainland Lewisian outcrops using interpretation from terrestrial laser scan datasets. This chapter introduces new techniques for comparing and contrasting fracture network attributes between outcrops in different structural settings.
- **Chapter 6** – Synthesises and discusses first the comparison between the fracture network characteristics presented in *Chapter 5*, and second between the mainland Lewisian and the Clair Field basement.
- **Chapter 7** - This chapter re-explores the aims of the project and discusses the extent to which the present work has been able to provide answers to the previously described questions. Recommendations for further work will also be outlined in this chapter.

### 1.3 – Introduction to deformation and reactivation processes in continental lithosphere

#### 1.3.1 Fault Zone Structure

Faults that form in the lithosphere typically comprise zones that consist of three main components – host rock, damage zone and core - (*Figure 1.1*) that represent increasing deformation towards the main fault plane (Sibson, 1977, Chester and Logan, 1987, Forster and Evans, 1991, Byerlee, 1993, Caine et al., 1996, Gudmundsson et al., 2009, Wibberley et al., 2008 and references therein). The complexity and structure of these fault domains can have important implications for fluid flow (Caine et al., 1996). Variations in fault zone architectures result in fault zones that are either barriers or conduits to fluid flow (*Figure 1.2a & b*). It is therefore important to understand the characteristic fault domain configuration of representative faults within the area of study.

##### 1.3.1.1 – Fault Core

The fault core (*Figure 1.1*) is defined as the portion of the fault zone that accommodates the largest displacements (Caine et al., 1996). It is typically a narrow zone (<10m) of deformation that can exhibit single slip surfaces (Caine et al., 1996), clay-rich gouges (Anderson et al., 1983), brecciated zones, zones of geochemical alteration (Sibson, 1977), mineral veins or zones of cataclasite (Chester and Logan, 1987) (*Figure 1.1b*). Typically fault cores act as barriers to fluid flow across and along the fault zone, due to the likely presence of fine-grained clay-rich gouge material, but in the absence of this fine-grained material, fault cores can be good conduits, i.e. permeability in the fault core is likely to be controlled by the grain-size and mineralogy of the fault rocks (Caine et al., 1996) (*Figure 1.2*).

### 1.3.1.2 – Fault damage zone

Many authors describe fault damage zones as the deformed rock volume surrounding the master fault plane, or fault core (e.g. Chester and Logan, 1987, Caine et al., 1996, Knott et al., 1996) and this definition is used throughout this thesis. As outlined by Caine et al. (1996) fault damage zones are the fault components that contain a network of subsidiary structures that bound the fault core (*Figure 1.1b*) and may enhance permeability relative to the fault core (and the undamaged protolith) (*Figure 1.2*). Structures found within fault damage zones may include small faults, veins, fractures, cleavage and folds that increase the anisotropy in the fault zone (Bruhn et al., 1990, Caine et al., 1996). Deformation within fault damage zones is a result of fault tip propagation and strain during slip along the master fault (Knott et al., 1996).

The geometry and size of damage zones surrounding master fault planes is likely to have important implications for the barrier/conduit potential of individual fault zones (*Figure 1.2*). Fracture density in the fault core is normally significantly lower than the fracture density in the damage zone (Andersson et al., 1991, Chester et al., 1993, Caine et al., 1996). It is therefore likely that permeability within the fault damage zone is controlled by the hydraulic properties of the structures within it (Caine et al., 1996). The width of fault damage zones is dependent on a number of variables that include lithology, fault kinematics and fault reactivation (Sleight, 2001). Within the context of this project, fault reactivation is likely to be the most important as it has been observed that wide damage zones are a potential indication of multiple periods of slip and the overprinting of successive deformation events (Caine et al., 1996).

DEPARTMENT OF EARTH SCIENCES, DURHAM UNIVERSITY

**Characterising fractured basement using the  
Lewisian Gneiss Complex, NW Scotland:  
Implications for fracture systems in the Clair Field  
basement**

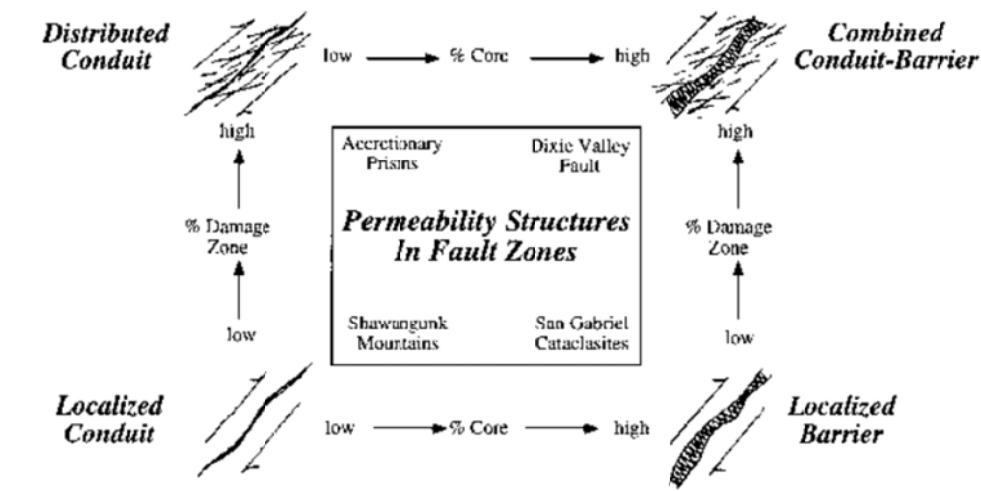
---



A thesis submitted to Durham University for the degree of  
Doctor of Philosophy in the Faculty of Science

**Jennifer Claire Pless**

**201**



Permeability Structure	Architectural Style	Fault Core	Damage Zone
<b>Localised Conduit</b>	Localised slip along single surfaces, or along discretely segmented planes	Poorly developed or absent	Poorly developed or absent
<b>Distributed Conduit</b>	Distributed slip accommodated along distributed surfaces and fractures	Poorly developed as narrow discrete, discontinuous bands, or absent	Well developed, discrete slip surfaces and fracture network
<b>Localised Barrier</b>	Localised slip accommodated within cataclastic zone	Well developed fault core cataclasites	Poorly developed, or absent
<b>Combined Conduit-barrier</b>	Deformation accommodated within localised cataclastic zone and distributed zone of subsidiary structures	Well developed fault core cataclasites	Well developed, discrete slip surfaces and fracture network

**Figure 1.2:** Are faults barriers or conduits to fluid flow? **(a)** Conceptual scheme for fault-related fluid flow showing four end members of fault architecture **(b)** Fault zone architectural styles and permeability structures (after Caine et al., 1996).



### 1.3.1.3 - Protolith

The fault core and damage zone are surrounded by relatively undamaged rock known as the protolith (Caine et al., 1996) (*Figure 1.1*). This protolith is the region of the host rock where fault-related permeability structures are absent (Caine et al., 1996) and any strain can be considered as ‘background deformation’ that has been produced by regional tectonic event(s). Most importantly, the fluid flow properties in the protolith are likely to be significantly reduced compared to the fault damage zone.

### 1.3.2 – Fault zone products

Deformation within fault zones can be separated into two main categories; brittle (frictional), which typically occurs near-surface and ductile (viscous) which normally occurs at depth (*Figure 1.3*). The depth of the transition zone between the frictional and viscous domains is dependent on a variety of parameters including temperature, lithology, pre-existing fabrics, fluid pressure and strain rate (e.g. Sibson, 1977). This thesis focuses primarily on the brittle deformation products associated with fault zones, which include; fractures (joints, shear fracture and faults), veins, cataclasites and pseudotachylites (frictional melting) (*Figure 1.3*). The definitions and formation processes of these fault zone products are described in the following sections.

#### 1.3.2.1 - Fractures

Fractures are defined as secondary structures (Davis and Reynolds, 1996) or as non-sedimentary mechanical discontinuities that represent a surface or zone of mechanical failure within a rock body. They can be defined by the origin of their causative forces, two of which (those that are relevant to this thesis) are described below.

*Tectonic Fractures* – are directly associated with a structural feature (e.g. a fault) and develop due to the application of surface or external forces related to a local tectonic event (Nelson, 1985 and references therein). This type of fracture is studied in detail within this thesis.

*Regional Fractures* – are unrelated to local tectonic events and develop over a large area with little change in orientation and no evidence of offset (Stearns and Friedman, 1972, Nelson, 1982). These faults are thought to have formed due to uplift (Aguilera, 1995), although other origins are possible. The lateral extent of

these fractures and the lack of fine-grained fault rock (due to there being no offset) means that these fractures can be conductive to fluid flow (Sleight, 2001). Fractures of this description are studied within this thesis, particularly within the mainland LGC.

The nature of fracture propagation displacements can be defined by three separate modes (mode I, II and III, *Figure 1.4*) which can occur independently or in combination with each other (Atkinson, 1987).

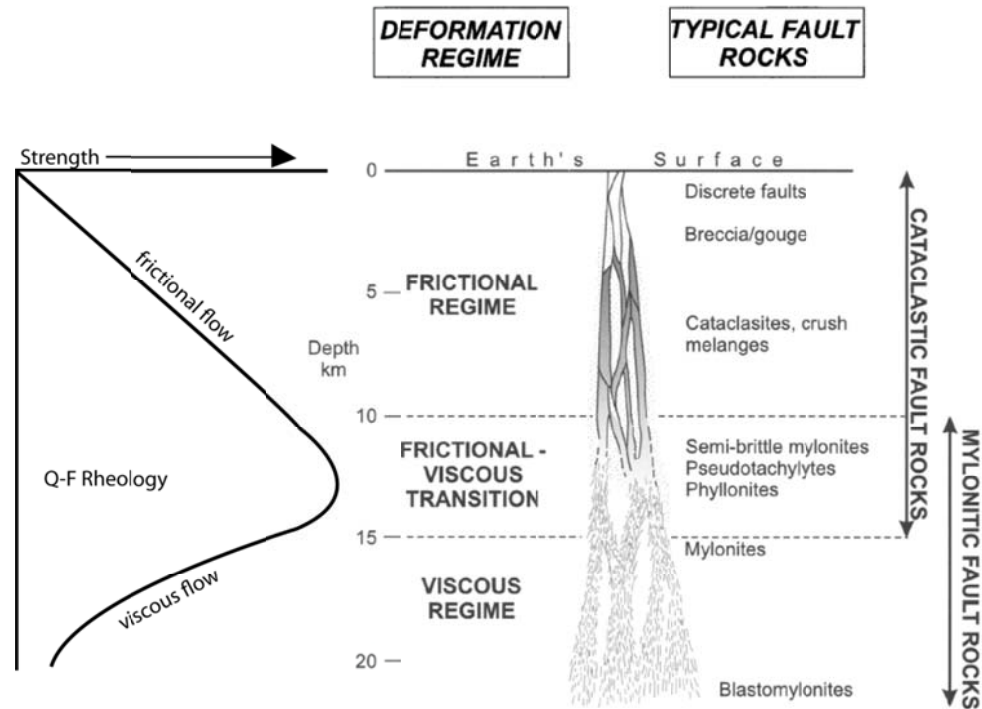
*Mode I fractures (Figure 1.4a)* are tensile with their relative motion perpendicular to the fracture walls (Twiss and Moores, 2007 and references therein). Most *joints* are mode I fractures as they exhibit small displacements perpendicular to their surfaces and no motion parallel to their surface. Mode I fractures occur in the mainland LGC and the Clair basement, although this motion is commonly over-written by later stages of shear or mixed-mode shearing.

*Mode II (Figure 1.4b) shear fractures* exhibit relative motion parallel to the fracture surface. In mode II fractures there is a sliding motion perpendicular to the propagating edge of the fracture (Twiss and Moores, 2007 and references therein).

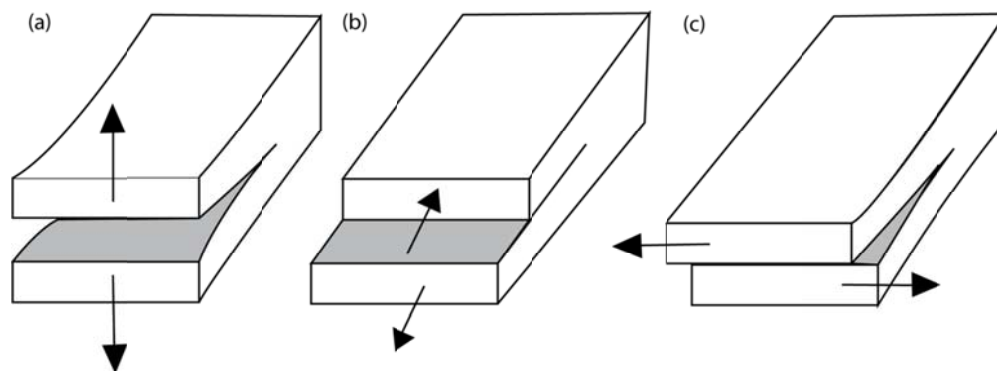
*Mode III (Figure 1.4c) shear fractures* are also shear fractures with relative motion parallel to the fracture surface. The sliding motion associated with these fractures occurs parallel to the propagating edge of the fracture (Twiss and Moores, 2007 and reference therein).

*Mixed mode shear fractures* exhibit motion both parallel and perpendicular to the fracture surface and experience oblique extension (Twiss and Moores, 2007 and references therein). Many of the fractures and faults studied within the mainland LGC and the Clair basement are mixed mode shear fractures.

Fractures which are represented by modes I or II or mixed-mode propagation and which exhibit large lateral extent and large displacements (meso-, macro- or mega-scale) are classed as faults. The deformed 'damage zone' surrounding faults normally contain examples of joints and/or shear fractures at a micro- and meso-scales.



**Figure 1.3:** Schematic illustration of the depth, fault rocks, deformation processes and strength profile along a vertical crustal-scale fault zone after Sibson (1977) and Holdsworth et al. (2001).



**Figure 1.4:** Schematic diagrams of the three fundamental modes of fracturing **(a)** Mode I, tensile, or opening mode. **(b)** Mode II, shear fracture. **(c)** Mode III, shear fracture. After Atkinson(1987).

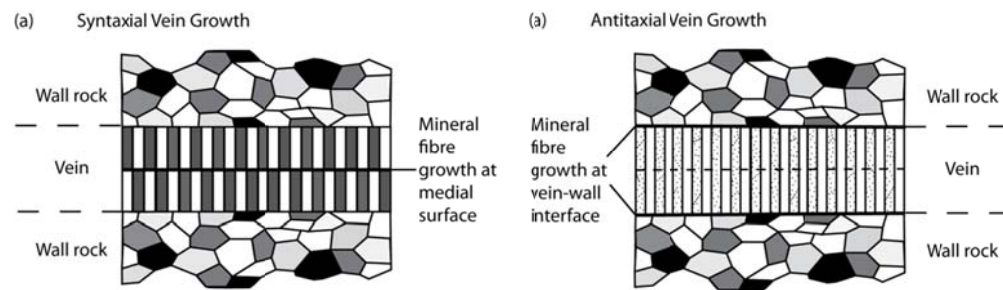
### 1.3.2.2 - Veins

Veins are defined as extension fractures that are filled with mineral deposits (Twiss and Moores, 2007) that precipitated from solution under favourable conditions of temperature and pressure (Davis and Reynolds, 1996). The mineral deposit may be massive or they may be composed of fibrous crystals that can be useful for interpreting the deformation kinematics associated with the opening of the vein (Twiss and Moores, 2007). Progressive growth of mineralisation in vein occurs in several distinct fashions. The two types of mineral growth seen within samples in this study are:

*Syntaxial (Figure 1.5a)* – In syntaxial veins (Durney and Ramsay, 1973, Bons, 2000), mineral growth occurs in or along the median plane (normally a thin fracture) where material is added by vein crystals on both sides of the growth plane. This means that the youngest material occurs in the centre of the vein, with the oldest mineralised at the vein edges. Syntaxial growth is normally found where the material in the vein is a constituent of the host rock.

*Antitaxial (Figure 1.5b)*– In antitaxial veins, mineral growth occurs along the vein walls, i.e. there are two growth surfaces (Durney and Ramsay, 1973, Bons, 2000). Mineral growth can occur simultaneously on each vein wall or it can be concentrated on only one wall of the vein. The key difference to syntaxial vein growth is that, in antitaxial veins, material in the centre of the vein is older than the material at the vein walls. Antitaxial growth normally occurs when the vein-forming material is not a constituent of the host rock.

It is also possible for composite vein growth to occur, where a combination of the above growth types can occur in the one vein. This normally occurs because there are two minerals growing at once: one is a constituent of the host rock and hence exhibits syntaxial growth, while the other is foreign to the host rock and therefore exhibits antitaxial growth (Bons, 2000).



**Figure 1.5:** Illustrations of mineral fibre growth in veins. **(a)** Syntaxial vein growth **(b)** Antitaxial vein growth. After Twiss and Moores(2007).

### 1.3.2.3 – Cataclasis

Classically, cataclasis is defined by Sibson (1977) as “the brittle fragmentation of mineral grains with rotation of grain fragments accompanied by frictional grain boundary sliding and dilatancy”. Cataclasis typically occurs in faults formed at depths less than 10 to 15 km and usually such fault rocks lack any internal planar or linear structure (Twiss and Moores, 2007). Fault rock products of cataclasis (*Table 1.1*) can be incohesive (breccia or gouge) or cohesive (cataclasites), all of which are described below.

*Fault Breccias* (*Table 1.1*) are incohesive (typically formed at 1 to 4 km depth, *Figure 1.3*) and they can be subdivided into the breccia series with megabreccia and breccia clasts being predominately rock fragments and microbreccia containing clasts that are primarily mineral grain fragments (Twiss and Moores, 2007). A breccia comprises > 30% visible clasts with the rest comprising a fine-grained matrix (Sibson, 1977). The clasts are typically angular fragments that originate in the wall rocks surrounding the fault.

*Fault Gouges* (*Table 1.1*) are also incohesive fault rocks representing a more deformed continuation of the breccia series to finer clast sizes (Twiss and Moores, 2007). They may also contain visible fragments but these comprise <30% of the total rock mass (Sibson, 1977). Fault gouge typically comprises clay-rich fine-grained material that acts as a barrier to fluid flow across the fault in which it occurs.

*Cataclasites* (*Table 1.1*) are generally cohesive brittle fault rocks that include a range of clasts sizes; from 30% fine-grained clasts to 100% matrix (e.g. Sibson, 1977, Twiss and Moores, 2007). They typically form in fault zones at depths between 4 and 10 km (*Figure 1.3*). Cataclasites form as a result of a brittle tectonic

reduction in grain size and differ from mylonites by the presence of a random fabric (Sibson, 1977).

Cataclastic rocks are present in fault zones that range from a few millimetres in thickness up to extensive zones that can be several kilometres thick. Typically the thicker the zone of cataclastic rocks and the smaller the grain size, the greater the amount of displacement that has occurred on the associated fault (Twiss and Moores, 2007).

#### 1.3.2.4 – Pseudotachylites

Pseudotachylites form as a result of frictional melting which typically occurs during earthquakes under dry conditions at moderate to high confining pressures, e.g. at depths of 10 to 15 km (*Figure 1.3*) (Twiss and Moores, 2007). Heating caused by friction slip along the active fault is thought to be sufficient enough to cause the rock to melt. The resulting product is generally a massive rock that is found in microbreccias and as dark veins of glassy or cryptocrystalline material with characteristic crystal sizes of < 1µm and/or glass (can be devitrified) (*Table 1.1*) cementing fractured material together (Twiss and Moores, 2007).

#### 1.3.2.5 – Mylonites

Cohesive fault rocks that form due to ductile deformation at depths exceeding 10 to 15 km are known as mylonites (*Table 1.1* & *Figure 1.3*) (e.g. Sibson, 1977, Passchier and Trouw, 2005, Twiss and Moores, 2007). Mylonites typically form at temperatures in excess of 250°C to 350°C as a result of the recrystallisation of mineral grains during crystal plastic deformation (e.g. Passchier and Trouw, 2005, Twiss and Moores, 2007). These foliated fault rocks form another series that was classified by Sibson (1977): protomylonites have 10-50% matrix, mylonites have 50-90% matrix and ultramylonites comprise >90% matrix (*Table 1.1*). Any coarser-grained relict grains are known as porphyroclasts. Blastomylonites continue the mylonite spectrum and are defined as a highly recrystallised mylonitic rock. The recrystallisation associated with blastomylonites may have accompanied or post-dated the ductile deformation mechanism (Passchier and Trouw, 2005). Phyllonites are formed by the same metamorphic recrystallisation as mylonites but are fine-grained and phyllosilicate rich (Passchier and Trouw, 2005).

		RANDOM - FABRIC		FOLIATED		
INCOHESIVE		FAULT BRECCIA (visible fragments >30% of rock mass)		?		
		FAULT GOUGE (visible fragments <30% of rock mass)		?		
COHESIVE	Glass/devitri fied glass	PSEUDOTACHYLITE		?		
	NATURE OF MATRIX  Tectonic reduction in grain size dominates grain growth by recrystallisation & neomineralisation	CRUSH BRECCIA FINE CRUSH BRECCIA CRUSH MICROBRECCIA		(fragments >0.5 cm) (0.1 cm < frags < 0.5 cm) fragments < 0.1 cm		0 - 10%
		PROTOCATACLASITE	Catclasite series	PROTOMYLONITE		10 - 50%
		CATACLASITE		MYLONITE	Mylonite series	50 - 90%
		ULTRACATACLASITE				ULTRAMYLONITE
		Grain growth pronounced		?		BLASTOMYLONITE

**Table 1.1:** Illustrates the textural classification of fault rocks. After Sibson (1977).

### 1.3.3 – Kinematic indicators

The following sections describe some of the most useful indicators for identifying sense of displacement along fractures, faults and shear zones (sinistral, dextral, normal, reverse or oblique). There are three principal ways that information on displacement direction of faults and fractures can be obtained, which are: observation of displacement markers, observation of the fault plane and by using the geometry and kinematics of secondary fault and fracture arrays (*Figure 1.6*).

#### 1.3.3.1 – Displacement markers

It is often possible to determine sense of movement along a fault by using structures or layers on either side of the fault plane. If two points that were initially coincident (e.g. a displaced dyke or foliation plane) can be identified, then the sense – and amount - of displacement can be established (*Figure 1.6a*).

#### 1.3.3.2 – Observation of fault planes

In many situations, it is possible to use structures that occur on the fault plane to determine the sense of displacement. These structures form as linear striations (slickenlines) on the fault/fracture plane, parallel to the direction of displacement (*Figure 1.6b*). Linear striations are identified in two different forms; slickenlines and slickenfibres (Price and Cosgrove, 1991). Slickenlines form as linear grooves on the surface of polished fault/fracture planes as a result of gouging by resistant materials during movement. Slickenfibres are mineral deposits (commonly quartz, calcite and hematite) that form as linear structures during movement along the fault/fracture plane. Both slickenline and slickenfibres occasionally have a stepped appearance that can be used to determine the sense of movement (*Figure 1.6b part C*) (Twiss and Moores, 2007), but more often other kinematic indicators have to be used in conjunction with these linear striations to establish whether a fault has left-lateral or right-lateral movement or is normal or reverse.



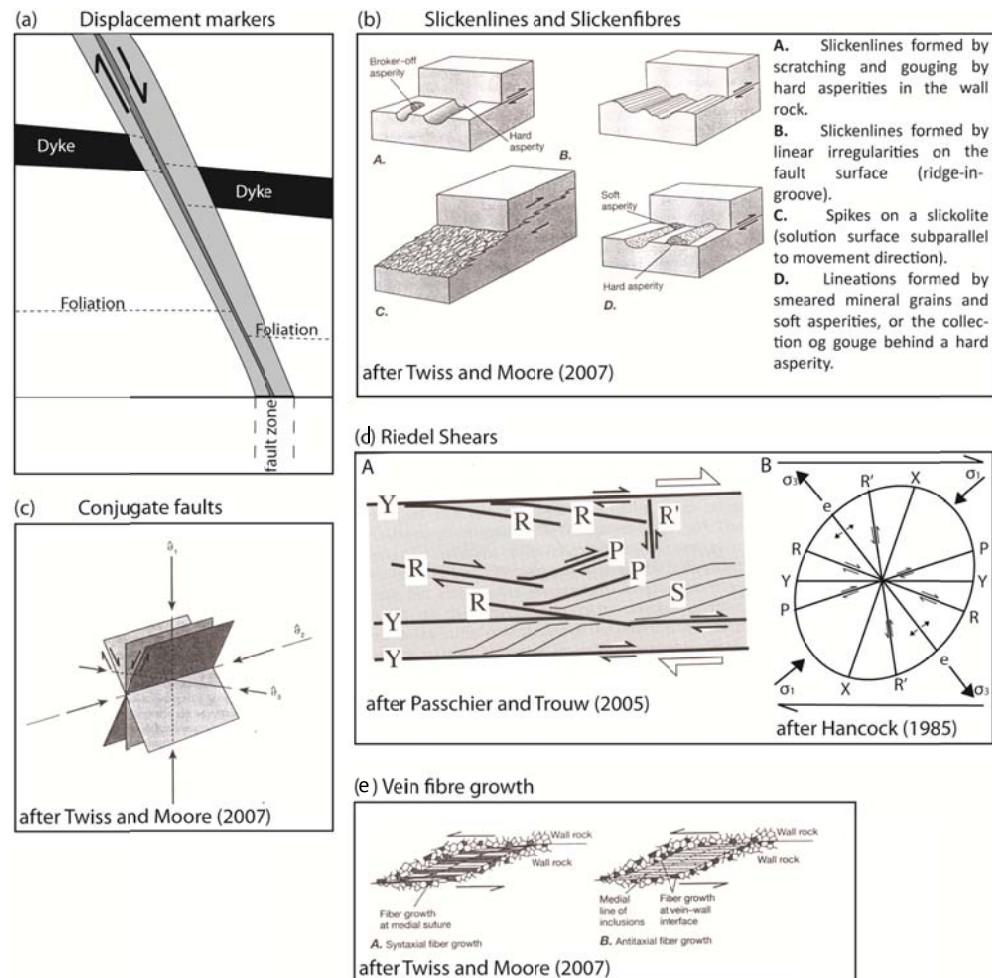
### 1.3.3.3 – Secondary fractures

The geometry and kinematics of secondary (subsidiary) fractures and other structures associated with larger faults and fractures can also be used to establish the sense of movement. Minor secondary fractures can develop along the main fault structure at low to moderate angles to the fault with either extension or shear displacements along them (Twiss and Moores, 2007). Conjugate faults are also useful as they typically intersect in a line that is parallel to the direction of intermediate finite stretch or stress (*Figure 1.6c*) (Davis and Reynolds, 1996), and by using the Coulomb-Navier theory of brittle failure, it is possible to determine the direction of slip on the main fault plane.

Subsidiary shear fractures, or Riedel Shears, can also be used to determine direction of movement along a fault plane (Riedel, 1929, Hancock, 1985, Passchier and Trouw, 2005). Riedel shears are identified with respect principal displacement direction which is parallel to the main fault boundary. They are subdivided into four different categories (R, R', P and Y shears, *Figure 1.6d parts A & B*) which each have their own characteristics, geometry and shear sense relative to the main fault (Passchier and Trouw, 2005, Twiss and Moores, 2007).

### 1.3.3.4 – Vein infills

Syntaxial and antitaxial vein infills (previously described, see *Section 1.3.2.2*) are sometimes controlled by displacement along faults and fractures (*Figure 1.6d*). In these situations mineral growth in the veins occurs in the opening direction of the fracture/fault and therefore they can be used to determine wall rock displacements (Passchier and Trouw, 2005, Twiss and Moores, 2007). In purely extension veins, mineral fibre growth is perpendicular to the vein walls, whereas mineral fibres in shear fractures grow oblique to the vein wall (Hancock, 1985, Twiss and Moores, 2007). Veins that form parallel to the maximum principal stress direction and at high angles to the extension direction are known as tension gashes. Mineral fibres that form on the shear surface and parallel to the movement direction are known as slickenfibres (*Section 1.3.3.2*). The continuity of mineral fibres across a vein or shear surface implies that the mineral growth accompanied and kept pace with the fracture displacement and crack opening (Twiss and Moores, 2007).



**Figure 1.6:** Examples of brittle kinematic markers (not exhaustive) **(a)** Displacement markers which can include igneous dykes and foliation planes. **(b)** Slickenlines and slickenfibres **(c)** Conjugate fault pair dissected by an extension fracture. **(d)** Examples of Riedel shear fracture characteristics and geometry **(e)** Syntaxial and antitaxial vein growth as a displacement marker.

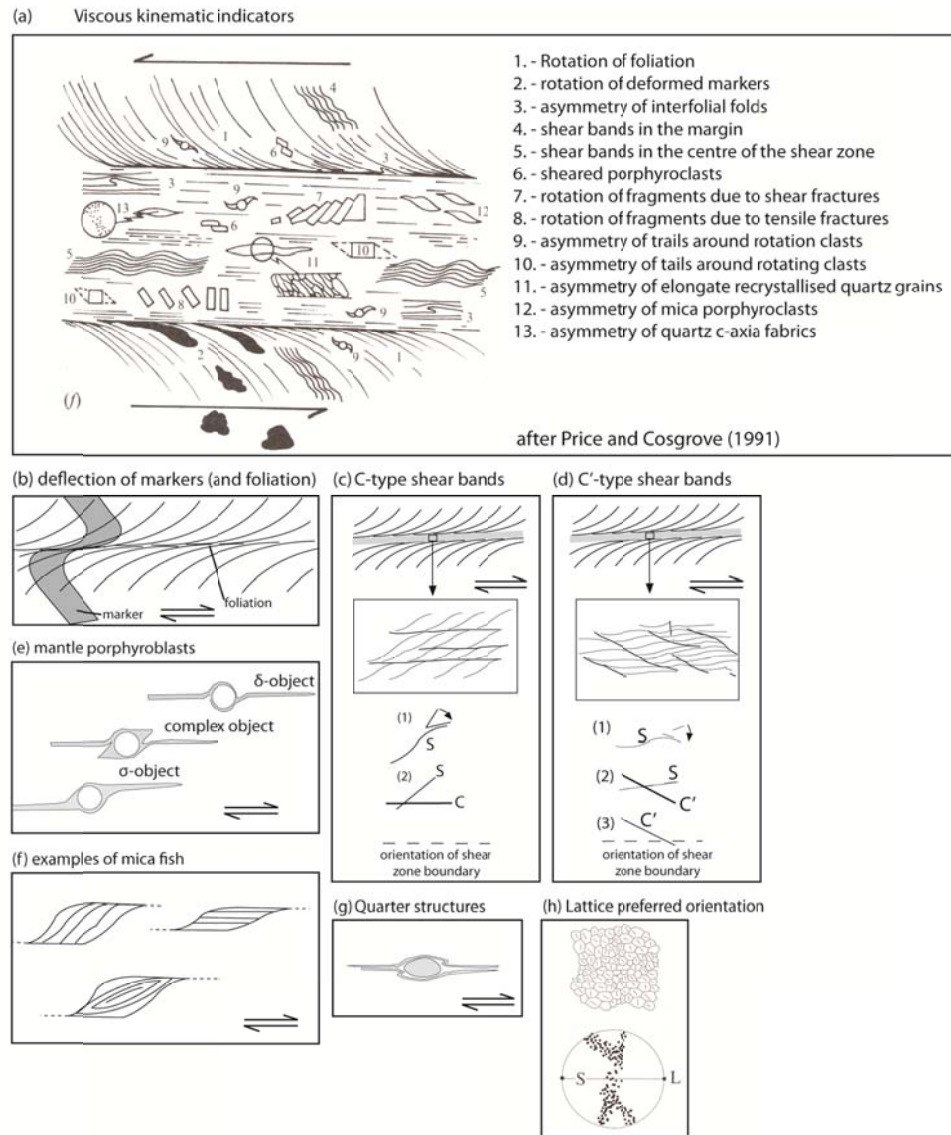
### 1.3.3.5 – Viscous kinematic indicators

There are many kinematic indicators for ductile or viscous shear zones (see Passchier and Trouw, 2005, Twiss and Moores, 2007). Those that are important for this thesis are outlined below (*Figure 1.7*).

*Foliation* can be used to determine shear sense direction from its orientation if it is deflected into a shear zone (*Figure 1.7b*). The deflection commonly has a curved shape that can be used to determine shear sense, only if the movement direction (defined by the lineation) is normal to the axis of curvature (Passchier and Trouw, 2005).

*Shear band cleavage* can be identified where compositional banding or orientated minerals (typically micas) are cross-cut by sets of sub-parallel minor shear zones (Passchier and Trouw, 2005). These shear band cleavages comprise two surfaces; C-surfaces (cisaillement) and S-surfaces (schistosity). Two types of shear band cleavage are recognised in the literature, C-type and C'-type (Figure 1.7c & d) (Berthé et al., 1979). C-type shear band cleavage is also known as C/S fabric (Berthé et al., 1979, Vernon et al., 1983, Lister and Snoke, 1984, Krohe, 1990, Passchier and Trouw, 2005) which may develop from the earliest stages of mylonite formation, reflecting inhomogeneous simple shear (Passchier and Trouw, 2005). C'-type shear band cleavage typically overprints C-type fabrics (Berthé et al., 1979) and usually forms late in the deformation process in strongly foliated mylonites. The latter fabric is oblique to shear zone boundaries and lies at typical angles of 15-35° (Dennis and Secor, 1987, Passchier, 1991, Blenkinsop and Treloar, 1995, Passchier and Trouw, 2005). Usually these shear bands fail to extend into weakly foliated areas (e.g. quartz layers) (Passchier and Trouw, 2005). During C'-type fabric development, synthetic rotation of shear bands indicates simple shear and antithetic rotation indicates extension parallel to the main shear zone (Passchier, 1991), thus making these shear bands reliable shear sense indicators.

*Porphyroblasts* (Figure 1.7e), *mica-fish* (Figure 1.7f), *quarter structures* (Figure 1.7g) and *lattice preferred orientations* (Figure 1.7h) can also all be used as indicators of shear sense within the viscous domain. Passchier and Trouw (2005) give a comprehensive study of viscous (and brittle) kinematic indicators).



**Figure 1.7:** Examples of viscous kinematic markers (not exhaustive). **(a)** Geometry and locations of viscous kinematic markers. **(b)** Deflections of markers, including foliation (after Passchier and Trouw (2005)). **(c)** C-type shear bands or C/S fabrics (after Passchier and Trouw (2005)). **(d)** C'-type shear bands or S/C fabrics (after Passchier and Trouw (2005)). **(e)** Mantle Porphyroblasts (after Passchier and Trouw (2005)). **(f)** Examples of Mica fish (after Passchier and Trouw (2005)). **(g)** Quarter structures (after Passchier and Trouw (2005)). **(h)** Lattice preferred orientations (after Passchier and Trouw (2005)).

### 1.3.4 – Fault zone reactivation

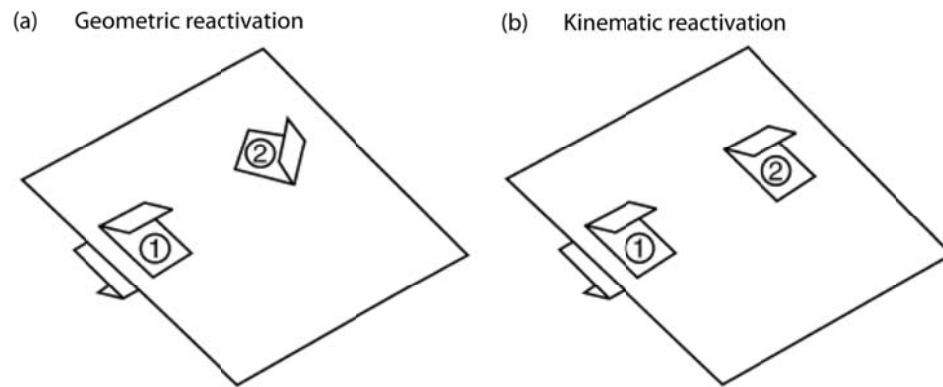
Reactivation is defined as “the accommodation of geologically separable displacement events (intervals >1 Ma) along pre-existing structures” (Holdsworth et al., 1997). This reactivation may occur along structures such as faults, shear zones, major compositional/rheological boundaries and magma ascent pathways (e.g. Daly et al., 1989, Butler et al., 1997, Holdsworth et al., 1997, Beacom et al., 2001, Gontijo-Pascutti et al., 2010). These discontinuities are found throughout the continental lithosphere and reactivate in preference to the formation of new deformation structures and zones (Holdsworth et al., 1997). The time scales between deformation events are important (>1 Ma) because shorter time intervals between events may relate to recurrent movements within the same seismic cycle and not to reactivation (Wallace, 1984, Beacom, 1999).

Two types of reactivation have been identified (Holdsworth et al., 1997):

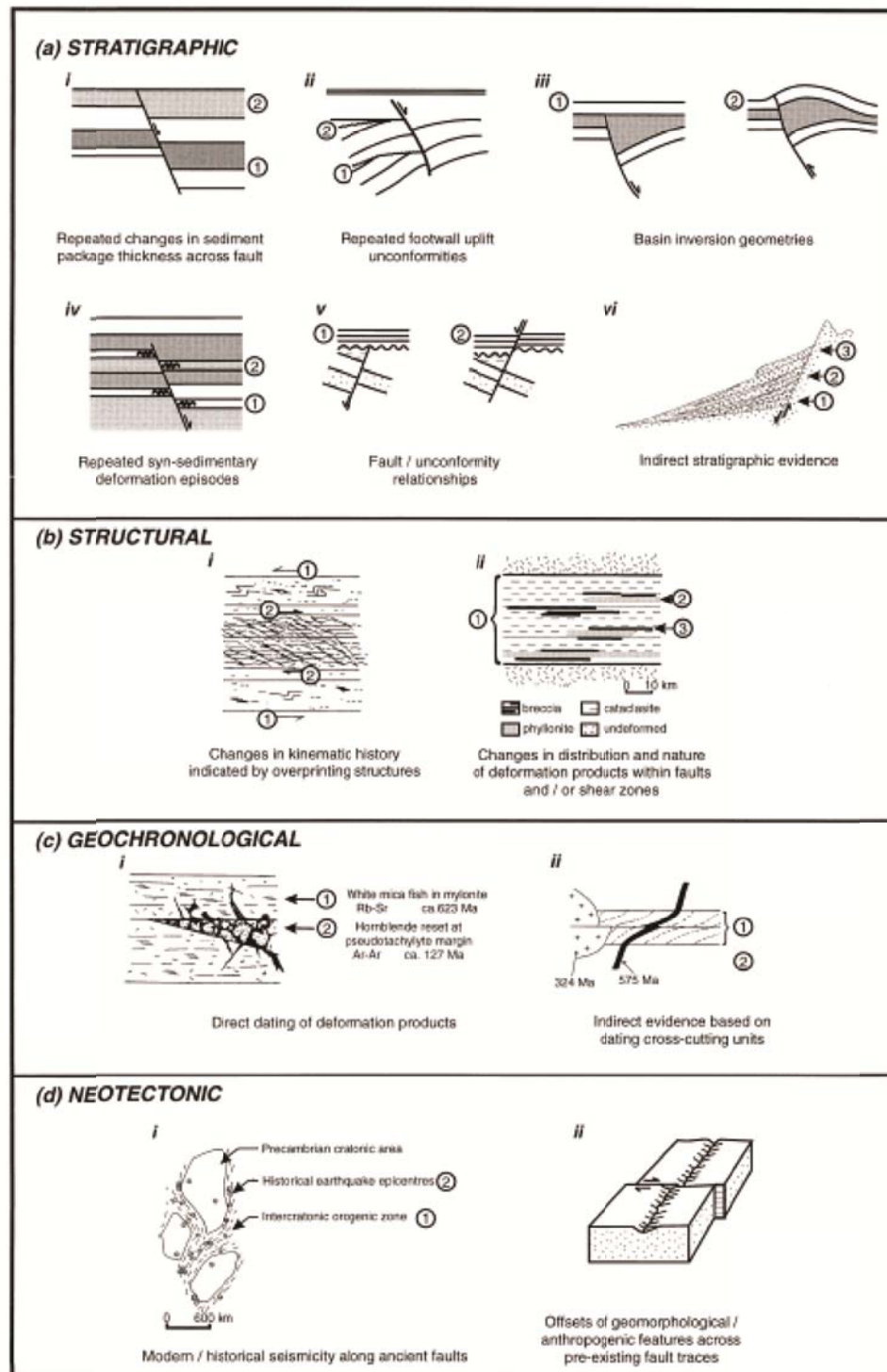
*Geometric reactivation (Figure 1.8a)* occurs when reactivated structures display different senses of relative displacement for successive events.

*Kinematic reactivation (Figure 1.8b)* occurs when reactivated structures display similar senses of relative displacement for successive events.

A number of stratigraphic, structural, geochronological and neotectonic criteria (*Figure 1.9a-d*) are considered to be reliable criteria for identifying reactivation (Holdsworth et al., 1997). Wherever possible, several different criteria should be used to define reactivation. Geometric similarity of the structures – i.e. similar trend - is not a reliable criterion for identifying reactivation, although the use of geometric similarities is common in the structural interpretations of seismic data from offshore hydrocarbon fields and sedimentary basins (e.g. Bartholomew et al., 1993, Lee and Hwang, 1993, Dore et al., 1997, Cobbold et al., 2001).



**Figure 1.8:** The two recognised types of reactivation **(a)** Geometric reactivation. **(b)** Kinematic reactivation. After Holdsworth et al. (1997).



**Figure 1.9:** The four main criteria considered reliable for recognising reactivation: stratigraphic (a), structural (b), geochronological (c) and neotectonic (d). The isotopic ages shown in (c) are for illustration purposes only. After Holdsworth et al. (1997).

### 1.3.4.1 - Estimating stress and strain trajectories from faults

The orientation of stress and strain trajectories can be determined from the symmetrical or asymmetrical architecture of fractures with respect to the principal stresses ( $\sigma'_1 > \sigma'_2 > \sigma'_3$ ), if you can assume that the principal stresses and strains were parallel when the faults/fractures were forming (Beacom, 1999). Techniques for determining the orientation of stress and strain axes from fault orientation and kinematic indicators are widely used in the literature (e.g. Angelier, 1979, Aleksandrowski, 1985, Fleischmann and Nemcok, 1991). These models should be considered cautiously because they are of limited use where there are complex fault/fracture network architectures and the symmetry of the fault/fracture pattern does not reflect the stress or strain trajectories (e.g. Pollard et al., 1993, Sperner and Zweigel, 2010, Kaven et al., 2011). Complexities in fault/fracture networks often develop as a result of geometric and kinematic interaction or reactivation of pre-existing heterogeneities in the continental lithosphere (Beacom, 1999).

### 1.3.4.2 – Reactivation of pre-existing structures

The reactivation of pre-existing structures (particularly faults) depends on two main factors: the fluid pressure and the orientation of the local stress regime acting on the fault (Jolly and Sanderson, 1997). The geometric limitations associated with frictional reactivation have been investigated by (Sibson, 1985) for a cohesionless fault using 2-dimensional analysis. In this example a cohesionless fault plane is used that is at an angle  $\theta$  to  $\sigma_1$  with its normal contained in the  $\sigma_1 \sigma_3$  plane with principal compressive stresses of  $\sigma_1 > \sigma_2 > \sigma_3$  (Figure 1.10a). The resulting stress ratio is:

$$R = (\sigma'_1 / \sigma'_3) = (1 + \mu \cot \theta) / (1 - \mu \tan \theta) \quad (1)$$

which is a rewritten version of Amonton's Law that has the failure criteria

$$\tau = \mu \sigma'_n = \mu(\sigma_n - P) \quad (2)$$

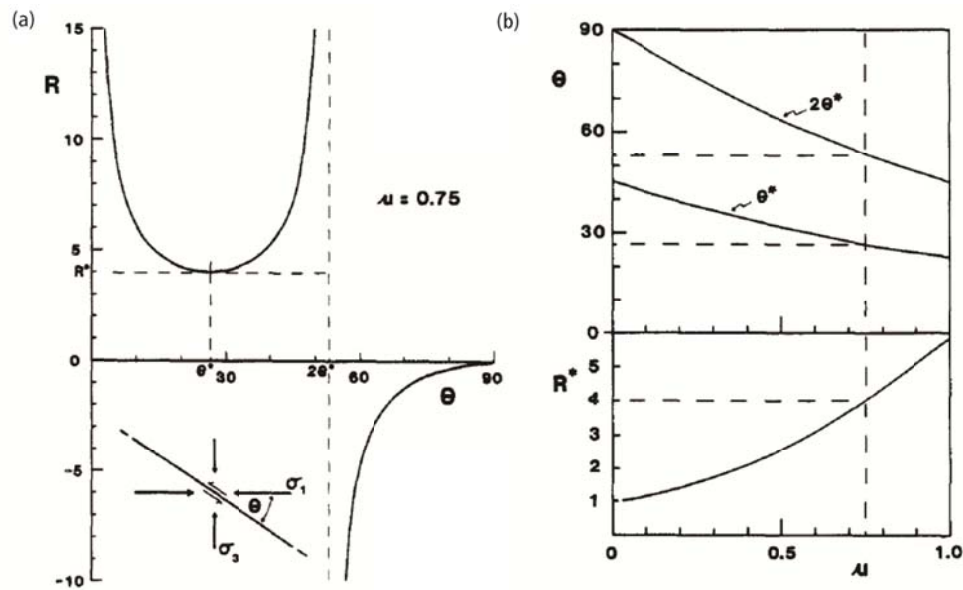
where  $\tau$  and  $\sigma_n$  are the shear and normal stresses to the plane, respectively,  $P$  is the fluid pressure and the coefficient of friction  $\mu$  is approximately 0.75 (Sibson, 1983). These relationships suggest that the ratio for reactivation has a minimum positive angle ( $R^* =$



$(\nu(1 + \mu^2) + \mu)^2$  (Sibson, 1985)) when the optimal angle for frictional reactivation is  $\theta^* = \frac{1}{2} \tan^{-1}(1/\mu)$  (Sibson, 1974). For fault reactivation to arise at large values of  $\theta$ , instead of the formation of favourably orientated new structures,  $\sigma'_3$  must become tensile ( $\sigma'_3 < 0$ ) or the frictional coefficient must be significantly lower than 0.75 (*Figure 1.10b*), expressing the need for high fluid pressures or abnormally low frictional coefficients, or the stress trajectories must deviate markedly from the horizontal and vertical (Sibson, 1985).

In examples where the fault/fracture network architecture is more complex it is important to consider both the geometric and kinematic interactions of differently orientated structures during reactivation (Nieto-Samaniego and Alaniz-Alvarez, 1995, Nieto-Samaniego and Alaniz-Alvarez, 1997, Beacom, 1999).

The reactivation of pre-existing structures fundamentally requires fault zone weakening processes to be considered. These weakening processes have been divided into those which have syn-tectonic effects and those which occur over a long term (Holdsworth et al., 1997). Syn-tectonic weakening processes include shear heating, increases in pore fluid pressure, fine-grained reaction product weakening, transformational plasticity, changes in pore fluid chemistry, fluid assisted diffusive mass transfer and the addition/production of melt (Holdsworth et al., 1997). Those processes which occur in the long term (and syn-tectonically) include generation of cohesionless fractures, grain size reduction, reaction softening, fabric softening and thermal perturbations (Holdsworth et al., 1997). One relevant example from the Outer Hebrides Fault Zone suggested that fault zone weakening occurred due to the formation of aligned phyllosilicates minerals and the occurrence of syn-tectonic reaction softening (IMBER et al., 1997). Most of these processes involve the interactions of hydrous fluids, metamorphism, stress, strain, temperature and pressure (Beacom, 1999). The importance of fluid interaction is outlined in the following section.



**Figure 1.10: (a)** Stress ratio required for frictional reactivation,  $R$ , vs. the reactivation angle,  $\theta$ , for static frictional coefficient  $\mu = 0.75$ . **(b)** Variation of optimum reactivation angle,  $\theta^*$ ,  $2\theta^*$ , and minimum possible stress ratio for reactivation  $R^*$  with frictional coefficient,  $\mu$ .

### 1.3.5 – Fluid activity in faults

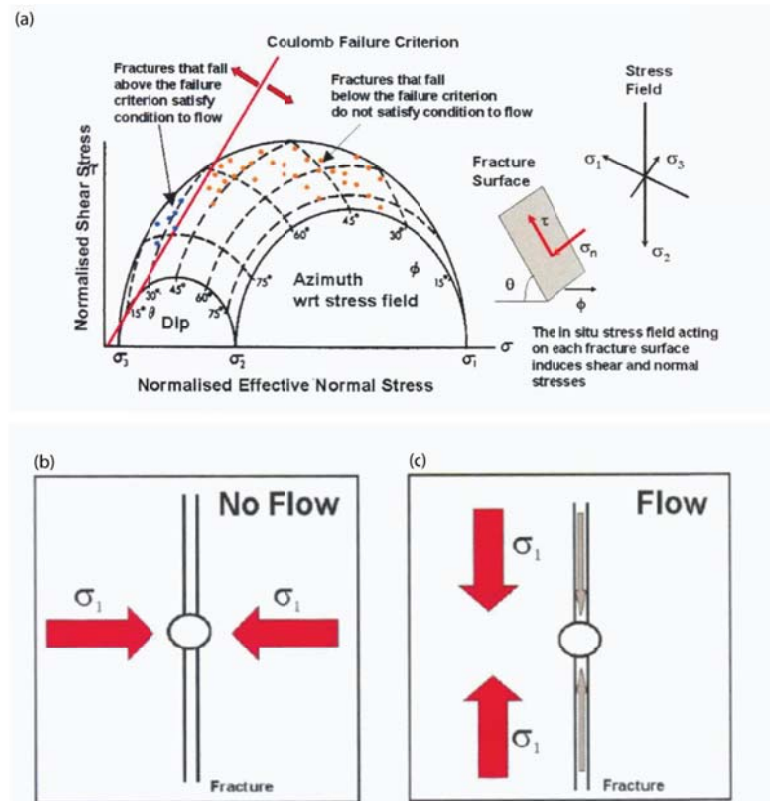
The chemistry and pressures of fluids found in fault and shear zones play a critical role in many weakening mechanisms. Fluids involved may originate from meteoric, metamorphic, igneous or hydrothermal sources and can be identified from associated mineralisation, fluid-assisted processes and their isotopic signatures (e.g. Carter and Dworkin, 1990, Pik and Marty, 2009, Sample, 2010).

Fault/fluid interactions are important within the mainland LGC where fluids are responsible for a variety of different mineralisation and metamorphic events. For example, surface-derived fluids are recognised due to the presence of hematite, as an oxidation product (Hay et al., 1988), within fractures and faults that are found throughout the Assynt and Rhiconich Terranes. Also much of the metamorphic retrogression that occurred syn-tectonically throughout the LGC (Beach, 1980) and particularly seen within Lewisian shear zones resulted from the presence of metamorphic fluids.

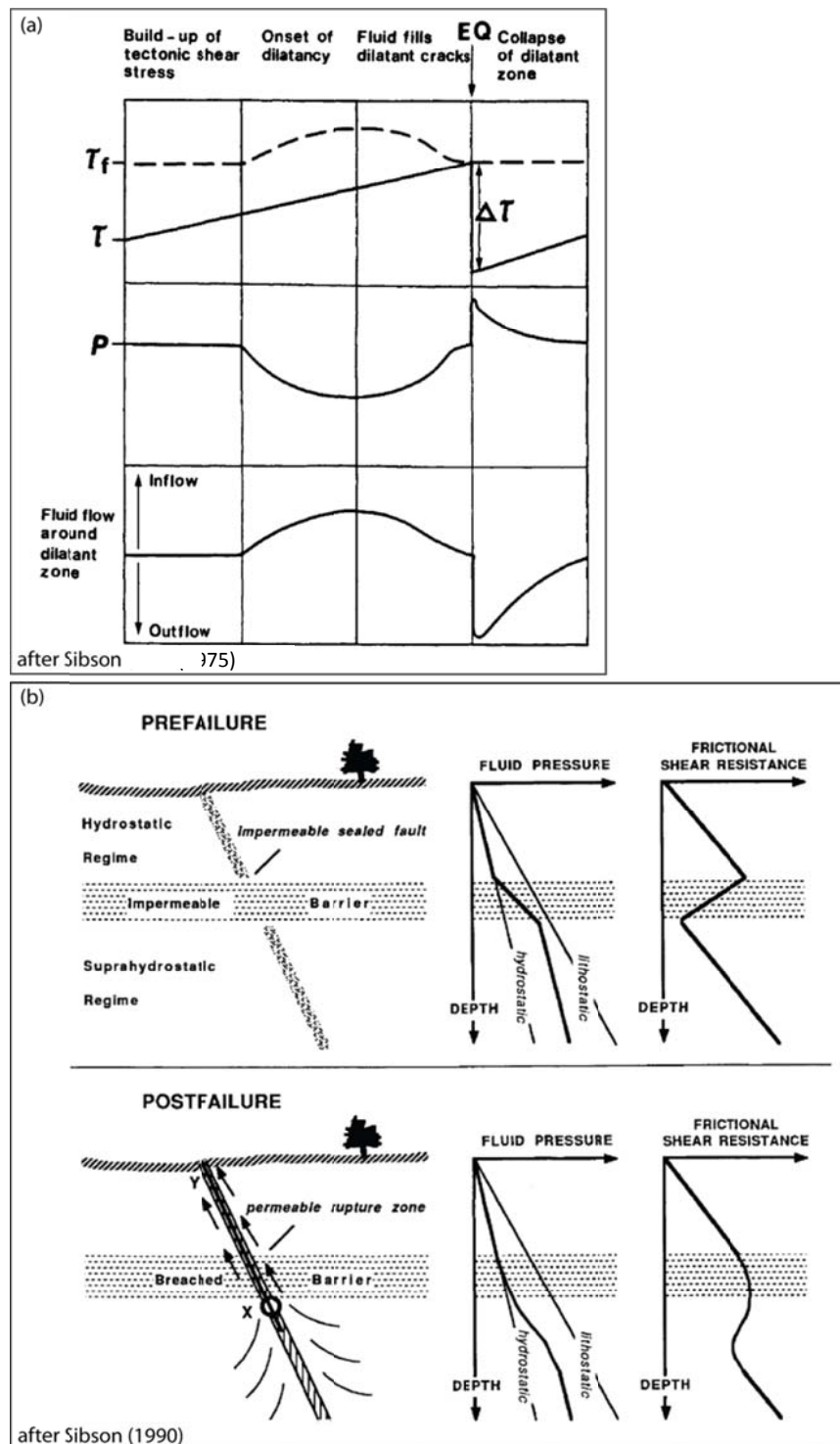
The orientation of the stress field is critical to a fault/fracture's ability to flow (Rodgers, 2000). Those fractures which fall above the Coulomb failure criteria satisfy the criteria for fluid flow (Figure 1.11a). Also if the maximum compressive stress,  $\sigma_1$  is

perpendicular to the fracture plane, then fluid flow is likely to be restricted (*Figure 1.11b*). Conversely, if  $\sigma_1$  is parallel to the fracture plane then fluid flow is potentially enhanced as the fracture is more likely to be open (*Figure 1.11c*).

Fluid movement along faults is accommodated by mechanisms including devolatilisation reactions and dilatancy. Dilatancy is not necessarily dependent on the nature of devolatilisation reactions, although the associated volume change is highly dependent on the properties of the rocks and fluids (Etheridge et al., 1983). Fluid flow in the upper crust is likely controlled by mechanisms such as seismic pumping (*Figure 1.12a*) (Sibson et al., 1975) and fault valve behaviour (*Figure 1.12b*) (Sibson, 1990). In the middle and lower crust likely fluid flow mechanisms include dilatancy pumping (Etheridge et al., 1983, Sibson, 1986) and inter- and intra-granular flow (Hadizadeh and Rutter, 1983), with the majority of flow accommodated along major faults and shear zones.



**Figure 1.11:** Stress field criteria for fluid flow through fractures. After Rodgers (2000). **(a)** Three dimensional Mohr circle plot of a cubic stress element on an inclined fracture plane. **(b)** Maximum compressive stress acting perpendicular to the fracture plane resulting in no flow. **(c)** Maximum compressive stress acting parallel to the fracture plane resulting in flow along the fracture.



**Figure 1.12:** Examples of fluid flow mechanisms. **(a)** Diagram depicting the seismic pumping process. After Sibson et al. (1975). **(b)** Potential for fault valve behaviour with an impermeable barrier separating hydrostatic and suprahydrostatic fluid pressure regimes. This barrier is then breached by allowing the upward flow of fluids along the ruptured fault plane. After Sibson (1990).

#### 1.4 – Fracture attribute characteristics

All fractures have a series of attributes that can be analysed to gain an understanding of individual fractures and full fracture networks in great detail. These attributes provide information on the geometry, spatial relationships, fluid storage and migration potential through the studied fracture networks. Important fracture attributes are: orientation, spacing, aperture, connectivity and infill.

##### 1.4.1 – Orientation

Fracture orientation is defined by its attitude in space (Twiss and Mooress, 2007). As fractures represent planar features their orientations are normally defined by the strike direction (measured from geographic north) and the dip of the line of steepest inclination (measured from a horizontal reference line) (e.g. Barton, 1978, Twiss and Moores, 2007). Dip and dip direction are also used within this thesis to define the orientation of fracture planes.

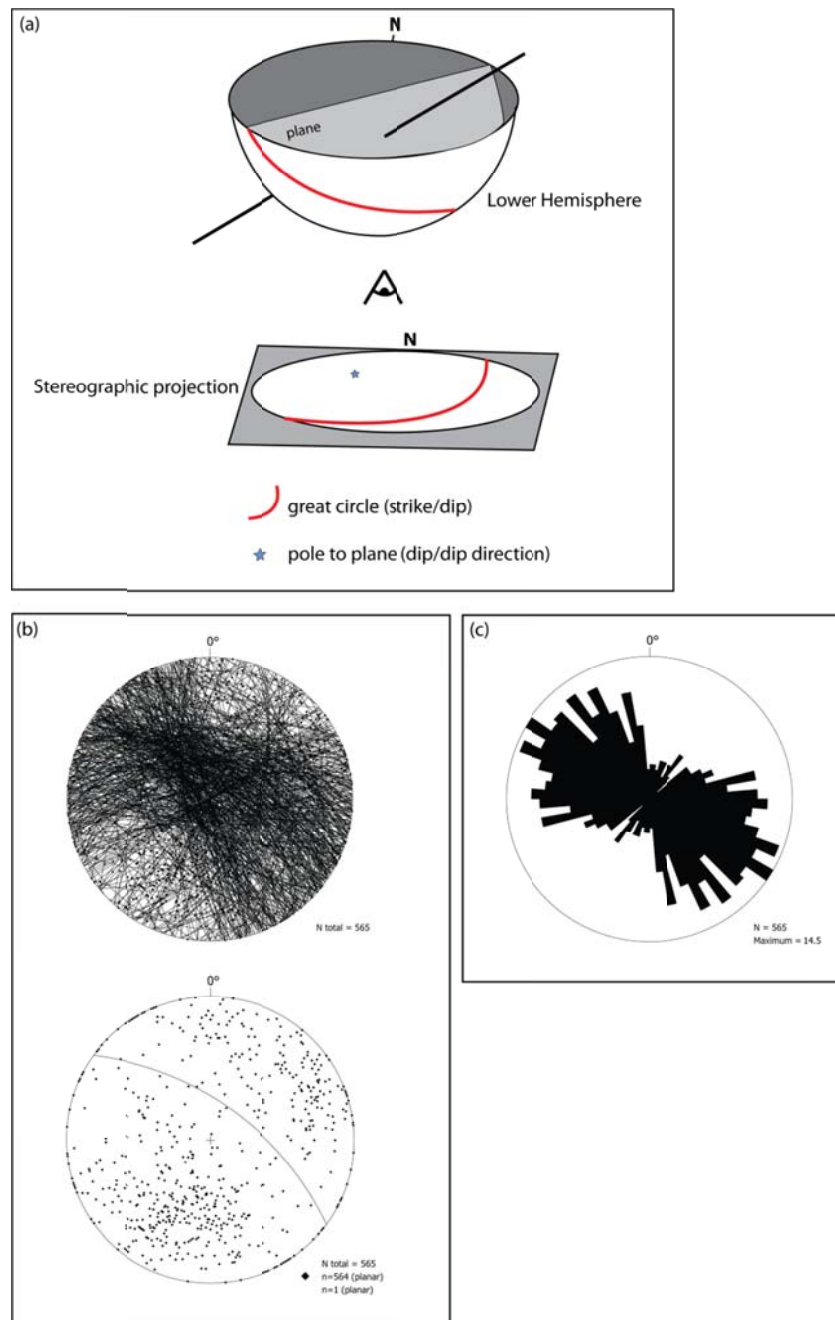
To analyse fracture orientation in three dimensions, dip and strike values can be plotted on lower hemisphere stereographic projections (*Figure 1.13a & b*), or stereonet. Fractures are normally shown as poles to planes in order to identify clusters or patterns within the fracture datasets. Using stereonet allows both fracture strike and dip to be visualised simultaneously on the same plot. Fracture strike data may also be plotted on rose plots to allow the identification of dominant fracture trends (*Figure 1.13c*). Although rose plots are useful for easily visualising dominant fracture trends, it is important to note that they create bias by exaggerating large orientation concentrations and suppressing smaller ones (Barton, 1978). They are also inherently two dimensional.

Regional fault orientation datasets included in this project are primarily analysed using rose plots due to a lack of fracture dip data (well data from the Clair basement also falls into this category). Stereonets are used to analyse fieldwork orientation datasets from both fractures and other structures (e.g. foliation) found within the mainland LGC.

Fracture orientation data collected using a variety of different sampling techniques are inherently biased due to the orientation of the sampling. This is particularly true from fieldwork sampling where 1-dimensional line samples (*Section 1.6.5*) dominate and therefore fractures are preferentially sampled where their azimuth is sub-perpendicular to the sample line. It is therefore critical to ensure fracture

sampling in different directions to ensure that all fracture sets are included in the analysis which reduces any orientation bias. Cliff sections provide the biggest risks for creating biases in the fracture orientation data as the vertical extent of each section is normally limited by the height of the person conducting the sampling and sampling a perpendicular cliff section in the same area is not always possible. As many of the fieldwork fracture datasets are from wave-cut platforms, horizontal fractures are commonly under-sampled.

The relationship between host rock and fracture and fault orientations is not always simple, with previous work showing that heterogeneities within rocks can play an important role in fracture and fault orientations (Anderson, 1951, Peacock and Sanderson, 1992 and references therein). Heterogeneities include layering, cleavage, bedding planes, foliation and pre-existing faults, with both foliation and earlier faults being the most relevant for this project.



**Figure 1.13:** Examples of the different methods for analysing orientation. **(a)** Schematic diagram illustrating the principles of a stereographic projection (stereonet). **(b)** Stereonets showing fracture data. The top stereonet shows fracture data plotted using great circles. The bottom stereonet shows the same fracture data plotted as pole to the planes, with an average orientation shown as a great circle. It is often more instructive (and less cluttered) to plot the data as per the bottom stereonet. **(c)** The same fracture data from (b) shown on a rose plot. This time only the fracture strike (or azimuth) is included.

### 1.4.2 – Spacing

Fracture spacing is defined as the distance between two adjacent fracture traces as sampled along a 1-dimensional sample line (e.g. Priest and Hudson, 1976, Ladeira and Price, 1981, Rouleau and Gale, 1985, Huang and Angelier, 1989, Gillespie et al., 1993, Johnston et al., 1994 and references therein). This spacing can be separated into fractures from the one fracture set (parallel orientations) or the full fractures sampled can be analysed as the one entity. Fracture spacing in this thesis is most commonly defined in terms of distance along 1-dimensional transects (*Figure 1.14*), but it is also characterised in terms of fracture density. These two methods of analysing the spatial variability of fractures are described below:

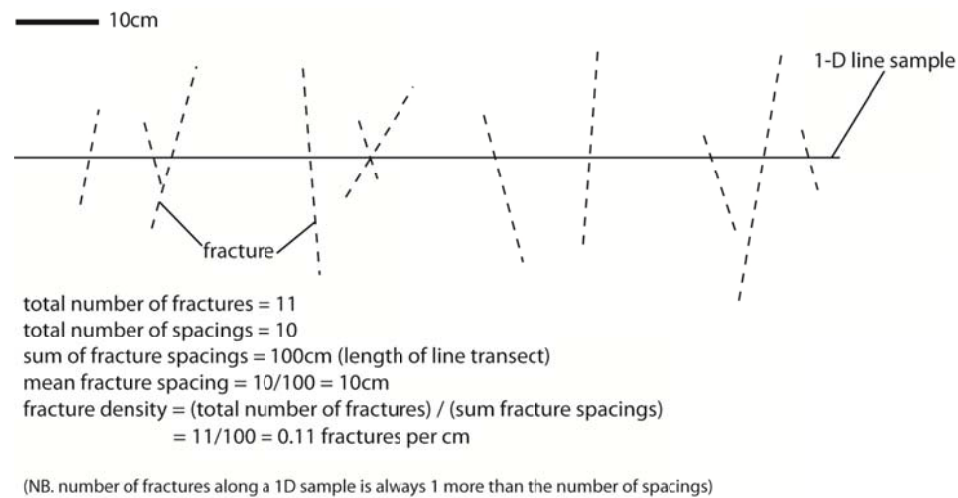
*Spatial variability based on distance* – Spacing is easy to measure along 1-dimensional line samples, but it is much more difficult to define in 2-dimensional and 3-dimensional datasets. Fracture spacing in this study has primarily been collected from 1-dimensional line samples (*Figure 1.14*) collected across outcrops in the mainland LGC (where possible, they were taken parallel, perpendicular and oblique to foliation) and core sections from the Clair basement. 2-dimensional regional datasets from the onshore and offshore study areas have also been analysed for fracture spacing characteristics using a series of 1-dimensional pseudo-wells taken in a variety of different orientations across the regional fault lineament maps. The resulting fracture spacing datasets have then been analysed on population distribution plots (spacing plotted against cumulative number, see *Section 1.5.2*).

*Fracture density* – It is also possible to describe fracture spacing distributions in 1D, 2D or 3D as a single number which is known as the fracture density. Fracture density is described in the literature as having several different meanings. For the purposes of this thesis fracture density is primarily expressed as the number of fractures per sample line length (for 1D samples, *Figure 1.14*), fracture trace length per unit area (for 2D samples) and fracture area per unit volume (for 3D samples) as per the definition provided in Gillespie et al. (1993).

Fracture spacing (including fracture density) can be influenced by many factors such as lithology, layer/bed thickness, pre-existing ductile structures and the presence pre-existing fault and fracture sets (Sleight, 2001). In many lithologies, the spacing between fractures in thick beds/layers is commonly larger than the fracture spacing in



thinner beds (Narr and Suppe, 1991). This relationship is not applicable to the rocks in this thesis because there is very little evidence of mechanical stratigraphy within the mainland LGC or the Clair basement rocks. Fracture density, especially in the mainland LGC, is affected by pre-existing foliation planes where there is a complex relationship between metamorphic mineralisation and preferential fracturing of foliation. Large, regional faults also have an effect on the fracture density attributes, both within the mainland LGC and the Clair basement.



**Figure 1.14:** Schematic illustration of fracture spacing along a 1-dimensional line sample and the calculation of fracture density from the same sample. Modified after Sleight (2001).

#### 1.4.3 – Aperture

In this thesis, fracture aperture is defined as the perpendicular distance across the fracture between the fracture walls. Fracture aperture has been categorised as being ‘open’, ‘partially open’ or ‘closed’ depending on the nature of fracture infill (if any), which has clear implications for the ability of fractures to transmit fluid (Neuzil and Tracy, 1981). The traditional classification of fracture apertures as defined by Barton (1978) is given in *Table 1.2*.

At outcrop, fracture aperture is commonly impossible to measure accurately as weathering and solution processes result in falsely wide openings. As a rule of thumb during this project, fracture aperture measurements gathered in the field are treated with caution and are normally considered to represent an overestimation of fracture width for most outcrops. This overestimation may not apply to outcrops where

recent blasting has occurred (road cliff sections) as there has been less time for weathering to have had an effect. However, caution is required at these road outcrops due to the creation of man-made fractures formed during blasting). Core samples from the Clair Field basement are also unaffected by weathering and therefore fracture aperture values of mineralised measured from these core samples are accepted as representing true fracture aperture values within the Clair basement fracture networks. This is because the fractures measured in core are no longer at subsurface pressures. Cemented or mineralised fractures will likely hold their aperture at the surface and therefore can be measured with a high degree of accuracy, but uncemented fractures, especially those which cross-cut the core, will fall apart once the core is brought to the surface and removed from the core barrel. Removing in-situ subsurface pressures will likely lead to relaxation of the core and result in the opening of some fractures to larger apertures than those encountered at depth. The converse can also occur where fractures held open by fluid pressure at depth or with orientations close to the present-day maximum horizontal stress direction may have smaller apertures at the surface than what they would have at depth. It is therefore important, if fracture aperture in core is being assessed, to account for any variations in true aperture due to changes in stresses as the core is brought to the surface.

No direct statistical analysis of aperture is presented in this thesis. This fracture attribute is used only to provide an estimated relationship between fracture length and fracture width to provide more information on fracture length parameters in the spatially limited datasets from the Clair basement (see *Chapter 4, Section 4.3.5*).

Aperture Width	Description	Summary
< 0.1 mm 0.1 – 0.25 mm 0.25 – 0.5 mm	Very tight Tight Partially open	“Closed” features
0.5 – 2.5 mm 2.5 – 10 mm > 10 mm	Open Moderately wide Wide	“Gapped” features
1 – 10 cm 10 – 100 cm > 1 m	Very wide Extremely wide Cavernous	“Open” features

**Table 1.2:** Aperture width classification (after Barton (1978)).

#### 1.4.4 - Infill

Any material that occurs in the space separating two adjacent walls is known as fracture infill. Commonly these infills are minerals such as quartz, calcite or hematite etc. or are fault rocks such as gouge, breccia or cataclasite. It is important to record all instances of fracture infill as they can provide valuable information about the relative timing of fracture-forming events and can give an indication of the types of fluids that have migrated through the fractures during their deformation history. Fracture infills can also help to separate different fracture sets that may have similar orientations and the cross-cutting relationships of these different fracture fills can provide more insight into the relative timing of different deformation events.

Fracture infills are also important from a fluid migration and storage perspective. Where fracture fills are clay-rich or consist of well cemented materials, their fractures are likely to form barriers to fluid flow. By contrast, fractures filled with vuggy vein material that indicates the presence of incompletely filled cavities may have potential for high levels of conductivity both along and across these fractures.

#### 1.4.5 – Length

Fracture length is defined as the measureable length of a linear trace produced by the intersection of a planar fracture with an outcrop surface (Priest and Hudson, 1981). Fractures either terminate against another fracture or within the main rock body. Understanding fracture length parameters provides the most important information for assessing fracture connectivity potential and the ability of the fracture to transmit fluids through the rock mass. Fracture length difficult is very difficult to quantify accurately and is typically subject to a number of sampling errors including censoring, truncation and size/geometric bias (e.g. Priest and Hudson, 1981, Rouleau and Gale, 1985, Pickering et al., 1995, McCaffrey et al., 2003, Manzocchi et al., 2009 and references therein):

*Censoring bias (Figure 1.15a)* occurs when large fractures extend beyond the limits of the sample area (in this study they extend beyond the edges of the outcrop or core section) and is applicable to both fracture length and spacing attributes. A sample is censored when some, or all, of the values within it are over- or underestimated (Pickering et al., 1995). The most common type of censoring in this thesis occurs due to the fact that no fracture can have a measured spacing wider

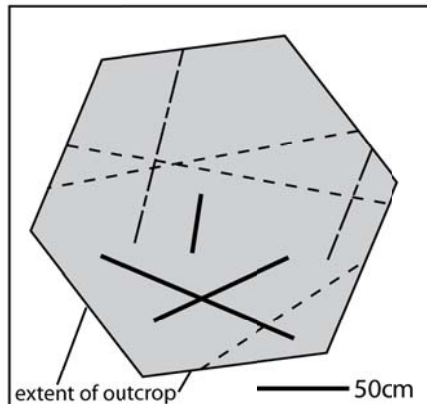
than the length of the sample and therefore fractures with spacing values larger than the sample length will be underestimated (Pickering et al., 1995).

*Truncation bias (Figure 1.15b)* occurs when the resolution of the sampling is too low to include small fractures below this cut-off value. It is formally defined as when the scale range of a sample of data is less than the scale range of the whole data population. The resolution cut-off of sampling in this thesis is the resolution of the human eye for fieldwork and core datasets, and for the regional datasets or LiDAR data, the cut-off is dependent on the resolution and quality of each of these datasets. Truncation can also occur at the large-scale end of the dataset and most commonly occurs due to large faults not being observed due to erosion (Pickering et al., 1995).

*Size/Geometric bias (Figure 1.15c)* occurs because fractures that are relatively longer are more likely to intersect 1-D sample lines or 2-D sample areas than shorter, less pervasive fractures. This bias also applies to fracture orientation with respect to 1-D line samples where fractures at a high angle to the line sample are more likely to be sampled than fractures which lie at low angles or sub-parallel to it.

Fault lineament length density maps have been used in this thesis to determine the occurrence of fault sets (based on length and orientation) within the onshore and offshore regional datasets. Fracture length data collected from outcrop, along with aperture measurements, have been used to estimate a relationship between fracture length and aperture that could be used to estimate the length of fractures from Clair basement core samples where fractures are consistently censored by the width of the core (10cm).

## (a) Censoring Bias



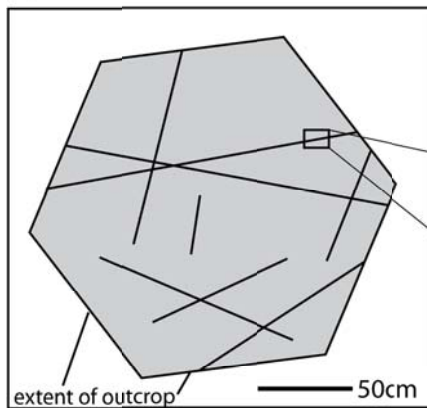
Long fracture traces are often underexposed by the limits of the outcrop.

— no exposure

- - - one end of the fracture is censored

- · - · both ends of the fracture are censored

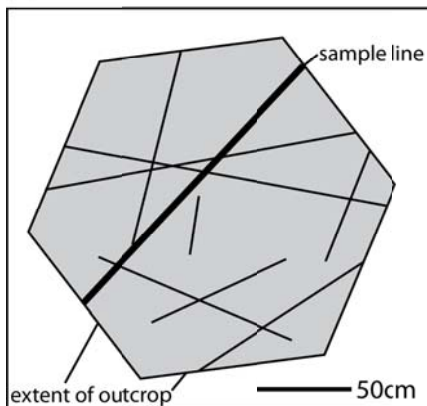
## (b) Truncation Bias



Small/short fracture traces are often below the scale of resolution and therefore under-sampled

— 5cm

## (c) Size/ Geometric Bias



Long fracture and those orientated at higher angles to the 1D sample line are preferentially sampled. This means that short fractures or those sub-parallel to the sample line are systematically undersampled.

**Figure 1.15:** Schematic diagrams illustrating the three main biases that occur when measuring fracture lengths. Modified after Sleight (2001).

#### 1.4.6 – Geometry

Fracture network geometry is a culmination of all the previously mentioned fracture attributes (*Sections 1.3.1 – 1.3.5*) which results in an overall pattern which either repeats regionally or is restricted to local areas. Geometry is defined in the literature as comprising five parts which are: (a) density of fractures; (b) orientation distribution of the fractures; (c) fracture size (i.e. length); (d) fracture shape; and (e) fracture aperture (e.g. Long and Billaux, 1987, Bour et al., 2002, Mäkel, 2007).

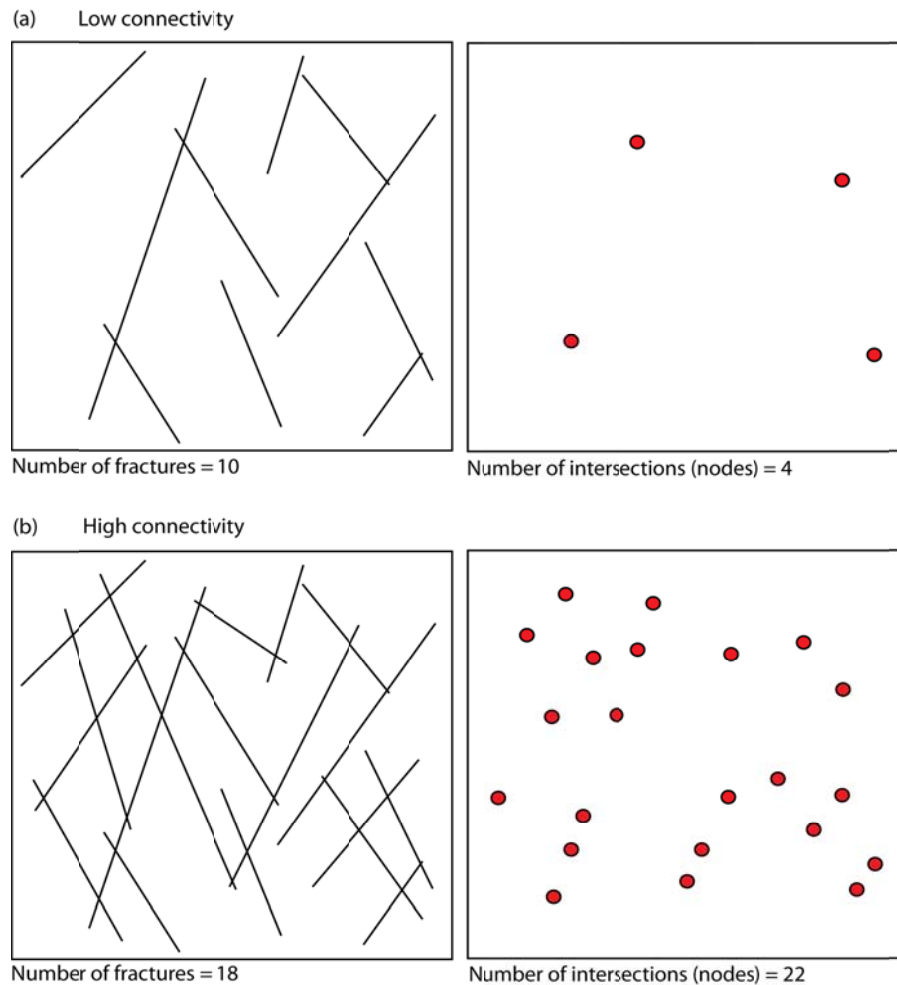
An understanding of fracture network geometry can be achieved when all fracture attributes are characterised in detail. Understanding the geometric relationships within a fracture network then allows an assessment of the fracture connectivity to be made, which ultimately provides a perception of how the fracture network may transmit and store fluid (*Section 1.3.7*).

#### 1.4.7 – Connectivity

Many fractures act as fluid pathways through the earth's crust. This is particularly relevant for this project where the study areas comprise crystalline basement rocks that have no primary porosity or permeability and therefore any fluid storage and flow has to occur within fractures (secondary porosity and permeability). Fractures can act as key conduits for fluid flow (e.g. oil, gas, water, CO<sub>2</sub> and toxic waste), but conversely fractures can be partially or wholly sealed and therefore restrict any fluid flow through the rock. Understanding the linkage of fractures forming continuous pathways through the rock is of the utmost importance for assessing the fluid flow (and storage) potential within the studied fracture networks.

From the literature, different authors regard some fracture attributes to be of more importance for fracture connectivity than others. For example, fractures that occur parallel to each other are unlikely to intersect, highlighting the importance of fracture orientation (e.g. Manzocchi et al., 1998, Mäkel, 2007). A fracture network with a high fracture density is more likely to have connected pathways than a network that only contains sparse fractures (*Figure 1.16*) (e.g. Mäkel, 2007). Also fracture apertures (and infills) play a key role in the ability of a fracture network to transmit fluids: narrow or mineral-filled fractures are less able to transport and store fluids than fractures that are open and/or have wide apertures (e.g. Odling et al., 1999).

Fracture connectivity, in this thesis, is primarily assessed using 2-dimensional maps with only the nodes (where fractures intersect) being considered statistically (*Figure 1.16*). This analysis only presents a 1-dimensional fracture connectivity on a 2-dimensional map and therefore only provides low-end estimates of fracture connectivity at particular outcrops, or from regional maps, for comparison between the different study areas. For deterministic fracture network modelling purposes, fracture connectivity is also calculated from fracture intersection curves and given as a percentage of the total volume connected, allowing comparisons to be made between the different structural settings that the models represent.



**Figure 1.16:** Schematic illustrations of the fracture connectivity analyses used in this thesis. **(a)** Low connectivity example. **(b)** High connectivity example where the introduction of more fractures significantly increases the number of nodes (i.e. connectivity).

### 1.5 – Fracture population statistical analysis

The statistical analysis of fracture attributes such as spacing, density, orientation and length allows the fracture system to be characterised quantitatively, allowing comparisons to be made between datasets collected from different study areas. These comparisons can also be made between different lithologies and structural settings within both the onshore and offshore areas.

All of the datasets collected for analysing the fracture systems that are collected at different scales (seismic reflection data, digital elevation models, outcrop, core samples, thin sections) represent samples from an underlying population. Within each of the study areas there is a *target population*, which is the collection of elements about which information is desired (e.g. all fracture orientations within a fracture network); a *sampled population*, which is the collection of elements that are available for sampling and a *sample* which is the collection of elements that are actually sampled (Swan and Sandilands, 1995). In order to fully understand sampled and target populations, collected samples are ideally taken at a variety of different scales (e.g. regional and outcrop) and at different dimensions (1-dimensional samples should also be taken in a variety of different orientations). Statistical analysis of the sample allows quantitative inferences to be made about properties of the sampled population (Einstein and Baecher, 1983, Swan and Sandilands, 1995). Samples can also be used to make inferences about the target population, although this is more difficult as it often involves extrapolating sample populations between scales and between dimensions (i.e. using 1-dimensional samples to make inferences about a 3-dimensional fracture networks).

In order to best describe the characteristics of the sampled and target populations, statistical distributions are typically used. However, the statistical distributions that best describe the collected sample may not best describe the sampled or target populations, if the collected sample is *biased* (e.g. Pickering et al., 1995). Any bias in the collected sample is generally inversely proportional to the sample size, i.e. the longer the 1-dimensional sample, the less bias is likely to occur (Sen and Kazi, 1984). Collected samples (e.g. fracture spacing) need to extend over more than one order of magnitude before different statistical distributions can be distinguished easily (Bonnet et al., 2001). This is particularly difficult at an outcrop scale where collected samples are often restricted by the size of the outcrop study area.



### 1.5.1 - Eigenvectors for fracture orientation analysis

Eigenvectors are determined from a non-parametric method specifically designed for orientation datasets. This rotationally invariant, matrix-based statistical method creates 3 unit vectors that are orthogonal to each other that describe the shape of the sample (*Figure 1.17*) (Woodcock and Naylor, 1983). Orientation distributions for individual fracture samples are determined by first creating normalised eigenvectors ( $S_1$ ,  $S_2$  &  $S_3$ ) so that;

$$S_1 + S_2 + S_3 = 1 \quad (3)$$

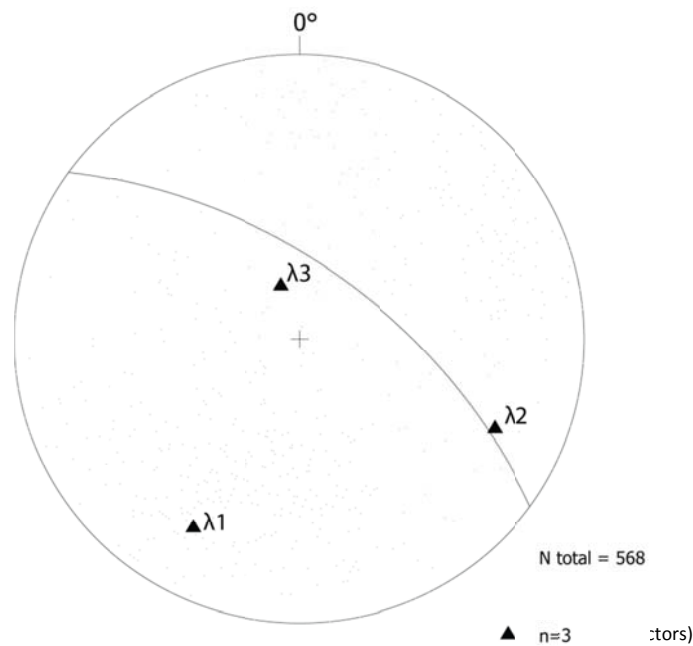
These normalised eigenvectors are then used to create the eigenvector ratios  $C$  (strength of the preferred orientation) and  $K$  ('shape' of the preferred orientation) (Woodcock and Naylor, 1983, Beacom et al., 2001) where

$$C = \ln(S_1 / S_3) \quad (4)$$

and

$$K = \ln(S_1 / S_2) / \ln(S_2 / S_3) \quad (5)$$

Following Beacom et al. (2001) this quantitative method is used in this thesis to assess the qualitative relationship between fractures and pre-existing foliation within mainland LGC shear zones. Where  $C$  and/or  $K$  values of fracture orientations are the same as the  $C$  and  $K$  values calculated from foliation, then the structures are geometrically coincident. This quantitative orientation analysis technique can be used, in conjunction with field observations, to assess the level of reactivation of pre-existing structures across the mainland LGC.



**Figure 1.17:** Stereonet exhibiting the same fracture orientation data as shown in Figure 1.12 and including its eigenvectors  $\lambda_1$ ,  $\lambda_2$  and  $\lambda_3$ . These eigenvectors can then be normalised to  $S_1$ ,  $S_2$  and  $S_3$  which are then used to determine orientation distributions.

### 1.5.2 – Fracture population distribution plots

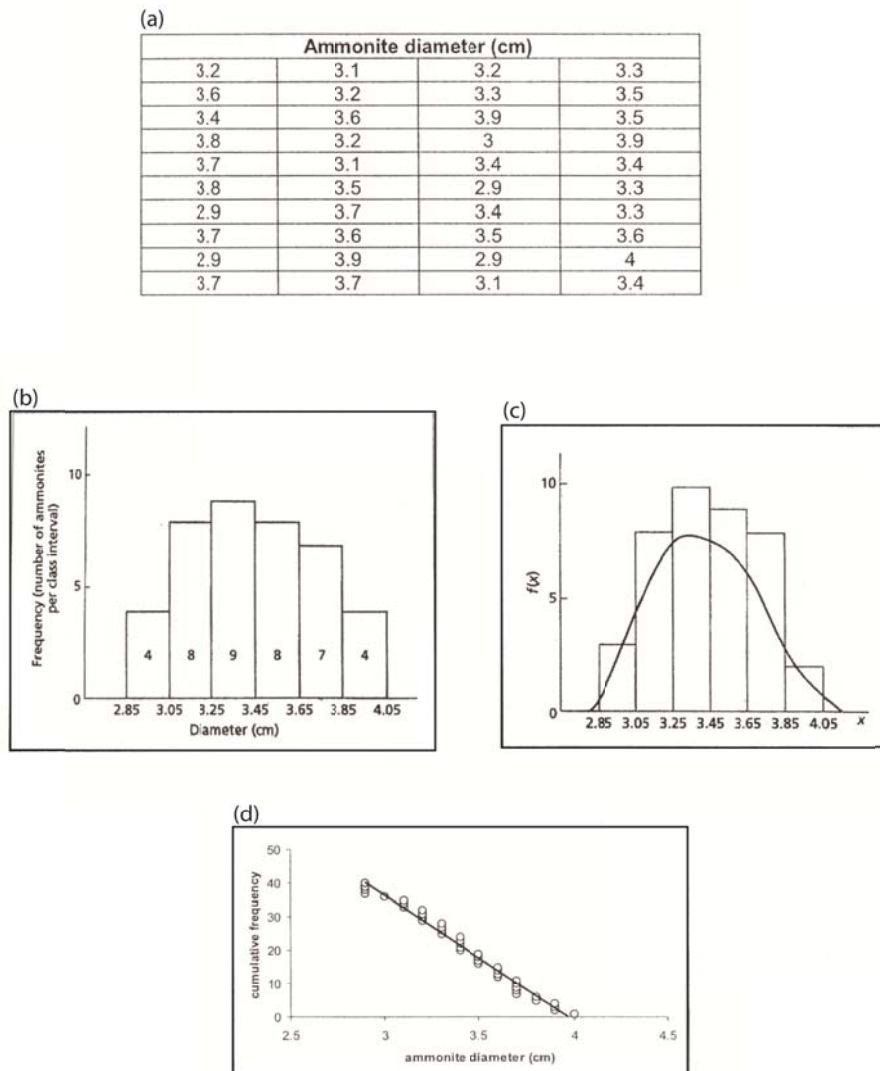
Within this thesis fracture spacing is analysed using statistical distributions from collected samples, with the result of this analysis used to infer the fracture spacing characteristics of the full fracture networks in the onshore and offshore study areas. There are two main methods used for analysing statistical distributions present within fracture network samples: *frequency distribution* and *cumulative frequency distribution* (Pickering et al., 1995).

*Frequency distribution plots (Figure 1.18)* – Measurements of the fracture attribute (e.g. spacing) are ‘binned’ into equal intervals along the x-axis of the histogram plot (Figure 1.18b). The number of measurements in each ‘bin’ is termed the frequency, which is given on the y-axis, and the series of measurements describe the frequency distribution (Swan and Sandilands, 1995, Sleight, 2001). When a large number of data are plotted on a frequency distribution histogram the intervals can be approximated into a smooth curve which is known as a probability density function (Figure 1.18c) (Swan and Sandilands, 1995), which

can be used to describe the fracture spacing distribution. These distributions cannot often be plotted on logarithmic axes because some size 'bins' may contain zero values (Gillespie et al., 1993). This type of plot is not used in this thesis.

*Cumulative frequency distribution plots* (referred to population distribution plots in this thesis, *Figure 1.18d*) are constructed by sorting fracture spacing values in descending order on the x-axis and plotted against cumulative number on the y-axis (Johnston et al., 1994, McCaffrey et al., 2003). These population distribution plots are the preferred method of describing fracture distributions (e.g. Walsh et al., 1991, Gillespie et al., 1993, Johnston et al., 1994, Pickering et al., 1995, Bonnet et al., 2001) as the data can be easily plotted and there is no need to divide the data into 'bin' sizes, the choice of which can be arbitrary.

Fracture attribute distributions (primarily fracture spacing in this thesis) are described using four main statistical distributions: normal, log-normal, exponential and power-law.



**Figure 1.18:** Methods used to analyse best-fit statistical distributions. **(a)** Table of data used to create the plots in (b), (c) & (d). **(b)** histogram. **(c)** Probability density function superimposed onto the histogram from (b). **(d)** cumulative frequency distribution plot. Note both the x and y axes are linear. (a), (b) and (c) are after Swan and Sandilands (1995); (d) is after Sleight (2001).

### 1.5.2.1 – Normal (or Gaussian) distribution

A normal distribution is used widely in the statistical analysis of probability distribution (Swan and Sandilands, 1995). A sample will have a normal distribution if it is unskewed and if the values are uniform and lie symmetrically around the mean value (bell-shaped curve on a histogram, *Figure 1.19*). The spread of the distribution (scale parameter) around the mean value is described by the variance and standard deviation. On a population distribution plot (cumulative frequency) normal distributions are represented by a slightly curved line on linear x and y axes (*Figure 1.19a*).

### 1.5.2.2 – Log-normal distribution

Geological variables do not often follow a normal distribution but instead follow a highly skewed probability density function. These skewed distributions are known as log-normal because if values on the x-axis are converted to logarithmic form, so that  $y = \log x$ , then the appearance of the distribution on a histogram is bell-shaped i.e. normal (*Figure 1.19*). On a population distribution plot, a log-normal distribution plots as a straight line, when the x-axis is plotted as a logarithmic scale and the y-axis is linear (*Figure 1.20b*). Fracture spacing distributions that exhibit log-normal distributions have been related to joint spacing distributions in sedimentary rocks (Narr and Suppe, 1991).

### 1.5.2.3 – Exponential distribution

When fractures are randomly spaced along a 1-dimensional sample line, the intersection points between the fractures and the scan-lines are described as random if there is no interaction between surrounding fractures (e.g. Priest and Hudson, 1976, Hudson and Priest, 1979, Einstein and Baecher, 1983). If each segment of a 1-dimensional line sample has a small but equal probability of being intersected by a fracture, the associated spacing values have an exponential distribution with a negative slope (Priest and Hudson, 1976, Hudson and Priest, 1979, Einstein and Baecher, 1983, Gillespie et al., 1993).

Exponential (random) distributions plot on histogram (*Figure 1.19*), with a probability distribution function of a steep slope that represents relatively more small values of spacing (and relatively fewer large values for spacing). On a population distribution plot exponential distributions are represented by a straight line when the x-axis (spacing) is on a linear scale and the y-axis is logarithmic (*Figure 1.20c*).

From an exponential population distribution plot, the slope of the line is known as the exponent. A high exponent value represents relatively large numbers of small spacing values and a low exponent represent relatively more large spacing values. The exponent value of exponential distributions can be used to compare spacing parameters across datasets. In this thesis 1-dimensional spacing samples that contain faults and fractures of varying orientation, typically exhibit exponential distributions.

#### **1.5.2.4 – Power-law distributions**

In recent years, power-law distributions have been increasingly used to characterise spatial characteristics of fracture networks (Bonnet et al., 2001) and many objects that occur naturally over a range of scale have been shown to have power-law relationships (Schroeder, 1991). If a fracture attribute dataset is described as having a power-law distribution, it implies that the fracture attribute (primarily spacing in this thesis) exhibits scale-invariance (or is fractal). This scale-invariance allows estimations of the fracture attribute parameters beyond the scale that the data was collected in.

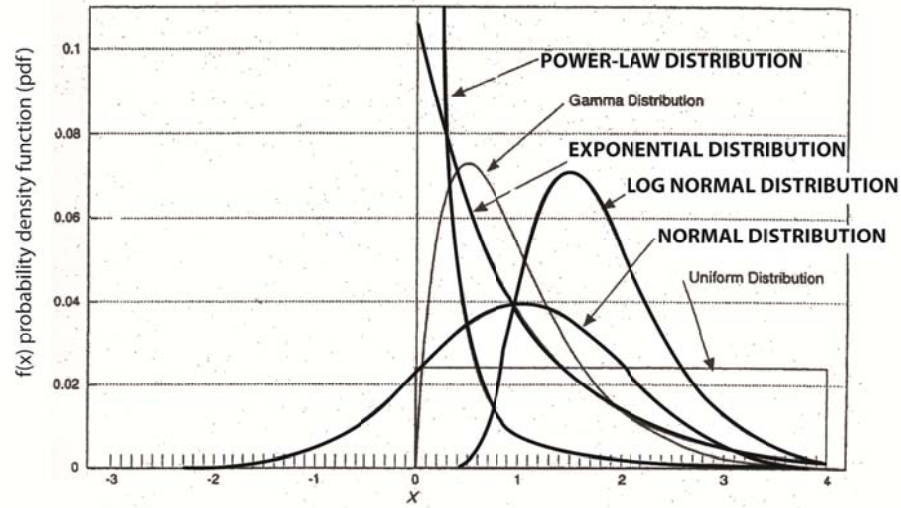
Self-similarity within fracture networks can be described using the concept of fractals. Fractal geometry (Mandelbrot, 1982, Turcotte, 1989) is a branch of mathematics that quantifies how the geometry of patterns repeats itself throughout a range of scales (Barton and La Pointe, 1995a). This theory of fracture geometry is used to study the scale-invariance of geological phenomena, including fault and fracture patterns. For a set of objects to exhibit a fractal geometry and show scale-invariance, the relative number of small and large elements (spacing values) remain the same at all scales between the upper and lower fractal limits (fractal dimension) (Barton and La Pointe, 1995b). It is important to note, however, that the term fractal should only be used to describe the spatial distribution of fractures (e.g. Mandelbrot, 1982, Odling et al., 1999, Bonnet et al., 2001), since the spatial correlation implied by the fractal geometry is independent of the distributions of fracture attributes such as spacing and length. Therefore, individual fracture attributes can be described as scale-invariant, but they cannot be fractal, as independently, they do not describe the spatial distribution of the fracture network.

On a population distribution plot, scale-invariant, power-law distributions are represented by a straight line when both the x and y axes are on a logarithmic scale (*Figure 1.20d*) with

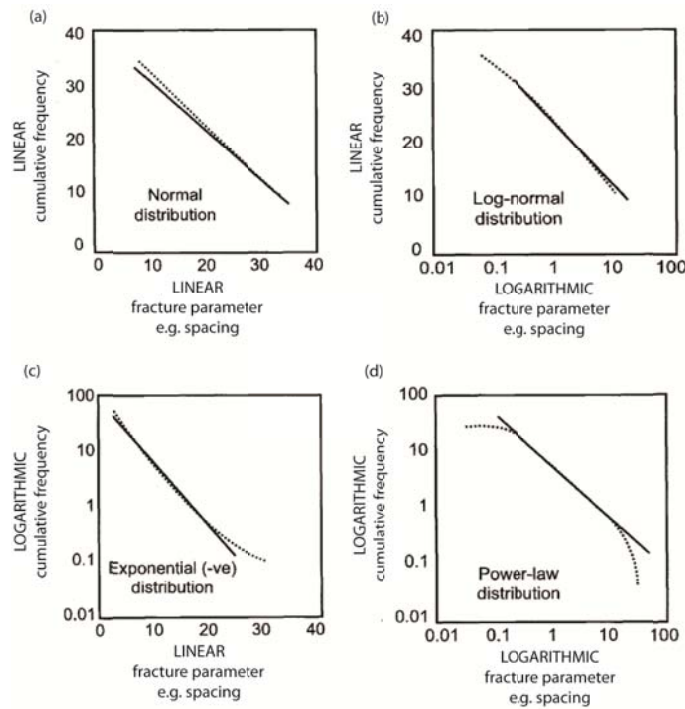
$$N_s \propto S^{-D} \quad (6)$$

Where  $S$  is the fracture spacing and  $N_s$  is the number of fracture spacings  $\geq S$ . The slope of the power-law distributions (the exponent or D-value) is a key parameter for describing a power-law distribution (Pickering et al., 1994, Pickering et al., 1995). This D-value provides a measure of the relative importance of large and small values (in this thesis the values are spacing). If the exponent is large, then there are more small values than there are for every large value.

This exponent is also interchanged by several authors with the fractal dimension which provides a measure of the clustering of structures in a sample. For example, low D-values represent larger spacing values and therefore tighter clusters in the dataset (Gillespie et al., 1993). The fractal dimension of a power-law relationship defines the scaling geometry of the fractal geometry and describes how an object fills the defined space. Fractal dimensions are typically non-integers as most objects (e.g. a fracture network) do not totally fill spaces (e.g. a 2-dimensional mapped area). Therefore fractal dimensions are typically not equivalent to Euclidean dimensions, which are 1 for a line segment (length), 2 for a square (area) and 3 for a cube (volume) (Turcotte, 1992). This means that 1-dimensional fractal dimensions fall between 0 and 1; 2-dimensional fractal dimensions are between 1 and 2 and 3-dimensional fractal dimensions are between 2 and 3.



**Figure 1.19:** Probability density functions for the different distributions possible with respect to geological datasets. In this thesis, only normal, log-normal, exponential and power-law distributions are considered.



**Figure 1.20:** Population distribution plots for the four main distributions possible in geological datasets. Solid line represents ideal datasets; dashed line represents typical 'real' datasets. **(a)** Normal distribution (linear-linear axes). **(b)** Log-normal distribution (log – linear axes). **(c)** Exponential distribution (linear – log axes). **(d)** Power-law distribution (log – log axes). Modified after McCaffrey et al. (2003).



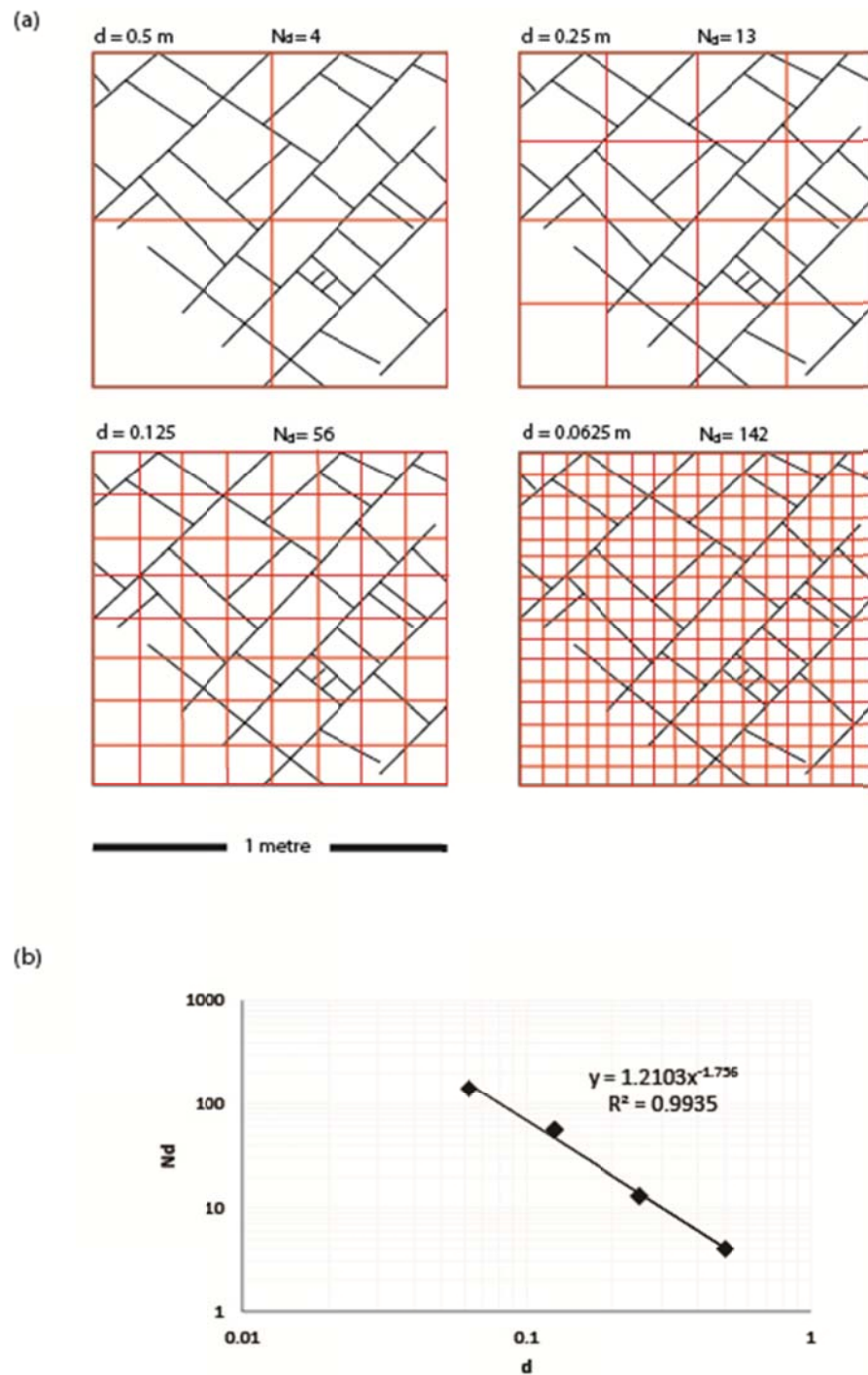
#### 1.5.2.4.1 – Box-counting

Fractal dimensions within fracture networks are most commonly determined using the box counting technique (Turcotte, 1992, Walsh and Watterson, 1993). This box counting technique was primarily developed to calculate the fractal dimension from 2-dimensional datasets but has been adapted to allow the determination of 3-dimensional fractal dimensions (Sanderson and McCaffrey, 2011). Grids of boxes (or cells) with a known side length ( $d$ ) are overlain on the fracture network map or (fracture volume) (*Figure 1.21a*) and the number of boxes containing fractures (or other geological features) are counted ( $N_d$ ). This is repeated for boxes of different sizes, and a graph of  $d$  against  $N_d$  is plotted on logarithmic axes (Liebovitch and Toth, 1989, Gillespie et al., 1993, Walsh and Watterson, 1993). Typically the largest box size used should be equivalent to the largest space between fractures in the dataset and the smallest box size should be equal to the length of the shortest fracture (Gillespie et al., 1993). If the geometry of the fracture network is fractal then the data points gathered from the box counting technique will fall on a straight line (*Figure 1.21b*). The slope of this straight line is the fractal dimension ( $D$ ), which for 2-dimensional datasets has a value of  $1 < D < 2$  (Gillespie et al., 1993).

Box counting is used within this thesis to assess the fractal dimension of fracture presence and fracture intersection models using terrestrial laser scan datasets (*Chapter 5*). The traditional technique has been slightly modified by Sanderson and McCaffrey, (2011) to allow the analysis of 2.5-dimensional terrestrial laser scan models in 2- and three-dimensions by reconstructing the outcrop and fracture data so that it fills the whole model area or volume. This is achieved by calculating the proportion of boxes containing fractures in each outcrop and multiplying it by the total number of boxes in the model, which are either in a model slice or in the full 3-dimensional volume. Typically this process should be conducted several times with various box sizes (in this thesis three model box sizes are used, see *Chapter 5*) and the resulting data points are plotted to determine the fractal dimension of the fracture sample.

#### 1.5.2.4.2 – Extrapolation of power-law distributions between scales

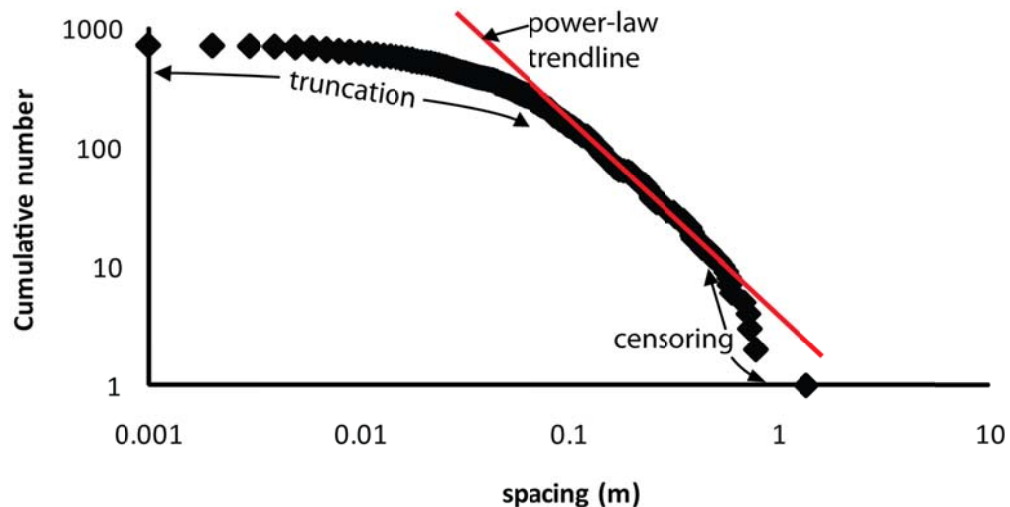
Typical power-law distributions plotted on a population distribution plot have three distinct segments: a shallow-sloping left hand section (due to truncation), a straight central section and a steeply-sloping right hand section (due to censoring) (*Figure 1.22*). The central segment determines the power-law distribution of the sample and therefore the data included within this portion are deemed scale-invariant and can potentially be used to estimate the attribute parameters above and below the sampling limits from this dataset. This central segment should extend over at least one order of magnitude before extrapolation is deemed to be reliable (Childs et al., 1990).



**Figure 1.21:** Illustration of the box-counting technique. (a) Fracture maps are overlain with grids of boxes of known side length ( $d$ ) and the number of boxes containing fractures is counted ( $N_d$ ). (b) Box size length is plotted against number of boxes containing fractures on logarithmic axes. If the fracture map is fractal then the data points plot as a straight line and the slope of the trend line is the fractal dimension.

The ability to extrapolate these scale-invariant power-law distributions is particularly useful in the oil industry where data are normally limited to large-scale seismic interpretations (kilometres to hundreds of metres) and small-scale core logging (centimetres to millimetres), and it is important to know what occurs between these two scales. Extrapolation of fracture data has been carried out by many authors (e.g. Knott et al., 1996, Needham et al., 1996, Odling and Roden, 1997, Sleight, 2001), which has enabled the distributions of fracture length, spacing and displacement to be determined over a large range of scales. It is important to note, however, that fracture scaling laws may have naturally occurring upper and lower limits due to variables such as lithology, unit thickness, fracture type or anisotropy (Sleight, 2001).

Ortega et al. (2006) state that in order for fracture spacing distributions (in terms of fracture intensity) to be truly scale-independent, fracture size also has to be quantified. This is because fracture intensity varies with changes in resolution because the number of fractures sampled will increase as the threshold size for fracture detection decreases, which produces fracture spacing results that vary depending on the resolution of the dataset. Not including fracture size analysis with the fracture spacing analysis potentially introduces a bias that reduces confidence in the scale-invariant power-law distributions that are used to extrapolate fracture spacing parameters over large scale ranges.



**Figure 1.22:** Population distribution plot illustrating the deviation of a power-law distribution caused by truncation and censoring. NB. Throughout this thesis only the section of data representing the power-law distribution are shown in figures. The full datasets are given in the associated appendices.

#### 1.5.2.4.3 – Extrapolation of power-law distributions between dimensions

The power-law exponents (D-values, slope of the power-law trend line) analysed for fracture networks in the onshore and offshore datasets of this thesis are mainly only collected in 1-dimension. Fracture networks are inherently 3-dimensional and therefore the spatial distribution data presented within this thesis is limited. Several authors have shown that the power-law exponent (and fractal dimension) for fracture populations collected in 1D will differ from 2- and 3-dimensional populations with fractures inherently underestimated in lower dimensions (e.g. Marett and Allmendinger, 1991, Marett, 1996, Borgos et al., 2000). In populations of well-samples, changing the sampling domain by 1 (e.g. from 1D to 2D) also changes the power-law exponent (D-value) by 1 (Mandelbrot, 1982, Marett and Allmendinger, 1991, Yielding et al., 1996, Borgos et al., 2000, Bonnet et al., 2001), but this relationship is unlikely to hold for fracture sets with strong spatial correlations and clustering (Borgos et al., 2000, Bonnet et al., 2001).

#### 1.5.2.4.4 – Factors affecting power-law distributions

The key factors that are known to affect power-law distributions are:

*Data quantity* – the number of data points in a sample must be large enough to provide a statistical representation of the whole population and have a good statistical fit to the theoretical power-law distribution (this also applies to other spacing distributions observed within this thesis). From the literature it is recommended that at least 50 fractures are sampled (e.g. Johnston et al., 1994) although over 200 fractures per sample would be preferable to determine an accurate power-law exponent (Bonnet et al., 2001). Collecting samples with these large numbers of data points is not always possible, especially at outcrop where the size of the sample is limited by the physical extent of exposure.

*Combining samples* - where data is sparse, data points from parallel 1-dimensional sample lines can be merged to form a larger dataset, which is known as multi-line sampling (Childs et al., 1990, Nicol et al., 1996). This type of sampling is not used in this thesis.

*Geological variables* such as lithology, pre-existing foliation or proximity to large faults may affect the sample characteristics (e.g. fractures in a shear zone may be

more clustered than fractures within the background area) (e.g. Knott et al., 1996, Nicol et al., 1996, McCaffrey et al., 2003).

*Reactivation* of a fracture system is likely to cause complexities in the sampled population, especially if the pattern and scale of the subsequent deformation events change the statistical properties of the system (e.g. Peacock and Sanderson, 1992, Yielding et al., 1996). It has been suggested by Vignes-Adler et al. (1991) that the greater the number of reactivation events in an area, the more random the fracture geometry will be which reduces the likelihood of a fractal fracture pattern (although this does not mean that the fracture attributes will not be scale-invariant).

#### 1.5.2.5 – Reliability of statistical fracture distributions

The majority of fracture network samples included in this thesis do not fit the statistical distributions described above exactly. Instead the data are described as ‘best-fit’ and normally it is reasonably easy to determine which type of statistical distributions is most appropriate for a given sample. This fitting is completed by eye and is therefore to some extent arbitrary. In order to check the reliability of the best-fit statistical distributions regression analysis is used ( $R^2$ ). The  $R^2$  value allows both rectilinear and curvilinear relationships to be tested. For power-law relationships, a linear regression is used, where a ‘best-fit’ straight line is drawn through the data points so that the deviation in the y-direction between the data points and the line is minimal.  $R^2$  (coefficient of determination) measures the amount of deviation of the data points from the ‘best-fit’ line. It can vary between 0 and +1, where +1 indicates a perfect fit of the data points to the regression line (see Microsoft Excel help manual for more information). Throughout the data analysis in this thesis,  $R^2$  values that are greater than 0.80 are understood to represent datasets that fit the determined statistical distribution well.

#### 1.5.3 – Coefficient of Variation (CV)

As well as producing population distribution plots to determine the statistical distribution that best describes the fracture spacing parameters within the onshore and offshore study areas, another statistical method was used. The coefficient of variation (CV) allows the clustering of 1-dimensional fracture data sets to be quantified (Johnston

et al., 1994). This statistical value is valid irrespective of whether or not the fracture datasets are considered to be fractal (or scale-invariant) and therefore it can be used to analyse all of the datasets included here.

The coefficient of variation is calculated by:

$$CV = \frac{SD(s)}{\langle s \rangle} \quad (7)$$

where SD is the standard deviation of  $s$ , the fracture spacing values calculated for a 1D sample and  $\langle s \rangle$  is the mean fracture spacing value (Christensen et al., 1992, Johnston et al., 1994). The coefficient of variation expresses the degree of clustering in the dataset so that randomly distributed fractures (best described by an exponential distribution) have standard deviation and mean values for spacing which are equal and therefore  $CV = 1$ . For fractures that are clustered,  $CV > 1$  and for those fractures that exhibit fracture spacing that are anti-clustered (uniformly distributed)  $CV < 1$  (Johnston et al., 1994).

## 1.6 – Data collection techniques and methodology

This section outlines the sampling techniques used in both the onshore and offshore study areas included in this thesis.

### 1.6.1 – Field mapping and sample collection

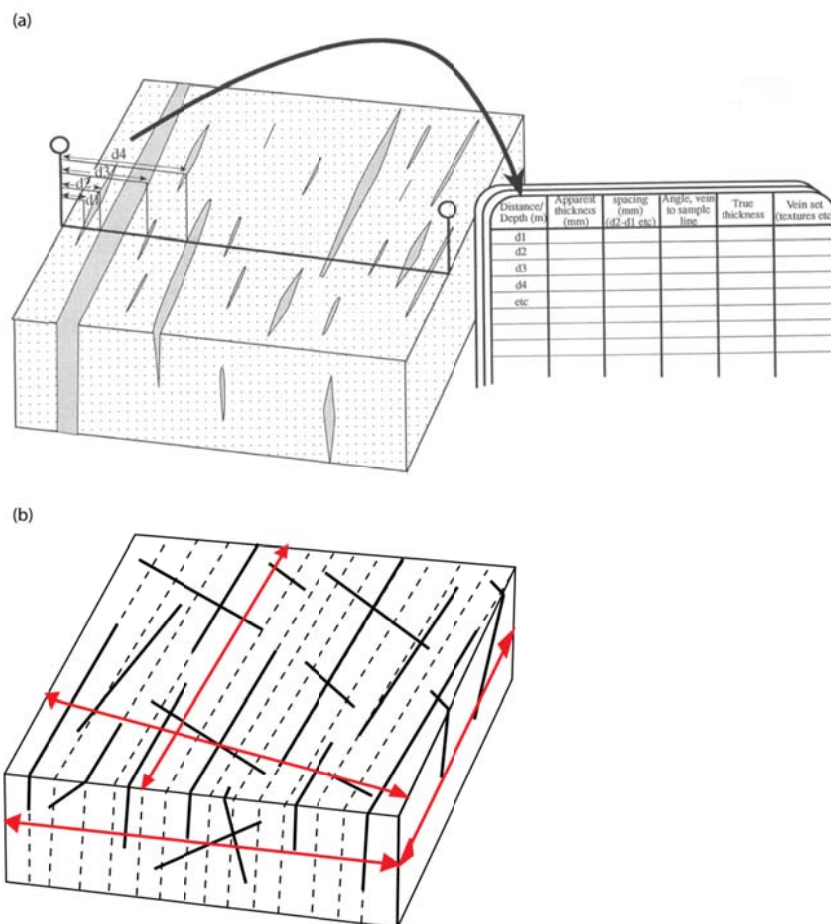
Two main field seasons were spent in NW Scotland: June-July 2008 and June-July 2009. These main field seasons were supplemented with shorter field trips with my industry sponsors and to collect the LiDAR datasets.

The first field season was spent sampling key outcrops in the Canisp Shear Zone, at Kinlochbervie, along the north coast and Lochinver using 1-dimensional line sampling techniques, collecting photo-mosaics and orientated (where possible) hand specimens for thin section work. The second field season was spent sampling other areas across the Assynt and Rhiconich Terranes that were deemed important from the first season and

industry fieldtrips. Time was also spent deciding on which key outcrops should be laser scanned for detailed fracture network analysis.

### 1.6.2 – Basement core logging

Approximately three weeks has been spent during this project logging lithology and fracturing within basement core samples from the Clair Field. 1-dimensional line sampling (*Figure 1.23a*) was utilised and a limited amount of core was collected for thin section analysis. The interpretation and analysis of fractures from the Clair basement core can be found in *Chapter 4*.



**Figure 1.23:** Schematic diagrams illustrating the 1-dimensional line sampling process. **(a)** Sampling strategy for collecting data from parallel vein/fracture sets. After Johnston et al. (1994). **(b)** Sampling strategy for outcrops where fractures do not form a parallel set. Where possible, sample lines have been taken parallel and perpendicular to foliation and across perpendicular cliff sections. The dashed line represents foliation.



### 1.6.3 – Onshore regional fault interpretation using NEXTMap® DEMs and aerial photographs

Onshore regional fault lineament sets were collected using NEXTMap digital elevation models (DEM) and interpreted on maps at 1:100,000, 1:50,000, 1:25,000 and 1:10,000 scales. Details of the DEM processing and fault lineament interpretation are presented in *Chapter 3*. The DEM analysis has also been supplemented with the interpretation of aerial photographs over key areas that were later analysed using LiDAR data at 1:5,000 scales. These onshore regional datasets were collected and processed at the British Geological Survey offices in Edinburgh.

### 1.6.4 – Offshore regional fault interpretation using a 3D seismic volume

The Clair field seismic volume analysis was conducted in the ConocoPhillips (U.K.) Ltd offices in Aberdeen. Pre-interpreted seismic horizons (BP interpretation) were used to create horizon attribute maps for the main basement and cover sedimentary units as there was no time to re-interpret the horizons myself. Also as the datasets gathered from this analysis and the rest of the project are to be given to the industry sponsors, it was deemed more reasonable to use their already agreed horizon interpretations so that my fault lineament interpretation could be used to enhance their existing understanding of the Clair Field fracture and fault networks. Horizon attribute maps were created and fault lineaments interpreted at 1:100,000, 1:50,000 and 1:25,000 scales. Details of the seismic horizon attribute map creation and fault lineament analysis can be found in *Chapter 4*.

### 1.6.5 – 1-dimensional line sampling

Much of the fracture data presented in this thesis was collected using a variety of different 1-dimensional line samples (also known as line transects traverses and scanlines). During fieldwork these 1D line samples were used to collect a variety of fracture attribute data including orientation, spacing, aperture, length, host rock lithology, fault rock lithology, slickenlines, displacement and cross-cutting relationships (*Figure 1.23a*). The outcrop data gathered using these 1D line samples form the basis of the majority of statistical analysis presented from fieldwork in this thesis. This sampling technique was also used with Clair basement core samples with 1D line samples taken parallel to the long axis of each core section.

Similar 1D sample lines have been utilised across the regional onshore and offshore datasets and across the LiDAR datasets in the form of *pseudo-wells*. These pseudo-wells only provide information on fault lineament azimuth and spacing, but this is sufficient to be able to make comparisons with smaller-scale datasets and to assess the validity of extrapolating spatial distributions determined from outcrop or core samples to a more regional scale.

The advantages of this 1D sample line method include:

- (a) The data is easy to collect, analyse and visualise.
- (b) The same sampling technique can be applied to outcrops and core samples to provide direct comparisons between the two study areas (McCaffrey et al., 2003).
- (c) Creating pseudo-wells across the regional datasets provides a quick and relatively automated method for collecting fault lineament orientation and spacing attributes.

Disadvantages include (Sleight, 2001, McCaffrey et al., 2003):

- (a) Problems occur when extrapolating the data across different dimensions.
- (b) Exposure often limits the size of the samples and can make it difficult to collect enough data points to obtain a statistically significant dataset (this is particularly relevant in areas of low fracture density). (*Section 1.4.1.4.3*).
- (c) Fracture spacing (and fracture density) can vary depending on the orientation of the line sample relative to the fracture orientations. For example, fractures that occur sub-parallel to the sample line will be under-represented. This problem can be overcome by taking 1D line samples in a variety of different orientations across each outcrop to ensure that every fracture orientation is sampled (*Figure 1.23b*). Where possible sample lines are taken perpendicular to the main fracture sets.
- (d) Using this method in the field is very time consuming.

#### 1.6.6 – Optical microscopy

Thin section analysis using an optical microscope has been utilised to supplement both fieldwork and core logging exercises. Where possible, orientated thin sections were prepared for samples of fault rocks and for the host lithologies. Optical microscopy has been used primarily to identify mineralogy, fault rock textures and possible deformation mechanisms. This analysis has also been used to allow identification of different deformation events during the evolution of large faults and fracture networks.

A side project analysing the fracture spacing distributions within thin sections from the mainland Lewisian has been conducted by Miss Rowan Vernon and this supplementary study is provided in *Appendix A*.

#### **1.6.7 – Terrestrial laser scanning (LiDAR)**

To allow detailed analysis of the fracture networks associated with key structural settings in the mainland LGC, a terrestrial laser scanner was used. The gathered LiDAR datasets from the Canisp Shear Zone (Alltan na Bradhan), Kinlochbervie and Caolas Cumhann have provided high-resolution virtual outcrop models that have then been interpreted to create fracture network models for each of these outcrops.

Principally these outcrop models are described as 2.5-dimensional datasets as they are typically irregular surfaces that occupy a greater proportion of a space than a 2D plane but they are inherently more limited than a volumetric dataset that samples the inside of an outcrop (Jones et al., 2008b). Within the confines of this thesis the fracture network interpreted from the virtual outcrops are also described as 2.5-dimensional as no extrapolation of the fractures out with the outcrop surface is conducted.

These fracture model data have been analysed to provide more 1-dimensional information on fracture spacing and 2- and 3-dimensional fractal values describing fracture presence and fracture intersection occurrence. The primary purpose of this analysis was to provide quantitative assessments of fracture networks in different structural settings that could be directly implemented into industry Clair basement modelling. Details of the processing and analysis involved in the creation of deterministic fracture network models from Lewisian outcrops can be found in *Chapter 5*.

### 1.7 - Collaboration

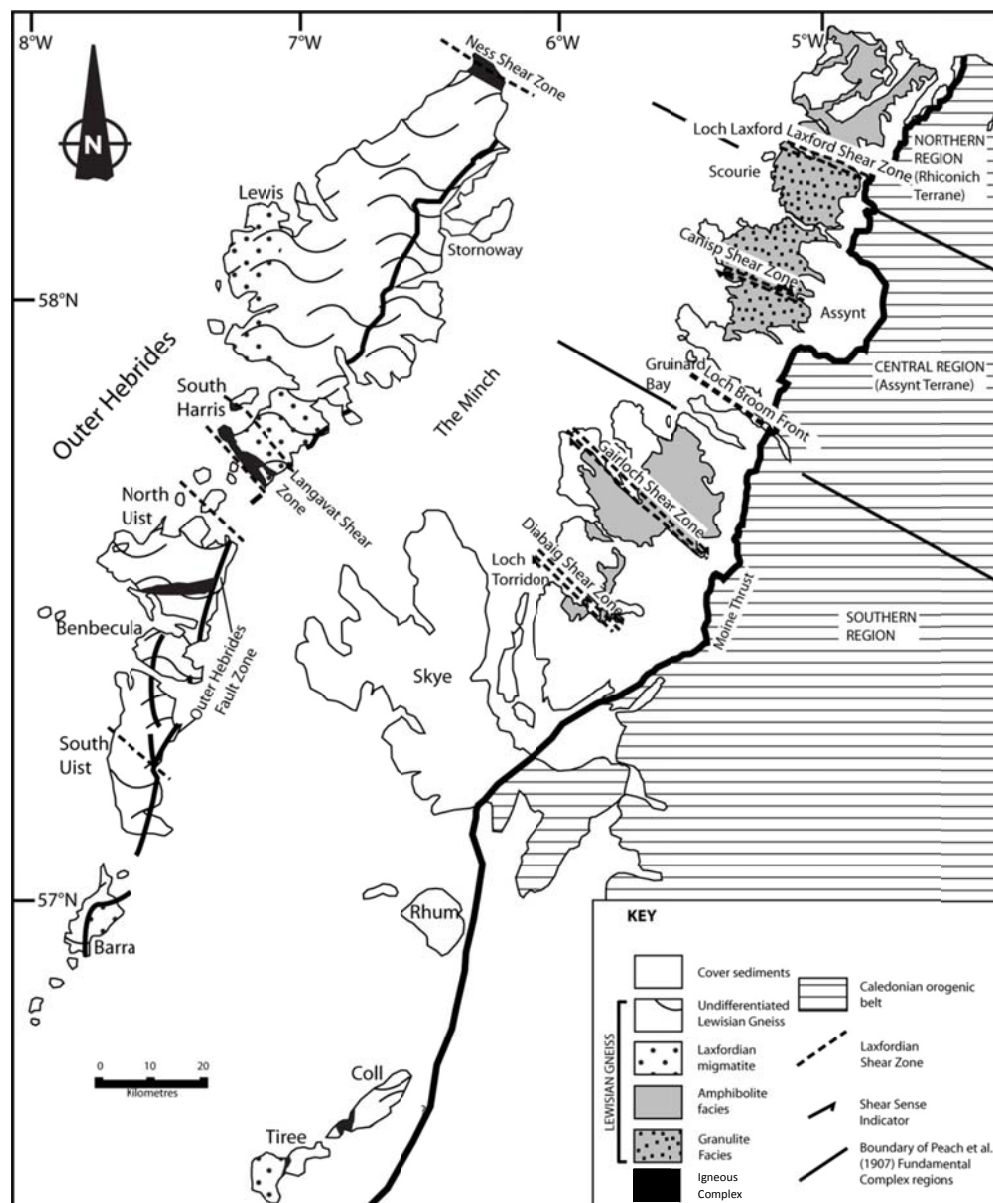
This project has been conducted with support and data from the Clair Joint Venture and the British Geological Society. Regular communication and updates between me and the Clair Joint Venture partners have taken place in the form of update meetings; both in Durham and Aberdeen and industry fieldtrips to the mainland LGC and also the Outer Hebrides. This project has been followed by and run in conjunction with another PhD project by Ben Franklin (Durham University, 2012) who is examining the controls and characteristics of fracture networks in the Lewisian and overlying sedimentary units of the Inner and Outer Hebrides. His work supplements the work presented in this thesis providing even more valuable structural information that can be utilised by the Clair Joint Venture to fully understand the fault and fracture networks in the Clair Field basement and cover sediments. This research is becoming more relevant due to the recent approval (October 2011) of a £4.5 billion development programme of the Clair Ridge area (and southwest Clair) where the basement plays a more prominent role.

## **Chapter 2 – Introduction to the geology of the NW Highlands and the Clair Field**

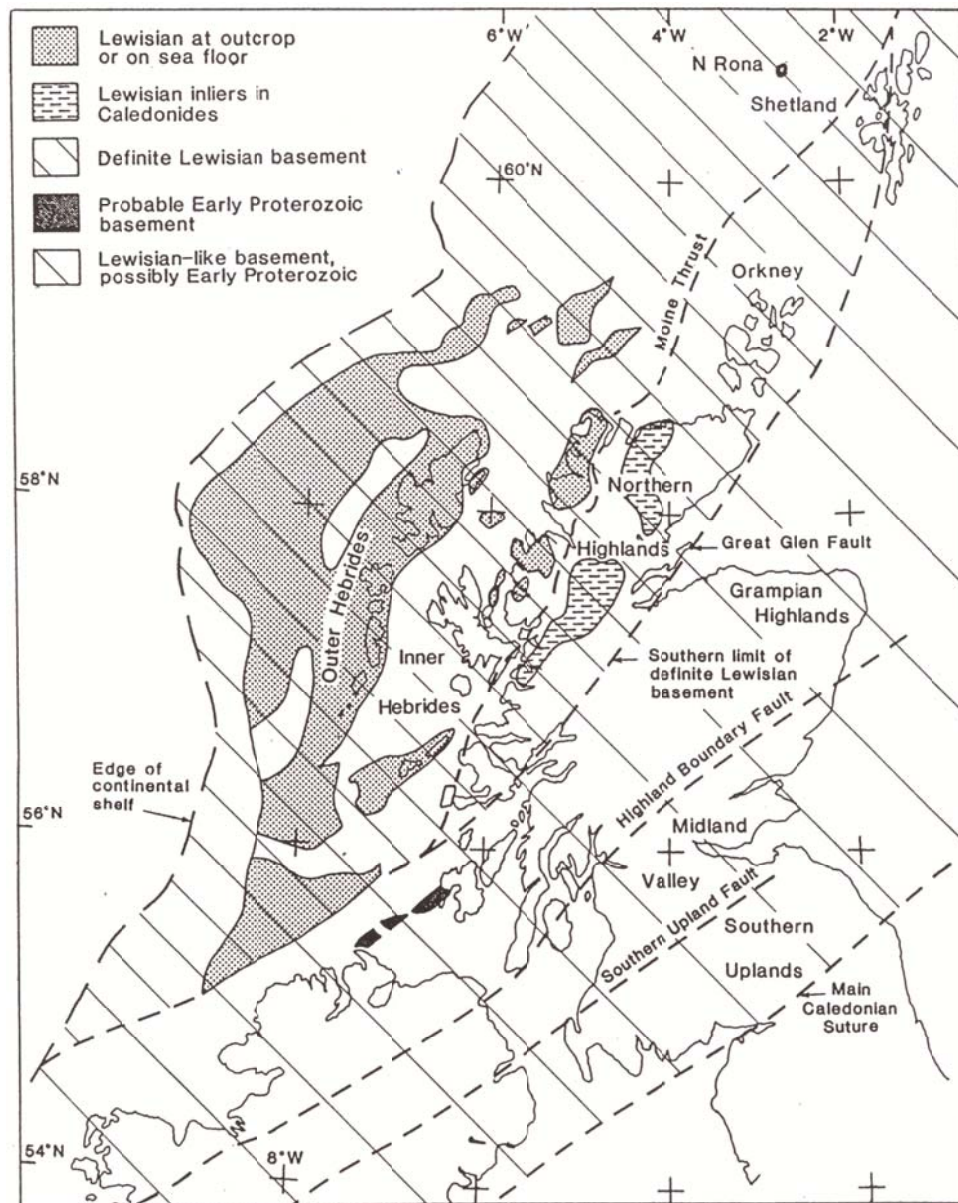
### **2.1 – Introduction to the Lewisian Gneiss Complex**

The main Lewisian Gneiss Complex (LGC) outcrops lie in the Caledonian foreland at the western edge of northern mainland Scotland (*Figure 2.1*). It forms an elongate region, approximately 650km<sup>2</sup>, of Archaean rocks that extend from Cape Wrath in the north to Loch Torridon in the south. The Lewisian also forms a large part of the Outer and Inner Hebrides (*Figure 2.1*). It also crops out in Shetland and within younger Precambrian Moine rocks east of the Moine Thrust where it forms tectonically emplaced basement inliers in the Caledonian orogenic belt (Park et al., 1994). It has been suggested from offshore deep seismic profiles (e.g. Hall, 1987) that the Lewisian Complex extends out to the edge of the continental shelf in the NW (*Figure 2.2*) and SE to at least the Great Glen Fault (Bamford et al., 1978, Dunning, 1985, Rollin, 1994, McBride and England, 1994).

The LGC is, for the most part, Archaean to Proterozoic gneissose basement rocks that have undergone granulite facies metamorphism followed, in some areas, by amphibolite facies retrogression. These crystalline basement rocks are unconformably overlain by a range of sediments that are Late Proterozoic (Torridonian) to Mesozoic in age, which partially obscure the complex in many areas. The nature of distribution of Lewisian rocks is thought to be largely controlled by extensional faults that formed basins (e.g. Minch Basin and the West Orkney Basin) in the Mesozoic and Early Cenozoic, off the northern coast of Scotland (e.g. Roberts and Holdsworth, 1999).



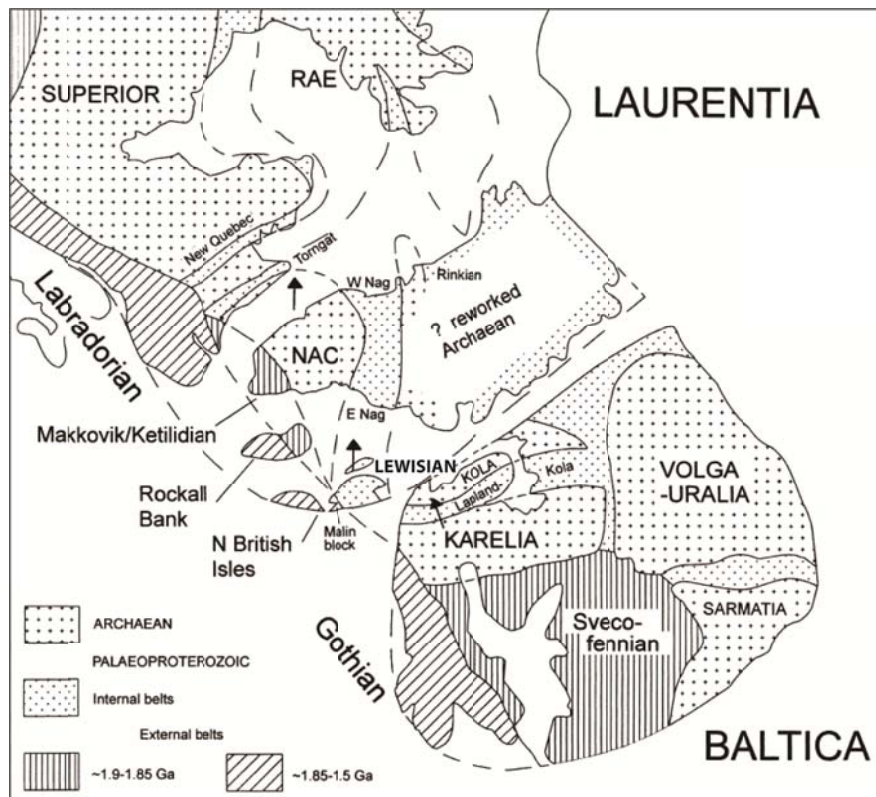
**Figure 2.1:** Simplified map of the NW Highlands of Scotland, west of the Moine Thrust showing the distribution of the Lewisian Gneiss Complex. It includes the classical subdivision of the Fundamental Lewisian Complex as first described by Peach et al. (1907). Modified after Park et al. (1994).



**Figure 2.2:** The distribution of the Lewisian Gneiss Complex across NW Scotland and its extension onto the continental shelf. After Dunning (1985).

### 2.1.1 – Regional setting

Regionally, the LGC is only a small fragment of a much larger early Proterozoic belt, that links the Canadian Shield (Churchill Province) (*Figure 2.3*) to Greenland (Ammassalik (Nagssugtoqidian) belt) and to Finland and Sweden (Svecokarelian belt (e.g. Park, 1994, Myhre et al., 2011). Even though the Lewisian is only a tiny part of this Proterozoic belt, the ease of access and quantity of outcrops makes it the most studied region across the whole belt. In Greenland, the Lewisian has been linked to the Ammassalik belt where there are similarities in rock ages and compositions (e.g. Myers, 1987, Kalsbeek et al., 1993). This is also true for the Cape Smith and Labrador belts of the Churchill province and the Svecokarelian belt, where rocks similar to the Loch Maree Group also occur (Johnson et al., 1987, Floyd et al., 1989, Whitehouse et al., 1997, Myhre et al., 2011).



**Figure 2.3:** Reconstruction of the North Atlantic Proterozoic belts and Archaean cratons at 1.265 Ga. Arrows represent the main tectonic movement (Park, 1994). NAC – North Atlantic Craton, E Nag and W Nag are the east and west portions of the Nagssugtoqidian Belt, respectively. After Buchan et al. (2000).



### 2.1.2 – The history of the Lewisian Complex

The Lewisian Gneiss Complex was first recognised and subdivided by Peach et al. (1907) into three regions; Northern (Cape Wrath to south of Loch Laxford), Central (Near Scourie to Loch Broom) and Southern (Gruinard Bay to Loch Torridon) (*Figure 2.1*). In the central region the gneisses were considered to be relatively unmodified compared to both the Southern and Northern regions where severe modifications of the so-called 'Fundamental Complex' were recorded (Peach et al., 1907).

This simple subdivision has been further developed and modified by subsequent research into the formation and genesis of the LGC (see *Table 2.1* for a summary of the developing understanding of the LGC). At its heart lies the proposal that the rocks of the LGC comprise a single crustal unit with the same ancient protolith that has then been heterogeneously reworked during a succession of younger events during the Archaean and Proterozoic. More recently, however, U-Pb single zircon geochronology has suggested that the LGC in fact comprises a series of disparate terranes that were assembled during the Proterozoic (e.g. Kinny and Friend, 1997, Friend et al., 2001, Kinny et al., 2005). This terrane model is discussed in the following section.

### 2.1.3 – The Terrane Model

The hypothesis that the LGC comprises a series of terranes was first proposed by Kinny and Friend (1997) using SHRIMP U-Pb single zircon ages to date different lithologies and events within the various LGC regions (Northern, Central and Southern). The results suggest that the protolith ages of gneisses in the Northern region (2800-2840 Ma) are significantly younger than protolith ages in the Central region (2960-3030 Ma, *Figure 2.4*), suggesting that the Northern region does not comprise reworked rocks from the Central region. Consequently, Kinny and Friend (1997) propose that the classical single terrane regional model used to explain the evolution of the LGC needs to be replaced. In later papers, the same authors propose a terrane-based nomenclature for the LGC based on other zircon ages, lithological and metamorphic variations (Friend et al., 2001, Kinny et al., 2005) (*Figure 2.4*). *Table 2.2* summarises the age and main characteristics of the suggested terranes across the mainland LGC (for details of proposed terranes in the Outer Hebrides see Kinny et al. (2005).

Author	Summary of the Lewisian subdivision
Peach et al. (1907)	Older acid gneisses of the FUNDAMENTAL COMPLEX are described as being intruded by basic and ultra-basic masses (e.g. Scourie dykes). The fundamental complex is divided into three regions, with the Central region containing relatively unmodified granulite-facies gneisses. Both the Northern and Southern regions comprise gneisses modified by early-granulite to amphibolite facies metamorphism. These modifications were defined as PRE-TORRIDONIAN as they did not affect the sedimentary cover.
Sutton and Watson (1950)	Subdivided the FUNDAMENTAL COMPLEX into older deformation which was termed SCOURIAN deformation and a younger re-working event (post-Scourie dyke) called the LAXFORDIAN.
(Tarney, 1963) (Park, 1964) (Evans and Tarney, 1964) (Evans, 1965b) (Evans and Lambert, 1974)	A major tectono-metamorphic event that occurs post-granulite/amphibolite metamorphism and pre-Scourie dyke emplacement was recognised and termed the INVERIAN (Evans, 1965b). It is only possible to identify Inverian structures, where cross-cutting Scourie dykes are present, as it has similar structural styles and geometry to the previously identified LAXFORDIAN event.
(Park, 1970)	Suggestion that the previously defined SCOURIAN deformation was subdivided into an early BADCALLIAN deformation event and the later INVERIAN event. The intervening break is considered to coincide with the Archaean-Proterozoic boundary.
Subsequent studies have assigned deformation and metamorphic events to these broad subdivisions.	

**Table 2.1:** Historical division of the LGC tectono-metamorphic stratigraphy. Modified after Beacom (1999).

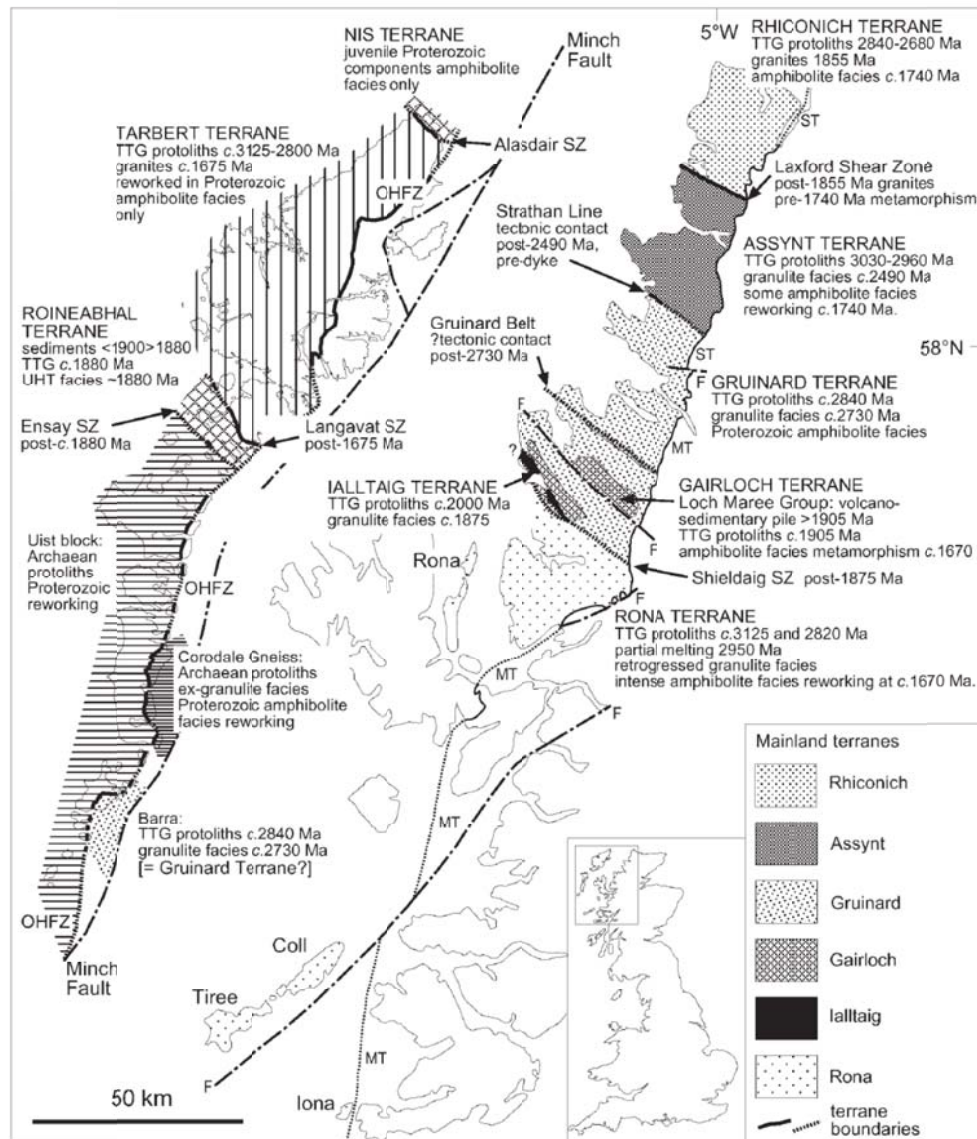
The model presented by Kinny et al (2005) suggests that the recognised terranes fall into two groups: reworked Archaean continental crust terranes and Palaeoproterozoic juvenile arcs. They suggest that most terrane boundaries coincide with already recognised shear zones (*Figure 2.4*), such as the Laxford Front, and that these zones separate diverse packages of lithologically and geochronologically distinctive rocks. This means that they fit the Coney et al. (1980) definition of terranes. Kinny et al. (2005) also state that there is evidence that the terrane boundaries formed

in transcurrent settings, suggesting significant lateral movements between adjacent terranes during their assembly.

Although this terrane model rationalises the confusing terminology and somewhat oversimplified view of the classical LGC subdivisions, some reservations expressed by Park (2005, 2005) concerning the use of terrane to describe the crustal blocks present within the LGC. Park (2005) suggests that differences in the geological history between two adjacent pieces of crust may not constitute sufficient evidence for large displacements between them. The lack of evidence of subduction between adjoined terranes is noted by Kinny et al (2005) and therefore Park (2005) suggests that the lack of evidence of subduction means that it is unlikely that adjacent terranes in the LGC experienced large relative displacements. Park (2005) therefore proposes that the terranes identified by Kinny et al. (2005) should be referred to as 'suspect terranes', or preferably, crustal blocks. Wheeler et al. (2010) suggest that there is no doubt that large relative movements occurred during the evolution of the LGC (e.g. during the Laxfordian, *Section 2.1.4.5*); but that there is no explicit need for these displacements to occur along specific boundaries in order to explain the current geochronological, structural and metamorphic datasets.

Other work, focussed on the Laxford Shear Zone (Laxford Front) agree with Kinny et al. (2005) that this shear zone is a potential terrane boundary, but state that many more questions need to be answered about the origin, displacement and kinematics of the Laxford Shear Zone before it can confidently be assigned terrane boundary status (Goodenough et al., 2010).

The terrane nomenclature and the proposed boundary (Loch Laxford Front) between the Assynt and Rhiconich terranes are used within this thesis to differentiate between rocks of different lithologies, metamorphism and deformation history in the southern and northern regions of study area used in this project (this however does not mean that the terrane model of Kinny et al. (2005) is accepted outright in this thesis). For the purposes of the onshore analysis, only the Assynt and Rhiconich Terrane are considered. This is for two main reasons: they are the most northerly of the proposed LGC terranes on the Scottish mainland and they represent the largest variations in lithology, tectono-metamorphic history and fracture network characteristics of any of the mainland terranes and therefore provide two end member datasets for comparison with the offshore Clair basement datasets.



**Figure 2.4:** Sketch map of the LGC depicting the locations of the proposed terranes. Inset shows the location of the LGC within northwest Scotland. ST - sole thrust of the Moine Thrust Zone. MT - Moine Thrust. OHFZ - Outer Hebrides Fault Zone. SZ - shear zone. After Kinny et al. (2005).

Terrane name	Protolith Age	Summary of Characteristics
Rhiconich terrane (Friend et al., 2001)	2840-2800 Ma	Bounded to the south by the Laxford Shear Zone. Comprises TTG gneisses, mafic and metasedimentary enclaves, Scourie dykes (emplaced prior to 1855 Ma) and pink granites (c. 1855 Ma). Laxfordian deformation is present (c. 1740 Ma (Corfu et al., 1994, Kinny and Friend, 1997)) which comprises amphibolite-facies metamorphism.
Assynt terrane (Friend et al., 2001)	3030-2960 Ma	Area between the Laxford Shear Zone and the Strathan Line (Evans and Lambert, 1974). Comprises granulite-facies TTG gneisses that have been retrogressed by younger events. These include Badcallian (2490-2480 Ma), Inverian (2490-2400 Ma), Scourie dyke emplacement (2400-2000 Ma) and Laxfordian (1740 Ma).
Gruinard terrane (Love et al., 2004)	c. 2860 Ma and 2825 Ma	South of the Strathan Line to the Gruinard Belt. Comprises TTG gneisses that underwent granulite-facies metamorphism in a pre-Badcallian event (c. 2730 Ma (Love et al., 2004)). Subjected to Inverian deformation (2490-2400 Ma) and Scourie dyke emplacement.
Gairloch terrane (Kinny et al., 2005)	>1905 Ma	Located between the Gruinard Belt and the Shildaig Shear Zone. Comprises Loch Maree Group sediments (> 1905 Ma), calc-alkaline granitoid sheets (c. 1905 Ma) and pegmatites (c. 1695 Ma (Park et al., 2001)).
Ilataig terrane	c. 2000 Ma	Shear-bounded block at Loch Shildaig. Comprises TTG gneisses (c. 2000 Ma) that underwent granulite-facies metamorphism (c. 1877 Ma (Park, 1964)). Not juxtaposed with the Loch Maree Group (Gairloch terrane) until after c. 1877 Ma.
Rona terrane	c. 3135 Ma and 2880 Ma	South from the Shildaig Shear Zone through the Torridon area. Includes the islands Raasay, Rona, Coll and Tiree. Comprises TTG gneisses (3135 Ma and c. 2880 Ma (Love et al., 2004)) and Scourie dykes. Amphibolite-facies occurred at c. 2955 Ma (Love et al., 2004).

**Table 2.2:** Summarising the characteristics and protolith ages of the mainland terranes proposed by Kinny et al. (2005). See *Figure 2.4* for the positions of the above terrane within northwest Scotland.

#### 2.1.4 – Regional geology of the mainland Lewisian Gneiss Complex

The Northern region (or Rhiconich Terrane as it is referred to in this thesis, see *Figures 2.1 & 2.4*) represents a belt where the original Archaean gneisses including granular hornblende-gneisses and biotite-gneisses (Peach et al., 1907) have been subjected to Laxfordian deformation and amphibolite-facies metamorphism (Park et al., 1994). This Rhiconich Terrane is separated from the Central Region, the northern section of which (*Figure 2.4*) is referred to as the Assynt Terrane in this thesis, by the Laxford Shear Zone which is an Inverian-Laxfordian-age shear zone, several kilometres wide, where the original Scourian (granulite-facies) gneisses are separated from gneisses typical of the Rhiconich Terrane (e.g. Evans and Tarney, 1964, Davies, 1976, Coward and Park, 1987, Goodenough et al., 2010).

The Assynt Terrane primarily comprises grey granulite-facies Badcallian gneisses that exhibit localised steeply-dipping NW-SE belts of Inverian and Laxfordian reworking, i.e. in the Canisp Shear Zone (Evans, 1965a, Attfield, 1987). These relatively unmodified rocks are intruded by mafic and ultramafic Scourie dykes, which have a general trend of NW-SE to E-W (Park et al., 1994). Scourie dykes are important time markers within the LGC and separate the deformation that occurred pre-emplacement (Badcallian and Inverian; (Evans and Lambert, 1974, Park, 1970) and the deformation that occurred post-emplacement (Laxfordian (e.g. Sutton and Watson, 1950)) (see *Section 2.1.4.1* for more details on the Scourie dyke suite).

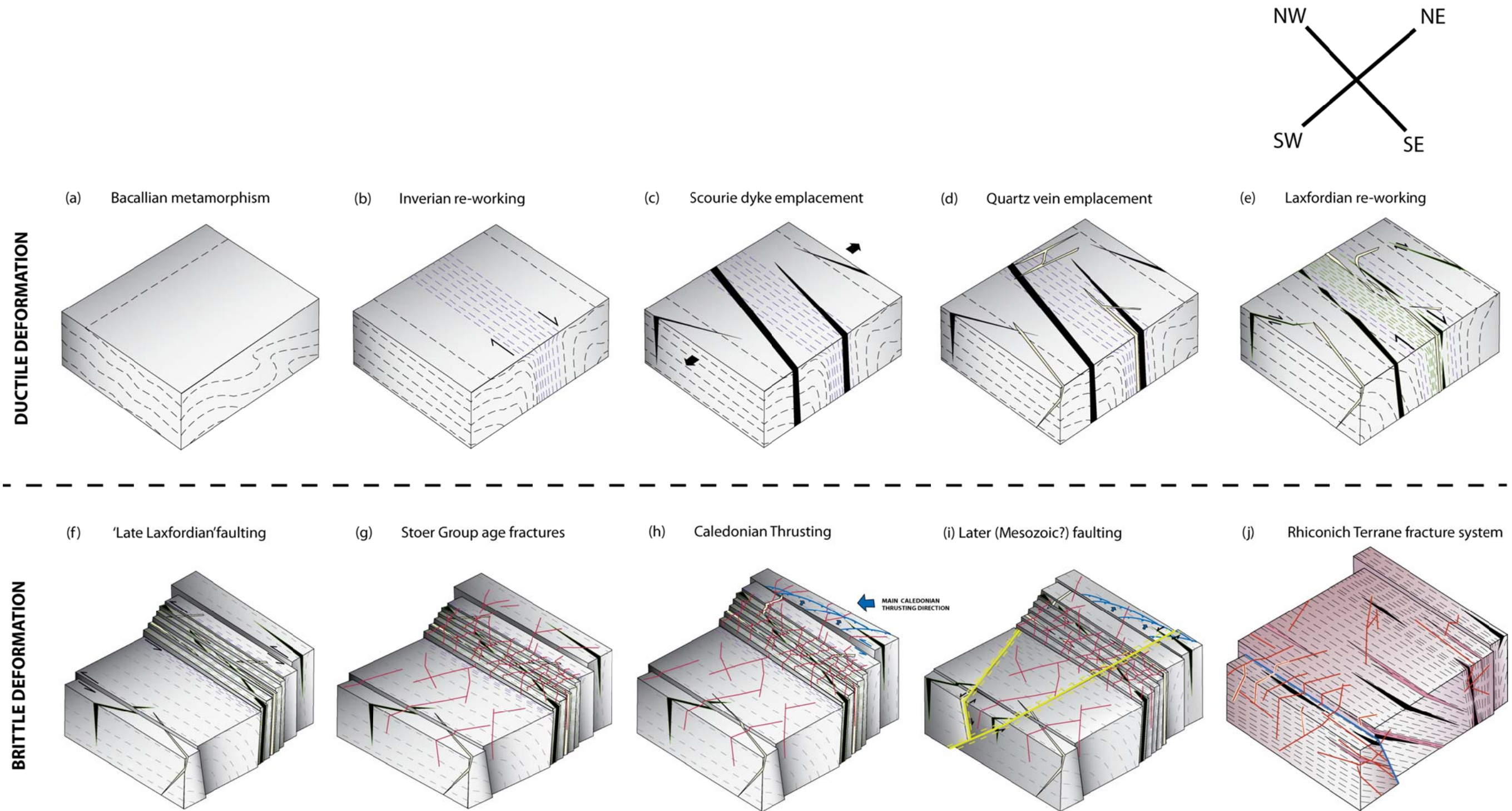
The Southern region (not visited in this thesis) includes LGC rocks on the islands of Raasay, Rona, Iona, Coll and Tiree (*Figure 2.1*) and comprises upper amphibolite-facies biotite-gneiss, hornblende-gneiss and pyroxene-gneiss (Peach et al., 1907, Park et al., 1994). A small region of metasedimentary and metavolcanic sequences (Loch Maree Group) also occurs as an integral part of the LGC (Sutton and Watson, 1950). This Southern Region is separated from the Central region by an 8km wide transitional zone in which intense deformation and amphibolite-facies metamorphism has significantly altered the original Archaean gneisses (Park et al., 1994). Scourie dykes in the Southern region are relatively unaffected by Laxfordian deformation which is mostly restricted to the Gairloch and Diabaig Shear Zones (Evans, 1965b, Cresswell and Park, 1973, Attfield, 1987, Wheeler et al., 1987, Beacom, 1999).

Deformation and metamorphism that occurred pre-Torridonian in the LGC is summarised in *Table 2.3* and *Figure 2.5* and is discussed in more detail in *Sections 2.1.4.1 to 2.1.4.5*.

Ma (≈)	Event	Kinematics
2900 - 2490	BADCALLIAN granulite-facies metamorphism and deformation. <b>NE-SW Shear Zones</b>	Folding and sub-horizontal thrusting
2490 – 2400	INVERIAN amphibolite-facies metamorphism and deformation <b>Steep NW-SE Shear Zones</b>	<b>Dextral transpression</b> (north up thrusting with small dextral component)
2400 - 1900	Emplacement of Scourie Dyke Swarm. <b>NW-SE to E-W trending.</b> Loch Maree Group deposition	<b>Dextral transtension</b>
1900-1800	Early-LAXFORDIAN amphibolite-facies metamorphism and deformation <b>NW-SE Shear Zones</b>	<b>Dextral transtension</b> (on oblique shears and asymmetric shear folds)
1600	Mid-LAXFORDIAN lower amphibolite-facies metamorphism and deformation <b>NW-SE Shear Zones</b>	<b>Dextral transpression</b> (north up over-thrusting and upright folds)
1400	Mid-LAXFORDIAN upper greenschist-facies metamorphism and deformation <b>NW-SE Shear Zones</b>	<b>Dextral transpression</b>
1400 - 1150	Late LAXFORDIAN lower greenschist-facies metamorphism and deformation <b>NW-SE Shear Zones</b>	<b>Sinistral Strike-Slip</b> (steeply plunging asymmetric folds and crust belts)
1200	Pre-Torridonian brittle deformation <b>NW-SE trending faults</b>	<b>Oblique extension</b>

**Table 2.3:** A summary of the mainland Lewisian structural and metamorphic chronology before the deposition of the Torridonian Succession. Modified After Beacom (1999).





**Figure 2.5:** Schematic block diagrams illustrating the ductile and brittle deformation history of the mainland Lewisian from the Late Archaean through to the Mesozoic. The Rhiconich Terrane exhibits a different brittle deformation history to the Assynt Terrane. These differences in fracture system are shown in part (j) where there is little evidence of the reactivation of well-developed foliations and hematite stained fractures can be attributed to percolation of fluids through the Torridon Group sediments. These block diagrams are not drawn to scale.



#### 2.1.4.1 – Badcallian gneisses

The LGC of the Central region (Assynt Terrane) is predominately comprised of Archaean high-grade metamorphic TTG (tonalite-trondhjemite-granodiorite) banded or massive gneisses (Sheraton et al., 1973a) which are believed to have igneous (plutonic) origins, i.e. they are orthogneisses (Peach et al., 1907, Weaver and Tarney, 1980, Tarney and Weaver, 1987, Barnicoat, 1987, Rollinson and Fowler, 1987, Goodenough et al., 2010).

Early granite sheets are occasionally incorporated into the gneisses, and there are numerous m to km-scale mafic and ultramafic bodies (Peach et al., 1907, Bowes and Ghaly, 1964, Whitehouse, 1989). Peach et al. (1907) first described these mafic bodies and recognised that some of them predated the surrounding TTG gneisses. Subsequent authors have interpreted these older mafic bodies to be remnants of subducted oceanic slab (e.g. Park and Tarney, 1987, Rollinson and Fowler, 1987). Wheeler et al. (2010) suggest that these old mafic rocks are important as they may represent the TTG source rock; which form as a product of the partial melting of a basaltic precursor (Rollinson, 2006, 2007). The LGC also contains small amounts of metasedimentary, semi-pelitic (Cartwright and Barnicoat, 1987) and kyanite-bearing (Bikerman et al., 1975) gneisses that may be associated with the mafic/ultramafic bodies, although it is unclear if they are an original part of the Lewisian complex (Park et al., 1994).

The earliest deformation that affected the Lewisian gneisses was termed the Badcallian (*Figure 2.5a*) which had been dated at  $\geq 2710$  Ma using U-Pb isotopic relationships (Corfu et al., 1994). This Badcallian deformation is best preserved in the Central Region and is characterised by granulite-facies metamorphism and poorly-defined structures including sub-horizontal foliation and intrafolial folds (Sheraton et al., 1973b). Potassium-rich pegmatite veins that are dated between 2450 Ma and 2310 Ma (Evans and Lambert, 1974) provide stratigraphic markers that separate the Badcallian and Inverian deformation events (see *Section 2.1.4.2* for a discussion of the Inverian).

The Badcallian gneisses of the mainland LGC are extremely heterogeneous, with varied ages and geobarometry (Whitehouse, 1989), which may reflect a period of crustal (or terrane) accretion that spanned approximately 310 Ma (from LGC protolith U-Pb isotopic ages presented in Kinny et al. (2005) and references therein). Alternatively, the recorded variations in geobarometry and therefore formation pressure (and temperature) may reflect the variation in origin of the Badcallian gneisses from mid-

crustal levels in the Central region (Scourie) to shallower crustal levels further south (Loch Maree)(Whitehouse, 1989). This does not apply as clearly to the Northern region (Rhiconich Terrane) where geochemical analysis suggests that the gneisses in this region were not subjected to granulite-facies metamorphism in the Badcallian (Sheraton et al., 1973a) and that oldest common deformation event between the Central and Northern regions was the Laxfordian (Kinny et al., 2005).

#### 2.1.4.2 – Inverian deformation

The Inverian was first defined by (Evans, 1965a) in the Central Region as a post-pegmatite vein, pre-Scourie dyke emplacement amphibolite-facies metamorphism that produced well-defined rock types and WNW-ESE-trending vertical structures (*Figure 2.5b*). Inverian deformation is dated between 2490 Ma and 2400 Ma (e.g. Evans, 1965a, Evans and Lambert, 1974) and is thought to be responsible for the initial formation of both the Gairloch and Laxford Shear Zones (Holland, 1966, Goodenough et al., 2010) at the southern and northern edges of the Central region, respectively. This Inverian event is also recognised in the Central region where it formed the Canisp Shear Zone (Tarney, 1963, Evans, 1965a, Attfield, 1987), including the Inverian type locality at Lochinver (Evans and Lambert, 1974).

Inverian deformation is not recognised north of the Laxford Shear Zone, i.e. in the Rhiconich Terrane. This lack of Inverian deformation and the younger protolith ages recorded for the Rhiconich Terrane (2840-2800 Ma compared to 3030-2960 Ma in the Assynt Terrane (Friend et al., 2001)) suggests that these terranes represent two different crustal blocks, with different formation histories that became aligned post-Inverian as a result of movements along the Laxford Shear Zone (Friend et al., 2001).

#### 2.1.4.3 – Scourie Dykes

A series of sub-vertical, NW-SE to E-W trending mafic and ultramafic dykes, known as the Scourie Dyke Swarm, were intruded into the mainland LGC between 2400 Ma and 1900 Ma (*Figure 2.5c*) (e.g. Evans, 1965a, Coney et al., 1980, Friend et al., 2007, Love et al., 2004). Using the shape of the dykes in areas of little or no Laxfordian deformation suggests that dyke emplacement occurred during a period of dextral transtensional crustal extension (Park et al., 1987). Only dykes in the Assynt Terrane have any direct age constraints (Kinny et al., 2005); e.g. the c. 2400 Ma Beannach dyke

and the c. 2000 Ma Strathan dyke (Friend et al., 2007) and it is not clear if dykes found in the Northern and Southern Regions belong to the same suite as the Scourie Dykes of the Central Region (Park et al., 2002). It is important to be aware that several authors (e.g. Tarney, 1963, Park, 1964) proposed that the emplacement of the oldest dykes (~2400 Ma) overlapped Inverian deformation. This potentially means that using the oldest dyke set as a tectono-stratigraphic marker to separate the Inverian and Laxfordian deformation events (see below) may not be valid.

The dykes have two main compositions: bronzite-picrite/olivine-gabbro and mafic dolerite (Peach et al., 1907, Tarney, 1973). Recent high-resolution TIMS U-Pb age data from Scourie dykes in the Assynt Terrane provide evidence of at least four periods of dyke emplacement: ~2420 Ma, ~2400 Ma, 2375 Ma and 1990 Ma (Davies et al., 2009). Many of the dykes emplaced in the LGC (particularly in the Central region) lack evidence of chilled margins which suggests crystallisation at mid-crustal depths into hot country rocks (O'Hara, 1961, Tarney, 1963, Park, 1964).

Dykes in the Northern and Southern regions are typically more deformed and metamorphosed due to the effects of overprinting Laxfordian shearing. Many are now amphibolites which have been sheared into near concordance with the foliation in the surrounding gneisses. In the Central region, there is less evidence of Laxfordian deformation and it is common to observe dykes with their original igneous contact relationships and mineral assemblages (Park and Cresswell, 1973). In the Central region, Scourie dykes commonly only exhibit Laxfordian deformation (typically narrow zones of schistose mylonites) along their margins. This provides observational evidence that these intrusions were emplaced prior to the onset of Laxfordian deformation.

Quartz veins that also bear pyrite are observed across the Assynt Terrane where they cross-cut the steeply-dipping Inverian fabrics, but are consistently reworked and over-printed by Laxfordian deformation (Vernon et al., 2011). Recent geochemical analysis of pyrite-bearing quartz veins using Re-Os isotopes suggest that these quartz veins have ages of  $2259 \pm 61$  Ma which falls into the broad age range of the Scourie Dyke swarm (Vernon et al., 2011). Quartz veins are not observed within the Rhiconich Terrane providing more evidence that the Assynt and Rhiconich Terrane do not have a shared history until the Laxfordian.

#### 2.1.4.4 – The Loch Maree Group

Incorporated into the LGC are two belts of metasedimentary and metavolcanic rocks around Gairloch and Loch Maree (Peach et al., 1907), which are known as the Loch Maree Group (LMG). These supracrustal rocks cover an area of approximately 150km<sup>2</sup>, and are thought to have originally been deposited unconformably on top of the older surrounding gneisses (Evans, 1965b). The LMG forms the only belt of Paleoproterozoic supracrustal rocks in the mainland LGC, deposited after the Inverian at around 2000 Ma (based on Sm-Nd isotopic relationships (Wheeler et al., 1987) and detrital zircon ages (Whitehouse et al., 1997)).

The LMG comprises volcanic-origin amphibolites (Park, 1966, Johnson et al., 1987) interbanded with metasediments that include: semipelitic quartz-biotite schists and narrow discontinuous bands of marble, banded iron formation graphite-schist and chlorite-schist (e.g. Johnson et al., 1987, Park et al., 2001). It is hypothesised that the LMG assemblages are an accretionary complex formed at a subduction zone (Park et al., 2001). Its presence between slabs of Archaean TTG basement suggests that the accretionary complex has been involved in a collision with continental crust (Wheeler et al., 2010).

The LMG comprises amphibolite-facies metamorphic assemblages reflecting Laxfordian pressure-temperature conditions. Retrogression to greenschist-facies occurs locally in the younger Laxfordian shear zones which is marked by the breakdown of hornblende, garnet and feldspar to form biotite, epidote, albite, muscovite and actinolite (Park et al., 2001).

#### 2.1.4.5 – Laxfordian deformation

The main phase of ductile Laxfordian deformation deforms Scourie dykes (post 2000 Ma) and converts the original rocks into hornblende- and biotite-gneisses and Scourie dykes into amphibolites or hornblende-schists (Sutton and Watson, 1950). It has been suggested by Park and Tarney (1987) that Laxfordian deformation that affects earlier Scourie dykes may pre-date some later members of the Scourie dyke suite. The Laxfordian is thought to be the first deformation event in common between the Assynt and Rhiconich Terranes (Kinny et al., 2005).

Deformation events in the Laxfordian include early amphibolite-facies reworking of the gneisses, dykes and LMG, the emplacement of granites and pegmatites and

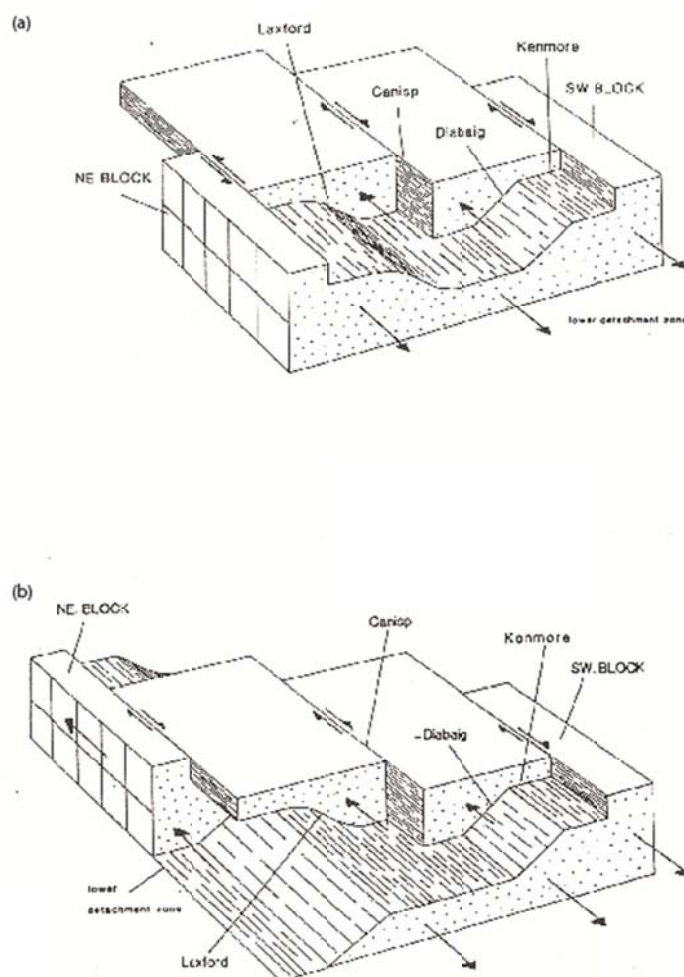
localised retrogression to phyllosilicate-rich greenschist-facies rocks within shear zones (*Figure 2.5e*) (Park and Tarney, 1987). In the Assynt Terrane, Laxfordian deformation is mainly confined to shear zones (such as the CSZ) and to the margins of Scourie dykes (*Figure 2.5e*). The effects of Laxfordian deformation are much more widespread in the Southern and Northern regions of the mainland LGC (e.g. Park et al., 1994, Kinny et al., 2005).

Rb-Sr, lead isotope and zircon ages suggest a maximum age of Laxfordian deformation (D1) as 1900 Ma and that the early deformation events had terminated by approximately 1800 Ma (Lambert and Holland, 1972, Weaver and Tarney, 1980). The Laxfordian granite/pegmatite sheets are dated at 1800 Ma using Rb-Sr and U-Pb isotopic analyses (Bikerman et al., 1975, Weaver and Tarney, 1980, Corfu et al., 1994) with a second amphibolite-facies deformation event (D2) at c. 1600 Ma (Holland, 1966). The later retrogressive Laxfordian event (D3), calculated from K-Ar whole rock and mineral datasets, occurred c. 1400 Ma (Holland, 1966). A final Laxfordian event (D4) is attributed to low-temperature (greenschist-facies), brittle folding and crush belts that transpired between 1400 Ma and ~1150 Ma (K-Ar datasets). The oldest of these dates comes from biotite samples in a retrogressed metasedimentary mica-schist and the youngest is from chloritised biotites from acid gneisses (Holland, 1966). Most of these younger ages are based on K-Ar dating, a technique that is not now generally considered to be reliable, so the accuracy of these ages is somewhat suspect.

Laxfordian deformation occurs on a set of NW-SE trending major shear zones which must form an inter-connecting network in order to transfer the resulting displacements through the crust between the adjacent undeformed (or less deformed) crustal blocks (*Figure 2.6*) (Coward and Park, 1987). A marked change of formation depth of these shear zones can be distinguished between D2 and D3 where the change of metamorphic facies suggests a change from mid-crustal to upper crustal deformation (Park et al., 1987) between ca. 1600 and 1400 Ma. The retrogression that occurs during this time in Laxfordian LGC shear zones (amphibolite-facies to greenschist-facies) includes hydration reactions, where anhydrous minerals (e.g. pyroxene) breakdown to hydrous minerals (e.g. biotite) (e.g. Beach, 1973).

NW-SE trending faults that are preferentially developed in Laxfordian shear zones (although they are not exclusive to them) have been termed 'Late Laxfordian' (*Figure 2.5f*) (Beacom, 1999). This is because cross-cutting relationships provide

evidence that these brittle structures formed after the main ductile phases of Laxfordian deformation, but before the deposition of the Stoer Group sediments on top of the LGC ca. 1200Ma. Park (1970) suggests that this brittle event is comparatively unimportant in Lewisian geochronology, but throughout this thesis, it will become apparent that these faults have significant implications for fracture network connectivity and later fault reactivation events. Further descriptions, including fault rock analysis of these 'Late Laxfordian' faults is provided in *Chapter 3, Section 3.3.3.1* of this thesis.



**Figure 2.6:** Schematic diagrams illustrating two possible models of shear zone networks and kinematics across the Lewisian. (a) Basic over-thrust model. (b) Basic strike-slip model. Dip-slip movements on the ramps are ignored for convenience. After Coward and Park (1987).

### 2.1.5 – Post Lewisian Geology

On the Scottish mainland, west of the Moine Thrust, the rocks of the LGC are unconformably overlain by Late Proterozoic to Mesozoic age sedimentary sequences and younger Quaternary drift materials (*Sections 2.1.5.1 to 2.1.5.5*). *Table 2.4* provides a summary of the sedimentary activity (including drift), igneous activity and tectonics in the northwest Highlands from first deposition in the Proterozoic right through to the Quaternary. The surface of the Lewisian was exposed before any sedimentary deposition occurred and so these sedimentary successions (especially the Torridonian Succession) cover a palaeotopography formed due to weathering of the exposed LGC.

It is important to be aware that the mainland LGC (west of the Sole Thrust of the Moine Thrust Zone between the Moine and the Sole Thrust the LGC is deformed) is essentially unaffected by tectonism and metamorphism associated with the Caledonian Orogeny. This contrasts with the Lewisian of the Outer Hebrides where Caledonian deformation is evident along the Outer Hebrides Thrust Zone (e.g. Batchelor et al., 2010, Imber et al., 1997). Post-Caledonian deformation is recognised on the mainland, with the formation of faults (and the reactivation of some pre-existing faults and shear zones) (e.g. Wilson et al., 2010) and the formation of extensive offshore sedimentary basins, including the Minch and West Orkney basins that lie immediately to the west and north of the Scottish mainland respectively (e.g. Roberts and Holdsworth, 1999, Wilson et al., 2010).

#### 2.1.5.1 – The Torridonian sedimentary sequence

Hickman in the 1907 Geological Survey memoir wrote, ‘the rocks included in the Torridonian series present a striking contrast to those of the Lewisian gneiss, inasmuch as they consist mainly of red sandstones and conglomerates which over much of their extent are gently inclined or horizontal’. This Torridonian sequence comprises the Stoer Group, the Sleat Group and the Torridon Group (oldest to youngest) (Stewart, 1988b, 1988a, 1991b, 1993), which form a sedimentary succession that comprises broken outcrops from Cape Wrath in the north to the Point of Sleat on Skye in the South (*Figure 2.7*) (Peach et al., 1907). On the mainland, the Torridon Group unconformably overlies the Stoer Group, whereas on Skye the Sleat Group is conformably overlain by the Torridon Group.

Time Period	Tectonics	Sedimentary and Igneous Activity
Quaternary	Last ice sheet retreat – isotactic rebound Uplift Rifting – N. Europe-Greenland sea opening  Beginning Atlantic opening – North Sea uplift and rifting	Skye, Rhum and Hebrides Igneous complexes  Epeiric seas and basins.  Playa lake, continental sediments
Tertiary		
Cretaceous		
Jurassic		
Triassic		
Permian	Pre-Atlantic rifts – North Sea basins	Evaporites, desert sedimentation and igneous activity Coals Carbonates and basinal mudrocks Turbidite sediments  Oceanic basin sediments Carbonates on NW foreland
Carboniferous	Lithospheric stretching	
Devonian	Final collision events – Moine Thrust Caledonian Orogenic events	
Silurian		
Ordovician	Iapetus closing	
Cambrian		
Proterozoic	Iapetus opening	
	Peripheral rifting to Iapetus opening	

**Table 2.4:** Generalised summary of the geological evolution of northern Britain. Modified after Beacom (1999).

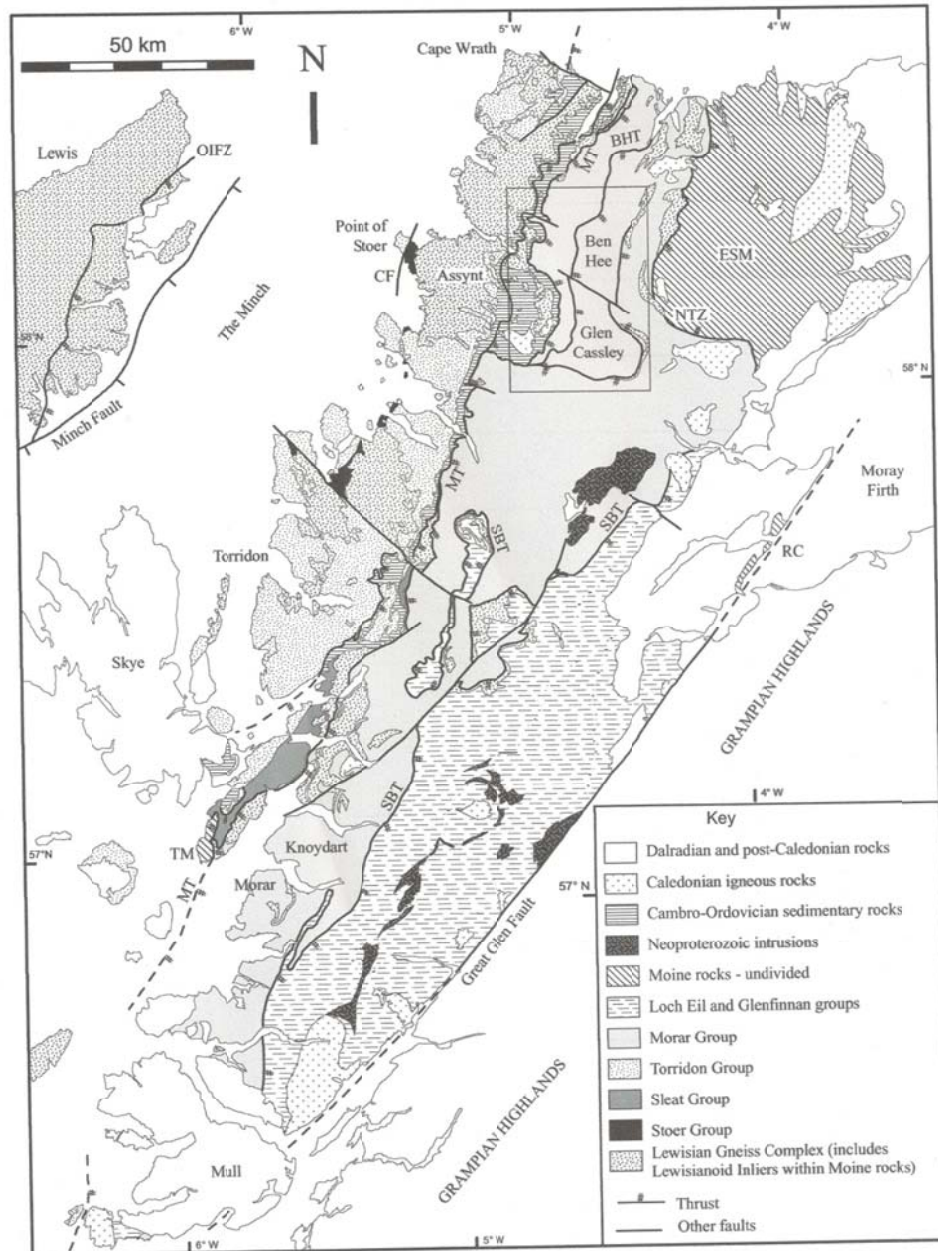
#### 2.1.5.1.1 – Stoer Group

The Stoer Group sediments are the oldest in the Torridonian succession. They are Proterozoic in age and post-date the later Laxfordian deformation events and were deposited in a series of palaeo-valleys created due to the weathering of the underlying Lewisian Complex (*Figure 2.8*). The most reliable radiometric age comes from lead isotope dating of a limestone unit and is thought to date early Stoer Group diagenesis at  $1199 \pm 70$  Ma (Turnbull et al., 1996).

The Stoer group comprises alluvial sandstones and lake sediments which had a maximum exposed thickness of 2km (*Figure 2.8*) (Stewart, 2002). Today, it is only found in a narrow strip that is truncated against the Coigach Fault. The deposition of the Stoer Group sediments is thought to have coincided with a period of late Proterozoic rifting during a phase of prolonged crustal extension before the opening of the Iapetus Ocean (Wheeler et al., 2010, Stewart, 1988b, Turnbull et al., 1996). Although no direct evidence for a syn-rift origin for the Stoer Group has been obtained several authors have provided interpretations of sedimentary (Wheeler et al., 2010, Stewart, 1991b) and tectonic

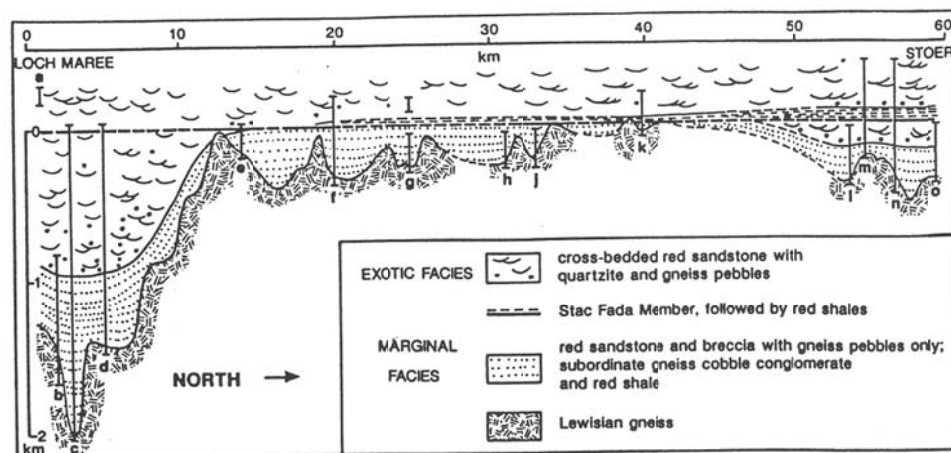


(Stewart, 1993, Soper and England, 1995) observations to support this syn-rift hypothesis.



**Figure 2.7:** Geological map of the Northern Highlands highlighting the sediment distribution. Moine undivided; included the East Sutherland Moine (ESM), the Tarskavaig Moine (TM), and the Rosemarkie-Cromarty Moine Inliers (RC). Other abbreviations: BHT, Ben Hope Thrust; CF, Coigach Fault; OIFZ, Outer Isles Fault Zone; MT, Moine Thrust; NTZ, Naver Thrust Zone; SBT, Sgurr Beag Thrust. After Krabbendam et al (2008).

Marginal sedimentary facies include local, Lewisian basement-derived breccia series which grade laterally into red alluvial sandstones and red shales (Stewart, 1991b). The Stoer Group sediments were deposited in a semi-arid environment at a palaeo-latitude of 10-20° (from palaeomagnetic data (Stewart and Irving, 1974, Smith et al., 1983, Torsvik and Sturt, 1987) and geochemical data (Stewart, 1991b)). The distinctive red colouration of the Stoer Group sediments (and the sediments of the younger Torridon Group) results from the high concentrations of ferric oxide that coats individual grains and due to staining of altered feldspars and fragments of felsites that are found within the sediments (Peach et al., 1907). These high levels of iron within the Torridonian sediments have important implications for fracture characteristics within the adjacent LGC, whose formation coincides with the deposition of these sediments (*Figure 2.5g*), and whose fault rock mineral assemblages are a result of fluid percolation through these overlying iron-rich sediments (see *Chapter 3, Section 3.3.3.2* for details of these Stoer Group age fractures).



**Figure 2.8:** Restored section of the Stoer Group facies from Loch Maree to Stoer, perpendicular to the palaeocurrent directions. Sections are (a) Rubha Reidh; (b) Bac an Leth-choin; (c) Inverian to Inverewe; (d) Loch Ghiuragarstidh to Loch Thurnaig; (e) Gruinard Bay; (f) Stattic Point; (g) Camas na Ruthaig; (h) Horse Island; (j) Rubha Dunan; (k) Enard Bay; (l) Clachtoll; (m) North side of Stoer Bay; (n) Rienachait; (o) Achnacarnin to Bay of Culkein. After Park et al. (1994).

#### 2.1.5.1.2 – Sleat Group

The Sleat Group comprises over 3500m of coarse-grained, grey alluvial sandstones and subordinate grey shales (Stewart, 1991a) which lies unconformably over the LGC (Stewart, 2002). Sleat Group sediments are best exposed on Skye and no outcrop of this sedimentary group on the mainland is found north of this location. Although no outcrop exhibiting a Stoer Group- Sleat Group contact has been discovered, palaeomagnetic data and field observations suggest that the Stoer Group is older than the Sleat Group (Stewart and Irving, 1974, Smith et al., 1983, Stewart, 1991a). It is also clear that the Torridon Group sediments are significantly younger than the Stoer Group (*Section 2.1.5.1.3*) and as the Sleat Group lies conformably beneath the Torridon Group then it is logical that the Sleat Group sediments are also younger than the Stoer Group (Park et al., 1994).

The dominant sedimentary feature of the Sleat Group is an upward decrease in grain size, from very coarse sandstones of the basal Rubha Guail Formation to very fine sandstones of the Kinloch Formation (Stewart, 2002). Sleat Group sediments are diverse and potentially represent a syn-rifting sequence prior to and conformable with the deposition of the overlying Torridon Group.

#### 2.1.5.1.3 – Torridon Group

The Torridon Group sediments are the youngest of the Torridonian Sequence. Where the Torridon Group is in contact with the Stoer Group it always has an angular discordance of 15-30° (Park et al., 1994). Onshore, the maximum thickness of the Torridon Group is approximately 7km (*Figure 2.9*) and offshore its maximum thickness is perhaps as much as 6km in the Sea of the Hebrides basin (Stein, 1988, fig. 11, 1992, fig 2B). Phosphate concretions found in the base of the Torridon Group have an age of  $994 \pm 48$  Ma (Rb-Sr dates) and  $951 \pm 120$  Ma (by Pb-Pb dating) (Turnbull et al., 1996). These ages suggest that the Stoer and Torridon Groups are 200 Ma apart in time. (Moorbath, 1969, Moorbath et al., 1967, Rodgers et al., 1990).

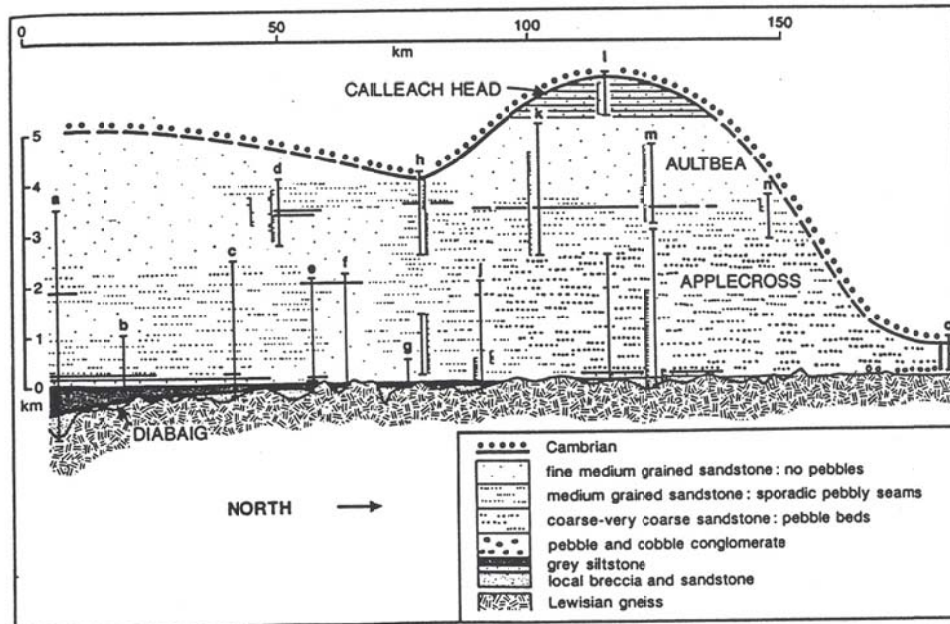
Several authors quote a change in palaeolatitude of up to 45° accompanying the unconformity between the Stoer and Torridon groups (Stewart and Irving, 1974, Smith et al., 1983, Torsvik and Sturt, 1987) which, assuming plate velocities similar to those occurring in Phanerozoic times would imply at least a 40 Ma time gap at the unconformity (Park et al., 1994). This change in palaeolatitude inferred from

palaeomagnetic datasets indicates that the Torridon Group was deposited in latitudes of 30-50° (Stewart and Irving, 1974, Smith et al., 1983).

The Torridon Group is subdivided into four formations (*Figure 2.9*); the Diabaig Formation, the Applecross Formation, the Aultbea Formation and the Cailleach Head Formation (Stewart, 2002). Breccias and sandstones derived from the immediately adjacent LGC form the Diabaig Formation. Coarse-grained, pebbly cross-bedded red sandstones of the Applecross Formation and the fine-grained, pebble free Aultbea Formation (all fluvial deposits) comprise the bulk of the Torridon Group (Park et al., 1994, Stewart, 2002). The Cailleach Head Formation lies at the top of the sequence and comprises coarsening-upward cyclothems of grey shale and red sandstone (Stewart, 2002) that have average thicknesses of 22m (Park et al., 1994).

Three separate basin models have been proposed for the depositional setting of the Torridon Group; a foreland basin (e.g. Sutton, 1963, Rainbird et al., 2001), a thermal relaxation basin (Nicholson, 1993), or a rift. Evidence put forward by Stewart (2002) suggests that the first two models do not fit the observations made from Torridon Group sediments. Stewart (2002) suggests that the slightly thinned crust under NW Scotland (e.g. Blundell et al., 1985), the presence of eastward-dipping fault sets (including boundary faults), the fluvial origin of the Torridon Group sediments and the convergence of palaeocurrent directions on the Minch Fault are all a result of the syn-deposition in a half-graben rift basin. In contrast, a newer study of the Altnaharra Formation in the Moine Supergroup finds that this formation is similar in terms of age, sedimentology, stratigraphical position, geochemistry, age constraints and overall transport direction to the Applecross-Aultbea Formations of the Torridonian Succession (Krabbendam et al., 2008). These authors conclude that the Applecross-Aultbea and Altnaharra Formations are direct correlatives repeated across the Moine Thrust Zone and therefore formed part of an axial trunk fluvial system forming an orogen-parallel foreland basin in front of the Grenville Orogen. As these two studies are in direct contradiction with each other it is suggested that further work is required before the depositional origin of the Torridon Group can be fully understood.

Areas of LGC overlain by Torridon Group sediments are encountered throughout the onshore study in this thesis, where the presence of ferric oxides within these sediments has similar implications for fault rock mineralisation (*Figure 2.5*) as fractures have associated with the deposition of the Stoer Group (see *Chapter 3, Section 3.3.3.3*).



**Figure 2.9:** Restored section of the Torridon Group from Rhum to Cape Wrath, perpendicular to the palaeocurrent direction. The base of the Applecross Formation is assumed to be horizontal. Key sections are: (a) Rhum; (b) Soay; (c) Scalpay; (d) Toscaig; (e) Raasay; (f) Shieldaig to Applecross; (g) Diabaig; (h) Torridon, west and east of the Fasag Fault; (j) Gailloch; (k) Aultbea; (l) Cailleach Head and Scoraig to Dundonnell; (m) Summer Isles and Achiltibuie to Strath Kanaird; (n) Rhubha Stoer; (o) Cape Wrath. After Park et al. (1994).

### 2.1.5.2 – Cambro-Ordovician Sequence

A sequence of Lower Cambrian to Lower Ordovician sediments lie unconformably on top of both the LGC and the Torridonian Succession in the west and, together with these older rocks, are found in imbricates within the Caledonian Moine Thrust Zone. These Lower Palaeozoic rocks lie with close proximity to the Moine Thrust Zone forming a 20km wide belt that runs from Durness in the north to the Isle of Skye in the south (*Figure 2.10a*). The Cambrian unconformity was suggested by Peach et al. (1907) to represent a marine denudation surface because of its relatively planar profile compared with the irregular Torridonian unconformity below.

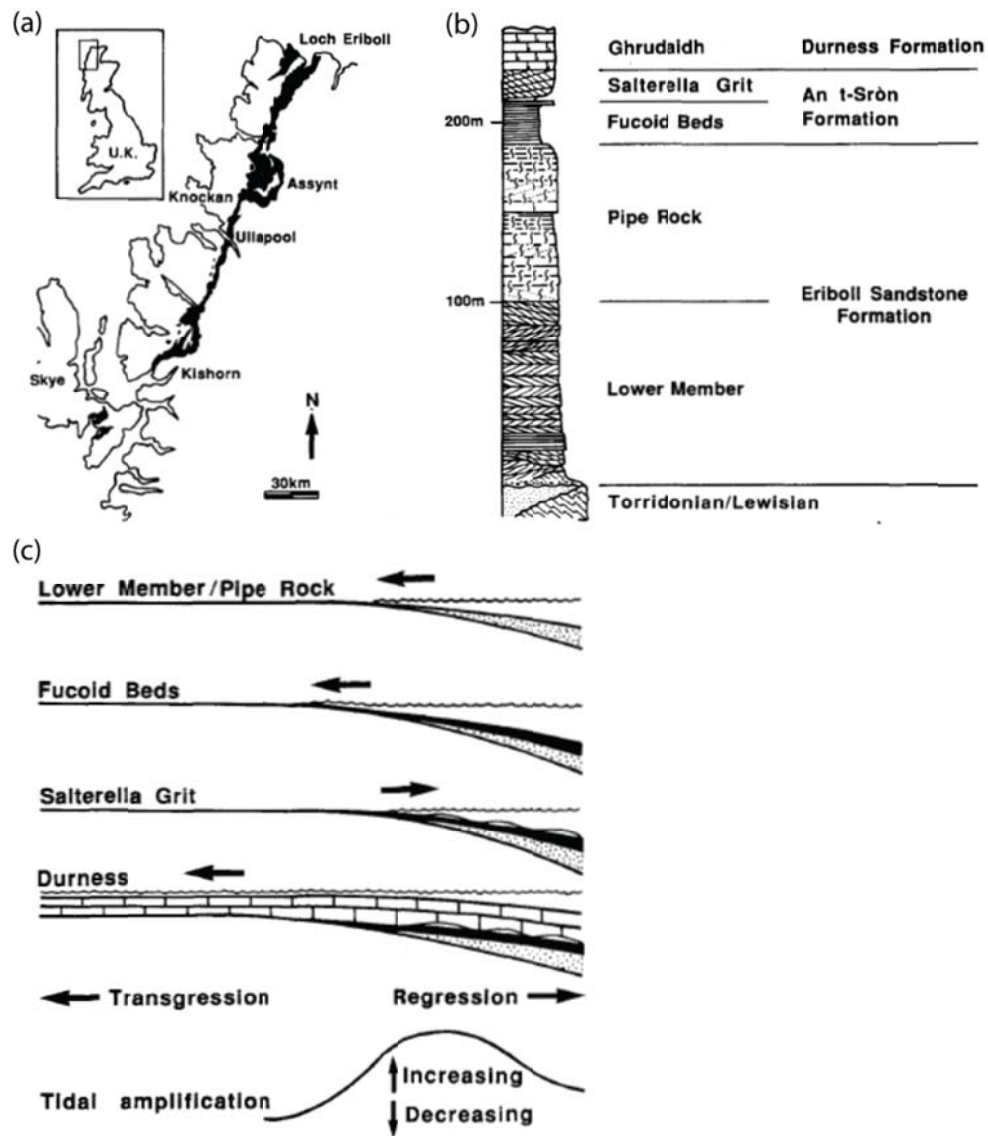
The stratigraphy of the Cambro-Ordovician sequence comprises a Cambrian basal clastic succession (Eriboll Sandstone and An t-Sron Formations) overlain by Cambro-Ordovician carbonates (Durness Formation) (*Figure 2.10b*). The Eriboll Sandstone consists of a 75-125m thick sequence of tidally influenced, cross-bedded

quartz arenites (Lower Member) which are overlain by the Pipe Rock, a 75-100m thick interval of tidal and storm influenced, bioturbated quartz-arenites (McKie, 1990). This sandstone is overlain by the storm-dominated (tidal) An t-Sron Formations that include 12-27m thick Furoid beds of mixed carbonate and clastic sediments and the 5-15m thick quartz-arenites of the Saltarella Grit (McKie, 1990). This sequence passes up into the 800m thick Cambro-Ordovician Durness Group which comprises dolostone with subordinate limestone and chert units that have a sub-tidal depositional origin (Wright and Knight, 1995).

The Cambro-Ordovician sequence represents an overall marine transgression, developed as the inner belt of an extensive shelf sequence on the northern passive margin of the Iapetus ocean (Park et al., 2002) (*Figure 2.10c*); with regressions within the Saltarella Grit explained by variations in the spreading rate during the opening of the Iapetus Ocean producing uplift on the shelf edge, where NW Scotland was situated (McKie, 1990). This overall transgression penetrated the craton interior, ending the deposition of clastic sediments (Eriboll Sandstone and An t-Sron Formations) allowing the continental shelf to be covered by a widespread carbonate platform (Durness Group) (McKie, 1990). The marine transgression described above was known to be widespread because similar sedimentary successions have been recorded in East Greenland and North America (Swett and Smit, 1972, Swett, 1981) on the same Laurentian margin as NW Scotland (McKie, 1990).

#### 2.1.5.3 – Silurian-Devonian

The Moine Thrust Belt formed during the Scandian (Silurian) during complex NW-SE foreshortening within the Caledonian Orogeny (e.g. van Breemen et al., 1979, Strachan et al., 2002). Sedimentary rocks associated with the Moine Supergroup include metamorphosed arenaceous and argillaceous sediments and minor calcareous units (Strachan et al., 2002). These rocks comprise psammites, semipelites and pelites that are affected thrust faulting and folding within the Moine Thrust Belt. Moine rocks were likely derived from the Grenville orogenic belt (c. 1.1 – 1.0 Ga) that formed during the assembly of the Rodinian supercontinent (Dalziel and Soper, 2001). The age of Moine sediments has a lower limit of c.870 Ma, calculated from igneous rocks that intrude the sediments (Strachan et al., 2002); therefore constraining the age of the Moine Supergroup between 1000 and 870 Ma.



**Figure 2.10:** (a) Location map of the Cambro-Ordovician succession in northwest Scotland. (b) Stratigraphic of the Cambro-Ordovician succession, not including the thickness of the Durness Formation. (c) Summary of the mainly transgressive depositional environment of the Cambro-Ordovician succession. After McKie (1990).

Sediments of the Moine Supergroup lie in the hanging wall of the Moine Thrust where they are dissected and repeated by a series of ductile thrusts (Barr et al., 1986). The structures within the Moine Thrust Belt are complex: in some places it comprises a single thrust plane; elsewhere there are complex plies of thrust sheets (Elliott and Johnson, 1980, Butler, 1982, Butler, 1984, Butler, 2010, Coward, 1985). The thrust sheets vary in thickness from km-scale to <10m with a wide range of geometries are also present (Krabbendam and Leslie, 2010). Caledonian movements associated with the Moine Thrust Belt are also observed across pre-existing structures, such as the Loch Assynt Fault; with sinistral movements recorded by the displacement of the Lewisian-Cambrian 'double unconformity' across the Loch Assynt Fault (Krabbendam and Leslie, 2010, Figure 7).

#### 2.1.5.4 – Permian-Triassic (Mesozoic) Sediments

Mesozoic sediments crop out over small areas in the NW Highlands with outcrops on the mainland occurring between Applecross and Coigach (*Figure 2.11*) (Steel, 1974). In the Outer Hebrides these Permian-Triassic sediments crop out prominently on the Isle of Lewis where they comprise the Stornoway Formation. During the Mesozoic several erosional cycles affected the Scottish Highlands during periods of uplift that stripped away cover rocks and ending with extensive marine transgressions in the Late Triassic, Late Jurassic and Late Cretaceous (Hall, 1991). These erosional cycles resulted in the small amount of Mesozoic sediments outcropping in the Scottish Highlands today.

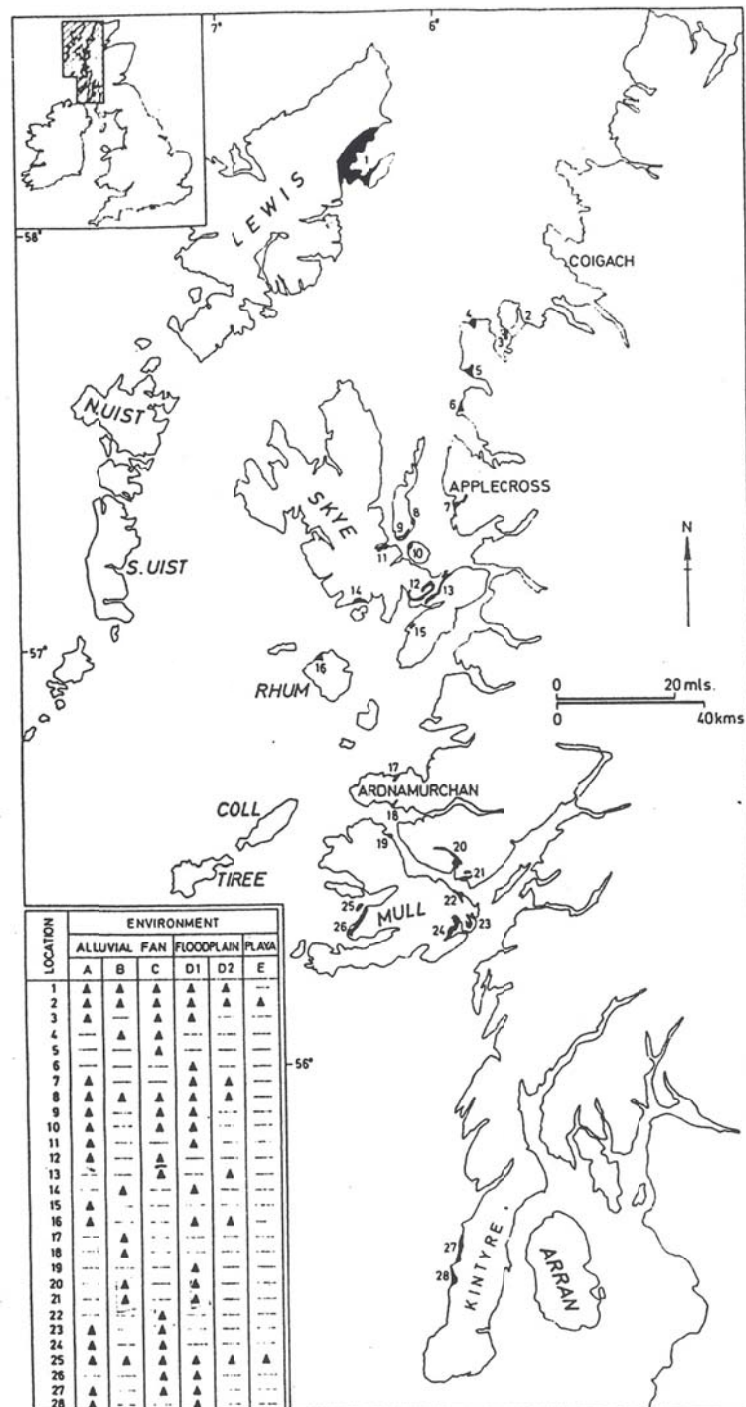
These outcrops of 'New Red Sandstone' occur conformably beneath Jurassic sediments. They consists of clastic sandstones and conglomerates that unconformably overlie Precambrian and Cambrian Rocks on the mainland and Hebridean islands (Warrington et al., 1980). The 'New Red Sandstones' are interpreted as alluvial fan deposits that evolved from mudflow to streamflow to braided stream deposits (Steel, 1974).

It has been suggested by many authors that Mesozoic sediments (particularly the Stornoway Formation) may be onshore representatives of sediment deposits in deep basins surrounding the NW Highlands such as the Minch Basin and the West Orkney Basin (e.g. Watts, 1971, Smythe et al., 1972, Binns et al., 1974, Stoker et al., 1993, Hitchen et al., 1995 and references therein). These basins are syn-tectonic half-grabens

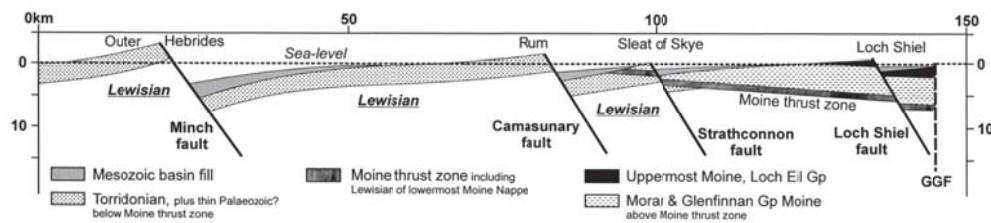


that typically thicken towards the west against reactivated NE-SW trending Caledonian thrusts such as the Outer Hebrides Fault Zone (Stein, 1988, 1992, Butler et al., 1997, Roberts and Holdsworth, 1999) and normal faults developed in the hanging walls of these major thrusts (e.g. Enfield and Coward, 1987). The faults controlling the development of basins such as the Minch are known to have been active in the Mesozoic and are thought to have helped to exhume the Precambrian rocks presently exposed on many of the Hebridean islands as a series of footwall highs (*Figure 2.12*) (Roberts and Holdsworth, 1999).

Mesozoic basins in the N Atlantic are important in terms of hydrocarbon systems, e.g. the west of Shetland hydrocarbon fields of Clair, Foinaven and Cuillin. Several authors suggest that Mesozoic faults bounding basins such as the Minch and West Orkney Basin extend onshore into the Outer Hebrides and the mainland (Roberts and Holdsworth, 1999, Wilson et al., 2010). It is therefore essential to study these onshore Mesozoic structures in order to better understand their kinematic evolution, including reactivation histories, and to provide an important analogue for the structural and tectonic modelling of the evolution of these Mesozoic basins.



**Figure 2.11:** Map of Triassic (New Red Sandstone) sandstone localities within northwest Scotland. Inset includes the distribution of the alluvial fan, floodplain and playa facies within the marked localities. After Steel (1974).



**Figure 2.12:** Schematic cross-section (true vertical scale) from the Outer Hebrides to the Great Glen Fault (GGF) during the Jurassic. It shows how the Precambrian/Caledonian basement became elevated in the footwalls of Mesozoic faults. After Roberts and Holdsworth (1999).

### 2.1.5.5 – Tertiary rocks

There are limited outcrops of Tertiary material across the Scottish Highlands which means that uplift, erosion/subsidence and deposition rates are poorly constrained across the area (Thomson et al., 1999). The Early Tertiary was characterised by a large igneous province that stretches from south of Arran in the Firth of Clyde to Lewis in the Outer Hebrides, although there is no evidence of this Tertiary igneous activity north of Shildaig on the Scottish mainland. This major magmatic activity in western Scotland accompanied the initial development of the Iceland plume and resulted in the extrusion of flood basalts and injection of dyke swarms across the Tertiary Igneous Province (Bell and Jolley, 1997).

Major uplift in the Early Tertiary resulted in downwarping and block movements along basin margins in the Highlands (Hall, 1991). This uplift and denudation was increased in areas associated with Tertiary igneous centres such as those on Skye and Rhum (Hall, 1991). The increase uplift associated with the igneous activity can be observed by increased sand accumulation in the Moray Firth Basin (Liu and Galloway, 1997) that has a provenance on the Orkney-Shetland Platform and in the Highlands (Jones and Milton, 1994). Regionally, Early Tertiary rocks are tilted, which is associated with rapid uplift. This rapid uplift is a result of igneous underplating below a substantial part of the northwestern continental shelf of Europe (Brodie and White, 1994).

#### 2.1.5.6 – Quaternary features

The Quaternary in the NW Highlands primarily includes the changes to the landscape and other products from the last British-Irish ice sheet (BIIS). It has long been understood that the retreat of this ice sheet was uninterrupted by readvances (Boulton et al., 2002), but this has been challenged by evidence for multiple retreat stages (primarily a chain of moraine ridges in Wester Ross) in Northern Scotland and the adjacent Atlantic shelf (Bradwell et al., 2007, Bradwell et al., 2008b).  $^{10}\text{Be}$  ages of 14 Torridonian sandstone boulders provide ages of this readvance as 13.5 to 14 ka (Ballantyne et al., 2009). Other features associated with the BIIS are megagrooves (glacial striations) that form the erosional landscape near Ullapool that is thought to be a signature of a fast-flowing tributary that once was the Minch palaeo-ice stream (Bradwell et al., 2008a).

Stewart et al. (2001) conducted a study of neo-tectonic fault reactivations in southeast Raasay (ENE-trending Hallaig Fault) that they attributed to post-glacial isostatic rebound due to unloading. They suggest that seismic activity recorded in this area coincides with other work conducted on Skye where the authors suggest a correlation between the distribution of ice cover and seismicity (Musson, 1996). This relationship potentially extends onto the mainland where significant Holocene fault displacements are consistent with a swarm of end glacial earthquakes (e.g. Davenport et al., 1989, Ringrose, 1989, Stewart et al., 2001). The glacio-isostatic rebound recorded from fault reactivations across northern Scotland are a response to ice loading and unloading (Main et al., 1999, Figure 9); although much of the deformation recorded in the upper crust in the last 600 years has been predominately aseismic (Main et al., 1999).

Glacial deposits are relatively sparse across the NW Scottish mainland study area with thin patchy tills (<5m thick) occurring locally on gentle slopes (Bradwell et al., 2008a). The majority of the LGC and Torridonian is bare, with the landscape exhibiting a glacially abraded bedrock surface (British Geological Survey, 1998). Glacial erratic boulders and glacial striae have been used to indicate that at the maximum glaciation ice flowed from east to west across the present-day watershed (Read, 1926).

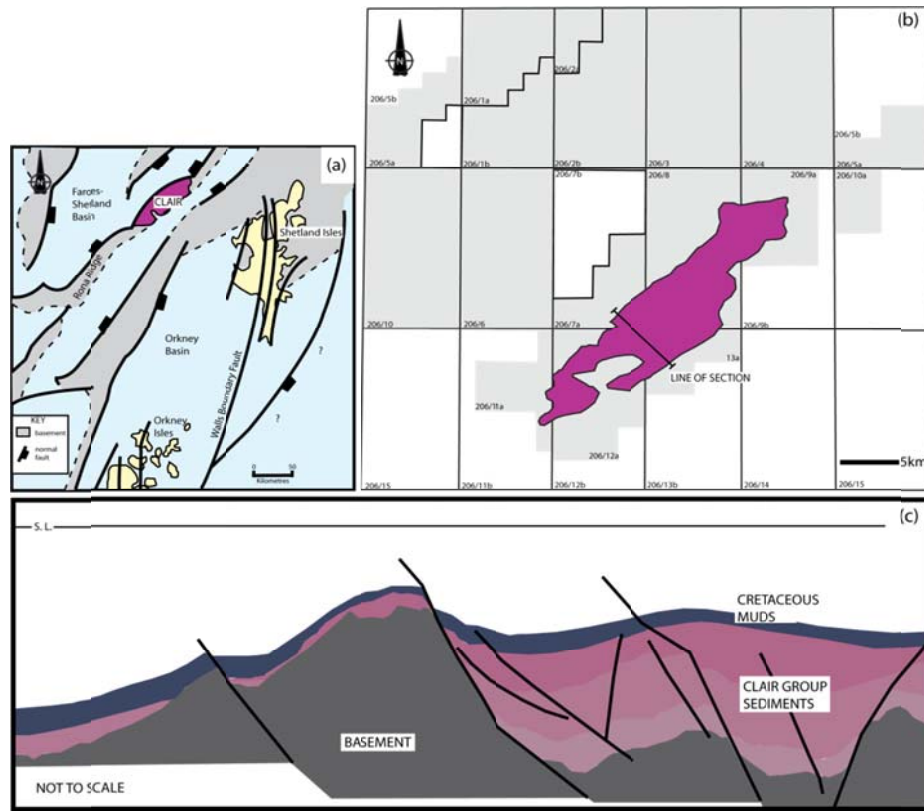
## 2.2 The Clair Field

The Clair Field was discovered in 1977 by BP (on behalf of the BP, Chevron, ICI licence group) (Coney et al., 1993), but it was not until the early 1990s when a 3D seismic survey was acquired over the area, and two exploration wells were drilled, that development was even considered viable. The Clair Field was considered to be the largest undeveloped hydrocarbon accumulation (oil and gas) on the U.K. continental shelf (UKCS) with estimates of likely oil exceeding 4 billion stock tank barrels (STB) original oil in place (OOIP). It is the largest fractured reservoir in the UKCS, but does also have significant matrix permeability in the sandstone reservoir units (Barr et al., 2007). This makes the Clair Field a key component of future U.K. hydrocarbon production strategy (Wylde et al., 2005).

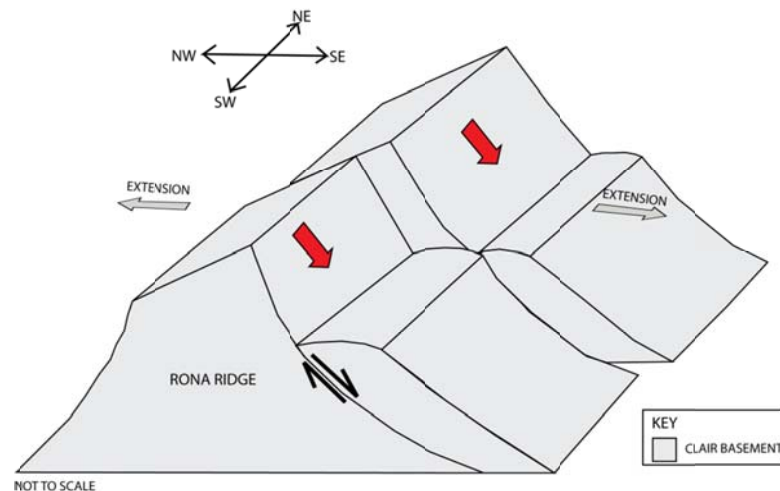
### 2.2.1 – Location of the Clair Field

The Clair Field lies 75km (47 miles) west of Shetland in the Faroe-Shetland Basin (*Figure 2.13a*) under a maximum water depth of 140 metres. It covers an area of 220km<sup>2</sup> spread over six licence blocks (*Figure 2.13b*) and is the third West of Shetland hydrocarbon development, following Foinaven and Schiehallion (Wylde et al., 2005).

The primary Clair reservoir is situated within Devonian and Carboniferous fluvial/lacustrine sediments (*Section 2.2.3.2*) that overlie and onlap a topographic basement high of Late Archaean to Early Proterozoic granodiorite/diorite/ granitic gneisses and pegmatites (*Figure 2.13c*) (*Section 2.2.3.1*) which itself is considered a potential fractured reservoir. This topographic basement high is known as the Rona Ridge and is the main structure of the Clair Field. It is thought to be a rotated footwall block related to a major NE-SW trending extensional fault (the Ridge Fault) that was first activated in the Devonian (Knott et al., 1993) and segmented by NW-SE trending faults (*Figure 2.14*). This NE-SW structural trend is prominent across the Clair Field, formed mainly by faults that activated through various extensional episodes in the Palaeozoic and Mesozoic (see *Section 2.2.4*). The hydrocarbon trap is a four-way dip closure of Late Cretaceous mudstones (Shetland Group, *Section 2.2.3.5*), forming the Greater Clair Closure (Witt et al., 2010).



**Figure 2.13:** (a) Schematic map illustrating the location of the Clair Field west of the Shetland Isles. (b) Schematic map showing the outline of the Clair Field over six U.K. licence blocks. (c) Illustration of the Clair Field structure (illustrated from seismic line whose location is shown in part (b)). Modified after Coney et al. (1993).



**Figure 2.14:** Schematic block diagram showing the basement structure in the Clair Field. The structure includes a rotated footwall block of a NE-SW extensional fault which is subsequently offset by NW-SE trending faults. The kinematics of the NW-SE ridge-offsetting faults is unclear as they are not imaged clearly on seismic but the ridge is known to be offset from the top basement seismic horizon depth map.

### 2.2.2 – Clair Field development history and future

The Clair Field was discovered in 1977 (well 206/8-1A) and ten wells drilled between 1977 and 1985 (including well 206/7-1) with disappointing results (Coney et al., 1993) so it wasn't considered again until the early nineties. Between 1991 and 1992 two wells were drilled into the field which demonstrated commercial flow rates but, these wells were not tested for long enough to provide confidence in the long-term reservoir performance of the field. It wasn't until 1996 when an extended reservoir performance test was conducted that produced average flow rates of 10,000 barrels per day (over 23 days) that the Clair Field was really considered as a commercially viable hydrocarbon field (Wylde et al., 2005).

The biggest breakthrough in the appraisal of the Clair Field came at the end of the 1980's when the four competing licence groups (led by BP, Esso, Mobil and Elf) that had been drilling the exploration wells realised that in order to develop their understanding of the field further they would have to develop a joint approach (Coney et al., 1993). Their first major collaboration was to shoot a joint 3D seismic survey across the central section of the Clair discovery area which allowed a significant improvement in the visualisation and understanding of the Clair structure (Coney et al., 1993). This collaboration still exists today under the heading 'Clair Joint Venture' with BP as the operators (28.6% share) and Shell (27%), ConocoPhillips (24%) and Chevron (19.4%) ownership partners in the field.

Due to the extent of the Clair Field, it is to be produced in a phased development. Phase-1 covers the Core, Graben and Horst areas (*Figure 2.15*) of the field, and is thought to contain recoverable reserves of 250 million barrels of oil. This started producing to a single fixed platform in 2005 with expected plateau production of 60,000 barrels of oil a day. This phase of the development focuses entirely on the Devonian and Carboniferous sediments, where there is a 600m maximum oil column (Wylde et al., 2005). Within the Phase-1 area, fracture clusters and discrete fluid inflows were observed in wells and associated with faults and other localised deformation features that are spaced tens or hundreds of metres apart (Barr et al., 2007). It was also observed that the reservoir sedimentary rocks have moderate to good matrix permeability, but the achieved well flow rates were fracture dominated (Barr et al., 2007). These observations highlight the importance of fracture modelling within the

Clair Field that has been extended to the Phase-2 and -3 areas and into the basement (this study).

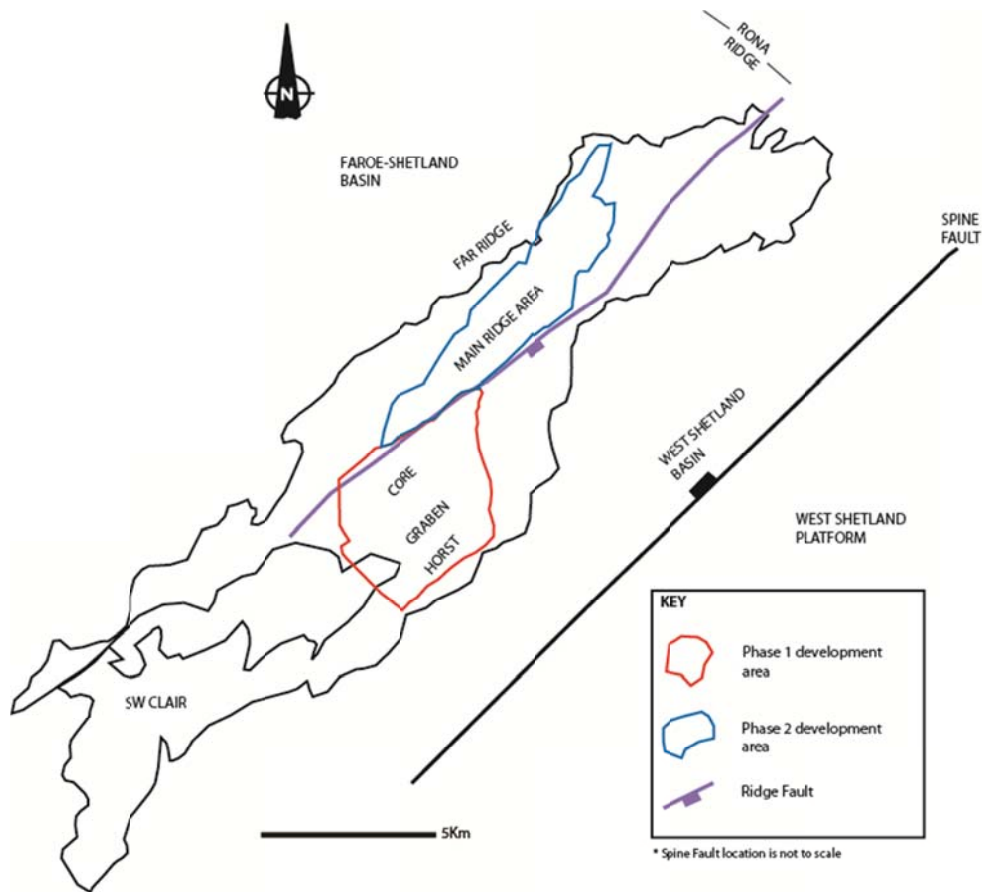
Phase-2 has recently been approved for development with an investment of £4.5 billion to build a new platform installation, drill production wells and extend the existing pipeline. It comprises the Main and Far Ridge areas and will likely involve the placement of a second oil platform. It encompasses both the cover sedimentary rocks and the underlying basement which is up to 1 kilometre higher on the ridge than in the rest of the Clair Field. On the ridge the basement intersects a maximum of approximately 750m of the oil column and approximately 50m of the gas column. Current Phase-2 well plans only involve the cover sedimentary rocks (Ogilvie, 2011), but the presence of this large oil column in the basement on the ridge means that there is the potential that the basement within this area is also acting as a very significant hydrocarbon reservoir.

Phase-3 covers the southwest Clair ridge which comprises a thin sedimentary cover, igneous sills and basement rocks. Appraisal of this phase is still in its infancy with interpretation of a new 3D seismic survey shot over the southern Clair area in 2008 still being completed. It is likely that the basement will play a much more dominant role in the development of this area.

#### **2.2.2.1 – Clair basement potential**

The basement is not currently considered in any of the reservoir capacity calculations or production models within the Clair Field. It is known to be heavily faulted and fractured (well studies, seismic analysis and this thesis) with many of these structures considered to be open features. Clair basement rocks were first sampled in 1978 when well 206/7-1 was drilled 160m vertically into the basement. When tested this well produced 963 barrels of oil per day entirely from fractures (Coney et al., 1993). Well 206/7a-2 was then drilled horizontally into the basement and during well testing when acid was introduced this well produced over 2000 barrels of oil per day, again entirely from fractures (Falt et al., 1992).





**Figure 2.15:** Clair Field outline showing the Phase 1 & 2 development areas and the location of basement wells.

Although wells 206/7-1 and 206/7a-2 struck oil in the basement, the relative lack of well data for the basement and poor imaging from seismic reflection data means that it has not been considered as a potential reservoir within the Clair Field. The work presented in this thesis aims to address some of the uncertainty involved with the basement fracture systems by conducting in-depth analyses of the available Clair basement datasets and using fracture networks within the mainland Lewisian Gneiss Complex as an onshore analogue. Being able to use an onshore analogue to expand the dataset available for the Clair basement allows educated assumptions and some predictions to be made about the fracture system characteristics in the basement rocks, increasing the ability to appraise the Clair basement as a potential hydrocarbon reservoir.

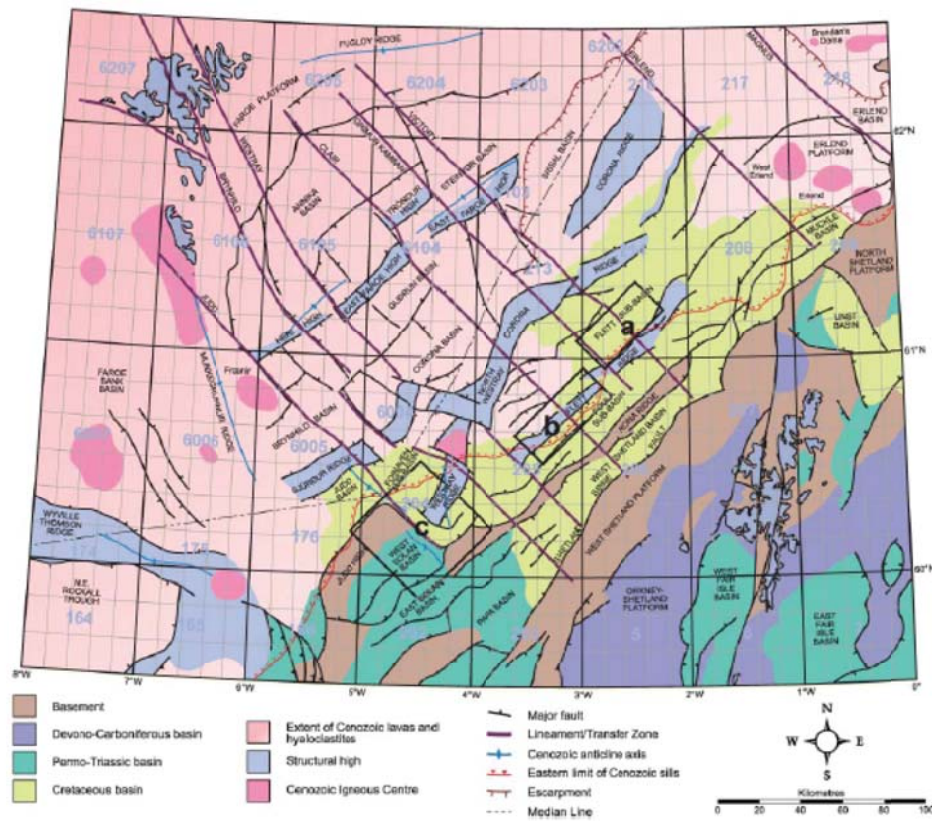
### 2.2.2.2 – Location of Clair basement wells

There are 23 wells across the Clair Field that have been drilled from initial discovery to first oil. A further 12 development wells have been drilled into the cover sedimentary rocks from a fixed platform (Witt et al., 2010). Seven of the initial wells enter the basement (206/7a-1, 206/7a-2, 206/8-8, 206/8-15, 206/8-2, 206/9-2 and 206/12-1, *Figure 2.15*) although only 206/7a-1 and 206/7a-2 go into the basement for any significant distance (160m and >400m, respectively). Well 206/8-8 samples the basement in the Phase-1 Core area; wells 206/7a-1, 206/7a-2, 206/8-15 and 206/8-2 sample the basement ridge in the Phase-2 area and well 206/12-1 is the only basement well in the Phase-3 (southwest Clair) area (*Figure 2.15*). Basement is also sampled by well 206/9-2, but this lies in the very north of the Clair Field, outside any of the current development phases. Details of individual basement wells, including descriptions of their lithologies, are presented in *Chapter 4* of this thesis.

Several of the basement-penetrating wells have core samples (not orientated), but only 206/7a-2 has a section of core that was taken horizontally through the basement. This core sample from 206/7a-2 is used throughout this thesis (and previous work conducted by Falt et al (1992)) to characterise the main fracture sets within the Clair basement that are present at the scale of a well (see *Chapter 4, Section 4.3* onwards).

### 2.2.3 – Regional setting of the Clair Field

The Clair Field lies within the eastern side of the extensional Faroe-Shetland Basin (FSB) which comprises a series of NE-SW trending sub-basins, formed during a sequence of Devonian-Carboniferous, Permian-Triassic, Cretaceous and Palaeocene rifting and subsidence events (*Figure 2.16*) (Moy and Imber, 2009) following the Caledonian Orogeny. The sub-basins are separated by a number of NE-SW trending, crystalline (metamorphic) basement 'highs' or horst blocks (Moy and Imber, 2009). The following sections (2.2.3.1 – 2.2.3.4) provide a summary of the main sedimentary deposition and igneous events that have occurred within the FSB, from the Archaean basement through to the Paleogene igneous events.



**Figure 2.16:** Schematic map showing the structural elements of the Faroe-Shetland Basin. Map projection is WGS84, UTM 30N. After Ellis et al (2009).

### 2.2.3.1 – Archaean basement

Little information is available about the nature and age of the West of Shetland basement as very few wells have actually cored the basement rock and in many of these core samples the basement is too weathered to use for dating purposes (Ritchie and Darbyshire, 1984). It has been thought for many years that the metamorphic basement rocks located offshore and to the West of Shetland comprised pyroxene granulites similar to the Archaean-Early Proterozoic gneisses seen onshore in NW Scotland (Watts, 1971).

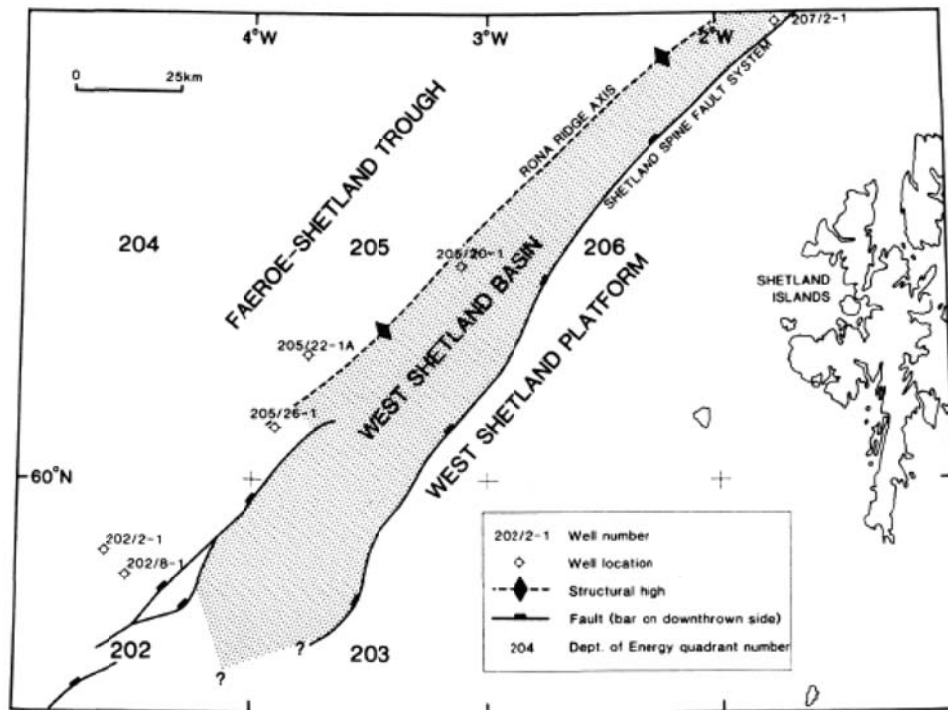
Seismic refraction analysis of the Faroe-Shetland basin showed that crust with velocities of approximately  $6.5 \text{ km s}^{-1}$  exists at depths of approximately 2.2km (Smith and Bott, 1975). This velocity value is comparable to those collected from Badcallian Gneisses within the Central region of the Scottish mainland (Figure 2.1) which have an average value of  $6.34 \text{ km s}^{-1}$  (Hall, 1978).

Core samples from across the Rona ridge area exhibit basement lithologies of quartzofeldspathic gneiss, granitic gneiss, tonalite grey gneiss, diorite gneiss and pegmatite, similar to the lithologies present within the Lewisian Complex of northwest Scotland. For detailed descriptions of basement lithologies in the Clair field and on the Scottish mainland see *Chapters 4* and *3*, respectively.

Rb-Sr dating has been used by Ritchie and Darbyshire (1984) to obtain an age for the FSB basement rocks. 6 basement core samples were used, including 3 in the vicinity of the Clair Rona Ridge area (*Figure 2.17*) which give a best estimate age of the basement rock as  $2527 \pm 73$  Ma. This rather poorly defined age provides semi-quantitative evidence that the basement rocks are late Archaean in age close to the period of pegmatite emplacement on the Scottish mainland, dated by Evans and Lambert (1974). Therefore it is probable that the basement within the Rona Ridge/Faroe-Shetland Basin area comprises another crustal block(s) or terrane(s) of similar origin to the Lewisian Gneisses present within both the Scottish mainland and Hebridean islands.

In the Clair Field, the Late-Archaean to Early Proterozoic basement is thought to influence hydrocarbon drainage zones (typically fracture corridors) within the cover sedimentary sequences. Coney et al (1993) suggest that effective permeability through fractures in the sedimentary rocks only occurs through fault zones and 'fracture corridors' which are potentially important for well drainage. These fault zones (and fracture corridors) in the sedimentary rocks are typically aligned with fault zones in the basement suggesting a basement influence either by the formation of new faults or by the reactivation of pre-existing structures.

Further qualitative analyses of the lithological relationships within basement core from the Clair Field and the LCG of mainland Scotland are used to strengthen comparisons between the two study areas. A discussion of these lithological relationships is presented in *Chapter 6*.



**Figure 2.17:** Location map of dated basement wells in the Rona Ridge section of the Faroe-Shetland Basin. The map includes the major structural present in this area. After Ritchie and Darbyshire (1984).

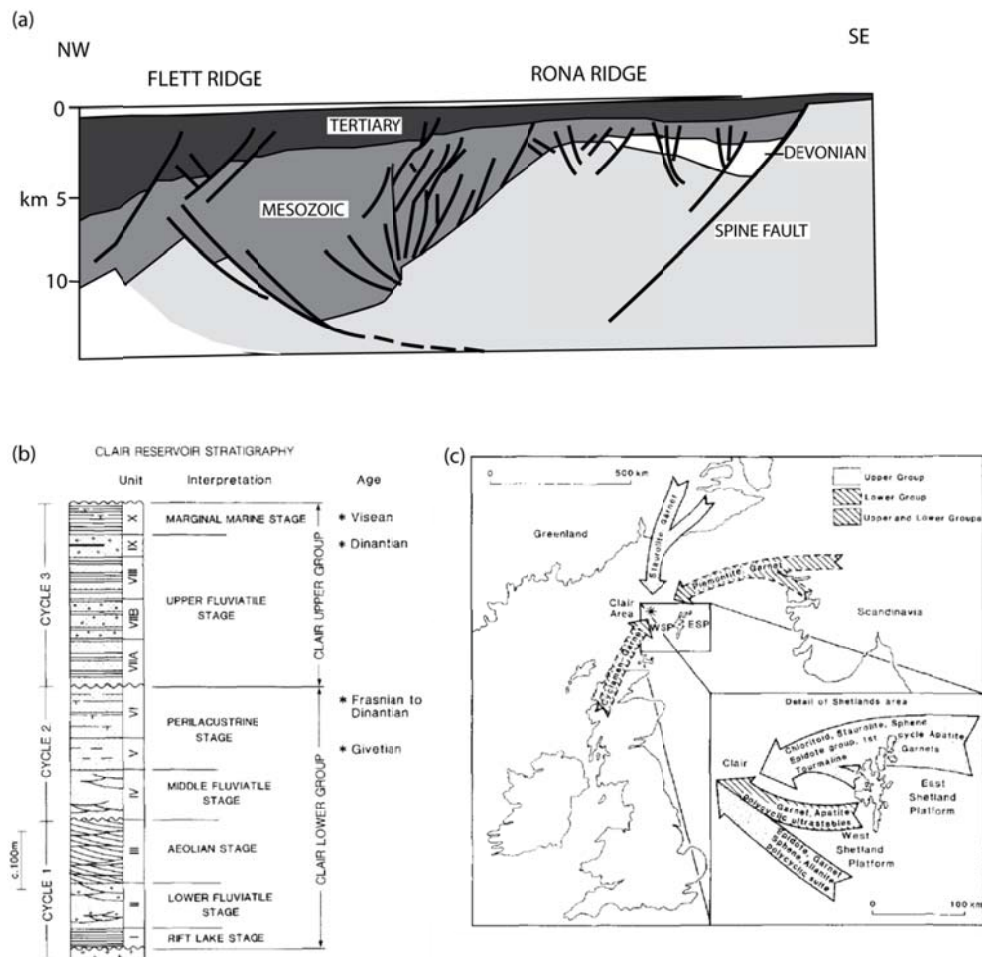
### 2.2.3.2 – Devonian-Carboniferous succession

The NE-SW to NNE-SSW trending elongate sub-basins of the FSB are defined by rift faults. The westward thickening of sedimentary strata into the hanging walls of these faults suggests that significant amounts of sedimentation occurred syn-rift (*Figure 2.18a*). Across different basins, such as the North Minch and the West Orkney Basin, the period of active sedimentation varies from commencement in the Devonian to the Cretaceous. In the FSB, extensional faults are thought to reflect rifting phases in the Permo-Triassic and Late-Jurassic to Early Cretaceous resulting in Permo-Triassic sedimentation (Ziegler, 1982). The Clair area is anomalous as it possess much older Devonian-Carboniferous sedimentary fills compared to surrounding areas in the FSB (Allen and Mange-Rajetzky, 1992).

Reservoir rocks in the Clair Field are of mid-Devonian to Early Carboniferous age sedimentary rocks that unconformably rest on the Late Archaean to Early Proterozoic basement (McKie and Garden, 1996). The Clair Group is divided into upper and lower groups (*Figure 2.18b*), that are separated by an angular-unconformity, which was first

recognised by Allen and Mange-Rajetzky (1992). Each group is divided into different units representing different depositional environments (*Figure 2.18b*). In the Lower Clair Group, Units I to VI represent two cycles, the first of which represents an upward change from fault-controlled floodplain lacustrine deposits (Unit I) to the deposition of multi-storey fluvial sandstones (Unit II) and finally sediment deposition in Aeolian dune and sabkha environments (Unit III) (Allen and Mange-Rajetzky, 1992). The second Lower Clair Group cycle shows a return to sand-rich fluvial deposits with evidence of interaction with Aeolian dunes (Unit IV), then a return to lacustrine deposits (Units V & VI) representing an upward fining of the sediments (Allen and Mange-Rajetzky, 1992). In the Upper Clair Group, the final cycle represents the evolution of well-developed high sinuosity fluvial systems (Units VII to VIII); followed by an influx of coarse sands and gravels and the increasing occurrence of carbonaceous sediments, including coals (Unit IX); and finally to a shallow marine depositional environment (Unit X) (Allen and Mange-Rajetzky, 1992).

The 'nested' cycles described above are interpreted to be the products of changes in the balance between tectonically-induced accommodation (start of Lower Clair Group deposition) and climatically-controlled sediment supply (deposition of lacustrine, fluvial and Aeolian sediments) (McKie and Garden, 1996, Nichols, 2005). Understanding the controls on the sediment cycles allowed better prediction of the distribution of the main reservoir units, (Units V & VI within the Lower Clair Group). The provenance of the Clair Group sediments (using heavy minerals) suggests that the sedimentary sequence evolved in two contrasting phases (*Figure 2.18c*) (Allen and Mange-Rajetzky, 1992). Lower Clair Group cycles were deposited by small intra-rift drainage systems with exclusively continental, clastic deposits (Nichols, 2005). Sediment supply during this time was predominantly from the north and west where the drainage network was eroding metamorphic basement rocks (presumably Lewisian) (Nichols, 2005). Upper Clair Group sediments represent an enlargement of the watersheds with river systems developed that were transporting sediments from Shetland and the Scottish mainland and reaching Scandinavia and Greenland during periods of maximum fluvial activity (Allen and Mange-Rajetzky, 1992). During the deposition of the Upper Clair Group there was no evidence of active tectonism in the Clair area and a climatic change occurred towards increasing humidity (Allen and Mange-Rajetzky, 1992).



**Figure 2.18:** (a) Present day structural cross-section showing the Devonian Clair Group forming an eastward thickening wedge from the Rona Ridge to the Spine Fault. After McKie and Garden (1996). (b) Summary stratigraphy of the Clair Group Devonian-Carboniferous sediments. After Allen and Mange-Rajetzky (1992). (c) Provenance areas of minerals comprising the Clair Group sediments. Arrows with broken lines are minor sources. WSP – West Shetland Platform; ESP – East Shetland Platform. Asterisk marks Clair area. After Allen and Mange-Rajetzky (1992).

### 2.2.3.3 – Late Cretaceous

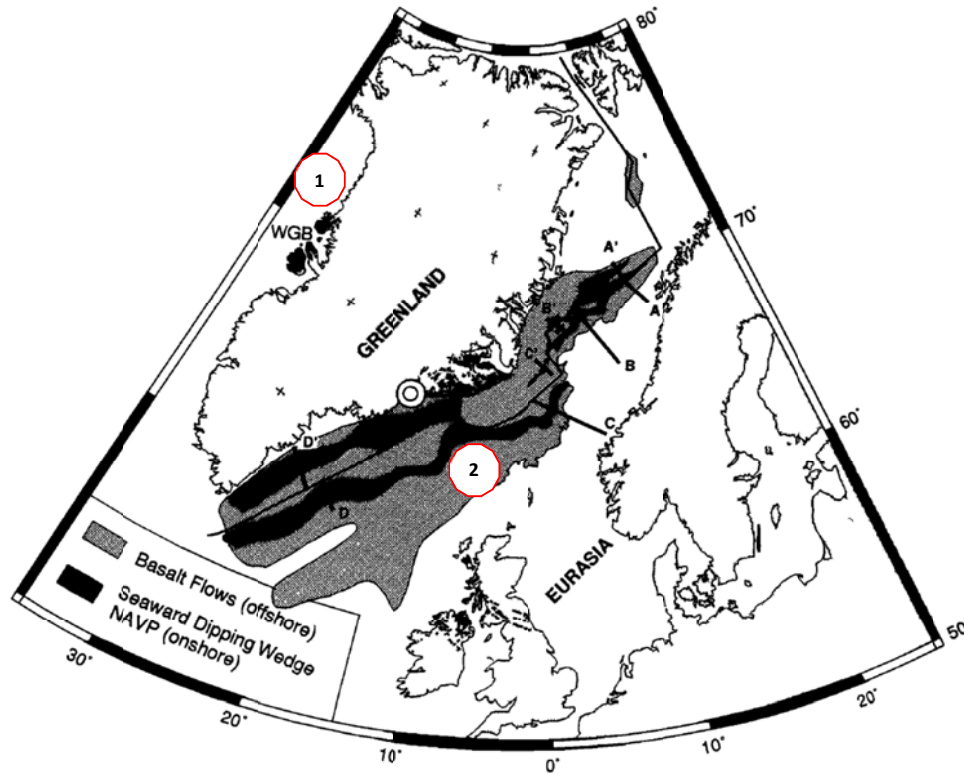
The Clair Group sediments are cut by the Base Cretaceous unconformity which is overlapped by a thick sequences of Cretaceous sediments (Barr et al., 2007). These Cretaceous sediments include shallow marine sands that are overlain by deep-water Shetland Group mudstones (in the Late Cretaceous) (Barr et al., 2007) that form the cap rock of the four-way dip closure of the Clair Field hydrocarbon trap (Witt et al., 2010). The mudstones are followed by Cenozoic (mainly Tertiary) sands and mudstones from a shallower water deposition environment (Barr et al., 2007). Evidence of fault

reactivation, folding and unconformities in the Cenozoic is related to North Atlantic rifting followed by a switch to a compressional, ridge-push environment (Barr et al., 2007).

#### **2.2.3.4 – Palaeocene to Eocene**

During the Paleocene and the Early Eocene, the North Atlantic Igneous Province (NAIP) developed, covering an area of  $1.3 \times 10^6 \text{ km}^2$  with a volume of basaltic rocks in excess of  $1.8 \times 10^6 \text{ km}^3$  (Eldholm and Grue, 1994). U-Pb, Ar-Ar and magneto-stratigraphy have been used to determine that the NAIP was emplaced in two distinct phases (*Figure 2.19*) (Saunders et al., 1997, Saunders et al., 2007). The first phase occurred at 62-59 Ma with magmatism occurring in the British Isles, Greenland and Baffin (Saunders et al., 2007). Phase two emplaced igneous rocks across the passive margin between east Greenland and northwest Europe at 56.5 – 54 Ma. It is this second phase of igneous activity that is present within the southwest portion of the Clair area with the presence of sills within the Tertiary sediments.

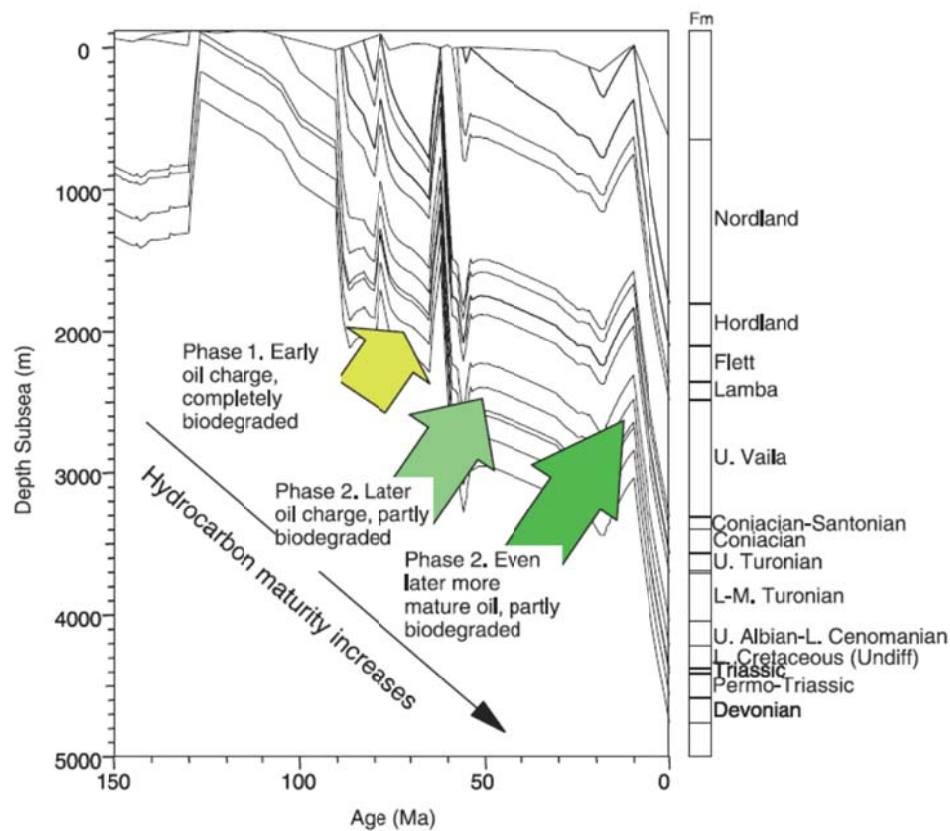




**Figure 2.19:** Extent of early Tertiary extrusive basalts on a reconstruction to magnetic anomaly 23 time (Eldholm and Grue, 1994). The two phases of NAIP emplacement are also indicated.

#### 2.2.3.5 - Source rocks and oil migration history

Source rocks for many of the FSB hydrocarbon fields, including the Clair Field is the Late Jurassic Kimmeridge Clay equivalent formation (Scotchman et al., 1998). The burial history for these source rocks in the Mesozoic is dominated by extension, particularly during the Cretaceous (Scotchman et al., 2002). Oil and gas generated from the Kimmeridge Clay Formation charged reservoirs (including those in Clair) during the Cretaceous-Tertiary (Scotchman et al., 1998). Multiple phases of hydrocarbon charging have occurred in the FSB with earlier charges becoming biodegraded before the final live oil charge (*Figure 2.20*). Re-Os geochronology shows that major volumes of oil generation in the FSB occurred at  $72 \pm 5$  Ma,  $64.3 \pm 3.5$  Ma,  $53 \pm 14$  Ma and  $42 \pm 6$  Ma (Finlay and Selby, 2011). The oldest two phases are relevant to the Clair Field with the live oil charge occurring in the Tertiary and filling the Carboniferous reservoirs (Conway et al., 2008).



**Figure 2.20:** Hydrocarbon charge model for the Foinaven area. The model shows three charge phases with similar biodegradation patterns to the hydrocarbons in the Clair Field. After Scotchman et al. (2006).

#### 2.2.4 – Clair Field tectonic history

The tectonic history of the Clair Field is long and complicated, spanning from the Archaean right through to the Cenozoic. There is little to no information about the tectonic history of the Clair area prior to the onset of sedimentation in the Devonian and so any attempt to assess the tectonic history of this area prior up to the mid-Devonian (i.e. the end of the Caledonian Orogeny, c. 390 Ma; Coward (1990a)) is limited. It is clear however, that basement structures, formed in the Proterozoic and Paleozoic, are likely to influence basin development (Coward, 1990a), and more importantly in this thesis, fault zones and ‘fracture corridor’ locations within the Clair reservoir units. *Appendix A* provides a tectonic, metamorphic, sedimentary and igneous history comparison of both the Clair Field and the mainland LGC.

Laxfordian deformation, which is present right across the onshore LGC in both the Scottish mainland and Hebridean islands is thought to be the first major orogenic

episode which affected the basement structure all across NW Europe (including the FSB) (Coward, 1990a). The onset of this deformation occurred at c. 1860 Ma before progressive exhumation passed the basement rocks through the viscous/frictional transition. Pre-Devonian brittle deformation is recognized in the Clair basement with the formation of epidote ultracataclasites and quartz/hematite mineralized fracture sets (see *Chapter 4* for a full analysis of brittle deformation in the Clair basement).

During the Caledonian Orogeny (closure of the Iapetus Ocean) compression was accommodated along NW-verging thrusts, such as the Moine Thrust and Outer Hebrides Fault Zone in northwest mainland Scotland and the Outer Hebrides, respectively (e.g. Dean et al., 1999). Seismic profiles from offshore northern Scotland show easterly-dipping dipping reflectors which are probably related to the Moine and other thrusts, reflecting an offshore continuation of the Caledonian Orogen into the West Orkney Basin (Coward, 1990a). It is also possible that the effects of the Caledonian Orogeny, namely the Outer Hebrides Fault Zone, were present in the Clair area with the formation of a NE-SW trending structural grain.

The next major tectonic event affecting the Clair area occurred in the early- to mid-Devonian when the Iapetus and Rheic Oceans finished closing with Laurentia, Baltica, Avalonia and Amörica being finally sutured (Knott et al., 1993). Also during this period, the Caledonian Mountain belt may have undergone some degree of extensional collapse (relaxation), resulting in block rotation along large-scale listric faults partially reactivating pre-existing thrusts. This may have resulted in the formation of localised basins in the area north of mainland Scotland (Bartholomew et al., 1993, Hinz et al., 1993, Knott et al., 1993) and created accommodation space for the deposition of the Devonian Old Red Sandstone. (Stoker et al., 1993) (*Figure 2.16*). It was during the same NW-SE extensional period that the deposition of the Lower Clair Group was initiated (Allen and Mange-Rajetzky, 1992). During this first rifting phase, the Clair area experienced block rotation and extension on N-S & NNE-SSW faults which potentially reactivated pre-existing basement weaknesses (Couzens, 2008).

The whole Clair Field area experienced multiple phases of NW-SE to E-W extension initiated by rifting events, from the Late Paleozoic through the Mesozoic, that formed new structures and possibly repeatedly reactivated pre-existing NE-SW, NNE-SSW and N-S faults (and fractures), both within the basement (Bartholomew et al., 1993) and the cover sedimentary sequences. This rifting continued through to the Late

Cretaceous when there was a final NW-SE rifting phase on the Clair Ridge Fault (Couzens, 2008).

Following this long extensional period, the Paleocene showed change to a compressive regime with the Clair area experiencing doming and uplift, resulting from sea-floor spreading in the northeast Atlantic. Accompanying this period was the formation of the NAIP between the British Isles and E. Greenland (with the thickest units occurring at the Faroes Platform) (Eldholm and Grue, 1994) (*Figure 2.19*). This uplift, compression and igneous activity episode continued until ~55 Ma (Eocene) when post-rift subsidence occurred (Davies et al., 2004). As the Atlantic has continued to open there have been further periods of compression and uplift, which have continued to reactivate pre-existing faults (particularly those trending NE-SW).

From the Pliocene to Recent, offshore and onshore regions have experienced NW down-tilting associated with glacial rebound (Couzens, 2008). In the Clair field this NW tilting is used to explain why the majority of open fractures seen in the basement and sediments trend in NE-SW & NNE-SSW directions (Couzens, 2008).

#### **2.4.4.1 – Hydrocarbon production from fractures in the Clair Field**

Well test analysis of an early well (206/8-8) drilled in the Core area of the Clair Field, showed that dynamic reservoir performance was largely due to the presence of abundant open natural fractures in the sedimentary rocks (Barr et al., 2007). The majority of fractures in the Clair Field (including the basement) are sub-vertical and so horizontal wells were used to cross-cut the known open fracture trend (from 206/8-8) of WNW-ENE. Wells that contained these open fracture sets typically flowed thousands of barrels of oil a day compared to relatively unfractured wells which only produced hundreds of barrels of oil a day (Barr et al., 2007).

Fractures within the Clair Field include granulation seams, cemented fractures, partially cemented fractures and open fractures. The proportion of each of these fracture types varies throughout the Clair Field depending on the lithotype in which they occur (*Table 2.5*). For example, brittle fractures dominate over granulation seams in lower-porosity, fined-grained facies where they are typically cemented and do not contribute to fluid flow (Barr et al., 2007). This is compared to clean high-permeability sands where granulation seams are common, but the equal presence of open fractures reduces any 'baffling' effects the granulation seams may have had on the reservoir (Witt

et al., 2010). In the basement, the presence of open or partially cemented fractures creates the potential for another reservoir unit which would not have been possible without the presence of fractures.

Open fracture sets fall into one or usually more preferred azimuths with open fractures on the ridge (in the basement) more commonly trending NE-SW. Barr et al (2007) suggests that the variations in open fracture azimuths are associated with adjacent sub-seismic faults and therefore this azimuth variation can be attributed to a model where open fractures formed during fault reactivation. This is instead of open fractures being uniformly orientated due to the relative orientation of a contemporary single, whole-field stress regime.

			Layer Averages (Core Area)			
			Net:Gross	Porosity	kh <sub>or</sub>	$\frac{K_{hor}}{K_{vert}}$
Lower Clair Group (c 600m)	VI-U	Lake margin fluvial	75%	14%	25mD	0.005
		Lacustrine key bed	NON-NET			
	VI-L	Lake margin fluvial	55%	13%	50mD	0.001
	V	Semi-arid fluvial	90%	15%	100mD	0.05
	IV	Semi-arid fluvial	80%	13%	10mD	0.001
	III	Aeolian	90%	14%	100mD	0.01
	I/II	Fluvial-lacustrine basal conglomerate	NON-NET			

**Table 2.5:** Stratigraphic subdivisions and reservoir properties of the Lower Clair Group. After Clifford et al. (2005).

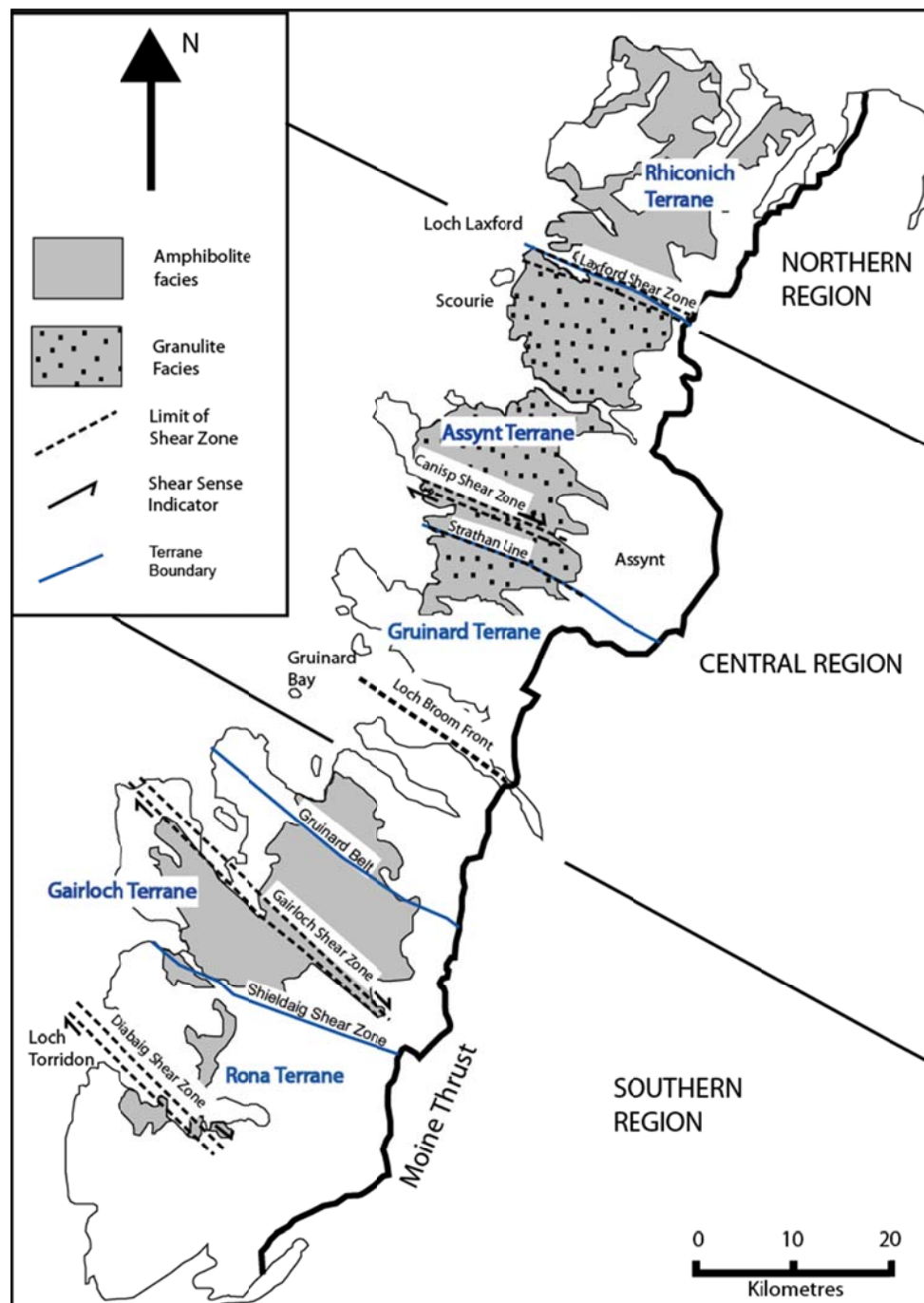
## **Chapter 3 – Mainland Lewisian Gneiss Complex fault and fracture analysis**

The aim of this chapter is to develop an understanding of the fracture network characteristics from the mainland Lewisian Gneiss Complex (LGC) using a variety of data sources. These include topographic lineaments derived from NEXTMap® digital elevation models across the northwest Highlands and field data from Lewisian outcrops; including hand specimens, thin sections and 1-dimensional line samples.

As discussed previously (*Chapter 2*), the Late Archaean-Early Proterozoic LGC comprises tonalite-trondjemite-granodiorite (TTG) gneisses with subordinate mafic & ultramafic dykes, meta-sedimentary and meta-volcanic sequences. It has long been thought to comprise a single unit of crust that has experienced differing ductile deformation histories that delimit three tectonic blocks or regions (Peach et al., 1907 and references thereafter). In recent years, however, this subdivision has evolved into a model where the LGC consists of at least six separate crustal blocks that were assembled during the Precambrian (*Figure 3.1*)

The LGC has experienced many episodes of deformation, with at least three distinct phases of brittle faulting. These include NW-SE trending 'Late Laxfordian' (*ca* 1.2 Ga.) structures which are most intensively developed in pre-existing NW-SE ductile shear zones developed in the LGC (Beacom et al., 2001). In turn, these are cross-cut by later NE-SW trending fractures formed at *ca* 1.1 - 1, synchronous with the deposition of the overlying Stoer Group sediments (Beacom, 1999, Beacom et al., 1999). Younger fracture sets also developed in association with Permian to Jurassic rifting events affecting both onshore and offshore NW Scotland (Beacom, 1999). The latter sets are less common, but where observed, they typically form as new cross-cutting features and also by reactivation of larger favourably orientated pre-existing structures.

The aim of this chapter is to present all of the data analysis from the regional and outcrop-scale studies in a manner that allows a comparison or contrast between the onshore (mainland LGC) and offshore (Clair basement, *Chapter 4*) datasets to be made later in this thesis (*Chapter 6*).



**Figure 3.1:** Schematic map detailing metamorphic facies and the three-fold classical subdivision of the mainland LGC as outlined by Peach *et al* (1907). These are overlain (in blue) by the current terrane model as introduced by Friend and Kinny (2001). Figure after Friend and Kinny (2001) & Rollinson (1996).

### 3.1 – Introduction to the onshore fracture analysis

The onshore nature of the datasets means that it is possible to gather fracture data from a variety of structural and lithological settings with the only restriction being the quality (or occasionally the location) of the outcrop.

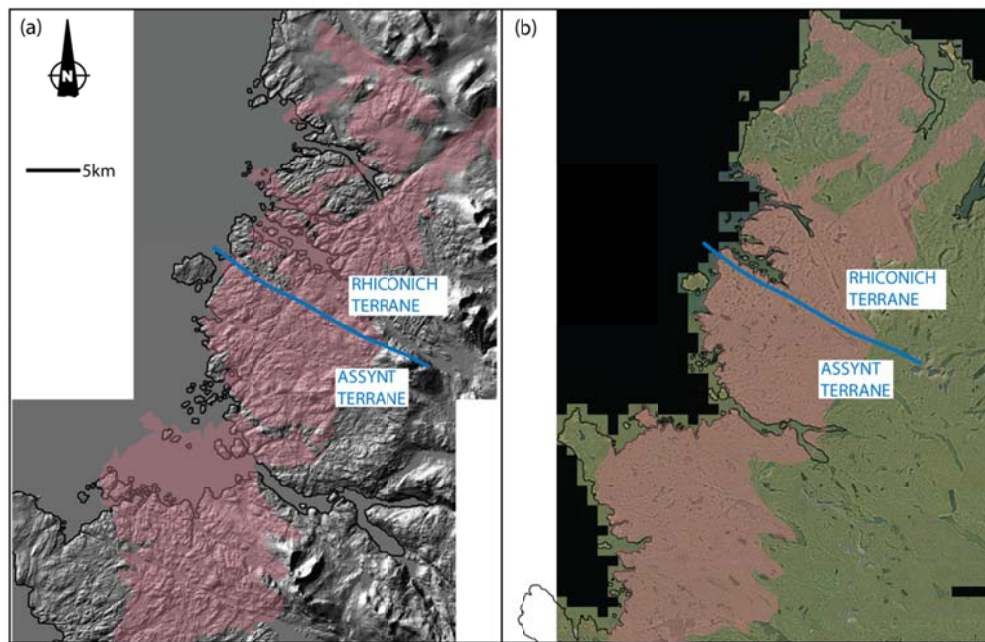
### 3.2 – Regional lineament analysis

A regional analysis of the faults and fractures present within the mainland LGC has been conducted using interpretations of NEXTMap<sup>®</sup> (Intermap Technologies, 2003) digital elevation models (DEM). *Figure 3.2* shows the extent of the DEM and aerial photographs across the mainland NW Highlands. Note that the aerial photographs were primarily used in conjunction with the analysis of key outcrops that have been terrestrial laser scanned and a semi-regional fault study using these can be found in *Chapter 5*.

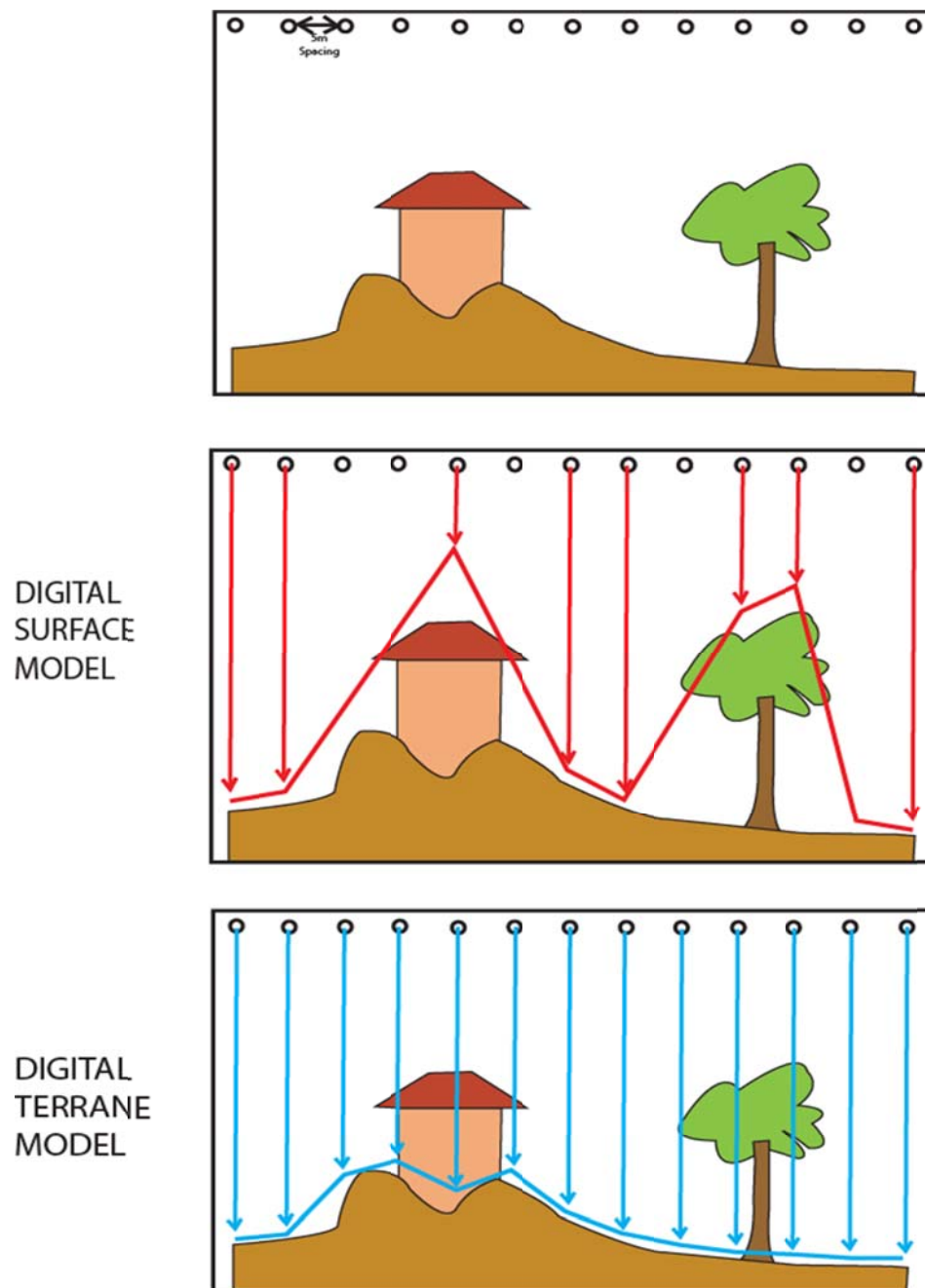
NEXTMap<sup>®</sup> Britain is a set of ortho-rectified radar images, digital surface models and digital terrain models. The data is collected by plane-mounted radar along predefined flight paths and is gridded on 5m spacings. It is then tied to the National Grid so that it is geo-referenced. The data are high resolution (5m horizontally and 2m vertically) and have been used to create fault lineament maps.

The DEM data are in the form of digital surface models (DSMs) or digital terrain models (DTMs). DSMs reflect the topography encountered by the radar without applying any smoothing. This can cause issues in populated areas or areas that are forested because the models contain anomalies created by houses and trees (*Figure 3.3a, b*). DTMs smooth the radar data to remove many of the artefacts created by houses and forests etc. (*Figure 3.3c*), thus reducing the errors that could be made during interpretation of features seen on the resulting maps. Due to the remote nature of the landscape in the NW Highlands (very few trees and houses) and the desire to be able to map the finest details that can be seen from the topography data, DSMs have been used exclusively for the onshore regional study.





**Figure 3.2:** Maps illustrating the extent of the regional data available for the mainland LGC. **(a)** Shows the extent of the NEXTMAP® Britain DEM dataset **(b)** Shows the extent of the aerial photographs. This dataset extends further than shown but the area in this figure covers the section of LGC that has been used in this study. The areas highlighted in pink show the extent of the LGC outcrop.



**Figure 3.3:** Schematic representation of the difference between Digital Surface Models and Digital Terrain Models. **(a)** An example of the typical topography encountered using the plane-mounted radar collecting the NEXTMap<sup>®</sup> Britain data. **(b)** Digital Surface Model (DSM) – topography reflects any buildings or trees, etc. encountered. **(c)** Digital Terrain Model (DTM) – model is smoothed to remove many of the artefacts caused by buildings or trees, etc. This model can also smooth some of the true topography and so features such as faults can be lost with this model.

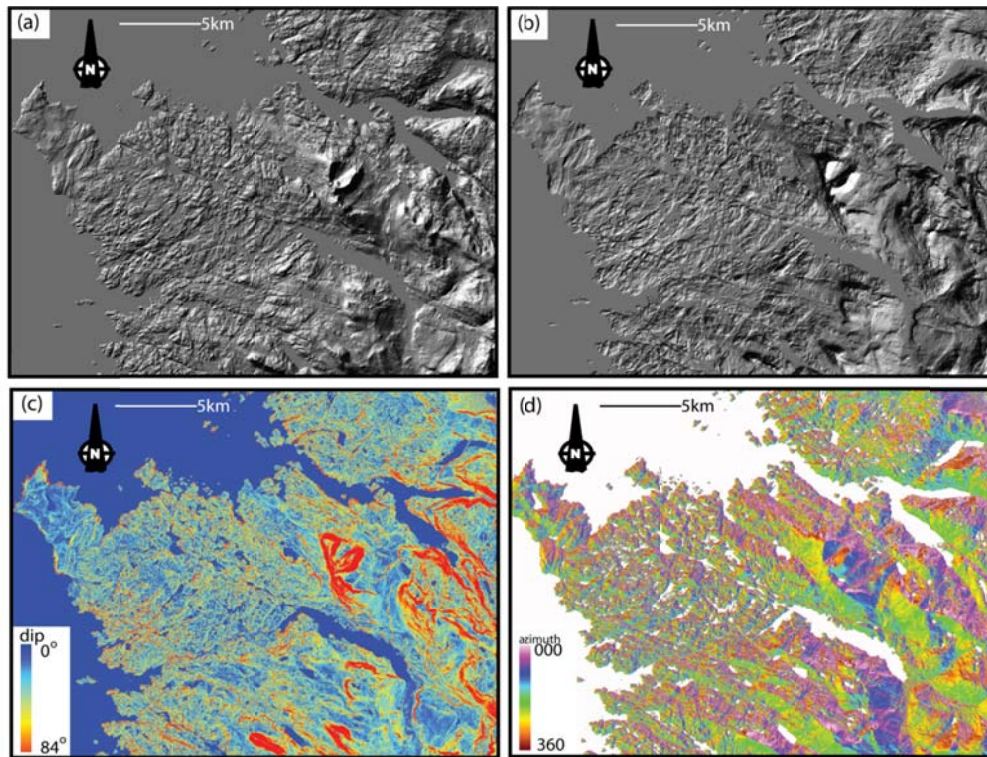
Onshore fault lineament interpretation was completed using ArcGIS® 9.2 where the DEM data was used to create different surface analysis maps which include: hill-shade, slope and aspect (*Figure 3.4*). The definitions of each surface analysis are given below.

*Hill-shade (Figure 3.4a & b)* – Highlights the changes in topographic height across the mapped area by illuminating the DSM from different orientations. For the purposes of this onshore regional study, the illumination was set in two orientations ( $60^\circ \rightarrow 315^\circ$  and  $60^\circ \rightarrow 135^\circ$ ) in order to maximise what can be seen from this surface analysis (see *Figure 3.4a & b* for comparisons). This surface analysis picks out grooves and ridges in the topography and in practice has been used first to interpret the most obvious features in the topography.

*Slope (Figure 3.4 c)* – This surface analysis highlights the variation in slope angle across the mapped area by colour-coding the different dips seen in the topography. It highlights steep slopes which in many cases can be attributed to scarps or gullies caused by faults.

*Aspect (Figure 3.5d)* – This surface analysis colour-codes the direction of slope within the mapped topography. It is particularly useful for interpreting small scale linear features (faults, dykes and/or foliation) as it picks out smaller changes in the topography than the hill-shade or slope analysis can.

During this onshore regional DEM study, none of these surface analysis maps were used independently of each other. To achieve the best interpretations it was found to be most effective if the different surface layers were overlain with each other. This was particularly effective with the aspect and slope analysis, as layering these two surface analyses allows small scale linear features to be interpreted that cannot be seen on the hill-shade analysis maps alone.



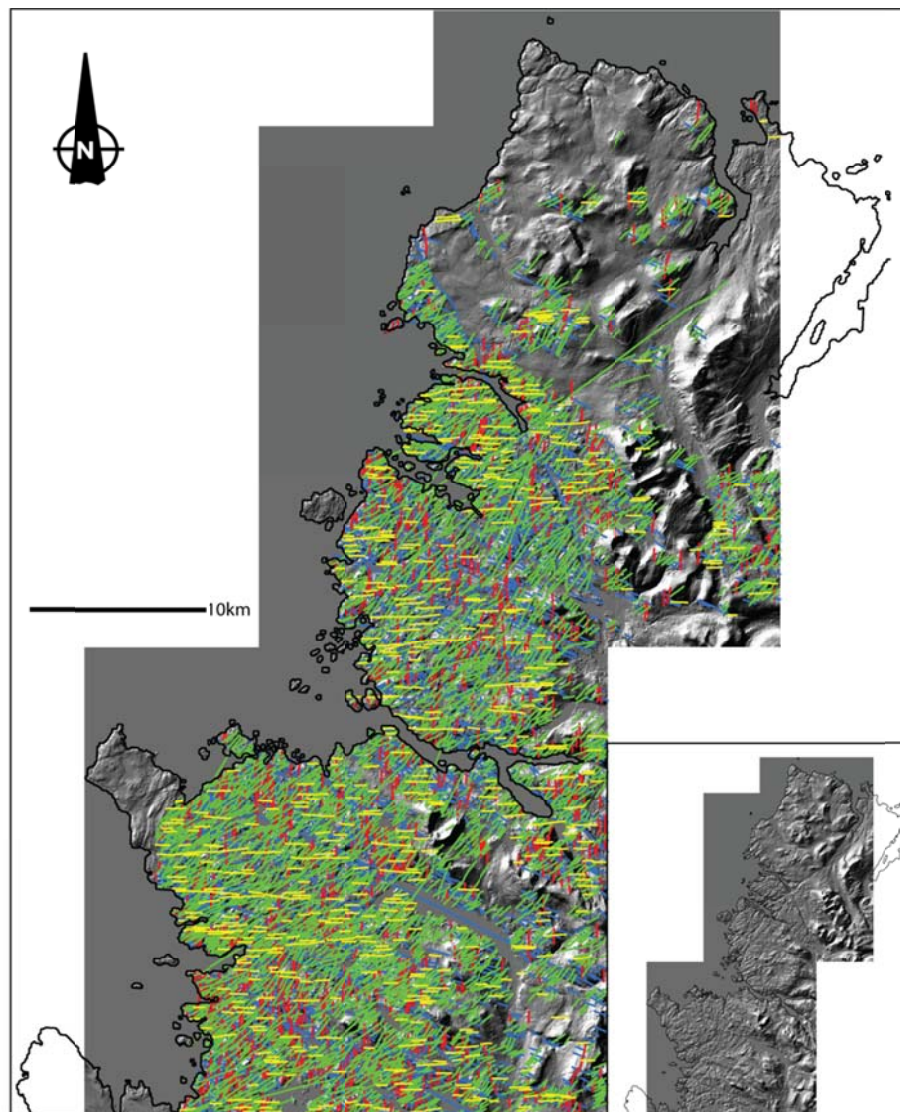
**Figure 3.4:** Examples of the surface analysis maps from the NEXTMap® Britain DEM data. **(a)** Hill-shade with the light pointing 60° → 315 **(b)** Hill-shade with the light pointing 60° → 135 **(c)** Slope analysis **(d)** Aspect analysis. Fault interpretation was best conducted by layering these different surface analysis maps on top of each other.

### 3.2.1 – Method for production and interpretation of DEM maps of NW Scotland

NextMap® DEM surface analysis maps were created at the British Geological Survey offices in Edinburgh where time was spent processing the raw DEM data. The surface analysis maps were created as rasters in ArcGIS® 9.2 using different techniques available in the Spatial Analyst toolbar (hill-shade, slope and aspect). Importantly, the resulting maps were in the same format as those created from the Clair basement seismic horizons so that direct comparisons between the datasets could be made (see below).

Surface analysis maps of the NW Highlands were created that best emphasised the regional faulting visible from the LGC regional data. Only areas of exposed LGC were interpreted as the overlying sedimentary units (Torridonian, Cambrian) and regions extensively covered with drift did not display obvious faults. Fault lineaments (*Figure 3.5*) were interpreted in ArcGIS® 9.2 at four different scales; 1:100,000 (first order faults), 1:50,000 (second order faults), 1:25,000 (third order faults) and 1:10,000 (fourth

order faults). The high-resolution nature of this data set (5m horizontally) means that it is possible to detect other linear geological features such as foliation and dykes from the surface analysis maps. Therefore using other resources, such as BGS geological maps, care was taken to exclude foliation, dykes and bedding in the cover sedimentary sequences from the lineament interpretation. It is possible, however, that a small number of interpreted lineaments have been incorrectly identified and do not represent faults (approximately 1.5%).



**Figure 3.5:** Map of the mainland LGC showing all interpreted fault lineaments over the hill-shade surface analysis map. In total there are 4012 interpreted fault lineaments on this map. Inset shows the hill-shade map without the fault lineament interpretation.



The high resolution of the NEXTMap® DEM data (5m horizontally and 2m vertically) is significantly higher than the resolution of the offshore seismic surveys. To directly compare the mainland DEM LGC dataset to the Clair basement seismic dataset, ArcGIS® 9.2 was used to reduce the resolution of the NEXTMap® DEM (cell size 25m x 25m) to create a second dataset that is more in line with the resolution of the seismic survey data from the Clair Field. This second dataset has been used within the fault spacing analysis to compare attributes such as the spacing distribution and fault density to the Clair Field seismic interpretation.

Once identified, the fault lineaments were assigned several different attributes, the most important of these being orientation (azimuth only) and length. The values for orientation and length were calculated using EasyCalculate50 scripts [polyline Get Azimuth 9x.cal](#) and [shape Return Length.cal](#) respectively. These attributes have been used to quantitatively analyse the fault lineament interpretation.

A fault lineament spacing analysis was also conducted using the data interpreted from the surface analysis maps. The work was completed in Paradigm® GOCAD 2009.2 and involved creating fault surfaces from the lineament data. This was executed by importing the interpreted fault lineaments in area groups (Assynt Terrane, Rhiconich Terrane, Canisp Shear Zone and Laxford Front; see Figure 3.6 for locations) into GOCAD and then using the structural modelling workflow to create fault surfaces (see *Appendix B* for the workflow).

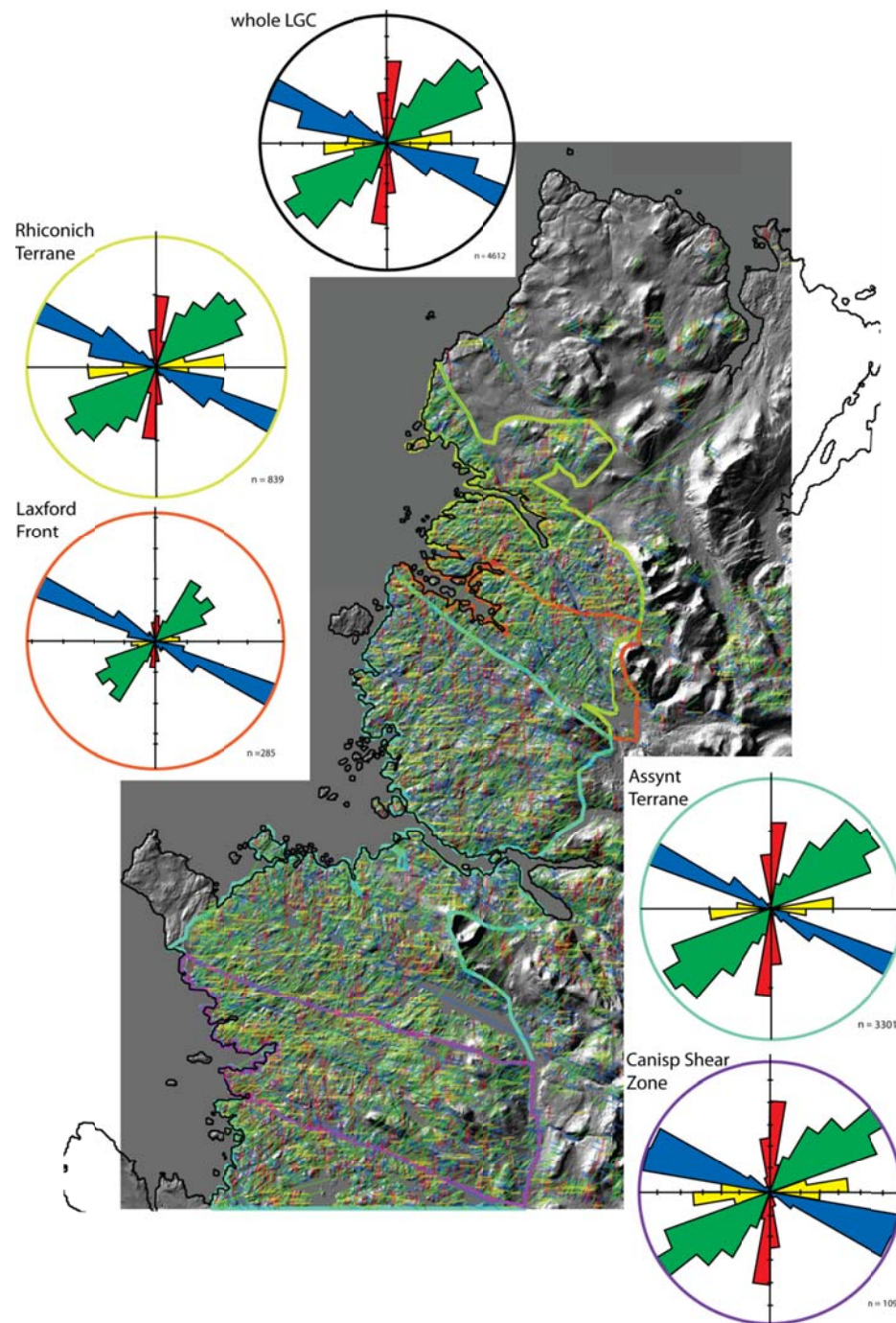
It is important to note that this technique of creating fault surfaces includes a major simplifying assumption. This assumption is that all the faults are plotted as vertical surfaces because there are insufficient data to be able to assign full 3-dimensional orientations to the interpreted fault planes. Due to the fact that I could only use height data from the DEM data whilst creating the surface analysis maps at the BGS offices, it was not possible to visualise the topography in 3-dimensions to allow fault orientations to be calculated from their topographic expressions. DEM data from the EDINA Digimap® download service were available, but these are of too low a resolution to be able to determine the orientation of all the interpreted faults. Another reason that the fault surfaces have been deemed vertical is that it means that this LGC regional analysis is more in line with the equivalent analysis carried out in the Clair Field. This means that it is possible to make a direct comparison between the onshore and offshore regional datasets. It is also worth pointing out that the outcrop-scale field observations

show that a majority (~67%) of the larger faults cutting the LGC are steeply dipping to sub-vertical (see *Section 3.3.4*)

Once fault surfaces were created in their separate area groups, a network of 'pseudo-wells' were draped over each area to create a 2-dimensional grid of 1-dimensional sample lines (*Section 1.6.5*). The pseudo-wells were made by creating linear 'wells' in GOCAD which can then be populated with fault surface intersections (see *Appendix B*). Pseudo-wells were created in four different orientations (NE-SW, NW-SE, N-S and E-W). This ensures that all orientations of fault surfaces were intersected and sampled by the pseudo-wells. The datasets collected from the pseudo-wells were then exported as dBASE table files into Excel and a spacing analysis of the interpreted faults was conducted. By using these pseudo-wells, fault spacing datasets, population distribution plots, the coefficient of variation and fault density values were easily created and analysed (see *Chapter 1* for more details on the methods involved in these statistical analysis techniques).

### 3.2.2 – Regional fault lineament orientation analysis

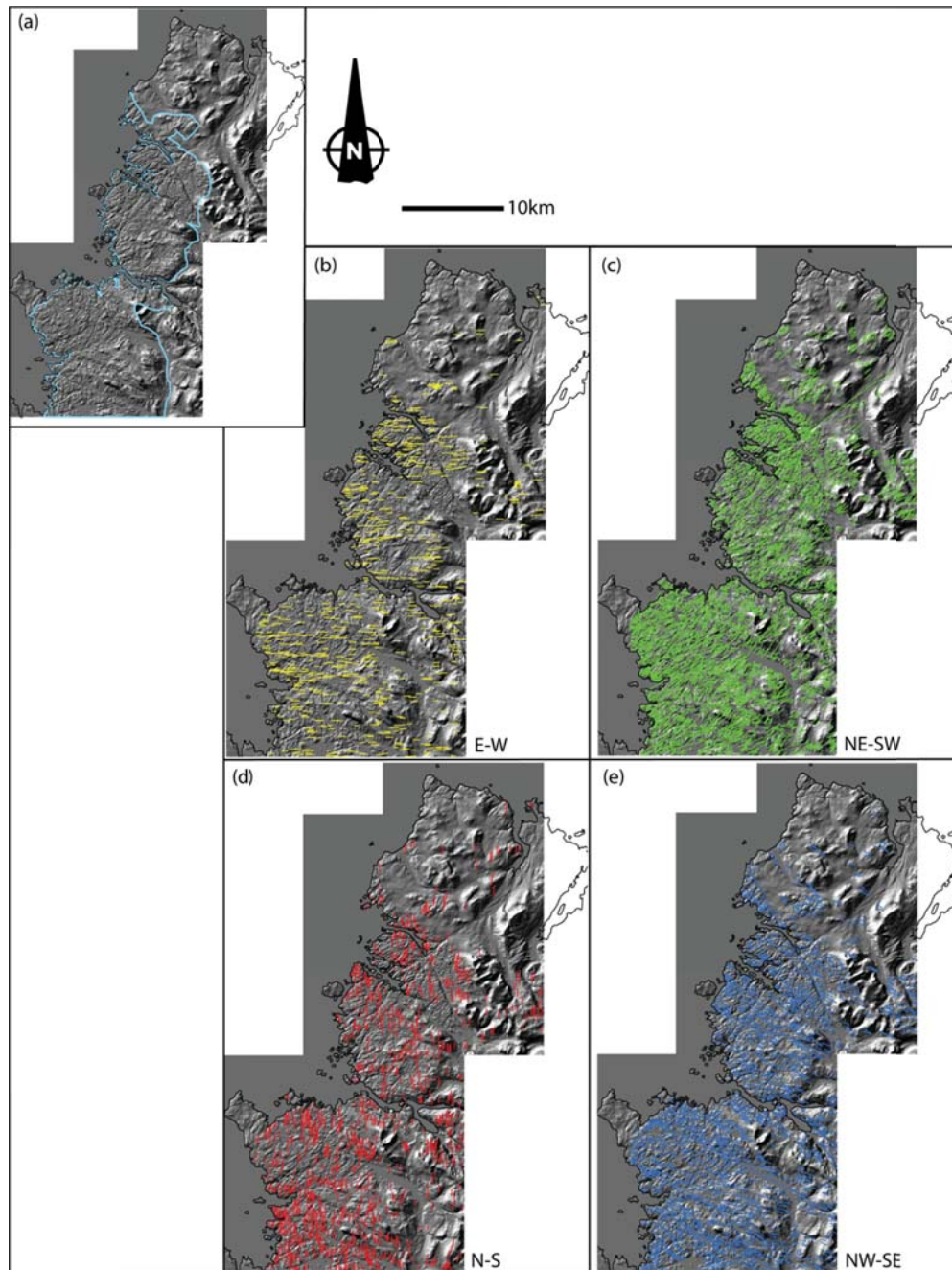
Orientation analysis has been conducted from the regional fault lineament analysis using rose plots and a series of lineament maps. For the purposes of the orientation analysis (and the subsequent fault spacing analysis), the mainland LGC has been separated into four areas; Assynt Terrane, Rhiconich Terrane, Laxford Front and Canisp Shear Zone (see *Figure 3.6*). In total, 4012 fault lineaments have been analysed for orientation (and spacing) across the whole mainland LGC. 3301 of these fault lineaments are in the Assynt Terrane and 839 are in the Rhiconich Terrane. Note that the Rhiconich Terrane represents a far smaller area of LGC outcrop compared to the Assynt Terrane. Geologically, both the Laxford Front (285 fault lineaments) and the Canisp Shear Zone (1092 fault lineaments) areas lie within the Rhiconich and Assynt terranes, respectively, but have been analysed separately because they contain major structures within the mainland LGC that show important variations in the fault and fracture network characteristics. Fault lineaments have been 'binned' into four separate azimuth groups; N-S (345-015° & 165-195°), NE-SW (016-075° & 196-255°), E-W (076-105° & 256-285°) and NW-SE (106-164° & 196-254°).



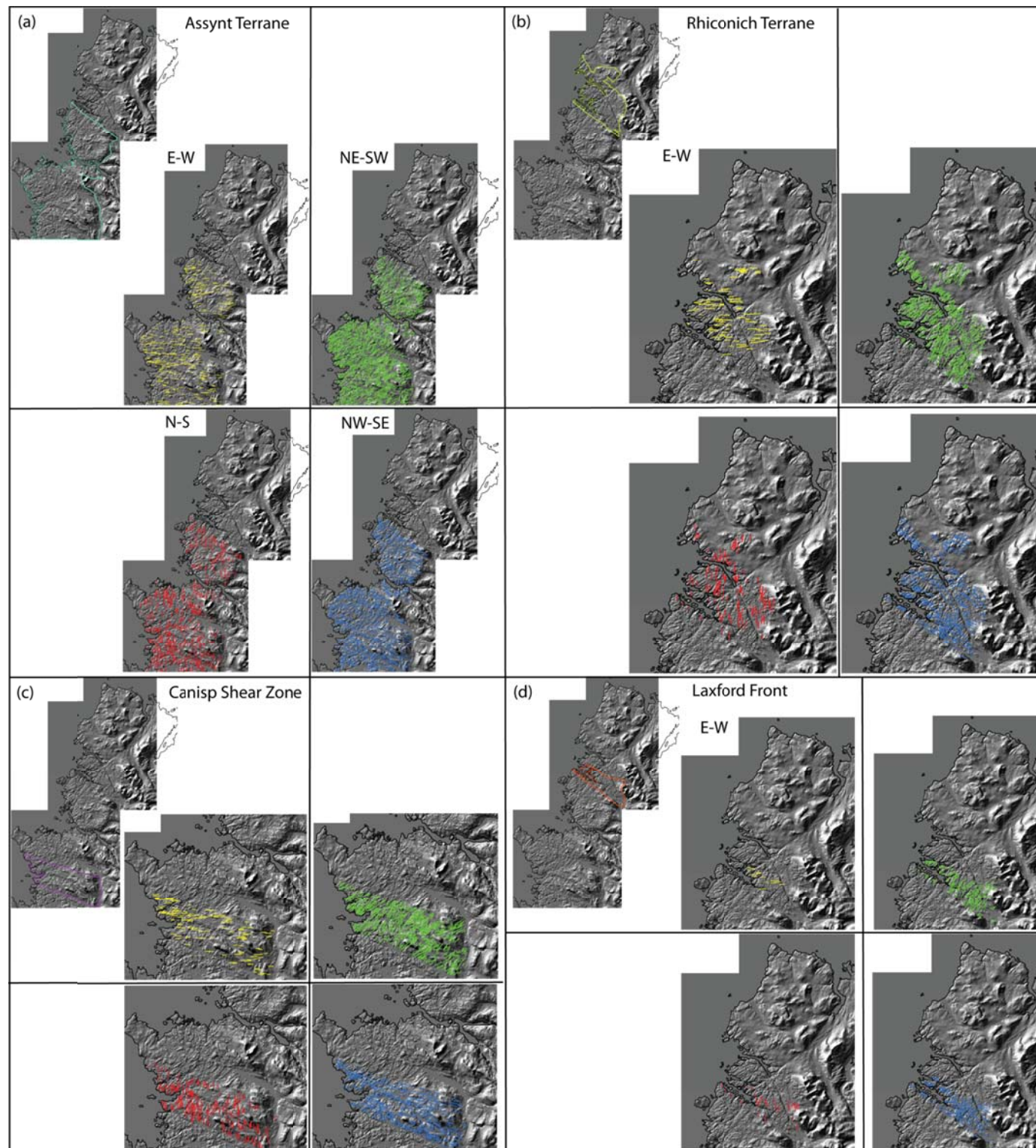
**Figure 3.6:** Map of the interpreted fault lineaments in the mainland LGC showing rose plots for different areas within the Lewisian. The rose plots are colour-coded per area. Black – Whole Lewisian Gneiss Complex (tick marks represent 10% of the dataset). Green – Rhiconich Terrane (tick marks represent 20% of the dataset). Orange – Laxford Front (tick marks represent 5% of the dataset). Turquoise – Assynt Terrane (tick marks represent 20% of the dataset). Purple – Canisp Shear Zone (tick marks represent 10% of the dataset). Fault trends are colour-codes per azimuth (Blue – NE-SW, Red - N-S, Green – NE-SW & Yellow – E-W).



From analysis of the NEXTMap® DEM data it is obvious that the mainland LGC is heavily fractured (e.g. see Figure 3.5). This is apparent from visual inspection of the DEM data, since areas that are known to have Lewisian outcrops are obviously cut by many more lineaments compared to the surrounding sedimentary rocks and areas covered by drift deposits. Consistently, NE-SW fault lineaments produce the most prominent trend across the mainland LGC areas (*Figure 3.6*). Commonly those NE-SW trending fault lineaments have azimuths that vary between 016° and 075° with a concentration around 048°. The colour-coded maps in *Figures 3.7 & 3.8* illustrate the variation in fault lineament orientation with respect to location. These maps show that NE-SW trending fault lineaments are densely distributed across the whole of the mainland LGC (4.05 faults per metre, *Figure 3.7*). NE-SW fault lineaments are particularly concentrated in the Canisp Shear Zone (2.80 faults per metre, *Figure 3.8c*) where there are 479 fault lineaments of this trend within this relatively small area (143km<sup>2</sup> compared to 658km<sup>2</sup> for extent of the mainland LGC shown in *Figures 3.5 and 3.6*). From *Figure 3.8* it is apparent that NE-SW trending fault lineaments are more densely distributed in the Assynt Terrane (2.91 faults per metre, *Figure 3.8a*) compared to the Rhiconich Terrane (2.41 faults per metre, *Figure 3.8b*). The Laxford Front also exhibits many NE-SW trending fault lineaments (132 lineaments), although they are less densely distributed compared to any other area in the mainland LGC (1.78 faults per metre, *Figure 3.8d*).



**Figure 3.7:** Hill-shade surface analysis map with the interpreted fault lineaments separated into their respective azimuth groups. **(a)** Hill-shade map showing the extend of the LGC outcrop (marked in blue) **(b)** E-W fault lineaments **(c)** NE-SW fault lineaments **(d)** N-S fault lineaments **(e)** NW-SE fault lineaments.



**Figure 3.8:** Hill-shade surface analysis maps for the mainland LGC highlighting the distribution of fault lineament azimuth groups for the main areas within the Lewisian. Each individual fault azimuth group is colour-coded (Yellow – E-W, Green – NE-SW, Red – N-S & Blue – NW-SE). **(a)** Assynt terrane map (outline shown in turquoise) **(b)** Rhiconich Terrane (outline shown in green) **(c)** Canisp Shear Zone (outline shown in purple) **(d)** Laxford Front (outline shown in orange).

NW-SE fault lineaments also represent a prominent trend within the mainland LGC with azimuth concentrations between 290° and 300° (*Figure 3.6*). Again, NW-SE fault lineaments are observed across the entire mainland LGC outcrop (*Figures 3.8a & b*), but are particularly prominent across the Laxford Front area where the fracture density is 1.59 faults per metre (*Figure 3.6*). From *Figure 3.8d* it is apparent that NW-SE and NE-SW fault lineaments occur in equal numbers in the Laxford Front area. This contrasts with the Canisp Shear Zone (*Figure 3.8c*) where there are far fewer NW-SE fault lineaments compared to those which trend NE-SW (261 and 479 fault lineaments, respectively).

Both N-S and E-W trending lineaments are present across all areas within the mainland LGC, albeit in smaller numbers. The Laxford Front exhibits the fewest N-S and E-W fault lineaments (0.19 and 0.34 faults per metre, respectively, *Figure 3.6*) with the Assynt Terrane showing the greatest numbers (E-W fault lineaments have a fracture density of 0.60 and N-S fault lineaments have a fracture density of 1.14, *Figure 3.8a*). N-S fault lineaments show little variation in azimuth (between 350° and 010°) and this is similar to E-W trending fault lineaments which all fall within a 20° azimuth window (between 080° and 100°) (*Figure 3.6*). Both N-S and E-W fault lineaments exhibit distributions that are more clustered, which contrasts with the NE-SW and NW-SE fault lineaments that are more regularly spaced throughout the mainland LGC (*Figures 3.7 & 3.8*).

The relationship between lineament orientation and lineament length has been analysed by displaying the length data as a density distribution across the mainland LGC (*Figure 3.9*). This length density distribution is calculated as a magnitude per unit area from polyline features (i.e. fault lineaments) in the neighbourhood of each output cell. It is calculated as units of length per unit of area. E-W fault lineaments are concentrated in three distinct regions in the study area where the fault lineaments are longer (*Figure 3.9c*). N-S faults also show some clustering of the longer lineaments, although the clustered regions are less well defined (*Figure 3.9a*). Both E-W and N-S fault lineaments show no consistency in their length, but they are typically shorter than both the NE-SW and NW-SE fault lineaments.

NE-SW lineaments exhibit length densities that are higher in the Assynt Terrane compared to the Rhiconich Terrane (*Figure 3.9b*). These lineaments show no consistent spacing patterns for the longer lineaments, although the longest lineaments occur in the

northern mainland LGC area. This contrasts with the NW-SE fault lineaments where it is clear that long lineaments have a consistent spacing distribution (*Figure 3.9d*). The NW-SE length density distribution also shows that the long fault lineaments have two separate orientations ( $\sim 285^\circ$  to the south and  $\sim 335^\circ$  to the north of the mainland LGC area). NW-SE lineaments fall into two length categories, those which have significant lengths ( $>10\text{km}$ ) and those which have lengths that are less than 2km. Those NW-SE fault lineaments that are in the first length category are the longest fault lineaments seen within the mainland LGC.

### 3.2.3 – Regional fault lineament orientation: Discussion

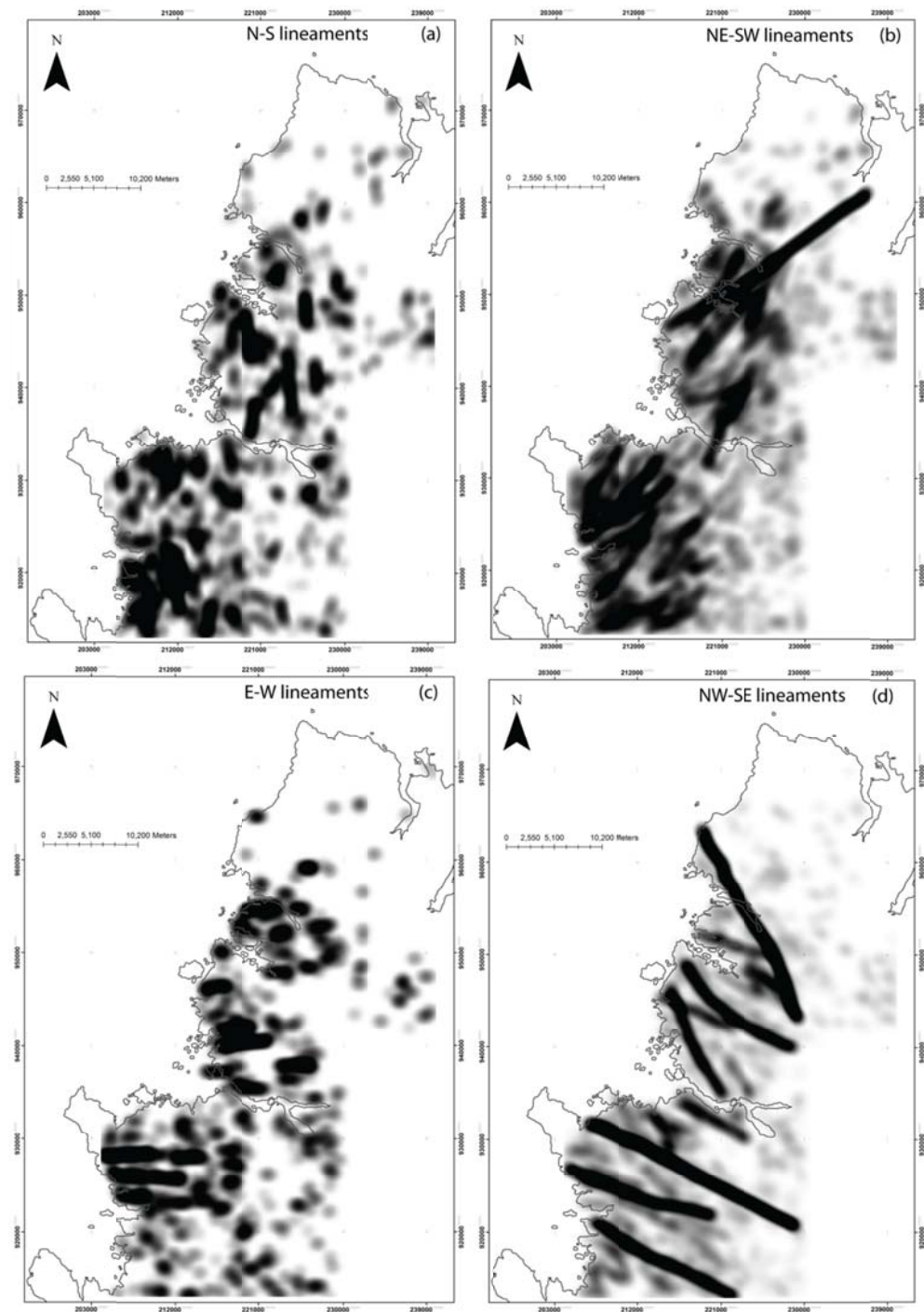
Regional fault interpretation from the mainland LGC has shown that both NE-SW and NW-SE trending faults are prominent across the study area. These fault azimuths coincide with at least two of the regionally recognised phases of brittle deformation within the LGC.

NW-SE trending faults in the Assynt Terrane are known to have first formed in the Proterozoic in an event known as the ‘Late Laxfordian’ (Beacom, 1999) with large-scale faults (and smaller fractures) forming sinistral strike-slip structures that are preferentially developed in, but not exclusive to, areas of well-defined foliation (e.g. the Canisp Shear Zone).

In the Rhiconich Terrane it is likely that the NW-SE trending faults have a younger origin and formed post-Torridonian. This potential origin is most obvious along the Loch Inchard Fault at Kinlochbervie (NC 2296 5621), which cross-cuts and offsets the Torridonian sediments and where the subordinate fractures in the fault damage zone are iron-stained and are epidote mineralised, which likely result of fault-related fluid flow through the Torridonian sediments.

Evidence from the British Geological Survey 1:50,000 bedrock geology maps and the length density maps (*Figure 3.9d*) suggest that the large NW-SE faults typically follow pre-existing weaknesses in the LGC. The azimuth of the large NW-SE trending faults appear to be controlled by the orientation pre-existing dykes and granite sheets in the LGC which accounts for the clockwise change in trend of NW-SE faults to the north of the Assynt Terrane and also in the Rhiconich Terrane (especially in the region of the Laxford Front) .





**Figure 3.9:** Length density maps for the mainland LGC using the interpreted fault lineaments. This type of analysis shows where a particular attribute (in this case length) is concentrated on a map. It clearly highlights larger features and areas where some lineament trends are more prominent than others. The search radius was set at  $\sim 500$  and the output cell size was 50 in order to produce a relatively high-resolution dataset. **(a)** N-S trending fault lineaments **(b)** NE-SW trending lineaments **(c)** E-W trending lineaments **(d)** NW-SE trending lineaments.

Some of the NW-SE faults – or parts of those faults - in the Assynt Terrane are known to reactivate subsequent to the Proterozoic. For example, the Loch Assynt Fault (see *Chapter 2, Figure* for a location map) is observed to offset the ‘double unconformity’ between the LGC and the Cambrian quartzites, which means that it was active post-deposition of the Cambrian sediments i.e. post Early-Ordovician (Krabbendam and Leslie, 2010). It is likely that many of the other large NW-SE faults in the mainland LGC have been at least partially reactivated through time (e.g. the Loch Inchar Fault (NC 2271 5663), see Kinlochbervie in *Section 3.3*), but there is a lack of clear geological evidence to determine the ages of these reactivations.

NE-SW faults are also present across the mainland LGC and this can be seen from *Figure 3.9b* where both long and short faults are distributed across both the Assynt and Rhiconich Terranes. These NE-SW faults can be attributed to at least two of the regionally recognised phases of brittle deformation. The first event occurred in conjunction with the deposition of the Stoer Group sediments on top of the LGC (c.a. 1100 -1000 Ma). The associated faults (and fractures) are syn-depositional features resulting from regional dextral transtension and are preferentially developed, but not exclusively, in areas of pre-existing NW-SE ductile shearing (Beacom, 1999 and references therein). N-S trending fault lineaments are also thought to have first formed during this Stoer Group deposition event. Collectively these N-S and NE-SW fractures form a conjugate set of multimodal faults and fractures (see Beacom et al., 1999, *Figure 11*)

Other NE-SW faults interpreted from the mainland LGC, particularly the Lochinver Fault (NC 0970 2316), are known to be much younger in age with a potential origin in the Mesozoic (see *Section 3.3.3.3*). These faults are likely related to Triassic NW-SE extension that is contemporaneous with movement on the Minch Fault which lies to the west of the mainland LGC (Wilson et al., 2010). Wilson et al. (2010) focus their study on the north coast of the mainland but it is possible that the extension recorded at the north coast is also evident throughout the mainland LGC resulting in large, possibly widely spaced NE-SW faults that cross-cut all pre-existing structures (or reactivate optimally orientated pre-existing faults).

### 3.2.4 – Regional fault lineament spacing analysis

A fault spacing analysis of the lineaments interpreted from the regional mainland LGC data has been conducted using population distribution plots created from the pseudo-wells draped on top of the mainland interpreted maps. The pseudo-wells intersect the interpreted fault lineaments at measured distances along each well, thus providing spacing data. Due to the fact that the LGC covers a large irregular area (658km<sup>2</sup>), the 4 sub-areas defined in the previous sections have been analysed for spacing distributions individually, rather than for the Lewisian as a whole. In total, 47 pseudo-wells in four different orientations (N-S, NE-SW, E-W & NW-SE) are used to analyse the fault lineament spacing distributions within the mainland LGC. Fault spacing data for the pseudo-wells used in this study are shown in the population distribution plots in *Figure 3.10* and the fault spatial attributes from the same pseudo-wells are shown in *Tables 4.1 & 4.2*.

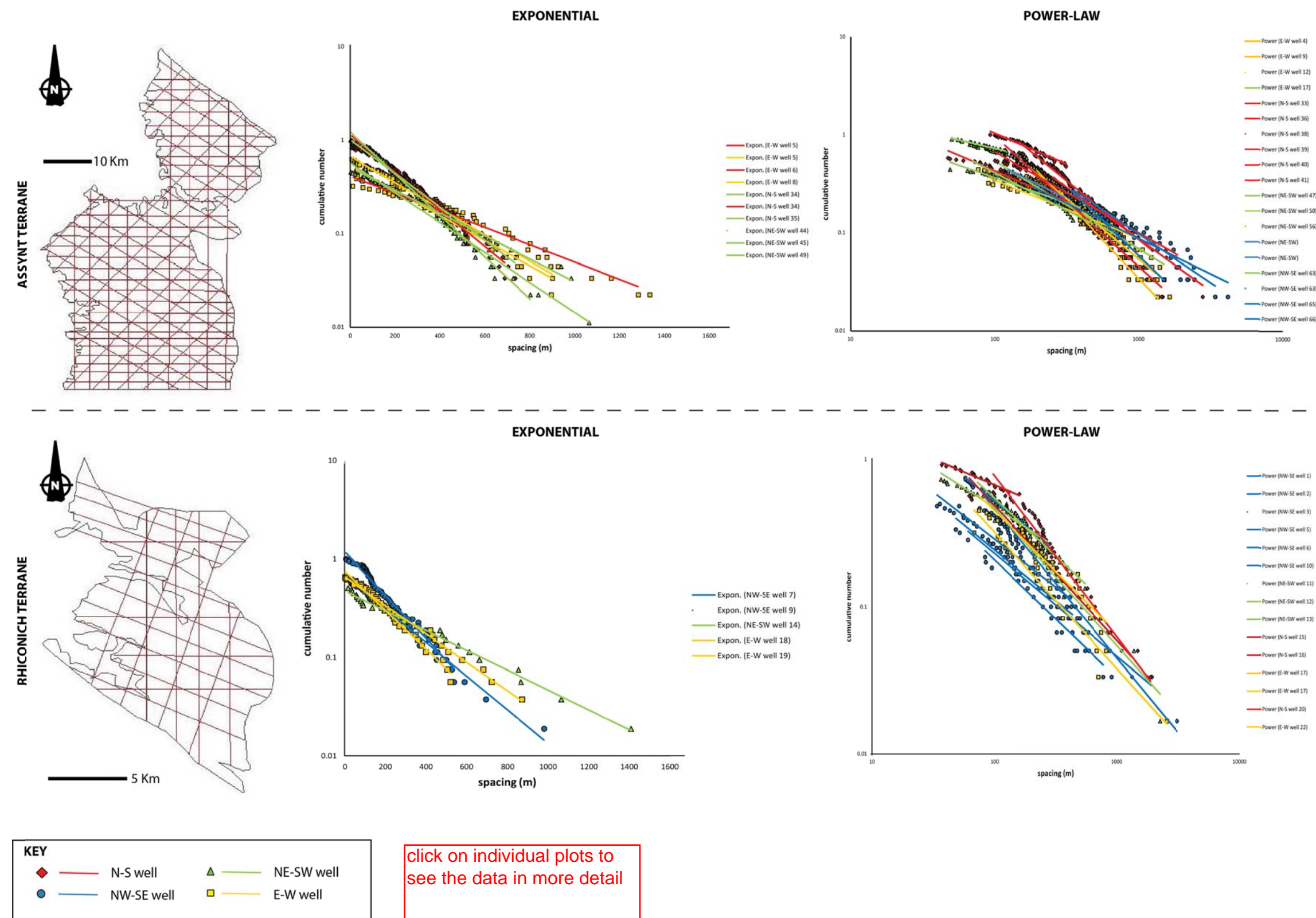
#### 3.2.4.1 – Regional fault lineament spatial distributions

Population distribution plots have been collated for all the pseudo-well samples from the mainland LGC (see *Figure 3.10*). The majority of the mainland LGC pseudo-well samples exhibit power-law spacing distributions (73%) for fault spacings between 100 and 1000 metres. Commonly the power-law distributions do not extend over more than one order of magnitude and they never extend over more than two orders of magnitude. All of the power-law distributions fit a power-law trend line well with R<sup>2</sup> values between 0.88 and 0.99 (*Table 3.1*). The Assynt and Rhiconich Terrane pseudo-wells exhibit power-law distributions for fault spacing that are consistent irrespective of the pseudo-well orientation (*Figure 3.10*). The power-law distributions from the Canisp Shear Zone are less consistent, with those pseudo-wells trending E-W and N-S showing power-law distributions across the largest orders of magnitude. Laxford Front power-law pseudo-wells show a wide range of distributions with fault spacings up to 10000 metres, but again, most of the distributions do not extend over more than one order of magnitude.

Approximately 25% of pseudo-wells in the mainland LGC show exponential distributions for fault spacings. The exponential distributions exhibit maximum fault spacing values between 800 and 2000 metres (*Figure 3.10*). These distributions fit an exponential trend line extremely well with R<sup>2</sup> values between 0.94 and 0.99 (*Table 3.2*).



The Assynt Terrane samples show exponential distributions (21% of Assynt Terrane pseudo-wells) for pseudo-wells that trend N-S, E-W and NE-SW, with fault spacing values concentrated at 400 metres. Rhiconich Terrane exponential pseudo-wells (26% of Rhiconich Terrane pseudo-wells) show fault spacing values that are concentrated at ~300 metres. The exponential pseudo-wells from the Canisp Shear Zone are separated into two groups; those samples from NW-SE trending pseudo-wells (mean spacing ~400 metres) and those samples from E-W trending pseudo-wells (mean spacing ~300 metres).



**Figure 3.10:** Population distribution plots from pseudo-well analysis of fault lineaments interpreted from the mainland LGC. The plots are split into areas within the LGC (see *Figure 3.6* for a map of the area locations) and also into power-law or exponential distributions. Each sample is colour-coded for the orientation of the pseudo-well from which the spacing data was collected. (a) Assynt and Rhiconich terranes (b) Canisp Shear Zone and Laxford Front.

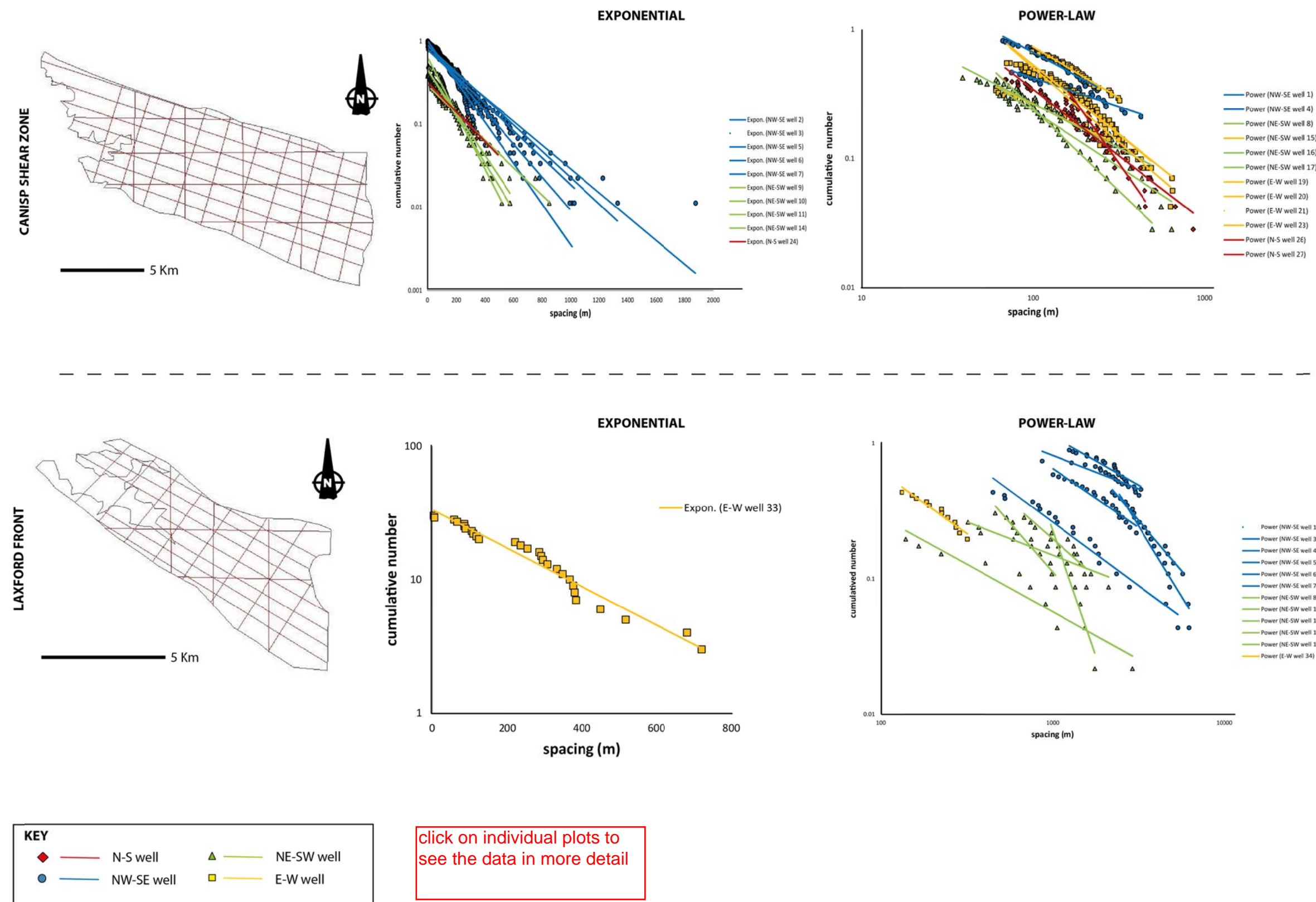


Figure 3.10: (b) contd

Area	Well #	Well orientation	N	Distribution	R <sup>2</sup>	D-value	CV	Clustering	Fracture Density (faults per metre)
Assynt Terrane	1	E-W	33	power-law	0.93	1.16	0.85	anti-clustered	0.002
	2	E-W	38	power-law	0.97	0.38	0.83	anti-clustered	0.002
	3	E-W	35	power-law	0.97	1.49	0.81	anti-clustered	0.002
	4	E-W	38	power-law	0.98	1.33	0.86	anti-clustered	0.002
	7	E-W	29	power-law	0.96	0.59	0.69	anti-clustered	0.002
	9	E-W	39	power-law	0.97	1.56	0.91	anti-clustered	0.002
	10	E-W	36	power-law	0.94	1.18	1.01	random	0.002
	11	E-W	37	power-law	0.95	1.22	0.8	anti-clustered	0.002
	12	E-W	29	power-law	0.95	0.70	0.92		0.002
	13	E-W	44	power-law	0.94	0.96	1.01	random	0.002
	15	E-W	40	power-law	0.96	1.20	0.73	anti-clustered	0.003
	16	E-W	32	power-law	0.96	1.18	0.63	anti-clustered	0.002
	17	E-W	42	power-law	0.99	0.92	1.03	random	0.002
	18	E-W	34	power-law	0.95	1.07	1.07	random	0.002
	33	N-S	59	power-law	0.96	0.99	1.68	clustered	0.003
	36	N-S	68	power-law	0.97	1.38	1.04	random	0.003
	37	N-S	73	power-law	0.93	1.51	0.78	anti-clustered	0.003
	38	N-S	100	power-law	0.93	1.22	0.95	anti-clustered	0.003
	39	N-S	85	power-law	0.97	1.21	1.32	clustered	0.002
	40	N-S	55	power-law	0.98	0.96	1.55	clustered	0.002
	41	N-S	44	power-law	0.98	1.10	1.69	clustered	0.001
	46	NE-SW	86	power-law	0.96	0.95	0.89	anti-clustered	0.004
	47	NE-SW	85	power-law	0.97	1.35	1.05	random	0.004
	48	NE-SW	89	power-law	0.95	1.55	0.82	anti-clustered	0.004
	50	NE-SW	45	power-law	0.95	0.99	0.97	anti-clustered	0.003
	56	NE-SW	41	power-law	0.96	0.56	0.95	anti-clustered	0.003
	63	NW-SE	30	power-law	0.97	1.51	1.15	clustered	0.002
	64	NW-SE	33	power-law	0.96	0.90	1.16	clustered	0.001
	65	NW-SE	29	power-law	0.96	0.72	1.2	clustered	0.001
	66	NW-SE	31	power-law	0.93	0.99	1	random	0.001

**Table 3.1:** Spatial attributes of faults from pseudo-wells created in the mainland LGC DEM study.

This table shows all pseudo-wells that exhibit a power-law spacing distribution for the faults that they sample.

**Table 3.1** (contd)

Rhiconich									
Terrane	1	NW-SE	22	power-law	0.93	0.69	2.2	clustered	0.002
	2	NW-SE	30	power-law	0.94	0.65	1.96	clustered	0.003
	3	NW-SE	17	power-law	0.88	0.8	2.13	clustered	0.003
	6	NW-SE	57	power-law	0.98	0.67	1.31	clustered	0.005
	8	NW-SE	33	power-law	0.93	0.65	1.66	clustered	0.003
	10	NW-SE	31	power-law	0.95	0.79	1.61	clustered	0.003
	11	NE-SW	30	power-law	0.97	0.93	1.37	clustered	0.002
	12	NE-SW	48	power-law	0.94	0.54	1.58	clustered	0.004
	13	NE-SW	41	power-law	0.97	0.79	1.44	clustered	0.003
	15	N-S	43	power-law	0.96	1.09	1.28	clustered	0.004
	16	N-S	60	power-law	0.97	0.35	1.48	clustered	0.004
	17	E-W	24	power-law	0.95	0.92	1.62	clustered	0.003
	20	N-S	36	power-law	0.96	1.09	1.39	clustered	0.003
	22	E-W	27	power-law	0.92	0.83	0.91	anti-clustered	0.003
Canisp									
Shear Zone	1	NW-SE	58	power-law	0.94	0.513	1.77	clustered	0.002
	4	NW-SE	38	power-law	0.96	1.021	1.47	clustered	0.004
	8	NE-SW	48	power-law	0.99	1.276	1.56	clustered	0.006
	12	NE-SW	26	power-law	0.95	0.607	1.11	clustered	0.005
	15	NE-SW	28	power-law	0.93	0.742	1.11	clustered	0.004
	16	NE-SW	38	power-law	0.98	0.574	1.12	clustered	0.005
	17	NE-SW	27	power-law	0.95	0.798	1.64	clustered	0.003
	19	E-W	39	power-law	0.93	1.151	0.88	anti-clustered	0.005
	20	E-W	39	power-law	0.96	1.066	1.02	random	0.004
	21	E-W	48	power-law	0.98	0.782	0.94	anti-clustered	0.004
	23	E-W	33	power-law	0.95	1.077	1.34	clustered	0.004
	25	N-S	29	power-law	0.93	0.922	0.74	anti-clustered	0.005
	26	N-S	33	power-law	0.98	1.897	0.71	anti-clustered	0.005
	27	N-S	29	power-law	0.97	1.026	1.13	clustered	0.004
Laxford									
Front	1	NW-SE	20	power-law	0.94	1.43	0.88	anti-clustered	0.002
	2	NW-SE	36	power-law	0.94	0.904	0.56	anti-clustered	0.003
	3	NW-SE	46	power-law	0.98	1.908	0.58	anti-clustered	0.004
	4	NW-SE	35	power-law	0.99	1.519	0.39	anti-clustered	0.004
	5	NW-SE	27	power-law	0.95	1.689	0.44	anti-clustered	0.004
	6	NW-SE	27	power-law	0.97	2.961	0.59	anti-clustered	0.003
	7	NW-SE	17	power-law	0.98	4.229	0.55	anti-clustered	0.001
	8	NE-SW	9	power-law	0.93	1.229	1.07	random	0.003
	11	NE-SW	15	power-law	0.97	1.454	0.41	anti-clustered	0.005
	34	N-S	34	power-law	0.94	0.914	0.52	anti-clustered	0.004

Area	Well #	Well orientation	N	Distribution	R <sup>2</sup>	Slope	CV	Clustering	Fracture Density (faults per metre)
Assynt Terrane	5	E-W	35	exponential	0.95	0.54	0.78	anti-clustered	0.002
	6	E-W	29	exponential	0.97	0.41	0.93	anti-clustered	0.002
	8	E-W	56	exponential	0.97	0.67	0.81	anti-clustered	0.003
	14	E-W	40	exponential	0.97	1.14	0.78	anti-clustered	0.002
	35	N-S	74	exponential	0.99	1.02	0.78	anti-clustered	0.004
	44	NE-SW	80	exponential	0.97	0.57	0.72	anti-clustered	0.003
	45	NE-SW	45	exponential	0.99	0.52	1	random	0.003
	49	NE-SW	90	exponential	0.99	1.22	0.82	anti-clustered	0.004
Rhiconich Terrane	7	NW-SE	53	exponential	0.98	1.19	0.92	anti-clustered	0.004
	9	NW-SE	31	exponential	0.98	0.69	0.76	anti-clustered	0.004
	14	NE-SW	27	exponential	0.99	0.48	0.96	anti-clustered	0.003
	18	E-W	35	exponential	0.99	0.76	1.01	random	0.004
	19	E-W	34	exponential	0.99	0.66	1.07	random	0.003
Canisp Shear Zone	2	NW-SE	80	exponential	0.97	78.40	0.96	anti-clustered	0.004
	3	NW-SE	83	exponential	0.97	88.08	1.08	random	0.004
	5	NW-SE	89	exponential	0.94	89.95	0.92	anti-clustered	0.006
	6	NW-SE	76	exponential	0.98	80.19	0.9	anti-clustered	0.005
	7	NW-SE	71	exponential	0.97	70.64	0.94	anti-clustered	0.004
	9	NE-SW	36	exponential	0.98	40.87	0.82	anti-clustered	0.006
	10	NE-SW	34	exponential	0.97	40.07	0.78	anti-clustered	0.006
	11	NE-SW	28	exponential	0.98	26.10	1	random	0.005
	13	NE-SW	35	exponential	0.97	41.00	0.77	anti-clustered	0.006
	14	NE-SW	45	exponential	0.98	57.27	0.74	anti-clustered	0.007
Laxford Front	33	E-W	33	exponential	0.96	33.26	1.11	clustered	0.003

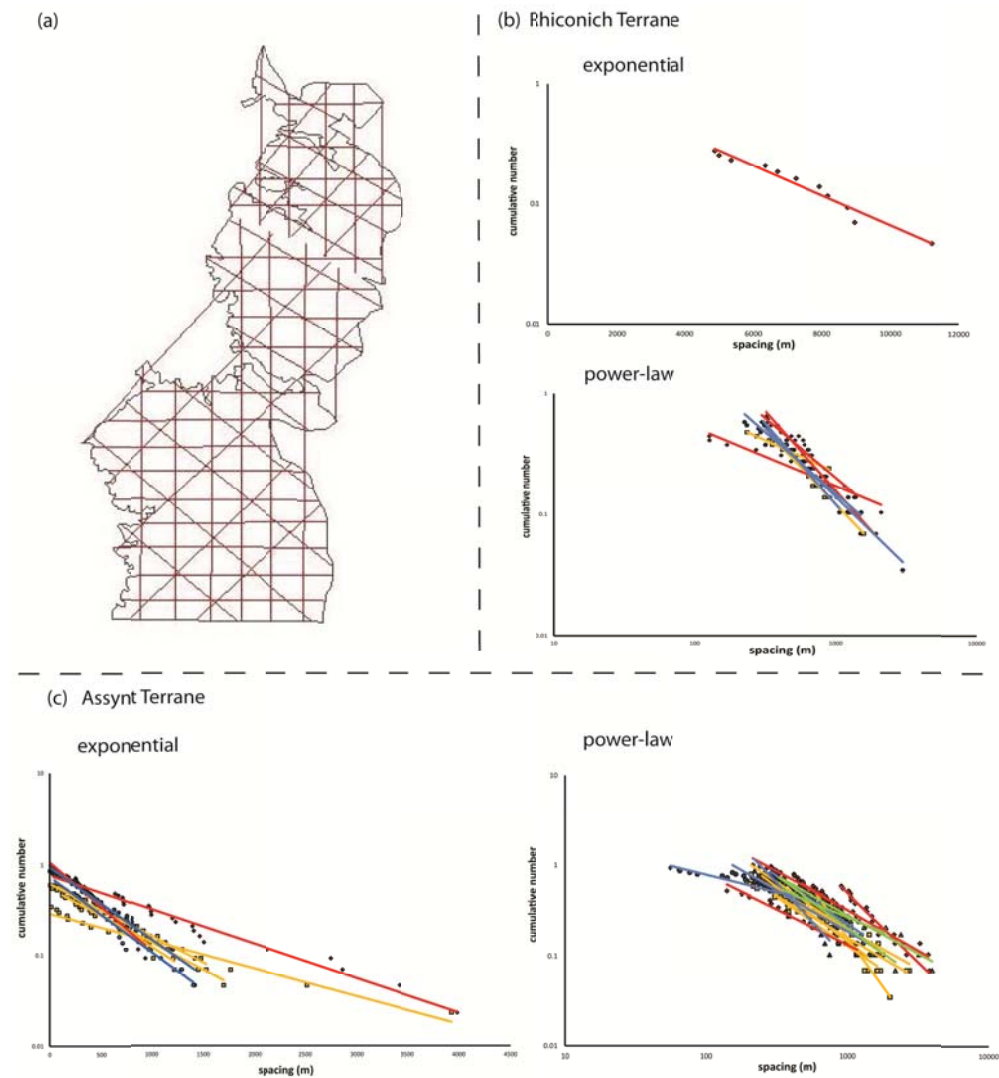
**Table 3.2:** Spatial attributes of faults from pseudo-wells created in the mainland LGC DEM study.

This table shows all pseudo-wells that exhibit a exponential spacing distribution for the faults that they sample.

To be able to make a direct comparison with the offshore Clair basement regional fault study, the resolution of the NEXTMap® DEM maps has been reduced (down to 25m cells), the visible faults re-interpreted and new pseudo-well samples were created. The Canisp Shear Zone and Laxford Front areas are not analysed separately because the resolution is too low to be able to determine any differences between the fault networks in these small areas. The population distribution plots of the low resolution dataset are given in *Figure 3.11* and the associated spatial attributes are given in Table 3.3.

Once again, the majority of pseudo-well samples exhibit power-law distributions (74%) with average fault spacing values between 100 and 1000 metres (*Figure 3.11c*). The power-law distributions fit a trend line with  $R^2$  values between 0.87 and 0.99 (*Table 3.3*). Within this low resolution dataset, no power-law distribution extends beyond one order of magnitude scale range.

The low resolution mainland LGC also exhibits pseudo-well samples with exponential distributions (they fit trend lines with  $R^2$  values between 0.93 and 0.98, *Table 3.3*). In the Rhiconich Terrane, only one pseudo-well shows an exponential distribution which shows fault spacing values between 400 and 11000 metres (*Figure 3.11b*). In the Assynt Terrane exponential distributions show two distinct types; a longer distribution with fault spacing values up to 4000 metres and shorter distributions with average fault spacing values of ~1000 metres.



**Figure 3.11:** Population distribution plots of the low resolution dataset from the mainland LGC NEXTMap® DEM map. **(a)** Map of the pseudo-wells placed on the mainland LGC **(b)** Population distribution plots from the Rhiconich Terrane. The dataset is split into exponential and power-law distributions. **(c)** Population distribution plots from the Assynt Terrane. The dataset is split into exponential and power-law distributions.

click on individual  
plots to see the data  
in more detail



Location	Well #	Well orientation	N	distribution	R <sup>2</sup>	D-value	Slope	Cv	Clustering	FD (fault per metre)
Assynt										
Terrane	1	E-W	22	power-law	0.98	0.87		1.03	random	0.001
	2	E-W	29	power-law	0.87	1.04		1.01	random	0.002
	3	E-W	28	power-law	0.96	1.18		0.88	anti-clustered	0.002
	4	E-W	20	power-law	0.94	0.50		0.95	anti-clustered	0.001
	5	E-W	26	exponential	0.99		26.81	0.87	anti-clustered	0.001
	6	E-W	17	power-law	0.92	1.15		1.05	random	0.001
	7	E-W	25	exponential	0.96		28.42	0.81	anti-clustered	0.002
	8	E-W	18	power-law	0.99	0.92		1.11	clustered	0.001
	9	E-W	15	exponential	0.97		12.60	1.14	clustered	0.001
	11	E-W	16	power-law	0.94	1.07		0.77	anti-clustered	0.001
	12	E-W	18	power-law	0.98	2.19		0.61	anti-clustered	0.001
	14	E-W	21	exponential	0.98		23.86	0.74	anti-clustered	0.001
	19	N-S	40	power-law	0.99	1.19		0.89	anti-clustered	0.002
	20	N-S	40	power-law	0.95	0.84		0.79	anti-clustered	0.002
	21	N-S	43	exponential	0.98		46.17	1.02	random	0.002
	22	N-S	34	exponential	0.98		33.13	0.95	anti-clustered	0.001
	23	N-S	27	power-law	0.99	1.53		0.9	anti-clustered	0.001
	24	N-S	28	power-law	0.96	0.90		1.06	random	0.001
	25	N-S	16	power-law	0.97	0.78		0.89	anti-clustered	0.002
	31	NW-SE	32	power-law	0.94	1.67		0.73	anti-clustered	0.002
	32	NW-SE	37	exponential	0.98		40.48	0.96	anti-clustered	0.002
	33	NW-SE	29	power-law	0.97	1.05		1.53	clustered	0.001
	34	NW-SE	30	power-law	0.94	0.39		0.99	anti-clustered	0.002
	38	NW-SE	26	exponential	0.95		31.94	0.94	anti-clustered	0.002
	39	NW-SE	25	power-law	0.92	0.89		0.75	anti-clustered	0.002
	45	NE-SW	23	power-law	0.96	1.13		1.09	random	0.001
	46	NE-SW	27	power-law	0.98	0.85		1.22	clustered	0.001
	47	NE-SW	21	power-law	0.94	0.65		1.5	clustered	0.001
Rhiconich										
Terrane	15	E-W	17	power-law	0.98	0.53		1.18	clustered	0.001
	16	E-W	17	power-law	0.99	1.23		1.01	random	0.002
	26	N-S	15	power-law	0.95	0.49		1.39	clustered	0.001
	27	N-S	13	exponential	0.96		51.04	0.42	anti-clustered	0.001
	28	N-S	19	power-law	0.97	0.99		0.77	anti-clustered	0.001
	29	N-S	22	power-law	0.94	1.32		1.11	clustered	0.001
	40	NW-SE	21	power-law	0.95	1.02		1	random	0.001
	41	NW-SE	31	power-law	0.98	1.34		1.03	random	0.002
	42	NW-SE	11	power-law	0.95	1.14		0.74	anti-clustered	0.001

**Table 3.3:** Spatial attributes of faults from pseudo-wells created in the low resolution mainland LGC DEM study.

### 3.2.4.2 –D-value

Those fault spacing distributions that exhibit power-law distributions have associated D-values (slope of the trend line). From the Assynt Terrane full resolution data set, the power-law distributions have D-values between 0.38 and 1.56, with E-W trending pseudo-wells showing the largest variations in D-value (*Table 3.1*). Over half of the power-law distributions from the Assynt Terrane exhibit D-values that are >1. The low resolution dataset from the Assynt Terrane shows a similarly wide variation in D-values for the power-law distributions (0.39 to 2.12, *Table 3.3*).

D-values from the Rhiconich Terrane power-law distributions vary between 0.35 and 1.09 (*Table 3.1*) with the low resolution dataset D-values varying between 0.49 and 1.34 (*Table 3.3*). The majority (84%) of spacing distributions from the Rhiconich Terrane high resolution dataset have D-values that are <1 (*Table 3.1*). This is in comparison to the low resolution spacing distributions where their associated D-values are commonly >1, (67%, *Table 3.3*).

The Canisp Shear Zone power-law distributions exhibit D-values between 0.51 and 1.9 with N-S and NE-SW trending pseudo-wells exhibiting the highest D-values (*Table 3.1*). D-values for the Laxford Front power-law pseudo-well samples vary between 0.9 and 4.23 with NW-SE trending pseudo-wells exhibiting the largest values. The majority (80%) of D-values for power-law distributions in the Laxford Front area are >1 (in the Canisp Shear Zone only 50% of D-values are >1).

### 3.2.4.3 – Coefficient of variation (CV)

The coefficient of variation (CV) has been calculated for every pseudo-well sample in the regional mainland LGC study to gain an insight into the clustering relationships of the interpreted faults. Power-law distributions from the Assynt Terrane (high resolution) have CV values between 0.63 and 1.69 (*Table 3.1*), with the low resolution Assynt Terrane power-law distributions exhibiting CV values between 0.61 and 1.53 (*Table 3.3*). Exponential distributions in the Assynt terrane have CV values between 0.72 and 1 (high resolution) and 0.77 and 1.11 (low resolution), with the majority (>75%) of CV values <1 (*Tables 3.2 & 3.3*, respectively).

Power-law samples from the Rhiconich Terrane have CV values that vary between 0.87 and 2.2 for the high resolution datasets (*Table 3.1*). The low resolution power-law datasets for the Rhiconich Terrane area exhibit CV values between 0.42 and

1.39 (*Table 3.3*). The majority of CV values (93%) for Rhiconich Terrane power-law distributions are  $>1$ . Exponential spacing distributions within the Rhiconich Terrane regional study exhibit CV values between 0.76 and 1.07 (high resolution, *Table 3.2*) and 1 (low resolution, *Table 3.3*). Most of the CV values (80%) from the Rhiconich Terrane exponential distributions have CV values around 1.

Canisp Shear Zone power-law samples have CV values that vary between 0.71 and 1.77, with many of the samples (47%) exhibiting clustered fault distributions ( $CV > 1$ , *Table 3.1*). This is in contrast to the exponential samples for the Canisp Shear Zone which have CV values between 0.74 and 1.08, with the majority (88%) of samples exhibiting CV values  $< 1$  (*Table 3.2*).

#### 3.2.4.4 – Fault density (FD)

*Tables 3.1, 3.2 & 3.3* also contain information on the fault density for each pseudo-well in the high resolution and low resolution samples. In the high resolution dataset, the Assynt Terrane and Rhiconich Terrane pseudo-wells have an average fault density of 0.003 faults per metre (or 3 faults per kilometre). There is little apparent difference between the fault density values calculated for the power-law (*Table 3.1*) or the exponential (*Table 3.2*) spacing distributions in either terrane. The low resolution sample exhibits fault density values of only 0.001 faults per metre (or 1 fault per kilometre) for both the Assynt and Rhiconich Terranes (*Table 3.3*).

The Canisp Shear Zone exhibits average fault density values of 0.005 faults per metre, with one pseudo-well exhibiting a fault density value of 0.007 faults per metre (exponential distribution, *Table 3.2*). In the Laxford Front sample area the fault density values for both power-law and exponential distributions have an average of 0.003 faults per metre.

#### 3.2.5 - Regional fault lineament connectivity

Fault connectivity in the mainland LGC has been analysed in 2-dimensions by interpreting all of the fault lineament intersections (nodes) from the high resolution datasets. This analysis illustrates how faults interact with each other, but does not consider fluid flow pathways between nodes. Therefore the resulting maps (*Figure 3.12*) only give an appreciation of the potential connectivity for the faults interpreted from the mainland LGC. It should also be noted that all of the faults interpreted from the

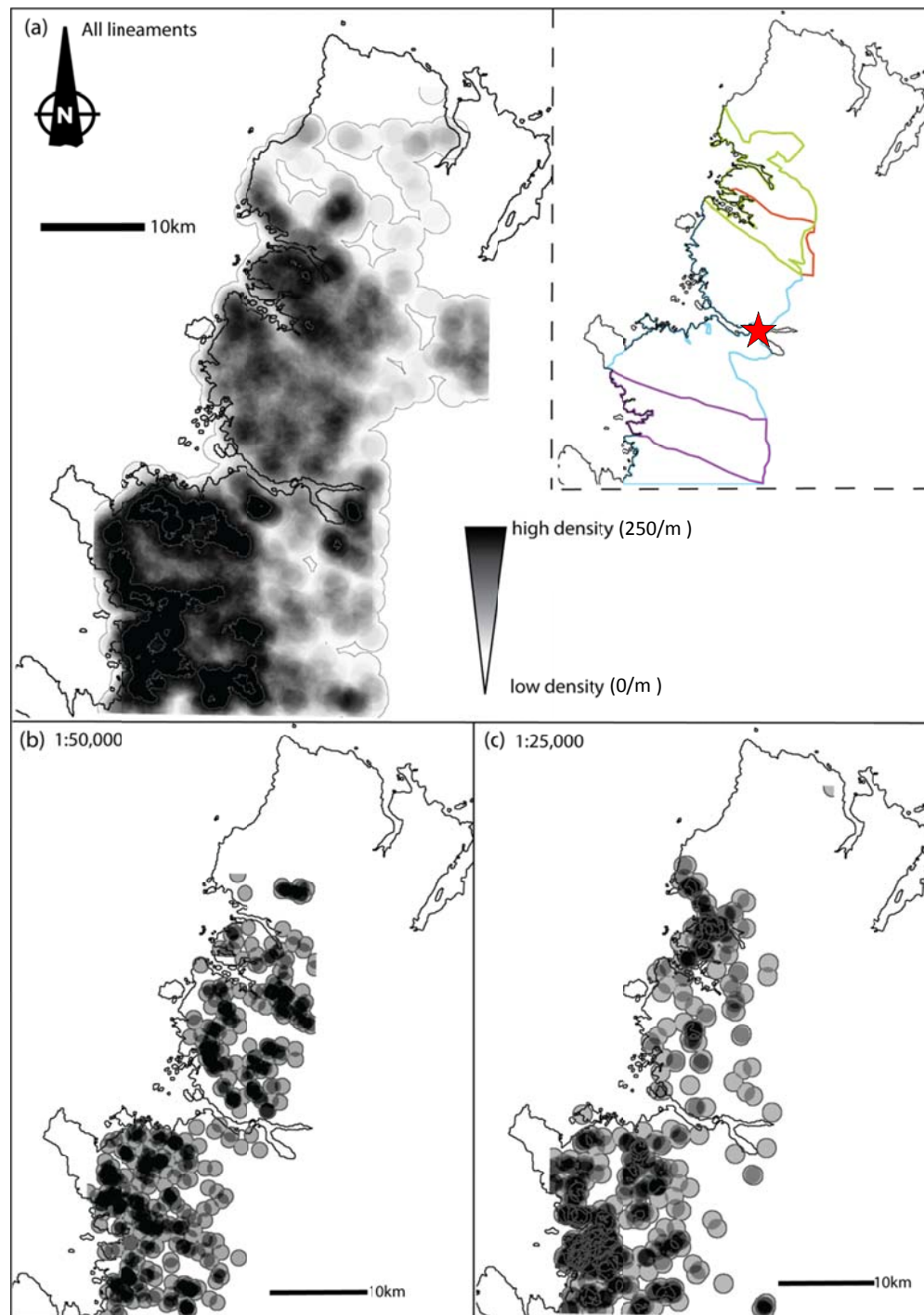
mainland LGC are assumed to be vertical and therefore the connectivity analysed in this study is also vertical.

The connectivity density maps show that when all of the fault lineaments are included (*Figure 3.12a*) the connectivity is higher within the Assynt Terrane, particularly south of Loch Glencoul (marked with a red star on the inset to *Figure 3.12a*). This pattern remains true when faults interpreted at 1:50,000 scale (*Figure 3.12b*) and 1:25,000 scale (*Figure 3.12c*) are analysed independently. Consistently the area surrounding the Canisp Shear Zone shows the highest connectivity density values. The 1:25,000 scale connectivity density map (*Figure 3.12c*) also shows an area of high density to the north of the LGC area in the Rhiconich Terrane. This area is associated with a major NW-SE trending normal fault (the Loch Inchar Fault).

### 3.2.5 – Regional fault lineament spatial analysis: Discussion

Population distribution plots from the mainland LGC exhibit both exponential and power-law spacing distributions (Figures 3.9 & 3.10). Power-law relationships are more common in the low resolution mainland LGC dataset, but the number of data points (less than 30 points) in each sample and the fact that they do not extend over more than one order of magnitude means that they represent a rather weak relationship and should be treated with caution. This is true for the majority of power-law distributions observed within the regional mainland LGC datasets.

The weak power-law spacing distributions may be a result of the sampling technique: because more than one prominent fault trend is being sampled by each pseudo-well, an exponential spacing distribution is more likely, as these are more commonly associated with fault sets that are distributed through a range of azimuths. At a regional scale, sampling one prominent fault orientation from the full fault network is difficult to do and therefore it is likely that exponential distributions will be more common.

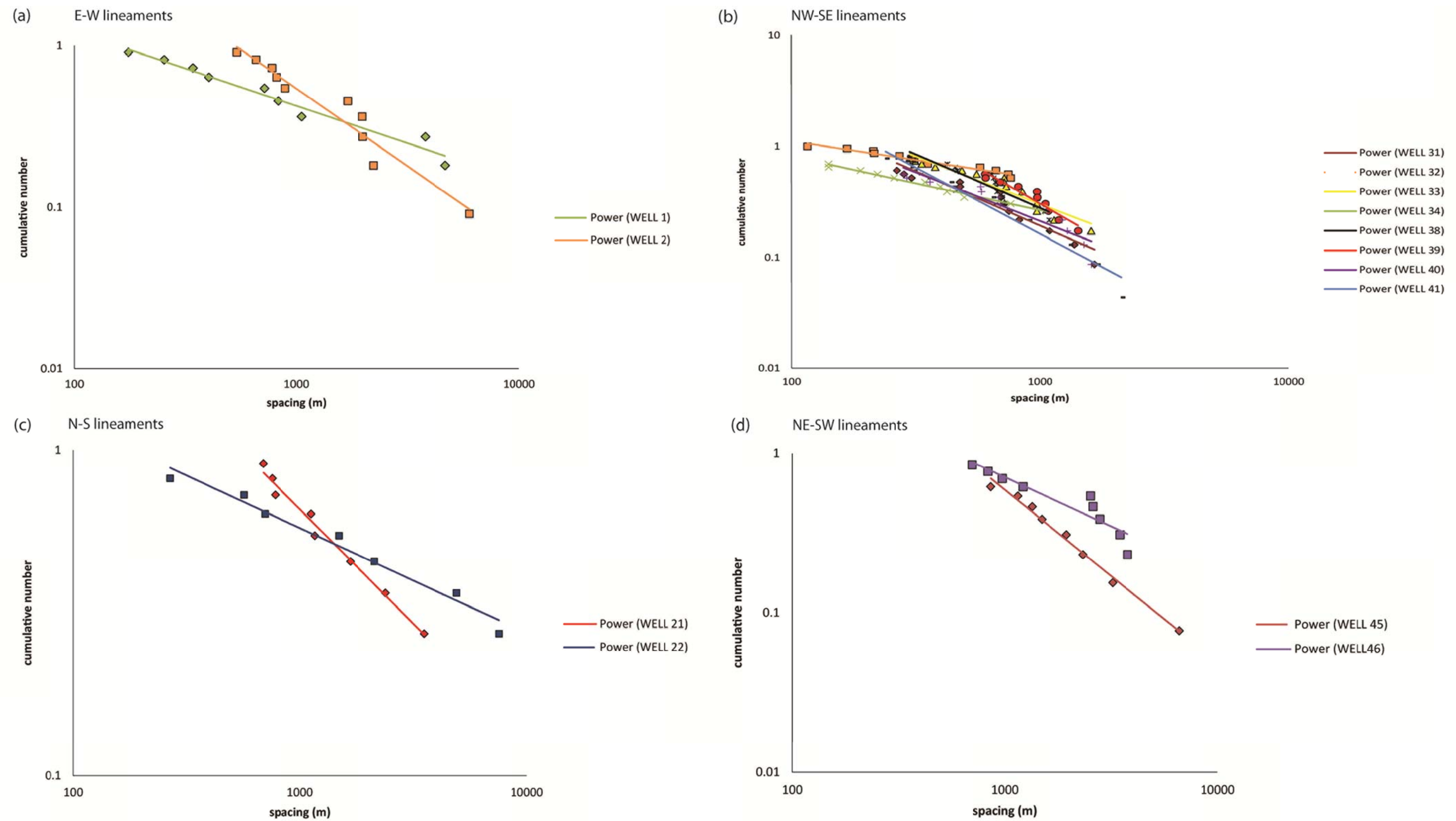


**Figure 3.12:** Density maps of lineament connectivity from the high resolution mainland LGC DEM dataset. These maps show the density of connectivity 'nodes' where different lineaments cross each other. **(a)** Connectivity of all the lineaments interpreted from the mainland LGC. Inset is a map showing the different interpreted areas in the mainland LGC (blue- Assynt Terrane, green - Rhiconich Terrane, purple – Canisp Shear Zone and orange – Laxford Front). **(b)** Connectivity of lineaments picked at 1:50,000 scale. **(c)** Connectivity of lineaments picked at 1:25,000 scale.

To test if the sampling process at the regional scale is responsible for the exponential and weak power-law spacing distributions, each fault azimuth group (N-S, NE-SW, E-W & NW-SE) has been sampled independently using perpendicular pseudo-wells (e.g. NW-SE trending pseudo-wells sample NE-SW trending faults). To allow direct comparison with the results from a similar analysis from the Clair basement fault lineament maps, only the low resolution dataset has been used for the mainland LGC study. The population distribution plots from this study are shown in *Figure 3.13*.

The spacing distributions are consistently power-law for all pseudo-well azimuths when each fault azimuth group is sampled independently. It should be noted, however that these power-law relationships often contain less than 30 data points which means that they are not statistically robust. These weak power-law relationships suggest that the spatial relationships of faults within the regional mainland LGC dataset cannot be confidently used as an estimation of the spatial relationships of fault and fractures at different scales.

The majority (63%) of power-law pseudo-wells in the Assynt Terrane and the Laxford Front areas have CV values  $<1$  (*Table 3.1*) which means that the faults exhibit anti-clustered (regularly spaced) or in some cases (when the CV value is close to 1) random spacing (Johnston et al., 1994). These anti-clustered fault spacing patterns are more commonly representative of exponential spacing relationships and do not reflect power-law datasets. Therefore it is likely that those pseudo-wells which have low CV values, and have been classed as power-law, instead, represent weakly defined exponential spacing distributions.



**Figure 3.13:** Population distribution plots for individual fault lineament trends from the mainland LGC regional study. **(a)** E-W trending lineaments. **(b)** NW-SE trending lineaments. **(c)** N-S trending lineaments. **(d)** NE-SW trending lineaments.

click on individual plots to  
see the data in more detail

Both the Rhiconich Terrane and the Canisp Shear Zone area power-law pseudo-wells have CV values that are normally  $>1$ , which suggests that these power-law relationships are significant and result from clustered faults that are sampled from the regional dataset. The consistent power-law spacing relationships evident in the Canisp Shear Zone area are a likely result of the increase in brittle deformation due to the reactivation of pre-existing weaknesses formed from the pre-existing development of a large ductile shear zone in the Proterozoic (Inverian, Laxfordian), resulting in more clustered fault spacing distributions (Beacom, 1999 and references therein). In the Rhiconich Terrane, the high CV values (and the power-law relationships) may be a result of the location of LGC outcrop as it is less continuous, which means that interpreted faults are not intersected the whole way along most pseudo-wells resulting in a clustered appearance to the fault samples.

Nearly all of the high resolution exponential pseudo-well datasets in the mainland LGC have CV values either close to or  $<1$ . This means that the fault spacing in these pseudo-wells is anti-clustered or random which is consistent with the exponential spacing distributions seen from these samples. The low resolution mainland LGC pseudo-wells commonly have CV values are  $<1$  for both exponential and power-law spacing relationships. This is consistent with the suggestion that the power-law relationships are in fact weakly defined exponential spacing relationships.

The D-values obtained from power-law pseudo-wells from the high and low resolution mainland LGC datasets also suggest that the power-law relationships are statistically weak. The D-values are widely varied, with some samples indicating distributions of faults that are more often widely spaced (D-values  $<1$ , for 1-dimensional samples  $D=1$ ) and some distributions with more faults that are closely spaced (D-values  $>1$ ). There is also a lack of evidence linking fault clustering relationships (CV and D-values) and pseudo-well orientation suggesting that fault spacing distributions do not show distinct spatial characteristics depending on the sampling direction used at a regional scale.

Fault density analyses conducted for each pseudo-well in the high resolution Assynt terrane dataset resulted in a mean value of three faults per kilometre. This is in line with the fault density results from the high resolution dataset in the Rhiconich terrane. It is likely representative of the true background fault density within the mainland LGC as the resolution of the NEXTMap DEM means that it possible to interpret



faults that are only a few metres apart. Fracture density calculated from outcrop analysis (*Section 3.3*) is normally at least an order of magnitude higher than the values calculated at the regional scale, but this includes many small fractures that can be less than a metre in length.

The fault density values calculated from pseudo-wells in the Canisp Shear Zone area are generally higher than those calculated from the Assynt Terrane as a whole (*Table 3.2*). This increase in fault density is again likely due to the presence of a large pre-existing zone of weakness (ductile shear zone) that has then been exploited by later phases of brittle deformation (Beacom, 1999 and references therein), thus increasing the density of the fault network in this area of the Assynt Terrane. This is not the case for the Laxford Front, where fault density values are more in line with the surrounding Assynt and Rhiconich Terranes (*Tables 3.1 & 3.2*). The ductile shear zone that forms the Laxford Front shows little evidence of being reactivated by later brittle deformation (*Section 3.3* of this chapter will discuss this in more detail), which is the likely reason why the fault density values are not elevated in this area in a similar manner to those from samples in the Canisp Shear Zone.

Fault density values from the low resolution pseudo-wells have an average of 2 faults per kilometre (*Table 3.3*). This low value does not reflect the true fault density within the mainland LGC. It does, however, allow a direct comparison of fault density values to be made between the onshore LGC and the offshore Clair basement datasets (see *Chapter 6*).

Analyses of 2-dimensional fault connectivity from the regional fault interpretations suggest that all the interpreted faults influence the connectivity potential within the mainland LGC. Faults interpreted at 1:25,000 scale exhibit larger areas of high connectivity density, suggesting that these third order faults are more important for connectivity between different structural areas; faults interpreted at 1:25,000 scales fill a 2-dimensional area, whereas faults interpreted at 1:50,000 scales have a more linear connectivity. This is particularly obvious in the Assynt Terrane where areas of low connectivity in the 1:50,000 scale map (*Figure 3.12b*) are filled by high connectivity areas from the 1:25,000 map (*Figure 3.12c*). This study highlights areas in the mainland LGC where fault connectivity is potentially high, but does not take into account which faults sets are considered open or closed. Analyses conducted at

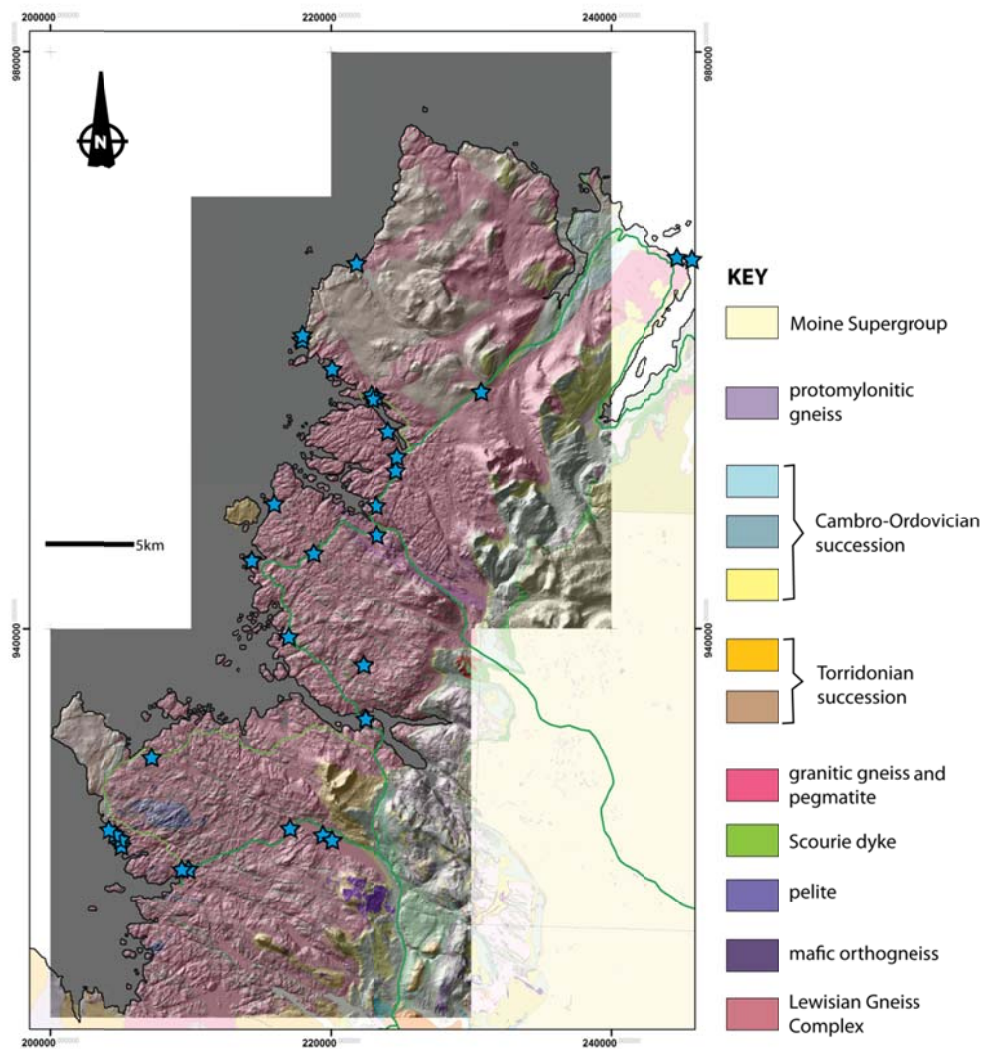
outcrops in the mainland LGC attempts to provide more information on the open and closed fault and fracture sets (see *Section 3.3* of this chapter).

### 3.3 – Fracture analysis from Lewisian outcrop data

In order to look at the fault and fracture networks in the mainland LGC in more detail, selected outcrops and thin sections have also been analysed. The majority of this outcrop study has been conducted using 1-dimensional sample lines and thin section analysis from selected locations. During 1-dimensional line sampling, time was spent describing the host lithology and fractures as they were encountered. The advantage of sampling and analysing the fracture network at outcrop is that there is a vast amount of opportunity to sample all the varying structural settings present within the mainland LGC (and potentially within the Clair basement). This allows a fuller understanding of the fracture network characteristics to be achieved. The onshore data is not limited by how many well samples there are or by the orientation of the samples, which helps to reduce any bias in the data and the number of assumptions that have to be made about how the fracture network may extend away from each sample site (or basement well).

Data from outcrop comes from across the different regions in the mainland LGC. The nature of outcrop in the Lewisian (heavily eroded and often extensively covered in lichen) means that the majority of outcrops used are from either road or coastal sections where the rocks are cleaner and individual fractures can be identified with confidence.

*Figure 3.14* shows a map of all the outcrops sampled in the mainland LGC. The following section describes the lithology of the host rocks and the various fracture systems encountered during the sampling of the fracture networks in the mainland LGC.



**Figure 3.14:** Map of outcrop locations within the mainland LGC. 1-dimensional line samples and rock samples have been collected for each of the locations marked with blue stars. The map has been created using British Geological Society 1:50,000 bedrock geology maps and hill shade maps from NEXTMap® DEM datasets.

### 3.3.1- Method for fracture logging and spatial analysis of fractures

1-dimensional sample lines have been used across many outcrops of the mainland LGC where they were taken in different orientations (normally parallel and perpendicular to foliation) in order to sample every fracture set present within the LGC outcrops (all brittle structures will be referred to as fractures, unless otherwise specified). These sample lines were used to analyse each encountered fracture in as much detail as possible. Several attributes were recorded for each fracture including: orientation, aperture, length; fault rock or infilling present, slickenlines (if present), and cross-cutting relationships (see *Section 1.6.5*). Fracture log tables and thin section analysis can be found in *Appendix B*. Fracture orientation and the orientations of other LGC structures were analysed using stereonet. Spatial characteristics of the fault sets have been analysed using population distribution plots and the spatial attributes D-value, CV and fracture density have also been calculated.

Along with the 1-dimensional sample lines, 2-dimensional photo-mosaics were used to analyse the fracture connectivity from some of the key LGC outcrops. Thin sections have also been used to analysis micro-textures associated with each fracture set.

### 3.3.2 – Key Lewisian outcrop locations and lithological descriptions

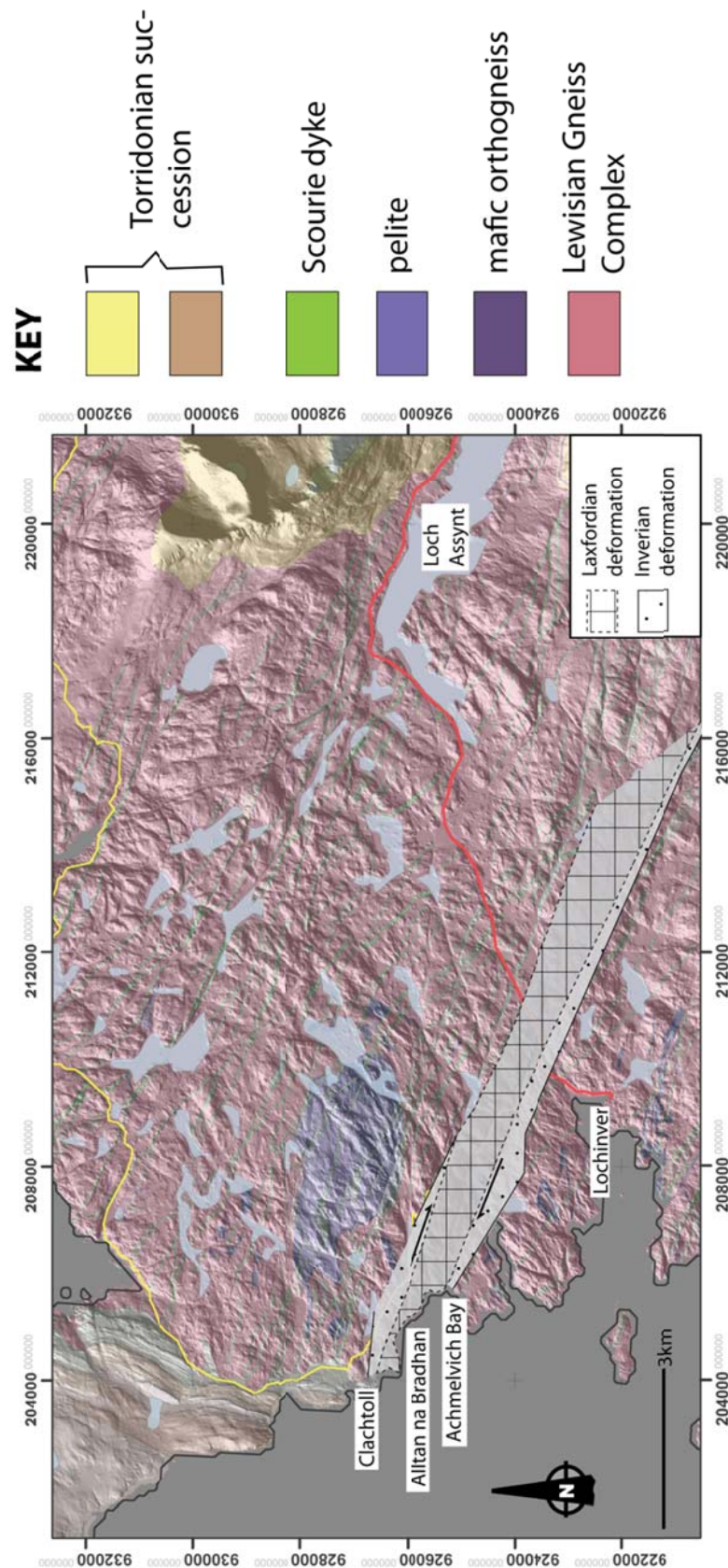
Outcrops in the Assynt Terrane include: Alltan na Bradhan (Canisp Shear Zone) including Achmelvich Bay and Clachtoll (NC 0508 2624, NC 0580 2504 & NC 0425 2677, respectively), Lochinver (NC 1000 2357), Loch Assynt (NC 2022 2586 & NC 1773 2650) and Caolas Cumhann (NC 2251 3392). In the Rhiconich Terrane the key outcrops are: Kinlochbervie (NC 2296 5621), Traigh Allt Chailgeag & Rispond (NC 4510 6577 & 4563 6577, respectively), Laxford Bridge (NC 2360 4827), Oldshoremore (NC 2010 5832) and Rhiconich (NC 2496 5211). Each of these outcrops have been used to collect data on fracture orientation, kinematics and spatial characteristics to provide a detailed understanding on the fracture networks present in the mainland LGC and how the fracture networks vary between different lithological and structural settings (data from all outcrops studied during this project are provided in *Appendix B*).

### 3.3.2.1 – Alltan na Bradhan, Achmelvich Bay & Clachtoll (Assynt Terrane)

The outcrops at Achmelvich Bay, Alltan na Bradhan and Clachtoll are situated along a 2km section of coastline within the Assynt Terrane. These outcrops have been chosen because they sample LGC close to the edge of the CSZ (Achmelvich Bay) and LGC within the CSZ (Alltan na Bradhan & Clachtoll). Sampling these outcrops in their various structural settings allows the development of an understanding of how varying the pre-existing ductile structures and metamorphic grade affects the characteristics of the fault and fracture networks within the LGC.

The lithology across the Alltan na Bradhan (NC 0508 2624), Achmelvich Bay (NC 0580 2504) and Clachtoll (NC 0425 2677) areas consists of banded grey, medium-grained orthogneisses, which also dominate the region (see *Figure 3.15* for a detailed location map of the Canisp Shear Zone (CSZ)). The gneisses are intermediate to mafic in nature and have mineralogical and textural differences depending on their level of deformation (Badcallian, Inverian or Laxfordian). Badcallian gneisses comprise a composition of plagioclase + quartz + hornblende  $\pm$  biotite  $\pm$  epidote (Sheraton et al., 1973b, Jensen, 1984). Jensen (1984) also suggests post-tectonic growth of hornblende, chlorite and muscovite. Bands within the orthogneisses are separated into two domains; plagioclase-quartz rich and hornblende-biotite rich with sharp mineral boundaries in zones of high strain (Beacom, 1999). The orthogneisses also include lensoidal to spherical ultramafic pods which consist almost entirely of hornblende (Sheraton et al., 1973b). At Achmelvich Bay these ultramafic pods can be up to 1 metre in length, but at Alltan na Bradhan and Clachtoll these pods have been stretched out completely.

Gneisses that have experienced Inverian deformation are amphibolized with pyroxene (augite and hypersthene) crystals commonly being replaced by hornblende (Evans and Lambert, 1974), indicating the rehydration of the rocks. Biotite is also observed fringing magnetite crystals (Evans and Lambert, 1974). In regions where Laxfordian deformation prevails, the original gneissic is recrystallised with the presence of epidote, biotite and muscovite. Chlorite was also observed in a few locations, suggesting Laxfordian deformation retrogressed the gneisses as far upper greenschist-facies metamorphism.



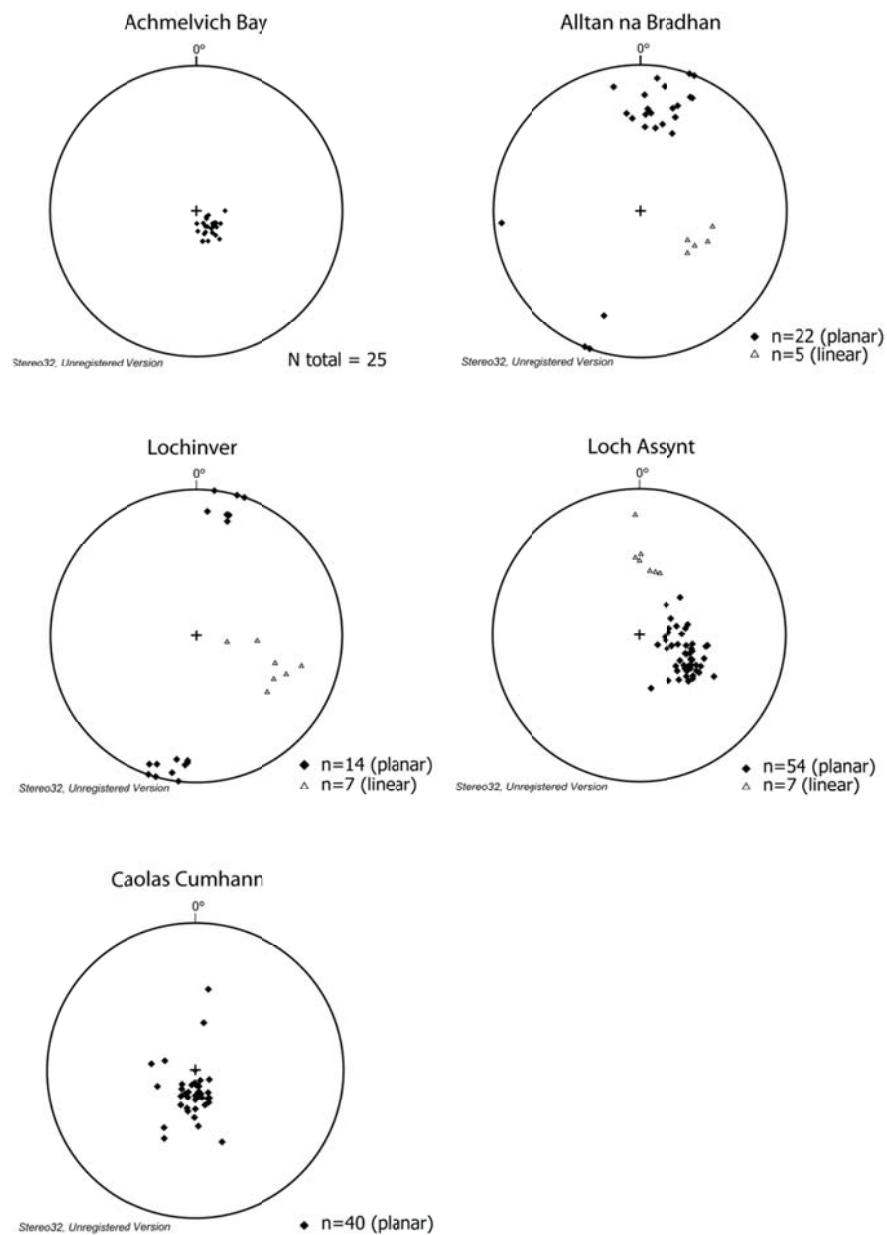
zones has been adapted from Attfield (1987). The summary map is overlain on BGS 1:50,000 bedrock geology map.

In thin section (sample 22-2a, NC 0508 2624), polycrystalline quartz and plagioclase feldspar are aligned in 1 to 3mm thick bands, forming the intense foliation present in CSZ outcrops. Small volumes of chlorite (<5%) are also observed to be aligned within the foliation where they appear to be overgrowing the feldspar bands (see *Appendix B* for thin section photographs of this locality and others throughout the mainland LGC). Hornblende is observed as large crystals that appear to form bands together with the phyllosilicates present in this sample. Epidote is also present (<5%) where it forms small crystals (up to 2mm across) that overprint some of the plagioclase feldspar as a result of saussuritization (a result of retrograde metamorphism of calcic plagioclase). Samples from other localities in the CSZ (sample 01-2b, NC 0583 2359) show little evidence of chlorite or epidote and their foliation is defined by quartz-plagioclase and biotite-hornblende bands. Further petrology and geochemistry of the orthogneisses in this region have been detailed by Peach *et al.* (1907), Sheraton *et al.* (1973a) and Attfield (1987) and further details on the microstructural textures can be found in Jensen (1984).

Orthogneisses across this region are cross-cut by two different phases of intrusive bodies (collectively known as Scourie Dykes) including early coarse-grained mafic/dolerite dykes with a composition of hornblende + plagioclase + epidote  $\pm$  quartz and later ultramafic/picrite dykes composed of olivine + bronzite + Ca-poor augite + plagioclase + biotite  $\pm$  chromite (Tarney, 1973). At Achmelvich Bay, these dykes are well preserved and little-deformed. This is in contrast to Alltan na Bradhan and Clachtoll, where the original igneous textures and mineralogy has been altered due to Laxfordian deformation within the CSZ.

At Achmelvich Bay, the predominant ductile structure in the gneisses consists of an irregular and gently N- to NW-dipping foliation and local SW-plunging folds related to Badcallian deformation (Jensen, 1984, Attfield, 1987). The mean foliation orientation at Achmelvich Bay is 050/18°NW (*Figure 3.16*). Moving north, less than 250 metres along the coast; the foliation steepens up (mean orientation 113/66° SW, see *Figure 3.16a*) with a moderately to steeply dipping lineation (Beacom, 1999) and becomes much more intense as the NW-SE trending CSZ begins (*Figure 3.17*). At the southern and northern edges (Clachtoll) of the CSZ, the foliation is thought to be associated with Inverian deformation representing SW-side-up, dextral senses of movement (Attfield, 1987, Beacom, 1999). This foliation is discontinuous and somewhat irregular along its length

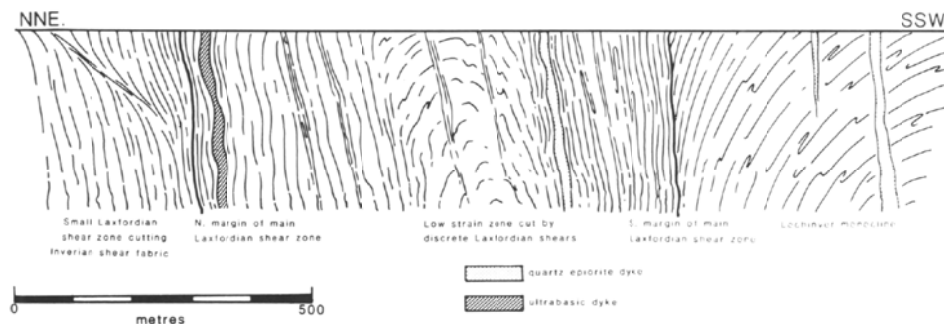
and also exhibits local SW-plunging folds (Sheraton et al., 1973b). The Inverian section of the shear zone was the product of amphibolite grade deformation (see *Figure 3.15* for the extent of Inverian deformation).



**Figure 3.16:** Equal angle stereonet projections of foliation and lineation data from key outcrops in the Assynt Terrane.



The central zone (~600m wide, see *Figures 3.15 & 3.17*) of the CSZ (Tarney, 1963), including Alltan na Bradhan, is characterised by steep, intense Laxfordian foliation (290/74° SW, *Figure 3.16b*) associated with more shallowly plunging lineations (41° → 118, *Figure 3.16b*) with shear sense indicators that suggest dextral shear (Jensen, 1984, Attfield, 1987, Wheeler et al., 2010). Narrow high strain zones (steep foliation) anastomose around regions of lower strain where the foliation is more irregular and sheath folds develop. Scourie dykes cross-cut the Inverian fabric (e.g. see Lochinver below) within the CSZ and are subsequently deformed. In many cases, the contacts and fine-grained chilled margins of the dykes are reactivated (e.g. near Achmelvich Bay NC 0508 2624), by the Laxfordian deformation. Hence, the Scourie Dykes are important structural markers that allow separation of the two main ductile deformation events that occur within the CSZ as well as forming significant pre-existing mechanical anisotropies. A more detailed analysis of the ductile deformation history within the CSZ can be found in Attfield (1987).



**Figure 3.17:** Diagrammatic cross-section of the extreme western end of the Canisp Shear Zone (Attfield, 1987).

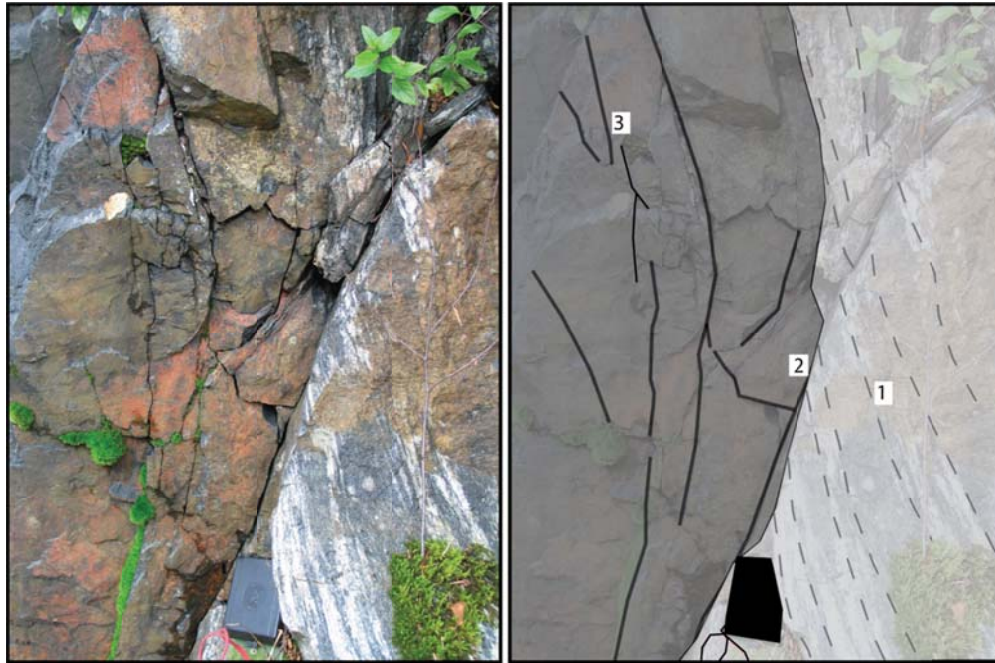
### 3.3.2.2 – Lochinver (Assynt Terrane)

The Lochinver outcrop lies approximately 900m west of Lochinver along the A837 on the junction of the B869 (NC 1000 2357) close to the edge of the Inverian deformation within the CSZ. The lithology present at this outcrop is dominated by banded grey quartz diorite or tonalite gneisses that exhibits amphibolite-facies metamorphism (Evans, 1965a, Evans and Lambert, 1974), similar to the orthogneisses present across the entire Assynt region. Banding within these gneisses is irregular and they contain spherical to lensoidal mafic to ultramafic pods (Evans and Lambert, 1974).

The main mineral assemblage at Lochinver is quartz + plagioclase + hornblende ± pyroxene ± biotite ± epidote. In thin section (sample 24-1, NC 0982 2334, see *Appendix B*) the lithology consists of hornblende- and pyroxene-rich bands (crystal size up to 3mm) interspersed within the mainly quartzofeldspathic rock (crystal size less than 1mm). Small clusters of biotite are also present (up to 4mm in size), although no alignment of the crystals is observed (this is also true for the crystals in the hornblende-pyroxene bands). There is also evidence of porphyroblastic muscovite and chlorite which suggests that the gneisses may have undergone metamorphic retrogression below amphibolite-facies (Evans and Lambert, 1974).

The predominant ductile fabric at the Lochinver outcrop consists of a steeply dipping foliation (mean foliation 105/85°N, *Figure 3.16c*) which varies between being discontinuous and intensely distributed. Lineations are steep to shallow (mean lineation direction 28° → 109, *Figure 3.16c*) and, along with shear sense indicators, indicate dextral movement.

The gneisses at Lochinver are cut by a series of NW-trending mafic and ultramafic Scourie dykes. One example at NC 1040 2357 cross-cuts the steep foliation (*Figure 3.18*) and is itself internally foliated. This dyke is a type example of evidence for the Inverian deformation event as it shows a Scourie dyke cross-cutting a pre-existing foliation and then being weakly deformed at a later stage (presumably during the later Laxfordian deformation). Evans and Lambert (1974) provide a comprehensive study of Inverian deformation as observed in the LGC outcrops of the Lochinver area.



**Figure 3.18:** Annotated photograph highlighting the structural relationship between the Inverian ductile fabric and a Scourie dyke. Outcrop photograph is from Lochinver (NC 1040 2357). Compass clinometer is for scale. 1. Inverian foliation within acid gneiss. 2. Foliation is cross-cut by a Scourie dyke indicating that the dyke is younger. 3. Many of the fractures in this section of outcrop are induced when the outcrop was blasted to make way for the road.

### 3.3.2.3 – Loch Assynt (Assynt Terrane)

Three main outcrops on the shores of Loch Assynt (NC 2022 2586 (two outcrops) & NC 1773 2650) have been studied to gain an understanding of the fault and fracture networks associated with granulite-facies, Badcallian LGC not affected by any major pre-existing ductile structures.

The lithology at Loch Assynt is the typical grey banded intermediate orthogneisses (tonalite) present across the Assynt Terrane. At this location the gneisses are segregated into bands of two domains; plagioclase-quartz-rich and biotite-rich. Key metamorphic minerals such as garnet, sillimanite, staurolite and corundum have also been recorded locally within the granulite-facies gneisses of the Assynt Terrane (Goodenough et al., 2010). At this location, the orthogneisses appear relatively homogeneous and only a few mafic pods are recorded across the entire area where they are typically <1m in dimension. There is little evidence from these outcrops for growth of muscovite or chlorite suggesting that these gneisses have experienced no widespread retrogression following granulite-facies metamorphism.

In thin section (sample M8, NC 2023 2602, see *Appendix B*), plagioclase and polycrystalline quartz form the majority of the lithology (65% and 20% respectively). Tabular pyroxene crystals (typically orthopyroxene) are interspersed among the plagioclase crystals where they do not exhibit any preferred orientation. Biotite is observed in small clusters (up to 5mm across) and again they show no preferred orientation.

The foliation in the gneisses on the shores of Loch Assynt is shallowly NW-dipping (mean dip of 47°, *Figure 3.16d*) and irregular. This foliation is typical of Badcallian deformation as described by Jensen (1984, 1987), Attfield (1987) and references therein.

The Loch Assynt gneisses are cross-cut by several NW-trending Scourie dykes that appear relatively undeformed. Again the dykes are mafic or ultramafic and there are examples where the dyke edges have been locally reactivated during later Laxfordian deformation.

#### 3.3.2.4 – Caolas Cumhann (Assynt Terrane)

Caolas Cumhann or Kylesku Bridge (NC2251 3392) has been studied as another example of LGC outcrop where the fault and fracture network is unaffected by pre-existing structures.

The lithology at Caolas Cumhann is predominately grey acid orthogneisses similar to those encountered within other outcrops across the Assynt region (Sheraton et al., 1973b, Jensen, 1984 and references therein). The acid gneisses are banded, in places, with mafic gneiss that has less quartz and plagioclase and a high proportion of pyroxene and biotite (up to 70%). The banded gneisses also contain small mafic or ultramafic pods which are generally lensoidal in shape. Microscopically (sample 21-2, NC 1931 3775, see *Appendix B*) the lithology primarily consists of quartz (45%), pyroxene (25%), hornblende (10%) and highly altered plagioclase feldspar (and microcline 20%). Generally pyroxene and hornblende are observed around the rims of plagioclase crystals. Biotite occurs in small clusters (up to 3mm across), again around the rims of the plagioclase crystals.

The outcrop exhibits relatively intense foliation that shallowly dips to the northwest and is typically irregular (mean foliation orientation 085/25°NNW, *Figure 3.16e*). Foliation is consistently in the same orientation as the banding within the gneiss

and flows around the mafic pods, which is typical of Badcallian deformation present throughout the Assynt region.

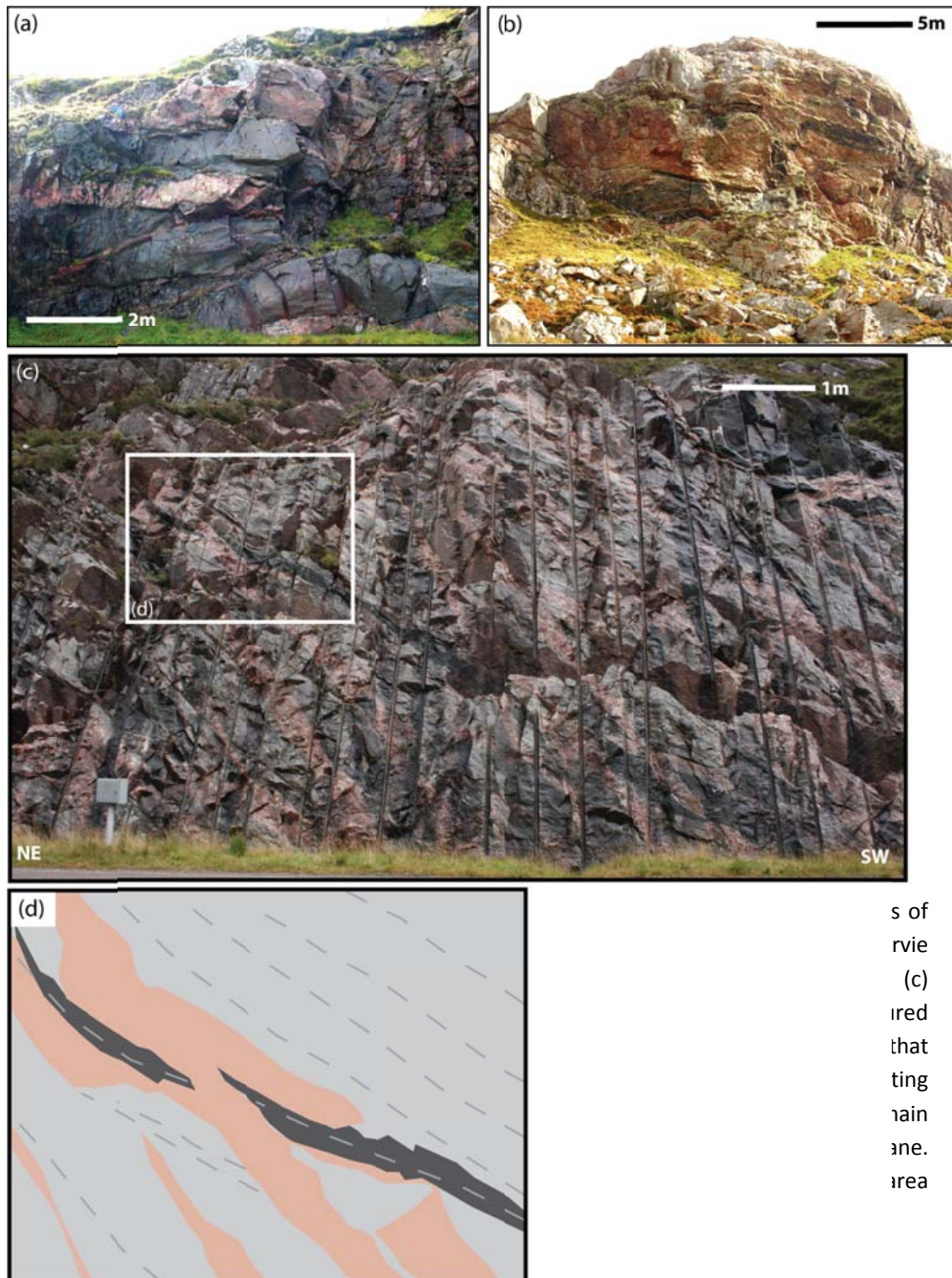
### 3.3.2.5 – Kinlochbervie (Rhiconich Terrane)

The outcrop at Kinlochbervie (NC 2296 5621) consists of three main cliff sections surrounding a small hill giving good access to all orientations of fractures present at this location. This outcrop is important for the understanding of fracture networks in the mainland LGC because of its position in the hanging wall of a large NW-trending post-Torridonian fault (Loch Incharid Fault which drops Torridon Group sediments to below the level of the LGC) and the resulting observed local variations in the fracture patterns.

The typical lithology observed at Kinlochbervie (*Figure 3.19a & b*) is consistent across the Rhiconich Terrane and therefore, the description given for this outcrop also applies to all other outcrops in the Rhiconich Terrane (unless otherwise stated). At Kinlochbervie the lithology is predominately dark to light grey diorite/granodiorite gneisses (*Figure 3.19a*) with a mineral composition of hornblende (50 -10%) + plagioclase (60 -20%) + quartz + biotite ± epidote. The dioritic/granodiorite gneisses are banded with younger mafic pods, containing phlogopite, that in many places have weathered out leaving spherical to lensoidal recesses in the outcrop. These mafic pods may be the remnants of dykes that were intruded into the earlier diorite gneisses.

In thin section (samples 13-1 and 14-3a, NC 2296 5621, see *Appendix B*) quartz, altered plagioclase crystals (including microcline) and biotite form the majority of the granodiorite rock volume. Hornblende is also observed as small prismatic crystals (<1mm across) that are included within the larger plagioclase crystals. In sample 14-3a, amorphous epidote-clinzoisite crystals are observed in close association with plagioclase crystals where it appears to be overprinting them. These epidote crystals are likely a product of the alteration of calcic plagioclase feldspar during retrograde metamorphism.

Granites are also present at Kinlochberive as sheets that are interbanded with, and in places cross-cut the diorite/granodiorite gneisses. In thin section (sample 14-4, see *Appendix B*), the lithology consists of plagioclase (40%), microcline (30%), quartz (15%) and biotite (15%). Plagioclase and microcline form the largest crystals present (up to 7mm across) with small quartz and biotite crystals forming poorly defined bands between the feldspar crystals.



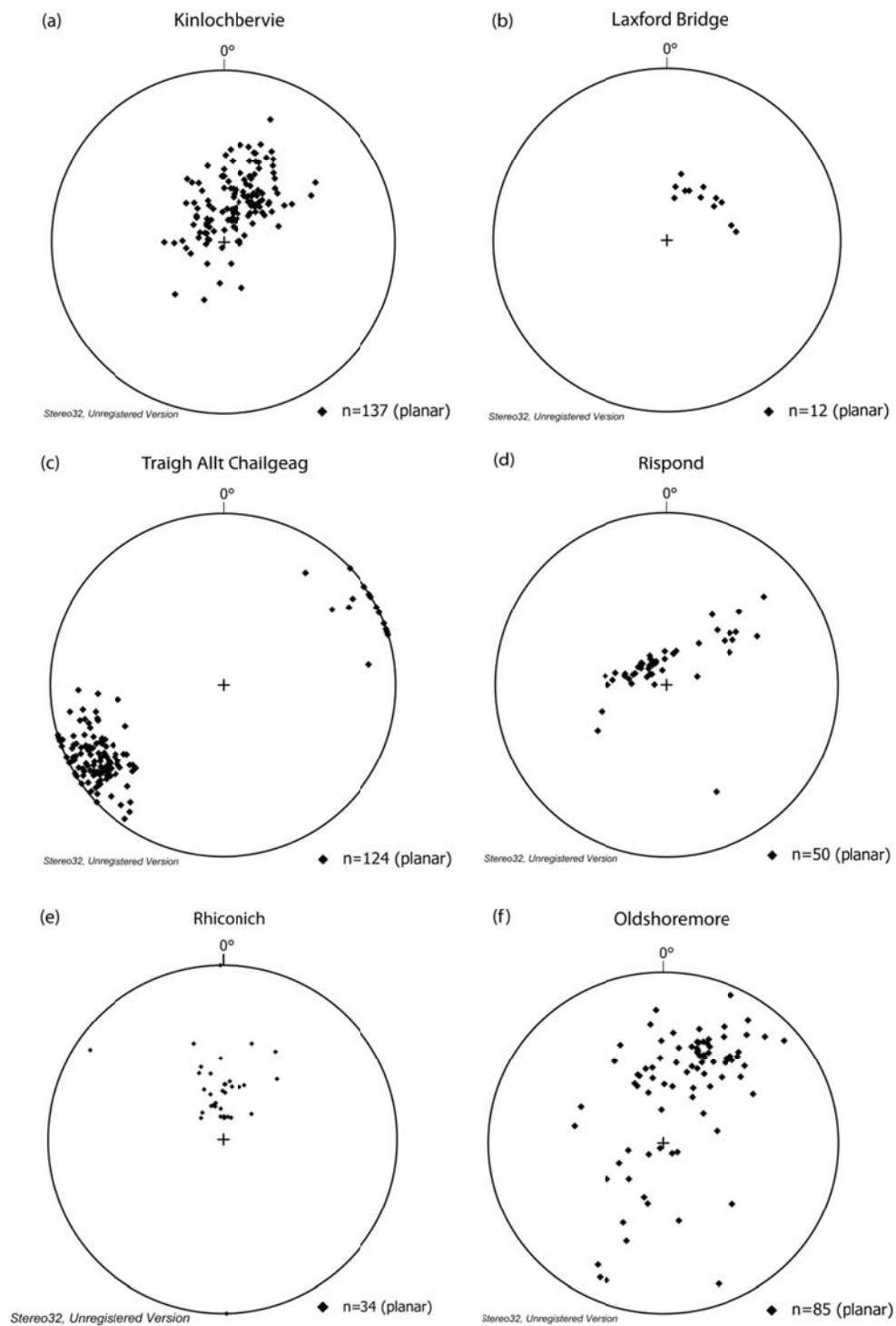
s of  
rvie  
(c)  
ired  
that  
ting  
rain  
ane.  
area

All of these lithologies are cross-cut by coarse-grained quartz-microcline pegmatite veins, which have a mineral composition of quartz + k-feldspar + biotite  $\pm$  plagioclase  $\pm$  hornblende  $\pm$  epidote. In thin section (sample 14-1, see *Appendix B*) the pegmatite is 70% quartz with microcline providing the majority of the rest of the rock volume. Unlike the other lithologies in the Rhiconich Terrane, the feldspars in the pegmatites show little evidence of alteration. Crystal size is up to 1cm with quartz having the largest crystal sizes. The pegmatite at Kinlochbervie, and at other localities in the Rhiconich Terrane, also exhibits bands that contain large hornblende and biotite crystals that are up to 5mm across.

The typical cross-cutting relationships of the different lithologies within the Rhiconich Terrane are best observed at the so called 'Multi-coloured Rock Stop' on the A838 (NC 2353 4902, *Figure 3.19c, d*). At Kinlochbervie the granite sheets and pegmatite veins comprise 40% of the rock volume: at other locations in the Rhiconich Terrane this value can be as much as 90% (e.g. at Laxford Bridge NC 2360 4827).

The diorite/granodiorite gneisses at Kinlochbervie exhibit a poorly defined foliation that dips shallowly to the SW (mean foliation orientation 284/33°SW, *Figure 3.20a*). This foliation flows around the mafic enclaves, but is cross-cut by granite sheets and pegmatite veins which themselves are weakly foliated to un-deformed (see Goodenough et al. (2010) for a description of this relationship as observed across the Rhiconich Terrane). Locally, there is macro-scale folding with fold plunges generally to the southeast.





**Figure 3.20:** Equal angle stereonet of foliation data from key outcrops in the Rhiconich Terrane.

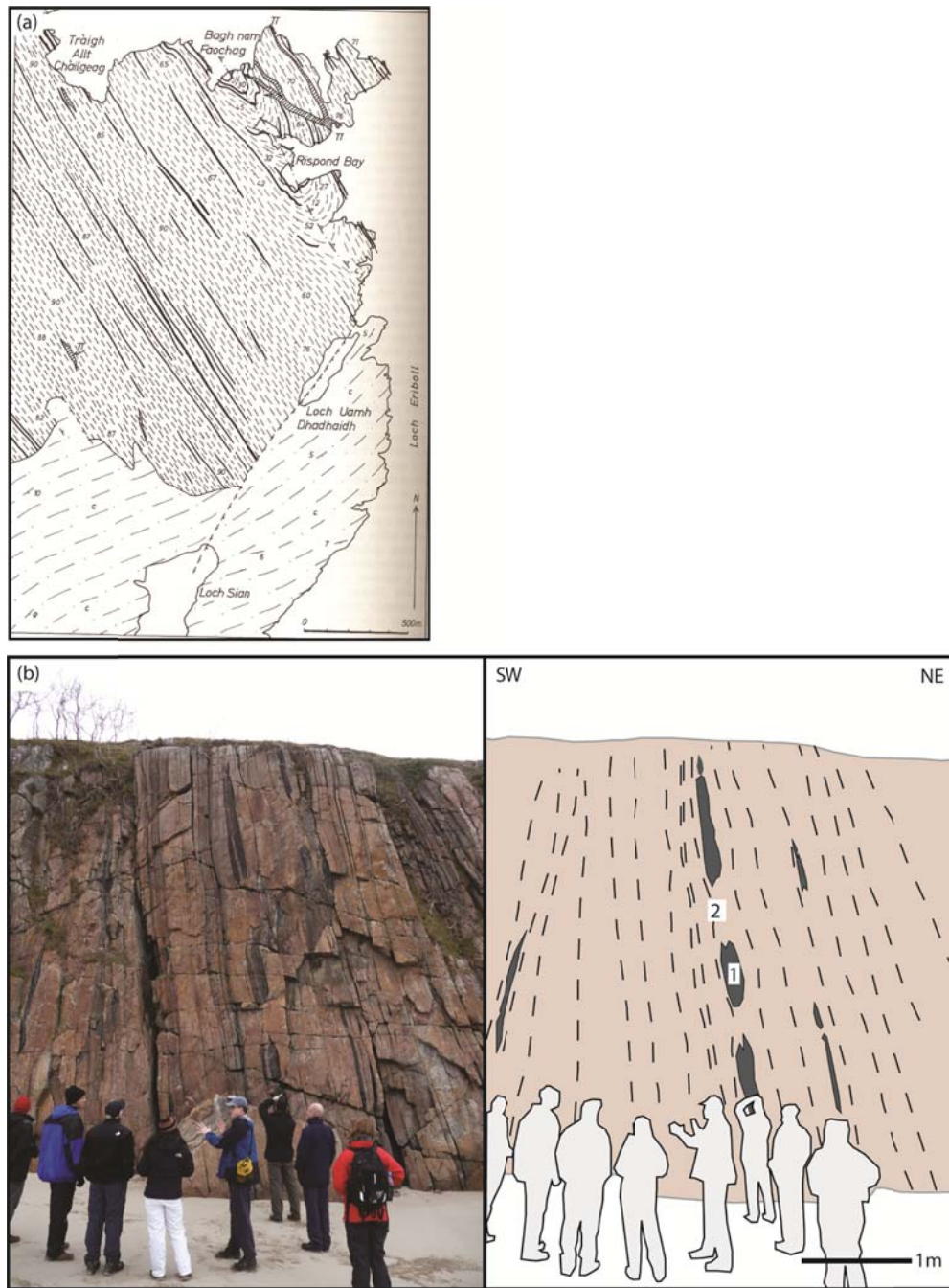


### 3.3.2.6 – Traigh Allt Chailgeag & Rispond (Rhiconich Terrane)

The outcrops at Traigh Allt Chailgeag (NC 4510 6577) and Rispond (NC 4563 6577) have been studied due to the presence of the Rispond Shear Zone (*Figure 3.21a*) providing a comparison of the effect of ductile shear zones on the fault and fracture networks between the Assynt and Rhiconich Terranes.

The lithology at Traigh Allt Chailgeag (TAC) and Rispond is predominately granitic gneiss with common mineralogy of quartz + feldspar + biotite interbanded with gneisses that are richer in hornblende. The outcrops are also characterised by abundant bands of hornblende-schist which are likely remnants of mafic dykes (Ramsay, 1997). At TAC these mafic dykes are highly deformed and stretched as they are observed forming large boudins (up to 5 metres long) along the foliation (*Figure 3.21b*). At Rispond Ramsay (1997) mapped out two main dyke strands across this area. The characteristic mafic boudins suggest that these mafic dykes were more competent than the surrounding gneissic material (Ramsay, 1997). Both the granitic gneiss and the deformed dykes are cross-cut by later pegmatite veins similar to those seen at Kinlochbervie.

Foliation at TAC is SE-trending with a near vertical dip (mean foliation orientation is 151/82°NE, *Figure 3.20c*). At this location the foliation is intense and the amount of stretching is highlighted by the large mafic boudins observed along the foliation planes. The foliation at Rispond dips more shallowly to the southeast (mean foliation orientation is 252/31°SE, *Figure 3.20d*) as this outcrop is on the other limb of a very tight, south-east plunging major antiformal fold (Ramsay, 1997). This change in foliation orientation is reflected in the orientation of the mafic bands which are also observed to be much shallower at Rispond.



**Figure 3.21:** (a) Map of the Rispond shear zone showing the change in foliation dip across the tight anticlinal fold. After (Ramsay, 1997). (b) Photograph from Traigh Allt Chailgeag highlighting the intense foliation and boudinage seen within the Rispond Shear Zone. **1.** Mafic bands within the gneiss form boudins. **2.** Foliation flows around the boudins suggesting that the mafic material in the boudins is more competent than the surrounding gneisses.

### 3.3.2.7 – Laxford Bridge (Rhiconich Bridge)

One road outcrop at Laxford Bridge (NC 2360 4827) has been studied to provide information on the fault and fracture network associated with a potential terrane boundary suture (Laxford Shear Zone (LSZ)) between the Assynt and Rhiconich Terranes (Friend et al., 2001, Kinny et al., 2005, Goodenough et al., 2010). The LSZ can be separated into three zones, the southern, central and northern zones with the Laxford Bridge outcrop occurring in the northern zone.

The lithology in this section of the LSZ corresponds to the Badnabay Zone (Sutton and Watson, 1950) is dominated by granite sheets and pegmatites that cut granodiorite gneisses. The granite sheets vary in thickness from 1m to 100m and are generally concordant with the foliation in the gneisses (Goodenough et al., 2010).

Foliation at Laxford Bridge is intense and dips to the southwest (332/47°SW, *Figure 3.20b*). The foliation in the northern zone of the LSZ has been identified as resulting from Laxfordian age deformation (Coward, 1990b), although the lack of Scourie dykes makes this difficult to confirm.

### 3.3.2.8 – Oldshoremore (Rhiconich Terrane)

Outcrops at Oldshoremore (NC 2010 5832) and adjacent sections of coast have been sampled to provide an understanding of the fault and fracture network in the Rhiconich Terrane where there is no influence from pre-existing ductile structures or major faults. Several outcrops at Oldshoremore and Sheigra Campsite (NC 1892 5900) have been sampled along this section of coastline.

The lithology at these locations is typical of what is observed throughout the Rhiconich Terrane with light grey granodiorite gneiss intruded with mafic lenses and subsequently cross-cut by granite sheets and pegmatite veins.

The foliation at these outcrops is generally weakly defined with relatively moderate dips towards the southwest or northeast (mean foliation orientation is 292/49°SW at Oldshoremore and 297/67°SW, *Figure 3.20f*). At Sheigra Campsite the gneisses and pegmatites are locally folded on a 10cm scale. These folds generally plunge steeply to the southeast and are likely the result of Laxfordian-age migmatisation.

### 3.3.2.9 – Rhiconich (Rhiconich Terrane)

Other outcrops at the roadside near Rhiconich (NC 2496 5211) have also been sampled to provide an understanding of the fault and fracture in the Rhiconich Terrane where there is no influence from major ductile or brittle structures.

These outcrops exhibit similar granodiorite gneisses, cross-cut by mafic lenses and then pegmatite veins. At NC 2496 5211, the outcrops exhibit mafic boudins, similar to those seen at TAC, although at this outcrop they are stretched along a weakly defined foliation that dips shallowly to the south (*Figure 3.20e*).

### 3.3.2.10 – Lithology Discussion

There are distinct differences between the main lithologies in the Assynt and Rhiconich Terranes. In the Assynt Terrane, banded grey granodiorite gneisses are predominant. Superficially similar granodiorite gneisses are also present in the Rhiconich terrane but these are inter-layered with granite gneiss sheets that are the defining feature of this terrane. All of the gneisses in the mainland LGC have a likely magmatic origin in terms of their protolith, i.e. they are all orthogneisses.

In the Assynt Terrane the orthogneisses typically exhibit granulite-facies metamorphism with pyroxene, hornblende and lesser volumes of biotite present throughout most samples. Within Assynt Terrane shear zones, such as the Canisp Shear Zone (CSZ), there is widespread evidence of retrogression of the granulite-facies gneisses. Within Inverian zones, pyroxene is less abundant and hornblende and biotite form larger volumes of the lithology consistent with amphibolite-facies metamorphism. At the centre of the CSZ, the Laxfordian deformation results in schistose, platy gneisses that exhibit biotite/muscovite mineralisation, with hornblende replacing pyroxene and small patches of chlorite and biotite replacing hornblende, all of which form compositional bands between quartz and feldspar. The presence of muscovite, biotite and chlorite suggests that ductile Laxfordian deformation may be associated with retrogression down as far as greenschist-facies metamorphic conditions.

In the Rhiconich Terrane, the orthogneisses have lithologies which are abundant in hornblende and biotite suggesting that amphibolite-facies metamorphism is prevalent. This is also true within the Rispond Shear Zone where there is no evidence of further retrogression to greenschist-facies, in distinct contrast to the Laxfordian deformation in the central part of the CSZ.

### 3.3.3 – Geological characterisation of onshore fracture sets

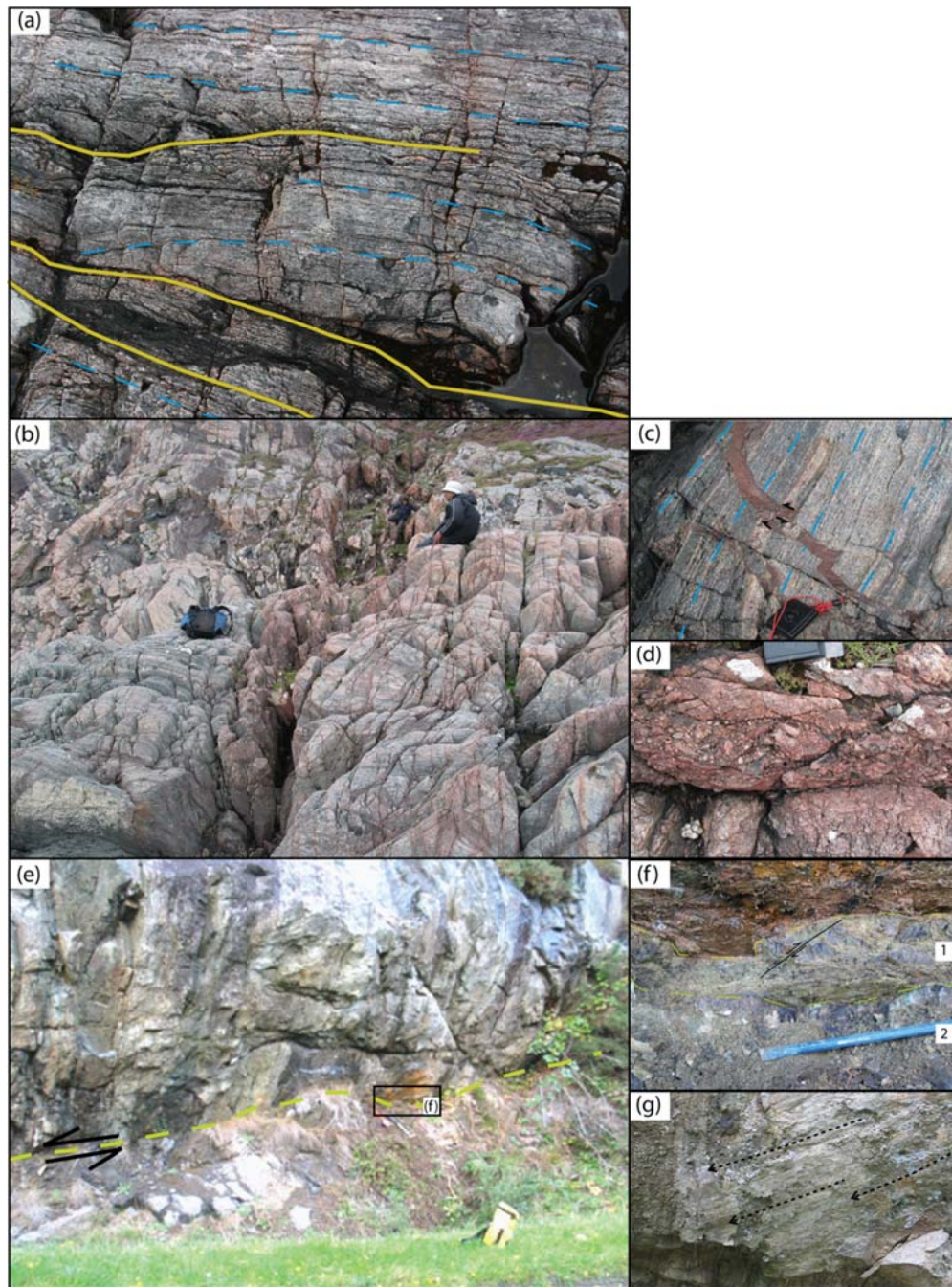
The mainland LGC has been affected by several phases of brittle deformation throughout its history. Each brittle deformation event creates new fractures or reactivates pre-existing structures. Understanding the fault and fracture networks in the mainland LGC provides important information on fluid flow pathways through this crystalline rock which is a particularly important consideration when comparing the mainland LGC with the potential hydrocarbon reservoir of the Clair Field basement.

There are three main fault and fracture sets recognised within the mainland LGC: the 'Late Laxfordian' faults; the Stoer Group age ladder fractures; and the late, possibly Mesozoic faults (*Figure 3.22*). Each of these fault and fracture sets has distinct fault rocks which are described in the following sections.

#### 3.3.3.1 – 'Late Laxfordian' Faults

'Late Laxfordian' faults occur most prominently in the Assynt Terrane with preferential development observed within the Canisp Shear Zone (CSZ) at Alltan na Bradhan (*Figure 3.22a*; *Beacom et al. 2001*). These faults have been termed 'Late Laxfordian' because they are known to be younger than the ductile Laxfordian deformation event that occurs within NW-SE trending shear zones across the LGC and they are older than the Stoer Group sediments overlying the LGC (from cross-cutting relationships), but their exact age within the Proterozoic is unclear (approximately 1200 Ma). 'Late Laxfordian' faults are most commonly observed as a fault zone within the Laxfordian deformation zone of the CSZ where they are spaced on a 10cm scale (outside the CSZ similar faults are spaced on a 100 to 1000m scale). Within the CSZ, these faults are generally foliation parallel structures (i.e. they trend NW-SE) and most commonly they occur in regions where pre-existing folding of the foliation is minor or absent (i.e. at Alltan na Bradhan, *Figure 3.22a*) where the foliation is well-developed and planar).





**Figure 3.22:** Examples of the three main fault sets present within the mainland LGC. **(a)** 'Late Laxfordian' faults in the Canisp Shear Zone. Yellow lines represent the faults. Blue dashed lines represent foliation. **(b)** Iron-stained Stoer Group 'ladder' fractures. **(c)** Clastic filled Stoer Group aged fracture. It cross-cuts and offsets the foliation and lithological banding. **(d)** Example of the indurated clastic fill within Stoer Group fractures that is common in the Canisp Shear Zone and on the north coast. **(e)** 'Later' (Mesozoic) fault at Lochinver. **(f)** Different sections of the Mesozoic fault **1**. Fault core which contains fault gouge and riedel shears **2**. Inner damage zone which contains heavily brecciated LGC. **(g)** Slickenlines providing evidence that the fault shows sinistral oblique strike-slip kinematics.

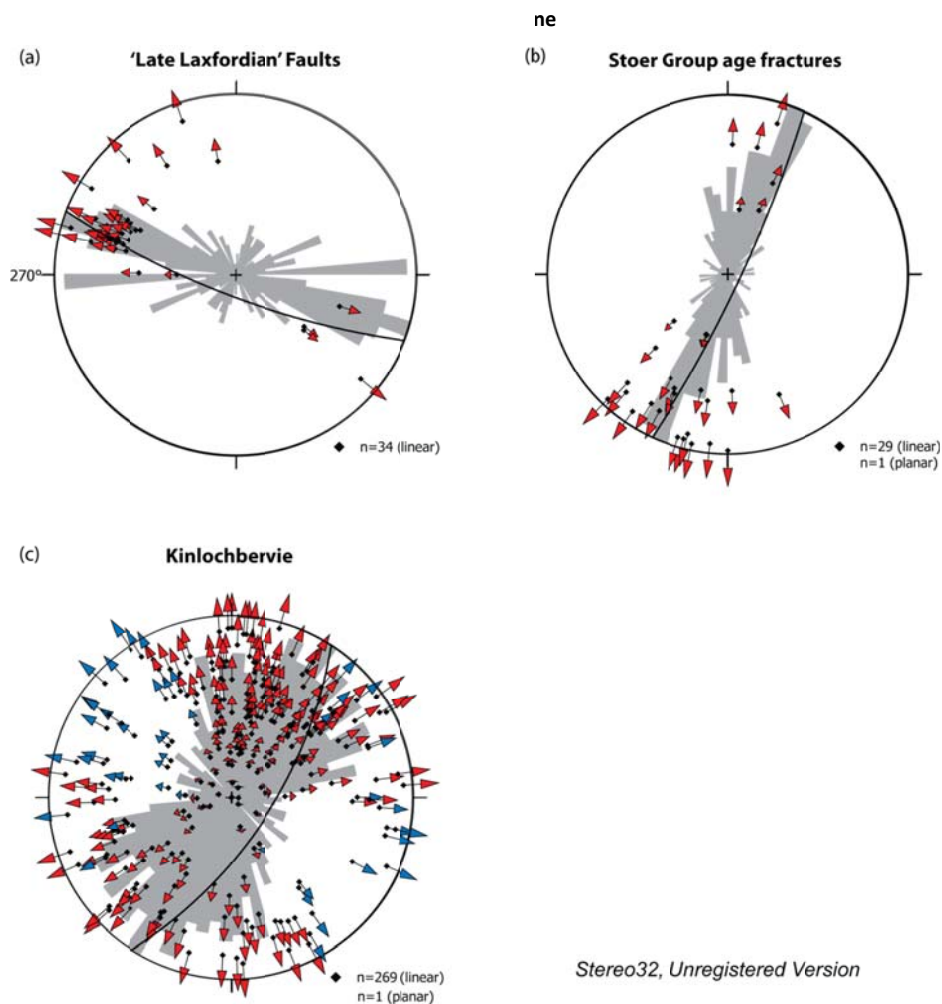
Outside Laxfordian shear zones 'Late Laxfordian' faults are rarer and they are most commonly discrete structures rather than broader interconnected deformation zones forming a larger fault zone. These discrete 'Late Laxfordian' faults trend NW-SE and generally extend over several kilometres (compared to 'Late Laxfordian' faults in the CSZ which are normally no more than 30m long). One example of a probable 'Late Laxfordian' fault is the Loch Assynt Fault which extends through Loch Assynt (NC 2330 2368) out to Clashnessie (NC 0681 3178) on the coast. At its southeast end, this particular fault exhibits evidence of displacement post Early-Ordovician (Krabbendam and Leslie, 2010), but it is likely that this phase of deformation reactivated a pre-existing fault plane of likely origin in the 'Late Laxfordian'.

Typical fault rocks within 'Late Laxfordian' faults include well-cemented, fine-grained breccia, cataclasite and, in some areas, thin pseudotachylites (see Beacom, 1999, Beacom et al., 2001 and references therein). There is little evidence of fluid flow through these 'Late Laxfordian' faults, although associated iron-oxide staining is widespread (Beacom, 1999). Those 'Late Laxfordian' faults outside the CSZ typically have fault rocks that consist of breccia and cataclasite. Whilst many of these structures have been reactivated during later events, it is difficult to link the fault rocks to individual deformation events.

Thin section samples from Clashnessie (samples M10 & M11, NC 0674 3178), where the Loch Assynt Fault outcrops, provides some insights into the microstructural textures associated with 'Late Laxfordian' Faults. Sample M10 (see *Appendix B*) exhibits thin (up to 1mm wide) cataclasite bands, that have a branching habit, cross-cutting otherwise undeformed granodioritic gneiss. The cataclasite bands contain clasts of unfractured quartz and feldspar with the majority of the fine-grained material enriched with epidote and chlorite. Also present are thin fractures (up to 2mm across) filled with brecciated gneiss clasts (<1mm in size) that are angular and show evidence of rotation (samples M10 & M11). Extremely fine-grained, red-black, opaque material is observed between the quartz, feldspar and hornblende clasts which is likely magnetite and iron-oxide (sample M11) that is also reported to be present in 'Late Laxfordian' faults within the CSZ (Beacom, 1999). These fault breccias are also enriched with black opaque minerals which are likely to be Fe-oxides that are common throughout 'Late Laxfordian' structures.

In samples M10 and M11, large (2-5mm across) equant crystals of calcite are observed overgrowing the granodiorite gneiss and truncating the cataclasite bands (*Appendix B*). Calcite is also observed within thin fractures (0.5mm wide) that cross-cut and offset the pre-existing fault breccias (*Appendix B*).

Sub-horizontal slickenlines and foliation offsets and mineral veins within the pre-existing LGC show that the 'Late Laxfordian' faults have predominantly sinistral strike-slip kinematics (*Figure 3.23a* and Beacom (1999)). Within the CSZ, these faults exhibit small displacements (no more than 1m, and more often 10cm) with larger boundary faults showing displacements of no more than 10m (Beacom, 1999).



**Figure 3.23:** Stereonets exhibiting slickenline data associated with fracture datasets from the mainland LGC. Fracture data is displayed as a rose plot and the average fracture orientation is given by a great circle on each stereonet. (a) 'Late Laxfordian' faults. (b) Stoer Group age fractures. (c) Kinlochbervie (the two different colours of arrows represent two different phases of deformation).



### 3.3.3.2 – Stoer/Torridon Group age fractures

Stoer Group age fractures and faults (1100 – 1000 Ma) are seen to cross-cut and offset the foliation parallel, 'Late Laxfordian' faults (*Figure 3.22b*). Many of the Stoer Group age structures are small features, but there are also large faults, such as the Coigach Fault, which are known to have been active during the deposition of the Stoer Group sediments (Stewart, 1993). Again these faults are preferentially developed within Assynt Terrane shear zones (particularly the Canisp Shear Zone (CSZ)) where they form meshes of 'ladder fractures', but are also found across both the Assynt and Rhiconich Terranes (Loch Assynt (NC 2022 2586), Caolas Cumhann (NC 2251 3392), Kinlochbervie (NC 2296 5621), Oldshoremore (NC 2010 5832), Traigh Allt Chailgeag (NC 4510 6577), Rispond (NC 4563 6577), Laxford Bridge (NC 2360 4827) and Rhiconich (NC 2496 5211)), where they form more discrete fracture planes. Typically Stoer Group age fractures are longer outside shear zones than they are within them. These fractures steeply dip to the northwest and have azimuths between NE-SW and N-S.

Stoer Group age fractures are extensively hematite-stained, with many also containing iron-stained sediment (breccia) and occasionally epidote ultra-cataclasite (*Figure 3.22c & d*). The hematite-staining and mineralisation within these fractures results in the characteristic red colourisation that these fractures display. These fractures typically form sub-planar to irregular dyke or sill-like structures that cut down into the LGC, and are pervasive over a few centimetres to 10's of metres. A key outcrop at Clachtoll (NC 0425 2677) exhibits large fractures (some are nearly 50cm wide) in-filled with clastic sedimentary material that is derived from the overlying Stoer Group sediments and clasts from the LGC (Beacom et al. 1999). Clastic material within these fractures consists of fine red mudstone and sandstone (*Figure 3.22c*). The LGC clasts are most commonly found at the edges of the fractures and are no bigger than 10cm (*Figure 3.22d*). The LGC clasts contain foliations which are mis-oriented with respect to the host rock foliation providing evidence of rotation and potentially evidence of transport during fracturing and in-filling of these structures. The clastic in-fills within Stoer Group age fractures are typically indurated which is likely a result of the level of iron and quartz mineralisation within the fractures (*Figure 3.22d*).

Epidote ultracataclasite is also observed locally within the Assynt Terrane Stoer Group age fractures where it appears to be earlier than the iron mineralisation and clastic in-fills since epidote cataclasite is truncated by iron-rich clastic in-fills and clasts of

epidote are entrained within the iron-stained mineralisation. There is evidence that the epidote has been remobilised, in some fractures, where the fill (surrounding LGC clasts) is green in colour, suggesting that epidote-rich fluid has been partially responsible for mineralising the clastic in-fills in these fractures (*Figure 3.24*). It is likely that this ultra-cataclasite is a result of an earlier deformation event (post 'Late Laxfordian' deformation) that represents the earliest phase of mineralisation associated with the Stoer Group rifting event.



**Figure 3.24:** Example of Stoer Group age fractures that also exhibit epidote mineralisation. Mobile phone is for scale.

In thin section, the Stoer Group fractures show a variety of microstructural textures. Fractures in the CSZ that contain clastic materials can consist of large clasts (up to 10cm across) of typical CSZ granodiorite gneisses with quartz and feldspar compositionally banded with biotite and hornblende (sample 01-01a, *Appendix B*). The compositional bands vary in orientation between gneiss clasts providing evidence of rotation within the fracture. Many of the clasts are also fractured with the majority of these micro-fractures mineralised with iron-rich minerals, primarily hematite, around their edges. The edges of all the gneissic clasts are also iron-stained but this iron-staining does not penetrate into the centre of the clasts. Arenitic sandstone is also present within the matrix of sample 01-01a (*Appendix B*) between some of the gneissic clasts

where smaller sub-rounded clasts of individual quartz and feldspar crystals are supported by a matrix of a quartzofeldspathic siltstone.

Slickenlines recorded on the iron-mineralised fault slip surfaces are generally steeply inclined (*Figure 3.23b* and Beacom (1999)). These slickenline orientations along with foliation and lithology offsets indicate normal kinematics consistent with oblique extension associated with the deposition of the Stoer Group sediments on top of the LGC.

A thin section sample from Kinlochbervie (sample 14-2, NC 2296 5621, see *Appendix B*) shows typical microstructural textures of other hematite stained fractures that do not contain clastic fills. These fractures are most likely associated with the deposition of the Torridon Group sediments on top of the Lewisian (or later phases of brittle deformation) and are therefore younger than their Stoer Group age counterparts in the Assynt Terrane. This particular sample is from the surface of a small fault plane and shows typical Rhiconich Terrane granodiorite gneiss that has been altered and stained with iron-rich minerals (hematite). It is highly fractured with two orientations of fractures (at 30° to each other) both containing drusy calcite mineralisation (Tucker and Wright, 1990). Other thin section samples from Kinlochbervie (sample 14-4, *Appendix B*) exhibit Torridon Group age (or later) fractures as inter-crystalline micro-cracks that are <1mm wide and show hematite mineralisation along their edges.

Slickenline data from Kinlochbervie (*Figure 3.23c*) exhibit similar orientations to those observed for Stoer Group age fractures in the Canisp Shear Zone (*Figure 3.23b*). This suggests that the Torridon Group fractures at Kinlochbervie have similar oblique extensional kinematics. *Figure 3.23c* presents two sets of slickenlines (red – older, blue – younger) which may represent different periods of oblique extension associated with deformation on the Loch Inchar Fault.

### 3.3.3.3 – ‘Later’ (Mesozoic) structures

Another major fault set present within the mainland LGC has been deemed to be Mesozoic in age. This age is based on the fact that these faults cross-cut and offset all other structures within the LGC in a similar manner to known Mesozoic structures that occur in the southern most sections of the mainland LGC and offshore into the Minch Basin (Roberts and Holdsworth, 1999). They are also consistently associated with incohesive, soft gouges and breccias (*sensu* Sibson, 1977) that contrast with the more

cohesive, highly cemented fault rocks associated with other faulting episodes. These faults are normally NE-SW to NNE-SSW trending and mostly steeply dip to the east. Several Mesozoic faults are known to exist in the southern most mainland LGC (Applecross and Kishorn Faults (Roberts and Holdsworth, 1999), but further north, in the area included in this study, only one convincing large Mesozoic fault has been identified (*Figure 3.22e*).

The large Mesozoic fault at Lochinver (NC 0982 2334) trends NE-SW (fault orientation is 044/62°NW) and is associated with incohesive fault gouges and breccias (*Figure 3.22f*). It has a large damage zone that extends over several metres either side of the main fault plane. This structure exhibits a fault core that is 7.5cm wide and a 50cm wide inner damage zone which contains Riedel shears and slickenlines (21° → 246) that indicate oblique sinistral strike-slip kinematics (*Figure 3.22g*). Fault rocks are highly altered and incohesive broken clasts of LGC that have, in the fault core, been ground into a grey gouge (*Figure 3.22f*).

In thin section, the damage zone of the Lochinver Fault (samples 24-3a & 24-3b see *Appendix B*) contains relatively undeformed granodiorite gneiss cross-cut by a series of sub-horizontal micro-fractures that contain brecciated fragments of the surrounding host rock. Significant grain size reduction is observed within these micro-fractures, although the clasts within the breccia appear to be relatively unfractured.

Sample M1 (*Appendix B*), which comes from the core of the same fault, exhibits large host rock clasts of quartz (up to 2cm in size) and highly altered feldspar cross-cut by a network of fault gouge filled micro-fractures. A large quartz clast, within this sample, lobate grain boundaries (Passchier and Trouw, 2005) typical of grain boundary diffusion creep during dynamic recrystallisation (*Appendix B*). Feldspar is highly altered, showing evidence of being replaced by epidote-clinozoisite. The quartz and feldspar clasts are cross-cut by micro-fractures containing yellow-green to colourless fault gouge. There is also evidence of hematite mineralisation along the edges of some of the larger micro-fractures.

Further along the same Lochinver Fault, two more thin sections (M5a & M5b) provide more evidence of the intense shearing that has occurred. Pristine hornblende crystals (up to 2cm in size), that appear to overprint the ductile fabric in the gneisses, become increasingly fractured (along their cleavage planes) and disaggregated towards the centre of the fault. The orientation of the crenulation cleavage indicates sinistral

strike-slip deformation which is consistent with observations made at the outcrop. Both these thin section samples contain red-brown, biotite-rich fault gouge that infills the fractures within the hornblende crystals and also follows the cleavage in the rock (*Appendix B*). Yellow/Green (epidote-rich?) fault gouge is also observed in patches within the fault core, particularly in plagioclase dominated zones where it lies along breaks in the cleavage (*Appendix B*).

Within the LGC there are potentially other localised deformation events that occur throughout geological history, especially as a result of the Caledonian Orogeny and deformation episodes during the Palaeozoic. The lack of younger sediments and cross-cutting relationships means that it is impossible to distinguish these fault and fracture sets from those described above.

#### 3.3.3.4: Fault rock discussion

The three main fracture sets within the mainland LGC have distinct fault rock characteristics that make them identifiable.

‘Late Laxfordian’ faults are likely to have developed in the mid to upper crust (5-15km depth) with most structural features (breccia, cataclasite and the local development of folds) indicative of faulting occurring in the frictional-viscous transition zone (Passchier and Trouw, 2005). Samples from the Loch Assynt Fault exhibit the microstructural textures typical of ‘Late Laxfordian’ faults in the Canisp Shear Zone (as described by Beacom (1999)) but also exhibit local calcite mineralisation (*Appendix B*) which is not documented in association with ‘Late Laxfordian’ faulting. The Loch Assynt fault is known to have reactivated post Early-Ordovician (Krabbendam and Leslie, 2010) and it is possible that the calcite mineralisation seen in thin section samples can be attributed to this later movement.

Stoer and Torridon Group fractures are likely to have formed near surface with fracture fills (breccia, sediments and hematite mineralisation, *Appendix B*) all associated with the deposition of the Stoer/Torridon Group on top of the LGC. Fractures containing clastic material are only found in close proximity to large faults that offset both the mainland LGC and the overlying Stoer Group sediments and in outcrops where the LGC is less than ~50 metres below the Stoer Group contact, again suggesting deformation in the upper crust. Stoer Group fractures are thought to have formed during dextral transtension (Beacom, 1999) and therefore it is possible that the clastic material within

these structures was washed down into open cavities rather than it being injected into weaknesses in the rock, as would be expected from traditional clastic dykes (Richter, 1966, Winslow, 1983, Molina et al., 1995 and references therein).

Potentially Torridon Group age (or later?) fractures with typical hematite staining and mineralisation are observed at Kinlochbervie (the age of these faults is unclear because of the lack of cross-cutting relationships with cover sedimentary units). In thin section, these fractures also show calcite mineralisation in micro-fractures within hematite-stained fault rock (*Appendix B*). Evidence from slickenlines suggests that these fractures at Kinlochbervie have been reactivated at least once and therefore it is possible that the calcite mineralisation is a result of later brittle deformation after the deposition of the Torridon Group sediments. The adjacent Loch Inchard normal fault which brings the Torridon Group sediments to the same height as the LGC is likely responsible for the reactivation and the growth of calcite on the Torridon Group fractures at this locality.

The 'Later', potentially Mesozoic fault described at Lochinver exhibits a variety of different microstructural textures (*Appendix B*). This fault exhibits a large damage zone that is heavily fractured although the majority of deformation is focussed along a single fault core that is up to 10cm wide. As previously described, deformation increases into the fault core with the development of a crenulation cleavage associated with iron-depleted chlorite and the fracturing of hornblende crystals that appear to have overprinted the pre-existing crenulation cleavage associated with the chlorite crystals (*Appendix B*). The presence of biotite-mineralised micro-fractures that disaggregate the pre-existing minerals suggests an upper crustal origin for the deformation along the Lochinver Fault.

### 3.3.4 – Fracture orientation analysis from outcrop data

Fracture data from across the whole of the mainland LGC study area have been used to conduct an orientation analysis. Particular focus is paid to the key outcrops described earlier in this chapter, but fracture samples from all over the mainland LGC are included in *Appendix B*. *Figures 3.25 & 3.26* show fault and foliation data for outcrops within the mainland LGC (Assynt and Rhiconich Terranes respectively).

In the Assynt Terrane, fracture orientation varies widely, but it is apparent that generally NE-SW and NW-SE trending fractures are somewhat dominant (*Figure 3.25*).

These fracture trends are observed across both outcrops within the Canisp Shear Zone (CSZ) and within the main body of the LGC, with relatively consistent orientations observed between all outcrops shown (this pattern is consistent across the Assynt Terrane, see *Appendix B* for stereonet from outcrops not shown here). The stereonets in *Figure 3.25* also show that the majority of fractures are steeply dipping with only a few structures exhibiting shallower dips (most commonly to the northwest).

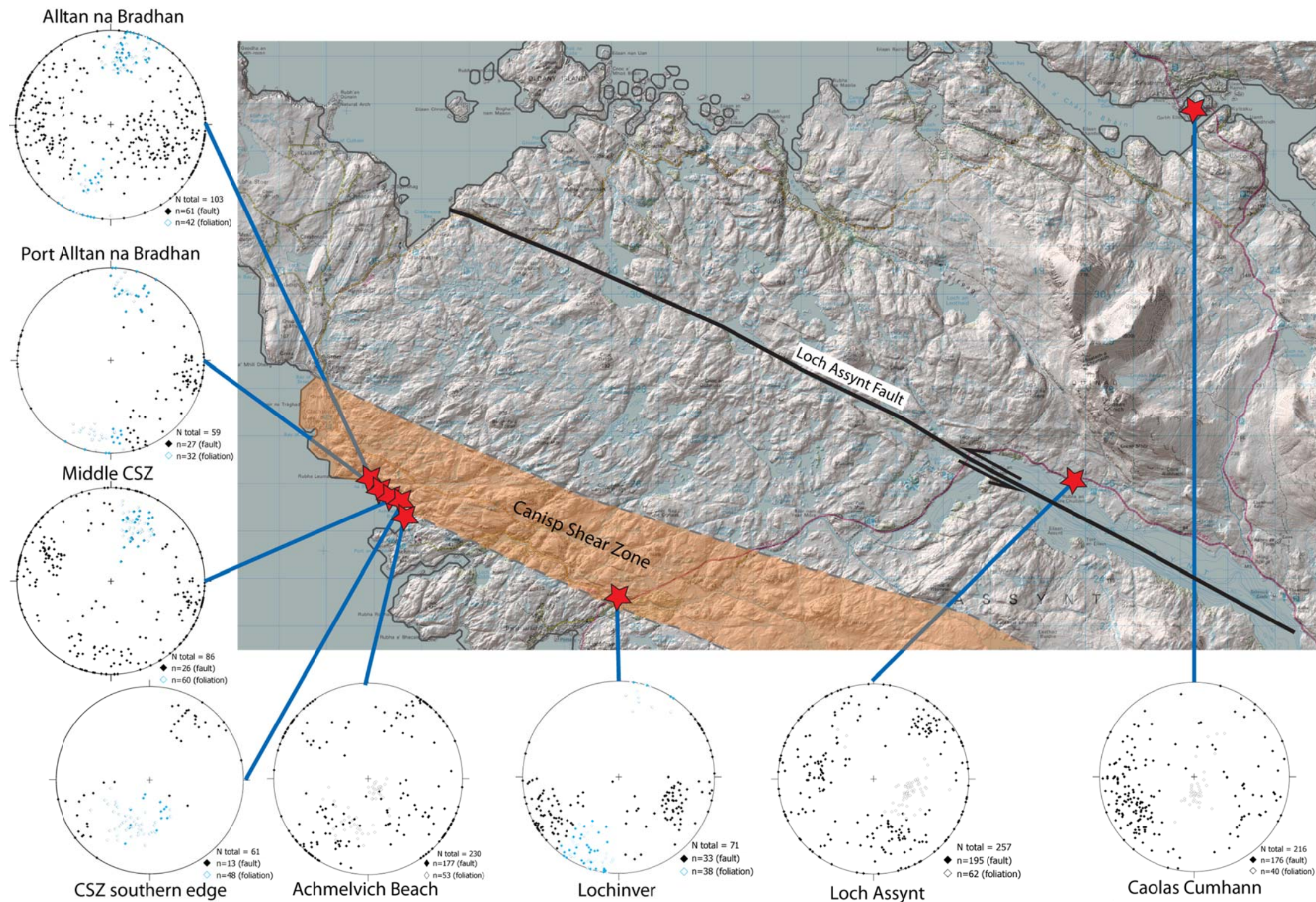
The stereonets in *Figure 3.25* also exhibit foliation data (hollow data points in black and blue) for each of the key outcrops to allow an assessment of the relationship between fracture and foliation to be made. Fracture orientations which coincide with foliation orientations at each outcrop are shown in blue (i.e. fractures which exploit pre-existing foliation planes). Throughout the CSZ, many of the NW-SE trending fractures are of the same orientation as the steeply inclined, intense foliation present at each of the CSZ key outcrops. One exception to this trend is at the southern edge of the CSZ (NC 0595 2529), where there is only a small number of similarly trending faults (NW-SE).

N-S trending fractures are also commonly seen in the CSZ key outcrops (*Figure 3.25*), with the exception of the outcrop at the southern edge of the CSZ. These N-S trending fractures are also less obvious in outcrops within the main body of the LGC (for example, Loch Assynt and Achmelvich Beach).

Across the Rhiconich Terrane fracture orientations vary more widely than those in the Assynt Terrane. Again, NE-SW and NW-SE trending fractures are present across the majority of the key outcrops shown in *Figure 3.26* (see *Appendix B* for more stereonets from other Rhiconich Terrane outcrops not shown in *Figure 3.26*). Fractures in the Rhiconich Terrane show a variety of dip angles; from vertical (>80% of fractures are steeply dipping) to sub-horizontal with this variation in dip evident across most individual outcrops.

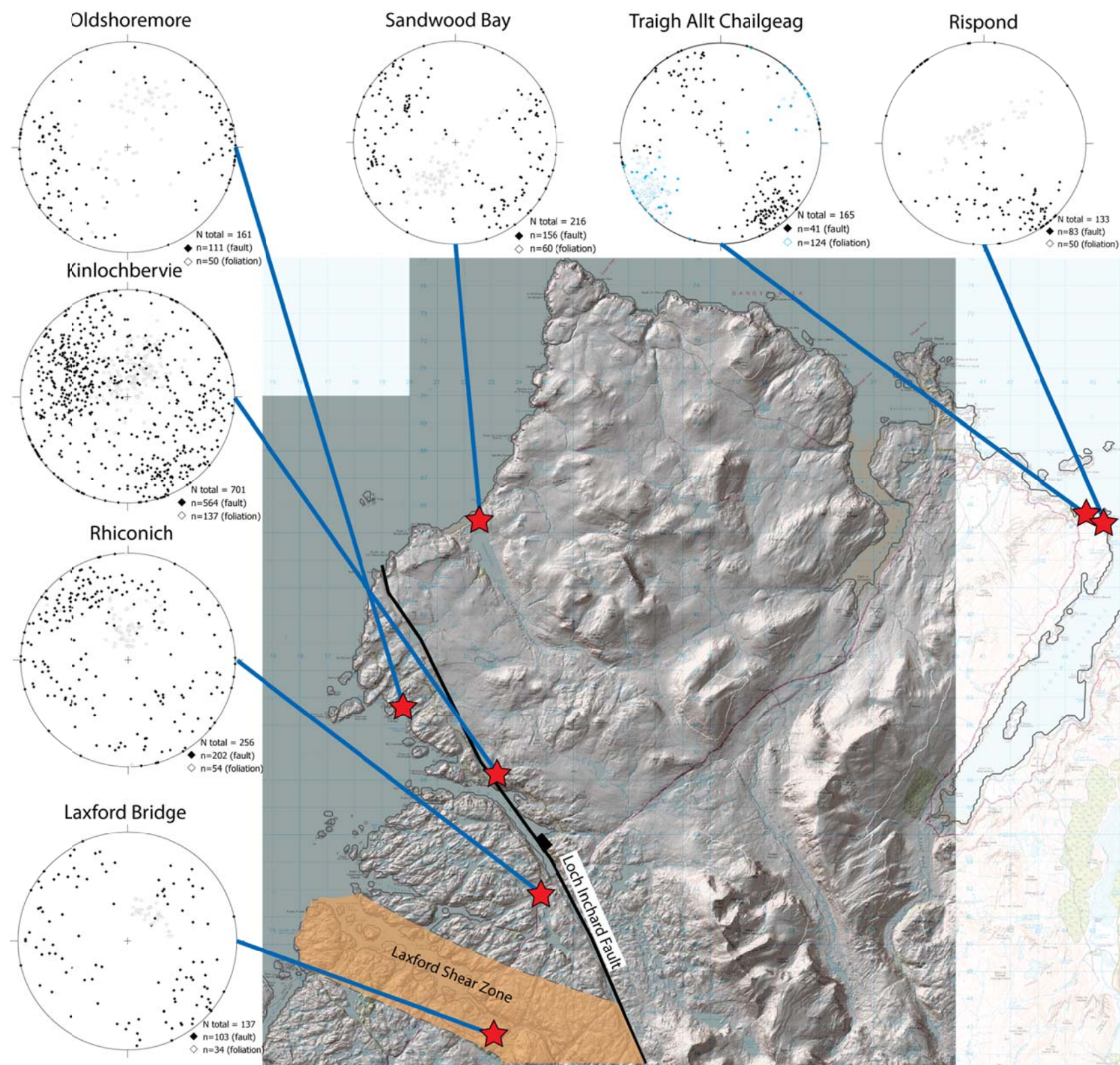
The key outcrop at Kinlochbervie exhibits fractures with strong NE-SW and N-S trends. These fractures are almost perpendicular the major NW-SE trending normal fault (Loch Inchard fault), which is in close proximity to this outcrop. Outcrops which represent the background fracturing in the Rhiconich Terrane (Rhiconich, Oldshoremore & Sandwood Bay) have predominant fracture orientations of NE-SW to N-S. This is consistent across all the Rhiconich Terrane outcrops that are not affected by any pre-existing foliation or major faults (see *Appendix B*).





**Figure 3.25:** Equal angle stereonet projections of fracture (solid data points) and foliation (hollow data points) data for LGC outcrops within the Assynt terrane. Each outcrop is highlighted with a red star on the map, which uses OS 1:50,000 scale colour raster maps overlain on NEXTMap® DEM hill shade analysis. Fracture orientations which are aligned with foliation are shown in blue.





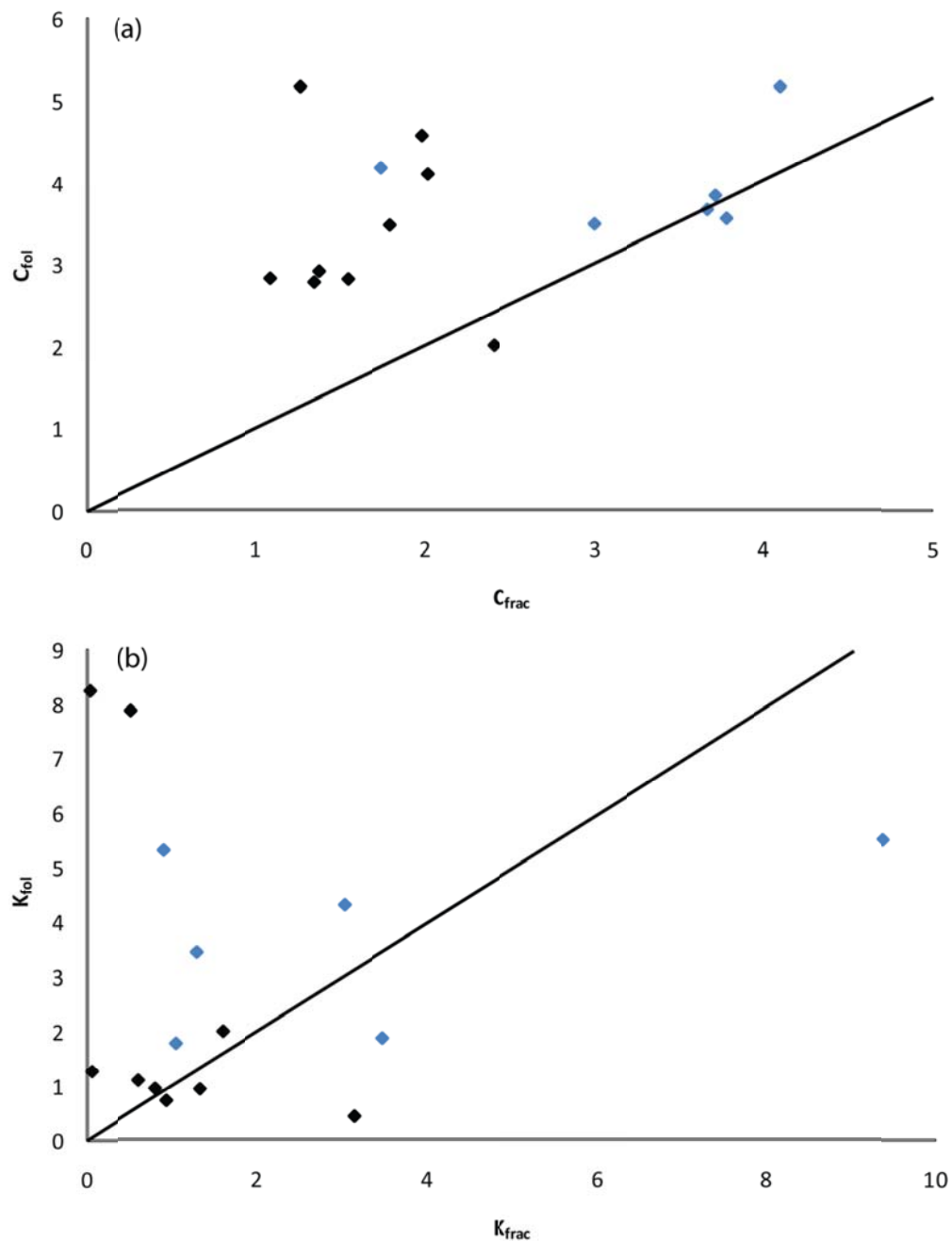
**Figure 3.26:** Equal angle stereonet projections of fracture (solid data points) and foliation (hollow data points) data for LGC outcrops in the Rhiconich Terrane. Each outcrop is highlighted with a red star on the map, which uses OS 1:50,000 scale raster image maps overlain on NEXTMap® DEM hill shade analysis. Fracture orientations which are aligned with foliation are shown in blue.

Only the outcrop at Traigh Allt Chailgeag contains fractures which have the same orientation as the intense NW-SE trending foliation of the Rispond Shear Zone (RSZ) that cross-cuts this outcrop (*Figure 3.26*). It should be noted that although several fractures at Traigh Allt Chailgeag do lie along pre-existing foliation planes, these only account for 20% of the fractures sampled at this outcrop (compared to ~40-50% of fractures within the CSZ, *Figure 3.25*). At Rispond, which is also affected by the RSZ, the foliation is near horizontal (Rispond is situated on the other limb of a very tight antiformal fold from Traigh Allt Chailgeag), and therefore the sub-vertical fractures do not exploit the pre-existing foliation (see *Figure 3.25*). The foliation at all other outcrops in the Rhiconich Terrane is not exploited by later fracturing, with most foliation orientations being quite shallow in comparison to the steeply dipping fractures.

In order to assess the relationship between fractures and foliation within mainland LGC outcrops in a more quantitative manner, C (strength of the preferred fracture/foliation orientation) and K (shape of the preferred fracture/foliation orientation) values were calculated. It should be noted that at outcrops that contain fractures which coincide with foliation only those fractures have been used to calculate the C and K values (i.e. in the CSZ only NW-SE trending fractures which are aligned with the NW-SE trending foliation are included). *Table 3.4* contains the results of this quantitative analysis, which are also graphically shown in *Figure 3.27*.

Terrane	Outcrop	Grid Reference	C <sub>frac</sub>	C <sub>fol</sub>	K <sub>frac</sub>	K <sub>fol</sub>
Assynt	Alltan na Bradhan	NC 0492 2627	3.7764	3.5646	1.0621	1.7551
	Port Alltan na Bradhan	NC 0513 2618	3.7106	3.8462	1.3027	3.4282
	Middle CSZ	NC 0543 2579	4.0954	5.1805	3.0418	4.2896
	CSZ southern edge	NC 0592 2530	2.9929	3.4974	3.4944	1.8511
	Achmelvich	NC 0580 2504	1.5383	2.8233	0.0659	1.2586
	Lochinver	NC 0982 2334	3.6627	3.6735	9.3781	5.4886
	Loch Assynt	NC 2022 2586	1.3689	2.9181	0.0453	8.2349
	Caolas Cumhann	NC 2251 3392	2.0106	4.1001	1.3345	0.9098
Rhiconich	Laxford Bridge	NC 2360 4827	1.2599	5.1682	0.615	1.0733
	Rhiconich	NC 2496 5211	1.3401	2.7861	0.5268	7.8523
	Kinlochbervie	NC 2296 5621	1.084	2.8321	1.6049	1.9704
	Oldshoremore	NC 2010 5832	2.3976	2.0089	0.9429	0.6962
	Sandwood Bay	NC 2254 6553	1.7893	3.4784	0.8112	0.9203
	Traigh Allt Chailgeag	NC 4510 6577	1.7389	4.1829	0.919	5.2866
	Rispond	NC 4563 6577	1.976	4.5715	3.1545	0.407

**Table 3.4:** C and K values for fractures and foliations collected from key outcrops across the mainland LGC. Outcrops where fractures exploit pre-existing foliation planes are highlighted in bold blue.



**Figure 3.27:** Plots showing the relationship between fault and foliation C and K values. Blue data points represent outcrops where fractures exploit pre-existing foliation planes (Canisp Shear Zone data). **(a)** Plot of fracture C-value versus foliation C-value. **(b)** Plot of fracture K-value versus foliation K-value. The trend line in both plots represents a line of 100% geometric correspondence.

Fracture and foliation C-values are generally similar to each other for outcrops within the CSZ. At Traigh Allt Chailgeag the C-values for fractures and foliation are completely different ( $C_{\text{frac}}$  is approximately half the  $C_{\text{fol}}$  value, *Table 3.4*). C-values for all other mainland LGC outcrops are different for fractures and foliations, with the majority of outcrops showing C-values for fractures that are significantly lower than the C-values for foliation (*Table 3.4*). These relationships are seen in *Figure 3.27a*, where data points from the CSZ form a positive correlation compared to the outcrops from the rest of the mainland LGC that show no correlation between fracture and foliation C-values.

K-values for CSZ outcrops are generally different for fractures and foliations and this is reflected in *Figure 3.27b*, where no clear correlation between  $K_{\text{frac}}$  and  $K_{\text{fol}}$  can be ascertained. Even the K-values from outcrops in the CSZ do not form a consistent relationship. *Table 3.4* shows that K-values for fractures and foliation show no consistent patterns between outcrops with some  $K_{\text{frac}}$  values higher than  $K_{\text{fol}}$  and some lower.

#### 3.3.4.1 – Orientation analysis from outcrop data: Discussion

Analysis of fracture orientations across the mainland LGC has shown that NE-SW and NW-SE trending fractures are dominant across both the Assynt and Rhiconich Terrane, with N-S fractures forming subordinate sets (*Figures 3.25 & 3.26*).

Within the Assynt Terrane most outcrops exhibit two predominant fracture trends (NE-SW & NW-SE) in approximately equal amounts (*Figure 3.25*). NW-SE fractures across most of the key Assynt Terrane outcrops are attributed to the sinistral strike-slip ‘Late Laxfordian’ faulting events (*Section 3.3.3.1*) that show preferential development within the Canisp Shear Zone (CSZ). The majority of NE-SW (and N-S) fractures sampled in the Assynt terrane are thought to be Stoer Group age (*Section 3.3.3.2*) formed during dextral transpression (Beacom et al., 2001), although some of the NE-SW (N-S) structures encountered are likely to be associated with much younger deformation events, potentially in the Mesozoic (this includes large structures, such as the Lochinver Fault and smaller NE-SW faults along Loch Assynt side).

CSZ outcrops exhibit many fractures that have the same orientation as the NW-SE trending, steeply-dipping foliation also present within these outcrops (‘Late Laxfordian’ faults). This observation is quantified by statistical analysis of the orientation using C and K values which, for values in the CSZ suggest that there is a strong correlation between the strength of the preferred orientation (C-values) for both

fractures and foliation (*Table 3.4 & Figure 3.27a*). The correlation can be explained by the fact that within the CSZ (especially the Laxfordian domain) the foliation is defined by the alignment of phyllosilicates (biotite, muscovite and chlorite) thus forming planes of weakness that have a strong pre-defined orientation (NW-SE). Subsequent brittle deformation, during the 'Late Laxfordian', exploited these planes of weakness (Beacom, 1999) forming sinistral strike-slip faults with the same orientation as the pre-existing foliation. K values, which represent the shape of the preferred orientation, show a much weaker correlation between fractures and foliation (*Figure 3.27b*). This is likely because, in most of the datasets used, the orientation spread of foliation or fracture data points are never equal which results in variable K values between the two datasets.

Outside the CSZ, in the Assynt Terrane, there is less evidence of fracture orientations coinciding with foliation because regionally the foliation does not have a strong preferred orientation (therefore there are fewer NW-SE trending fractures, *Figure 3.25*). Also the lithology has not been subjected to near greenschist-facies metamorphism therefore; there are fewer phyllosilicates along the foliation, forming planes of weaknesses that can be subsequently exploited by brittle deformation.

NE-SW and N-S trending fractures within the CSZ belong to the Stoer Group age fracture set. There are as many of this group of fractures in the CSZ as there are 'Late Laxfordian' faults which suggest that these Stoer Group age fractures are also preferentially developed in this shear zone. Observational evidence shows that these fractures get 'pinned' by foliation planes and therefore have restricted lengths. This means that in order for this fracture set to be able to accommodate the same amount of strain within the CSZ as out with it, then, more of these shorter fractures have to develop (this hypothesis is discussed in more detail in *Section 3.3.7*). Outside the CSZ many of these Stoer Group age fractures have been recorded, although they form longer structures and are normally less densely populated presumably because they are not restricted by foliation planes.

In the Rhiconich Terrane NW-SE and NE-SW fractures are the predominant trends (*Figure 3.26*). Most Rhiconich Terrane outcrops exhibit likely Torridon Group age fractures which exhibit typical iron-staining and in most places trend NE-SW or N-S. Other N-S trending faults that have been identified on the north coast of the Rhiconich Terrane have been interpreted as Mesozoic in age (Wilson et al., 2010). 'Late Laxfordian'



faults are not evident in the Rhiconich Terrane, except at Laxford Bridge where there are a few NW-SE trending faults (*Figure 3.26*) with sinistral strike-slip kinematics.

At Kinlochbervie, the dominant NE-SW trending fractures (*Figure 3.26*) are likely antithetic structures to the major NW-SE trending Loch Inchard fault that lies adjacent to this outcrop (Kinlochbervie lies in the hanging wall of this fault). The majority of the NW-SE trending faults are hematite-stained and therefore are likely to have formed during a time when fluid was percolating through the overlying Torridon Group sediments which are the source of the iron minerals (i.e. these fractures and the main Loch Inchard fault are potentially Torridon Group age). There is evidence that these fractures have been active more than once with at least two sets of slickenlines evident (*Figure 3.28*).



**Figure 3.28:** Photograph of a fracture surface from Kinlochbervie (NC 2296 5621) showing two sets of slickenlines representing different fracture kinematics. The black arrows represent the oldest movement with oblique fault kinematics. The purple arrows represent the youngest movement with more normal slip kinematics.

At Traigh Allt Chailgeag (TAC) a few fractures coincide with the orientation of the strong, steeply-dipping NW-SE foliation which represents the Rispond Shear Zone (RSZ) (*Figure 3.26*). Unlike the CSZ, the RSZ does not exhibit evidence of greenschist-facies metamorphism (it is amphibolite-facies metamorphism) and therefore there are less phyllosilicates (only biotite is present). This means that the foliation planes in the RSZ are more annealed and less prone to being reactivated by subsequent brittle

deformation events. C and K values quantify this observation as there is no correlation between the foliation and fracture values here (*Figure 3.27*). Throughout the rest of the Rhiconich Terrane very few fractures reactivate foliation and the majority cross-cut it entirely.

### 3.3.5 – Spacing analysis of fracture data from Lewisian outcrop

A study of the fracture spatial attributes has been conducted in the mainland LGC, across both Assynt and Rhiconich Terrane outcrops. Spacing data was collected using 1-dimensional line samples taken across key outcrops in the mainland LGC. Where possible, these 1-dimensional line samples were taken perpendicular and parallel to foliation in order to assess the relationship between fractures and foliation in terms of spatial attributes (see *Appendix B* for full fracture spacing tables). This technique was especially useful in the Canisp Shear Zone (CSZ) where taking sample lines parallel and perpendicular to the foliation samples 'Late Laxfordian' faults and Stoer Group age fractures independently. Although, this sampling technique allows independent analysis of individual fracture sets, it does bias the fracture spacing distributions because only a select part of the fracture network is sampled, thus the true fracture spacing distribution is underestimated (Pickering et al., 1995).

Line sample lengths vary between 3 and 70 metres and all samples contain at least 30 data points (the most statistically significant line samples have over 50 data points; the nature of some outcrops sometimes makes it difficult to collect larger samples on one sample line).

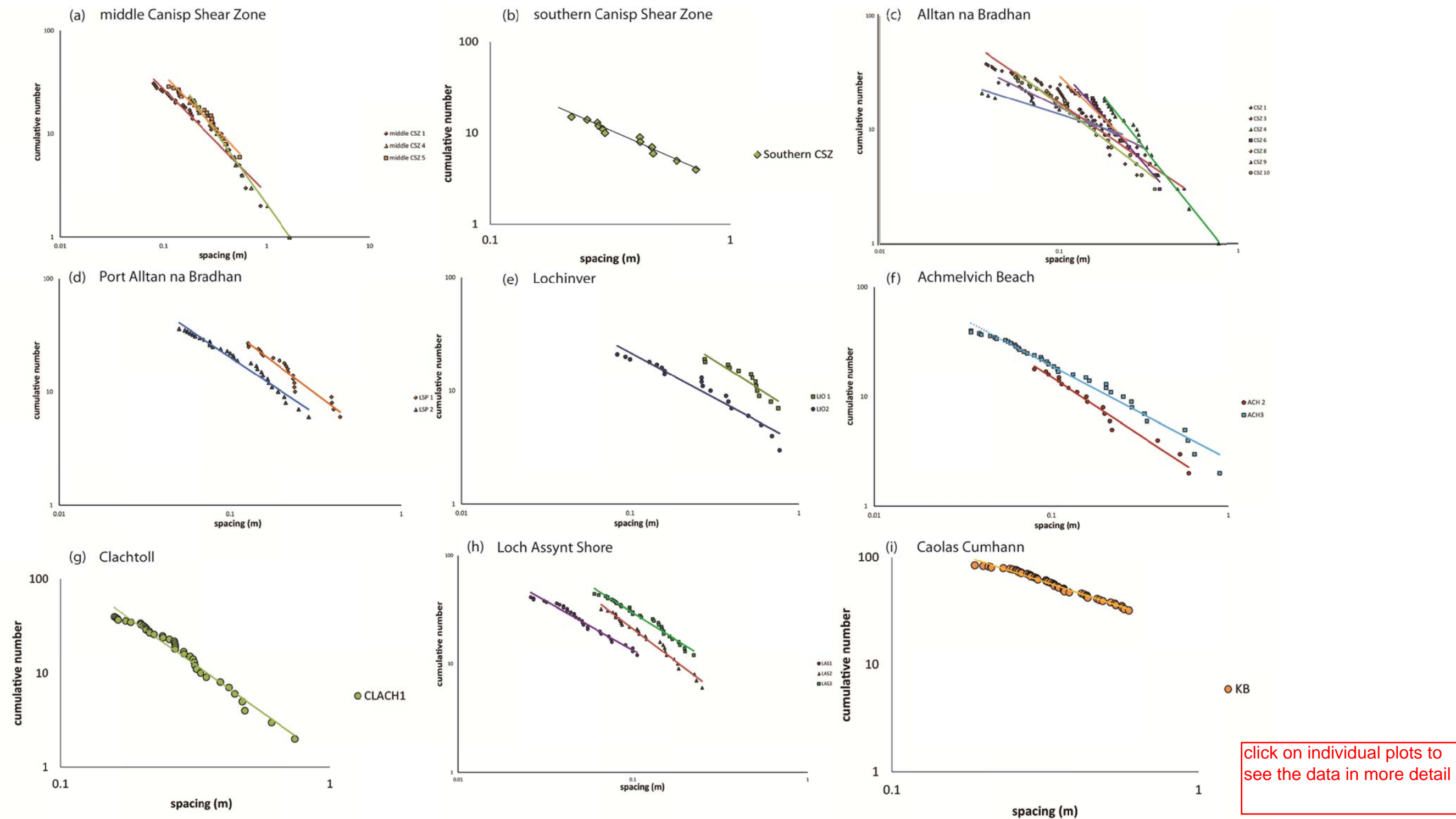
The spacing data from these sample lines has been used to analyse spacing population distributions, the coefficient of variation (CV) and fracture density and how these vary between outcrops and structural settings. Although many outcrops across the mainland LGC have been analysed using 1-dimensional line samples, only the same key outcrops used for the fracture orientation analysis have been included in the main body of this thesis (see *Appendix B* for tables and graphs for all outcrops sampled during this study). A fracture connectivity study has also been carried out using photo-mosaics collected from key outcrops in the mainland LGC and is presented in *Section 3.3.5.6*.

### 3.3.5.1 – Fracture spatial distributions

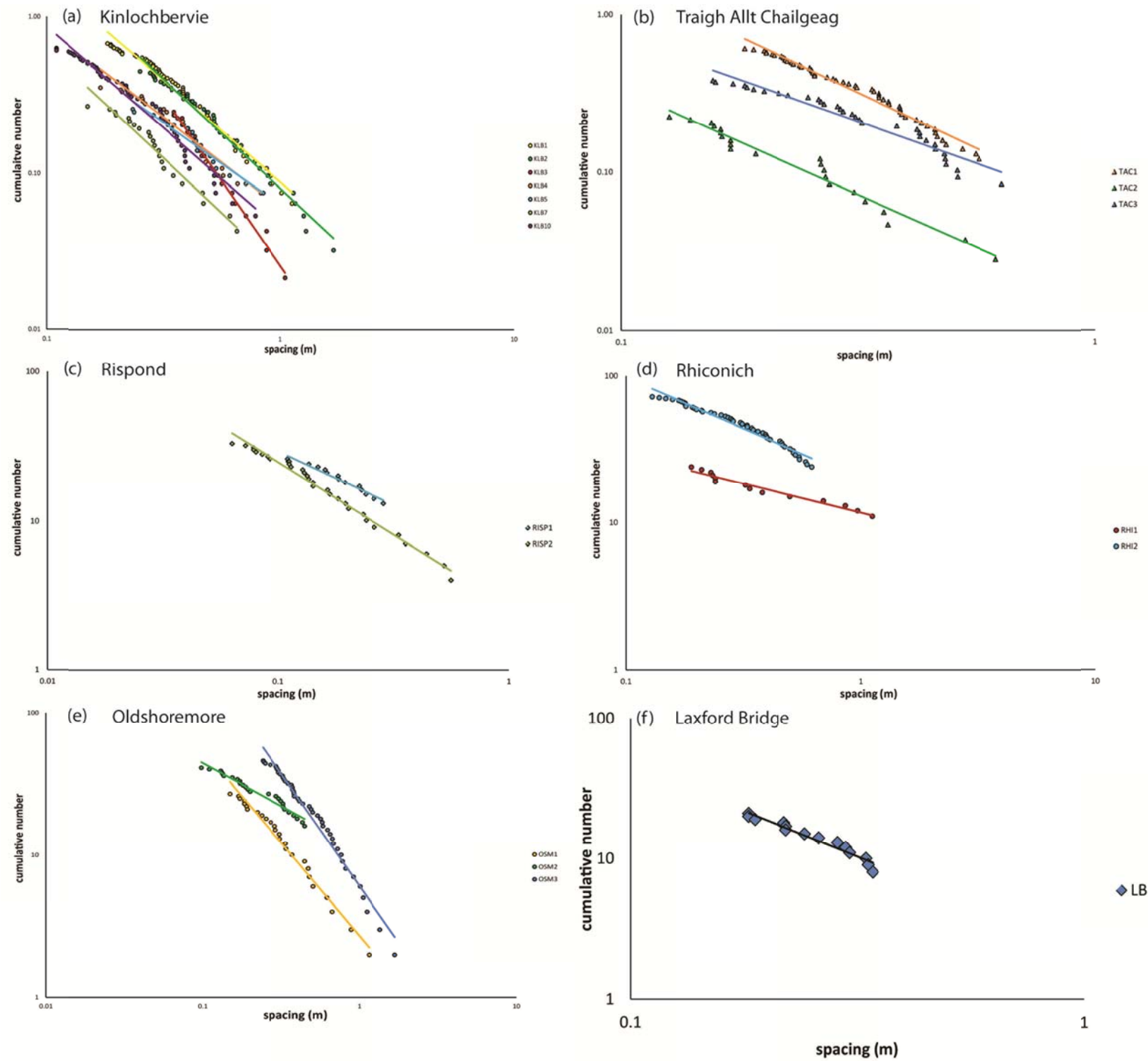
1-dimensional line samples from LGC outcrops in both the Assynt and Rhiconich Terranes consistently display power-law distributions for fracture spacing when displayed on population distribution plots (*Figures 3.29 & 3.30*). Generally, the straight line section of each dataset (on a log-log plot) fits a power-law trend line well, with  $R^2$  values between 0.86 and 0.99 (*Tables 3.5 & 3.6*). In the Assynt Terrane, the majority of these power-law relationships extend over no more than one order of magnitude with spacing values between 1 and 0.1 metres (*Figure 3.29*). Most sample lines in the Assynt Terrane do not extend more than 10 metres. Within the Rhiconich Terrane, population distribution plots show similar power-law relationships with spacing values centred between 1 and 0.1 metres.

Some samples, especially in the Canisp Shear Zone (CSZ), are differentiated by their orientation with respect to foliation (parallel, perpendicular or oblique to foliation). Fracture spacing values calculated from sample lines parallel to foliation represent Stoer Group age fractures (most commonly trend NE-SW at  $\sim 90^\circ$  to the NW-SE trending foliation) and fracture spacing values calculated from sample lines perpendicular to foliation mainly represent 'Late Laxfordian' faults (foliation parallel structures). Spacing relationships for all of the different line samples show power-law relationships with little evidence of large variations in the spacing relationships between the different (orientation, age) fracture sets (*Figure 3.29a-e*). This is also true in the Rhiconich Terrane in the Rispond Shear Zone (*Figure 3.30b & c*) where there are no large variations between the fracture spacing distributions from sample lines that are either parallel or perpendicular to foliation.





**Figure 3.29:** Population distribution plots of 1-dimensional lines samples from LGC outcrops in the Assynt Terrane. Diamond data points represent sample lines taken parallel to foliation. Triangle data points represent sample lines taken perpendicular to foliation. Circle data points represent sample lines taken in no specific direction. **(a)** Sample lines from the middle Canisp Shear Zone (mCSZ). **(b)** Sample lines from the southern edge of the Canisp Shear Zone (sCSZ). **(c)** Sample lines from Alltan na Bradhan (CSZ). **(d)** Sample lines from Port Alltan na Bradhan (LSP). **(e)** Sample lines from Lochinver (LIO). **(f)** Sample lines from Achmelvich Beach (ACH). **(g)** Sample lines from Clachtoll (CLACH). **(h)** Sample lines from Loch Assynt Shore (LAS). **(i)** Sample lines from Caolas Cumhann (KB).



**Figure 3.30:** Population distribution plots from 1-dimensional line samples from LGC outcrops in the Rhiconich Terrane. Diamond data points represent line samples taken parallel to foliation. Triangle data points represent line samples taken perpendicular to foliation. Circle data points represent line samples taken at no particular orientation. **(a)** Sample lines from Kinlochbervie (KLB). **(b)** Sample lines from Traigh Allt Chailgeag (TAC). **(c)** Sample lines from Rispond (RISP). **(d)** Sample lines from Rhiconich (RHI). **(e)** Sample lines from Oldshoremore (OSM). **(f)** Sample lines from Laxford Bridge (LB).

Outcrop	Sample Orientation	N	Distribution	R <sup>2</sup>	D-value	CV	Clustering	Fracture Density/ fractures per metre
middle CSZ 1	perpendicular to foliation	37	power-law	0.95	1.01	0.99	anti-clustered	3.79
middle CSZ 4	parallel to foliation	24	power-law	0.98	1.41	0.98	anti-clustered	2.76
middle CSZ 5	parallel to foliation	40	power-law	0.95	1.03	0.89	anti-clustered	3.88
southern CSZ (sCSZ)		19	power-law	0.97	1.12	0.65	anti-clustered	2.46
Alltan na Bradhan 1 (CSZ1)	parallel to foliation	49	power-law	0.97	0.76	0.81	anti-clustered	6.24
Alltan na Bradhan 3 (CSZ3)	parallel to foliation	23	power-law	0.93	1.07	1.05	clustered	7.54
Alltan na Bradhan 4 (CSZ4)	perpendicular to foliation	31	power-law	0.99	1.20	0.78	anti-clustered	4.62
Alltan na Bradhan 6 (CSZ6)	parallel to foliation	43	power-law	0.98	1.79	0.8	anti-clustered	7.27
Alltan na Bradhan 8 (CSZ8)	parallel to foliation	39	power-law	0.95	1.59	0.67	anti-clustered	6.86
Alltan na Bradhan 9 (CSZ9)	perpendicular to foliation	27	power-law	0.91	0.50	1.20	clustered	6.27
Alltan na Bradhan 10 (CSZ10)		35	power-law	0.98	1.20	1.23	clustered	7.26
Port Alltan na Bradhan 1 (LSP1)	parallel to foliation	38	power-law	0.94	1.14	1.17	clustered	4.34
Port Alltan na Bradhan 2 (LSP2)	perpendicular to foliation	42	power-law	0.97	1.01	0.95	anti-clustered	7.01
Lochinver 1 (LIO1)		23	power-law	0.86	0.95	1.04	clustered	1.73
Lochinver 2 (LIO2)		27	power-law	0.93	0.80	1.12	clustered	3.15
Achmelvich 2 (ACH2)		25	power-law	0.97	1.06	1.08	clustered	5.34
Achmelvich 3 (ACH3)		44	power-law	0.98	0.85	1.27	clustered	5.47
Clachtoll 1 (CLACH1)		65	power-law	0.97	1.93	1.03	clustered	4.55
Loch Assynt Shore 1 (LAS1)		50	power-law	0.97	0.90	0.96	anti-clustered	15.02
Loch Assynt Shore 2 (LAS2)		42	power-law	0.98	1.22	0.89	anti-clustered	7.88
Loch Assynt Shore 3 (LAS3)		53	power-law	0.97	1.00	1.04	clustered	6.74
Caolas Cumhann (KB)		113	power-law	0.98	0.92	1.01	clustered	2.33

**Table 3.5:** Spacing attributes measured and calculated from all 1-dimensional line samples taken from LGC outcrop in the Assynt Terrane.

Outcrop	Sample Orientation	N	Distribution	R <sup>2</sup>	D-value	CV	Clustering	Fracture Density/ fractures per metre
Kinlochbervie 1 (KLB1)		94	power-law	0.98	1.30	1.08	clustered	2.81
Kinlochbervie 2 (KLB2)		61	power-law	0.98	1.39	1.16	clustered	2.04
Kinlochbervie 3 (KLB3)		37	power-law	0.99	2.17	0.78	clustered	2.43
Kinlochbervie 4 (KLB4)		40	power-law	0.94	1.16	0.89	clustered	2.26
Kinlochbervie 5 (KLB5)		32	power-law	0.94	1.05	1.11	clustered	2.14
Kinlochbervie 7 (KLB7)		36	power-law	0.96	1.40	1.16	clustered	3.62
Kinlochbervie 10 (KLB10)		81	power-law	0.96	1.31	1.09	clustered	4.06
Traigh Allt Chailgeag 1 (TAC1)	perpendicular to foliation	107	power-law	0.98	1.42	1.05	clustered	3.57
Traigh Allt Chailgeag 2 (TAC2)	parallel to foliation	34	power-law	0.96	1.34	1.10	clustered	4.27
Traigh Allt Chailgeag 3 (TAC3)	perpendicular to foliation	57	power-law	0.93	1.06	1.22	clustered	2.92
Rhiconich 1 (RHI1)		28	power-law	0.96	0.40	0.92	clustered	1.17
Rhiconich 2 (RHI2)		77	power-law	0.97	0.69	1.04	clustered	1.96
Rispond 1 (RISP1)	parallel to foliation	34	power-law	0.96	0.72	1.14	clustered	3.97
Rispond 2 (RISP2)	parallel to foliation	40	power-law	0.99	0.97	0.93	clustered	5.15
Oldshoremore 1 (OSM1)		53	power-law	0.98	1.31	1.08	clustered	4.09
Oldshoremore 2 (OSM2)		51	power-law	0.96	0.60	1.17	clustered	2.62
Oldshoremore 3 (OSM3)		83	power-law	0.98	1.58	1.08	random	2.77
Laxford Bridge	perpendicular to foliation	31	power-law	0.95	1.81	1.06	clustered	3.92

**Table 3.6:** Spacing attributes measured and calculated from all 1-dimensional line samples taken from LGC outcrop in the Rhiconich Terrane.

### 3.3.5.2 – D-value

D-values (slope of the power-law distribution) in the Assynt Terrane vary from 0.50 to 1.99 (*Table 3.5*). Generally, samples from the CSZ have higher D-values (commonly >1) than samples from outcrops in the main body of the Assynt Terrane (*Table 3.5*).

In the Rhiconich Terrane D-values vary between 0.40 and 2.16 across all the sample lines (*Table 3.6*). Outcrops that have fracture sets that are parallel to pre-existing foliations or adjacent to major faults typically have D-values that are higher than D-values from outcrops in the main body of the Rhiconich Terrane (*Table 3.6*).

Outcrops within the Rispond Shear Zone show variations in their D-values depending on the orientation of the foliation. The samples from Traigh Allt Chailgeag, where the foliation is steeply inclined, have D-values that vary between 1.06 and 1.421 (*Table 3.6*). This is compared to the samples from Rispond, where the foliation is shallowly inclined and D-values vary between 0.72 and 0.97 (*Table 3.6*).

### 3.3.5.3 – CV

The coefficient of variation (CV) has been calculated for all 1-dimensional line samples taken across the mainland LGC. In the Assynt Terrane, CV values range between 0.67 and 1.27 (*Table 3.5*), with ~50% of sample lines having CV values >1 and an average CV value of 0.98. CV values from samples in the Rhiconich Terrane range between 0.78 and 1.22 (*Table 3.6*), with ~71% of samples having CV values >1. The average CV value in the Rhiconich Terrane is 1.12 (*Table 3.6*).

### 3.3.5.4 – Fracture density

Fracture density values have been calculated for samples in both the Assynt and Rhiconich Terranes. In the Assynt Terrane fracture density values vary between 1.73 and 15.02 fractures per metre (*Table 3.5*). Samples from the CSZ, especially from Alltan na Bradhan, have high fracture density values with average values of ~6 fractures per metre. Line samples from Loch Assynt Shore, close to the Loch Assynt Fault, have the highest fracture density values from the Assynt Terrane samples.

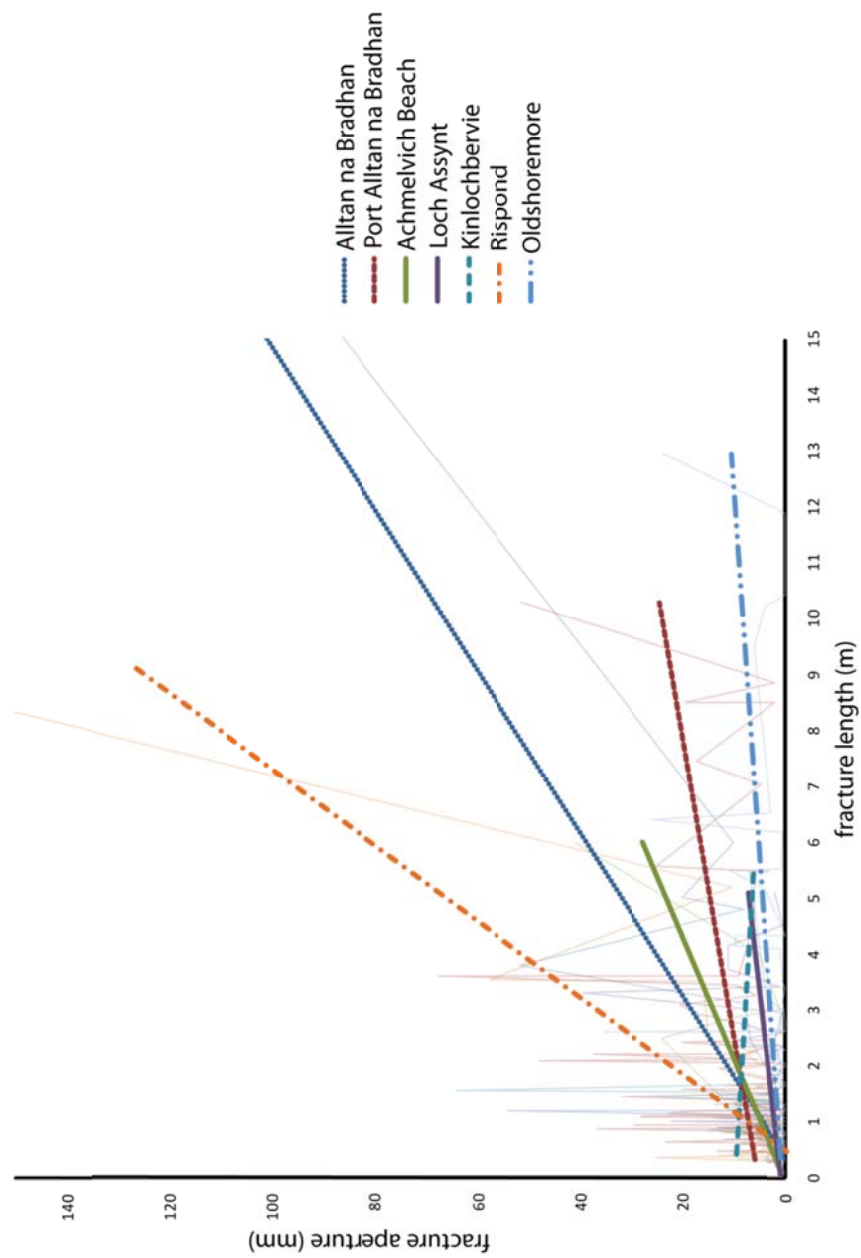
In the Rhiconich Terrane fracture density values range from 1.17 to 5.15 fractures per metre (*Table 3.6*). Generally, samples from outcrops that include pre-

existing foliation or faults (for example, Rispond and Traigh Allt Chailgeag) have higher fracture density values than outcrops in the main body of the Rhiconich Terrane.

#### 3.3.5.5 – Fracture aperture versus length analysis

Another analysis that has been conducted to gain more insight into the fracture network characteristics within the mainland LGC involves comparing fracture length versus fracture aperture. Representative line samples from key outcrops within the mainland LGC have been used for this study, with the results shown in *Figure 3.30*. One complication to this outcrop analysis is that the fracture aperture sizes are estimates of their true widths because weathering and erosion make it near impossible to measure exact fracture apertures (especially because the majority of line outcrops used in this study are coastal sections where erosion rates are high).

The plot in *Figure 3.31* shows that for most outcrops in the mainland LGC there is a relatively weak positive correlation between length and aperture so that as fracture length increase so does the width of the fracture aperture. Kinlochbervie is the only outcrop where fracture aperture decreases, albeit slightly, with increasing fracture length. Generally, line samples that are from outcrops within shear zones (for example, Alltan na Bradhan and Rispond) exhibit trend lines that suggest that small increases in fracture length result in larger increases in fracture aperture. This is compared to outcrops from the main body of the mainland LGC where the trend line is much shallower and larger increases in fracture length are needed to increase the fracture aperture width. No significant difference in the length versus aperture correlation is recorded between the Assynt Terrane and Rhiconich Terrane sample lines.



**Figure 3.31:** Plot showing aperture versus length for fractures sampled from the mainland LGC. Data shown on this graph is from representative outcrops from key locations from both the Assynt and Rhiconich Terrane.

### 3.3.5.6 – Fracture Connectivity

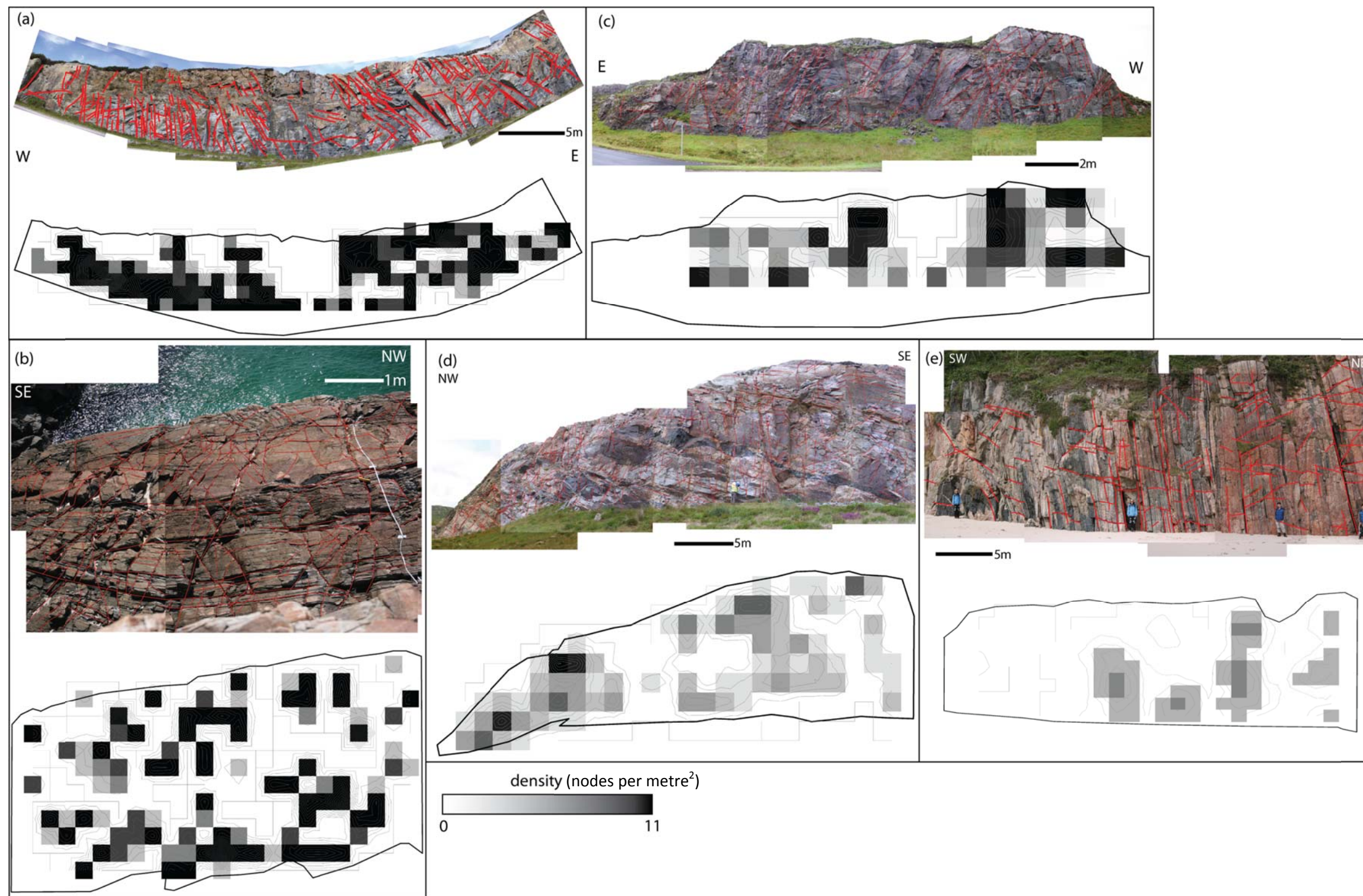
In order to assess basic 2-dimensional fracture connectivity within key outcrops in the mainland LGC, photo-mosaics have been used to interpret fracture sets. This study has been completed by first, stitching outcrop photographs together, in Adobe® Illustrator, to make photo-mosaics. Then all visible fractures have been interpreted and the resulting images saved as .tif files. These images were then imported into ArcGIS® 9.2 and the nodes (the points where fractures connect each other) were mapped. Using ArcGIS®, density maps for the fracture nodes have then been created to represent 2-dimensional fracture connectivity across different structural settings in the mainland LGC. The outcrops used in this study are Caolas Cumhann (representative of background fracturing in the Assynt Terrane, *Figure 3.32a*), Port Alltan na Bradhan (representative of fracturing in the Canisp Shear Zone, *Figure 3.32b*), Kinlochbervie (representative of fracturing influenced by a major fault, *Figure 3.32c*), Rhiconich (representative of background fracturing in the Rhiconich Terrane, *Figure 3.32d*) and Traigh Allt Chailgeag (representative of fracturing in the Rispond Shear Zone, *Figure 3.32e*).

The connectivity analysis shows that fracture networks within the Assynt Terrane are more connected than those in the Rhiconich Terrane with many more nodes present within each outcrop (*Figure 3.32a & b*). Caolas Cumhann shows the highest level of connectivity with the majority of the outcrop showing a high density of fracture nodes (*Figure 3.32a*). Within the Canisp Shear Zone (Port Alltan na Bradhan, *Figure 3.32b*) there is evidence of a high density of fracture nodes, but these appear to be confined to small zones, rather than being dispersed across the whole outcrop.

In the Rhiconich Terrane, only Kinlochbervie which is influenced by a major NW-SE fault, shows areas of high fracture connectivity (*Figure 3.32c*). Both the Rhiconich (*Figure 3.32d*) and Traigh Allt Chailgeag (*Figure 3.32e*) outcrops show low connectivity densities, with the little connectivity that there is being localised to small zones within the outcrops.

It is important to note that this study only uses points (nodes) on a 2-dimensional horizontal map or vertical section so the connectivity densities shown in *Figure 3.32*, are either vertical or horizontal, respectively.





**Figure 3.32:** 2-dimensional photo-mosaics that their fracture interpretation overlain. The nodes connecting fractures have then been interpreted and node density maps for each photo-mosaic have also presented. The density scale is the same for each node density map. **(a)** Caolas Cumhann **(b)** Port Alltan na Bradhan **(c)** Kinlochbervie **(d)** Rhiconich **(e)** Traigh Allt Chailgeag.

### 3.3.5.7 – Discussion of the Lewisian outcrop fracture spacing datasets

Spacing analysis of fractures networks across the mainland LGC has provided valuable quantitative data on the spatial characteristics of all three regional fault and fracture sets that have been identified to be present within the Lewisian. Consistently, power-law relationships are interpreted for outcrops across the mainland LGC (*Figures 3.29 & 3.30*). These consistent power-law relationships for 1-dimensional samples, in both the Assynt and Rhiconich Terranes, are an indication of scale-invariance. Therefore the fracture spacing relationships collected at outcrop scale can potentially be used as an estimation of the spacing attributes of fractures at different scales across the mainland LGC. It should be noted that although scale-invariance is indicated, none of the power-law relationships extend over more than one order of magnitude (normally between 0.1 and 1 metres) and therefore it is difficult to assess how significant these power-law relationships for spacing are, over a wider range of scales.

In the Assynt Terrane, 'Late Laxfordian' faults and Stoer Group age fractures show little variation in their power-law spacing distributions (Canisp Shear Zone outcrops *Figure 3.29a to e*), with D-values that are most commonly indicative of power-law relationships that have a higher number of fractures that are closely spaced; compared to fractures with large spaces between them (D-values >1, *Table 3.5*). This relationship is also true in the Rhiconich Terrane where foliation parallel faults and those that cross-cut the foliation, have similar power-law distribution attributes.

In the Rispond Shear Zone (RSZ) the main variations in the fracture spacing attributes occur between outcrops Traigh Allt Chailgeag (TAC) and Rispond. At TAC power-law D-values are >1 (*Table 3.6*) indicating that the power-law relationships have a higher ratio of closely spaced fractures. This is compared to the samples from Rispond where D-values are <1 (*Table 3.6*), indicating that the power-law relationships include more fractures that have wide spaces between them. The variation in the power-law relationships within the RSZ is likely due to the change in foliation orientation between TAC and Rispond. At TAC the foliation is steeply dipping which is intermittently reactivated by fractures and also cross-cut by many less steeply-dipping fractures, which results in closely spaced fractures within the line samples. The shallowly-dipping foliation at Rispond is less frequently reactivated and so the sample lines mainly intersect those fractures that cross-cut the foliation. This results in power-law

relationships which are represented by fractures that are more widely spaced (and therefore D-values that are  $<1$ ).

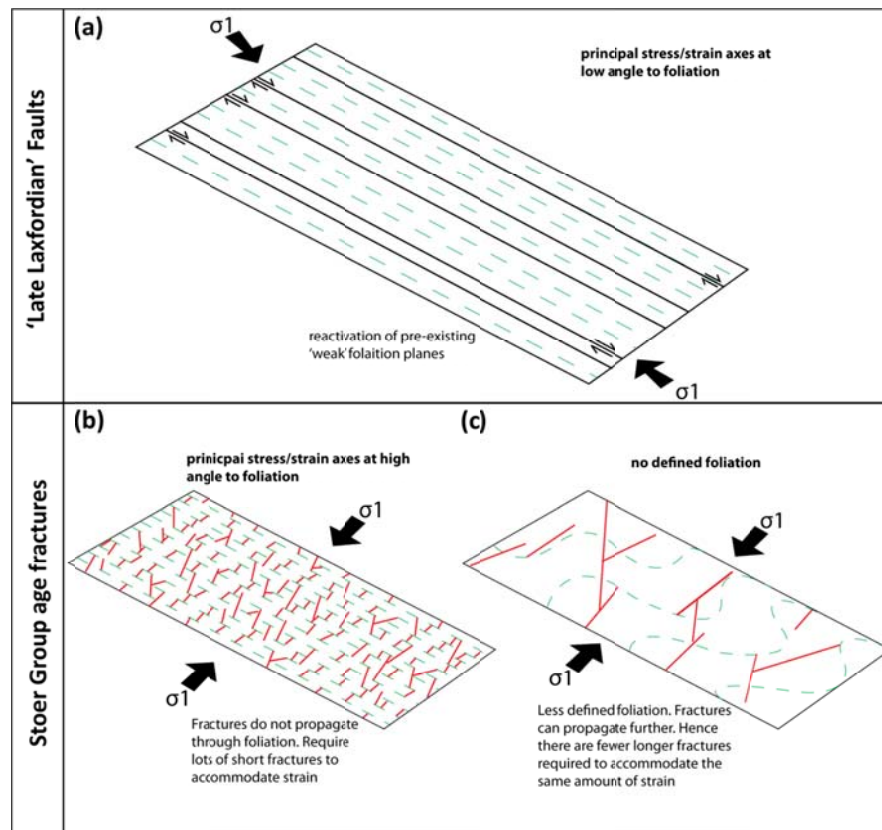
Coefficient of variation (CV) values across the mainland LGC are varied, although the majority (59%) of line samples have CV values that indicate that their fractures are clustered (CV values  $>1$  (Johnston et al., 1994)). In the Assynt Terrane, many of the line samples from the coastal section of the CSZ have CV values that suggest the fractures are anti-clustered. This is compared to the samples from elsewhere in the Assynt Terrane where the majority of CV values are  $>1$  (78%) and indicate clustered fracture sets (*Table 3.5*). The low CV values within the coastal CSZ line samples are likely a result of the length of the outcrop sample lines. Most line samples here are  $<10$  metres in length (due to the shape of the outcrops) which means that they only sample a small selection of fractures within the larger fracture networks and rarely cross any larger structures within the outcrops, thus limiting the amount of variation in fracture spacing relationships (and the number of data points) that each sample line intersects, therefore reducing the imprint of clustering in the statistical values.

CV values from line samples within the Rhiconich Terrane are most commonly  $>1$  suggesting that most of the fractures within these 1-dimensional samples are clustered (*Table 3.6*). These clustered fracture spacing relationships are in accordance with the power-law distributions consistently interpreted across the Rhiconich Terrane (and the Assynt Terrane). The minority of anti-clustered fracture spacing relationships (CV  $<1$ ) present within the Rhiconich Terrane are again attributed to 1-dimensional samples that are short ( $<10$ m) and as a result contain a reduced number of data points that do not adequately represent the fracture network.

Fracture density values in the Assynt Terrane are typically higher within the CSZ, where there is an average value of 6 fractures per metre. These high fracture density values in the CSZ are due to the presence of intense, steeply-dipping foliation. *Figure 3.33* illustrates a geometrical explanation for the higher fracture density values in the CSZ.

Stress/ strain axes during the development of the 'Late Laxfordian' fault sets were oriented preferentially for the reactivation of pre-existing 'weak' (lots of phyllosilicates, particularly biotite and muscovite) NW-SE trending foliation planes within the CSZ, resulting in relatively closely spaced NW-SE trending faults (*Figure 3.33a*). The presence of abundant phyllosilicates along the intense foliation planes also

means that the CSZ is volumetrically weak. During the development of Stoer Group age fractures, the principal stress/strain axes were approximately parallel to the CSZ foliation. As these fractures developed they did not propagate easily through the foliation planes (they are perpendicular to the long axis of the phyllosilicates) and therefore the fractures remain short. In order to accommodate approximately the same amount of strain, during this deformation event, many more short fractures have to form within the CSZ compared to outcrops outside the CSZ (where there is no defined foliation trend) where longer fractures can develop (*Figure 3.33b & c*). The development of foliation perpendicular Stoer Group age fractures is also likely enhanced within the CSZ because this region is volumetrically weak. This relationship between the foliation, stress/strain axes and fracture development results in higher fracture density values within the CSZ compared to most other outcrops within the Assynt Terrane.



**Figure 3.33:** Schematic diagrams representing (a) fault development when principal stress/strain axes are at a low angle to foliation (b) fracture development when principal stress/strain axes are at a high angle to foliation (c) fracture development when there is no well-developed foliation.

The fracture density values at Loch Assynt Shore are the highest from all the outcrops within the Assynt Terrane. These outcrops are in close proximity to the unconformity between the LGC and the Torridonian sandstones and also to the large Loch Assynt Fault. There is evidence that the top of the LGC has been subjected to some degree of weathering before the deposition of the Torridonian which may have resulted in some weakness within the LGC at this location. It is more likely, however, that the high fault density recorded from these outcrop samples are related to the development and subsequent reactivation of the Loch Assynt Fault during the Proterozoic and Palaeozoic (Krabbendam and Leslie, 2010).

In the Rhiconich Terrane, fracture density values are generally lower than those seen within the Assynt Terrane (*Table 3.6*). Samples from within the RSZ show the highest fracture density values (*Table 3.6*), although they are lower than the fracture density values seen within the CSZ. The RSZ exhibits less evidence of reactivated foliation, with the majority of recorded fractures completely cross-cutting and offsetting the foliation. This lack of foliation parallel fractures is likely due to the near absence of phyllosilicates along the foliation planes meaning that the foliation was annealed and strong and therefore does not reactivate easily.

Fracture length versus fracture aperture analysis suggests that fractures within shear zones show the biggest increases in aperture with the smallest increases in fracture length (*Figure 3.31*). This result parallels previous observations that fractures within shear zones (particularly the CSZ) are shorter than those outside shear zones and therefore there are more of them to accommodate the same amount of strain (*Figure 3.33*). Outside shear zones, fractures are able to extend further and therefore they are able to increase their length substantially (they are not pinned by foliation planes, *Figure 3.33*) while only incurring small increases to their apertures.

2-dimensional connectivity analysis of fracture networks using photo-mosaics within the mainland LGC has suggested that outcrops within the Assynt Terrane have more fracture connectivity (*Figure 3.32a & b*). The main difference between outcrops in the Assynt Terrane and the Rhiconich Terrane is that in the Assynt Terrane the majority of outcrops exhibit at least two different pervasive fracture orientations compared to the Rhiconich terrane where most outcrops have still have more than one prominent fracture trend but one fracture trend is more pervasive than the other. The starkest difference between the Assynt and Rhiconich Terrane is in their respective shear zones.



The CSZ (Assynt Terrane) exhibits zones of high fracture connectivity, where ‘Late Laxfordian’ faults and Stoer Group age fractures intersect (*Figure 3.32b*), compared to the RSZ (Rhiconich Terrane) where there is one dominant fracture set and therefore the fracture connectivity is much lower (*Figure 3.32e*).

As a small side project, further fracture spatial analyses have been performed on several thin section samples by Miss Rowan Vernon. The results from these analyses are given in *Appendix B*. Unfortunately the thin section fracture datasets proved too small (not enough fractures on each thin section slide) to be able to use the data in a meaningful way to enhance the onshore mainland LGC fracture characterisation presented in this chapter.

#### 3.3.5.8 – Comparison to previous fieldwork fracture studies in the mainland LGC

Previous work that also focuses on the fracture networks within the mainland LGC has concentrated mainly on compositional and fabric heterogeneities to explain variations in fracture spatial attributes and to elucidate on the likeliness of these fractures forming due to reactivation (Beacom, 1999, Beacom et al., 2001). As this previous analysis focussed on the affect of lithology on the fracture spatial characteristics; this study (which uses similar mainland LGC outcrops) deliberately does not dwell on lithology and instead focuses on fracture orientation and spatial attributes between different mainland LGC terranes and different structural settings.

Beacom et al. (2001) present C and K eigenvector analyses of fracture orientation distributions within the Gailoch Shear Zone of the Gruinard Terrane (*Figure 2.4*) and within the Canisp Shear Zone (CSZ) of the Assynt Terrane (Beacom et al., 2001, *Figure 6*). Similar orientation analyses are presented in this thesis for outcrop examples within the Assynt and Rhiconich Terranes (*Table 3.4* and *Figure 3.27*). Both studies show that there is a positive correlation between foliation and later NW-SE trending faults within the CSZ, which confirms that these structures are geometrically coincident and provides evidence that the later faults have reactivated the foliation. Work presented in this thesis develops this analysis further by comparing highly foliated rocks in the CSZ (Assynt Terrane) with highly foliated rocks in the Rispond Shear Zone (Rhiconich Terrane). Fault and foliation C and K values from within the Rispond Shear Zone are dissimilar to each other suggesting they have limited geometric relationships. It is therefore suggested that the prevailing upper greenschist-facies metamorphism (and

the resulting abundance of phyllosilicates minerals) that is present within the CSZ, but absent from the RSZ, is at least partially responsible for the reactivation of foliation planes within the CSZ (*Section 3.3.4.1*).

Fracture spatial characteristic analyses conducted in Beacom et al. (2001) suggest that mainland LGC lithology has a control on fracture spatial characteristics (Beacom et al., 2001, Figure 8) within the Gairloch and Canisp Shear Zones. These results are considered within this thesis as a comparison with the Clair basement datasets (*Chapter 4*) and similar analysis is used (*Chapter 6*) to assess the variations in fracture spatial characteristics due to changing structural setting or dataset scale.

Beacom et al. (2001, Figure 9) also show that areas with high C values (strength of the orientation distribution) are also highly clustered (CV) suggesting that localities with stronger preferred orientations (more planar foliations) also have more strongly clustered faults. Although the data presented in Figure 9 of Beacom et al (2001) show a positive correlation to support this hypothesis, the plot only contains 5 data points and therefore this analysis is considered with caution.

Beacom et al (2001) suggest that further work is required across a variety of tectonic settings to fully characterise the relationships between spatial distributions, geometry and scaling attributes to assess the importance of pre-existing heterogeneities influencing the architecture of the resulting fracture networks. Fracture network characterisation of the mainland LGC presented within this thesis aimed to develop upon the work of Beacom et al (2001) by sampling fractures within a variety of structural settings across the mainland LGC; with the primary aim of comparing and contrasting the results with the available Clair basement fracture datasets. Outcrop fracture characterisations shown in this Chapter are supplemented with terrestrial laser scan outcrop modelling in *Chapter 5*. The results of these onshore analyses are compared and contrasted to the Clair basement fracture datasets and are presented in *Chapter 6*; where conclusions about the affect changing structural setting has on the fracture network characteristics are also proposed.

### 3.4 – Fault and fractures in the mainland Lewisian: Regional to outcrop scale synthesis

Both the regional lineament analysis (*Section 3.2*) and outcrop line sample analysis (*Section 3.3*) provides important insights into the understanding of the fracture networks within the mainland LGC. This section aims to compare and contrast the datasets with particular focus on how the fracture attributes can be transferred across scales.

Fracture orientation analysis of NEXTMap® digital elevation models and outcrop line samples shows that there are two predominant fault and fracture trends of NE-SW and NW-SE across the whole of the mainland LGC (*Section 3.2.2, Figure 3.6*). Regionally, NW-SE trending faults form the longest lineaments seen across the mainland LGC (*Figure 3.9*). The majority of these NW-SE lineaments in the Assynt Terrane are known from outcrop analysis to be ‘Late Laxfordian’ faults formed during sinistral strike-slip deformation with preferential development seen in the Canisp Shear Zone. In the Rhiconich Terrane NW-SE (NNW-SSE) trending lineaments are also present across the regional dataset although from outcrop analysis it is likely that these faults have a younger origin (Torridon Group age deformation and younger (most probably Caledonian or Mesozoic reactivations) than lineaments of equivalent orientation in the Assynt Terrane.

NE-SW trending lineaments are present across the regional dataset where they occur in large numbers in both the Assynt and Rhiconich Terranes (*Figures 3.7 & 3.8*) and commonly form the shortest lineaments seen within the regional dataset (*Figure 3.9*). At outcrop, these lineaments can be attributed to NE-SW trending fractures formed during at least two events: regional dextral transtension during the deposition of Stoer Group sediments on top of the mainland LGC and to ‘Later’ (potentially Mesozoic) faulting resulting faults that cross-cut and offset all other structures present in the mainland LGC.

N-S and E-W lineaments form the least prominent sets interpreted from the regional datasets (*Figure 3.7 & 3.8*), but they are observed in both the Assynt and the Rhiconich Terranes. At outcrop, only N-S trending fractures are sampled in significant numbers (*Figure 3.25 & 3.24*) and these are known to have the same Stoer Group age origin as the majority of the NE-SW sampled across the mainland LGC. Although E-W trending fractures or faults are not readily identified from the outcrops used in this



study, it does not mean that they are not present at outcrop scale. It is possible that E-W trending fractures or faults are more obvious further inland, where less outcrop sampling took place. In this respect it is worth noting that in the regional study, the majority of E-W lineaments have been interpreted as lying away from coastal regions (*Figures 3.7 & 3.8*).

Spacing analysis has been conducted using 1-dimensional line sampling with the resulting population distribution plots showing variation in spatial attributes between the regional and outcrop datasets (*Figures 3.10, 3.11, 3.29 & 3.30*). From the regional lineament analysis, spacing distributions vary between power-law and exponential (for both the high and low resolution datasets), with line samples from the Rhiconich Terrane and the Canisp Shear Zone having the most statistically significant power-law relationships (although the number of data points in each sample is still relatively low, *Figure 3.10*). Across the rest of the mainland LGC statistically significant exponential relationships dominate (*Figure 3.10*); suggesting that for the majority of the Assynt Terrane, the regional fault spatial attributes cannot be used as an estimation of the spatial attributes at different scales.

At outcrop, 1-dimensional line sampling provides rather different spacing distribution results. Population distribution plots for all outcrops samples result in power-law relationships for spacing (*Figures 3.29 & 3.30*), suggesting that the spatial attributes from outcrop-scale samples are consistently scale-invariant. This is particularly important in the Canisp Shear Zone where both high resolution regional and outcrop samples exhibit power-law relationships (*Figures 3.10c & 3.29a-e*) resulting in scale-invariance that extends between 0.1 and 1000 metres which therefore provides more confidence when using the spatial attributes from both the regional and outcrop datasets to estimate the fracture network spatial attributes at different scales.

2-dimensional connectivity analysis from both the regional and outcrop studies agree that fault and fracture connectivity is higher within the Assynt Terrane (*Figures 3.12 & 3.32*). In the Canisp Shear Zone this high connectivity is due to the presence of two perpendicular sub-vertical fault sets ('Late Laxfordian' faults and Stoer Group age fractures) that cross-cut each other which results in high levels of vertical connectivity. Elsewhere in the Assynt Terrane the connectivity is due to two main fracture sets; one sub-vertical and one near horizontal resulting in relatively high levels of horizontal (or sub-horizontal) connectivity. The increased fracture connectivity in the Assynt is also

likely due to the fact that, in general, it is far more fractured than the Rhiconich Terrane. This increased fracturing is likely to reflect the primary lithology present across the Assynt Terrane (granodioritic gneiss) in comparison to the primary lithology across the Rhiconich Terrane (granitic gneiss). The suggestion that lithology may affect fracture density and, subsequently fracture connectivity, is developed further in *Chapter 6*.

### 3.5 – Mainland Lewisian summary

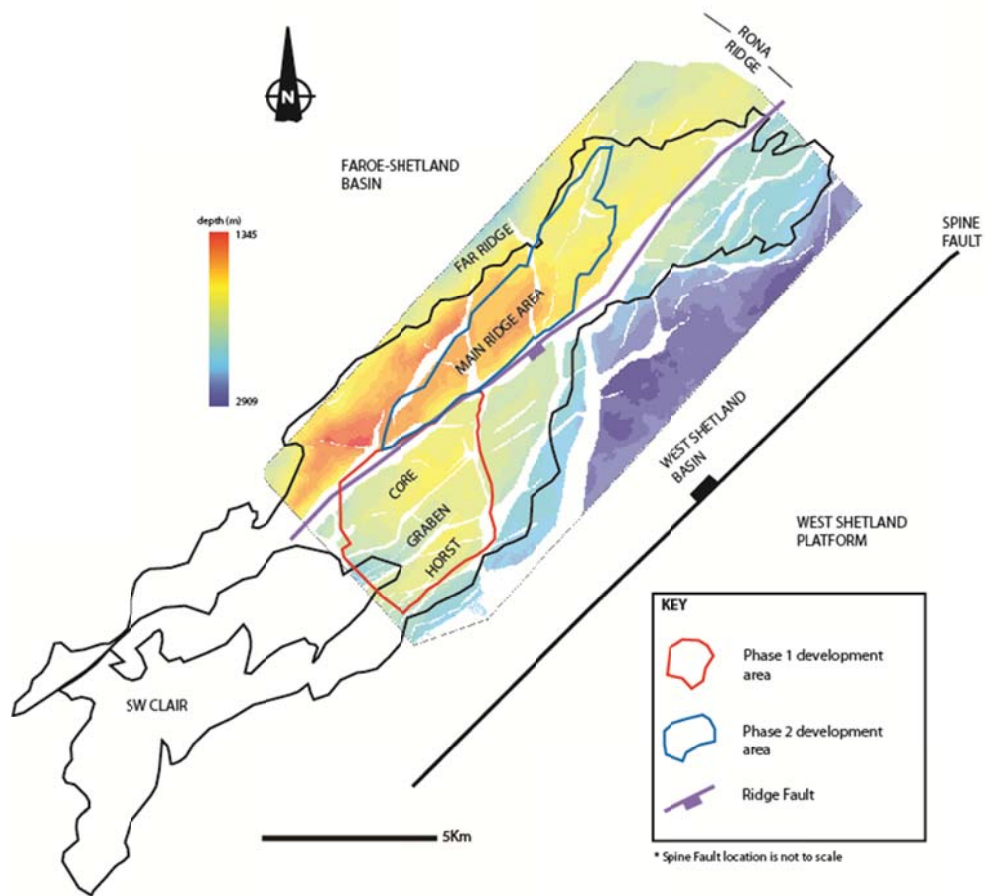
- The analysis of the mainland LGC regional and outcrop datasets provides a detailed understanding of the fracture networks across both the Assynt and Rhiconich Terranes. It highlights the variations across the mainland LGC due to changes in lithology and structural settings, which in turn shows how important an onshore analogue is for developing the understanding of the fracture network within an offshore equivalent (Clair basement) where fracture data is significantly limited.
- NW-SE trending faults and fractures are found across both the regional and outcrop datasets. These structures are Proterozoic 'Late Laxfordian' faults in the Assynt Terrane and potentially younger faults (associated with the deposition of the Torridon Group sediments on top of the LGC and younger, Caledonian or Mesozoic, reactivations) within the Rhiconich Terrane.
- NE-SW (and N-S) faults also present across the regional and outcrop datasets can be related to Stoer (Assynt Terrane) or Torridon (Rhiconich Terrane) Group age fractures which were a result of dextral transtension, due to regional ESE-WNW extension. Some NE-SW faults can also be linked to 'later' deformation with large structures observed cross-cutting and offsetting all other structures present in the mainland LGC.
- Other fault and fracturing events are likely to be present, especially within the regional dataset, but there is little outcrop evidence to be able to distinguish these from previously described fault and fracture sets. There is some limited field evidence, for example, for the local reactivation of Late Laxfordian structures, or parts of those structures during regional Caledonian (Silurian) thrusting (e.g. the Loch Assynt Fault ; Krabbendam et al. (2010)etc).

- Spatial analysis of regional data mainly produces exponential or weak power-law distributions which cannot be considered scale-invariant (except in the Canisp Shear Zone). This contrasts with the outcrop samples which consistently exhibit power-law relationships, indicating that the outcrop spacing samples are scale-invariant. Therefore there is a range of scales (0.1 to ~100m) where scale-invariance confidently applies. This does not mean that the regional scale datasets cannot be used to estimate fault and fracture spatial characteristics at different scales. It is important to be aware that not all of the 1-dimensional regional datasets are scale-invariant and therefore using these data as an estimate of fracture spatial characteristics at different scales will not be 100% reliable.
- The lithology in the mainland LGC shows distinct variations between the Assynt and the Rhiconich Terrane, although both sets of rocks are predominantly orthogneisses. In the Assynt Terrane, the lithology consists of granulite-facies granodiorite gneisses cut by local networks of phyllosilicate-rich low amphibolite-upper greenschist facies shear zones. This contrasts with the Rhiconich Terrane where uniformly mid-amphibolite-facies granodiorite gneisses and granite sheets dominate. The variation in metamorphic grade is particularly important in the Assynt Terrane where greenschist-facies metamorphism in the Canisp Shear Zone results in highly fractured rocks as a result of reactivation and pinning by the phyllosilicates-rich foliation.

## **Chapter 4 – Clair Basement Fault and Fracture Analysis**

The aim of this chapter is to explore the fracture network characteristics from the subsurface Clair basement using 3-dimensional seismic reflection data from across the majority of the Clair Field and basement well datasets, including core samples and image logs.

As discussed previously (*Chapter 2*), geophysical and geological interpretations of well data and seismic reflection datasets covering the Clair Field suggest that the metamorphic basement sits at depth as a fault-controlled topographic high which is onlapped and overlain by the Devonian to Carboniferous Clair Group sedimentary cover sequences (e.g. Falt et al., 1992, Coney et al., 1993). Many of the fractures that cut the Clair Group Reservoir also cut down into the basement (*Figure 4.1*). This basement-cover relationship implies that fractures in the basement have the potential to provide or influence important fluid flow pathways across the Clair Field, connecting sedimentary packages located on either side of the Rona Ridge. Furthermore it is possible that basement-hosted fracture systems form a significant hydrocarbon reservoir that is independent of the cover sequences. It is therefore important to gain an understanding of these basement fracture networks and their associated attributes in order to be able to model the basement in terms of both its potential to influence fluid flow pathways, and also to estimate the oil-in-place in the basement. A full description of the Clair Field area, including a tectonic history, is given in *Chapter 2*.



**Figure 4.1:** Map of the Clair Field showing the main development areas. The area outlines are displayed on a depth map of the top Clair basement. White sections in the depth map represent fault polygons.

#### 4.1 – Introduction to the offshore fracture analysis

The analysis in this chapter is based on two main datasets; top-basement seismic attribute maps, and well data, primarily core samples. These datasets are of a restricted nature because there are only three significant wells that sample the basement and only top basement is reliably imaged in the seismic reflection data. This means that the data available only represent a small sample of the total basement volume and big assumptions have to be made if it is to be extended across the entire field. This is why the onshore analogue study in the previous chapter (*Chapter 3*) is essential as it provides details about the potential fault and fracture networks in the Clair basement that could not be ascertained from offshore data alone.

#### 4.2 – Regional lineament analysis of seismic attribute maps

The issue of fracture scalability is important because it provides constraints on how useful different datasets are when carrying out whole-field or small-scale modelling exercises. This study uses a 3-dimensional seismic survey shot over the Clair Phase 1 and 2 areas (*Figure 4.1*), with particular focus on the basement ridge to create a fault lineament map that can be directly compared to the onshore regional study in the mainland Lewisian Gneiss Complex (LGC). Spatial analysis of this dataset provides insights into the scalability of the faults at this regional scale which will have direct implications for any basement fracture modelling in the future.

Seismic horizon analyses were completed using the Landmark® software package, particularly Seisworks® 3D. It has been used to create top basement seismic attribute maps which include: depth, difference, edge, azimuth, dip and coherency (*Figure 4.2*). The definitions of each attribute are given below.

*Depth (Figure 4.2a)* – In this case the depth map shows depth, in a metre scale, from sea level to the horizon that is to be interpreted (i.e. top basement). It particularly highlights the Ridge area and can be used to conduct a relatively low resolution analysis of the Clair basement (and the Clair sedimentary cover

sequences). The seismic time-to-depth conversion was carried out using a combination of ties to known horizons in the well data and using a Root Mean Square method to stack the velocities of the units known to be within the seismic volume.

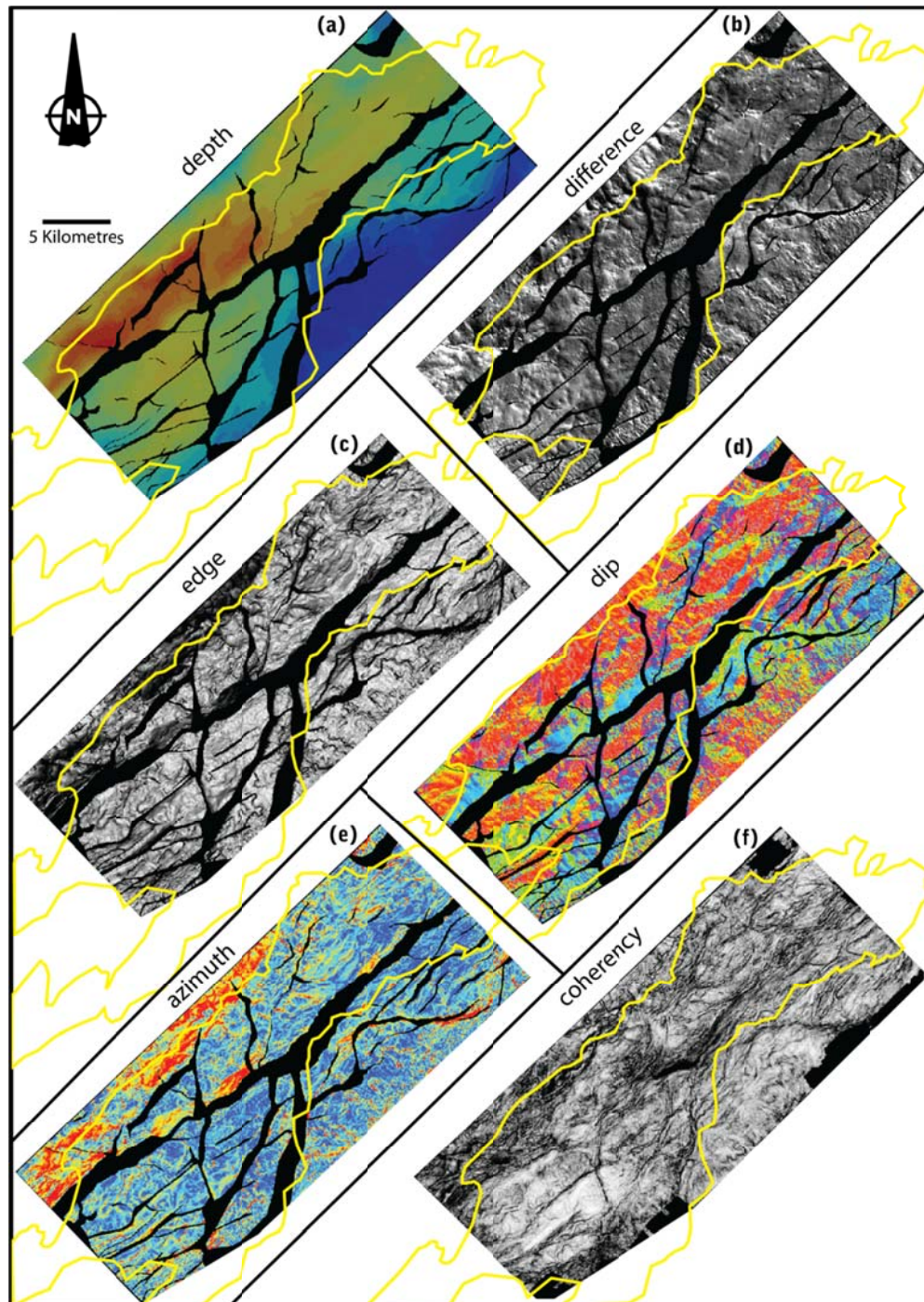
*Difference (Figure 4.2b)* – Measures the difference between adjacent seismic wavelets, in degrees. This attribute has two maps; one for difference along seismic lines and one along seismic traces. This is useful as it can help detect small faults only a few lines or traces wide and can highlight very subtle lineations (faults).

*Edge (Figure 4.2c)* – Edge detection exaggerates sharp dip changes such as reef edges (in carbonates), faults or steep horizon dips caused by topography (Carter and Lines, 2001). Units – degrees.

*Azimuth (Figure 4.2d)* – This gives the direction of the gradient vector calculated at each grid-point of the interpreted (time) horizon (Mondt and Jaap, 1993). It is a useful tool to distinguish sharp changes in slope angle. Azimuth is expressed in degrees from geographic north.

*Dip (Figure 4.2e)* – This gives the magnitude of the slope calculated at each grid-point of the interpreted horizon (Mondt and Jaap, 1993) and is expressed as degrees from a horizontal plane. It is an attribute that is useful for interpreting geological features that result in sharp changes in slope angle such as faults.

*Coherency (Figure 4.2f)* – This attribute works by comparing seismic wavelets with adjacent wavelets to determine the degree of similarity between them (measured in degrees (Chopra and Marfurt, 2007)). Coherency has been shown to be very effective at delineating faults (and palaeochannels) in seismic horizon data (Sassen, 2008). Areas which show high coherency are normally coloured white; those areas with low coherency such as faults are coloured black.



**Figure 4.2:** Top basement seismic attribute maps used for Clair basement fault lineament interpretation. (a) depth, (b) difference, (c) edge, (d) azimuth, (e) dip & (f) coherency. Yellow line marks the approximate outline of the Clair Field.



During this regional study none of these seismic attributes were used independently from each other; the best results were achieved when these attributes were used in conjunction with each other. For example, lineaments visible in azimuth, dip and edge attribute maps were confirmed if they were also visible in the difference and coherency attribute maps. This is because both the difference and coherency attribute maps highlight smaller scale features than the other attributes used, and thus provided the best datasets to 'ground-truth' the lineament picks. Care was also taken not to assume that every linear feature seen in the coherency and difference attribute maps was a fault lineament before its presence was confirmed using other seismic attributes. A more detailed description of the method used for the analysis of the seismic attribute maps is given in the following section.

#### **4.2.1 – Method for production and interpretation of top basement seismic attribute maps**

The creation of the top basement seismic attribute maps took place in the ConocoPhillips (U.K.) Ltd. offices in Aberdeen where I had access to 3-dimensional seismic data for the Phase 1 and 2 areas of the Clair Field (*Figure 4.1*). The seismic has lines (inlines) that trend NE-SW and traces (crosslines) that trend NW-SE across the main ridge structure which have been interpreted on a 50m spacing in both directions. To create the attribute maps, pre-interpreted seismic data were used as there was no need to re-interpret already well-scrutinised data i.e. the BP top basement depth horizon interpretation was used to create all subsequent seismic attribute maps. The attribute maps were created in Seisworks® for the top basement horizon and then converted into a raster format that could be used in the ArcGIS® 9.2 ([www.esri.com](http://www.esri.com)) suite of software. The reason for this conversion was to enable a fault lineament interpretation for the Clair basement to be conducted using the same method as was used in the regional study of the mainland LGC. This allowed direct qualitative (visual) and quantitative (statistical analysis techniques) comparisons of the onshore and offshore datasets to be made.

Attribute maps were created for depth, dip, azimuth, difference, edge and coherency for top basement, top Unit 5 (Lower Clair Group), top Unit 6 (Lower Clair Group), base Upper Clair Group and base Cretaceous. These were used to interpret fault

lineaments across the Clair units, with the main focus on the basement maps. These attribute maps were imported into ArcGIS® 9.2 and fault lineaments were interpreted at three different scales; 1:100,000 (first-order faults), 1:50,000 (second-order faults) and 1:25,000 (third-order faults). It should be noted that for the purposes of the present study, linear features visible on the attribute maps were all assumed to be faults: the low resolution of the data means that it is unlikely that foliation (on the basement maps) would be identifiable and no geophysical data (such as magnetic and gravity) were available, so it was not possible to differentiate dykes or other linear geological features from faults. Therefore it is possible that the regional dataset from the Clair Field contains a small number of lineaments that do not represent faults.

To reduce the effect of artefacts in the data, attribute maps were made transparent and layered with each other. This made artefacts associated with individual attributes more apparent and gave more confidence when interpreting 'real' fault lineaments. Although the attribute maps were not used independently of each other, it was clear that the coherency attribute proved to be the most useful for identifying and interpreting faults in the basement. This is because it highlights small-scale variations between adjacent seismic wavelets which can often be attributed to areas that are heavily faulted or cut by single fault lineaments (Sassen, 2008) and thus allows fault sets to be interpreted in greater detail. It should be noted that coherency maps were not available for the Clair sedimentary cover sequences and therefore the basement coherency interpretations were not used when comparing the fault networks between different units in the Clair Field.

Once identified each fault lineament was assigned various attributes, the most important of these being orientation (azimuth only) and length. These values were calculated using the EasyCalculate50 scripts polyline Get Azimuth 9x.cal (calculates the azimuth of a polyline in a user specified space) and shape Return Length.cal (calculates the length of polylines or the perimeters of polygons) respectively (see, <http://arcscripts.esri.com/details.asp?dbid=12224> for full details). These attributes have been used to analyse the lineament interpretation in detail.

A fault spacing analysis was also conducted on the lineaments that were created from top basement seismic attribute maps. The work was completed in Paradigm® GOCAD 2009.2 and involved creating fault surfaces from the lineament data. To do this the fault lineaments interpreted in ArcGIS® were imported into GOCAD and using the

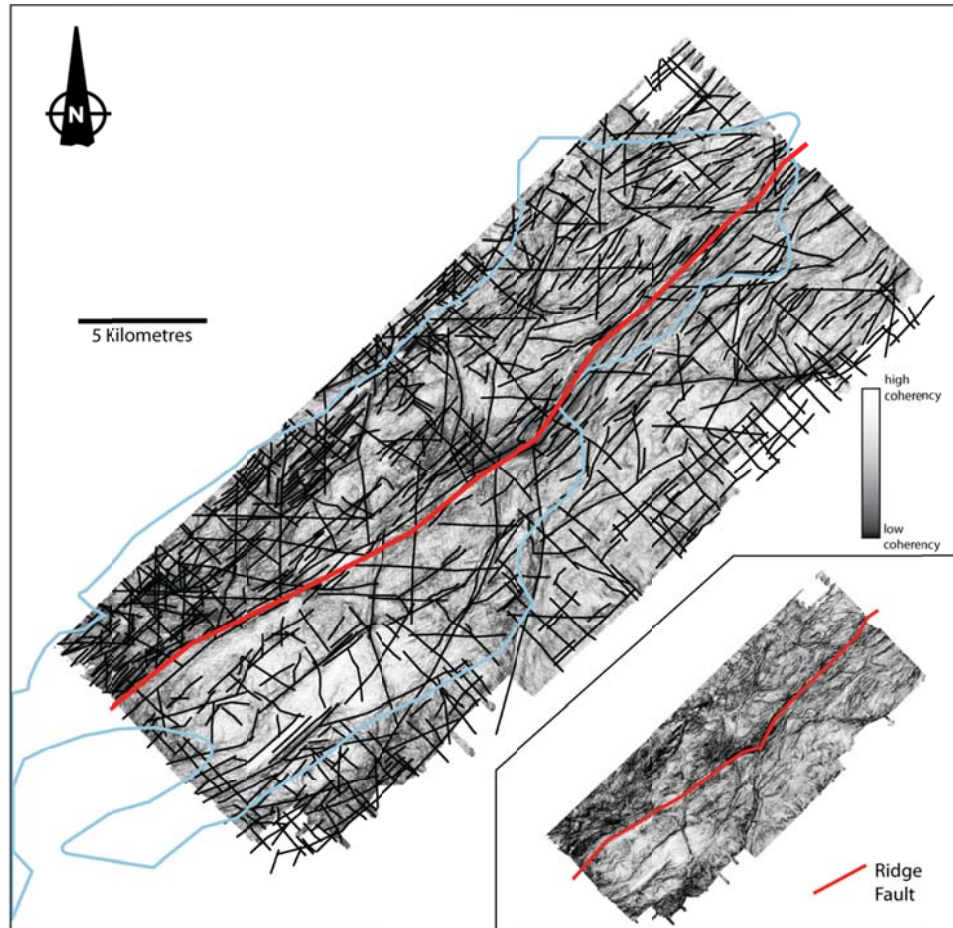
structural modelling workflow, fault surfaces were created. See *Appendix 3* for the lineament to fault surface workflow. One major simplifying assumption that this technique makes is that all of the faults are plotted as vertical structures because there is insufficient data available to be able to assign full 3-dimensional orientations (strike, dip, dip direction) to the fault planes. It is possible to determine the strike and dip of the large faults which display a surface expression on the horizon depth maps, but because the majority (>70% for the top basement horizon) of the fault lineaments picked during the regional interpretation do not exhibit a tangible surface expression, all the faults included in this study are inferred to be vertical for the purposes of the statistical spatial analysis.

Once fault surfaces were successfully created, a network of 'pseudo-wells' were draped on top of the horizon surfaces to create a 2-dimensional grid of 1-dimensional sample lines (see *Chapter 1, Section 1.6.5* for details of advantages and disadvantages of using these pseudo-wells). These were produced by creating wells in GOCAD which were then populated with surface intersections and, where available, other fault-attribute data (the full workflow is given in *Appendix 3*). Pseudo-wells were created for four different orientations (NE-SW, N-S, NW-SE and E-W) in order to ensure that all orientations of lineaments were sampled. The datasets created from the pseudo-wells were then exported into Excel and a spacing analysis was conducted. By using these pseudo-well fault spacing datasets, population distribution plots, the coefficient of variation and fault density values were created and analysed (see *Chapter 1* for more details on the methods involved in these statistical analysis techniques).

#### 4.2.2 – Regional fault lineament orientation analysis

Over 700 lineaments have been interpreted from the top basement horizon attribute maps and an average of 180 lineaments from each of the Clair sedimentary cover sequence horizons. The lineaments cover the Rona Ridge and areas to the southeast of the topographic high (*Figure 4.3*). Fault lineaments have been 'binned' into four separate azimuth groups; N-S (335-035° & 155-210°), NE-SW (031-080° & 211-260°), E-W (081-1-5° & 261-285°) AND NW-SE (106-156° & 286-334°), which allows lineament azimuths to be compared against location in the Clair Field and against lineament length. The following section describes the fault lineament orientation

distributions for the top basement horizon. These are then compared to the lineament patterns in the overlying cover sequences.



**Figure 4.3:** Map of the Clair basement horizon showing all interpreted fault lineaments over the coherency attribute. In total there are 771 interpreted lineaments on this map. Blue line marks the approximate outline of the Clair Field. Inset shows the coherency map without the fault lineament interpretation.

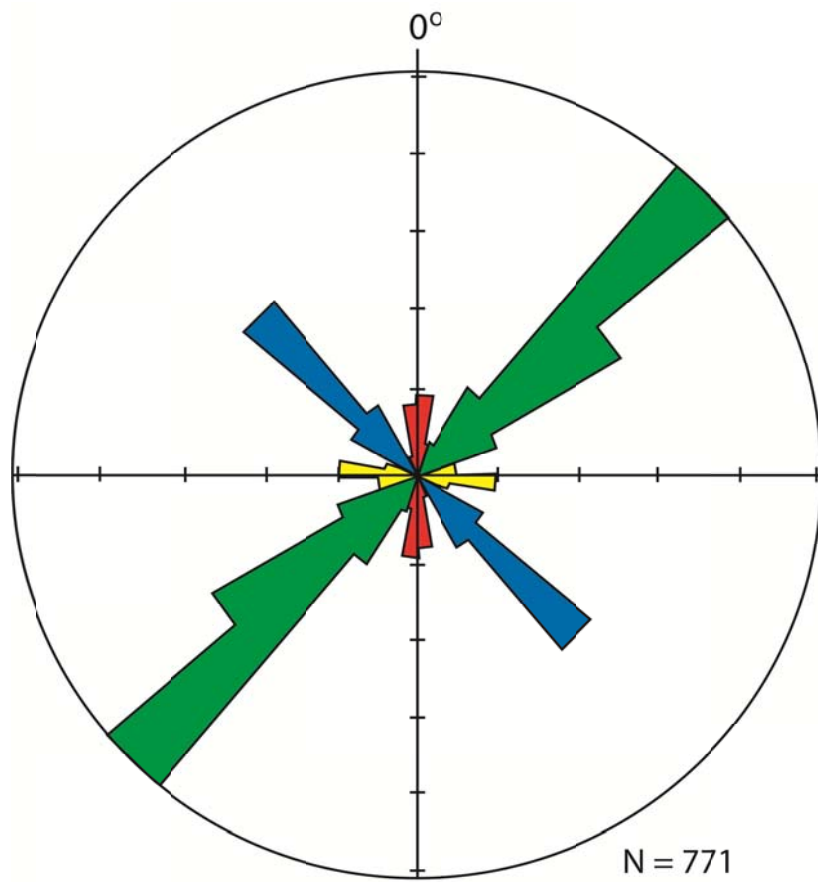
#### 4.2.2.1 – Clair basement

If we accept the assumption that the lineament interpretation of the relatively low-resolution seismic dataset identifies faults, it suggests that the basement is highly fractured. As previously mentioned there is the possibility that some of the interpreted lineaments could potentially be dykes, but evidence from well data and assumptions made from comparisons with the mainland LGC suggests that non-fault lineaments do not form a significant proportion of the regional dataset.

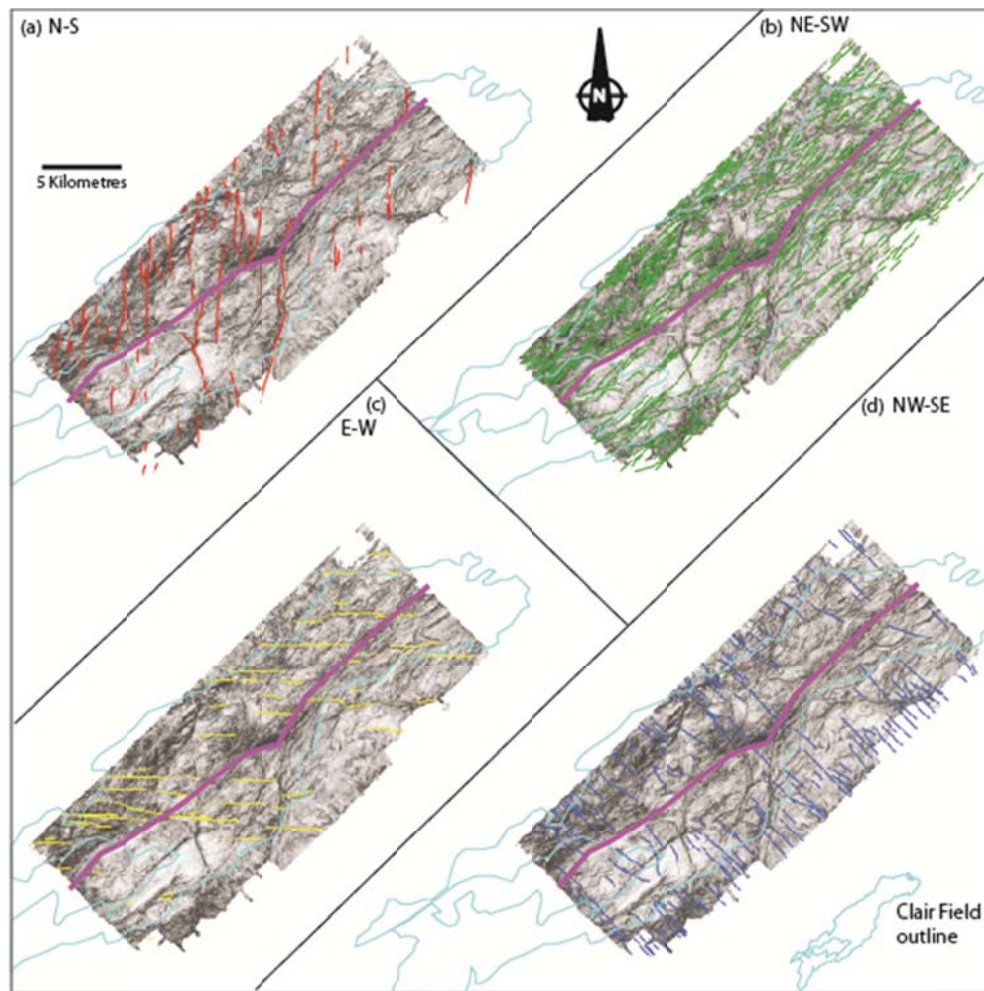
Interpretation of the top basement horizon clearly suggests that NE-SW orientated lineaments are the most abundant (460 lineaments) (*Figure 4.4*), with E-W structures representing the least prominent fault trend (54 lineaments). The colour-coded maps shown in *Figure 4.5* illustrate the variation in fault lineament orientation with respect to location. Most fault lineament orientations are consistent across the basement, i.e. there is little variation in the azimuth of the lineaments in each orientation group (NE-SW, N-S, NW-SE and E-W). *Figure 4.5* shows that NE-SW lineaments are more densely distributed across the ridge area with areas to the southeast of the main Ridge Fault exhibiting fewer NE-SW trending structures.

NW-SE fault lineaments have the second strongest azimuth trend (174 lineaments) in the basement. They are distributed across the whole Clair Field and do not show any increase in lineament density on the Rona Ridge (*Figure 4.5d*). Using the basement horizon depth map suggests that a small number of NW-SE trending lineaments right-laterally offset the main NE-SW trending Ridge Fault

N-S and E-W trending fault lineaments are less common (or possibly more poorly imaged) in the basement (see *Figure 4.5a & c* respectively). Generally both these fault lineament trends are distributed across the whole of the Clair Field, although N-S lineaments occur more frequently along the Rona Ridge.



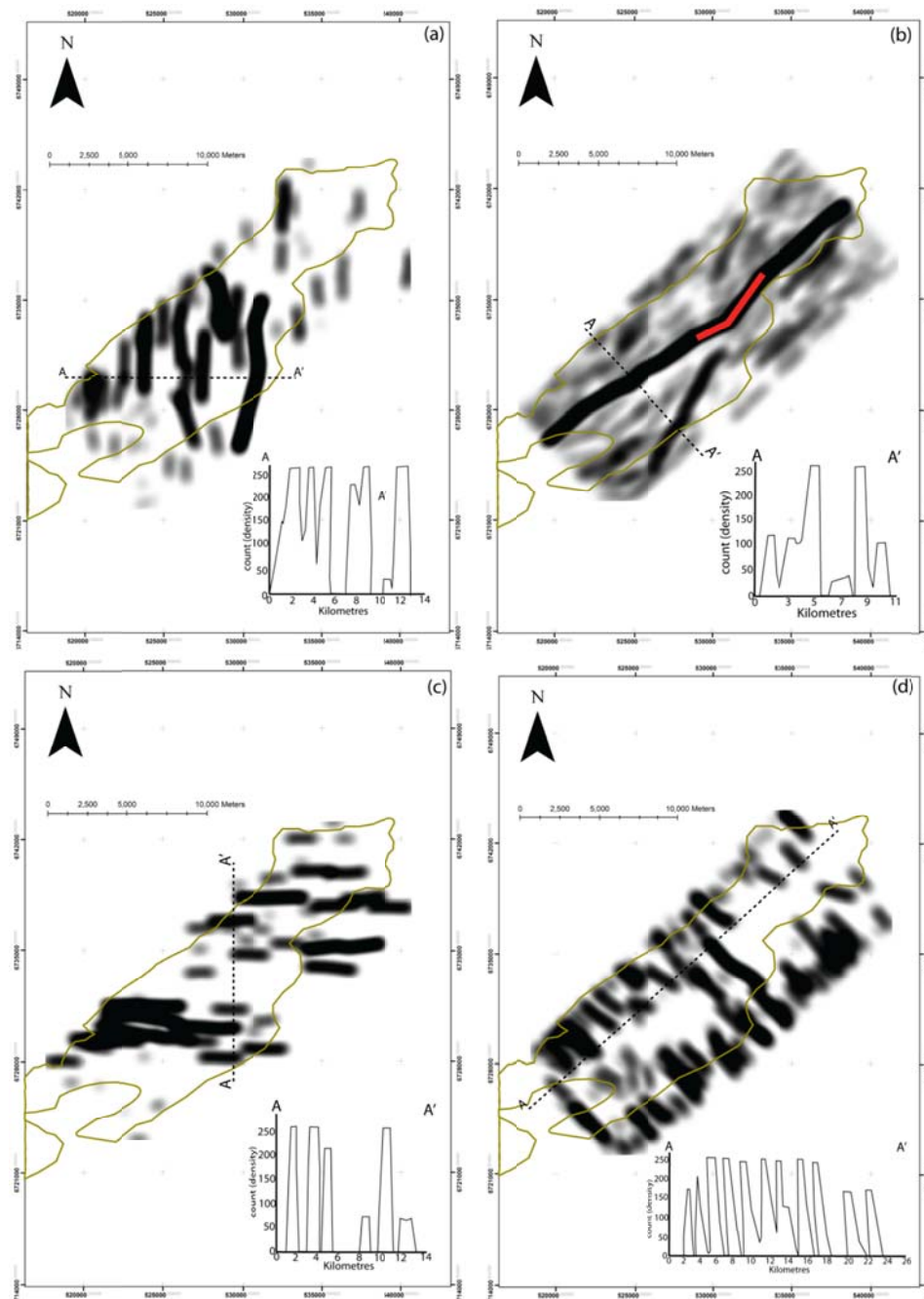
**Figure 4.4:** Rose plot of the interpreted Clair basement fault lineaments. The colours represent the bins that the azimuths have been separated in to. Red: N-S, green: NE-SW, blue: NW-SE & yellow: E-W.



**Figure 4.5:** Top basement horizon coherence maps with the interpreted fault lineaments separated in to their respective orientation bins. **(a)** Lineaments that trend N-S (total 83) **(b)** Lineaments that trend NE-SW (total 460) **(c)** Lineaments that trend E-W (total 54) **(d)** Lineaments that trend NW-SE (total 174). Ridge Fault is shown in purple.

The relationship between fault lineament azimuth and lineament length has been tested using a statistical method to display the length data as a density distribution on the top basement horizon map (*Figure 4.6*). This length density distribution is calculated as a magnitude per unit area from polyline features (i.e. fault lineaments) in the neighbourhood of each output cell. It is calculated as units of length per unit of area ([http://resources.esri.com/help/9.3/arcgisengine/com\\_cpp/gp\\_toolref/spatial\\_analyst\\_tools/how\\_line\\_density\\_works.htm](http://resources.esri.com/help/9.3/arcgisengine/com_cpp/gp_toolref/spatial_analyst_tools/how_line_density_works.htm) for more details on this statistical analysis).





**Figure 4.6:** Length density maps for the Clair top basement horizon using the interpreted fault lineaments. This type of analysis shows where a particular attribute (in this case length) is concentrated on a map. It clearly highlights larger features and areas where some lineament trends are more prominent than others. The search radius was set at ~500 and the output cell size was 50 in order to produce a relatively high-resolution dataset. **(a)** N-S trending fault lineaments **(b)** NE-SW trending lineaments (red line indicates 'kinked' section of the Ridge Fault **(c)** E-W trending lineaments **(d)** NW-SE trending lineaments.



This analysis shows that the lineaments trending N-S are concentrated to the south of the seismic study area and are more common on the basement ridge (*Figure 4.6a*). It also shows that the majority of the N-S faults are approximately the same length (mean length is ~1500m). NE-SW lineaments are consistently longer adjacent to the Ridge Fault but are found throughout the basement (*Figure 4.6b*). What *Figure 4.6b* shows is that there are only a few major NE-SW faults (lengths up to 25km) within the basement, but these are associated with lots of shorter faults (mean length is ~1400m). Fault lineaments that trend E-W are found across the ridge structure and appear to be focussed into two main clusters; one tight cluster in the south of the seismic study area and a more dispersed zone further north (*Figure 4.6c*). E-W fault lineaments have consistent lengths (~2000m) across the seismic study area. Two large NW-SE trending faults (*Figure 4.6d*) can be seen to coincide with a bend in the Ridge Fault (marked in red on *Figure 4.6c*). Other NW-SE trending faults are distributed throughout the seismic study area and generally have shorter lengths when compared to other fault lineament azimuth trends (mean NW-SE fault lineament length is ~1200m).

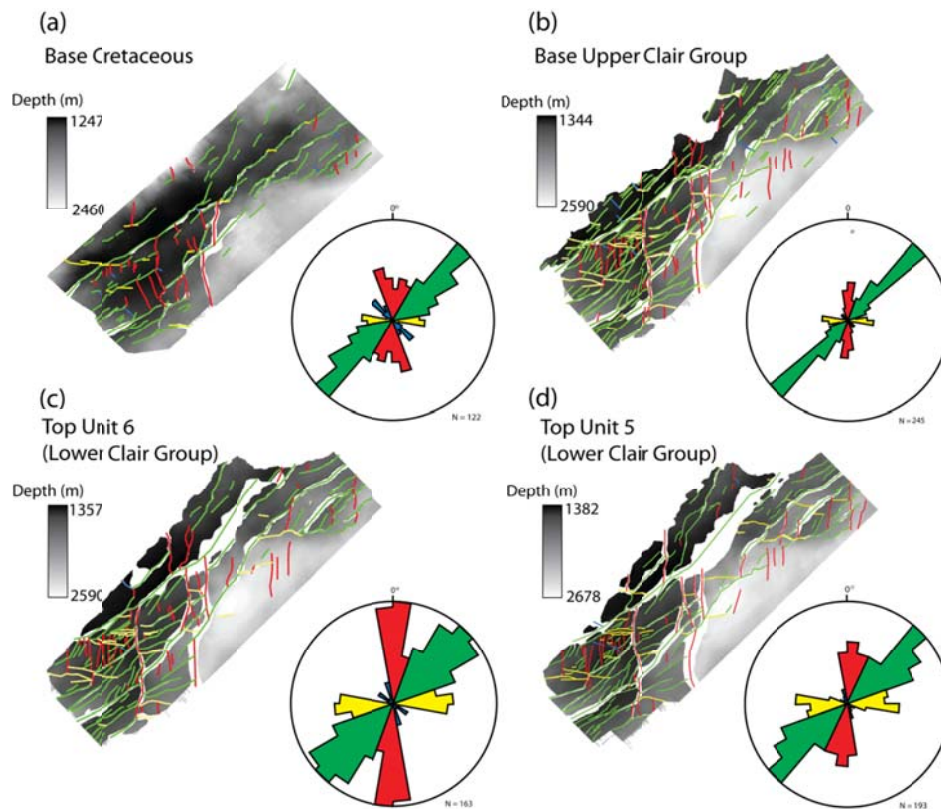
The data presented here only refers to the azimuths of the fault lineaments picked from top basement seismic attribute maps. It is possible to use information from seismic interpretation (and from the horizon depth maps) to estimate the dip and dip direction of the major faults that can be imaged in the seismic data (see *Appendix 4* for example seismic lines and transects including fault interpretations). Generally faults interpreted from seismic are steep ( $>60^\circ$ ) and dip to the southeast. In many places the faults are interpreted as being almost vertical. The fact that many of the faults present in the basement are vertical (or close to vertical) has implications for the well analysis study in *Section 4.3* of this chapter as it means that vertical wells in the basement are likely to under-sample the full fracture network.

#### 4.2.2.2 – Clair sedimentary cover sequences

In order to be able to gain some insight into the age of the fault lineament sets (based on lineament azimuth) a study of the fault lineaments from seismic horizons through the Clair sedimentary cover sequences has also been conducted. This analysis uses four seismic horizons from within the Clair Group sediments; top Unit 5 (mid-Devonian), top Unit 6 (mid to late Devonian), base Upper Clair Group (early Carboniferous) and base Cretaceous. Seismic attributes available for these horizons include; depth, dip, edge, azimuth and difference. Coherency was not available for the sedimentary units, so in order to be able to compare the interpreted fault lineament maps from the sedimentary cover with the basement, those lineaments picked from the basement using the coherency attribute were discounted from this part of the study. Also, it should be noted that the sedimentary seismic horizon maps do not cover exactly the same area as the basement map. This is because most of the Clair Group sedimentary units do not extend over the basement ridge (except the base Cretaceous), so therefore there is no data for this area from the Clair Group maps.

Fault lineaments were picked for the four sedimentary cover horizon maps in the same manner as the basement interpretation and they were again 'binned' into four separate azimuth categories (NE-SW, N-S, NW-SE and E-W). *Figure 4.7* shows the fault lineament maps for the sedimentary cover horizons and the associated rose diagram plots of the lineament azimuths.

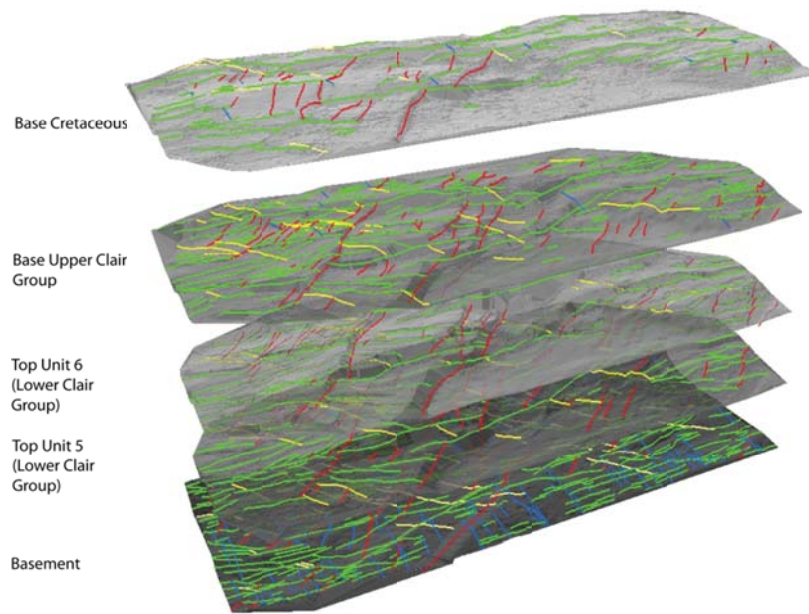
NE-SW lineaments clearly extend through all the selected sedimentary horizons and in most instances it is obvious that it is the same fault that has been interpreted through all the horizons (*Figure 4.8*). This pattern is also true for the N-S fault lineaments which also appear to cut through each of the seismic horizon samples. Both the NE-SW and N-S fault lineament trends show high lineament numbers in the Clair Group sediments (*Figure 4.7b, c & d*) with far fewer present within the base Cretaceous horizon map (*Figure 4.7a*). Also, it is clear from all the seismic horizon maps that the N-S trending fault lineaments are consistently cut by the NE-SW fault lineaments.



**Figure 4.7:** Fault lineament interpretations and depth horizon maps for Clair sedimentary cover sequence seismic horizons. Each map also shows a rose plot of the interpreted fault trends. The youngest horizon is shown in (a), with the oldest in (d).

E-W trending fault lineaments are present throughout the Clair Group sediments (*Figure 4.7b, c & d*) and are mainly concentrated in the Core area of the Clair Field (see *Figure 4.1* for a map of the different areas in the Clair Field). It is clear from the seismic horizon interpretations shown in *Figure 4.7* that E-W trending fault lineaments are less apparent within the base Cretaceous horizon with only a small number present within the Core area. What is apparent is that those E-W lineaments present within the base Cretaceous horizon are continuations of faults that are present within the Clair Group sediments and the basement (*Figure 4.8*).

NW-SE fault lineaments are not obvious throughout the sedimentary cover sequences at this regional scale. Only a few short lineaments have been interpreted (*Figure 4.7*) compared to the hundreds picked from the top basement map. This suggests that the great majority of these fractures are restricted to the basement in the region of the Clair field analysed.



**Figure 4.8:** Horizon topography maps for each of the interpreted horizons in the Clair Field. Each horizon shows their interpreted fault lineaments. N-S lineaments are in red, NE-SW lineaments are in green, E-W lineaments are in yellow and NW-SE lineaments are in blue.

#### 4.2.3 - Regional fault lineament orientation analysis: Discussion

Regional fault interpretation of the top basement seismic horizon has shown that there is a prominent NE-SW fault orientation trend (460 lineaments) which coincides with the main extensional structure that defines the basement ridge. It is therefore possible that the main extensional fault that trends NE-SW across the Clair field (the Ridge Fault) is controlling the development of similar trending faults across the basement ridge. This prominent NE-SW fault trend is visible on all the Clair sedimentary cover horizons interpreted in this study (*Figure 4.7*), therefore suggesting that this NE-SW fault trend is Late Jurassic/ Early Cretaceous or possibly younger in age.

N-S trending fault lineaments are also present throughout all the sampled seismic horizons (*Figure 4.8*), albeit in fewer numbers (83 lineaments picked from basement; mean value of 18 lineaments picked from the cover sequences), again suggesting an age of Cretaceous or younger. A possible origin of these N-S fault lineaments is a result from a period of E-W extension during the latest Jurassic (the youngest seismic dataset is from the base Cretaceous so this event may have been recorded on this horizon map) which occurred before the main NE-SW fault trend seen

on the North Atlantic margin (Dore et al., 1997). Evidence from the interpretation of the seismic horizons in the basement and sedimentary cover suggests that these N-S fault lineaments are locally cross-cut by NE-SW trending faults (*Figure 4.8*). Therefore N-S faults are older than NE-SW structures, providing more evidence for these N-S faults originating in the Jurassic. Also, well test data made during hydrocarbon production in the cover sequences suggests that N-S trending faults are conducive to fluid flow (Conway, 2010), and so if these open structures extend down into the basement, they could potentially provide major fluid flow pathways across the whole Clair Field.

Fault lineaments that trend E-W are present through all the sampled seismic horizons (*Figure 4.8*), but evidence from the reduced number of interpreted faults of this trend from the base Cretaceous horizon (11 lineaments picks compared to 30 from the top Unit 5 horizon) suggests that these faults are 'dying out' and therefore may not be younger than the Cretaceous. Previous work from the Clair Partners suggests that the E-W trending lineaments are structures that reactivate pre-existing basement fabrics (Hart, 2008), which may explain their clustered nature: there are two E-W fault clusters within the basement map and E-W faults are clustered in the Core Area of the Clair Field in all of the sedimentary cover horizon maps (*Figure 4.7*). This work also suggests that E-W trending faults are 'older' (than the Cretaceous), which is consistent with fault of this trend 'dying out' in the Cretaceous.

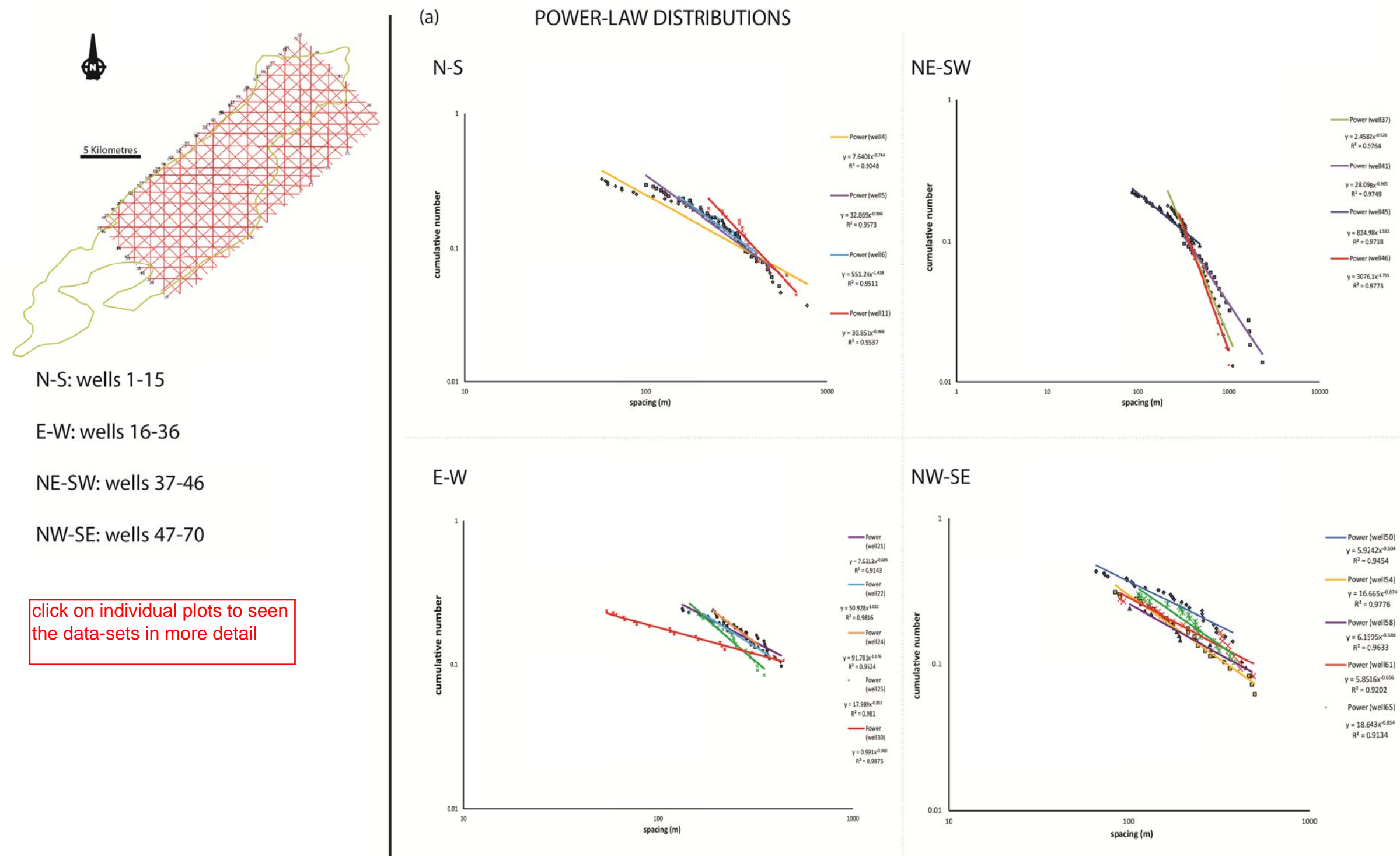
NW-SE fault lineaments are distributed across the whole of the basement and from the interpretation it is possible that a few of these lineaments right-laterally offset the main NE-SW Ridge Fault suggesting an age of Devonian or younger. This can be constrained further because, although NW-SE trending fault lineaments are abundant in the basement (174 lineaments), they are not obviously present within any of the sedimentary cover seismic horizon maps. Therefore these NW-SE trending faults that apparently off-set the Ridge Fault must have an age after the initiation of the Ridge Fault but before the deposition of the Lower Clair Group Unit 5 sediments, i.e. in the early Devonian. This only applies to those faults which offset the Ridge Fault, which may result from the reactivation of basement shear zones of the same orientation (in a similar manner to the Canisp Shear Zone, see *Chapter 3*). Most of the NW-SE lineaments interpreted from the basement horizon do not offset the Ridge Fault and therefore, at this regional scale, the majority of NW-SE trending faults are inherently basement features and have pre-Devonian age.

Previous work by Coney et al. (1993), examining core samples, showed that NW-SE (WNW-ENE & NNW-SSE) trending faults and fractures are present within the sedimentary cover rocks and are, more importantly, the open features within the rocks. Therefore it is possible that these approximately NW-SE trending faults exist within the sedimentary cover sequences but are at a scale that is not resolvable in the seismic dataset.

Although the orientation analysis gives some insight into the distribution of fault lineaments in the basement, the low resolution of the 3-dimensional seismic survey and poor seismic imaging in the basement means that it is difficult to see any local variations in the basement fault orientations. The lack of high-resolution regional data is one of the biggest weaknesses in the analysis of the Clair basement.

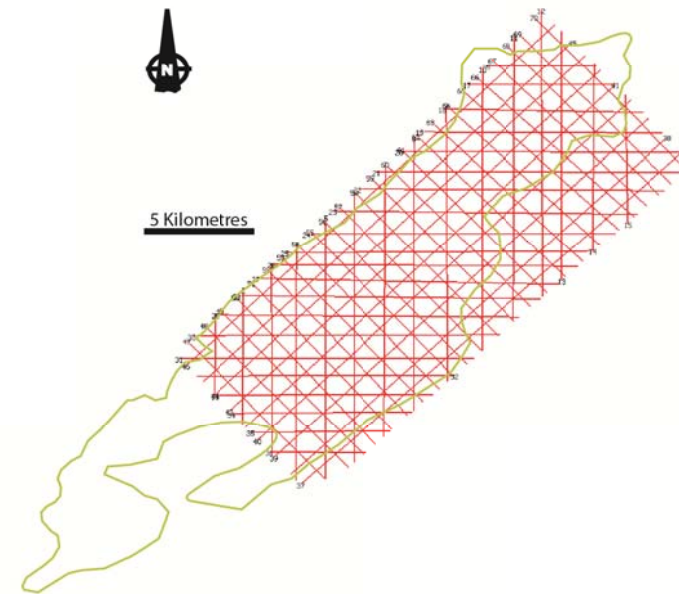
#### 4.2.4 – Regional fault lineament spacing analysis

Fault lineament spacing analysis has been conducted primarily using fracture population distribution plots created from data collected from pseudo-wells drawn across the basement horizon. The pseudo-wells record fault lineaments that they intersect so this information can be used to calculate the fault spacing for individual 1-dimensional sample lines. In total, 70 pseudo-wells have been used to analyse the basement (*Figure 4.9a*), although some of these wells did not contain enough fault surfaces to be of use for the statistical analysis shown in the following sections. Fault spacing data for the useable pseudo-wells is shown in the population distribution plots in *Figure 4.9* and the fault spatial attributes from the same pseudo-wells are shown in *Tables 4.1 & 4.2*.



**Figure 4.9:** Population distribution plots for the spatial relationships of faults within pseudo-wells created for the Clair top basement seismic horizon map. The pseudo-wells shown in the plots have fault numbers which exceeds 30 per sample. **(a)** Population distribution plots which show power-law distributions for fault spacing. The plots are split into the different orientations of the pseudo-wells. **(b)** Population distribution plots which show exponential distributions for fault spacing.





N-S: wells 1-15

E-W: wells 16-36

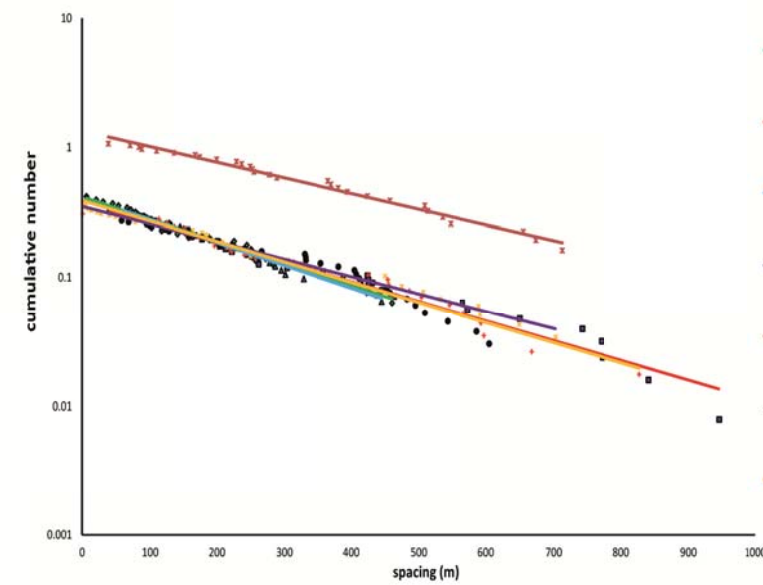
NE-SW: wells 37-46

NW-SE: wells 47-70

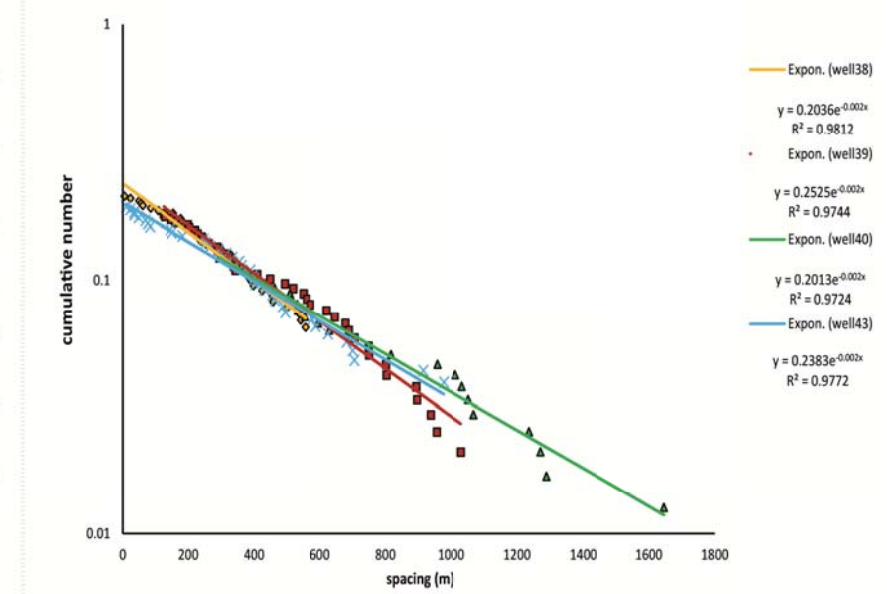
click on individual plots to see the data-sets in more detail

## (b) EXPONENTIAL DISTRIBUTIONS

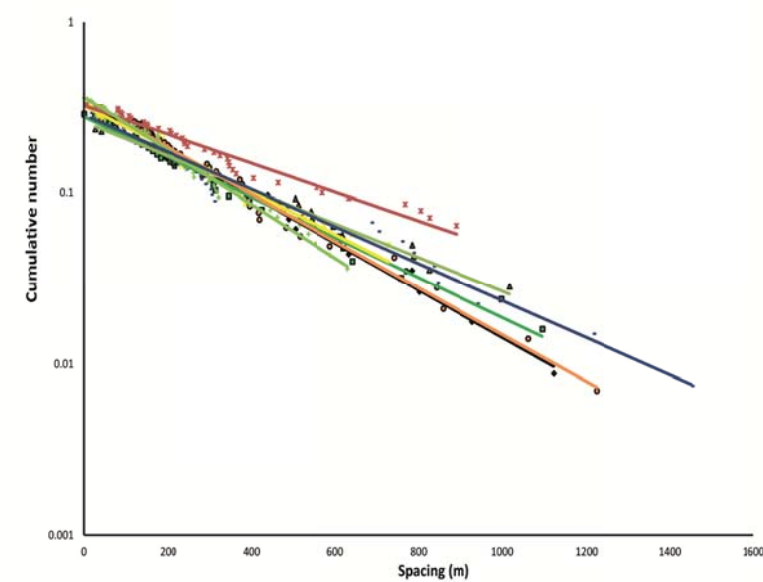
N-S



NE-SW



E-W



NW-SE

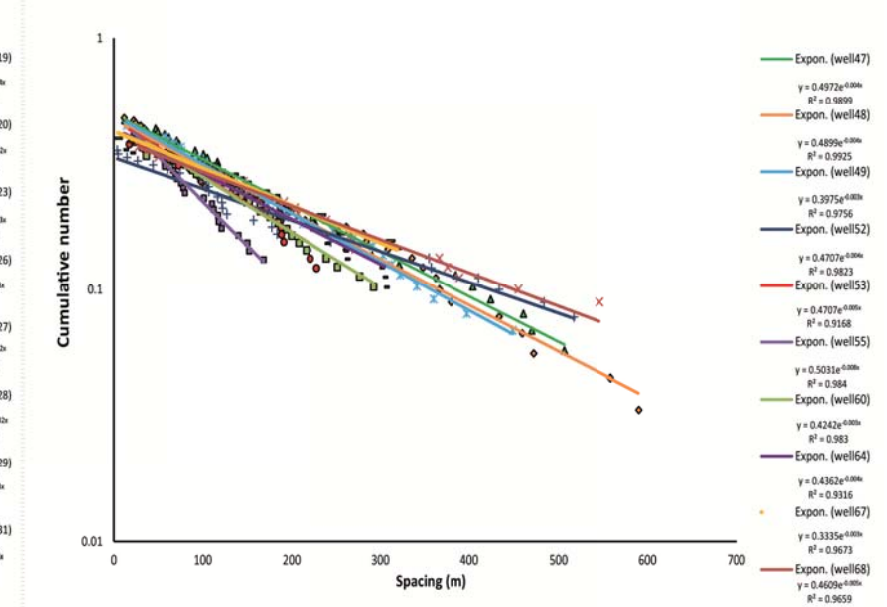


Figure 4.9: (b) contd



Well #	Well orientation	N	Distribution	R <sup>2</sup>	d-value	Cv	Clustering	Fracture Density (fracture /m)
4	N-S	39	power-law	0.90	0.74	0.97	anti-clustered	0.004
5	N-S	44	power-law	0.96	0.99	0.91	anti-clustered	0.004
6	N-S	41	power-law	0.95	1.44	0.82	anti-clustered	0.003
11	N-S	33	power-law	0.95	0.97	0.87	anti-clustered	0.003
21	E-W	43	power-law	0.91	0.69	0.71	anti-clustered	0.003
22	E-W	43	power-law	0.98	1.02	0.78	anti-clustered	0.003
24	E-W	55	power-law	0.95	1.18	0.66	anti-clustered	0.004
25	E-W	49	power-law	0.98	0.85	0.98	anti-clustered	0.003
30	E-W	39	power-law	0.99	0.37	1.05	random	0.003
37	NE-SW	62	power-law	0.98	0.53	0.82	anti-clustered	0.003
41	NE-SW	41	power-law	0.97	0.97	1.05	random	0.001
45	NE-SW	59	power-law	0.97	1.53	0.86	anti-clustered	0.002
46	NE-SW	79	power-law	0.98	1.76	0.99	random	0.003
50	NW-SE	39	power-law	0.95	0.60	0.97	anti-clustered	0.004
54	NW-SE	41	power-law	0.98	0.87	0.95	anti-clustered	0.004
58	NW-SE	31	power-law	0.96	0.69	0.98	anti-clustered	0.003
61	NW-SE	37	power-law	0.92	0.66	0.85	anti-clustered	0.004
65	NW-SE	38	power-law	0.91	0.85	0.70	anti-clustered	0.004

**Table 4.1:** Spatial attributes of faults from pseudo-wells created in the Clair top basement seismic horizon. This table shows all pseudo-wells that exhibit a power-law spacing distribution for the faults that they sample.

Well #	Well orientation	N	Distribution	R <sup>2</sup>	slope	Cv	Clustering	Fracture Density (fracture /m)
3	N-S	33	exponential	0.98	1.34	1.09	random	0.004
7	N-S	42	exponential	0.95	0.39	0.80	anti-clustered	0.003
8	N-S	41	exponential	0.97	0.39	0.84	anti-clustered	0.003
9	N-S	42	exponential	0.99	0.35	0.91	anti-clustered	0.004
10	N-S	34	exponential	0.98	0.42	0.74	anti-clustered	0.003
12	N-S	38	exponential	0.98	0.41	0.82	anti-clustered	0.003
13	N-S	35	exponential	0.98	0.38	0.79	anti-clustered	0.003
19	E-W	34	exponential	0.99	0.36	0.78	anti-clustered	0.003
20	E-W	36	exponential	0.99	0.26	1.13	clustered	0.003
23	E-W	33	exponential	0.99	0.35	0.77	anti-clustered	0.002
26	E-W	46	exponential	0.99	0.28	0.89	anti-clustered	0.003
27	E-W	40	exponential	0.96	0.32	0.95	anti-clustered	0.003
28	E-W	41	exponential	0.97	0.28	0.77	anti-clustered	0.003
29	E-W	50	exponential	0.97	0.32	1.03	random	0.004
31	E-W	39	exponential	0.99	0.35	0.93	anti-clustered	0.003
38	NE-SW	49	exponential	0.98	0.20	0.87	anti-clustered	0.002
39	NE-SW	43	exponential	0.97	0.25	0.60	anti-clustered	0.002
40	NE-SW	32	exponential	0.97	0.20	0.67	anti-clustered	0.001
43	NE-SW	44	exponential	0.98	0.24	0.83	anti-clustered	0.002
47	NW-SE	41	exponential	0.99	0.50	0.74	anti-clustered	0.005
48	NW-SE	43	exponential	0.99	0.49	0.96	anti-clustered	0.005
49	NW-SE	39	exponential	0.98	0.40	0.89	anti-clustered	0.004
52	NW-SE	32	exponential	0.98	0.47	0.91	anti-clustered	0.003
53	NW-SE	34	exponential	0.92	0.47	1.07	random	0.004
55	NW-SE	37	exponential	0.98	0.50	1.22	clustered	0.004
60	NW-SE	33	exponential	0.98	0.42	0.95	anti-clustered	0.003
64	NW-SE	35	exponential	0.93	0.44	0.76	anti-clustered	0.003
67	NW-SE	38	exponential	0.97	0.33	0.80	anti-clustered	0.004
68	NW-SE	33	exponential	0.97	0.46	0.70	anti-clustered	0.004

**Table 4.2:** Spatial attributes of faults from pseudo-wells created in the Clair top basement seismic horizon. This table shows all pseudo-wells that exhibit an exponential spacing distribution for the faults that they sample.

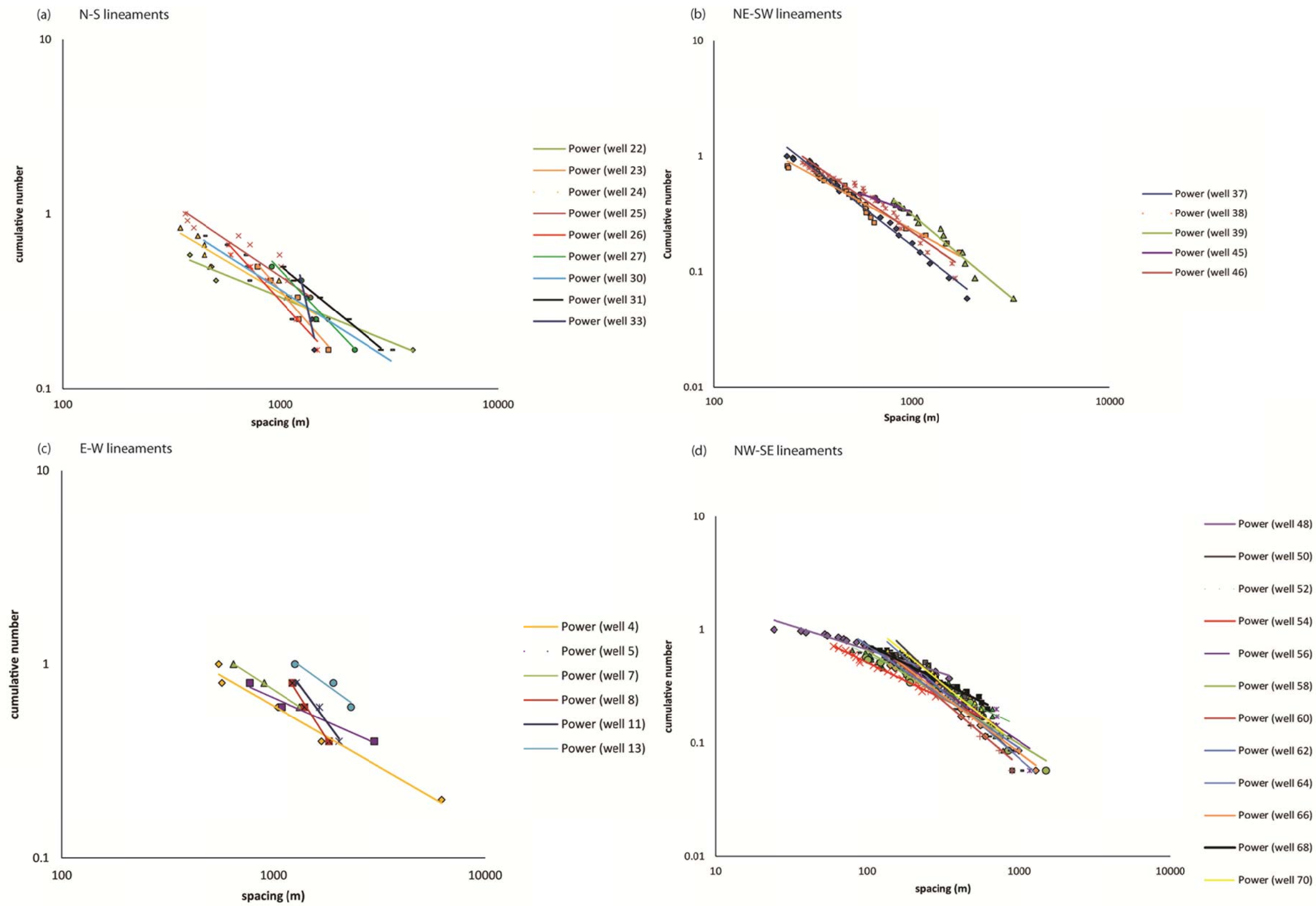
#### 4.2.4.1 – Regional fault lineament spatial distributions

The population distribution plots show two main types of spatial distributions; exponential and power-law (for examples see McCaffrey et al., 2003, Johnston et al., 1994). Pseudo-wells of every orientation show a combination of both these spacing distribution trends, with the majority (62%) of samples exhibiting exponential distributions. Those samples, which are represented by power-law distributions, never extend over more than one order of magnitude, most commonly between 100 and 1000 metre spacing values (*Figure 4.9b*).

The exponential distributions are strong and statistically significant with maximum spacing values in the range of 1000 to 1600 metres (*Figure 4.9b*). This is confirmed by the  $R^2$  value of each exponential trend line which varies from 0.92 to 0.99 (see *Table 4.2*), suggesting that the majority of trends fit an exponential distribution extremely well. The portions of other spacing distributions which could be considered power-law also have good fits to their trend lines ( $R^2$  values between 0.90 and 0.99, *Table 4.1*), but these sections include, in most cases, fewer than 30 data points, and therefore, should be classed as insignificant.

In order to test the effect that the sampling technique has on the spacing distribution results, each fault set (based on azimuth) was analysed individually. For example, NE-SW trending lineaments were sampled by NW-SE trending pseudo-wells. The results of this study are shown in *Figure 4.10*.

NE-SW trending lineaments, when analysed on their own, show consistent power-law distributions for pseudo-wells trending NW-SE (*Figure 4.10b*). The power-law distributions for this dataset extend over one order of magnitude (or slightly more) between 100 and 1000 metre spacing values. NW-SE trending lineaments (measured from NE-SW trending pseudo-wells) also show consistent power-law distributions with spacing values between 100 and 1000 metres (*Figure 4.10d*). Both N-S and E-W trending lineaments do not show any prominent spacing distributions (*Figures 4.10 a & c* respectively), which is probably directly related to the small number of fault lineaments in each of these fault sets.



**Figure 4.10:** Population distribution plots for individual fault lineament trends from the basement regional study. **(a)** N-S lineaments **(b)** NE-SW lineaments **(c)** E-W lineaments **(d)** NW-SE lineaments

#### 4.2.4.2 – Fractal dimensions (D-value)

The fractal dimension D-values is the slope of those samples with robust power-law distributions. For 1-dimensional samples D-values should converge around  $D = 1$ , with values  $>1$  representing samples that over-sample closely spaced fractures and values  $<1$  representing samples that under-sample closely spaced fractures (Pickering et al., 1995). Where pseudo-wells show power-law distributions, there is a wide variation in the D-values (0.37 to 1.76, *Table 4.1*) suggesting that many of these samples contain biases created by the over- or under-estimation of closely spaced fractures.

#### 4.2.4.3 – Coefficient of variation (CV)

The coefficient of variation for the pseudo-well data that exhibit power-law distributions ranges from 0.66 to 1.05, with the majority of samples having CV values less than one (*Table 4.1*). Those pseudo-wells with exponential fault spacing distributions show CV values between 0.61 and 1.22 (*Table 4.2*). Again most samples in this exponential group have CV values less than one. In both the power-law and exponential samples there does not appear to be a pattern to the CV values in relation to the pseudo-well orientation.

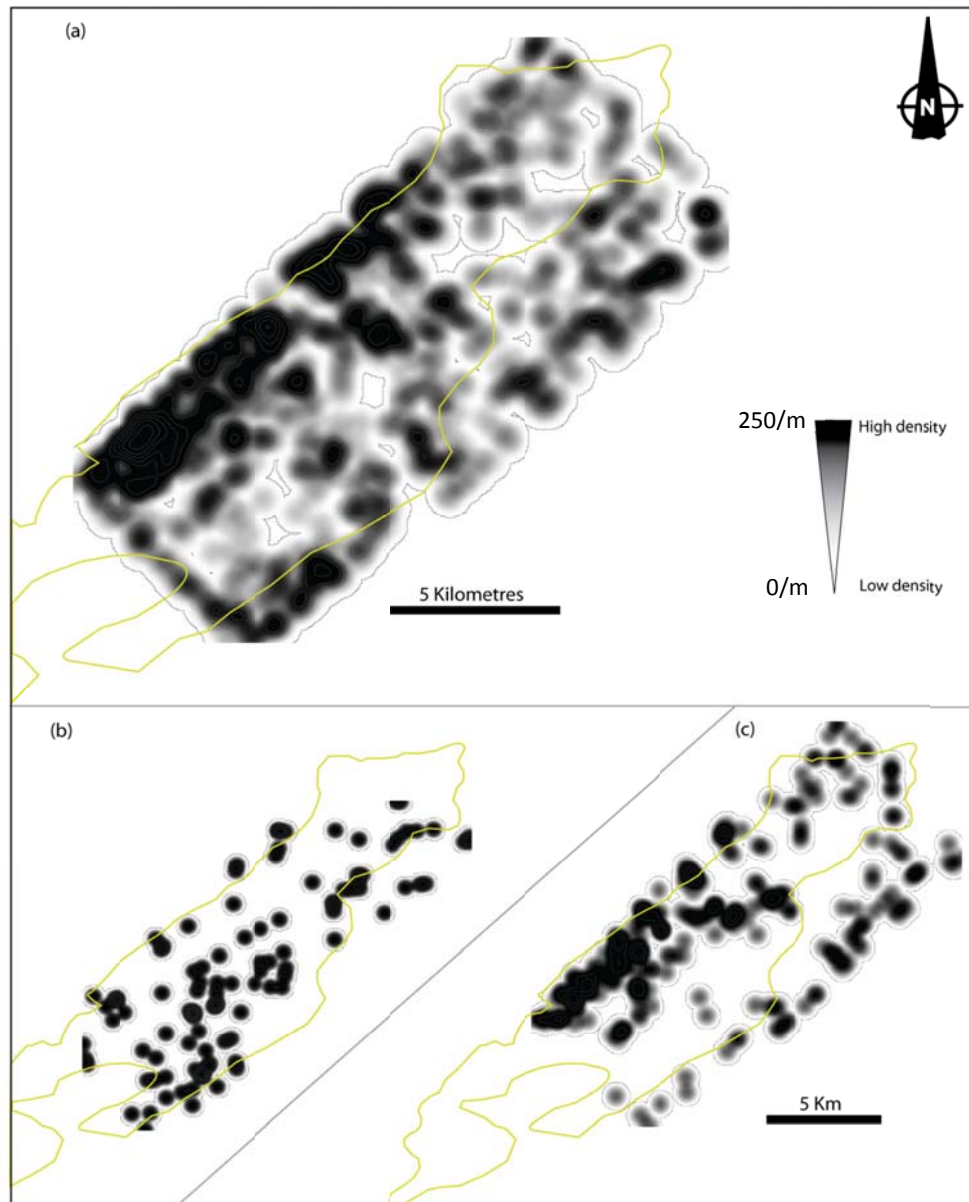
#### 4.2.4.4 – Fault density (FD)

*Tables 4.1 & 4.2* also contain data on the fault density for each pseudo-well. For both power-law and exponential samples, the mean fault density is 0.003 faults per metre which means that there are approximately 3 faults for every kilometre of line sample. This low fault density is a likely reflection of the low resolution of the seismic dataset and is not a true reflection of the natural spacing of the fault sets.

#### 4.2.5 – Regional fault lineament connectivity

Fault connectivity has been analysed in 2-dimensions by picking all the fault lineament intersections (nodes). This analysis shows where faults come into contact with each other, but does not consider fluid flow pathways between nodes, therefore the results only give a generalised appreciation of the fracture connectivity in the basement (*Figure 4.11*). For example, all the fault lineaments in this regional study are assumed to be vertical and therefore the connectivity using this analysis technique is also vertical. The connectivity density maps show that when all interpreted fault

lineaments are included, the connectivity is clearly more concentrated on the southwest Ridge area (*Figure 4.11a*). Fault lineaments picked at 1:50,000 scale show connectivity sporadically across the Clair Field (*Figure 4.11b*) which suggests that the larger, second order faults may provide connected pathways throughout the field rather than to specific, local areas. It is also known that second order faults have a more prominent trend (NE-SW) and therefore are less likely to be connected to each other. At 1:25,000 scale, fault lineament connectivity is denser towards the southwest of the Ridge area (*Figure 4.11c*), showing that smaller, third order faults have a wider range of orientations and hence, are more interconnected.



**Figure 4.11:** Density maps of lineament connectivity from the top Clair basement seismic horizon. These maps show the density of connectivity ‘nodes’ where different lineaments cross each other. **(a)** Connectivity of all the lineaments interpreted from the Clair basement. **(b)** Connectivity of lineaments picked at 1:50,000 scale. **(c)** Connectivity of lineaments picked at 1:25,000 scale.

#### 4.2.6 – Regional fault lineament spatial analysis: Discussion

Population distribution plot analysis shows that the majority of 1-dimensional sample lines (pseudo-wells) produced exponential distributions for regional fault spacing (*Figure 4.9*). It is important to emphasise that the exponential distributions obtained in this study may be primarily a consequence of the sampling process. These regional studies differ from those conducted at well scale or at outcrop as it is very difficult to sample only one prominent fault trend with each pseudo-well. At outcrop scale, for example, it is possible to take sample lines that are parallel or perpendicular to foliation or one particularly dominant fault set and therefore only sample the prominent fractures that are geometrically associated with these relative orientations. In those cases, as only one main fracture trend was sampled, the fractures show more clustered spacing attributes, resulting in power-law distributions. The Clair basement regional seismic results compare better to a regional study onshore where it is difficult to only sample one prominent fault orientation in each pseudo-well and therefore the datasets are less spatially clustered, resulting in stronger exponential distributions.

One way to test if there are underlying power-law relationships for spacing in the Clair basement regional dataset (similar to those determined from well or outcrop data) is to only sample faults in one particular orientation trend. This will ascertain if by separating out the main fault sets power-law distributions exist or that the regional Clair basement spacing data is inherently exponential in its distribution. The results of this test show that power-law distributions are more consistently apparent for both the NE-SW and NW-SE trending fault lineaments (*Figures 4.10b & d*) and not as obvious for the E-W and N-S trending fault lineaments (*Figures 4.10a & c*). This is likely because of the reduced number of lineaments in each of the E-W and N-S fault sets, resulting in many of pseudo-wells sampling less than ten faults. Although this technique results in more prominent power-law distributions for the larger fault sets, it raises questions about its geological validity. It is impossible to know from this analysis if all the different fault trend sets are independent of each other. Therefore it is not valid to treat each fault set as individual samples as it takes no account of the geological relationships between them. What this test does show is that the sampling technique is partially responsible for the exponential spatial distributions evident from many of the pseudo-well samples.

Population distribution plots also provide information on how each sample is biased by the over- or under-sampling of spacing values with respect to their fractal



(power-law) distribution (Pickering et al., 1995). Those spacing distributions which are power-law are associated with a D-value (*Table 4.1*), which for these 1-dimensional samples should converge on  $D = 1$ . Power-law samples from the regional fault lineament analysis of the Clair basement have a wide range of D-values (0.37 to 1.76, *Table 4.1*), which means that there is no consistency in how the spacing values of the faults are weighted: those with low D-values ( $< 1$ ) sample more faults which are widely spaced (relative to the pseudo-well) and those with high D-values that have more faults which are closely spaced. This wide variation in D-value across the power-law pseudo-well samples is likely to be an artefact of the fact that the power-law distributions have insufficient data points within them to be statistically significant.

The coefficient of variation (CV) provides more evidence to suggest that the power-law distributions seen in some pseudo-wells may in reality be weak exponential distributions. This is because nearly all of the pseudo-wells in this category have CV values less than one (*Table 4.1*), meaning that the faults are anti-clustered (regularly spaced), or in some cases (where the CV values gets close to one) random (Johnston et al., 1994). These anti-clustered relationships are more normally representative of exponential distributions and do not usually reflect datasets which are power-law in nature. Therefore it is likely that those samples which exhibit power-law distributions, instead, represent weakly defined exponential fault spacing distributions, which is consistent with the other pseudo-well samples from across the Clair basement regional study.

All of the spatial attributes (namely CV) from the exponential pseudo-wells are consistent with the interpretation of exponential fault spacing distributions (*Table 4.1*). The majority of the exponential samples show CV values less than one, suggesting that the fault spacing for these samples is slightly anti-clustered. The lack of a relationship between clustering (CV values) and pseudo-well orientation suggests that fault spacing distributions do not show distinct characteristics depending on the sampling direction.

Fault density analysis conducted for each pseudo-well sample resulted in a mean value of three faults per kilometre across the Clair Field (*Table 4.1 & 4.2*). As previously mentioned this low fault density value is likely a result of the low-resolution of the seismic survey data rather than a true reflection of the natural fault spacing within the basement. This is strongly supported by the evidence from the Clair core datasets (see

*Section 4.3* of this chapter), which exhibit fault spacing values on a metre scale and fracture spacing values on a centimetre scale (up to 15 per metre).

Fault connectivity analysis results suggest that first, second and third order faults are all involved simultaneously in the connectivity of the Clair Field and that larger faults are not independently responsible for creating potential fluid flow pathways through the basement (*Figure 4.11*). This study highlights the areas in the basement where fault connectivity is potentially high, but does not consider which fault sets are thought to be open or closed because there is little regional evidence to be able to determine these attributes for the basement faults. Work conducted on the basement core samples attempts to provide more information on the open and closed fault and fracture sets (see *Section 4.3* of this chapter). Evidence from fault lineament interpretations of the sedimentary cover sequence horizons suggests that many of the faults interpreted from the basement (with the exception of the NW-SE trending faults) extend up into the overlying sediments (*Figures 4.7 & 4.8*). It is therefore possible that the connectivity pattern interpreted from the top basement horizon is also present within the Clair Group sediments. It should be noted that at a regional scale, connectivity is likely to be lower in the sediments because no NW-SE faults extend past the basement and therefore do not provide any pathways (potentially for fluid flow) in the cover sediments.

#### **4.3 –Fracture analysis from Clair basement well data**

To supplement the regional fault analysis, the basement well data has also been analysed in detail. The majority of this analysis has been conducted using basement core samples, where time has been spent logging the core and describing the lithology and nature of each fracture as they are encountered. There are three main caveats affecting the understanding of the fracture network within the Clair basement. The first is that there are very few well cores which sample the basement, thus limiting the data available for studying the fractures at this scale. Secondly, most of the basement core data comes from vertical wells so it is likely that the majority of basement samples under-sample steeply-dipping or vertical fractures. Finally, very little of the Clair basement well core data is orientated, thus making it nearly impossible to determine the main fracture trends present within the basement at this scale.

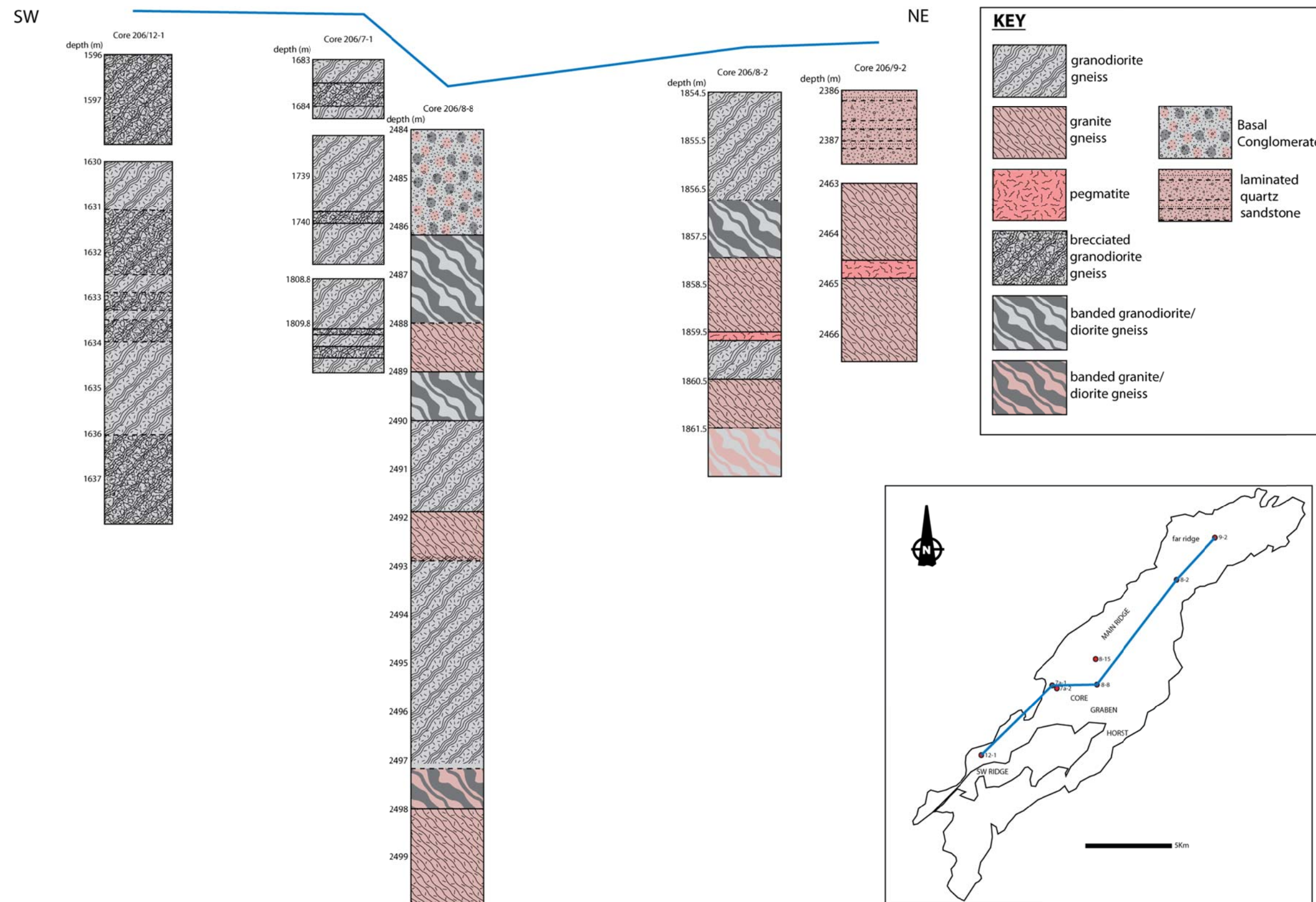
Core samples used in this well analysis are from wells 206/7a-2, 206/8-8, 206/12-1 and 206/9-2. 206/8-15 has image log data from the basement, specifically OBMI (oil based micro-imager) and UBI (ultrasonic borehole imager). This section describes the geology and fault rocks seen within core samples of the basement and illustrates the orientation analysis and statistical analysis of the fracture and fault spacing at well scale.

#### 4.3.1 – Method for core logging and spatial analysis of fractures

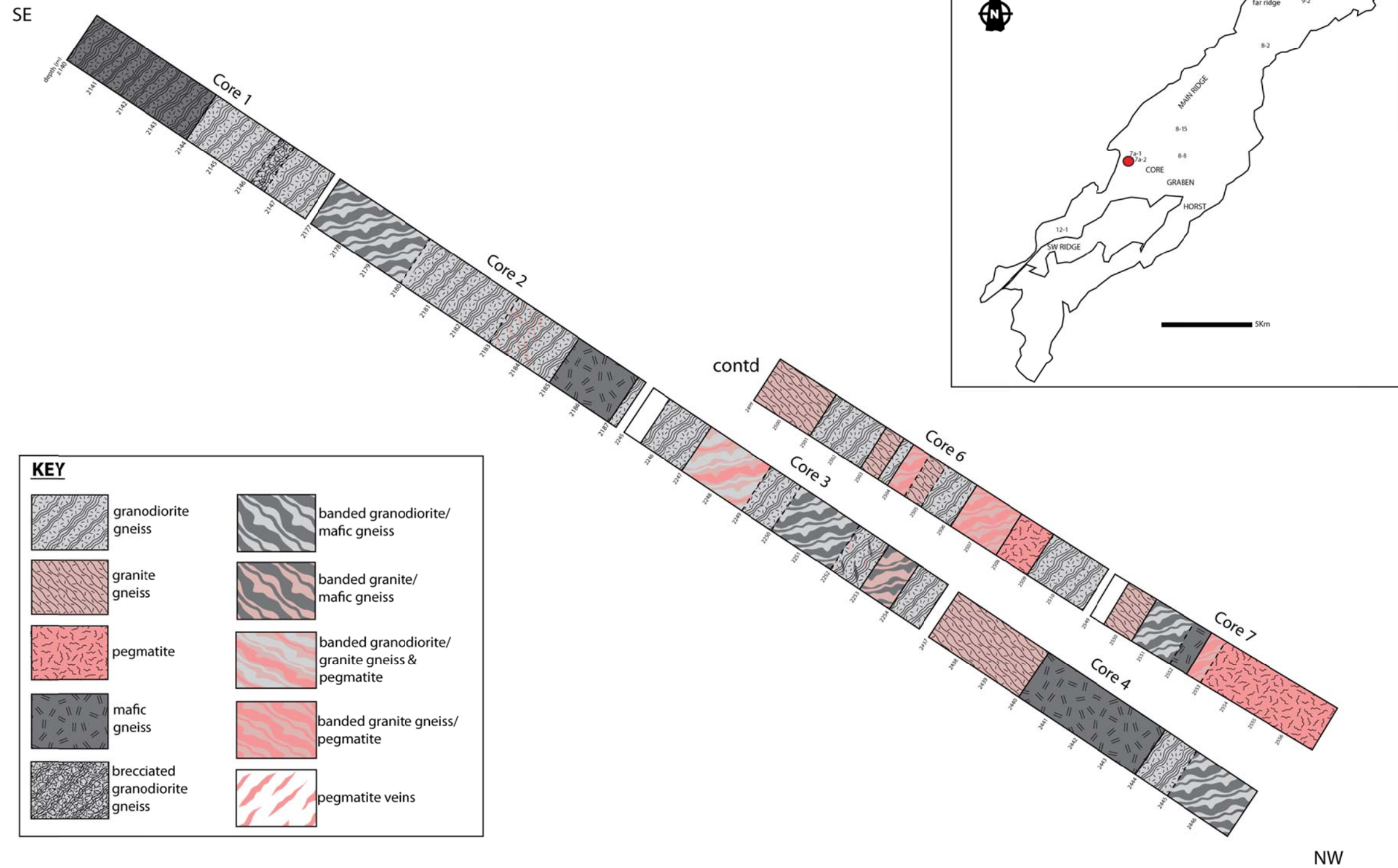
Both image logs and cores were available for different regions within the Clair basement and were used to scrutinise the fault and fracture sets present within the basement in as much detail as possible. Core samples have been found to be the most useful source of fracture data as they can be studied down to millimetre scales compared to the image log data where the resolution is lower (high-resolution OBMI has a resolution down to 4cm) and therefore only larger fractures are recognisable. As a result, most of the fracture analysis presented below comes from core.

All changes in lithology and ductile fabric in the core samples were recorded in addition to logging all visible veins, fractures and faults (these brittle structures will be referred to as fractures unless, specified), including their fault rock type, aperture, orientation (if applicable) and cross-cutting relationships (see *Section 1.6.5* for more details). Descriptive logs for all basement core samples (including photograph logs) and thin section analysis can be found in *Appendix 4*. Also *Figures 4.12 & 4.13* show generalised lithological logs for each of the basement core samples.

Along with lithological logs, a detailed fracture log was produced for 206/7a-2 and this is shown in *Figure 4.16*. Fracture spacing was logged using a 1-dimensional sample line placed down the centre of each core and data was collected in the same manner as the onshore outcrop 1-dimensional line samples (*Section 1.6.5* and *Section 3.3.1*). The fracture data were recorded in an Excel spreadsheet and then used for statistical analysis of fracture spacing attributes. The data analysis has been conducted in a similar manner to that of both the regional data and the onshore datasets (*Section 1.6.5*). Once again, population distribution plots, fracture density and the coefficient of variation were all used (see *Chapter 1* for details on the statistical methods).



**Figure 4.12:** Generalised lithological logs for all the vertical wells that sample the Clair basement. Blue line links the well locations on the map inset.

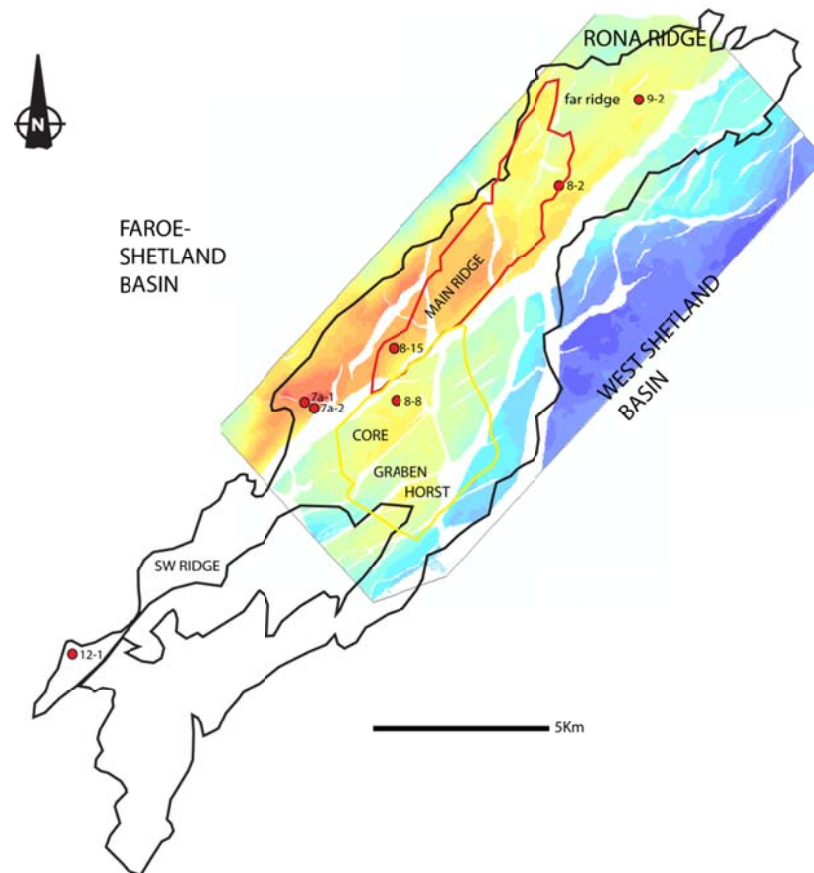
**Core 206/7a-2**

**Figure 4.13:** Generalised lithological log for well 206/7a-2. Note that it is a series of 7 core sections (although only 6 are included here) with Core 1 at the SE end of the well.



#### 4.3.2 – Clair basement well locations and descriptions

Well data is relatively sparse in the basement with those samples available spread across the entire Clair Field area. *Figure 4.14* shows the location of all the wells in the basement and their position relative to the major structures and development regions identified across the field. The majority of basement wells are vertical, with only one well drilled horizontally through the basement. This horizontal well (206/7a-2) is also the only basement core sample that is orientated (N290°) and therefore it provides a more complete sample of the basement fractures. Much of the description and analysis given in the following sections of this chapter focuses on well 206/7a-2.



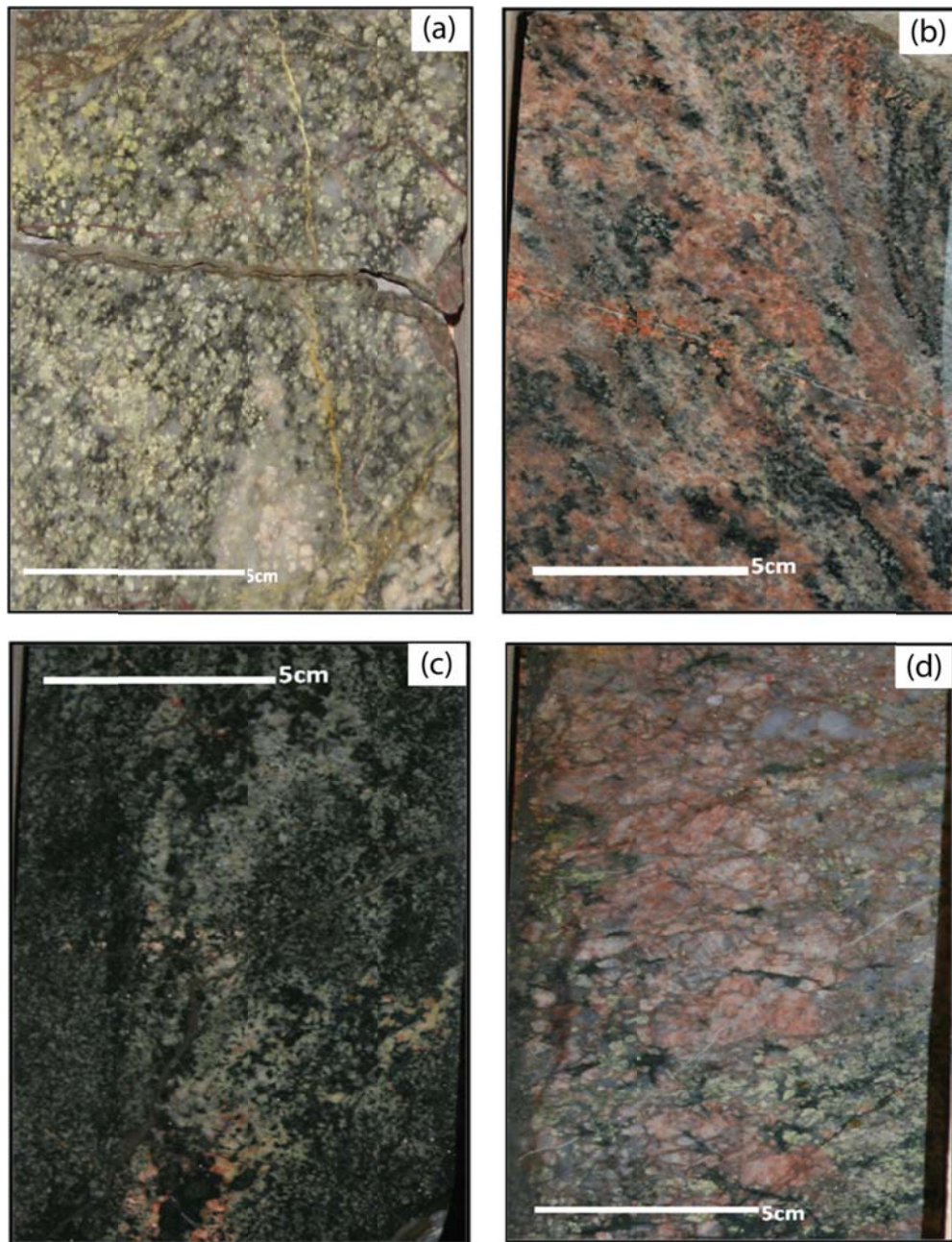
**Figure 4.14:** Outline of the Clair basement (provided by ConocoPhillips (U.K.) Ltd.) overlain on the depth to basement seismic horizon map. The map shows the locations of wells that sample the basement. All of the well numbers shown have the prefix 206/: for example 206/7a-2. Yellow outline indicates Clair Phase 1 development area. Red outline is for Clair Phase 2 development area.

#### 4.3.2.1 – Well 206/7a-2

Well 206/7a-2 lies towards the south of the Phase 2 region on the basement ridge (*Figure 4.14*). It was drilled at high angles of deviation in the Clair Group sediments and then levelled off to horizontal in the basement, with its primary purpose to sample so called ‘fracture corridors’ that were believed from previous well tests to provide hydrocarbon drainage zones connecting the basement and the Devonian/Carboniferous sediments (e.g. Falt et al., 1992, Coney et al., 1993). 206/7a-2 was drilled so that it ran adjacent and approximately parallel to a large NW-SE trending fault that was thought to offset the main ridge structure. It has a trend of N290° which has been used to orientate the fractures found within this core sample. ‘Spot’ cores were collected throughout the basement portion of the well with a combined length of 50 metres. The basement core samples start at a down well depth of 2148m and finish at 2559m meaning that at least 411m of the well was drilled into basement.

##### 4.3.2.1.1 – Lithology

Well 206/7a-2 core samples provide a good insight into the basement lithology and preserves evidence to show how fracture density is affected by changes in lithology. The majority of the basement in this core comprises granodiorite gneiss with minor components of granite gneiss, diorite gneiss and pegmatite. *Figure 4.13* shows generalised lithological basement logs for well 206/7a-2 core samples. Also see *Figure 4.15* for examples of the different basement lithologies.



**Figure 4.15:** Photographs of basement core samples from well 206/7a-2 showing the variation in lithology seen within the Clair basement. **(a)** Granodiorite gneiss **(b)** Granite gneiss **(c)** Diorite (basic) gneiss **(d)** Pegmatite.



Granodiorite gneiss (*Figure 4.15a*) occurs preferentially towards the 'top' of the basement section of the well (SE portion of the well, see *Figure 4.13*). The lithology is characteristically light grey in colour with dark grey patches peppered throughout. It occurs in 'layers' that are thicker than any of the other lithologies present in the basement (the widest continuous granodiorite gneiss layer is 5m wide, *Figure 4.13*). In the southeast 'top' section of 206/7a-2 (mainly core samples 2, 3 and 4) the granodiorite gneiss is inter-layered with thin basic gneiss layers that are no more than 15cm thick (*Figure 4.13*). It is also observed with small lenses (no more than 10cm long) of granite gneiss and basic gneiss (*Figure 4.13*).

The mineralogy of the granodiorite gneiss in core samples from well 206/7a-2 typically comprises: quartz (30%) + plagioclase (40%) ± pyroxene ± k-feldspar ± chlorite ± orthoclase ± epidote ± amphibole (*Figure 4.15a*). Plagioclase, macroscopically, displays large numbers of intra-crystal fractures and is closely associated with secondary epidote. Orthoclase feldspar occurs throughout all of the granodiorite gneiss in the cores from well 206/7a-2 and this locally has a large crystal size (up to 2cm). Epidote occurs in patches throughout the granodiorite gneiss in varying volumes between <5% and >80% (for example, 32.90m along 206/7a-2, *Appendix 4*).

In thin section, the granodiorite gneiss from well 206/7a-2 is coarsely crystalline (see *Appendix 4*). Quartz is almost completely recrystallised and shows a polycrystalline texture. Other large crystals seen in thin section are of plagioclase and k-feldspar and these appear highly altered (intra-crystalline micro-fractures and very fine clinozoisite crystal overgrowths). Small crystals of chlorite are also evident throughout the granodiorite gneiss thin section samples from 206/7a-2. They appear to overprint all pre-existing minerals and structures. Small quantities of hornblende crystals (<5%) are also observed over-printing pyroxene.

Granite gneiss (*Figure 4.15b*) is the second most common lithology seen in well 206/7a-2, and across the basement samples (*Figures 4.12 & 4.13*). In well 206/7a-2 granite gneiss was only observed towards the 'bottom' northwest part of the core samples (cores 3, 4, 5 and 7, see *Figure 4.13*). The rock appears pink/light grey in colour and occurs in close association (inter-layering) with pegmatite layers. Commonly, the granitic gneiss is either coarse-grained (1cm crystals) or very coarse-grained (2cm crystals) and it may contain finer patches of epidote. In well 206/7a-2 the granitic gneiss is observed to be inter-layered with pegmatite and granodiorite gneiss in the northwest

section of the core (cores 3 and 5 have the best examples, *Appendix 4*). This inter-layering is on a 10cm scale. Generally, there is a sharp contact between the granodiorite gneiss and granite gneiss layers (e.g. 2439m down well 206/7a-2, see *Appendix 4*).

The key mineralogy is quartz (40%) + biotite (10% - 15%) ± alkali feldspar (orthoclase- 35 - 40%) ± plagioclase (<10%) ± epidote (<2%). Quartz and biotite occur as relatively fine crystals when compared to the larger feldspar crystals. Orthoclase and quartz crystals are segregated from biotite and plagioclase crystals into distinct bands. Biotite occurs as fine grained crystals which are generally aligned and highlight the ductile fabric within the basement core samples (this fabric generally trends NW-SE). Epidote occurs in discrete patches and appears to be overprinting plagioclase feldspar.

A dark grey/ black basic gneiss (*Figure 4.15c*) is also present within well 206/7a-2, but it occurs less frequently and normally in thinner bands (<2m) than either granodiorite gneiss or granite gneiss. Most commonly the basic gneiss occurs as thin bands (20cm) inter-layered with granodiorite gneiss and occasionally the granite gneiss (see *Figure 4.13*). The basic gneiss most commonly occurs in streaky lenses (up to 30cm in size) within the granodiorite gneiss (for example see, 2252m down 206/7a-2, *Appendix 4*) and granite gneiss where it forms a noticeably finer-crystalline rock (crystals 2-5mm in size).

The main mineralogy seen within the basic gneiss is as follows: plagioclase – mainly albite (40%-60%) + orthopyroxene (up to 20%) ± epidote (up to 30%) ± sericite (up to 20%) ± opaque minerals (maximum 10%). In some parts of the 206/7a-2 core plagioclase alteration is extensive with upwards of 50% of the feldspar completely replaced by either chlorite or epidote.

Thin section sample 7a-2-4 (from 2442m down well 206/7a-2, see *Appendix 4*) shows 60% albite crystals which are up to 5mm in size. Chlorite overgrowths are responsible for the majority of the plagioclase alteration in this sample. The chlorite crystals are less than 1mm in size and do not appear to have a preferred orientation. It is apparent that the plagioclase crystals have grown around ortho-pyroxene crystals which do not appear to have a preferred orientation. Epidote is also seen within this thin section sample in minor volumes (<5%). Where present, epidote is in small patches (no bigger than 5mm) closely associated with the chlorite mineralisation.

Pegmatite layers (*Figure 4.15d*) are observed towards the bottom of well 206/7a-2 (northwest end) where they occur in association with the other main

lithologies present in the basement (*Figure 4.13*). Generally pegmatite occurs as bands inter-layered (a maximum of 4m thickness) through the granite gneiss, but it can also occur as lenses (up to 20cm in width) in either granodiorite or granite gneisses (e.g. 2247m down well 206/7a-2, *Figure 4.13* and *Appendix 4*). The contacts between the pegmatite layers and other basement lithologies are most commonly sharp.

The common mineralogy is orthoclase (up to 90%) + quartz (up to 70%) ± biotite/chlorite (~10%) ± plagioclase (~5%) ± epidote (5%). Orthoclase crystals are highly fractured and have large crystal sizes up to 10cm. Epidote is also apparent throughout the pegmatite layers where it occurs in patches with crystal sizes between 1.5 and 2cm.

In thin section (sample 7a-2-6 from well 206/7a-2, see *Appendix 4*) orthoclase has very large crystal sizes and composes 90% of the rock volume. These large orthoclase crystals show signs of chemical alteration with the edges of the feldspar crystals being replaced by very fine (<0.1mm) epidote crystals. The rest of the rock volume consists of quartz (crystals up to 1cm in size) that exhibits undulose extinction and chlorite, which has crystallised between the large orthoclase crystals. In this thin section sample the chlorite crystals form small clusters where they have over-printed previous biotite growth.

Well 206/7a-2 exhibits a foliation that is weakly defined and trends predominately N-S to NNW-SSE, although it does have variations to this trend (see photo-logs in *Appendix 4*). The foliation dips steeply and is pervasive across the width of the core. It is most apparent in the granodiorite gneiss sections of the core and also in zones of the core where different lithologies are inter-layered with each other (e.g. 2550m down well 206/7a-2, *Appendix 4*). Foliation is never apparent in the pegmatite layers.

#### 4.3.2.2 – Well 206/8-8

206/8-8 is a vertical well which lies in the Core Area of the Clair Field (Phase 1 development area, see *Figure 4.14*). The well sits directly adjacent to the Ridge Fault and enters the basement approximately 400m lower than it would on the ridge. It includes a 16m long piece of core from the basement at a depth of 2484m (see *Appendix 4* for the full descriptive log). The core is not orientated, so this well can only be used descriptively and for fracture spacing analysis.

The top 2 metres of the 206/8-8 core shown here includes the Clair Group Basal Conglomerate (there is a much larger section of the core from the Basal Conglomerate in this well, but it has not been included in this study, see *Figure 4.12*). This conglomerate consists of large clasts (10->20cm) of granite gneiss (60%), granodiorite gneiss (25%), and basic gneiss (15%), all supported by smaller clasts (<1cm) and laminated (mm-scale), grey arenitic siltstone matrix. The conglomerate is occasionally inter-bedded with fine grained units of laminated (on mm scale) arenitic sandstones and there is some evidence of compaction (laminations get thinner between conglomerate clasts) within the matrix of the conglomerate. The contact between the Basal Conglomerate and the basement is gradational because the top of the basement has been weathered and eroded before the conglomerate was deposited on top.

Below the Basal Conglomerate, the basement consists of inter-layered granodioritic and basic gneisses (basic gneiss layers are up to 10cm thick, *Figure 4.12*). The granodiorite gneiss has a similar mineralogical composition to that seen in the core from well 206/7a-2. It forms layers that are up to 4 metres thick (*Figure 4.12*). Core from well 206/8-8 also contains granite gneiss in layers that are no more than 2 metres thick (*Figure 4.12*). This granite gneiss is depleted in quartz (25% of the total volume) in comparison to the granite gneiss seen within well 206/7a-2. There are zones with the 206/8-8 core where coarse crystalline granite gneiss (5-10mm) is inter-fingered with fine crystalline (<1mm) basic gneiss. The contacts between granodioritic and granitic gneiss layers in this core are gradational with no discrete boundary; pegmatite layers are absent.

Foliation is not well defined in core 206/8-8. Where it can be recognised, it has a dip between 50° and 85° relative to the walls of the core.

#### 4.3.2.3 – Well 206/8-2

206/8-2 is located in the main basement ridge ~8km north of well 206/7a-2 (*Figure 4.14*). It is, again, a vertical well and samples nearly 8m of the basement only.

The lithologies seen within this well includes granite gneiss, granodiorite gneiss, basic gneiss and pegmatite (*Figure 4.12*). Granite gneiss is the most prominent lithology here with the other rock types occurring as thinner layers (up to 1m thick) inter-layered with each other throughout the core sample (*Figure 4.12*). The granite gneiss is typically coarsely crystalline (crystal size up to 1cm) and is composed of quartz + orthoclase +

biotite and minor volumes of epidote. Some of the granite gneiss contains patches that are rich in epidote (>80%). Pegmatite occurs as a 20cm thick layer 1859m down well 206/8-2. It is recognisable by its dark pink colour and the very large crystals (10cm) of orthoclase and quartz (crystal size up to 5cm). The orthoclase crystals within the pegmatite layers typically exhibit intra-crystal fractures which are associated with concentrations of small epidote crystals (crystal size up to 5mm).

The 206/8-2 core shows little evidence of a ductile fabric. Where it is apparent, its orientation is highly variable (average dip 45°).

#### 4.3.2.4 – Well 206/12-1

Well 206/12-1 has been drilled vertically in the southwest region of the Clair Field (*Figure 4.14*) and is situated on the basement ridge in an area not covered by the seismic data accessible in this project. It consists of two short ‘spot’ cores of the top of the basement with a total length of 10m (*Figure 4.12*).

The lithology in the 206/12-1 core is almost entirely granodiorite gneiss with a similar composition to the comparable lithology in well 206/7a-2 (*Figure 4.12*). In some sections of the 206/12-1 core the granodiorite gneiss has approximately 15% orthoclase content and these feldspars have crystal sizes up to 3cm (~1893m depth, *Appendix 4*).

In thin section 206/12-1 granodiorite gneiss (sample 12-1-1, see *Appendix 4*) contains large crystals of plagioclase (albite) and quartz (up to 5mm), which are entirely recrystallised. The majority of the euhedral albite crystals are highly altered and are being replaced by very fine crystalline (<0.1mm) epidote crystals. ‘Mats’ of very fine crystalline sericite (<0.1mm) are also present within the sample where they are replacing the albite crystals at their edges. The chlorite crystals do not have any preferred orientation. Pyrite is clearly visible in this thin section sample, where it is found in vugs within the granodiorite gneiss. The origin of this pyrite mineralisation will be discussed in *Section 4.3.2.7*.

There is little evidence of a ductile fabric within core from well 206/12-1 and because this core is highly brecciated (this will be discussed in *Section 4.3.2.7*), where foliation does exist it is impossible to determine any relative orientations.

#### 4.3.2.5 – Well 206/9-2

206/9-2 was drilled in the north of the Clair Field, again on the ridge (*Figure 4.14*). It is a vertical well with 4.5m of core in the basement.

At this location, the basement is composed of coarsely crystalline granite gneiss (crystals up to 2cm in size) beneath a conglomerate containing entirely granite gneiss clasts. The clasts within the conglomerate are on average 2cm in size. The conglomerate at the top of the core sample is matrix supported and has a matrix of poorly-sorted arenitic sandstone. The nature of the contact between the conglomerate and basement rocks is unknown because ~76m of the well is missing from the core samples.

The mineralogical composition of the granite gneiss is quartz (40%) + plagioclase (up to 30%) + orthoclase (20%) ± chlorite/muscovite (up to 20%) ± epidote (5%). The feldspar crystals within the granite gneiss can be up to 3cm in size with an average size of 1cm. Pegmatite is also present within this basement core sample in thin layers (5-10cm thick), with crystal sizes coarser than the surrounding granite gneiss (crystal size up to 10cm).

In thin section, the granite gneiss is 60-65% polycrystalline quartz (sample 9-2-1a & b, see *Appendix 4*). The feldspar (albite 80% & microcline 20%), which forms large euhedral crystals, is altered and overprinted with very fine crystals of epidote (over 90% of the feldspar is altered). These feldspar crystals are also fractured (intra-crystalline) and some of the plagioclase crystals exhibit a perthitic texture. Chlorite and muscovite compose the rest of the rock. Both have much smaller crystal sizes and in some places the chlorite replaces pre-existing biotite. Both of these minerals are observed around the crystal edges of the larger feldspars where they do not exhibit a preferred orientation.

The core from well 206/9-2 shows a weakly defined foliation. This foliation has a range of dips between 65° and 30° relative to the walls of the core.

#### 4.3.2.6 – Well 206/8-15

206/8-15 is a vertical well which lies on the eastern edge of the basement ridge 2km northeast of well 206/7a-2 (*Figure 4.14*). It has only image log data (OBMI & UBI) which covers both the basement and cover sediment sections seen in the Clair Field. It does not have any core samples, so no examination of the basement lithologies and fault rocks can be made from this well.

#### 4.3.2.7 – Lithology Discussion

There are four distinct lithologies present within the basement core samples (granodiorite gneiss, granite gneiss, basic gneiss and pegmatite, *Figures 4.12 & 4.13 and Appendix 4*) with mineralogies that are generally consistent between different wells. All seem most likely to have a magmatic origin in terms of the protolith, i.e. they are orthogneisses. Throughout the core samples there is evidence of compositional banding, with the four lithologies commonly seen to be inter-fingering with each other (particularly in well 206/7a-2, see *Figure 4.13*). This compositional banding suggests that the rocks have been flattened and stretched through time and highlights the intense ductile deformation that the basement rocks were subjected to early in their geological history. Similar compositional banding is observed in the onshore Lewisian where it is attributed to the many phases of ductile deformation known to have affected these rocks (e.g. Park, 2009). They are completely recrystallised suggesting deformation under elevated temperatures and pressures consistent with amphibolite facies (or higher) (Passchier and Trouw, 2005). They are therefore typical mid- to lower crustal basement gneisses and appear on lithological and textural grounds to be comparable to the Lewisian Gneiss Complex seen within the onshore analogue used for this study. See *Chapter 2* for a full description and discussion of the early history of the Clair basement rocks.

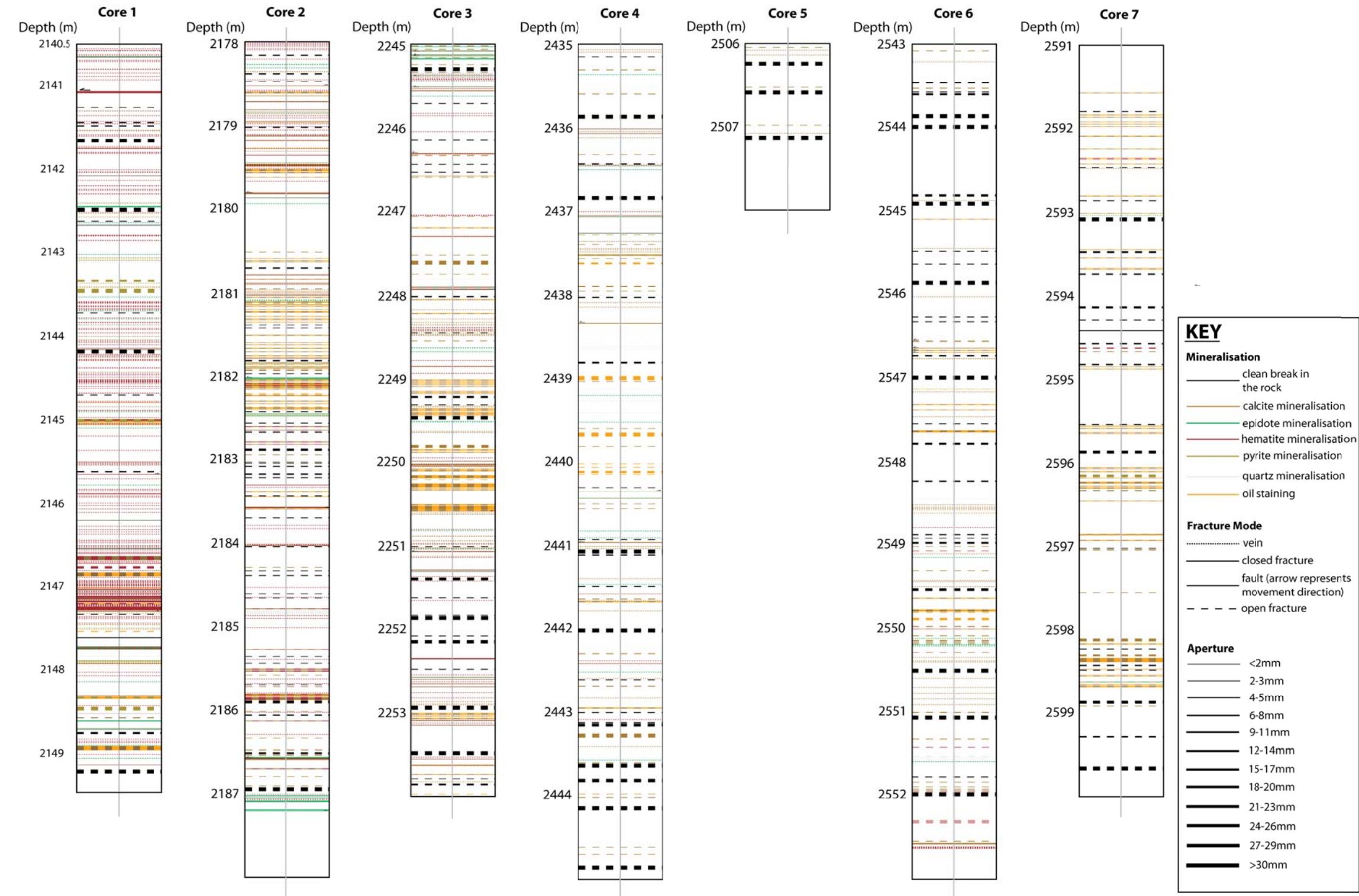
In all basement samples, there is evidence of retrogression during exhumation. For example, plagioclase is widely replaced by secondary epidote, clinozoisite and sericite which are known products of the alteration of anorthite-rich plagioclase to albite-rich plagioclase due to retrograde metamorphism. Green amphibole (hornblende) is seen replacing pyroxene (e.g. in sample 7a-2-3 from well 206/7a-2, *Appendix 4*) and chlorite partially to completely replaces biotite in many lithologies.

#### 4.3.2.8– Veins, fractures and faults

Fractures from the Clair basement have been geologically classified using all the material from the available basement core samples. These lengths of core have been logged in detail for fracture mineralisation, orientation, spatial attributes and other characteristics to gain as much information as possible from this limited dataset. Photographs and thin sections have also been used to fully characterise the host rock and the fracture sets. *Figure 4.15* shows an abstract fracture log from well 206/7a-2 which characterises all of the main fracture sets seen within the Clair basement. The detailed core fracture logs and photographs can be found in *Appendix 4*.

This chapter section focuses on describing and characterising the different types of fractures seen within the basement cores (using observation of the core samples and thin sections) and looks at any crosscutting relationships to ascertain the relative age of different fracture sets. The fractures have been split into categories based on mineral fill as each of the fracture and vein systems identified are associated with specific mineral fills and the associated cross-cutting relationships allows inferences on the fracture chronology to be made. The characteristics of each fracture set are described in the following sections, with the oldest sets described first. The fracture set descriptions given below focus mainly on the core samples from well 206/7a-2 because this well provides the most complete sample of the fracture sets within the Clair basement.



**CORE 206/7a-2**

**Figure 4.16:** Fracture log for well 206/7a-2. It highlights the complex nature of the fracturing present within this basement core sample. Note that this is an abstract log representing a 1D line traverse: none of the faults, fractures or veins have been orientated.

#### 4.3.2.8.1 – Epidote/hematite and quartz fractures and veins

Epidote, hematite and quartz mineralised veins and shear fractures are evident throughout all the basement core samples and within clasts of basement gneiss included within the Basal Conglomerate (in well 206/8-8). Although these fractures are present throughout the basement core samples, the descriptions below focus on data from well 206/7a-2 because it has the largest and most varied dataset. From this well dataset, it is apparent that the majority of hematite, epidote and quartz filled fractures are found towards the southeast (top) end of the core samples (the fracture density for the epidote/hematite/quartz fractures in Core 1 is 15.93 per metre compared to Core 6 where there is 1.35 fractures per metre – see *Figure 4.15*).

Most commonly, hematite is found in mineral veins which have an average thickness (aperture) of <1mm but, in some case it forms an outer layer of much thicker veins that are in-filled mainly with carbonate (*Figure 4.17a*). Some examples of hematite mineralised fractures visually appear to be sealed, but the surrounding rock is oil stained (e.g. 206/7a-2, 48m (2143m depth) along the core, see *Appendix 4*). Where this is apparent, there tends to be several hematite mineralised fractures clustered together, all at different orientations and with a high degree of fracture connectivity. It is also typical that brecciated and hematite mineralised gneiss is found on one side of well-defined fault surfaces (see *Figure 4.17e*). The majority of faults associated with hematite veins exhibit an apparent sinistral shear sense (for an example, see *Figure 4.17e*) but there are also some examples in well 206/7a-2 where hematite mineralised faults show an apparent dextral shear sense. The fine-grained fault breccia consists of shattered clasts of host rock that vary from <0.1mm to 5mm in size.

Epidote mineralisation is commonly seen in association with hematite and at a macro-scale it appears to have the same relative age within veins in the basement core samples (*Figure 4.16 & 4.17d*). Epidote veins locally form the thickest vein sets (up to 2cm) and these veins can also be filled with the later mineralisation of carbonates (mainly calcite). The veins filled with epidote sometimes show ‘anastomosing’ patterns which are commonly associated with faults where the adjacent gneiss becomes brecciated. This association is similar to the veins that are mineralised with hematite. Fractures associated with the brecciated gneiss and epidote/hematite mineralisation can exhibit significant offsets that are too large to be measured from core samples (>10cm).

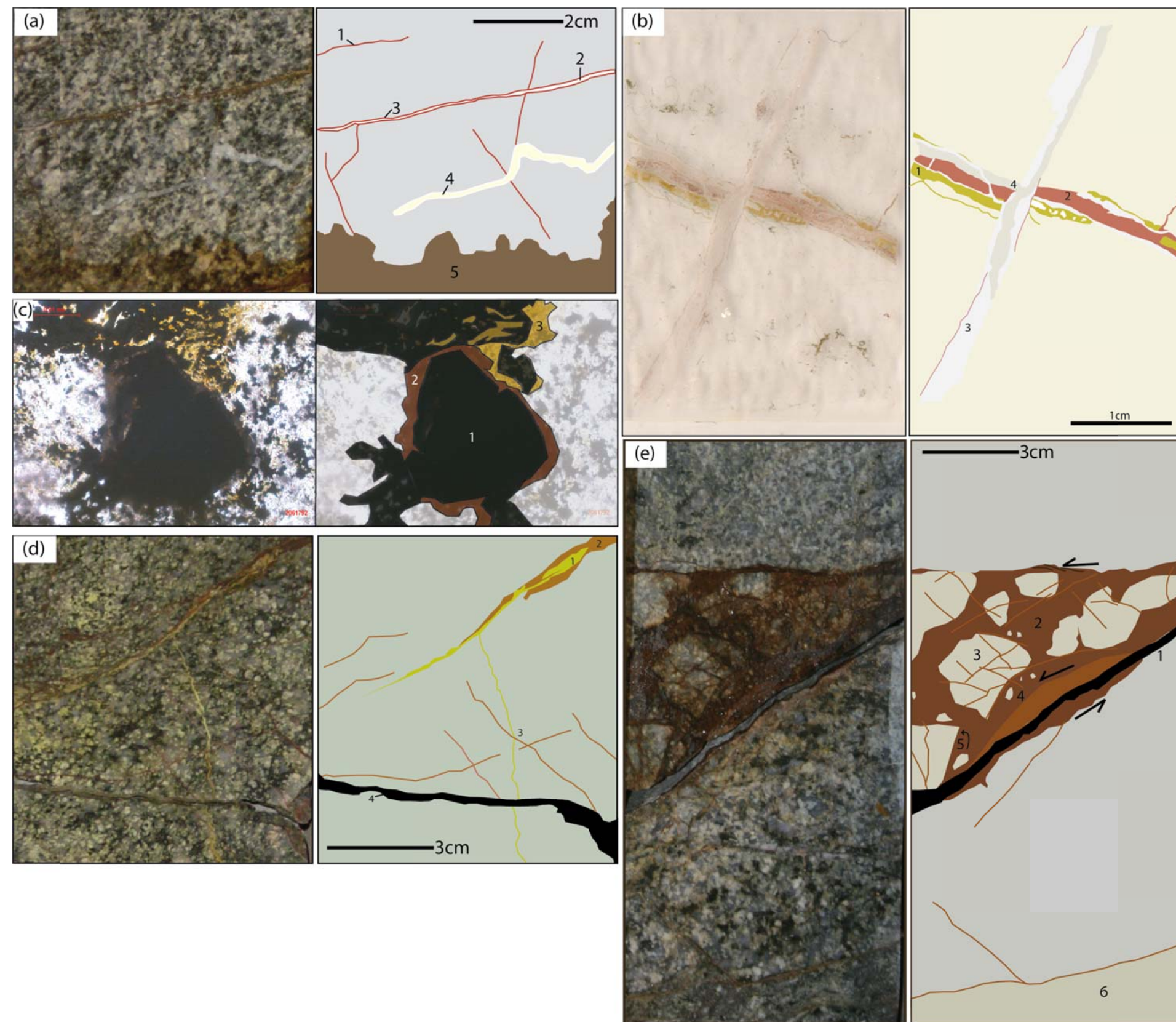
Epidote mineralisation is often observed as an ultra-cataclasite smeared along larger (up to 4cm thick) fault planes (for example, see well 206/8-8).

Quartz mineralisation is also present although the veins are less numerous in the basement core than either hematite or epidote mineral veins. They have narrow apertures (<2mm) and are commonly associated with hematite mineralisation which forms as a coating on the outside edges of the veins.

In thin section (sample 7-a2-1) it is apparent that epidote, which is included in a fault as an ultra-cataclasite, is the oldest mineralisation seen within the basement. The epidote ultra-cataclasite (*Figure 4.17b*) is truncated by later hematite/quartz and then carbonate mineralisation. The fact that clasts of the epidote ultra-cataclasite are entrained within the quartz/hematite vein provides further evidence suggesting that the epidote is the oldest fracture mineralisation seen within the sample (and within the basement). Hematite and quartz are observed together within single veins and appear to be contemporaneous (e.g. sample 7-a2-1). The quartz within this vein consists of very fine (<0.1mm) euhedral crystals which are interspersed with smaller hematite crystals (these are too small to visualise properly using an optical microscope). Hematite appears to be more concentrated towards the centre of the vein. The quartz/hematite vein is exploited and cross-cut by a larger carbonate vein which also offsets the earlier fracture mineralisation sinistrally by ~1.5mm.

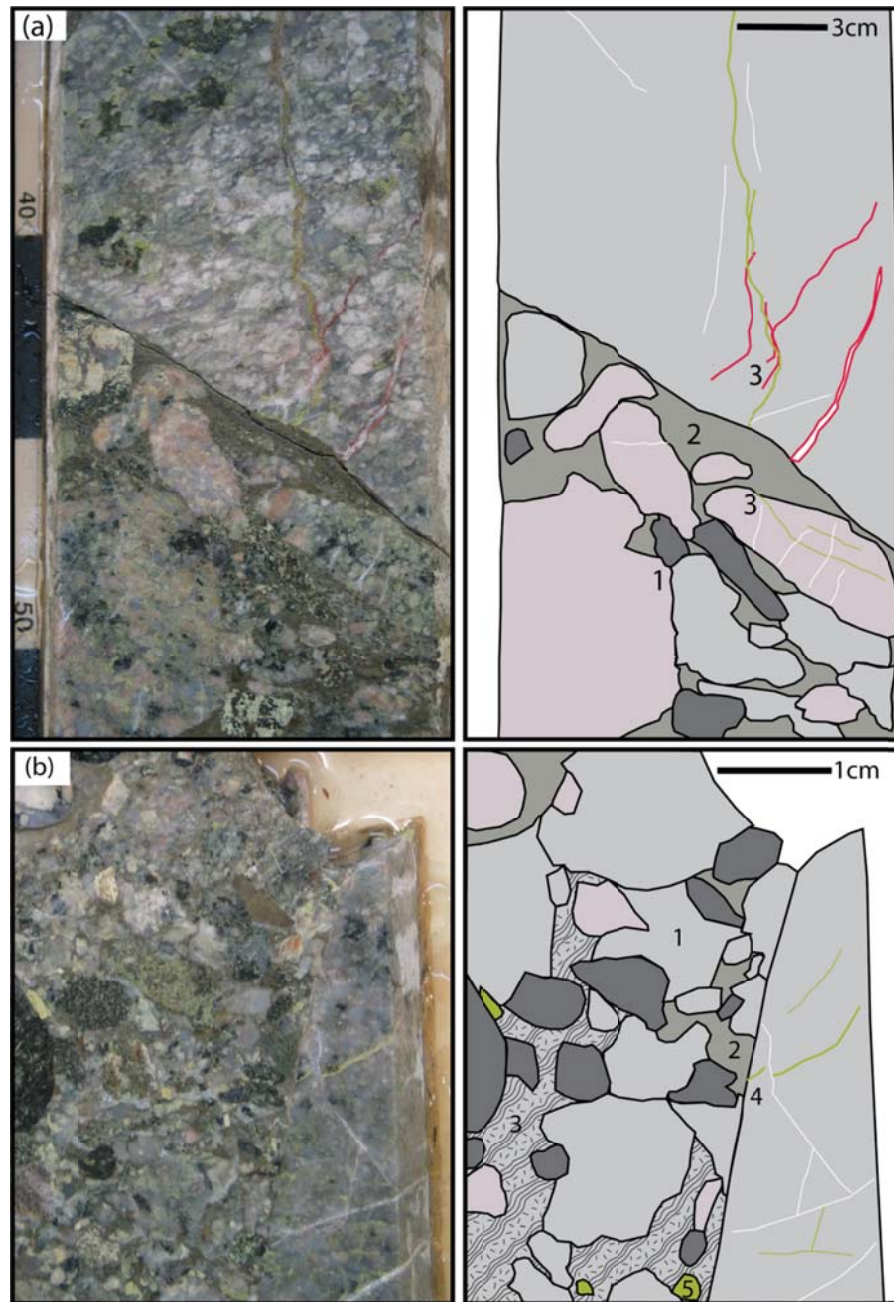
Hematite, epidote and quartz mineralisation are all observed within the basement core samples, but are not documented within the overlying Clair Group sedimentary sequences (see Milodowski et al., 1998). Many of the basement gneiss clasts within the Basal Conglomerate in well 206/8-8 contain fractures mineralised with hematite, epidote and quartz. None of these fractures extend beyond the edges of the clasts into the surrounding sandstone matrix (e.g. see *Figure 4.18*). This suggests that these three in-fills are older than the formation of the presumably Devonian Basal Conglomerate.





**Figure 4.17:** Examples of fracture modes seen within the Clair basement. **(a)** Photograph of Clair basement granodiorite core from well 206/7a-2. **1.** Hematite mineralised vein. **2.** Calcite-filled vein. The vein cross-cuts a hematite vein but does not offset it. **3.** Calcite vein has an outer coating of hematite. **4.** Quartz vein cross-cutting a hematite vein. **5.** Oil staining related to a cluster of open fractures just below where this photograph was taken. **(b)** Scanned thin section of Clair basement granodiorite from well 206/7a-2 (7-a2-1). **1.** Epidote cataclasite formed in a shear fracture. **2.** Hematite mineralisation. **3.** Older carbonate exhibiting small crystals. **4.** Clean carbonate, large crystals (0.1mm). **(c)** Thin section photo-micrograph of granodiorite from well 206/7a-2 (2061792). **1.** Individual pyrite crystal **2.** Bitumen coating on the outer edges of individual pyrite crystals. **3.** Oil staining the surrounding granodioritic rock. **(d)** Clair basement core sample of granodiorite from well 206/7a-2. **1.** Epidote mineralisation within a closed fracture. **2.** Hematite mineralisation within the same closed fracture. **3.** The mutual cross-cutting relationships between epidote and hematite veins suggest that they may have been introduced into the Clair basement at the same time. **4.** Non-mineralised open fracture which shows no evidence of shearing or oil-staining. **(e)** A sample of granodiorite from the Clair basement from well 206/7a-2. **1.** Open fracture at the base of the shear fracture. **2.** Brown cataclasite which is well indurated and potentially mineralised with hematite. **3.** Fractured clasts of granodiorite host rock. **4.** Some of these clasts have been broken further and form proto-cataclasite. **5.** There is evidence that some of the host rock clasts are rotated and this is one criteria used to determine the shear direction of the fault.





**Figure 4.18:** Core sections of Basal Conglomerate that provide evidence for the age of the epidote, hematite and quartz mineralisation seen within the Clair basement. **(a)** Shows a core section from 206/8-8 of the Basal Conglomerate. **1.** Granite and granodiorite gneiss clasts. **2.** Arenitic laminated sandstone matrix. This also contains smaller clasts of basement gneiss. **3.** Epidote, hematite and quartz filled fractures do not extend past the edge of the basement clasts. **(b)** Another example of Basal Conglomerate (well 206/8-8). **1.** Clasts of granodiorite and granite gneiss clasts. **2.** Sandstone matrix **3.** Matrix of small basement gneiss clasts. **4.** Epidote and quartz fractures that do not extend into the conglomerate matrix. **5.** Clasts of epidote.

#### 4.3.2.8.2 – Carbonate-pyrite fills

Nearly half of all the discontinuities measured from core samples contain carbonate mineralisation (calcite). Many of these also contain closely associated pyrite. The descriptions of carbonate mineralisation given in this section are predominately from well 206/7a-2 and well 206/12-1 where carbonate mineralisation is prolific.

Carbonate veins display apertures of up to 1cm. They commonly exhibit open vugs that can be up to 5cm across, containing both calcite and pyrite crystals (up to 5mm across). Both minerals are also found in association with some regions of brecciated gneiss where carbonate veins fill the voids left between the basement clasts (e.g. well 206/12-1).

From analysis of the core and associated thin sections it is clear that the carbonate-+/- pyrite veins form the youngest set(s) within the basement, as they cross-cut and exploit the pre-existing hematite-, epidote- and quartz-filled veins and fractures. Evidence from thin section samples and core samples suggest that at least two phases of carbonate mineralisation are present throughout the basement (see the full descriptive core logs in *Appendix 4*).

In thin section (e.g. sample 7a-2-1) the older carbonate veins consists of large, equant spar (Tucker and Wright, 1990) calcite crystals (up to 0.7mm across) along one or both vein edges and drusy calcite crystals (Tucker and Wright, 1990); antitaxial growth patterns dominate. The later cross-cutting veins consist entirely of drusy calcite crystals that are difficult to resolve using an optical microscope. In sample 12-1-1, large equant calcite crystals appear to be filling in voids left by the brecciation of the surrounding granodiorite gneiss. Associated and intergrown with these calcite veins are clusters of pyrite crystals (up to 1cm across (*Figure 4.17c*)).

Carbonate-filled faults are widespread in the Basal Conglomerate (seen in well 206/8-8) cutting both the basement gneiss clasts and the surrounding sandstone matrix. This suggests that the carbonate +/- pyrite filled fractures are younger than the formation of the Basal Conglomerate.

#### 4.3.2.8.3 – Oil-fills and ‘open’ fractures

One of the most important features present within the basement is the oil-staining seen in over a third of the fractures within core samples from 206/7a-2 and many of the fractures within well 206/12-1. This oil-staining is most commonly associated with carbonate mineralised fractures where it is clear that many vugs have acted as storage space for fluids (oil). A smaller number are associated with hematite veins in regions of brecciated gneiss adjacent to faults where they are clustered together and the vein connectivity is increased.

The oil-staining presents itself as a superficial stain that spreads out (normally for 1/2cm from the host fracture, coating the surrounding host rock. This is likely to have occurred due to oil pressurised by burial leaking out of the fractures after the coring and cutting process at the surface.

‘Open’ fractures are present in many of the basement core samples (especially well 206/7a-2). Commonly they exhibit visible spaces or vugs in the rock where there is no mineralisation or large crystals of either pyrite or calcite ‘pinning’ the fracture open. Over half of the fractures measured in basement core samples are considered to be at least partially open. The majority of the open fractures seen in core samples from well 206/7a-2 exhibit oil-staining, except where the fractures have a small aperture (<1mm) and there is no evidence of connectivity with other fractures. Areas in the core where open fractures are evenly spaced and orientated in approximately the same direction, oil staining is at a minimum or non-existent. Whereas, in areas where there is a large open fracture or lots of smaller interconnected open fractures in a wide range of orientations, oil staining is profuse.

The larger open fractures in well 206/7a-2 (2441m down well 206/7a-2) contain chemically degraded ‘rubble’ that is mineralised with pyrite, carbonate and also coated with hydrocarbons, mainly bitumen (it has a distinctive smell of degraded oil). In some examples, particularly in well 206/7a-2, the host rock at the edge of oil-stained fractures, that also contain carbonate and pyrite, looks highly degraded (almost rotten) suggesting that the host rock has reacted chemically with the hydrocarbons (or carbonate/pyrite) present within the fracture (*Figure 4.19*).



**Figure 4.19:** Photograph of 206/7a-2 basement core highlighting the degraded nature of the core in association with oil-staining. **(a)** Shows the full core section (1m in length). **(b)** More detailed view of the degraded material.

In thin section (sample 2061792), the oil-bitumen presents itself as brown, opaque globules (0.5mm in size) that are closely associated with both calcite and pyrite mineralisation (*Figure 4.17c*). The most extensive regions of oil-staining (up to 2mm across) are closely associated with pyrite mineralisation, which in sample 2061792, is commonly seen at the ends or edges of the carbonate veins (*Figure 4.17c*).



#### 4.3.2.9 – Fault and fracture Discussion

The basement and sedimentary cover sequence core samples provide evidence that there are many different phases of brittle deformation and associated mineralisation within the Clair field. The focus of the present study has been on the basement well cores, but samples from the overlying Basal Conglomerate have been used to help provide constraints on the relative ages of the different fracture fills present within the basement gneisses. Analysis of the cross-cutting relationships in the basement core samples suggests that there are at least six different mineral (or organic) fills seen within the basement veins, fractures.

Epidote mineralised faults (mainly lined with ultra-cataclasite) are the oldest set in the basement and occur throughout the basement cores. Much of the epidote that accumulates in these faults probably originated in the basement rocks as a product of the breakdown of plagioclase feldspar (see *Chapter 1*). Hematite often occurs in association with quartz within fractures. The relationship between the hematite and the quartz is unclear, although in sample 7a-2-1 the iron oxide appears to be concentrated in the centre of a vein. This may suggest that the hematite entered the system slightly earlier than the quartz as it appears that this particular vein exhibits antitaxial growth. These hematite/quartz veins can be seen to cross-cut and truncate epidote-filled faults and in thin section, clasts of epidote ultra-cataclasite can be observed entrained within hematite/quartz veins (e.g. sample 7a-2-1). The origin of the quartz and hematite is unknown but it is likely that it originates from outside the host rock which is echoed in the antitaxial growth of veins (Durney and Ramsay, 1973).

Carbonate mineralisation present within fractures in the basement exhibits two (or possibly three) phases of formation. This is particularly clear in thin section (sample 7a-2-1) where a large calcite vein is cross-cut and offset by a much thinner carbonate fracture. Previous work in the Clair Group sedimentary cover sequences (Milodowski et al., 1998) used fluid-inclusion studies to analyse the different phases of mineralisation present within the Clair sediments. This previous work stated that there are three calcite phases present within the Clair sediments; one prior to hydrocarbon migration (Calcite I) and two synchronous with hydrocarbon migration (Calcite II & III). From the basement core samples it is likely that all three of these carbonate phases are present within the basement.

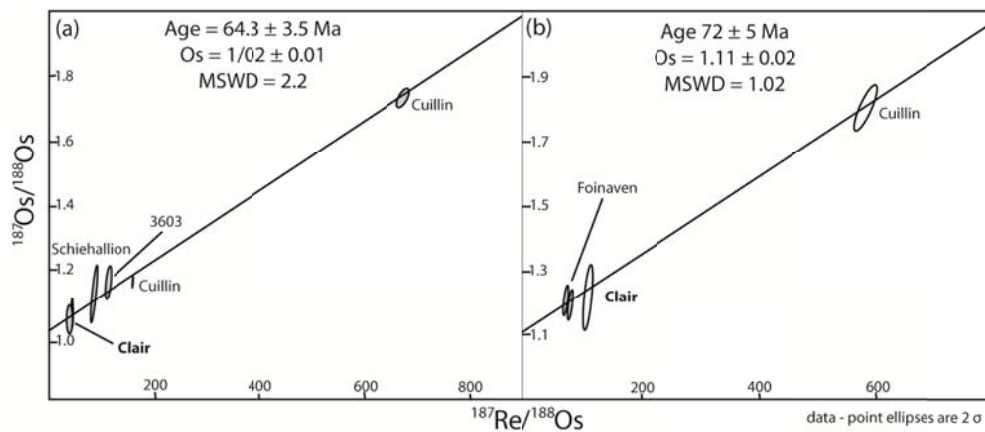
It is proposed, in this study, that Calcite I from Milodowski et al. (1998) can be attributed to those carbonate fills within the basement that fill voids created by the brecciation of the basement gneiss (e.g. well 206/12-1). The brecciation of the gneiss is thought to be the result of over-pressured fluids (e.g. Sibson, 1986, Woodcock and Mort, 2008) which result in the breaking of the basement gneiss and emplacement of the carbonate-rich fluids into the voids. This is in agreement with the sediment study (Milodowski et al., 1998) which states that Calcite I entered the system under conditions of overpressure prior to the hydrocarbon migration during the Late Cretaceous to Early Tertiary.

I also suggest that Calcite II & III mineralisation is found throughout veins and fractures within the basement. From the previous analysis of fracture mineralisation in the sediments (Milodowski et al., 1998) it is known that this later calcite formation is synchronous with hydrocarbon migration and pyrite mineralisation. Analysis of basement core samples and thin sections shows no evidence of Calcite II or III cross-cutting each other, but does show evidence of their different habits. Calcite II forms drusy calcite spar crystals that fill veins and fractures and shows evidence of oil within inclusions. Veins containing Calcite II show evidence of small vugs in the fracture centre that may be a result of the percolation of CO<sub>2</sub>-rich water during maturation of the hydrocarbons (Tucker and Wright, 1990). The migration of these CO<sub>2</sub>-rich fluids creates porosity in these carbonate filled fractures ahead of the migrating oil (Tucker and Wright, 1990). Calcite III type mineralisation is seen in the basement rocks as larger calcite crystals (up to 5mm in size) lining the walls of open fractures and faults. This large crystal size suggests that the calcite crystals were growing into fluid filled cavities and that these cavities must have been open for significant periods of time. The nature of this later carbonate mineralisation within the basement is comparable to that seen from the overlying sediment fracture study (Milodowski et al., 1998) and is therefore likely to be the same age (Late-Cretaceous to Early Tertiary).

Both Calcite II & III episodes are also associated with the mineralisation of sulphides (mainly pyrite). This pyrite mineralisation is younger than Calcite I mineralisation (in well 206/12-1 pyrite can be observed overprinting the calcite mineralisation in the voids caused by brecciation, see well photographs in *Appendix 4*) and Calcite II and appears to be synchronous with Calcite III. Pyrite seen within fractures in the basement core samples typically lines the walls of fractures and is almost always

associated with calcite mineralisation and oil-staining. This is comparable to the description of Sulphide III mineralisation given by Milodowski et al. (1998) for the sediments so the pyrite in the basement is therefore understood to be of the same origin.

A separate study using core samples from the Clair basement has dated samples of pyrite and bitumen using Re-Os isotopes (Finlay and Selby, 2011). The isotope study produces pyrite and Clair oil ages of  $72 \pm 5$  Ma (and  $64 \pm 3.5$  Ma, bitumen only sample) which is within error of the hydrocarbon ages found within other fields west of the Shetland Isles (*Figure 4.20*). What this separate study has shown is that the pyrite and hydrocarbons within the Clair basement system are from the same source, which is consistent with the textural and cross-cutting relationships observed and described through the core sample analysis presented in this chapter.



**Figure 4.20:** Plots showing Re-OS ages of pyrite and bitumen taken from core samples in the Clair basement and compared to other hydrocarbon fields within the Faroe-Shetland basin (Finlay and Selby, 2011). **(a)** Bitumen only samples from the Clair basement fit the 64.3 Ma isochron found from other oil samples across the Faroe-Shetland basin **(b)** Pyrite samples from the Clair basement fit the 72 Ma isochron which is also present in other samples from across the Faroe-Shetland basin (the younger oil shown in **(a)** is likely to have been cleared from the pyrite by later hydrocarbon migrations).

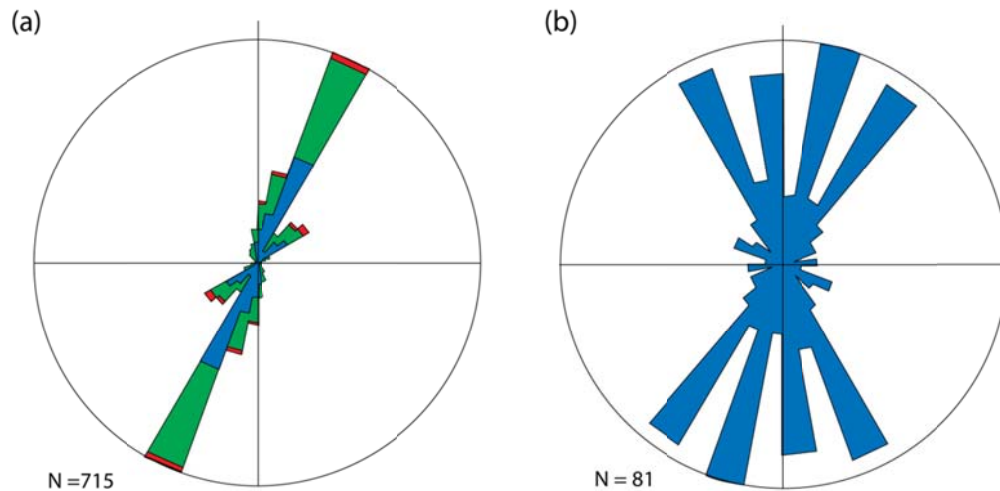
From comparison with previous work in the sediments (Milodowski et al., 1998) and analysis of the Basal Conglomerate and basement core samples, it is clear that carbonate mineralisation occurred post-sedimentation and can be separated into two (possibly three) distinct categories. This is in comparison to those veins, fractures and faults that are mineralised with epidote, hematite and quartz which from the evidence presented in this chapter are likely to have formed pre-sedimentation (pre-Devonian). These older brittle structures are still important in terms of later fluid (hydrocarbon) flow because they are locally re-exploited by the later episodes of carbonate and sulphide mineralisation, and hydrocarbon migration into the Clair Field.

Open fractures are apparent throughout the basement core samples (particularly in well 206/7a-2) although their origin is less obvious. Fractures that appear open in core samples may not have been open at depth and may be a result of the coring process where weakness in the basement rock have opened up as the core sections were extracted. It is also possible that open fractures observed in core samples were open at depth, allowing fluid to flow through them, and have subsequently opened further again due to extraction during the coring process (see *Chapter 1, section 1.4.3*). Throughout this chapter only open fractures that are known or interpreted to be open at depth are included in any fracture orientation or spacing analysis of open fracture sets.

#### 4.3.3 –Fracture orientation analysis from well datasets

Data from both basement core and image log samples have been used to analyse fracture orientations in the basement. Only data from two wells have been used for this part of the offshore study because orientation data are not available from any other samples. The two wells used, 206/7a-2 and 206/8-15, sample the basement ridge; thus only provide an insight into the southern Ridge Area of the Clair Field.

*Figure 4.21* shows rose plots of fracture orientations from the basement well samples. It shows that there is one prominent fracture orientation of NE-SW (NNE-SSW) with some evidence of NW-SE trending fractures.



**Figure 4.21:** Rose plots of the fracture orientations from well data from the Clair basement. Colours represent the different types of fractures: Red – faults, Green – closed fractures (includes veins) and Blue – open fractures. **(a)** Well 206/7a-2 **(b)** Well 206/8-15.

Well 206/7a-2 provides the largest amount of data for the orientation study (Figure 4.21a). Fracture orientations were measured relative to the sample line, which in the case of 206/7a-2, was the same as the drilling direction (N290°). By determining the fractures' true orientations, relative to the drilling direction, it is clear that there is a prominent fracture orientation of NNE-SSW. There are a smaller number of fractures measured from core 206/7a-2 that trend N-S (Figure 4.21a) with the majority of these being hematite, epidote and quartz veins. As 206/7a-2 trends NW-SE (N290°), it is unlikely that the well samples any NW-SE trending fractures to the same degree that it sample fractures of other orientations, and therefore, it is likely that the core inherently due to its 1D nature, represents an incomplete fracture network dataset.

Core 206/8-15 also samples fractures on the Clair Ridge. As this well is vertical and the data comes from image logs, the sample size is much lower than at 206/7a-2 (Figure 4.21b). It again shows NE-SW (NNE-SSW) trending fractures. N-S and NW-SE trending fractures are also prominent in this well sample. All of the fractures included in the study of well 206/8-15 are classed as open fractures (known from previous image log interpretation not completed during this study (e.g. Falt et al., 1992) and therefore their orientations can all be assumed to be conductive to fluid.

#### 4.3.3.1 – Orientation analysis from well data: Discussion

It appears from the very limited available well data that NE-SW fractures are the most prominent set within the basement (*Figure 4.21*). This NE-SW fracture trend is also quoted in a paper by Falt et al. (1992) as being the main fluid flow pathway through the basement based on image log analysis of well 206/7a-2 and subsequent well testing.

NE-SW trending fractures from well 206-7a-2 are mineralised with hematite/epidote and/or calcite/pyrite suggesting two separate ages of this prominent fracture trend. From cover-sediment/basement relationships described earlier in this chapter (*Section 4.3.2.8*) it is known that NE-SW mineralised with hematite/epidote are pre-Devonian in age, potentially during a period of NW-SE extension similar to tectonic episodes recorded in the mainland LGC (Beacom, 1999). Those NE-SW trending fractures in well 206/7a-2 that are mineralised with calcite are known to have formed at the same time as oil emplacement and therefore have an age of Late Cretaceous to Early Tertiary (Milodowski et al., 1998) during which time NW-SE extension was occurring within the North Atlantic (Davies et al., 2004).

The lack of NW-SE trending fractures in well 206/7a-2 is likely because this well is biased due to its orientation (N290°) and therefore no fractures parallel to the well (NW-SE) have been interpreted. The few fractures in well 206/7a-2 that trend N-S are normally mineralised with hematite, epidote and quartz and show little or no evidence of oil-staining. This suggests that these particular fracture sets are less conducive to fluid flow and therefore do not improve the understanding of fluid flow pathways through the basement.

The N-S and NW-SE fracture trends present within well 206/8-15 are consistent with the regional analysis for this part of the Clair basement (*Figure 4.21b*). For example, the well coincides with a region of the basement where there is a concentration of N-S fault lineaments consistent with the fracture trends seen from the 206/8-15 core. These N-S fault lineaments could be related to E-W Devonian (Dewey and Strachan, 2003, Wilson et al., 2010) and/or Jurassic (Dore et al., 1997) extension (N-S trend). Fractures within well 206/8-15 have been interpreted to be open to fluid flow. The open nature of these structures is likely due to the location of the well within a structurally complex region of the Clair Field basement next to a distinct 'kink' in the main Ridge Fault (*Figure 4.6*).

The understanding of fracture orientation in the basement at the scale of a well is limited. Only orientation data for part of the Clair Ridge was available, so the regional seismic attribute fault lineament analysis forms the only basis on which assumptions about the fracture trends through the entire basement can be made. This limited amount of orientation data highlights the importance of being able to use an onshore analogue to catalogue and interpret the full fault and fracture networks that are potentially present within the basement at a range of different scales.

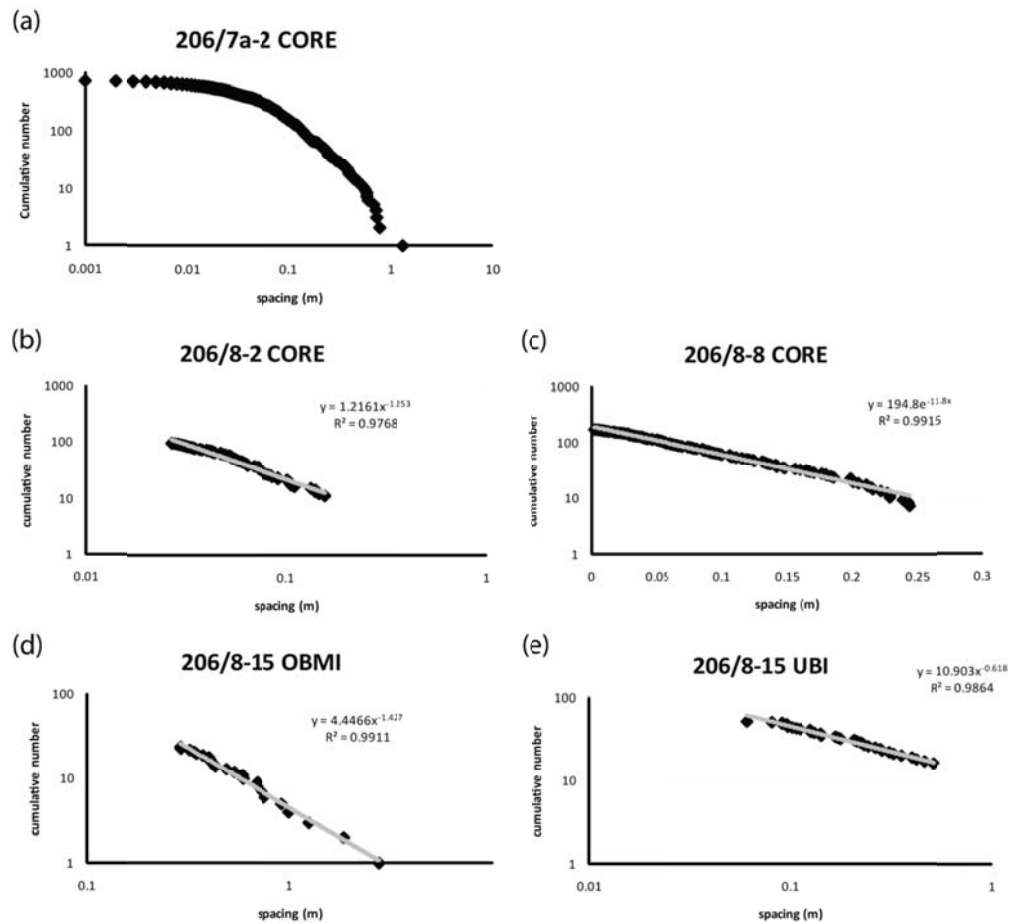
#### 4.3.4 - Spacing analysis of fracture data from Clair basement well samples

A study of the fracture spatial attributes has been conducted in the basement cores. Spacing data for the fracture sets was gathered using 1-dimensional sample lines taken down the centre of suitable basement core samples and from image log data from other wells (see *Appendix 4* for full spacing tables). This spacing data has been used to analyse spacing population distributions, the coefficient of variation, fracture density along samples and how fracture density is affected by basement lithology. Suitable wells for this basement fracture spacing analysis are 206/7a-2 (core), 206/8-2 (core), 206/8-8 (core), 206/8-15 (OBMI) and 206/8-15 (UBI) as these samples contain a statistically significant number of fractures.

##### 4.3.4.1 –Fracture spatial distributions

The primary analysis of spatial attributes involves creating population distribution plots for each well in the study and these plots for the full fracture sets are shown in *Figure 4.22*.

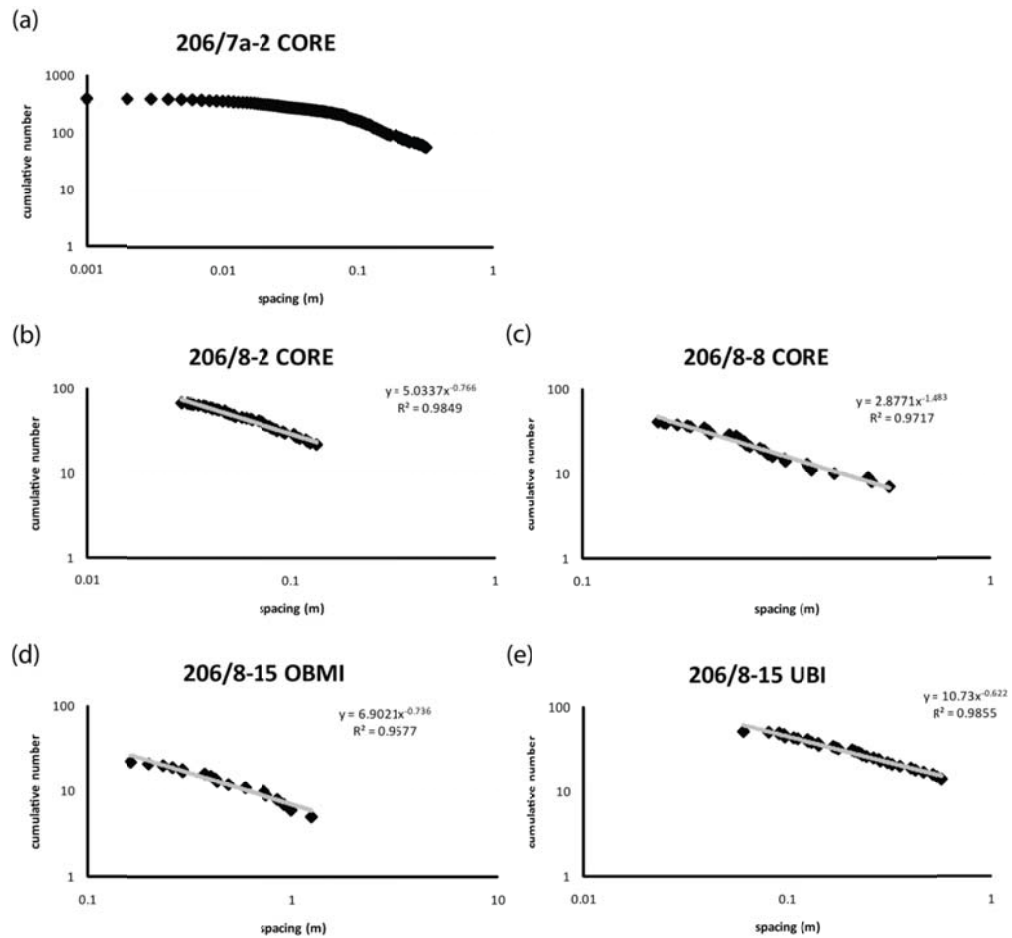
The population distribution plots are best described by power-law relationships (both axes on the graphs are logarithmic) for nearly every well sample, when both open and closed structures are analysed together. These power-law relationships generally extend over no more than one order of magnitude, normally between 0.01 and 1 metre spacing values. When only open fractures are analysed, the spacing distributions are consistently power-law, albeit with smaller datasets. *Figure 4.23* shows population distribution plots for the open fractures only. The open fracture datasets also show power-law distributions that extend over no more than one order of magnitude between 0.01 and 1 metre spacing values.



**Figure 4.22:** Population distribution plots for all fractures sampled from Clair basement wells. **(a)** Well 206/7a-2 full fracture spacing distribution. The ‘spot’ core nature of this core means that every section of core has to be statistically analysed separately. The population distribution plots for individual sections of core in well 206/7a-2 are given in *Figure 4.24*. **(b)** Well 206/8-2 core spacing dataset. Only the data that represents the distribution is shown on this plot (and the plots for 206/8-8 and 206/8-15). **(c)** Well 206/8-8 core spacing dataset. **(d)** Well 206/8-15 OBMI spacing dataset. **(e)** Well 206/8-15 UBI spacing dataset.

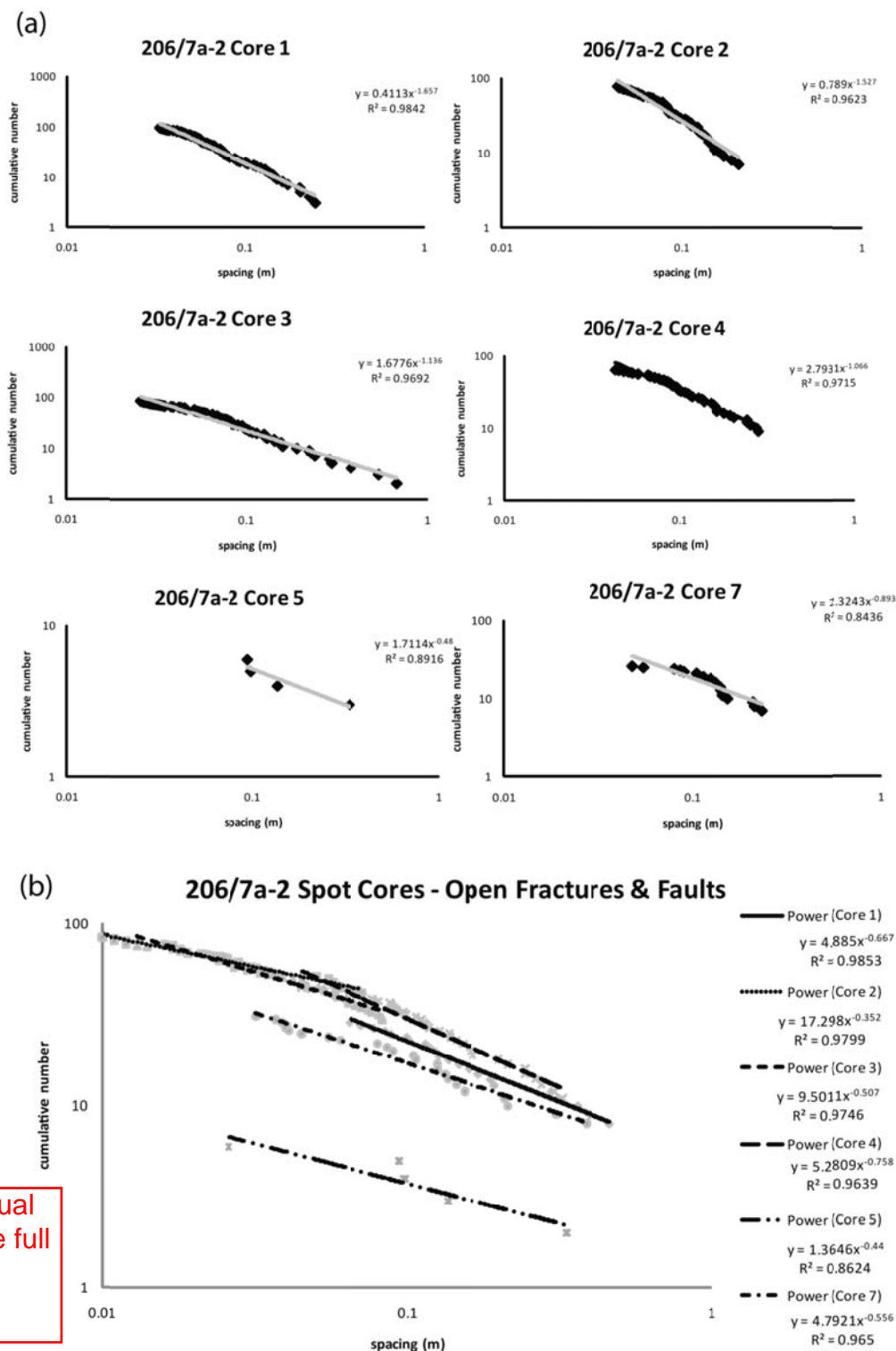
click on individual plots  
to see the full dataset





**Figure 4.23:** Population distribution plots for open fractures sampled from Clair basement wells. **(a)** Well 206/7a-2 full open fracture spacing distribution (see *Figure 4.24* for individual spot core distributions for open fracture sets). **(b)** Well 206/8-2 core spacing dataset. Only the data that represents the distribution is shown on this plot (and for the plots for 206/8-8 and 206/8-15). **(c)** Well 206/8-8 core spacing dataset. **(d)** Well 206/8-15 OBM spacing dataset. **(e)** Well 206/8-15 UBI spacing dataset.

click on individual plots  
to see the full dataset



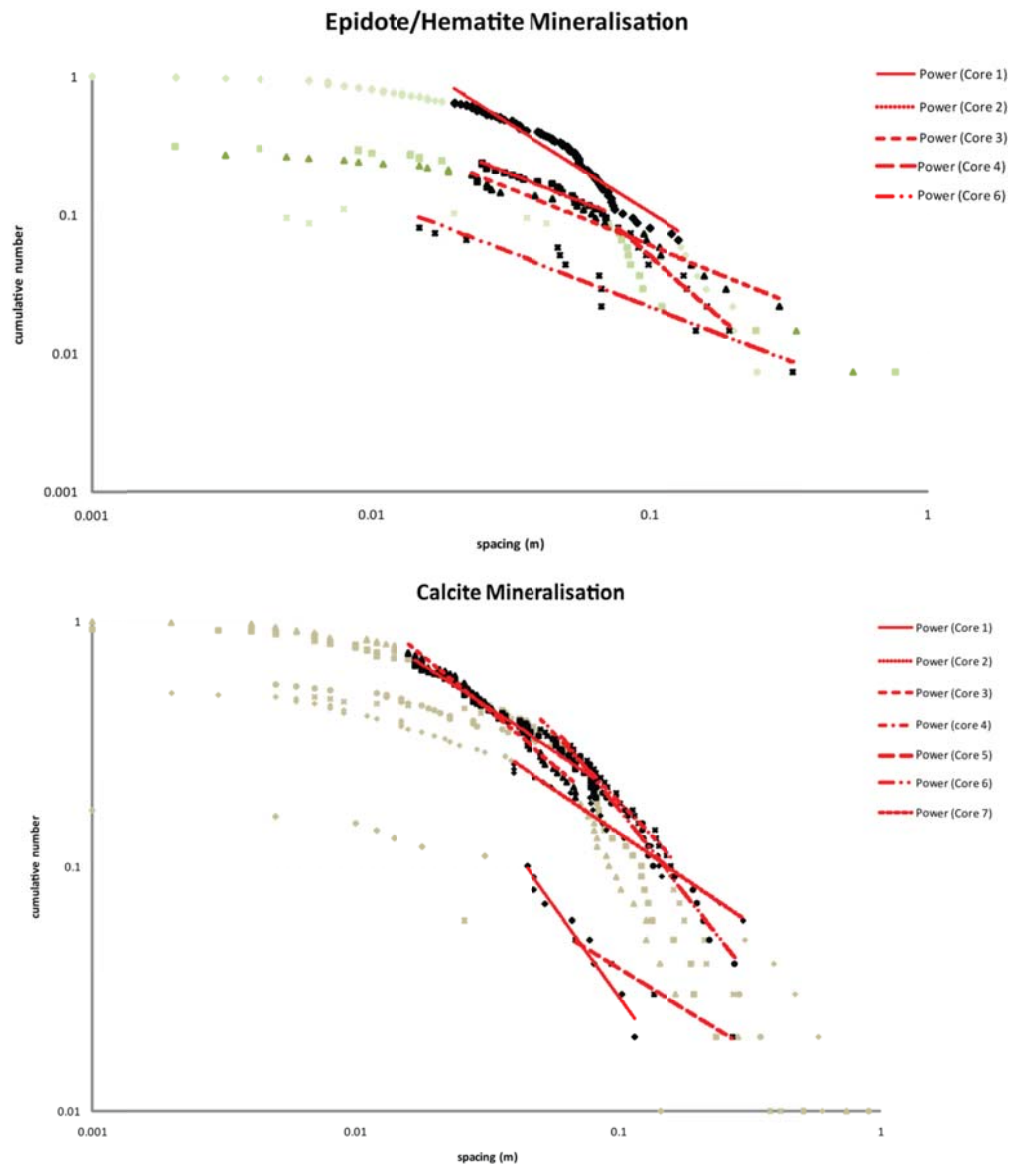
**Figure 4.24:** Population distribution plots for individual basement spot cores in well 206/7a-2. **(a)** Plots for all the fractures in each section of core. **(b)** Plot showing the spacing distributions for open fracture sets in each individual section of basement core in well 206/7a-2.

Well #	Fracture Sets	Type	Location	Length (m)	Main Lithology	Spacing distribution	R <sup>2</sup> value	D-value	Slope	Cv	Fracture Density
206/7a-2	All	Core1	Clair Ridge	8.6	granodiorite	Power-law	0.9842	1.657		1.033	22.91
	All	Core 2	adjacent to	9.3	gneiss	Power-law	0.9623	1.527		1.104	16.45
	All	Core 3	a NW-SE	9		Power-law	0.9692	1.136		1.429	15.78
	All	Core 4	ridge	9.6		Power-law	0.9715	1.066		0.919	8.65
	All	Core 5	off-setting	1.1		Power-law	0.8916	0.48		0.806	5.45
	All	Core 7	fault	7.1		Power-law	0.8436	0.893		1.408	8.03
	Open	Core1		8.6		Power-law	0.9853	0.667		1.043	3.84
206/8-2	Open	Core 2		9.3		Power-law	0.9799	0.352		1.476	10.11
	Open	Core 3		9		Power-law	0.9749	0.507		1.746	10.33
	Open	Core 4		9.6		Power-law	0.9639	0.758		1.001	5.83
	Open	Core 5		1.1		Power-law	0.8624	0.44		0.94	5.45
	Open	Core 7		7.1		Power-law	0.965	0.556		1.33	6.2
	All	Core	mid Clair		granite gneiss	Power-law	0.9768	1.253		0.855	15.88
	Open	Core	ridge			Power-law	0.9849	0.766		0.699	9.19
206/8-8	All	Core	Core area		granodiorite	Exponential	0.9915		194.8	0.868	10.54
	Open	Core	Clair field		gneiss	Power-law	0.9717	1.483		0.77	3.98
206/8-15	All	OMBI	East Clair		n/a	Power-law	0.9911	1.427		0.953	1.75
	Open	OBMI	ridge			Power-law	0.9577	0.736		0.954	1.35
	All	UBI	just north			Power-law	0.9864	0.618		1.323	2.46
	Open	UBI	of 206/7a-2			Power-law	0.9855	0.622		1.309	2.42

**Table 4.3:** Spacing attributes for all fractures measured from Clair basement well data. This table is arranged so that the full fault and fracture set attributes are displayed directly above the open fault and fracture sets for the same well or core sample.

Note that well 206/7a-2 has not been 'cleaned-up' to only show the power-law portion of the distribution in either *Figure 4.22* or *Figure 4.23*. This is because 206/7a-2 consists of seven separate 'spot' cores which have to be treated as individual datasets. *Figure 4.24* shows the population distribution plots for each individual 'spot' core from the basement in well 206/7a-2. Each section of the 206/7a-2 core is best described by a power-law distribution with similar attributes to those seen from other basement wells (see *Table 4.3* for all spatial attributes from basement wells). This applies to the full fracture sets and open fracture sets from this basement well. Again these power-law distributions extend over no more than one order of magnitude centred on spacing values of 0.1 metres. Only well 206/8-8 exhibits fracture spacing relationships which are exponential, indicating that fracture spacing in this well is not scale-invariant.

Population distribution plots have also been created to analyse the spacing patterns of different mineral fills in the 'spot' cores from 206/7a-2. Fractures filled with hematite and/or epidote (these are considered to be pre-Devonian in age) and those mineralised with carbonate (considered to be amongst the youngest present in the basement) are included in this study. Other mineral fills are omitted from this analysis because their numbers were too few to be considered statistically significant. The population distribution plots from this analysis are shown in *Figure 4.25* and the associated spatial attributes are given in *Table 4.4*.



**Figure 4.25:** Population distribution plots for different mineralisation types in well 206/7a-2. Each sample line is for individual cores in the basement from well 206/7a-2. **(a)** Shows spacing distributions for those fractures filled with hematite and epidote. **(b)** Shows spacing distributions for those fractures filled with carbonate (calcite). Black datapoints represent the power-law portions of the datasets. Green points represent the truncation and censoring within the datasets.

Core #	Length (m)	Fracture Fill	Main Lithology	Spacing Distribution	R <sup>2</sup> value	D-value	CV	Fracture Density
1	8.6	hematite/epidote	basic/ granodiorite gneiss	power-law?	0.93	1.28	1.00	15.81
2	9.3	hematite/epidote	granodiorite gneiss	power-law	0.96	0.79	1.70	4.52
3	9	hematite/epidote	granodiorite gneiss	power-law	0.96	0.82	1.34	4
4	9.6	hematite/epidote	granite/ basic gneiss	power-law	0.97	1.76	0.60	1.46
6	9.6	hematite/epidote	granite gneiss	power-law	0.91	0.79	1.18	1.25
1	8.6	carbonate	basic/ granodiorite gneiss	power-law	0.96	1.51	0.77	1.86
2	9.3	carbonate	granodiorite gneiss	power-law	0.98	0.71	1.23	9.89
3	9	carbonate	granodiorite gneiss	power-law	0.98	0.90	1.67	11
4	9.6	carbonate	granite/ basic gneiss	power-law	0.98	1.14	0.78	5
5	1.1	carbonate	granite gneiss/ pegmatite	power-law	0.99	0.67	0.83	5.45
6	9.6	carbonate	granite gneiss	power-law	0.98	1.37	1.35	5.63
7	7.1	carbonate	granite gneiss	power-law	0.97	0.74	1.44	7.04

**Table 4.4:** Spacing attributes for fractures measured from 206/7a-2 well data. This table is arranged to show the variations in spacing attributes for fractures mineralised with hematite/epidote or carbonate.

Those fractures mineralised with hematite and/or epidote exhibit less convincing power-law relationships (*Figure 4.25a*). Only five of the 'spot' cores are included in this part of the study because the other two samples had too few data-points to be statistically useful. Those core samples that are included show weak power-law relationships (the data do not lie on a particularly straight line) that extends over no more than one order of magnitude. Again the spacing values for those structures mineralised with hematite and/or epidote is between 0.001 and 1 metres.

All of the carbonate mineralised fractures from each of the 206/7a-2 'spot' cores are best described by power-law relationships for their spacing relationships (*Figure 4.25b*). These power-law relationships do not extend over more than one order of magnitude and they show no consistency with each other between individual 'spot' cores. In a similar manner to the full fracture analysis, the power-law relationships for carbonate mineralised structures are centred at a value of 0.1 metres.

#### 4.3.4.2 – D-value

D-values (slope of the power-law distribution) range from 1.7 to 0.5 for full basement fracture sets and from 0.8 to 0.4 for open fracture sets (*Table 4.3*). Cores 1 to 3 from well 206/7a-2 show comparatively high D-values ( $>1$ ) suggesting that their power-law relationships over-sample fractures that are closely spaced. Core 5 shows a low D-value which is likely due to the size of the sample dataset. This core only contains 7 fractures and so does not represent a statistically significant sample of the fracture sets in the Clair basement.

The D-values for open fault and fracture sets in well 206/7a-2 are significantly lower than those D-values for the same cores when the full fault and fracture set is considered. These low D-values indicate that widely-spaced fractures have been over-sampled and therefore these power-law relationships are biased towards fractures which have larger spacing values. This is observed in these core samples where zones of oil-stained rock are widely spaced throughout the core and are normally found where groups of smaller fractures cluster together to form a larger open features in the rock (normally associated with carbonate mineralisation).

This pattern of high D-values for the full fracture sets and low D-values for open fracture sets is not as obvious in other well samples (*Table 4.3*). In particular, 206/8-15 UBI fracture datasets do not have D-values that vary depending on whether it is the full

fracture set or only open fractures that are sampled. This could be related to the quality of the dataset. As previously mentioned, when examining basement well fracture orientations, the OBMI and UBI have sampling issues related to the location of their pads against the edge of the well. Therefore, it is likely that the fracture sets in well 206/8-15 have been inadequately sampled and spacing attributes from this dataset have to be treated with some caution.

When the fracture sets from well 206/7a-2 are separated into different sets based on mineral fill (hematite/epidote and carbonate) their D-values do not show any consistent pattern. Those samples of hematite/epidote mineralisation have D-values between 0.785 and 1.759 (*Table 4.4*). Fractures that are mineralised with carbonate also show a wide range of D-values between 0.667 and 1.508.

#### 4.3.4.3 – CV

The coefficient of variation (CV) has been calculated for each basement well sample. In 206/7a-2 CV values range between 0.81 and 1.7 (*Table 4.3*). Generally, the CV values for the open fracture sets are higher than those for the full sets for each individual 'spot' core sample. For example, the full fracture set from 206/7a02 Core 2 has a CV value of 1.104 compared to a CV value of 1.476 for the open fracture set for the same 'spot' core.

CV values for other basement wells are normally less than one (*Table 4.3*) which means that fractures in these samples exhibit anti-clustered to random spacing.

CV values for hematite/epidote mineralised fractures from well 206/7a-2 have a range between 0.644 and 1.738, although typically they are greater than one (*Table 4.4*). Those fractures mineralised with carbonate also show a wide range of CV values that range between 0.799 and 1.687 (*Table 4.4*).



#### 4.3.4.4 – Fracture density

Fracture density values vary between 22.9 and 1.7 fractures per metre for full sets measured in Clair basement wells (*Table 4.3*). 206/7a-2 shows high fracture density values towards the top of well (southeast end, Core samples 1-3) and far lower values at the bottom of the well (northwest end, Core samples 4, 5 and 7). The other core samples from wells 206/8-2 and 206/8-8 also show high fracture density values for the full fracture sets (15.88 and 10.54 respectively). Open fracture sets show consistently lower fracture density values (*Table 4.3*) than the full sets for the same samples but in some samples they are still relatively high (for example, Cores 2 and 3 from well 206/7a-2).

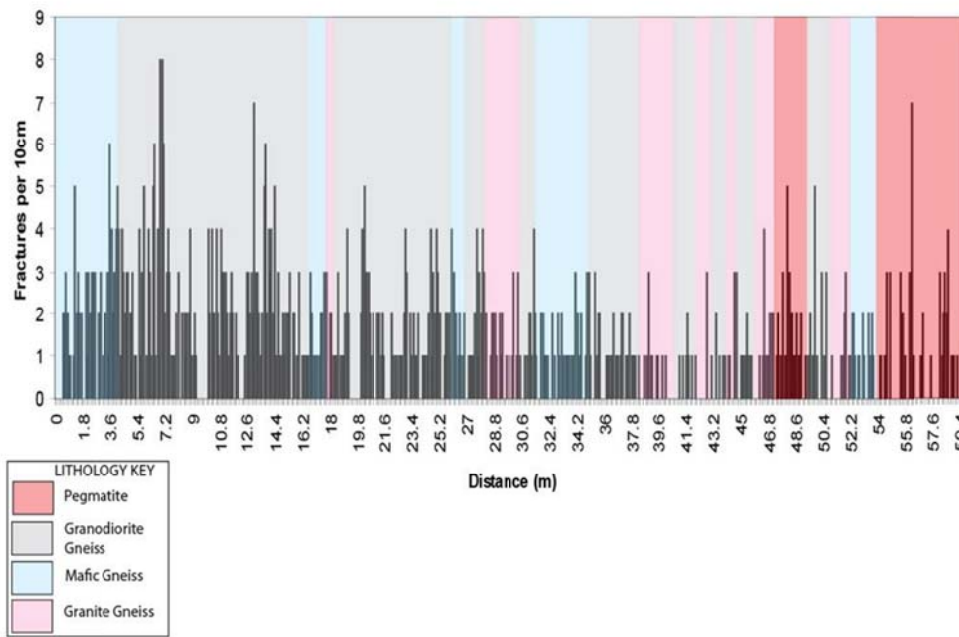
The samples from well 206/8-15, which are interpreted from image logs, exhibit much lower fracture density values than any of the basement core samples (*Table 4.3*). This is likely a direct result of the considerably lower resolution of the image log datasets in comparison to the core which is interpreted by the naked eye (the image logs have an order of magnitude lower resolution).

Carbonate mineralised fractures from well 206/7a-2 have fracture densities values that range from 1.98 to 11.11 fractures per metre (*Table 4.4*). Hematite/epidote mineralised fractures have density values between 1.3 and 15.93 with Core 1 from 206/7a-2 exhibiting the highest fracture density value (*Table 4.4*). Core samples from well 206/7a-2 that have high fracture density values for hematite/epidote mineralised structures generally have low fracture density values for carbonate mineralised fractures; and vice versa (see *Table 4.4*).

#### 4.3.4.5 –Fracture density versus Clair basement lithology

As well 206/7a-2 shows clear variation in the basement lithology along the core samples (see *Figures 4.12 & 4.13* for generalised lithological logs from well 206/7a-2), it is possible to use this well to evaluate the variation in fracture density in relation to the lithology. *Figure 4.26* is a plot showing the relationship between fracture density and lithology. Comparing the fracture density with the 206/7a-2 core lithologies shows that there is a relationship between densely fractured rock and a predominately granodioritic rock type. Sections of the basement core where the lithology stays constant over larger areas also tend to be more intensely fractured. It is also clear that the granite gneiss is far less fractured than the rest of the lithologies in the basement. It is unclear if lithology

affects the fracture density values in any of the other basement samples because the sections of core are not long enough or do not show any large variations in lithology.



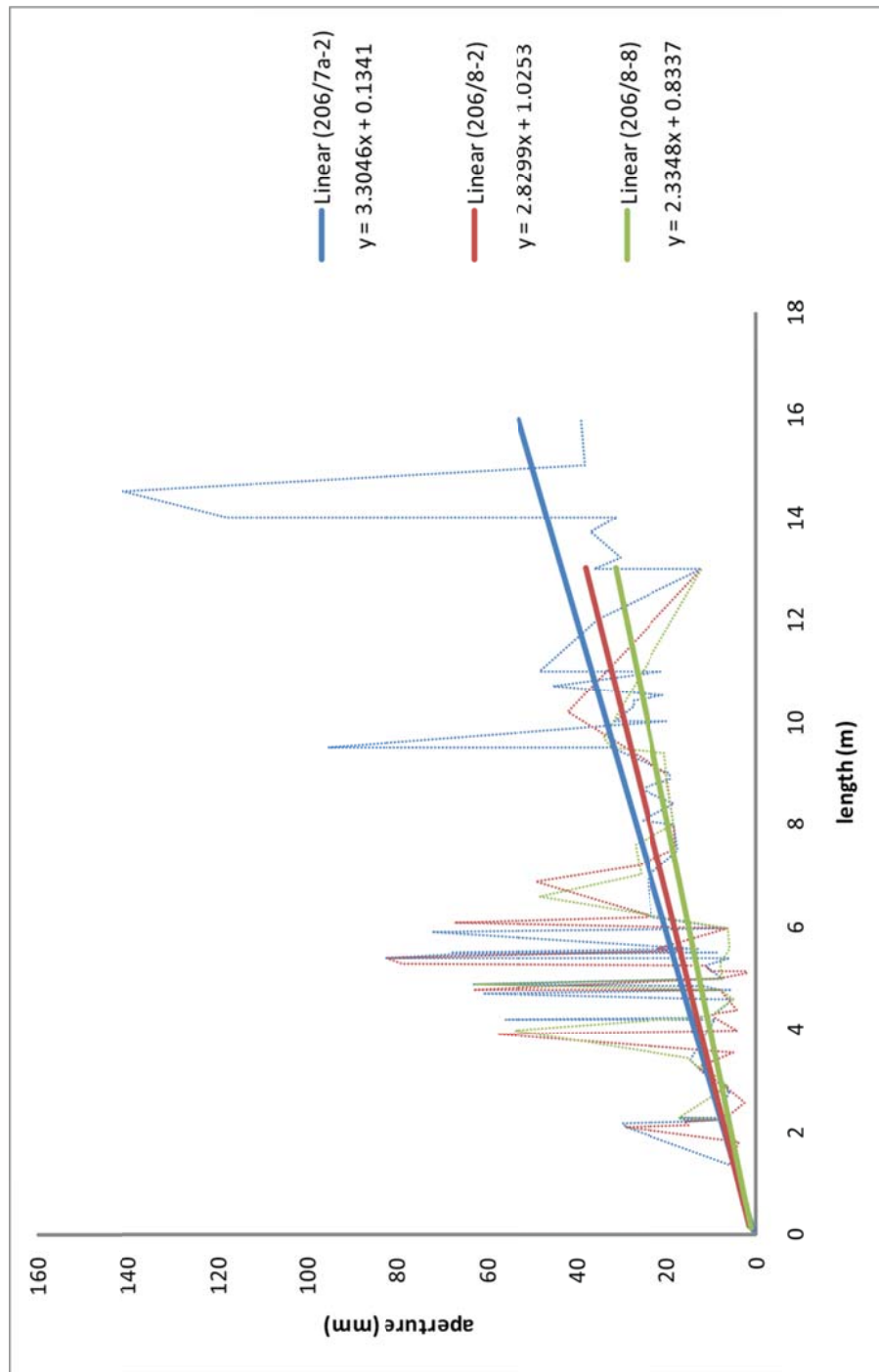
**Figure 4.26:** Plot of distance along core versus fracture density. This plot is superimposed with the variations in basement lithology along core 206/7a-2.

#### 4.3.5 –Fracture aperture versus length analysis

One problem with well data is that it is difficult to gain any understanding of fracture length from core samples. In most samples the fracture length visible is governed by the width of the core and therefore, no more than ~10cm of the discontinuities can be measured. To address this issue an evaluation of fracture length versus aperture has been undertaken.

This technique involves using mean apertures for fracture lengths binned every 10cm from data collected from the mainland Lewisian study. The onshore data selected for this study originates across the mainland Lewisian and encompasses many of the fractures analogous to structures measured from the basement core (although there is no onshore equivalent to the carbonate filled fractures observed in this study). By using onshore data from an analogue to the basement it is possible to estimate the length of the fractures sampled in basement core by using their measured apertures. *Figure 4.27*

shows the estimated relationship between aperture and fracture length from Clair basement core samples.



**Figure 4.27:** Plot showing aperture versus length for fractures sampled from the Clair basement core samples. The results shown in this plot have been estimated from mainland Lewisian data, where it is possible to measure both azimuth and fracture length.

*Figure 4.27* predicts that there is a positive correlation between fracture length and fracture aperture. The majority of fractures measured from core have apertures less than 10mm and therefore are estimated to have lengths less than 2m. Modelling using this dataset suggests that only fractures and faults with apertures >30mm have lengths over 10m.

Fracture aperture data have other implications for understanding strain in the basement. We can assume that all the fractures are tensile and that they opened parallel to the well core axis. By calculating the total width of fracture apertures and dividing it by the total length of core sample, it is possible to calculate the % strain seen at the site of the well (Johnston et al., 1994). Obviously this is an oversimplification, but the results are nevertheless instructive. For 206/7a-2 this strain value for the full fracture array is 5.71%. It is important to be aware that the total strain values quoted here are calculated from all fractures measured from core samples and so cannot be attributed to one tectonic event. It is possible from well 206/7a-2 to separate the strain into two categories; pre-Devonian and post-Devonian. Those fractures mineralised with epidote and hematite are considered pre-Devonian and these account for a 0.65% strain. Carbonate mineralised fractures which are known to be post-Devonian in age show a strain value of 2.05%. The total strain calculated from these two fracture sets does not equal the total strain calculated for the 206/7a-2 core samples. This is because there are fractures measured from 206/7a-2 core samples that have unknown ages and therefore cannot be split into either the pre-Devonian or post-Devonian categories.

At 206/8-2, the value 13.6% strain is significantly higher than seen from other wells. This core sample is particularly heavily fractured but the majority of the structures in this well sample exhibit no mineralisation and are potentially a result of the coring process rather than natural discontinuities in the basement. Well 206/8-8 shows a slightly lower strain value (4.85%) than seen from the full fracture sets from other wells.

#### 4.3.6 – Discussion of the Clair basement well fracture spacing datasets

Spacing analysis of fractures within basement well samples using population distribution plots are best described by consistent power-law distributions for almost all of the well samples (*Figures 4.22, 4.23 & 4.24*). This includes the spacing relationships for the full fractures sets and the open fracture sets alone. These consistent power-law spacing distributions evident in all the basement wells means that the fracture data collected at this scale can potentially be used as an estimation of the spacing attributes of fractures in the basement at different scales. It is also important to note that none of these power-law distributions extend over any more than one order of magnitude (normally between 0.1 and 1 metres), which means that from the well datasets it is difficult to determine if these power-law distributions are actually significant over a range of scales.

Well 206/8-8 exhibits an exponential spacing distribution for the full fracture datasets which indicates that this sample contains fractures that are randomly spaced (rather than clustered). It is likely that the location of this well is responsible for the spacing distribution of fractures seen within this well. 206/8-8 is located in the Core Area of the Clair Field, which is not on the basement ridge; therefore this well may well have been subject to a different stress field in comparison to the rest of the basement wells which lie on the Ridge area of the Clair Field, resulting in different spacing parameters for the fractures sets within the core sample.

When pre- and post-Devonian mineral fills are analysed separately, the spacing distributions are still power-law (*Figure 4.25*), albeit with a wide variation in the distribution attributes (D-values and CV values). This large variation in attribute values is likely a result of the variation in the distribution of these differently mineralised fractures through the 206/7a-2 core samples. Each core sample exhibits different numbers of each fracture set and this is likely to be responsible for the lack of a consistent power-law trend from both the carbonate and hematite/epidote fracture datasets.

D-values calculated from the power-law distributions obtained from full fracture sets in well 206/7a-2 vary over a wide range. This can be attributed to observations made from the core samples. Cores 1 to 3 show D-values >1 meaning that the power-law distributions are biased (as a result of over-sampling) towards fractures that are closely spaced, which coincides with observations from these three core sections that

shows that they have fracture densities which are significantly higher than the fracture density values (See *Table 4.3*) seen in the core samples further down the well (Cores 4 to 7, where D-values are commonly  $<1$ ).

What the analysis of D-values from the open fractures in basement wells (in particular 206/7a-2) shows is that the power-law distributions for these fracture sets have more fractures that are widely spaced (low D-values, see *Table 4.3*). In well 206/7a-2, CV values are generally higher, when only the open fractures are considered compared to the full fracture sets (*Table 4.3*). This means that the open fracture sets are more clustered. These low D-values and high CV values for the open fracture sets in the basement wells implies that any potential fluid flow through these open structures in the basement may occur in narrow, well-defined zones, of clustered open fractures, rather than through individual fractures dispersed throughout the basement. This may be consistent with previous studies (Falt et al., 1992, Coney et al., 1993) where well tests in 206/7a-2 showed that hydrocarbon flow originated in 5 ‘fracture corridors’ along the length of the 206/7a-2 well, rather than from individual fractures sampled throughout the well. Many of these ‘fracture corridors’ are consistent with the locations of open fractures, and subsequently the oil-staining, in the core samples used in this study (see Plate 1 in Falt (1992)).

Previous work conducted, during fieldwork, in the onshore analogue of the overlying Clair Group sediments suggested that ‘fracture corridors’ evident in the sedimentary packages are likely to have effective permeability and therefore are important for well drainage (Coney et al., 1993). The same study also concluded that these ‘fracture corridors in the sediments are aligned with those in the basement thus improving the confidence in the spacing attribute datasets, for the basement, provided in the study in this chapter.

The CV values from the other well samples (normally  $<1$ ) indicate that the fractures in these samples are anti-clustered or randomly spaced. This lack of evidence of fracture clustering, which has been reported to be present within the Clair basement (see Falt et al., 1992, Coney et al., 1993), potentially results from the orientation of the wells. Only well 206/7a-2 is horizontal; the remainder are vertical, and therefore it samples a larger set of fractures (the majority of fractures in the basement are steeply-dipping to sub-vertical). It is therefore concluded that only 206/7a-2 provides a representative sample of the fracture spacing attributes for the basement.

Fracture density values in well 206/7a-2 are higher in Cores 1 to 3 (the top of well, southeast end) than in Cores 4, 5 and 7 (the bottom of the well, northwest end) and this can be linked to the basement lithology. Cores 1 to 3 mainly consist of granodiorite gneiss which is in comparison to the bottom of the well where the lithology is mainly granite gneiss and pegmatite. It is possible that the mineralogy of each lithology is responsible for the relative variations in the fracture density across well 206/7a-2. The granodiorite gneiss contains up to 80% plagioclase and the majority of this is heavily fractured and highly altered. This high level of alteration potentially created weaknesses in the granodiorite gneiss which were later exploited by brittle deformation. This is in comparison to the other lithologies where the volumes of altered feldspar (mainly plagioclase) are generally lower so there are fewer weaknesses in the pre-existing lithology for the later brittle deformation to exploit.

Open fracture sets show relatively high fracture density values for each well sample (except 206/8-15) in comparison to the full fracture sets (care has been taken to remove fractures that were induced due to core extraction). This is an indication that there are potentially large volumes of fluid flow possible through the basement rock, if these open fracture sets are connected to each other. As previously mentioned, well tests from 206/7a-2 in the basement suggest that hydrocarbon production was coming from 4 or 5 'fracture corridors' spaced along the well (Falt et al., 1992). It is therefore possible those zones of highly clustered faults and fractures are where most of the fluid movement occurs and that smaller open fractures provide hydrocarbon storage space and a level of connectivity between these larger fractured zones. It is therefore important to understand these more discrete structures; their extent, density and connectivity by using an onshore analogue to obtain a large and full dataset of the potential fracture network in the Clair basement.

Using the fracture apertures measured from the basement core samples to estimate fracture length suggested that only fractures with apertures >30mm have lengths over 10m (*Figure 4.27*). This is important as it suggests that the majority of the fractures sampled from Clair basement cores have dimensions that are not significant for fluid transport. It is only fractures with the largest apertures that have estimated lengths that may have some significance in terms of connectivity (up to 18m in length). Their length coupled with the fact that the majority of these longer structures have open or partially open apertures (often with carbonate, pyrite and/or oil mineral fills) suggests

that these fractures could have an impact on fluid flow and fluid storage throughout the basement.

Fracture aperture has also been used to calculate percentage strain within the basement core samples. The strain value (5.71%) for the full fracture sets in well 206/7a-2 could be attributed mainly to Mesozoic extension across the Clair Field because the orientation of the well lies close to the direction of the maximum principal stress axis (NW-SE extension) that affected the Greater Clair area during that time (e.g. Knott et al., 1993, Davies et al., 2004).

Well 206/8-2 shows a significantly higher strain value than the other vertical wells. This core is highly fractured and many of the fractures have large apertures (mean aperture is 20mm) and the location of this well next to a section of the Ridge Fault which exhibits larger off-sets (~500m), may be responsible for the significantly higher strain values calculated.

By separating fractures into two separate groups; pre-Devonian and post-Devonian (based on mineral fills) it is possible to determine the strain relationships of the fracture sets in the basement before and after Devonian sedimentation. Epidote, hematite and quartz filled fractures show little impact on the total strain value for the Clair basement (0.65%) compared to over 3 times the strain value (2.05%) calculated for the carbonate mineralised fractures. This higher strain value and the fact that carbonate mineralisation overprints a lot of the earlier epidote, hematite and quartz mineralisation suggests that the structures included in the post-Devonian group are more likely to have a stronger influence on the fracture networks present within the Clair basement.



#### 4.4 - Fault and fractures in the Clair basement: Regional to well scale synthesis

Both the regional lineament (*Section 4.2*) and basement well analysis (*Section 4.3*) provide insights into the understanding of the Clair basement fault and fracture networks. This section aims to compare and contrast the datasets, and in particular focus on what fracture attributes can be transferred across different scales and also discuss where the pitfalls of this study lie.

Fracture orientation analysis of seismic (*Section 4.2.2*) and well datasets (*Section 4.3.3*) show that there is a strong preferential development of NE-SW (NNE-SSW) trending faults and fractures (*Figures 4.4 & 4.21*). Regionally, this fault trend is consistent with the main Mesozoic and Cenozoic extension direction (based on regional models (Bartholomew et al., 1993) and plate reconstructions (Knott et al., 1993)) in the Greater Clair area (NW-SE), resulting in many small NE-SW faults and a focus of deformation along the main NE-SW Ridge Fault. At a well scale, the lack of data for the whole of the basement makes it more difficult to attribute the fracture trends to regional stress fields. A mineralogical study of the infills present within NE-SW trending fractures from well 206/7a-2 indicate that these fractures formed during at least two phases of extension; the first associated with hematite/epidote mineralisation which originates from the pre-Devonian and the second associated with calcite/pyrite mineralisation which originates at the same time of oil emplacement in the Late Cretaceous to Early Tertiary (Milodowski et al., 1998). Previous work conducted by Falt et al. (1992) suggests that the NE-SW is the main fluid flow pathway through the Clair basement and therefore it is possible that the NE-SW fracture sets present in core from well 206/7a-2 occur regionally across the ridge area of the Clair Field basement.

The other prominent trend seen from the regional interpretation is NW-SE (*Figure 4.4*). This trend is also observed in well 206/8-15, albeit in a smaller dataset (*Figure 4.21b*). Although this NW-SE fault trend is prominent within the basement it has not been interpreted within the sedimentary cover horizons from the regional analysis (*Figure 4.7*), suggesting that NW-SE faults are inherently basement structures, and therefore, are pre-Devonian in age.

N-S and E-W fault trends are represented in the basement on the regional lineament analysis (*Figures 4.4 & 4.5*) but are not as obvious from basement well data (*Figure 4.21*). This does not mean that they are not present in the basement at the scale

of a well; it means that they have not been clearly sampled by the few well samples that extend into the basement. Both N-S and E-W have been interpreted from regional seismic horizons in the overlying sedimentary cover sequences and can be seen as far through the sequence as the Cretaceous (*Figure 4.7*). This means that faults of these orientations are Cretaceous or younger in age and are definitely not restricted to the basement.

Spacing analysis of the regional and well datasets has been conducted using 1-dimensional line sampling (*Sections 4.2.4 & 4.3.4* respectively). The resulting population distribution plots show distinctly different spacing distributions for the regional and well datasets (*Figures 4.9, 4.22, 4.23 & 4.24*). From the regional lineament analysis, spacing distributions vary between exponential and power-law (*Figure 4.9*), with the exponential trends consistently being the most statistically significant. This implies that the fault lineament spacing, from the regional basement study, cannot be used for estimation the fracture spacing attributes of fracture sets at different scales.

The well data show different spacing distribution results. Spacing distribution plots for well datasets consistently show power-law relationships (*Figures 4.22, 4.23 & 4.24*), suggesting that the datasets are scale-invariant. This has important implications for fracture modelling in the Clair basement as the scale-invariant nature of the fracture sets means that they can be used as an estimation of the fracture spacing attributes at different scales within the Clair basement (between 0.1 metres and 100m, although the spacing value at which fracture and fault sets stop showing power-law relationships at the top end is unknown).

The difference in the spacing analysis, regionally (exponential distribution) and at a well scale (power-law distribution), means that there may be a range of scales where scale-invariance applies (around the well scale). Therefore, caution should be used if extrapolating the well analysis for basement models, as it is difficult to know which scale range, beyond the well scale, the scale-invariance can be applied to.

This clear difference between the fracture spacing distributions regionally and at the well scale highlights the importance of being able to use an onshore analogue to increase the availability of data to help improve the understanding of the fracture networks in the Clair basement. Having an onshore analogue allows a high resolution study of the fracture networks to be conducted and more importantly allows the fracture networks, which are potentially present in the offshore basement, to be viewed

and analysed in three dimensions. The importance of an onshore analogue is also emphasised by the lack of connectivity data available from offshore datasets. Terrestrial Laser Scan (TLS) data collected from key outcrops on the mainland Lewisian allows a far more detailed examination of the fault and fracture networks and therefore provides an opportunity of both fracture presence variations and intersections to be analysed in great detail. The results from the TLS study can be found in *Chapter 5*.

#### 4.5 – Clair basement summary

- The analysis of the Clair basement datasets provides a useful insight into the fracture networks present within the Clair basement. It more importantly highlights the major drawbacks of working with offshore data and the difficulty in being able to fully image and understand the faulting and fracturing patterns and characteristics within the Clair basement rocks.
- A prominent fault trend of NE-SW is present in all offshore datasets and this is consistent with Mesozoic NW-SE extension, meaning that these NE-SW structures are potentially open to fluid storage and flow. These open structures seen in basement core samples are partially mineralised with carbonate and/or pyrite and are commonly oil-stained.
- Fault spacing analysis at a regional scale results in exponential spacing distributions that are not scale-invariant. This is in comparison to the well datasets which exhibit power-law spacing distributions for the fractures, indicating that they are scale-invariant. Therefore, caution has to be used when using the well data as an estimation of the fracture spacing attributes at different scales for basement modelling, as the spacing attributes gathered from well data cannot be used to estimate the fault spacing parameters at a regional seismic scale.
- Lithological and fracture analysis from the well (core) datasets shows that the Clair basement has undergone many different episodes of ductile and brittle deformation. Compositional banding and recrystallised textures provide evidence that the basement lithologies have been subjected to high degrees of metamorphism (amphibolite-facies or above) early in their history. Fracture mineralisation indicates that there have been at least five phases of

mineralisation associated with brittle deformation within the Clair basement; three pre-Devonian (epidote, hematite and quartz) and two post-Devonian (carbonate and carbonate/pyrite/oil-staining).

- Qualitative and quantitative analysis of the Clair basement datasets in this study have provided a better understanding of the fracture networks within the basement rocks. This study has also highlighted the importance of having an onshore analogue to fill in the gaps created by the lack of high resolution datasets for the whole of the Clair basement structure. An onshore analogue (mainland Lewisian Gneiss Complex) provides information on the 3-dimensional discrete fracture networks at an outcrop scale that cannot be obtained from well data alone.

## **Chapter 5 –Deterministic fracture network models from the Lewisian Gneiss Complex of the NW Scottish mainland**

### **5.1 – Introduction to terrestrial laser scanning (ground-based LiDAR)**

The aim of this chapter is to present deterministic fracture/fault network models that have been created from three key outcrops within the mainland LGC. Terrestrial Laser Scanning (TLS) provides an accurate method of collecting large volumes of outcrop information in a relatively short period of time. The creation of fully geo-referenced models of fractures and faults in this way provides a greater understanding of the complexity of the fracture networks which cannot be obtained from 1-dimensional line samples or 2-dimensional photo-mosaics alone because they have an increased 3-dimensional component to them. It is also suggested that the TLS models will partially span the gap in data between fieldwork and regional analysis.

The fracture and fault models have been generated from the TLS datasets in order to try to improve models of subsurface fluid flow within the Clair field. To date fracture models have been created using stochastic methods. For example, there is an understanding that large NW-SE shear zones exist within the Clair basement and that these zones potentially result in areas of significantly increased fracture density and connectivity. Currently, locations of these shear zones in the Clair basement and their attributes are modelled stochastically (Bergbauer and King, 2009) and therefore the true nature of the complexity of the fracture networks within the Clair basement is not captured. This is because the stochastic models do not account for the variation in fracture spacing characteristics due to changes in structural setting (shear zones, proximity to major faults, etc.) i.e. they only consider the rock mass to be either heavily fractured or poorly fractured with no control on how fracture spacing values may change across the model.

Through the analyses conducted (regional onshore & offshore studies and well & outcrop studies) in this project it has been ascertained that the heterogeneity of the Clair fracture networks requires models that consider the fracture patterns in a

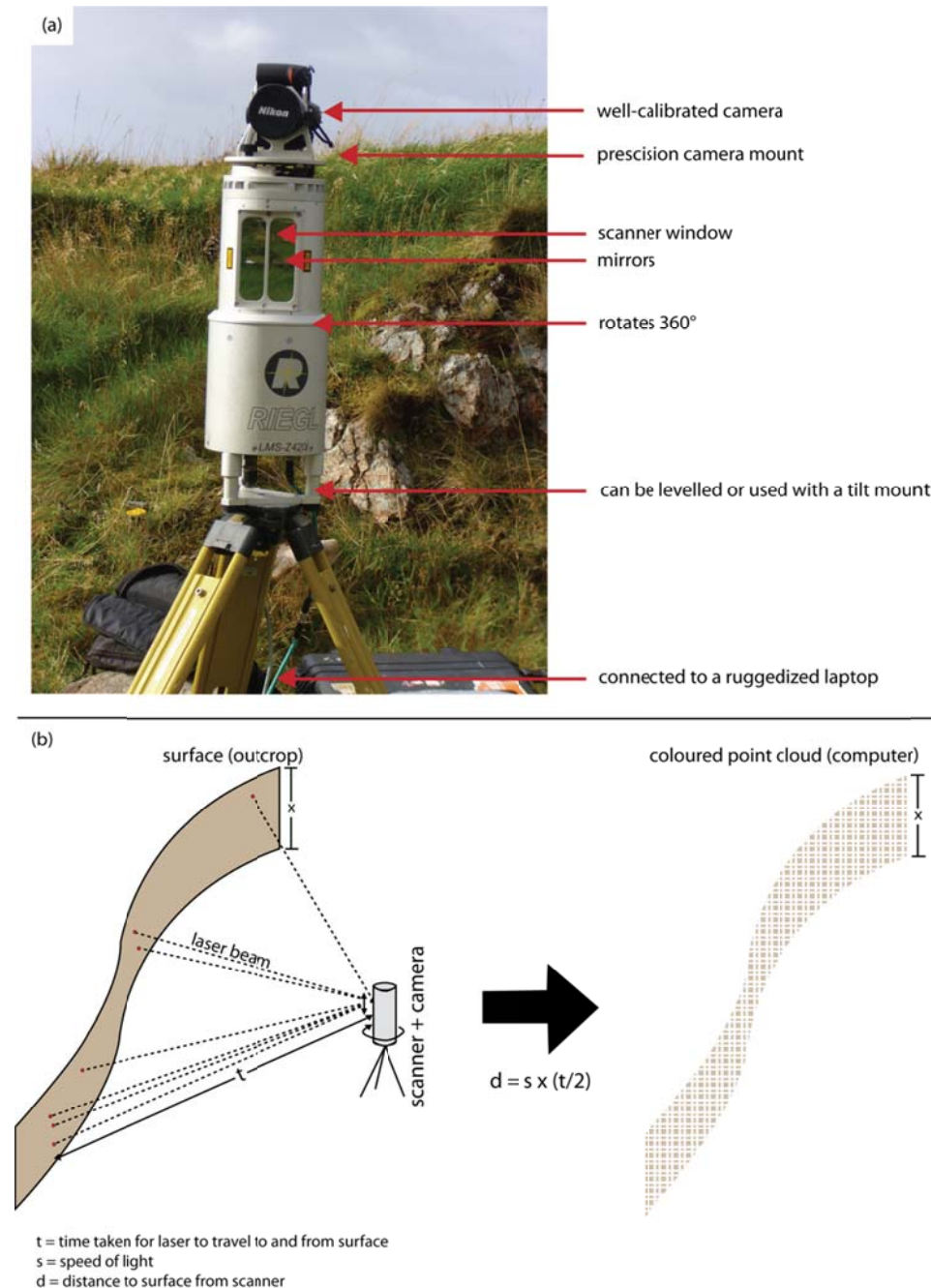
deterministic manner (using quantitative datasets), so that relatively small-scale (for example using 50m model grid cells in fluid flow models of the basement) changes in fracture attributes can be accurately accessed.

TLS allows the collection of '2.5' dimensional datasets (it can only capture a 2-dimensional surface with the small-scale topography of the outcrop in a 3-dimensional space (Jones et al., 2008a), see *Chapter 1, Section 1.6.7*), which by virtue of their high spatial resolution, can then be manipulated and analysed in great detail. This allows the creation of highly realistic geo-referenced fracture models from the mainland Lewisian Gneiss Complex (LGC) that can be assessed for their suitability as analogues for the varying structural settings thought to be present within the Clair basement.

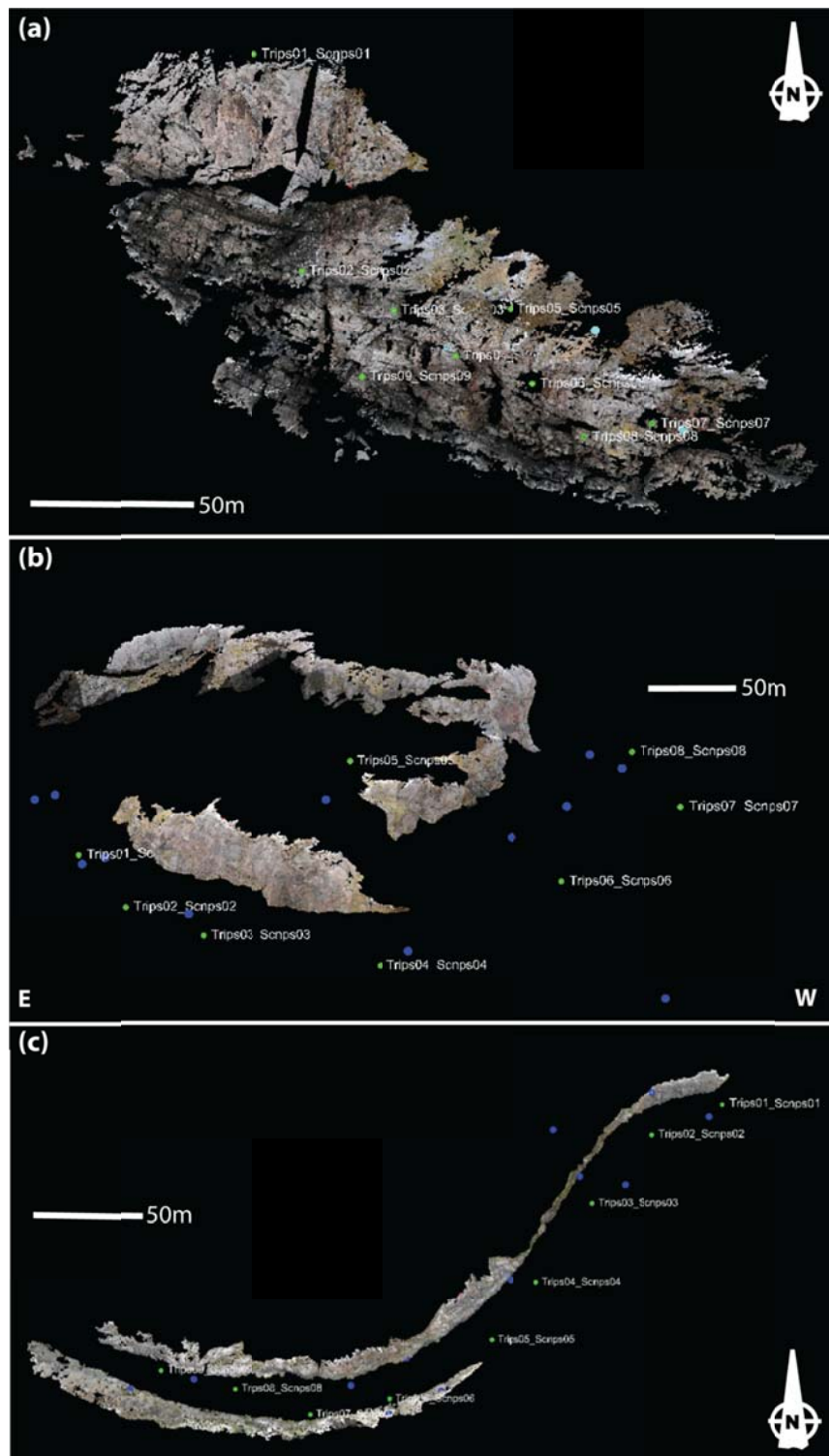
The raw TLS data collected during the current project was collected as point-clouds gathered using a [Riegl](#) LMS-z420i scanner (*Figure 5.1a*). Outcrop data is collected by the scanner by using a continuously oscillating mirror to send laser beam to the outcrop surface and to then collect the returning light. The time taken for the laser beam to leave the scanner and return ('time of flight') is measured which then allows the scanner to calculate how far away the surface is (*Figure 5.1b*). This calculation is made for points across the surface at a typical acquisition rate of 12,000 points/s, creating a point cloud that defines the shape of the measured surface (*Figure 5.1b*). Each data point in the cloud is then coloured from photographs taken with a well-calibrated Nikon D100 digital SLR camera precision-mounted on top of the scanner (*Figure 5.1a*). More information on the scanner used and methodology is given by Trinks et al. (2005) Kokkalas et al. (2007), McCaffrey et al. (2008) and Wilkinson et al. (2010).

The data is gathered by the scanner which is placed in a series of pre-selected scan-points around the outcrop (*Figure 5.2*). Each of the individual datasets are then registered, i.e. 'stitched' together and geo-referenced into the correct coordinate system (WGS 1984 Complex UTM zone 30N). This geo-referencing is possible because the reflectors (*Figure 5.2*) used to locate and register the scans in the scanner software (RiSCAN Pro v1.2.1b9) are given precise GPS (global positioning system) coordinates that can then be used to orientate the point clouds into their correct global location. These fully orientated point clouds can then be used to pick fault and fractures sets (and any other important geological features) from the coloured point cloud. Detailed descriptions of TLS data acquisition and interpretation techniques are given in (Ahlgren

and Holmlund, 2002, Kokkalas et al., 2007, Bellian et al., 2005, McCaffrey et al., 2008, Wilkinson et al., 2010).



**Figure 5.1:** (a) Annotated Riegl LM-Z420i laser scanner used to collect the outcrop model datasets in this chapter. (b) Diagram showing the basic calculation made by the scanner to create the virtual point cloud that is a replica of the scanned surface. In reality the scanner has to make approximately 40,000 calculations a second (if the scan rate is 10,000 points per second) to accurately determine how far away the point on the outcrop is from the scanner unit.



**Figure 5.2:** Examples of 'cleaned' TLS point clouds showing the location of scan positions (in green) and reflectors (in blue/cyan) used to geo-reference the data. **(a)** Alltan na Bradhan **(b)** Kinlochbervie **(c)** Caolas Cumhann.

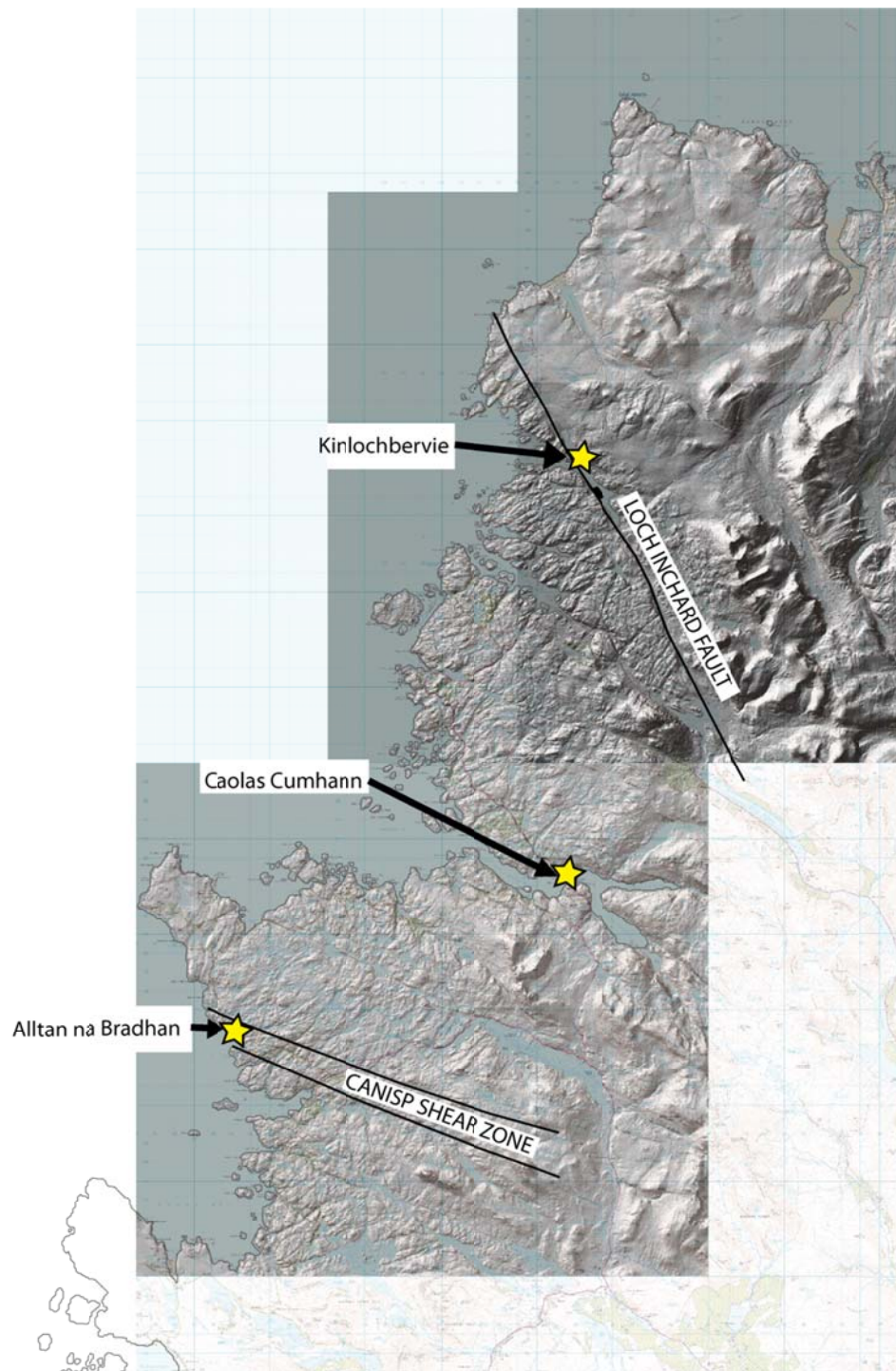


## 5.2 – Rationale for the selection of scanned outcrops

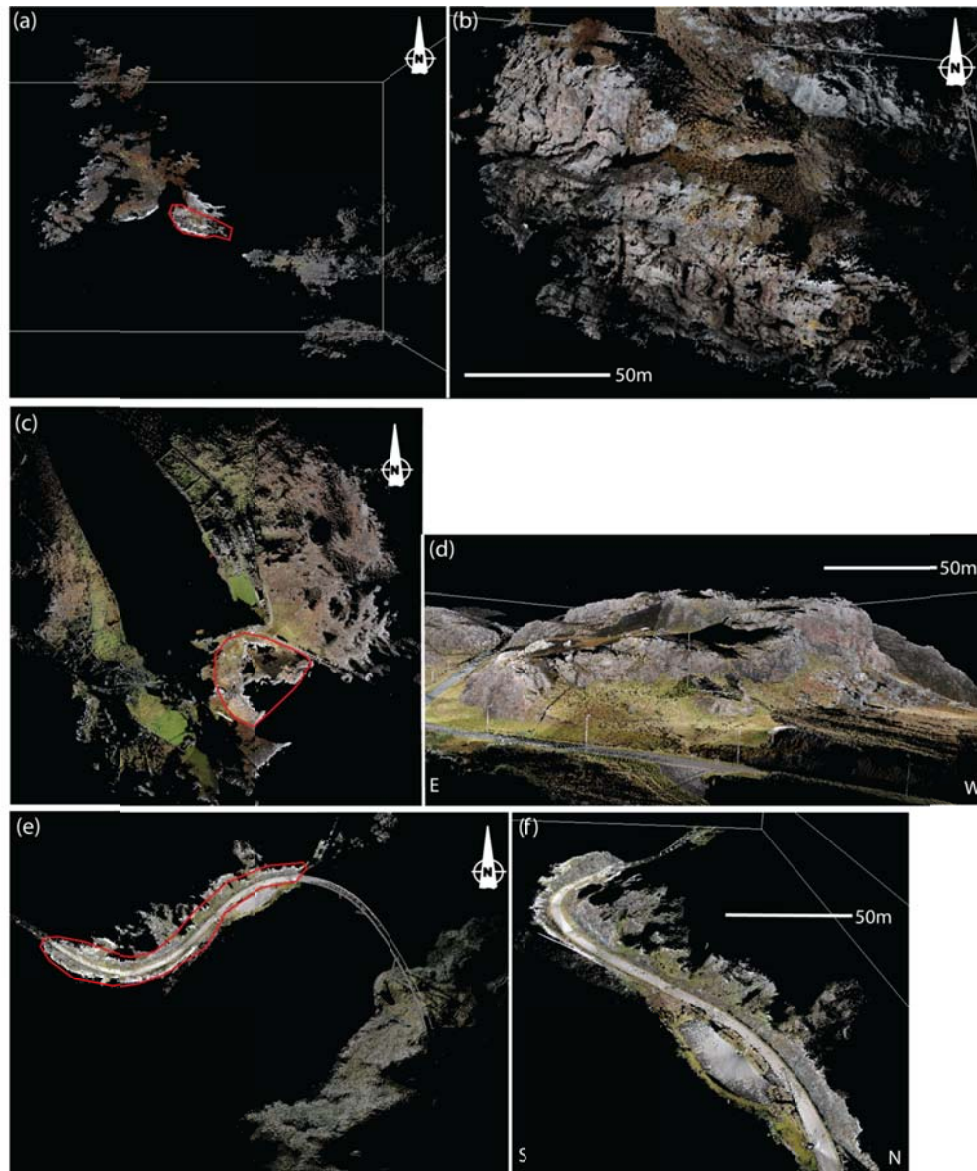
TLS data have been collected from three key outcrops across the LGC. The rationale for the chosen outcrops is that, from an industry and academic perspective, it is essential that we capture datasets that are representative of the diversity of structural settings present within the Lewisian Complex. For industry, it is important to provide details of the 3-dimensional fracture network attributes and statistics, e.g. fracture intensity, connectivity, density, etc. in order to provide the key information that can be implemented into the already existing fracture network models created by the Clair Joint Venture Group. From an academic perspective, it presents an opportunity to explore variation of the fracture network characteristics in three dimensions to aid the overall understanding of the small-scale fault and fracture network relationships to larger controlling structures and geological settings in the mainland LGC.

Given the limited amount of time available to collect this data, the most important and representative structural settings for the Clair field basement have been selected for scanning and detailed structural interpretation and analysis. It should be noted that all three of the key outcrops had been previously sampled during fieldwork using 1-dimensional sample lines and rock samples were collected for thin section analysis. This allows the TLS analysis to be 'ground-truthed' to observations and analyses from the actual outcrop without having to rely entirely on the collected point cloud data to create the fracture network models.

TLS data has been gathered from three outcrops on the mainland LGC; Alltan na Bradhan, Kinlochbervie and Caolas Cumhann (*Figures 5.3 & 5.4*). The details of each key outcrop at Alltan na Bradhan, Kinlochbervie and Caolas Cumhann are briefly summarised in the sections below.



**Figure 5.3:** Mainland LGC map showing the location of the the three key outcrops used to create terrestrial laser scan outcrop models.



**Figure 5.4:** Images of the TLS datasets collected from the three key outcrops selected in the mainland LGC. **(a)** Full scan dataset from Alltan na Bradhan. Red outline highlights the area used for fracture modelling shown in (b) (this area has been scanned in detail). **(b)** Detailed scan of the section of outcrop used for fracture modelling from Alltan na Bradhan. **(c)** Full scan dataset from Kinlochbervie. Red line highlights the main outcrop used for fracture modelling shown in (d) (this area has been scanned in detail). **(d)** Detailed scan of the main Kinlochbervie outcrop used for fracture modelling. **(e)** Full scan dataset from Caolas Cumhann. Red outline highlights the area used for fracture modelling shown in (f) (this area has been scanned in detail). **(f)** Detailed scan of the Caolas Cumhann outcrop used for fracture modelling.

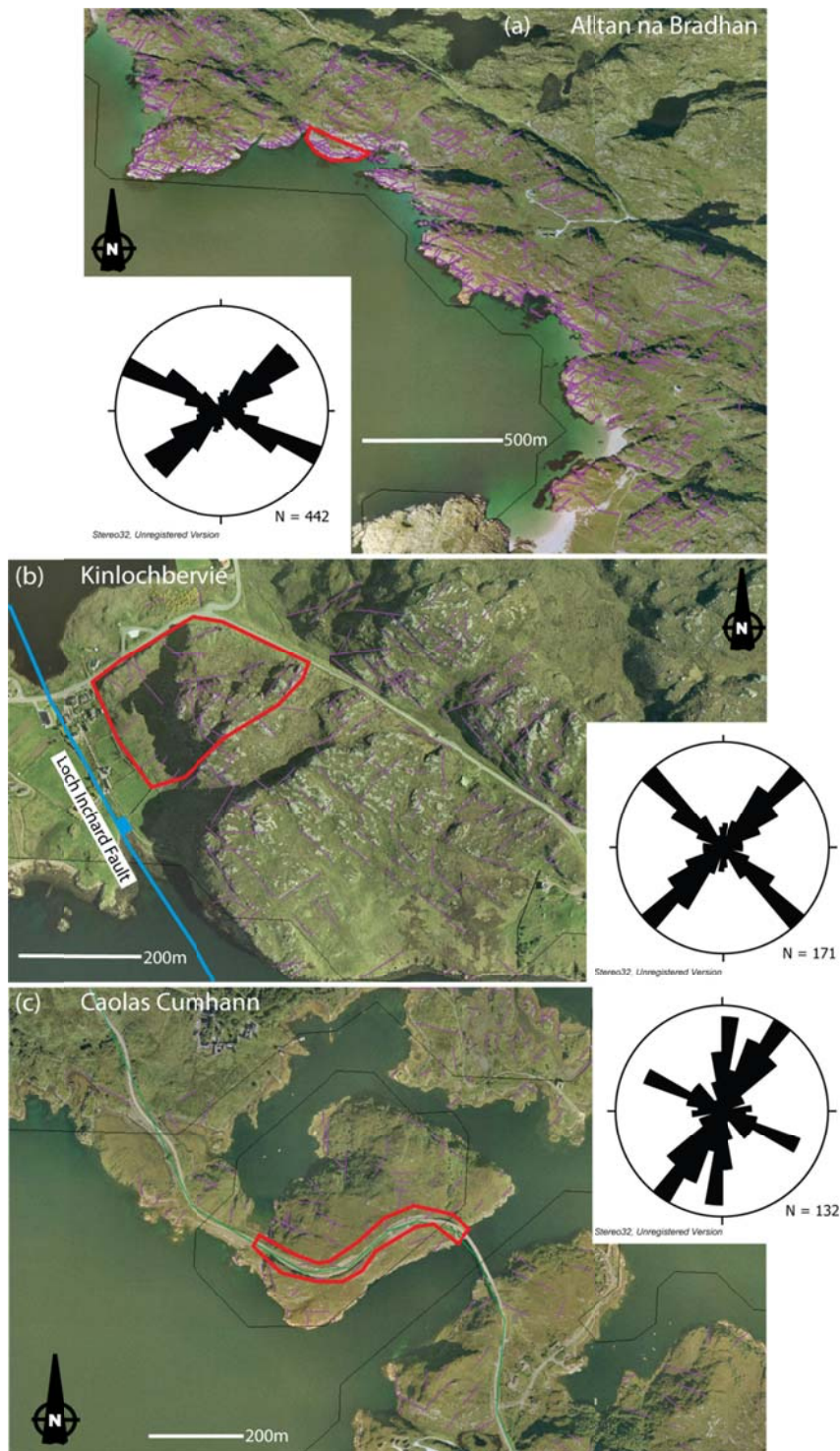
### 5.2.1 – Alltan na Bradhan (Canisp Shear Zone)

The complex fracture network associated with Laxfordian shear zones within the Assynt Terrane was sampled at a suitable outcrop in the Canisp Shear Zone (CSZ). The outcrop at Alltan na Bradhan (NC 0508 2624) is also almost 100% exposed and contains good examples of both ‘Late Laxfordian’ faults and ‘Stoer Group age’ faults and is a fine representation of the complex relationship between pre-existing weaknesses (foliation) and the fracturing that occurs. It is thought that similar shear zones are present within the Clair basement and that there is an associated increase in fracture density and connectivity that potentially results in so called ‘fracture corridors’ which have been shown to be responsible for almost all of the fluid flow in the basement (Falt et al., 1992, Coney et al., 1993).

Aerial photograph interpretation (*Figure 5.5a*) across the Canisp Shear has identified two main sets of lineaments that trend NE-SW and NW-SE. As understood from fieldwork analysis (see *Chapter 3*), the NW-SE lineaments can be attributed to the foliation parallel ‘Late Laxfordian’ faults and the NE-SW lineaments are known to be Stoer Group age fractures. Both these lineament trends form a densely populated fracture network across the Canisp Shear Zone and therefore interpretation of these faults and fractures from the TLS dataset are essential to capture the full fracture network at this location.

This particular outcrop in the Canisp Shear Zone is a wave-cut platform, which caused logistical issues. The effect of erosion has formed small scale topography which means that, when scanning, the data collected contains lots of shadowing, which occurs in areas not in the laser’s line of sight from each tripod position (*Figures 5.2a, 5.4a & b*). As a result the dataset from this outcrop is of poorer quality than those collected from the other key outcrops in the Lewisian, thus making it difficult to interpret a full fracture network within the CSZ.





**Figure 5.5:** Aerial photographs of the local areas surrounding the locations of the three TLS datasets. The areas that have been scanned are highlighted with red outlines. **(a)** Alltan na Bradhan in the Canisp Shear Zone. Inset is a rose plot of the lineaments picked at 1:5000 scale. **(b)** Kinlochberrie. Inset is a rose plot of the lineaments picked at 1:5000 scale. **(c)** Caolas Cumhann. Inset is a rose plot of the lineaments picked at 1:5000 scale.

### 5.2.2 – Kinlochbervie

Kinlochbervie, in the Rhiconich Terrane (NC 2296 5621), was chosen as a suitable outcrop for this study for several reasons. Most importantly, it sits in the hanging wall of an adjacent large, NW-SE trending normal fault, which is a similar structural setting to that which is thought to occur within regions of the Clair field basement. Another reason this outcrop was chosen is because of its shape. Its location on a hill between two lochs means it can provide almost 360° coverage, and hence, provide a better approximation to a fully 3-dimensional dataset (*Figures 5.2b, 5.4c & d*). The fractures at Kinlochbervie show evidence for at least one reactivation phase and a later stage of calcite mineralisation, which can be used as a proxy for the deformation and mineralisation in the Clair field basement (see *Chapter 4, Section 4.3.2*).

Aerial photograph interpretation at a 1:5000 scale (*Figure 5.4b*) allowed the identification of two main fracture lineament trends of NW-SE and NE-SW forming synthetic and antithetic structures to the main Loch Inchar fault, respectively. A smaller number of N-S trending lineaments were also interpreted from the aerial photographs and therefore they should also be present within the TLS fracture network model from Kinlochbervie. Field observations suggest that the majority of fractures at Kinlochbervie are likely to be post-Torridonian structures (*Chapter 3, Section 3.3.3.3*) and therefore should be identifiable on the TLS dataset by their distinctive red, hematite-staining. The aerial photograph interpretation also suggested that the fracture density associated with the Kinlochbervie outcrop is higher than other areas within the Rhiconich Terrane located away from large faults or other structures.

### 5.2.3 –Caolas Cumhann

The final key outcrop is a road cutting located directly north of Kylesku, adjacent to the main A894 road bridge and the Loch Glencoul viewpoint (NC 2251 3392). This outcrop is useful because it is not influenced by any adjacent large-scale structures and therefore provides an assessment of the background fracture network for the Assynt Terrane. The shape of the outcrop makes it possible to collect data on all the fault and fracture orientations present within the Assynt Terrane LGC (*Figure 5.4e & f*).

The aerial photograph interpretation indicates strong N-S and NNE-SSW fracture trends across the Caolas Cumhann area (*Figure 5.5c*). NW-SE trending lineaments are also present in the aerial photograph interpretation. The shape and orientation of the

scanned road section is optimal for these fracture trends to cross-cut the outcrop and therefore these three fracture trends should also be present within the TLS fracture network model. The aerial photograph interpretation suggests that fracture density is low, which should also be reflected in the TLS fracture model from this outcrop.

An outcrop within the Rhiconich terrane, which shows the background fracture network, has not been scanned for this study. This is because no suitable outcrop has been identified and from field observations it is apparent that the Rhiconich Terrane is poorly fractured away from major faults. Therefore scanning an outcrop of the background fracture pattern would not have produced a dataset that would be useful for basement modelling in the Clair Field.

### 5.3 – 3-dimensional fracture network model construction

The high-resolution nature of the TLS data makes it possible to interpret many of the fractures and faults visible to the naked eye at the outcrops with the advantage that part of the outcrop that cannot be reached in the field are also included in the dataset. All of the key outcrops contain fractures that have visible surface expressions, which mean that the fracture and fault orientations can be reconstructed with interpretation from the TLS data. Although the resultant models contain 3-dimensional data (primarily orientation) the fracture networks realistically only contain '2.5-dimensional' data and can only be extrapolated into 3-dimensions with significant assumptions about the size and lateral extent of the fracture sets. The work completed for the purposes of this thesis uses the fracture sizes, as interpreted from the point clouds, without extending them into the rock mass.

Other assumptions made while creating the TLS models include the shape of the interpreted fractures. It is generally accepted that fracture planes form ellipses where the fracture displacements decrease towards the tips. For simplicity, the fractures interpreted for the models in this study are given rectangular shapes which have been deemed acceptable because the majority of the interpreted fractures have limited surface expressions and therefore the change in area between rectangles and ellipses would be negligible.

It should also be noted that due to the nature (and resolution) of the TLS dataset, it is impossible to pick every single fracture present within each outcrop. Fractures which are observed in the outcrop as linear features (i.e. the fracture plane shows no surface expression) are typically not interpreted from the TLS dataset. This has obvious implications for the fracture spacing characteristics of the resulting fracture network as not every fracture present in the outcrop is included in the analysis. Although poorly defined fractures are omitted from the resulting fracture network models this is considered to be a resolution (scaling) issue. From fieldwork, the majority of the poorly defined fracture planes (~80%) also have short lengths (<30cm) and therefore are assumed to not contribute greatly to the overall fracture network. Throughout the TLS interpretation fractures with lengths <50cm have been disregarded from the fieldwork datasets as they are also assumed to not contribute to the overall fracture network. The cut-off length (50cm) is slightly higher than the cut-off length used during fieldwork as a direct result of the lower resolution of the TLS outcrop dataset compared to looking directly at the outcrop.

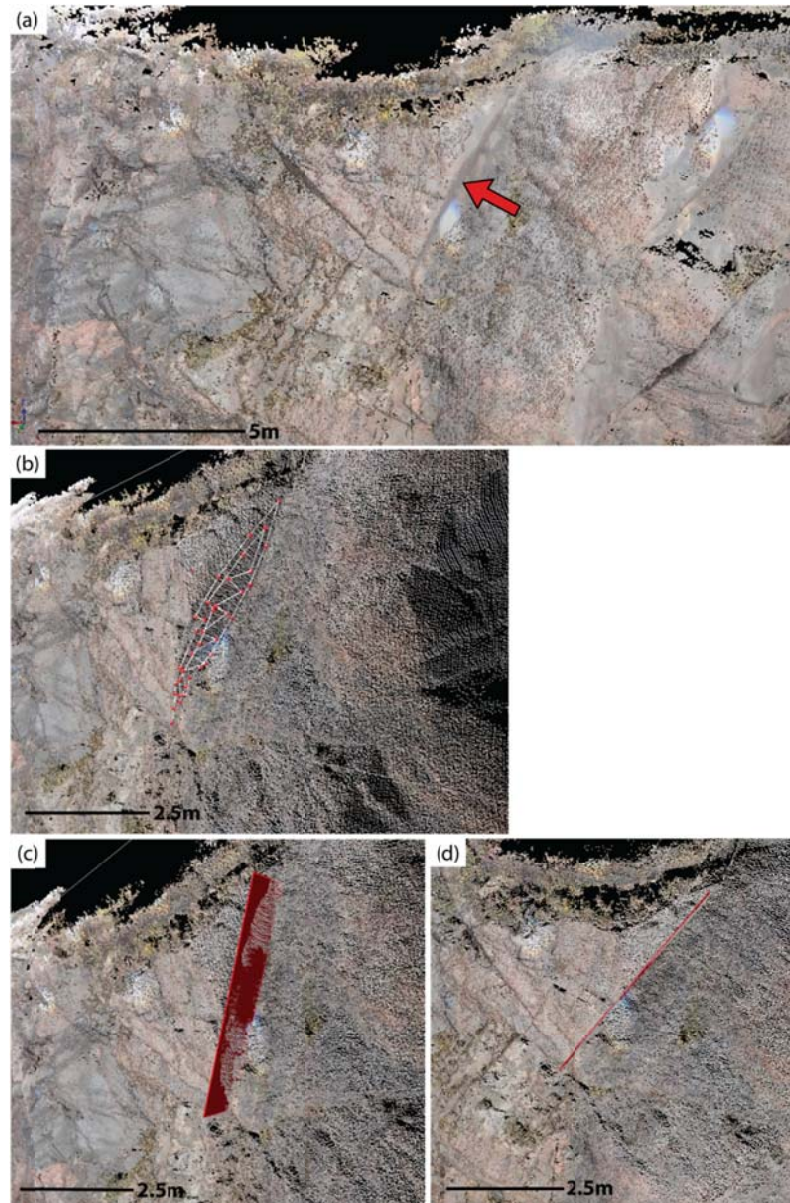
### 5.3.1 – Interpreting and creating fracture planes

To get as much information out of the TLS datasets as possible, a significant portion of time was spent interpreting (picking) fractures from coloured point clouds. This interpretation took place in the RiSCAN Pro software. Fractures were interpreted by picking polylines in a circular or zigzag pattern so that as much of the visible fracture surface as possible was included (*Figure 5.6b*). The interpretation was completed directly on the point clouds, but field photographs of the scanned sections were also used to confirm the extent and geometry of small-scale, less obvious fractures. The resulting set of polylines for each outcrop can then be converted into fracture planes using a stringent fitting criteria developed by Jones (2011) so that there is a ‘best-fit’ to the true fracture planes (*Figure 5.6c & d*). It works by looking at the aspect ratio of the polylines so that if the length/width ratio is below a certain criteria it is rejected as the uncertainty to fit a plane to the polyline is too high. The details of the stringent fitting criteria are given in *Appendix D*.

The created fracture planes can be visualised in RiScan Pro; however the rest of the fracture analysis is processed using Paradigm GOCAD 2009.2. The fracture planes are exported from RiScan Pro and then directly imported into GOCAD, along with a low



resolution point cloud, from which, outcrop topography surfaces can be interpolated as part of the fracture model analyses.

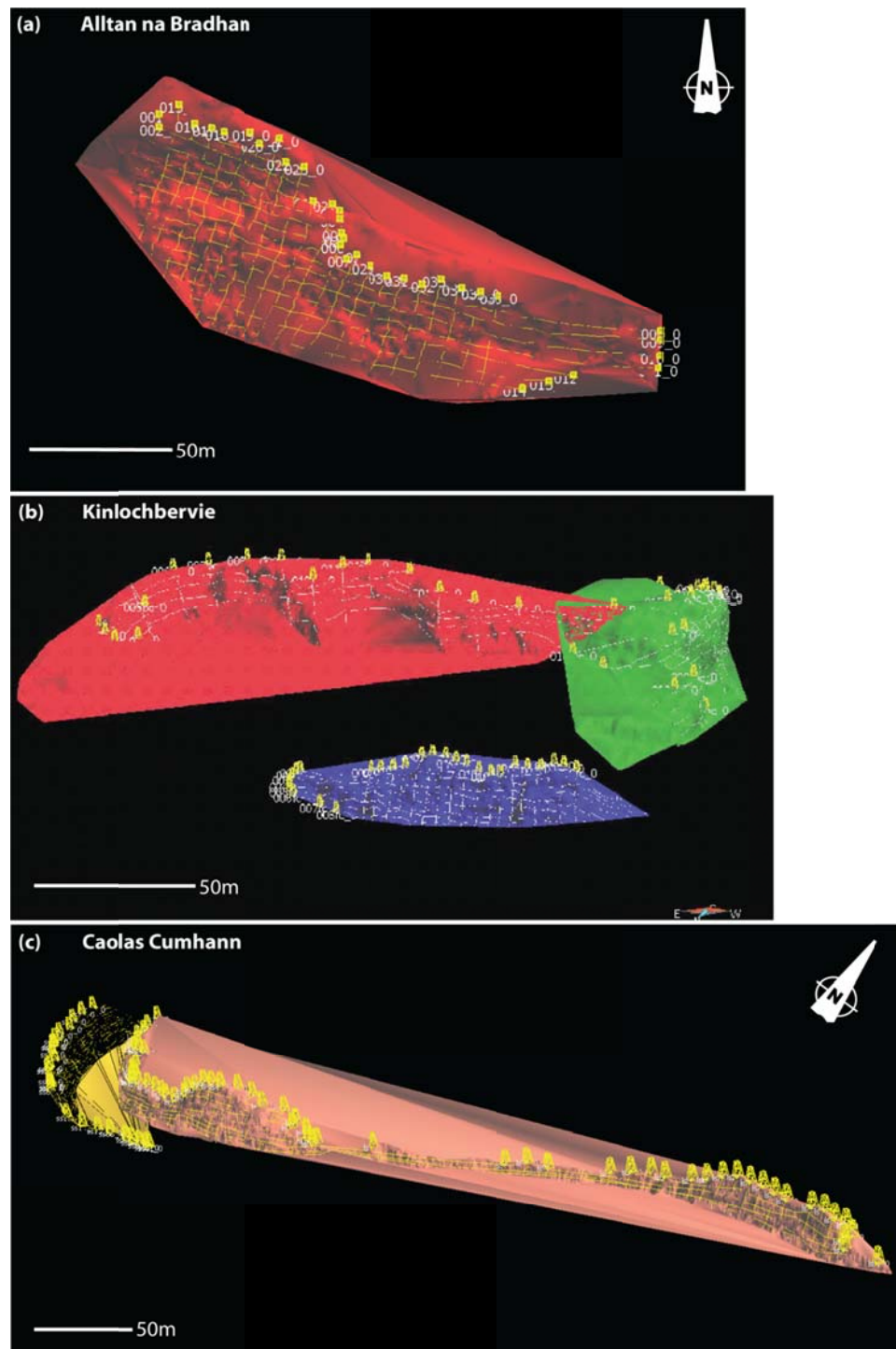


**Figure 5.6:** Images outlining the process undertaken to interpret and create fracture planes from the TLS datasets. The images used are taken from the Kinlochbervie TLS dataset. **(a)** Fracture planes with surface expressions are identified. **(b)** Polylines are used to define the surface expression of the fracture plane. **(c)** These polylines are then exported from RiScan® and imported into a Geospatial Research Limited proprietary spreadsheet where they are subjected to a stringent fitting criteria before being converted into fracture planes. **(d)** These fracture planes provide the best fit for the surface expression observed from the TLS datasets. This figure shows how the created fracture plane (from a polyline) fits the surface expression of the outcrop.

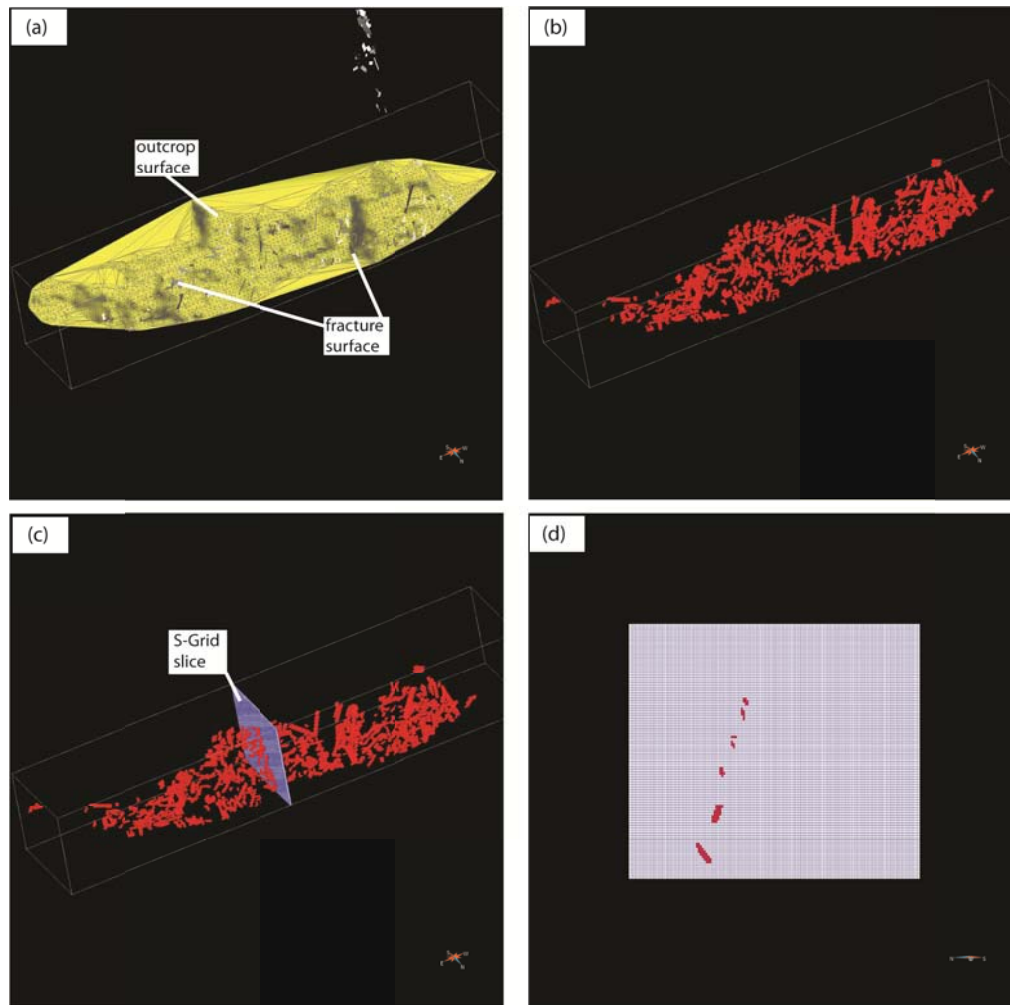
### 5.3.2 – Analysing the fracture networks

To allow direct comparisons between the TLS and outcrop data, similar statistical analysis techniques have been applied to both datasets. The first of these involves the creation of ‘pseudo-wells’ draped over the outcrop topographic surface which allow collection of 1-dimensional line samples across the datasets (*Figure 5.7*). These can then be analysed for fracture spacing and density attributes. The workflow for creating ‘pseudo-wells’ was identical to that used for the onshore and offshore datasets and can be found in *Appendix C*. Once spacing data have been obtained from the line samples, population distribution plots were created that can be directly compared to those created from outcrop and from the regional onshore dataset (and ultimately the analysis from the Clair basement). An analysis of the coefficient of variation (CV) was also carried out to ascertain the fracture clustering relationships, together with a 1-dimensional study of the fracture density variations along the study outcrops. These 1-dimensional line samples are also useful for direct comparison with sub-surface datasets from the Clair basement where the only direct rock analyses comes from 1-dimensional well samples.

The 2.5D nature of the point cloud data permits a volumetric analysis of fracture presence and a workflow has been developed to calculate the variation in fracture presence across the key outcrops (Sagi, 2010). Fracture presence is here defined as whether or not a given area or volume of rock contains one or more fractures. This fracture presence analysis works by creating S-Grids for outcrops or outcrop sections that can then be filled with different types of information (*Figure 5.8* shows the fracture presence analysis workflow). Three different resolution S-Grids were created (very low-resolution 20 x 20 x 20 cells; low-resolution 50 x 50 x 50 cells; high-resolution 300 x 150 x 100 cells – the size of each cell varies depending on the size of the outcrop) to allow the development of a 2- and 3-dimensional box-counting analysis that assesses how much of each outcrop is filled by fractures. A review of box-counting is given in *Chapter 1; Section 1.5.2.4.1* and the techniques relevant to the fracture modelling presented in this chapter are reiterated below.



**Figure 5.7:** Outcrop surfaces in Paradigm GoCad 2009.2 showing the network of pseudo-wells taken across each of the TLS datasets **(a)** Alltan na Bradhan where pseudo-wells are taken parallel and perpendicular to foliation. **(b)** Kinlochbervie where the outcrop is split into three cliff sections; front cliff (blue), main cliff (green) and back cliff (red). **(c)** Kylesku. The outcrop is split into two cliff sections; long road section and short road section.



**Figure 5.8:** 3D model fracture presence analysis workflow. (a) Fracture planes are imported into Paradigm GOCAD 2009.2 along with a low resolution TLS point cloud which is converted into an outcrop topographic surface. (b) An S-Grid is created using the topographic outcrop surface (shown in white) and then a region of the S-Grid is created where it is intersected by fracture planes (shown in red). (c) The region in the S-Grid is painted with a property to make it visible and then slices are taken through the grid. (d) The number of coloured cells (for fractures and outcrop) on each slice is counted (the coloured cells represent the fractured region) and the proportion of cells containing fractures per outcrop is calculated.

To determine how much of each outcrop is filled by fractures the cells in the S-grid that were intersected with a fracture(s) were collated into a region in the S-Grid (*Figure 5.8b*). Those cells that are intersected by the outcrop are collated into a separate region. These regions are then 'painted' with an arbitrary property so they are visible on slices through the S-grid (*Figure 5.8c & d*). Slices of the S-Grid are taken along a set orientation (*Figure 5.8c*) (this can be conducted for different orientations along the outcrop to assess variations due to the presence of geological features, i.e. foliation) and the number of 'painted' cells on each slice counted (*Figure 5.8d*). This process is conducted for both the fractures and the outcrop and then the number of fracture-filled cells on each slice is divided by the number of outcrop-filled cells. As the outcrop only fills a 2.5-dimensional space in a 3-dimensional volume, the proportion of fracture-filled cells (compared to outcrop-filled cells) are multiplied by the total number of cells on the slice to make the fracture/outcrop proportion fill the entire 2D slice. This method uses the fracture proportion calculated from the outcrop surface and estimates how fractures would fill the model slice if the fracture proportion was consistent away from the scanned outcrop surface.

The advantage of this particular analysis technique is that it eliminates the affect the 2.5-dimensional outcrop shape has on the fracture fill of each outcrop. It should be noted, however, that the values of fracture fill for each outcrop are inherently biased by the shape of the outcrop that was initially scanned. This is because the apparent shape of fractures at the surface of the outcrop (e.g. fracture trace or fracture plane) is dependant on both the amount of weathering/erosion and the shape of the outcrop. The majority (>90%) of the outcrop shape/weathering effect is removed by the resolution of the initial TLS fracture interpretation where the lower fracture length scale is cut off at 50cm. This is because fractures <50cm in length typically presented as fracture traces (due to outcrop shape/ weathering processes), and therefore cannot be interpreted as planes from the outcrop pointclouds. Having a fracture network model scale cut-off at 50cm almost removes the bias caused by these small fractures and the modified box-counting technique used to analyse these interpreted fracture network models therefore provides realistic 2- and 3-dimensional values for fracture presence (and fracture intersections) in each of the scanned outcrops for fractures 50cm in length or longer. These models therefore do not represent fractures <50cm but this is

considered acceptable because these short fractures show little evidence of offset and do not likely contribute to any potential fluid flow through the fracture network models.

A similar method can be used for each outcrop to determine how much of the full 3-dimensional model volume is filled by fractures. The 3D value is obtained by determining the total number of cells in the model that include fractures and dividing it by the total number of cells that include outcrop. The resulting proportion of fracture-containing cells is then multiplied by the total number of cells in the volume to reconstruct the fracture-fill proportion to fill the entire 3D volume. In a similar manner to the 2-dimensional analysis this method uses the fracture proportion calculated from the outcrop surface and estimates how fractures would fill the full model if the fracture proportion was consistent away from the scanned outcrop surface.

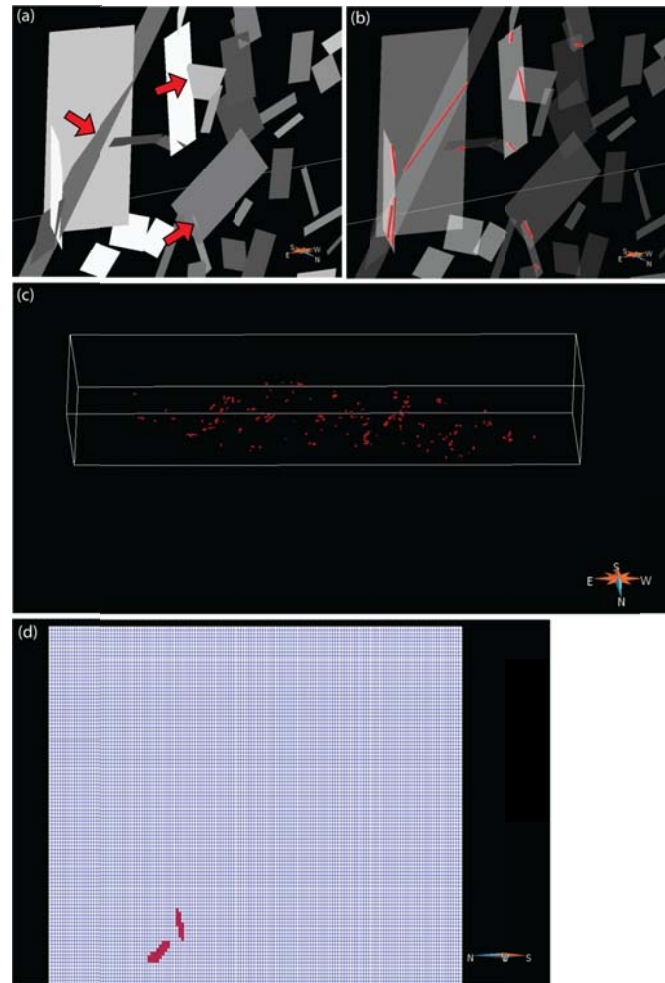
Reconstructed fracture presence values for all three fracture model resolutions are then plotted as log cell size versus log fracture presence (2D and 3D values are plotted on separate graphs). The resulting graph should plot the three model values as a straight line with the slope of the straight line representing the fractal dimension of the dataset. This fractal dimension ( $D_2$  or  $D_3$ ) value provides a handle on how area (or volume) filling the fractures are. For the 2D slices  $1 < D < 2$ ; where  $D_2 = 2$  fractures fill the entire slice and where  $D \rightarrow 1$  fractures are less area filling. In 3D,  $2 < D < 3$  with  $D_3 = 3$  representing fractures that fill the entire volume.

Another important fracture attribute that can be analysed using the TLS datasets is the fracture intersection distribution. This is modelled in GOCAD by calculating intersection curves between adjoining fracture planes (*Figure 5.9*). The workflow after this stage is the same as that conducted for the fracture presence analysis and provides a percentage value of the volume of the S-Grid which contains intersected fractures. A step-by-step workflow for the fracture presence and intersection modelling can be found in *Appendix D*.

The modified box-counting technique used to determine the 2- and 3-dimensional fractal dimension values is only valid if the fracture sets interpreted from the outcrop fracture network models exhibit scale-invariance i.e they are represented by power-law distributions on population distribution plots. From 1-dimensional fieldwork analysis (*Chapter 3*) and outcrop pseudo-well analysis shown in *Section 5.4.2* of this chapter it is known that fractures within the outcrops chosen for TLS analysis exhibit power-law distributions and are therefore scale-invariant, at least in terms of fracture



spacing. The occurrence of these scale invariant fracture sets in the outcrop fracture network models gives confidence that the 2- and 3-dimensional fractal dimension values calculated from the following modelling provide a realistic representation of both the fracture presence and fracture intersection relationships across all of the modelled outcrops.



**Figure 5.9:** Fracture intersection analysis workflow using the TLS datasets. This analysis uses the same S-Grid in Paradigm® GoCAD 2009.2 as the fracture density analysis but focuses on intersection curves instead of full fracture planes. **(a)** First, intersections between fracture planes are identified (examples are highlighted by the red arrows) **(b)** Then using semi-automatic processing the intersection curves illustrating these fracture connections are created as polylines (curves) **(c)** The intersection curves are then used to create a new region in the S-Grid which represents connectivity. **(d)** Slices are then taken through the S-Grid and the proportion of coloured cells (containing intersections) in each outcrop is calculated.

## 5.4 – Results

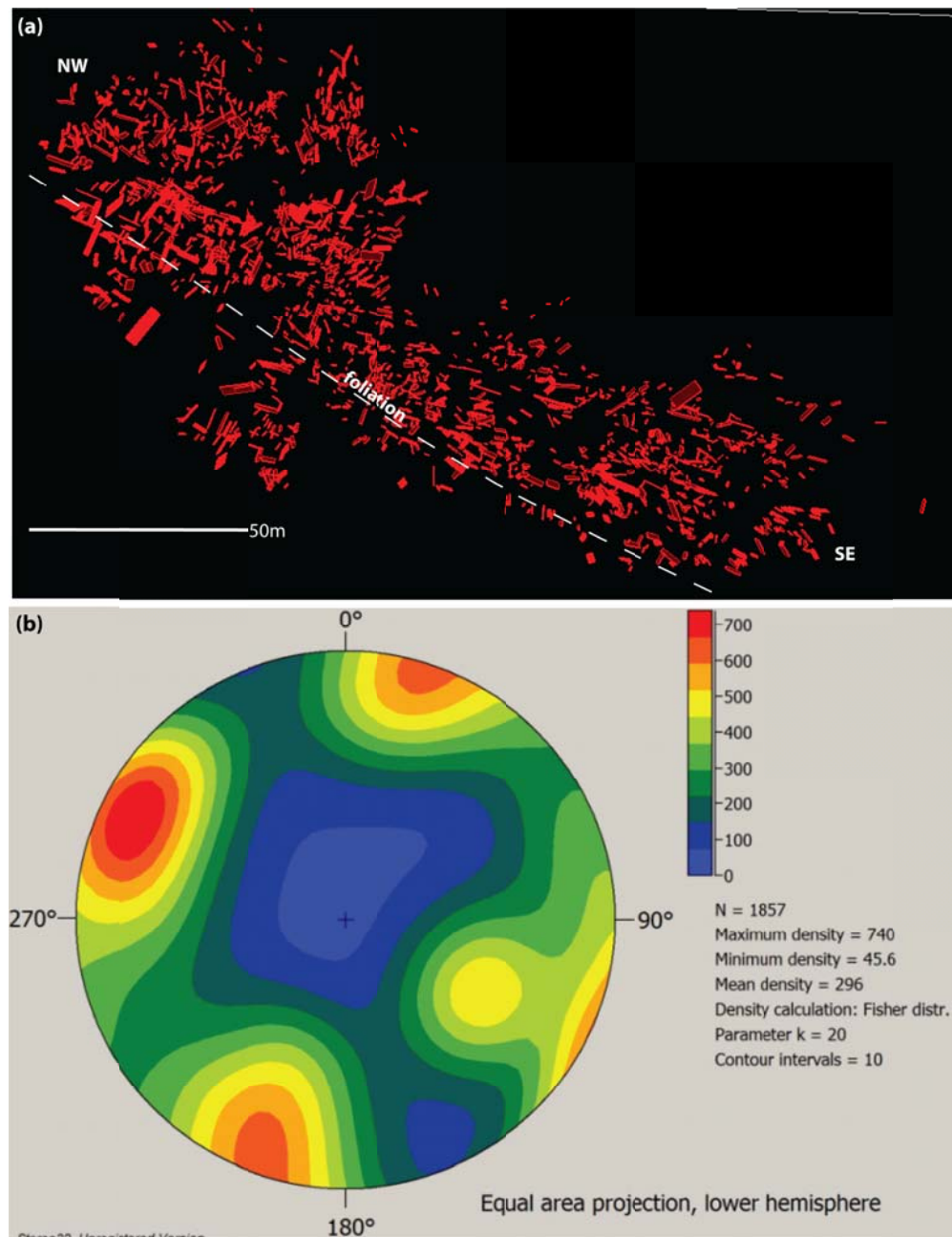
The following sections outline the results from the analyses undertaken on the TLS datasets from Alltan na Bradhan, Kinlochbervie and Caolas Cumhann and discusses the findings.

### 5.4.1 – 3-dimensional fracture networks

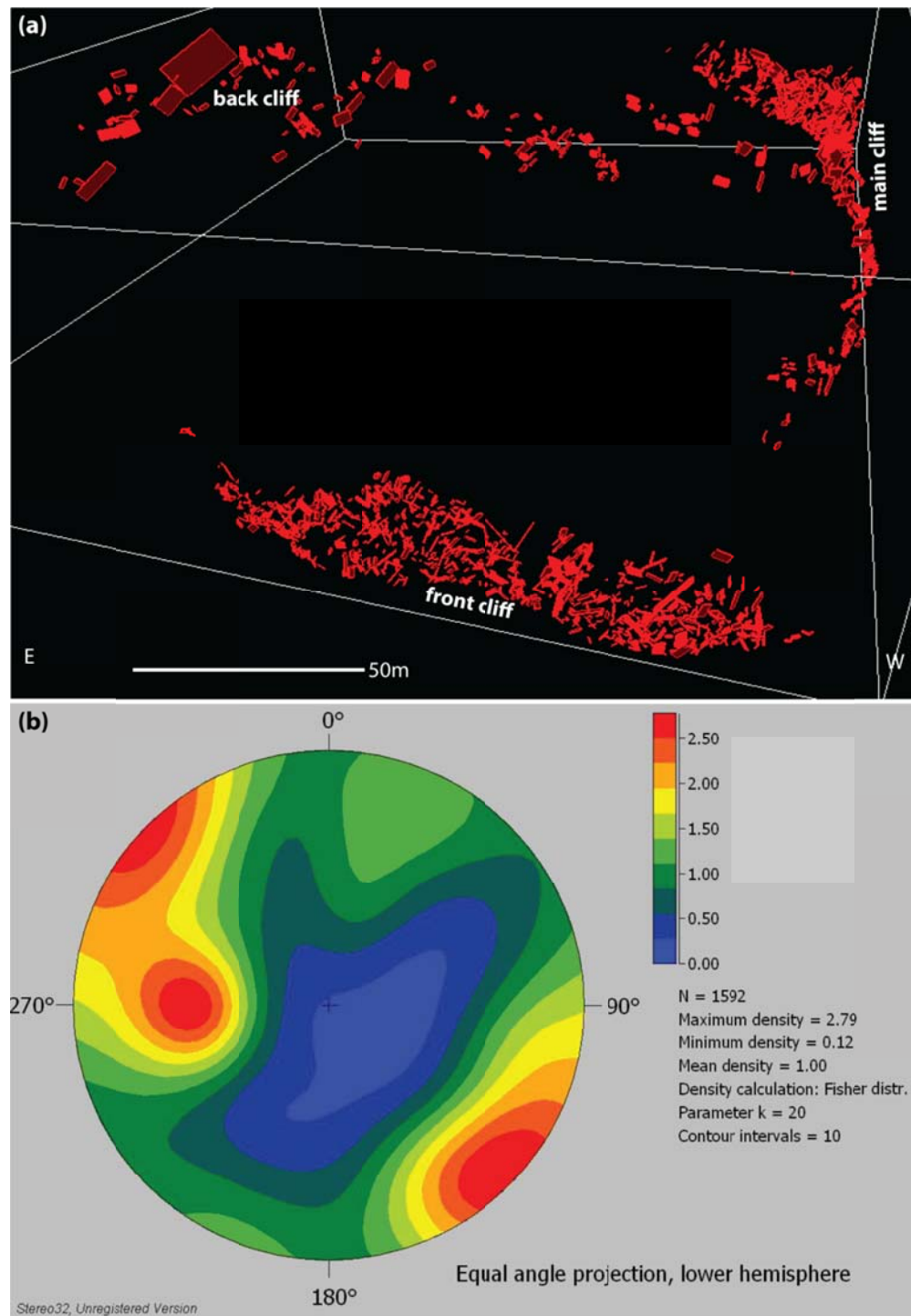
Thousands of individual fractures have been interpreted across all three TLS datasets and provide a detailed 3-dimensional model of the fracture network present at the surface of each outcrop. These fracture network models have then been manipulated and analysed to provide an understanding of fracture spatial, density and connectivity attributes in more detail and at a slightly larger scale (100's of metres instead of typically 10's of metres from fieldwork) than the traditional fieldwork analyses shown in *Chapter 3*. *Figures 5.10, 5.11 And 5.12* show the full fracture network models from Alltan na Bradhan, Kinlochbervie and Caolas Cumhann respectively and their visual characteristics are described below. Digital video animations showing the full 3-dimensional properties of each fracture network model are provided in *Appendix D*.

The fracture network model from Alltan na Bradhan shows two prominent fracture trends (*Figure 5.10b*): NW-SE (parallel to foliation) and NE-SW (perpendicular to foliation) and a subordinate N-S trend. All fracture sets are predominantly steeply dipping to sub-vertical. There are approximately 1800 fractures interpreted from this relatively small TLS dataset (*Figure 5.10*) which suggests high fracture density values across this outcrop. As the two main fracture sets are perpendicular to each other, the vertical fracture connectivity is also likely to be high.

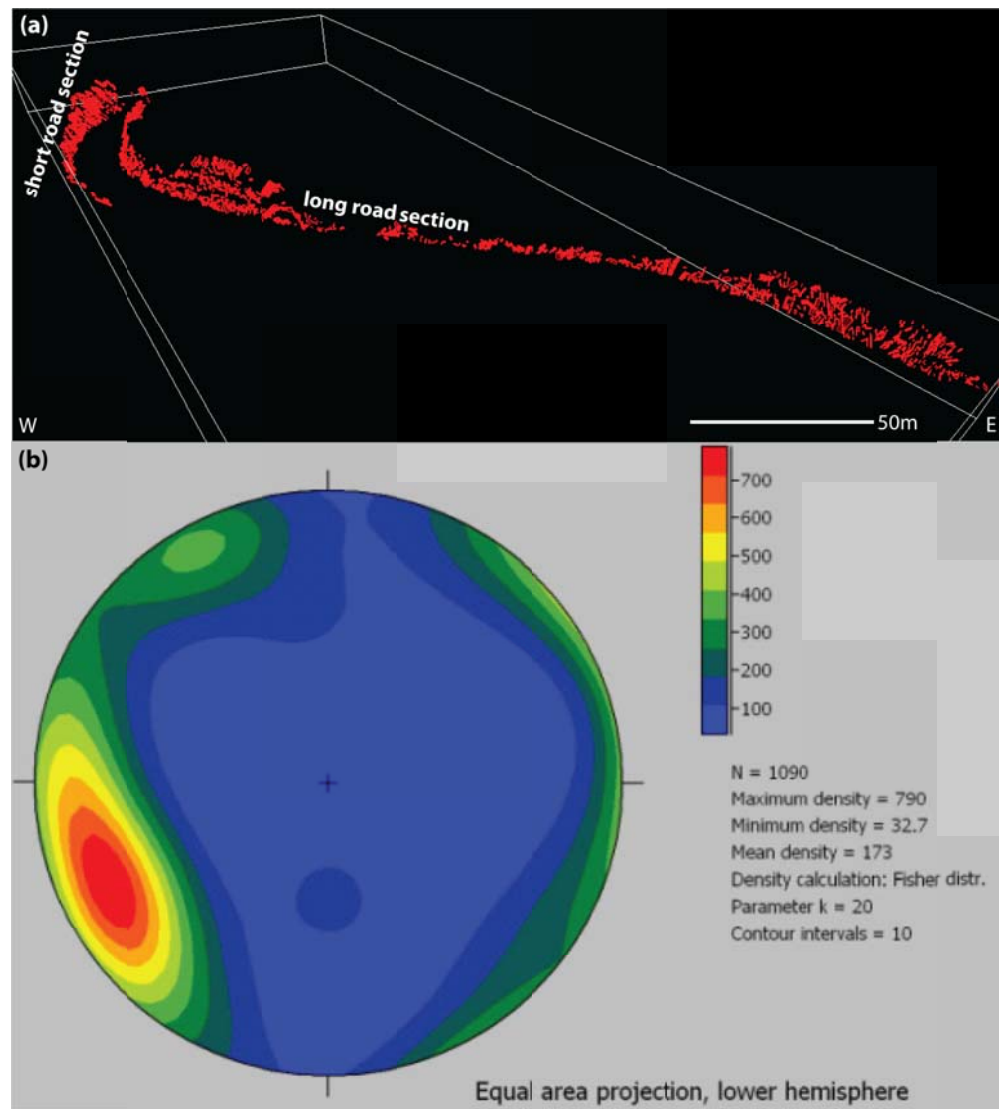




**Figure 5.10:** Resulting fracture network from Alltan na Bradhan. **(a)** Shows the full fracture network from the detailed TLS dataset including ~1800 individual fractures. The foliation at this outcrop is intense and trends NW-SE (marked by the dashed white line). **(b)** Stereonet showing the density of poles to fracture planes collected from the interpretation of the Alltan na Bradhan TLS dataset.



**Figure 5.11:** Resulting fracture network from Kinlochbervie. **(a)** Shows the full fracture network from the detailed TLS dataset including ~1600 individual fractures. **(b)** Stereonet showing the density of poles to fracture planes collected from the interpretation of the Kinlochbervie TLS dataset.



**Figure 5.12:** Resulting fracture network from Caolas Cumhann. **(a)** Shows the full fracture network from the detailed TLS dataset including ~2200 individual fractures. **(b)** Stereonet showing the density of poles to fracture planes collected from the interpretation of the Caolas Cumhann TLS dataset.

More than 1500 fractures have been interpreted from three cliff sections at Kinlochbervie to form a fracture network model that encompasses at least 270° of the outcrop (Figure 5.11). To avoid large assumptions being made about fracture extent, each cliff section (front cliff, main cliff and back cliff) has been treated as a separate entity for the purposes of the pseudo-well, fracture presence and fracture intersection

analyses. At Kinlochbervie the majority of fractures trend NE-SW and N-S with a subordinate NW-SE fracture set (*Figure 5.11b*; note that the stereonet here combines data from the three cliff sections). The fracture orientations collected from the Kinlochbervie TLS dataset differ from the orientation values collected from the aerial photo: NW-SE are far less obvious and only form a small subordinate set in the TLS fracture dataset compared to the aerial photograph dataset where NW-SE fractures form a dominant trend (*Figure 5.5b*). This difference is likely due to the scale and nature of each dataset, with the N-S fractures more visible at an outcrop scale compared to semi-regional-scale (aerial photographs) where NW-SE are more apparent. This extends to the regional study where NW-SE lineaments account for more than double the number of N-S trending lineaments, *Chapter 3* (*Chapter 6* discusses the scalability of orientation data in more detail). The fracture network model from Kinlochbervie also visibly exhibits high density levels which can be attributed to their presence in the hanging wall of a large NW-SE trending normal fault (Loch Inchara Fault), i.e. they form part of the fault's damage zone.

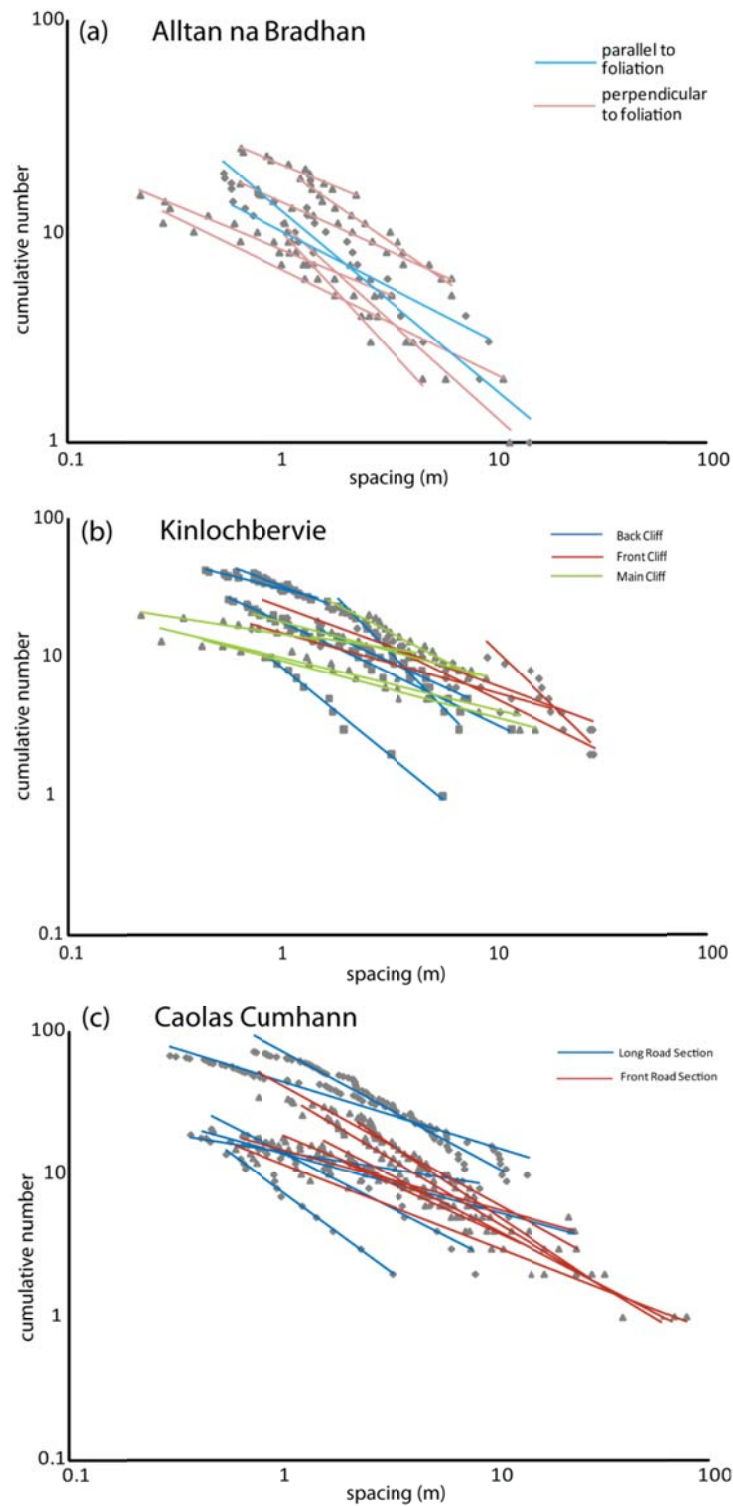
The TLS at Caolas Cumhann provides a more linear shaped fracture network model as a result of the data collection being carried out along a road section (*Figure 5.12*). However, since the road section falls on two relatively tight bends in the road this makes the scanned section suitable for capturing all orientations of fractures that are likely to be present in this area of the Assynt Terrane. The cliffs either side of the roads running through this outcrop are treated separately ('long road section' (north side) and 'short road section' (south side); see *Figure 5.12*) for the fracture network analyses which reduces any assumptions made about how far each fracture extends away from the visible fracture plane on the outcrop. NNW-SSE, N-S and NE-SW dominate the Caolas Cumhann fracture network model which is reasonably consistent with the aerial photograph interpretation (*Figure 5.5c*). The fractures interpreted from this TLS dataset visually appear to be less densely populated than the fracture network models for both Alltan na Bradhan and Kinlochbervie although this can only be confirmed by conducting quantitative analysis of the fracture density attributes as shown in the following sections.

#### 5.4.2 – Pseudo-well analysis

1-dimensional line samples have been collected in the form of pseudo-wells taken across the TLS datasets. For cliff sections (Kinlochbervie and Caolas Cumhann) pseudo-wells have been taken along strike and up/down dip of the digital outcrop surfaces. At Alltan na Bradhan (where the outcrop is a wave-cut platform) pseudo-wells were taken parallel and perpendicular to foliation. Each fracture encountered by the pseudo-well is recorded as a depth value and from this fracture spacing values have been calculated. Both the Kinlochbervie and Caolas Cumhann datasets have been separated into different cliff sections to aid processing and to reduce assumptions about fracture extent. At Kinlochbervie the outcrop has been split into front cliff, back cliff and main cliff (*Figures 5.7b & 5.11*) and at Caolas Cumhann the outcrop has been split into 'long road section' and 'short road section' (*Figures 5.7c & 5.12*). Samples from pseudo-wells from both of these datasets have been labelled according to these different outcrop sections. Alltan na Bradhan pseudo-well samples have been labelled according to their orientation with respect to foliation (either parallel or perpendicular). The resulting spacing data has then been used to produce population distribution plots (shown in *Figure 5.13*) and other spatial attributes have been calculated (*Table 5.1*).

##### 5.4.2.1 – Spacing distribution

The population distribution plots (*Figure 5.13*) show consistent power-law relationships (the plots have log-log axes) for fracture spacing across all three TLS datasets. All of the spacing samples from the TLS datasets are best described by power-law trend-lines with  $R^2$  values between 0.88 and 0.99 (*Table 5.1*). These power-law relationships have spacing values which are centred between 1 and 10 metres (*Figure 5.13*). The majority of the power-law relationships extend over more than one order of magnitude, but none extend over more than two orders of magnitude. Alltan na bradhan exhibits the shortest power-law relationships. The longest power-law relationships (those which extend over approximately two orders of magnitude) originate from the Caolas Cumhann TLS dataset, where the majority of pseudo-wells taken across the short road section have power-law spacing values between 1 and 100 metres (*Figure 5.13c*).



**Figure 5.13:** Population distribution plots from pseudo-wells taken through the TLS datasets. The different coloured trend-lines (and different shaped datapoints) represent different pseudo-well locations and orientations (key is shown on each individual plot). **(a)** Alltan na Bradhan (Canisp Shear Zone) **(b)** Kinlochbervie **(c)** Caolas Cumhann.

Outcrop	Well Location/ Orientation	N	Well #	Distribution	R <sup>2</sup>	D- value	CV	Fracture Density (fractures per metre)
Alltan na Bradhan	parallel to foliation	19	5	power-law	0.97	0.53	1.39	0.34
	parallel to foliation	22	6	power-law	0.96	0.85	1.36	0.41
	perpendicular to foliation	23	8	power-law	0.98	0.71	1.66	0.17
	perpendicular to foliation	30	9	power-law	0.96	0.42	1.92	0.22
	perpendicular to foliation	19	12	power-law	0.99	0.47	1.36	0.24
	perpendicular to foliation	15	16	power-law	0.98	0.43	1.24	0.4
	perpendicular to foliation	12	19	power-law	0.97	0.50	1.36	0.33
	perpendicular to foliation	10	23	power-law	0.94	0.92	0.97	0.29
	perpendicular to foliation	13	28	power-law	0.97	1.10	0.81	0.51
Kinlochbervie	back cliff	16	1	power-law	0.88	1.48	.82	0.07
	back cliff	24	2	power-law	0.95	0.56	1.43	0.12
	back cliff	16	3	power-law	0.98	0.4	1.27	0.11
	back cliff	16	4	power-law	0.92	0.76	1.30	0.1
	front cliff	19	2	power-law	0.98	0.73	1.77	0.18
	front cliff	23	3	power-law	0.98	0.71	1.62	0.21
	front cliff	34	4	power-law	0.99	1.57	1.10	0.30
	front cliff	46	5	power-law	0.97	0.58	1.32	0.40
	front cliff	45	6	power-law	0.97	0.40	0.94	0.43
	front cliff	30	7	power-law	0.97	0.71	1.91	0.35
	front cliff	13	16	power-law	0.99	1.25	0.88	0.61
	main cliff	12	1	power-law	0.97	0.4	1.17	0.15
	main cliff	15	3	power-law	0.93	0.38	1.26	0.18
	main cliff	21	4	power-law	0.97	0.23	1.80	0.17
	main cliff	22	5	power-law	0.99	0.41	0.95	0.19
	main cliff	29	6	power-law	0.96	0.79	0.90	0.21

**Table 5.1:** Spatial attributes from the pseudo-wells taken across TLS data collected from Alltan na Bradhan, Kinlochbervie and Caolas Cumhann.

**Table 5.1** (contd)

Caolas Cumhann	long section	75	1	power-law	0.963	0.47	1.65	0.19
	long section	92	2	power-law	0.96	0.80	1.5	0.24
	long section	21	4	power-law	0.96	0.24	1.59	0.12
	long section	22	5	power-law	0.97	0.41	1.77	0.13
	long section	16	8	power-law	0.98	1.11	0.77	0.78
	long section	24	9	power-law	0.95	0.76	1.14	0.41
	short section	20	1	power-law	0.95	0.41	1.34	0.12
	short section	38	2	power-law	0.95	0.83	1.23	0.19
	short section	47	3	power-law	0.99	1.01	1.59	0.24
	short section	38	4	power-law	0.98	0.89	2.12	0.2
	short section	24	5	power-law	0.97	0.70	2.37	0.15
	short section	21	6	power-law	0.96	0.77	2.03	0.13
	short section	23	7	power-law	0.96	0.65	1.3	0.24
	short section	16	8	power-law	0.94	0.59	1.65	0.17

#### 5.4.2.2 – D-value

D-values (slope of the power-law relationship) from the TLS datasets vary within and between outcrops (*Table 5.1*). From Alltan na Bradhan, the D-values vary between 0.42 and 1.10 (*Table 5.1*). Both Kinlochbervie and Caolas Cumhann exhibit larger variations in their sample D-values which vary from 0.23 to 1.57 and from 0.24 to 1.11 respectively (*Table 5.1*). Typically the largest sample lines in each TLS dataset exhibit D-values (slopes) that converge around an average value ( $\sim 0.5$ ), with the smaller samples (<10 data points) accounting for the largest variations in slope value (see *Figure 5.13* & *Table 5.1*).

#### 5.4.2.3 – CV

The coefficient of variation (CV) has also been calculated for all of the pseudo-well samples collected from the TLS datasets (*Table 5.1*). CV values from Alltan na Bradhan vary between 0.81 and 1.92 with the majority (80%) of values greater than 1 (*Table 5.1*). This is also true for the samples from Kinlochbervie where CV values vary



between 0.82 and 1.91 (*Table 5.1*). The CV values from Caolas Cumhann are typically higher than the values from the other TLS datasets with values between 0.77 and 2.37 (*Table 5.1*). At Caolas Cumhann the majority (~93%) of pseudo-well samples have CV values that are greater than 1.

#### 5.4.2.4 – Fracture density analysis

Fracture density values have also been calculated for each pseudo-well sample collected from all three TLS datasets. The fracture density values across all TLS datasets vary between 0.07 and 0.78 fractures per metre (*Table 5.1*). Average fracture density values are highest at Alltan na Bradhan (0.32 fractures per metre) with both Kinlochbervie and Caolas Cumhann exhibiting similarly low values (~0.24 fractures per metre).

#### 5.4.2.5 – Pseudo-well sampling discussion

Fracture spacing analysis of pseudo-well samples has provided quantitative data on the 1-dimensional spatial characteristics of the fracture sets interpreted from all three TLS datasets. Consistently, power-law relationships are interpreted from population distribution plots for the TLS pseudo-well samples (*Figure 5.13*). The consistent power-law relationships indicate scale-invariance and therefore these 1-dimensional spacing relationships can potentially be used as an estimation of 1-dimensional spacing attributes at different scales (Johnston et al., 1994). This is particularly relevant for the Caolas Cumhann pseudo-wells where some power-law relationships extend over two orders of magnitude (*Figure 5.13c*).

D-values, which are an indication of how the spacing values forming the power-law relationships are weighted (i.e. ratio of small to large fracture spaces (e.g. Pickering et al., 1995)), vary widely across all TLS datasets. Most commonly the D-values are <1 indicating that the power-law relationships are formed by fractures that are widely spaced (towards 10m spacings or 100m for some Caolas Cumhann samples). D-values also provide an indication of how clustered the data is with these common low D-values representing tight clusters in the fracture spacing data (Gillespie et al., 1993). Due to the nature of the TLS datasets, the majority of pseudo-wells contain a small number of fracture data points in comparison to the length of the sample line. Therefore it is likely that fractures are sampled sporadically along each pseudo-well resulting in power-law

relationships with D-values indicating that the majority of fractures in the sample are widely spaced and clustered. There are a few pseudo-wells, however, which have D-values  $>1$  (15%), indicating that their power-law relationships are formed mainly by fractures that are closely spaced (towards 1m spacing, and 0.1m spacing for a minority of pseudo-wells from Alltan na Bradhan and Kinlochbervie).

CV values are commonly  $>1$  which suggests that the fracture sets are clustered (Johnston et al., 1994) which supports the power-law spacing relationships. These power-law relationships and CV values are in agreement with the fieldwork data (this will be discussed further in *Chapter 6*) suggesting that the TLS fracture network model analysis is valid for assessing the 1-dimensional fracture spatial characteristics across all three key outcrops.

Fracture density analyses conducted for the TLS pseudo-well samples yield results between 0.07 and 0.78 fractures per metre. As expected from fieldwork observations, the pseudo-wells from Alltan na Bradhan in the Canisp Shear Zone exhibit the highest fracture density values, although they are still an order of magnitude lower than the density values collected in the field.

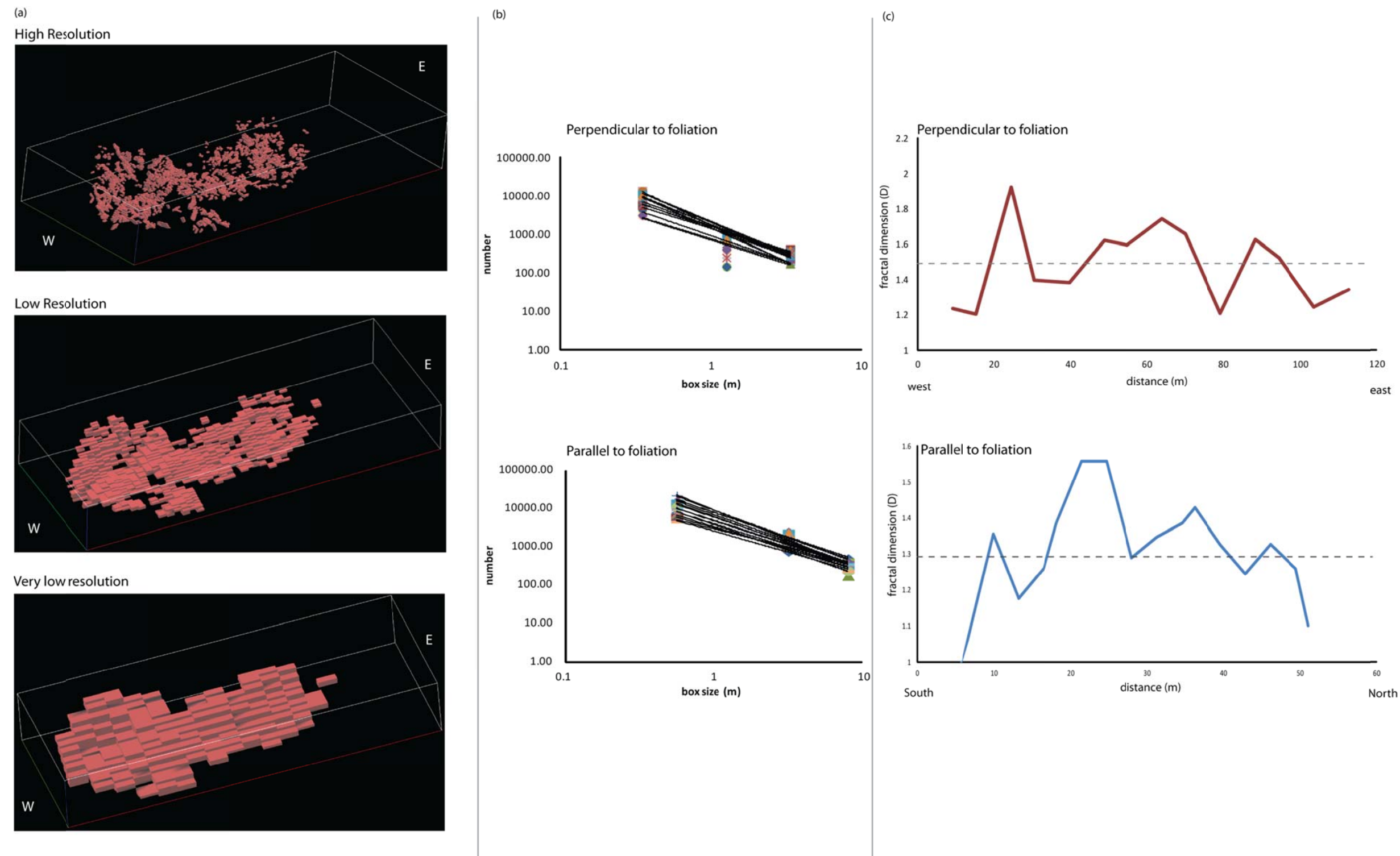
The density results are consistently lower in the TLS datasets (compared to fieldwork samples), which is likely due to the limitations imposed by interpretation of fractures in the TLS network model rather than a reflection of the true fracture density present at each of the three key outcrops. This is because only fractures that exhibit a visible surface expression and are over 50cm in length (see *Figure 5.5* for an example of a viable fracture) are interpreted from TLS virtual outcrops. This means that any fractures that only present themselves as linear surface trace in the outcrop are disregarded from the TLS fracture networks, thus reducing the fracture density values for each outcrop. As there is a lower limit (50cm) to the fracture lengths which are picked from the TLS datasets the reduced fracture numbers can mostly be accounted for by the scale of the dataset. It is possible, however, that a small number ( $<10\%$ ) of the fractures visible at outcrop that are longer than 50cm have not been interpreted because they are poorly defined and therefore do not have a visible fracture surface that can be picked within the TLS dataset.

Although using 1-dimensional pseudo-wells across the TLS datasets provides more information, at a larger scale, on the fracture spatial attributes at outcrop than fieldwork analyses, it does not use the outcrop models to their full potential. These TLS

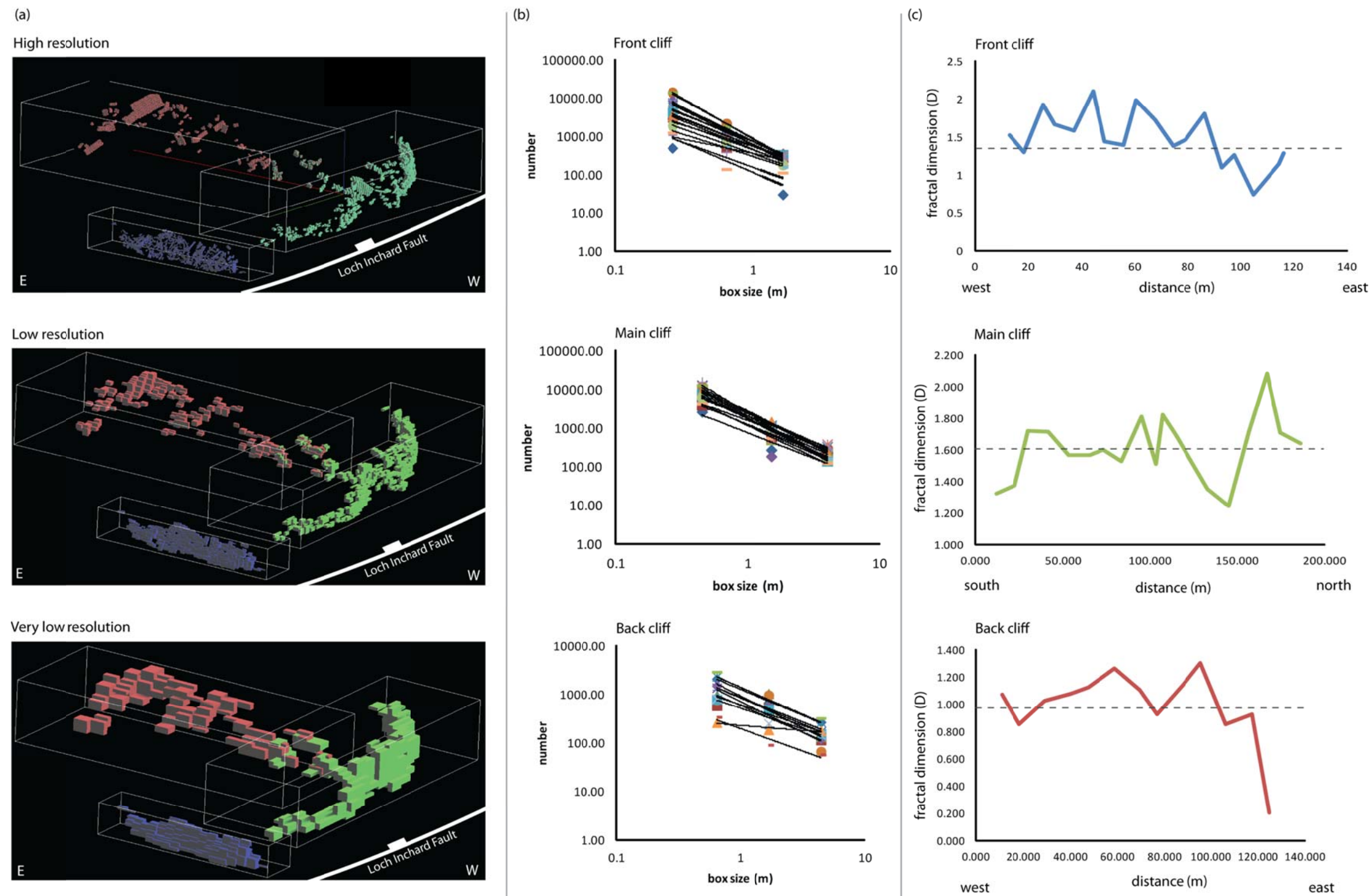
outcrops represent 2.5-dimensional datasets (3-dimensional if you include large assumptions about fracture extent) and therefore it should be possible to use these datasets to gain an understanding of the fracture attribute characteristics in 2- and possibly even 3-dimensions. The following sections use the TLS fracture models in a volumetric analysis by calculating changes in the fracture network characteristics (namely presence and intersections) across the outcrops in different directions.

#### 5.4.3 – Fracture presence models

As previously described, the fracture presence analysis of the TLS datasets was conducted in Paradigm® GoCAD 2009.2. S-Grids are used to calculate fracture presence variations across the key outcrops by calculating 2- and 3-dimensional fractal dimensions (*Section 5.3.2* and *Appendix D* for the full workflow). Where applicable, outcrop sections have been treated individually (e.g. At Kinlochbervie where there are the front cliff, back cliff and main cliff sections, *Figure 5.11*) and graphs have been plotted showing the changes in fractal dimension for each outcrop section. For each outcrop three fracture presence analyses have been conducted: one at very low resolution (20 x 20 x 20 cells) one at low resolution (50 x 50 x 50 cells) and one at high resolution (300 x 150 x 100 cells) with the resulting values used to calculate the 2- and 3-dimensional fractal dimensions ( $D_2$  and  $D_3$ , respectively). Ideally, several more grids should be created to improve the fractal dimension relationships, but the limit of time within the project meant that three S-Grids of different resolutions were optimum for this study. The fracture presence regions of the three S-Grid resolutions and the resulting fractal dimension plots for each outcrop are shown in *Figures 5.14, 5.15 & 5.16*.

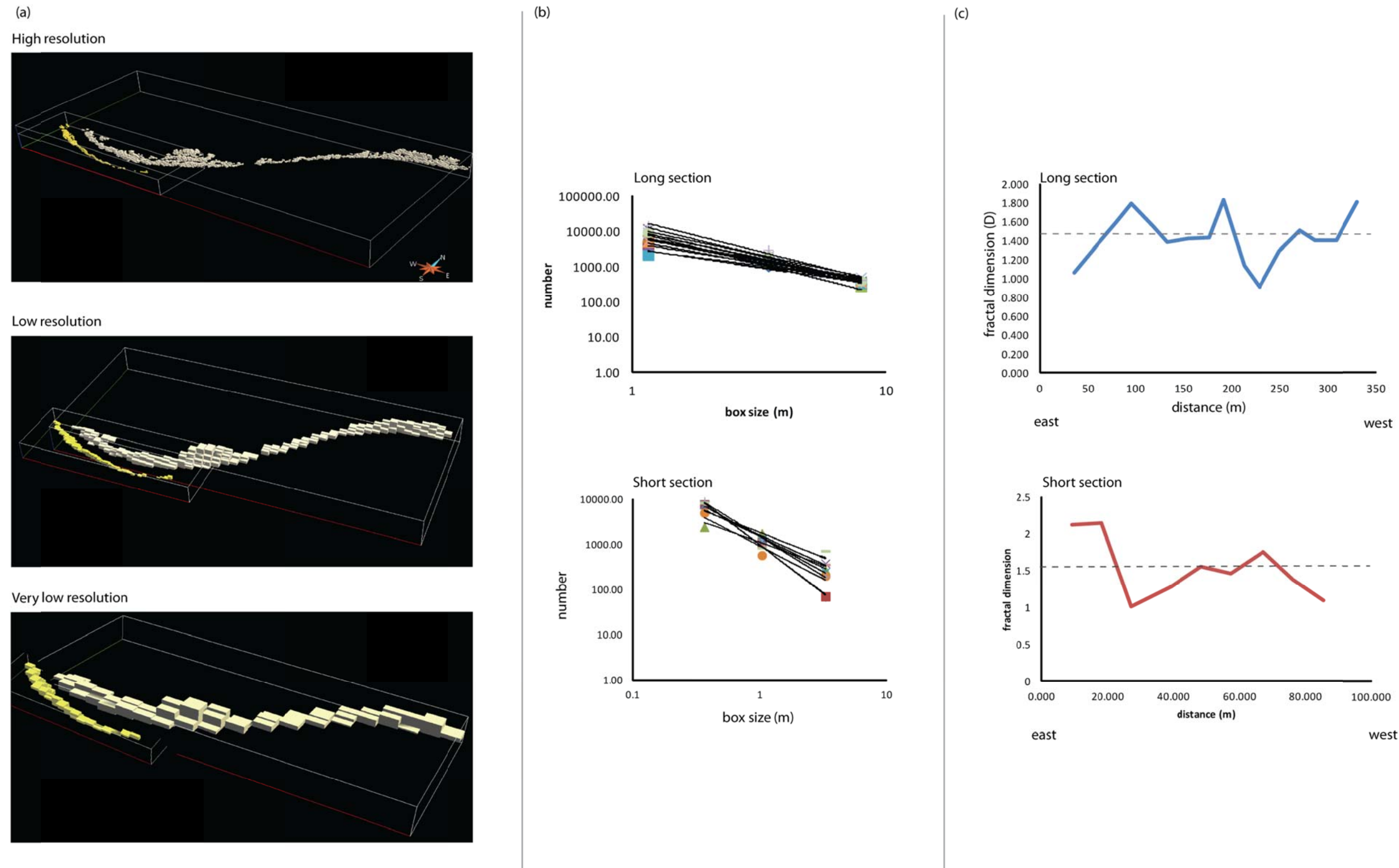


**Figure 5.14:** 2-dimensional fracture presence models for the TLS outcrop at Alltan na Bradhan. (a) The high (300 x 150 x 100), low (50 x 50 x 50) and very low (20 x 20 x 20) fracture presence models showing the distribution of cells that intersect fractures. (b) Box counting analysis of the high, low and very low resolution fracture presence models. The box (or cell) size is plotted against the proportion of cells containing fractures in the outcrop for one slice of the model multiplied by the total number of cells in that slice. The slope of the trend line plotted between the data points of all three models is the fractal dimension and is used to assess how much of the model is filled by fractures in two dimensions. (c) Plots of the variation in 2-dimensional fractal dimension along each outcrop model. The dashed line represents the average fractal dimension value.



**Figure 5.15:** 2-dimensional fracture presence models for the TLS outcrop at Kinlochbervie. (a) The high (300 x 150 x 100), low (50 x 50 x 50) and very low (20 x 20 x 20) fracture presence models showing the distribution of cells that intersect fractures. Green cells – main cliff section; red cells – back cliff section and blue cells – front cliff section. (b) Box counting analysis of the high, low and very low resolution fracture presence models. The box (or cell) size is plotted against the proportion of cells containing fractures in the outcrop for one slice of the model multiplied by the total number of cells in that slice. The slope of the trend line plotted between the data points of all three models is the fractal dimension and is used to assess how much of the model is filled by fractures in two dimensions. (c) Plots of the variation in 2-dimensional fractal dimension along each outcrop model. The dashed line represents the average fractal dimension value.





**Figure 5.16:** 2-dimensional fracture presence models for the TLS outcrop at Caolas Cumhann. (a) The high (300 x 150 x 100), low (50 x 50 x 50) and very low (20 x 20 x 20) fracture presence models showing the distribution of cells that intersect fractures. Cream cells – long road section and yellow cells – short road section. (b) Box counting analysis of the high, low and very low resolution fracture presence models. The box (or cell) size is plotted against the proportion of cells containing fractures in the outcrop for one slice of the model multiplied by the total number of cells in that slice. The slope of the trend line plotted between the data points of all three models is the fractal dimension and is used to assess how much of the model is filled by fractures in two dimensions. (c) Plots of the variation in 2-dimensional fractal dimension along each outcrop model. The dashed line represents the average fractal dimension value.

#### 5.4.3.1 - Results

At Alltan na Bradhan, fractal dimension ( $D_2$ ) values vary between 1.20 and 1.92 for 2-dimensional slices taken perpendicular to foliation and between 0.94 and 1.56 for slices taken parallel to foliation (see *Appendix D* for the full dataset). The highest fractal dimension values at Alltan na Bradhan occur towards the centre and western end of the TLS outcrop area (*Figure 5.14c*). 2-dimensional slices taken perpendicular to foliation have an average of  $D_2 = 1.47$  which is higher than the average parallel to foliation value of  $D_2 = 1.29$ . 3-dimensional fracture presence analysis of the Alltan na Bradhan yields values of  $D_3 = 1.97$  (perpendicular to foliation) and  $D_3 = 2.36$  (parallel to foliation) (*Table 5.2*).

2-dimensional modelling of fracture presence at Kinlochbervie produces values of  $D_2$  that vary significantly across all three outcrop cliff sections (*Figure 5.15*). Front cliff section slices have values of  $D_2$  that vary between 0.74 and 1.99 with a decrease in  $D_2$  evident as the 2D slices move west to east across the cliff section (*Figure 5.16c*). The average front cliff fractal dimension value is 1.49. Main cliff model slices produce values of  $D_2$  between 1.24 and 2.08 with an average value of  $D_2 = 1.61$ . Back cliff  $D_2$  values are much lower than  $D_2$  values from both the front cliff and main cliff sections and vary from anomalously low  $D_2 = 0.205$  to  $D_2 = 1.31$ . 3-dimensional  $D_3$  values for the Kinlochbervie cliff sections are 2.11, 2.72 and 2.07 (front cliff, main cliff and back cliff, respectively, *Table 5.2*).

At Caolas Cumhann,  $D_2$  values vary between 0.91 and 1.83 for the 'long' (north) road section and between 1.10 and 2.12 for the 'short' (south) road section (*Figure 5.16c*). The 'long' road section has an average  $D_2$  value of 1.43 which is similar to the 'short' road section where the average  $D_2$  value is 1.53. In 3-dimensions the 'long' road section has a  $D_3$  value of 2.32. The 'short' road section 3-dimensional fractal dimension value is lower with  $D_3 = 2.19$  (*Table 5.2*).

#### 5.4.3.2 – Discussion

Using fractal dimensions to assess fracture presence has generated both 2- and 3-dimensional values that provide a constraint on what proportion of each outcrop model contains fractures. As the virtual outcrops collected using TLS only represent a 2.5-dimensional slice through a 3-dimensional volume it would have been impossible to quantitatively determine the 2- and 3-dimensional fracture presence potential by

directly using the virtual outcrop (and fracture) surfaces. Therefore this fracture presence analysis increases the ability to assess how much of each 2D slice or 3D volume is fractured because the box counting calculation used to determine the fractal dimension values makes the outcrop fill the entire model area or volume. In effect, it assumes that the fracture distribution that is observed in the outcrop is typical of the volume as a whole i.e. the box-counting estimates how fracture presence may fill the model volume; if the values interpreted from the outcrop surface remain consistent across the whole slice or model volume. The resulting fractal dimension values therefore provide quantitative datasets that can be used across a full model volume without the limitation of the fracture presence values only representing a small section of the model volume.

Alltan na Bradhan, which lies within the Canisp Shear Zone, is known, from fieldwork, to be highly fractured with both 'Late Laxfordian' faults (parallel to foliation) and Stoer Group age fractures (perpendicular to foliation) that formed due to the reactivation and exploitation of the pre-existing upper greenschist-facies foliation (see *Chapter 3* for a detailed synthesis of the fracture network characteristics within the Canisp Shear Zone). The highly fractured nature of this outcrop is not particularly well represented by the TLS fracture presence model with average  $D_2$  values of 1.47 and 1.29 (*Figure 5.14*) and  $D_3$  values of 1.97 and 2.36 (*Table 5.2*). In 2-dimensions  $1 < D_2 < 2$  and so the Alltan na Bradhan  $D_2$  values represents an outcrop which has a relatively low fracture content. *Figure 5.17* exhibits a merged plot of all the 2-dimensional fractal dimension values for each of the mainland LGC TLS models which highlight the unexpected low  $D_2$  values for the Alltan na Bradhan models compared to the rest of the outcrops in this study.

These low fractal dimension values continue into the 3-dimensional fracture presence analysis where the  $D_3$  values are closer to 2 ( $2 < D_3 < 3$ ), suggesting that the 3-dimensional Alltan na Bradhan model represents an outcrop that is relatively unfractured. As previously mentioned, the Alltan na Bradhan point cloud is full of shadows (missing outcrop data) caused by the low-scale topography present across the wave-cut platform. It is likely that this reduced TLS outcrop quality, coupled with the lower fracture length cut-off of 50cm, is responsible for the low fracture presence fractal dimension values calculated from this TLS model. The fracture presence analysis of the Alltan na Bradhan outcrop suggests that the TLS model results may not be suitable to



provide 2- and 3-dimensional fractal dimension values that are consistent and representative of the fracture network characteristics observed in the field. If more time could have been allocated to this section of this thesis then it is likely that a second dataset from the Canisp Shear Zone would have been collected where more care would have been taken to ensure only minimal data shadows were present within the TLS outcrop model.

Location	Model	3D fractal dimension ( $D_3$ )
Alltan na Bradhan	perpendicular to foliation	1.965
	parallel to foliation	2.358
Kinlochbervie	front cliff	2.109
	main cliff	2.715
	back cliff	2.066
Caolas Cumhann	long road section	2.321
	short road section	2.185

**Table 5.2:** 3D fractal dimension values for all of the fracture presence TLS models from the mainland LGC.

Although the fracture presence models from the Alltan na Bradhan outcrop are not considered to be entirely representative of the fracture network present at this location, the dataset can still be used to determine relative variations in the fracture presence values across the outcrop. Sampling perpendicular to foliation results in higher fracture presence  $D_2$  values than the sampling parallel to foliation, suggesting that ‘Late Laxfordian’ faults, which generally form parallel to foliation (these would have the largest expression on the perpendicular to foliation sampling), are the most present across this TLS dataset. Stoer Group age fractures, which have their largest expressions in the parallel to foliation slices have fracture presence  $D_2$  values which are on average 0.2 lower than the ‘Late Laxfordian’ faults. The likely explanation for this is that Stoer Group age fractures generally have less of a surface expression and are shorter than the ‘Late Laxfordian’ faults (observed from fieldwork). It is also therefore, possible that fewer of these Stoer Group fractures have been interpreted because only fractures over 50cm in length have been interpreted for this (and all of the) TLS outcrop models.

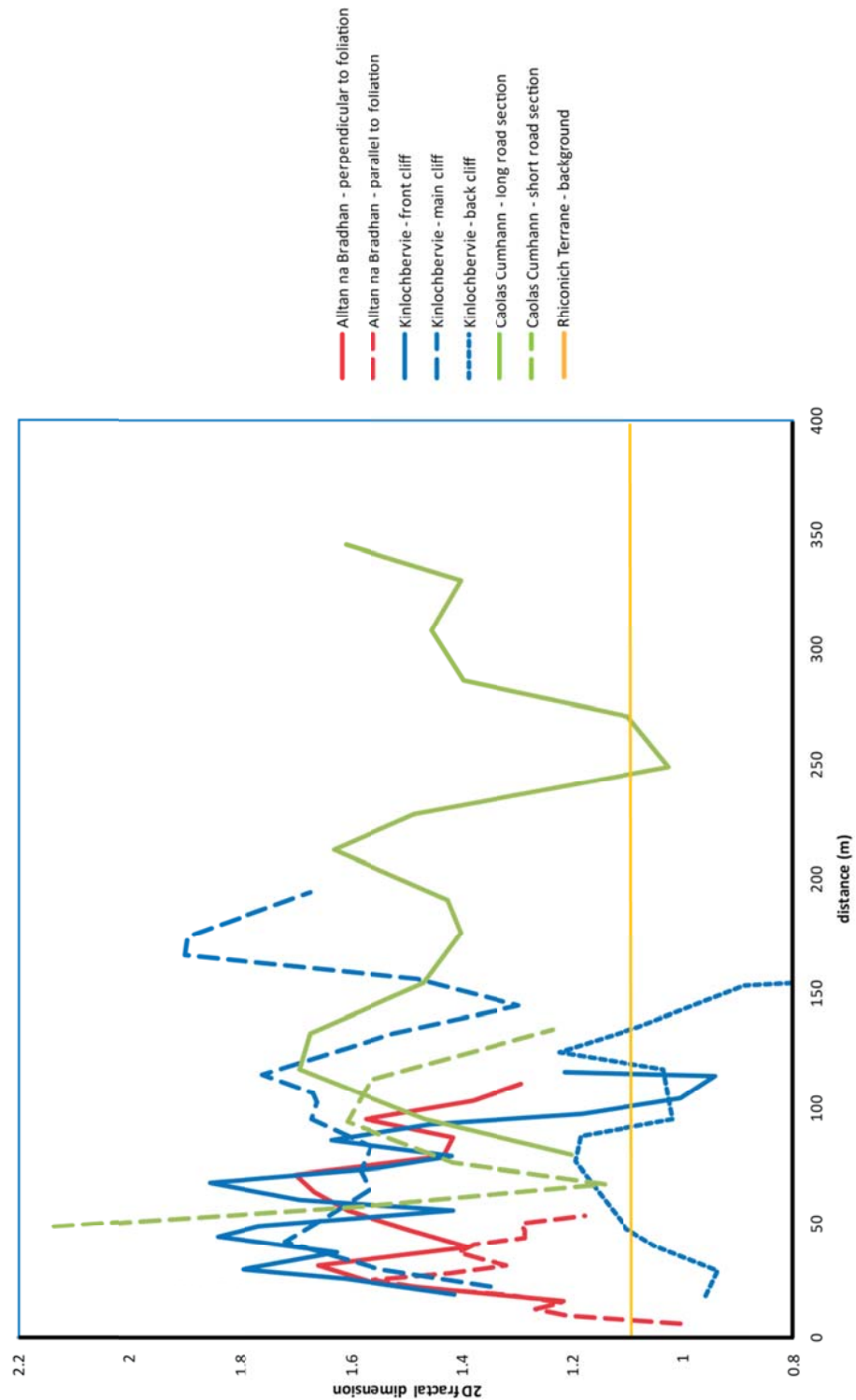
Fracture presence  $D_2$  and  $D_3$  values at Kinlochbervie vary considerably between the different outcrop cliff sections within the TLS outcrop model. The main cliff section exhibits the highest average fracture presence  $D_2$  value at Kinlochbervie with the front

cliff section average  $D_2$  value 0.12 lower. These similar 2-dimensional fractal dimension values of the main and front cliff sections are illustrated in *Figure 5.17*.

The 2-dimensional fracture presence model for the front cliff exhibits a small decrease in the fracture presence  $D_2$  values moving west to east across the cliff section (*Figure 5.15c*) which is likely to result from this outcrop lying in the damage zone of the Loch Inchar Fault that is adjacent to the west side of the Kinlochbervie outcrop. Fracture presence  $D_2$  values decreases by approximately 0.55 from the west to the east side of the outcrop (1.75 to 1.20) over a distance of 140m. Following this trend, it is estimated that the damage zone of the Loch Inchar fault extends ~220m to the east of the main fault plane; with fracture density values returning to background levels (estimated from fieldwork observations) beyond this distance (*Figure 5.18*).

On first inspection, the west to east decreasing fractal dimension trend is not reflected in the back cliff section with both  $D_2$  (0.99) and  $D_3$  (2.07) values representing an outcrop that is relatively unfractured along its entire length (*Figure 5.15c*). This is likely due to poorly exposed nature of the cliff section (it is covered in heather and moss and therefore it is difficult to visualise fractures along its surface), rather than a true reflection of the fracture presence distribution.

The Kinlochbervie main cliff section, which is orientated parallel to the adjacent Loch Inchar Fault exhibits relatively consistent  $D_2$  values across the model with an average  $D_2$  value of 1.61. Any peaks in the Kinlochbervie fracture presence  $D_2$  values for the main cliff section coincide with larger exposed cliff surfaces in the outcrop (*Figure 5.4b*). The lower than average fracture presence  $D_2$  values occur where the outcrop is more eroded and obscured by vegetation.

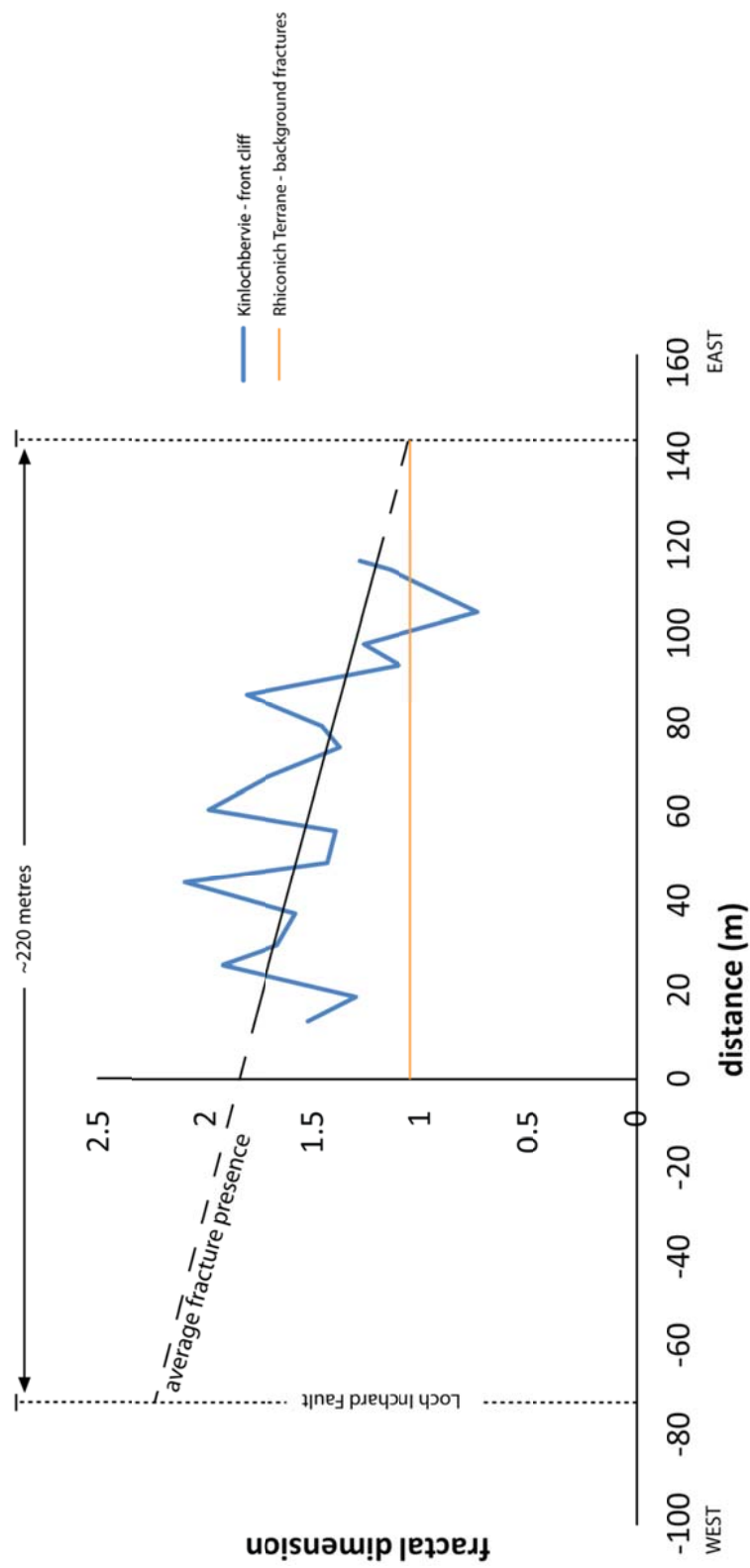


**Figure 5.17:** Plot showing the variation in 2D fractal dimension across all of the TLS model datasets in the mainland LGC. The data is shown of the plot as a moving point average (period of 2).

As this main cliff section lies the closest to the main Loch Inchar Fault plane, the higher  $D_2$  value (than both the front and back cliff sections) supports the hypothesis that the Kinlochbervie fracture presence models record the effect that the Loch Inchar Fault has on the surrounding fracture network. This effect is represented by increased fracture presence close to the main fault plane and decreasing fracture presence away from this main fault back down to background fracture presence levels. This is also seen with the  $D_3$  main cliff value which is significantly higher than any other 3-dimensional fractal dimension value across the Kinlochbervie TLS outcrops (*Table 5.2*) which suggests that the majority of the main cliff section is intersected by fractures. It should be noted however that in *Figure 5.17*, fracture presence  $D_2$  values for the main cliff section appear lower than the fracture presence  $D_2$  values from the front cliff section.

This is because the trend-line used to display the data in *Figure 5.17* uses a moving average and therefore the peaks in fracture presence from the main cliff section, shown in *Figure 5.15c*, are reduced as they are counteracted by the lower fracture presence  $D_2$  values seen in the highly eroded sections of the main cliff section.

At Caolas Cumhann, fracture presence  $D_2$  values are similar to those collected at the other TLS outcrops in this study (*Figure 5.17*). Any peaks in the fracture presence calculations at this outcrop can again be attributed to areas where there are large exposed cliff sections, and therefore more fractures to interpret. Areas in between are covered in more vegetation and are more heavily eroded, thus reducing the number of interpreted fractures. The average fracture presence  $D_2$  values at Caolas Cumhann are most similar to the front and main cliff sections of Kinlochbervie, suggesting that, in 2-dimensions, the Assynt Terrane is heavily fractured, even in outcrops that are not affected by large faults or pre-existing structures. In three dimensions, the  $D_3$  values (2.32 and 2.19) are similar to the  $D_3$  values calculated from the Kinlochbervie front section (2.11) which implies that both outcrops have similarly low proportions of fractures within them.

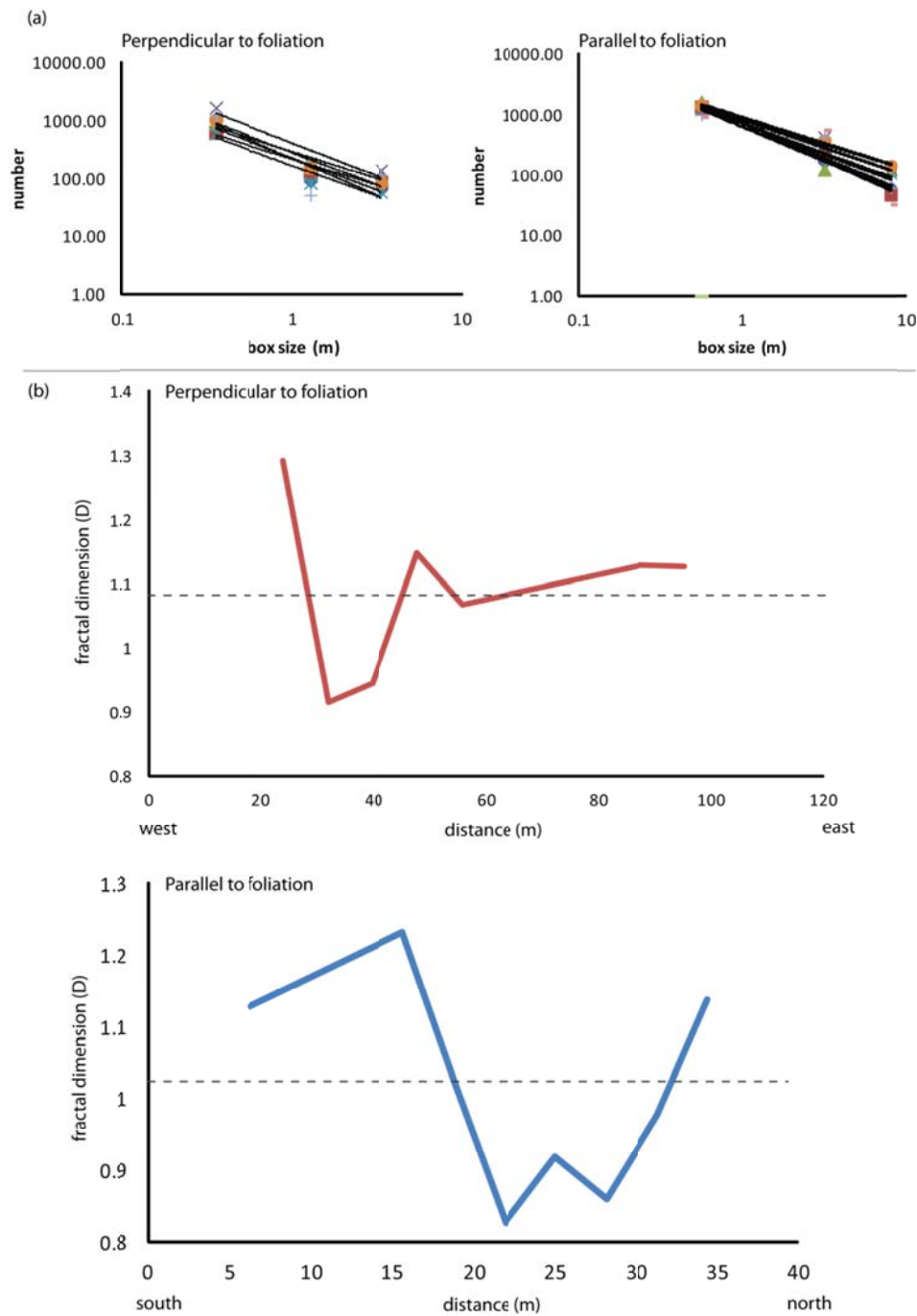


The fracture presence modelling of the TLS datasets from Alltan na Bradhan, Kinlochbervie and Caolas Cumhann has shown that the proportion of fractures present varies across all outcrops, but more importantly, between the outcrops in relation to the structural settings in which they occur. Alltan na Bradhan exhibits fracture presence values that are lower than would have been expected from fieldwork observations. This can be related to the poor quality of the TLS point cloud and the inability to pick every fracture presence within the outcrop. Kinlochbervie exhibits relatively high fracture presence  $D_2$  and  $D_3$  values across the main cliff section, in particular. These higher fracture presence values are to be expected as Kinlochbervie sits in the hanging wall, and damage zone, of the large NW-SE trending Loch Inchar Fault. Average fracture presence values at Caolas Cumhann are similar to those seen at Kinlochbervie. This may suggest that outcrops exhibiting background fracturing in the Assynt Terrane are as fractured as outcrops affected by major faults in the Rhiconich Terrane. The merged plot shown in *Figure 5.17* also includes a 2-dimensional estimated fracture presence value for background fracturing in the Rhiconich Terrane. It suggests that outcrops within the Rhiconich Terrane, that are not influenced by any major ductile or brittle structures, have the lowest fracture density values seen across the entire mainland LGC study area. This is consistent with fieldwork observations where outcrops in the Rhiconich Terrane that are not affected by larger or pre-existing structures have fracture density values (which can be attributed to fracture presence) of approximately 1 fracture per metre.

The modelling shown above provides a quantitative understanding of how fracture networks associated with the mainland LGC have different fracture presence parameters, in both 2- and 3-dimensions, depending on the structural setting the outcrop model originates in. This fracture presence analysis has important implications for the understanding of the Clair field basement as the fractal dimension values can be input directly into existing fluid flow models of the basement to help improve understanding and control of the various structural settings thought to be present within the Clair basement.

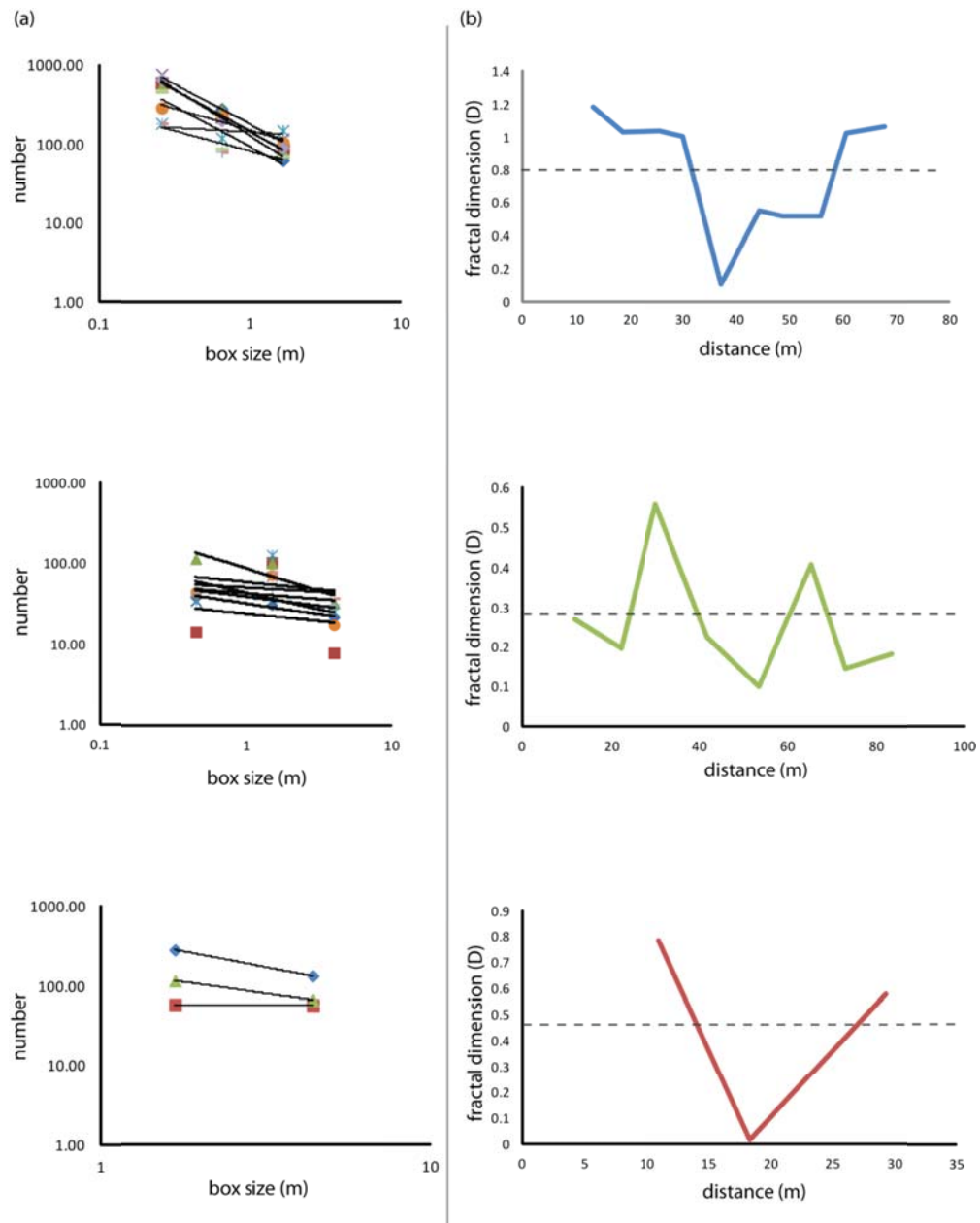
#### 5.4.4 – Fracture intersection models

Fracture intersection analysis of the TLS datasets has been conducted using a similar approach as the fracture presence analysis; although this time only the intersection curves between fractures are considered (see *Figure 5.9* for an illustration of the intersection curve workflow). The same three different resolution S-Grids used for the fracture presence models are also used to model fracture intersections with the intersection proportions used to determine the fractal dimensions in 2- and 3-dimensions. The resulting fracture intersection fractal dimension plots for Alltan na Bradhan, Kinlochbervie and Caolas Cumhann are given in *Figures 5.18, 5.19 & 5.20* respectively.

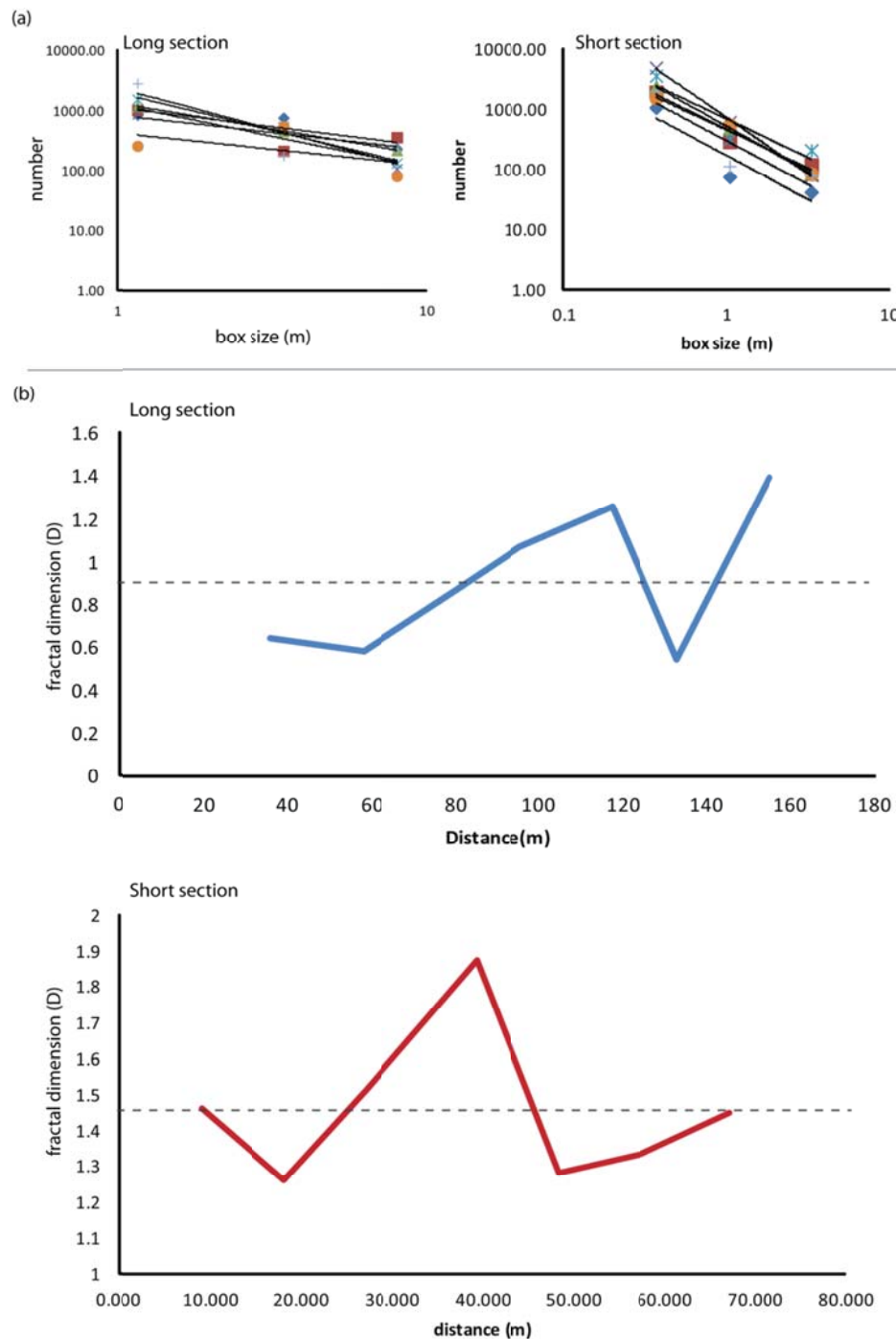


**Figure 5.19:** Fracture intersection modelling from Alltan na Bradhan. (a) 2-dimensional box counting plots of the proportion of fracture intersections within the outcrop calculated to fill each 2D slice. Modelling is completed both perpendicular and parallel to foliation. The values from all three resolutions of S-Grid are plotted and then the slope of the trend line that represents the three data points provides the fractal dimension. (b) Plots of distance across the outcrop versus 2-dimensional fractal dimension ( $D_2$ ) again for models taken perpendicular and parallel to foliation.





**Figure 5.20:** Fracture intersection modelling from Kinlochbervie. (a) 2-dimensional box counting plots of the proportion of fracture intersections within the outcrop calculated to fill each 2D slice. Modelling is completed for three separate cliff section models (front cliff, main cliff and back cliff). The values from all three resolutions of S-Grid are plotted and then the slope of the trend line that represents the three data points provides the fractal dimension. (b) Plots of distance across the outcrop versus 2-dimensional fractal dimension ( $D_2$ ).



**Figure 5.21:** Fracture intersection modelling from Kinlochbervie. (a) 2-dimensional box counting plots of the proportion of fracture intersections within the outcrop calculated to fill each 2D slice. Modelling is completed for two separate cliff section models (long road section and short road section). The values from all three resolutions of S-Grid are plotted and then the slope of the trend line that represents the three data points provides the fractal dimension. (b) Plots of distance across the outcrop versus 2-dimensional fractal dimension ( $D_2$ ).

#### 5.4.4.1 – Results

At Alltan na Bradhan, the perpendicular to foliation fracture intersection model produces  $D_2$  values between 0.91 and 1.29 for the perpendicular to foliation model and between 0.83 and 1.23 for the parallel to foliation model (*Figure 5.18b*). Both the perpendicular to foliation and parallel to foliation models have an average fracture intersection  $D_2$  value of 1.01. Parallel to foliation, the fracture intersection  $D_2$  values are more varied with many of the  $D_2$  values  $<1$  (50%) compared to the perpendicular to foliation model where 29% of the  $D_2$  values are  $<1$ . Unlike the fracture presence modelling, the fracture intersection models show their smallest values towards the centre and western end of the outcrop models (*Figure 5.19b*). Low values are also observed in 3-dimensions with the  $D_3$  values from Alltan na Bradhan consistently  $<2$  (*Table 5.3*).

Location	Model	3D fractal dimension
Alltan na Bradhan	perpendicular to foliation	1.348
	parallel to foliation	1.625
Kinlochbervie	front cliff	1.947
	main cliff	1.599
	back cliff	1.726
Caolas Cumhann	long road section	2.021
	short road section	2.204

**Table 5.3:** 3D fractal dimension values for all of the fracture intersection TLS models from the mainland LGC.

Fracture intersection modelling at Kinlochbervie varies across the three outcrop cliff sections (*Figure 5.20b*). The average  $D_2$  values for all three cliff sections are  $<1$  with the average  $D_2$  values for the front cliff section the highest calculated from the Kinlochbervie models (*Figure 5.20b*). Fracture intersection modelling of the main cliff section yield extremely low  $D_2$  values which are between 0.1 and 0.56 and an average  $D_2$  value of 0.26. Similar to the fracture presence modelling, the back cliff section exhibits the low  $D_2$  values for fracture intersections which average 0.46. Three dimensional fracture intersection modelling at Kinlochbervie produces  $D_3$  values that are consistently  $<2$  (*Table 5.3*). The front cliff section exhibits the highest  $D_3$  value (1.95, *Table 5.3*) with the main cliff section showing the lowest  $D_3$  value (1.6, *Table 5.3*).

Fracture intersection  $D_2$  values vary significantly across the Caolas Cumhann model (*Figure 5.17c*). The short road section has an average fracture presence  $D_2$  value of 1.45 compared to the long road section where the fracture intersection average  $D_2$  value is 0.91 (*Figure 5.21b*). At Caolas Cumhann the  $D_3$  fracture intersection values are  $>2$  with the short road section exhibiting the highest 3-dimensional fractal dimension value (*Table 5.3*).

#### 5.4.4.2 – Discussion

Fracture intersection modelling across the mainland LGC TLS outcrop datasets quantitatively expresses the variation in fracture intersection occurrence as a result of the quality of the TLS datasets and the structural setting in which each outcrop resides.

Fracture intersection modelling at Alltan na Bradhan produces  $D_2$  and  $D_3$  values that are consistently low for both the perpendicular to foliation and parallel to foliation samples. In 2-dimensions the average  $D_2$  value of 1.01 suggests that only a very small proportion of the outcrop contains fracture intersections. Fracture intersection  $D_2$  values that are lower than fracture presence  $D_2$  values are to be expected because fracture intersections are defined as curves and therefore occupy a much smaller volume than a full fracture surface. However, the calculated fracture intersection  $D_2$  values at Alltan na Bradhan are lower than would have been expected from fieldwork observations. The Canisp Shear Zone (CSZ), where Alltan na Bradhan originates, is cross-cut by two main fault and fracture sets ('Late Laxfordian' foliation parallel faults and Stoer Group age foliation perpendicular fractures). These faults and fractures occur perpendicular to each other and are found throughout the majority of the CSZ and therefore they should result in high numbers of vertical fracture intersections across the whole of the Alltan na Bradhan TLS model. Therefore it is likely that the low fracture intersection  $D_2$  values from this outcrop is consistent with the hypothesis that the quality of the TLS dataset has an impact on the fracture presence and fracture intersection fractal dimension values across the Alltan na Bradhan outcrop i.e. these extremely low values are an artefact of the terrestrial laser scan coverage.

The Alltan na Bradhan  $D_3$  values also reflect the low quality of the TLS point cloud as for both the parallel and perpendicular to foliation models the  $D_3$  values are  $<2$  (1.65 and 1.35, respectively, *Table 5.3*).

As the majority of faults and fractures at Alltan na Bradhan are vertical, the majority of fracture intersections will also be vertical. Without a workflow to understand the variation in fracture connectivity away from the interpreted fracture intersections, it is impossible to determine whether the fractures at Alltan na Bradhan are connected across the whole outcrop or whether fracture connectivity only occurs in narrow vertical columns, where the fractures intersect.

At Kinlochbervie, fracture intersection  $D_2$  values are highest across the front and back cliff sections, although they are still  $<1$  (*Figure 5.20b*). These low  $D_2$  values represent fracture networks which are poorly intersected. The Kinlochbervie fracture intersection models exhibits the lowest  $D_2$  values observed across all three TLS outcrops in the mainland LGC. 3-dimensional  $D_3$  fracture intersection values for Kinlochbervie show similar relationships with the main cliff section producing the lowest  $D_3$  value (*Figure 5.20b*). Again the front cliff section has the highest fracture intersection  $D_3$  value, although it is still  $<2$  (1.95, *Table 5.3*) representing an outcrop which contains little or no fracture intersections. As previously discussed the prominent fracture trends across the Kinlochbervie TLS dataset are NE-SW and N-S which are likely small conjugate structures to the main Loch Inchar Fault. These two main fault orientations are parallel enough to each other that intersections between them are reduced, thus reducing the  $D_2$  values for the fracture intersection models created for this outcrop. The majority of fractures at Kinlochbervie are steeply dipping to sub-vertical, suggesting that any fracture intersection is also going to occur sub-vertically. The fact that fracture intersection values are low ( $D_2$  and  $D_3$ ) indicates that there are unlikely to be many connected fracture pathways across the outcrop. This modelling does not provide an understanding of whether any connectivity occurs along fracture planes. If many of the fracture planes in this model are open to fluid flow (critically stressed under present day stress conditions) then it is possible that connected pathways across the whole outcrop could form without the need for there being a high number of fracture intersections within the fracture network.

At Caolas Cumhann 2-dimensional fracture intersection  $D_2$  values vary considerably between the two main road sections (long and short). The short road section has  $D_2$  fracture intersection values that are the highest calculated from any of the TLS outcrop models that suggest that in two dimensions the short road section outcrop has a fracture network that is well connected (nearly half of the outcrop is

cross-cut by fracture intersections, *Figure 5.21b*). This is in comparison to the long road section where the average  $D_2$  value (0.91) indicates that the outcrop contains very few or no fracture intersections. The  $D_3$  values for Caolas Cumhann echo this pattern with the short road section exhibiting the highest value (2.20, *Table 5.3*).

The higher fracture intersection  $D_2$  and  $D_3$  values for the short road section are likely due to the fact that, at Caolas Cumhann, there are two main fracture sets present within the TLS outcrop datasets (NW-SE and N-S, see *Figure 5.12*) which are most evident in the short road section. In the long road section there is a reduced number of NW-SE trending fractures in this outcrop section which has resulted in the reduced fracture intersection  $D_2$  and  $D_3$  values from the TLS modelling (the majority of fractures on the long road section are therefore sub-parallel).

Fracture intersections at Caolas Cumhann are typically sub-horizontal due to the presence of two main fracture sets with variable dips; one set is sub-vertical and one is sub-horizontal. It is again however, impossible to determine (from this study) the level of fracture connectivity between the interpreted intersection curves. Without knowing if the fracture sets are open to fluid flow, it is impossible to predict whether fluid flow at the outcrop is restricted to fracture intersections or can occur along and up fracture planes, thus increasing the number of pathways for fluid migration (and storage) within this particular fracture network.

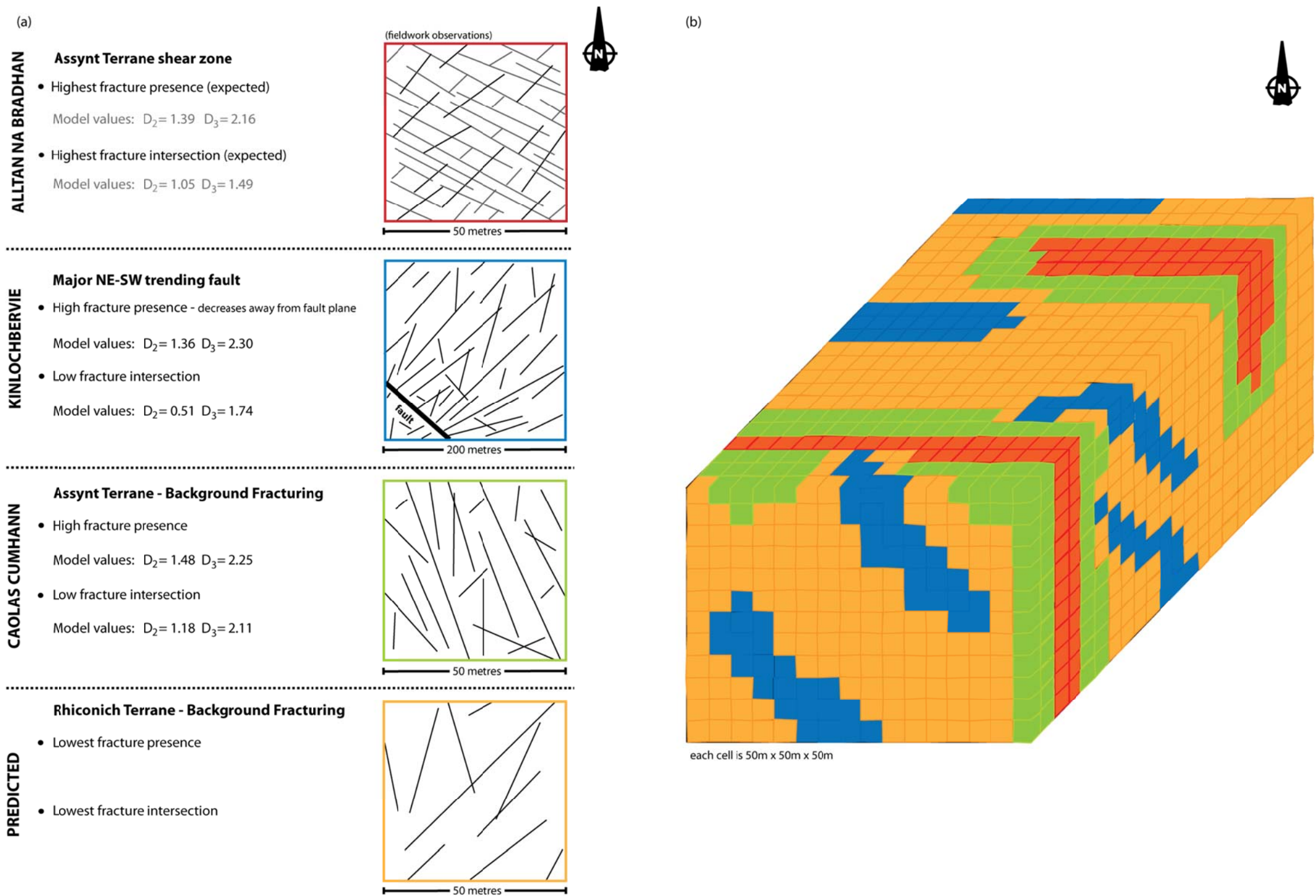
From fieldwork observations it was expected that the outcrop models from Caolas Cumhann would have lower fracture intersection fractal dimension values than the outcrop models from Alltan na Bradhan. The fracture intersection analysis shown in this chapter does not show this and in fact suggests that the Caolas Cumhann outcrops have a higher number of fracture intersections (see *Figures 5.19b* and *5.21b* for a comparison). It is likely that the poor quality of the Alltan na Bradhan TLS point cloud is responsible for this disagreement between fieldwork observations and modelling results.

### 5.5 – Overall discussion

Fracture presence and fracture intersection analysis using the TLS outcrop datasets from the mainland LGC illustrates the differences in the fracture network attributes associated with the structural settings in which these three outcrops originate (see *Figure 5.22* for an illustrated summary of the main fracture presence and fracture intersection variables calculated from Alltan na Bradhan, Kinlochbervie and Caolas Cumhann). TLS modelling has shown that different structural settings can have a profound effect on the number of fractures and interactions between fractures and also highlights the importance of having a high quality dataset. The creation of these outcrop models for the mainland LGC provides important (and useful) quantitative datasets that can be directly implemented into existing Clair basement fluid flow models. This is critical when the mainland LGC is being employed as an onshore analogue for the Clair Field basement that contains a potential hydrocarbon reservoir which is entirely dependent on secondary porosity and permeability created by faults and fractures.

The following section compares and contrasts both the fracture presence and fracture intersection variations within the mainland LGC outcrops and highlights their importance with relation to hydrocarbon exploration in an offshore crystalline basement setting (a direct comparison of the onshore and offshore datasets will also be made in *Chapter 6*).

In addition to the structural setting, fracture geometry is important and produces fracture networks that have distinctive attributes within the mainland LGC. At Alltan na Bradhan both fracture presence and fracture intersections were expected to be the highest observed across any of the TLS outcrop datasets (fieldwork line samples yield an average fracture density value of 6.64 fractures per metre, *Table 3.5*) in this study. Unfortunately this was not the case because many of the fractures at Alltan na Bradhan are too small a resolution to be picked up from the TLS point cloud data coupled with the presence of abundant shadows in the Alltan na Bradhan TLS dataset. This means that the reduction in fracture presence value for the outcrop models is a result of an inherent resolution issue, which at this outcrop is exacerbated by the abundance of shadows within the dataset.



**Figure 5.22:** (a) Illustrations of the fracture presence and fracture intersection geometries for the key structural settings within the mainland Lewisian. (b) Conceptual fracture model showing the potential relationships of the different structural settings that are thought to exist within the Clair basement. Each coloured cell represents the 3-dimensional fractal dimension values for fracture presence and fracture intersection from the different structural settings shown in (a). Red cells – Alltan na Bradhan, Blue cells – Kinlochbervie, Green cells – Caolas Cumhann and Orange cells – Rhiconich Terrane background fractures.



The reason the outcrop at Alltan na Bradhan was expected to yield the highest fracture presence and fracture intersection  $D_2$  and  $D_3$  values is because of this outcrop's location within the Canisp Shear Zone (CSZ). This large crustal-scale shear zone plays a critical role in creating these predicted optimal fracture network values. Foliation within the CSZ exhibits greenschist-facies metamorphism and therefore contains a high percentage of phyllosilicates which makes this pre-defined foliation relatively weak. The weak foliation is subsequently re-activated by 'Late Laxfordian' faults and restricts the foliation perpendicular growth of Stoer Group age fractures (a full analysis of the role of weak foliation planes in the Canisp Shear Zone is discussed in detail in *Chapter 3*). All of this foliation control produces a highly populated fracture network, with two main fracture sets that are perpendicular to each other. As this relationship is not reflected in the TLS models it is recommended that the Alltan na Bradhan dataset is considered with care and that fracture attributes calculated from fieldwork (see *Chapter 3*) are taken into account when modelling shear zones in the Clair basement.

At Kinlochbervie, the TLS fracture network models exhibit fracture presence values that are the highest calculated across all three TLS models however the fracture intersection values are among the lowest. As previously mentioned, Kinlochbervie sits in the hanging wall of the adjacent NW-SE trending Loch Inchard fault which is likely responsible for the higher fracture presence values calculated from this outcrop model (Kinlochbervie sits in the damage zone of the Loch Inchard Fault, *Figure 5.17*). The majority of fractures at Kinlochbervie are orientated as minor conjugates to the main normal Loch Inchard fault plane (NE-SW) and have been interpreted as conjugate fractures that formed during deformation along the Loch Inchard Fault. This strong NE-SW (and sub-ordinate N-S) alignment of fractures within the Kinlochbervie TLS fracture model is responsible for the low fracture connectivity as the sub-parallel nature of the majority of the fractures means that there are a limited amount of fracture intersections. The fact that within this fracture network the majority of fractures are sub-parallel to each other suggests that even if connectivity between fracture planes was considered, the overall fracture connectivity within the fracture network would still be low, because there would still be limited intersections between suitably open fractures.

The background fracture network in the Assynt Terrane as modelled from the Caolas Cumhann TLS dataset exhibits fracture presence values, which are similar or

higher to those calculated from Alltan na Bradhan suggesting that even where the Assynt Terrane is not affected by any pre-existing structures or major faults, the rock is still relatively highly fractured. This is consistent with fieldwork observations across both the Assynt and Rhiconich Terranes where it is obvious that fracture density in the Assynt Terrane is significantly higher than the fracture density of the Rhiconich Terrane (see *Chapter 3* for a comparison). Fracture intersection  $D_2$  and  $D_3$  values are highly variable across the Caolas Cumhann model. This can be related to areas within the outcrop where there are large cliff sections where the rock is relatively 'clean' (high intersection numbers i.e. the short road section) compared to areas where the outcrop is disguised by vegetation (low intersection numbers i.e. parts of the long road section). At this outcrop fracture intersections are generally sub-horizontal as a result of the two main opposing fracture orientations (sub-horizontal and sub-vertical) that cross-cut the cliff sections. As this outcrop represents the background fracture pattern within the Assynt Terrane it is likely that many of the fractures within the network would be closed structures (most are tight joints with little evidence of aperture). Therefore even if fracture connectivity between the intersection curves was considered it is likely that there would be little communication between the fracture intersections (i.e. along fracture surfaces). This means that the fracture intersection values calculated from the Caolas Cumhann outcrop models are potentially a realistic representation of the fracture connectivity present within this outcrop.

The fracture presence and fracture intersection modelling shown in this chapter has important implications for fracture modelling within the Clair basement. This statement is particularly applicable to the 3-dimensional fractal dimension values ( $D_3$ ) which can be input directly into existing Clair basement fluid flow models (see *Figure 5.22b* for a conceptual Clair basement model using the onshore TLS model datasets). These  $D_3$  values are deterministic (they are based on measured fracture spacing and orientations) and therefore their implementation into the existing stochastic models will improve the understanding of the characteristics of Clair basement fracture networks. It is important to note however that the models presented in this chapter do not include any information on whether or not the fractures are open to fluid flow. In order to be able to use these models in Clair basement fluid flow models it is recommended that the main fracture sets within each of the structural settings are tested for their porosity and permeability characteristics.

## 5.6 – Conclusions

- Three outcrop datasets have been gathered using TLS to create more deterministic fully geo-referenced fracture network models for different structural settings within the mainland LGC. These structural settings were chosen because equivalent settings are thought to be also present within the Clair Field basement.
- Pseudo-well analysis results in power-law distributions for fracture spacing which is consistent across all three TLS fracture network models. This power-law distribution indicates scale-invariance and means that 1-dimensional spacing data gathered from these TLS datasets can potentially be used as an estimation of the fracture spacing at different scales.
- 1-dimensional fracture density analysis produces values between 0.1 and 0.5 fractures per metre. This is likely due to limitations imposed by the scale of the datasets (only fractures over 50cm in length have been interpreted compared to fractures over 30cm that are interpreted from fieldwork), rather than a true reflection of the 1-dimensional fracture density present within these key outcrops.
- Fracture presence modelling using the TLS datasets exhibits significant variations in the proportion of fractures within the three outcrops. These fracture presence variations can mainly be attributed to the structural setting in which the TLS outcrop datasets originate, although in the case of Alltan na Bradhan TLS point cloud quality plays a vital role in the fracture presence fractal dimension values (the model produces fracture presence values that are lower than expected from fieldwork observations). Kinlochbervie exhibits the highest fracture presence values which can be attributed to this outcrops location adjacent to a major NW-SE trending normal fault. The outcrop at Caolas Cumhann, which represents background fracturing in the Assynt Terrane, has fracture presence values that suggest the outcrop is relatively highly fractured. This can be compared to field observations of background fracturing in the Rhiconich Terrane which is predicted to have significantly lower fracture presence values (this was not laser scanned due to a lack of suitable outcrops).

- Average fracture presence  $D_2$  values at Kinlochbervie have a trend-line that decreases in fracture density away from the Loch Inchar Fault (*Figure 5.17*), suggesting that the damage zone of this fault (area of increased fracture presence) extends approximately 220m to the east of the main fault plane (normal fracture presence values determined from the predicted Rhiconich Terrane background fractures values).
- Fracture intersection models provide a low-end estimate of fracture connectivity across each of the three TLS outcrop models. These models suggest that fracture intersection occurrences with each of the TLS outcrops are very low or negligible. At Alltan na bradhan the low fracture intersection values were unexpected, again suggesting that the resolution of the TLS models and lower quality of the TLS point cloud for this outcrop has a large effect on both the fracture presence and fracture intersection values.
- The results suggest that outcrops that reside adjacent to large NW-SE trending faults (i.e. Kinlochbervie) the potential for fluid migration and storage is the highest. Areas where only the background fracturing is encountered (Caolas Cumhann and the Rhiconich Terrane) are likely to provide the least favourable fractured environment for a basement reservoir.
- All of the analyses conducted in this chapter have important implications for the Clair Field basement, where similar structural settings are thought to occur and the lack of high resolution 3-dimensional data makes it essential to use fracture network attribute information from an onshore analogue.
- It would be instructive for those modelling the Clair basement to recollect a TLS dataset from within the Canisp Shear Zone as similar structures are thought to exist within the Clair basement. The affect the shadowing in the Alltan na Bradhan TLS point cloud has had on the data was unfortunately not recognised until a point when there was no time left within the confines of this thesis to collect a fresh dataset.
- Another recommendation for further work on these datasets would be an extensive study looking at how varying the aspect ratio of the fractures affects the fracture presence and fracture intersections (connectivity) of the fracture networks. This would provide an insight into the fluid flow and ultimately the 'connected volume' present within the Clair basement which is dependent on

the values of the variables used. Such an analysis would increase the number of assumptions used within the modelling, particularly fracture extent. However, by history matching it to pre-existing development data from the Clair basement and by using the fracture characteristics from the mainland LGC to keep it geologically accurate, it should be possible to extend this analysis into fully 3-dimensional deterministic fracture network models. These models would provide the most accurate understanding of these offshore basement fracture networks, which ultimately will improve any potential hydrocarbon production from the Clair basement.

## **Chapter 6 – Data synthesis**

The onshore, offshore and TLS model analyses presented within this thesis suggest that fracture network characteristics can be incredibly heterogeneous in the mainland LGC and highly dependent on both the scale and structural setting from which the dataset was gathered. Little data are available for the Clair basement and therefore there is a need to interpolate, using data between regional scales (seismic interpretation) and well scales (core and image logs), to estimate the geometry and characteristics of the fracture network at all scales between. This is important as the geometry and characteristics of the fracture networks control fluid flow; particularly at a sub-seismic scale. The use of an onshore analogue, such as the mainland Lewisian Gneiss Complex (LGC), is intended to provide a geological basis for such an interpolation since there is ready access here to large datasets across a lot of different scales. Hence the analogue can also provide key fracture network parameters that could not have been discovered from the offshore datasets alone.

In this chapter, the similarities and differences between the onshore and offshore fracture orientation and spatial attributes are compared and contrasted at different scales. This provides a test of how good the onshore analogue for the fracture network in the Clair basement.

### **6.1 – Comparison of TLS modelling, fieldwork and regional analysis**

All of the onshore regional remote sensing, fieldwork and TLS model datasets provide detailed information about fault and fracture orientations and the spatial characteristics of the fracture networks present within the mainland LGC. As these three dataset types cover a range of scales, the primary aim of this section is to consider the scalability of the fracture networks from a series of key outcrops in the mainland Lewisian Gneiss Complex (LGC). Any similarities or differences in fault and fracture orientations across the scale range (mega- to meso-scale) will also be assessed. For the remainder of this chapter, the term fracture will be used to describe all brittle structures, unless otherwise stated.

### 6.1.1 – Orientation synthesis

Rose plots and stereonet have been used to analyse fieldwork, regional and TLS orientation datasets from the mainland LGC. *Figures 6.1, 6.2 and 6.3* show orientation data across a range of scales used within the mainland LGC which highlight the similarities and differences in the fracture orientation between the three datasets used.

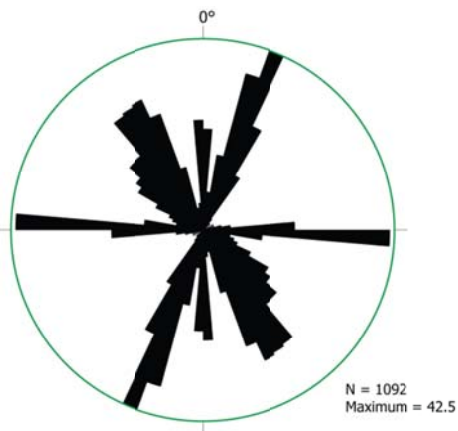
Within the Canisp Shear Zone (CSZ), orientation datasets come from: NEXTMap® digital elevation models (DEM), which cover the entire CSZ area; a terrestrial laser scan (TLS) model that only includes a specific outcrop at Alltan na Bradhan and fieldwork fracture samples from along part of the coastal section of the CSZ. Orientation data from these datasets are comparable across the different scales (*Figure 6.1*). The same prominent NE-SW and WNW-ESE fractures are recognised across the macro- and meso-scale datasets with a subordinate N-S fracture trend also present, consistent with previous fracture network analysis within the CSZ (Beacom et al., 2001). At a mega-scale more NW-SE trending faults are also recognised. A subordinate E-W fracture trend is also appreciated from the regional and fieldwork datasets, but it is not evident in the TLS data (*Figure 6.1*). The lack of E-W trending fractures in the TLS model can be explained because the CSZ fracture network is extremely spatially heterogeneous and this TLS model only samples a small, single outcrop, portion of this large shear zone. This spatial heterogeneity may also explain the lack of WNW-ESE trending faults in the mega-scale datasets, suggesting that the regional stress field is perturbed within individual outcrops due to pre-existing heterogeneities within the rock (e.g. intense foliation, etc)

Full three-dimensional orientation data gathered from the TLS and fieldwork datasets exhibit similarly steeply-dipping to sub-vertical fracture sets (*Figure 6.1*) suggesting fracture orientation (strike and dip) within the CSZ are scalable at least between macro- and meso-scales. It could be argued that this scalability can be extended to the regional dataset since fault lineaments typically plot as straight features on a map are therefore can also be assumed to be steeply-dipping/sub-vertical.

**MEGA-SCALE**

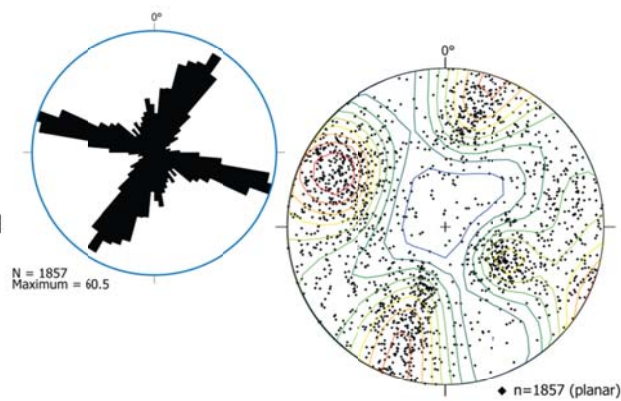
NEXTMap Digital Elevation Models

- Canisp Shear Zone data

**MACRO-SCALE**

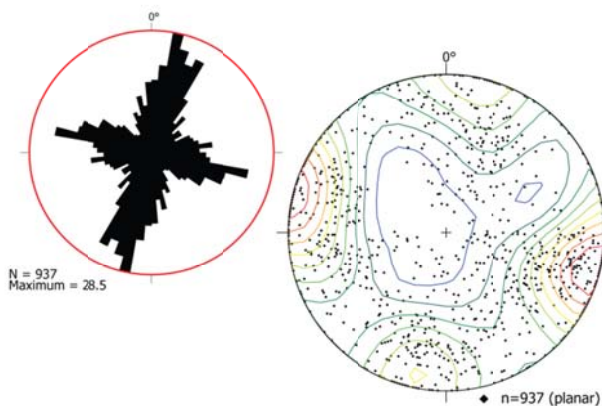
Terrestrial Laser Scan Model

- Alltan na Bradhan

**MESO-SCALE**

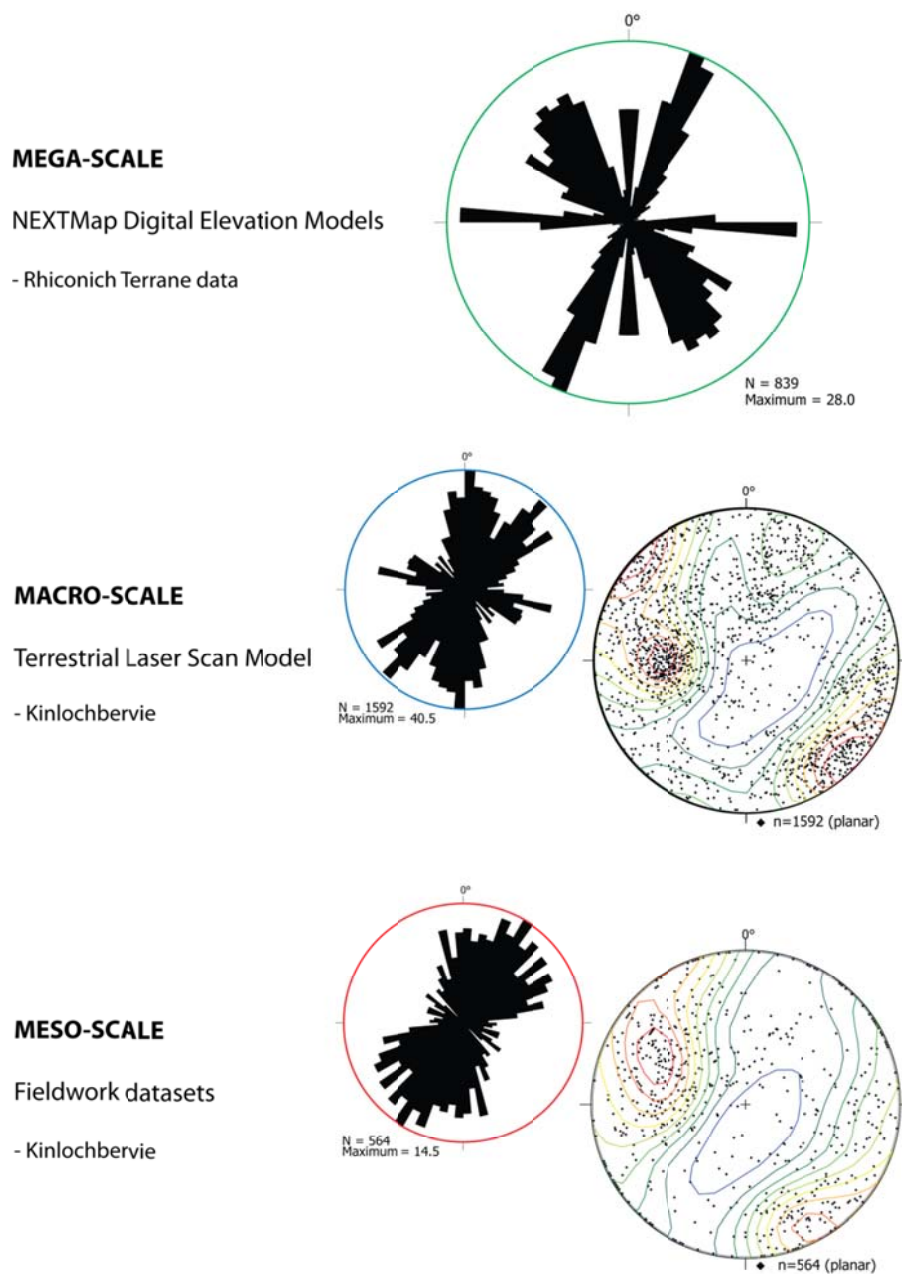
Fieldwork datasets

- Canisp Shear Zone



**Figure 6.1:** Rose plots and stereonets exhibiting fault and fracture orientation from the Canisp Shear Zone. The mega-scale dataset covers the full Canisp Shear Zone; the macro-scale dataset is limited to the outcrop at Alltan na Bradhan (NC 0508 2624) and the meso-scale dataset is from outcrops within the Canisp Shear that are found along its coastal section.



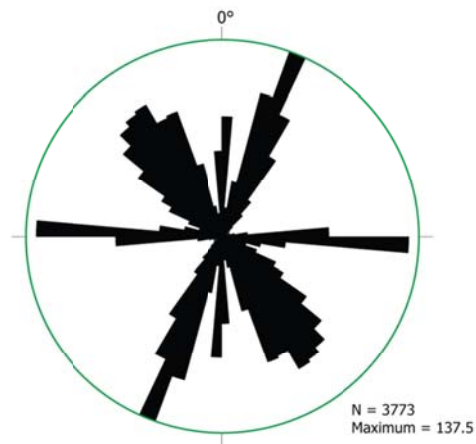


**Figure 6.2:** Rose plots and stereonets exhibiting fault and fracture orientation from Kinlochbervie. The mega-scale dataset covers the whole of the Rhiconich Terrane; the macro-scale dataset is limited to the outcrop at Kinlochbervie (NC 2296 5621) and the meso-scale dataset covers the same Kinlochbervie outcrop.

**MEGA-SCALE**

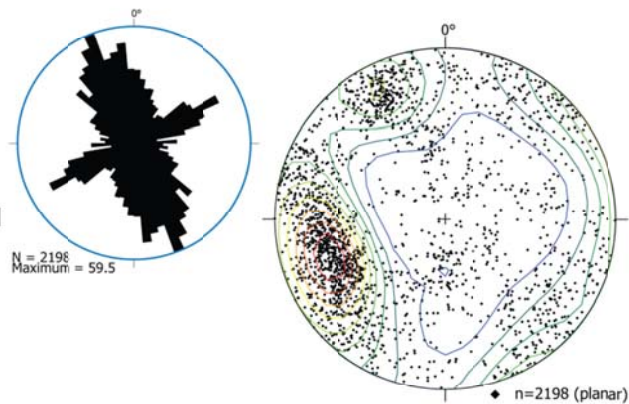
NEXTMap Digital Elevation Models

- Assynt Terrane data

**MACRO-SCALE**

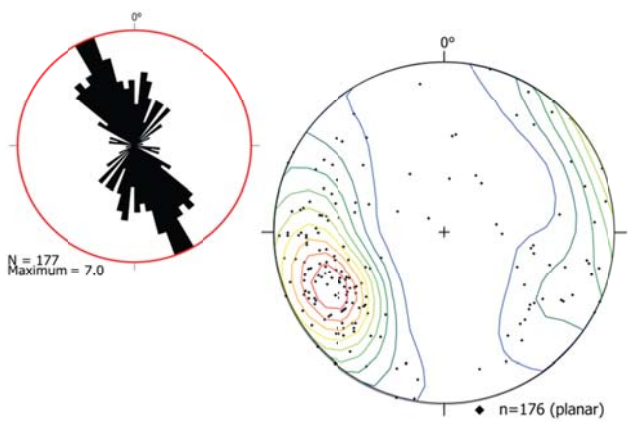
Terrestrial Laser Scan Model

- Caolas Cumhann

**MESO-SCALE**

Fieldwork datasets

- Caolas Cumhann



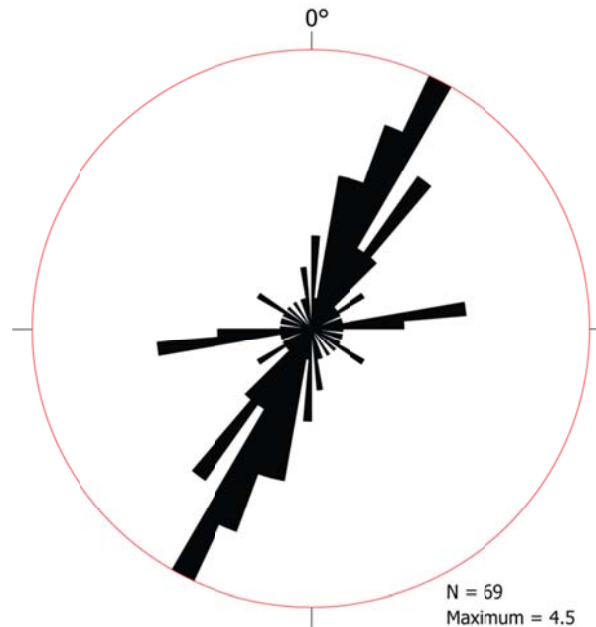
**Figure 6.3:** Rose plots and stereonets exhibiting fault and fracture orientation from Caolas Cumhann. The mega-scale dataset covers the whole of the Assynt Terrane; the macro-scale dataset is limited to the outcrop at Caolas Cumhann (NC 2251 3392) and the meso-scale dataset covers the same Caolas Cumhann outcrop.

At Kinlochbervie (NC 2296 5621), orientation data are again comparable across three different scales (*Figure 6.2*). All three datasets produce fracture orientations that trend NE-SW and N-S with a subordinate NW-SE trending fracture set also present. At a mega-scale NW-SE trending fault lineaments form a prominent trend. This can be related to the fact that the regional orientations cover the entire Rhiconich Terrane compared to the macro- and meso-scale datasets which are limited to the outcrop at Kinlochbervie. The presence of similarly steeply dipping fractures in the meso- and macro-scale datasets and the assumed near vertical dip of the regional fault lineaments (they are typically straight features on the DEM maps) across the Rhiconich Terrane (*Figure 6.2*) suggests that the orientation of fracture sets present across the Kinlochbervie area are scalable from <1m to several kilometres.

The fracture network datasets from the area surrounding Caolas Cumhann (NC 2251 3392) show more variety to their fracture trends than other areas included in this analysis. All three scales of datasets exhibit a NW-SE (NNW-SSE) fracture set and a subordinate N-S fracture trend (*Figure 6.3*). The NE-SW fault lineament trend present in the regional dataset is less obvious in the smaller scale datasets and only the TLS dataset exhibits an ENE-WSW set (*Figure 6.3*). Those fractures which trend ENE-WSW in the TLS model also have shallow dips which may explain why they are not obvious from fieldwork datasets. The TLS outcrop models allow fractures to be interpreted up the entire height of the outcrop, whereas in the field, only fractures in the bottom 1.5 metres of the cliff face can be sampled (due to sampler height restrictions). This means that the fieldwork sampling is biased towards fractures which are steeply dipping. This also applies to the regional dataset where the 2-dimensional DEM maps are again biased towards faults which are steeply dipping because they form the most prominent lineaments.

The lack of prominent NE-SW trending fractures in the macro- and meso-scale datasets is likely due to the fact that the Caolas Cumhann outcrop lies on a curved road section that primarily trends NE-SW and E-W. This means that there are only small portions of the road outcrop where NE-SW fractures would be oblique enough to the outcrop to be sampled, thus reducing the number of NE-SW trending fractures within the outcrop-based datasets. One recommendation from this hypothesis would be to conduct a further outcrop analysis further north on the same road (A894) where it is orientated more NW-SE allowing more NE-SW fractures (if they are present) to be

interpreted. A small fracture dataset collected from the A894, north of Caolas Cumhann, is shown in *Figure 6.4* which highlights the presence of NE-SW trending fractures within outcrop scale datasets. This supports the suggestion that the shape of the outcrop at Caolas Cumhann is at least partially responsible for the lack of a predominant NE-SW fracture trend in the outcrop-based datasets shown in *Figure 6.3*.



**Figure 6.4:** Rose plot exhibiting fracture data from the A894, north of Caolas Cumhann (NC 1728 3958).

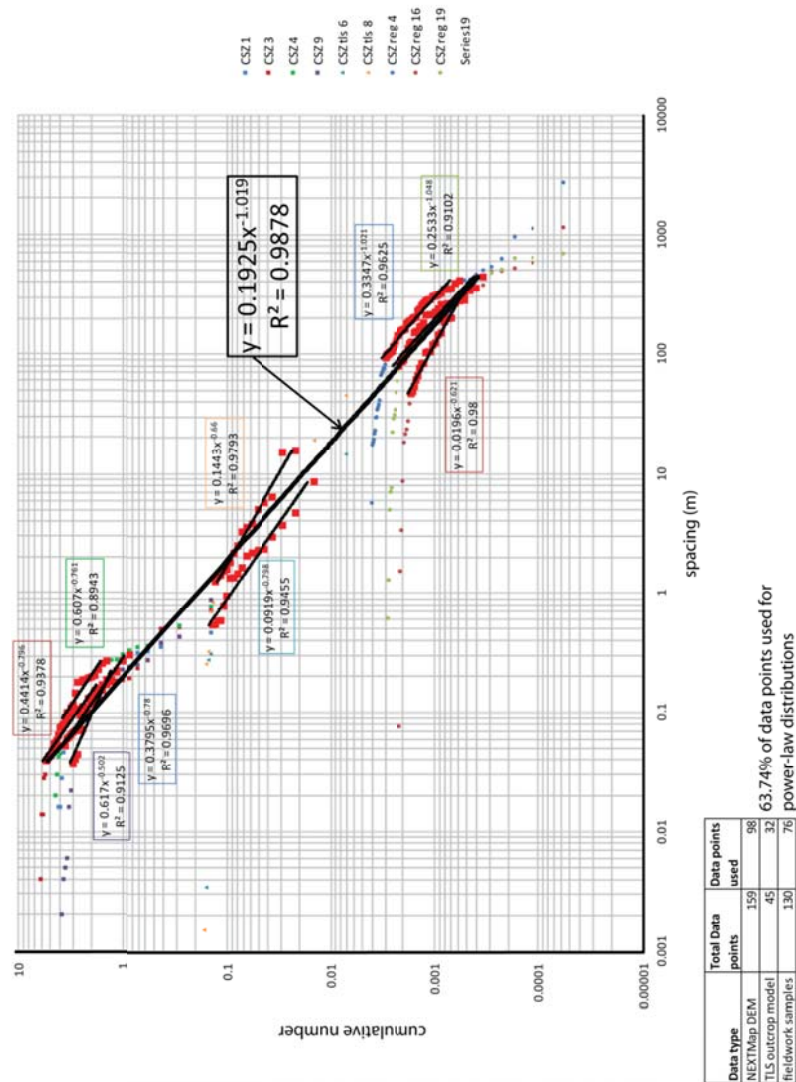
Other onshore outcrop fracture orientation datasets are given in *Chapter 3* and *Appendix 3* and show similar relationships to those seen at Caolas Cumhann. Most outcrop datasets include portions of the full fracture sets seen within the regional data, i.e. outcrop data may only contain fractures that trend NE-SW and N-S compared to the regional data, where fractures trend NE-SW, N-S, NW-SE and E-W. A possible explanation is that fracture orientation patterns observed at smaller scales are typically more complex than orientation patterns at larger scales because of heterogeneous local deformation controls including the presence of pre-existing features such as lithology, layering, foliation and faults (Beacom et al., 2001). This results in fractures that develop non-parallel to the regional bulk strain (Hesthammer et al., 2000, Jones et al., 2005) and over time results in a local fracture network which differs from that seen at a regional

scale. Therefore, although many outcrop samples within the mainland LGC exhibit fracture patterns that are similar to the regional scale datasets, care should be taken to ensure that the effects of local controls such as pre-existing structures are known before fracture orientations at a local scale are used to estimate the fracture orientations at a more regional scale.

### 6.1.2 – Spatial synthesis

Population distribution plots, fracture density estimates and coefficient of variation (CV) value analyses of 1-dimensional sample lines (including pseudo-wells) were used as a primary assessment of the spatial characteristics of the fracture networks within the mainland LGC. Although such 1-dimensional analyses provide a valuable insight into the spatial characteristics, it is important to be aware of the inherent limitations due to the fact that one 1-dimensional samples can only include small portions of the full 3-dimensional fracture network (Gillespie et al., 1993). Therefore, throughout this thesis, 1-dimensional line samples or pseudo-wells have been collected for fracture data in different orientations (normally perpendicular to the main fracture set; see *Chapter 1*) to try and combat some of the limitations imposed by the relative simplicity of the sampling technique.

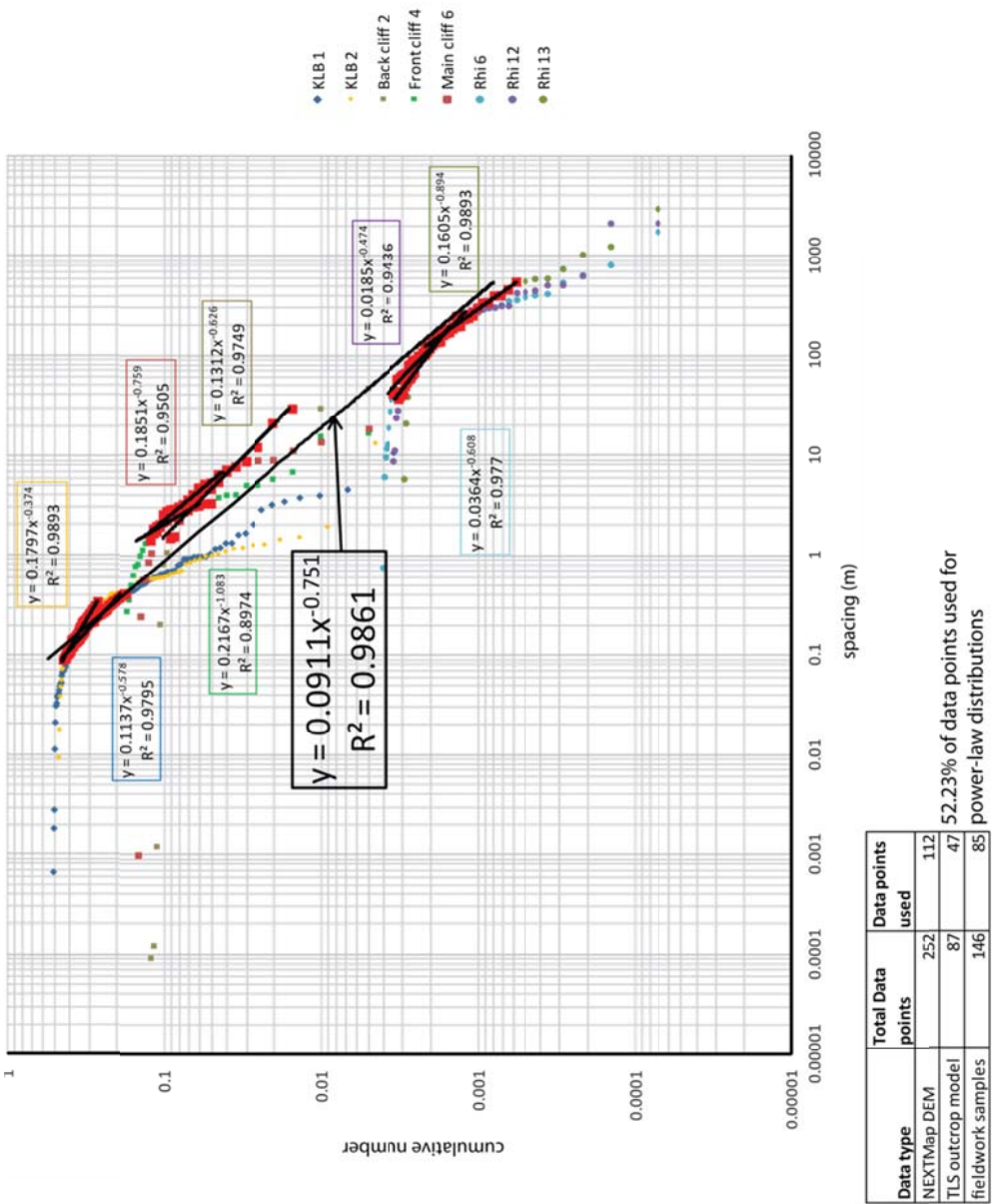
*Figures 6.5, 6.6 and 6.7* show 1-dimensional fracture spacing population distributions from the three scales of data sources used to analyse the mainland LGC fracture networks. The population distribution plot for the CSZ (*Figure 6.5*) demonstrates that the power-law spacing distributions of fracture spacing samples from all studied scales have comparable relationships and lie on a straight trend line with a D-value of 1.019. This distribution of the different scale power-law datasets along one trend line suggests that Canisp Shear Zone data set is scale-invariant at least between 0.1 and 1000 metre fracture spacing values. Somewhat similar power-law relationships are apparent for the Kinlochbervie and Caolas Cumhann spacing datasets (*Figures 6.6 and 6.7*, respectively).



power-law distribution shown in red. The trend line equation and  $R^2$  values are given in boxes which are colour-coded as per the sample that they are from.

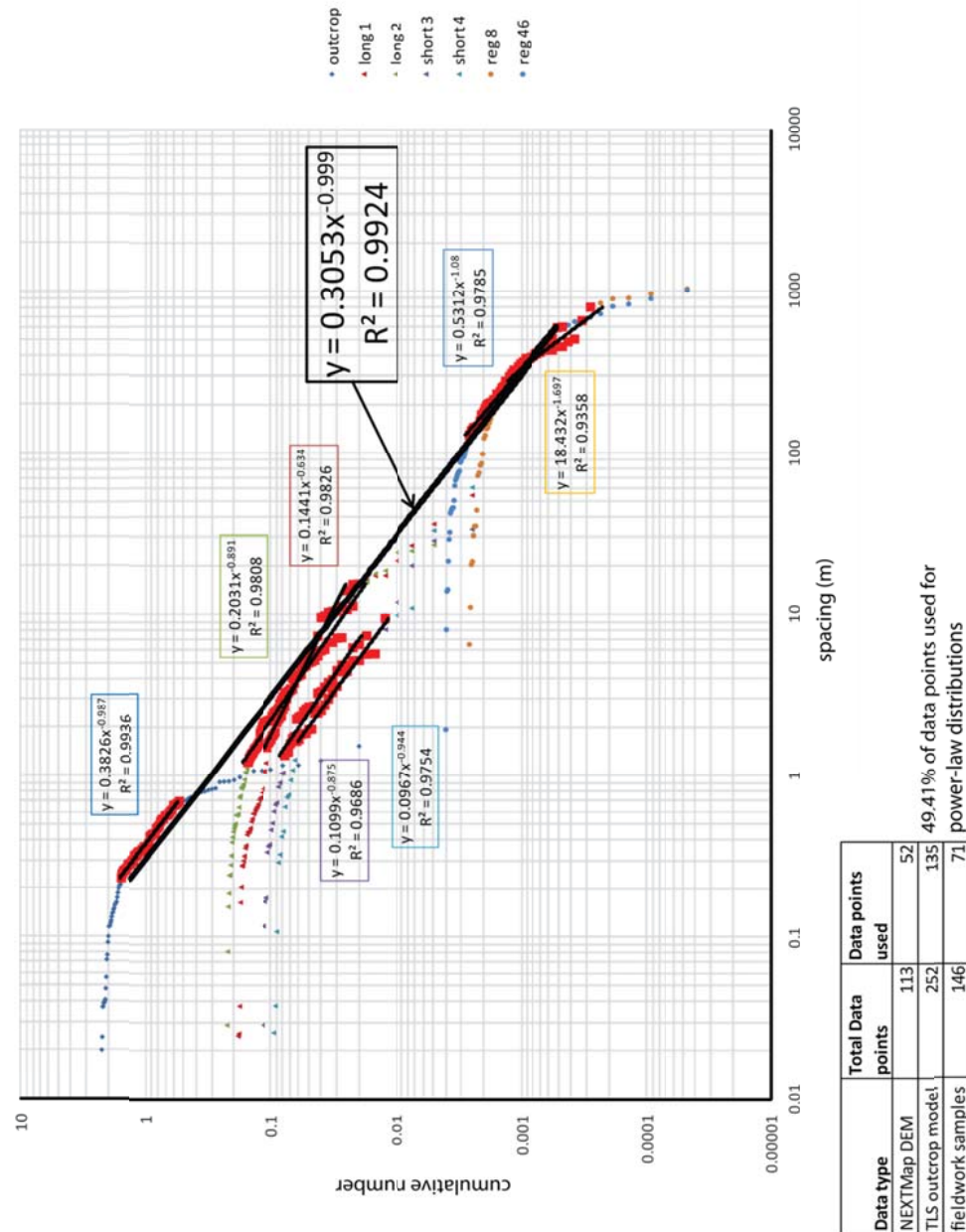
At both Kinlochbervie (Figure 6.6) and Caolas Cumhan (Figure 6.7) the TLS samples are slightly offset from the trend line that describes the full spatial relationship of the three included scales of dataset. As slopes (D-value) of the TLS model power-law distributions are similar to those from the NEXTMap® DEM and fieldwork datasets (see Table 6.1) it is suggested that this offset does not have a detrimental impact on the fracture spatial relationship. It is in fact a relict caused by the fact that the fractures interpreted from the Kinlochbervie and Caolas Cumhann TLS models have power-law relationships that form from ranges of fracture spacing values that are slightly larger than predicted from the trend line used to describe the fracture spacing across all three

scale ranges i.e. the fracture spacing size ranges for the TLS datasets are above the average seen across all dataset ranges.



**Figure 6.6:** Power-law population distribution plot showing example fracture spacing datasets from the three scales of data collected from Kinlochbervie: fieldwork sampling, TLS models and NEXTMap® regional analysis. All data points in each sample are shown with those that represent the power-law distribution shown in red. The trend line equation and  $R^2$  values are given in boxes which are colour-coded as per the sample that they are from.





**Figure 6.7:** Power-law population distribution plot showing example fracture spacing datasets from the three scales of data collected from Caolas Cumhann: fieldwork sampling, TLS models and NEXTMap® regional analysis. All data points in each sample are shown with those that represent the power-law distribution shown in red. The trend line equation and  $R^2$  values are given in boxes which are colour-coded as per the sample that they are from.



Data Source	Location	Sample Number	D-value	R <sup>2</sup>	CV	Fracture density
NEXTMap® DEM	Canisp Shear Zone	CSZ reg 4	1.02	0.96	1.47	0.004
	Canisp Shear Zone	CSZ reg 16	0.62	0.98	1.19	0.005
	Canisp Shear Zone	CSZ reg 19	1.05	0.91	1.14	0.005
	Rhiconich Terrane	Rhi 6	0.61	0.98	1.31	0.005
	Rhiconich Terrane	Rhi 12	0.47	0.94	1.58	0.004
	Rhiconich Terrane	Rhi 13	0.89	0.99	1.44	0.003
	Assynt Terrane	reg 8	1.70	0.94	1.12	0.003
	Assynt Terrane	reg 46	1.08	0.98	1.01	0.004
TLS outcrop model	Alltan na Bradhan	CSZ tls 6	0.80	0.95	1.36	0.41
	Alltan na Bradhan	CSZ tls 8	0.66	0.98	1.66	0.17
	Kinlochbervie	Back cliff 2	0.63	0.97	1.43	0.12
	Kinlochbervie	Front cliff 4	1.08	0.90	1.1	0.3
	Kinlochbervie	Main cliff 6	0.76	0.95	0.93	0.21
	Caolas Cumhann	long 1	0.63	0.98	1.65	0.18
	Caolas Cumhann	long 2	0.89	0.98	1.5	0.24
	Caolas Cumhann	short 3	0.88	0.97	1.59	0.24
	Caolas Cumhann	short 4	0.94	0.98	2.12	0.2
Fieldwork samples	Alltan na Bradhan	CSZ 1	0.78	0.97	1.28	5.8
	Alltan na Bradhan	CSZ 3	0.80	0.94	1.05	7.17
	Alltan na Bradhan	CSZ 4	0.76	0.89	1.33	4.43
	Alltan na Bradhan	CSZ 9	0.50	0.91	1.15	6
	Kinlochbervie	KLB 1	0.58	0.98	1.98	4.26
	Kinlochbervie	KLB 2	0.37	0.99	2.32	3.43
	Caolas Cumhann	outcrop	0.99	0.99	1.31	2.26

**Table 6.1:** Fracture network spatial attributes for mainland LGC 1-dimensional fracture samples from three different scales of data sources.

The spatial relationships illustrated in *Figures 6.5, 6.6 and 6.7* imply that, in 1-dimension, fracture spacing is scale-invariant between ~0.1 and 1000 metres across all three of the areas included in this study. This is important because it means that fracture spacing values collected at one scale can then confidently be used to estimate the fracture spacing characteristics at another scale, in a similar structural setting within the mainland LGC (and potentially the Clair basement), in an area where fewer fracture data are available. It is also likely that this scale-invariance could be expanded to micro-scales or even larger regional scales because of the strength of the relationship demonstrated (the straight line section of each dataset have similar D-values at all scales of analysis) on these population distribution plots (*Figure 6.5, 6.6 and 6.7*); although any spacing

estimation made outside of the 0.1 to 1000 metre range would have to be considered carefully.

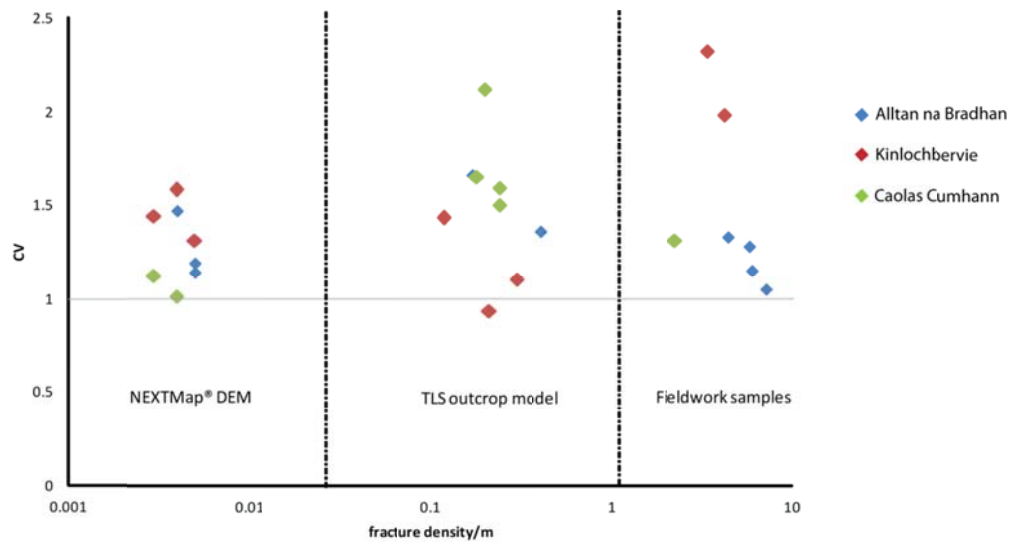
This population distribution analysis also proves how valuable the TLS outcrop model data are. If only the fieldwork samples and regional fracture datasets were available then the extent of the power-law relationships shown in *Figures 6.5, 6.6 and 6.7* would be the same, but there would be a large data 'gap' across the middle of the scale range. This would inevitably reduce the confidence of the scalability of the onshore fracture spacing characteristics. Therefore, having TLS model data available, that encompasses fracture spacing values between 1 and 100 metres fills in most of the 'gap' in the power-law relationships, increasing the confidence in the scale-invariance of the mainland LGC fracture spacing datasets.

The D-values from the trend lines through the three scales of fracture spacing data can also be used to assess how the power-law distributions are weighted (i.e. are they based on more larger or more smaller spaces between fractures?). For the CSZ, the trend line that describes the three scales of power-law relationships has a D-value of 1.019 (*Figure 6.5*) which suggests that there are more small fracture spacing values for every large spacing value (although the increased number of small fracture spacings is minimal). This contrasts with the trend line from Kinlochbervie which has a D-value of 0.751 (*Figure 6.6*), suggesting that this power-law distribution contains more fractures that are widely spaced compared to small spaces. The power-law distribution for Caolas Cumhann has a D-value that is close to one (0.999, *Figure 6.7*) indicating that the fractures at this location are approximately equally distributed between those that are widely spaced those that are close together.

CV value calculations presented in *Table 6.1* and *Figure 6.8* are consistent with the population distribution plots. When the CV values from the three key areas are compared (*Figure 6.8*), the Canisp Shear Zone exhibits the lowest values which means that the fractures at this location are the least clustered within the included datasets. These low CV values concur with the Canisp Shear Zone power-law distribution as its D-value indicates that the majority of fractures are closely spaced and have a more regular (but still slightly clustered) distribution.

The CV values for Kinlochbervie are more variable across the scales of datasets (Table 6.1 and Figure 6.8). Fracture CV values for the NEXTMap® DEM interpretation and fieldwork samples increase with increasing resolution suggesting that the fracture sets at Kinlochbervie become more clustered with more detailed fracture sampling. The Kinlochbervie TLS model fracture sets do not follow this increasing CV value trend, which is likely due to sampling restrictions imposed on the interpretation so that fractures < 50cm in length were not interpreted (see Chapter 5, Section 5.3). Thus not every fracture seen at the outcrop is interpreted and this reduces the clustering relationship.

Generally the Kinlochbervie CV values concur with the D-values from the population distribution analysis. The D-value (0.751, Figure 6.6) suggests that the 1-dimensional power-law fracture spatial characteristics include more fractures that are widely spaced than those which are clustered. This coincides with the CV values ( $> 1$ , Figure 6.8), which indicates that fractures at Kinlochbervie are clustered.



**Figure 6.8:** Plot of fracture density versus CV value which highlights the difference in spatial attributes of the three scales of data sources used to assess the fracture network spatial characteristics in the mainland LGC.

The CV values from Caolas Cumhann are also variable across the three scales of datasets (*Figure 6.8*). In this instance the TLS model fracture samples have the highest CV values. This is likely because in the steep-sided outcrops at this locality the TLS model allows access to many more fractures than traditional fieldwork and therefore a far larger dataset has been gathered at this intermediate scale. If a larger fracture dataset had been gathered during fieldwork then it is likely that the fieldwork samples would have CV values that were more comparable to those from the TLS fracture datasets.

The D-value determined for the Caolas Cumhann power-law distributions across the three scales of datasets does not coincide as well with the majority of the CV values calculated across the area. The D-value suggests that the fracture spacing distribution is equally split between fractures that are widely spaced and fractures that are close together. This relationship would suggest that the fractures are also more regularly spaced which is not apparent from the TLS model datasets where the samples have CV values that indicate fracture clustering. It is possible that the D-value for Caolas Cumhann has a reduced slope because of the small fieldwork fracture sample (i.e. it may not be entirely representative of the overall fracture pattern at this location). Therefore both the D-value and CV values from fieldwork samples may be lower than what would be expected from the full fracture network characteristics where fractures are more likely to be highly clustered ( $CV \gg 1$ ).

1-dimensional fracture density values (fractures per metre) clearly show the difference in resolution of the three scales of data (*Figure 6.8*). Not surprisingly the regional dataset exhibits the lowest fracture density values with an average value of 0.004 fractures per metre (equivalent to 4 fractures per kilometre, *Table 6.1*). At this scale there is little difference in the fracture density values across the three key areas, although the Canisp Shear Zone samples typically have slightly higher fracture densities.

Both the TLS model and fieldwork samples originate in the same outcrops and would have been expected to have similar fracture density values. In fact the TLS model samples have fracture densities which are an order of magnitude lower than the fieldwork samples (*Figure 6.8*). This is most likely due to the resolution limitations of the TLS models where only fractures >50cm in length are interpreted, compared to the fieldwork samples where fractures >30cm in length are included. In both the TLS model and fieldwork samples, Alltan na Bradhan (CSZ) exhibits the highest fracture density values with Caolas Cumhann and Kinlochbervie typically displaying similar fracture

densities (*Figure 6.8* and *Table 6.1*). As explained in both *Chapter 3* and *Chapter 5*, the fieldwork and TLS model (respectively) fracture density values reflect the structural settings in which the samples are collected.

*Alltan na Bradhan* (Assynt Terrane) has the highest fracture densities due to its location within a large crustal-scale shear zone where fractures preferentially develop due to the presence of a pre-existing phyllosilicate-rich foliation (*Chapter 3, Section 3.3.7*).

*Kinlochbervie* (*Rhiconich Terrane*) also has relatively high fracture density values which are due to this outcrop's location within the hanging-wall of an adjacent NW-SE trending normal fault: the majority of fractures within this outcrop are thought to be small conjugate structures to the main fault plane (*Chapter 3, Section 3.3.7*).

*Caolas Cumhann* (Assynt Terrane) exhibits fracture densities similar to those calculated for Kinlochbervie, but unlike the latter locality, these fractures represent background fracturing in the Assynt Terrane. These relatively high fracture density values indicate that even in regions where there are no pre-existing structures or major faults, the Assynt Terrane is still heavily fractured (*Chapter 3, Section 3.37* and *Chapter 5*).

The comparative spatial analysis has shown most importantly that 1-dimensional spatial characteristics of fractures in the mainland LGC are scale-invariant over at least 4 orders of magnitude. This has important implications for modelling the Clair basement: if similar structural settings are present in the subsurface then it is possible to assume that similar scaling relationships of fracture spacing also exist here and therefore fractures measured from well samples and seismic can be used to estimate the fracture spacing characteristics at all scales in between. The suitability of the mainland LGC as an analogue for the Clair basement is assessed in the following sections.

## 6.2 – Onshore/Offshore Synthesis

Although it is apparent that the onshore datasets are scale-invariant over at least four orders of magnitude, these data are only useful for the Clair basement if the orientation and spatial fracture network characteristics are comparable. This section aims to synthesise the onshore and offshore datasets and to highlight any differences in the fracture history that need to be considered when using the onshore fracture datasets as an analogue for the fractures in the Clair basement.

### 6.2.1 – Comparison of lithologies

In order to assess the potential of the mainland LGC as an analogue for the Clair basement, we need to compare and contrast the main lithologies present in the onshore and offshore study areas. *Chapter 3* and *Chapter 4* provide details of the onshore and offshore lithologies, respectively, so the aim of this section is to evaluate to what extent the lithologies described in the earlier chapters are comparable between the two study areas. From *Chapter 3* it is known that the mainland LGC lithological characteristics are not simple with several different terranes (or crustal blocks) recognised. Two of these - namely the Assynt and Rhiconich Terranes have been studied during the present study as they lie closest to the Clair field. This pre-existing complexity in the basement gneiss protoliths is important because previous work in the mainland LGC has shown that there is a potential link between gneiss lithology and fracture network spatial characteristics; particularly clustering and fracture density (Beacom et al., 2001). Therefore it is essential to determine which mainland terrane the Clair basement has the most affinities with, to help ascertain which fracture networks within the mainland LGC may provide the best analogue for the Clair basement.

As discussed in *Chapter 4*, the Clair basement comprises four distinct lithologies which are: granodiorite gneiss, granite gneiss, basic gneiss and pegmatite. All experienced at least amphibolite-facies metamorphism. These rocks have an orthogneissic origin with characteristics similar to the gneisses seen in northwest Scotland. *Chapter 3* focuses attention on the Assynt and Rhiconich Terranes from the mainland LGC, which exhibit different lithologies of generally different metamorphic grades. The Assynt Terrane typically comprises granulite-facies grey, banded

intermediate orthogneisses that are occasionally cross-cut by crustal-scale NW-SE trending lower amphibolites to upper greenschist-facies shear zones that are 100's of metres to kilometres wide, e.g. the CSZ. Typically the Assynt Terrane exhibits poorly-defined shallow-dipping foliation that steepens up (to near vertical) into the later shear zones. This is in comparison to the Rhiconich Terrane where the lithology predominately comprises granodiorite/diorite gneisses and granite gneiss sheets with subordinate mafic units and pegmatite veins (*Figure 6.9a*). In the Rhiconich Terrane the rocks are amphibolite-facies and are typically more foliated than the rocks of the Assynt Terrane.

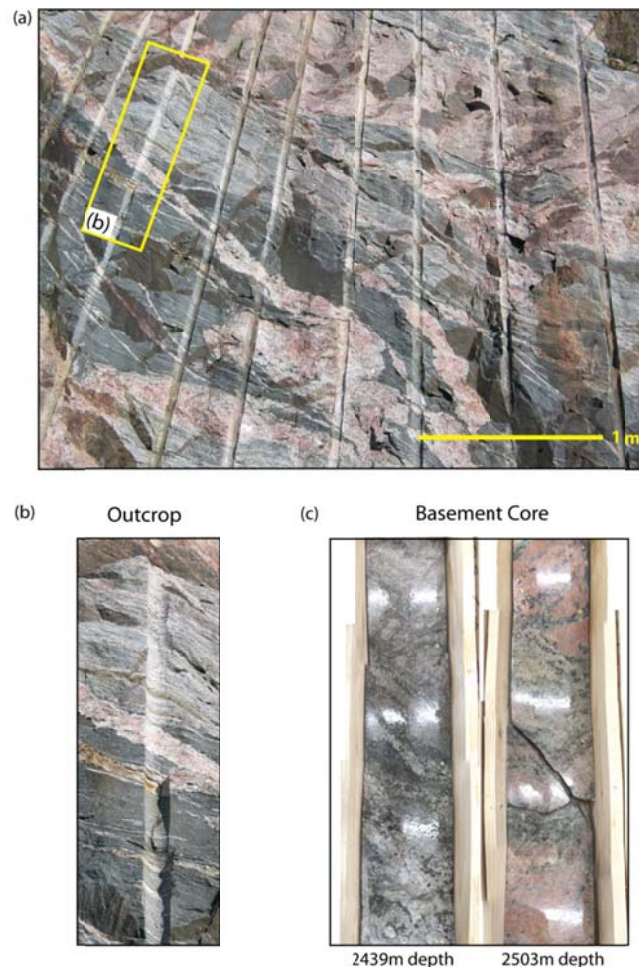
Using the above summaries (and the details of the mainland LGC presented in *Chapter 3*) it is apparent that the core samples (at least) from the Clair basement seem to have the most affinities with the Rhiconich Terrane of the mainland LGC. *Figure 6.9b & c* best illustrates the similarities between the Rhiconich Terrane and Clair basement lithologies using drill holes in the 'Multi-coloured rock stop' cliff face as an inverted analogue for the basement core samples. This figure shows the similar banding of the different lithologies, including the presence of later, cross-cutting, pegmatite veins.

*Figure 6.9a* also highlights how poorly fractured the Rhiconich Terrane can be. The lack of fractures is not limited to this outcrop; in fact fracturing is typically very limited across the bulk of the Rhiconich Terrane. Only areas adjacent to faults display highly fractured areas (e.g. Kinlochbervie which lies in the hanging wall of the Loch Inchar Fault). Therefore if the Clair basement lithology is considered to be the same (or similar) to the Rhiconich Terrane *and* the lithology is deemed to control the fracture network spatial characteristics, then the majority of the Clair basement is unlikely to be heavily fractured. It also means that (seismic-scale) faults in the Clair basement are fundamentally important as they created fracture corridors that have potential for providing fluid flow pathways through these crystalline rocks.

It is unlikely that the mainland LGC/Clair basement relationship is as simple as described above. Interpretations of the basement from seismic suggest that the main Ridge Fault is offset dextrally several times along its length. It has been postulated by the industry sponsors that these offsets represent WNW-ESE trending shear zones that are potentially similar in nature to those present within the Assynt Terrane. If these shear zones do exist within the Clair basement then they are likely zones of increased fracture density (from fieldwork samples and TLS models) and they may also follow pre-existing upper greenschist-facies, highly foliated rocks. At the present time the presence

of these shear zone can only be assumed; as there are no direct basement samples (core or image logs) through one of these zones that offset the main Ridge Fault.

It should also be noted that it is possible that one region of the Clair basement may be more analogous with one mainland LGC terrane than another. This means that this thesis does not aim to provide a unique solution, as it may be that different onshore analogues will be appropriate for different regions of the Clair basement ridge. The datasets presented in this thesis provide model types that can then be input into sensitivity models to assess which onshore dataset provides the best geological and statistical match for the Clair basement.



**Figure 6.9:** Photographs of mainland LGC outcrop and Clair basement core samples illustrating the similarities in lithology. (a) Multi-coloured rock stop in the Rhiconich Terrane. This is a blasted outcrop. (b) The blasted cliff face provides a useful analogue for the core samples from the Clair basement: the drill holes used for the explosives resemble inverted core samples.



### 6.2.2 – Comparison of fault rock characteristics

As well as assessing the similarities between the mainland LGC and Clair basement lithologies it is also important (if not more important) to compare and contrast the fault rock and fracture fill characteristics between the onshore and offshore datasets.

Fractures interpreted from Clair basement core samples fall into three main categories. The oldest of these are pre-Devonian (known from relationship with the Basal Conglomerate that overlies the Clair basement, *Figure 4.18*) and are mineralised with epidote, hematite and quartz; with many of the faults containing epidote ultra-cataclasite. The second set of fractures are mineralised with calcite and are known to have developed before any hydrocarbons migrated into the Clair fracture system (Late Cretaceous to Early Tertiary, Milodowski et al., 1998). A final set of basement fractures is recognised which are mineralised with calcite and pyrite and developed at the same time as hydrocarbon migration into the Clair fracture network (Milodowski et al., 1998 and Chapter 4 Section 4.3.2.8).

Onshore, hematite (and epidote)-mineralised Stoer/Torridon group age fractures are recognised across the mainland LGC (Assynt and Rhiconich Terranes). These fractures have similar fault rock compositions to the pre-Devonian fractures recognised from Clair basement core samples. As no lower age limit is known for the offshore pre-Devonian fracture sets it is possible that they are directly comparable with the onshore Stoer/Torridon Group age fractures that bear similar fault mineralogies. This suggestion is further enhanced by the fact that both the onshore and offshore hematite/epidote bearing fracture sets have dextral extensional kinematics (and similar NE-SW orientations), suggesting that they formed under similar stress regimes.

The mainland LGC exhibits little evidence of calcite mineralised fracture sets; with only reactivated fractures associated with the Loch Assynt and the Loch Inchar Faults exhibiting any calcite mineralisation (*Chapter 3, Section 3.3.3.4*). This limited evidence of Mesozoic/Cenozoic extensional fractures in the mainland LGC highlights the fact that much of the mainland LGC has not experienced Mesozoic tectonism meaning that it may only be a suitable onshore analogue for the background fracture sets (pre-Devonian) that are present within the Clair basement.

### 6.2.3 – Synthesis of orientation data

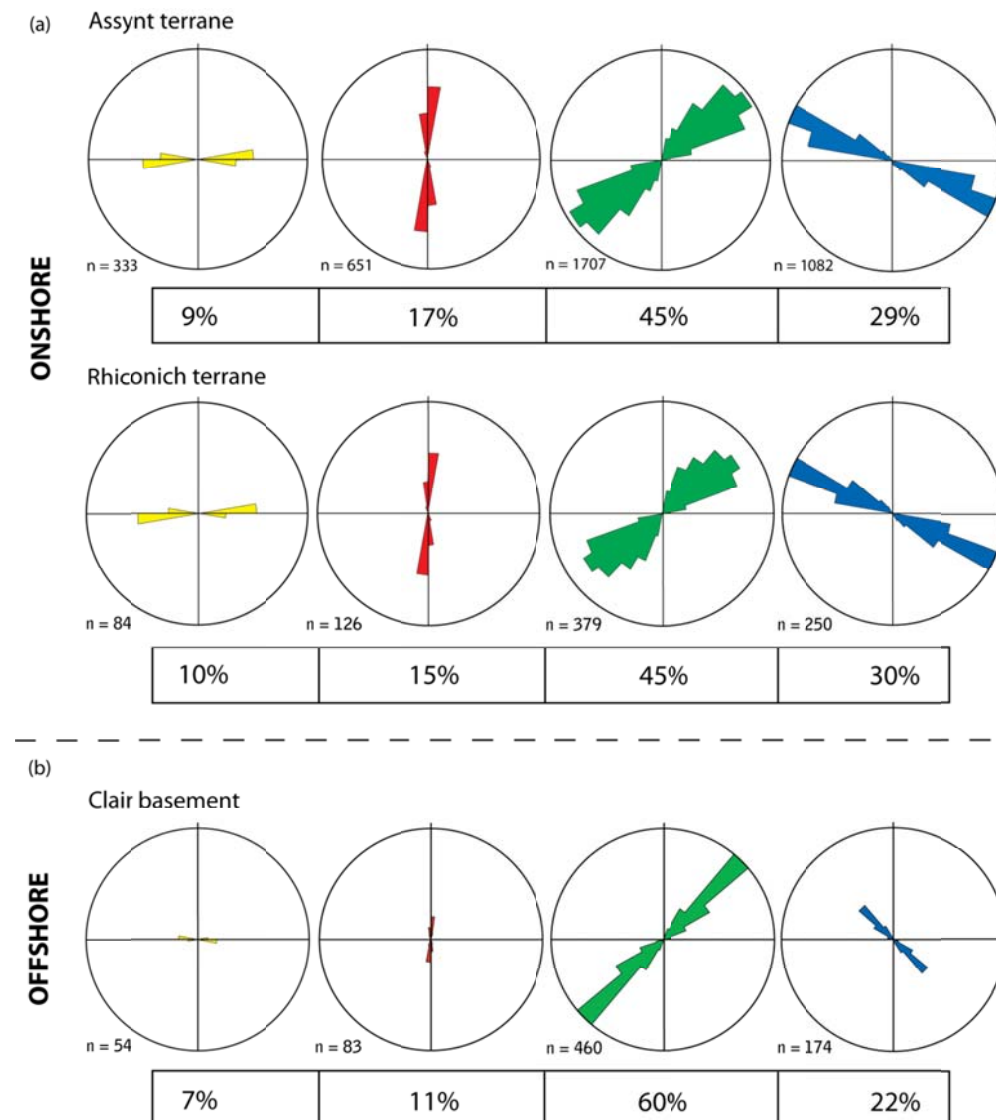
Fault and fracture orientations for the onshore and offshore datasets are also compared to test the suitability of the mainland LGC as an analogue for the Clair basement. The following sections compare and contrast the mega- (regional) and macro- (TLS models) & meso-scale (outcrop and well) orientation datasets and assesses how consistent the fracture orientations are across the scale range.

#### 6.2.3.1 – Regional orientation analysis

Onshore regional orientation datasets come from NEXTMap® DEM maps and offshore the regional orientation data are from seismic attribute maps of the top Clair basement horizon. *Figure 6.10* exhibits the entire available fault lineament orientations from the regional datasets with the data split into four separate azimuth groups.

The onshore regional data are split into the Assynt and Rhiconich Terranes to assess any variations in fault lineament orientations across the mainland terranes. As *Figure 6.10a* shows, there is little difference in the fault orientations between the Assynt and Rhiconich Terranes. The accompanying percentage values in *Figure 6.10a* illustrate the similarities in the number of fractures in each azimuth group, i.e. the ratio of fractures in each azimuth group is approximately the same for both the Assynt and the Rhiconich Terrane. This means that, at a mega-scale, the difference in fault network orientations between the Assynt and Rhiconich Terranes is not readily distinguishable.

The Clair basement regional data exhibits similar fault orientation patterns as the onshore datasets (*Figure 6.10b*), although the percentage of fractures in each azimuth group are much less comparable with the Assynt and Rhiconich Terrane datasets. The NE-SW azimuth group from the Clair basement comprises 60% of the full dataset (*Figure 6.10b*). This is in comparison to the onshore datasets where the NE-SW azimuth group consistently comprises 45% of the full fault dataset. The increased percentage of NE-SW trending faults subsequently reduces the percentage of the other azimuth groups in Clair basement (particularly NW-SE and N-S faults, *Figure 6.10*).



**Figure 6.10:** Rose plots of regional fault lineament orientation data separated into four azimuth groups. The orientation is from (a) onshore NEXTMap DEM and (b) offshore seismic attribute maps. Also included in this figure are percentage values of the number of fault lineaments in each azimuth group.

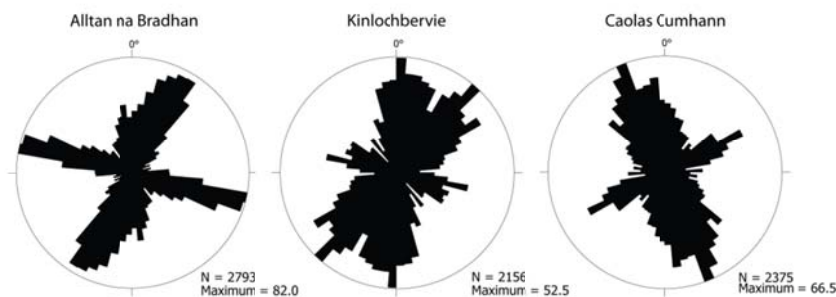
It is likely that the very strong (and well defined) NE-SW fault trend present in the Clair basement (compared to the onshore datasets) can be explained by prolonged NW-SE trending extension across the Faroe-Shetland Basin during the Palaeozoic and especially the Mesozoic (e.g. Knott et al., 1993, Davies et al., 2004, Couzens, 2008) which potentially reactivated existing faults (and fractures) and formed new NE-SW trending structures. Evidence of Mesozoic extension is limited in the mainland LGC, with

movements restricted to a relatively small number of widely-spaced larger structures, with most smaller NE-SW faults interpreted to have formed in the Proterozoic (*Chapter 3*).

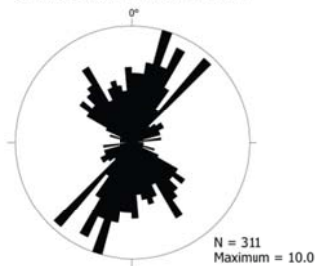
### 6.2.3.2 – Well and Outcrop (includes TLS) orientation analysis

Meso- (and macro-) scale orientation datasets from mainland LGC outcrops are compared to fracture orientation datasets from well samples of the Clair basement. This is completed, first to assess the similarity of the onshore and offshore datasets and second to help determine which onshore terrane (Assynt or Rhiconich) is the most comparable at this scale range with the Clair basement.

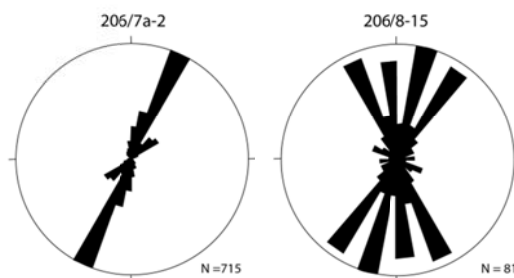
#### (a) ONSHORE - fieldwork samples



#### Oldshoremore + 'Multi-coloured rock stop'



#### (b) OFFSHORE - well samples



18  
0-  
:S.  
15  
el  
C.  
15  
25

*Figure 6.11* contains rose plots of fracture orientations from key outcrops across the mainland LGC and from core and image log samples from the Clair basement. The outcrop rose plots from Alltan na Bradhan (Canisp Shear Zone), Kinlochbervie (adjacent to a major NW-SE trending fault) and Caolas Cumhann (Assynt Terrane background fracturing) comprise both fieldwork and TLS model fracture samples; Oldshoremore and the 'Multi-coloured rock stop' represent the background fracturing in the Rhiconich Terrane (*Figure 6.11a*). All of these onshore rose plots exhibit different prominent fracture trends which represent the various structural settings in which they are located (see *Chapter 5* for descriptions of the relationships between fracture orientations and structural setting).

Alltan na Bradhan in the Canisp Shear Zone comprises NE-SW and NW-SE trending fractures with a subordinate N-S fracture trend (*Figure 6.11a*). Similar fracture trends are present at Kinlochbervie, although at this location N-S and NE-SW trending fractures are most prominent and NW-SE fractures form the subordinate set (*Figure 6.11a*). At Caolas Cumhann the majority of fractures trend NNW-SSE with far fewer NE-SW fractures present at this outcrop (*Figure 6.11a*). Although Oldshoremore and the 'Multi-coloured rock stop' are geographically not adjacent to each other, their datasets have been combined in the one rose plot to represent background fracturing in the Rhiconich Terrane (*Figure 6.11a*). This rose plot shows that at these outcrops fractures trend mainly NE-SW (NNE-SSW), NW-SE and N-S.

The offshore well orientation datasets from the Clair basement are extremely limited with data only available from two basement wells. The core sample from well 206/7a-2 comprises fractures with a strong NNE-SSW fracture trend (*Figure 6.11b*) which have been attributed as antithetic structures of an adjacent, Clair ridge off-setting fault (see *Chapter 4, Section 4.3.4.1*). Well 206/8-15 comprises fractures interpreted from image log data which have trends of NNE-SSW, N-S, NNW-SSE and a minor NW-SE trend (*Figure 6.11b*). The fractures in well 206/8-15 are likely related to periods of E-W extension in the Devonian (Dewey and Strachan, 2003, Wilson et al., 2010) and/or Jurassic (Dore et al., 1997).

Using the rose plots in *Figure 6.11* to determine the similarities and differences between the onshore and offshore fracture network orientations suggests that the outcrop (and TLS) orientation data from Oldshoremore, the 'Multi-coloured rock stop' and to a certain degree orientation data from Kinlochbervie are the most similar to the

fracture orientations in the Clair basement. This assessment is in agreement with the lithology analysis shown in *Section 5.2.1* which suggests that the Rhiconich Terrane in the mainland LGC is the most likely correlative for the Clair basement.

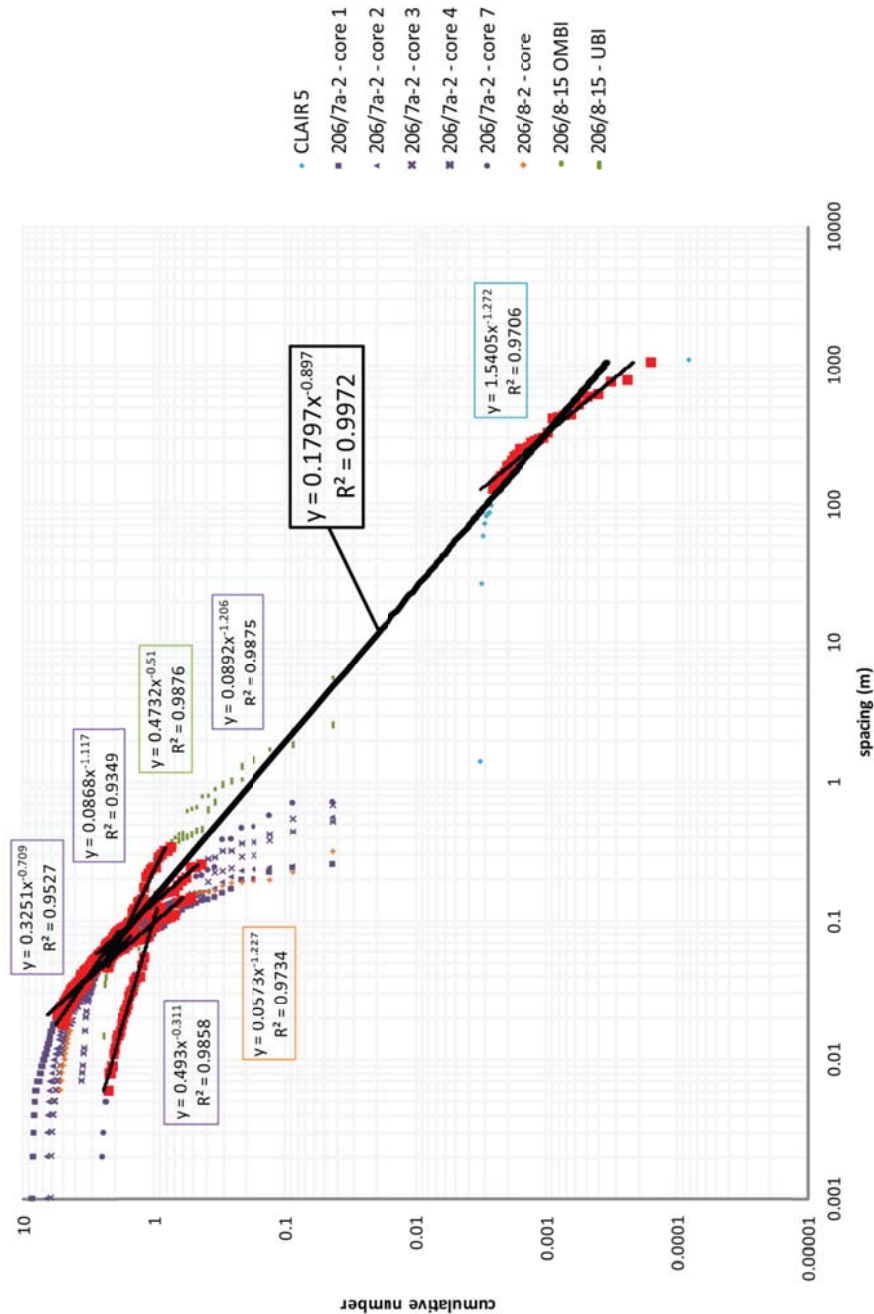
Although there is a reasonable comparison between the onshore and offshore meso-scale (macro-scale) fracture orientation datasets, there is no exact match across the study areas. Some of the variations in fracture orientation in the Clair basement can be attributed to position and orientation of the well from which the dataset originates. This particularly applies to the core sample from well 206/7a-2 which as a horizontal well that is orientated N290° and is therefore biased towards fractures that trend NE-SW (*Figure 6.11b*). It is therefore possible that fractures trending NW-SE, similar to fractures seen in mainland LGC outcrops, are excluded from core 206/7a-2 due to the orientation of the well. Other differences in fracture orientation between the onshore and offshore datasets may be a product of the more extended tectonic history of the Clair basement compared to the mainland LGC: the Clair basement exhibits brittle deformation that is likely of Proterozoic, Palaeozoic, Mesozoic and Cenozoic age compared to the mainland LGC samples where the majority of fractures appear to be Proterozoic in age.

### 6.2.3.3 – Comparison of fracture network spatial characteristics

Although comparing onshore and offshore fracture orientations provides a basic means of determining the suitability of the mainland LGC as an analogue for the Clair basement, it says very little about the scalability of the datasets. It is therefore more instructive to use fracture spatial distributions, first to assess how scalable the fracture datasets are across the onshore and offshore areas and to then ascertain how valid the fracture networks in the mainland LGC are for use as an analogue for fracture patterns in the Clair basement.

The three different scales of onshore datasets (NEXTMap DEM, TLS model and fieldwork samples) were compared in *Section 6.1.2*, which demonstrated that the fractures in the mainland LGC are probably scale-invariant over at least four orders of magnitude. *Figure 6.12* exhibits a similar analysis conducted for the offshore, Clair

basement datasets which is used to assess if the offshore fracture sets display a similar degree of scale-invariance as fractures in the mainland LGC.



map and well samples. All data points in each sample are shown with those that represent the power-law distribution shown in red. The trend line equation and  $R^2$  values are given in boxes which are colour-coded as per the sample that they are from.

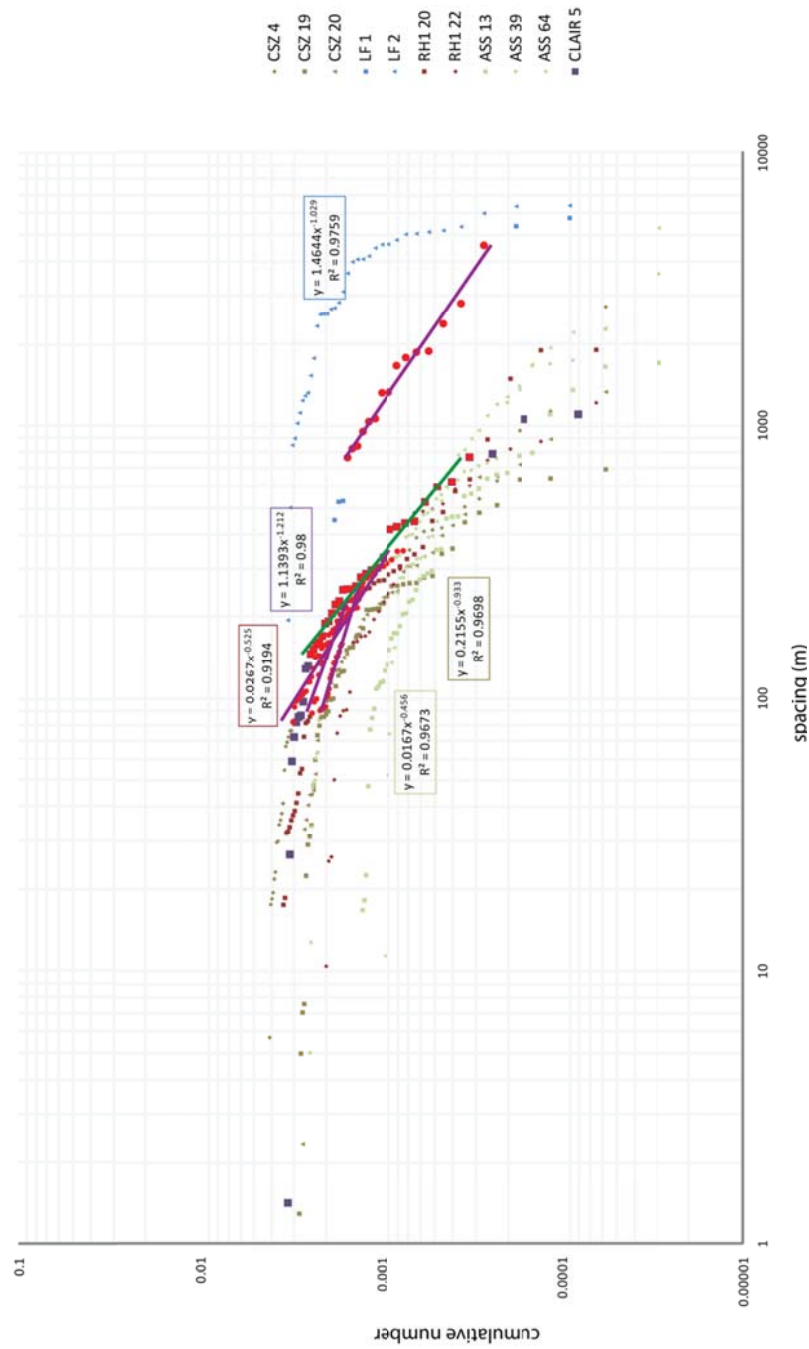
Fractures in the Clair basement do not have consistent power-law spatial relationships across the well datasets (*Figure 6.12*). In these meso-scale fracture samples the power-law distributions have D-values that vary widely from 0.31 to 1.23 suggesting that fracture spacing is not repeatable across the Clair basement. The one regional pseudo-well sample included in *Figure 6.12* (Clair 5 is the only Clair basement pseudo-well sample with a noteworthy power-law distribution) has a D-value that is steeper (1.272) than any of the basement well fracture samples) suggesting that this distribution is formed mainly by fractures that are relatively closely spaced. These variable D-values across the well and seismic datasets means that the trend line between the well and seismic fracture spacing datasets is ill-defined and not a good representation of the power-law distribution spanning five orders of magnitude.

The large variation in fracture spacing power-law distributions in the Clair basement coupled with the lack of regional fracture data means that although individual datasets are scale-invariant, caution must be taken if using these datasets to estimate the spatial characteristics of fractures at different scales within the Clair basement. Having limited Clair basement datasets significantly reduces confidence in the fracture scaling relationships which are critical to being able to build an understanding and models of the possible fracture networks present within the Clair basement. This above statistical analysis again emphasises the importance of being able to use an onshore analogue, with ample fracture datasets, to develop models of the fracture networks within the Clair basement.

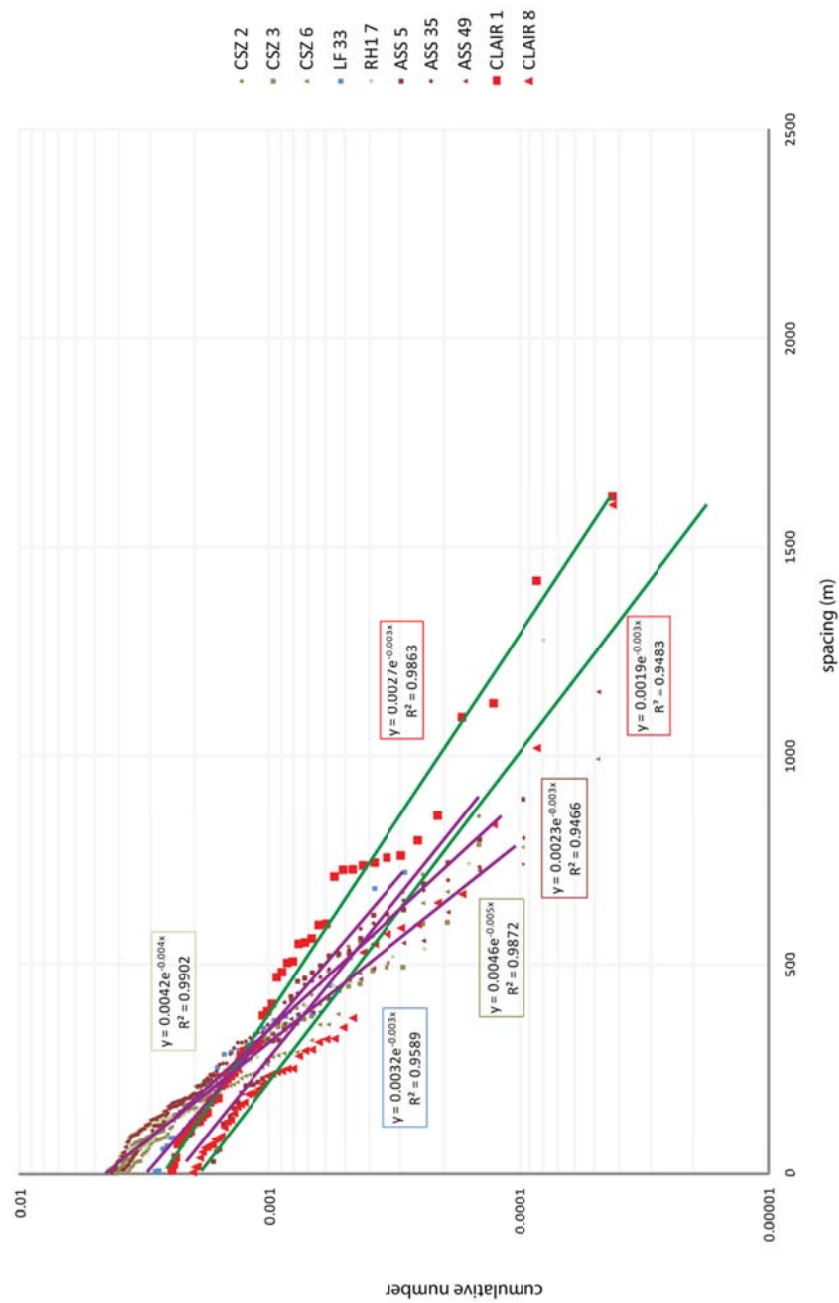
#### 6.2.3.4 – Regional fault data spatial synthesis

The onshore and offshore regional fault lineament spacing datasets are compared below by compiling an example set of normalised (to sample length) pseudo-well samples on one population distribution plot. This has been completed for both power-law and exponential fault lineament spacing distributions with results shown in *Figures 6.13* and *6.14*, respectively. Spatial attributes, including CV and fracture density values, for all individual regional spatial datasets are also provided in *Table 6.2*.





Trend lines for the onshore datasets are shown in purple and those for the offshore datasets are shown in green. CSZ – Canisp Shear Zone, LF – Laxford Front, RH1 – Rhiconich terrane, ASS – Assynt terrane and CLAIR – Clair basement.



sample that they are from. Trend lines for the onshore datasets are shown in purple and those for the offshore datasets are shown in green. CSZ – Canisp Shear Zone, LF – Laxford Front, RH1 – Rhiconich terrane, ASS – Assynt terrane and CLAIR – Clair basement.

Location	Well Number	spacing distribution	R <sup>2</sup>	D-value	Slope	CV	FD
<b>Canisp Shear Zone</b>	CSZ 2	exponential				0.96	0.004
	CSZ 3	exponential	0.987		0.0046	1.08	0.004
	CSZ 4	power-law	0.97	0.933		1.47	0.004
	CSZ 6	exponential				0.9	0.005
	CSZ 19	power-law (?)				0.88	0.005
	CSZ 20	power-law				1.02	0.004
<b>Laxford Front</b>	LF 1	power-law (?)	0.976	1.029		0.88	0.002
	LF 2	power-law (?)				0.56	0.003
	LF 33	exponential	0.959		0.0032	1.11	0.003
<b>Rhiconich terrane</b>	RHI 7	exponential	0.99		0.0042	0.94	0.004
	RHI 20	power-law	0.919	0.525		1.39	0.003
	RHI 22	power-law (?)				0.91	0.003
<b>Assynt terrane</b>	ASS 5	exponential	0.947		0.0023	0.78	0.002
	ASS 13	power-law				1.01	0.002
	ASS 35	exponential				0.78	0.004
	ASS 39	power-law	0.967	0.456		1.32	0.002
	ASS 49	exponential				0.82	0.004
	ASS 64	power-law				1.16	0.001
<b>Clair basement</b>	Clair 1	exponential	0.986		0.0027	0.86	0.003
	Clair 5	power-law (?)	0.98	1.212		0.85	0.003
	Clair 8	exponential	0.948		0.0019	1	0.003

**Table 6.2:** Regional fault lineament spatial attributes from onshore and offshore datasets. The values highlighted in red from the onshore locations are the most comparable to the Clair basement. FD – fracture density (fractures per metre).

The regional fault spacing power-law distributions (*Figure 6.13*) for the onshore and offshore datasets generally cluster between spacing values of 80 and 800 metres. This excludes the datasets from the Laxford Front (LF 1 & 2) which have fracture spacing values between 800 and 4000 metres. The Clair basement fault power-law distribution has a D-value of 1.21 (*Table 6.2*) which is most similar to the D-value from LF1 (1.03, *Table 6.2*) but because the Clair basement power-law distribution spans between 80 and 800 metres the spatial distribution from LF1 is not directly comparable to this offshore dataset.

The regional fault spacing distributions which are exponential are presented in *Figure 6.14* which shows that the offshore data typically forms exponential distributions that have shallower slopes than the onshore fault datasets. Regional Clair basement exponential spacing distributions have slope values of 0.0019 and 0.0027 compared to

most mainland LGC samples which have exponential slope values between 0.0023 and 0.0046 (*Table 6.2*). Onshore sample ASS 5 from the Assynt Terrane has a slope value of 0.0023 which is the most comparable with the Clair basement samples (*Table 6.2*).

CV values and fracture density values are also used to assess the similarities between the onshore and offshore regional fault datasets. Clair basement regional samples have CV values between 0.85 and 1 (*Table 6.2*), with the power-law distribution exhibiting the lowest value. Comparable onshore CV values are found across the mainland LGC areas, although no individual datasets are comparable across all the statistical spatial attributes used in this analysis. Fracture density values in the Clair basement are consistently representative of three fractures per kilometre which coincides with fracture density values calculated for Laxford Front and Rhiconich Terrane samples (*Table 6.2*).

As discussed in *Chapters 3 and 4*, it is likely that some of the power-law relationships determined from onshore and offshore regional datasets in fact exhibit weak exponential relationships (mainly based on CV values being  $< 1$  and the extent of the straight line parts of the distributions being less than an order of magnitude). This may account for some of the irregularities observed within the regional fracture spacing distributions and almost certainly means that the regional power-law distributions should be considered with caution.

The presence of weak power-law distributions has implications for the ability to use the regional datasets to assess the scalability of the onshore and offshore datasets. If the regional data offshore do not form good power-law spacing distributions then the faults are not scale-invariant which means that the fault spatial characteristics determined at a regional scale cannot be used to estimate the fracture spatial characteristics at any other scale. It should be noted that this does not apply to the onshore regional pseudo-well fault spacing samples used to determine the scaling relationships between all of the onshore datasets (*Section 6.1.2*) as the regional samples included in that analysis were vetted to ensure that they were strong power-law relationships with CV and D-values that supported their scale-invariant distributions.

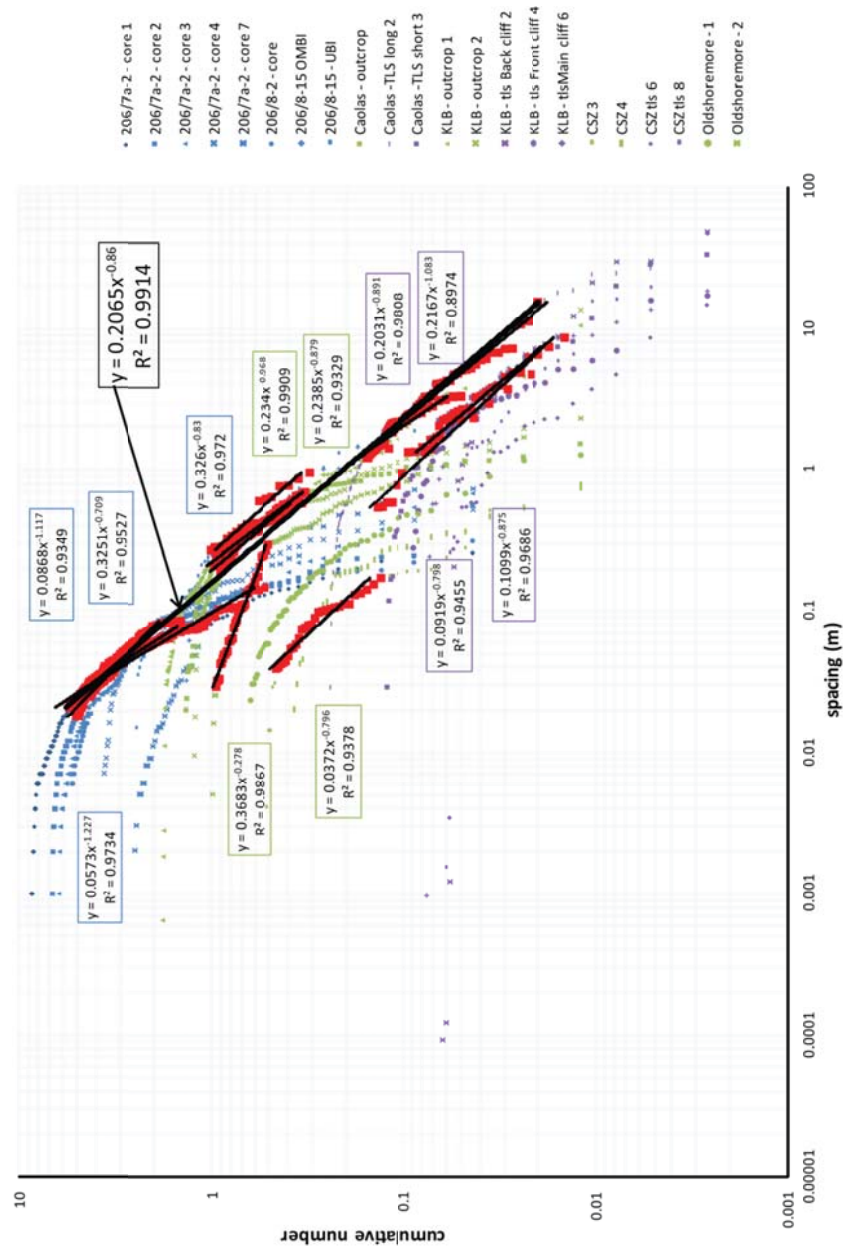
These regional analyses suggest that the onshore and offshore datasets are not directly comparable to each other, although similarities in fracture density values exist between the Laxford Front, Rhiconich Terrane and the Clair basement. It is also important to be aware that the regional spacing data cannot be reliably considered

scale-invariant meaning that the Clair basement regional data can only be used with caution to estimate fracture spacing characteristics at different scales within the offshore study area. This increases the need for fracture spacing characteristics within the onshore TLS models and fieldwork data to be comparable with the well sample data to improve the suitability of the mainland LGC as an analogue for the Clair basement.

#### 6.2.3.5 – TLS model, fieldwork and well fracture data spatial synthesis

Clair basement well data, TLS model samples and fieldwork fracture spacing datasets are analysed side-by-side in *Figure 6.15*. The majority Clair basement well datasets have power-law distributions that form between fracture spacing values of 0.02 and 0.1 metres, with the data from 206/8-15 forming power-law relationships between 0.2 and 1 metre. This discrepancy in the Clair basement well datasets is due to the fact that the 206/8-15 well data comprises fracture interpretations from image logs which have a significantly lower resolution (>1 order of magnitude) than fracture interpretations from basement core samples that are collected by eye.

Fieldwork datasets from the mainland LGC have power-law distributions that typically extend between 0.1 and 1 metre, similar to the samples from well 206/8-15 (*Figure 6.15*). This similarity in power-law distribution range can be explained by the weathered nature of most outcrops. In the field, outcrops are subjected to weathering effects and vegetation growth which can often disguise or obscure small fractures resulting in a reduced number of fractures at a millimetre-scale being interpreted: this is therefore equivalent to the well samples from 206/8-15 where image log resolution restricts the lower scale to which fractures can be interpreted. Both the fieldwork datasets from Oldshoremore and one sample from the Canisp Shear Zone do have power-law distributions that extend to fracture spacing values of 0.01 metres (*Figure 6.15*). All three of these samples were collected from coastal platforms, away from the tidal zone, where the rocks are especially 'clean' meaning that even very small (thin) fractures can be identified for interpretation.



law distribution shown in red. The trend line equation and  $R^2$  values are given in boxes which are colour-coded as per the sample that they are from. Caolas – Caolas Cumhann, KLB – Kinlochbervie and CSZ – Canisp Shear Zone.

The overall power-law distribution of the well and outcrop datasets is extended further by the TLS model datasets which have power-law distributions approximately between 1 and 10 metres (*Figure 6.15*). These TLS model power-law distributions are normalised so that they align with both the fieldwork samples and the basement well samples which allow a power-law trend line to be plotted through all three different datasets. This best fit power-law extends between 0.01 and 10 metre fracture spacing values (*Figure 6.15*) and means that the fracture spacing characteristics presented in this population distribution plot are scale-invariant over three orders of magnitude. The extent of the main power-law distribution over three orders of magnitude again highlights how important (and useful) the TLS models are to the fracture spacing statistical analysis presented in this chapter. If the TLS model datasets were not available, then the Clair basement well and mainland LGC outcrop fracture datasets would have power-law relationships that barely extended over two orders of magnitude. Reducing the scale range of the power-law distributions drastically reduces confidence in the scale-invariance of the datasets and means that more caution needs to be implemented when using the meso-scale fracture datasets to estimate fracture spacing characteristics at any other scale.

Clair basement well fracture datasets have power-law distribution D-values between 0.71 and 1.23 (*Table 6.3*) which are comparable to the majority of mainland LGC fieldwork samples and TLS models (values between 0.278 & 0.968 and 0.798 & 1.083, respectively; *Table 6.3*). Fracture spacing samples from Oldshoremore, which represent background fracturing in the Rhiconich Terrane, have D-values that are significantly lower than those seen in the Clair basement samples or the rest of the mainland LGC (includes TLS models). This suggests that at Oldshoremore, large fracture spacing values are far more common than closely spaced fractures and also suggests that the fracturing at Oldshoremore is not comparable with the fracture spatial characteristics present within Clair basement well samples.

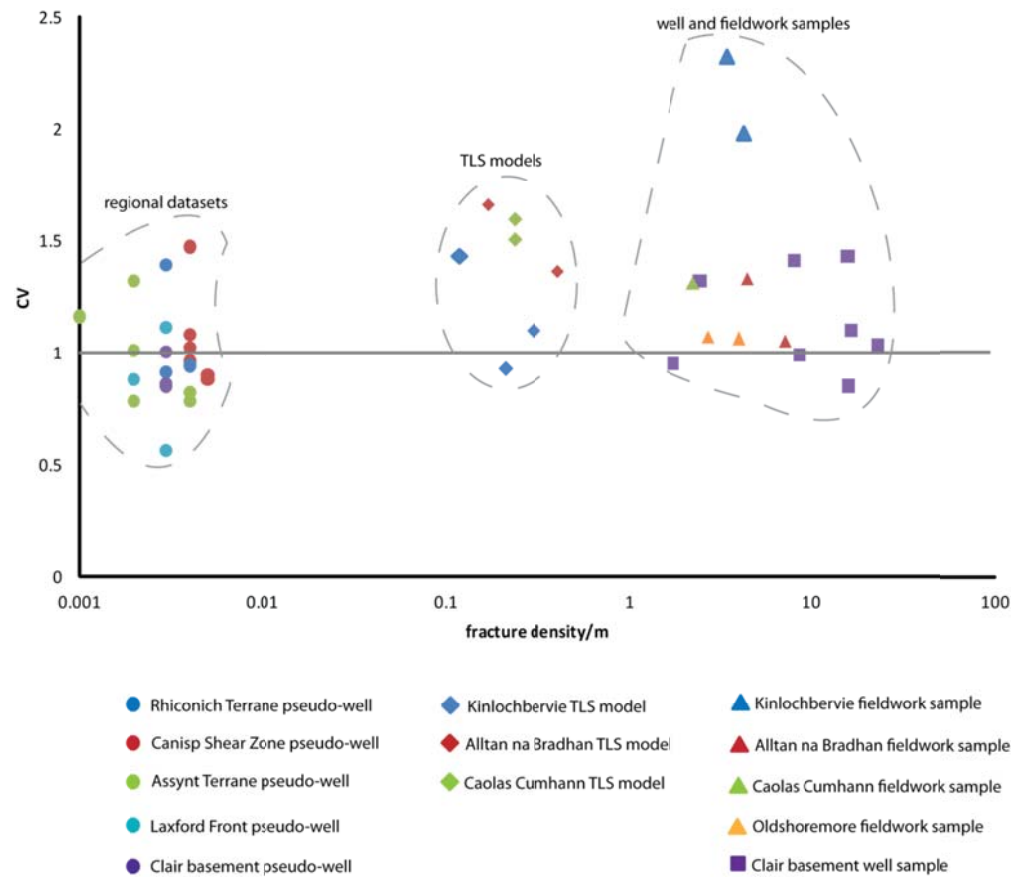
Data source	Location	Sample Number	D-value	R <sup>2</sup>	CV	FD
Clair basement well	south Clair Ridge	206/7a-2 core 1	1.17	0.9349	1.03	22.91
		206/7a-2 - core 2	0.709	0.9527	1.1	16.45
		206/7a-2 - core 3			1.43	15.78
		206/7a-2 - core 4			0.99	8.65
		206/7a-2 - core 7			1.41	8.03
	mid Clair Ridge	206/8-2 core	1.227	0.9734	0.85	15.88
	east Clair Ridge	206/8-15 - OBMI	0.83	0.972	0.95	1.75
		206/8-15 UBI			1.32	2.46
LGC fieldwork samples	Caolas Cumhann	Caolas - outcrop	0.968	0.9909	1.31	2.26
	Kinlochbervie	KLB - outcrop 1			1.98	4.26
		KLB - outcrop 2	0.879	0.9329	2.32	3.43
	Alltan na Bradhan	CSZ 3	0.796	0.9379	1.05	7.17
		CSZ 4			1.33	4.43
	Oldshoremore	Oldshoremore -1			1.06	3.99
		Oldshoremore -2	0.278	0.98	1.07	2.73
TLS model	Caolas Cumhann	Caolas - TLS long 2	0.891	0.9808	1.5	0.24
		Caolas - TLS short 3	0.875	0.9686	1.59	0.24
	Kinlochbervie	KLB - tls back cliff 2			1.43	0.12
		KLB - tls front cliff 4	0.798	0.9455	1.1	0.3
		KLB - tls main cliff 6			0.93	0.21
	Alltan na Bradhan	CSZ tls 6	1.083	0.8974	1.36	0.41
		CSZ tls 8			1.66	0.17

**Figure 6.3:** Fracture spatial attribute datasets from Clair basement well samples, mainland LGC fieldwork studies and TLS model samples. FD – fracture density.

CV and fracture density values are also used to compare the onshore and offshore well and outcrop datasets. *Figure 6.16* comprises a plot of fracture density versus CV to illustrate the variations in these spatial attributes across the study areas and different datasets. The majority (82%) of the macro- and meso-scale datasets have CV values >1 which means that the fractures within each sample are clustered (those datasets with CV < 1 are anomalous because power-law distributions are normally coincident with CV values >1). For the datasets with CV>1, most (89%) have values between 1.03 and 1.66 with only the fieldwork samples from Kinlochbervie exhibiting higher values. The fieldwork CV values at Kinlochbervie (1.98 and 2.32, *Table 6.3*) are extremely high and suggest that the fractures at this location are exceptionally clustered. These strongly clustered fracture sets are likely due to their formation in the



damage zone of a major NW-SE trending normal fault (Loch Incharid Fault), which produces a relatively large number of fractures that become more closely spaced towards the main fault plane.



**Figure 6.16:** Plot of fracture density versus CV value which highlights the difference in spatial attributes of the onshore and offshore from all the available datasets.

Typically, the TLS model fracture datasets exhibit moderately higher CV datasets compared to both the Clair basement well and mainland LGC samples (*Table 6.3*). This does not apply to Kinlochbervie where the exclusion of fracture <50cm in length results in much lower TLS model CV values than fieldwork CV values (see *Section 6.1.2*), but the well and fieldwork sample fracture datasets are directly comparable to each other. Assynt Terrane background fracture sets (Caolas Cumhann) and fracture sets from the Canisp Shear Zone provide the closest matches to the Clair basement well samples (*Figure 6.16*), suggesting that fracturing within the Assynt Terrane exhibits similar fracture clustering patterns to fractures in the Clair basement.

Fracture density value analysis is the most effective tool for distinguishing the onshore and offshore datasets. This is apparent in *Figure 6.16* where the TLS model, fieldwork and Clair basement fracture datasets are mainly separated by their differing fracture density values. Almost all of the basement core samples from the Clair basement contain higher fracture density values than any other fracture samples from the onshore and offshore datasets (8.03 to 22.91 fractures per metre, *Table 6.3*): only fracture density values from Canisp Shear Zone fieldwork samples (*Table 6.3*) even remotely compare. Fieldwork and Clair basement image log samples comprise similar fracture density values, which is to be expected because these datasets have similar resolutions to each other (the outcrop samples are affected by weathering disguising smaller (thinner) fractures). TLS model fracture datasets have even lower fracture density values (*Table 6.3* and *Figure 6.16*), which is due to the resolution of the raw data and the fact that fractures shorter than 50cm were not interpreted.

Evidence from fieldwork suggests that the mainland LGC has a complex and punctuated history of brittle deformation with a majority of fractures that are included in the statistical spatial analyses presented throughout this thesis formed in the Proterozoic. Although episodes of Palaeozoic and Mesozoic faulting and fracturing are recorded in certain regions of the mainland LGC, the resulting brittle structures tend to be localised and are not exposed widely across the onshore study area. This means that very few younger fractures are included in this onshore study. The onshore outcrop analyses are therefore different from the Clair basement well analyses where fractures of a large variety of ages are almost certainly present in all of the well datasets. This is particularly true for core from well 206/7a-2 where vast arrays of fractures, of different ages which span from the Proterozoic until the Tertiary, are interpreted. It is therefore likely that the extremely high fracture density values present within the Clair basement well core datasets, compared to the mainland LGC fieldwork samples, is a result of the extended brittle deformation history in the Greater Clair area (see *Chapter 2, Section 2.2.4* for the tectonic history of the Clair Field).

The suggestion that the Clair basement contains fractures of a much wider range of ages than the mainland LGC samples does not mean that the mainland LGC is necessarily a poor analogue for the Clair basement. Mesozoic and younger fractures within the Clair basement are known to have reactivated older fractures as well as forming entirely new structures (see *Figure 4.17b* for an example of a Mesozoic to

Cenozoic calcite-filled fracture reactivating a pre-Devonian hematite/epidote filled fault). Similarly mineralised fractures (hematite/epidote) are present throughout the mainland LGC, which again are suggested to have pre-Devonian ages. These fractures, along with other Proterozoic fractures within the mainland LGC (e.g. 'Late Laxfordian' faults) potentially are found within the Clair basement and may have been reactivated and exploited by younger brittle deformation events forming the contemporary Clair basement fracture network that is sampled by well core and image logs.

#### 6.2.3.6 – Regional and local scale synthesis

Regional and local fracture orientation datasets from the mainland LGC provide a strong comparison to orientation datasets of similar scales from the Clair basement (*Figures 6.10 and 6.11*). Local fracture orientation datasets provide the best evidence that the Clair basement can be compared to the mainland LGC with outcrops of background fracturing in the Rhiconich Terrane providing the closest affinities to the fracture azimuths sampled from the Clair basement (*Figure 6.11*). This implication coincides with lithological observations of the mainland LGC and the Clair basement that also suggests that the Rhiconich Terrane is most comparable with the Clair basement rocks (*Figure 6.9*). It is more difficult to distinguish differences between the regional Assynt and Rhiconich Terrane orientation datasets, but it is apparent that the onshore regional fault orientation datasets compare satisfactorily to regional fault orientation datasets from the Clair basement (*Figure 6.10*).

Spatial statistical analysis of the regional and local datasets across the Clair basement and mainland LGC provide a more detailed insight into the offshore and onshore fracture networks. Population distribution analysis of the offshore datasets suggests that those samples that have power-law relationships have comparable D-values across both scales of data and therefore can be assumed to be scale-invariant over 5 orders of magnitude (*Figure 6.12*). This scale-invariance should however be treated with caution because there are no offshore data available for the spacing values between 1 and 100 metres.

Onshore and offshore regional spacing datasets have population distributions that are either exponential or power-law (*Figures 6.12 and 6.13*). Many of the regional power-law population distributions, both onshore and offshore, are coupled with CV values which are <1 (*Table 6.2 and Tables 3.2, 3.3, 4.1 and 4.2*). These low CV values are

normally associated with exponential distributions; which suggests that these power-law relationships may in fact be weak exponential relationships. Therefore any scale-invariance associated with these spacing distributions should be considered carefully. These results are in contrast to outcrop (including TLS models) and well spatial datasets which consistently exhibit strong power-law relationships and are regarded to be robustly scale-invariant.

As discussed in this chapter, those fracture spacing datasets which are regarded to be power-law can be combined on population distribution plots to assess if the power-law relationship is constant across a range of spacing values. Clair basement well datasets, mainland LGC TLS model and fieldwork samples are shown to have relatively consistent power-law distribution D-values across the different datasets (*Figure 6.14*). This comparison also demonstrates that these macro- and meso-scale datasets have power-law distributions, and are therefore scale-invariant, over at least 3 orders of magnitude.

D-values from the Clair basement regional and local datasets have a best fit value of 0.897 (*Figure 6.12*). This value can be compared to best-fit values from onshore datasets that comprise similar regional and local datasets. D-values from Kinlochbervie (0.751, *Figure 6.6*) and Caolas Cumhann (0.999, *Figure 6.7*) are the most comparable to D-values from the offshore datasets, suggesting that spacing values from fracture networks adjacent to large NW-SE normal faults and from areas of background fracturing in the Assynt Terrane are the most similar to the fracture network within the Clair basement. Fracture spacing analyses of datasets that represent background fracturing within the Rhiconich Terrane do not yield results that are comparable to the Clair basement samples. This suggests that in terms of fracture spatial distributions, the Rhiconich Terrane does not have clear affinities with the Clair basement.

Previous studies of statistical fracture analyses within the mainland LGC suggest that lithology has some control on the development of fractures within the rock mass (Beacom et al., 2001). It is proposed that within the offshore and onshore datasets lithology has an effect on fracture density value variations between mainland LGC fieldwork samples and Clair basement well datasets. As discussed in *Chapter 4*, core samples 4 to 7 from well 206/7a-2 (*Figure 4.13*) mainly comprises granitic gneiss. These core samples have fracture density values which are the lowest present within this basement well (and the lowest from all Clair basement core samples, *Table 6.3*). Granite

gneiss is also present within the Rhiconich Terrane where fracture density values are some of the lowest calculated across the mainland LGC fracture datasets (*Table 6.3*): some outcrops within the Rhiconich Terrane exhibit no fractures, suggesting that samples containing granite are less heavily fractured than other samples either in the Clair basement or within the mainland LGC.

The disparities between the lithological, orientation and spatial analyses imply that the relationship between the Clair basement and the mainland LGC is complex. Lithology and orientation comparisons suggests that the Rhiconich Terrane has the most affinities with the Clair basement; but fracture spatial analyses suggest that Kinlochbervie and background Assynt Terrane fracture networks provide the best likeness to the Clair basement fracture networks. Many of the variations in fracture spatial distributions (including fracture density, *Figure 6.16*) between the onshore and offshore datasets can be attributed to the extended brittle deformation history within the Greater Clair area in comparison to the mainland LGC. This may also explain why the Rhiconich Terrane exhibits markedly different spatial attributes compared to the Clair basement because its more limited brittle deformation history has resulted in this terrane being relatively under-fractured.

The onshore and offshore dataset synthesis has demonstrated that there are many similarities and some differences between the fracture networks in the mainland LGC and the Clair basement. Lithology and orientation datasets from the Rhiconich Terrane are comparable with the Clair basement, but the link between fracture network spatial characteristics is less clear. Importantly, many of the fracture spacing datasets are power-law, and therefore scale invariant, and these relationships extend over the regional and local scale datasets (i.e. much of the fracture spacing data is scale-invariant over at least three orders of magnitude). The large extent of these power-law fracture datasets means that it is possible to use the fracture spatial values measured from local and regional scale datasets to estimate, with confidence, the spatial characteristics of the fracture network at any other scale.

## 7 – Conclusions

Four main research questions were proposed at the start of this thesis (*Chapter 1*) which examines in detail the complex fracture network characteristics of both the mainland LGC and the Clair basement. The main purpose was to assess the suitability of the mainland LGC as an analogue for the Clair basement. Qualitative and quantitative analyses of fracture datasets from both the mainland LGC and the Clair basement have been utilised to provide answers to the four main research questions which are discussed below.

### *(1) What is the offshore Clair Field basement?*

Previous work concerning the basement rocks within the Rona Ridge suggested that the Clair basement has its closest affinities with the Lewisian Gneiss Complex of northwest Scotland (Watts, 1971, Ritchie and Darbyshire, 1984). More recently, isotopic studies have suggested that the LGC both on the mainland and Hebridean islands comprise a series of tectonostratigraphic terranes (e.g. Kinny and Friend, 1997, Friend et al., 2001, Kinny et al., 2005), two of which; the Rhiconich and Assynt Terranes, are studied within this thesis. Therefore one of the main aims of this thesis was to establish which one of these terranes was the most likely geological correlative with the Clair basement.

Quantitative observations of characteristic lithologies across the Clair basement samples were compared to outcrop descriptions from the mainland LGC terranes to provide the basis for the understanding of the suitability of the mainland LGC as an analogue for the Clair basement. Both the Clair basement and the Rhiconich Terrane comprise amphibolite-facies granodioritic, granitic and basic gneisses with cross-cutting pegmatite veins (see *Chapter 3, Section 3.3.2.6* and *Chapter 4, Section 4.3.2* for onshore and offshore lithological descriptions). This is compared to the Assynt Terrane where there is no evidence of the granitic gneisses or pegmatite veins that are prolific throughout the Clair basement samples. In terms of lithology it is therefore proposed that the Rhiconich Terrane is the most appropriate onshore analogue for the Clair basement.

The similarities between the Rhiconich Terrane and the Clair basement continue with analysis of outcrop and well fracture orientation datasets where outcrops that encompass background fracturing in the Rhiconich Terrane possess fracture orientations that are the most comparable with those measured from Clair basement core and image log samples (*Figure 6.11*).

1-dimensional fault and fracture network spatial analysis of the onshore and offshore study areas do not provide such a clear correlation between the mainland LGC and the Clair basement. Outcrop and TLS model fracture spacing datasets have consistent power-law (scale-invariant) datasets that are generally comparable with similar power-law fracture spacing relationships from Clair basement well samples. This 1-dimensional spatial analyses suggests that fracture datasets from the Assynt Terrane and from damage zones around large NW-SE trending normal faults (i.e. Kinlochbervie) are the most comparable with the Clair basement (*Figures 6.6, 6.7 and 6.12*). Fracture samples that represent background fracturing in the Rhiconich Terrane are shown to be the least comparable to the Clair basement samples (*Figure 6.14 and Table 6.3*).

All of the quantitative and qualitative and quantitative onshore and offshore fracture analysis suggests that the mainland LGC is a suitable analogue for the Clair basement to some degree, but that there is not a simple relationship with the fracture networks in an individual onshore terrane. The rest of the research questions proposed at the start of this thesis aimed to examine the complexities of onshore and offshore fracture networks with the research conclusions presented below.

*(2) What are geological characteristics and attributes of the fracture systems developed in the onshore mainland Lewisian Gneiss Complex?*

Fieldwork observations in this study and in previous outcrop- and mapping-based studies suggest that there are a number of regionally recognised fracture sets present within the mainland LGC (Beacom, 1999, Roberts and Holdsworth, 1999, Beacom et al., 2001 and references therein). These fracture sets have been characterised, both qualitatively and quantitatively across both regional and outcrop scale fracture datasets (*Chapter 3*) and the characterisations used to assess the onshore

fracture network comparability with fractures, from similar scale datasets (*Chapter 4*), analysed within the Clair basement.

Onshore faults and fractures can be separated into four main sets: 1) NW-SE trending 'Late Laxfordian' faults which preferentially develop in Assynt Terrane shear zones; 2) hematite-stained Stoer Group age or Torridon Group age fractures (NE-SW to N-S trending) which developed due to ESE-WNW extension associated with the deposition of the Torridonian on top of the mainland LGC; 3) post-Torridonian Faults such as the Loch Inchard Fault which displaces Torridonian sediments and uplifts the LGC; and 4) Mesozoic faults which typically trend NE-SW and cross-cut (and offset) all other structures in the mainland LGC (*Chapter 3*). Offshore, fractures interpreted from core are divided into three main groups, those which are pre-Devonian and contain hematite/epidote/quartz mineralisation; those which are mineralised with calcite and developed before hydrocarbons migrated into the basement fracture system (Late Cretaceous to Early Tertiary; *Chapter 4, Section 4.3.2.8*) and those fractures which developed synchronous with hydrocarbon migration (Early Tertiary) and associated with calcite and pyrite mineralisation. Pre-Devonian fractures of the Clair basement have comparable mineral fills and dextral extensional kinematics to the Stoer/Torridon Group age fractures found across the mainland LGC, but there is limited evidence for calcite-mineralised Mesozoic/Cenozoic age extensional fractures within the mainland LGC.

The majority of fractures within the mainland LGC formed in the Proterozoic with local reactivation of some these structures observed associated with deformation along the Loch Inchard Fault (*Figure 3.26*) and Caledonian thrusting (e.g. Loch Assynt Fault (Krabbendam and Leslie, 2010)). Within the Clair basement core samples, there is also evidence of reactivation of hematite/epidote bearing faults by far younger (Early Tertiary) deformation events that re-mineralise the faults with calcite (*Figure 4.17*). It is therefore proposed that the lack of abundant Mesozoic (and younger) fractures within the mainland LGC does not discount this onshore area as an analogue for the Clair basement. Instead it is hypothesised that in fact the abundant Proterozoic fractures sampled across the mainland LGC may provide the background fracture network attributes (orientation and spacing) within the Clair basement that are preferentially aligned to be exploited by further periods of brittle deformation in that area and that this potentially results in the development of similarly trending, younger fracture sets that are seen within the Clair basement datasets.



Statistical spatial analyses of onshore and offshore fracture datasets yield many power-law relationships for regional and local scale 1-dimensional samples which suggest that much of the fracture spatial characteristics are scale-invariant. It should be noted, however, that many (but all not all) of the regional datasets have a combination of spatial attributes that implies the power-law spacing relationships are extremely weak and therefore their scale-invariant properties should be considered with caution. For all the other fracture spacing datasets across the onshore and offshore 1-dimensional datasets power-law relationships are strong and suggest scale-invariance between three and five orders of magnitude (*Figures 6.5, 6.6, 6.7 and 6.14*).

The extent of the onshore power-law relationships and the similarities in the main power-law trend line D-values enhances the proposal that the mainland LGC is a powerful onshore analogue for the fracture network spatial characteristics in the Clair basement. As previously stated, differences noted in fracture density (and to some extent D-values and CV values) can be attributed to the longer brittle deformation history in the Clair basement compared to the mainland LGC where brittle deformation events are older.

This research question also asked: are the fracture networks in the offshore and onshore study areas scale-invariant across different dimensions? Due to the lack of offshore datasets it is only possible to quantitatively characterise onshore fracture network characteristics in 2- and 3-dimensions. This analysis is presented in *Chapter 5* where TLS models have been utilised to determine fracture presence and fracture intersection characteristics across outcrops within three key structural settings in the mainland LGC. TLS models from Alltan na Bradhan, Kinlochbervie and Caolas Cumhann produce 2- and 3-dimensional values for fracture presence that can be considered fractal (scale-invariant) with those fractal dimension values from Kinlochbervie and Caolas Cumhann suggesting that these outcrops have the highest proportion of fractures (*Chapter 5, Section 5.5*). The occurrence of fractal fracture datasets in 2- and 3-dimensions from three key mainland LGC outcrops suggests that the scale-invariance recorded from 1-dimensional line samples extends through different dimensions. 2- and 3-dimensional onshore datasets cannot be compared to similar offshore datasets because they are not available. If the spatial characteristics of the mainland LGC is to be used as an analogue for the fracture networks in the Clair basement, then any extension of spatial attribute estimations into 2- and 3-dimensions have to be based solely on the

strength of the 1-dimensional power-law relationships and the fractal dimension values calculated from the three key mainland LGC outcrops.

(3) *What are the dominant controls on these fracture patterns?*

It is now understood, from this thesis and previous work (Beacom et al., 2001) that the fracture networks within the mainland LGC are controlled by a range of factors that include lithology, metamorphic grade, intensity of pre-existing fabrics and proximity to major faults. This study uses fracture spatial attributes (spacing distributions and fracture density) to develop the understanding of how different lithological and structural environments affect the fracture networks in both the mainland LGC and the Clair basement.

As previously stated, lithology (and metamorphic grade) has important control on fracture density, particularly in the Clair basement, where core samples of granitic gneiss have the lowest fracture density values (see *Figure 4.26*). This is partially echoed in the mainland LGC where the presence of amphibolite-facies granitic gneisses in the Rhiconich Terrane, are coincident with spacing distributions that form from widely spaced fractures and lower fracture density values than are calculated from anywhere in the Assynt Terrane (*Tables 3.6 and 6.3*).

Statistical spatial analysis from across the mainland LGC has shown that the structural setting that each fracture sample resides within has important controls on both the fracture distribution and fracture density. Fracture datasets from the Canisp Shear Zone have power-law distributions that are formed from fractures that are closely spaced ( $D\text{-values} \gg 1$ ) and have fracture density values that are among the highest calculated throughout the mainland LGC. These spatial attribute values all indicate increased fracturing within this shear zone. This is attributed to the presence of strongly aligned phyllosilicates-rich (upper greenschist-facies) foliation planes which form pre-existing planes of weakness that are subsequently exploited by the 'Late Laxfordian' faults and Stoer Group age fractures resulting in high fracture density values and closely spaced fractures within the Canisp Shear Zone (see *Chapter 3, Section 3.37* for the main discussion on shear zone controls). Increased fracture density values are not as evident from the amphibolite-facies shear zones present in the Rhiconich Terrane where the intense foliation planes appear to be more annealed. This implies that increased fracture

attribute values in Assynt Terrane shear zones are controlled by three factors; the presence of intense, steeply-dipping foliation, the metamorphic grade and the presence of large volumes of phyllosilicates.

The presence of major faults that exhibit evidence of reactivation through their tectonic history (e.g. Loch Inchard Fault at Kinlochbervie where associated fractures exhibit at least two sets of slickenlines, *Figure 3.26*) also have important controls on the surrounding fracture networks. Fracture spatial attributes from the fracture networks in the damage zones of these major faults (examples included in the onshore study are the Loch Inchard Fault at Kinlochbervie and the Loch Assynt Fault on Loch Assynt Shore, *Chapter 3, Section 3.3.3*) are increased relative to the surrounding background fracture network in both the Assynt and the Rhiconich Terranes. The increase in fracture density and fracture presence values surrounding the Loch Inchard Fault at Kinlochbervie is evident in both the 1-dimensional fieldwork samples and the 2- and 3-dimensional TLS model datasets where it has been possible to estimate the width of the fault damage zone at 220 metres (*Figure 5.17*). Increases in fracture density associated with adjacent faults are also observed in the Clair basement where fracture density values in core from wells 206/7a-2 and 206/8-2 (which lie adjacent to major Clair basement faults) are generally higher than fracture density values from other core samples (*Table 4.3*).












Out with of the shear zones and fault damage zones the fracture networks in the mainland LGC have spatial attributes which are at background levels (i.e. they indicate the rocks are the least fractured away from major structures). Typically background fracturing has higher fracture density values within the Assynt Terrane compared to the Rhiconich Terrane which again comes back to the abundance of amphibolite-facies granitic gneiss within the Rhiconich Terrane.

*(4) How can the mainland Lewisian Gneiss Complex be best used as an onshore analogue for the Clair basement?*

The qualitative and quantitative analyses presented in this thesis demonstrate that there are many similarities and some differences between the mainland LGC and the Clair basement (*Table 7.1*). Fracture orientation and fracture spatial characteristics provide the best datasets for comparisons between the onshore and offshore study

areas. The similarities in fault and fracture orientation across the Clair basement and the mainland LGC, and the scalability of the majority of these orientation distributions between regional and local scales means that the onshore fracture orientation datasets provide an good analogue for the Clair basement. Scalability is the key advantage of the onshore fracture spacing datasets, with power-law distributions exhibiting scale-invariance over 5 orders of magnitude. The large extent of this scale invariance, and the fact that many of the fracture spacing datasets are comparable with the limited data from the Clair basement, means that the onshore fracture spacing datasets (particularly from Caolas Cumahnn and Kinlochbervie) can be used to estimate fracture spacing characteristics at all scales (regional to well) within the Clair basement. It is important to note, however, that fracture density values within the Clair basement are higher than those calculated in the mainland LGC. This is thought to be a result of the presence of abundant Mesozoic (and Cenozoic) fractures within the offshore study area. Therefore the mainland LGC fracture sets can only be used to confidently estimate background fracturing within the Clair basement.

The advantages of the mainland LGC as an onshore analogue are strengthened by the development of terrestrial laser scan virtual outcrop fracture models. These models have yielded 2- and 3-dimensional fractal dimension values for fracture presence (and intersections) which can be directly input into Clair basement fluid flow models to provide deterministic values of fracture occurrence for different structural settings that are thought to be present within the Clair basement (e.g. fractal dimension values from Kinlochbervie can be input into cells surrounding (and away from) the known location of seismic-scale faults). The availability of these datasets will improve the current stochastic Clair basement geological and fluid flow models and will help develop the understanding of the Clair basement as a potential future producing hydrocarbon reservoir.

CLAIR BASEMENT		MAINLAND LEWISIAN GNEISS COMPLEX
<b>LITHOLOGY</b>		
Amphibolite-facies granodiorite, granite & basic gneisses and pegmatite veins		ASSYNT TERRANE Granulite-facies granodiorite & tonalite gneisses and Scourie Dykes
		RHICONICH TERRANE Amphibolite-facies granodiorite, granite & basic gneisses and pegmatite veins
<b>FRACTURE-FILL &amp; AGE</b>		
Pre-Devonian hematite/epidote and quartz filled fractures		Proterozoic hematite/epidote filled fractures
Late Cretaceous - Early Tertiary Calcite & pyrite filled fractures		Mesozoic faults
<b>ORIENTATION</b>		
NE-SW & NW-SE trending faults dominant in regional datasets		NE-SW & NW-SE trending faults dominant in regional datasets
NNE-SSW trending fractures dominate the well datasets		ASSYNT TERRANE NE-SW & NW-SE fractures dominate
		RHICONICH TERRANE NE-SW, NW-SE & N-S fractures dominate
<b>SPATIAL CHARACTERISTICS</b>		
power-law relationships across five orders of magnitude		strong power-law relationships across at least three orders of magnitude
		Alltan na Bradhan (CSZ) best fit D-value of 1.019
best fit D-value of 0.897		Kinlochbervie best fit D-value of 0.751
		Caolas Cumhann best fit D-value 0.999

**Table 7.1:** Summarises the main similarities and differences between the Clair basement and the mainland LGC.

Many of the statistical analysis techniques used throughout this thesis to quantitatively describe the fracture networks present within the Clair basement can be applied to different geological studies including hydrocarbon exploration, the storage of radioactive materials and carbon capture and storage projects. For example, without too much work, pseudo-wells can be created through existing fault attribute maps created from seismic datasets and a simple population distribution analysis conducted. These regional results can then be compared to fracture spacing distributions from core logs to assess the level of scale-invariance present (if any) within the local and regional datasets. This relatively quick survey would provide key information about whether or not the local or regional datasets can be used to estimate fracture spatial attributes at different scales or whether more caution should be employed when creating fault models from the existing datasets.

All of the analyses presented in this thesis are particularly relevant for studies within crystalline basement rocks, where primary porosity and permeability is non-existent. This means that understanding the orientation and spatial characteristics of the fracture sets within your basement study area is critical to being able to determine suitability as a hydrocarbon reservoir, fluid flow pathways, storage capacity, etc.

### 7.1 – Impact

Portions of the work presented in this thesis, and of the work currently being completed by Benjamin Franklin (Durham, Ph.D.), along with observations and discussions from industry fieldtrips (*Figure 7.1*) run in conjunction with this Ph.D. program have been used by the industry sponsors (Clair Joint Venture) to understand the Clair basement fracture network potential to help better constrain their geological models of the Clair Field as a whole. This in turn improved the Clair co-venture's economic assessment of the Clair field. The newly constrained geological model and the improved economic assessment mean that the Clair Ridge project (Clair Field Development - Phase 2) has recently been sanctioned for development resulting in an investment of approximately £4.5 billion into the UK economy.



**Figure 7.1:** A group of oil industry professionals from the Clair Joint Venture soaking up the characteristics of the fracture network within the Canisp Shear Zone on a Durham University led fieldtrip.

The introduction of mainland LGC fracture network data into the Clair Field geological model used to sanction this new development suggests that the mainland LGC can be an appropriate analogue for the Clair basement. The work presented throughout this thesis has therefore not only created useful onshore and offshore fracture networks characterisation datasets, it has also added real value that has been utilised by the Clair Joint Venture.

## 7.2 – Recommendations for further work

The main disparity between the mainland LGC and the Clair basement is the absence of abundant Mesozoic and Cenozoic faults and fractures within the onshore study area. Large Mesozoic faults are known to exist west of the Scottish mainland (e.g. Minch Fault), which formed syn-tectonic half grabens and elevated Lewisian rocks bringing them adjacent with the Mesozoic basin-fill sediments (e.g. Stein, 1992, Butler et al., 1997, Roberts and Holdsworth, 1999) and form the Scottish Hebridean islands. These elevated Lewisian highs adjacent to Mesozoic faults are more analogous with the structural setting in the Greater Clair area where the Clair basement forms a topographic high as a rotated footwall block of the Mesozoic Ridge Fault (*Figures 2.12 and 2.13*). It is therefore recommended that faults and fractures associated with the Mesozoic faults that form the Hebridean Islands are characterised to assess Mesozoic fracture orientation and spatial attributes that are found within the Lewisian Gneiss Complex as a direct comparison with the Mesozoic fracture networks in the Clair basement. Much of this work is ongoing in a separate Ph.D. project (Ben Franklin, Durham University), who is also analysing the basement cover sediment interaction using the Permo-Triassic Stornoway Formation (that overlies the LGC on the Isle of Lewis) as an analogue for the Clair Group sediments in the Clair Field.

Other potential onshore Clair basement analogue study areas can be found along the north coast of the Scottish mainland where Mesozoic faults have been recognised (Wilson et al., 2010). These Mesozoic faults are recognised to have reactivated Caledonian structures similar to the Outer Hebrides Fault Zone, which is thought to underlie the Rona Ridge (e.g. Dean et al., 1999), and therefore they may provide a fitting analogue for the Clair basement. Another potential Clair Field analogue lies, again on the north coast of the Scottish mainland and encompasses Devonian rocks of the Orcadian basin which are directly analogous to the Clair Group sediments. These Devonian rocks, found at Caithness, overlie Moine basement and have been used as an analogue for the Clair field for several years (e.g. Bergbauer and King, 2009). A current Ph.D. research project (Anna Dichiarante, Durham University) focuses on the fracture systems in these Devonian sediments around the north coast of the Scottish mainland and on Orkney where they are exposed in close proximity to the Moine and Lewisian basement rocks.



With regards to the terrestrial laser scan models presented in Chapter 5, it would be useful to recollect a TLS dataset from within the Canisp Shear Zone as similar structures are thought to exist within the Clair basement. The effect the shadowing in the Alltan na Bradhan TLS point cloud has had on the data was unfortunately not recognised until a point when there was no time left within the confines of this thesis to collect a fresh dataset.

Another recommendation for further work on these TLS datasets would be an extensive study to assess how varying the aspect ratio of the fractures interpreted from the virtual outcrop models affects the fracture presence and fracture intersections (connectivity) of the fracture networks. A study of fracture aspect ratio would be instructive because the fracture networks used for the TLS analysis in *Chapter 5* have not been extended beyond their surface expression and therefore only provide minimum values for fracture presence and fracture intersection. Creating models with varying fracture aspect ratios, and comparing the resulting values with the 1-dimensional samples directly collected from outcrops, would provide better control on 2- and 3-dimensional fractal dimension values that best represent the 'true' fracture network present within the key outcrop models. This would then provide an insight into the fluid flow and ultimately the 'connected volume' present within the Clair basement. By history matching this expanded TLS outcrop modelling to pre-existing development data from the Clair basement and by using the fracture characteristics from the mainland LGC to keep it geologically accurate, it should be possible to extend this analysis into fully 3-dimensional deterministic fracture network models. These models would provide the most accurate understanding of these offshore basement fracture networks, which ultimately will improve any potential hydrocarbon production from the Clair basement.

## **APPENDICES**

## APPENDIX A

I: Tectonic, metamorphic, sedimentary and igneous summary table for the Clair basement and the mainland LGC

TIME ERA	Metamorphism and Tectonism				Sedimentary and Igneous activity	
	TIME PERIOD	YEARS (Ma)	Clair Field	northwest Scotland	Clair Field	northwest Scotland
Archaean		3125 - 2900			Formation of early rocks. Emplacement of tonalitic/granodioritic plutons	
		2900 -2490		granulite-facies metamorphism		
Proterozoic	E. Proterozoic	2490-2400		amphibolite-facies metamorphism - formation of steep NW-SE foliation in shear zones		
	E. Proterozoic	2400-1900		emplacement of Scourie Dyke Swarm - dextral transtension		emplacement of the Loch Maree Group
	E. Laxfordian	1900-1800	growth of hornblende (may be of similar age)	amphibolite-facies metamorphism - reworking of shear zones and retrograde metamorphism		
	M. Laxfordian	1600		upper greenschist-facies		
	L. Laxfordian	1400-1200	overgrowth of existing mineralogy by chlorite	lower greenschist-facies		
		1200	NW-SE faults in Clair basement (from seismic) may have initiated at same time?	Late Laxfordian' faults preferentially developed in Assynt Terrane shear zones		
		1100 -800	Similar NE-SW hematite stained fractures present in Clair basement may be of similar age.	Formation of N-S and NE-SW hematite stained fractures		Deposition of the Torridonian succession
	Cambrian	545-470		Opening of Iapetus creating uplift on the passive margin shelf edge.		deposition of Cambro-Ordovician sequence in NW Highlands (shallow marine transgressive sequence)
		475-450				
	Calendonide	440-415	compression accommodated along NW-verging thrusts during formation of the Caledonian Orogeny.			
	E. to M. Devonian	416-385	Iapetus and Rheic Oceans close and Laurentia, Baltica, Avalonia and Amazonia are accreted. Caledonide mountain belt underwent extensional collapse forming localised basins north of mainland Scotland			
Palaeozoic	Devonian	416-359.2	Rifting initiated. Rifting orthogonal to NE-SW Ridge fault.		Lower Clair Group deposited	
	E. Carboniferous	359.2-345			Deposition of the Upper Clair Group	
	E. Carboniferous	359.2-345				
	L. Carboniferous	306.5-299	non-specific compressional regime possibly orthogonal to the Ridge fault			
	E. Permian	299-270.6				

Mesozoic		251-65		formation of large Mesozoic fault zones that extend offshore		
	E.Triassic	251-245	NW-SE extension accommodated on a few widely spaced faults			
	Permian - Triassic	299-199	Prominent fracture trend of NNE-SSW seen in basement core from the ridge.			deposition of New Red Sandstone in a transgressive marine environment
	or Jurassic	199-141				
	L. Jurassic	161-145			no Jurassic sediments	
	E. Cretaceous	145-99	rifting			
	Cretaceous	145-65	rifting			
	L. Cretaceous	99.6-65.5	final rift phase in Clair		deposition of caprock mudstones - first oil charge into Clair Field (72 Ma)	
Cenozoic		65.5	formation of calcite-filled fractures			
	E. Tertiary	65	doming and uplift - does not reactivate existing faults.	uplift resulting in block rotations along basin margins		formation of Tertiary igneous province
	Tertiary	65-1.8	compression and uplift		second oil charge into Clair field	
	M. Paleocene to E. Eocene	61.7-48.6				
		55.8	post-rift subsidence		emplacement of sills in southwest Clair - associated with North Atlantic Igneous Province	
		54.8	localised uplift caused by oblique slip deformation			
	L. Eocene	37.2-33.9	E-W compression			
	Oligocene	33.9-23	NNW-SSE compression (Boldreel & Anderson, 1993)			
	M. to L. Miocene	15.9-5.3	existing faults and fractures reactivated in extension			
	Pliocene to Recent	5.3-0	NW tilting due post-ice sheet isotatic rebound	potential reactivation of basin margin faults		deposition of glacial till.

## **APPENDIX B**

### **I: Fault lineaments to Surfaces in Paradigm GOCAD™ 2009.2**

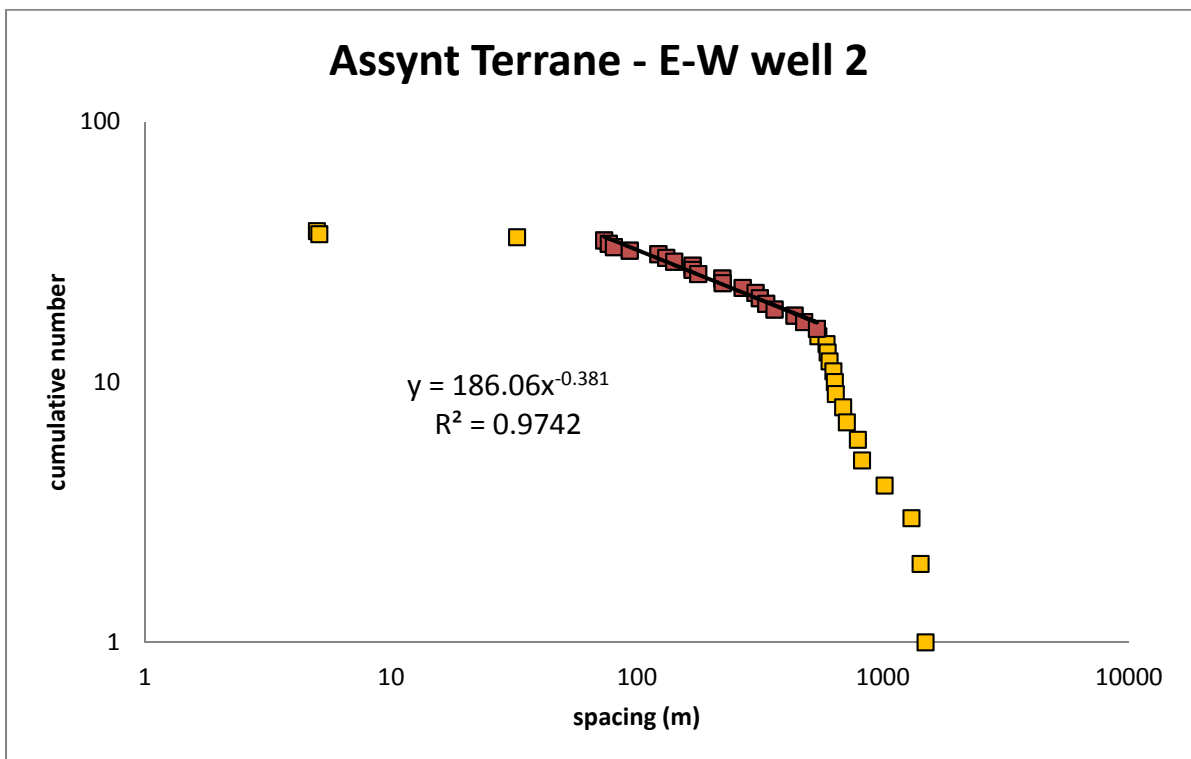
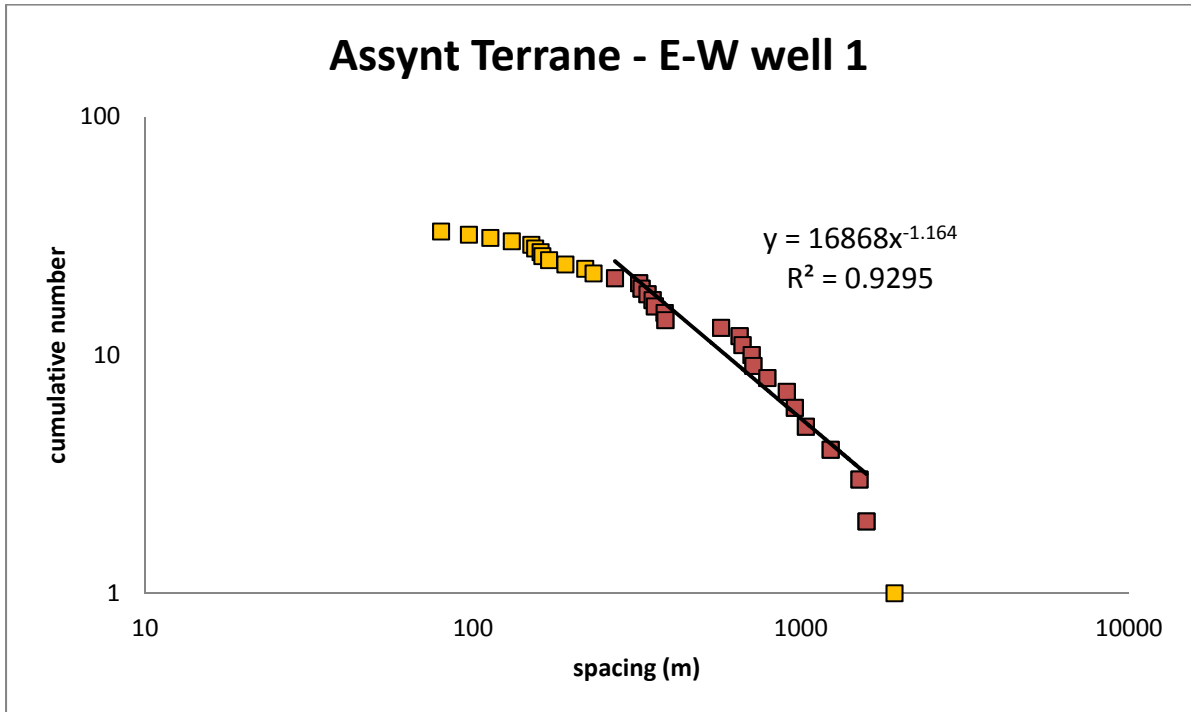
1. Fault lineaments are interpreted in ARCGIS™ and created as shape-files – see ARCGIS™ help for detailed instruction on how to produce fault lineament interpretations (polylines).
2. Start a new Paradigm GOCAD 2009.2 project – make sure all options have been ticked and measurements have been set to your requirements.
3. Import shape-files from ARCGIS™ - File/ Import objects/ Cultural data/ Arcview Shape – and select your fault lineament interpretation file(s)
4. GOCAD™ will process the data and create curves from your lineament picks.
5. Click on the workflow tab and right click on structural modelling to start a new project.
6. Click NEXT at the bottom of the window and select the depth button. Click YES to the next question (do you want to add fault data?)
7. Highlight your lineament data file(s) which should be visible in the next pop-up window. Change fault sticks to fault centre lines (at the bottom of the window) and click the adjacent arrow.
8. With the data file(s) still highlighted click the arrow pointing right. GOCAD will then process the lineament data into faults – this step may take a while to process depending on the number of lineaments in the sample.
9. Once GOCAD has finished processing the faults, click OK. Then click NO to do you want to add horizon data and define volume of interest?
10. You should now see Fault modelling highlighted – click NEXT.
11. Make sure all fault sticks are highlighted and click BUILD FAULT SURFACES (if you click the adjacent downward pointing arrow you can set size limits for you surfaces if you plan on doing a detailed study of aspect ratios etc.) – this processing may take some time again depending on how many faults are in the study.

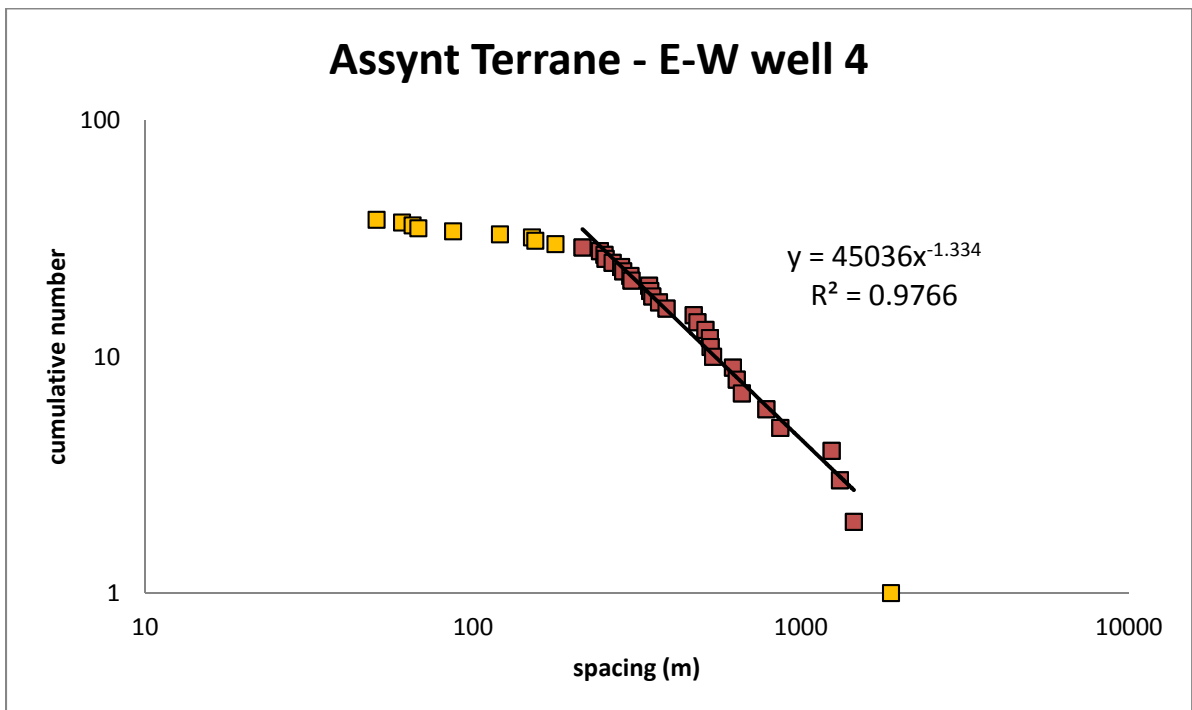
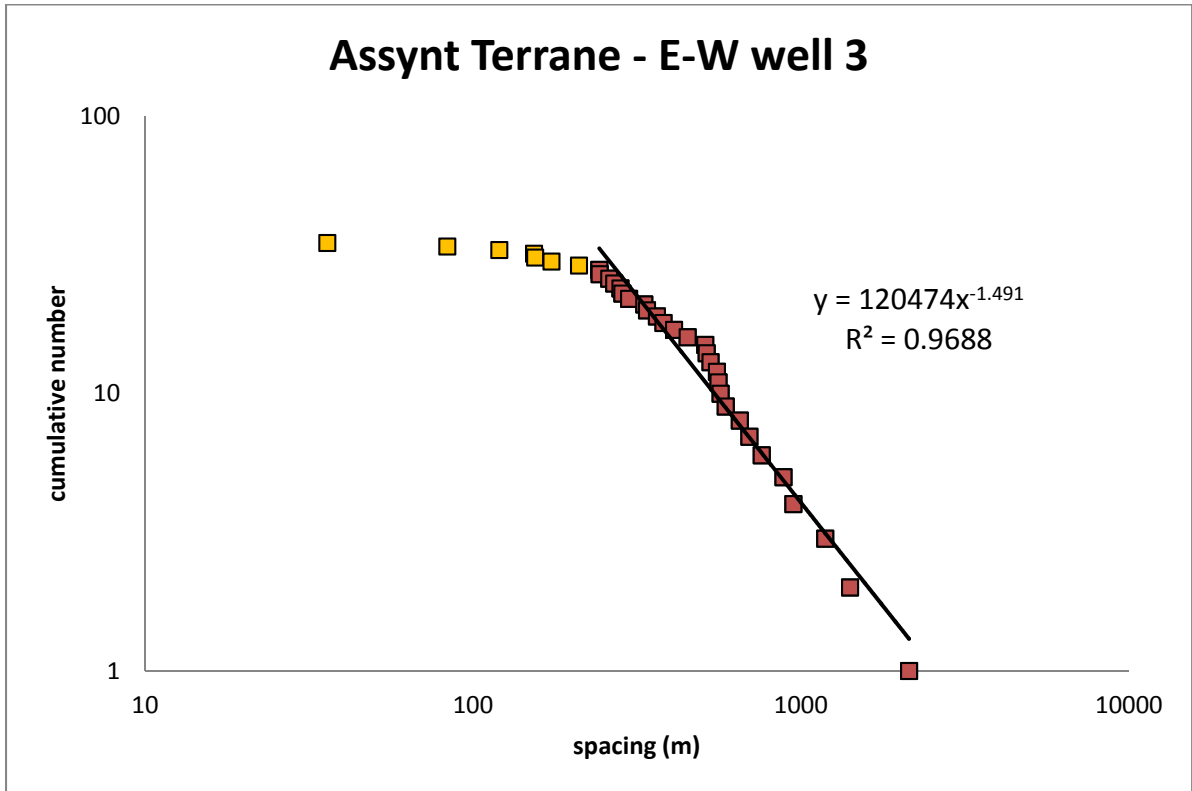
## II: Creating Pseudo-wells in Paradigm GOCAD 2009.2 for fault spacing attribute analysis

### CONTINUED FROM I

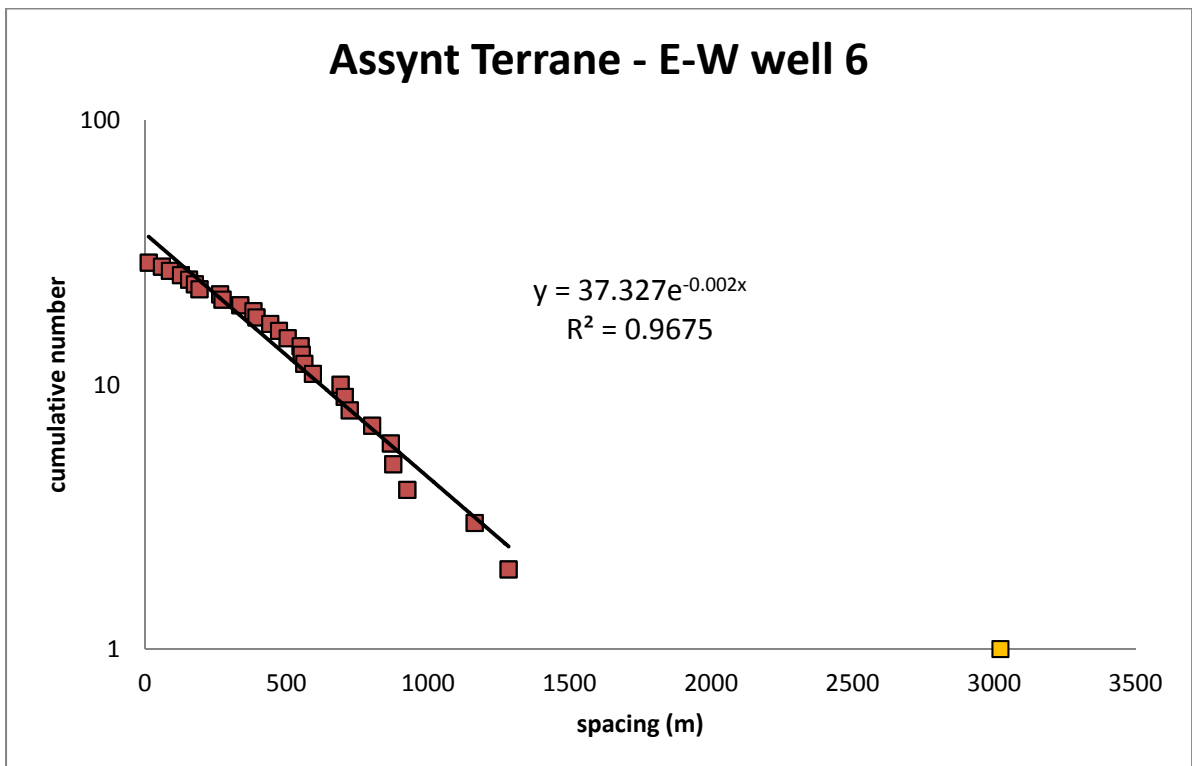
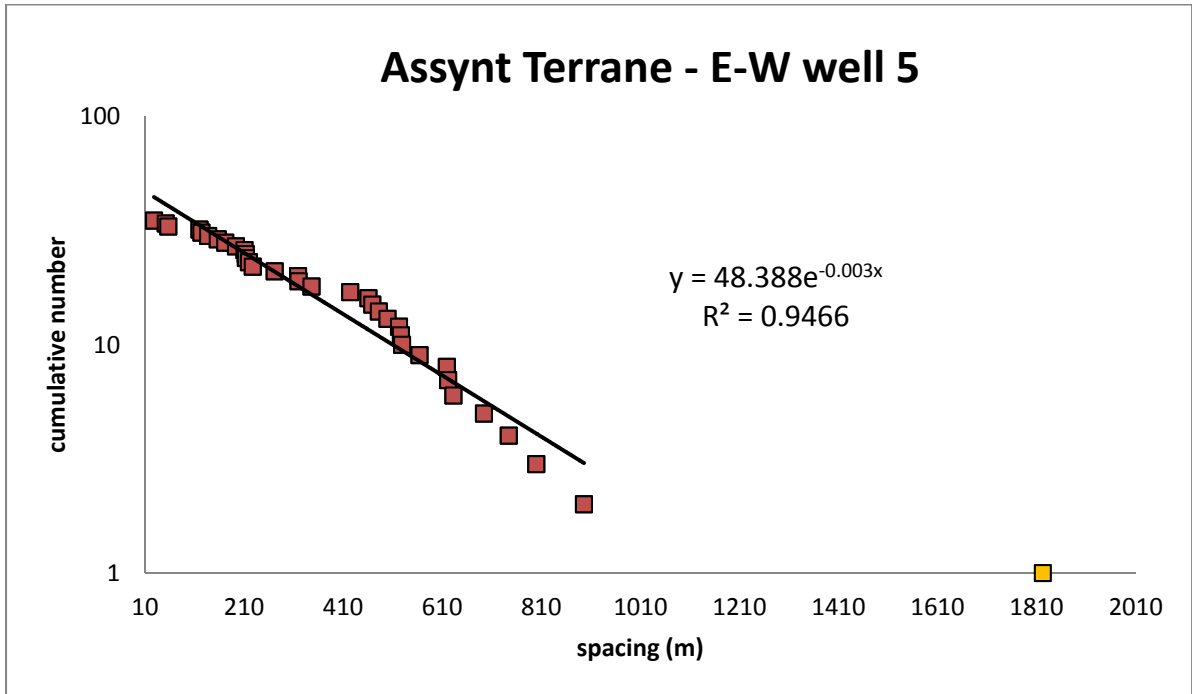
12. Close the structural modelling workflow and set view to map view.
13. Open the objects tab and right click – new/ from digitised polyline
14. Draw polylines where you want your wells by using the left click and then right clicking to finish – it is a good suggestion to draw pseudo-wells perpendicular and parallel to the main fault trends to collect better sampled datasets.
15. Create wells from the newly drawn curves – right click on Well/ New/From Curve – use the cross to click on one of your newly drawn polylines
16. Add faults to wells – Well/ Markers/ add markers from surface intersections – now each well should include the faults that it intersects.
17. These intersections can be exported as an ASCII file and analysed in Excel™ (right click on markers and choose the export option)- it includes fault intersection depths so fault spacing can be calculated and statistically analysed.

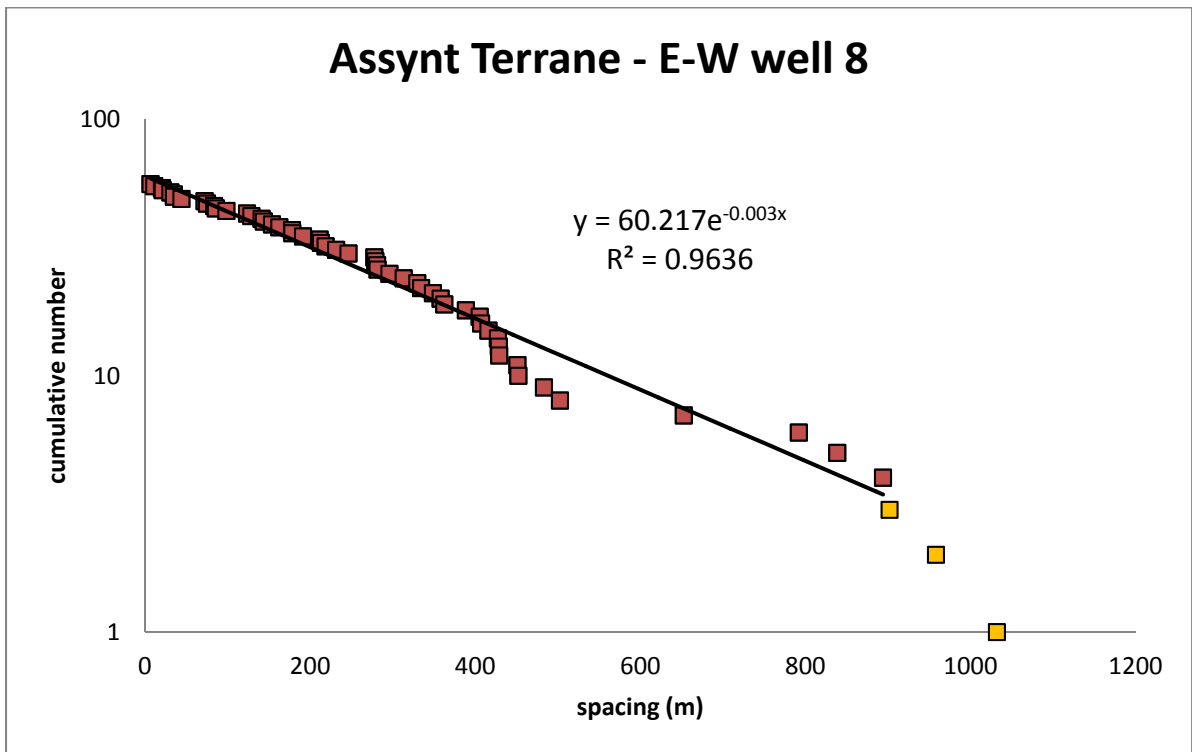
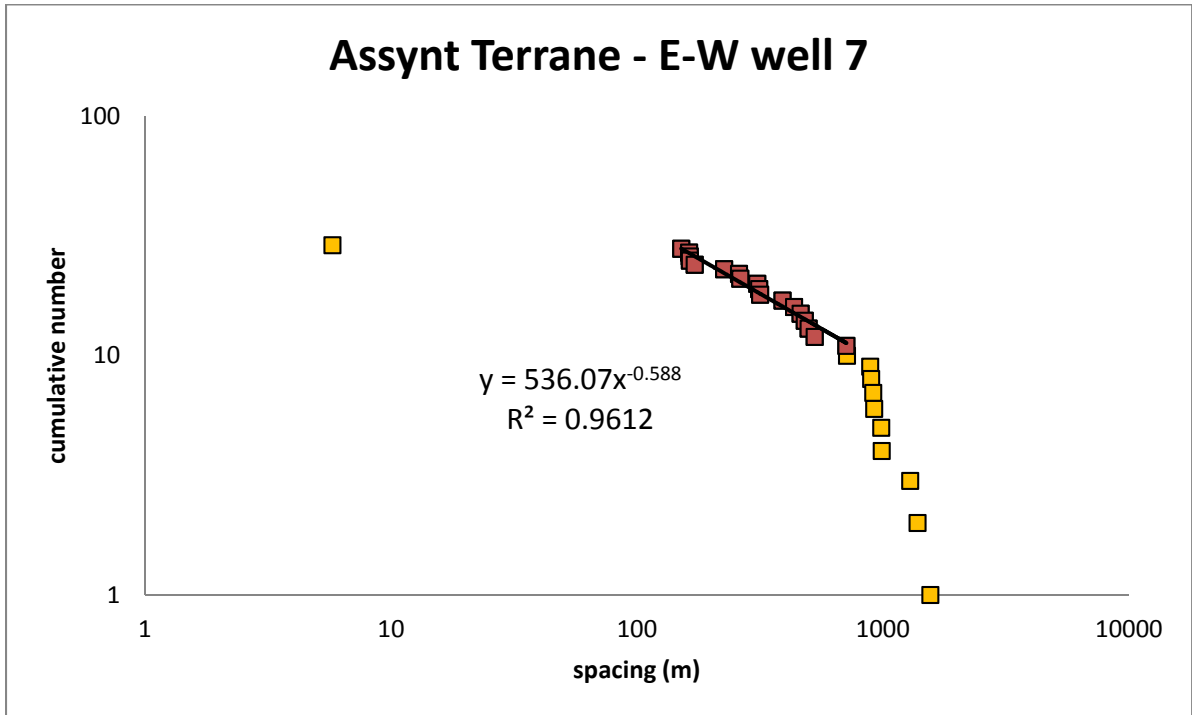
### III: Regional 1-dimensional fault population distribution plots

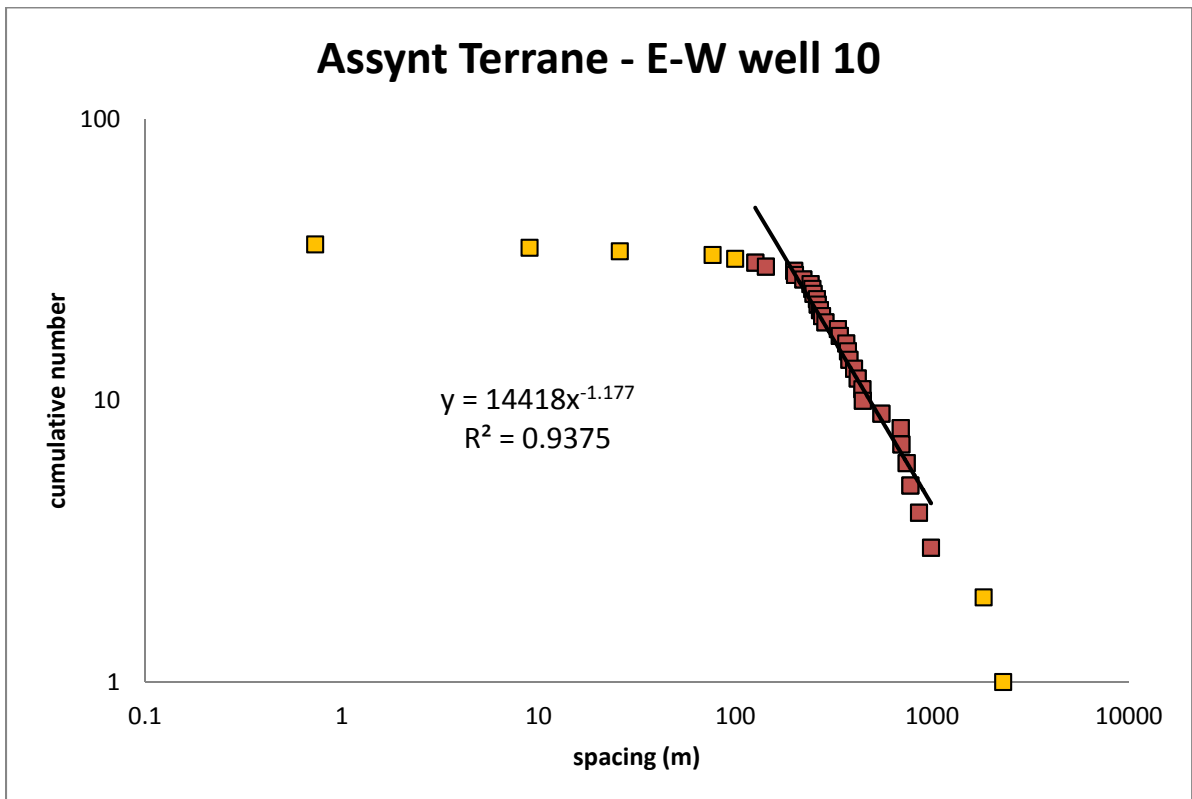
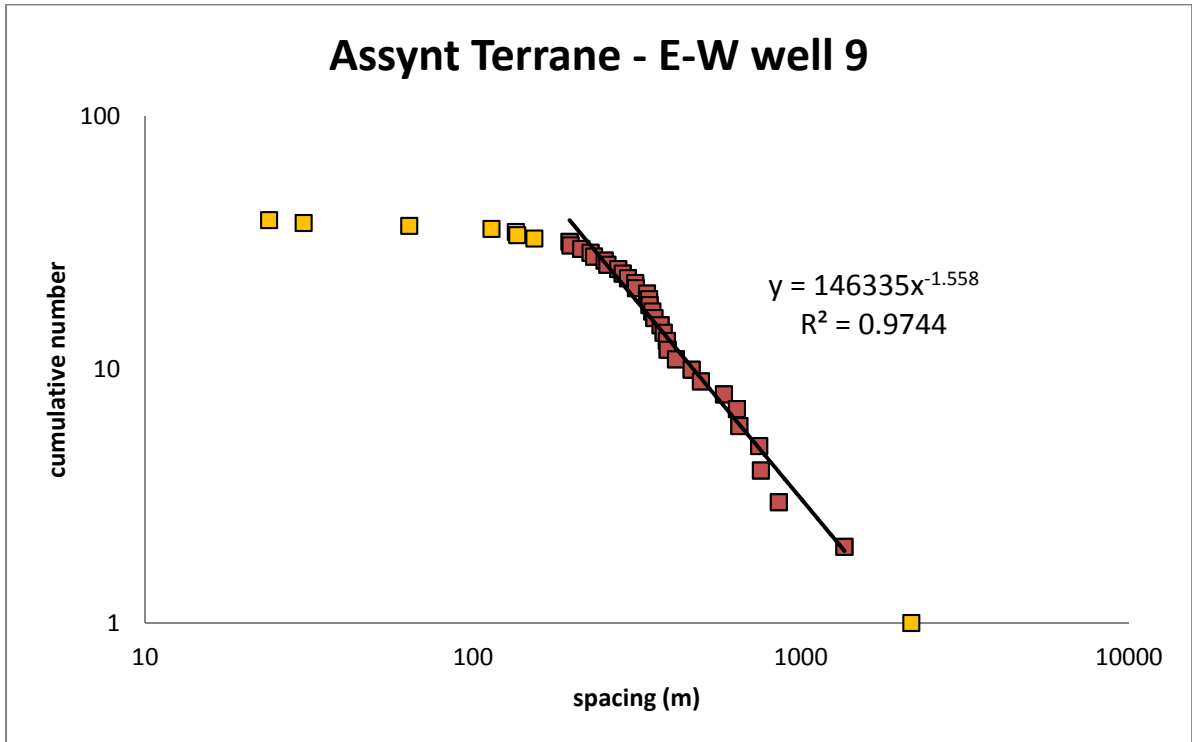


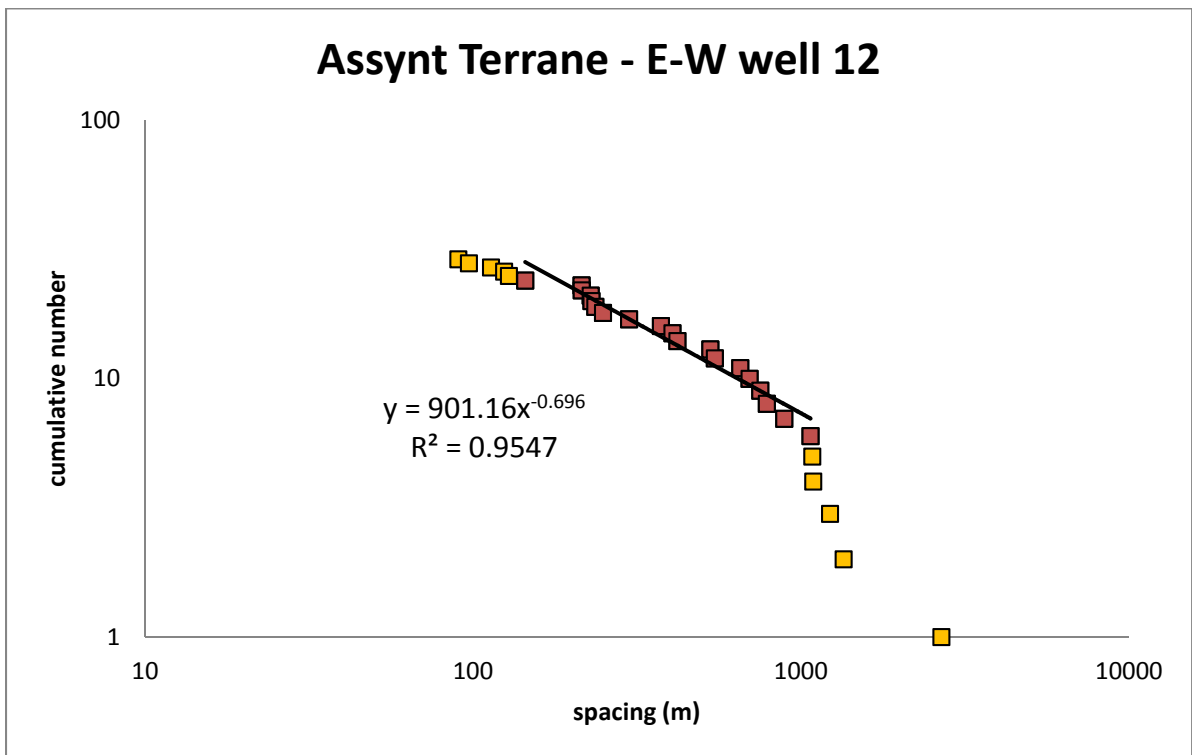
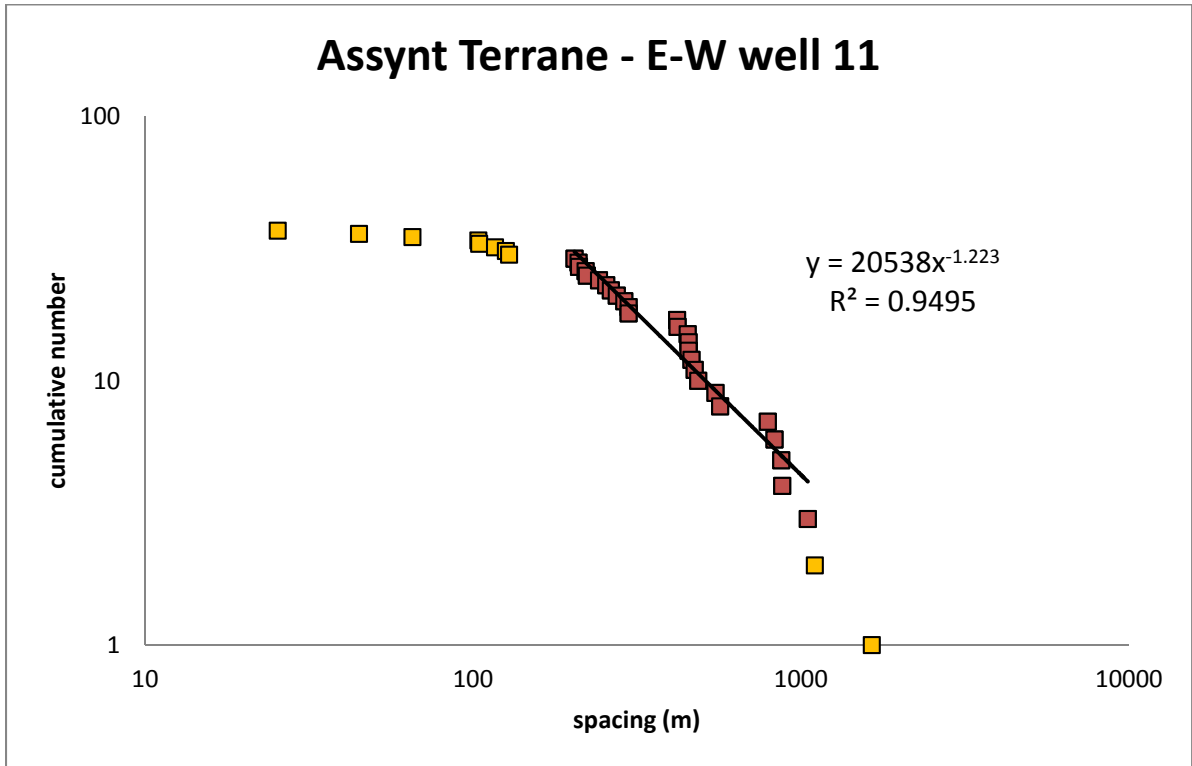


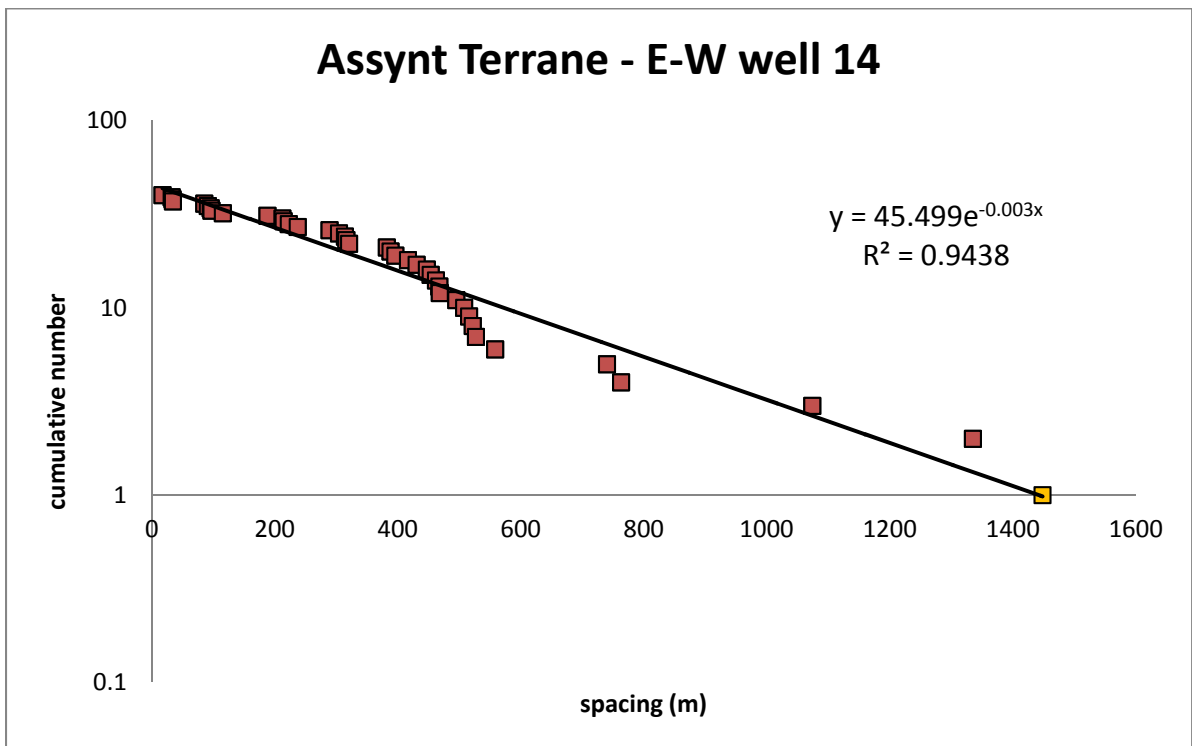
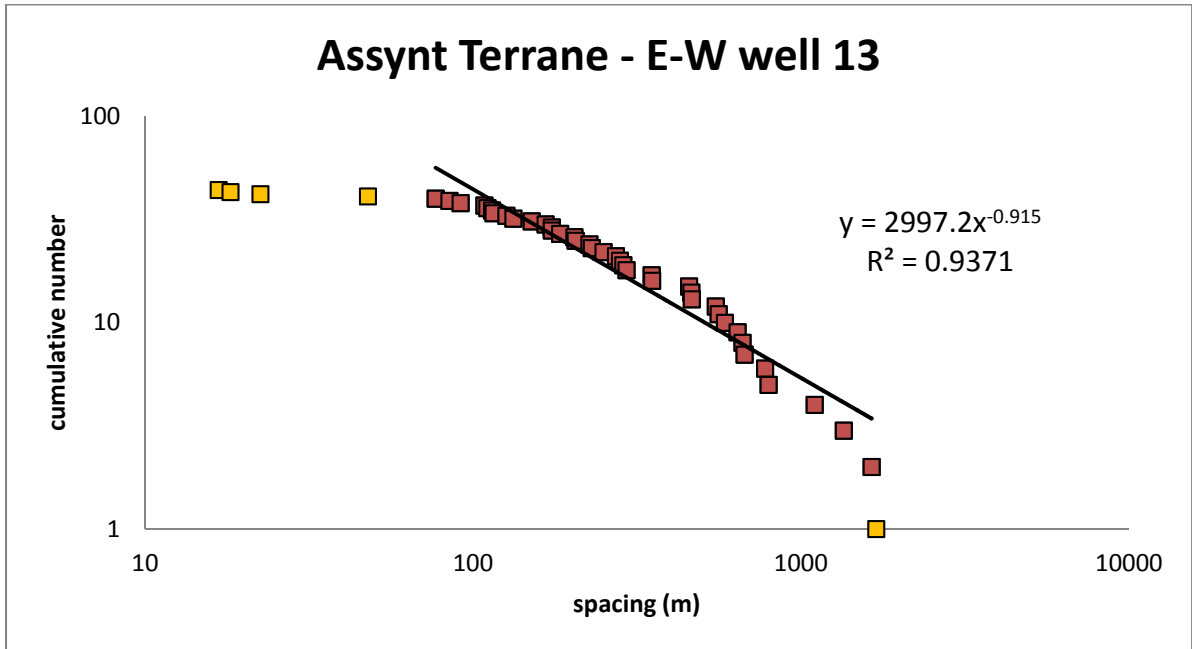


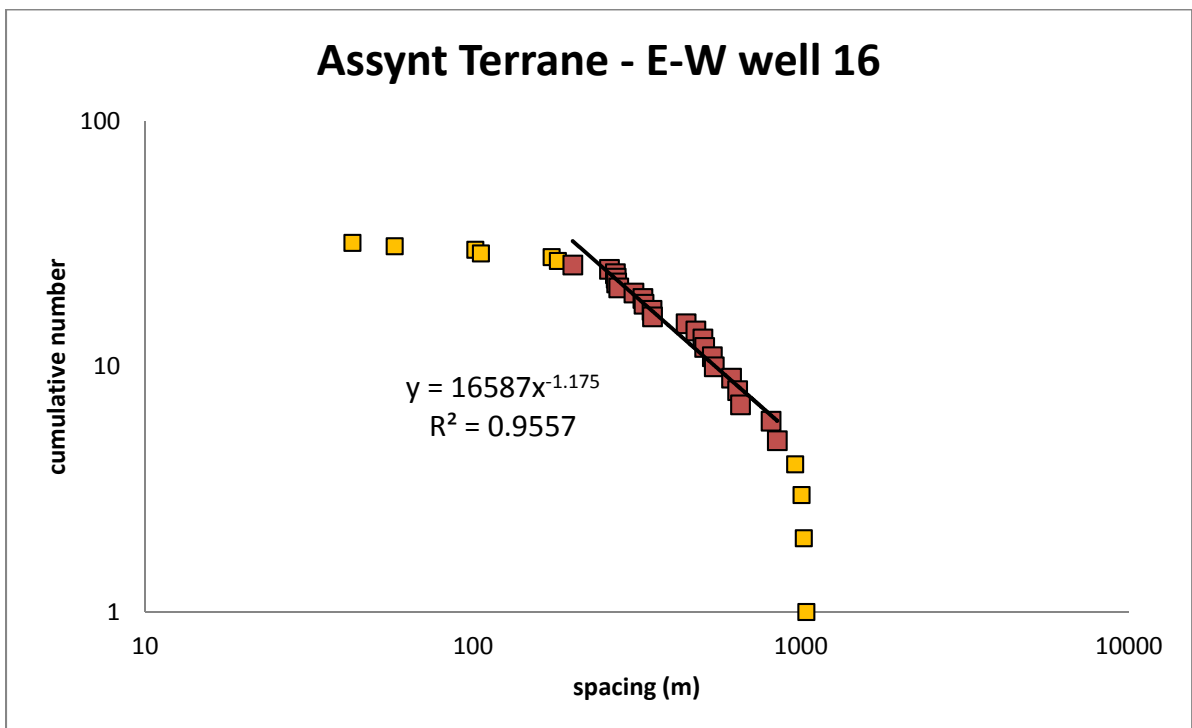
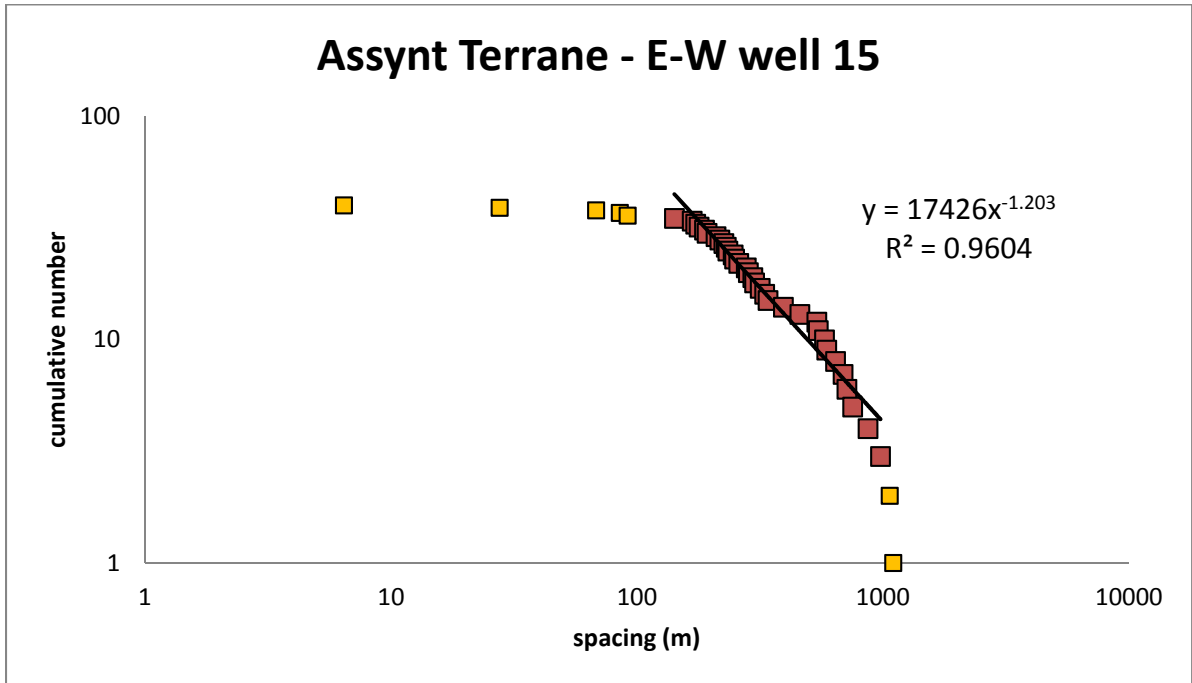


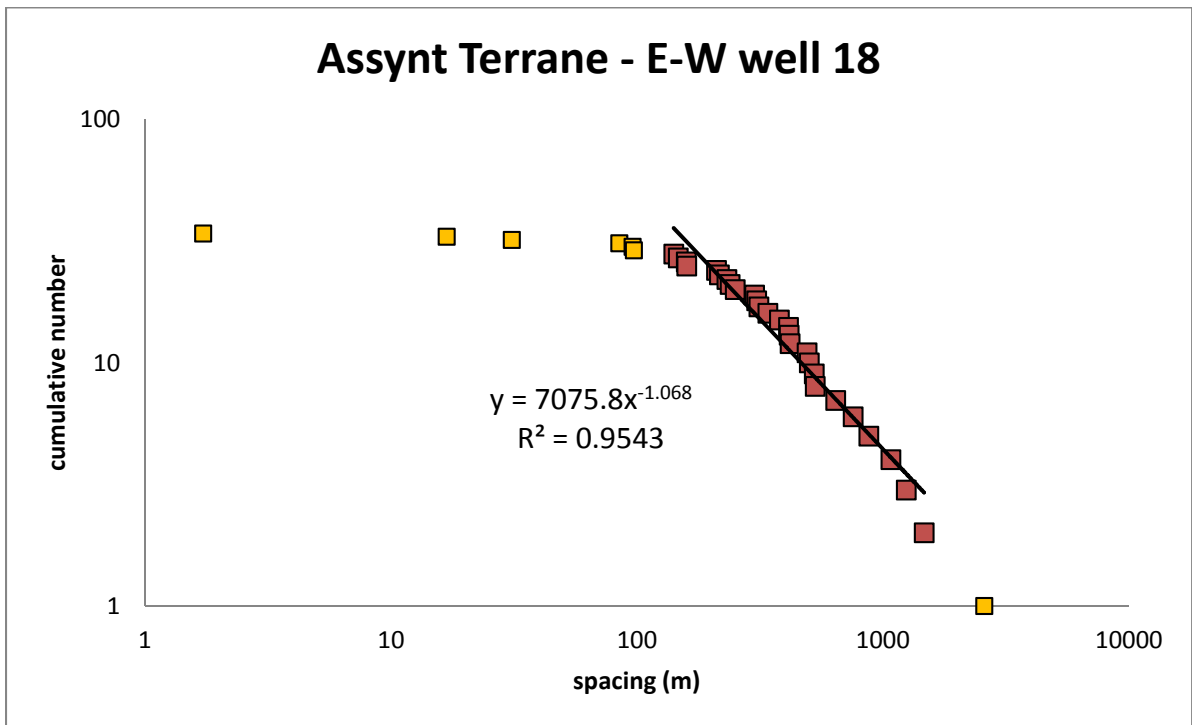
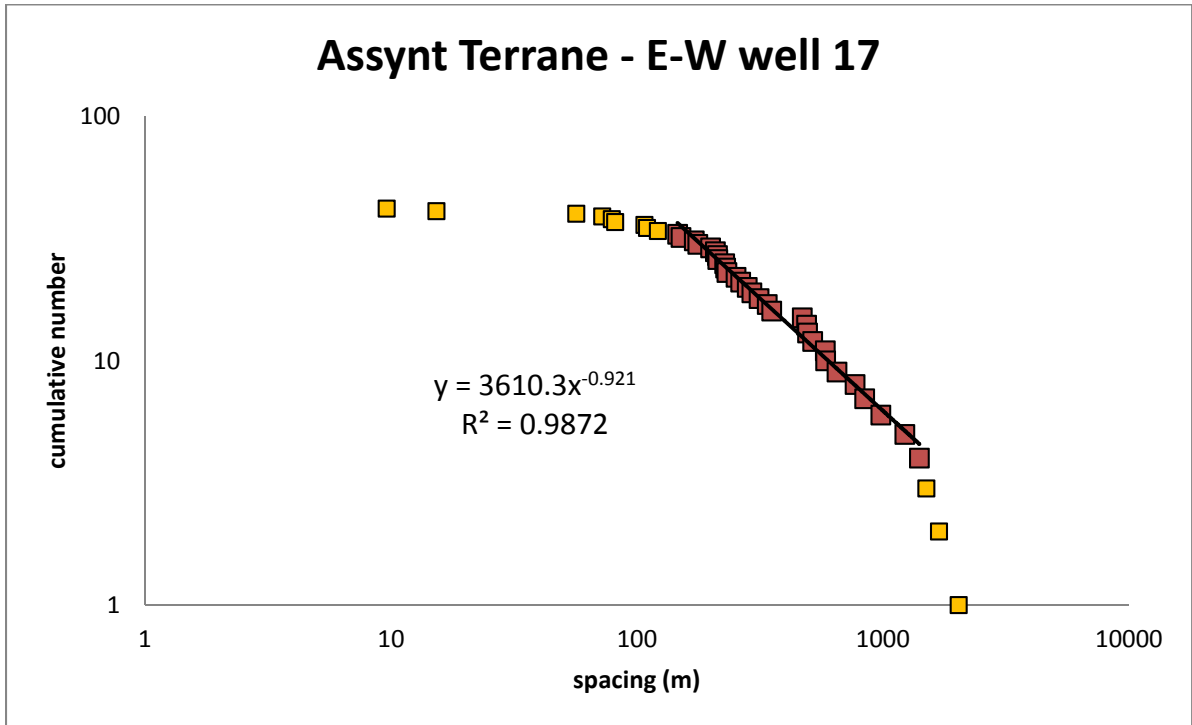


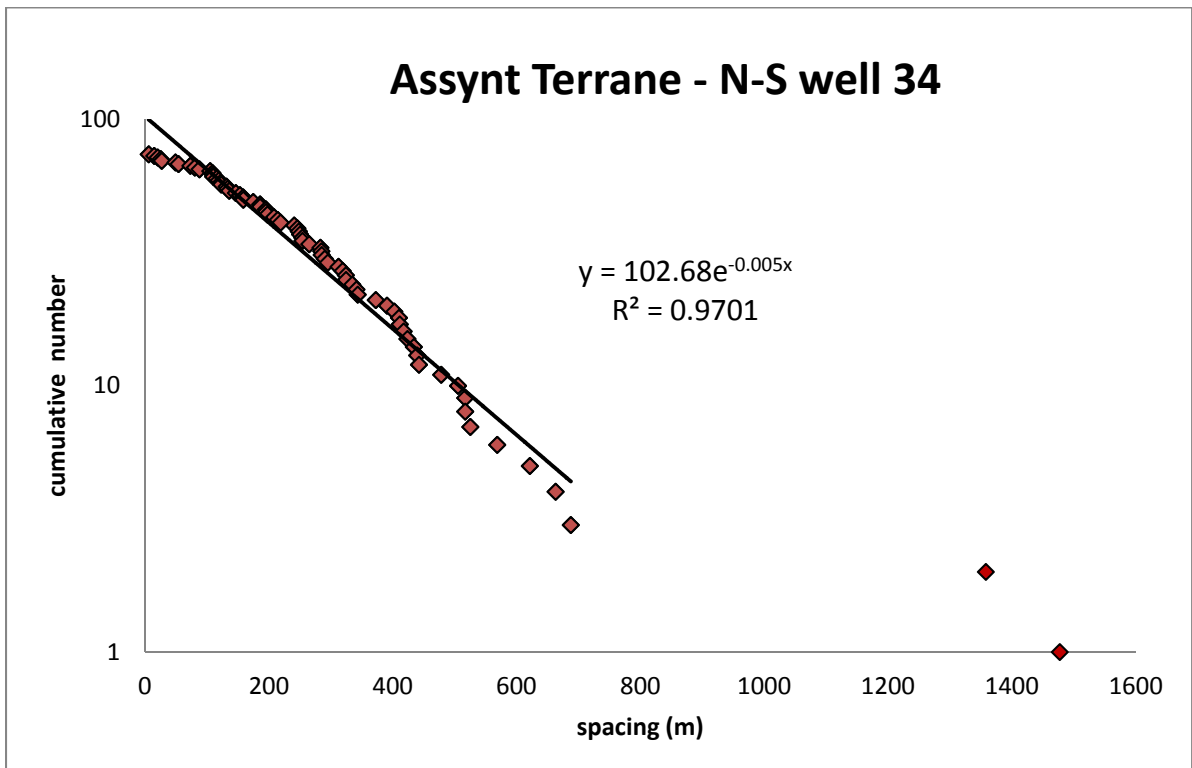
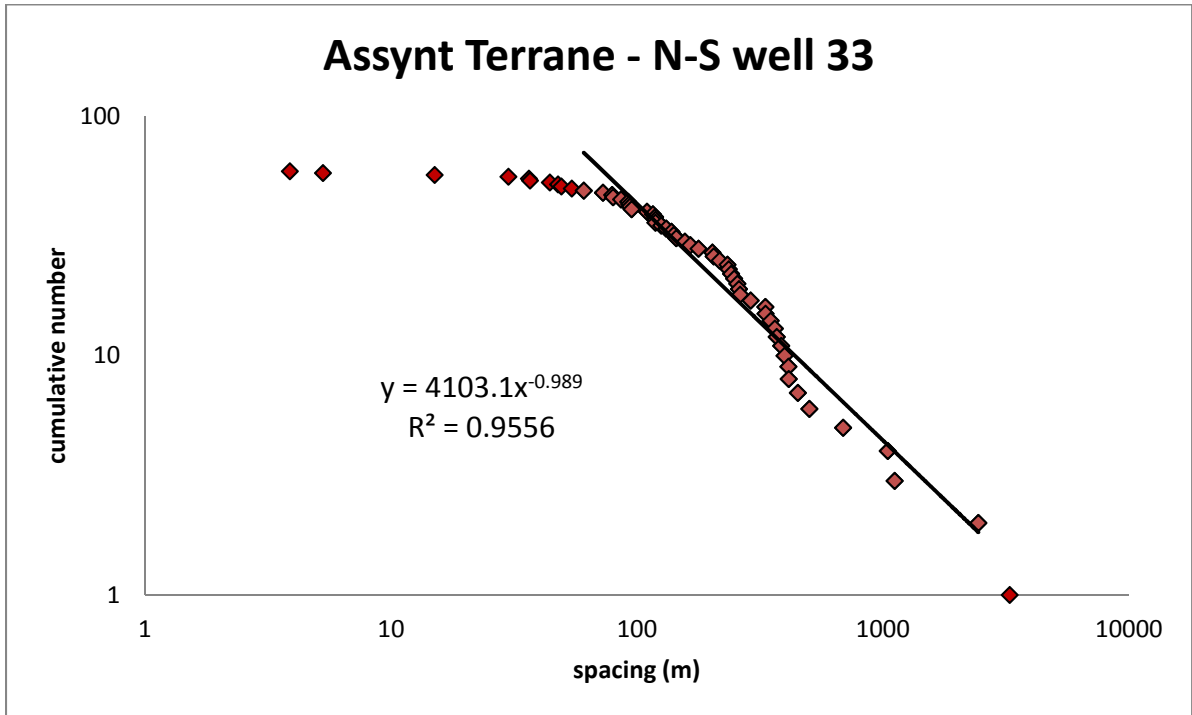




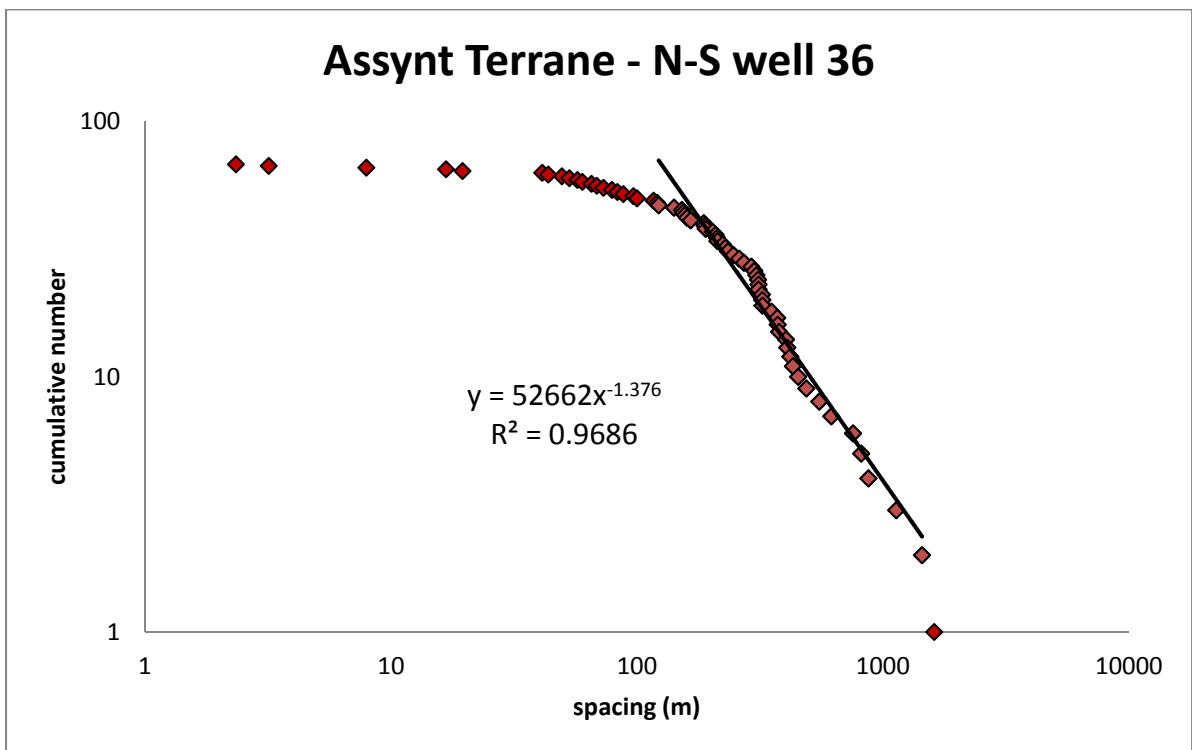
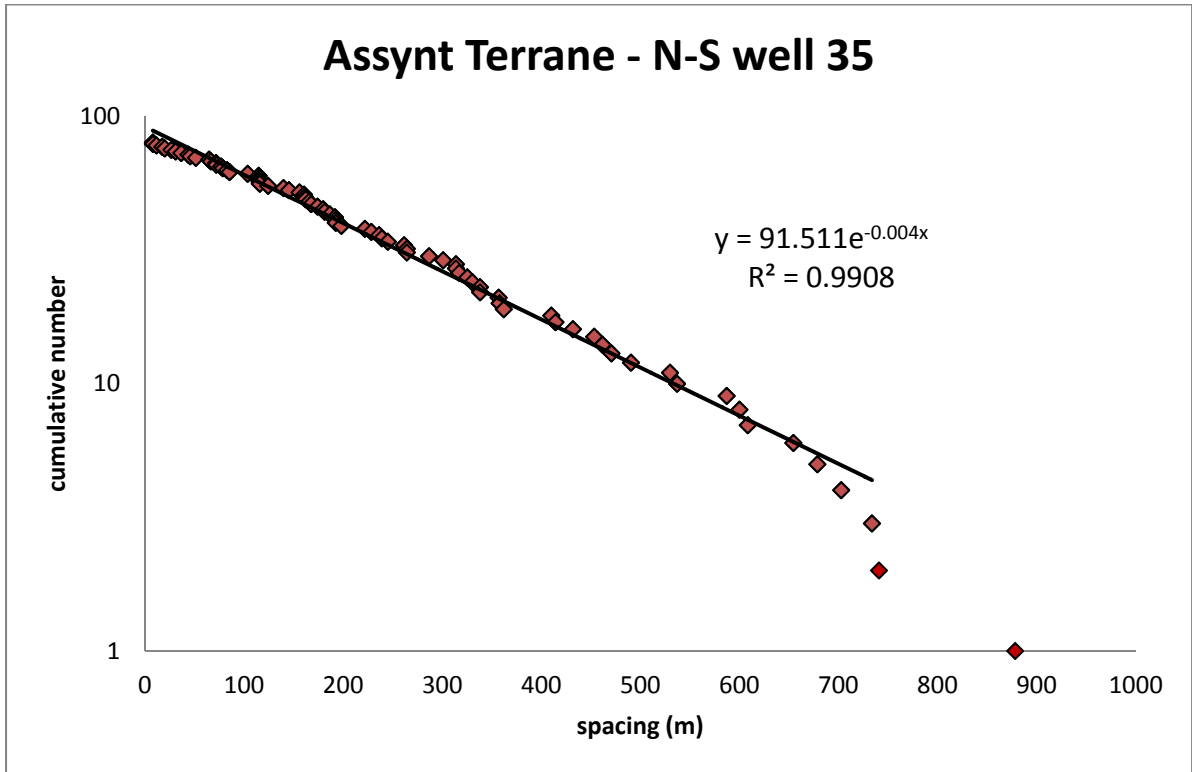


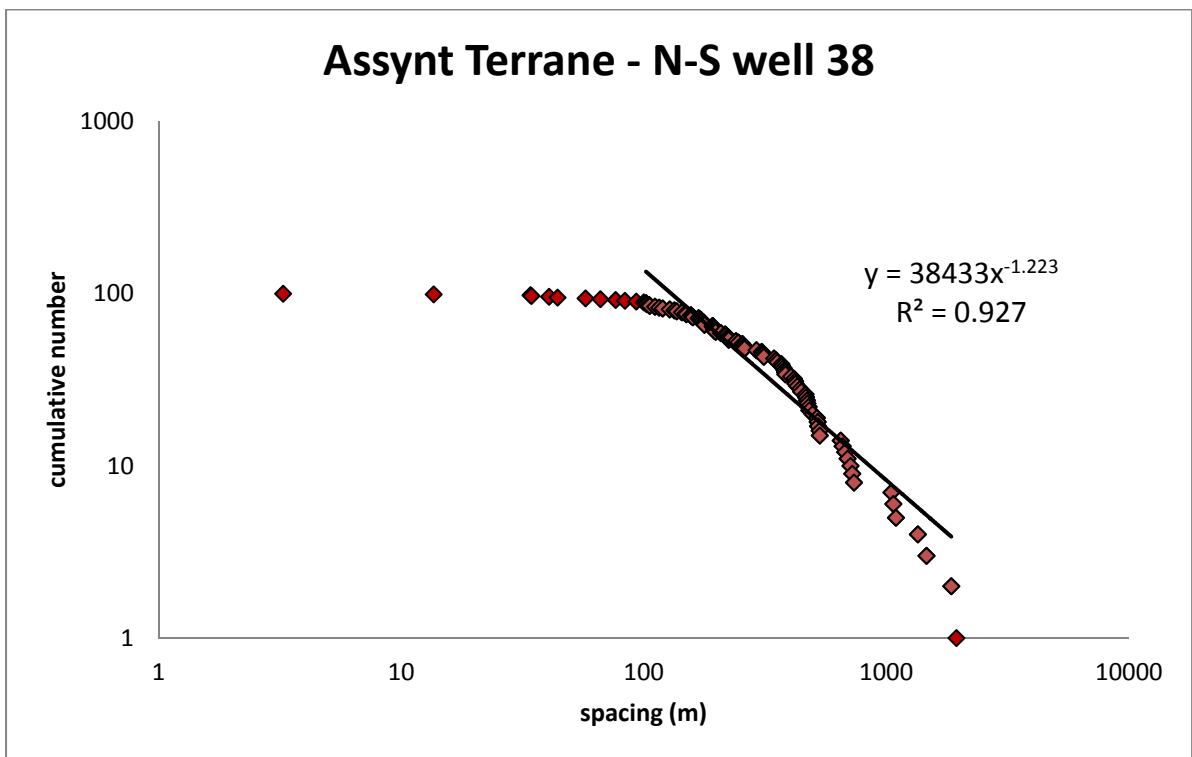
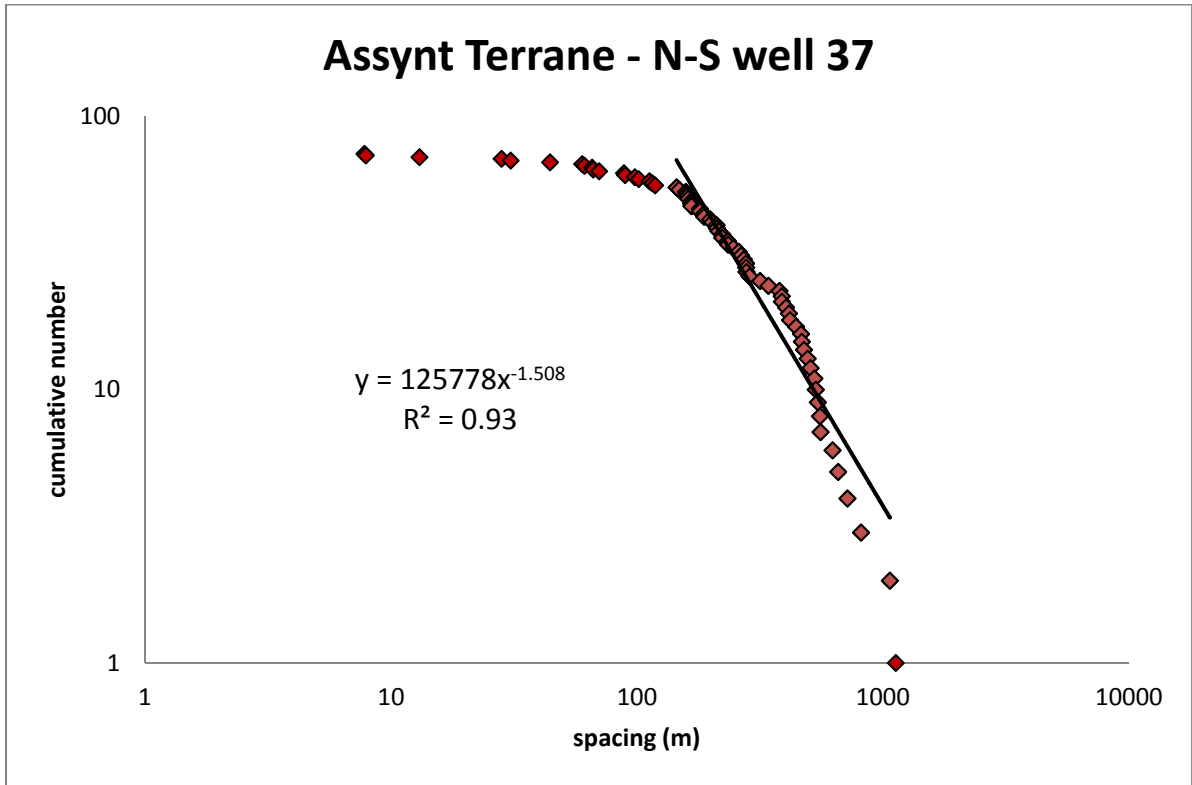


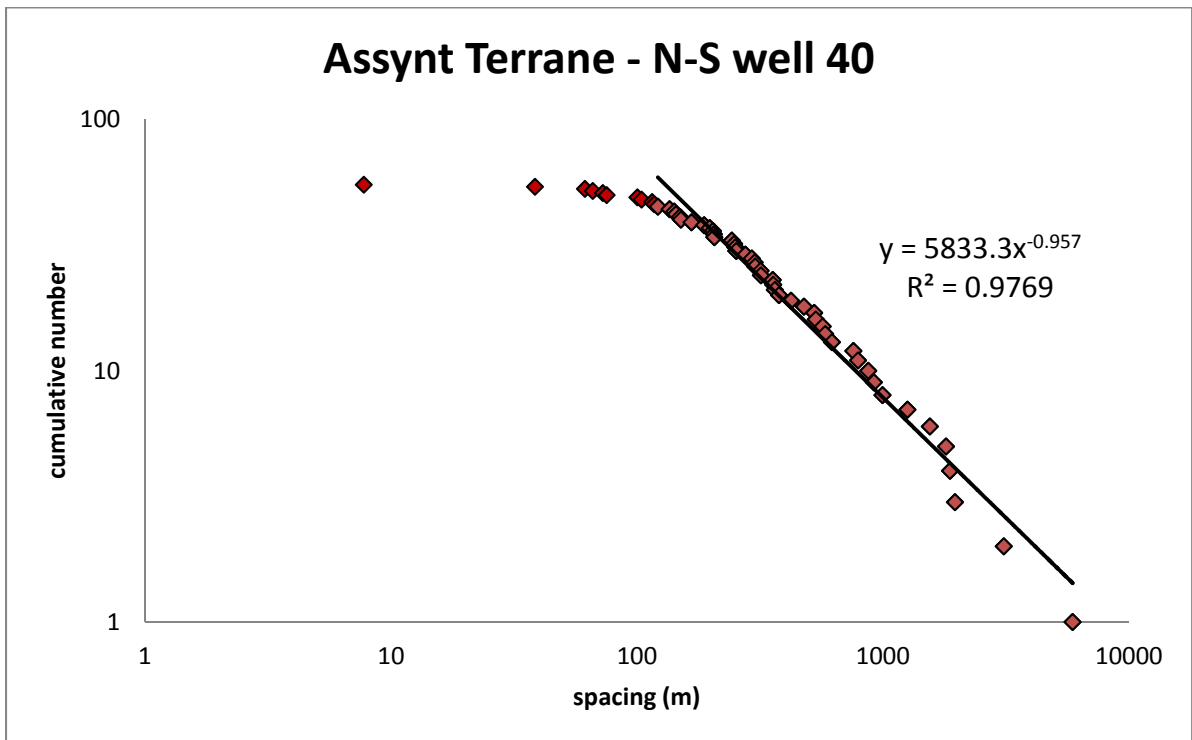
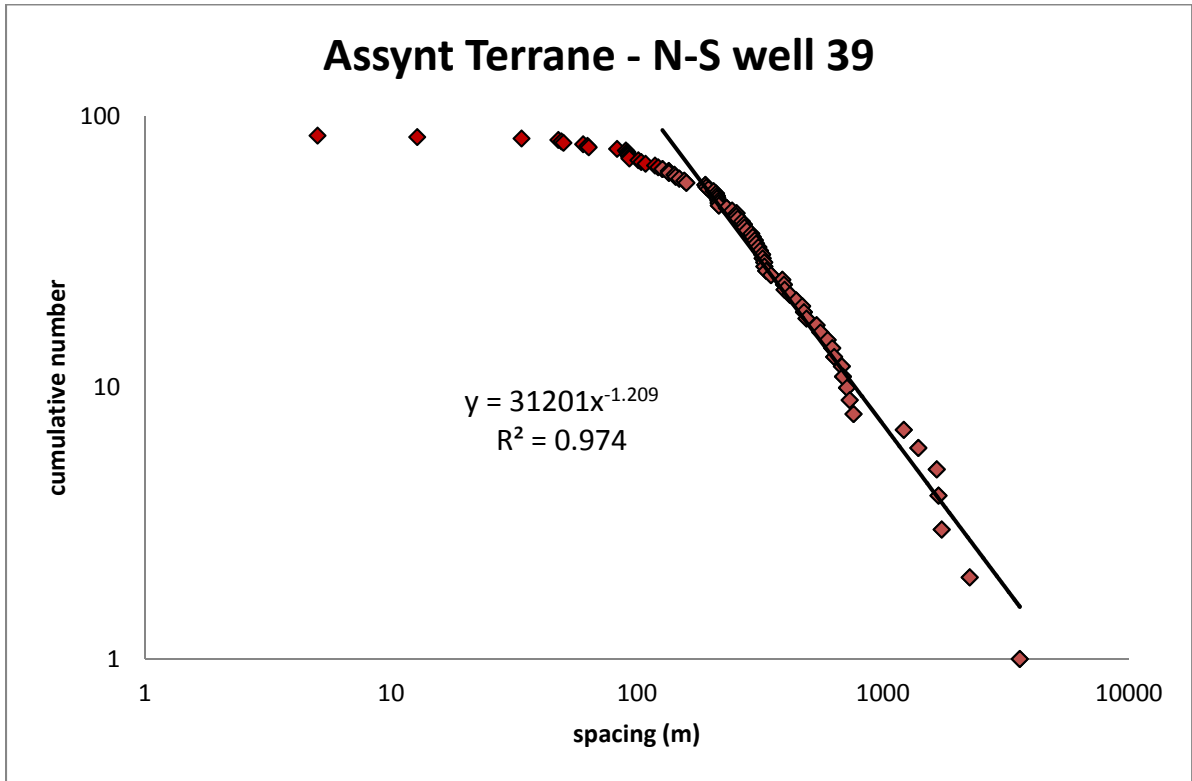


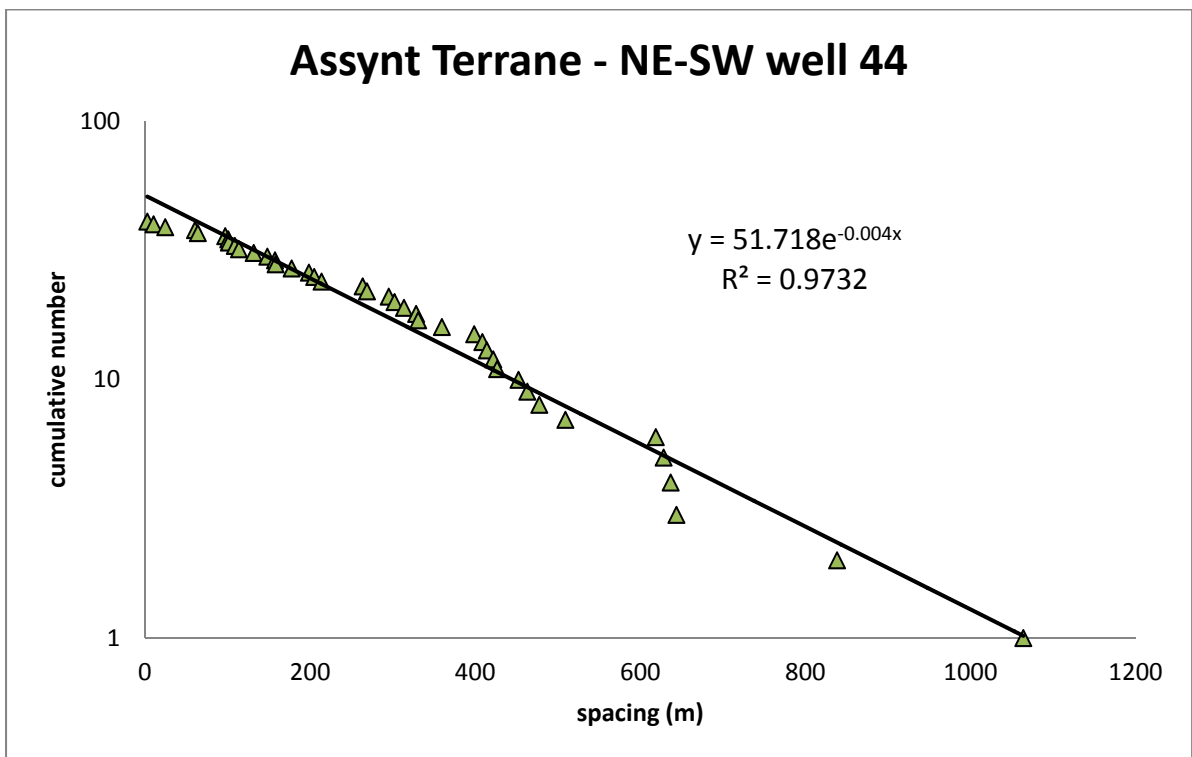
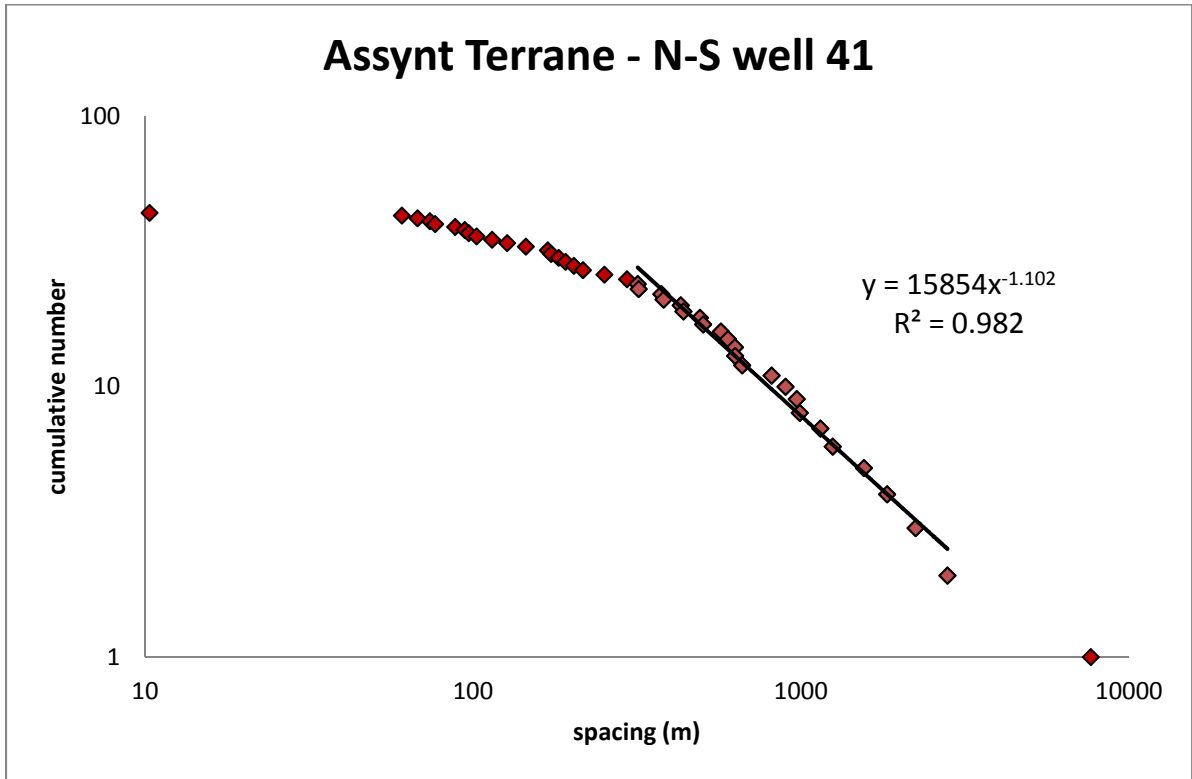


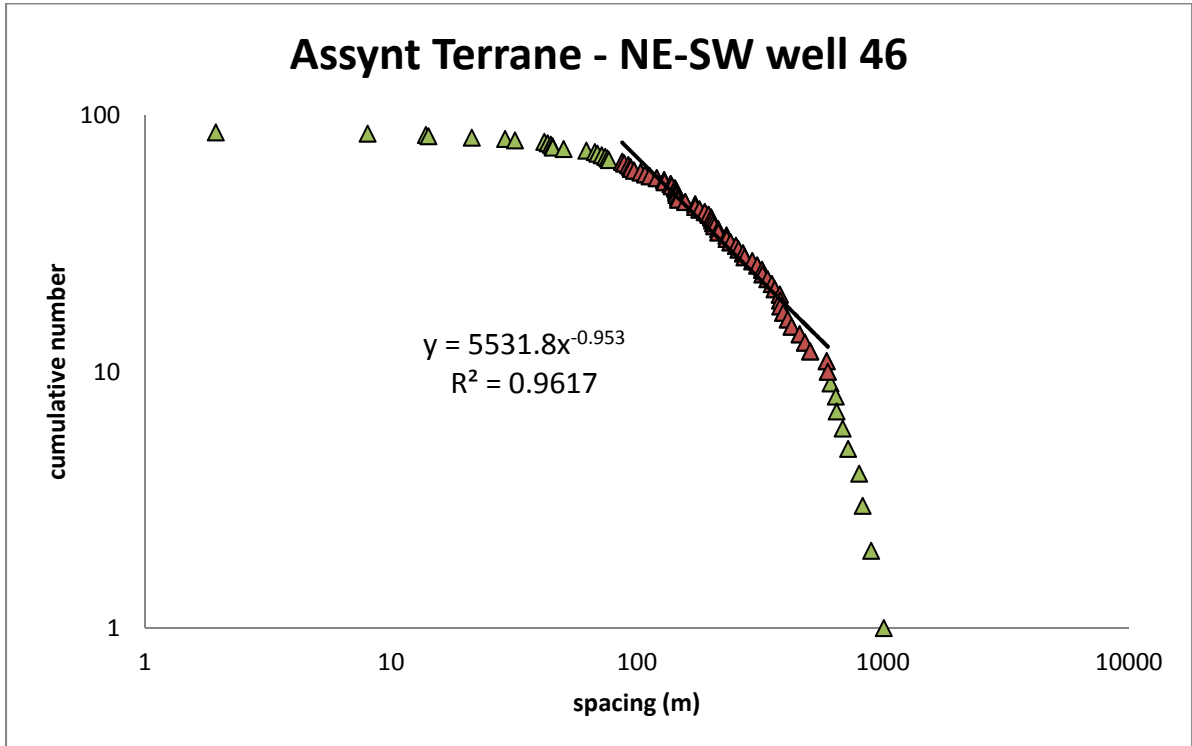
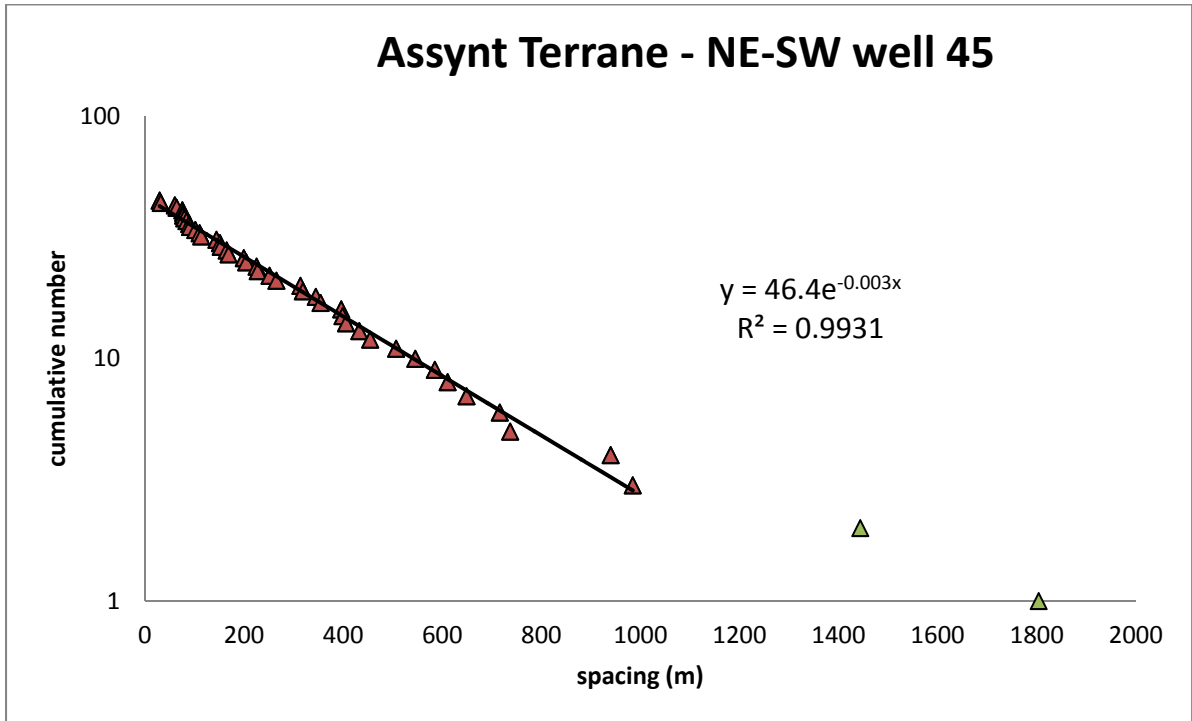


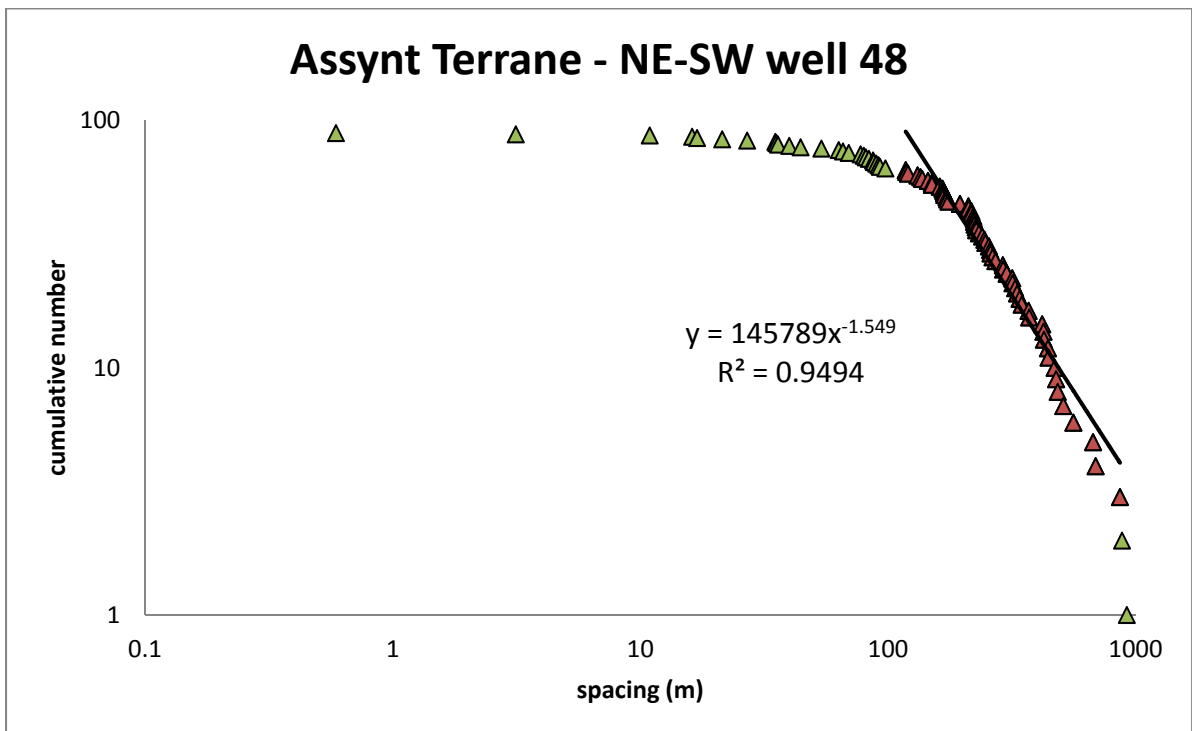
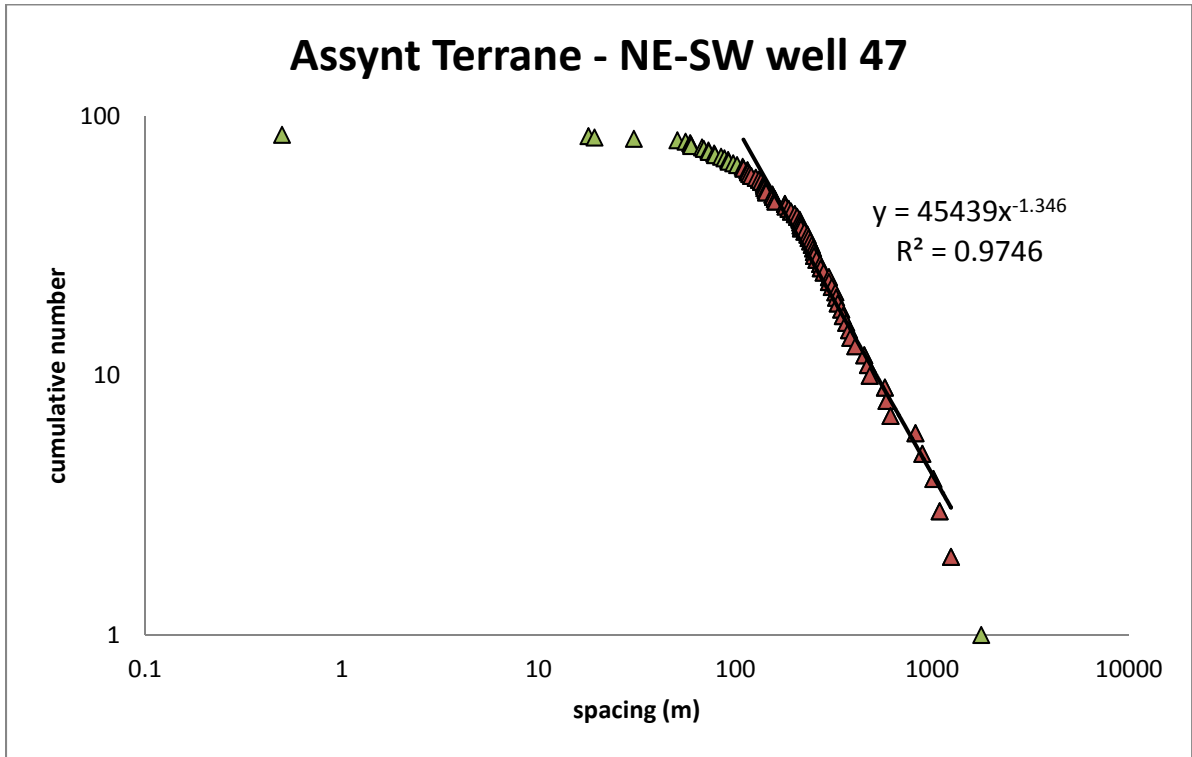


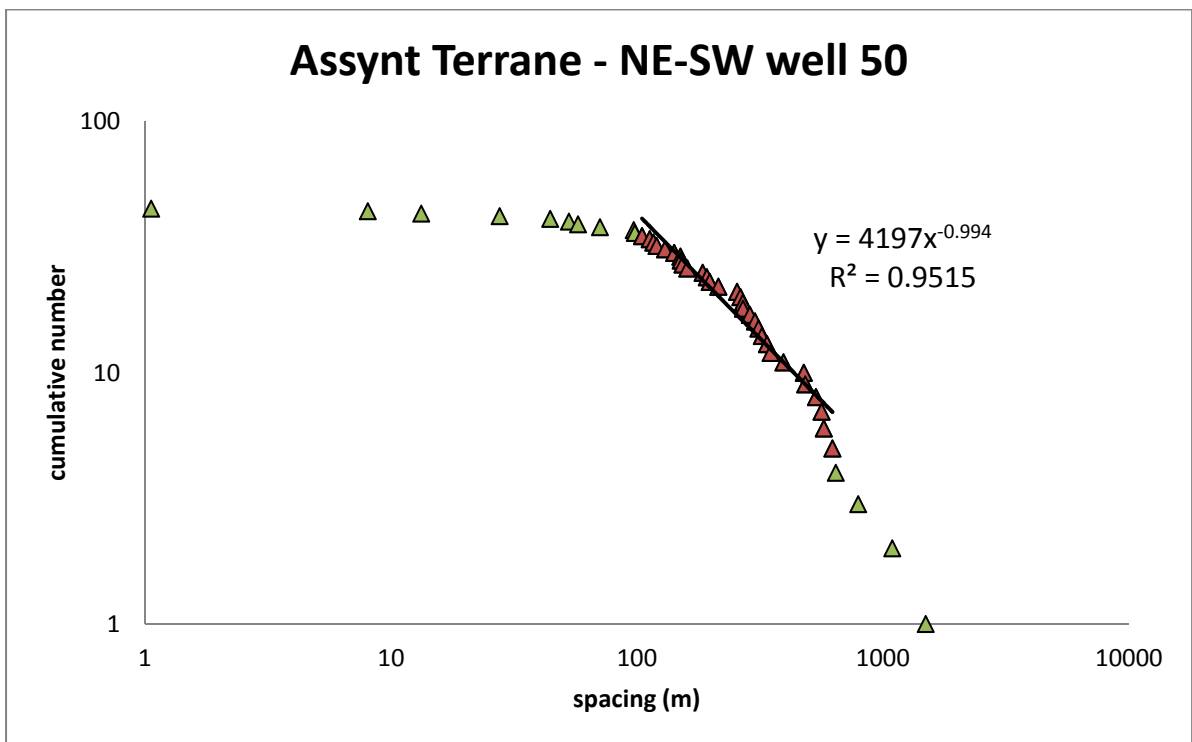
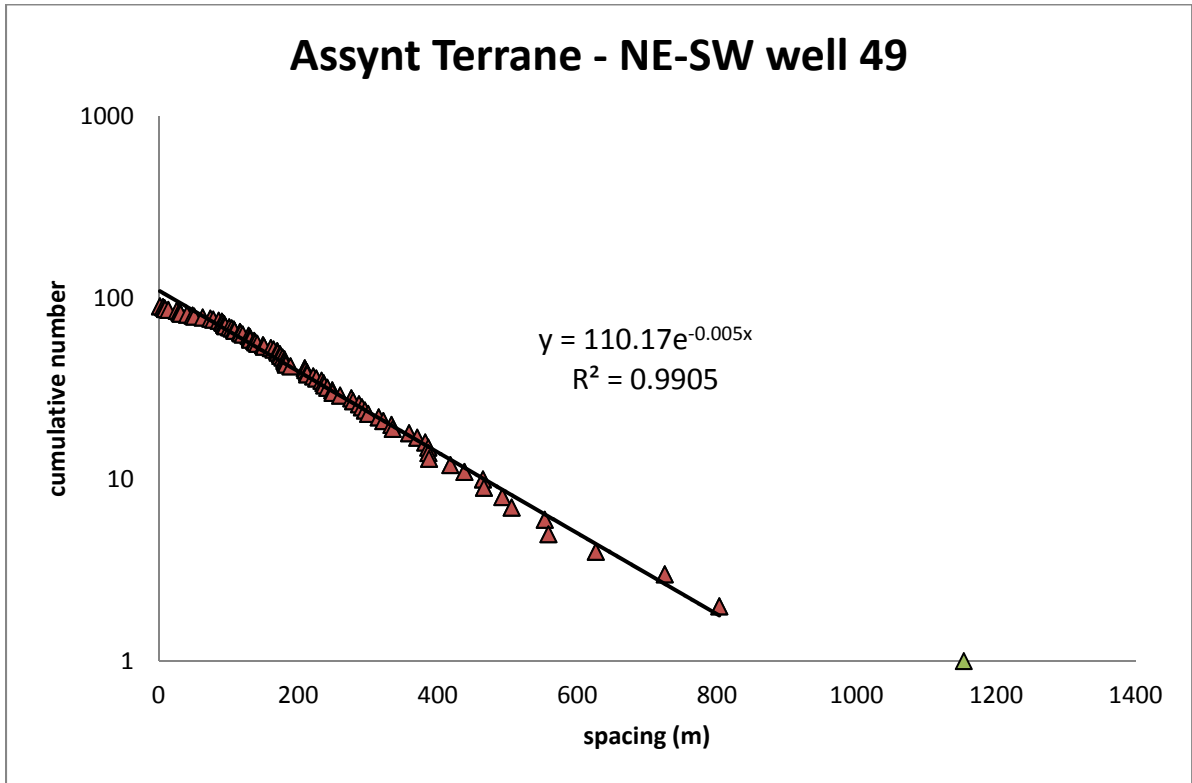


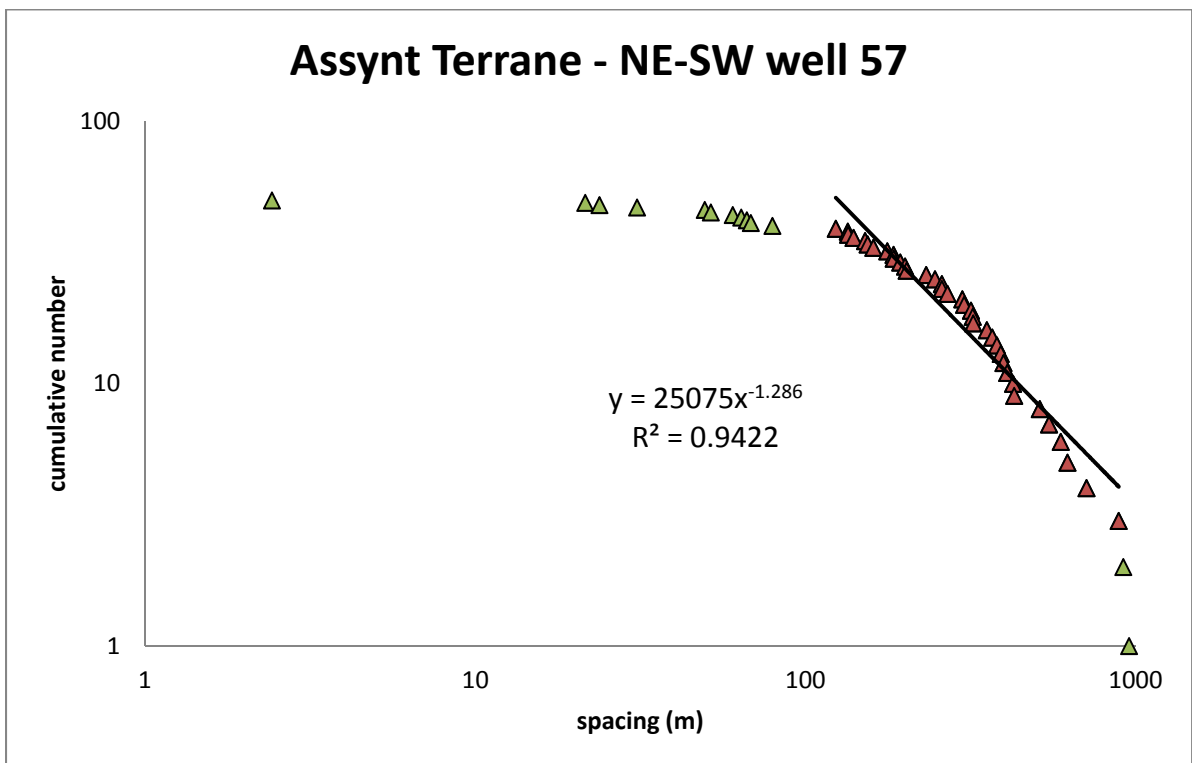
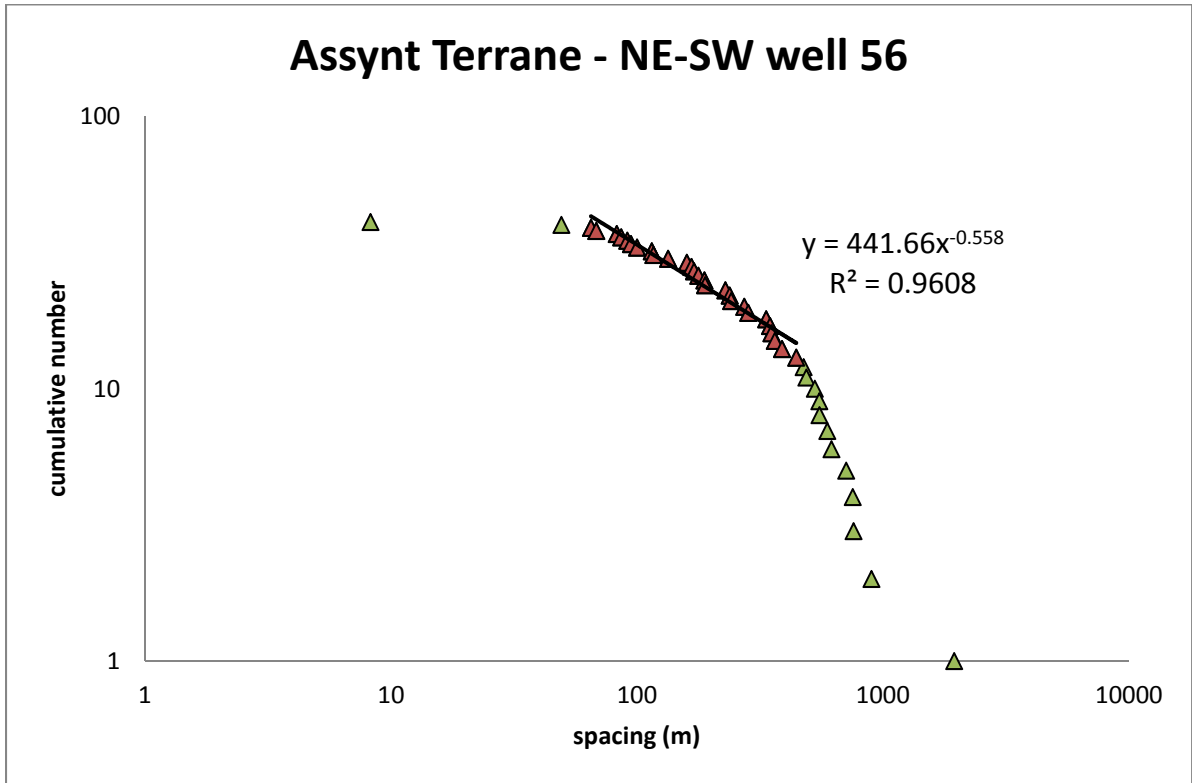




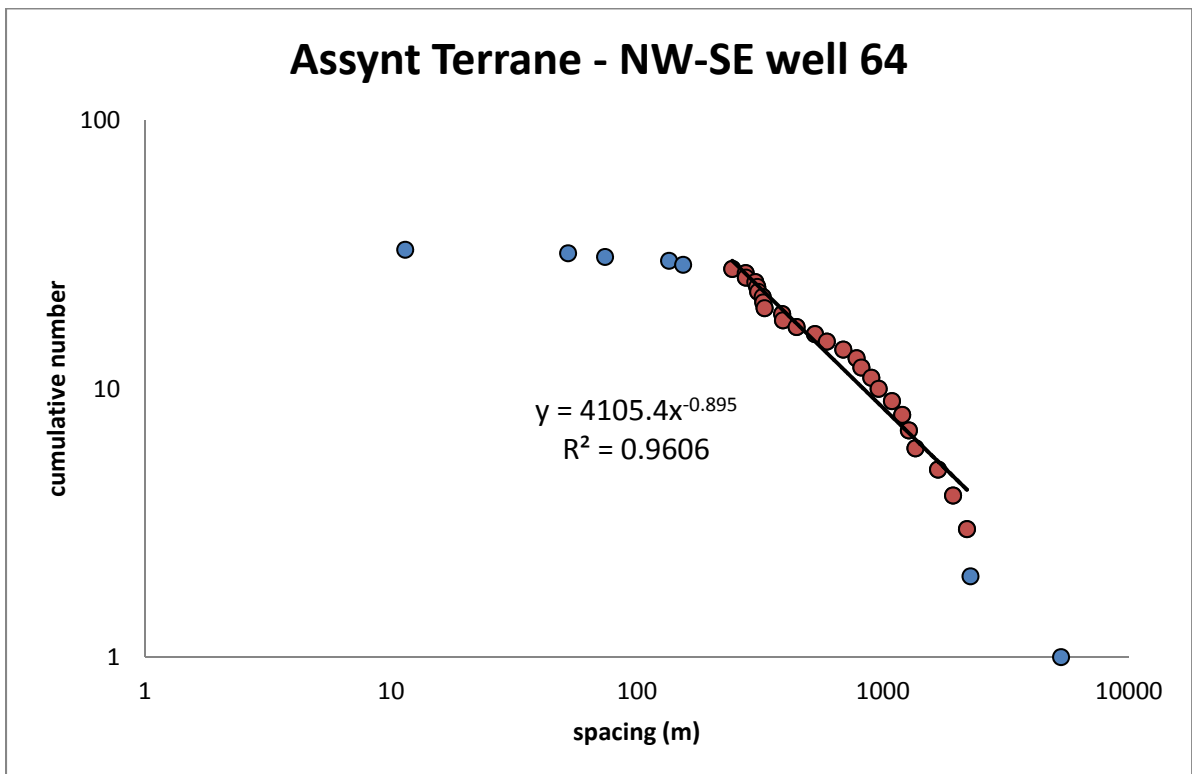
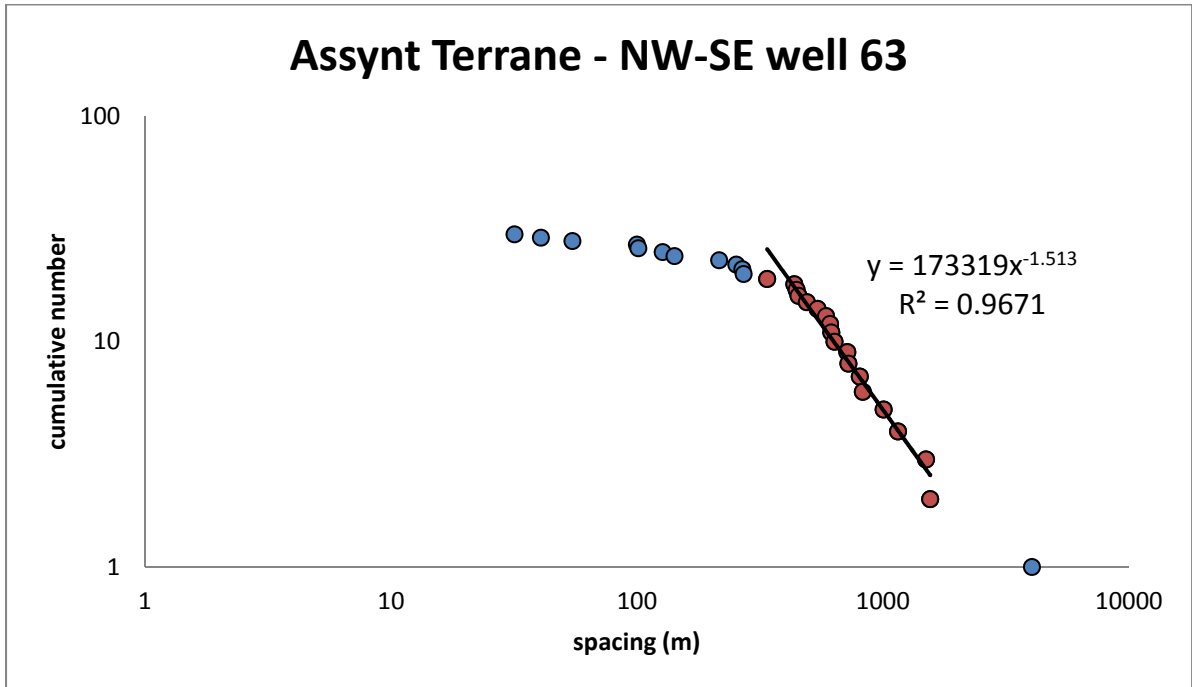


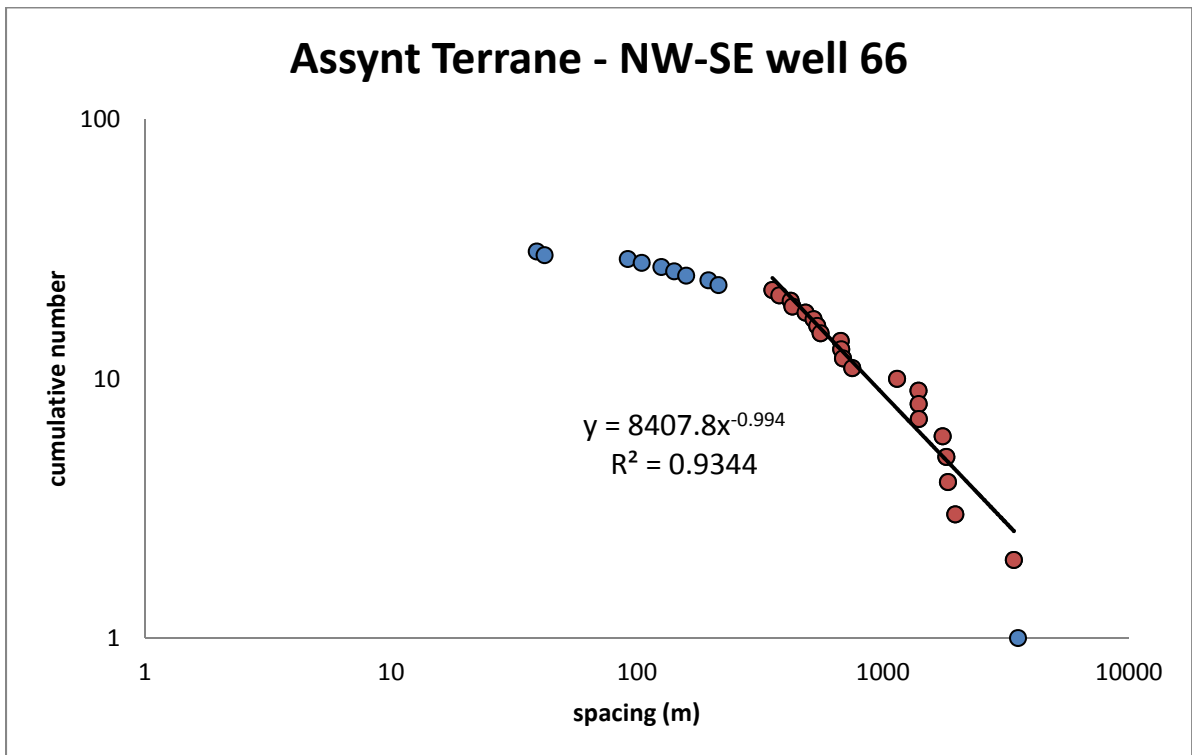
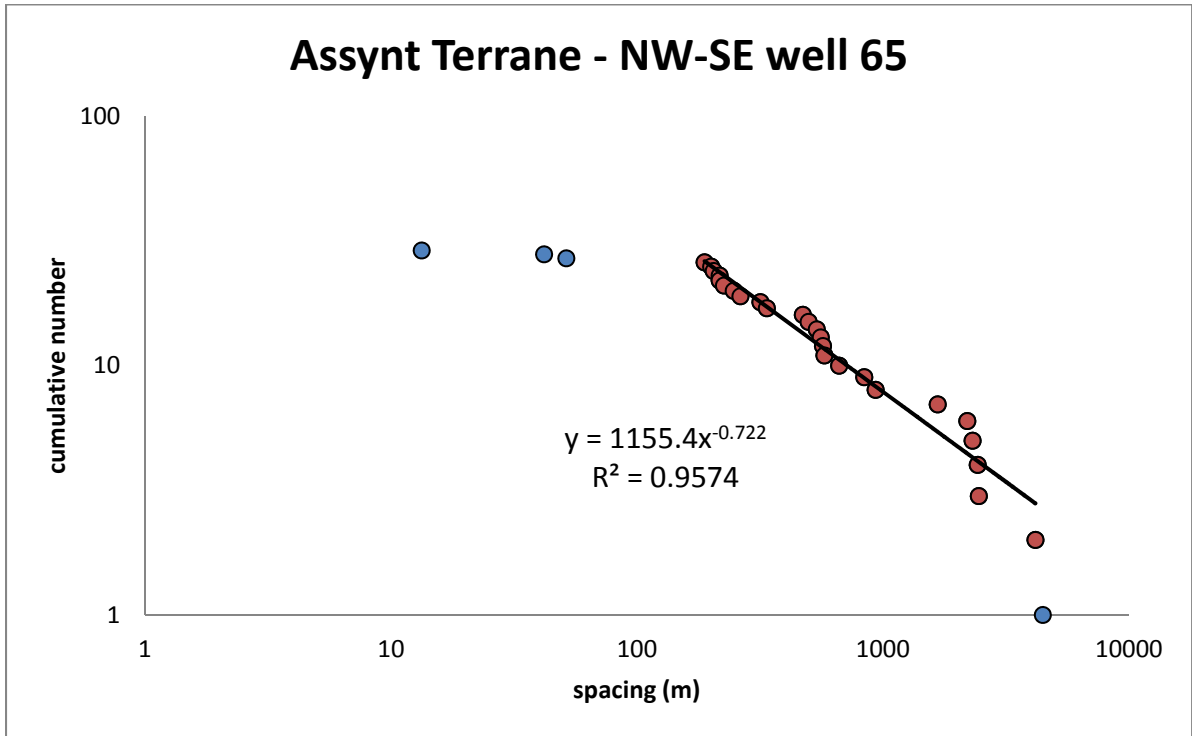




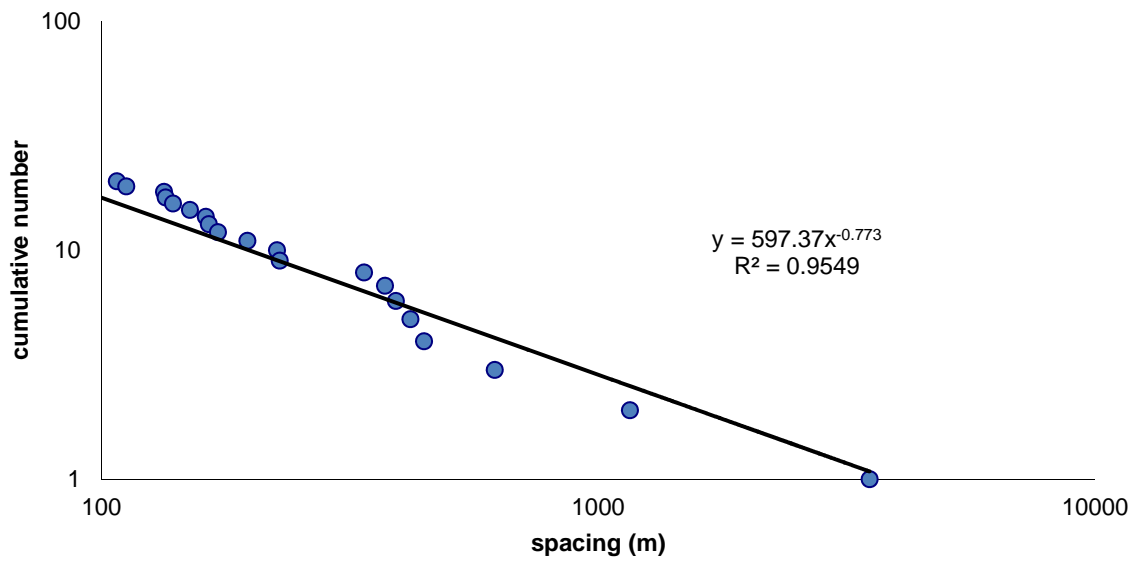




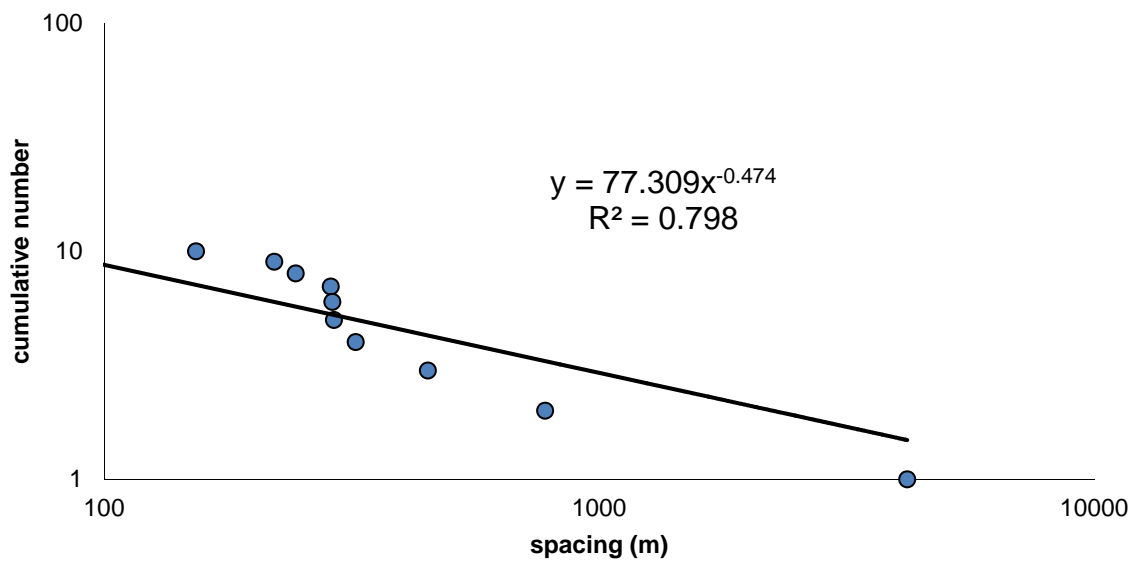




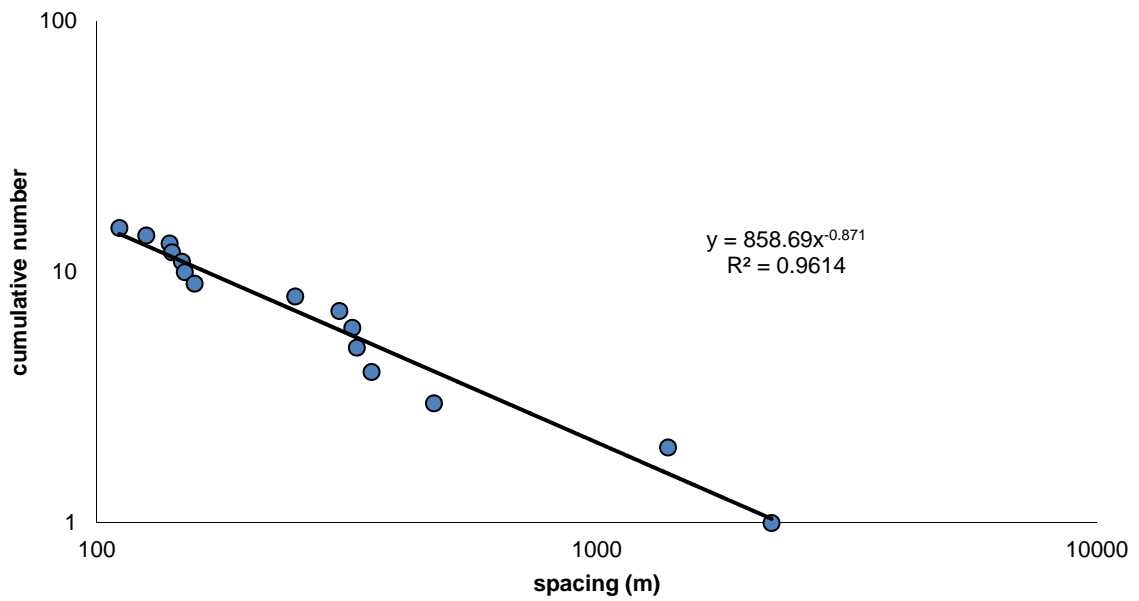
### Rhiconich Terrane - NW-SE well 2



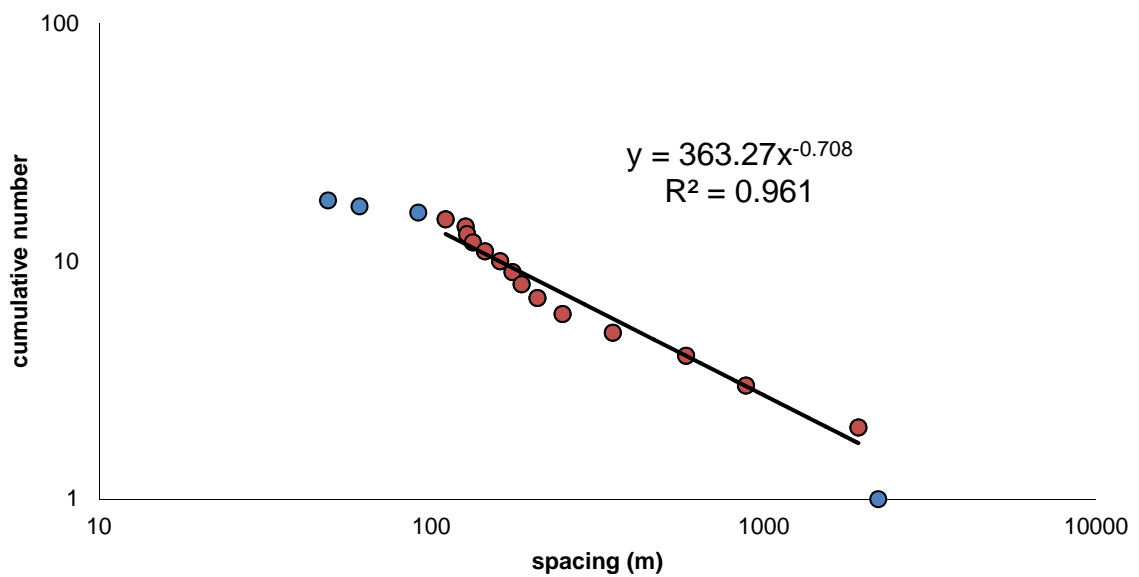
### Rhiconich Terrane - NW-SE well 3

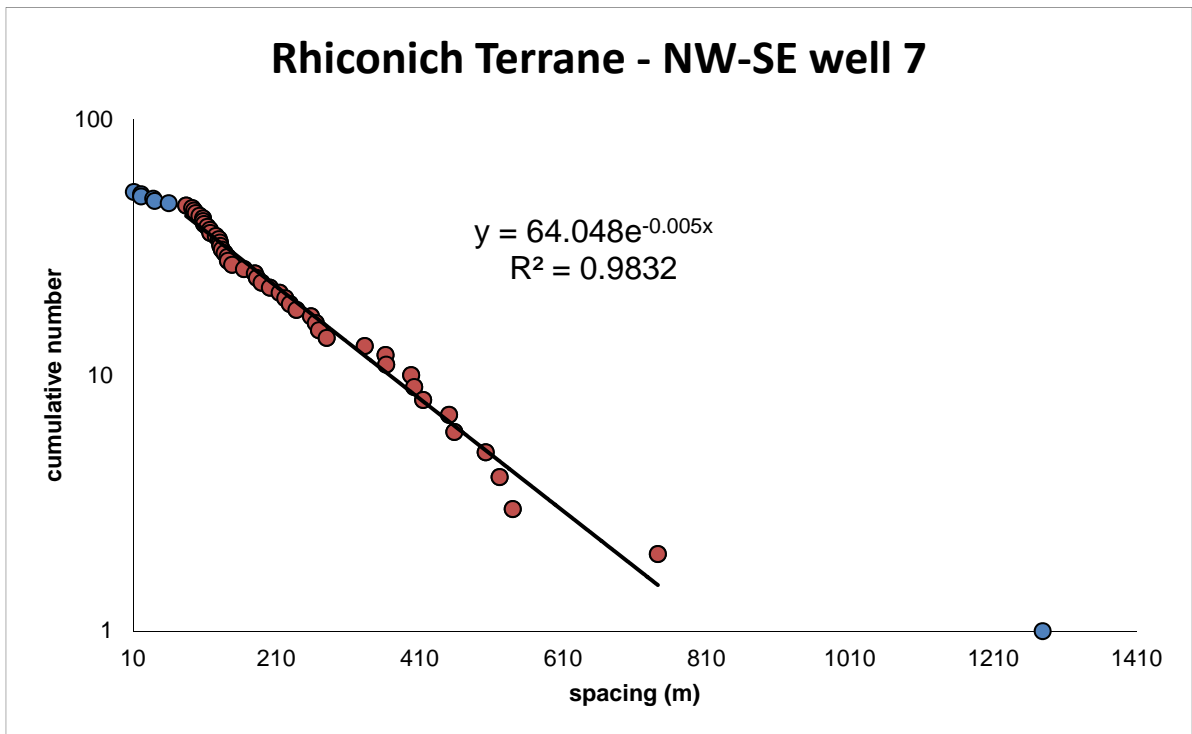
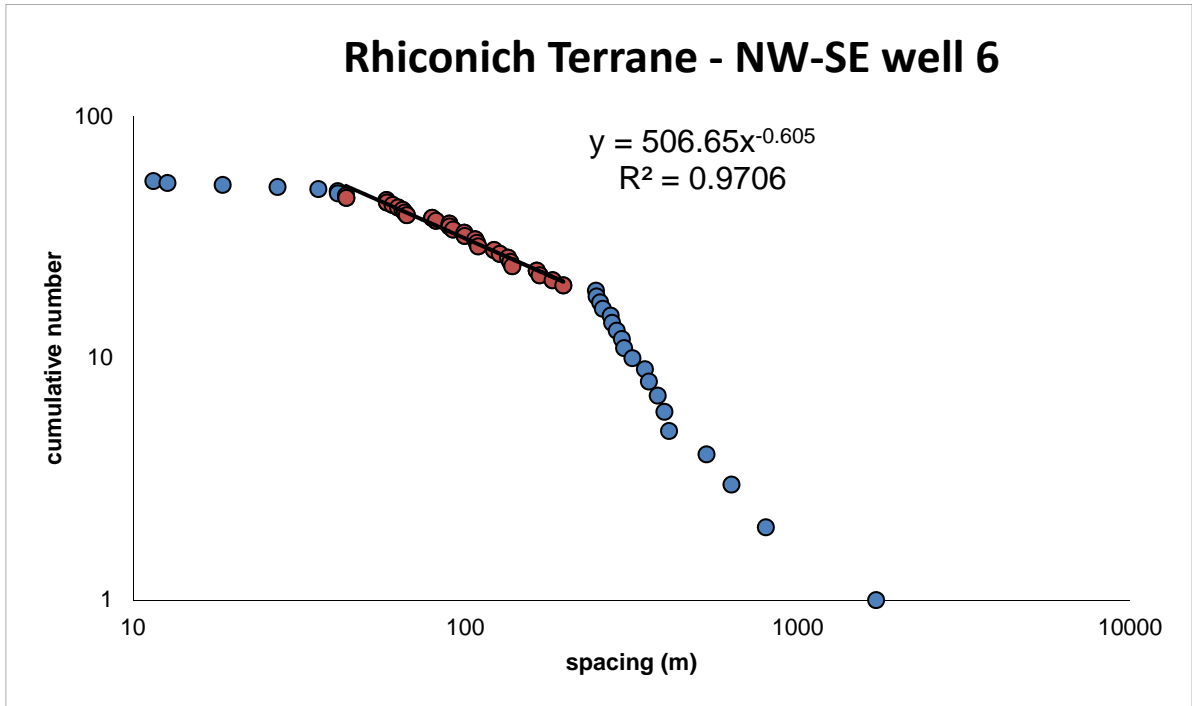


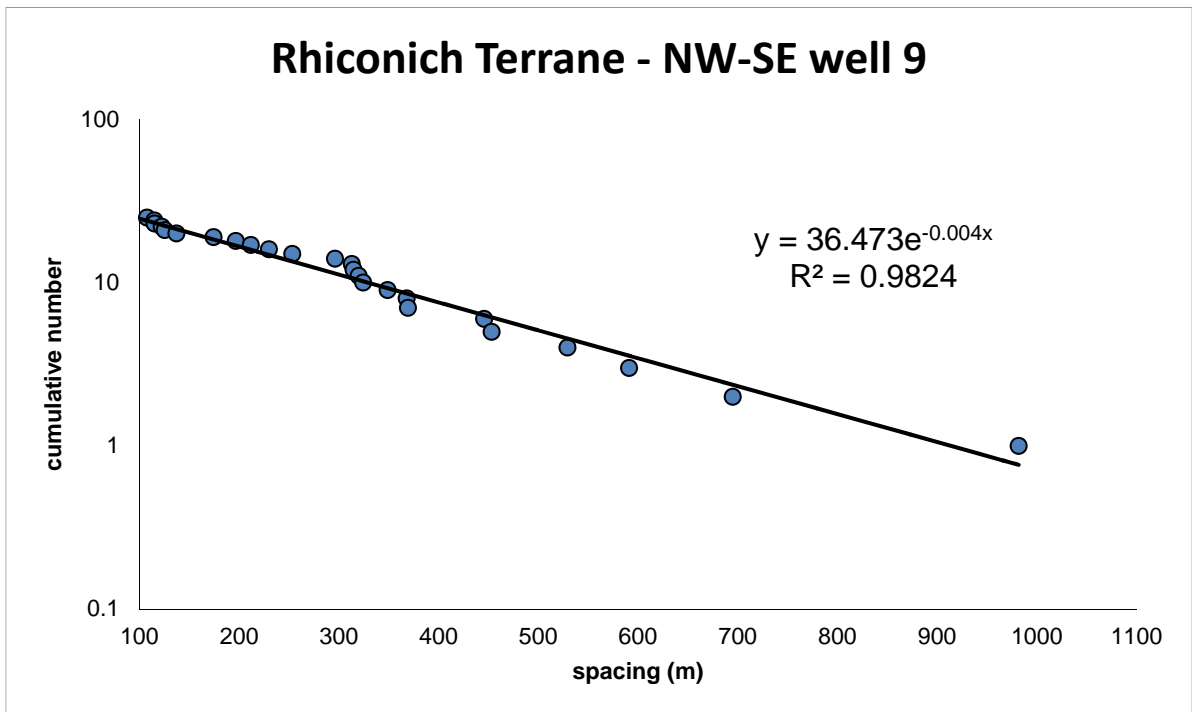
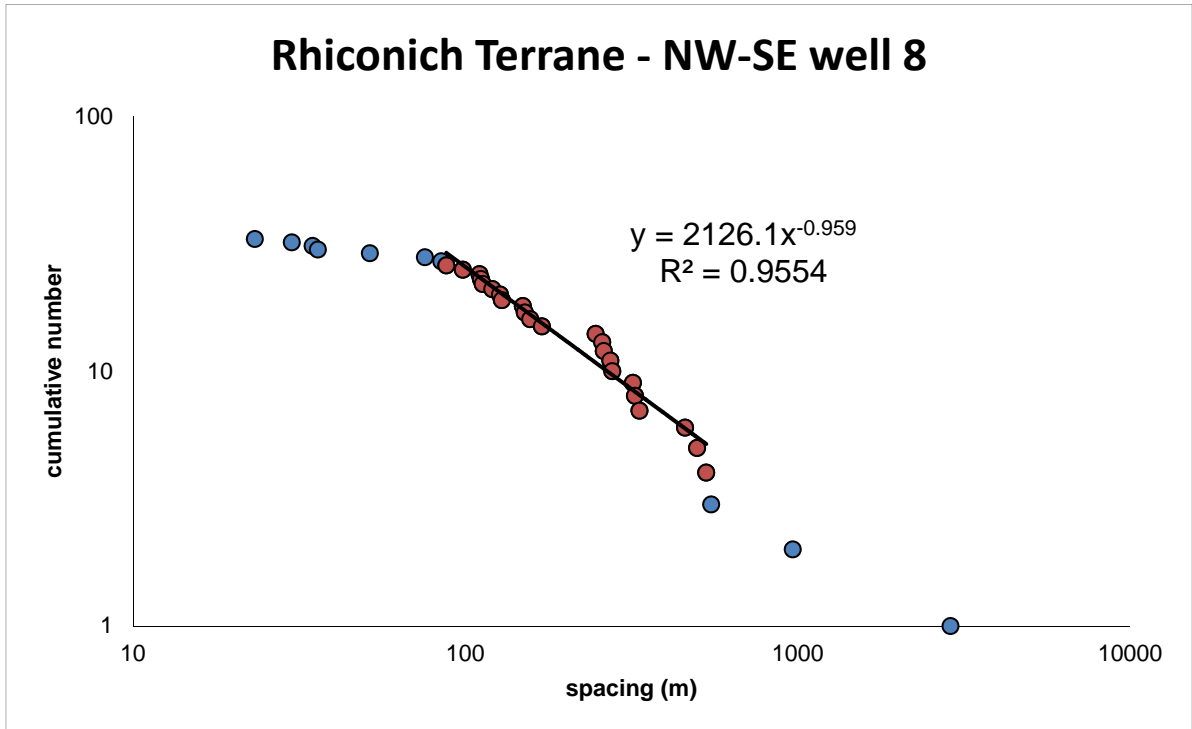
### Rhiconich Terrane - NW-SE well 4

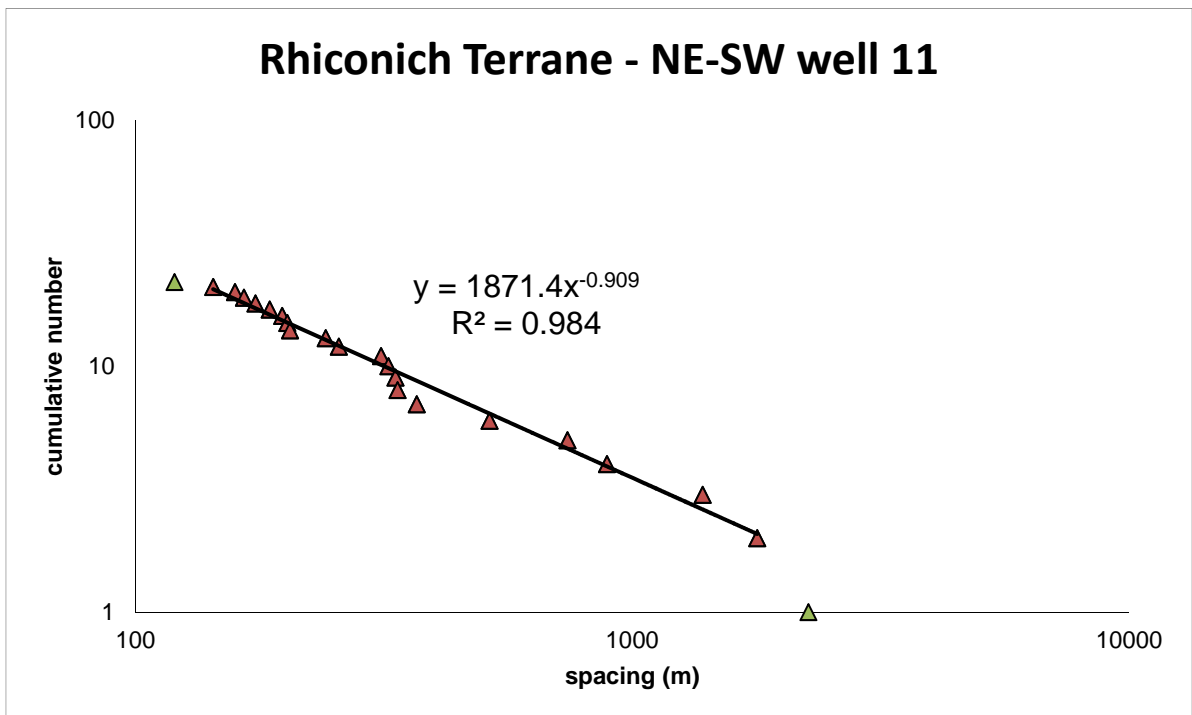
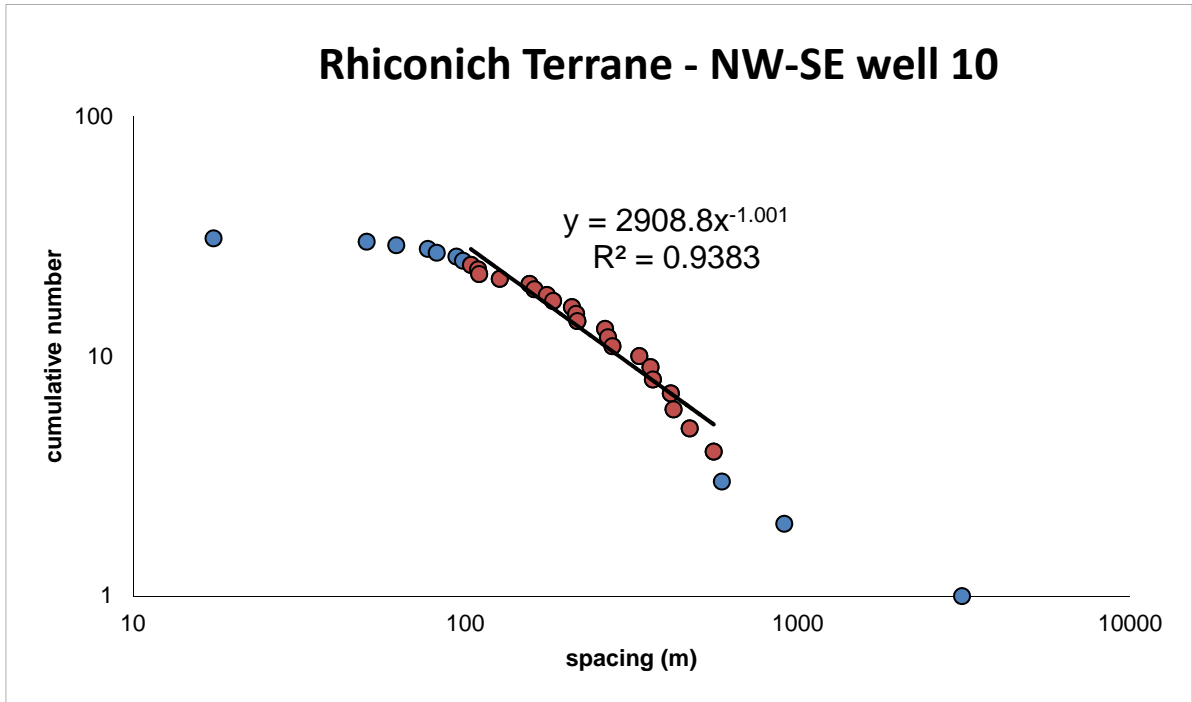


### Rhiconich Terrane - NW-SE well 5

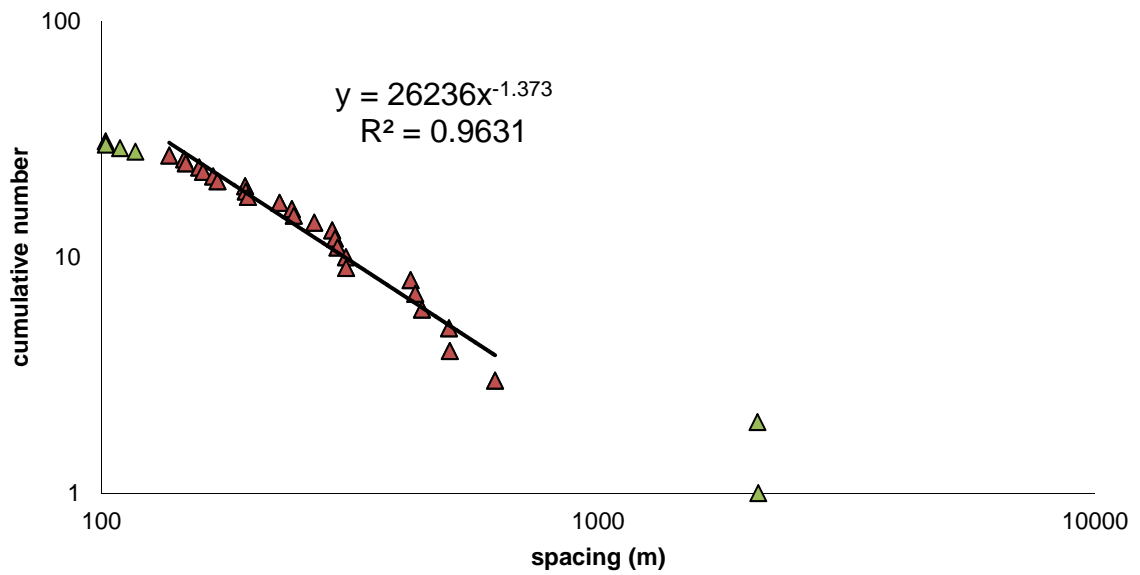




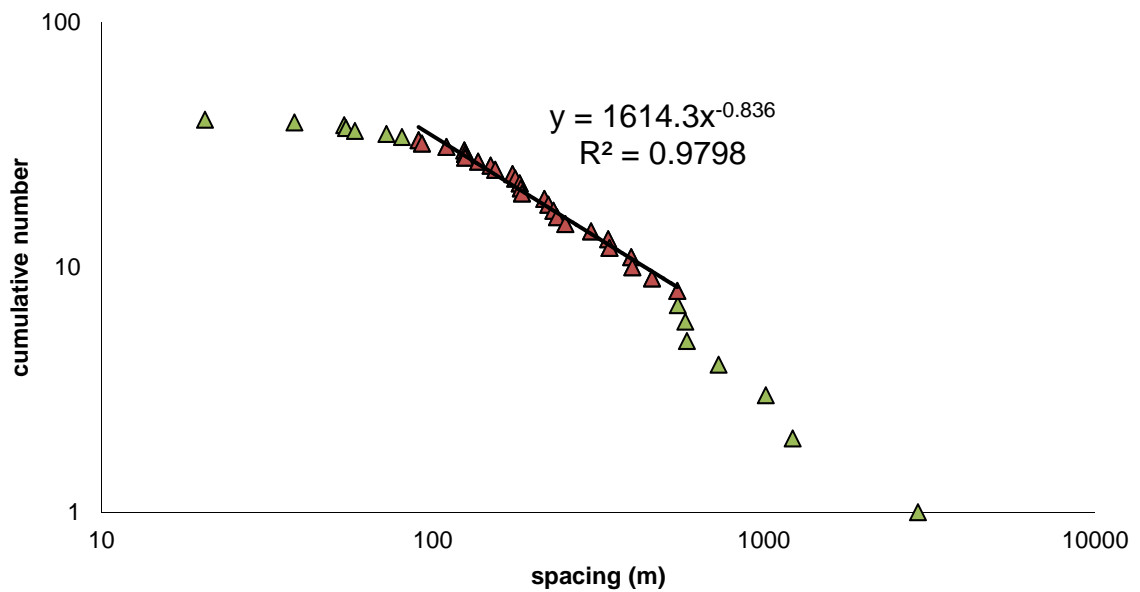




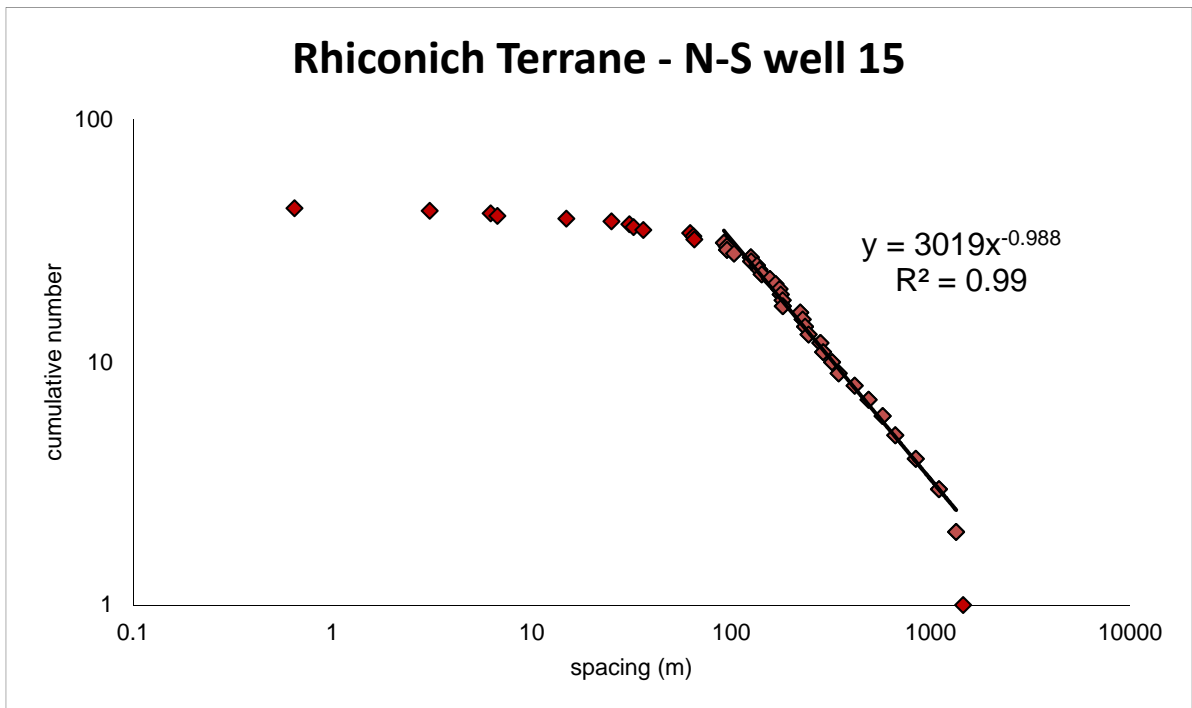
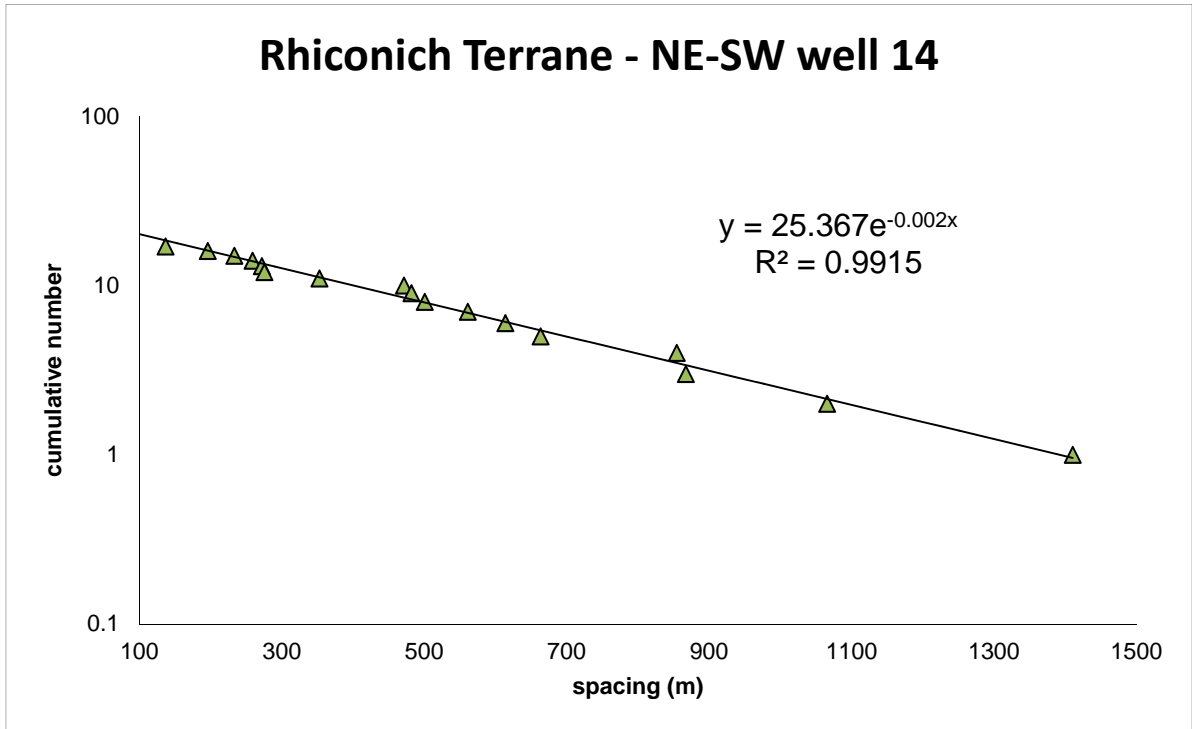
### Rhiconich Terrane - NE-SW well 12

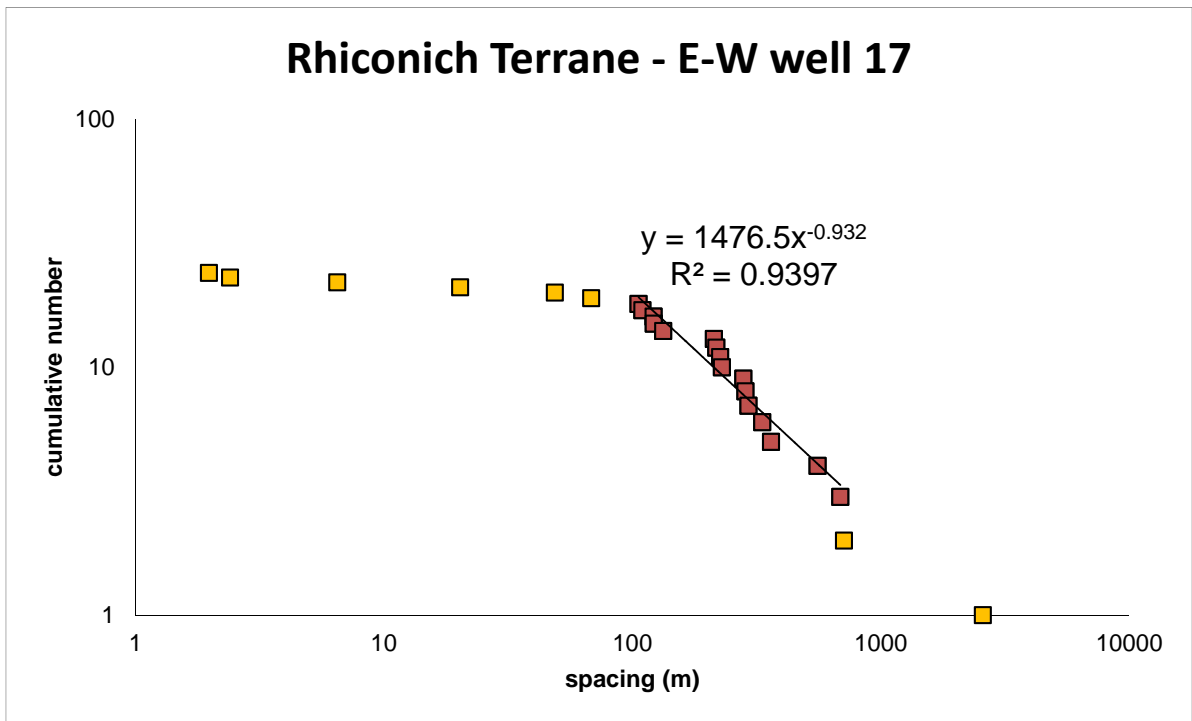
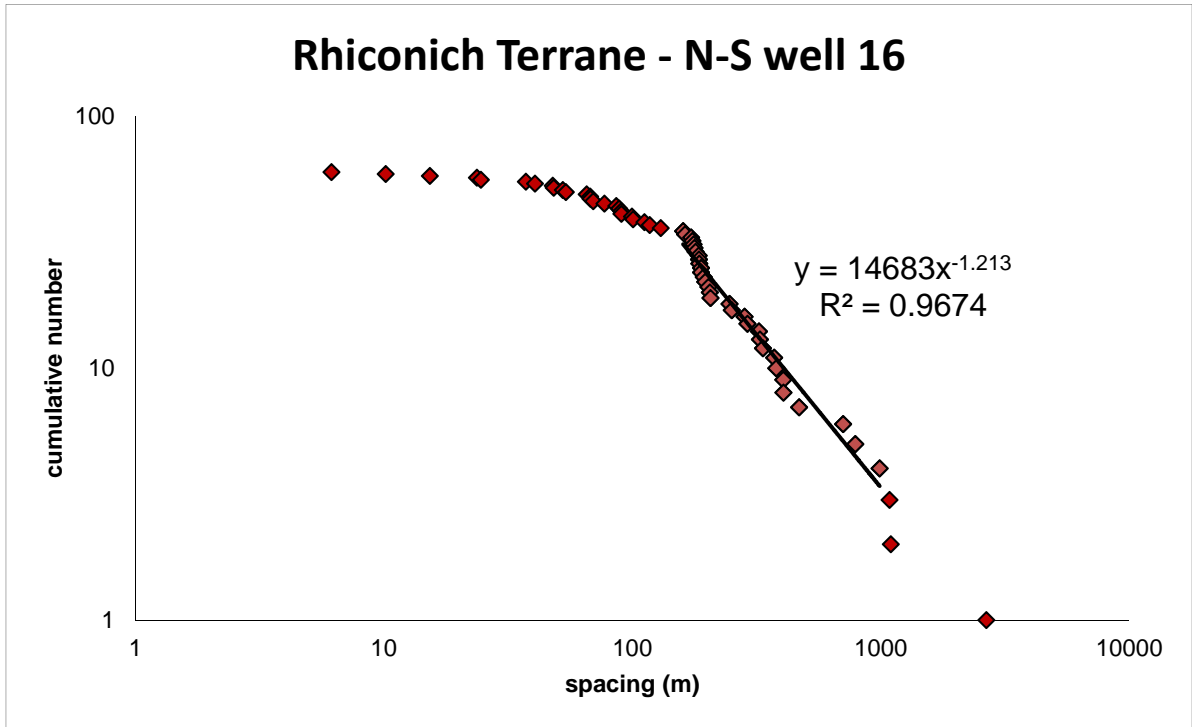


### Rhiconich Terrane - NE-SW well 13

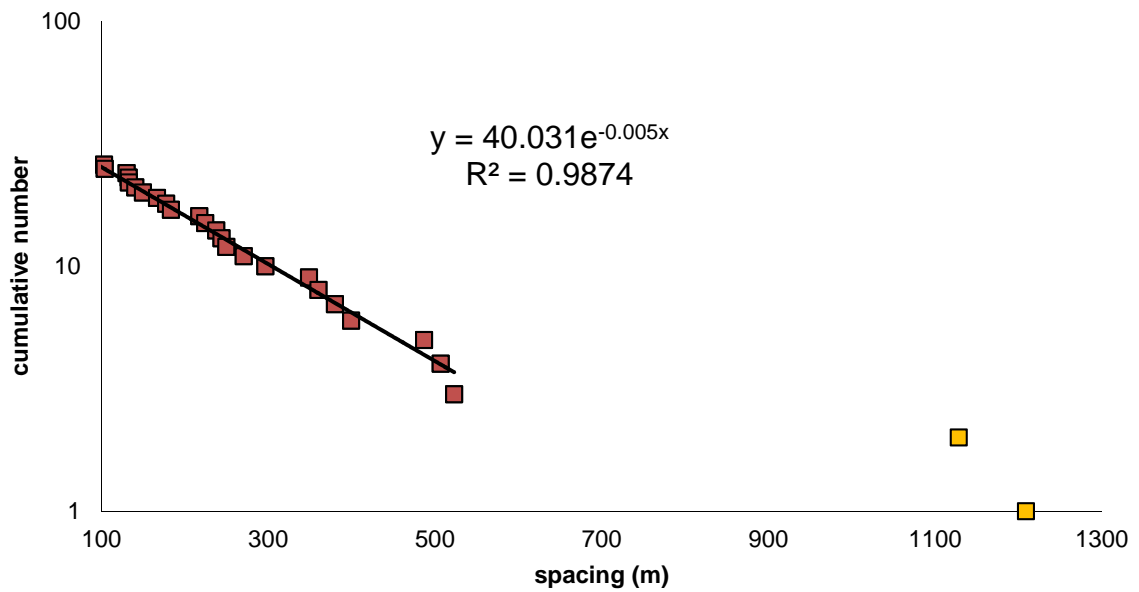




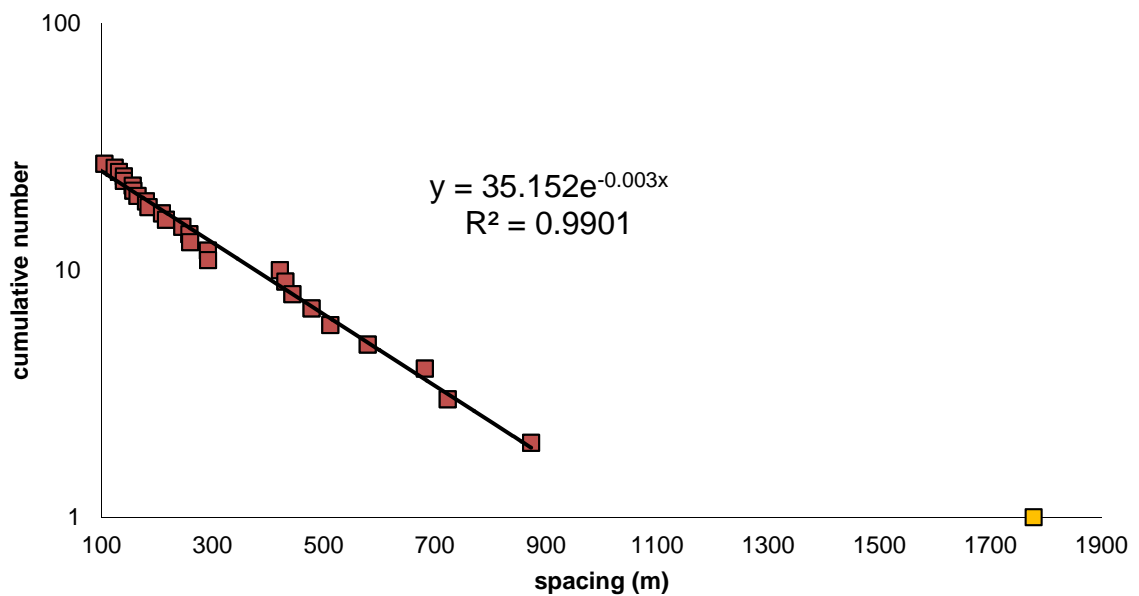


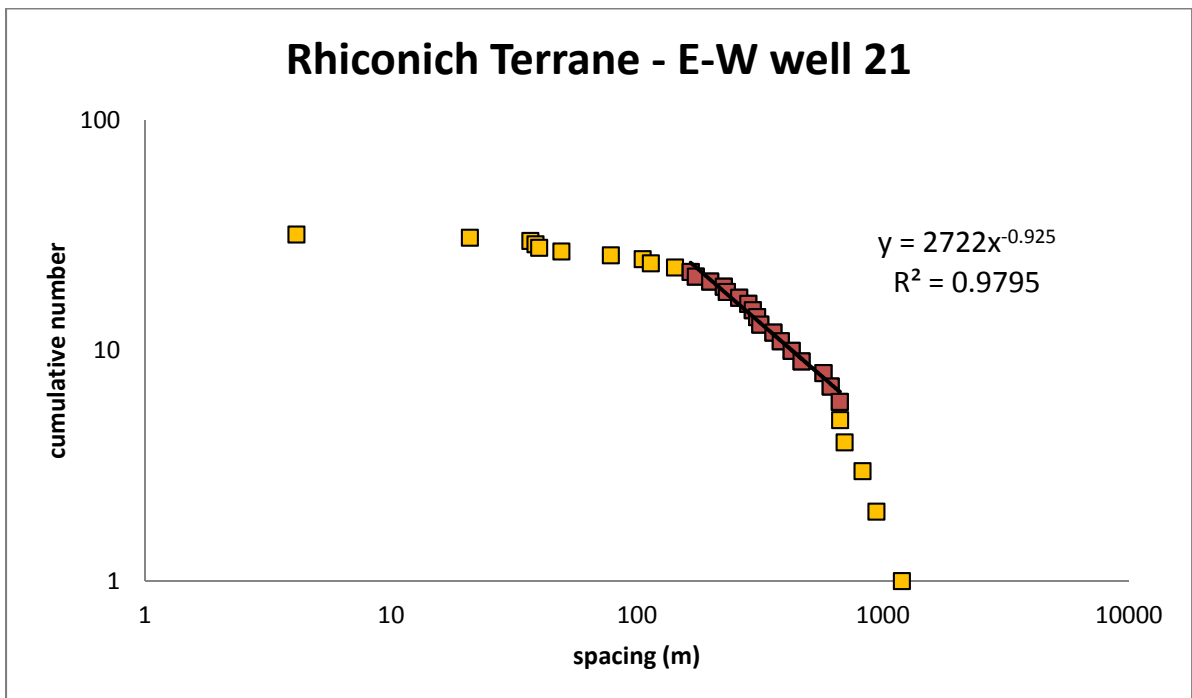
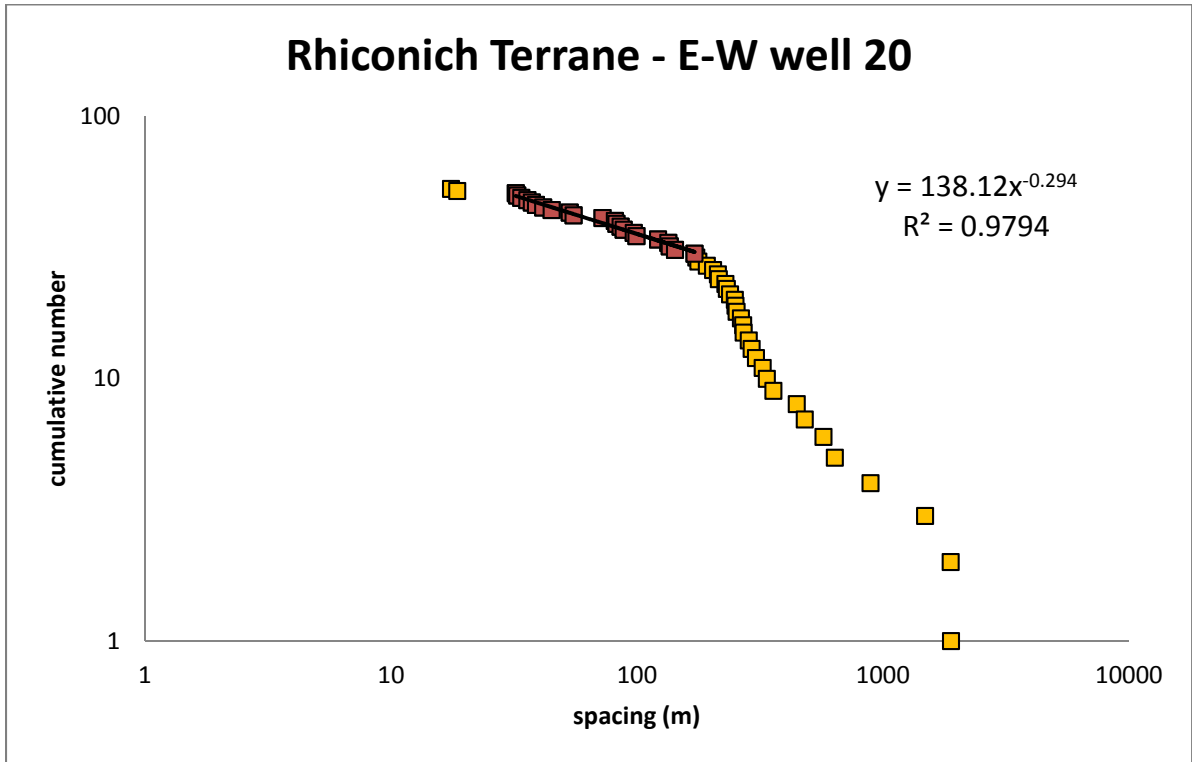


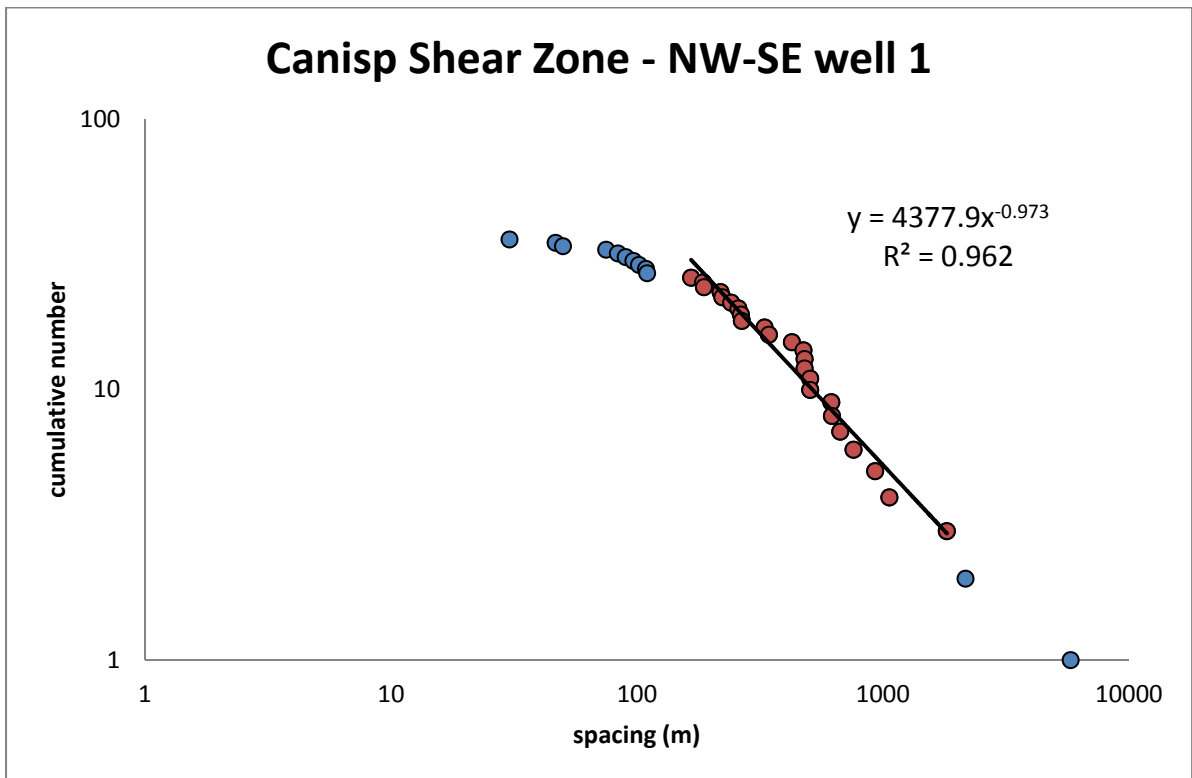
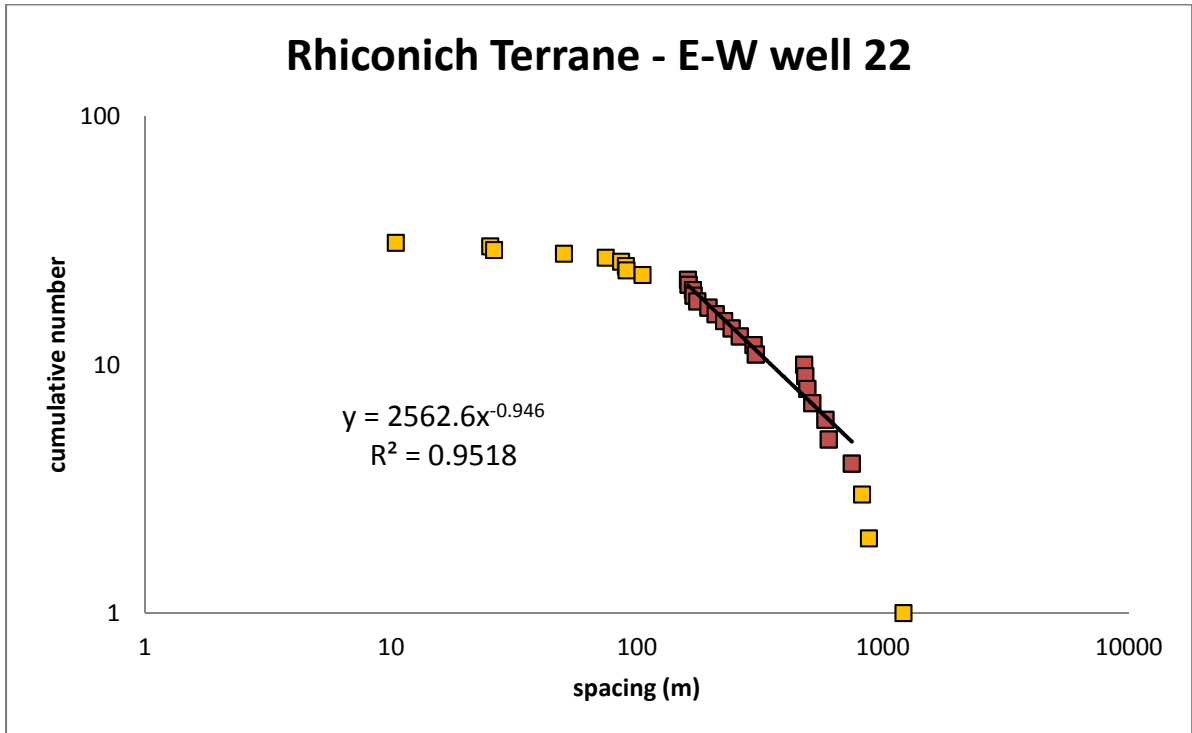
### Rhiconich Terrane - E-W well 18

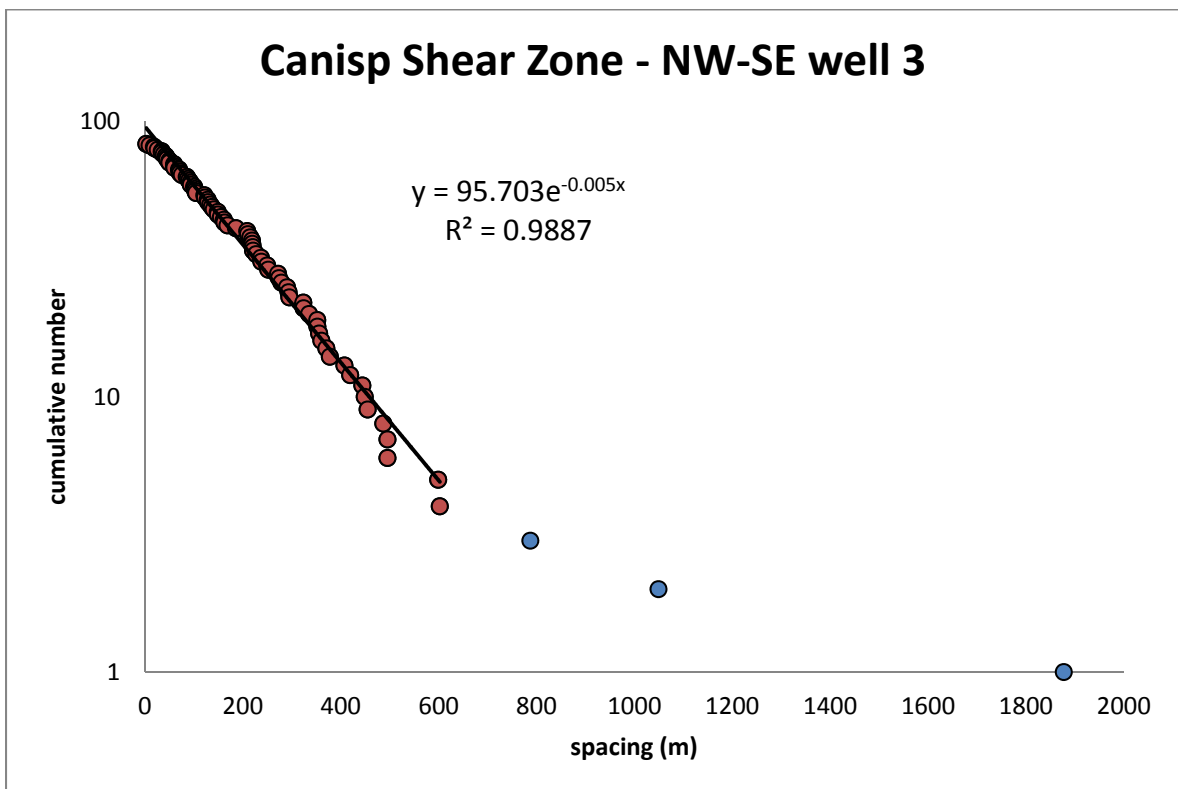
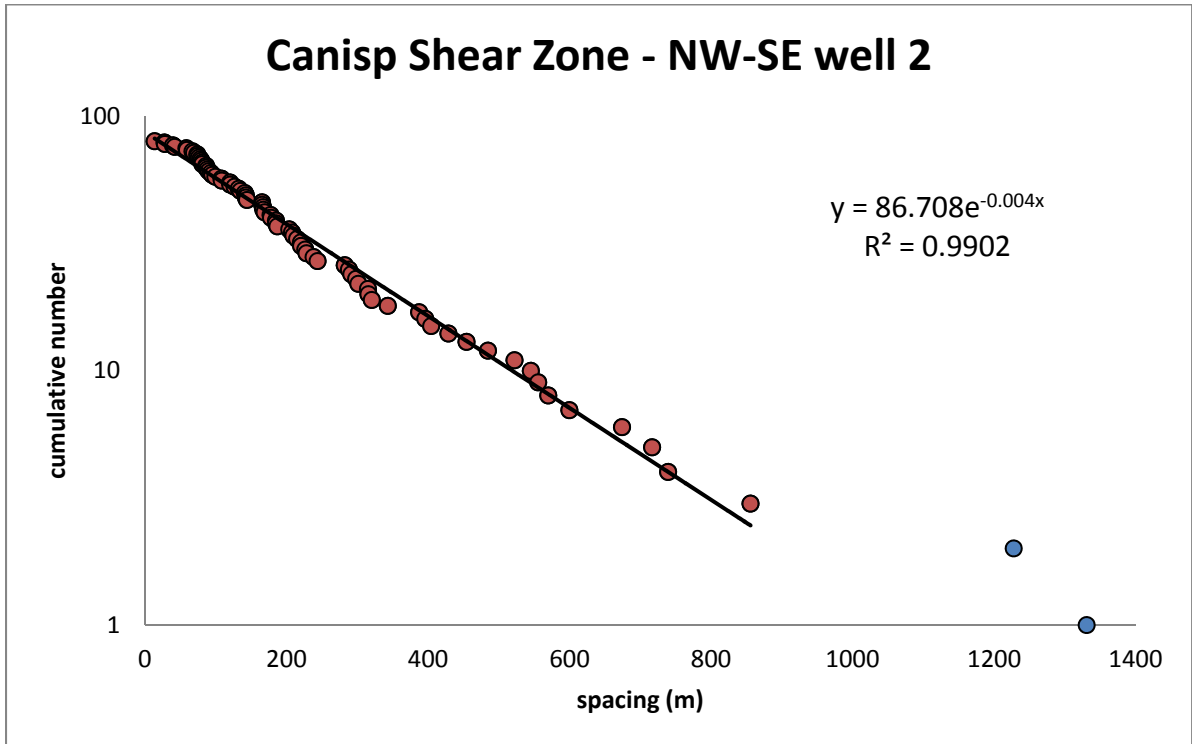


### Rhiconich Terrane - E-W well 19

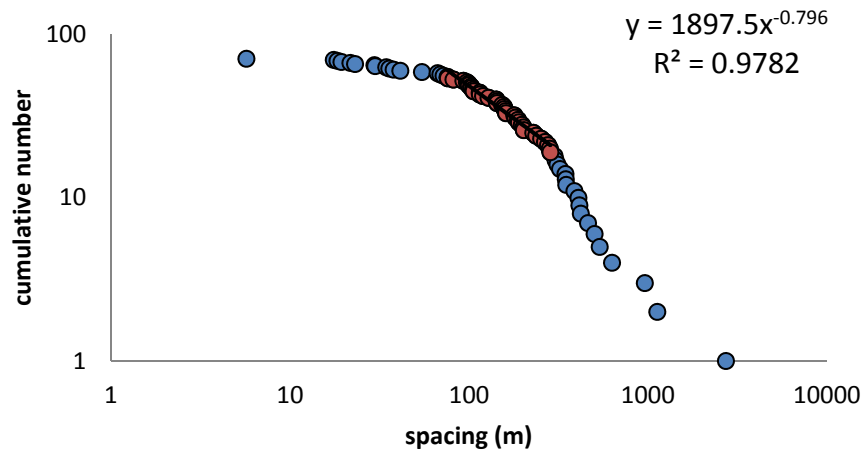




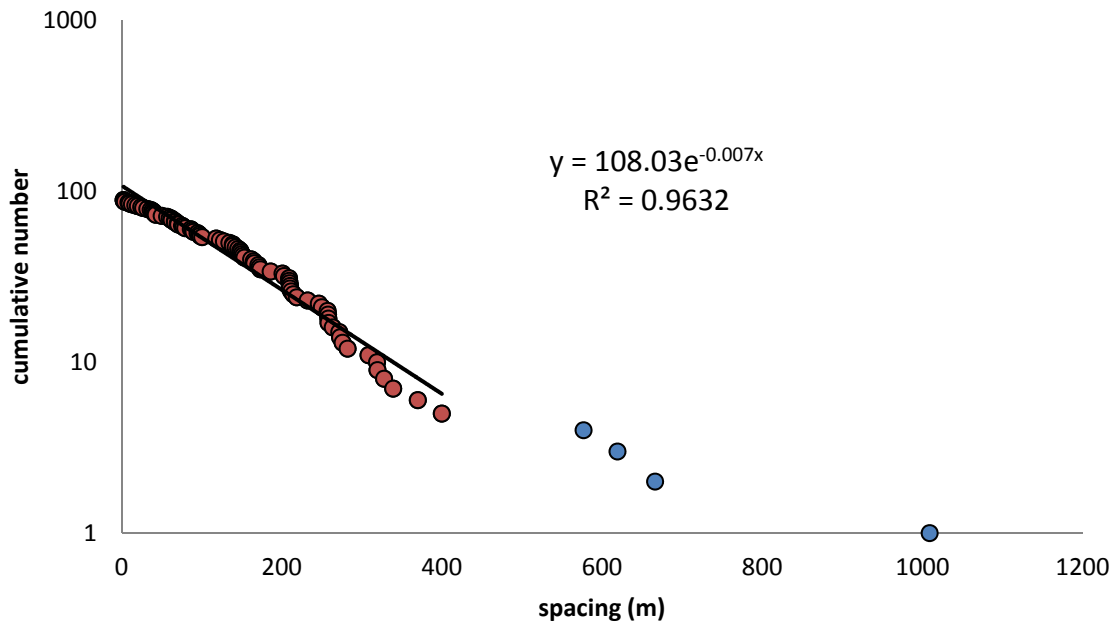


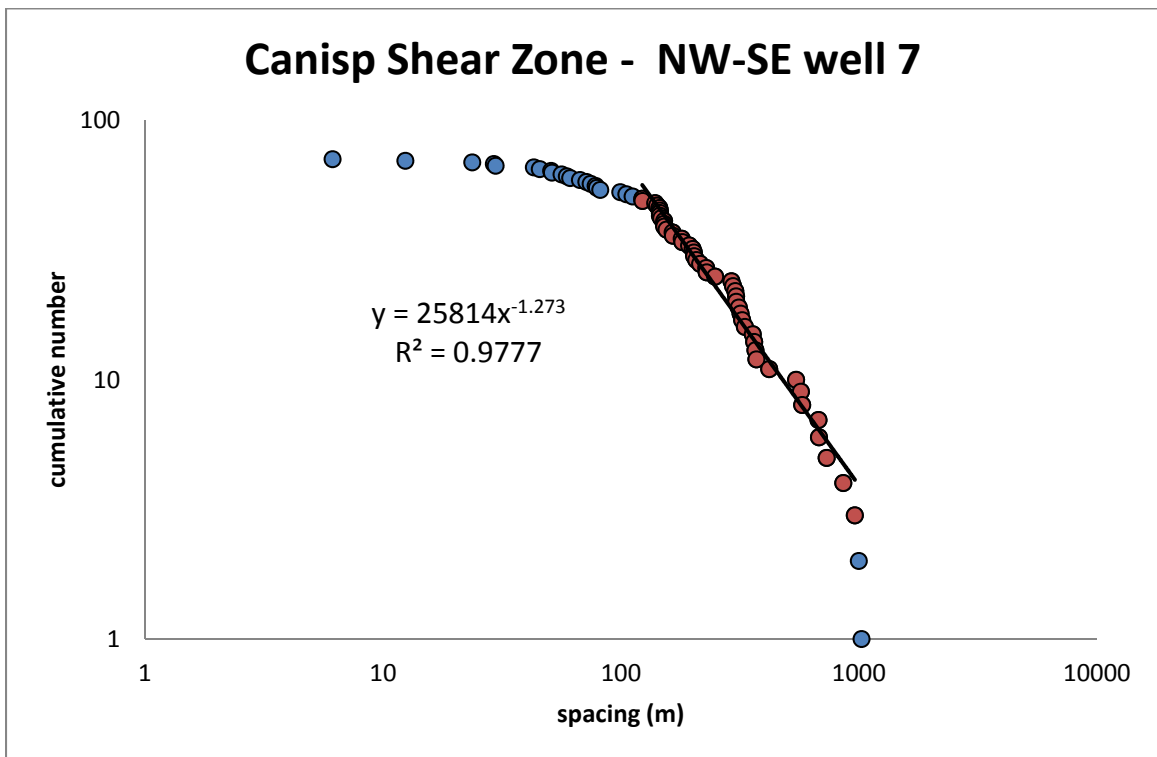
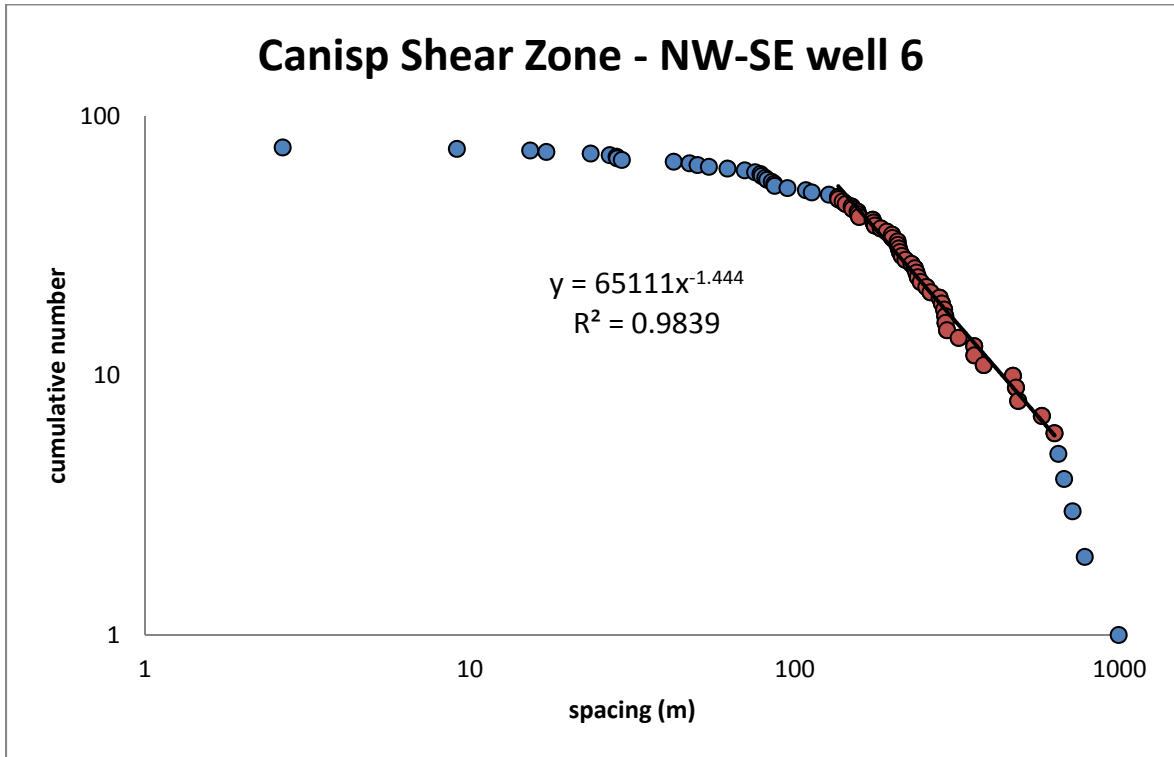


### Canisp Shear Zone - NW-SE well 4

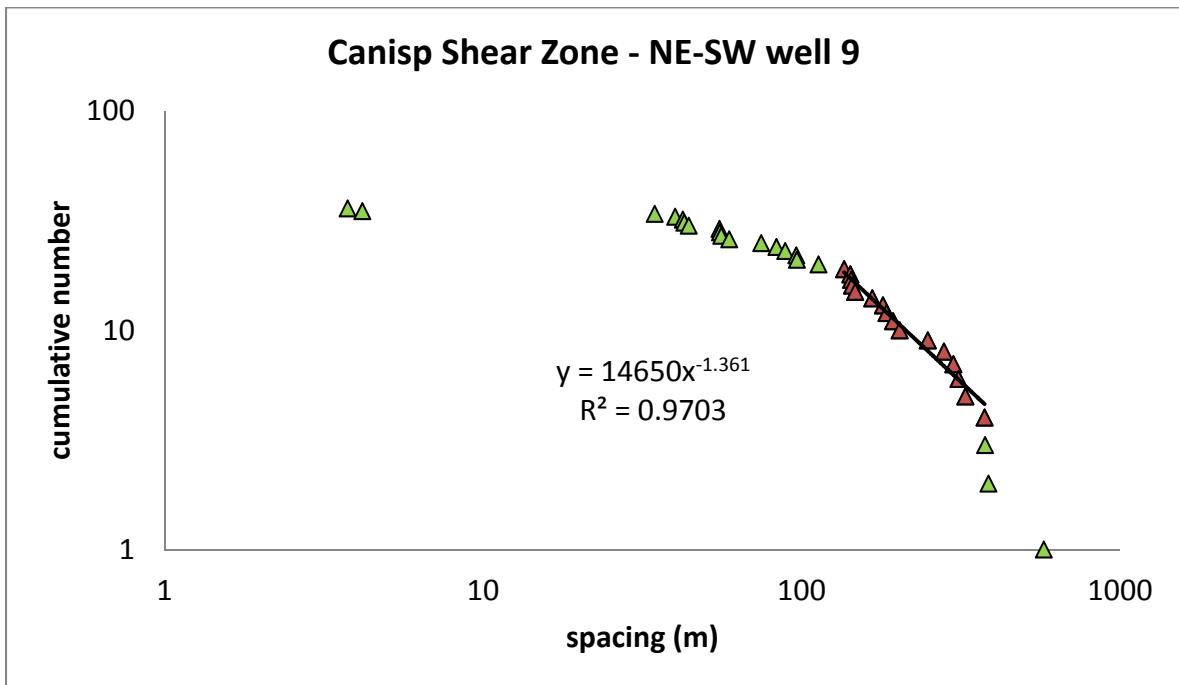
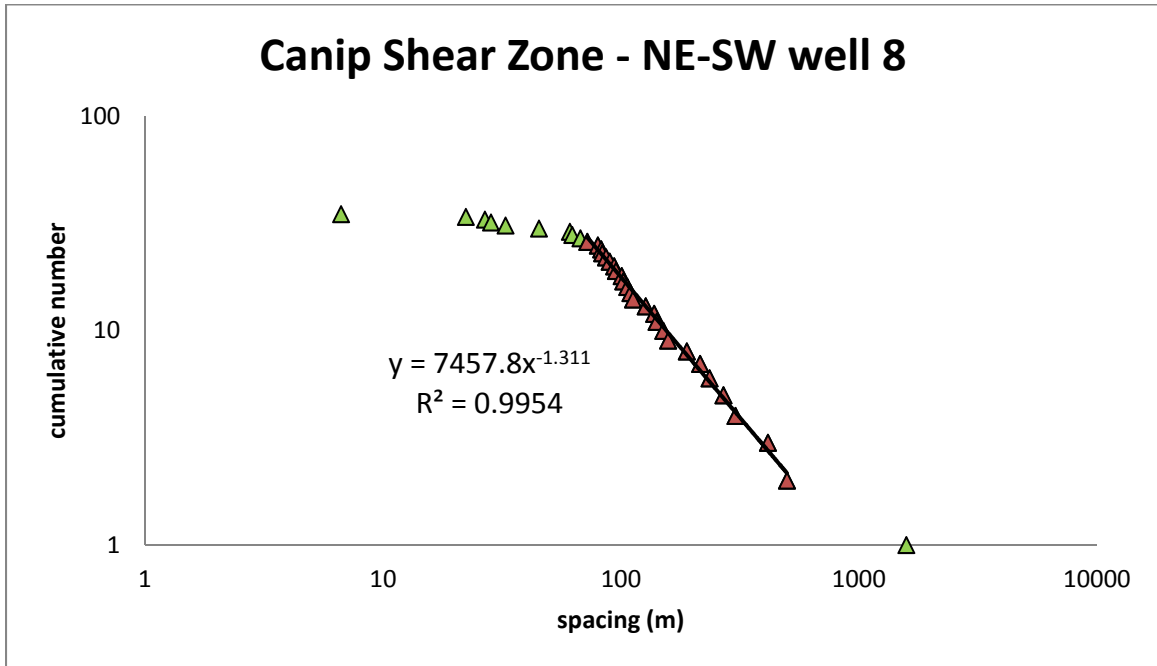


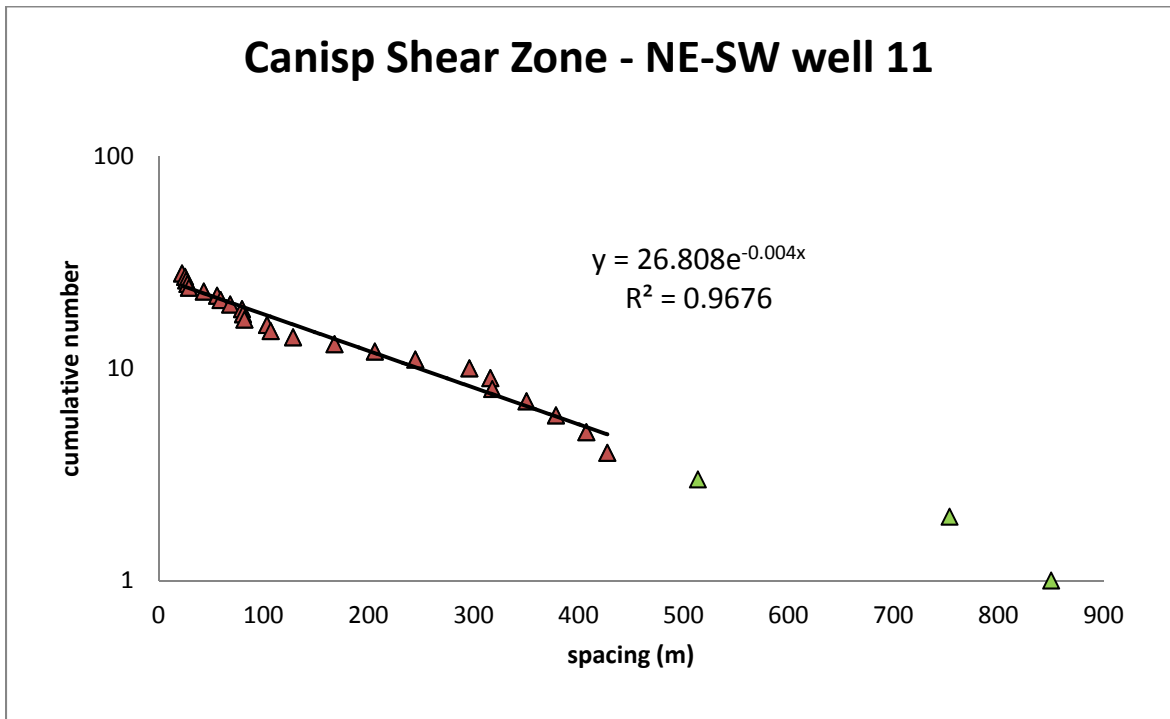
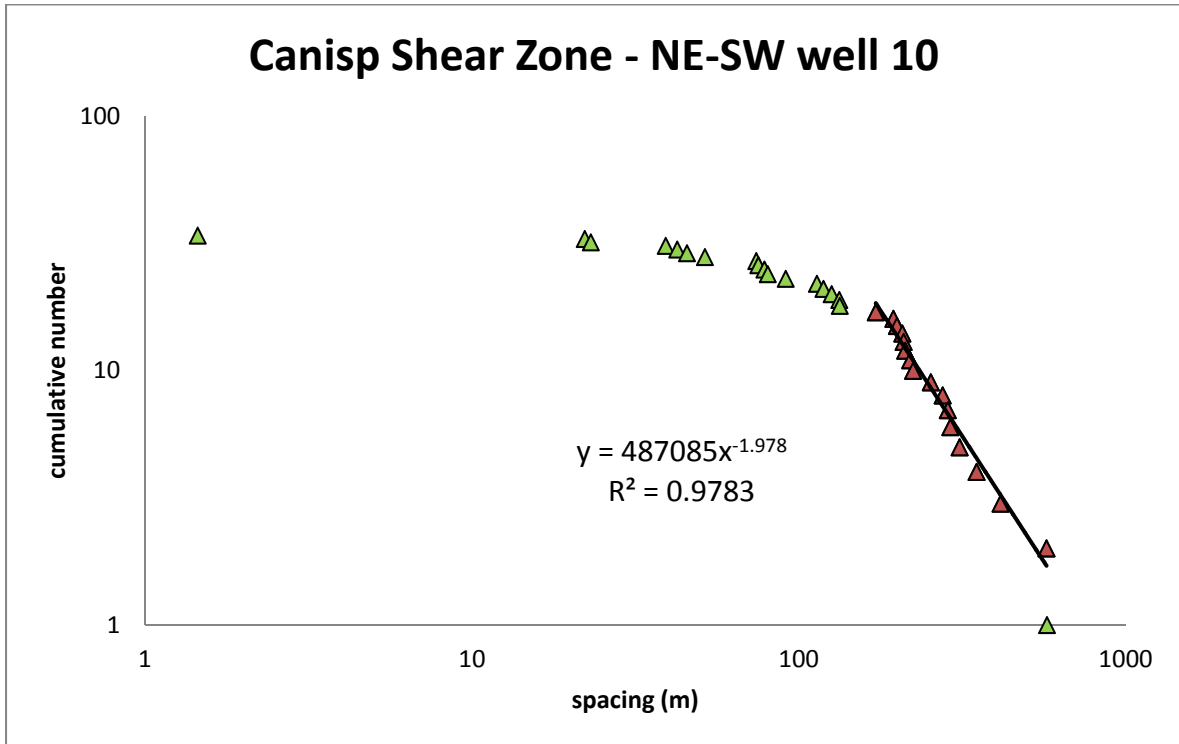
### Canisp Shear Zone - NW-SE well 5

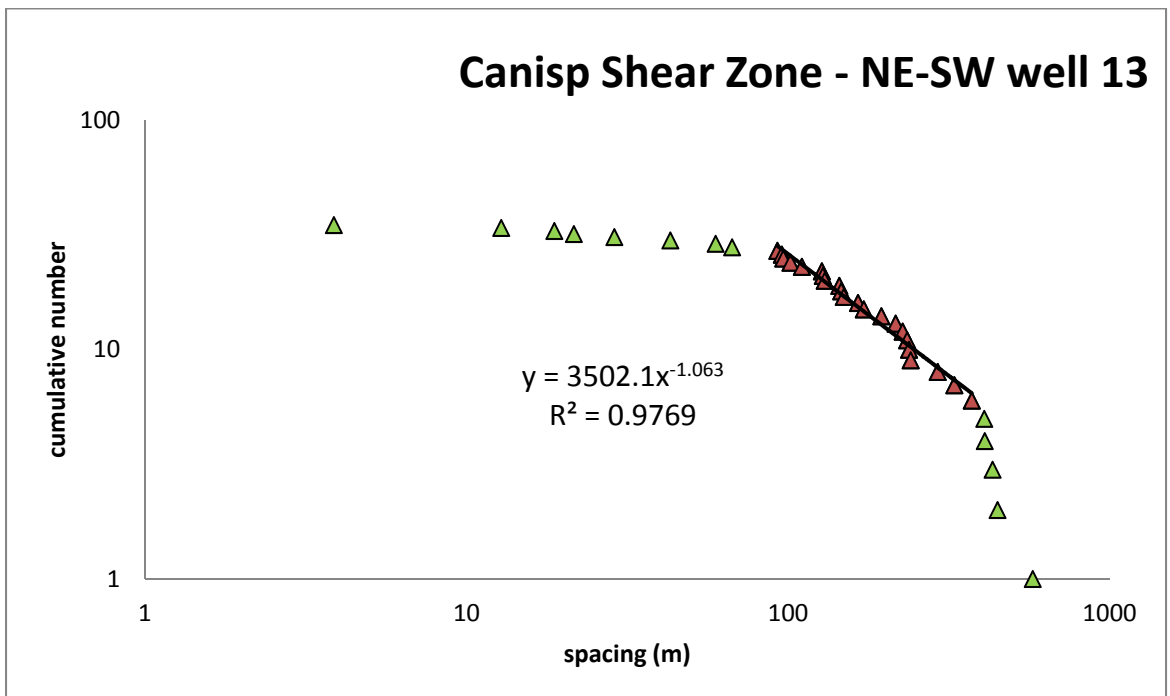
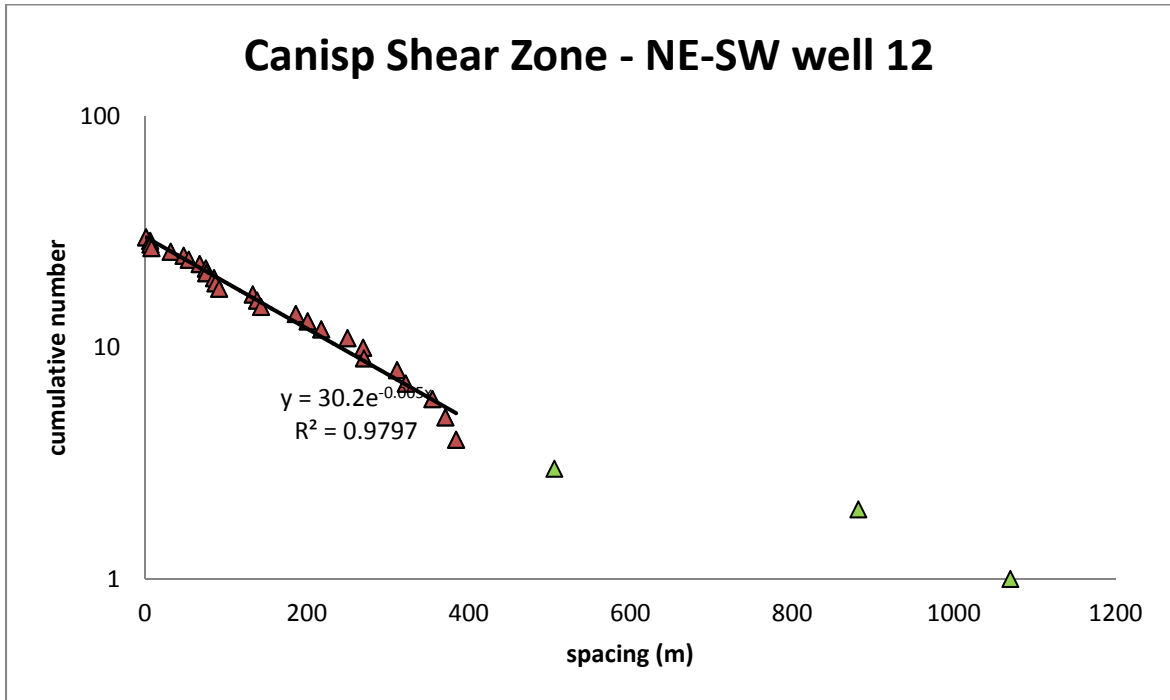


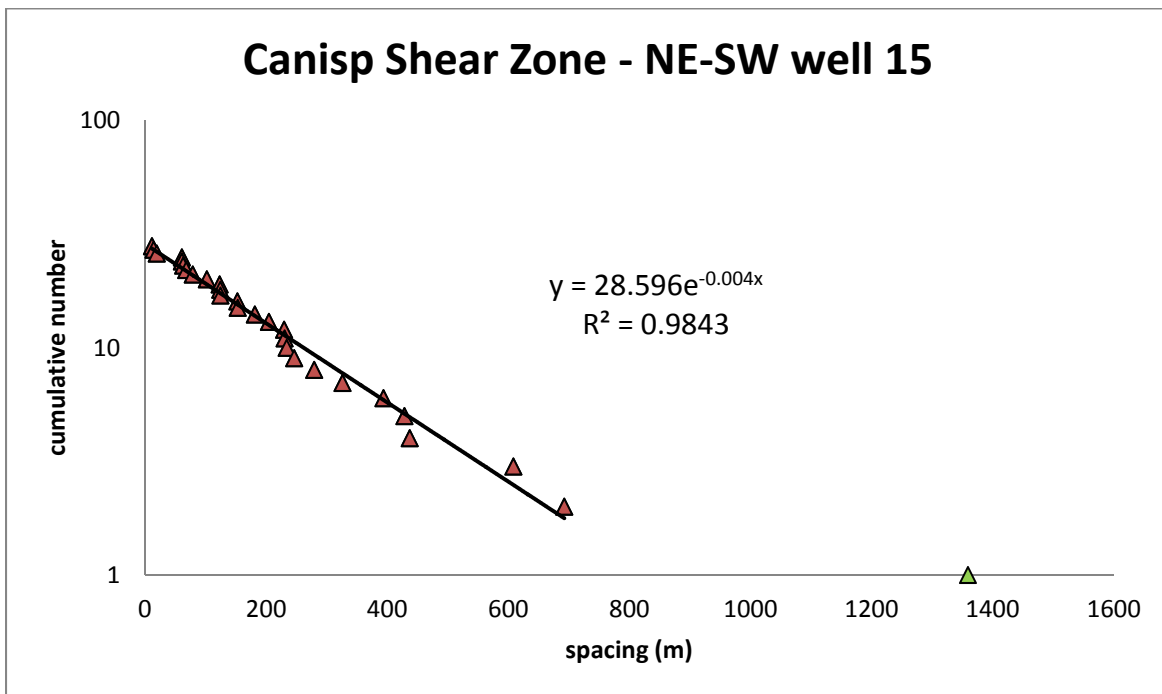
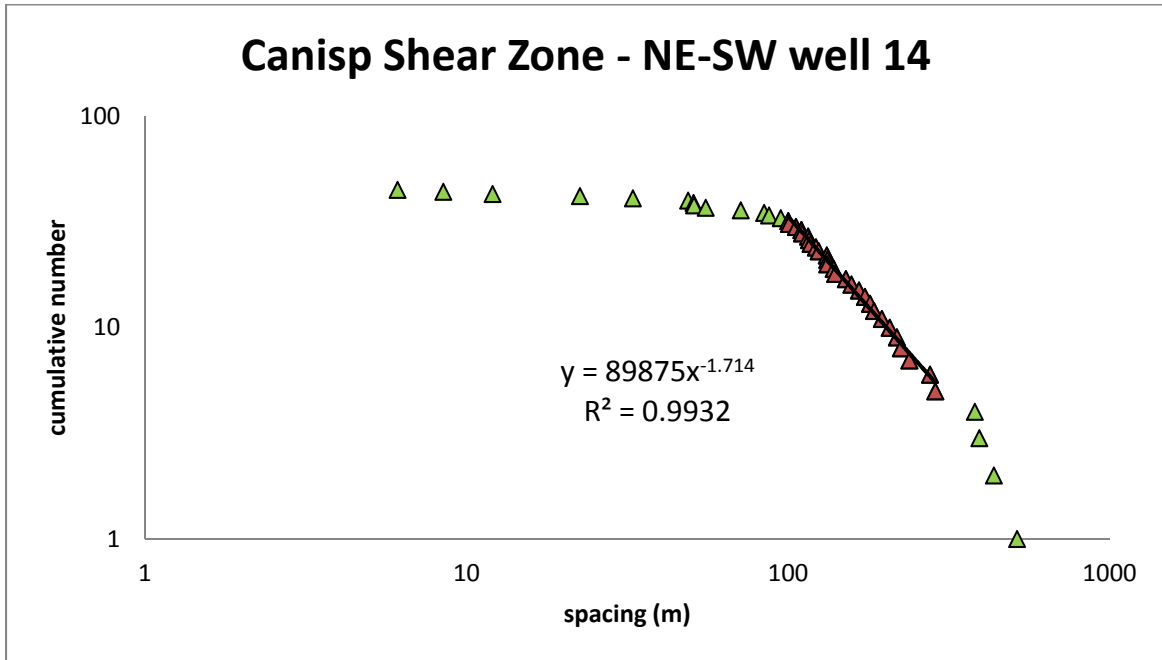


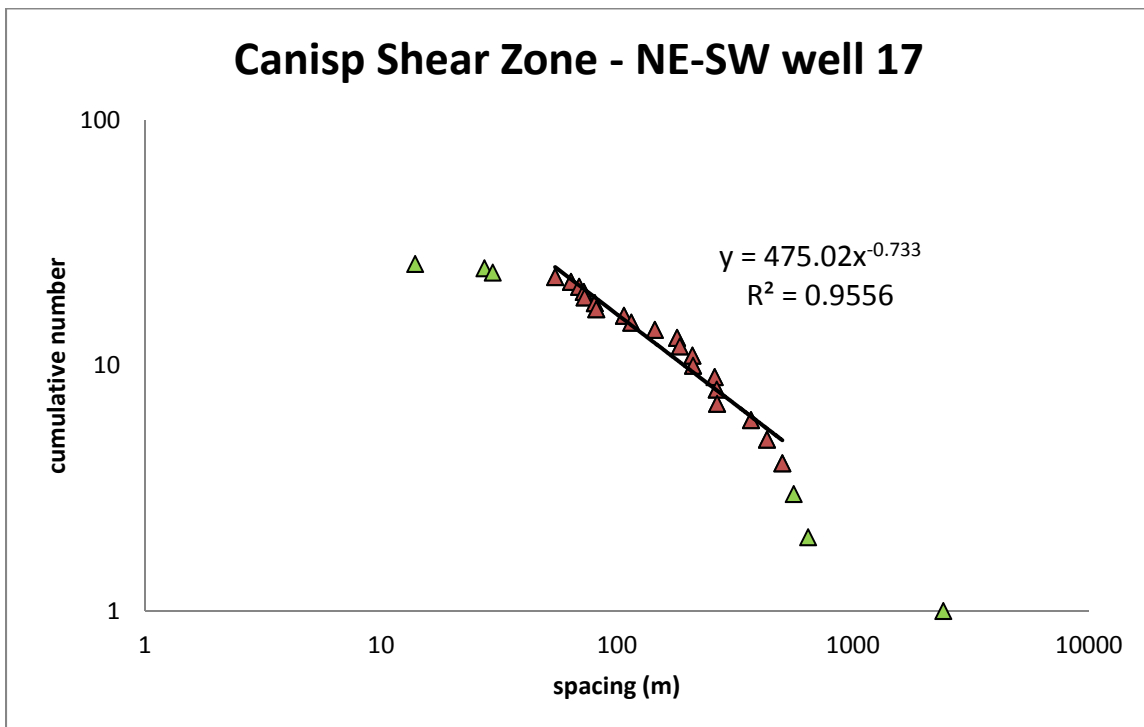
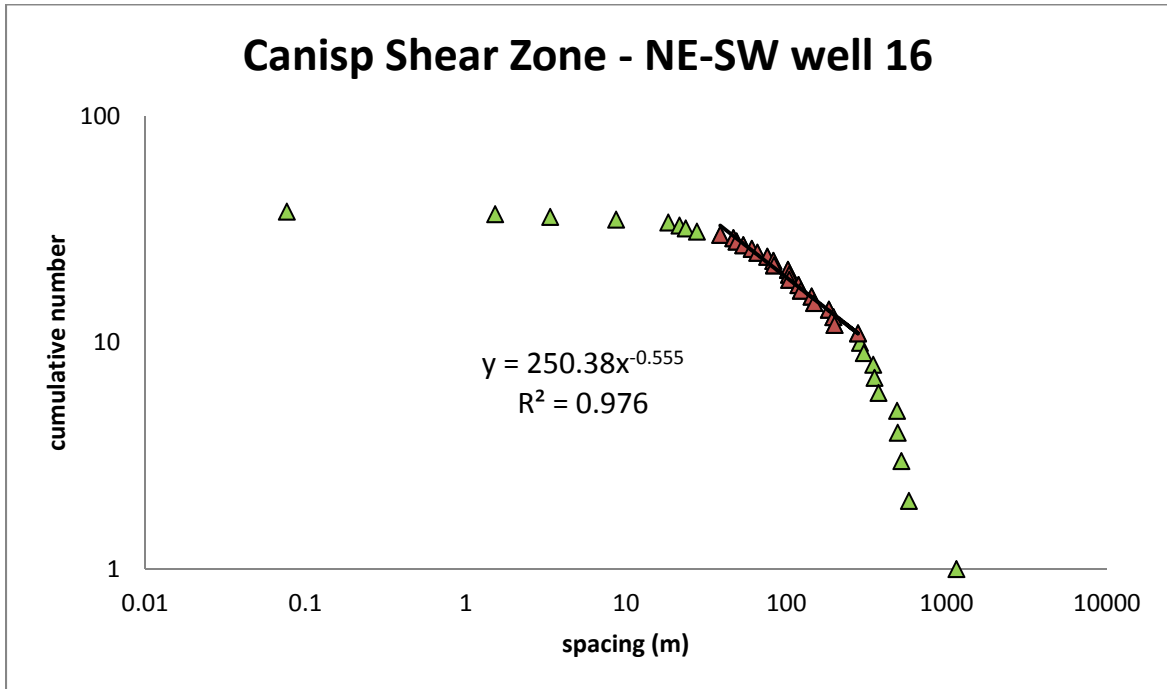


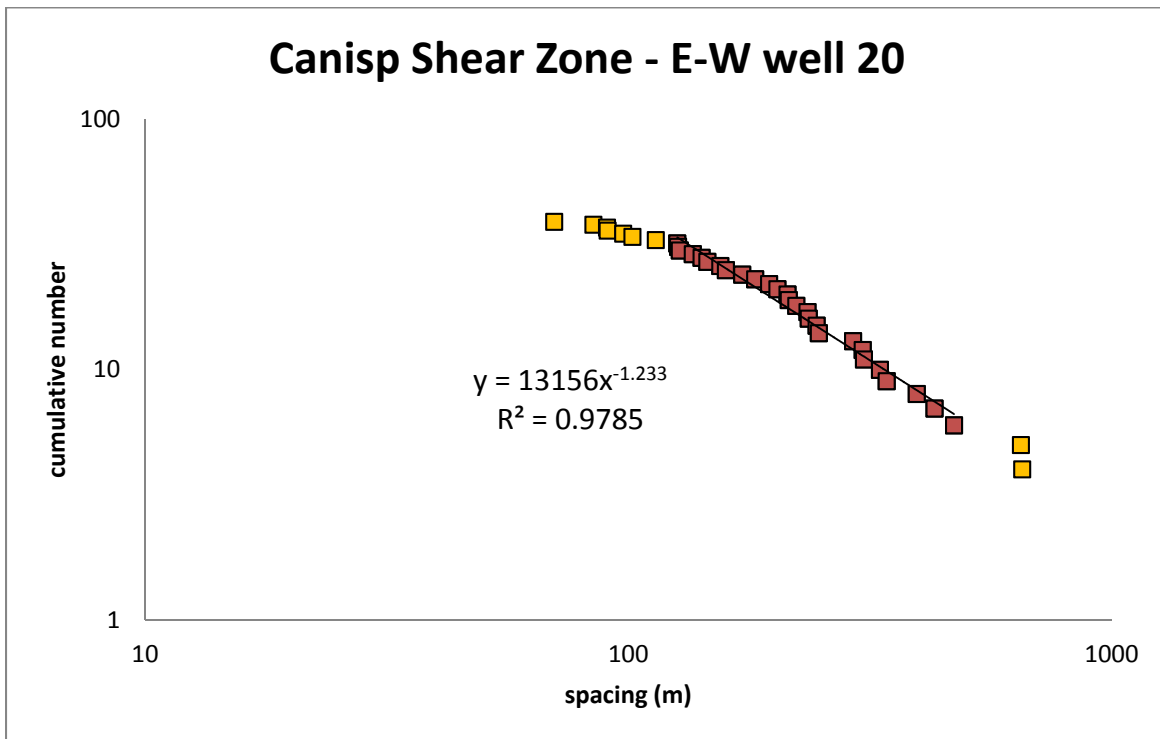
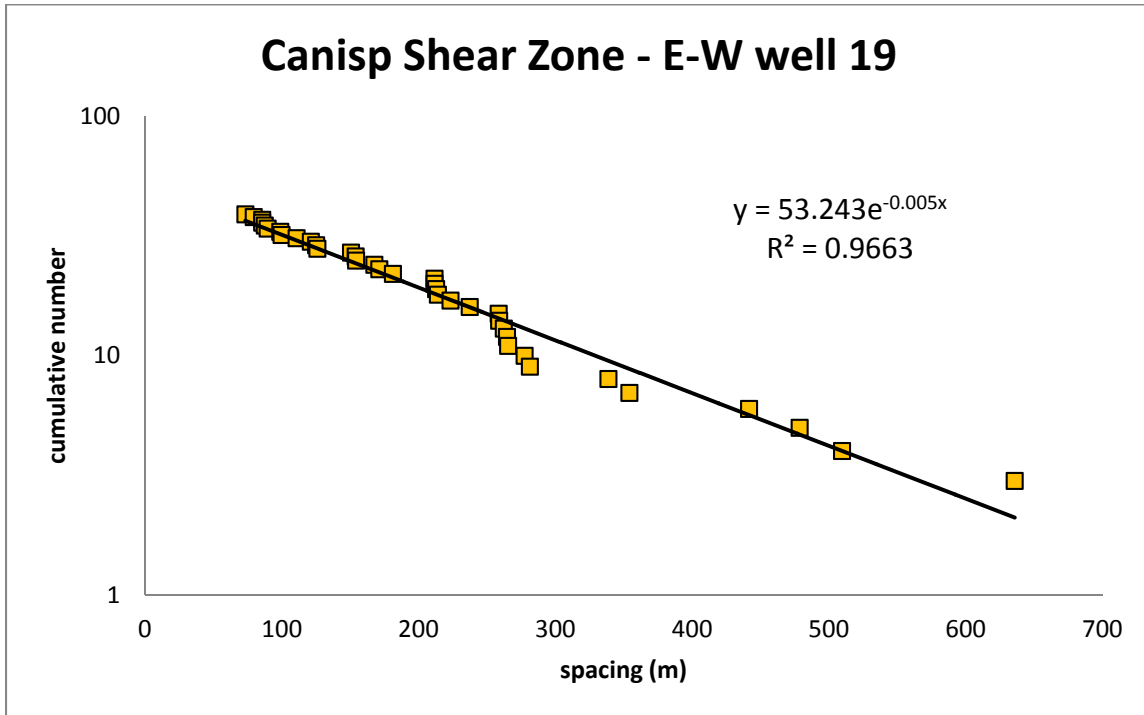


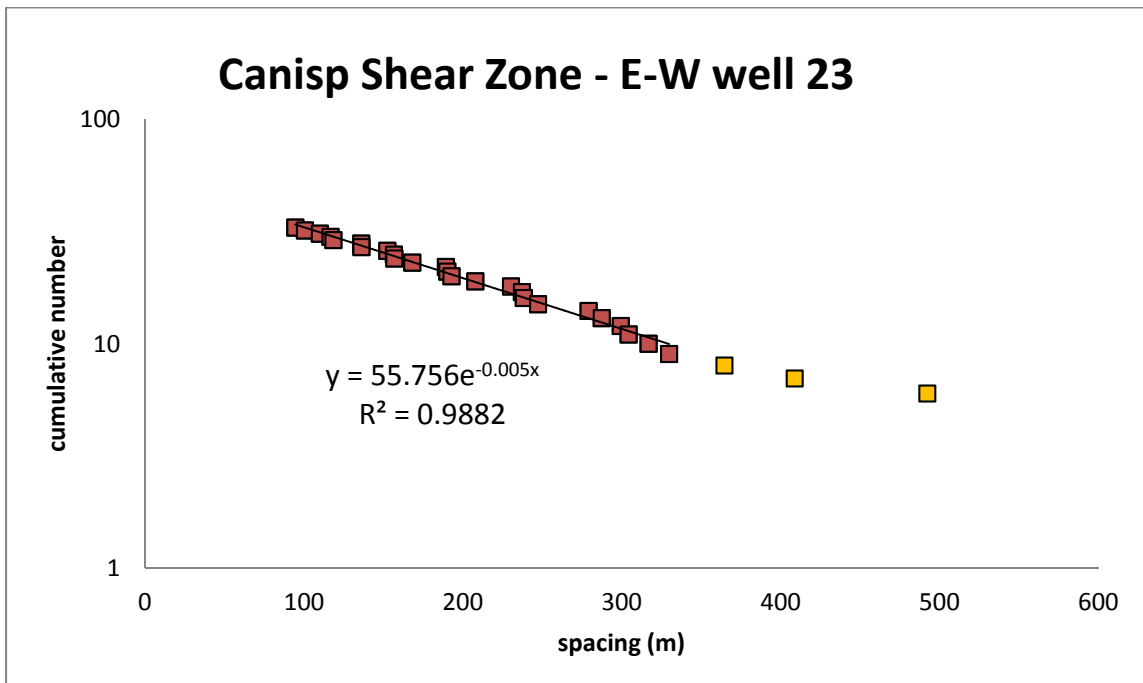
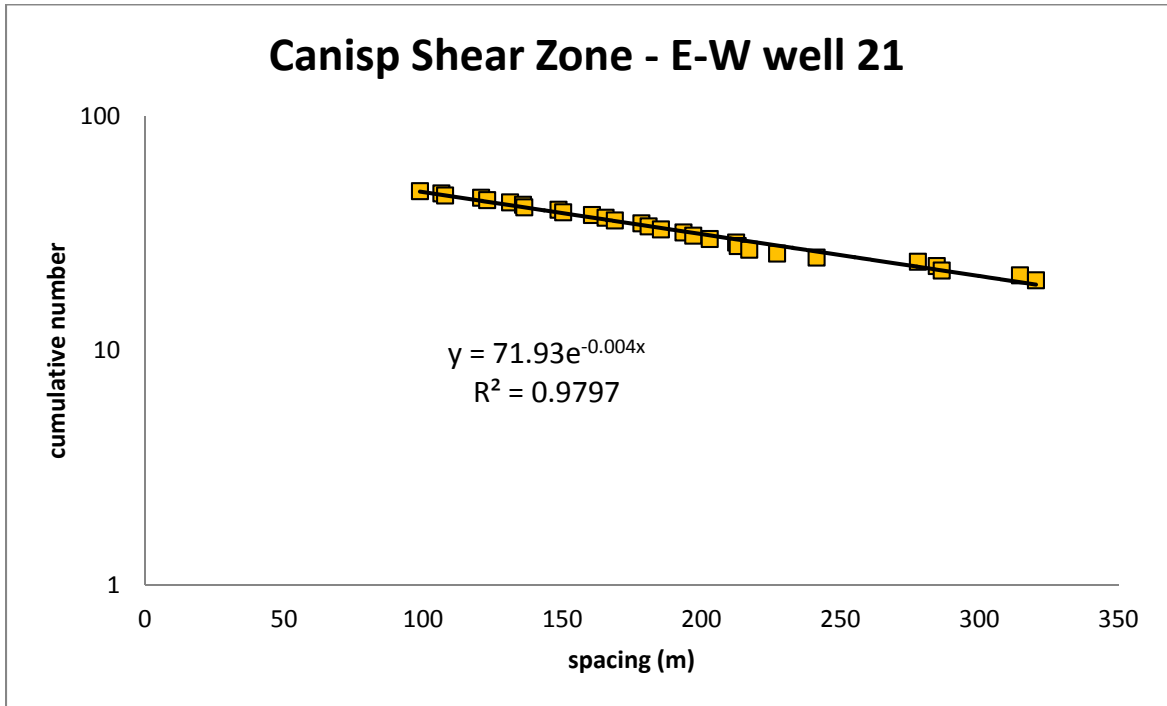


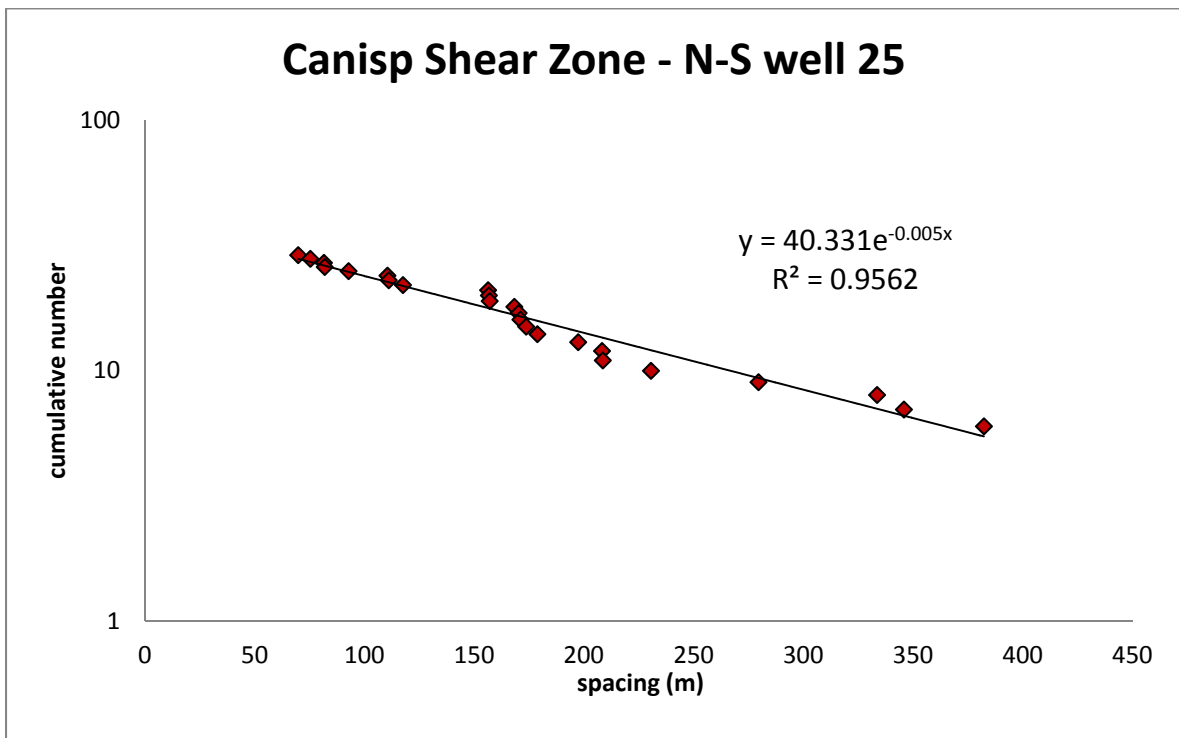
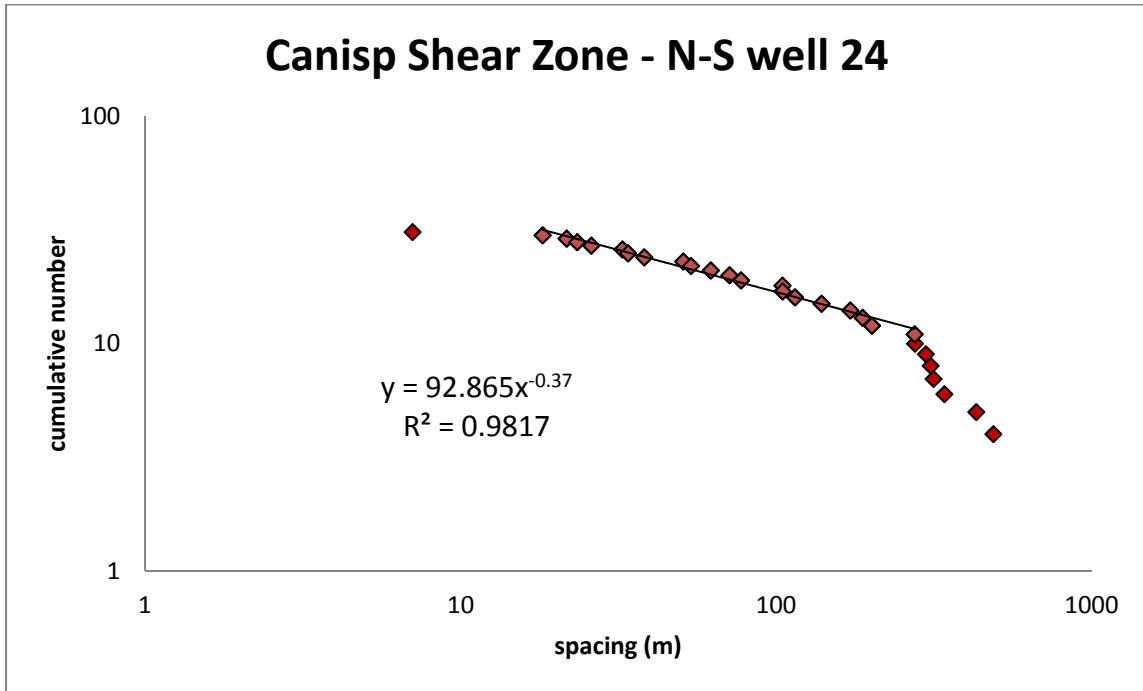




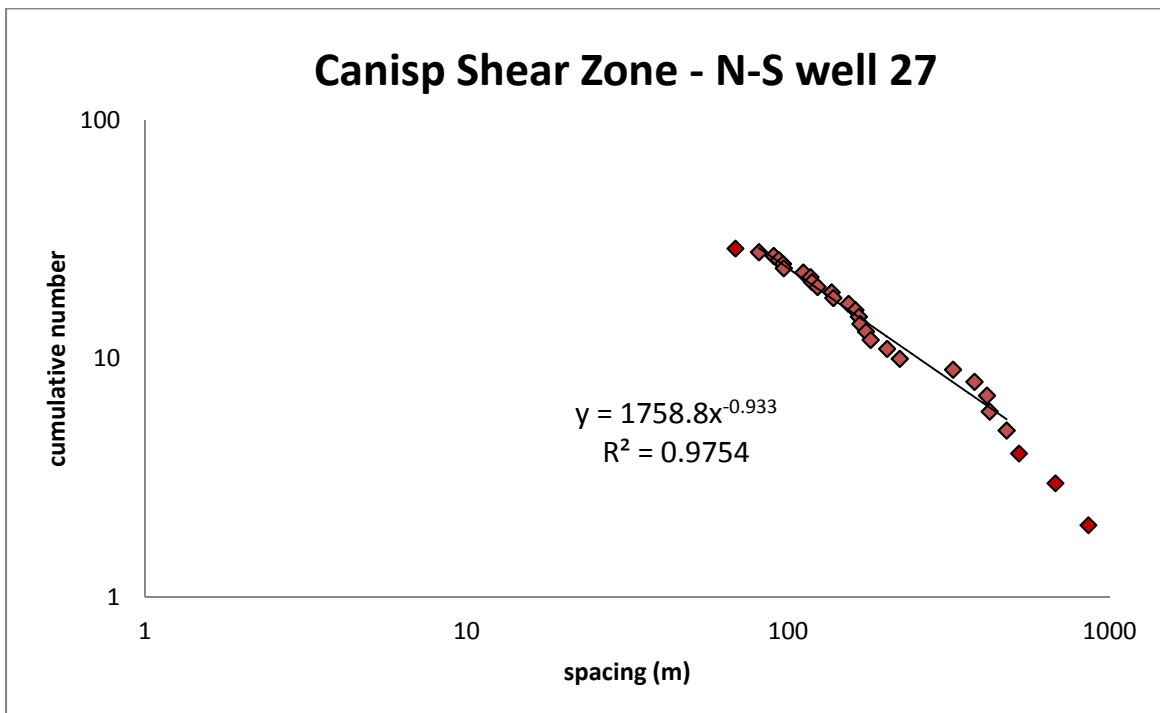
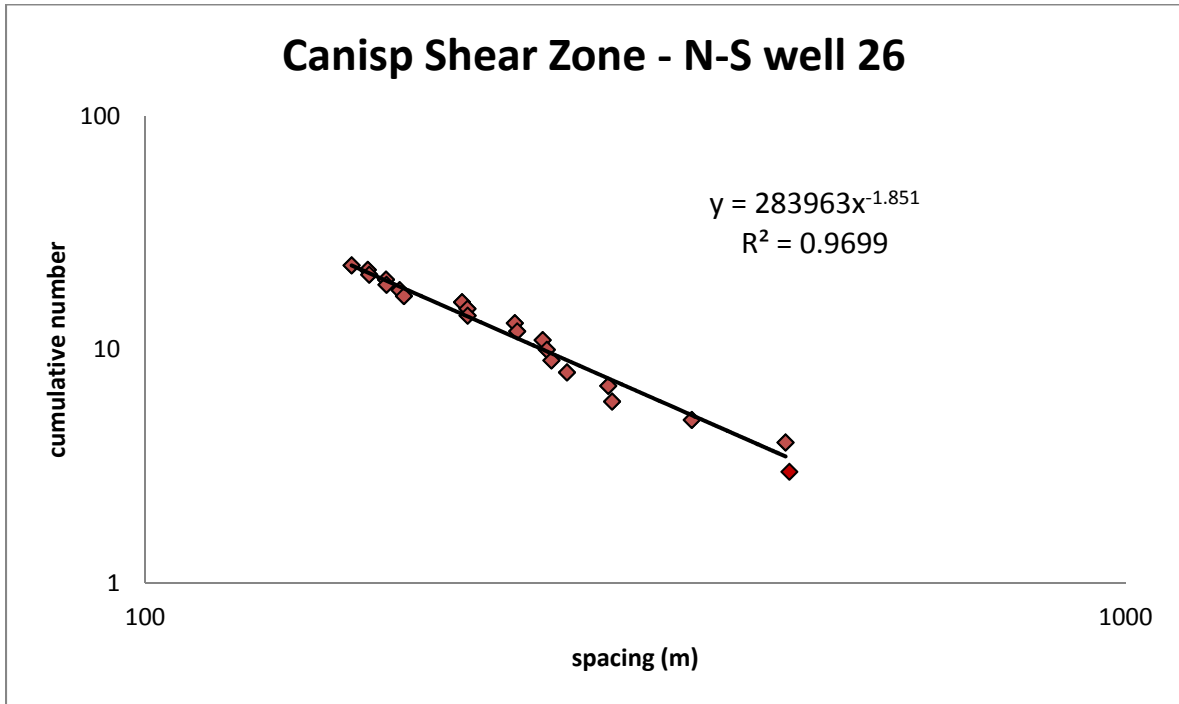




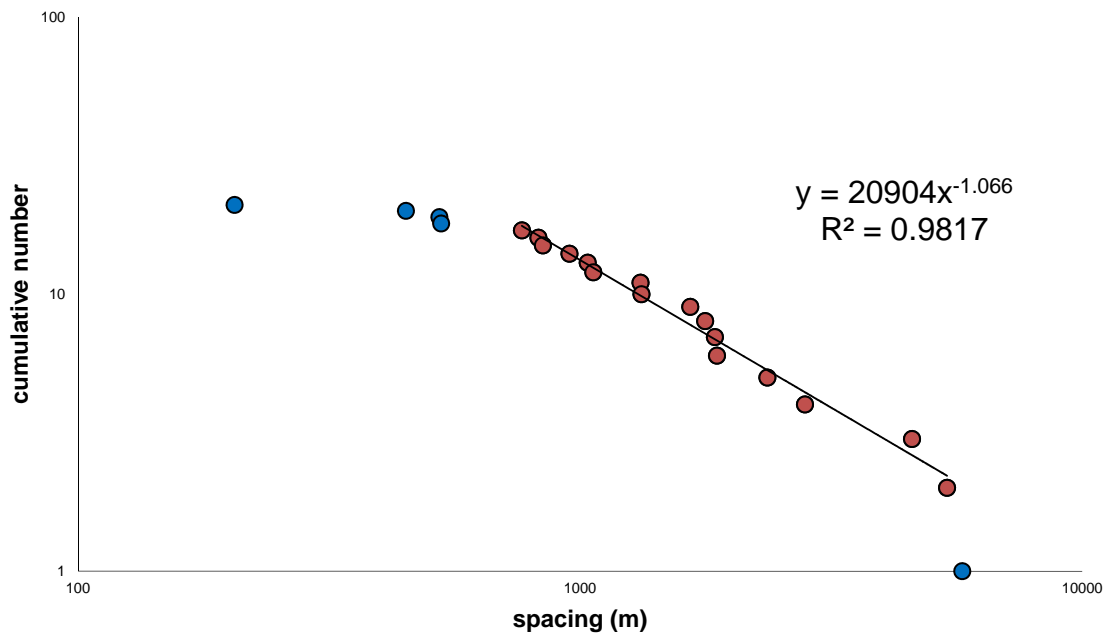




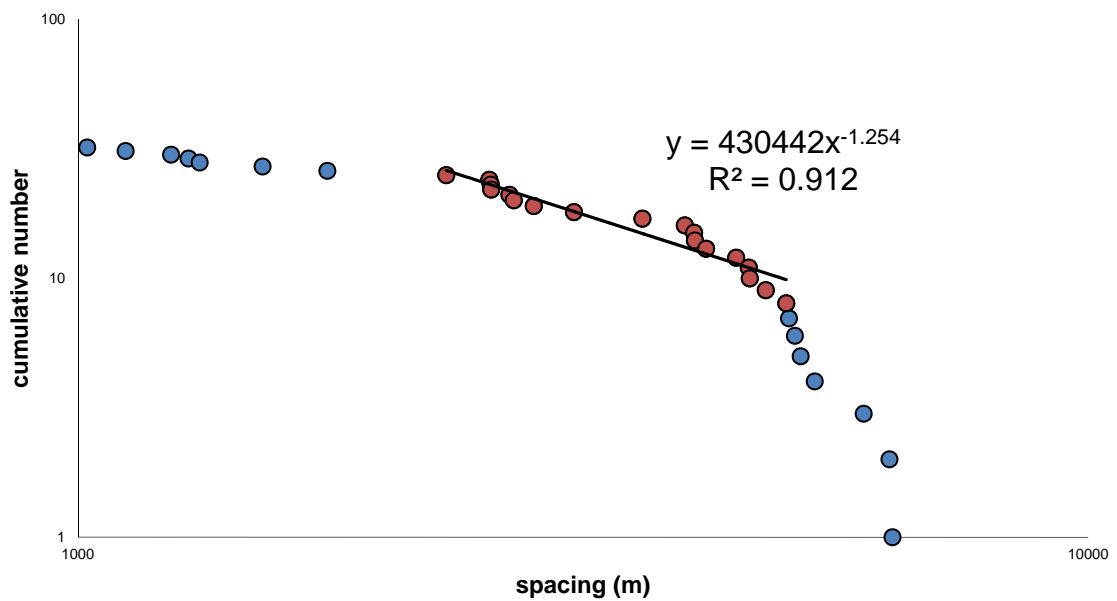


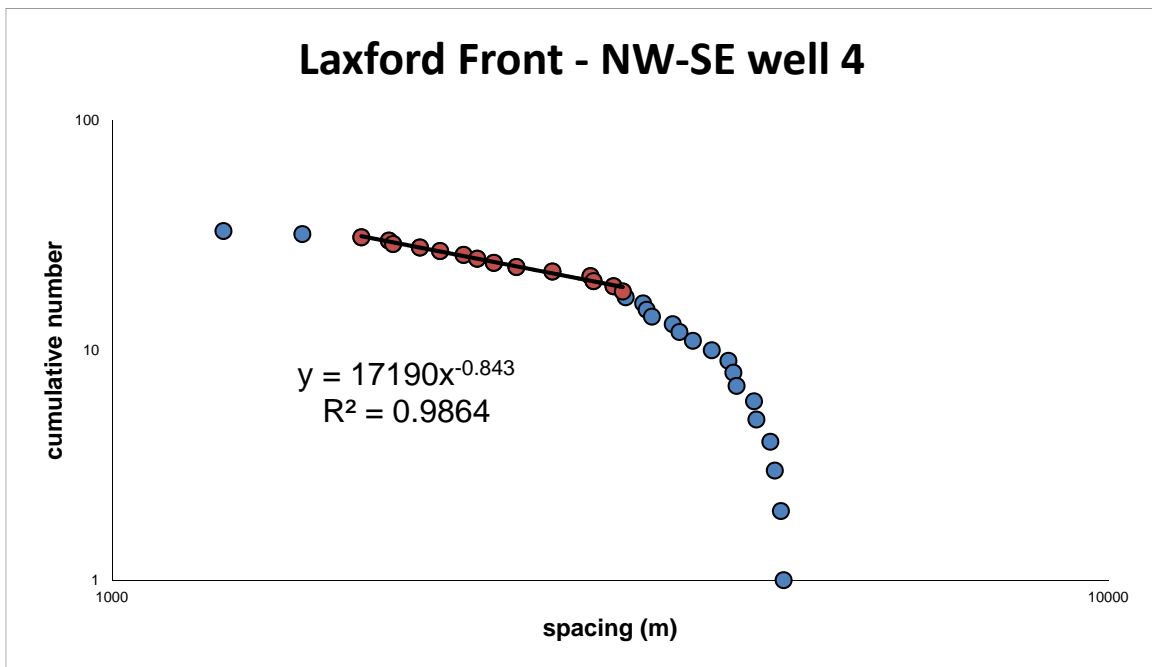
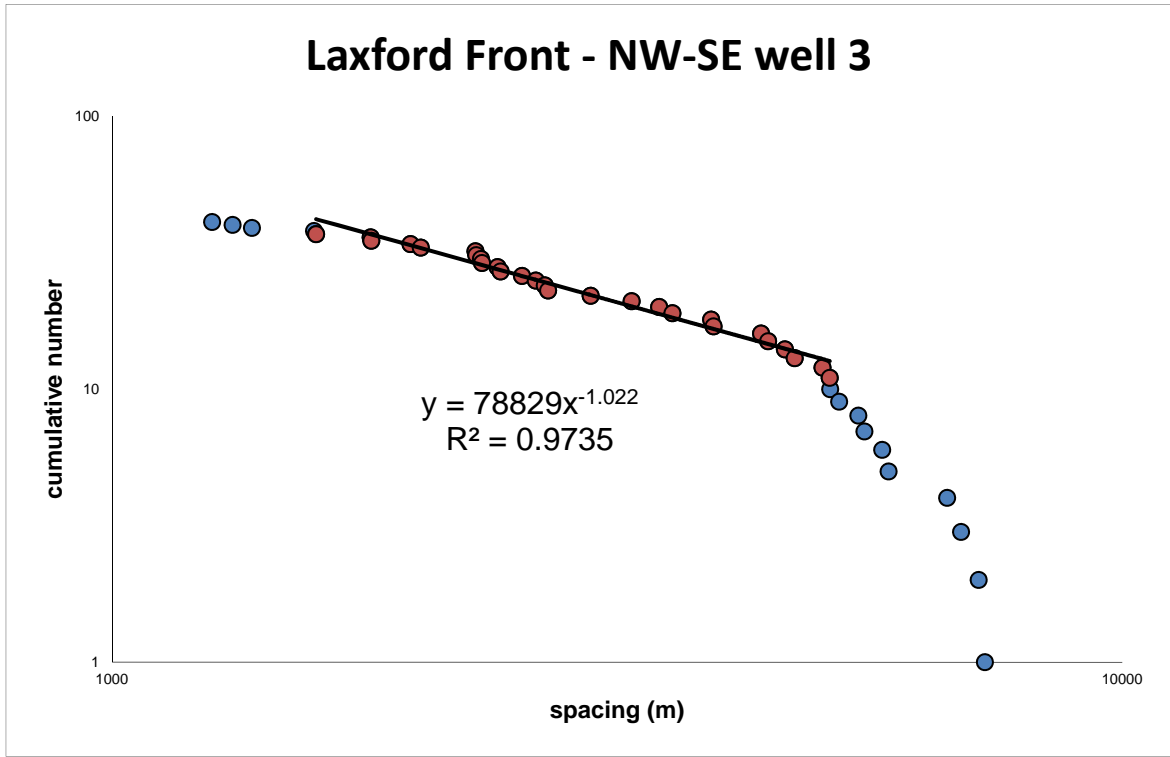


### Laxford Front - NW-SE well 1

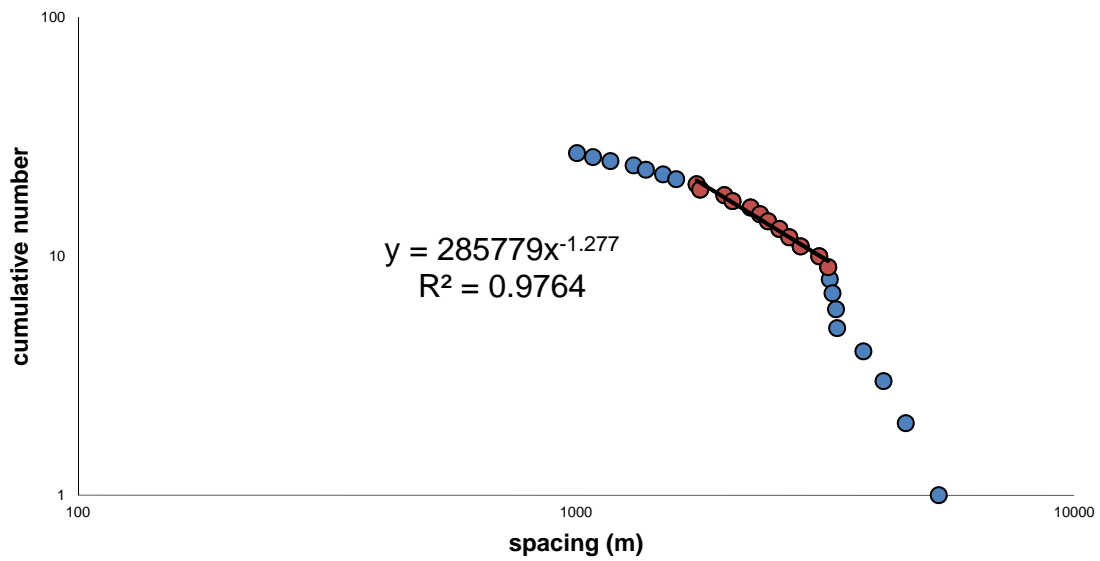


### Laxford Front - NW-SE well 2

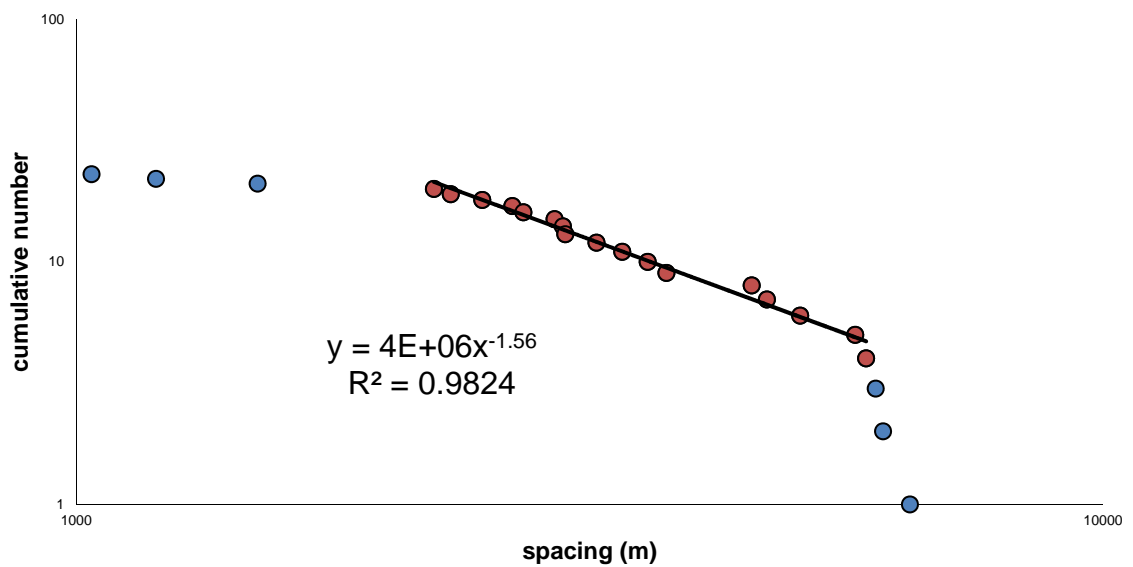




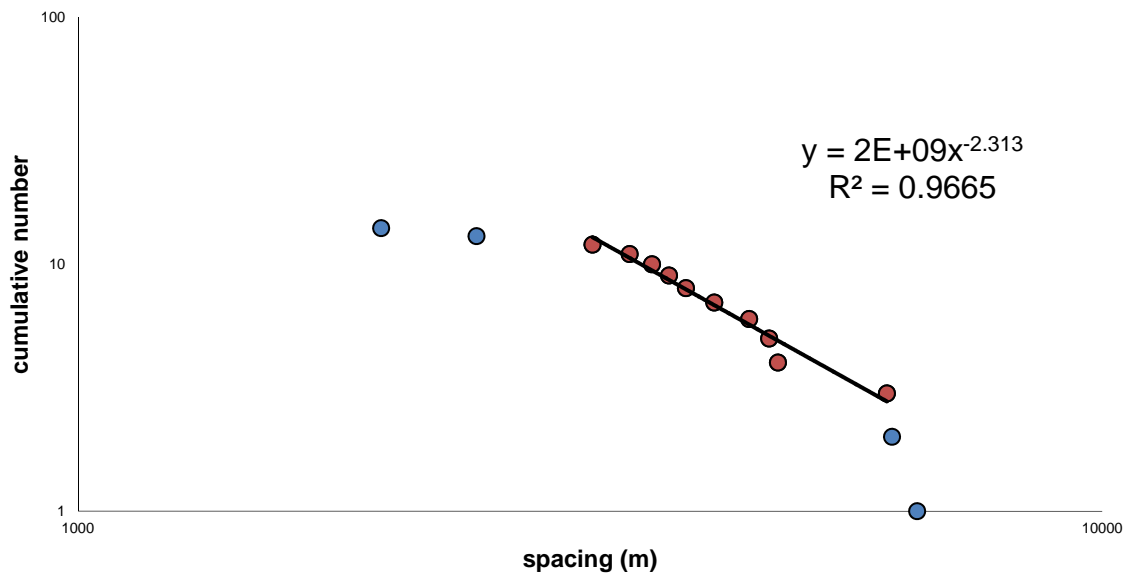
### Laxford Front - NW-SE well 5



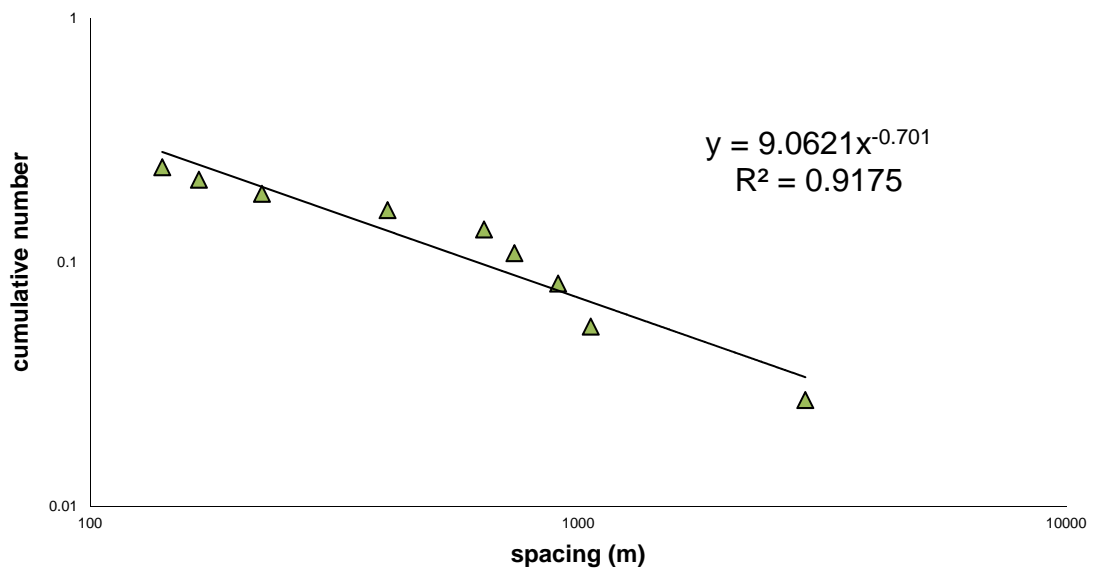
### Laxford Front - NW-SE well 6



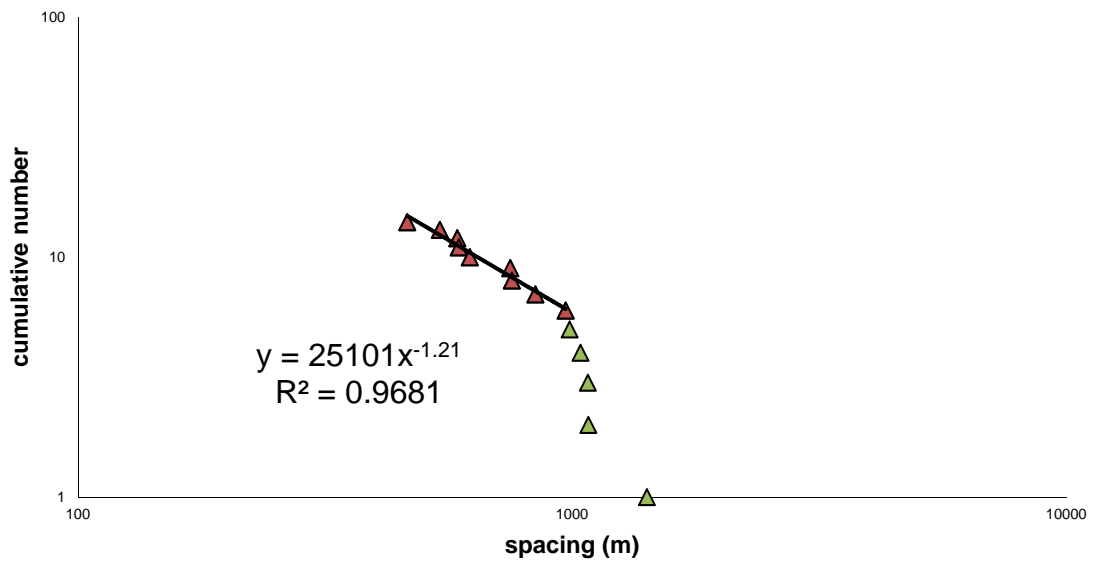
### Laxford Front - NW-SE well 7



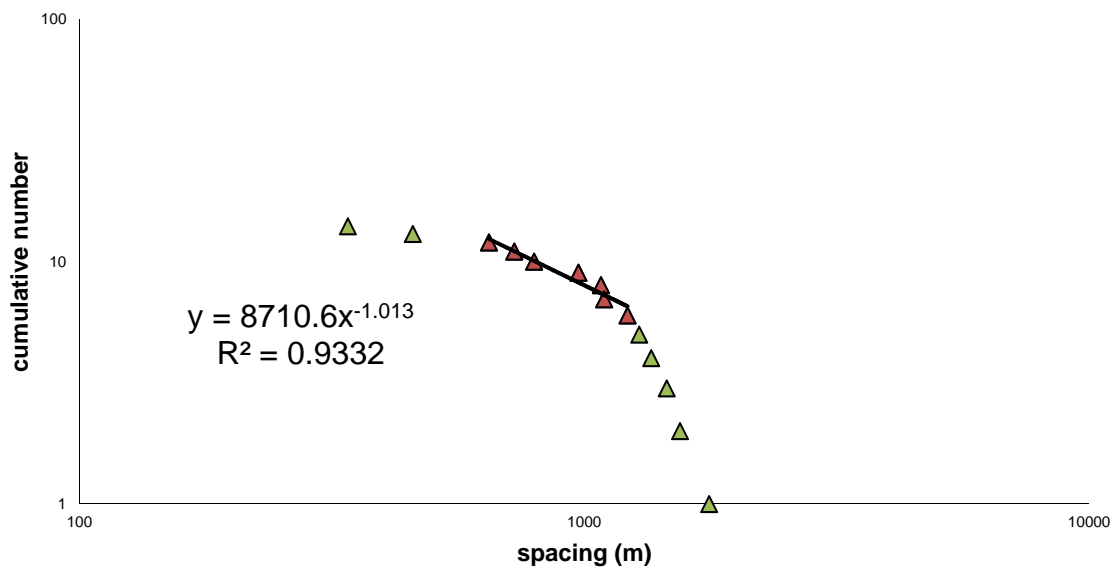
### Laxford Front - NE-SW well 8



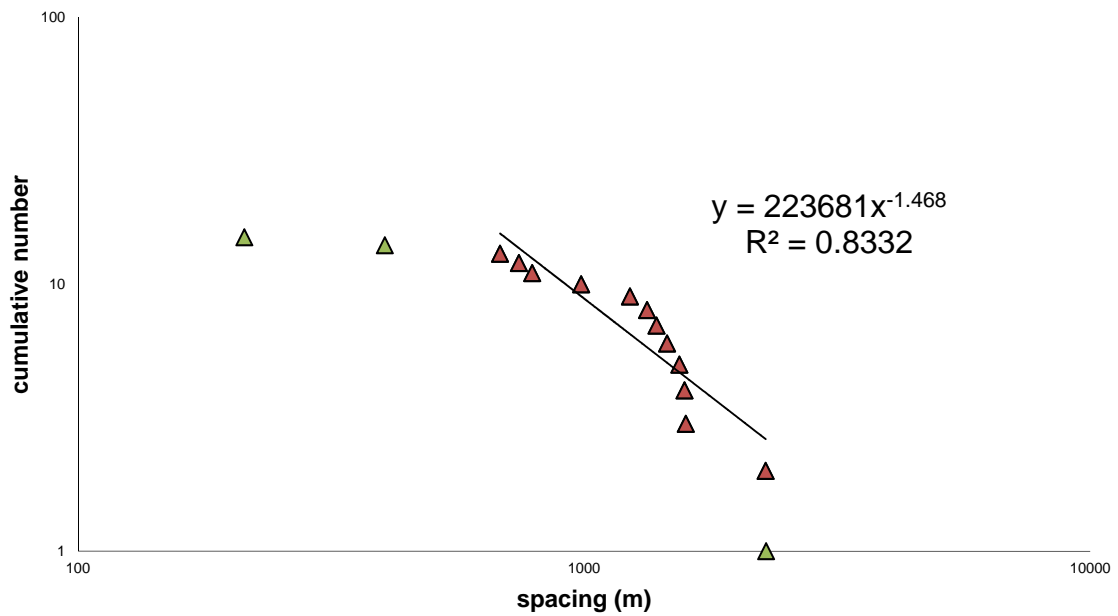
### Laxford Front - NE-SW well 11



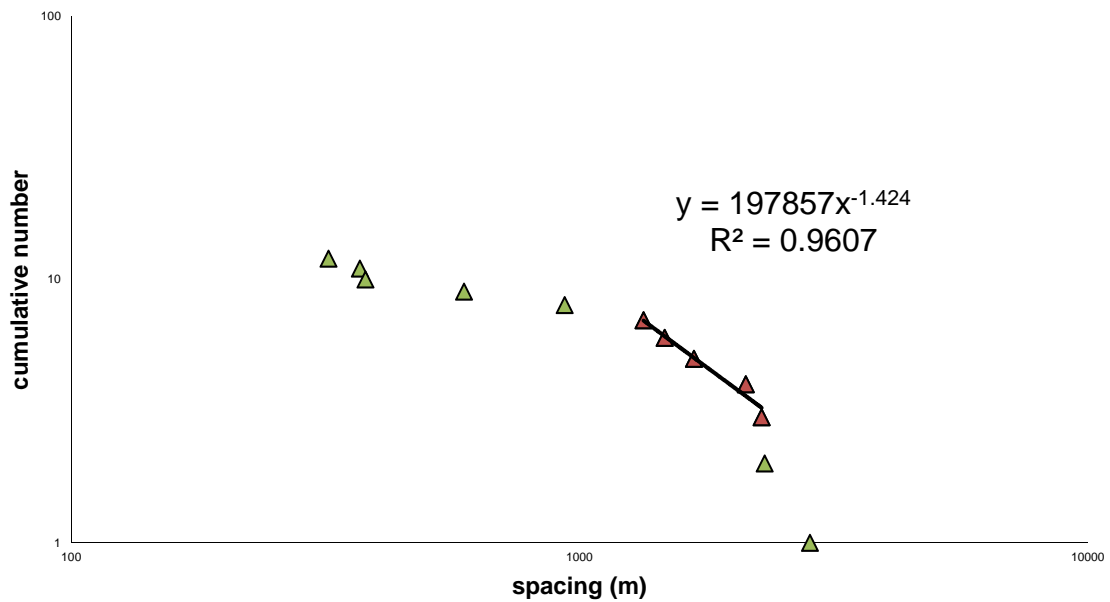
### Laxford Front - NE-SW well 12

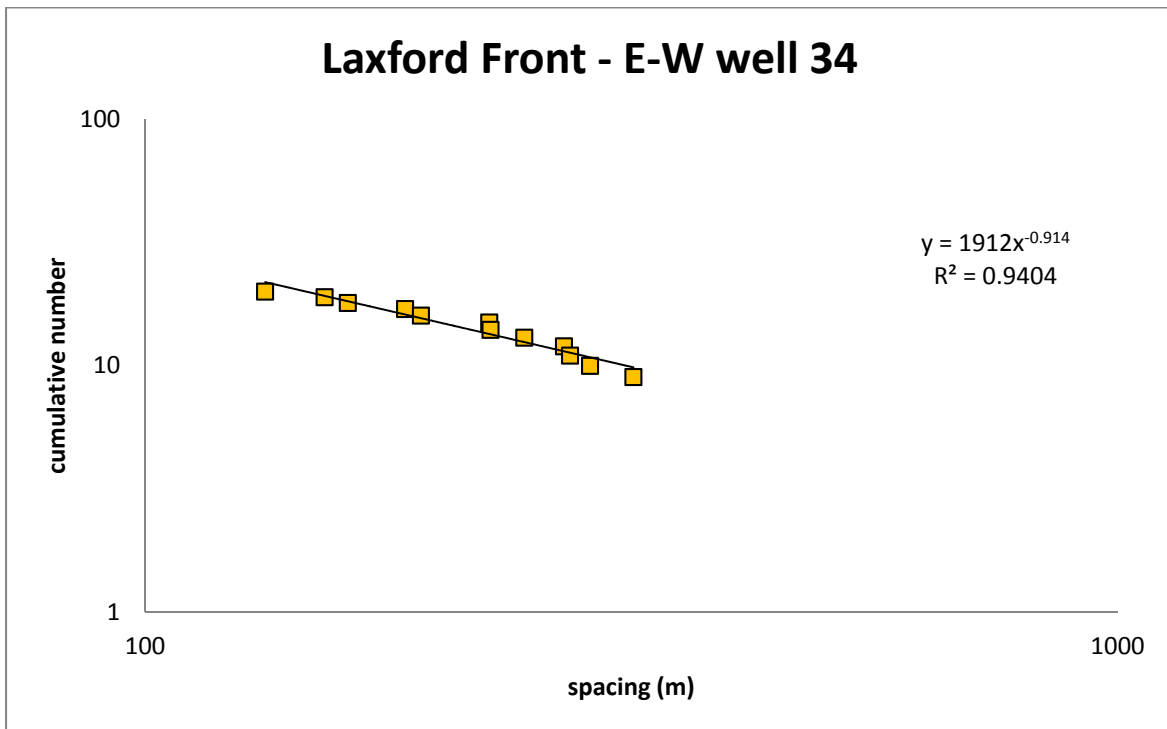
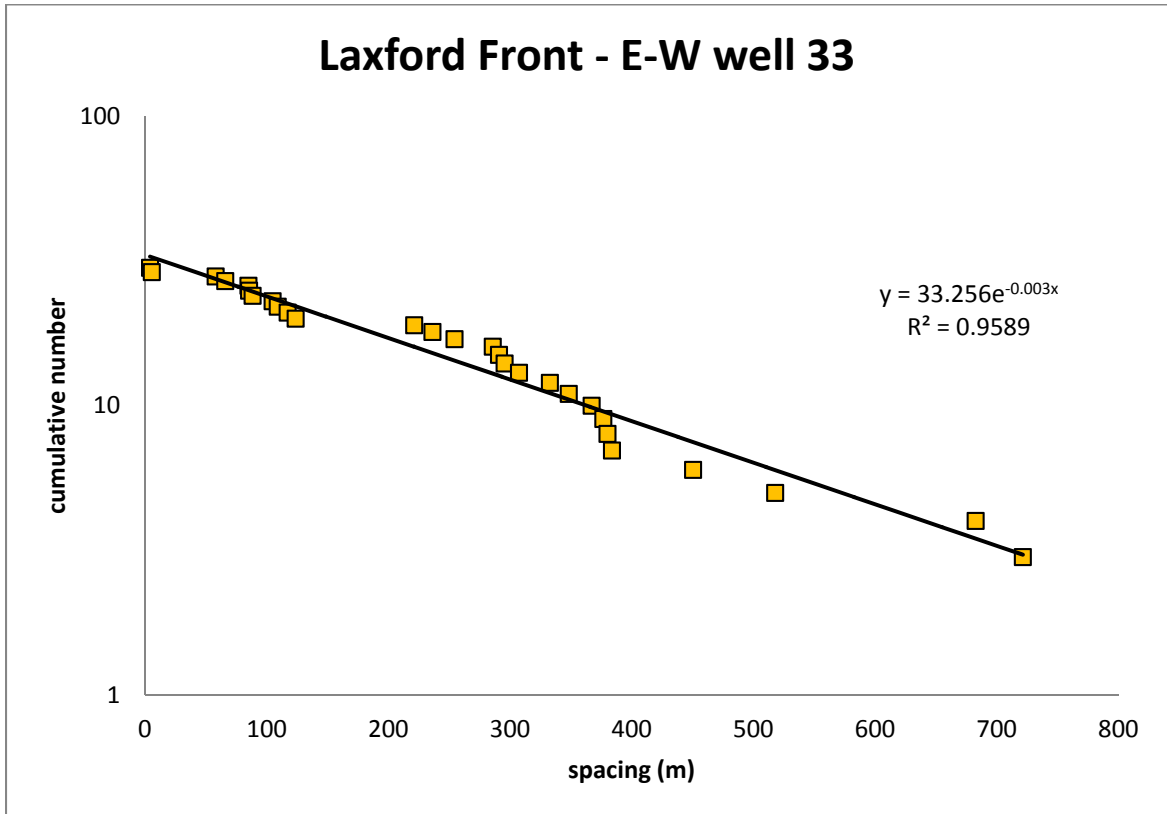


### Laxford Front - NE-SW well 13

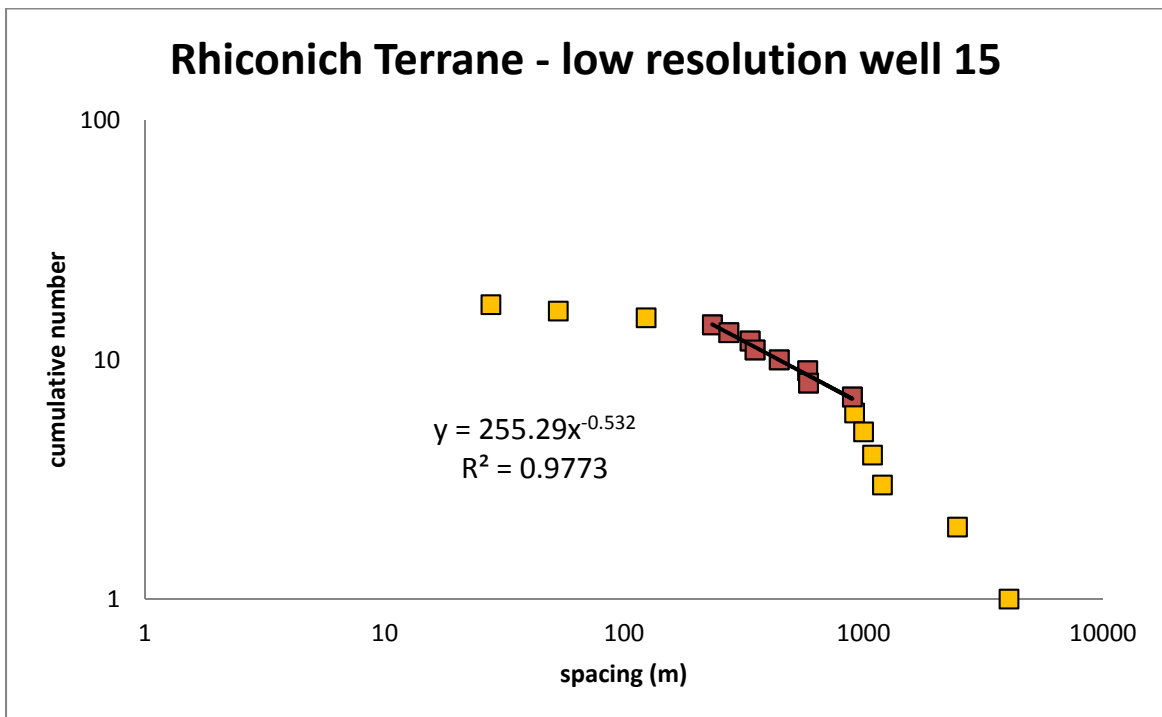
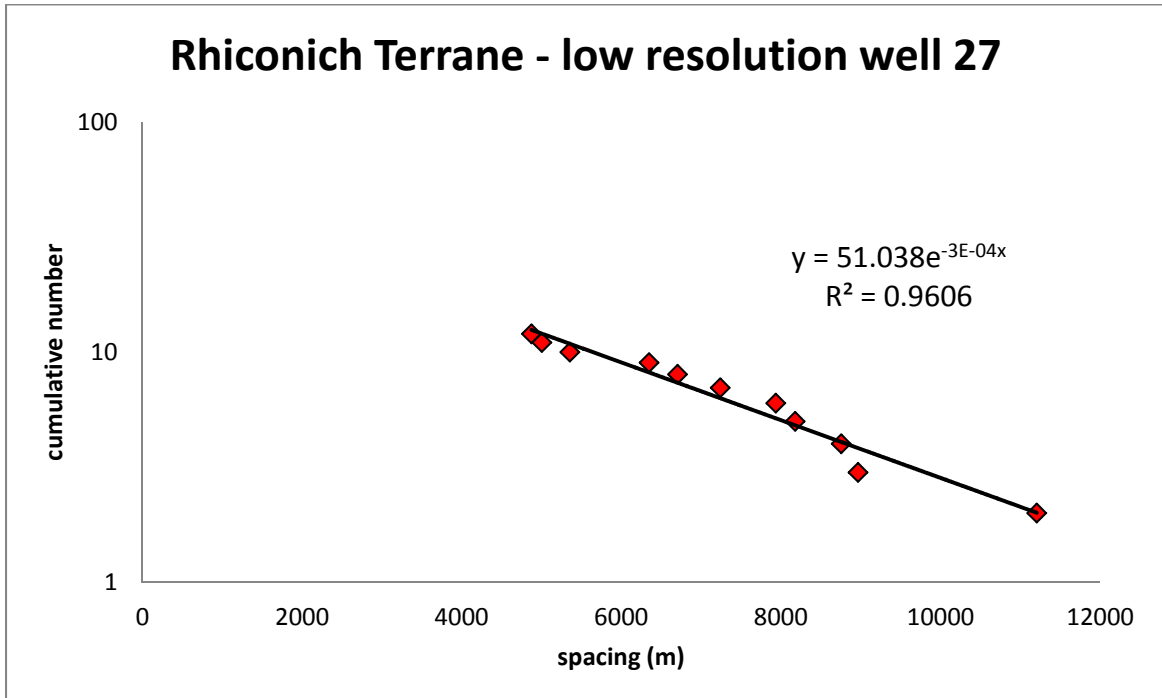


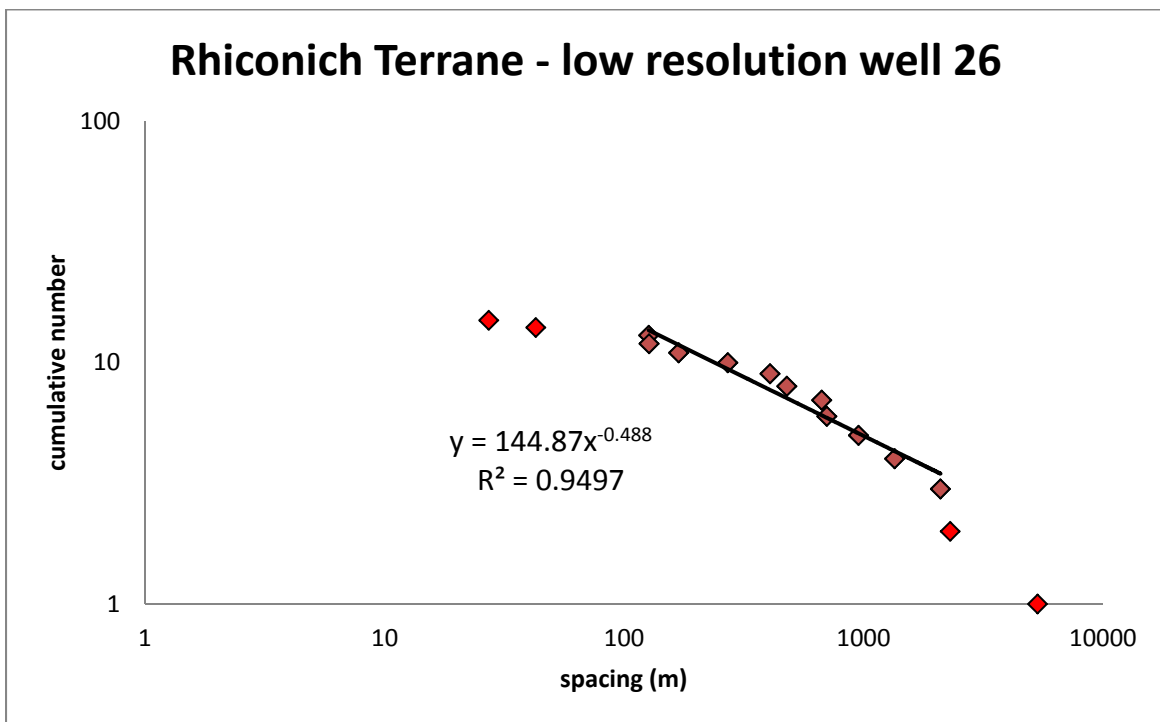
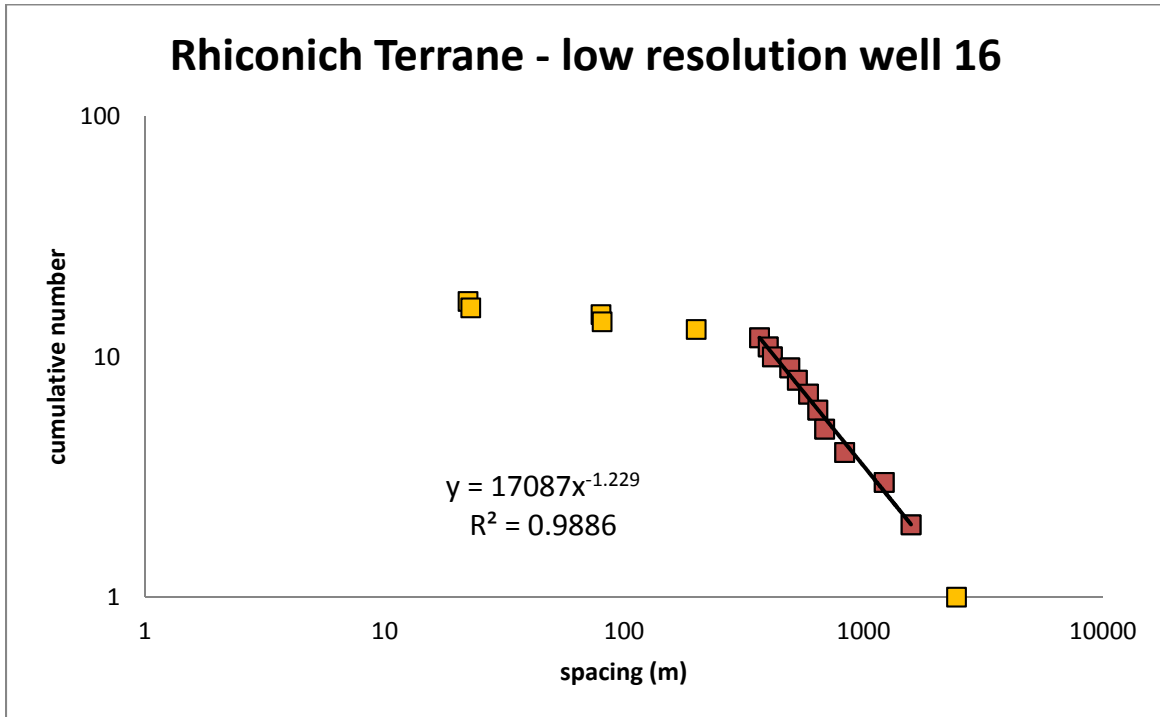
### Laxford Front - NE-SW well 14

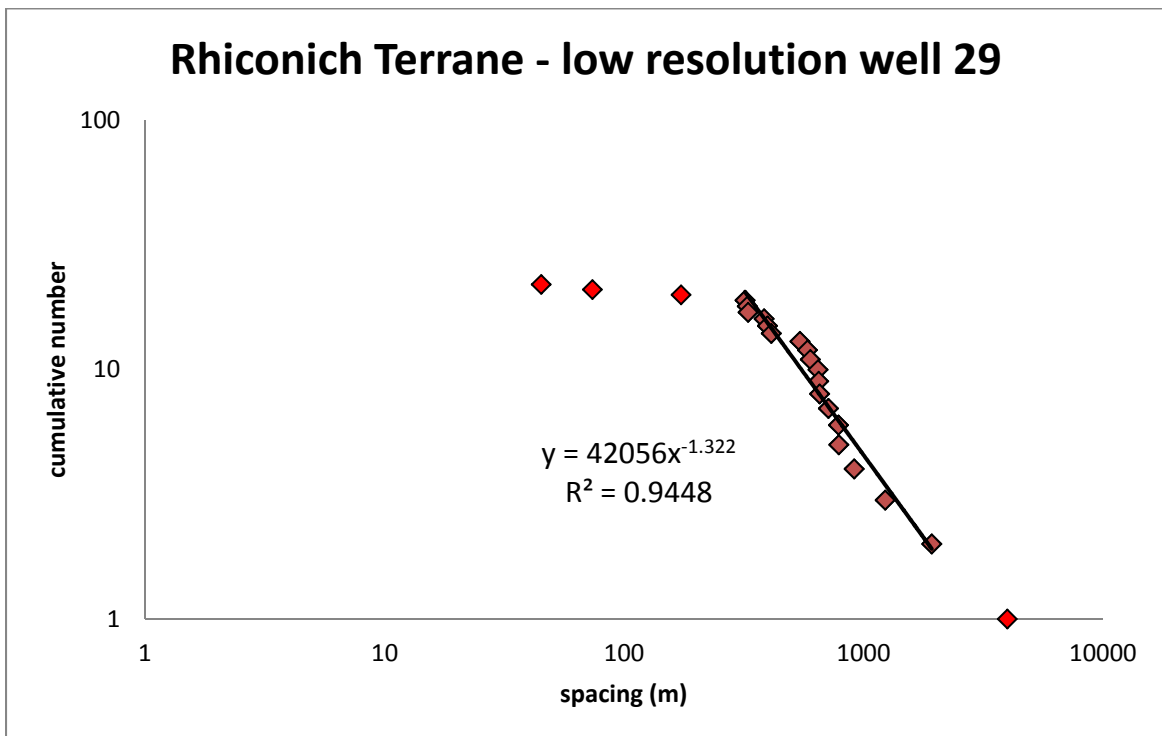
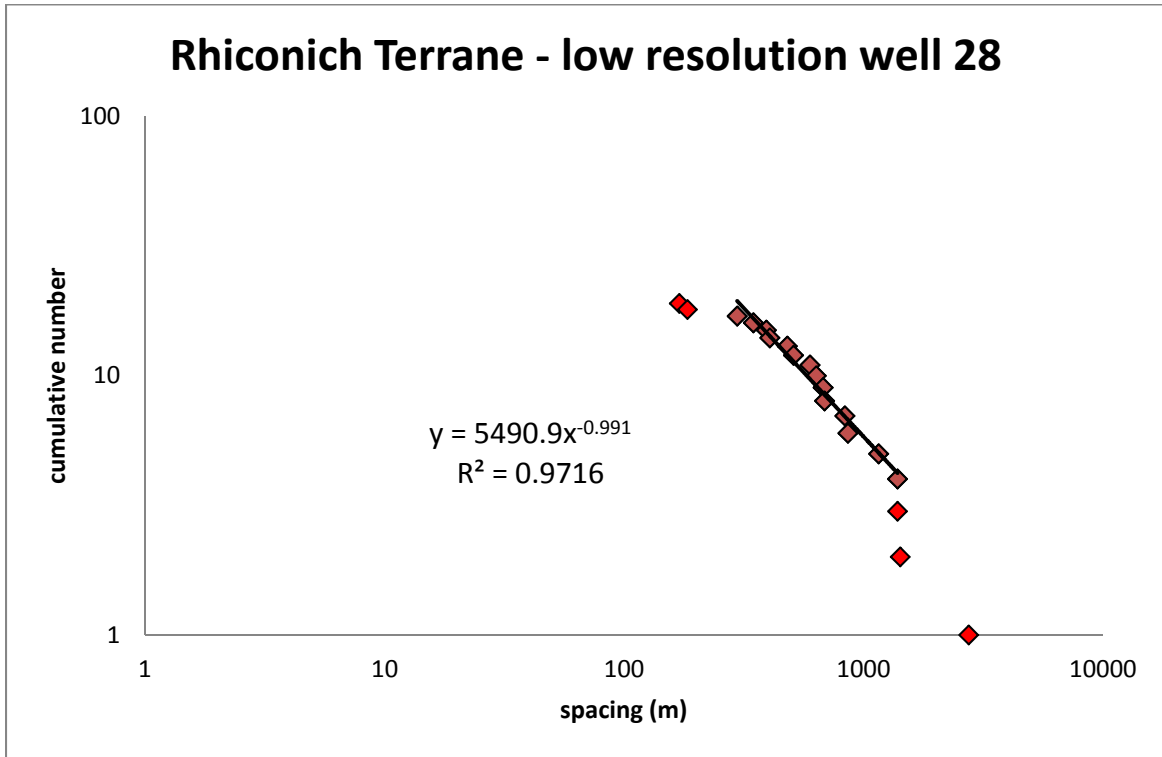


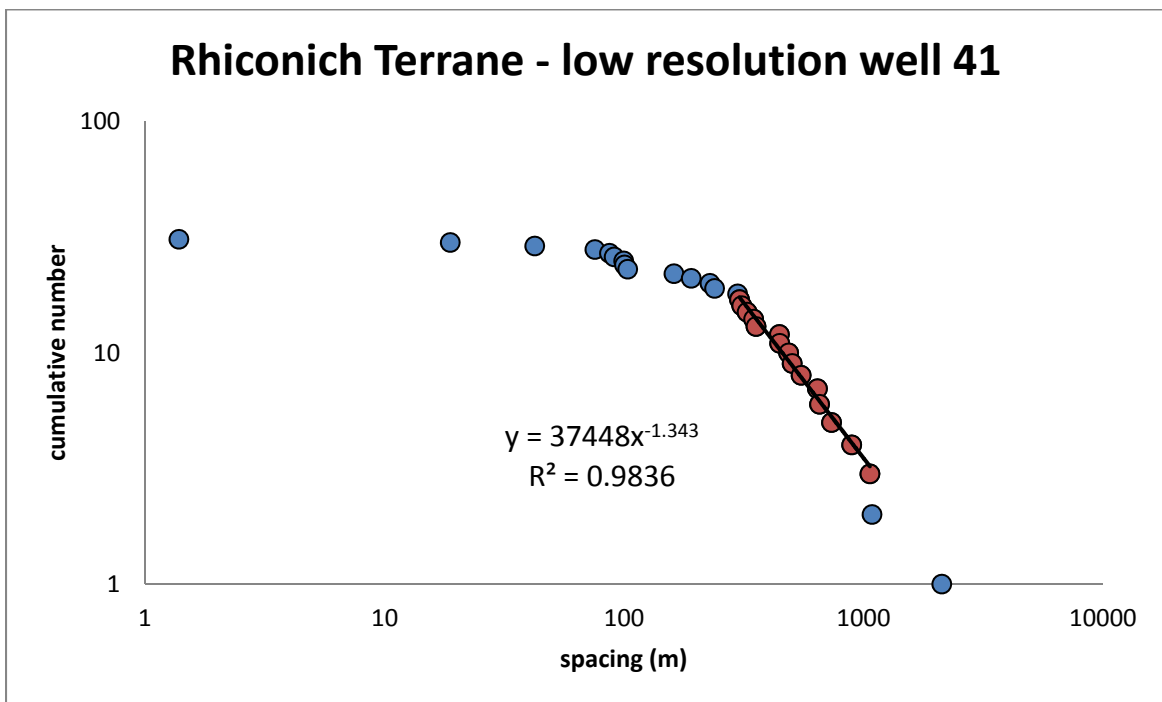
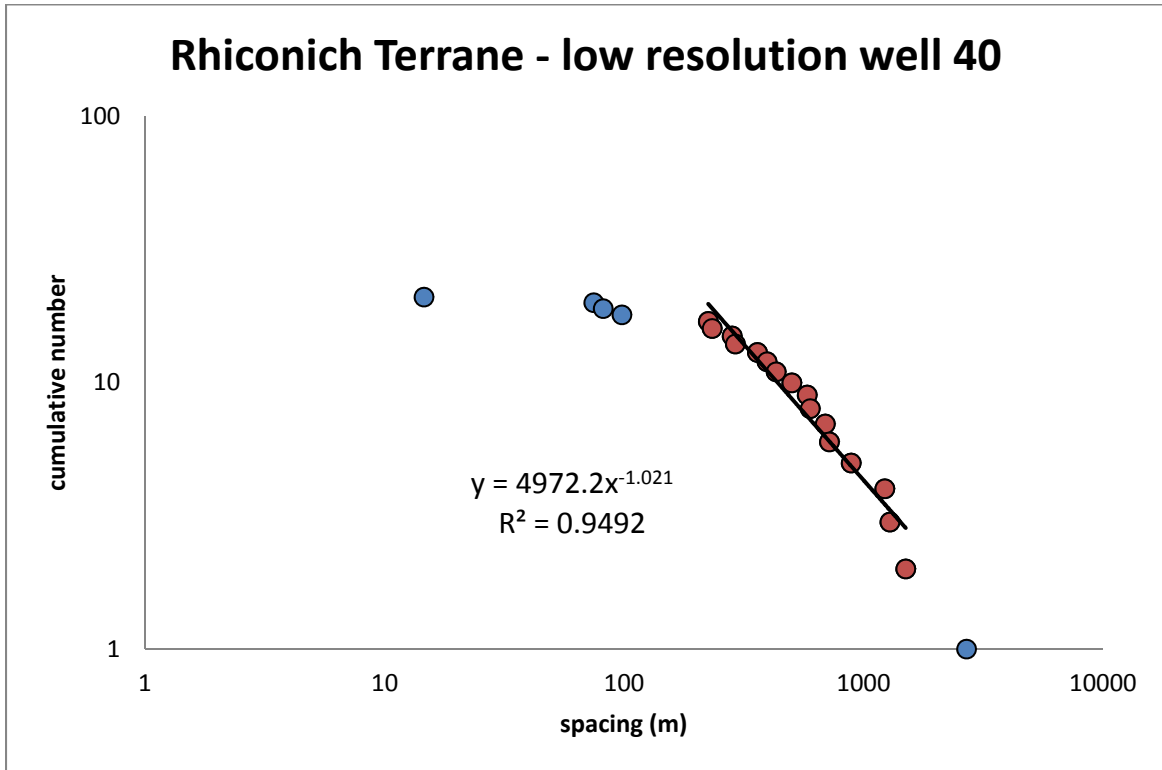


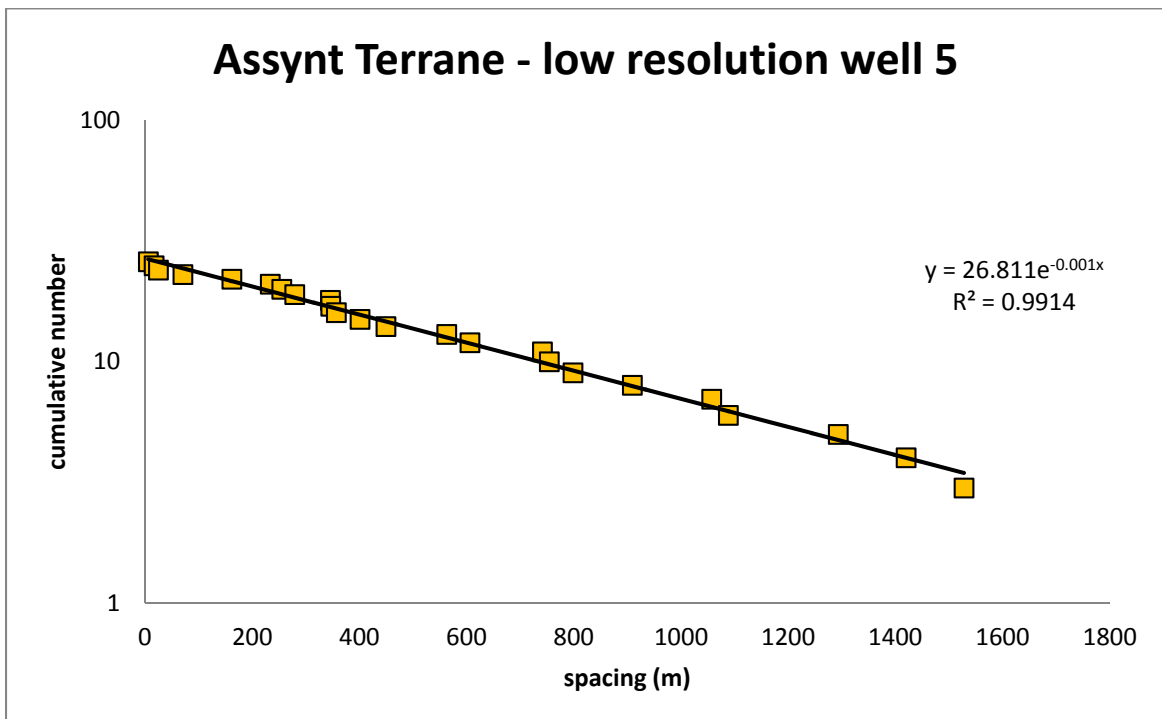
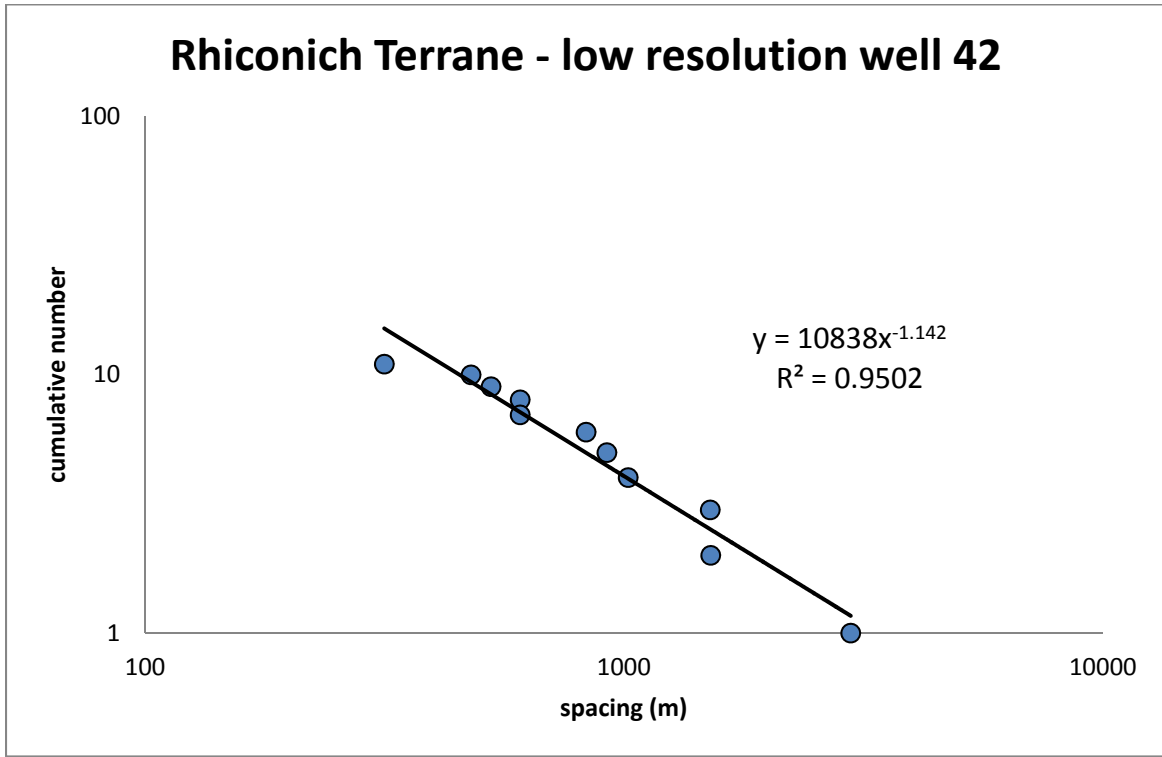


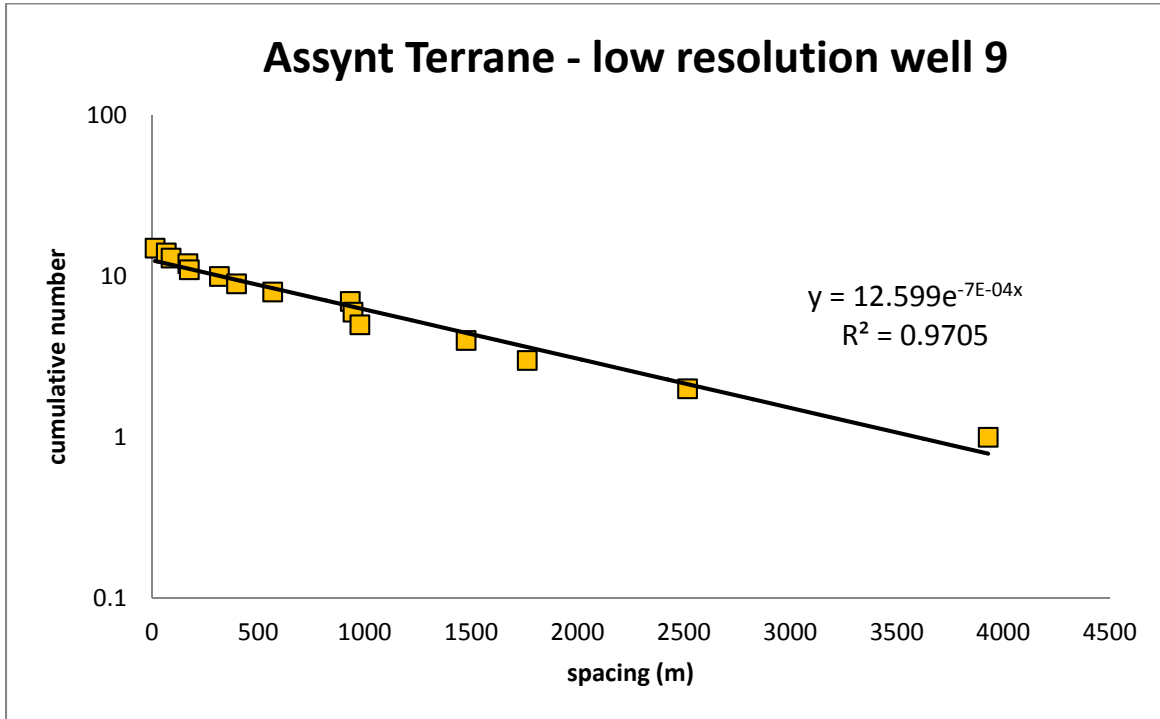
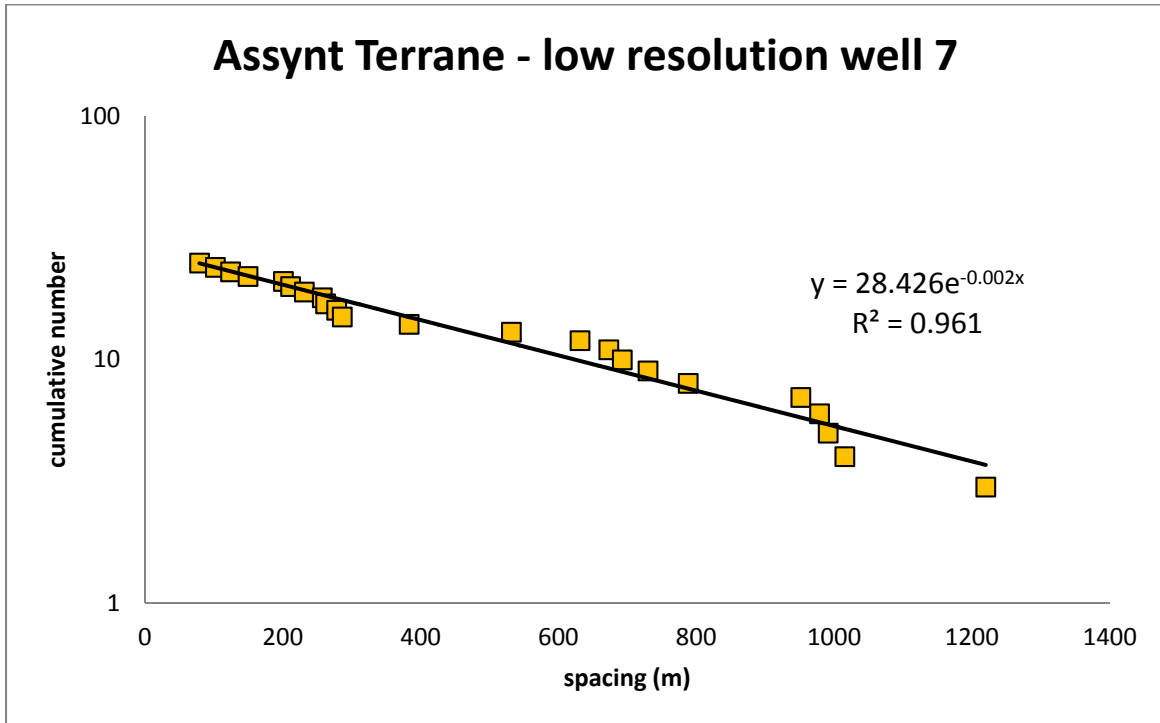




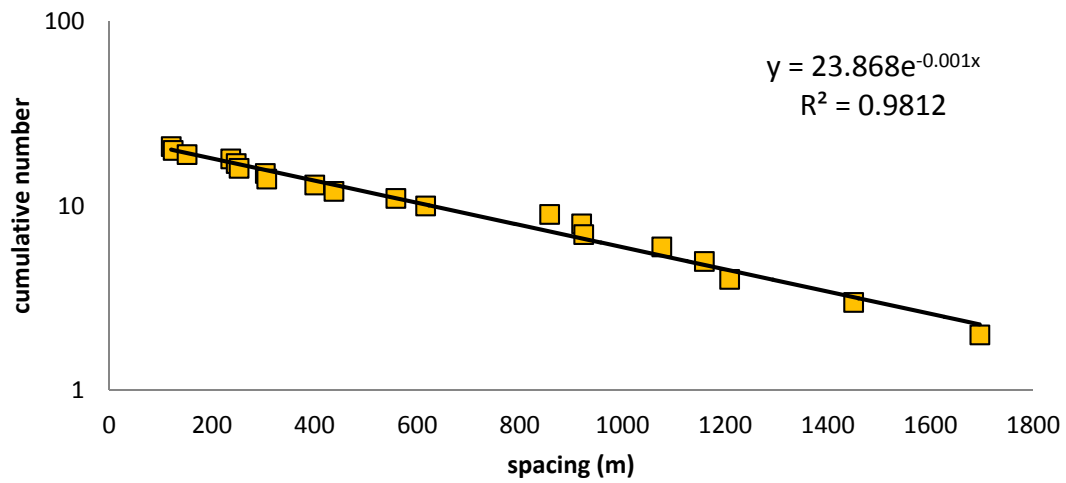




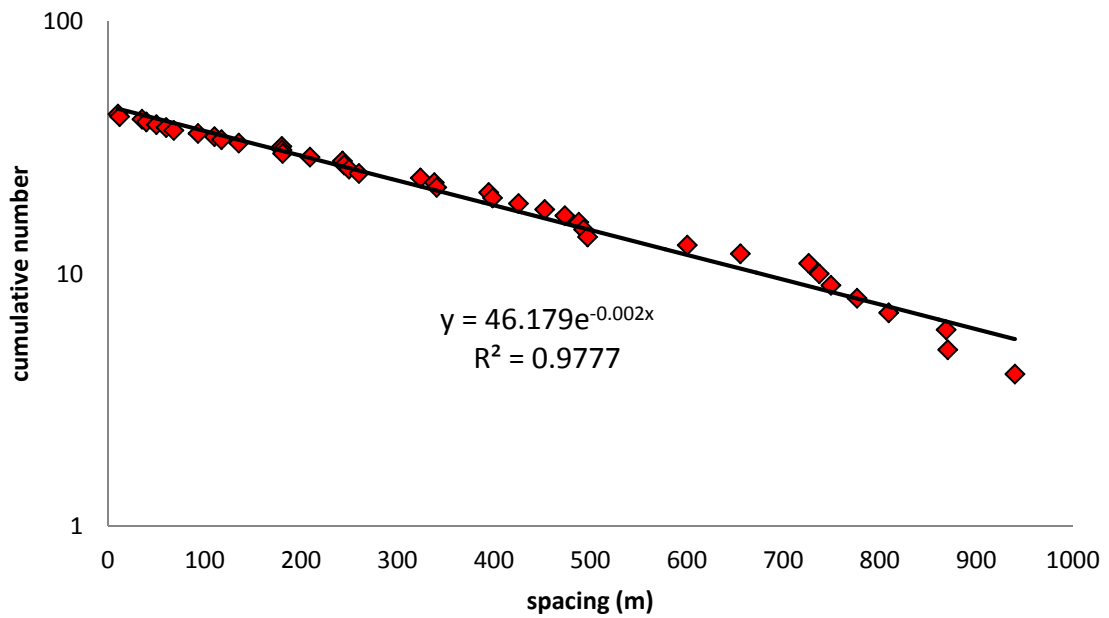




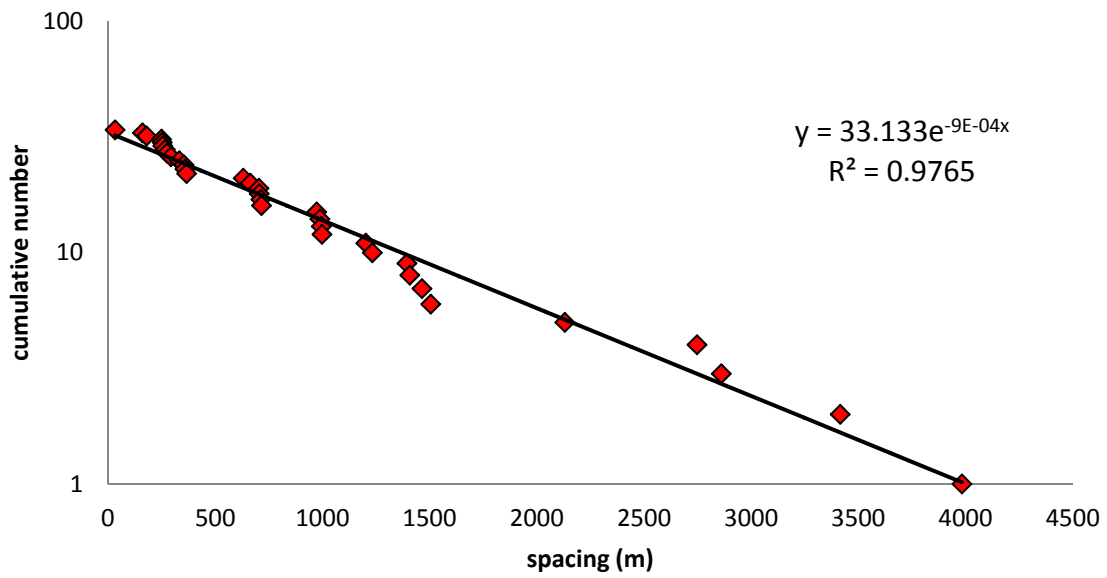
### Assynt Terrane - low resolution well 14



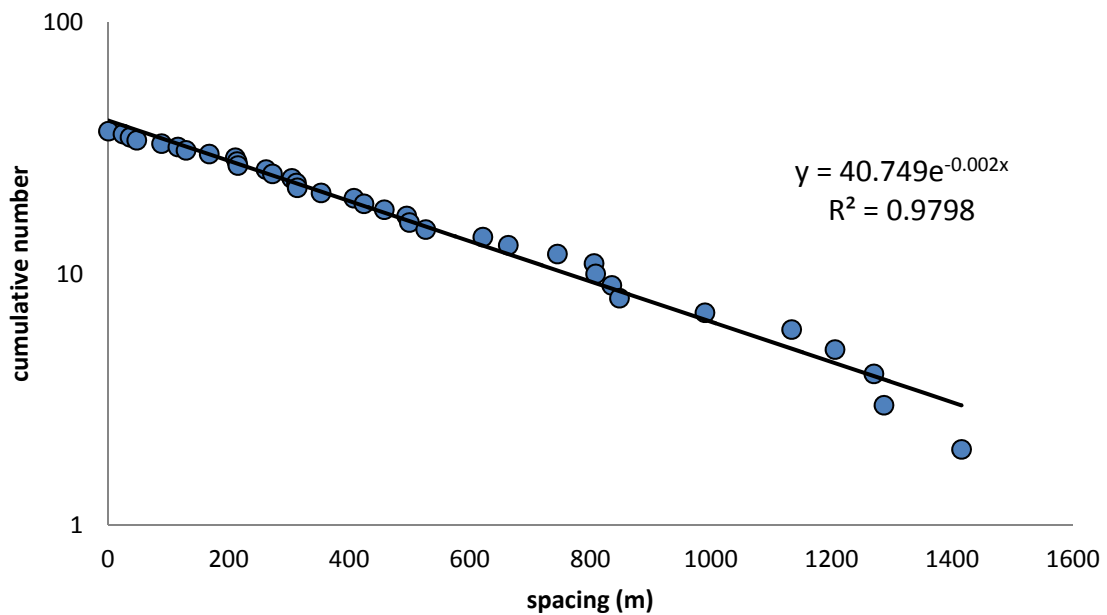
### Assynt Terrane - low resolution well 21



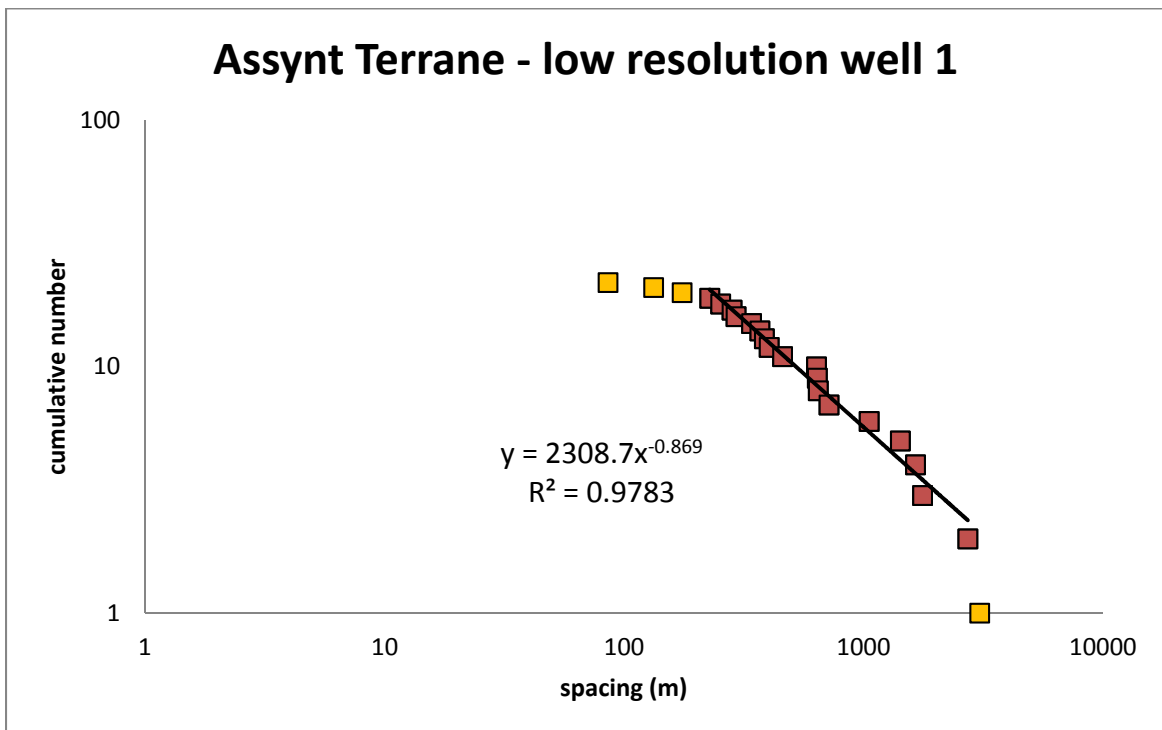
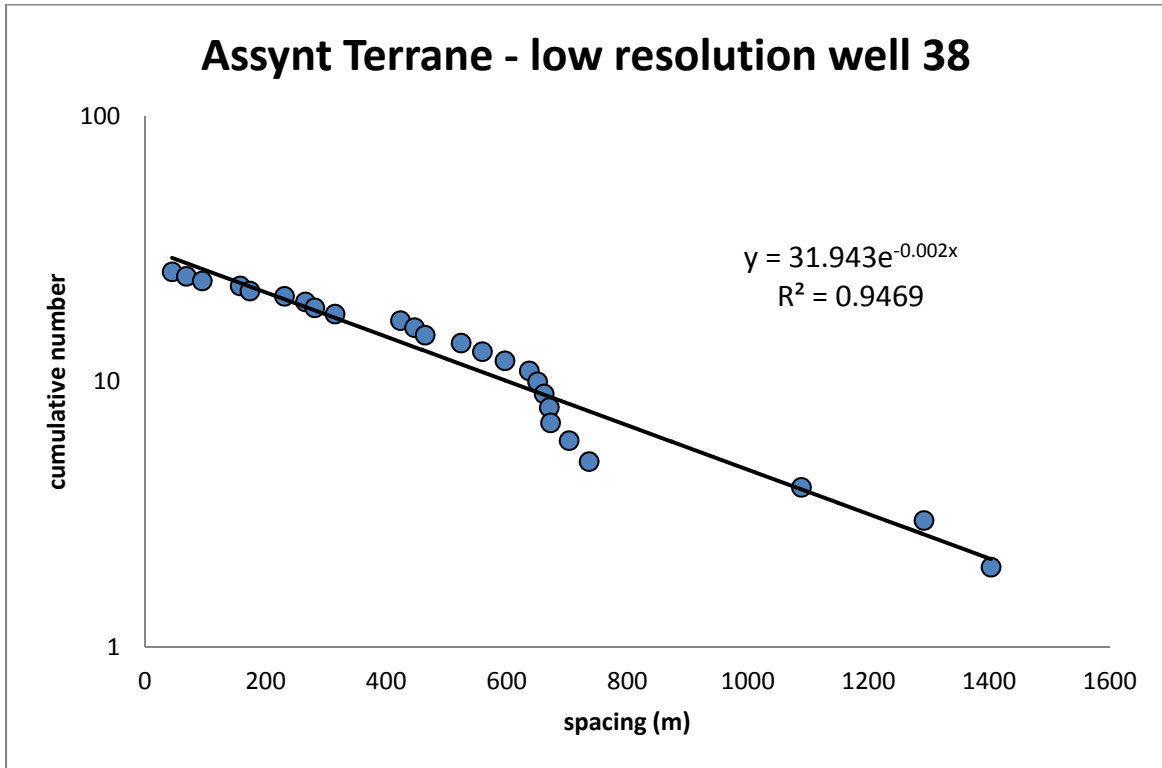
### Assynt Terrane - low resolution well 22

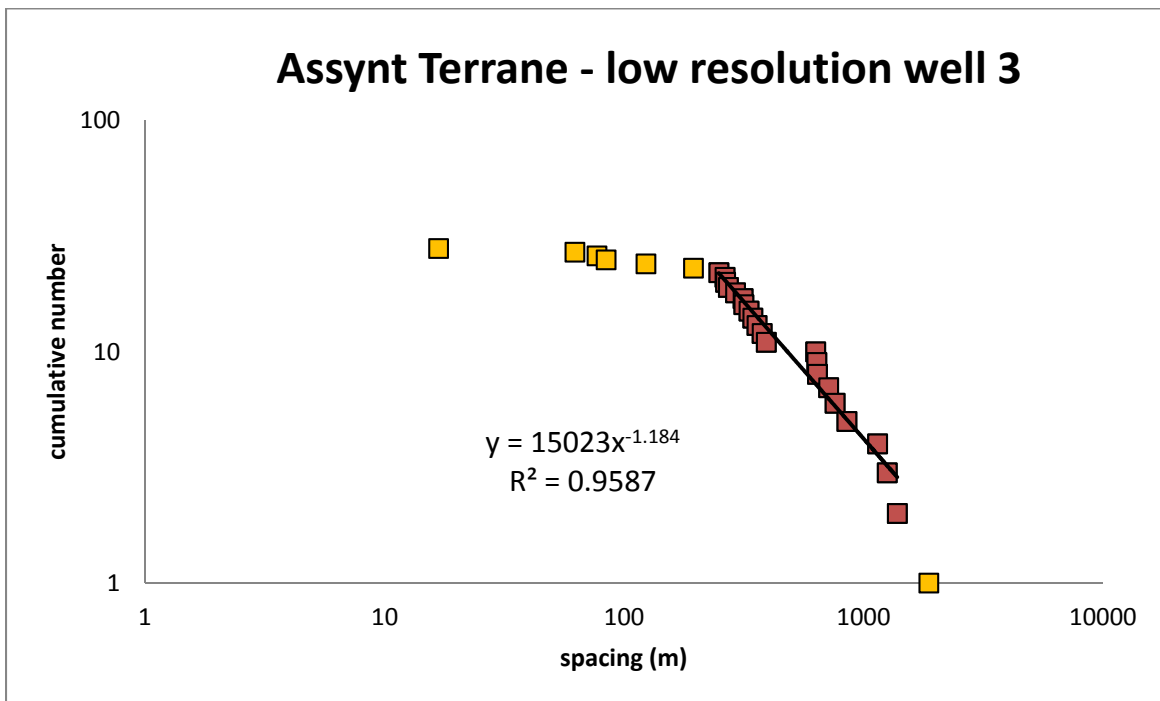
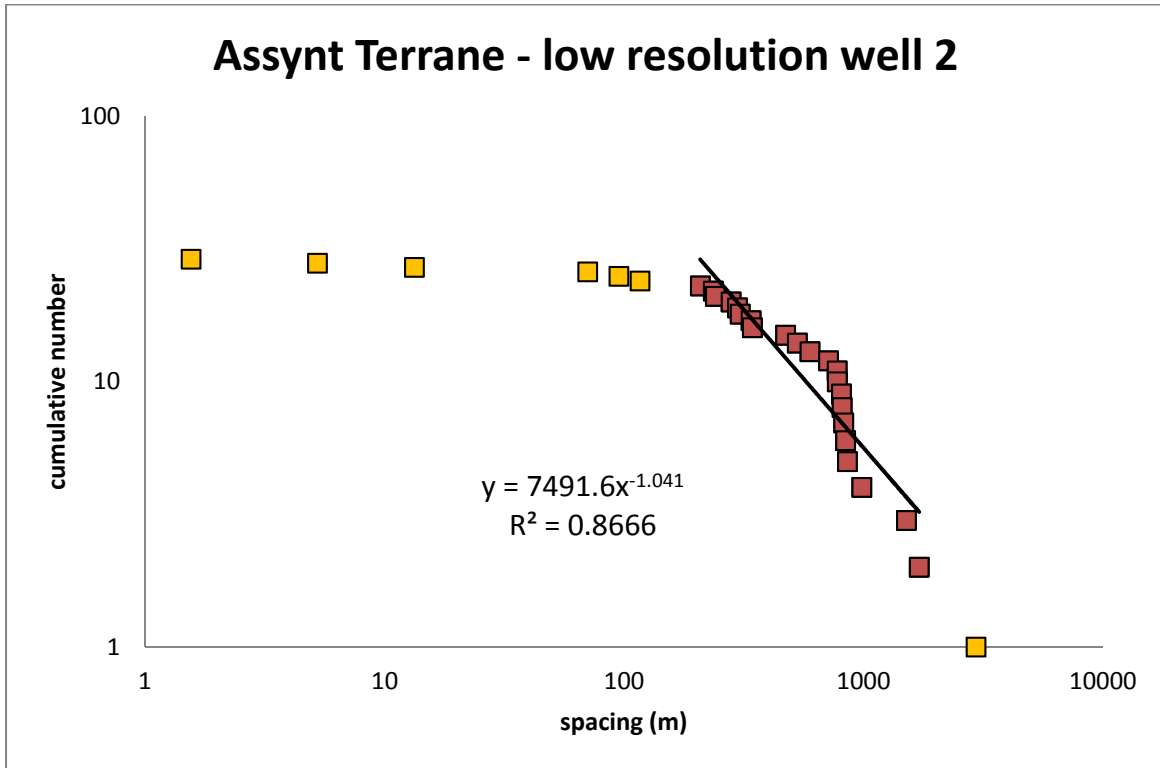


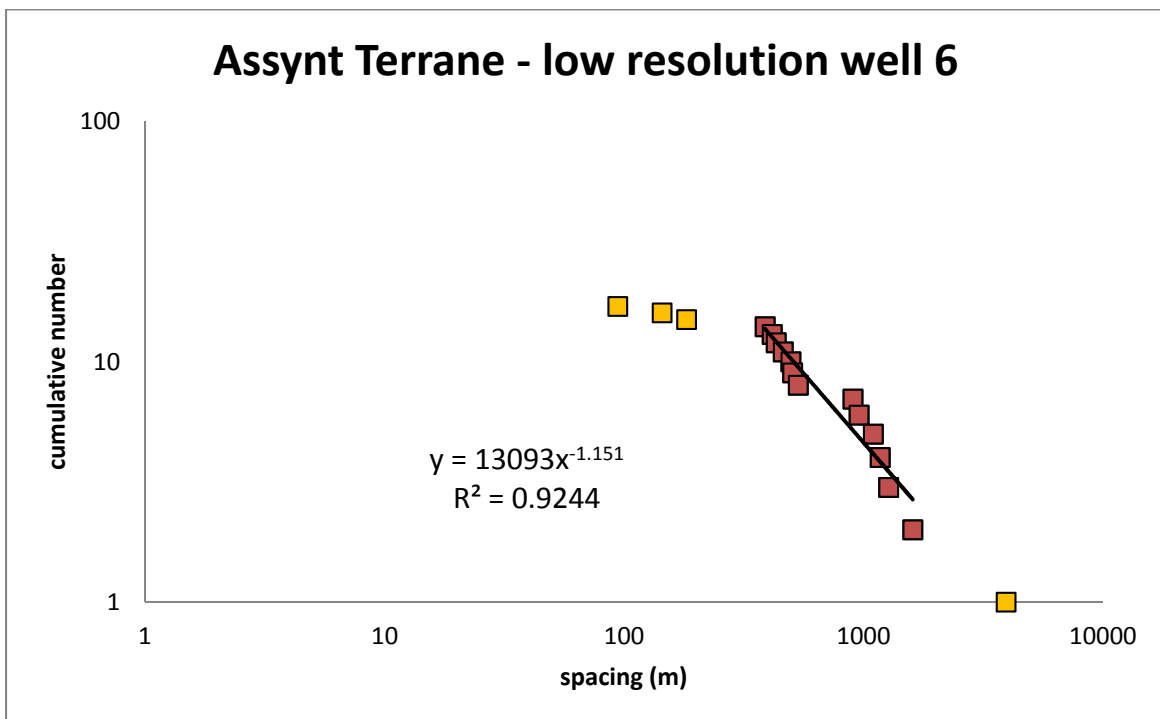
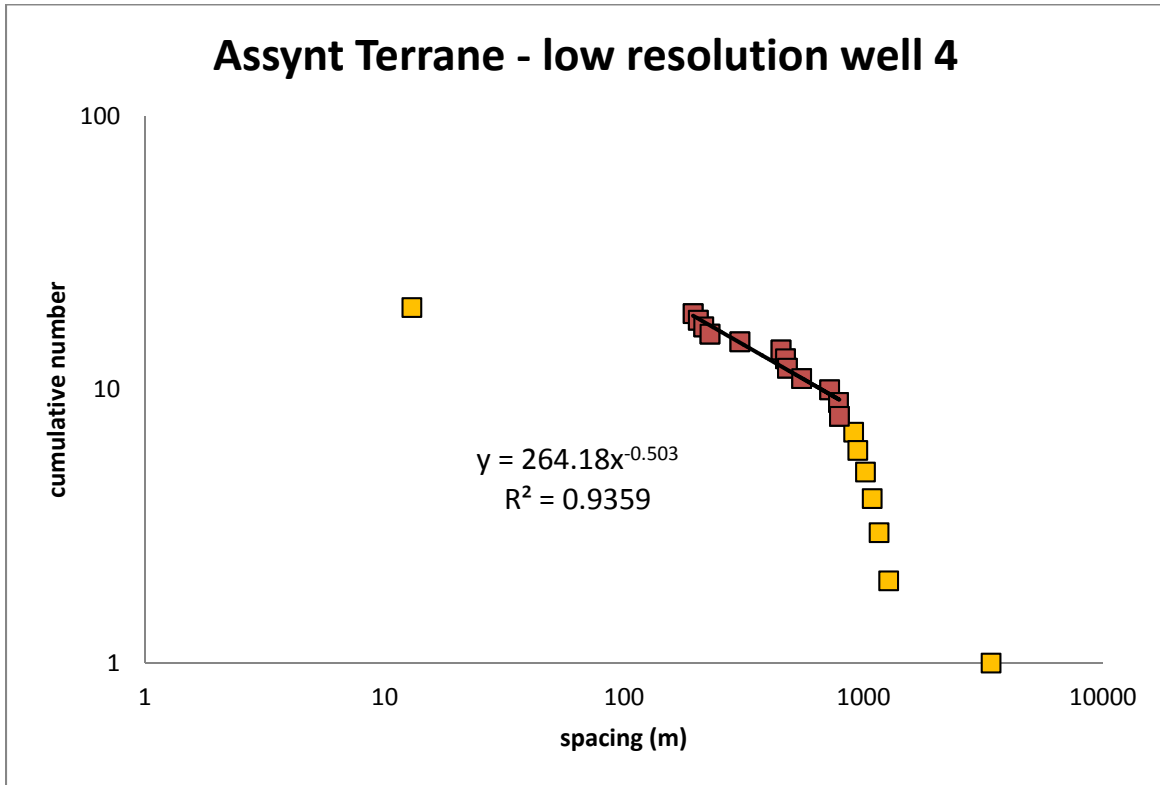
### Assynt Terrane - low resolution well 32

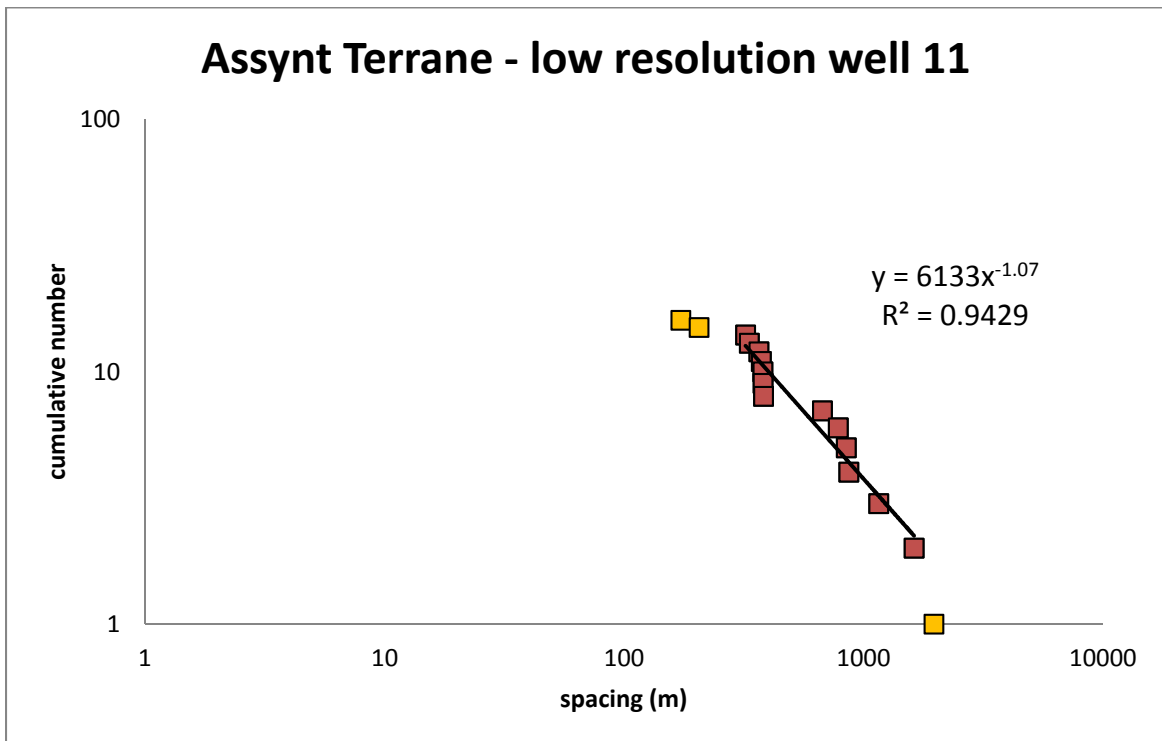
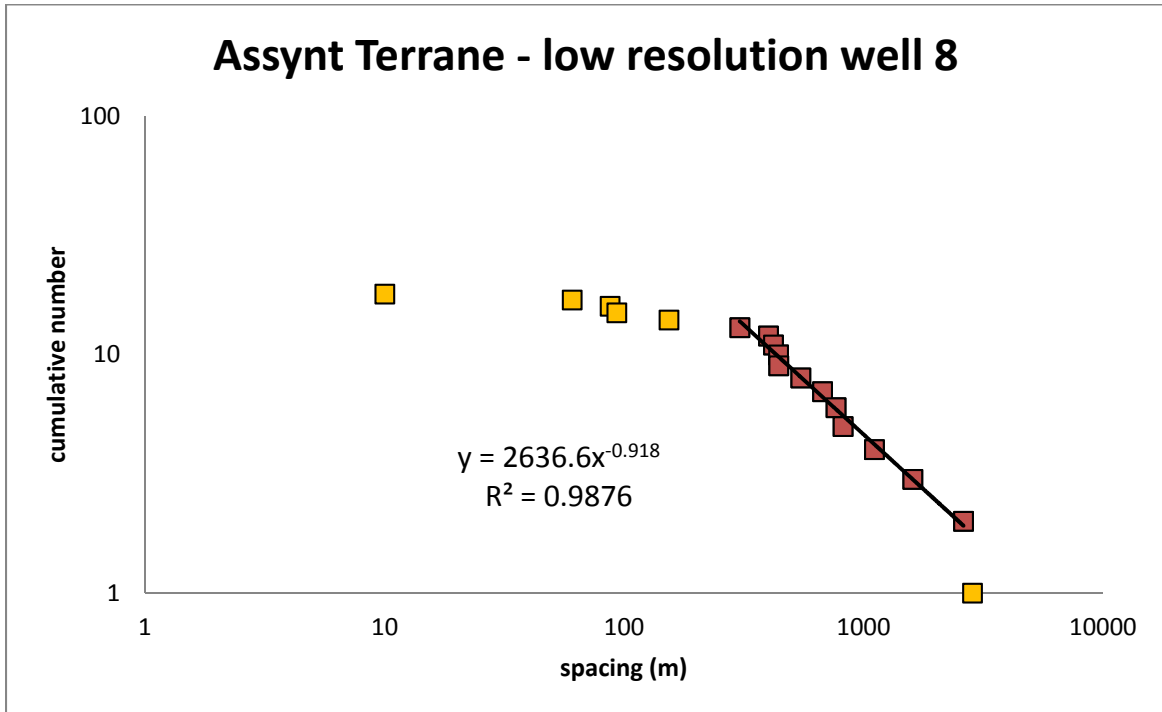


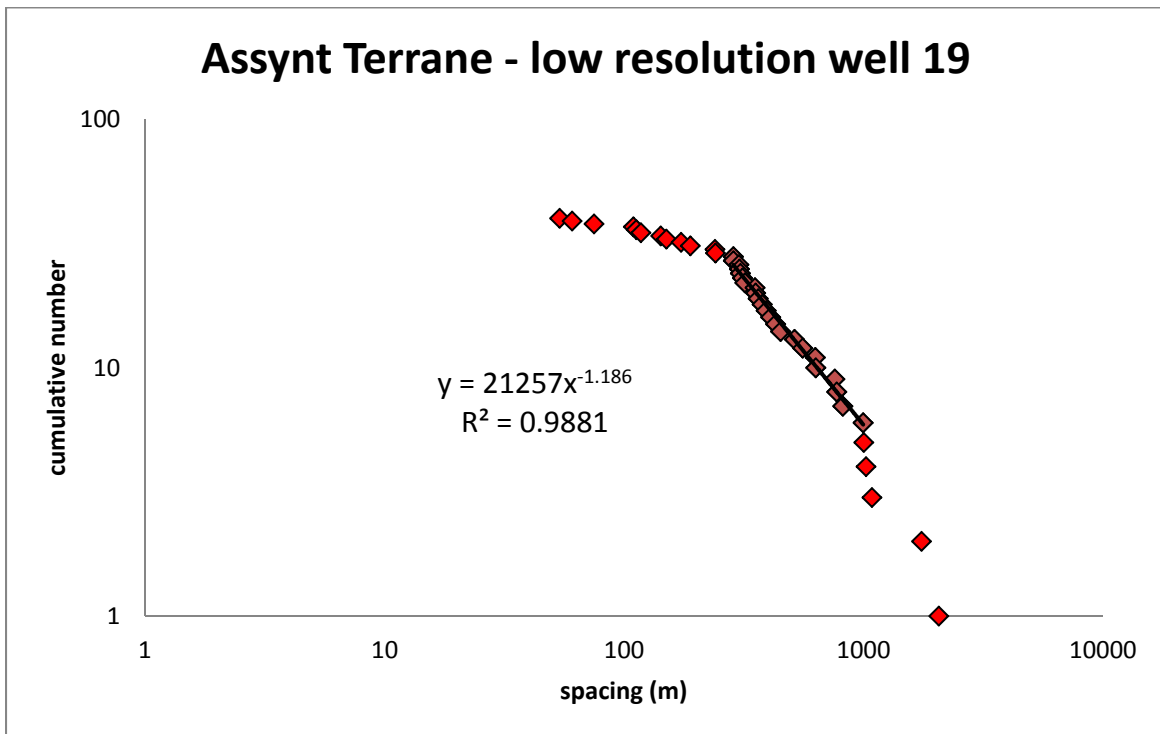
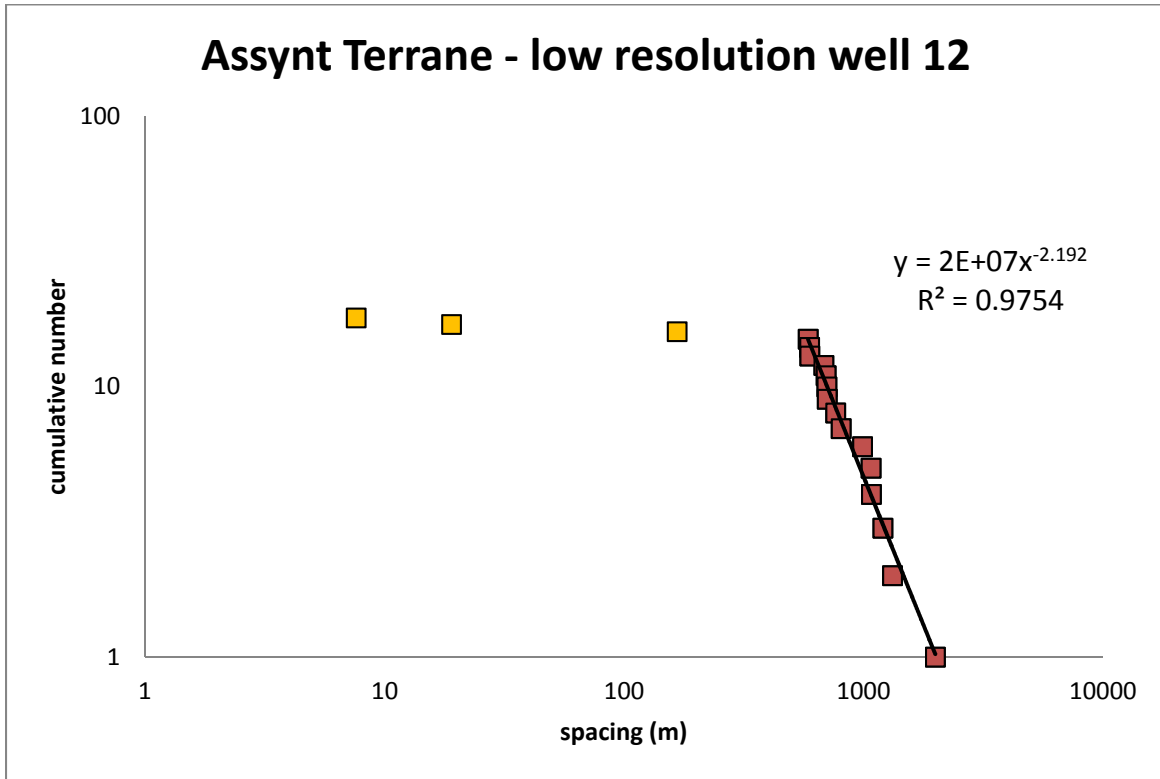


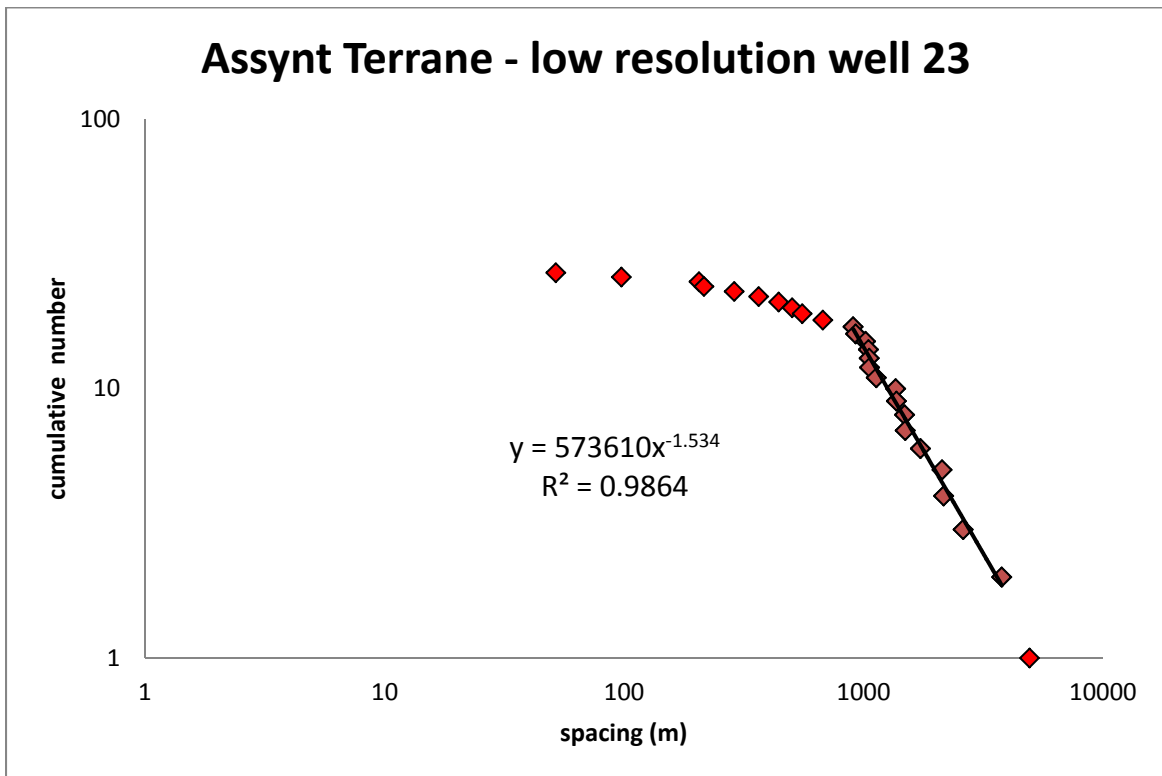
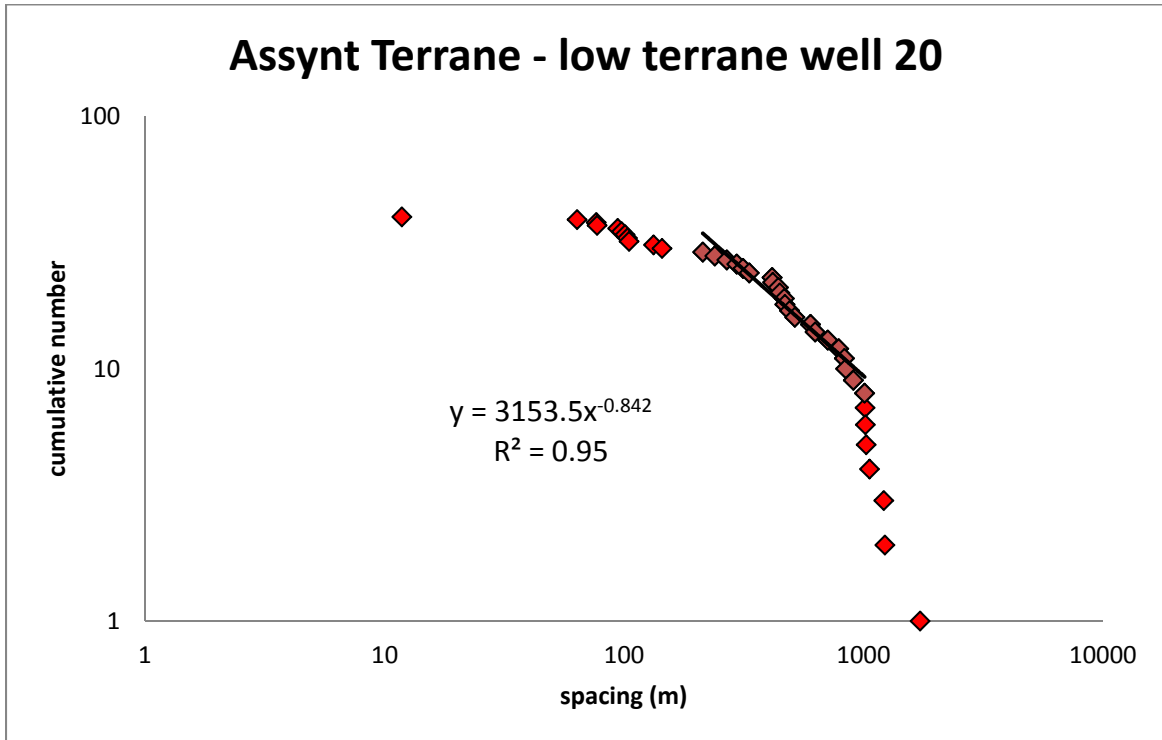


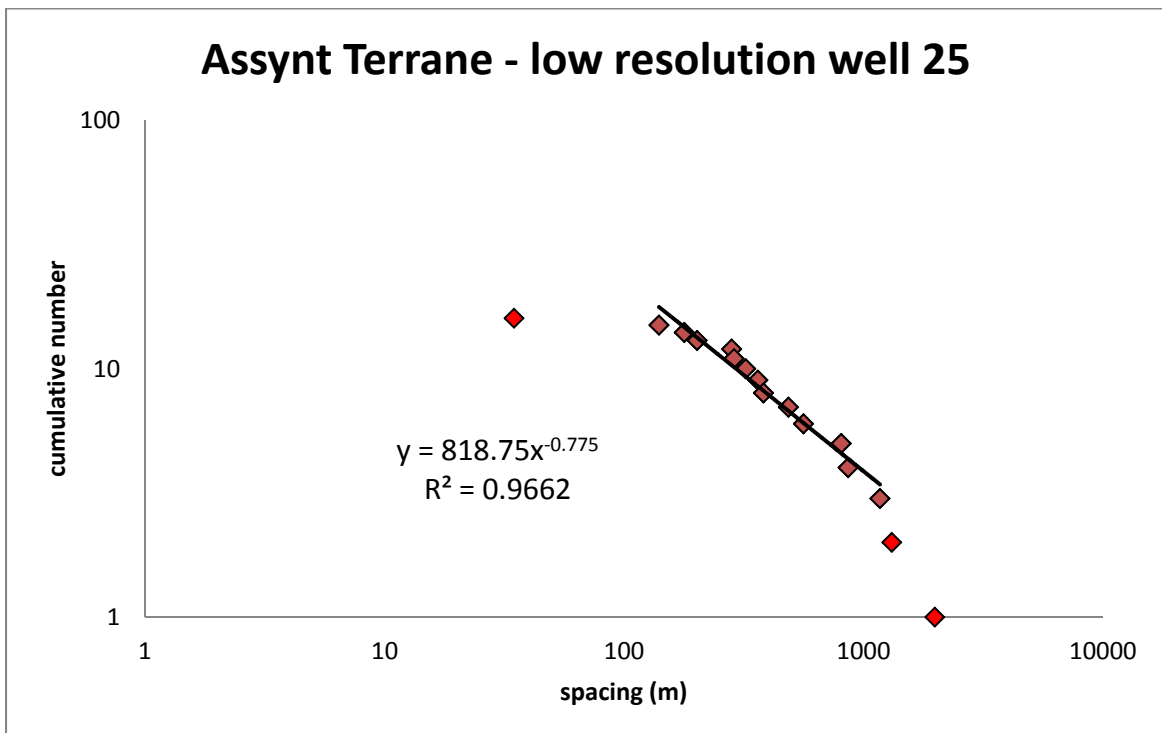
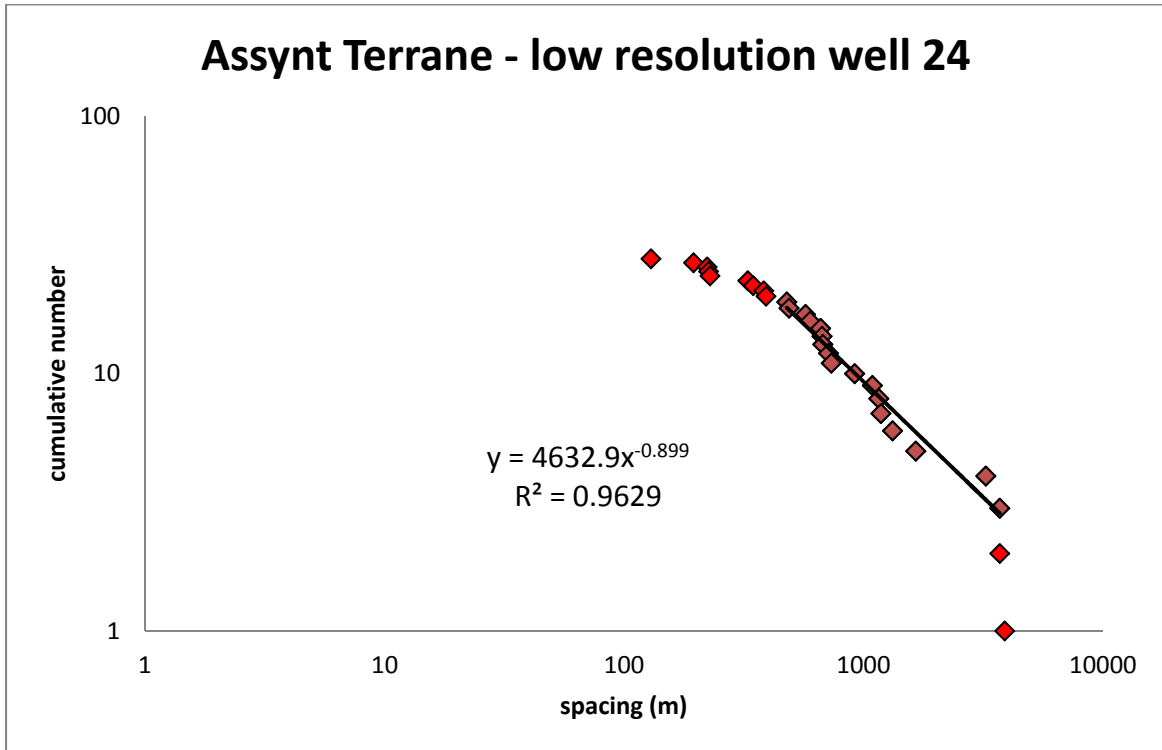


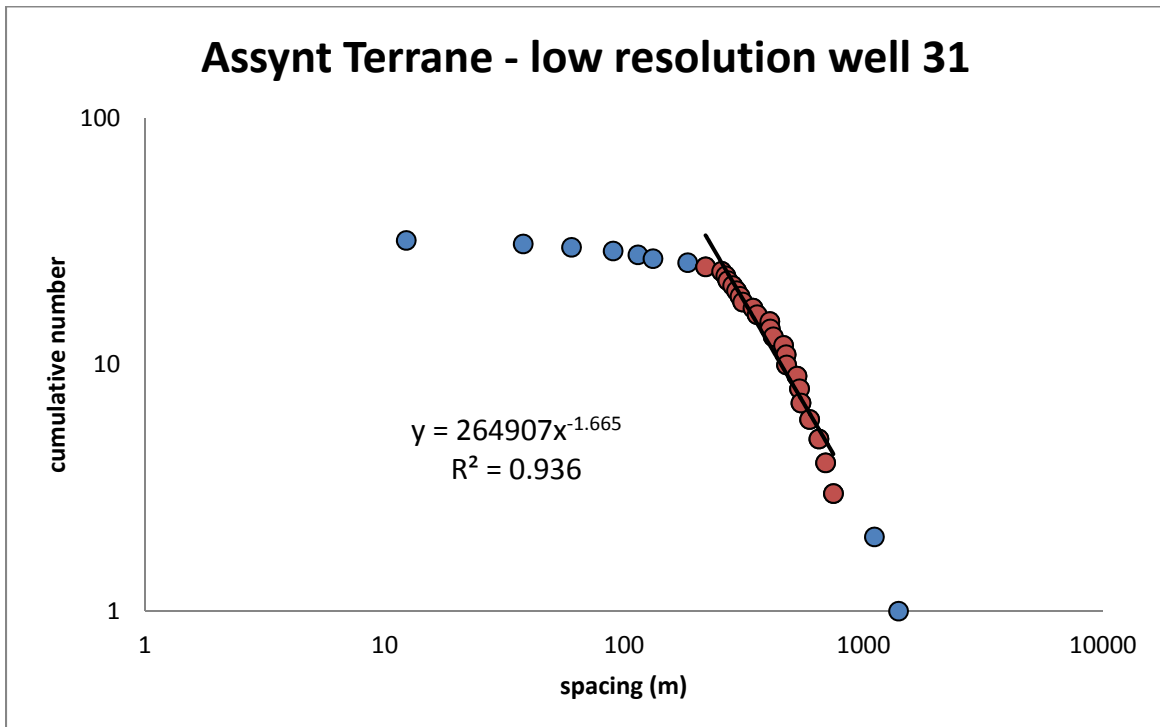
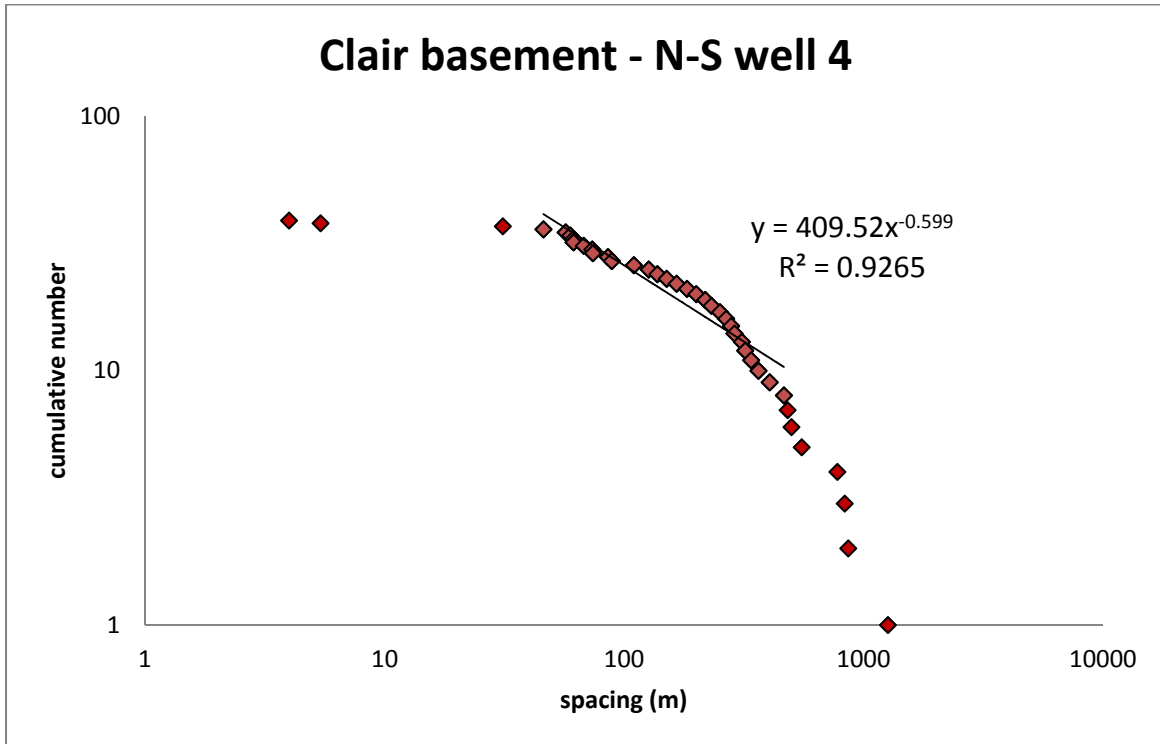




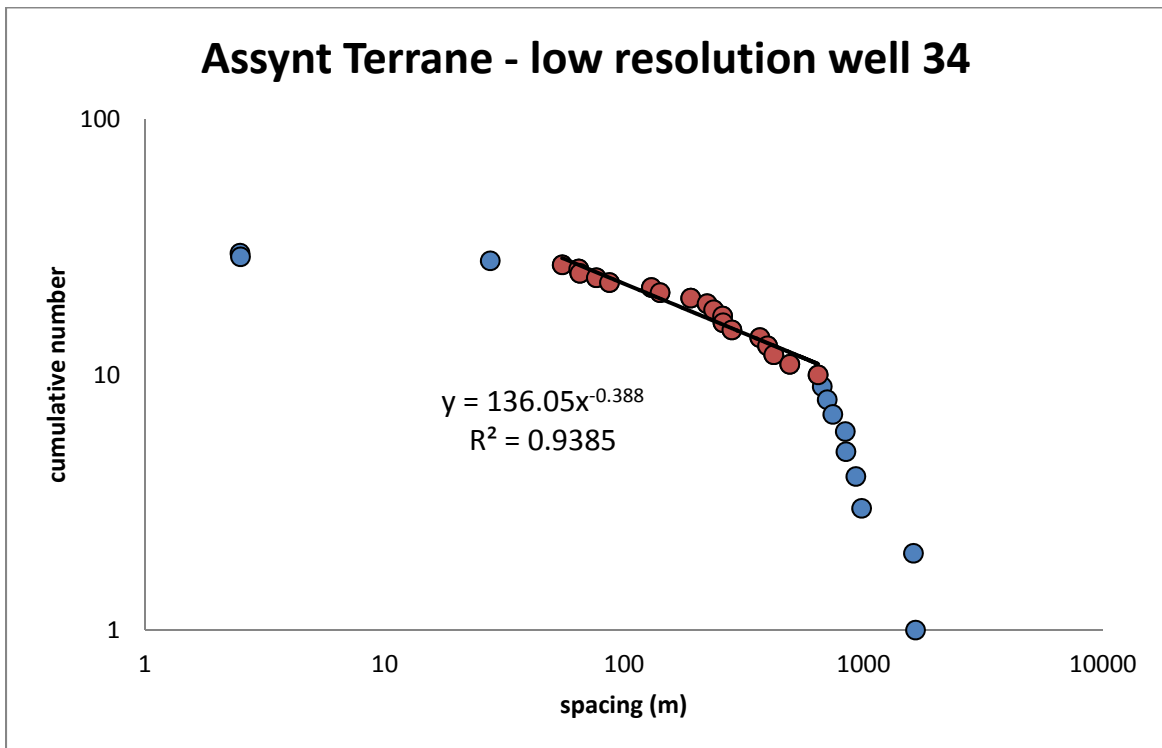
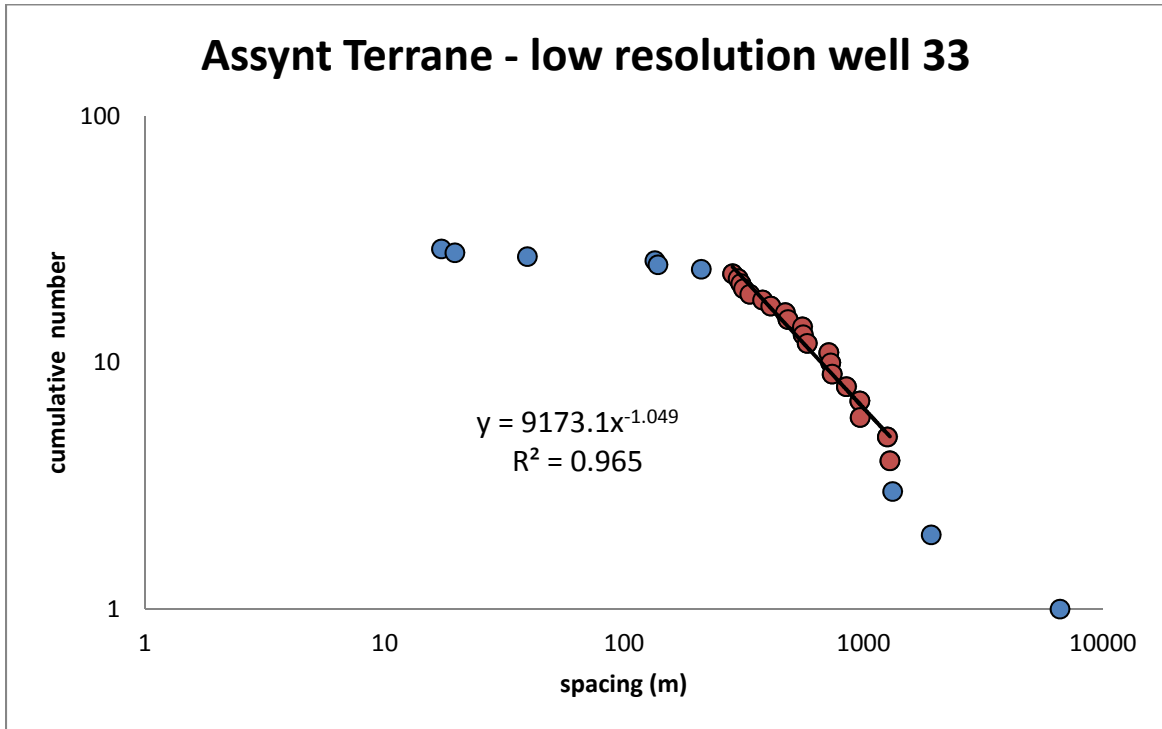


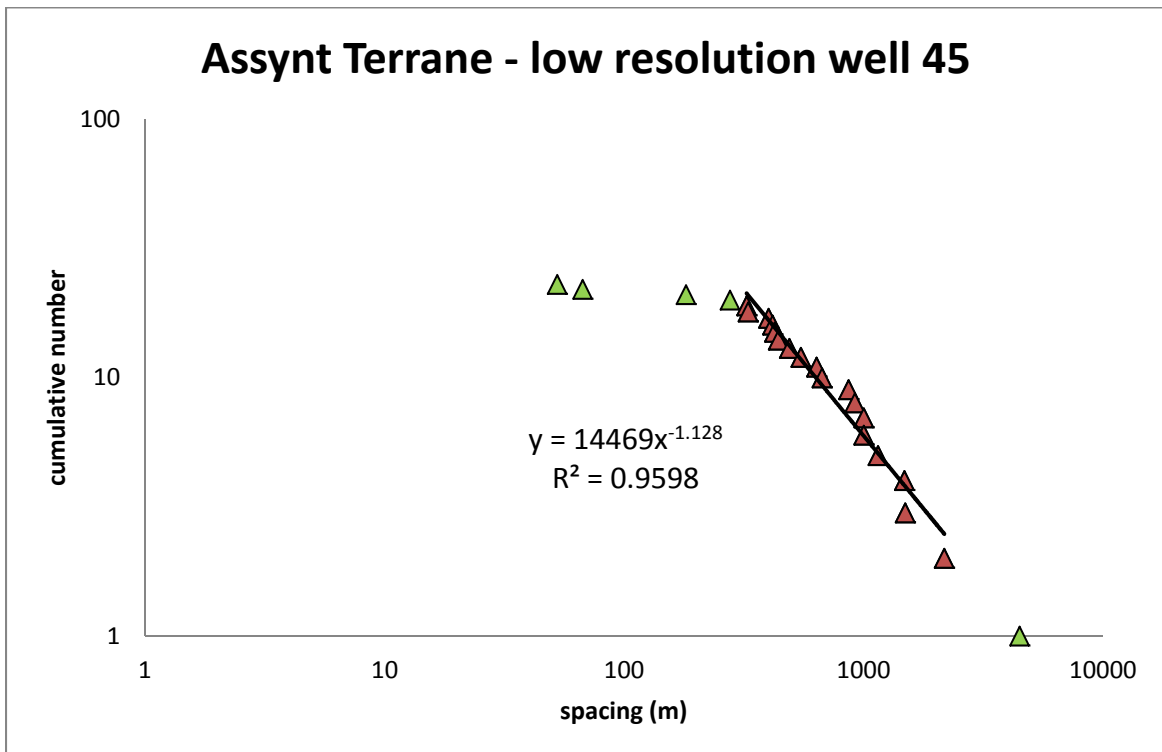
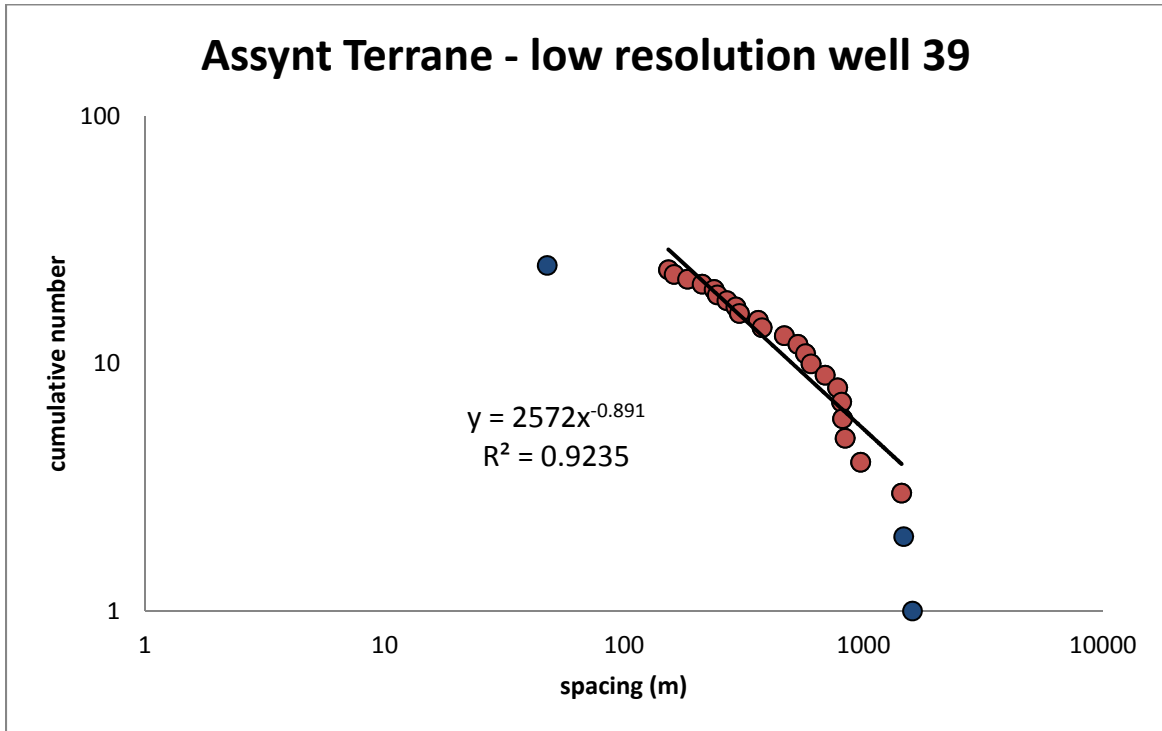


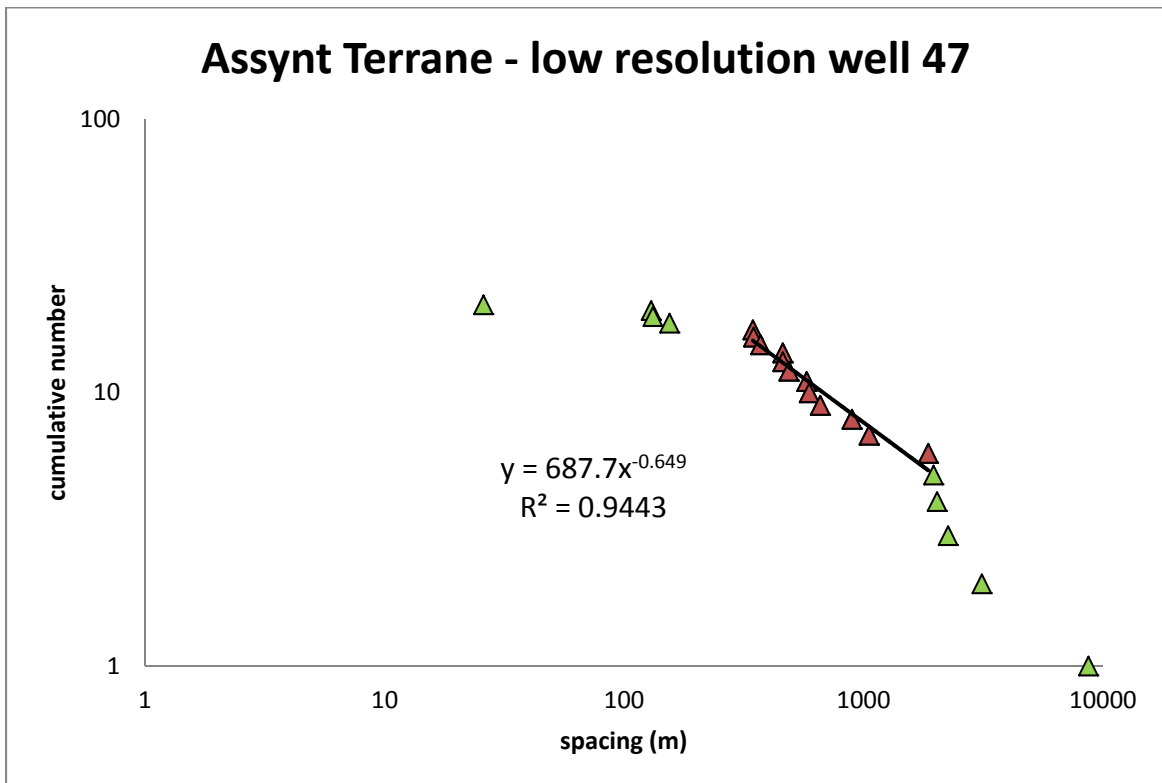
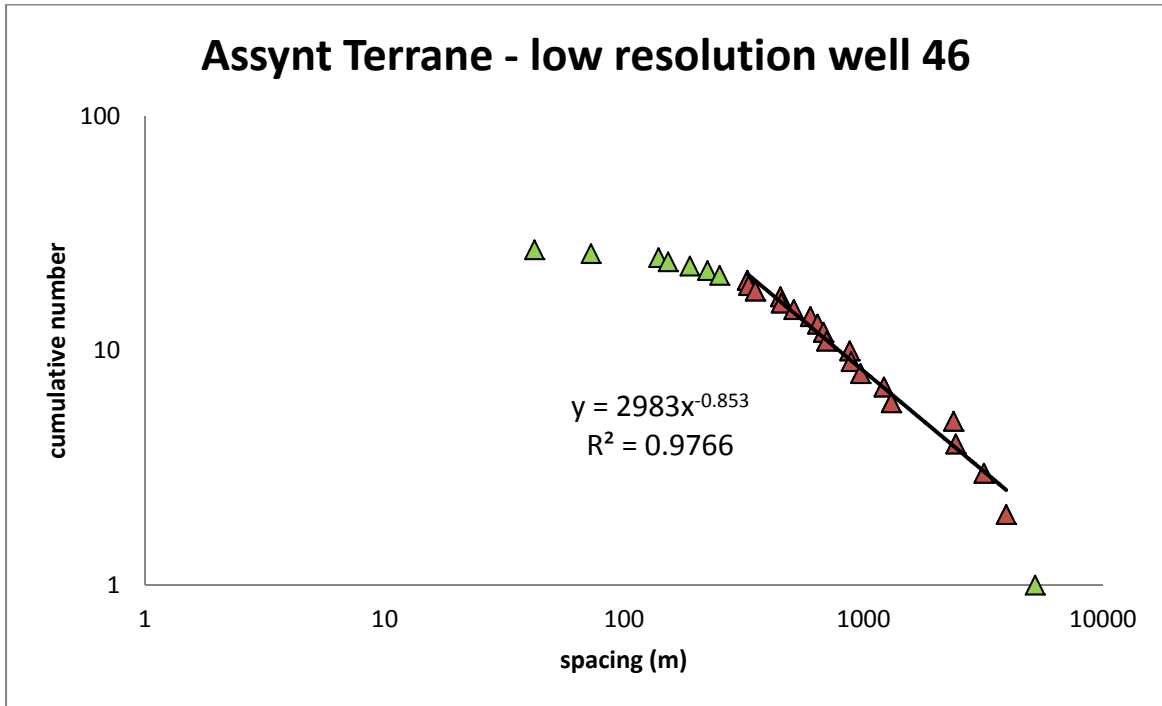


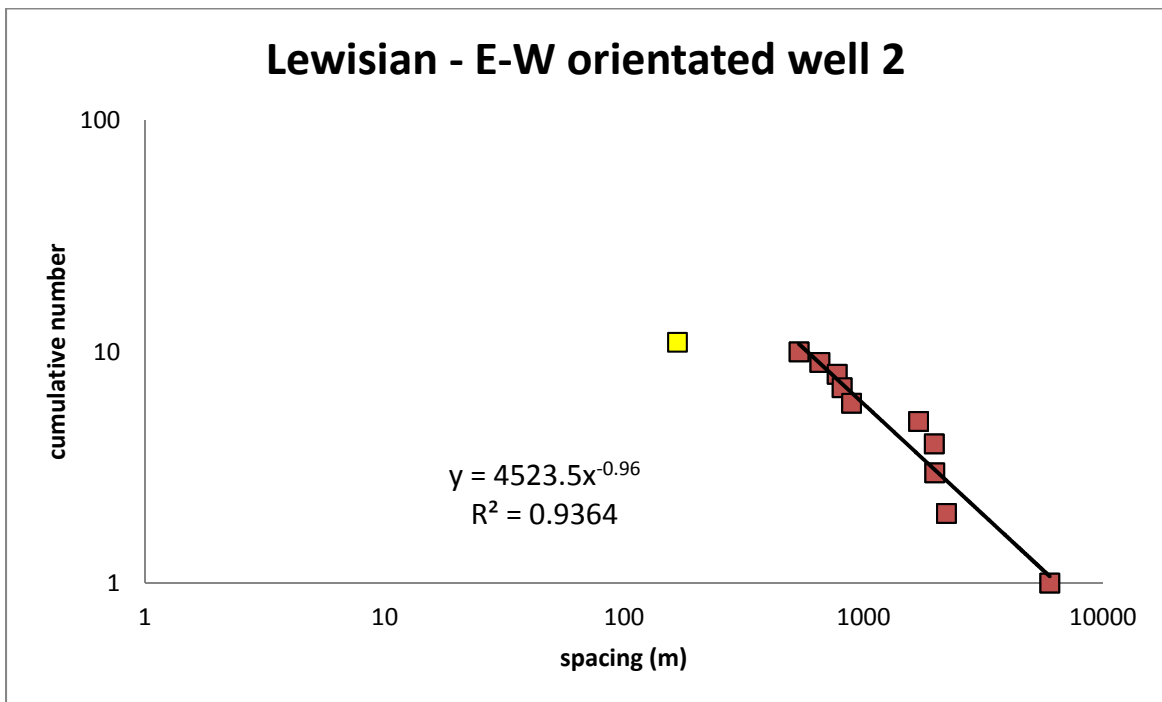
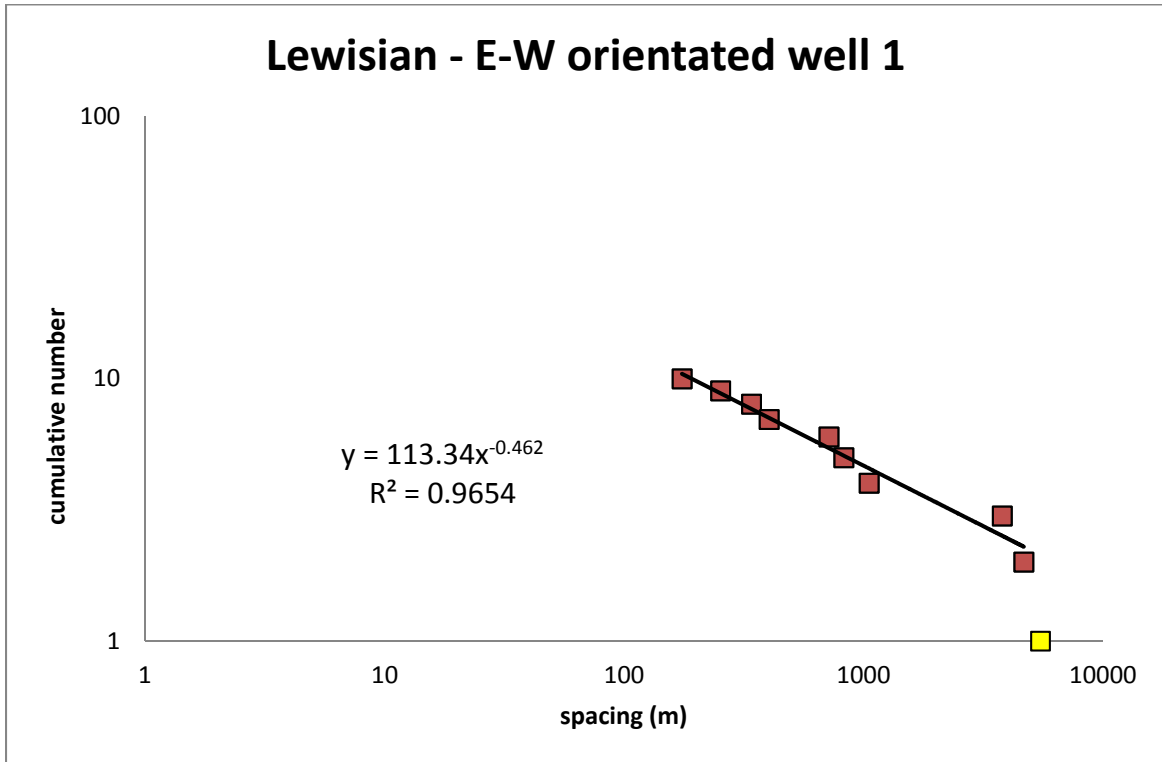


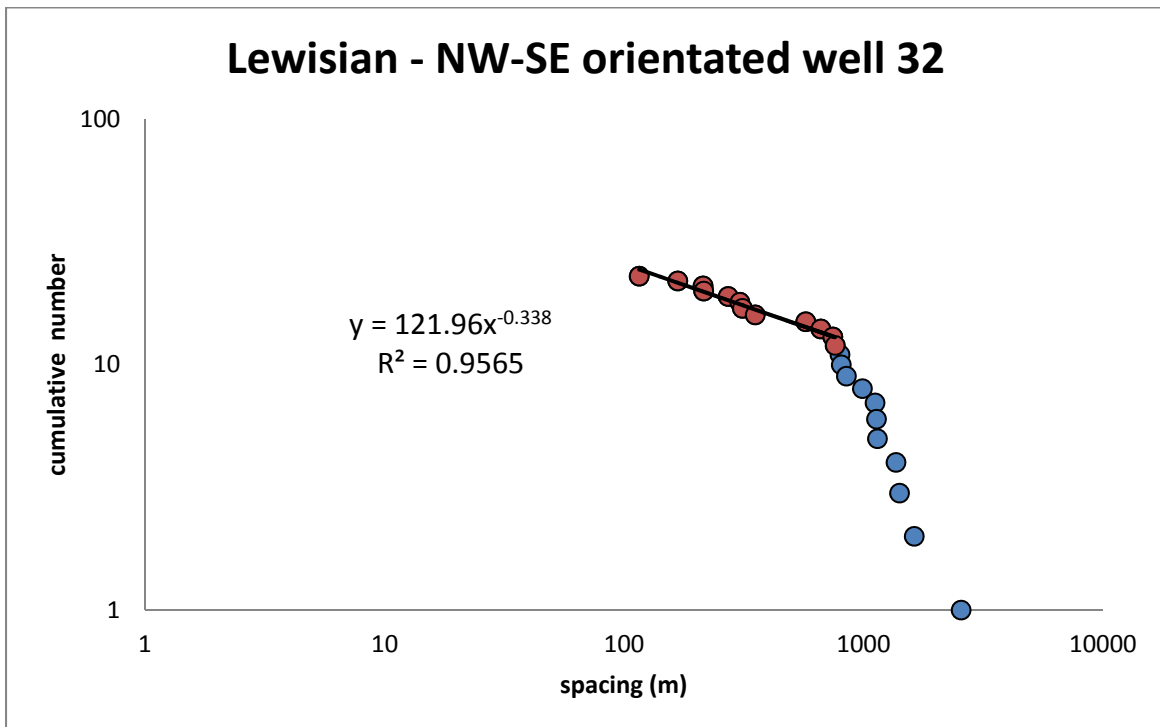
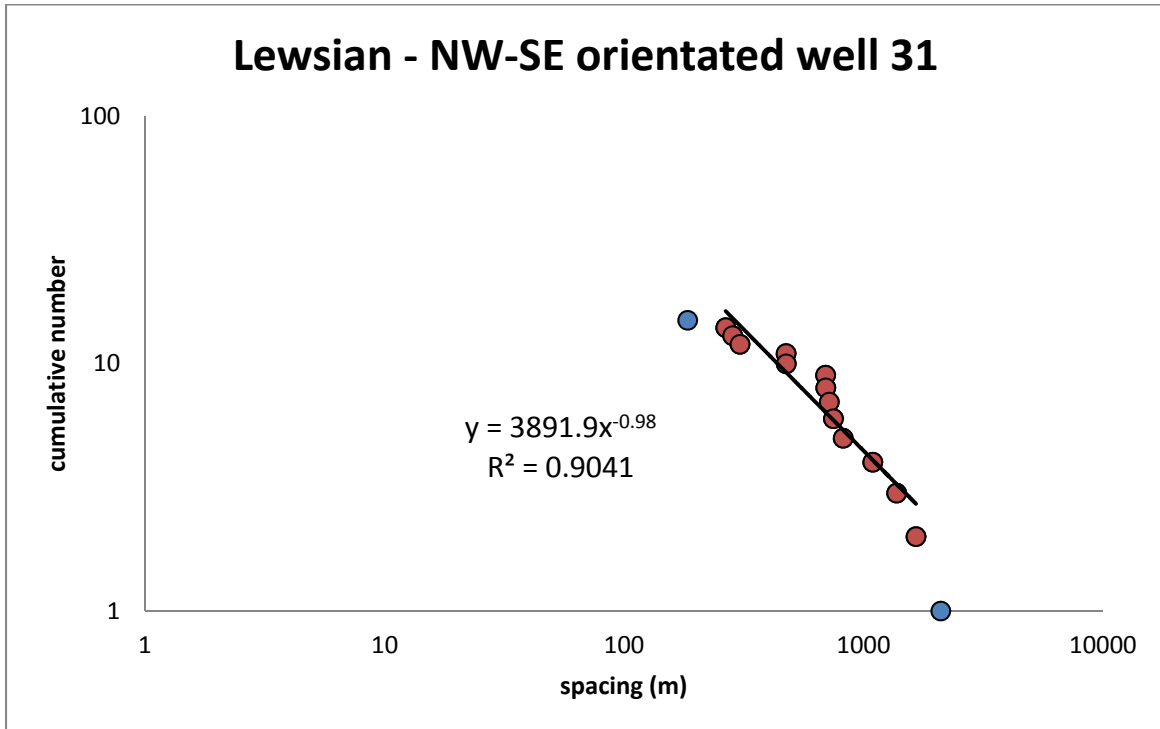


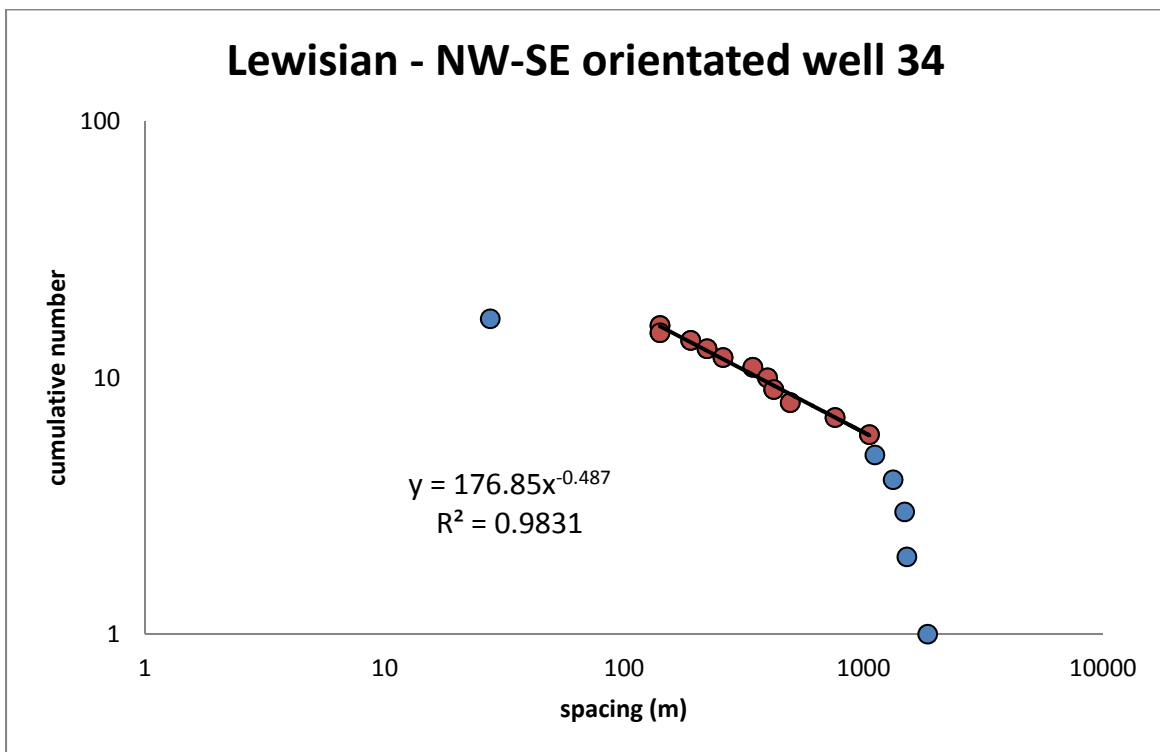
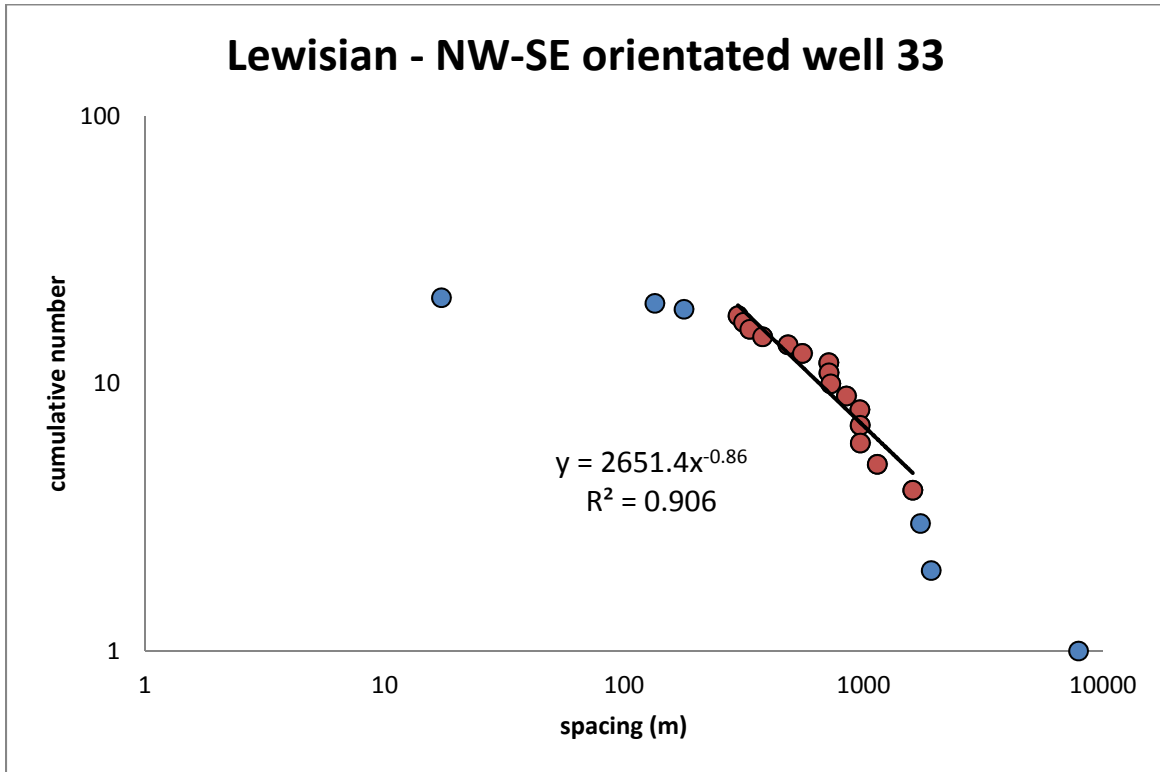


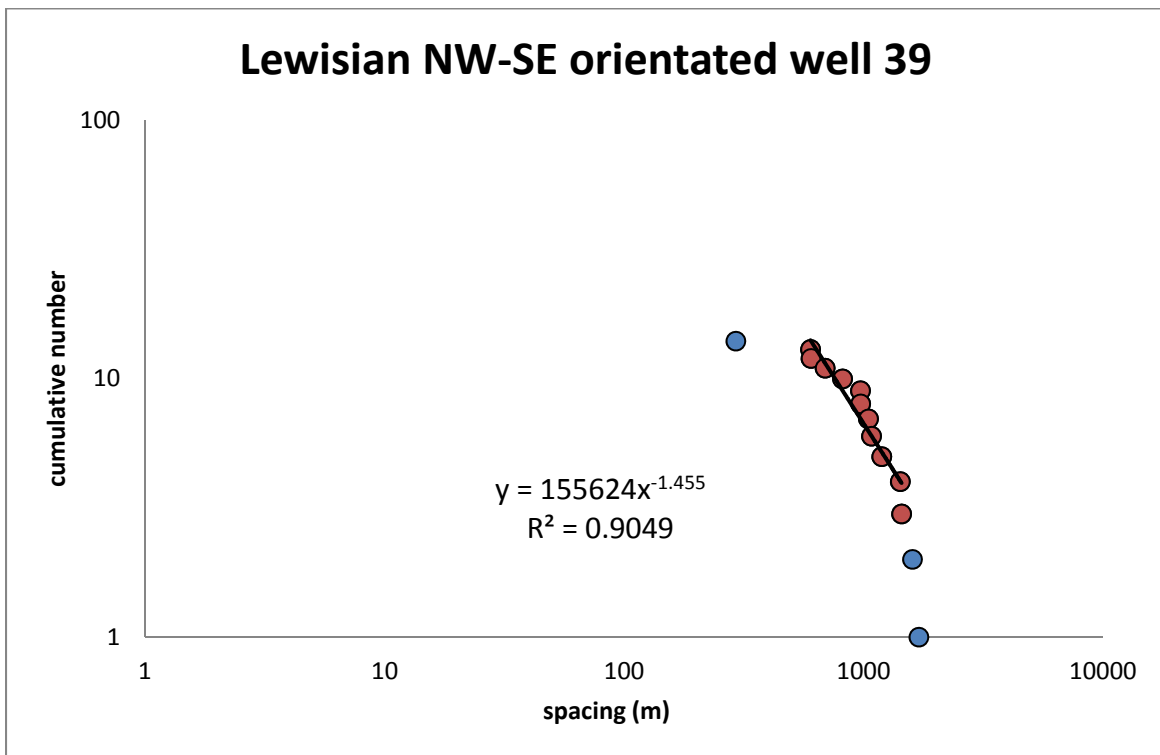
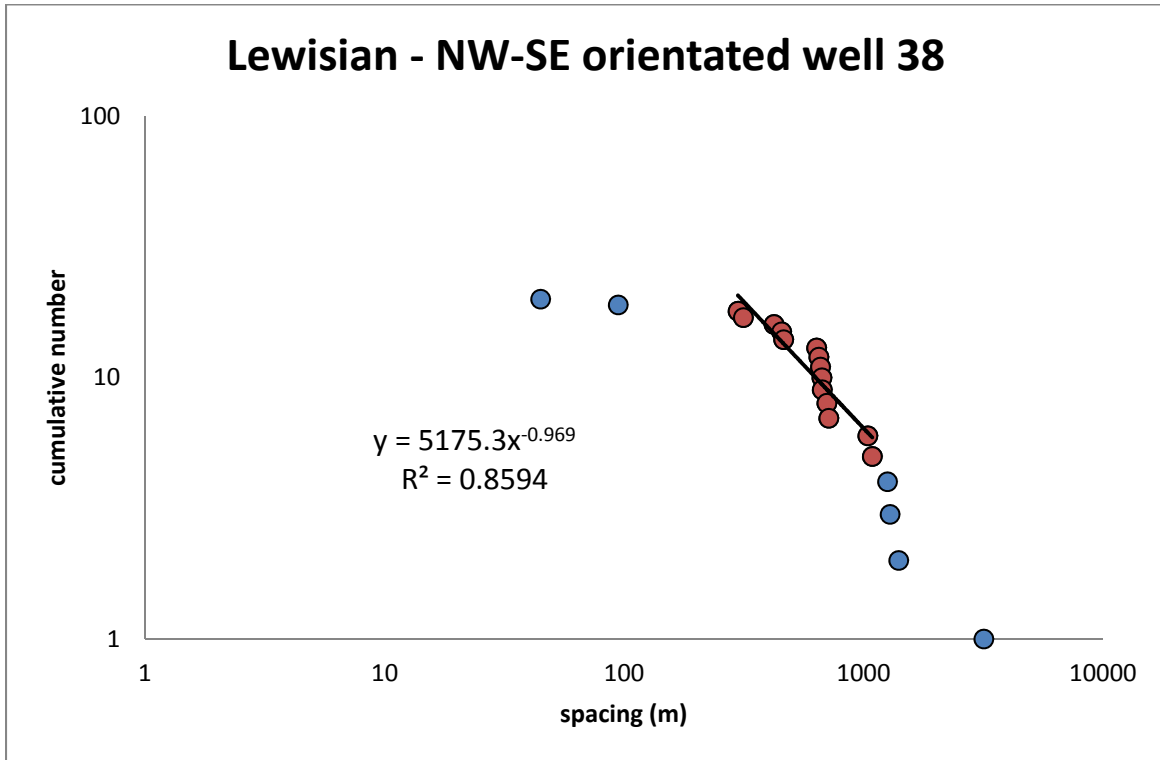


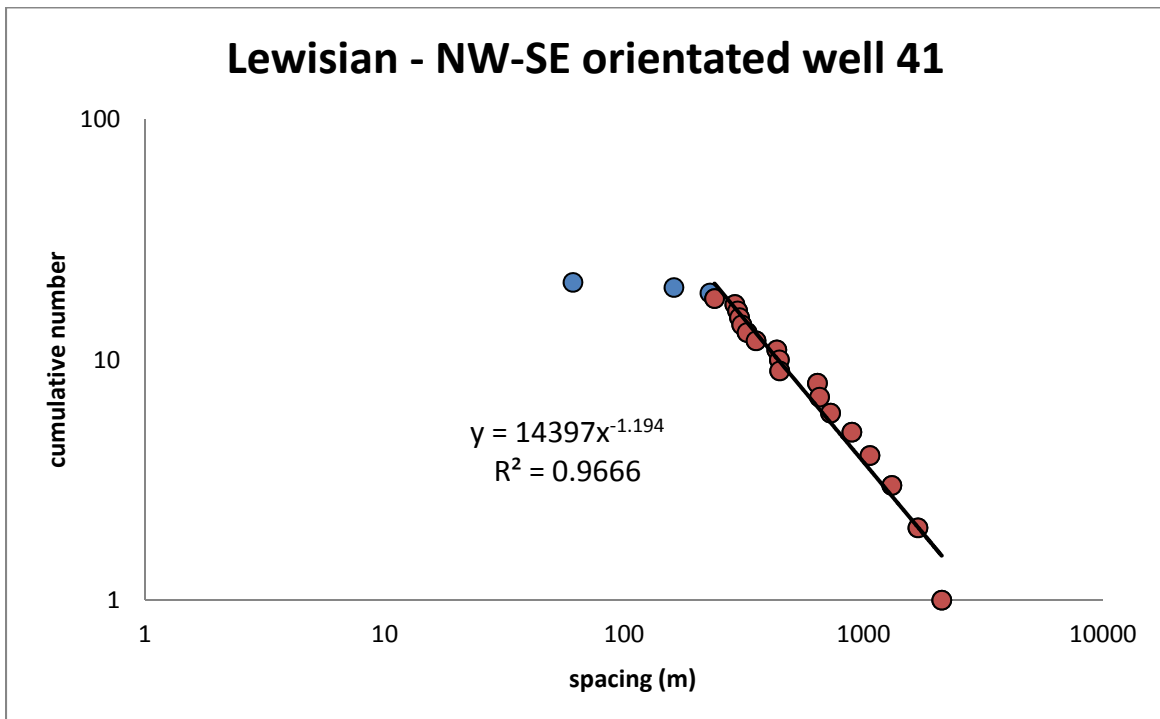
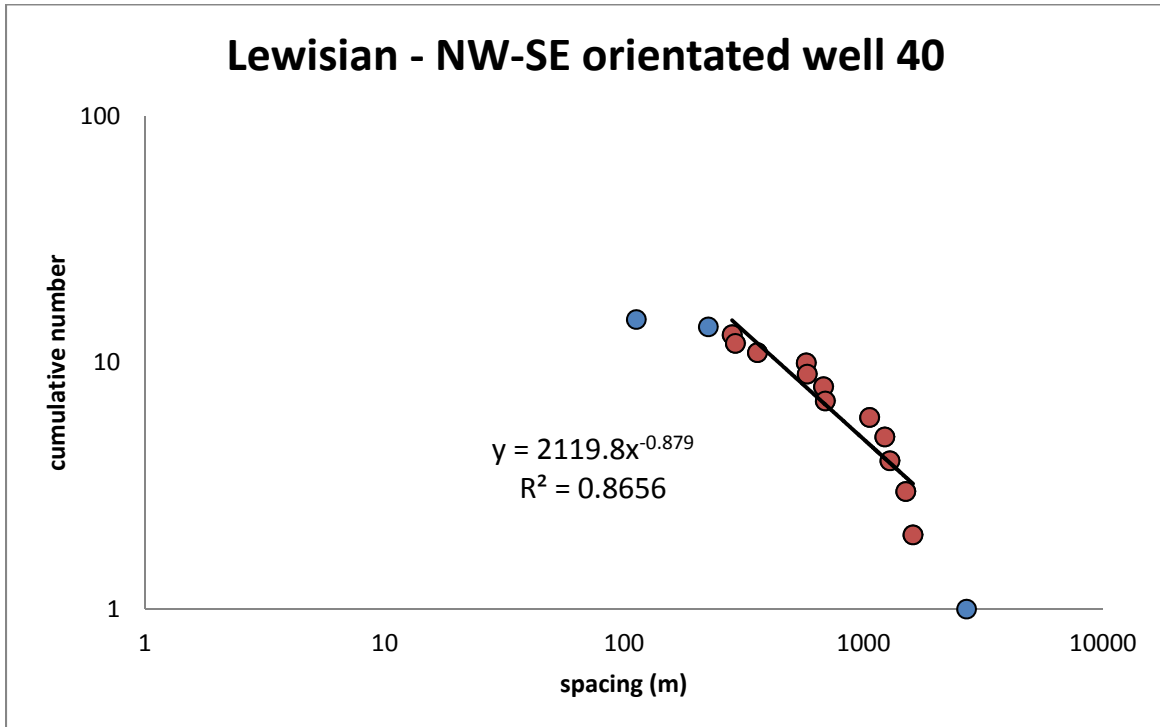




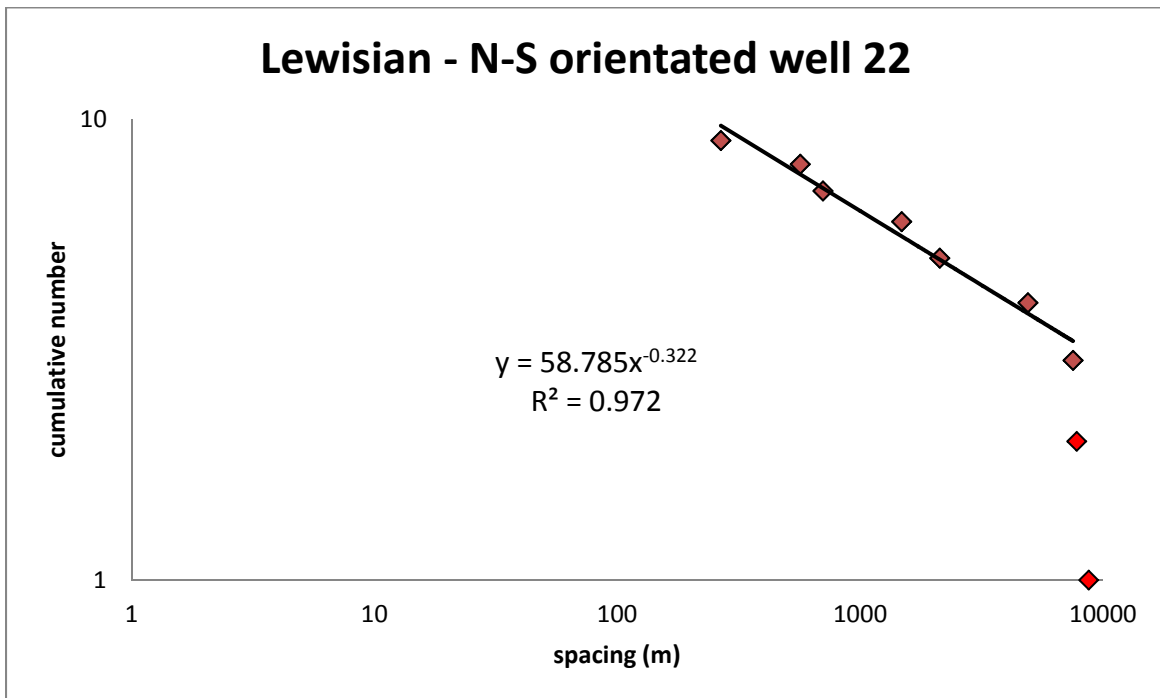
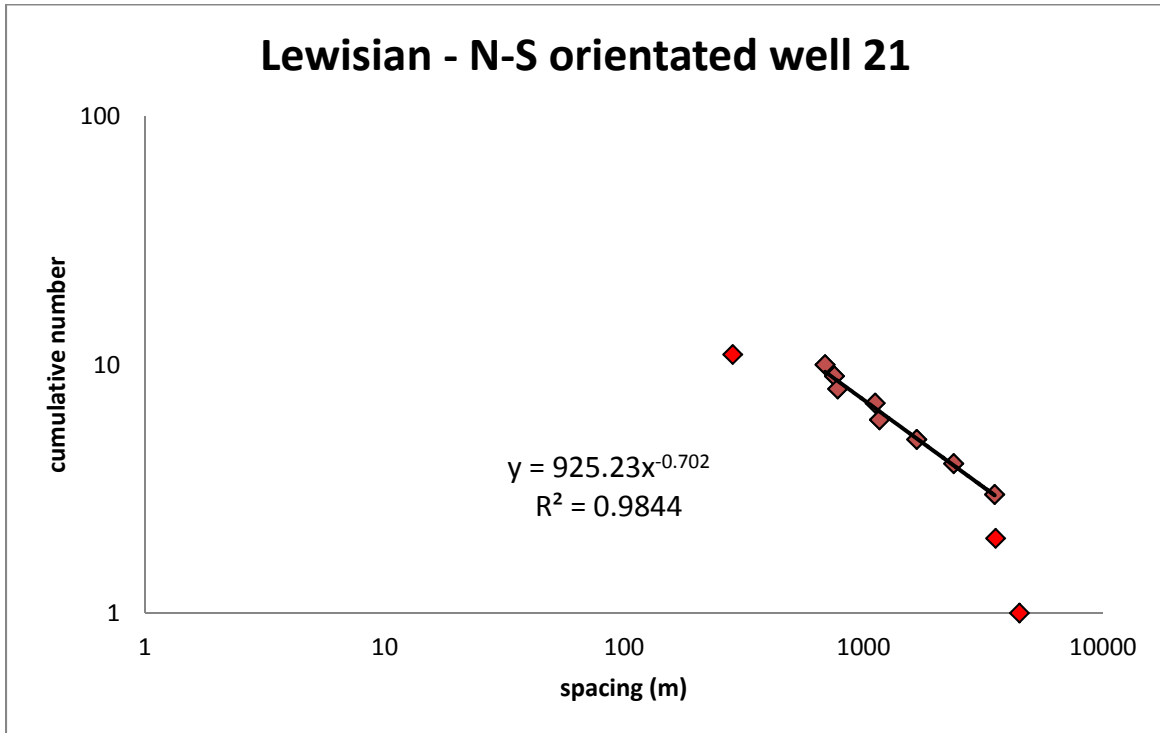


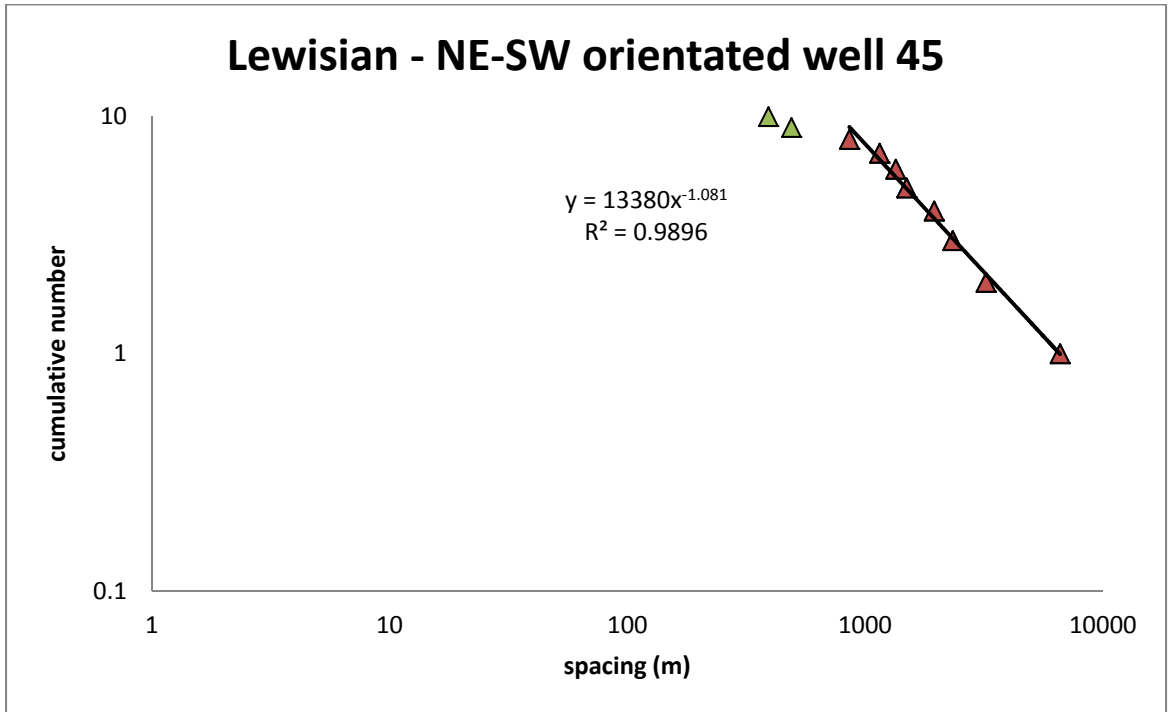






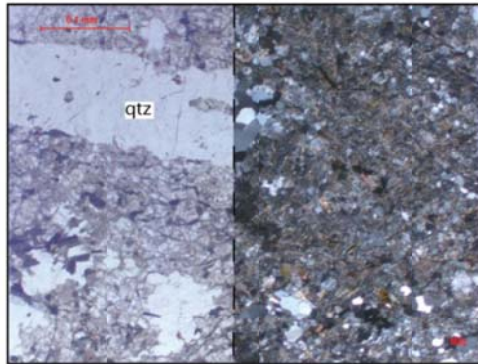




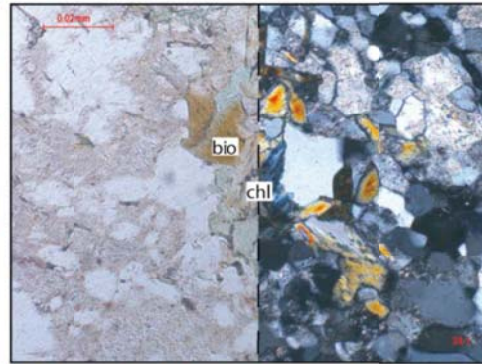
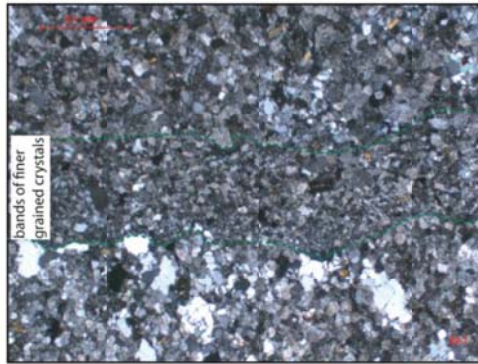


# IV: Thin section Photographs

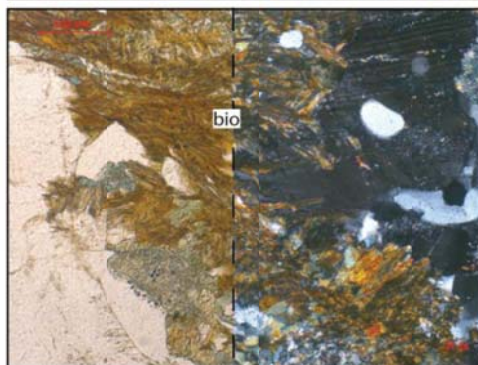
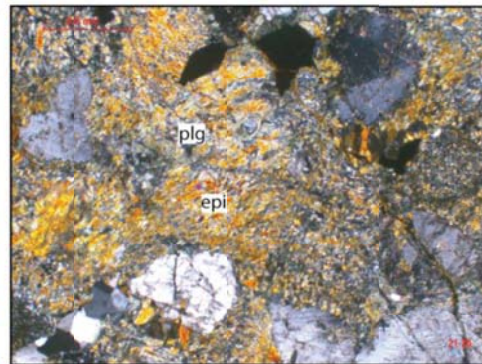
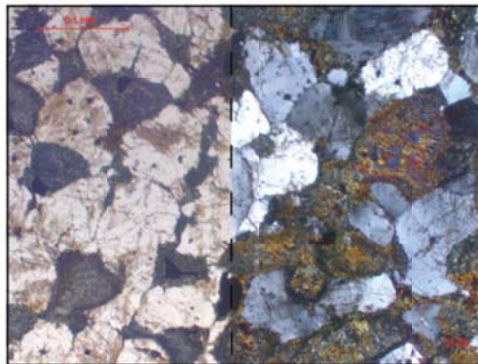
Loch Assynt



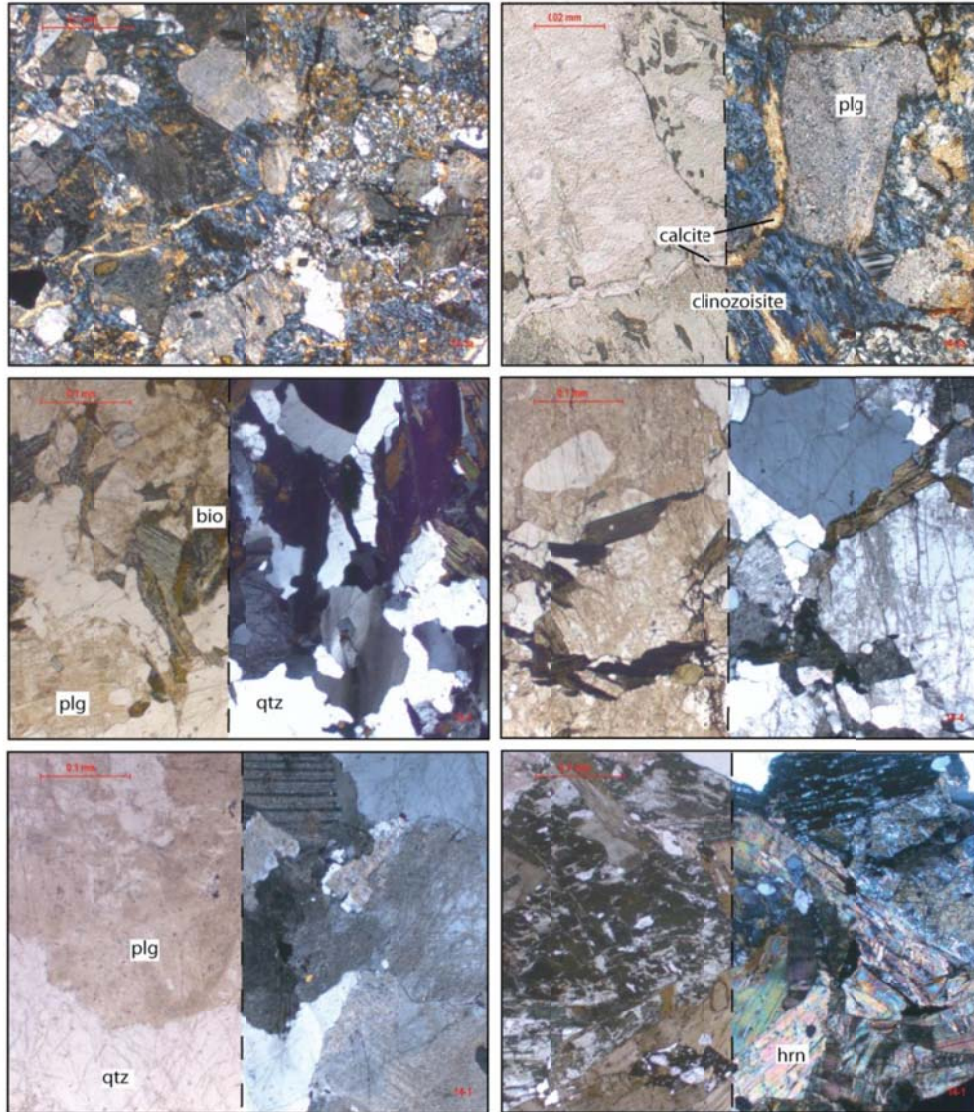
Lochinver



Caolas Cumhann



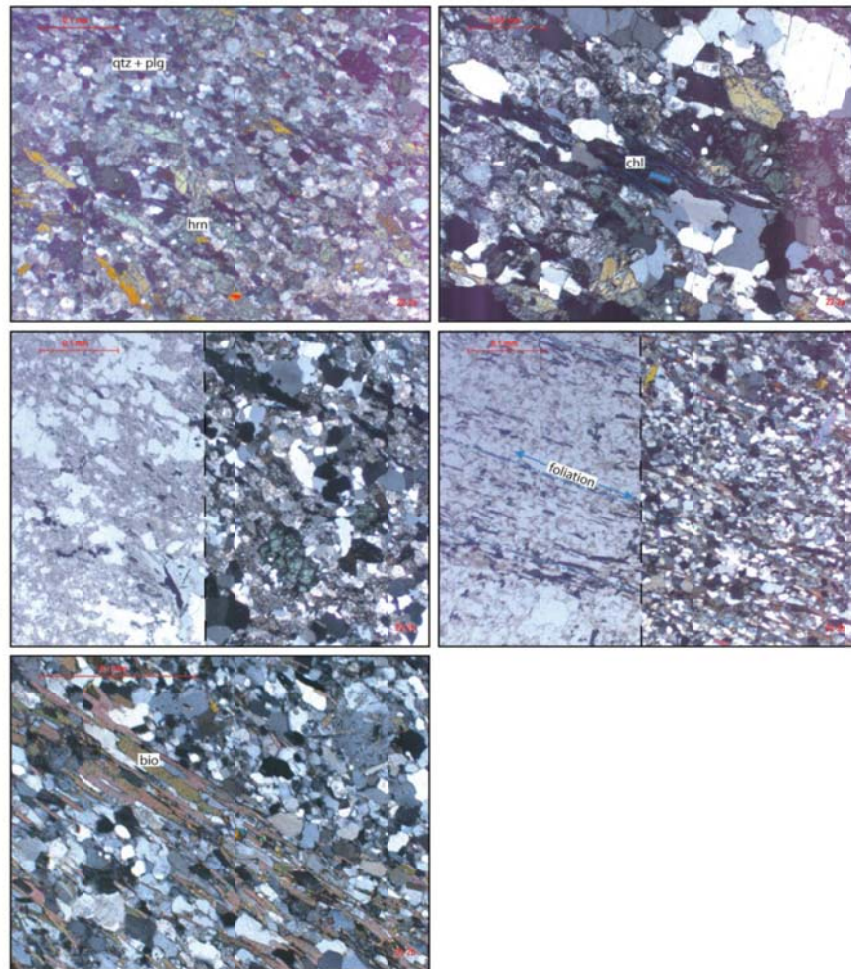
# Kinlochbervie



plg - plagioclase, bio - biotite, qtz - quartz, hrn - hornblende

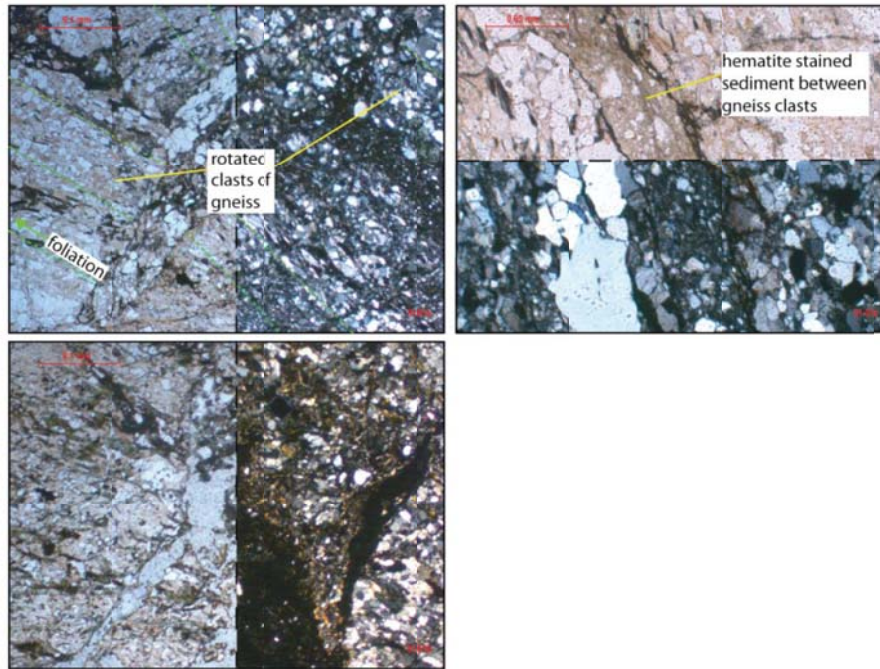


# Canisp Shear Zone

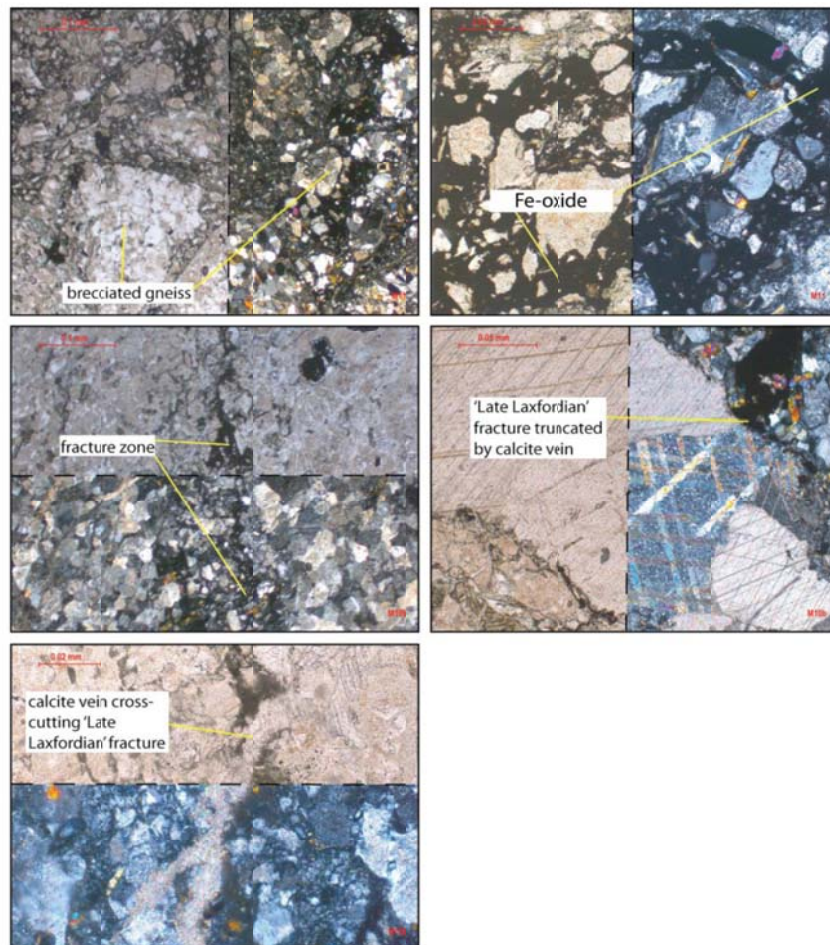


plg - plagioclase, qtz - quartz, horn - hornblende, chl - chlorite, bio - biotite

# Alltan na Bradhan

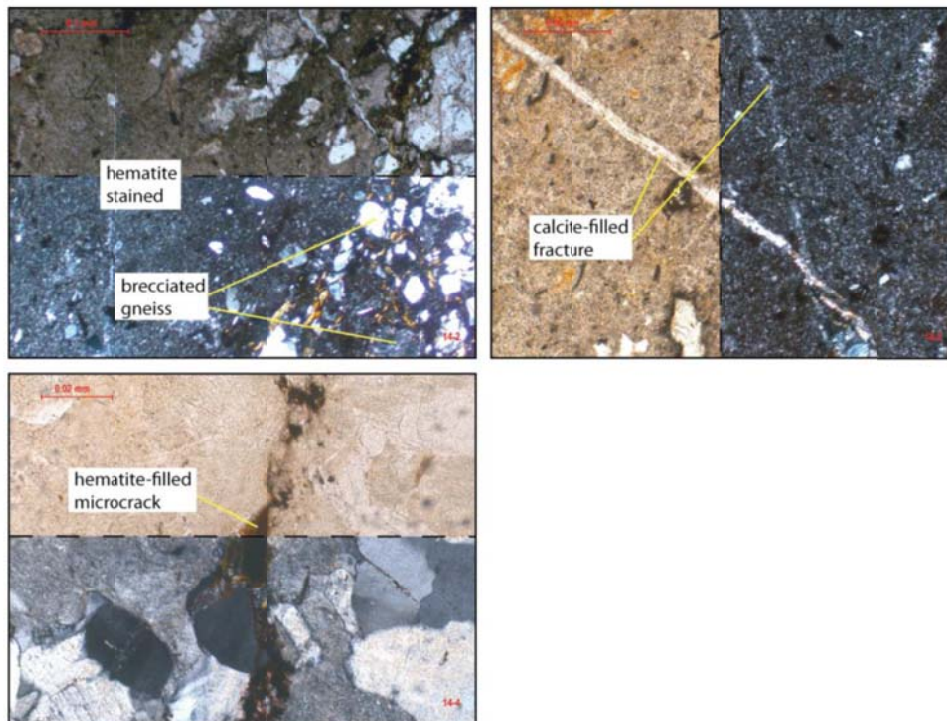


# Loch Assynt Fault - Clashnessie

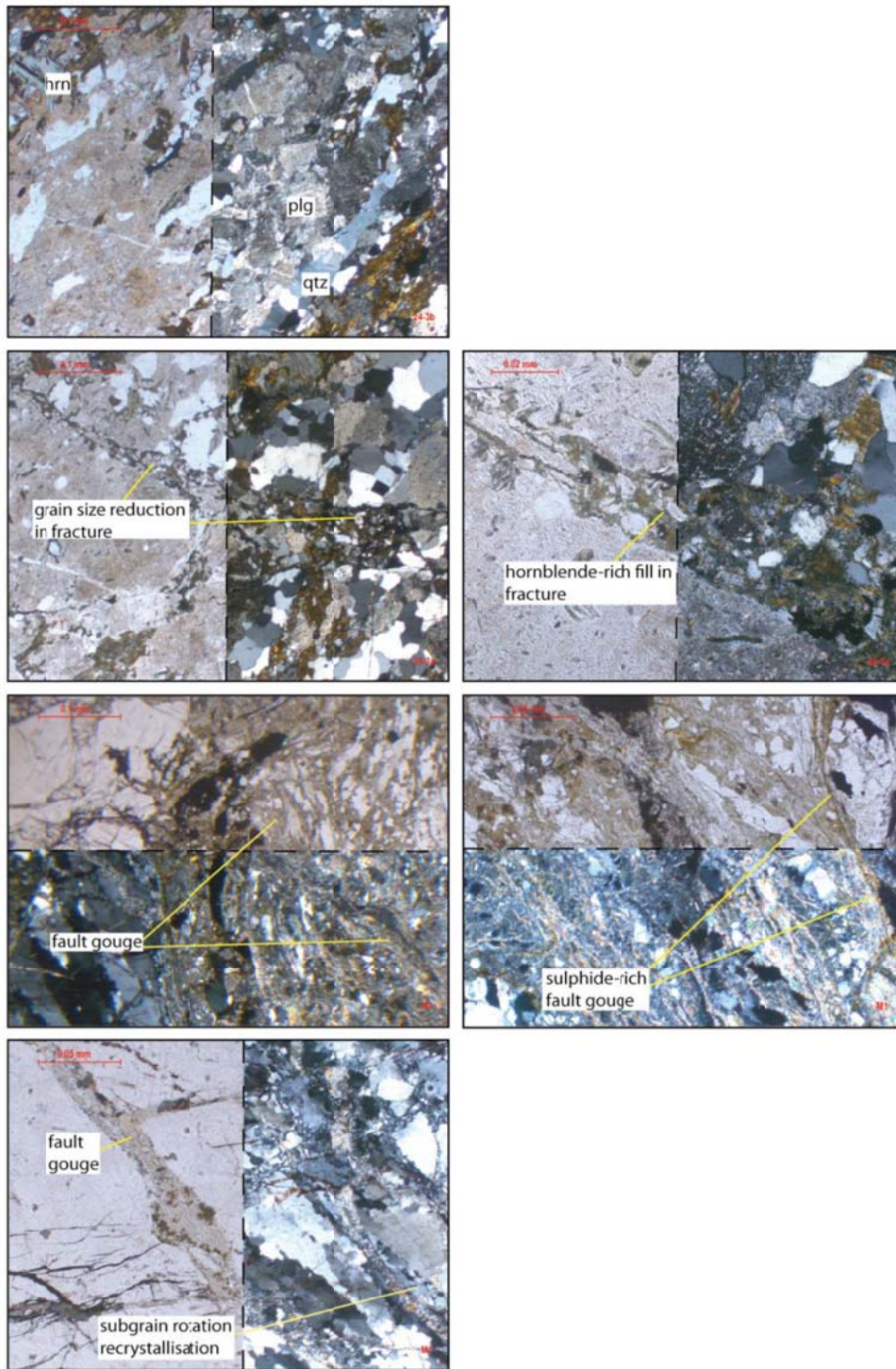




# Kinlochbervie



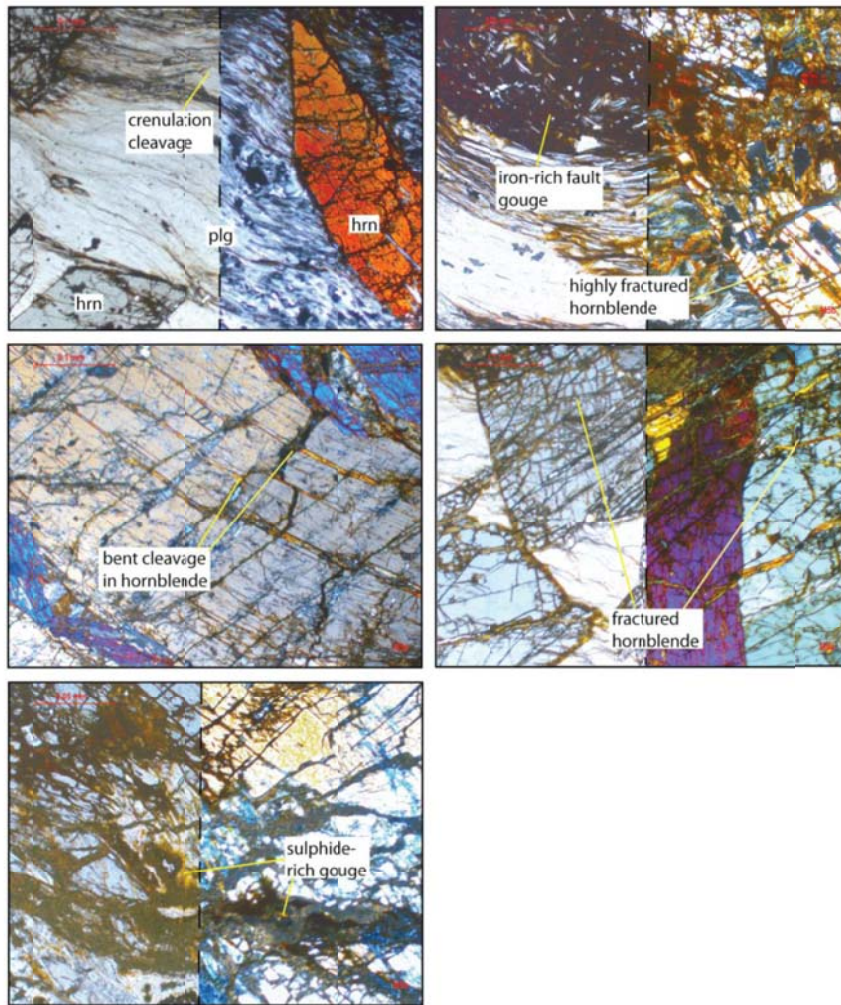
# Lochinver Fault (Mesozoic?)



plg - plagioclase, hrn - hornblende, qtz - quartz



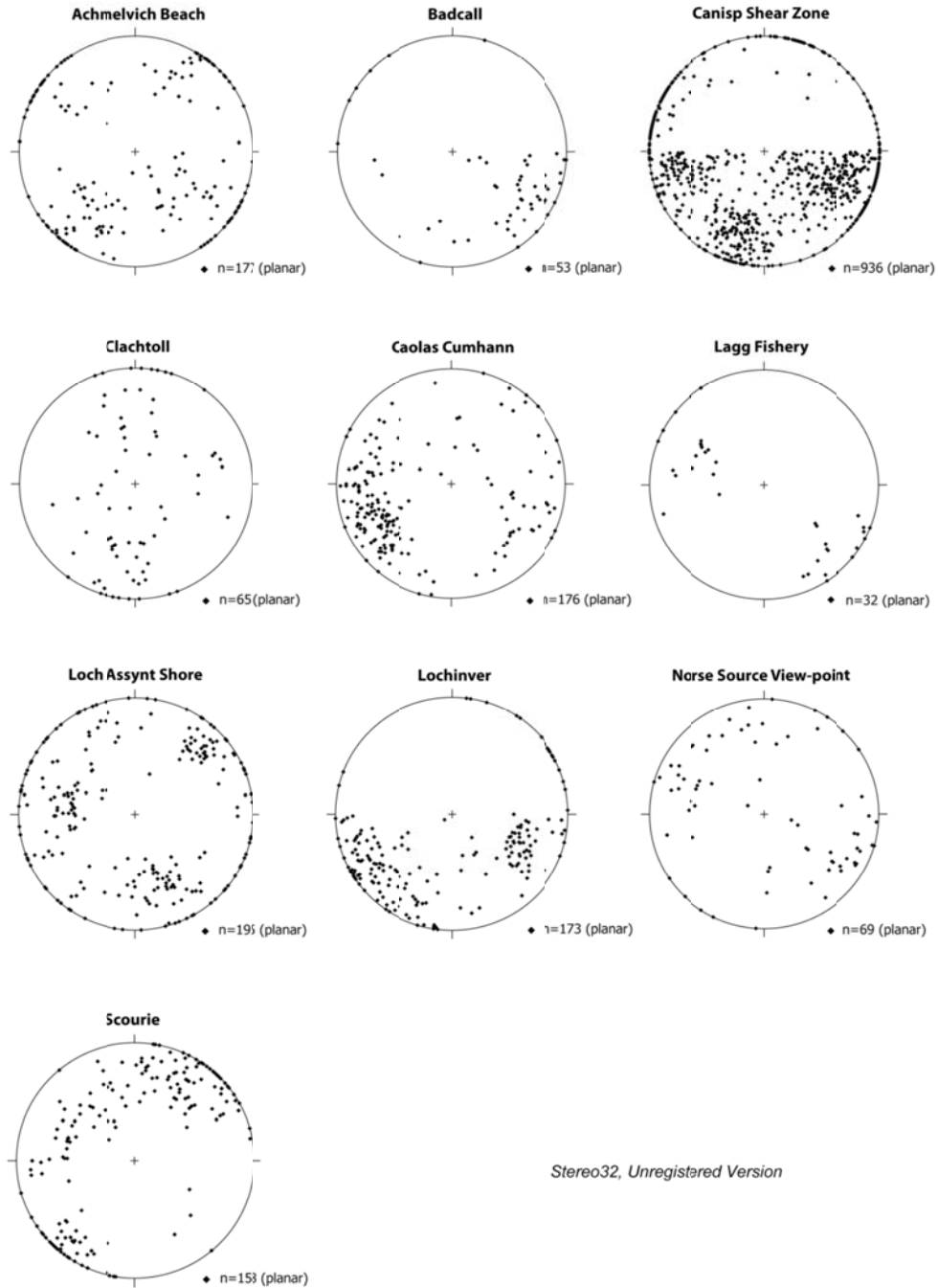
# Lochinver Fault (Mesozoic?)



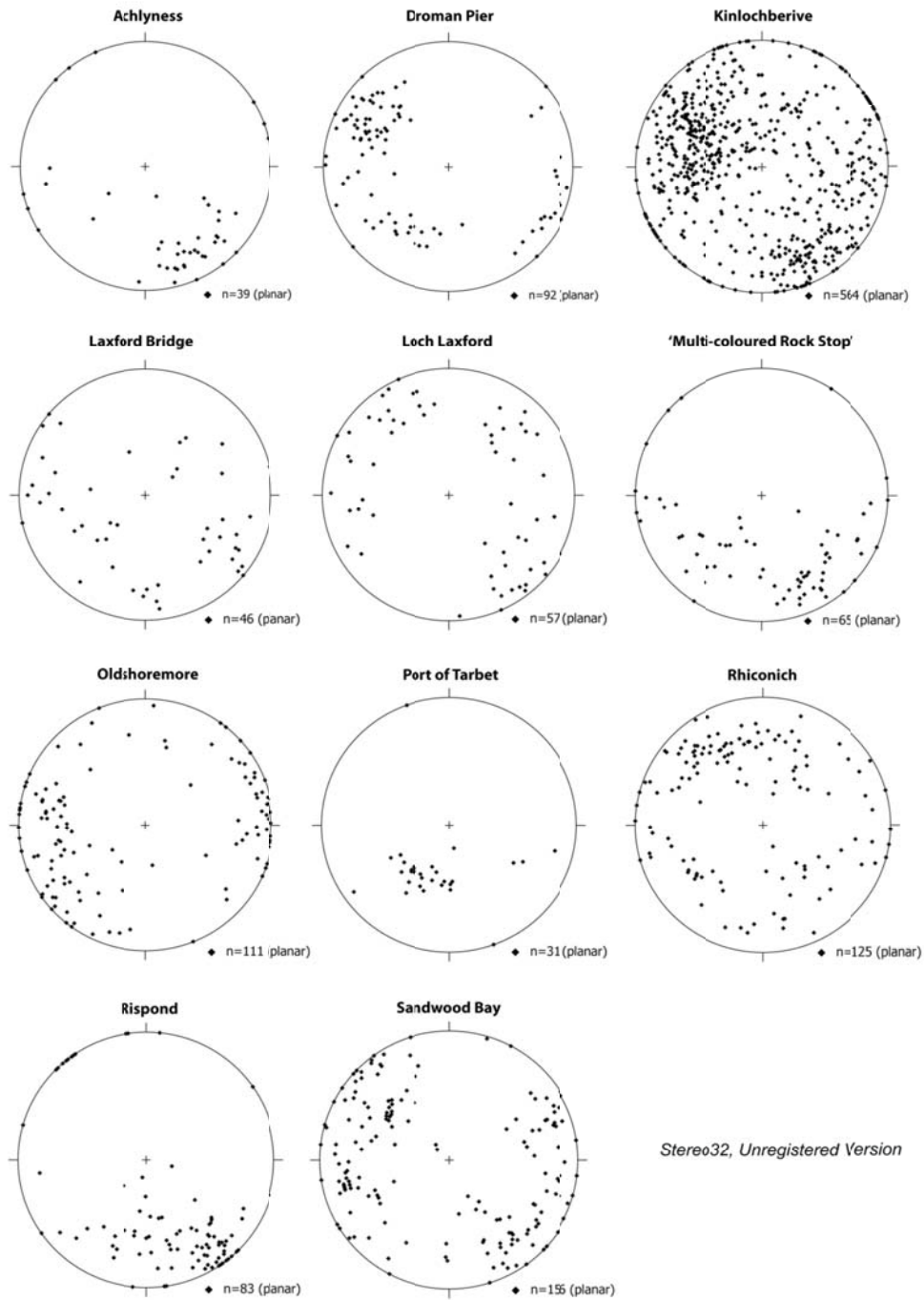
hrn - hornblende, plg - plagioclase

## V: Outcrop Stereonets

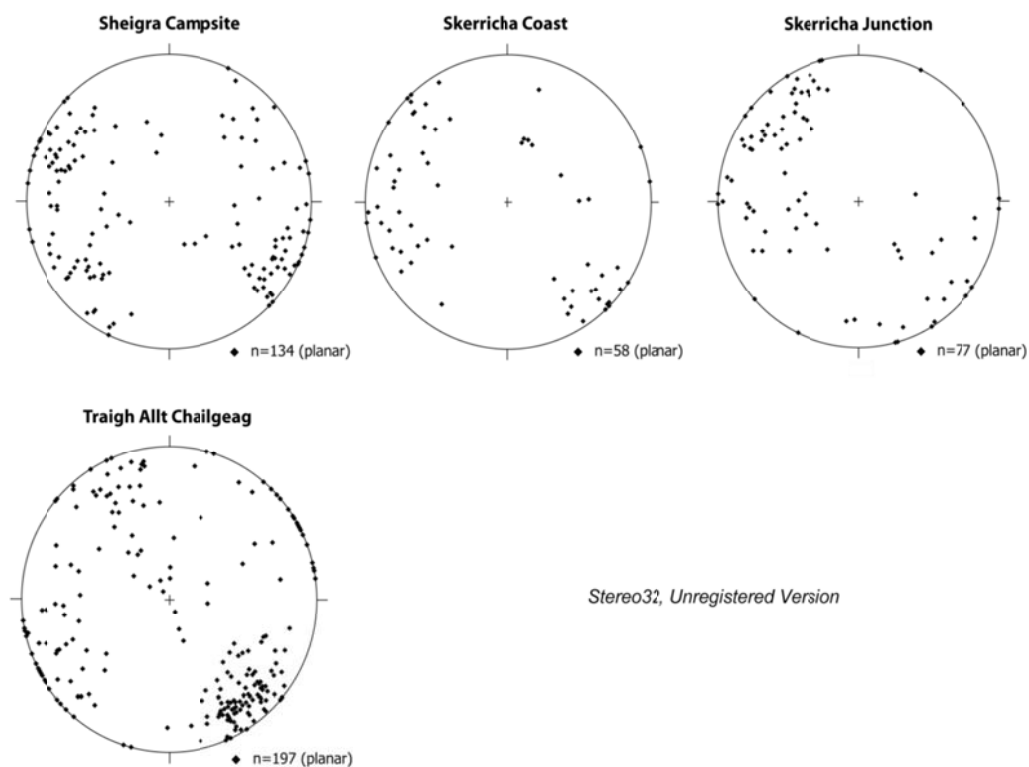
### Assynt Terrane



## Rhiconich Terrane

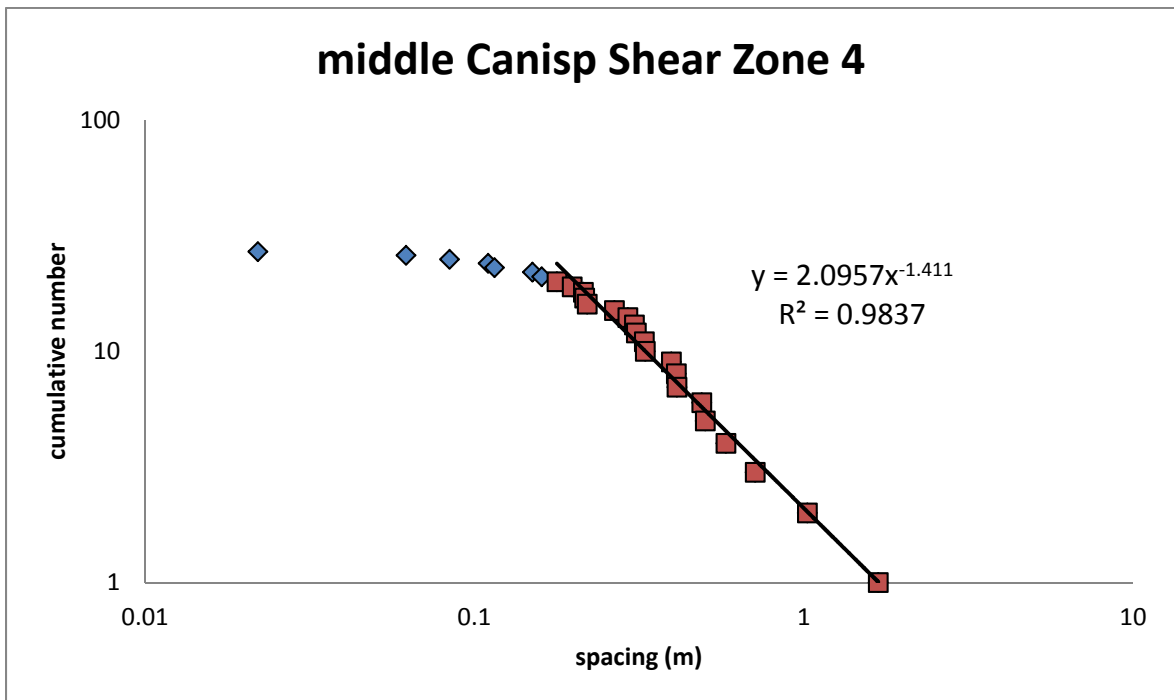
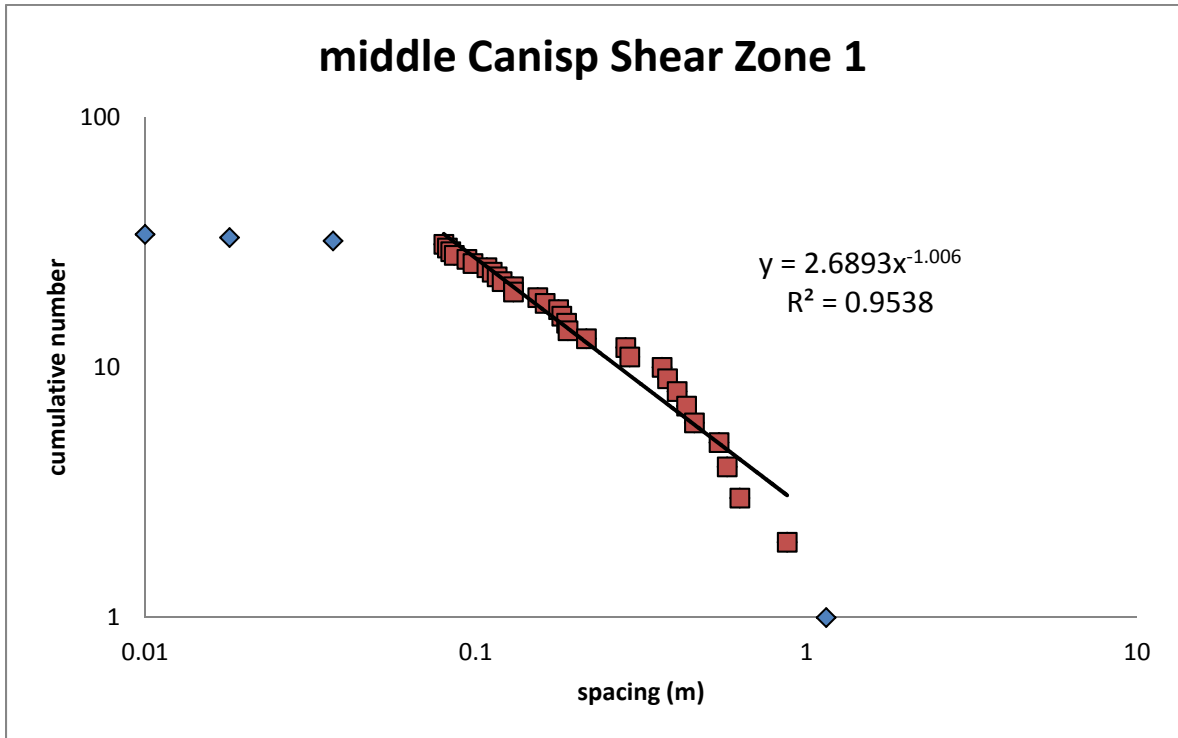


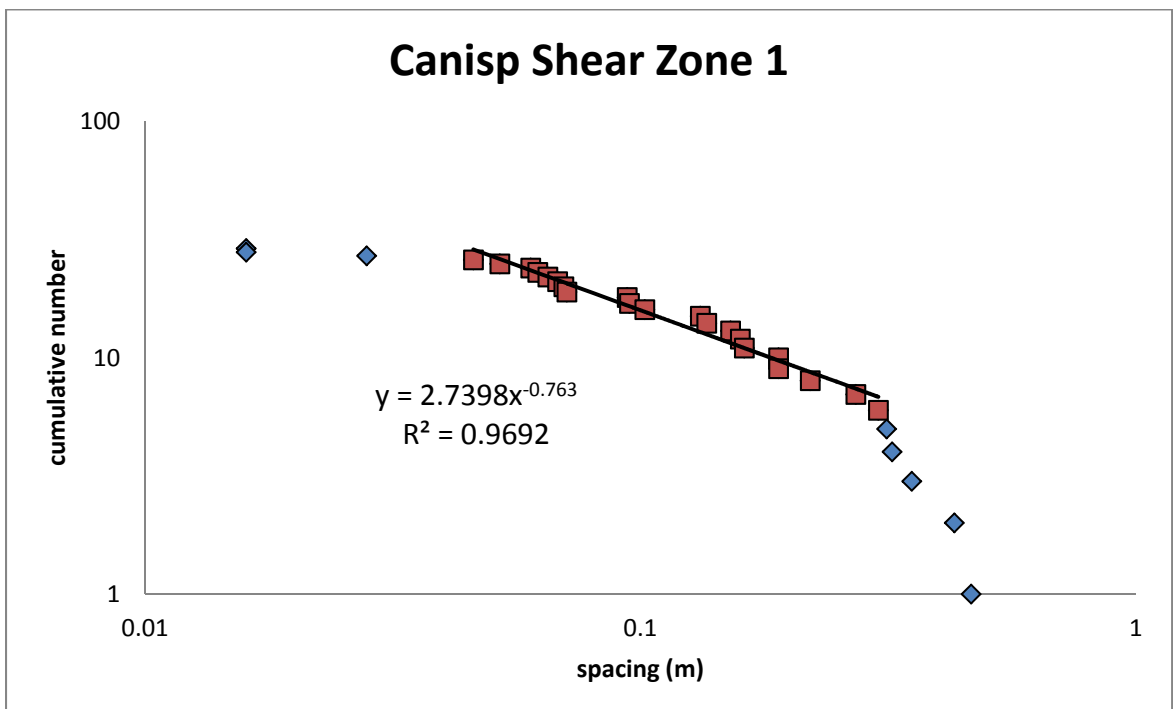
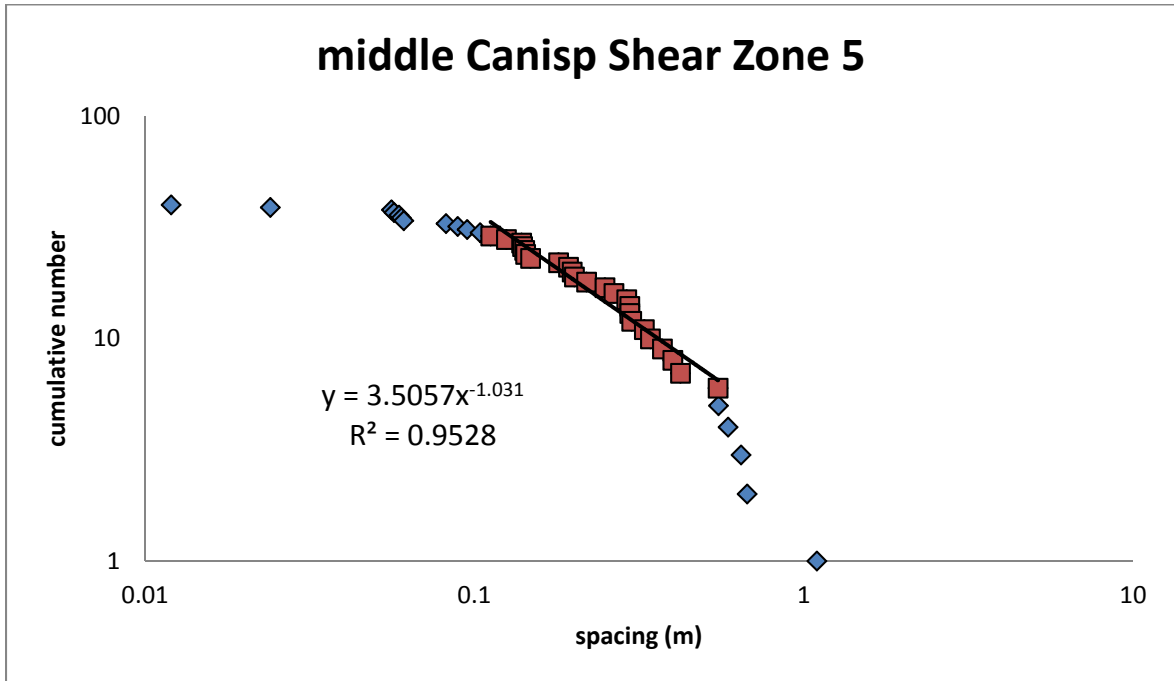
Contd

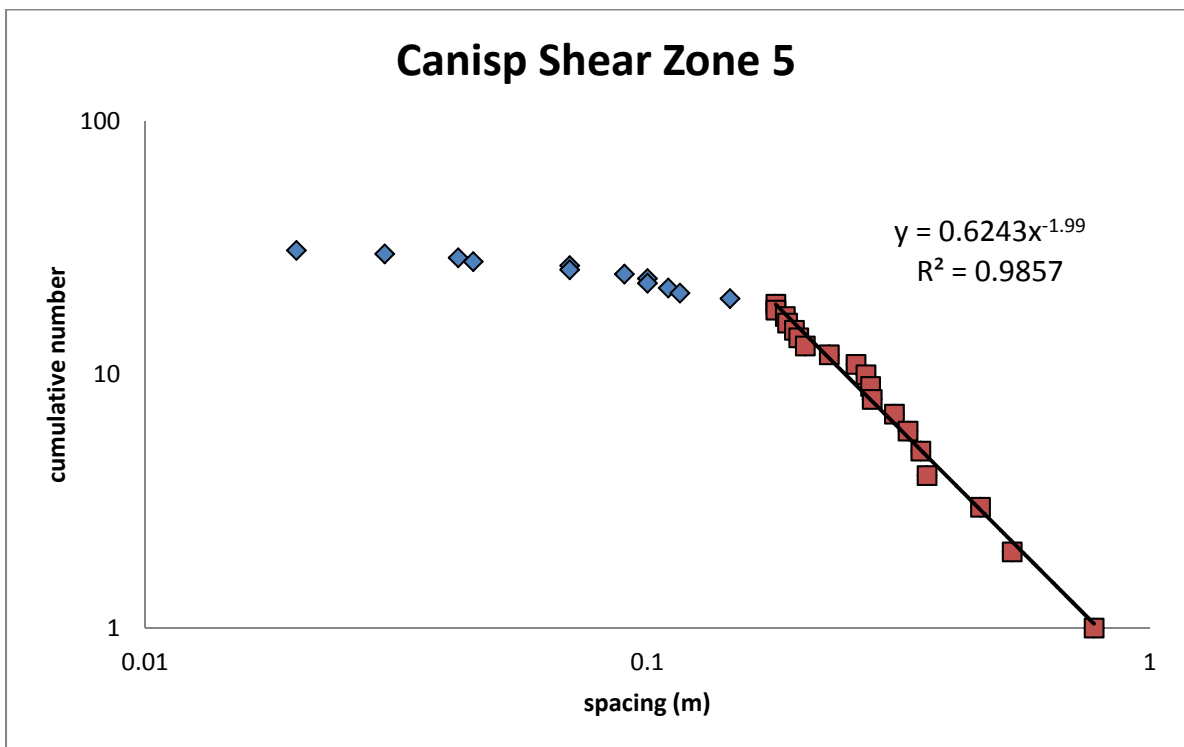
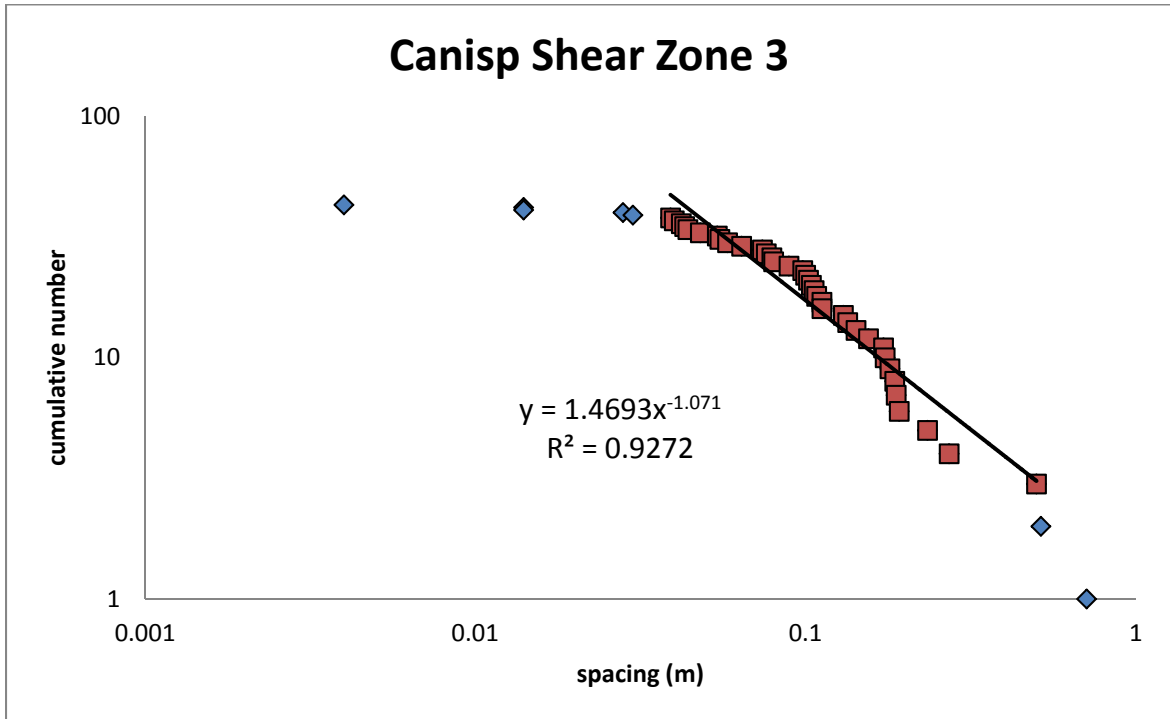


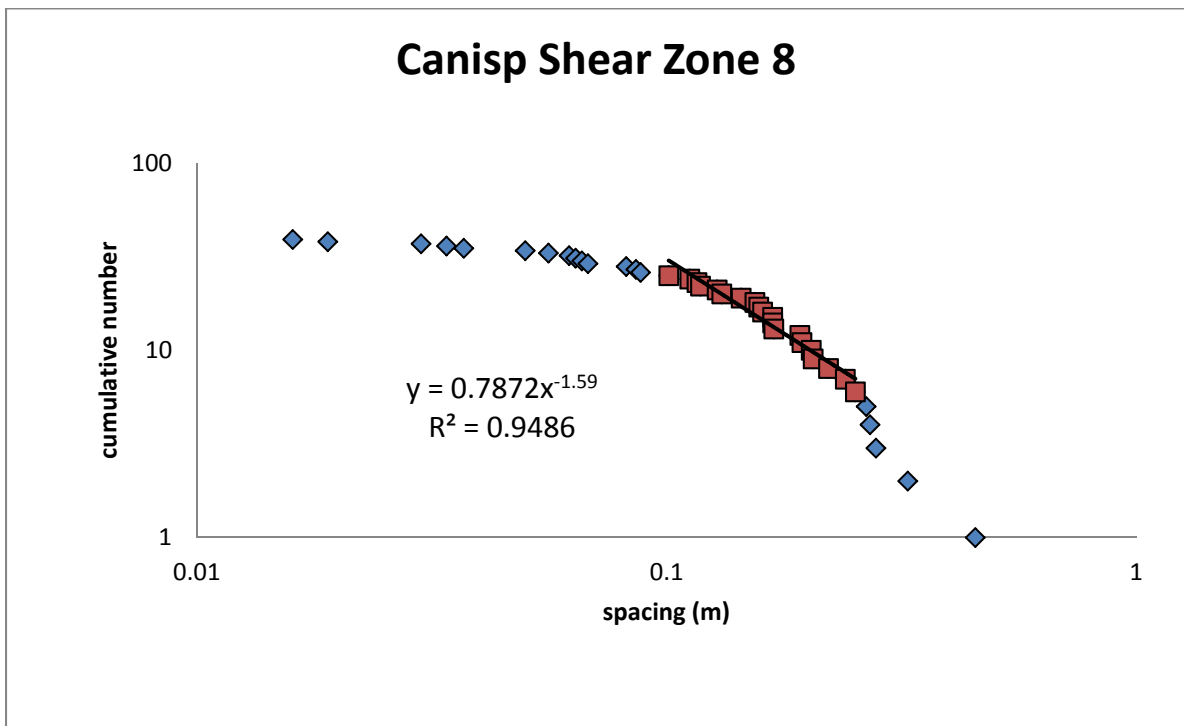
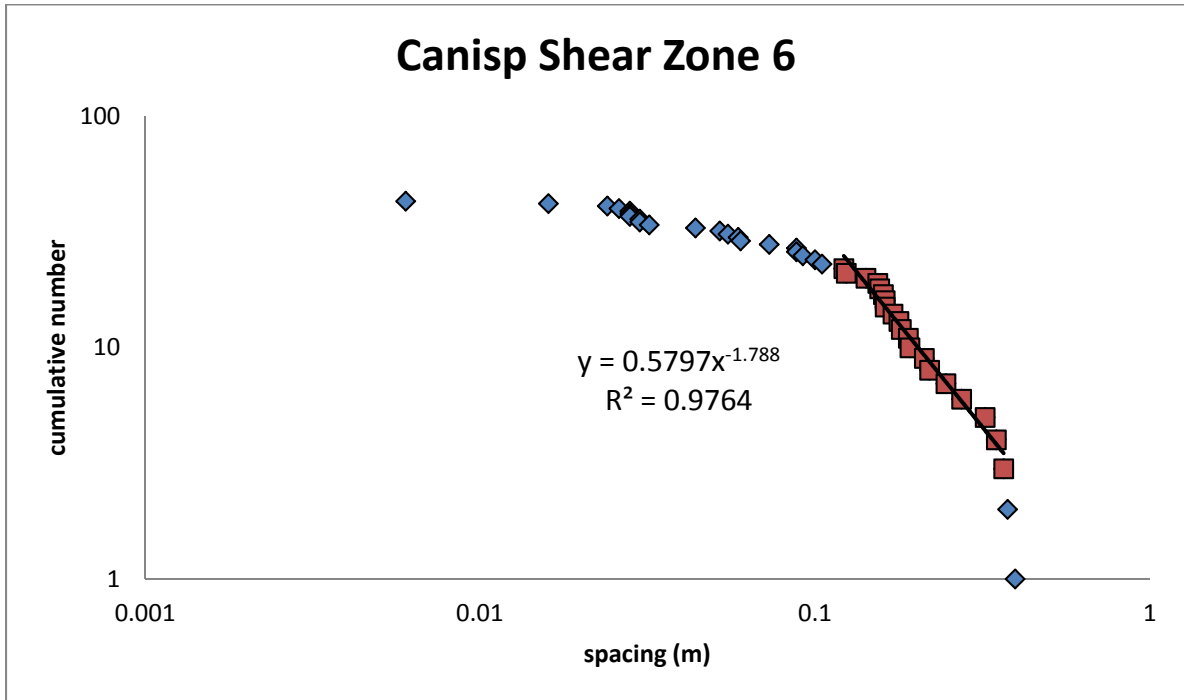
*Stereo32, Unregistered Version*

VI: 1-dimensional fracture spacing population distribution plots

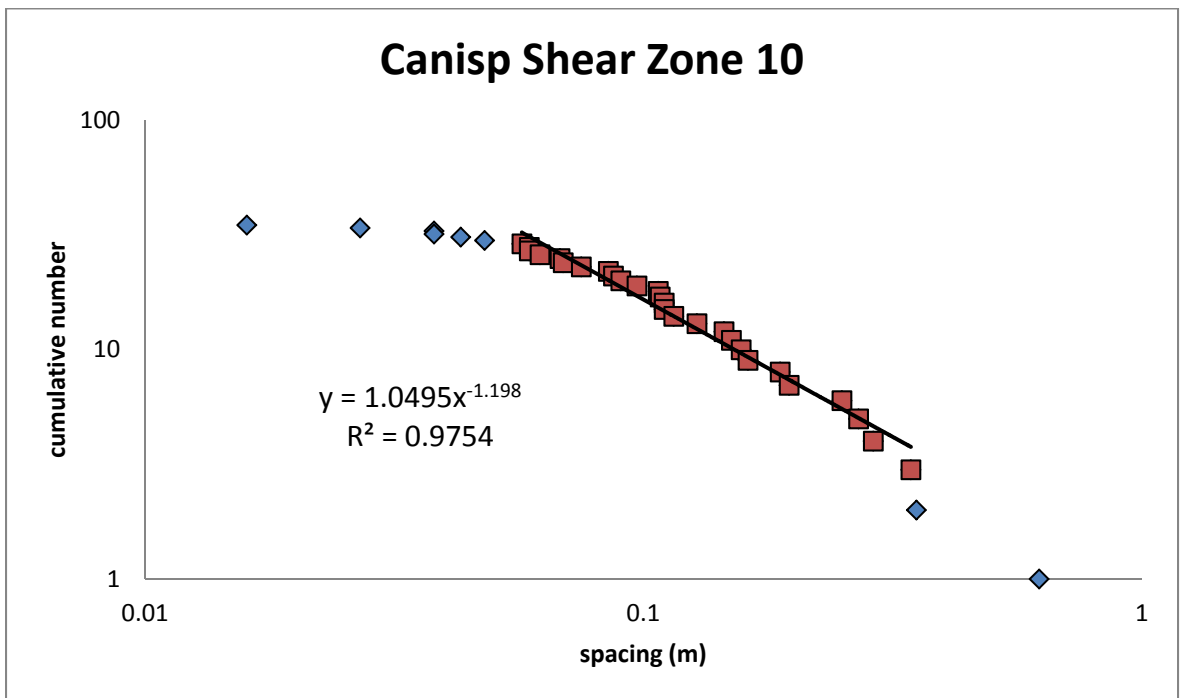
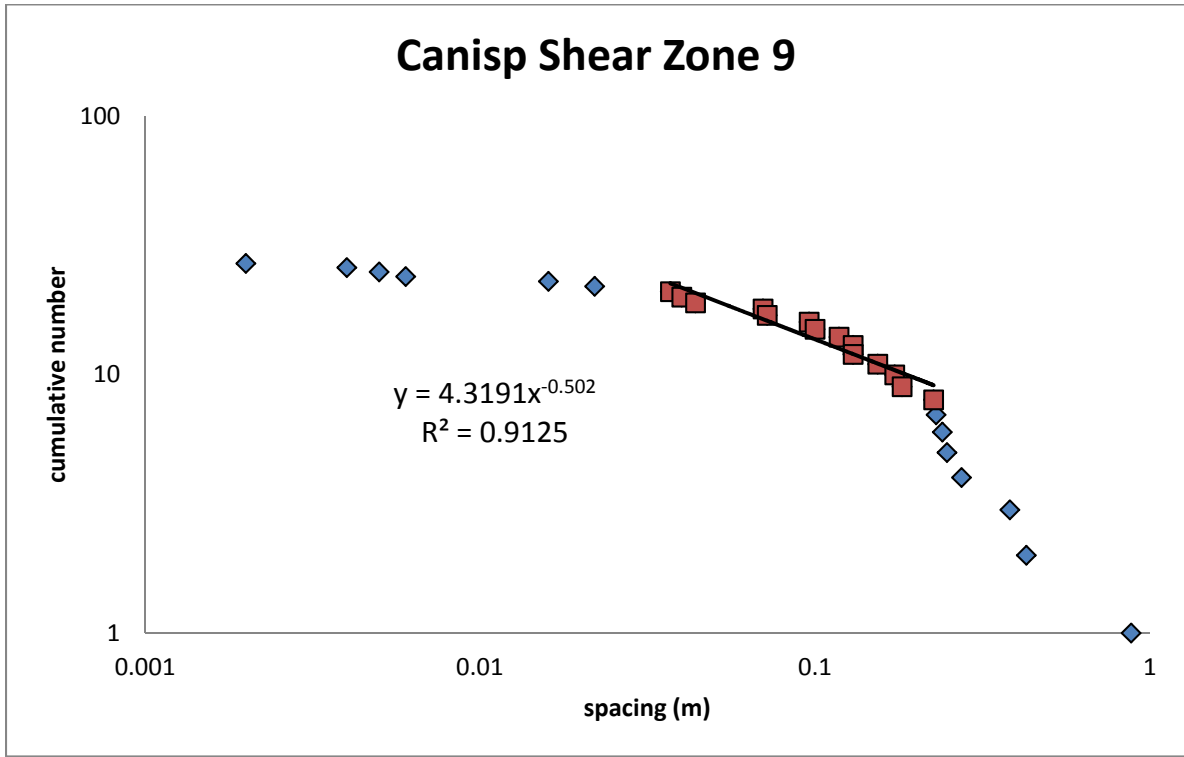


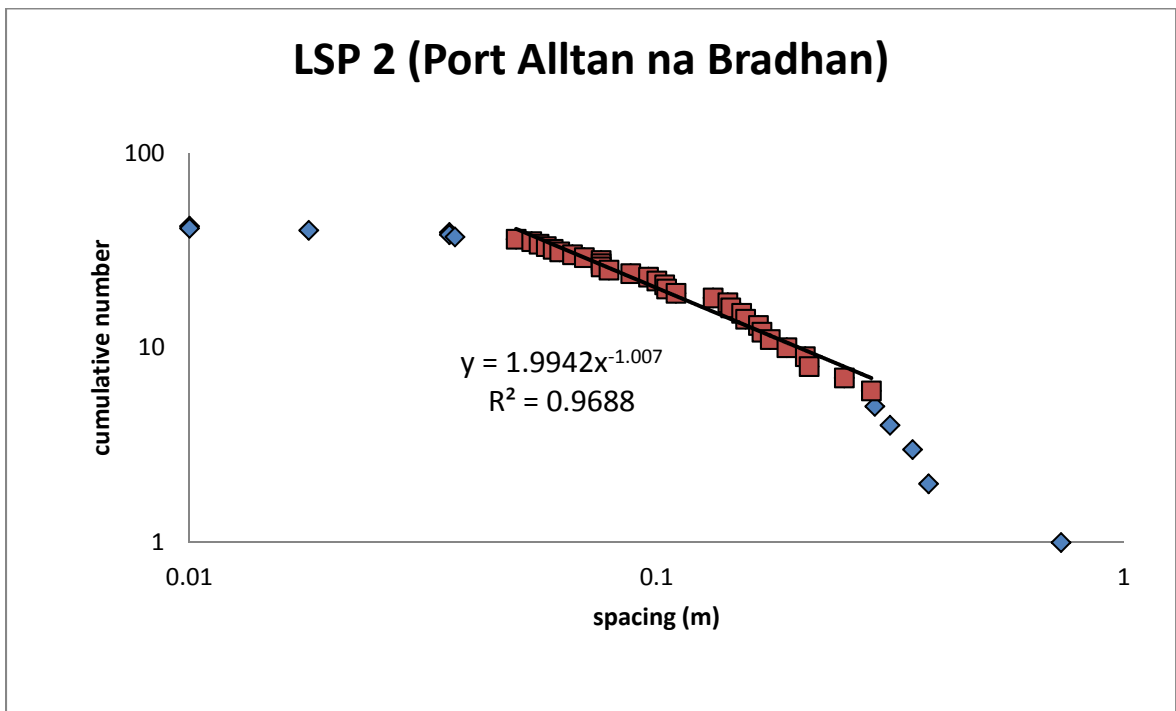
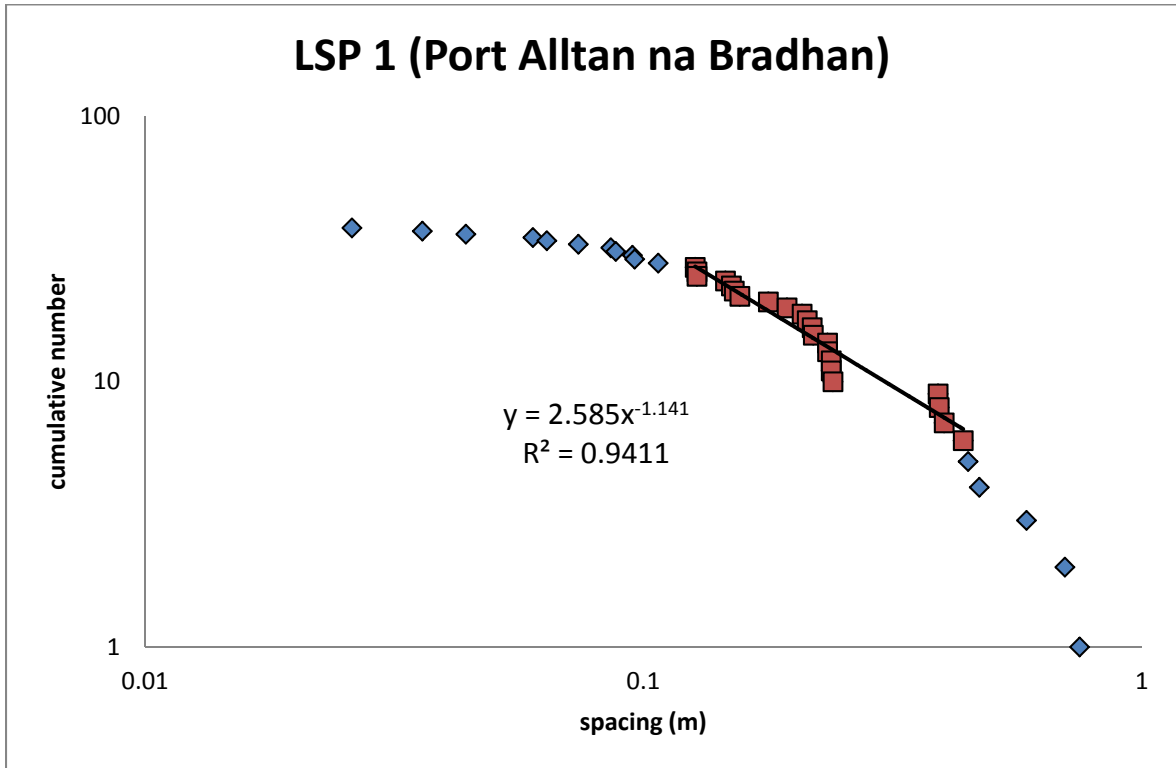


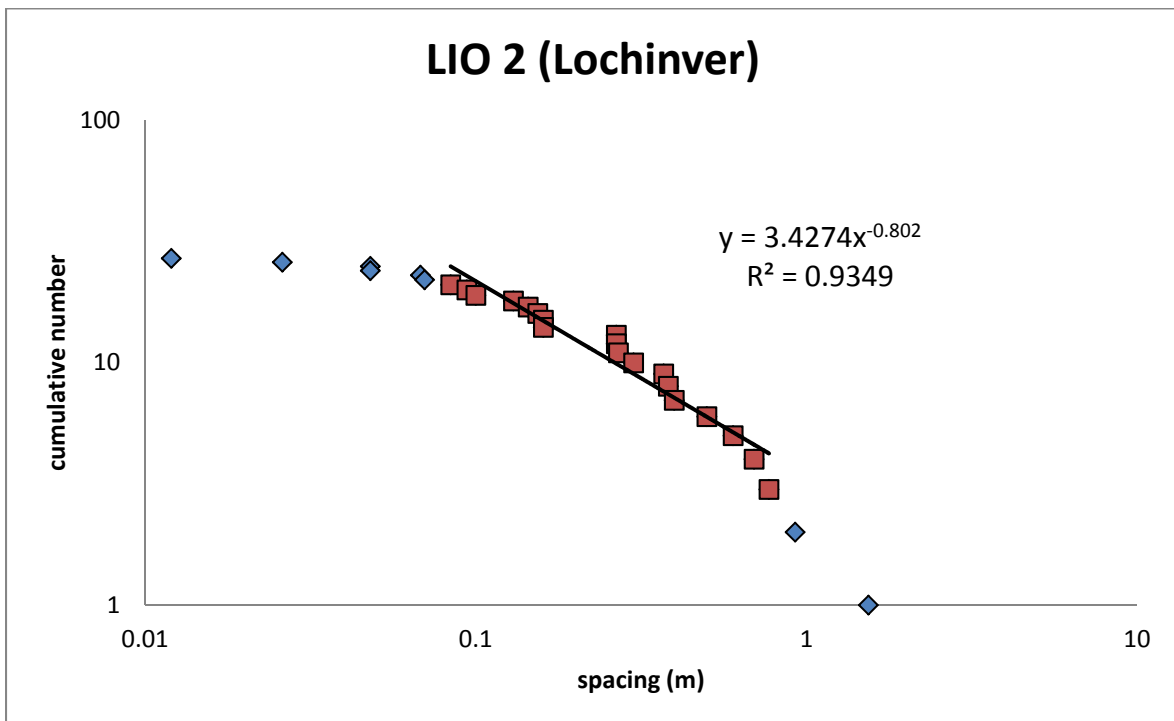
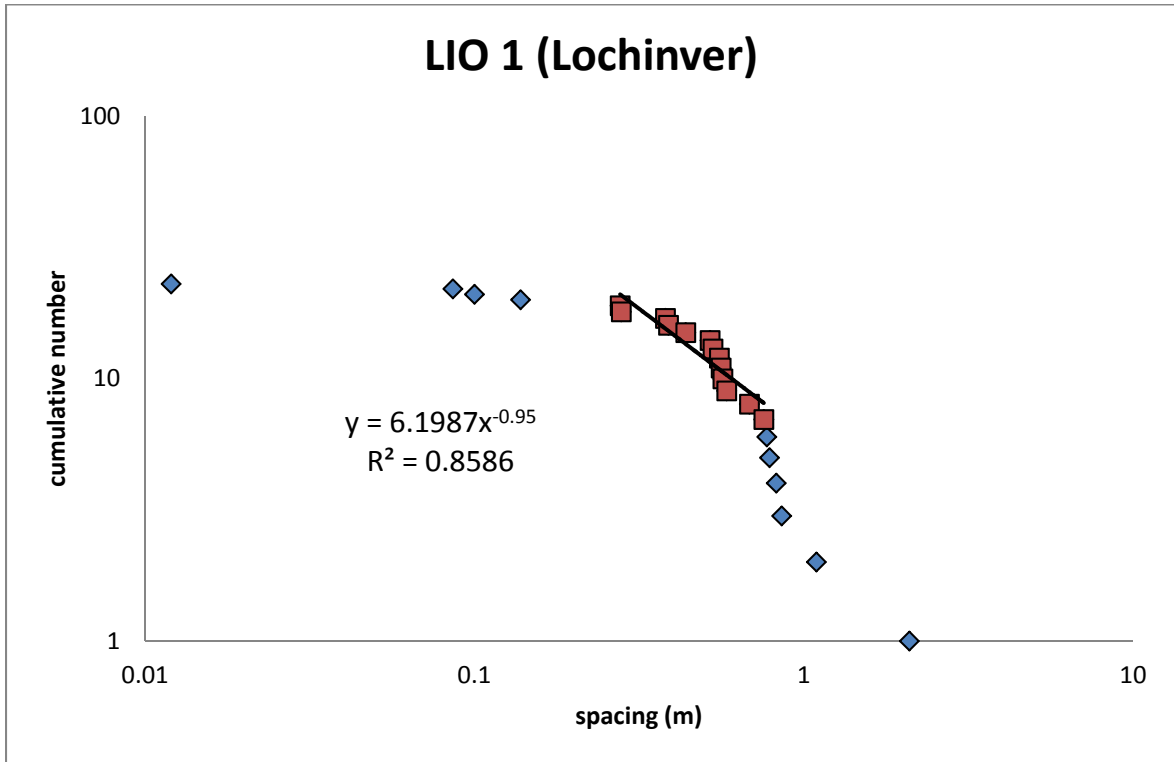


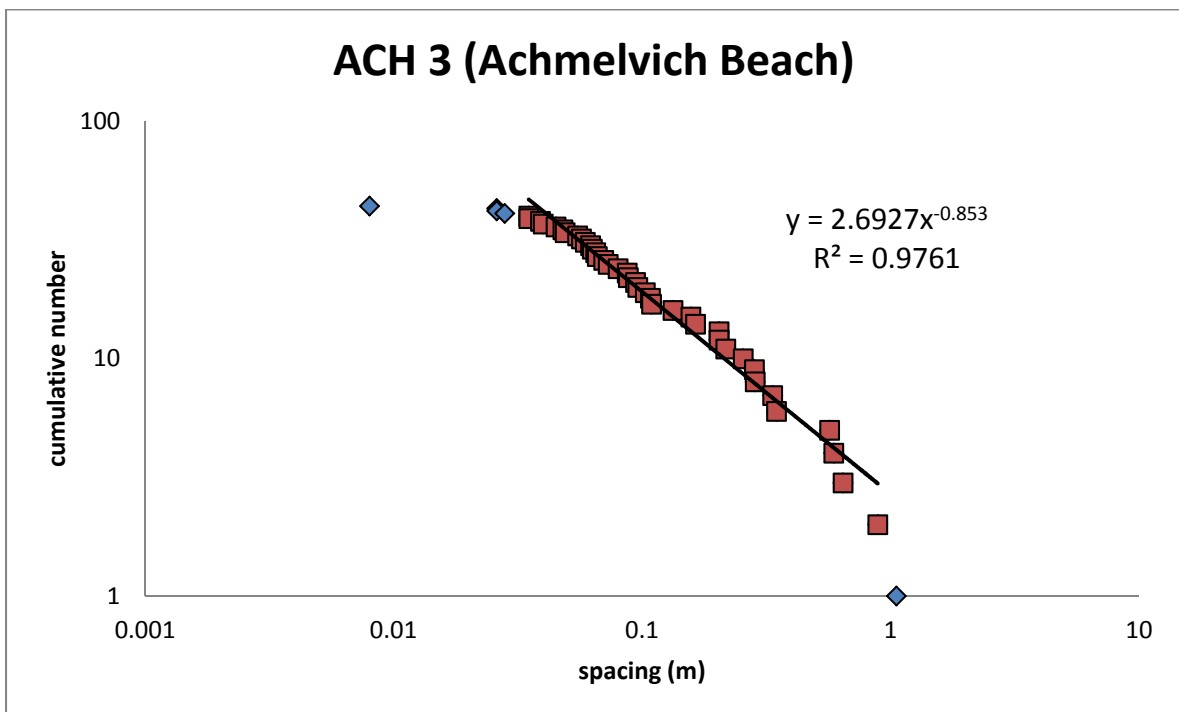
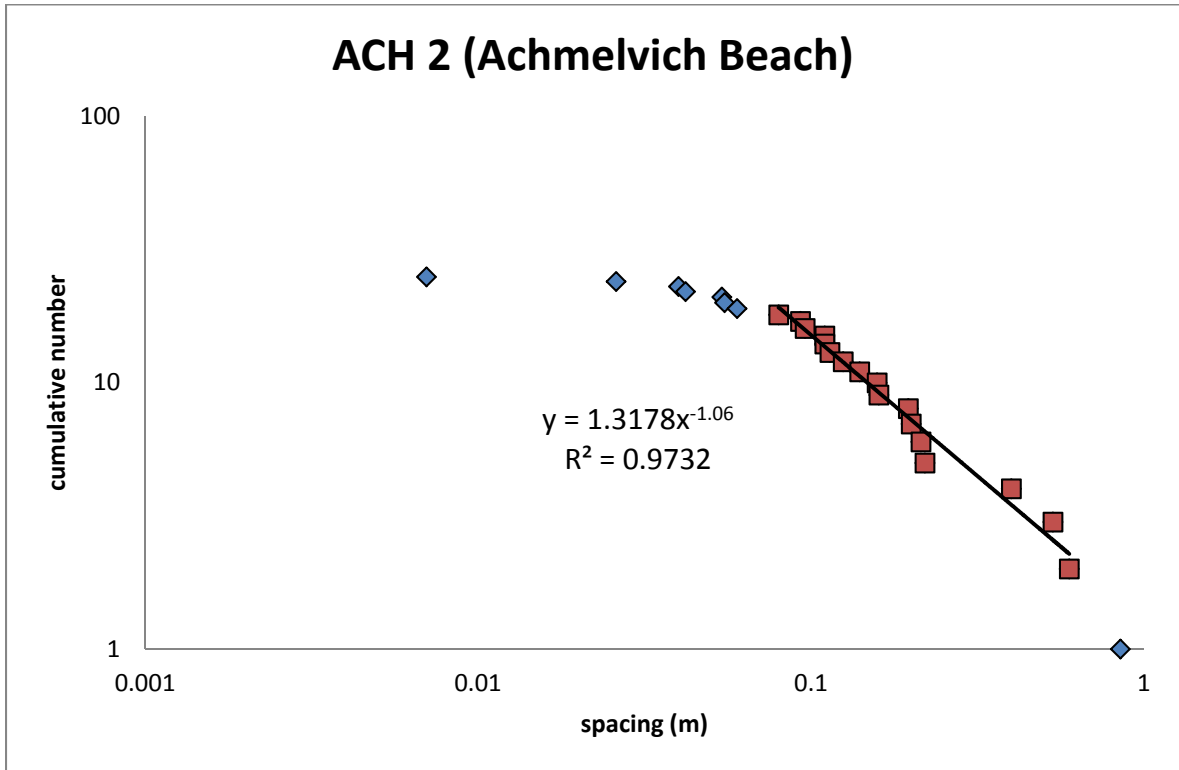


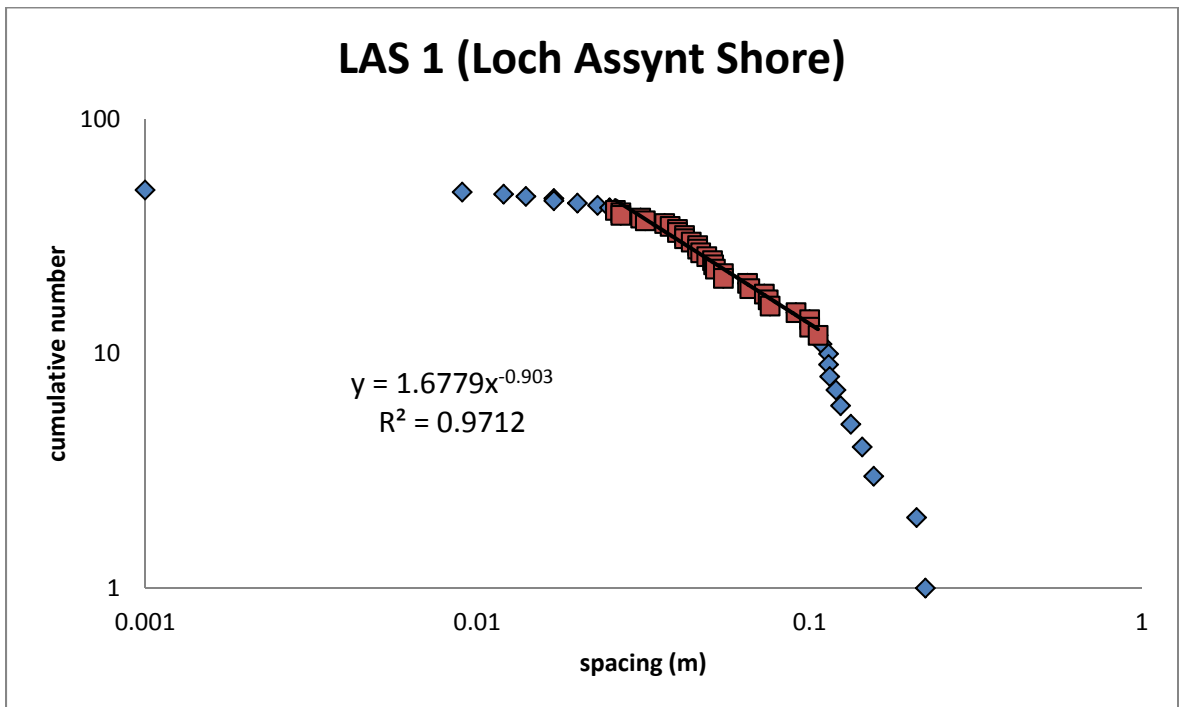
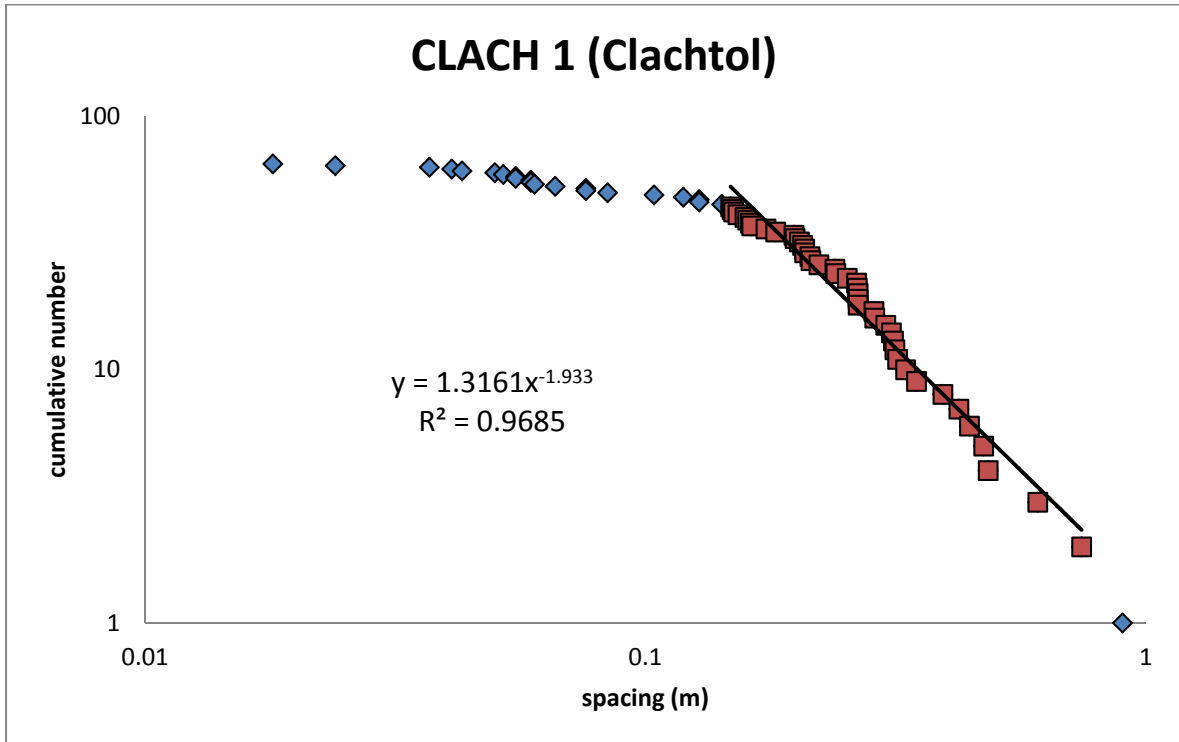


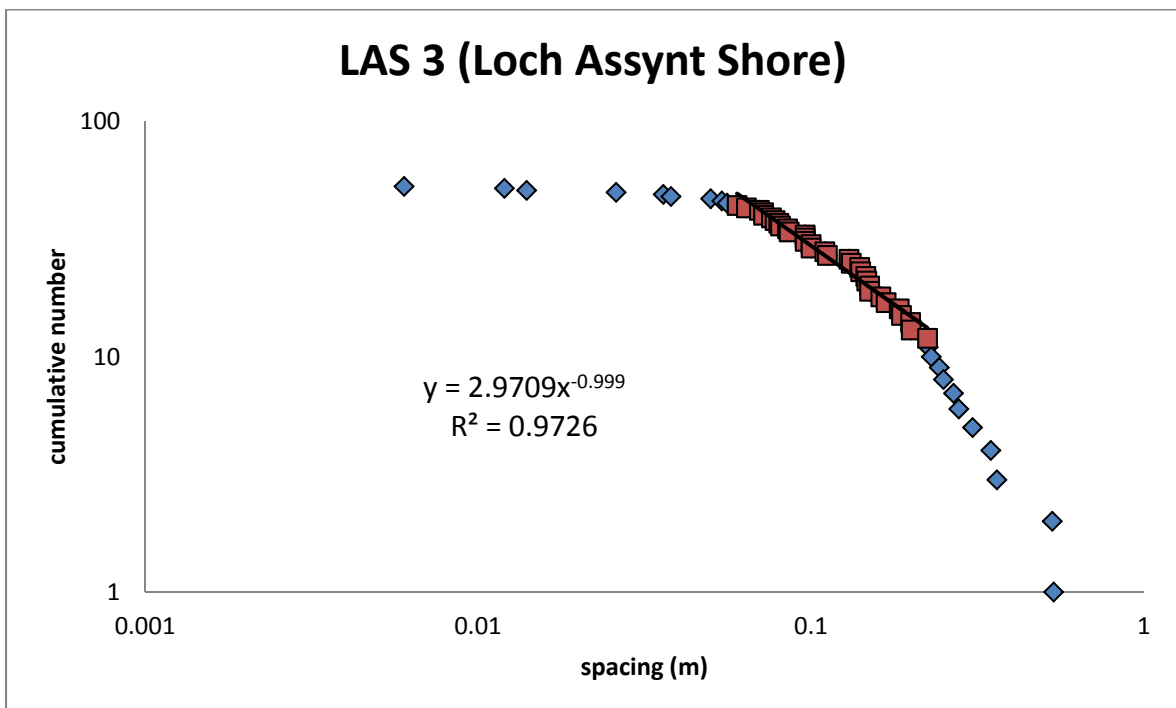
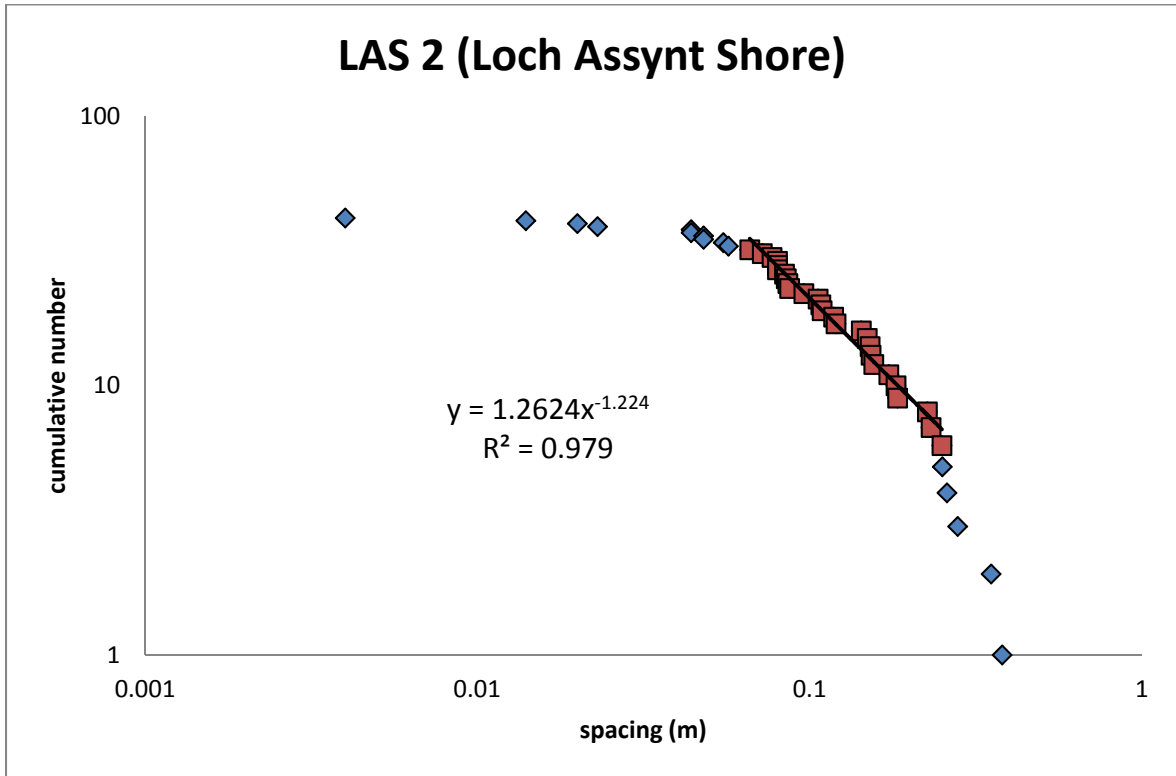


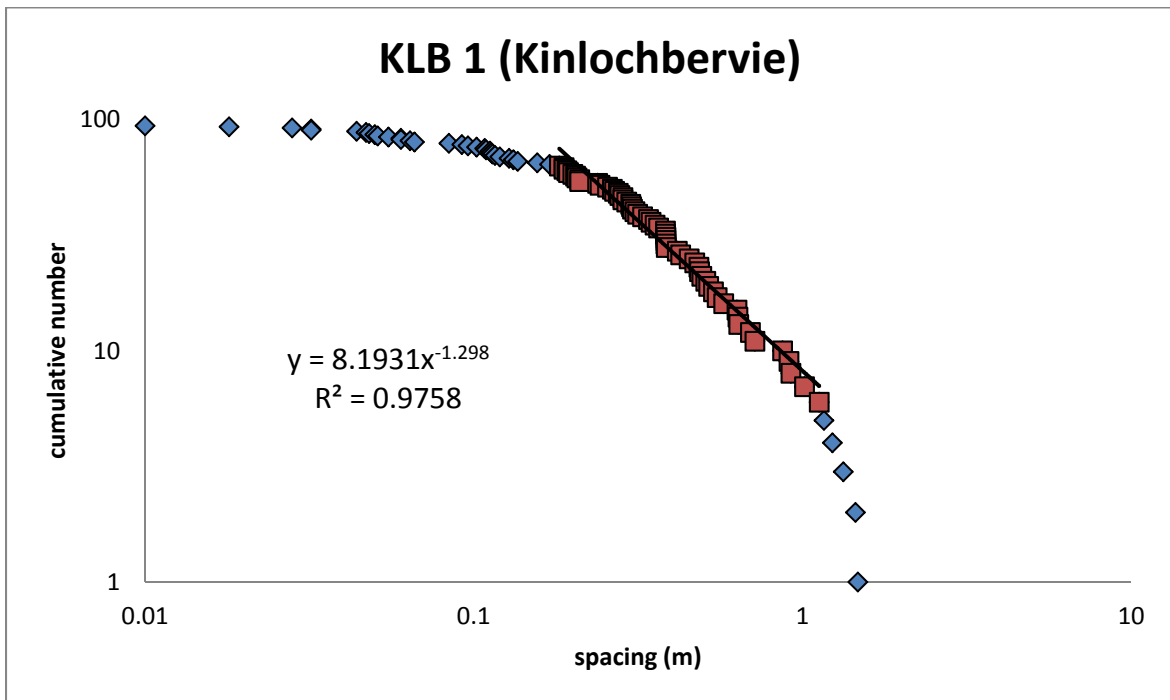
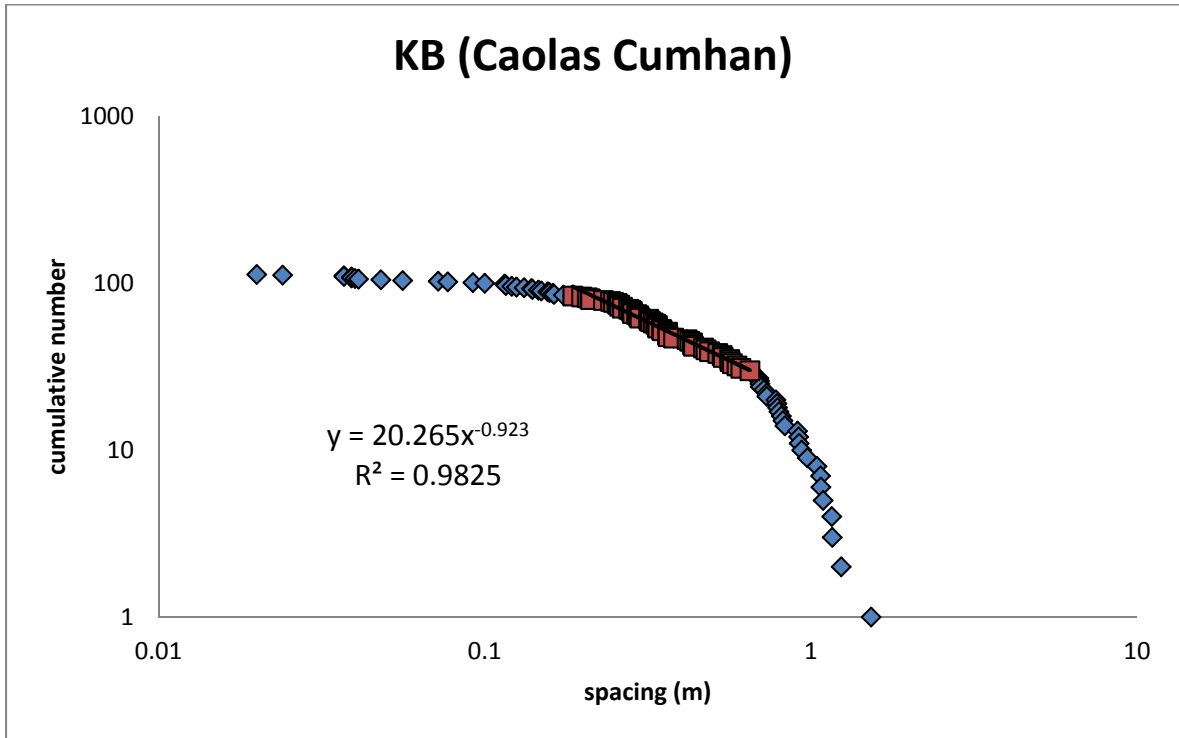


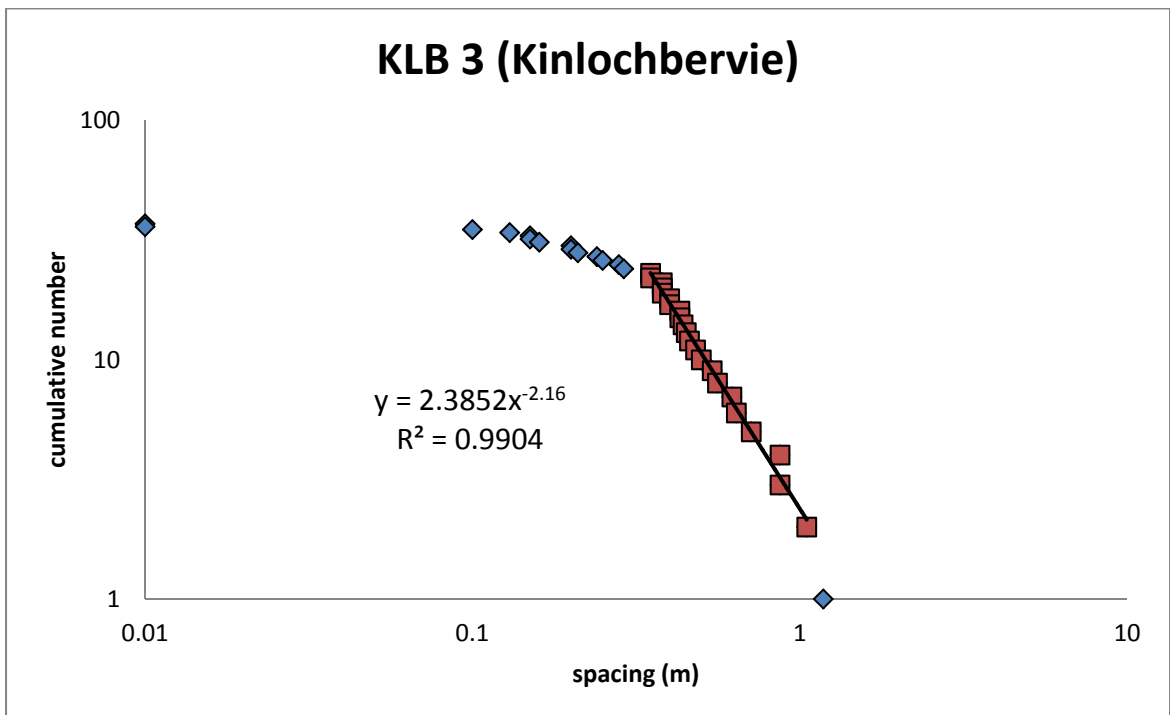
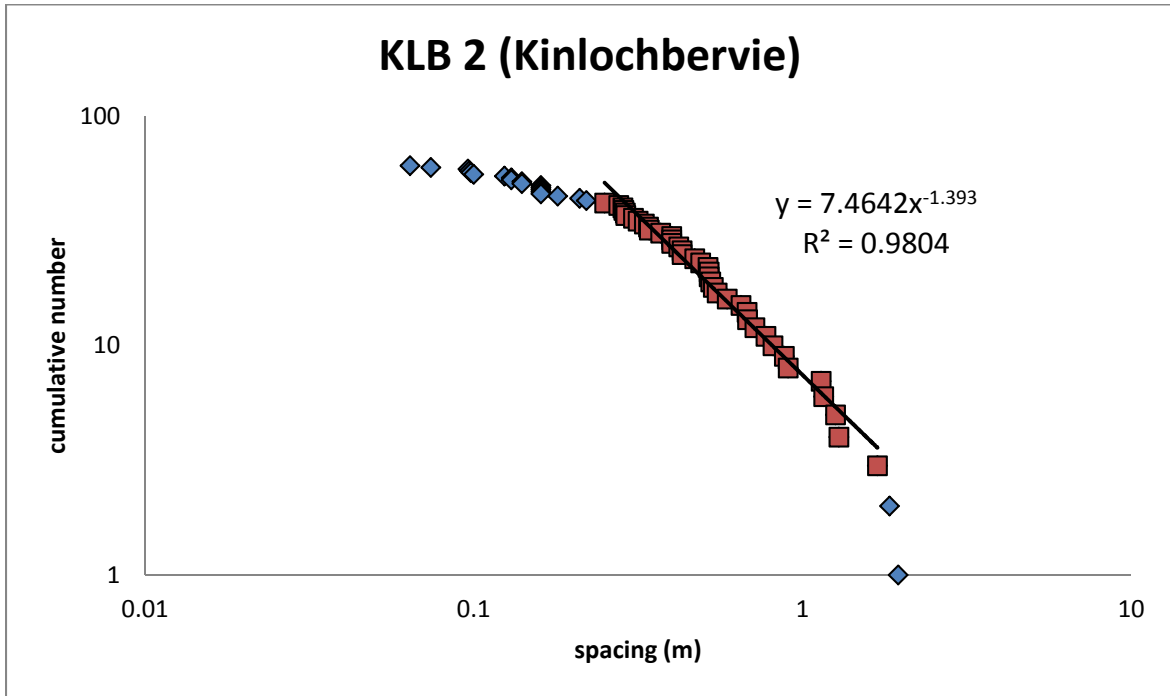




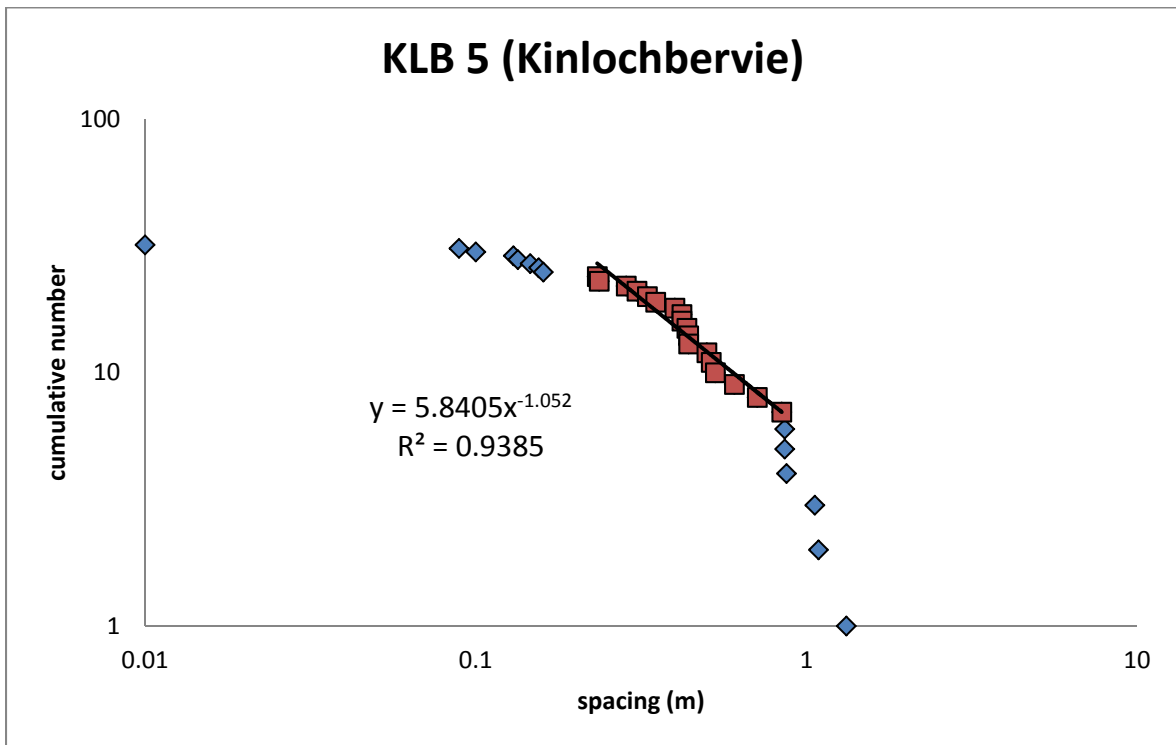
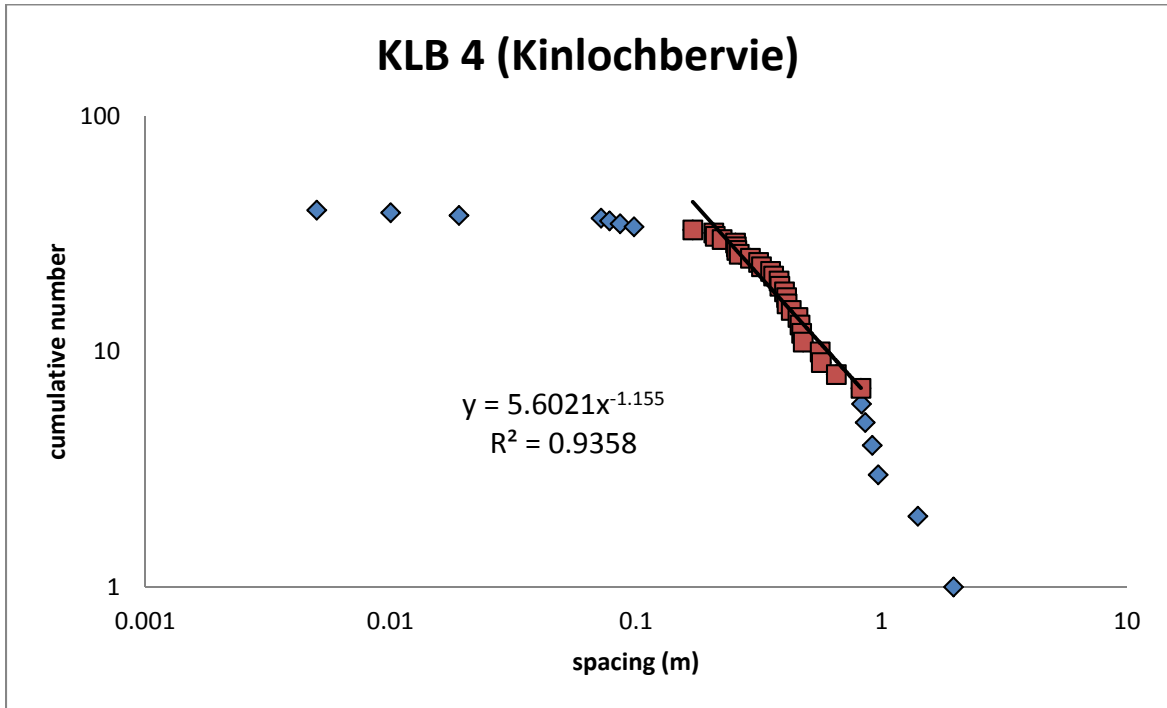


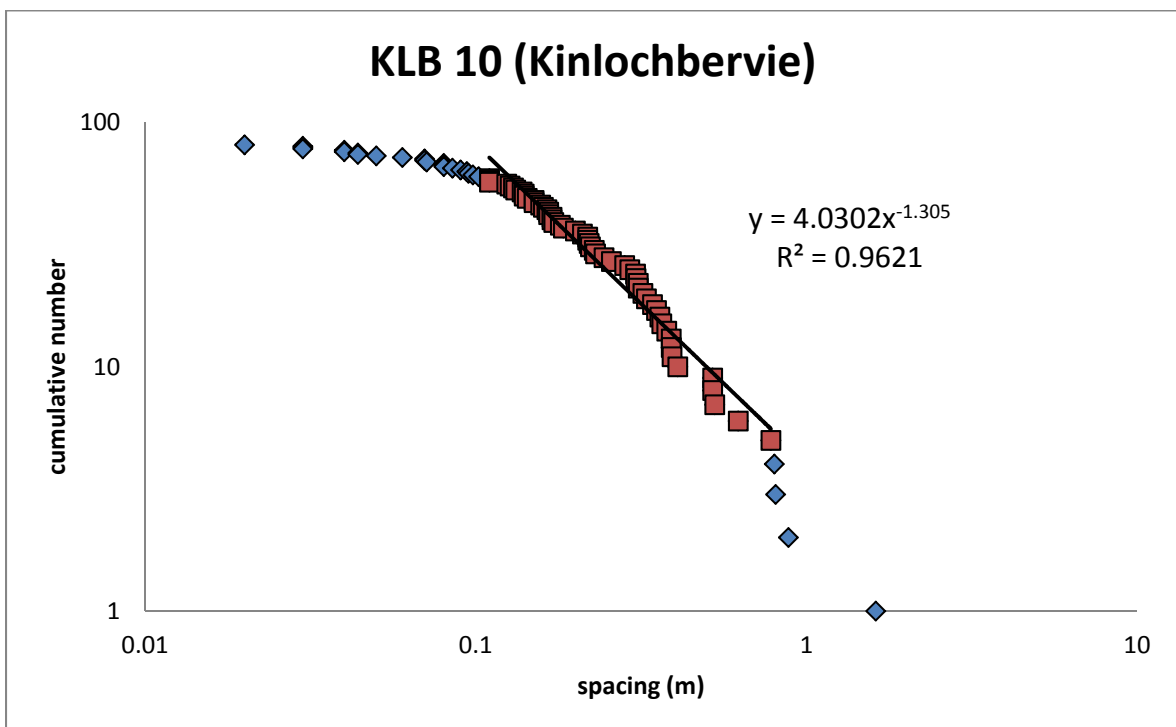
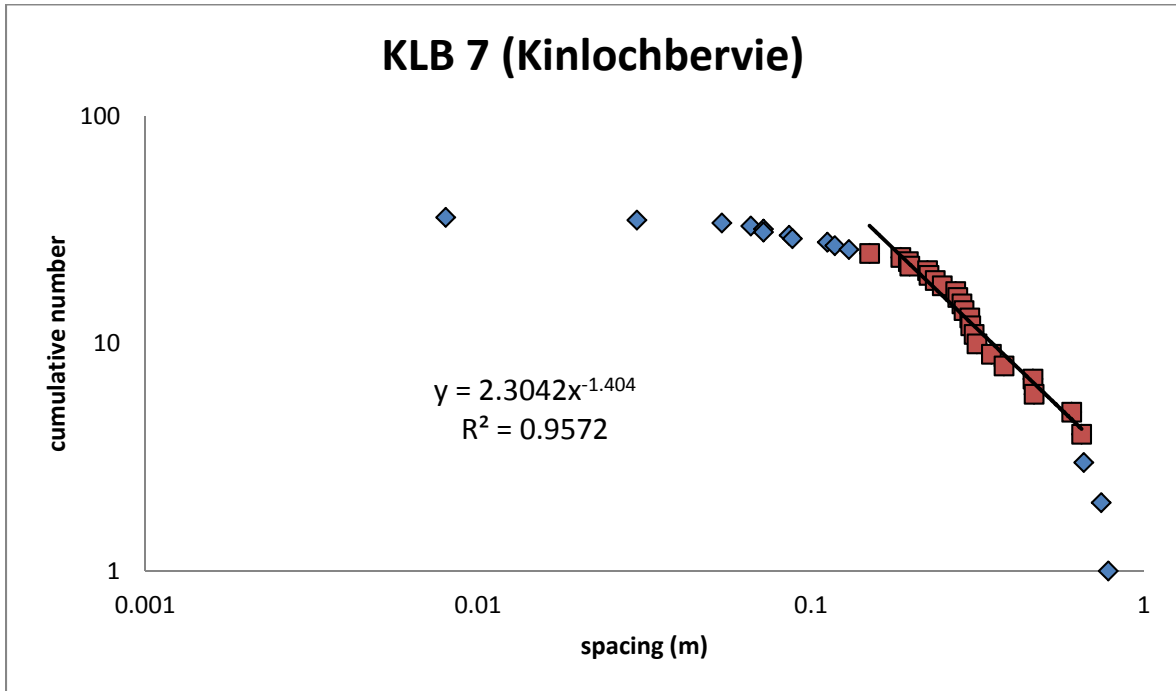


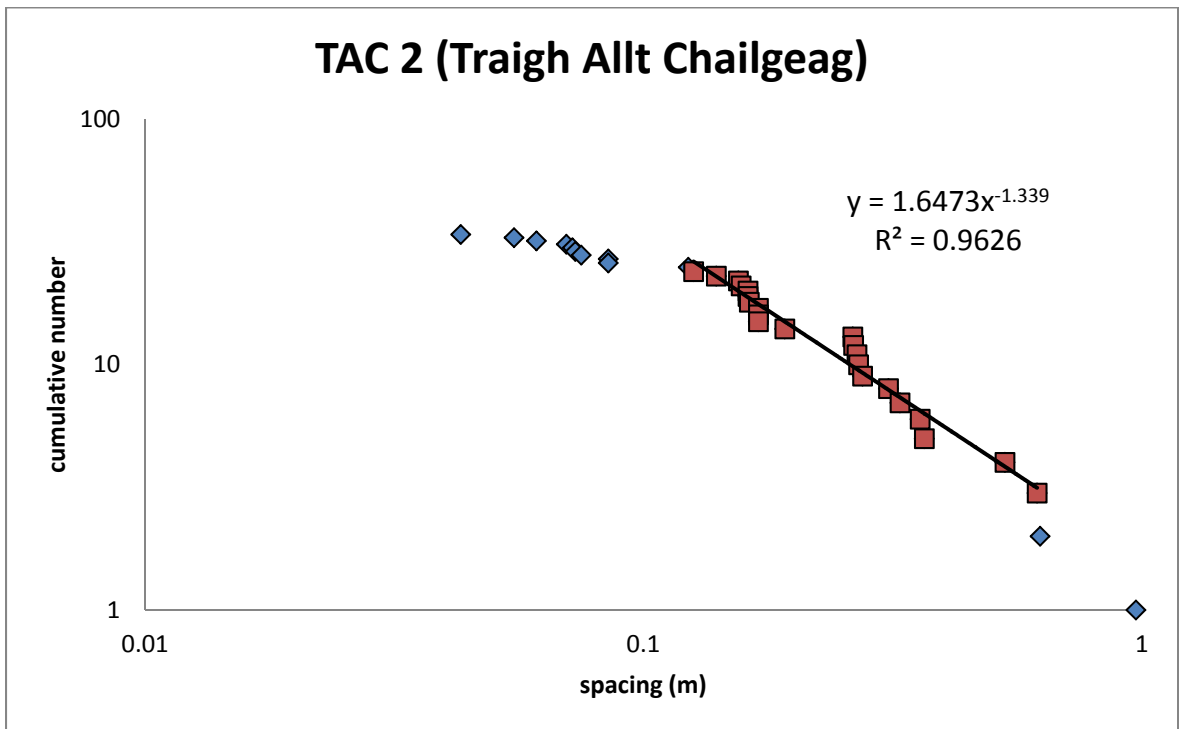
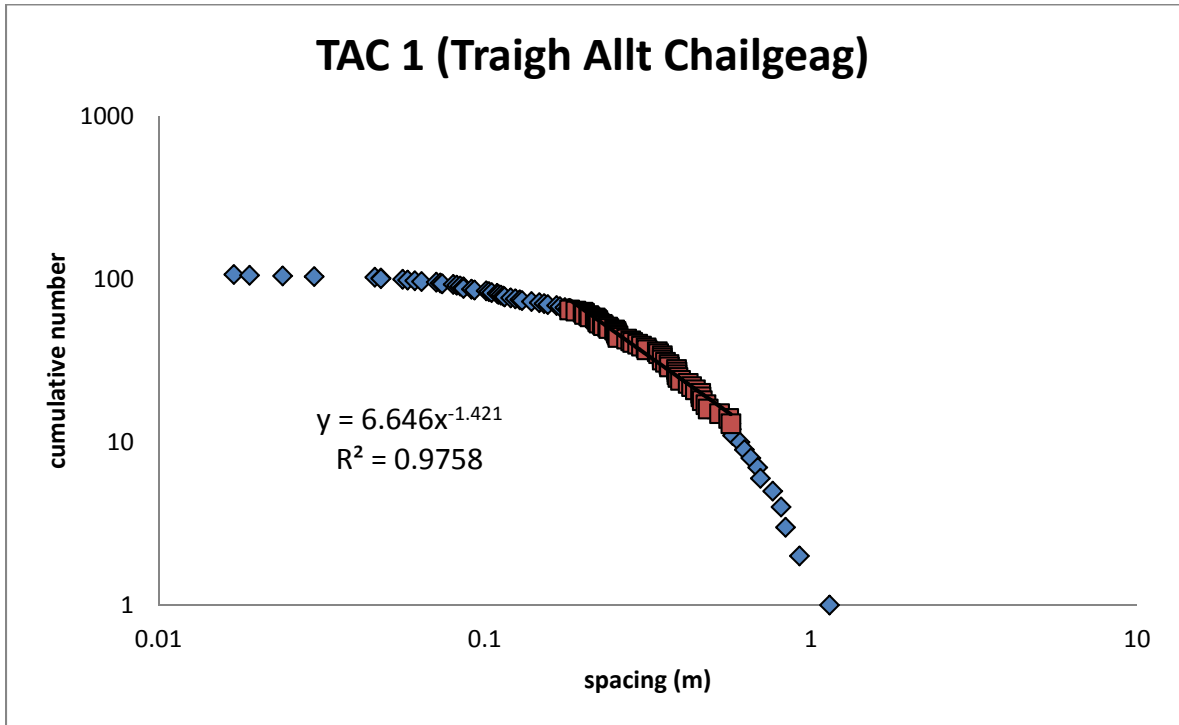


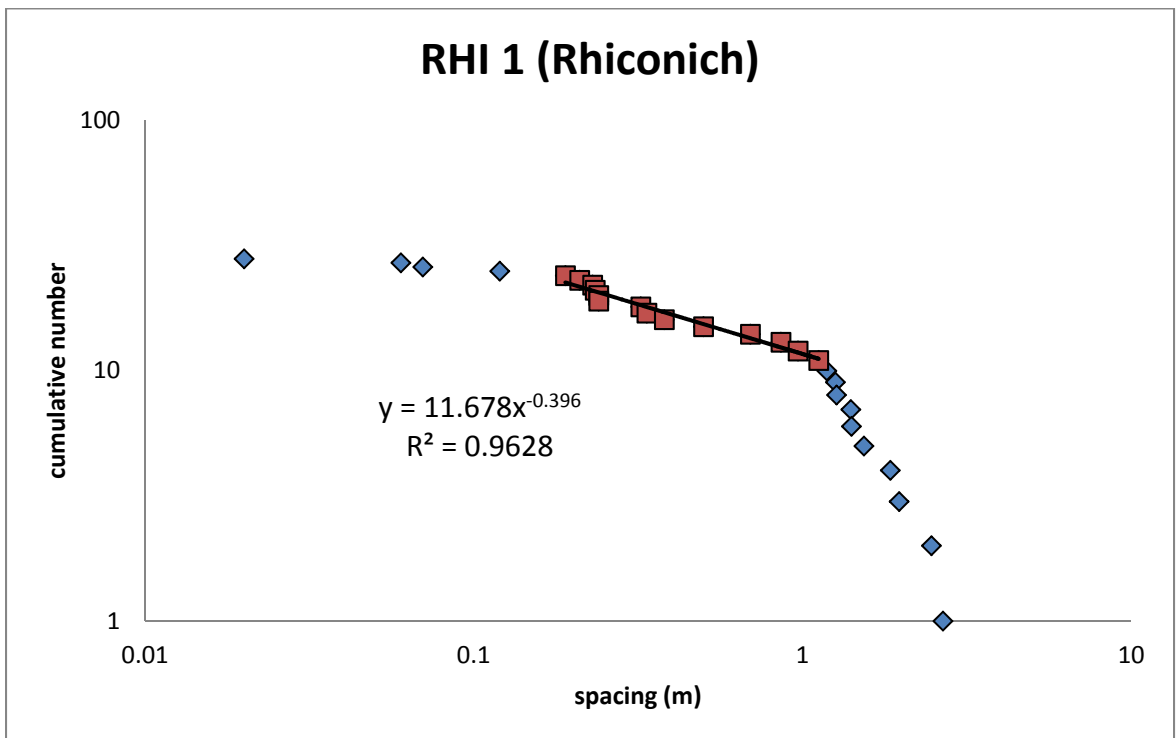
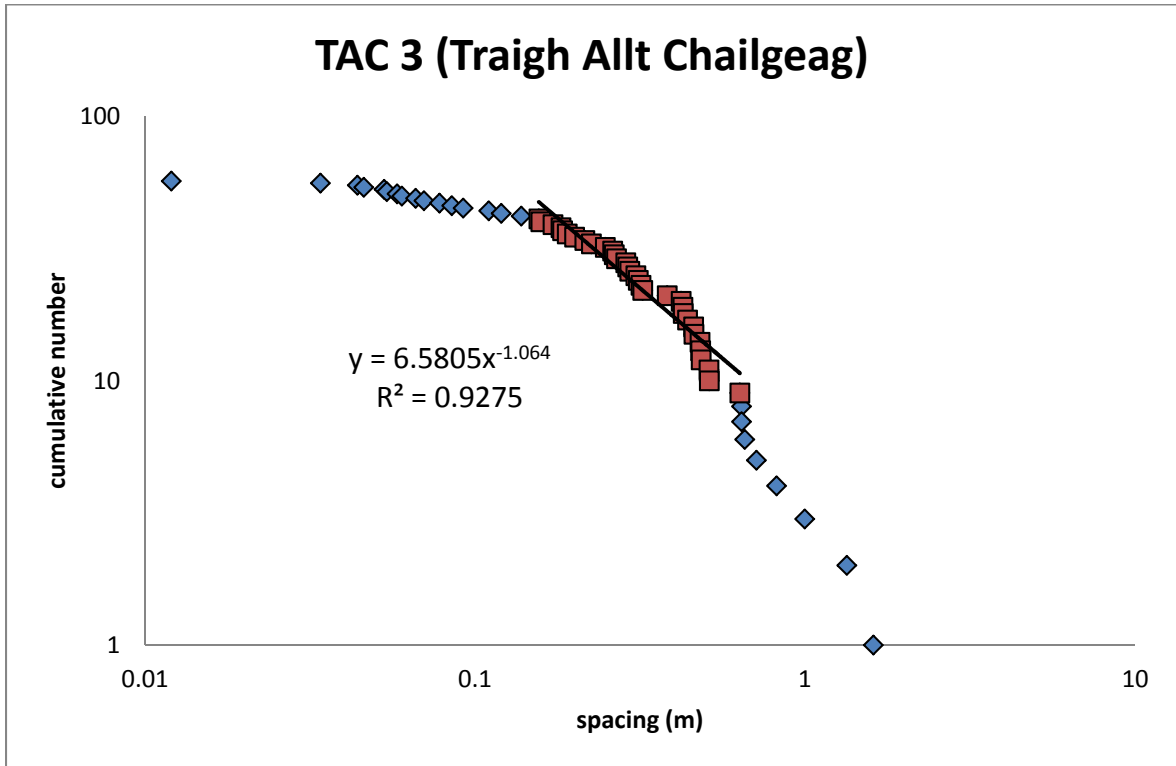


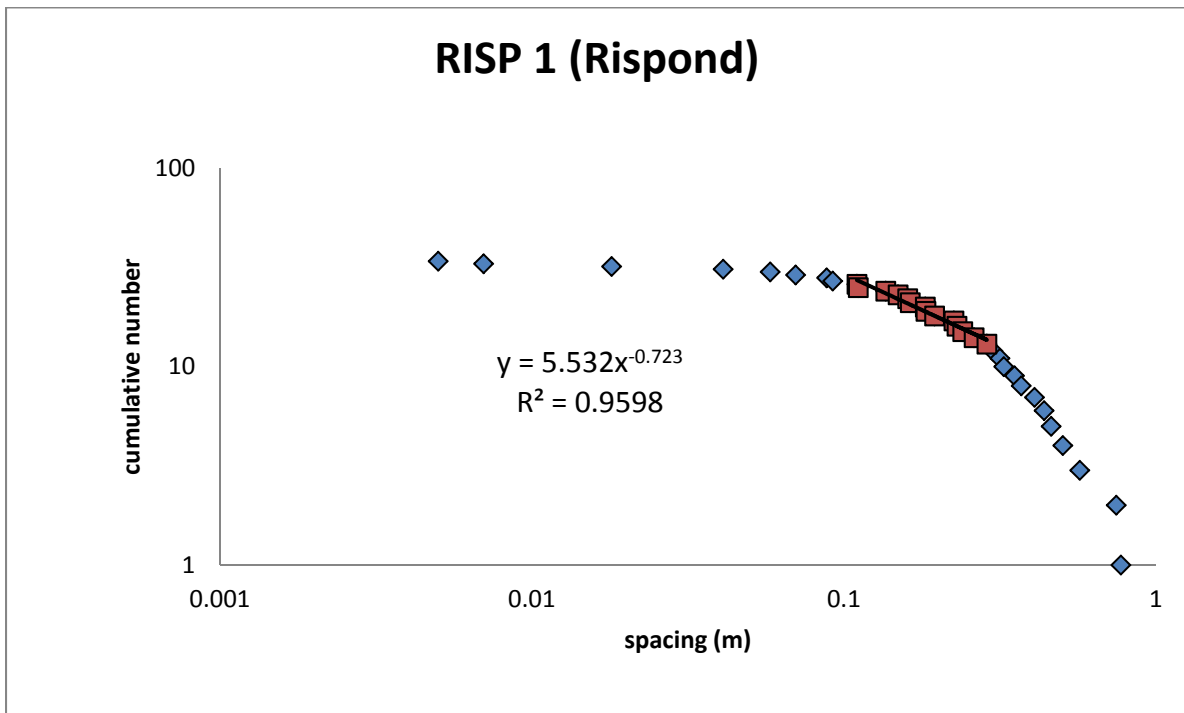
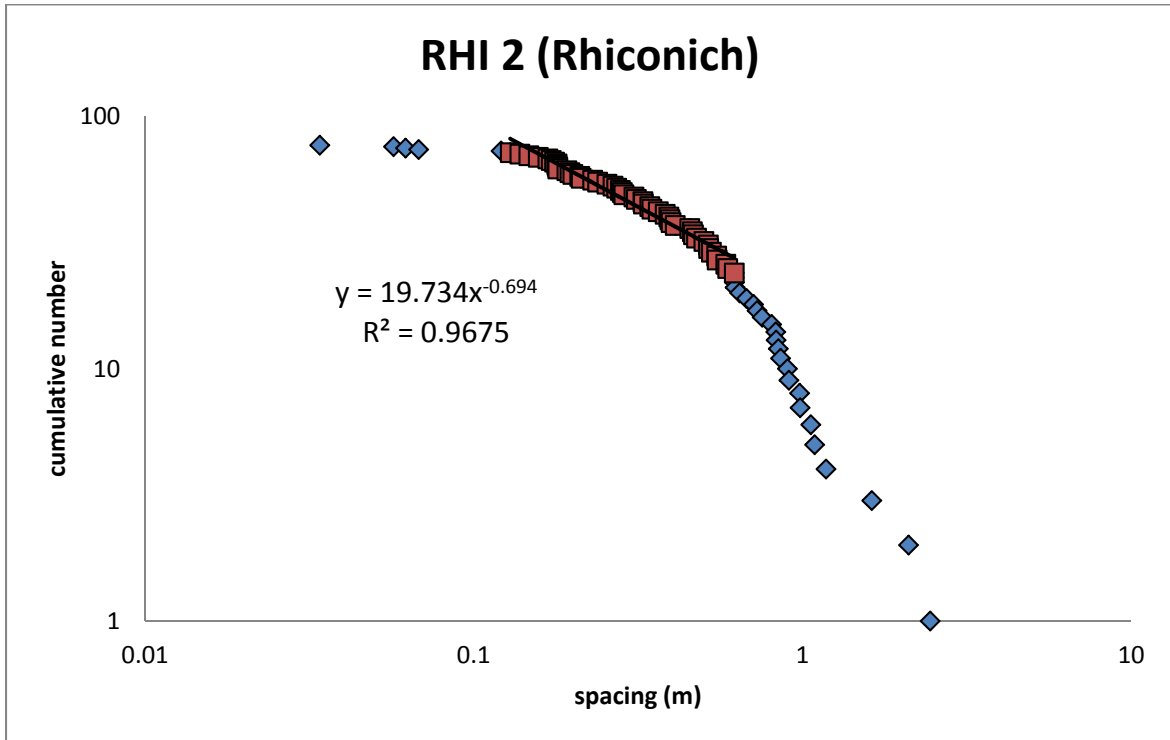


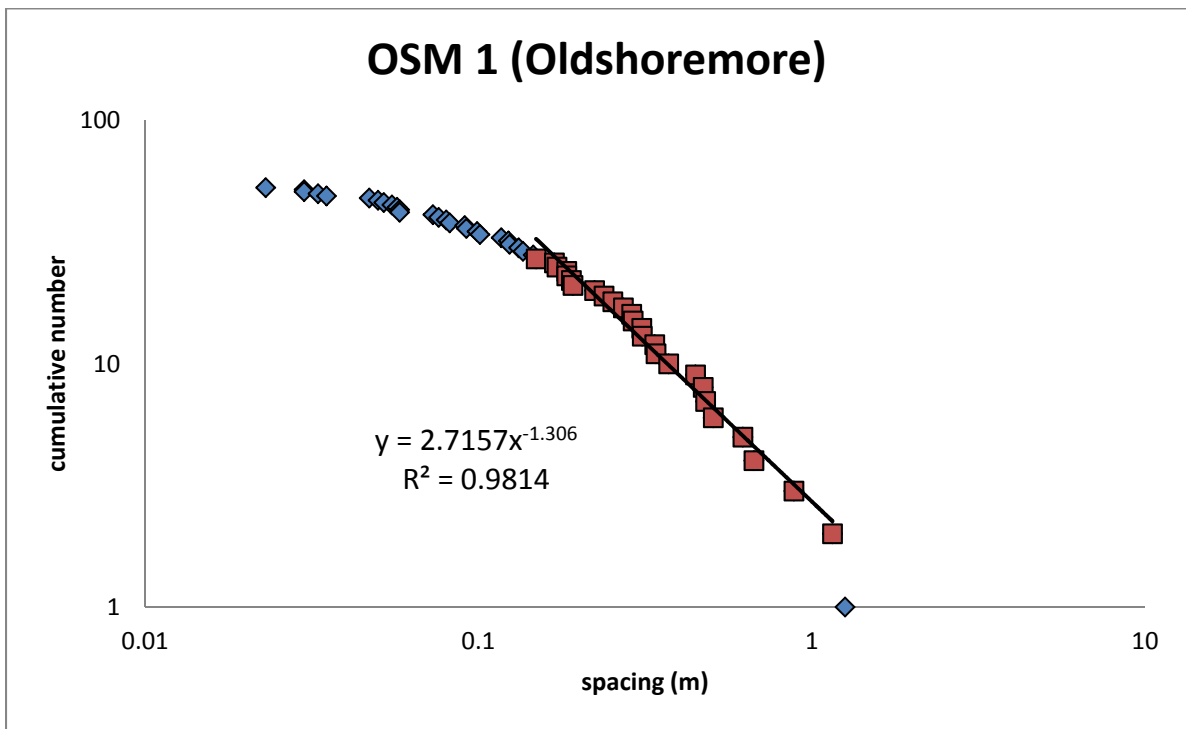
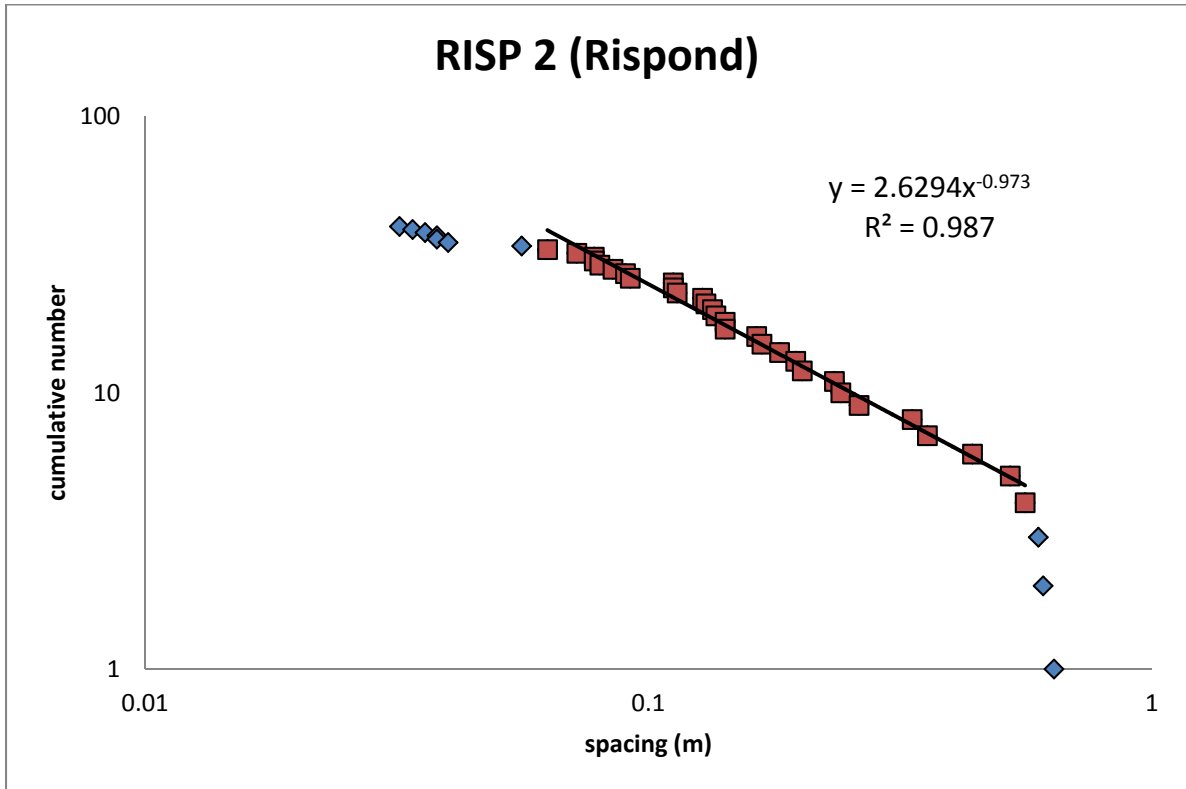


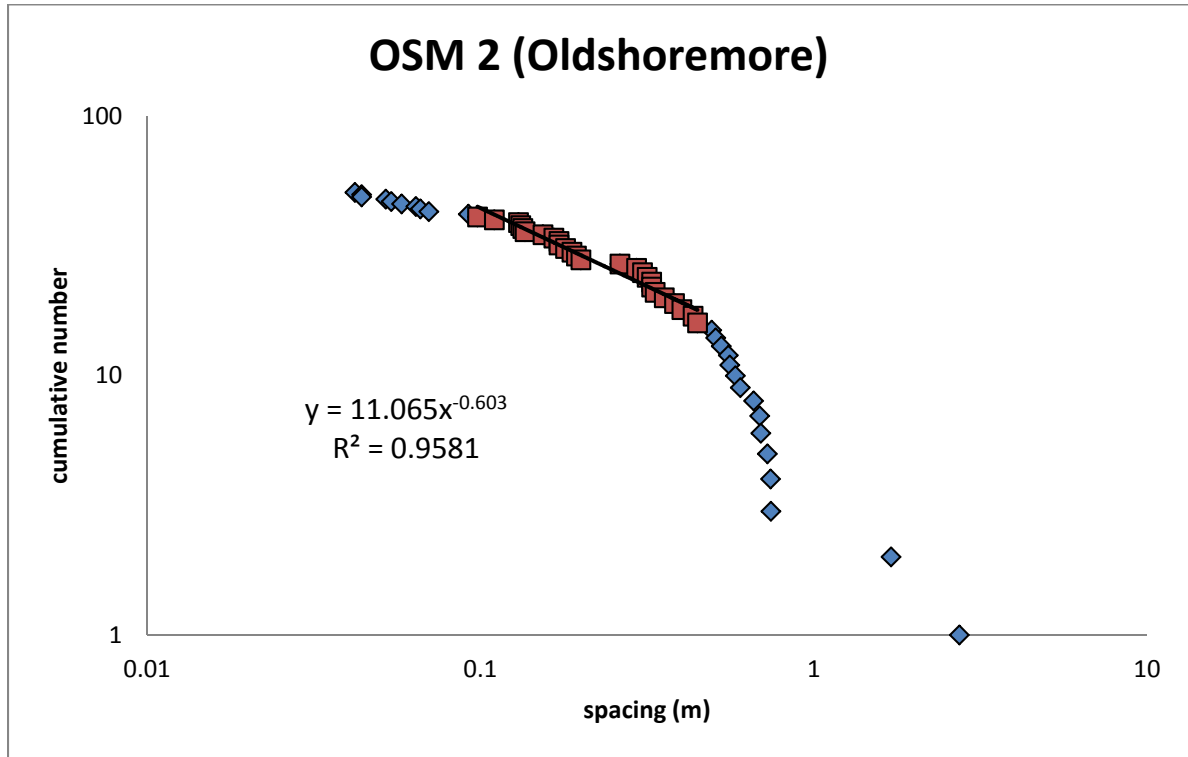












## VII: Fracture Characterisation of mainland Lewisian Gneiss Complex thin section samples – Rowan Vernon

### Introduction;

- This study looks at the characteristics of fractures taken from different settings within the Lewisian Complex of northwest Scotland.
- All the thin sections analysed have been deformed in some way, whether as part of the gouge zone of a fault or due to shearing.

### Rock Types of Thin Sections;

Sample Number	Rock Type
M5a	Lewisian fault gouge
14-2	Highly altered block from within fault plane
M10a	Deformed Lewisian
21-1a	Lewisian fault rock with haematite staining
M10b	Deformed Lewisian
M6a	Sheared Torridonian
M7	Lewisian gouge



### Observations:

- There is a large variation in the number of fractures in each thin section and thus crossed by each sample line. Some do not contain any, while others contain upwards of fifteen fractures.
- The maximum number of fractures which any one sample line crosses is eleven, meaning that the datasets for this study are small and only the larger ones have been used for statistical analysis.
- The majority of the fractures do not show an apparent aperture, or show an aperture too small to be measured using a ruler.
- Thin Section M7 is an exception to this, and has fractures with measurable apertures, the smallest being 0.09mm and the largest 0.72mm. These are generally filled with calcite and perhaps limited quartz.
- Thin Section 21-1 has fractures which are filled with epidote.
- Thin Section 13-2b has fractures which are delineated by strongly orientated mica (mostly biotite) which aligns with the fracture direction.
- None of the thin sections are densely fractured on an inter-crystal basis, although Thin Sections M5a and M5b are heavily fractured on an intra-crystal basis owing to the large crystal size (>5mm) and their composition (pyroxene which is in the process of breaking down).
- Only Thin Sections M5a, 14-2, 10a, 21-1a, M10b, M6a and M7 were densely fractured enough to allow for statistical analysis, with none of these having more than 11 fractures intersecting the sample lines.
- In many of the thin sections the same fractures are crossed by both the long ways and cross ways sample lines.

### Fracture Distribution;

- For each sample line three trendlines are plotted on the graph (Linear, Exponential and Power Law) and the  $R^2$  values for each of these lines is also displayed on the graph. These are all included in **Appendix 1**.

- The majority of the sections have an exponential distribution ( $R^2 > 90\%$ ), with the exception of M10a longways and M6a longways which have a linear distribution, although it is likely the datasets are not large enough for these sample line (containing only 4 and 3 fractures respectively).

- M10b crossways is the exception in that the  $R^2$  value is greatest for power law distribution,  $R^2 = 0.9969$ .

- In some cases  $R^2 > 90\%$  for another type of distribution (either linear or power law), however, in these cases the exponential distribution has the largest  $R^2$  value.

- M5a crossways has linear  $R^2 = 0.9436$ , while exponential has  $R^2 = 0.9527$ .
- M10a crossways has linear  $R^2 = 0.9436$ , while exponential has  $R^2 = 0.9529$ .
- 21-1a crossways has  $R^2 > 90\%$  for linear, exponential and power law distributions, but exponential has the highest  $R^2 = 0.9766$ , while linear  $R^2 = 0.9014$  and power law  $R^2 = 0.9158$ .
- M10b long ways has linear  $R^2 = 0.9053$ , while exponential  $R^2 = 0.9184$ .

- 14-2 crossways has an  $R^2 = 0.8567$  for the exponential distribution, which is far higher than for either the linear or power law distributions.

- Thus, with the exception of M10a long ways, M6a long ways and M10b crossways, the highest  $R^2$  value for each sample line belongs to the exponential distribution.

- The z number in  $e^{-zx}$  for the exponential distributions tends to be very small ( $\sim 0.1x$ ) which the largest value being  $-0.527x$ ). These low values imply fractures which are not very closely spaced.

#### Density Log;

- Density logs which show the number of fractures per millimetre have been plotted as bar charts for each sample line and are displayed in **Appendix 2**.
- The sample lines do not often show more than one fracture per millimetre, and never more than two fractures per millimetre.
- Many of the millimetres on the majority of sample lines do not contain any fractures at all.
- This suggests that the density of fracturing is not high.

#### Angle to Sample Line;

- The angles of each fracture to its sample line have been plotted on Rose Diagrams (**Appendix 3**), with the sample line taken as N-S.
- In many of the thin sections, the long ways and cross ways sample lines cross the same fractures. This can be seen by the similar groups of fractures on the rose diagrams for the long ways and cross ways directions of each section, but rotated by ninety degrees.
- Many of the rose diagrams show preferred orientations of fractures relative to the sample line, although in some cases (e.g. M10a longways, 14-2 crossways and M6a longways) there is no apparent preferred orientation in the fractures, but these sample lines are also the one which cross the fewest fractures.

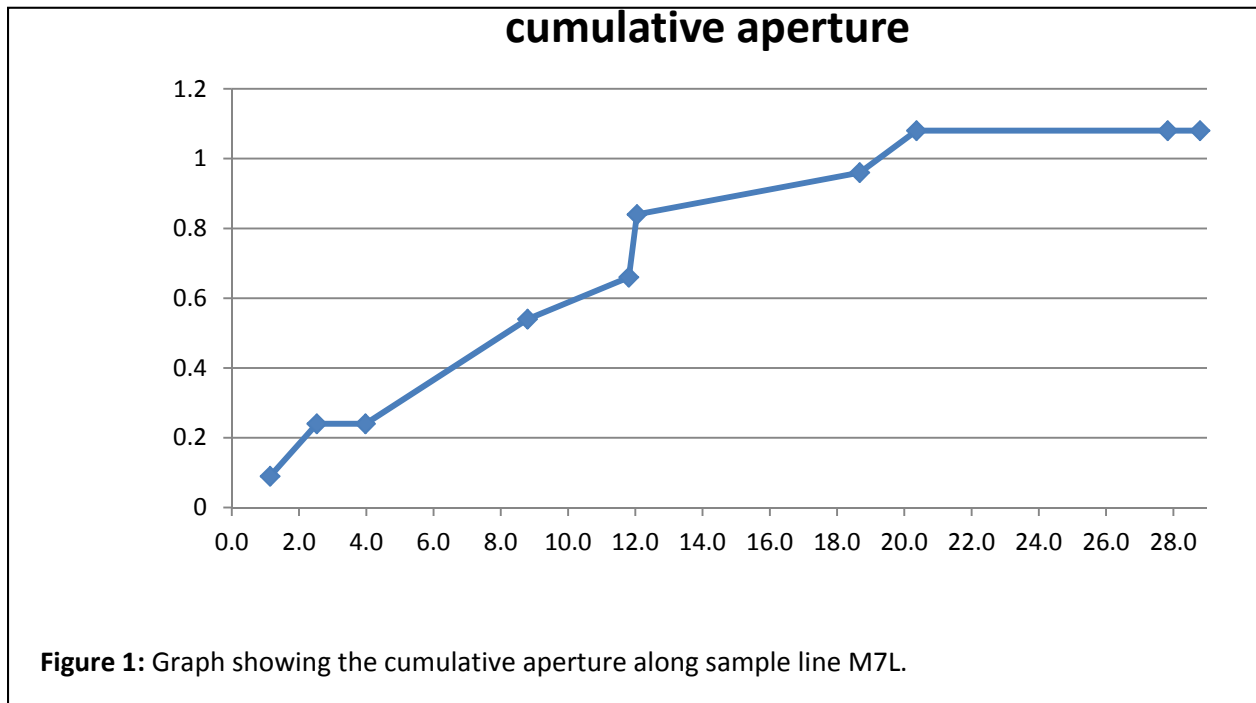
#### Coefficient of Variation;

- The coefficients of variation for all the sample lines are displayed in **Table 1**, along with whether they are interpreted to be Clustered, Non-Clustered or Random.
- The majority of sample lines show a coefficient of variation  $<1$ , implying a non-clustered and non-random distribution.
- Sample line 14-2 crossways is the only one which shows a clustered distribution.

- There is a reasonable spread in the coefficient of variation (0.379-0.988), and thus in the degree of randomness.
- Sample lines 14-2 longways, 21-1a longways M10b crossways and M7 longways and crossways have coefficients of variation which are close to one, thus they tend toward a random distribution.

Coefficient of Variation				<b>Table 1</b>
Sample	L		X	
M5a	0.791559	Non-clustered	0.57588	Non-clustered
14;2	0.906294	Random	1.296485	Clustered
M10a	0.379206	Non-clustered	0.529252	Non-clustered
21-1a	0.823735	Random	0.482689	Non-clustered
M10b	0.767125	Non-clustered	0.988251	Random
M6a	0.51263	Non-clustered	0.855843	Random
M7	0.883469	Random	1.067273281	Random

Cumulative Aperture;



- As mentioned above, only Thin Section M7 shows apparent aperture for the majority of the fractures.

- The fracture apertures range from 0.09 mm to 0.72mm in width, measured perpendicular to the strike of the fracture at the point it crosses the sample line, and are filled with mostly calcite and some quartz.

- A cumulative aperture graph has been drawn, showing the accumulation of opening distance throughout the thin section (**Figure 1**).

- This shows that along the 30mm long sample line, 1.08mm is taken up by fracture apertures, suggesting extension of the rock by 3.6% in the direction of the sample line. Given the size of the section sampled, this is a significant amount of extension.

- This may be a useful value to have obtained, as it may be compared with the percent of extension due to fracturing on larger scales throughout the Lewisian.

### Discussion;

- Sample line M10b crossways is the only sample line which has a very strongly power law distribution. It also has a coefficient of variation which is very close to 1 (0.988) implying a strong degree of randomness to the distribution of the fractures. The fractures also display a reasonable preferred orientation (NNE-SSW).
- Sample lines which display a very strong ( $R^2 > 9.5$ ) exponential distribution tend to also display a wide variation in the orientation of the fractures and also tend to have a moderate coefficient of variation ( $\sim 0.6$ ), suggesting a non-clustered, and more evenly spaced distribution of the fractures throughout the rock.
- Those sample lines which display less strong exponential distributions experience less spread in the orientations of their fractures and have coefficients of variation which are close to one, and thus have distributions throughout the rock which tend towards being random.
- The sample lines which display a linear distribution (sample lines M10a longways and M6a longways) also display a very wide variation in the orientations of the fractures and tend to have the lowest coefficients of variation ( $< 0.5$ ), suggesting a non-clustered distribution of fractures throughout the rock which trend towards being evenly spaced as opposed to random. However, these sample lines also tend to be those which contain very few fractures (3 to 4) and thus are not statistically significant.

### Conclusions;

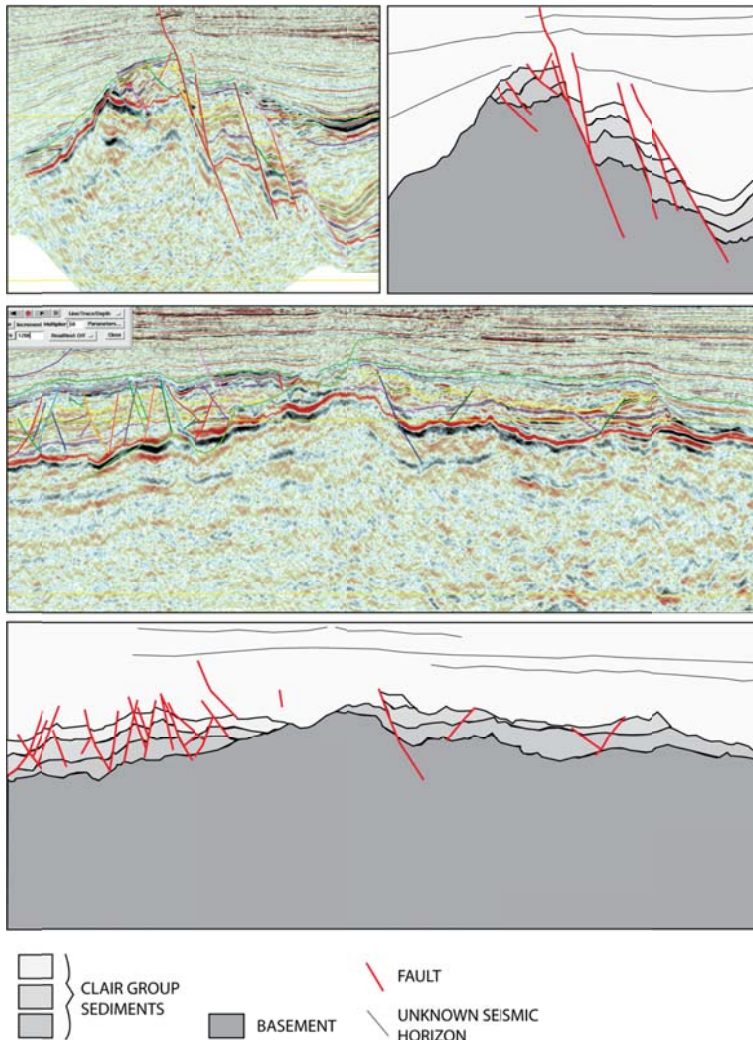
- The majority of sample lines statistically analysed show an exponential distribution with regards to spacing and have a distribution in the rock which is random, or non-clustered but tending towards being random.
- The rose diagrams show that the often large variation in the orientation of the fractures relative to the sample lines may be influencing this exponential distribution as well as the distribution throughout the rock to be tending towards being random.
- The percent extension calculated from the cumulative aperture in Thin Section M7 could be an important way to link this study into fracture characteristics on larger scales throughout the Lewisian.

- Only seven out of the eighteen thin sections looked at contained enough fractures for statistical analysis, and even then the maximum was eleven which is a very small dataset. Thus, it is suggested that, in many cases, the thin section sample area is too small to provide a reliable datasets in many instances.

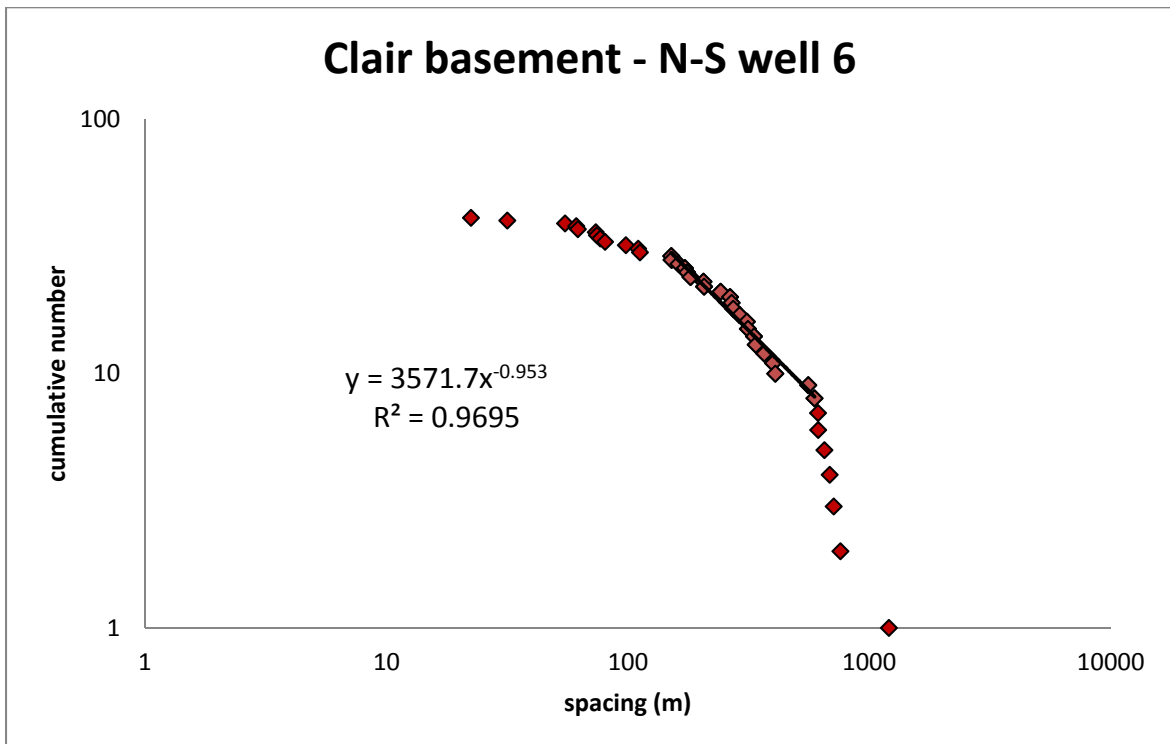
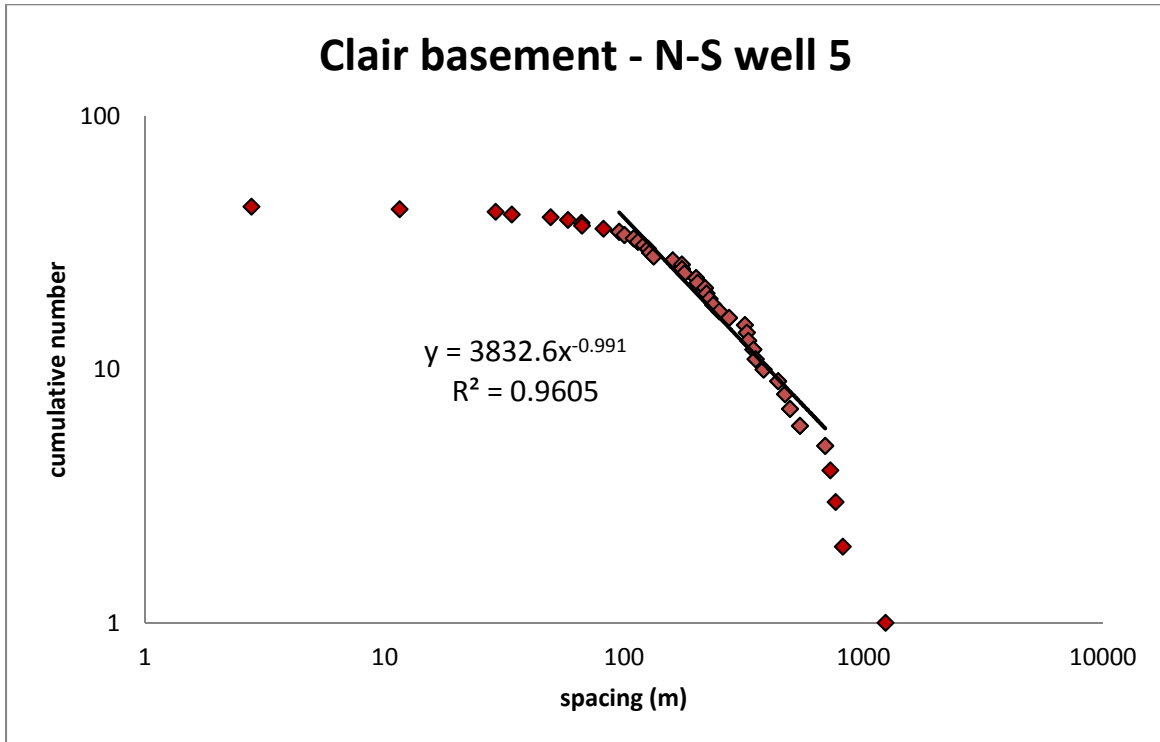
## APPENDIX C

### I: Examples of seismic interpretation for the Clair Field

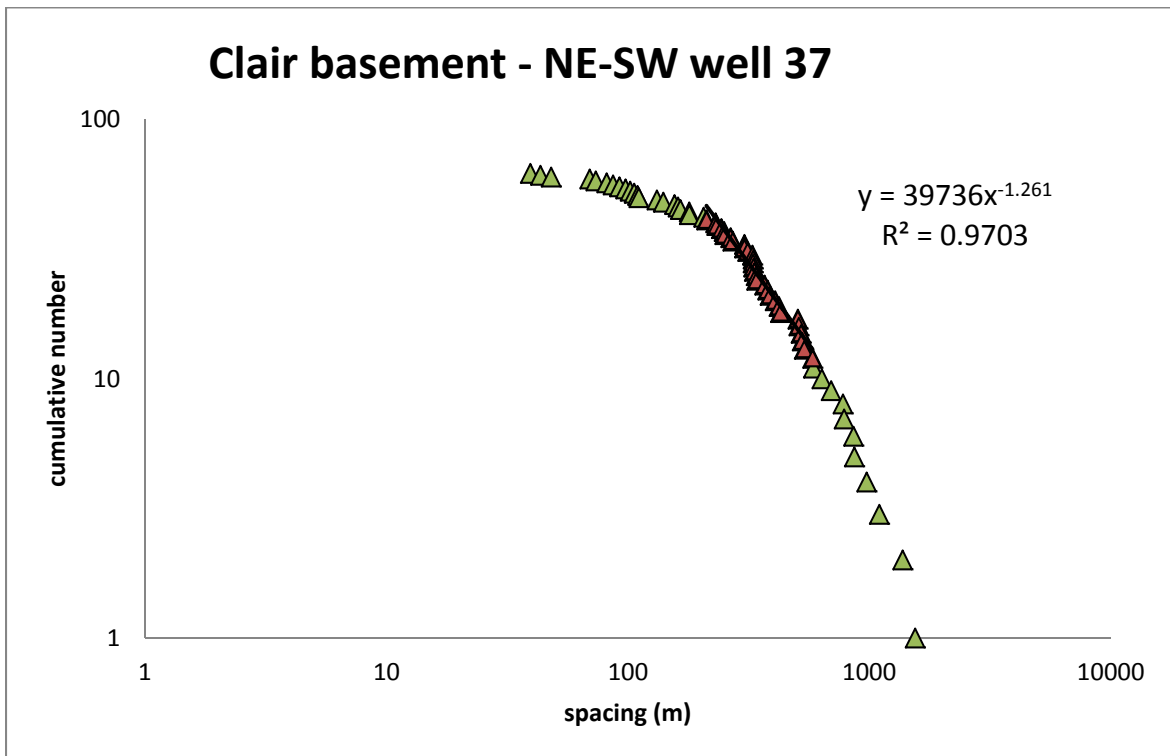
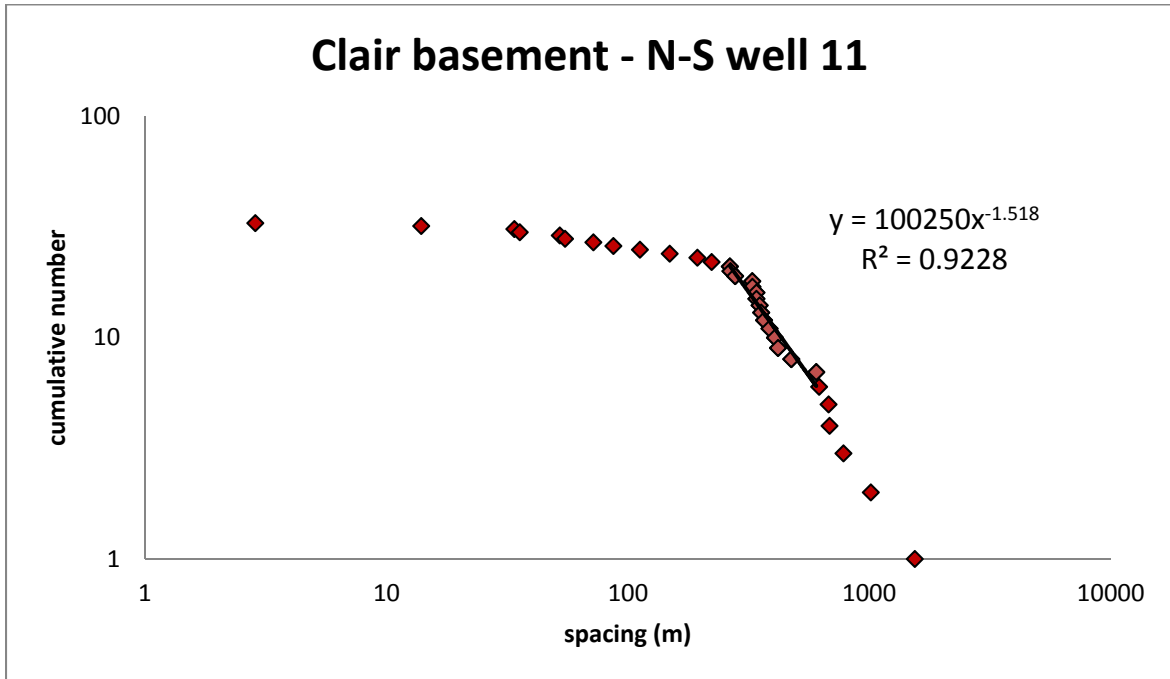
#### EXAMPLES OF THE CLAIR FIELD STRUCTURE FROM SEISMIC INTERPRETATION

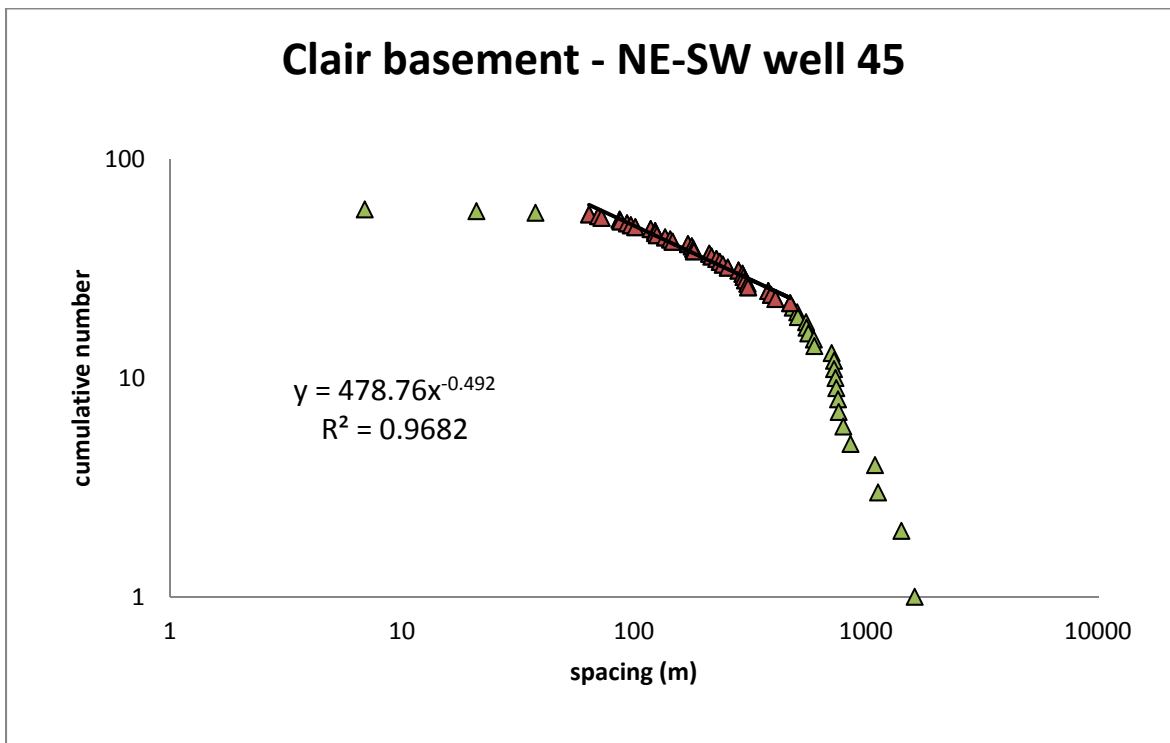
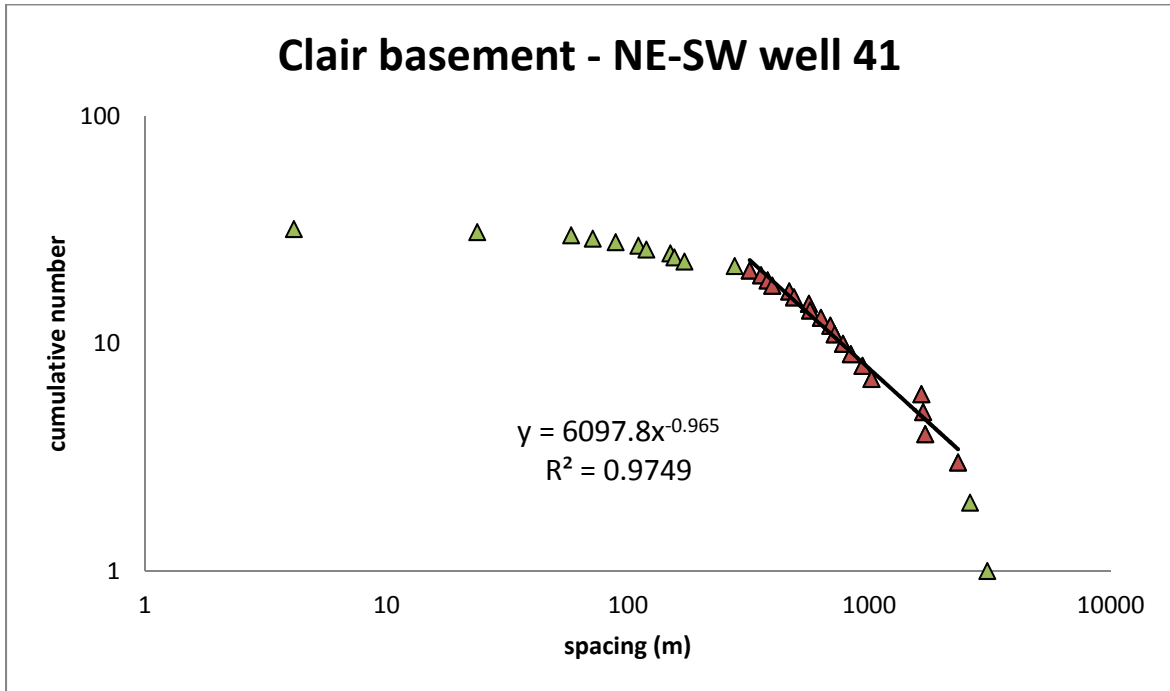


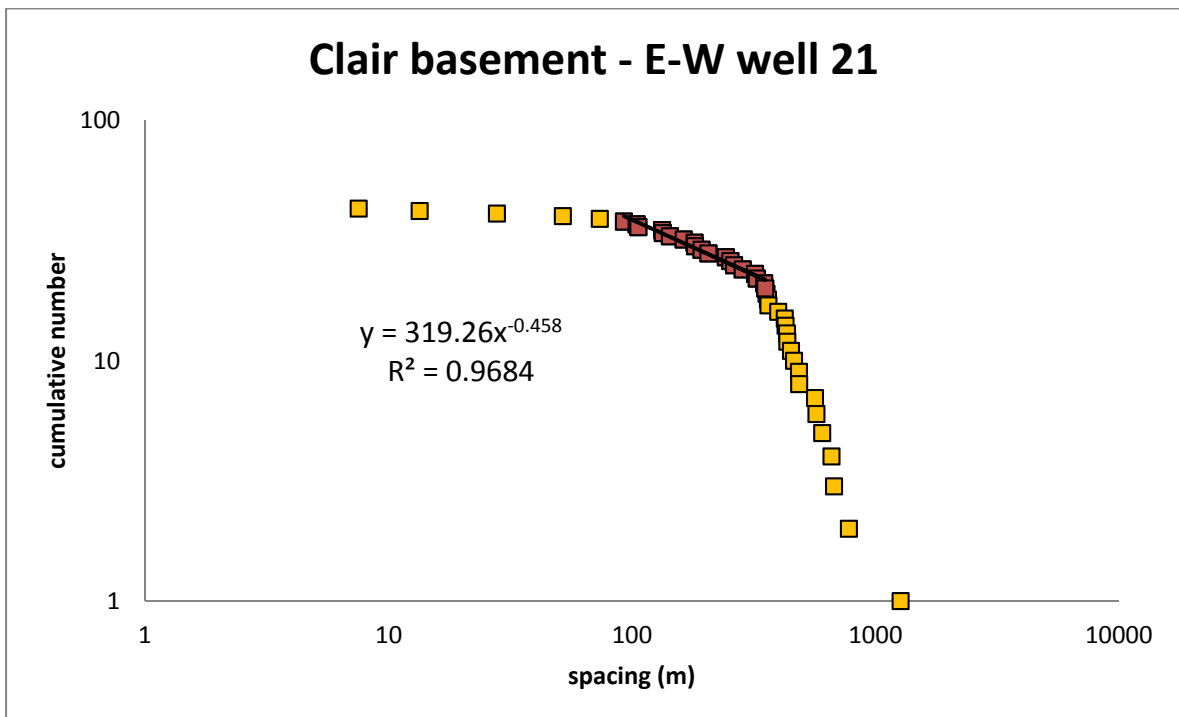
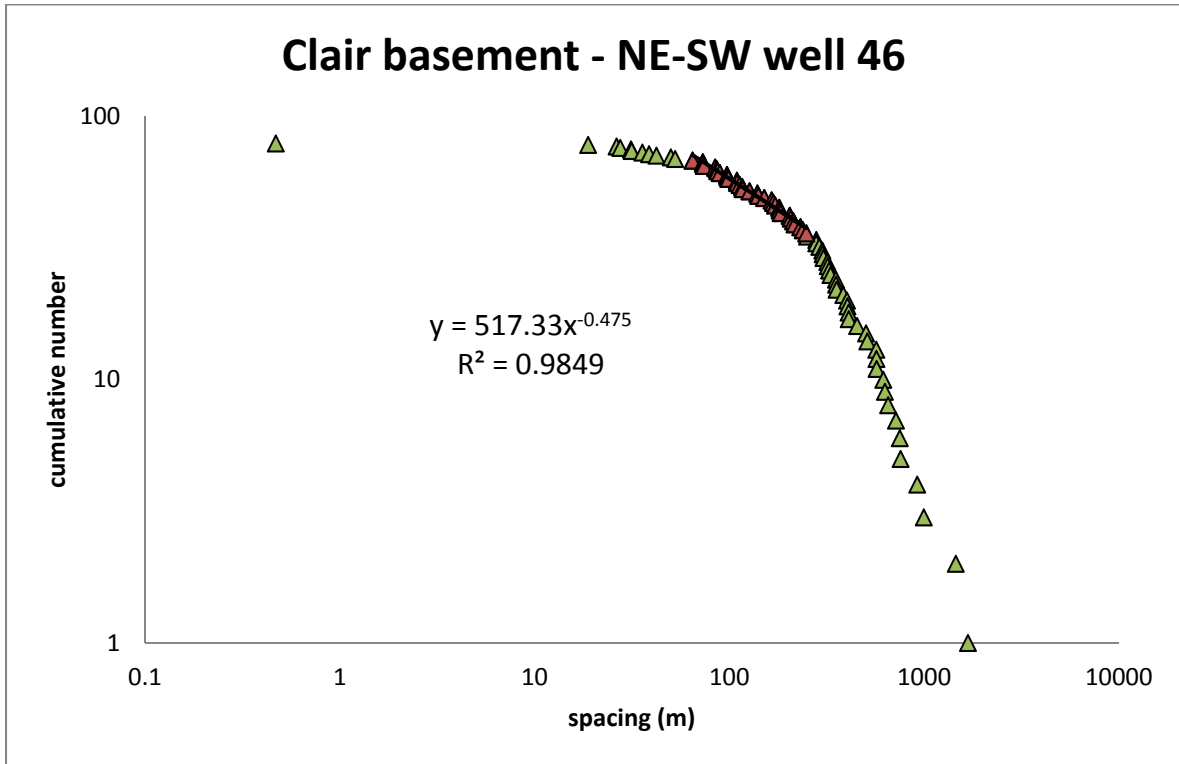
II: Regional fault population distribution plots for Clair basement

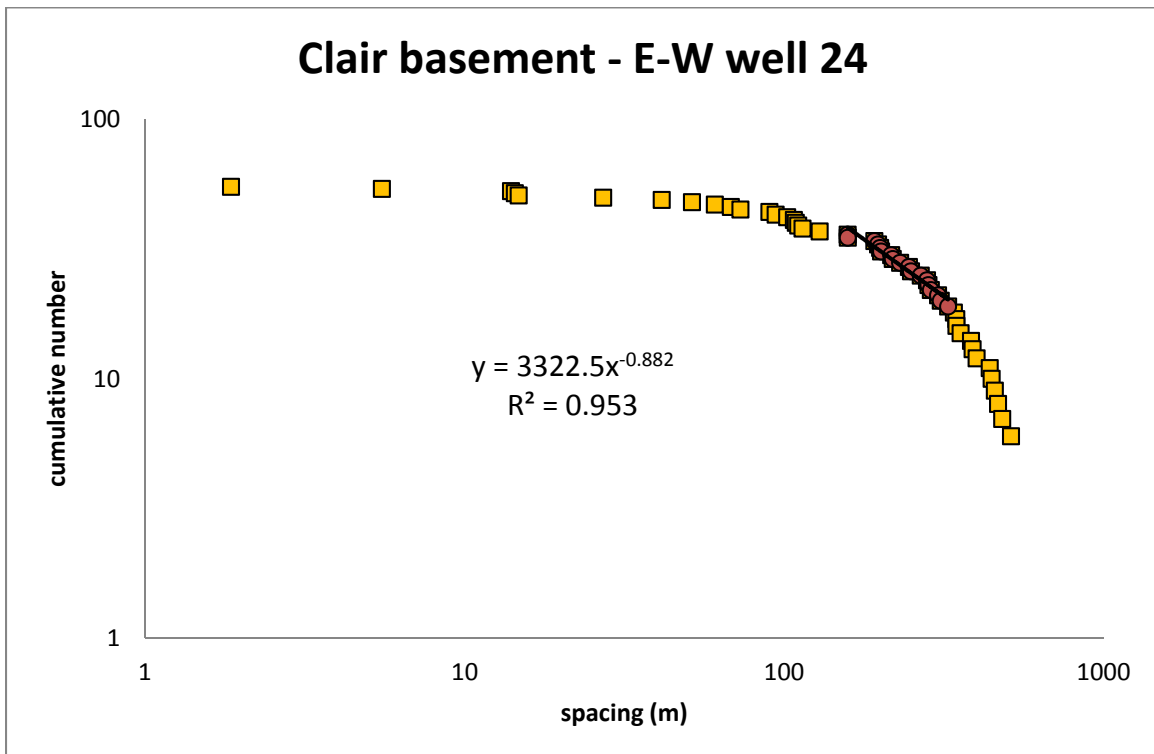
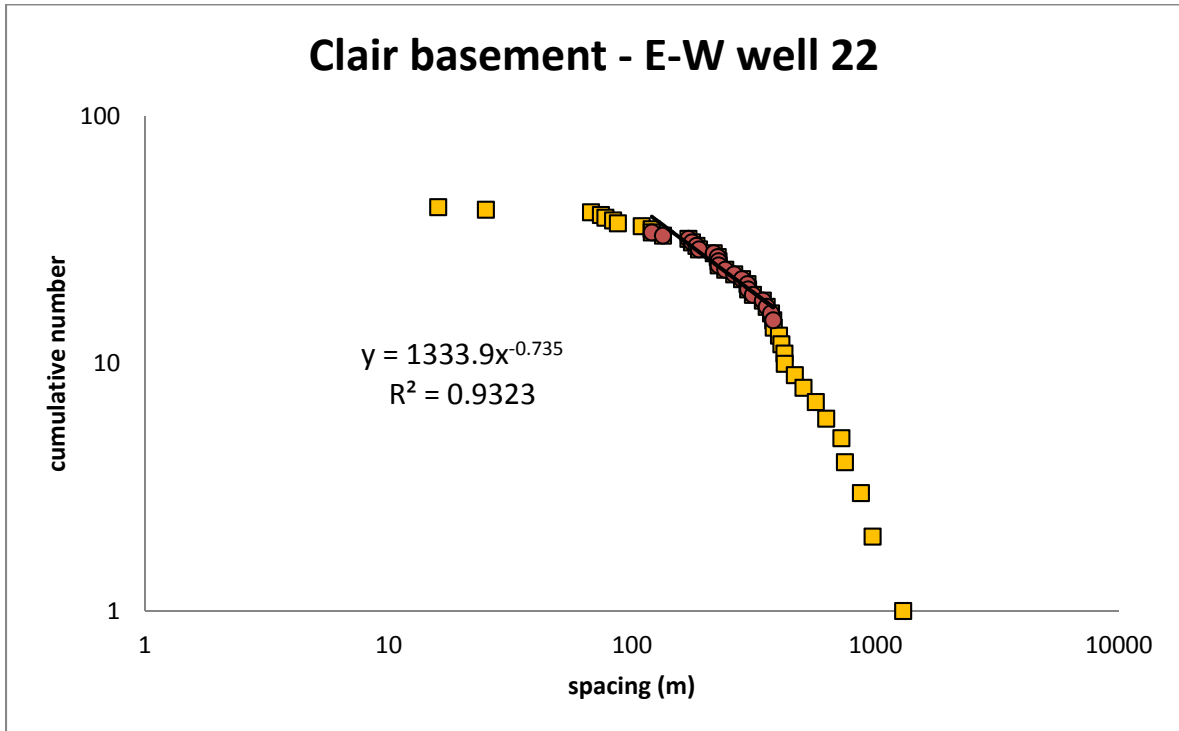




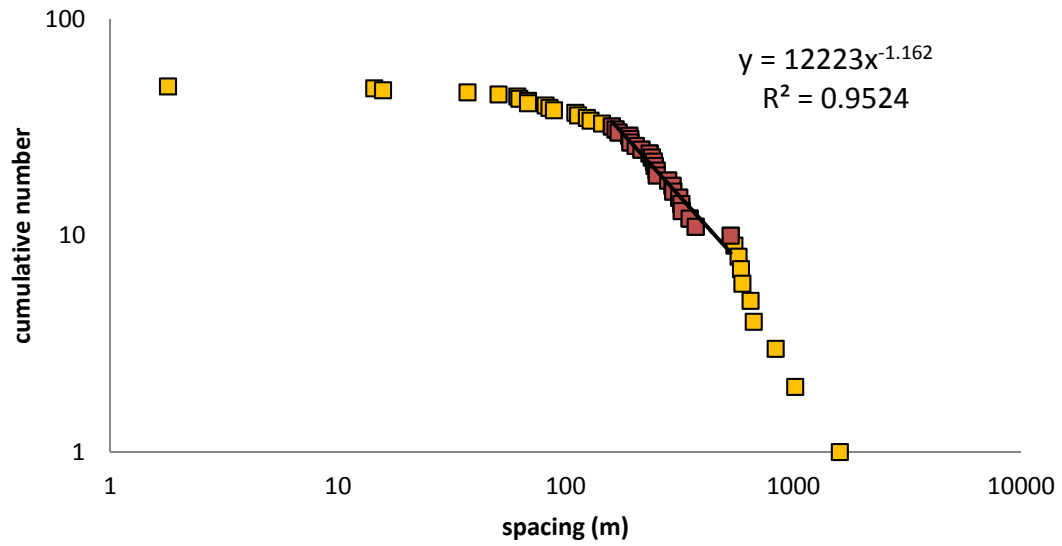




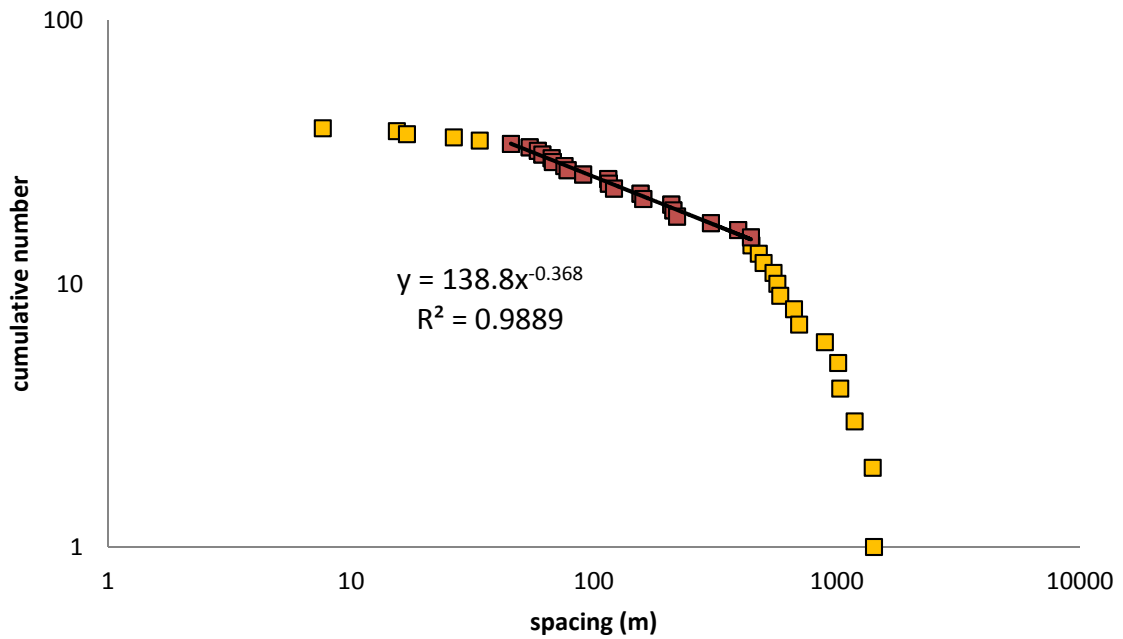


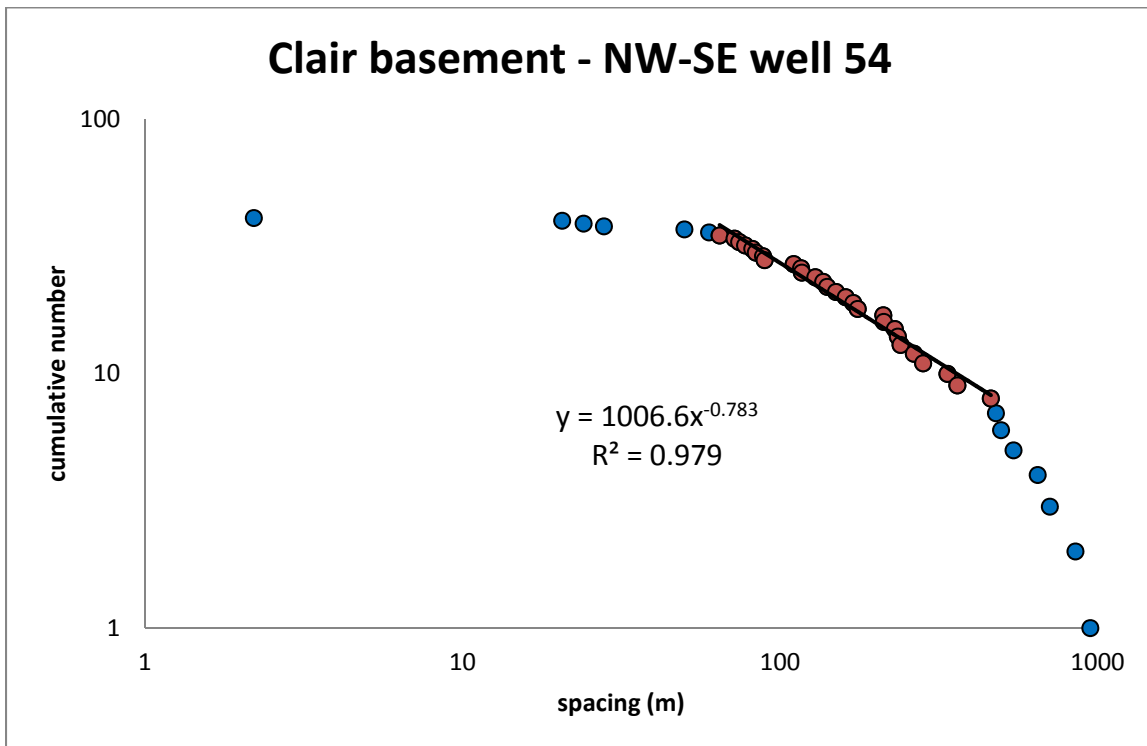
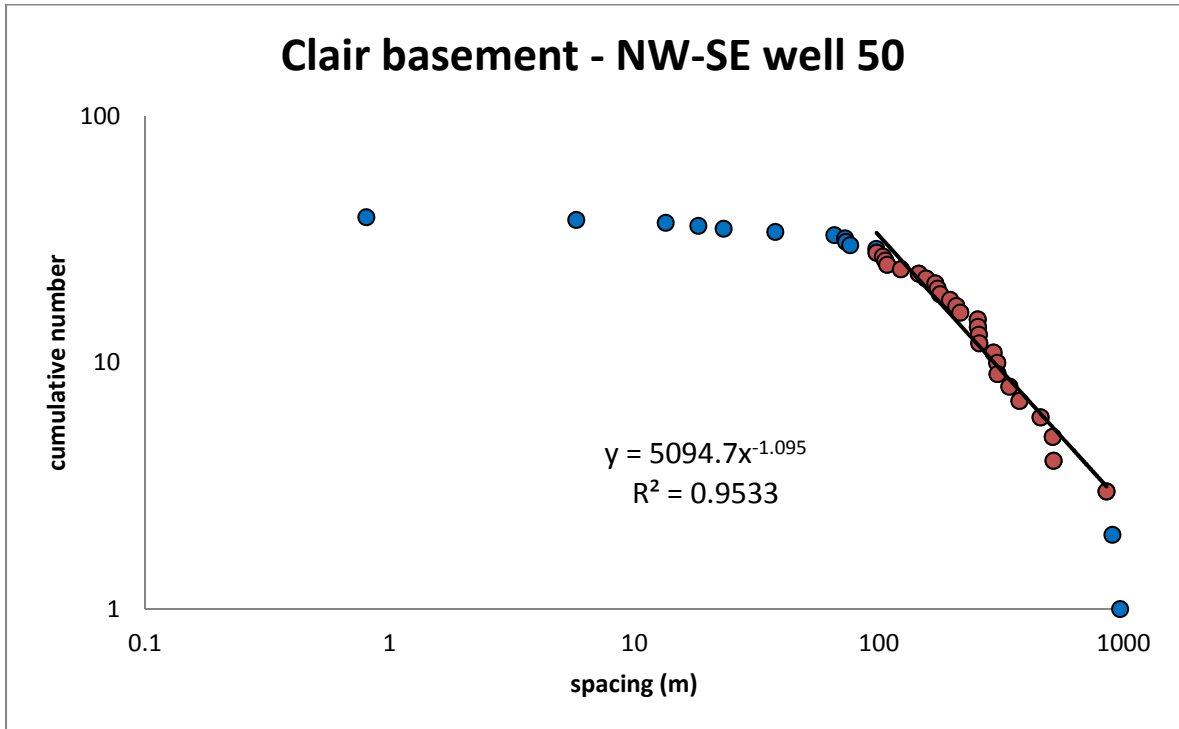


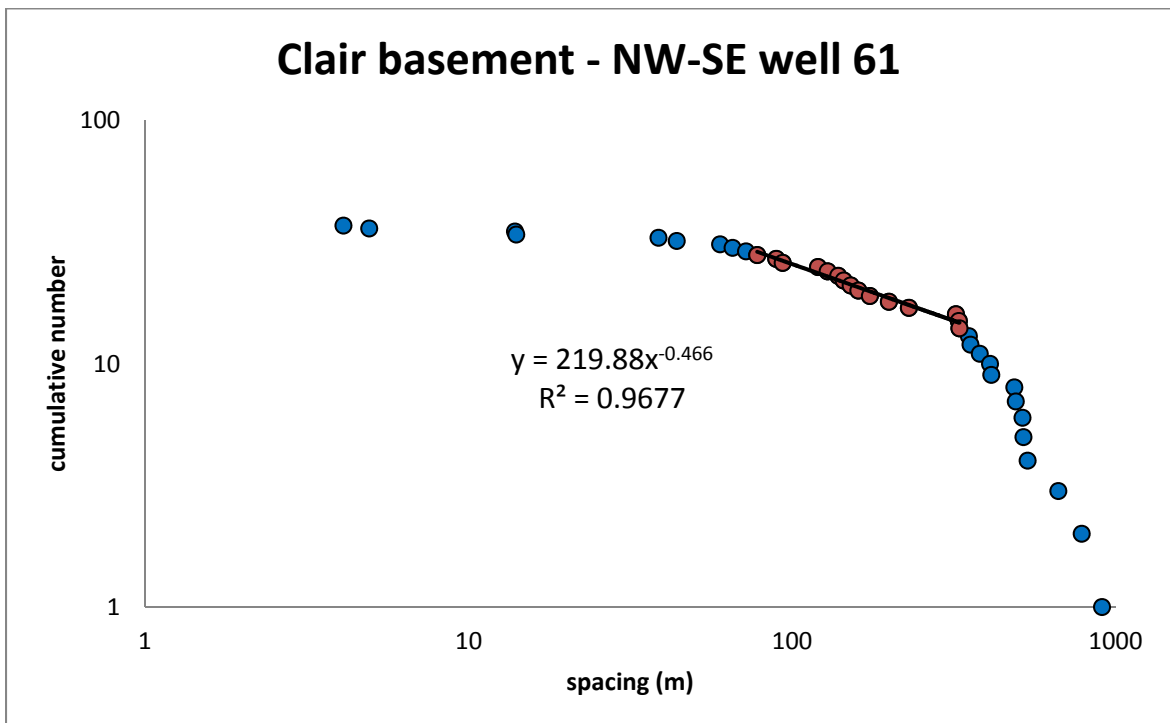
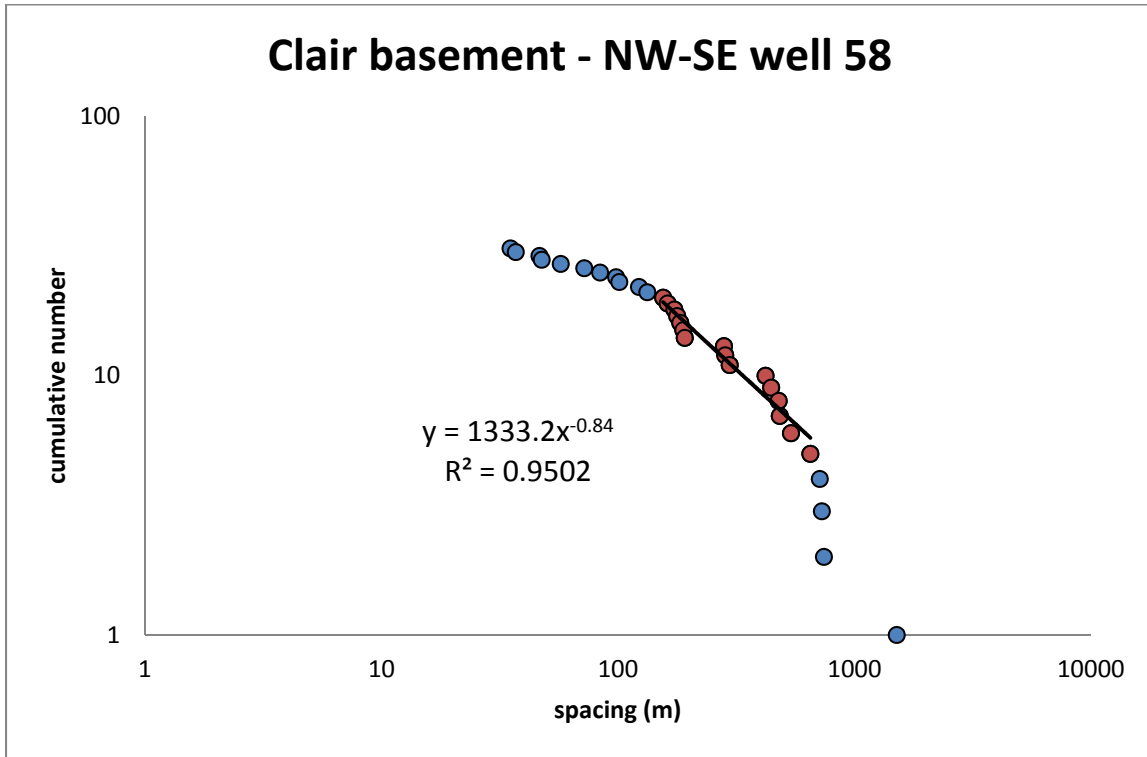
### Clair basement - E-W well 25

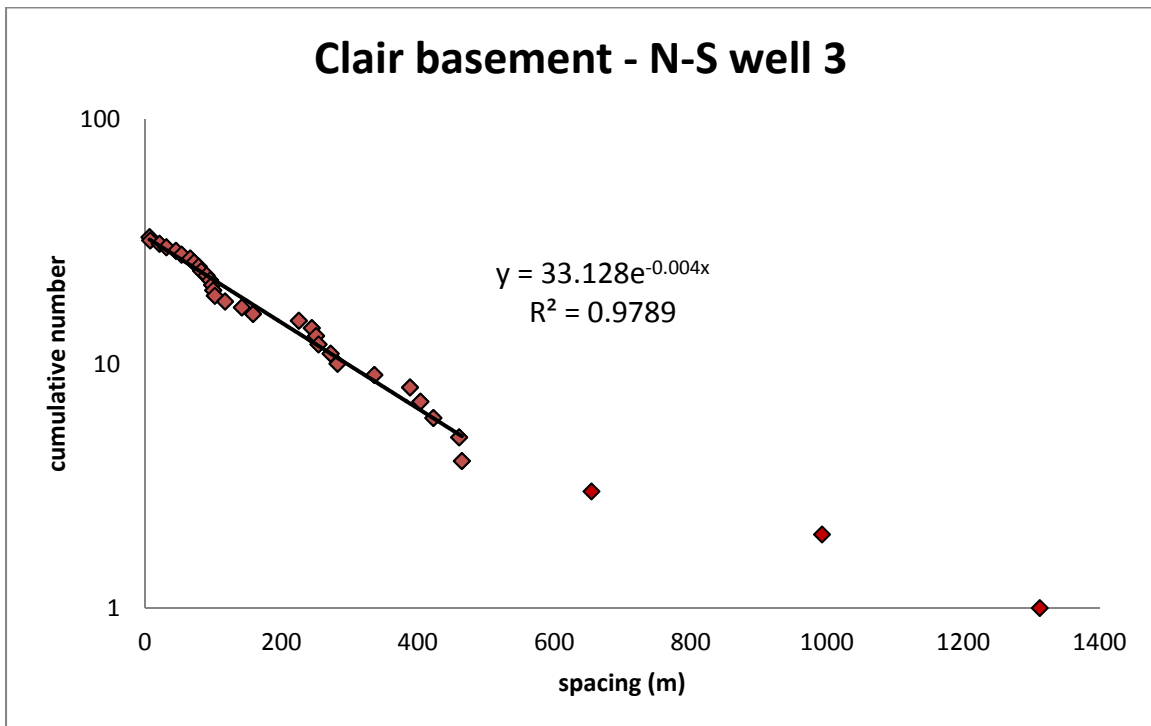
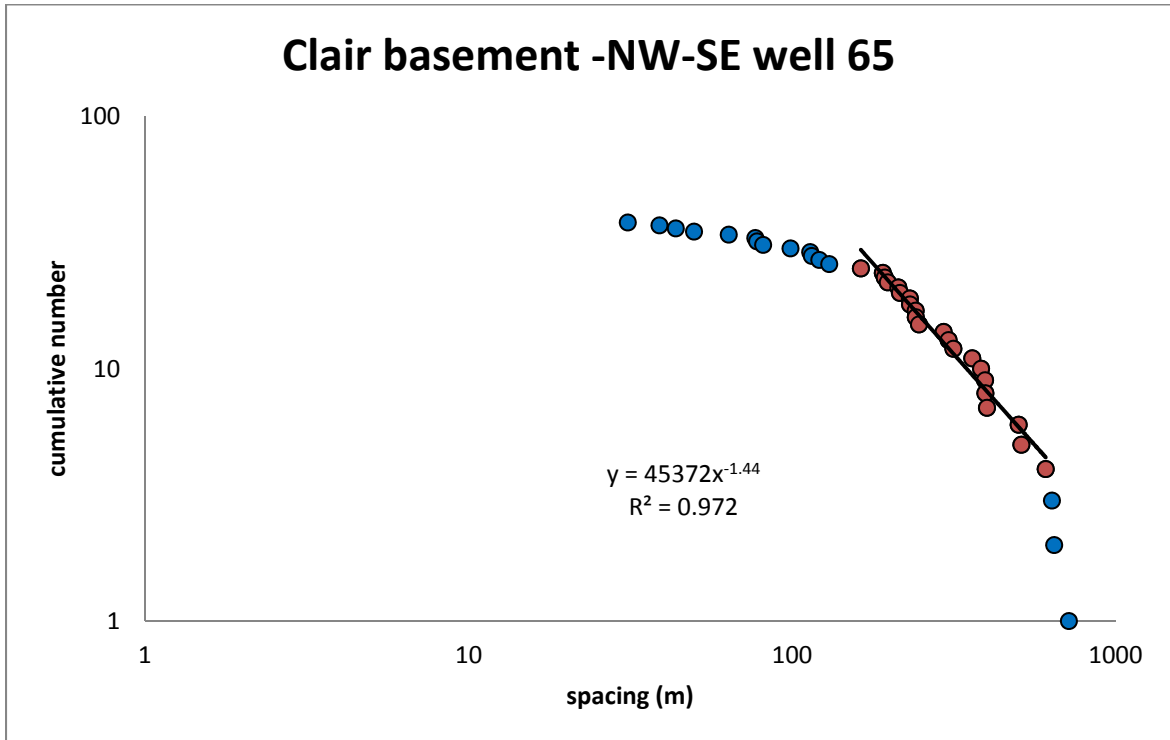


### Clair basement - E-W well 30

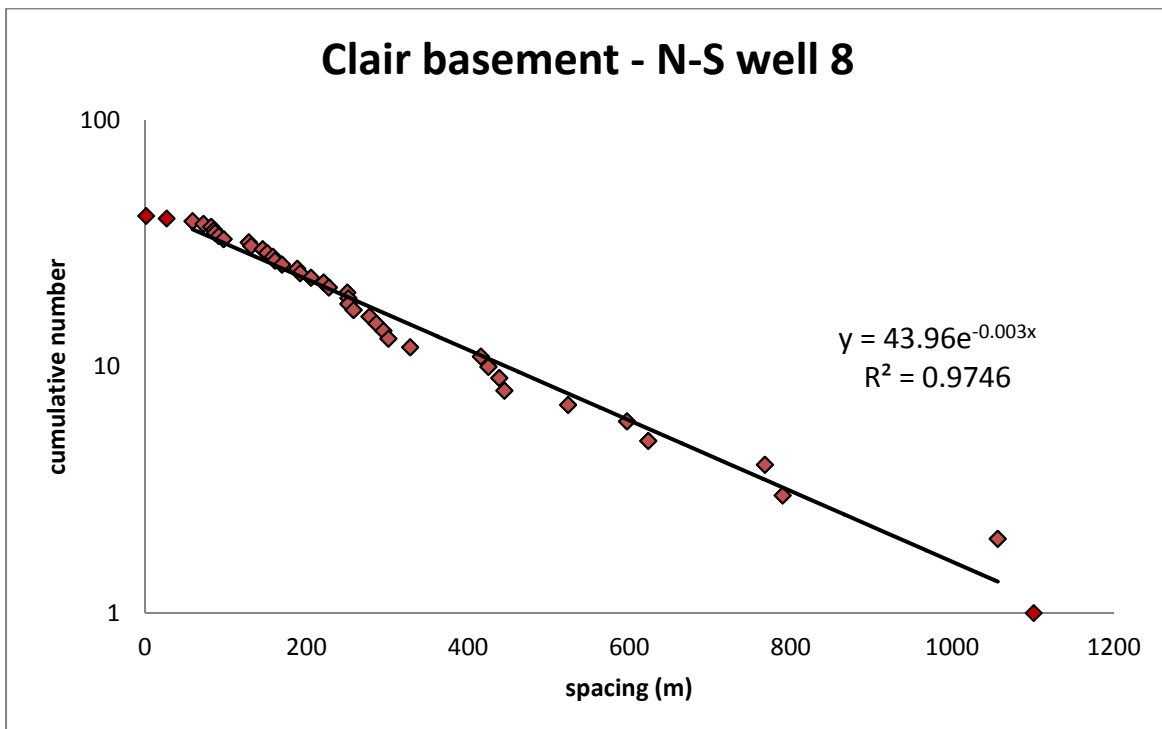
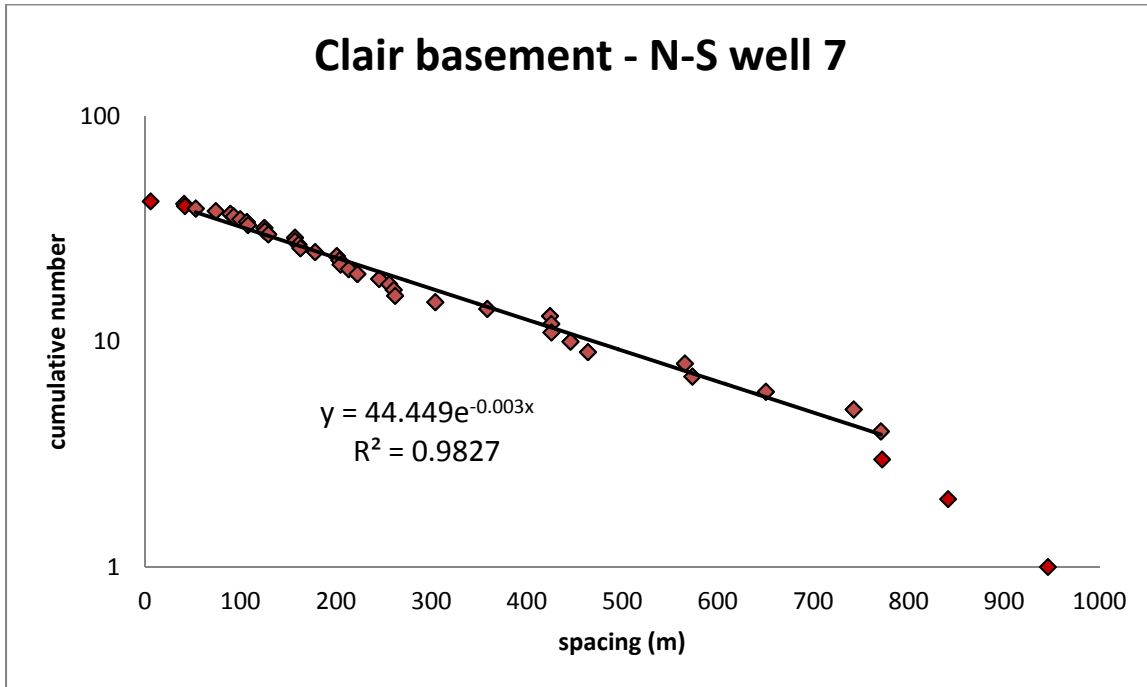


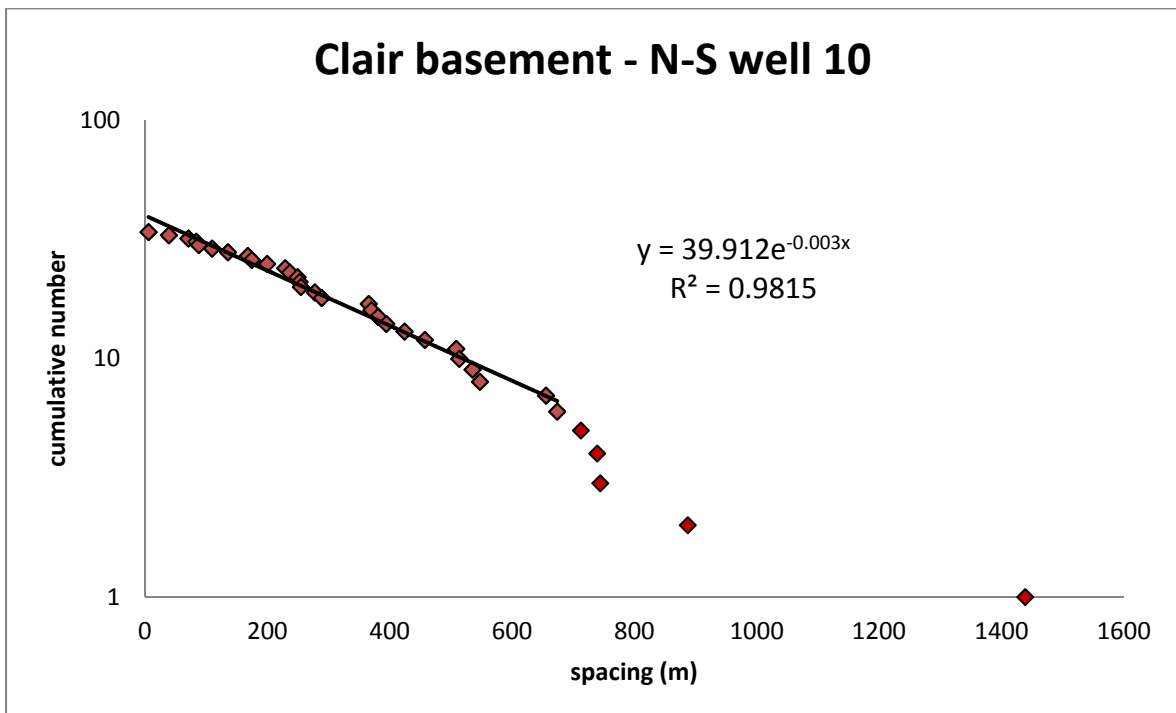
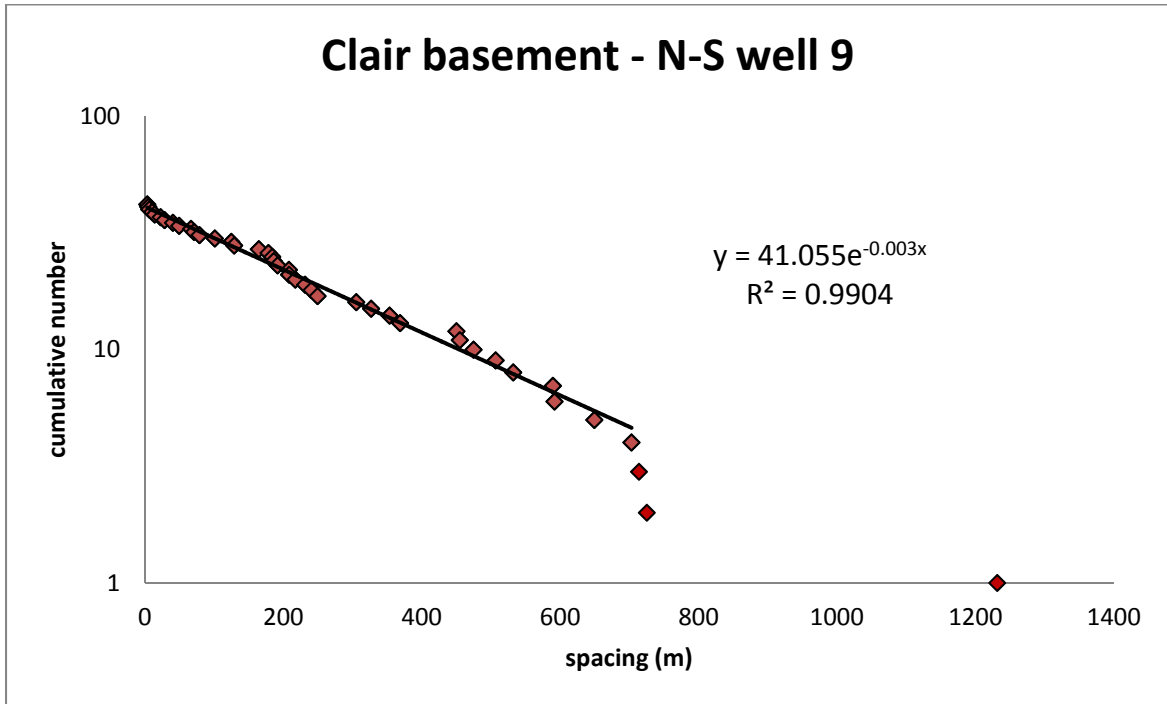


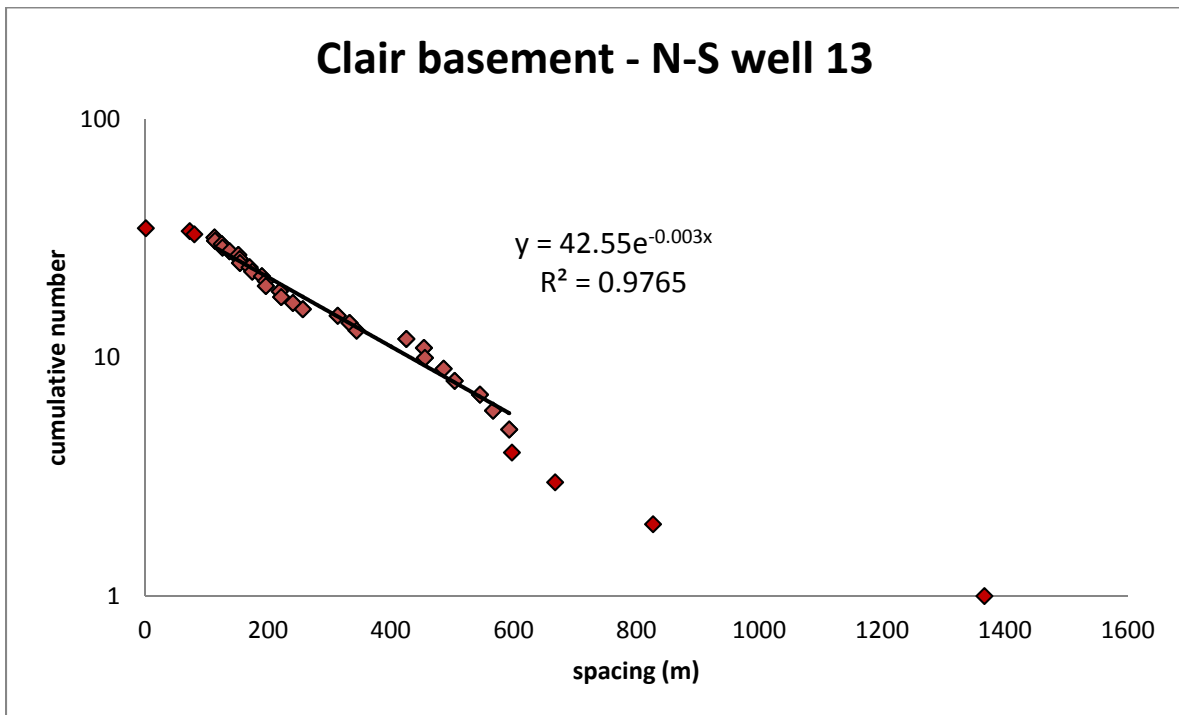
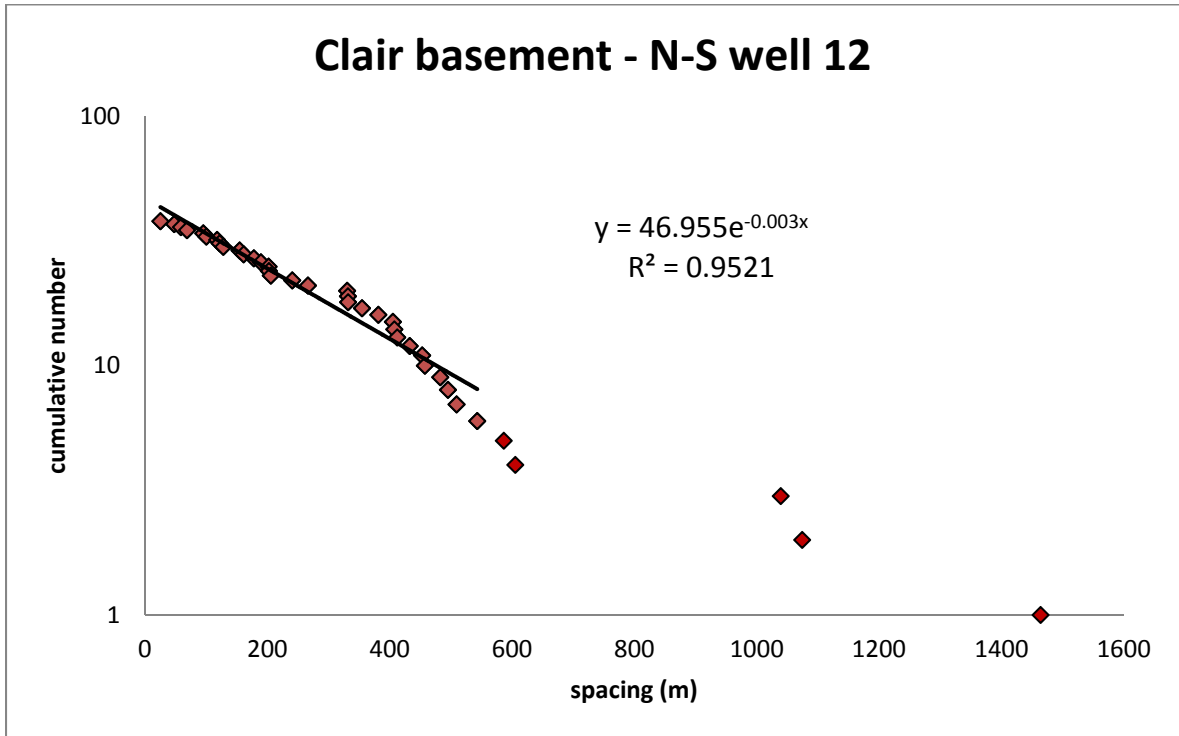


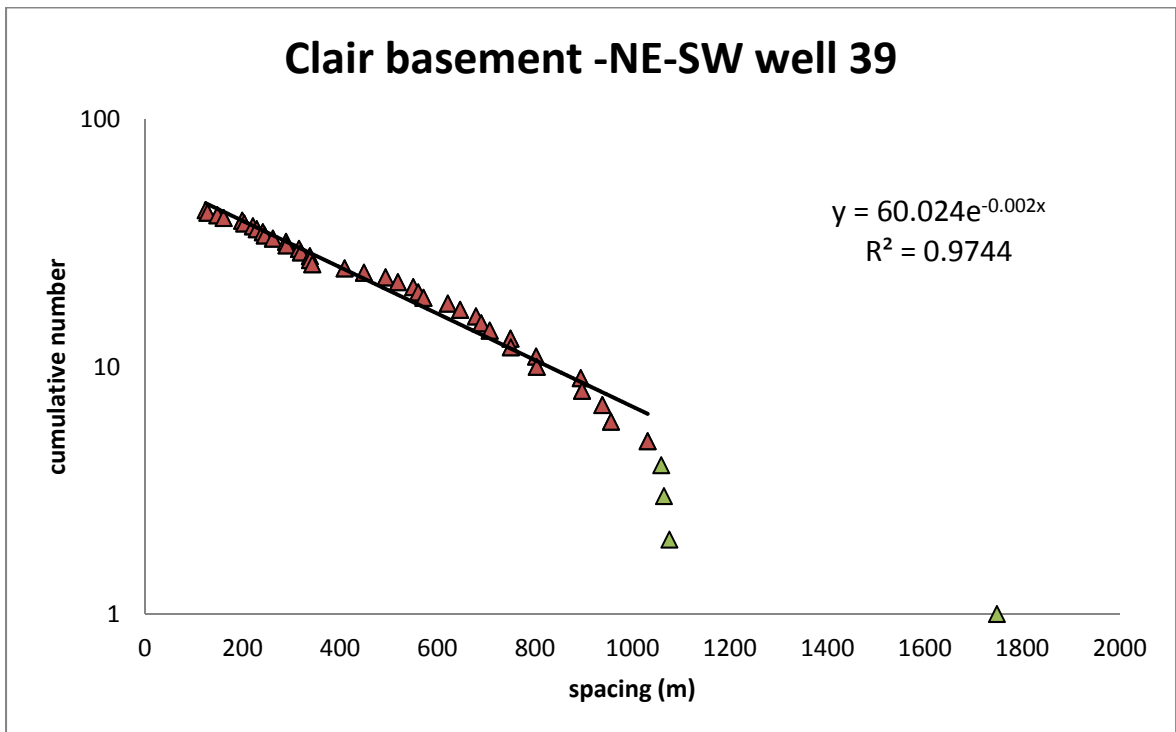
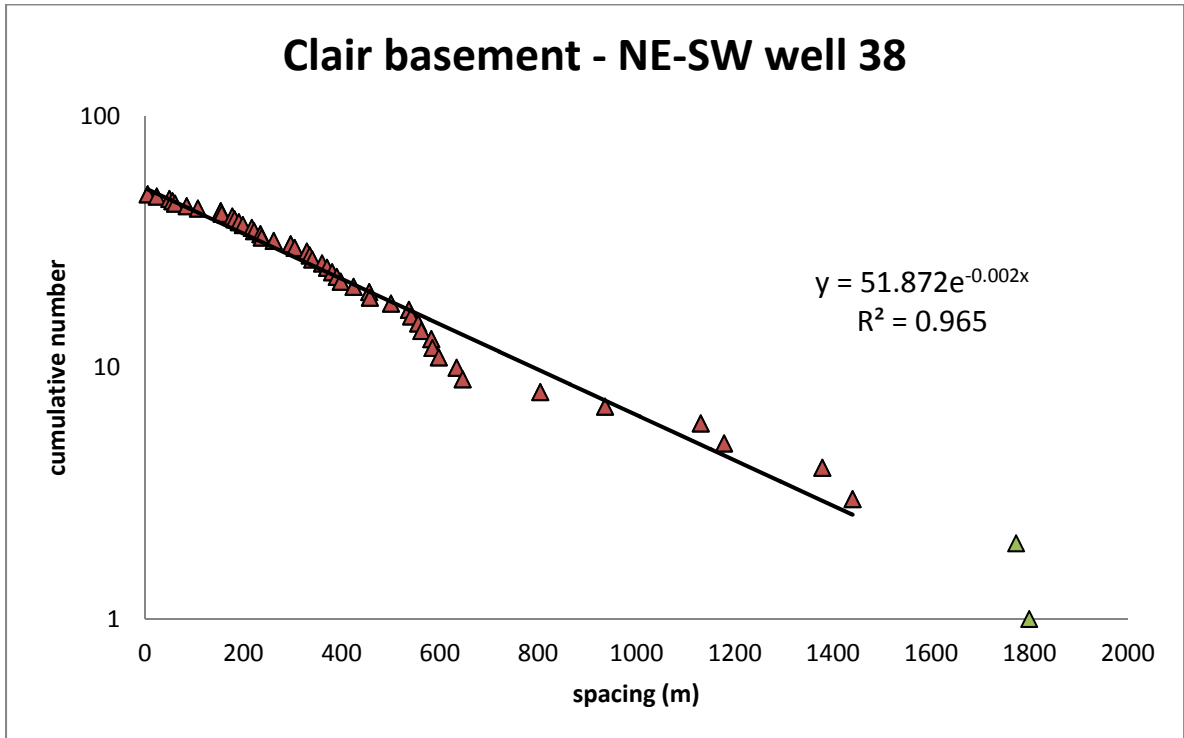


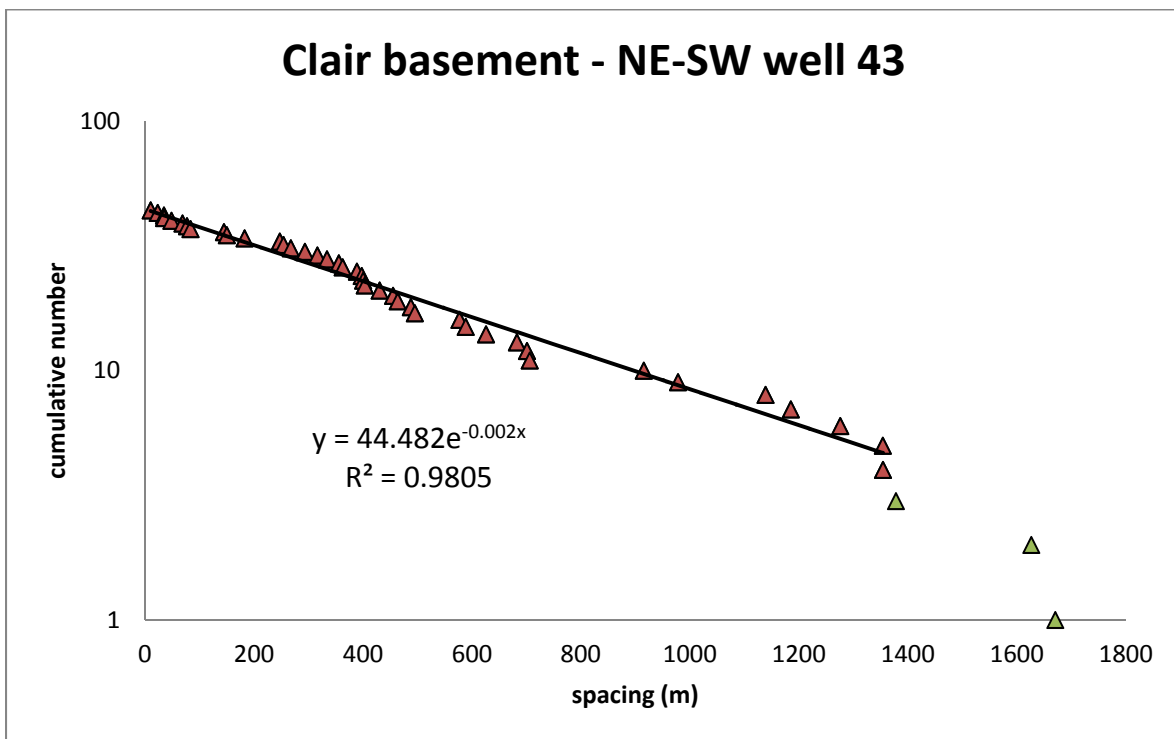
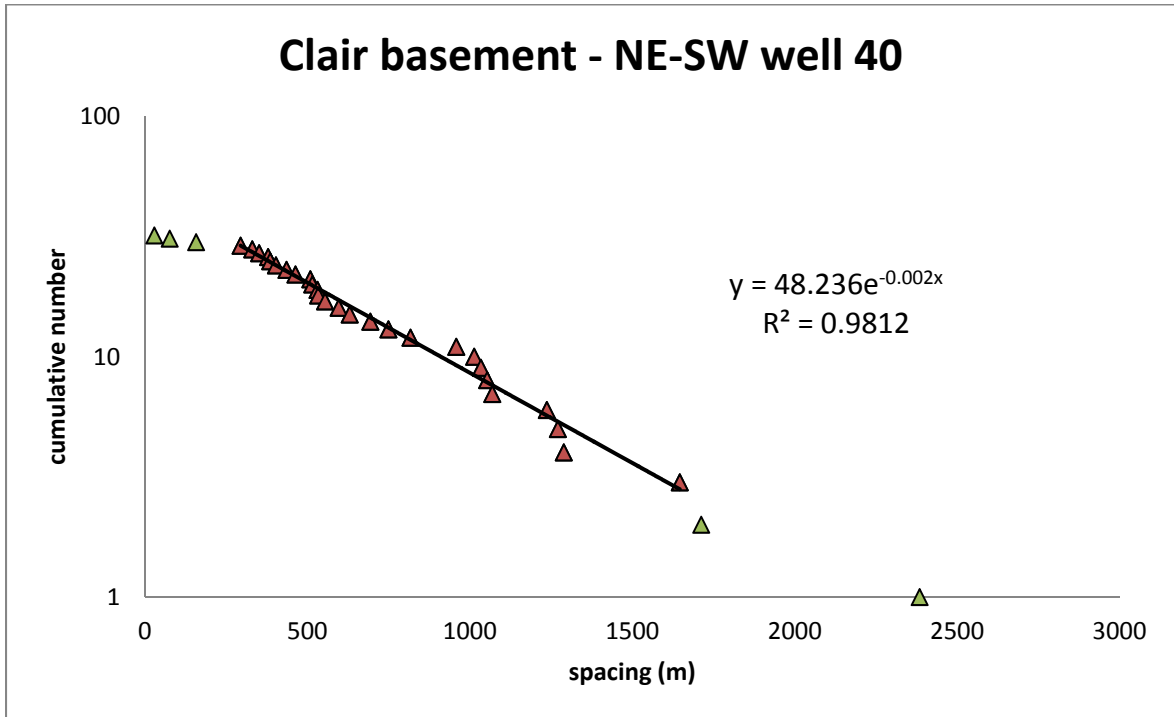


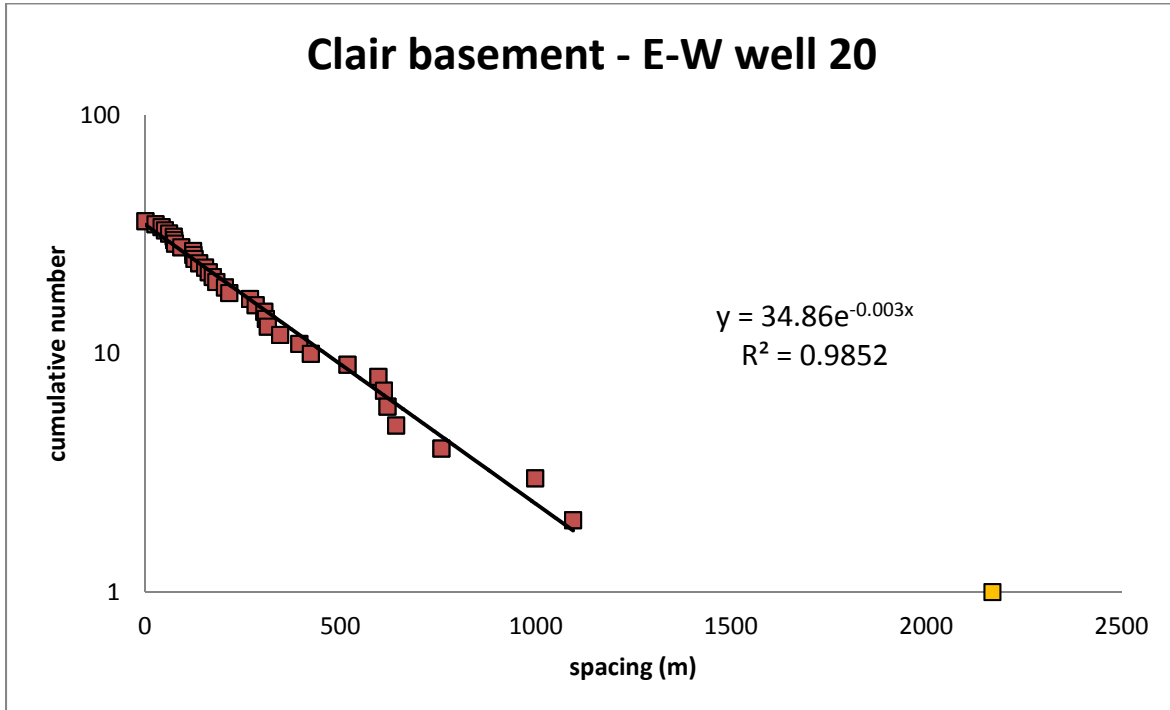
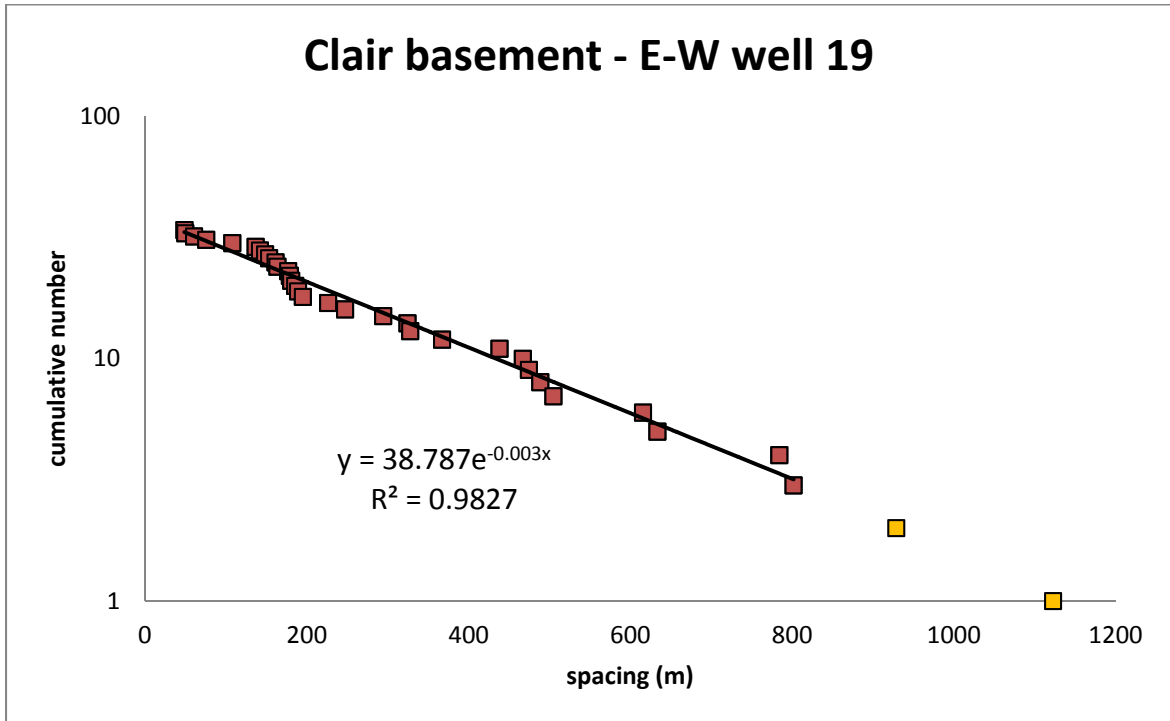




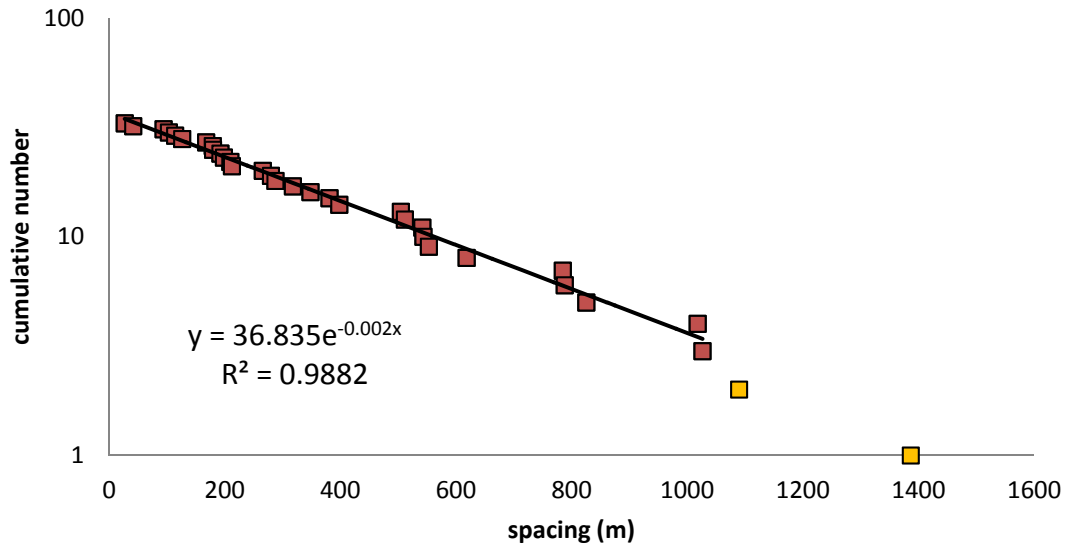




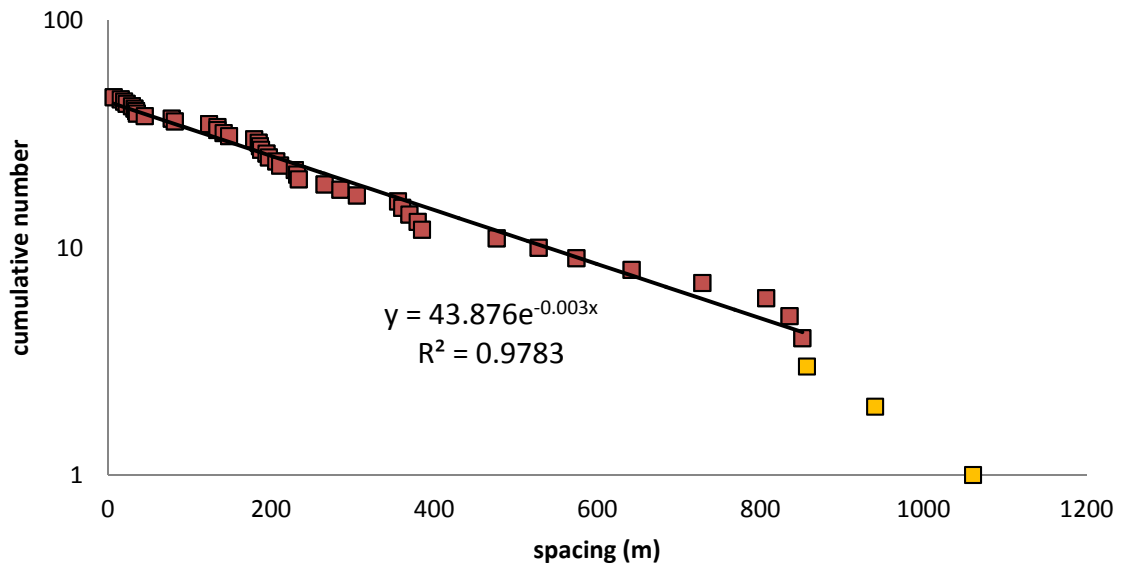


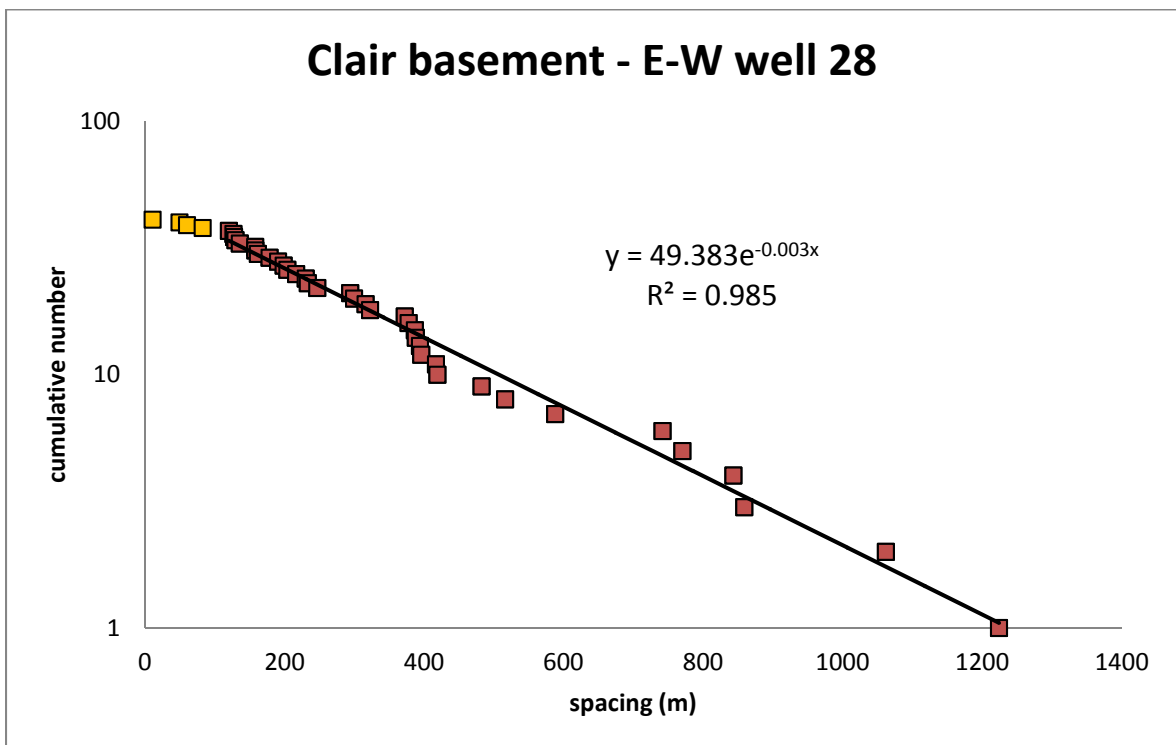
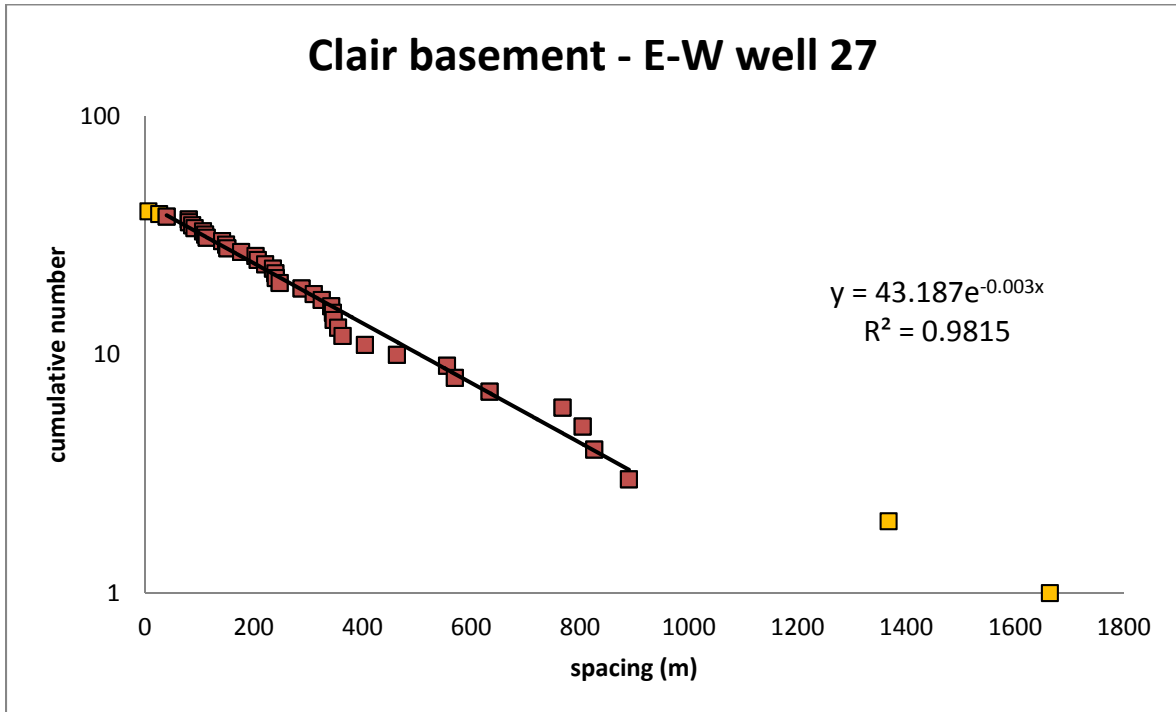


### Clair basement - E-W well 23

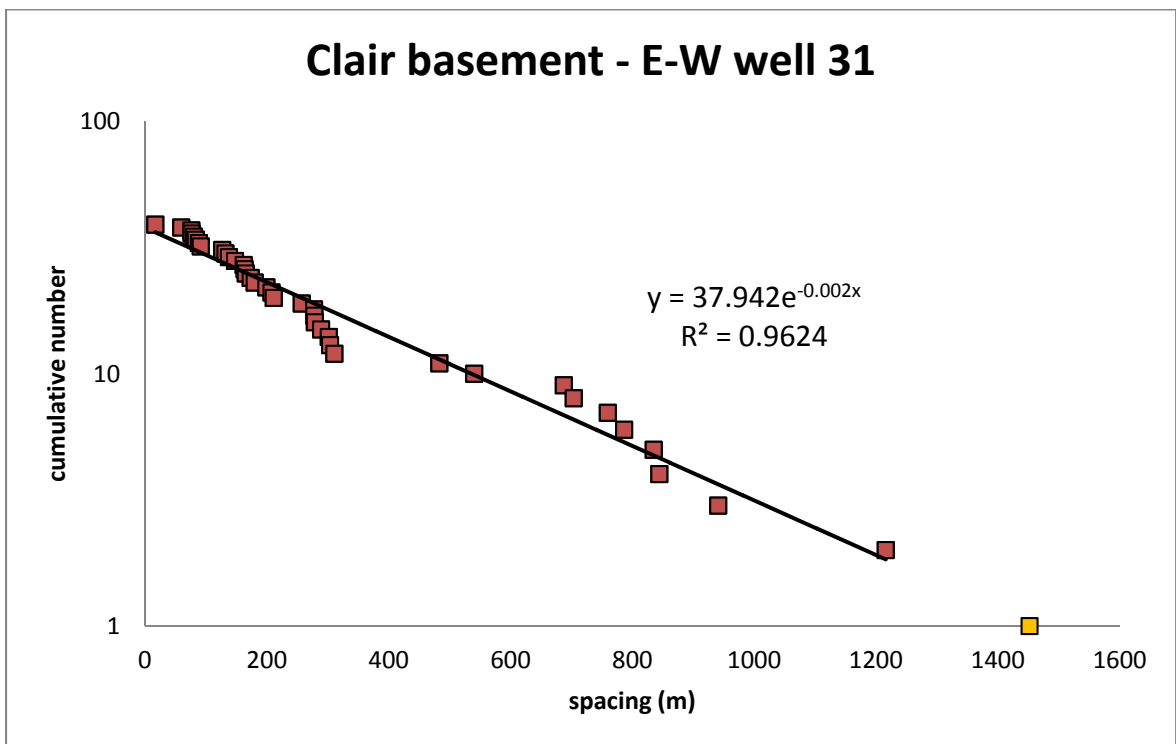
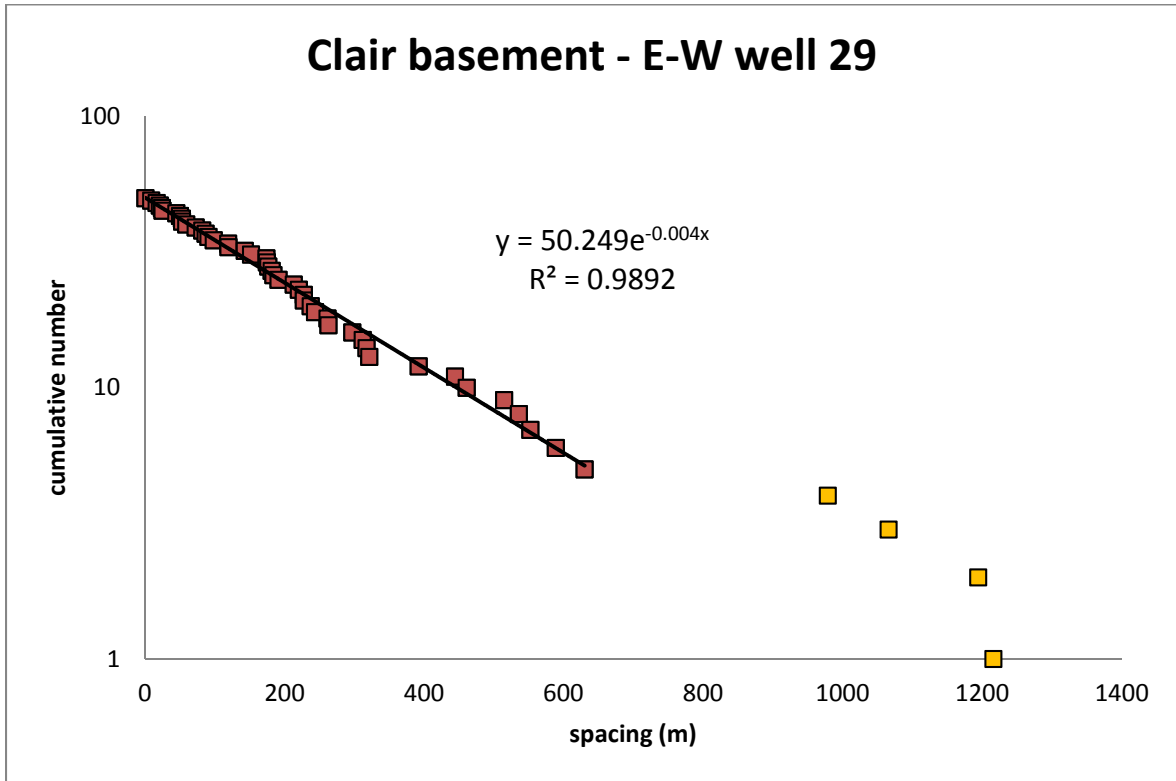


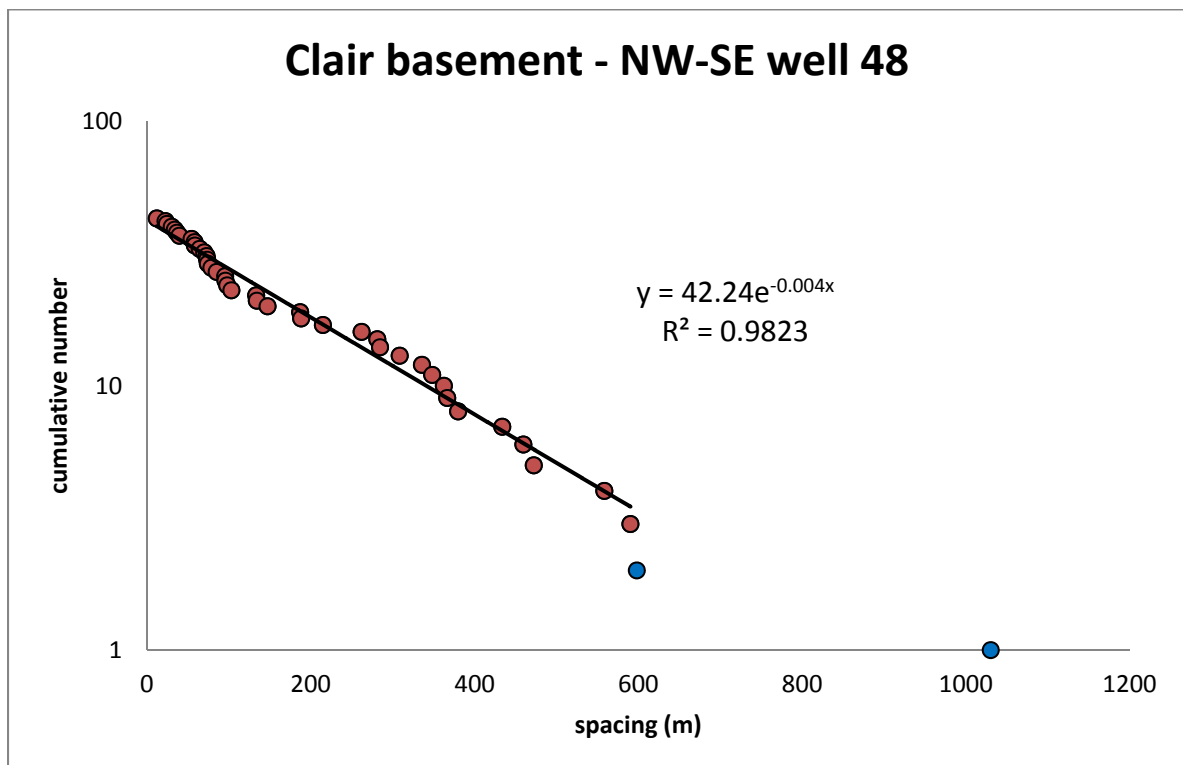
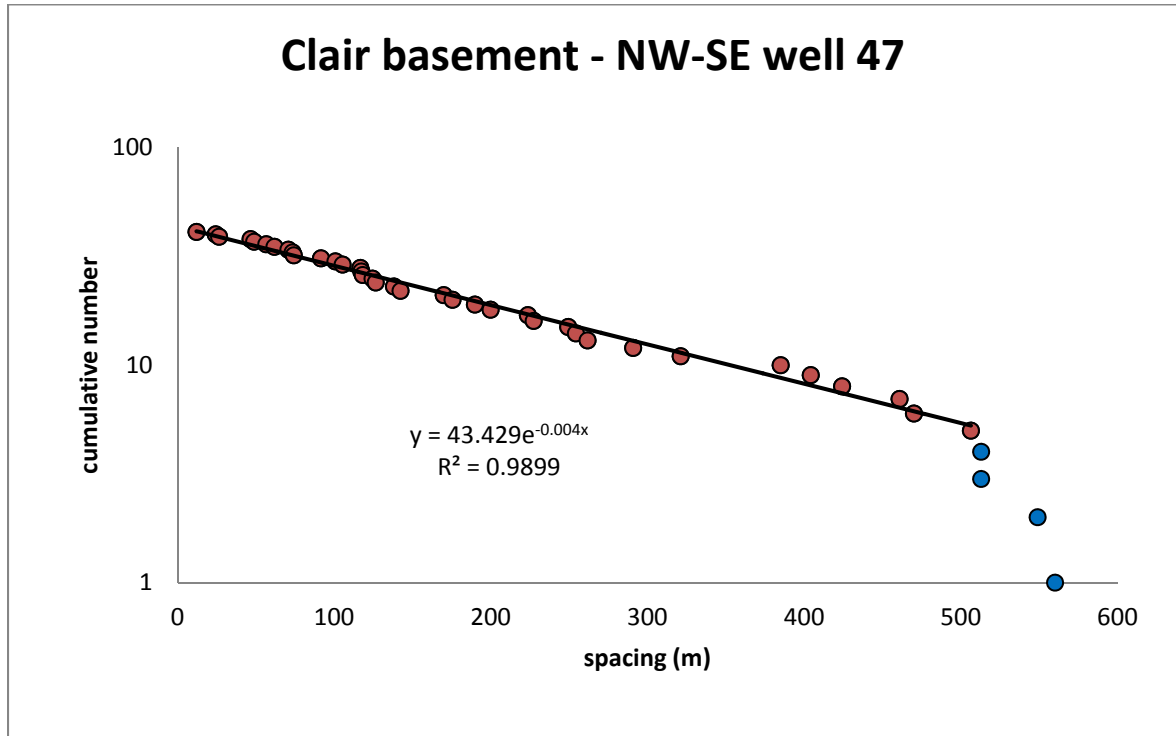
### Clair basement - E-W well 26

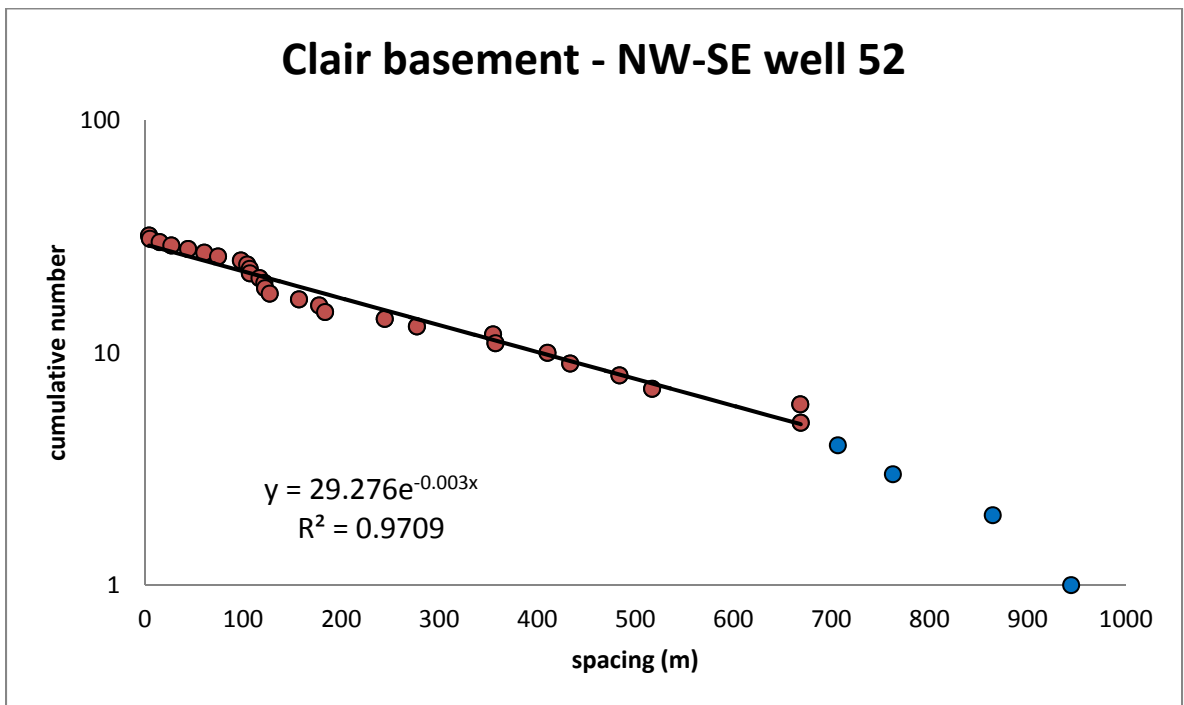
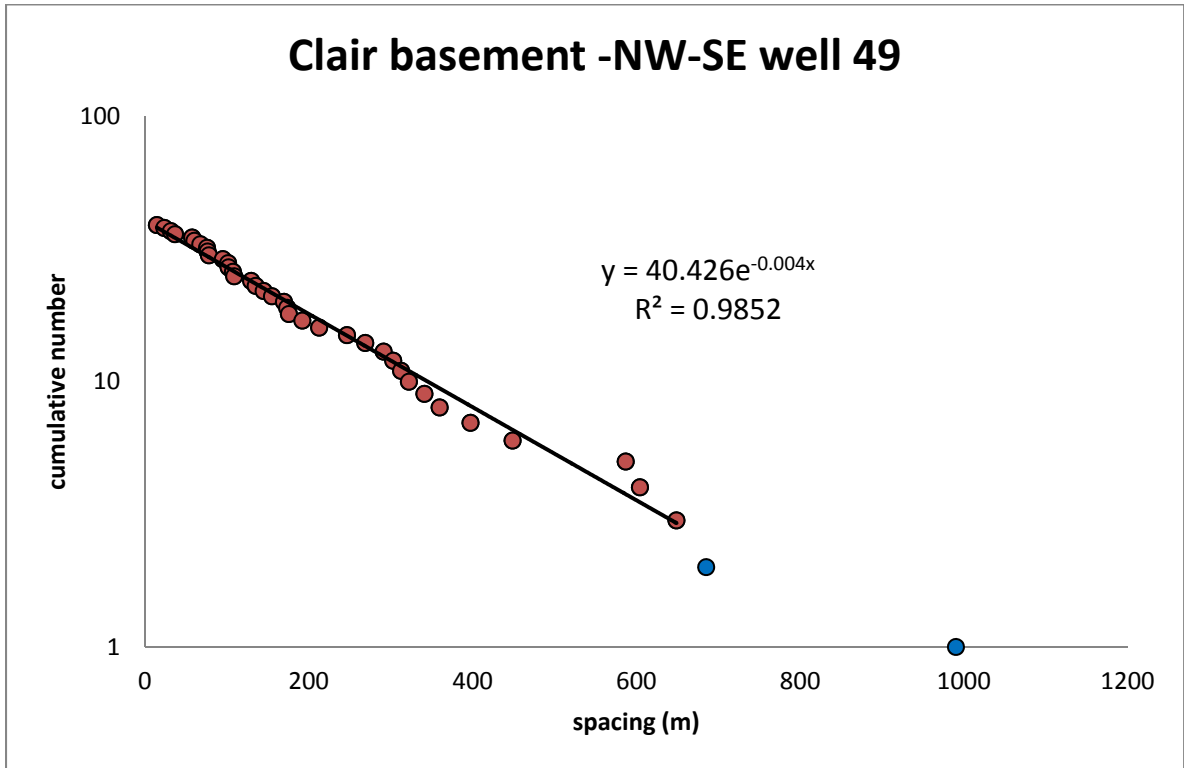


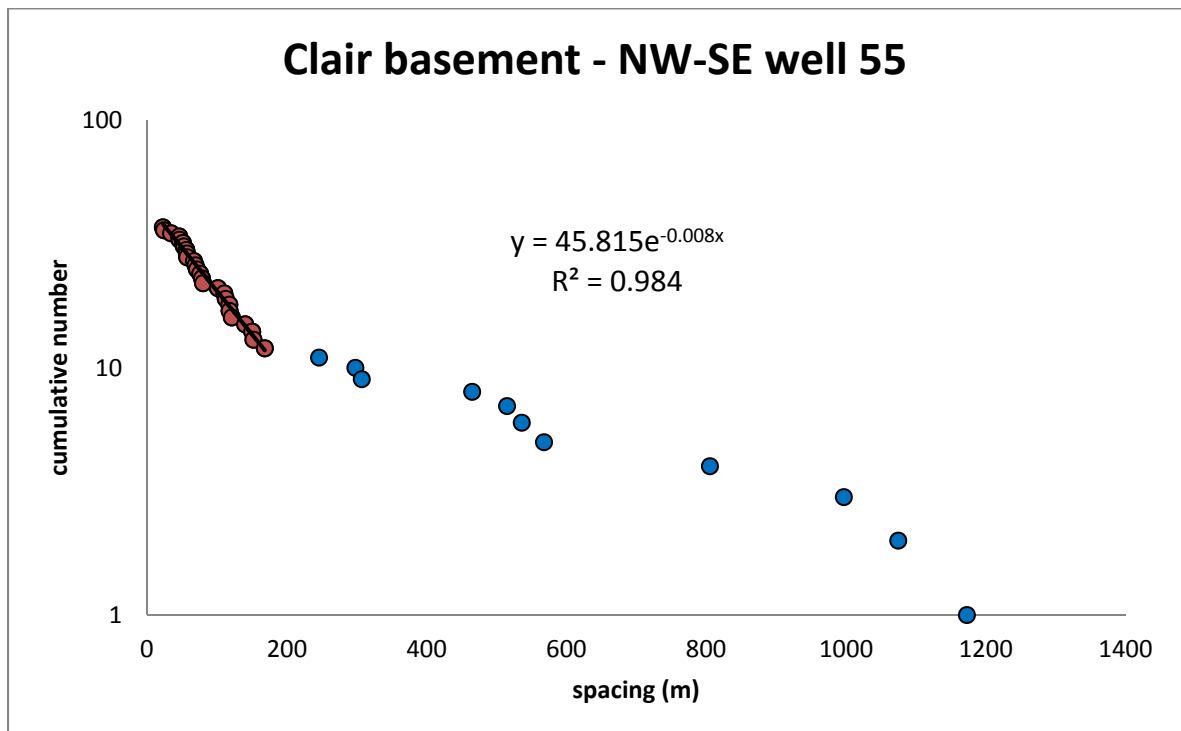
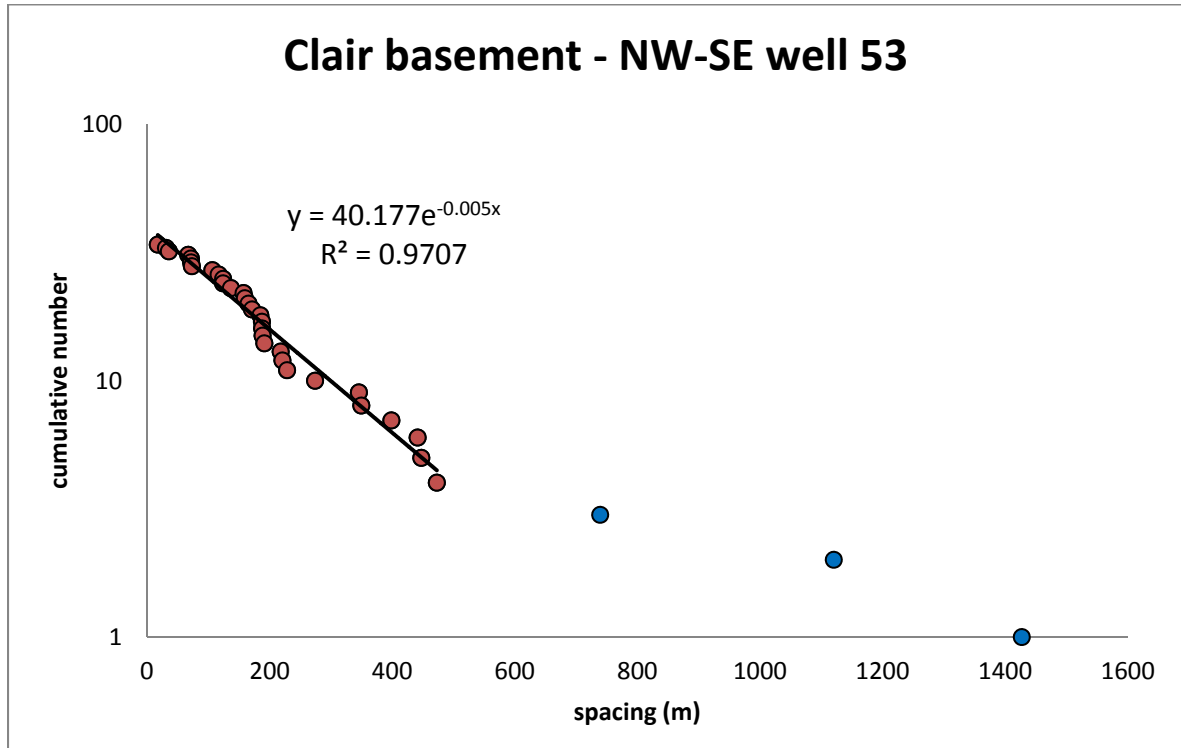


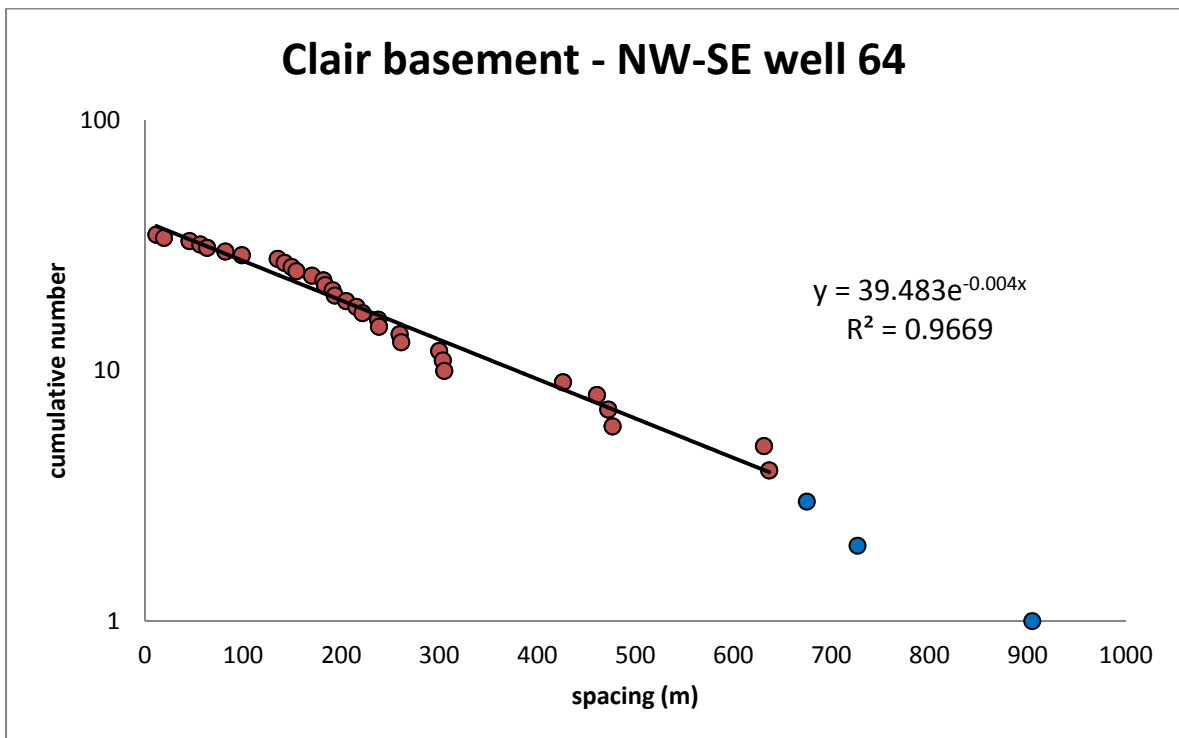
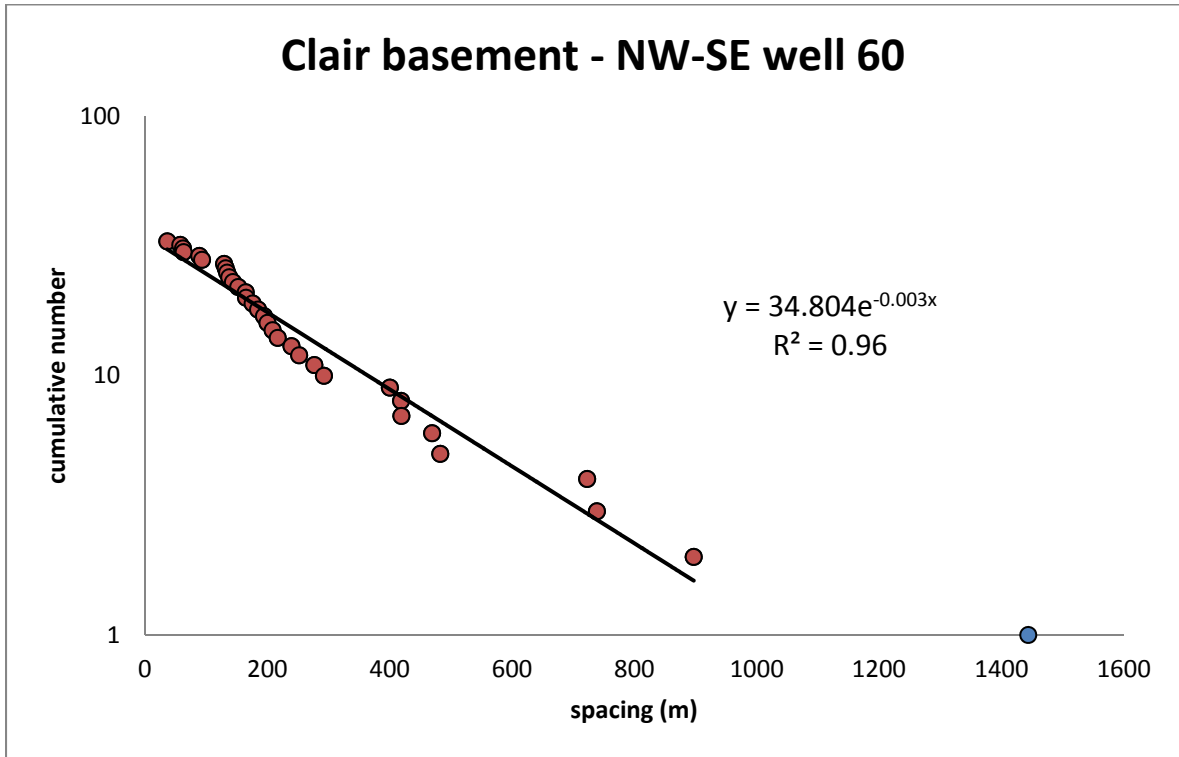


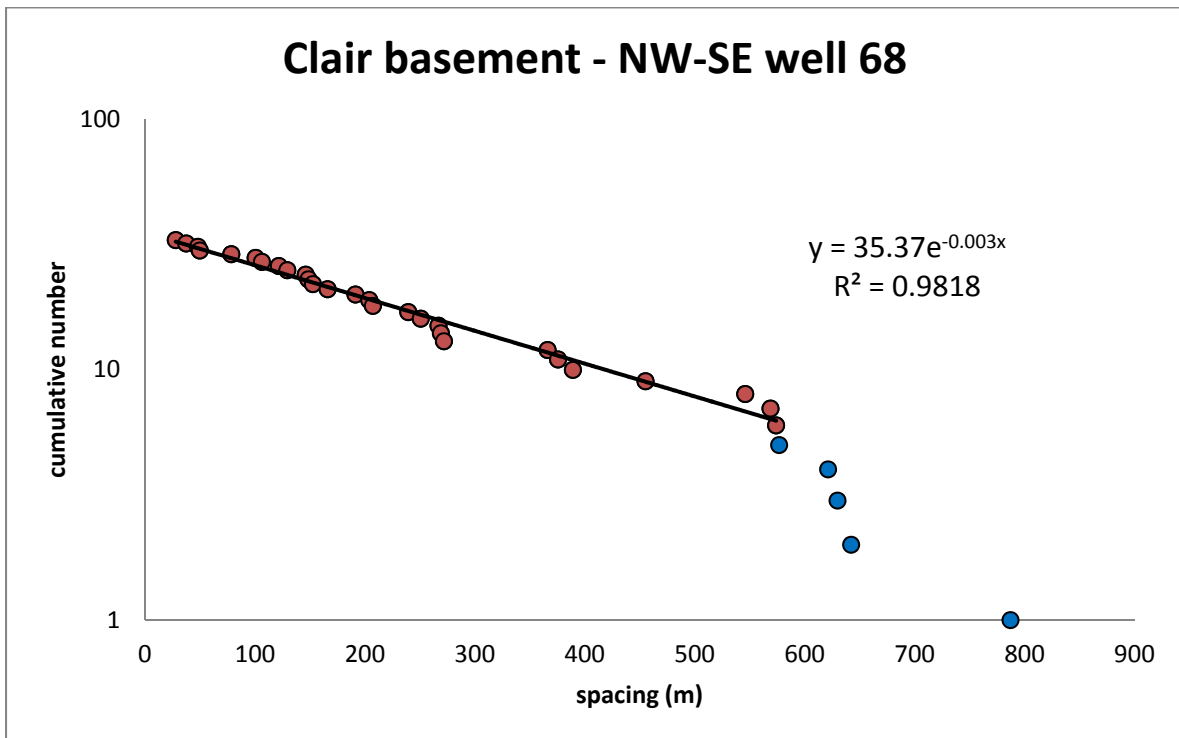
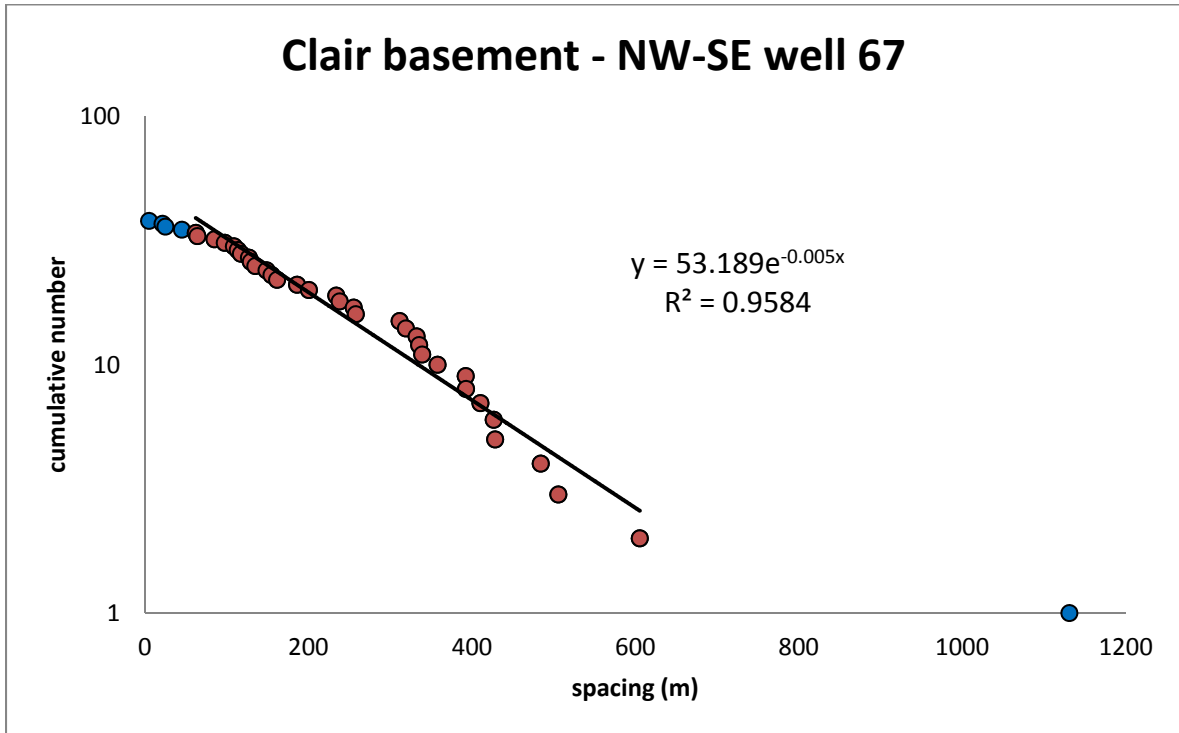


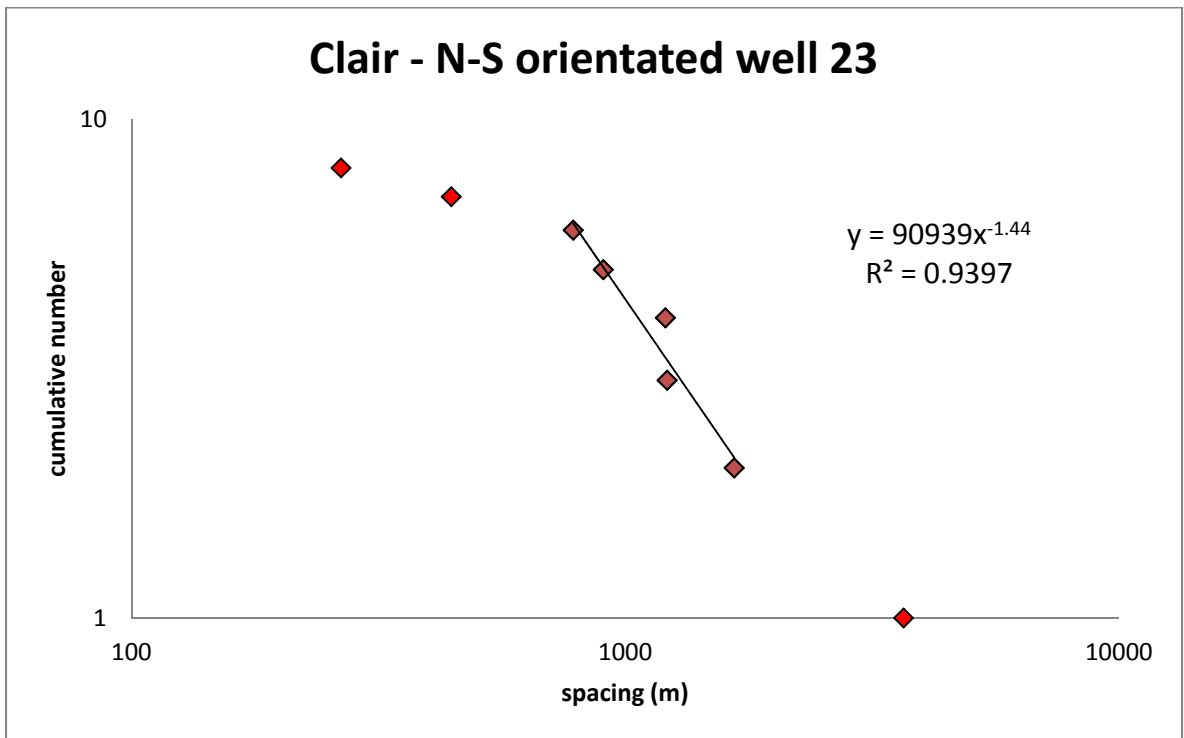
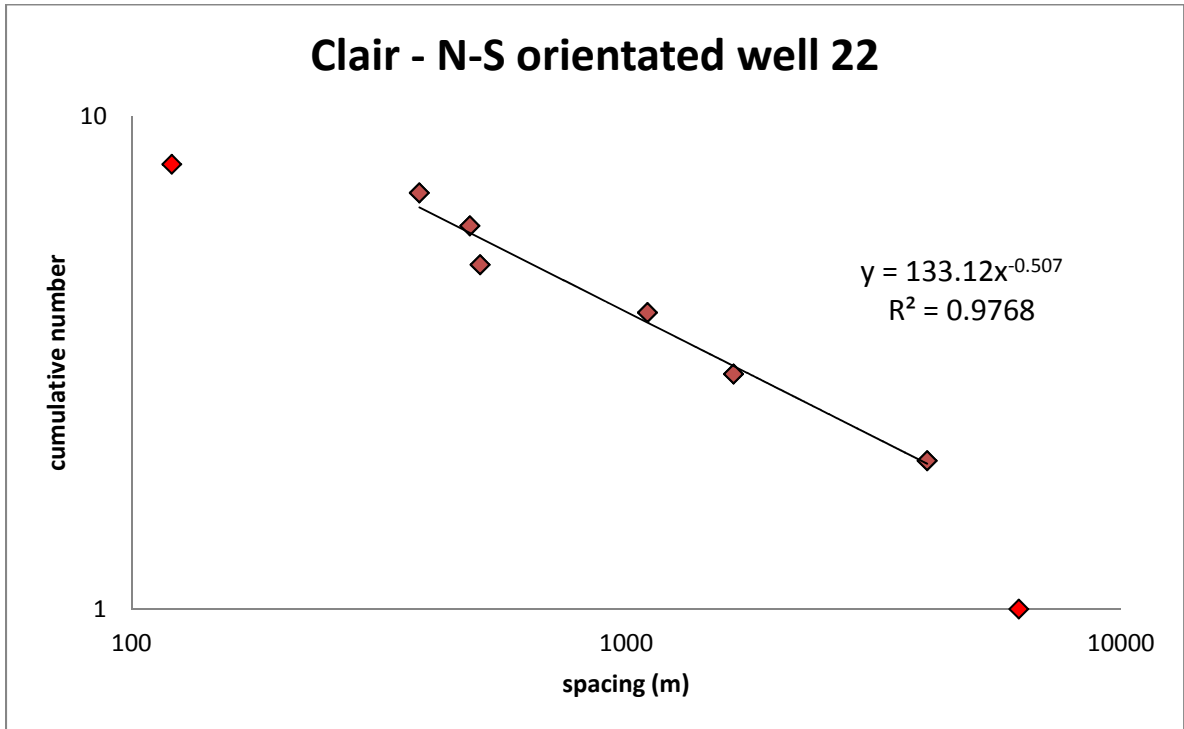


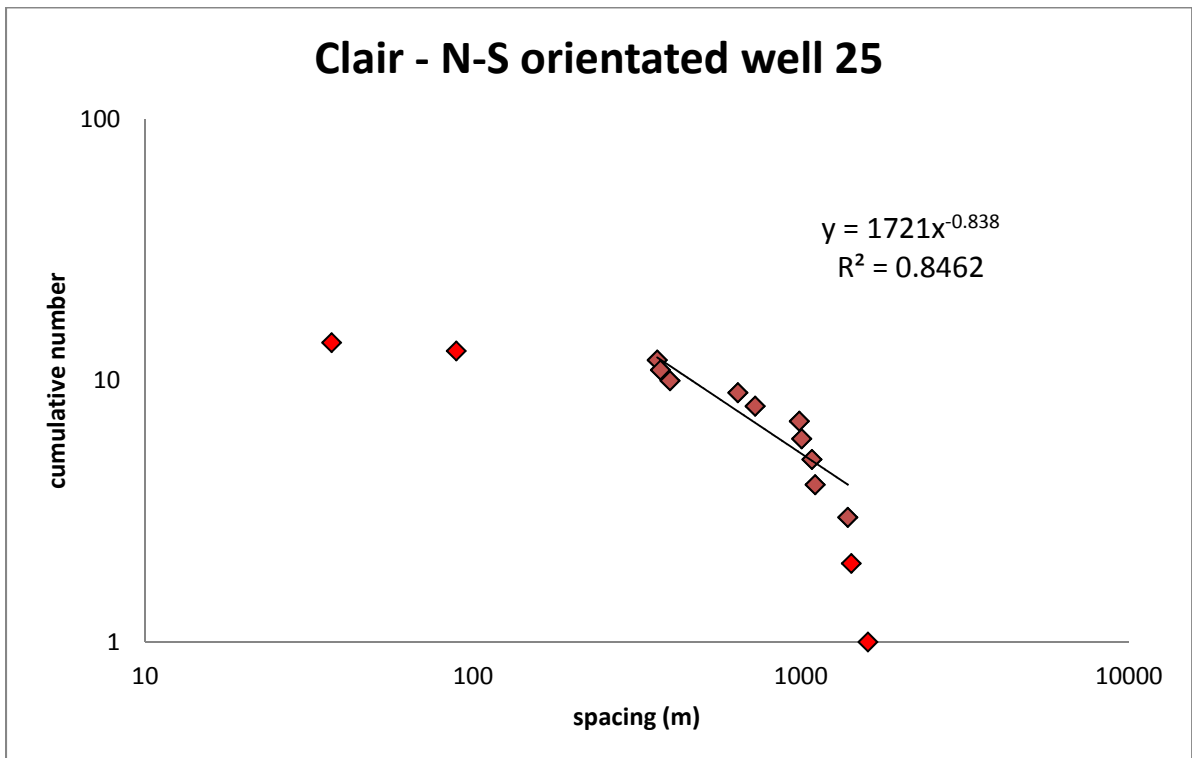
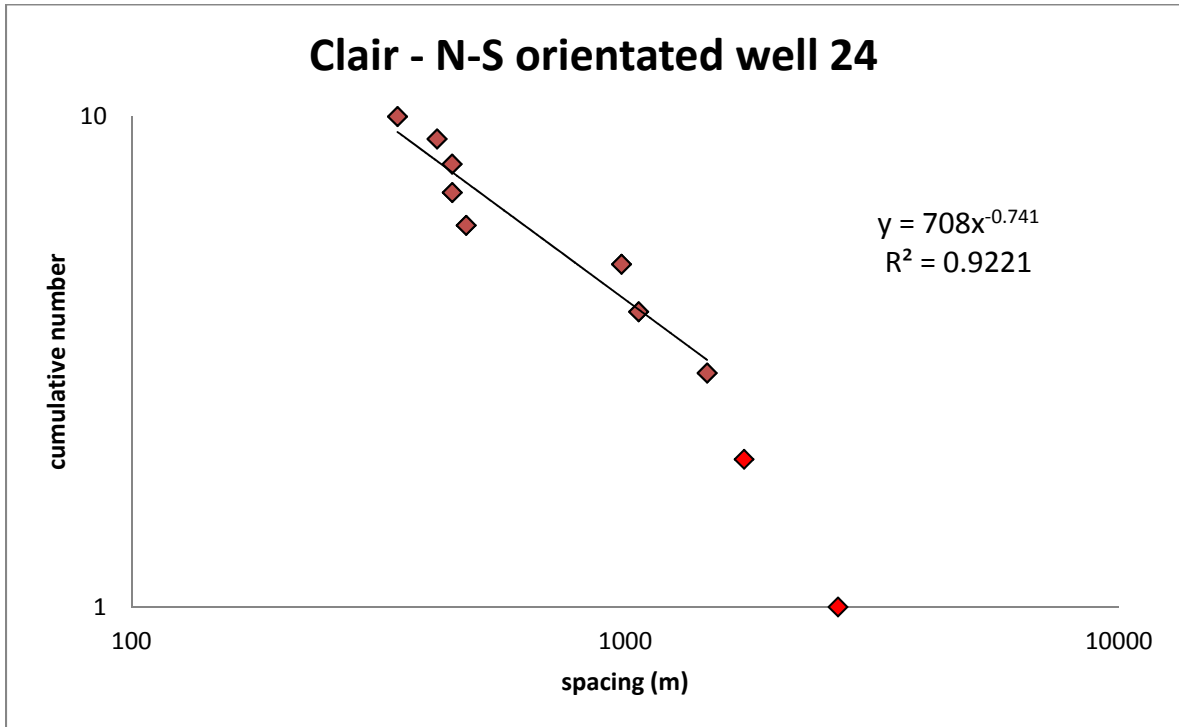




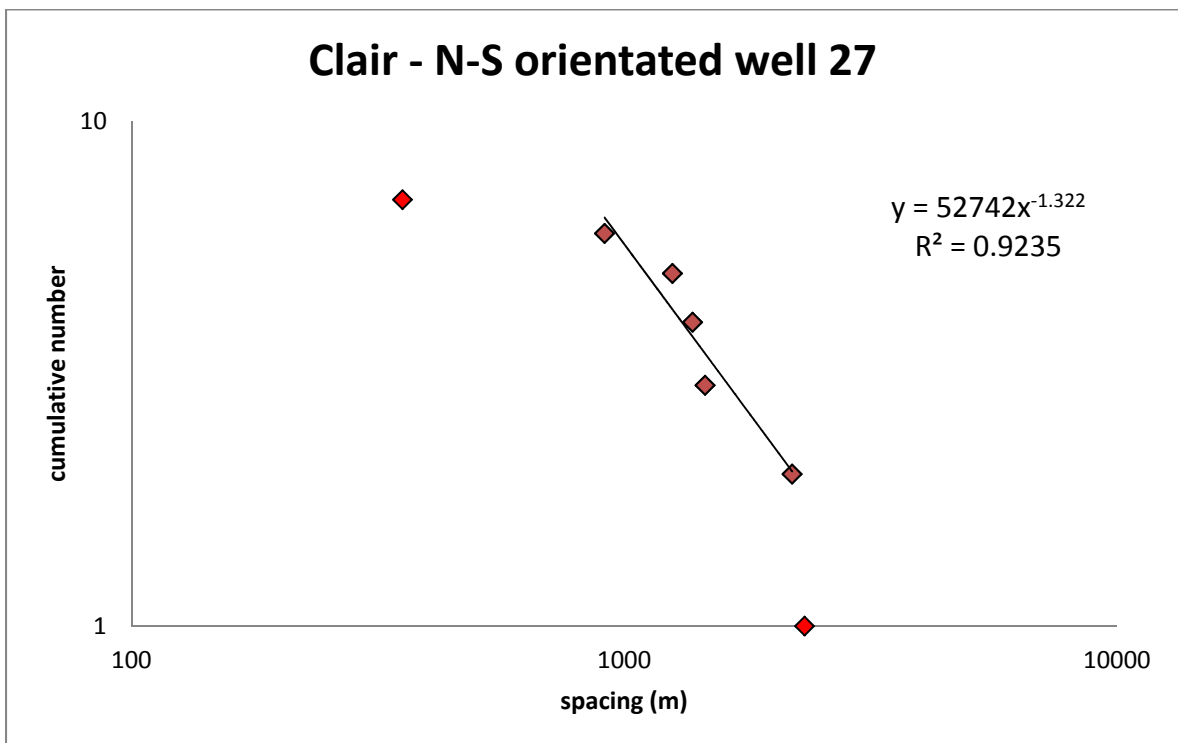
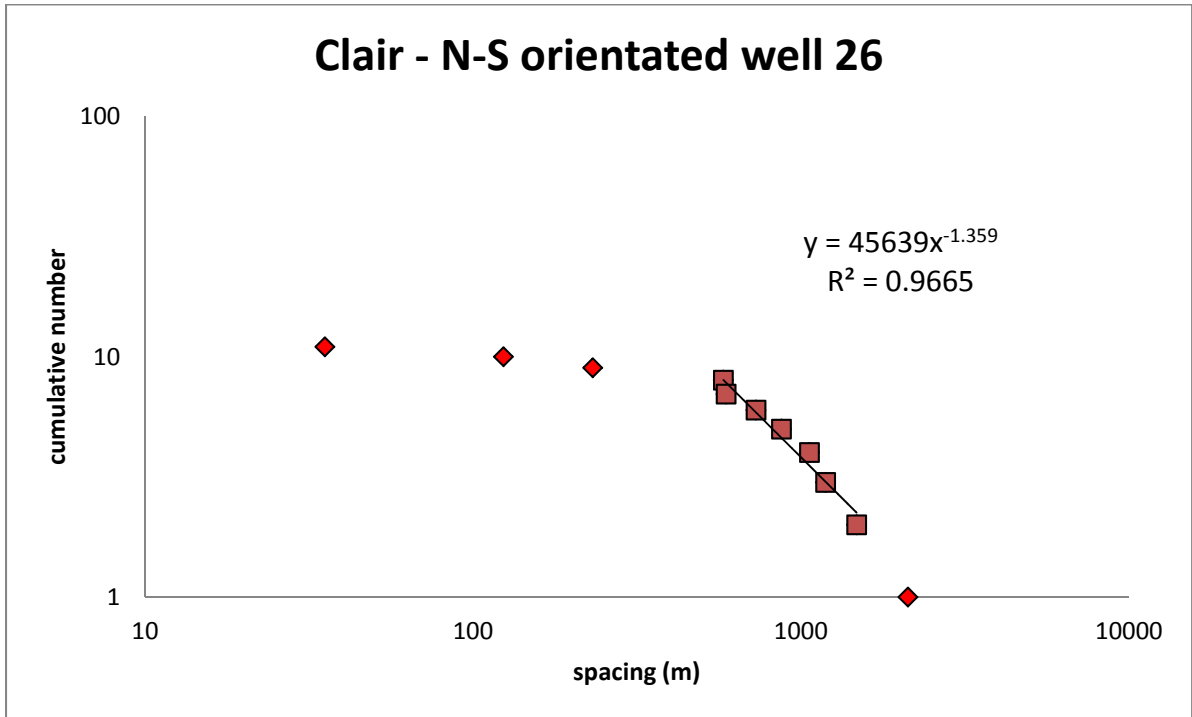


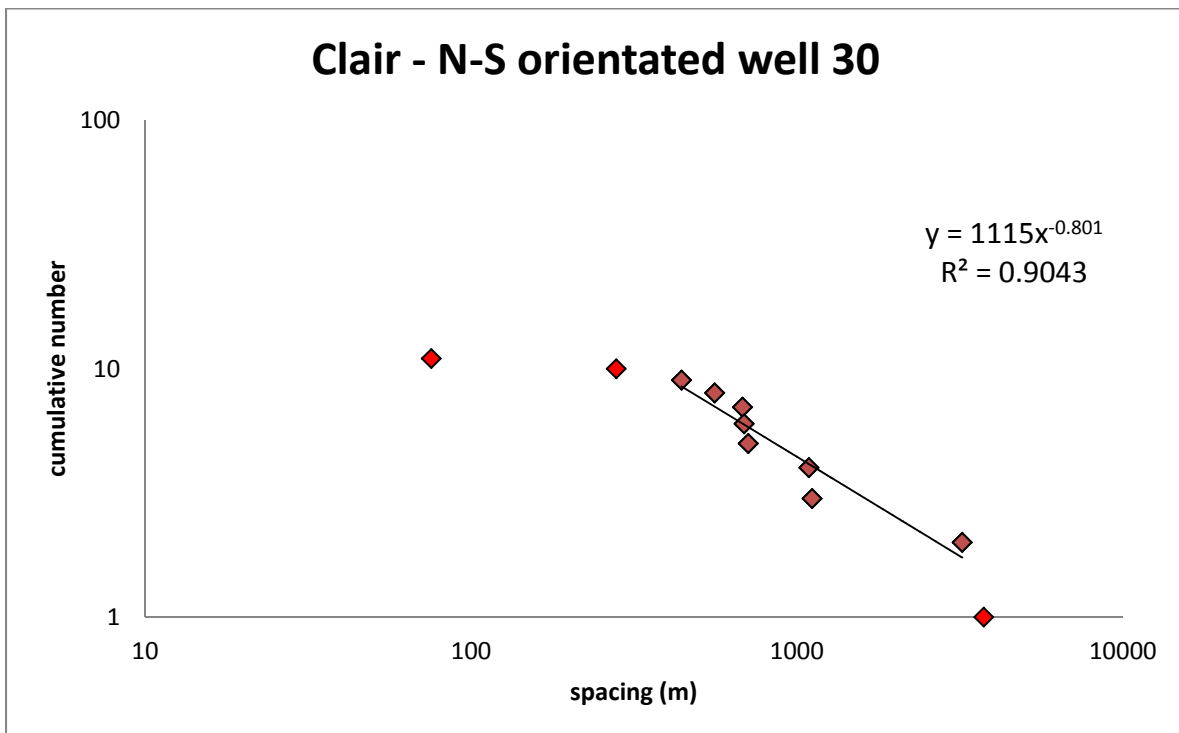
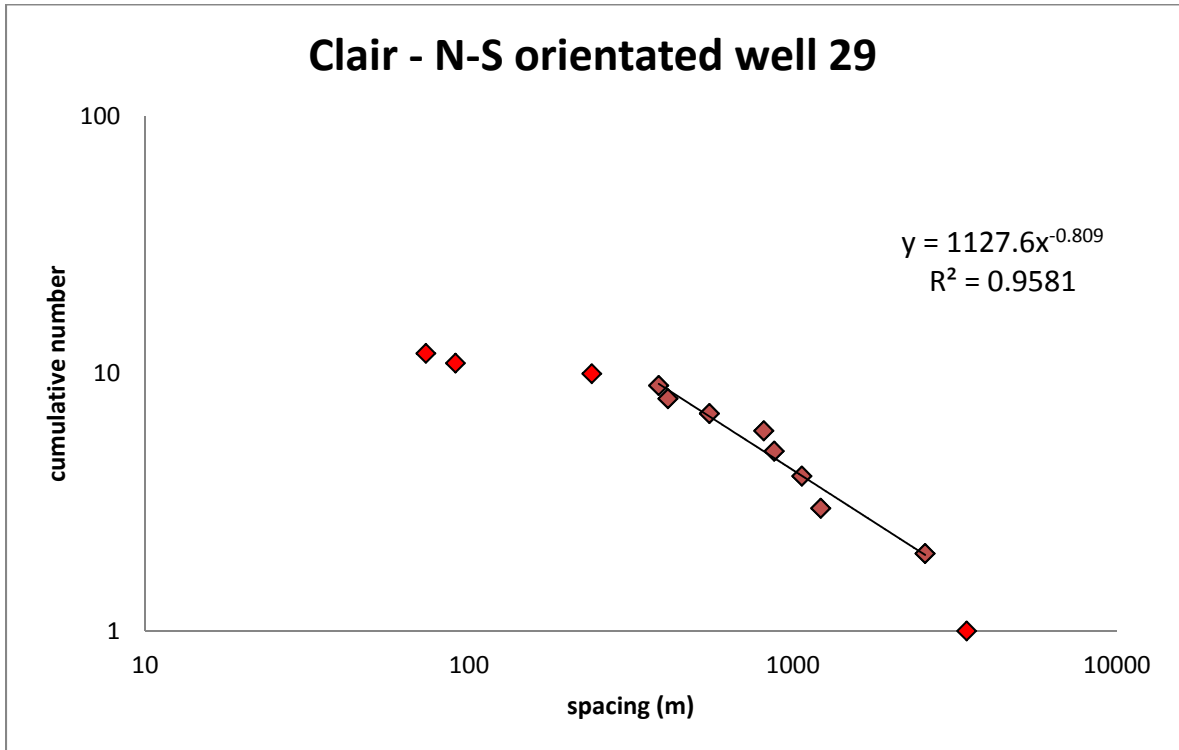


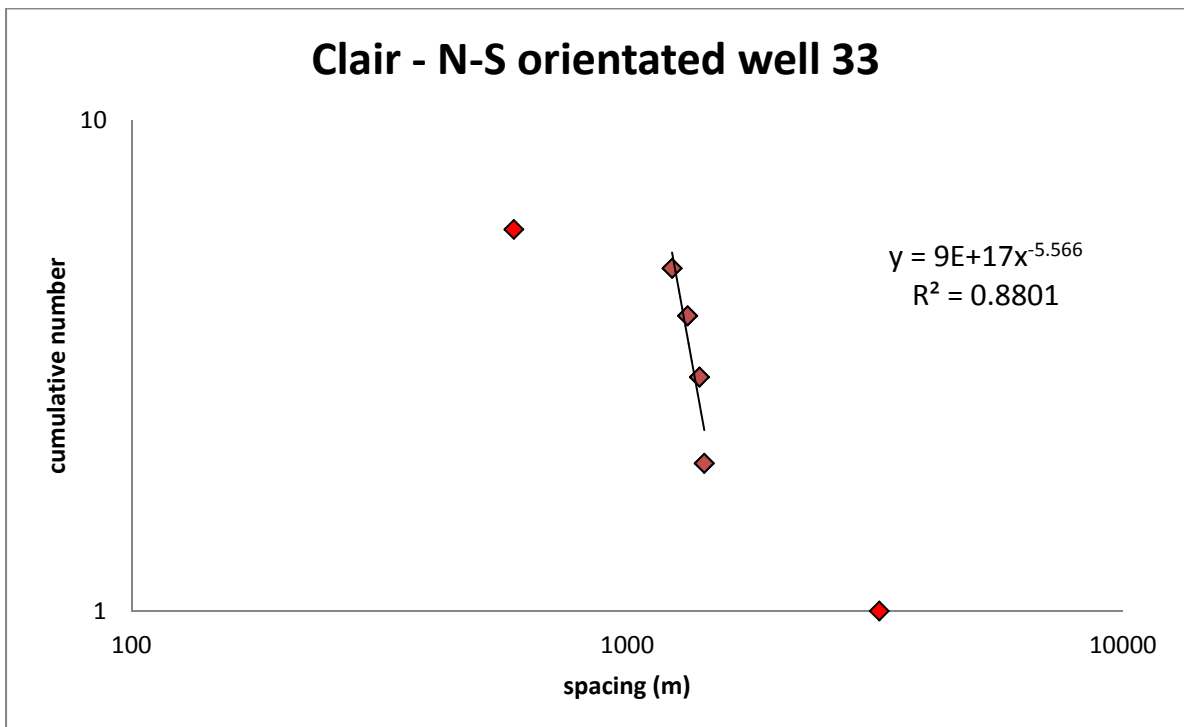
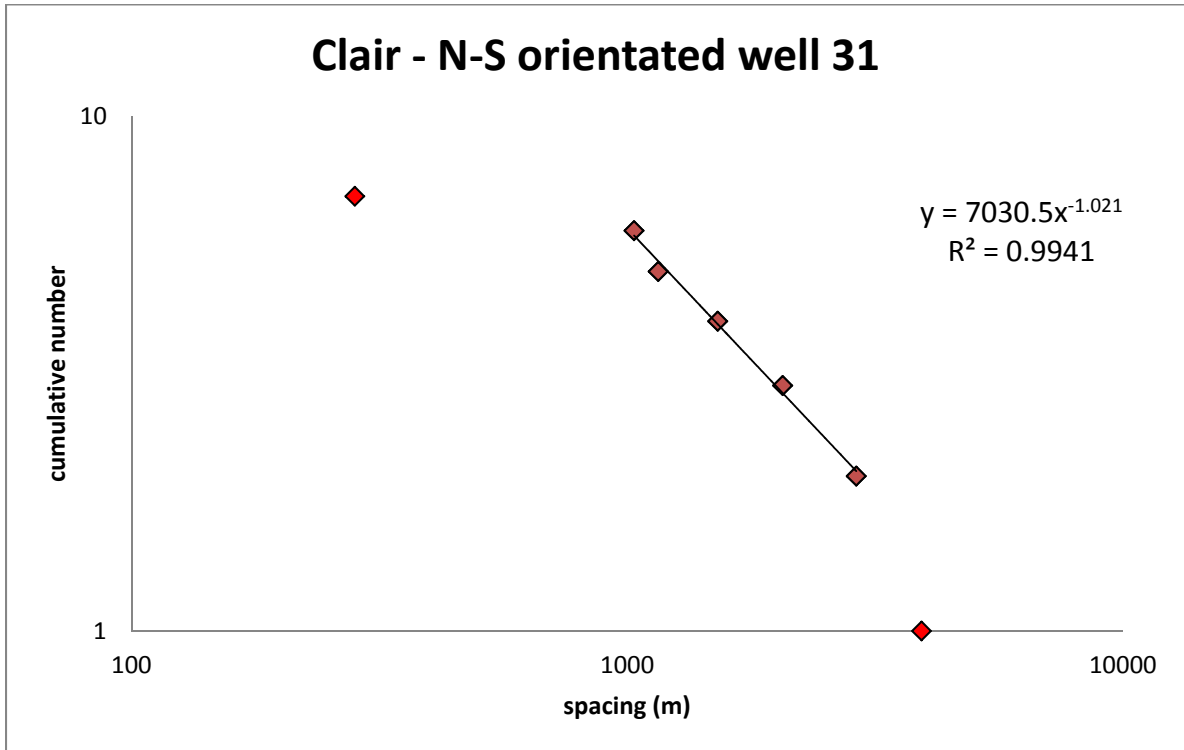


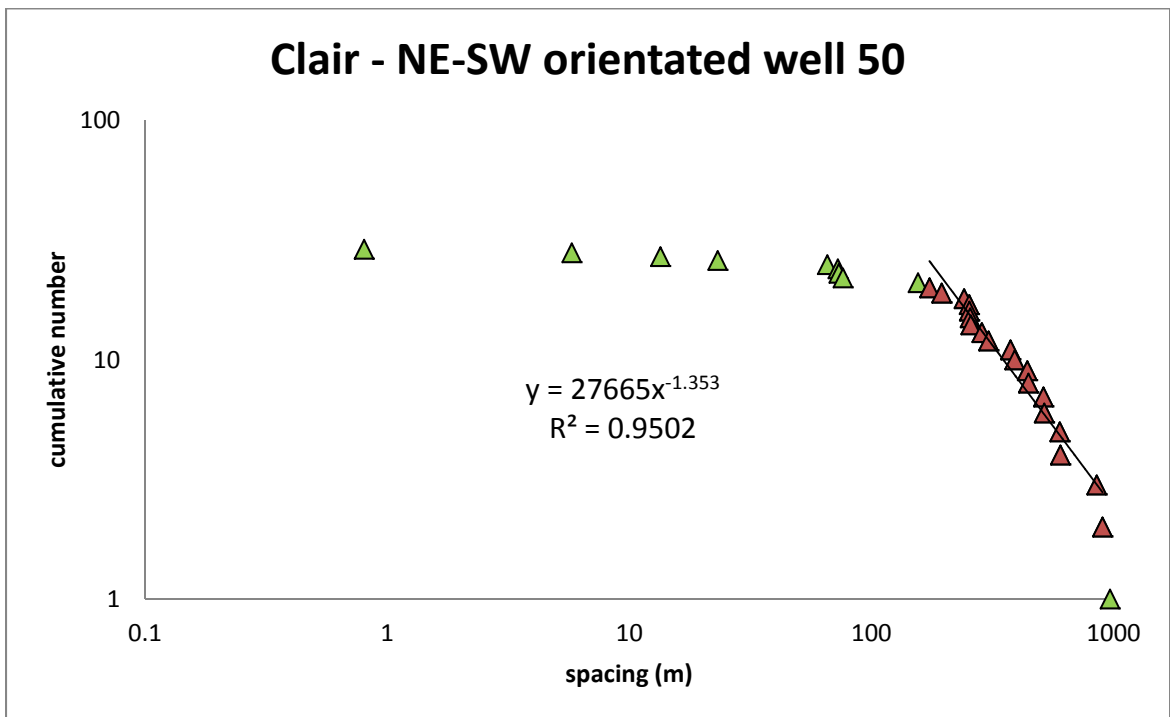
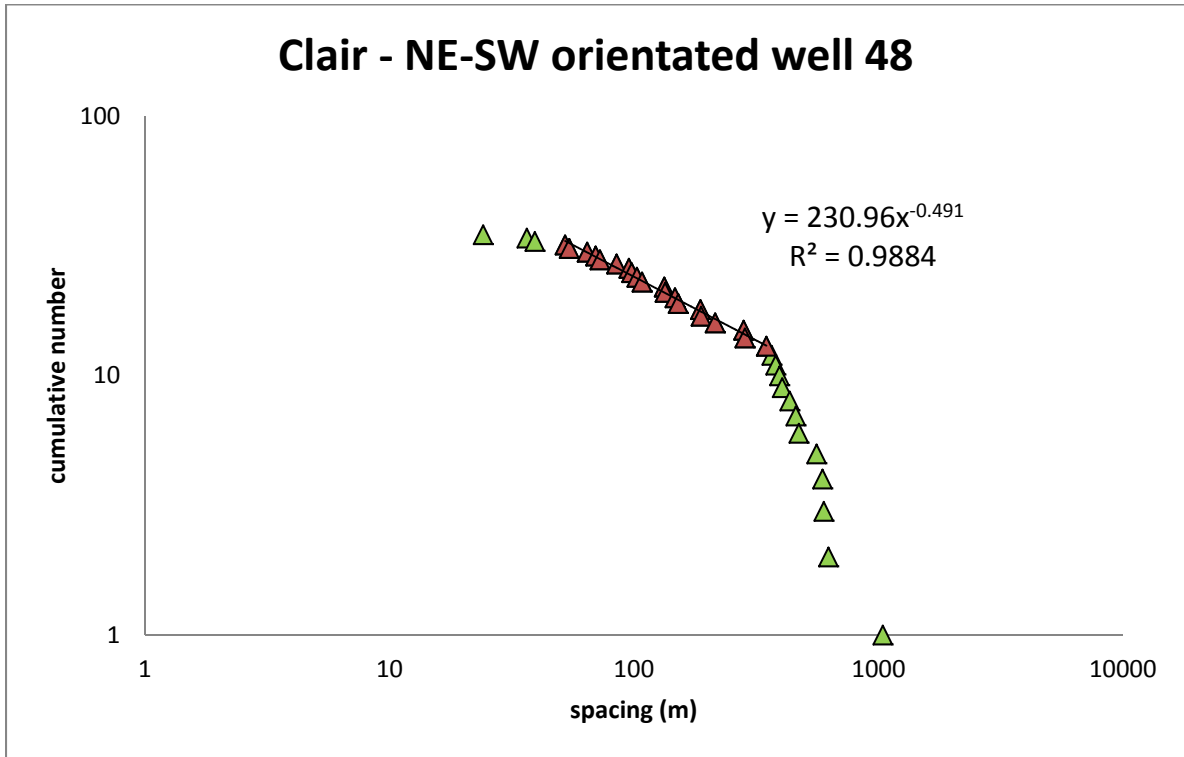


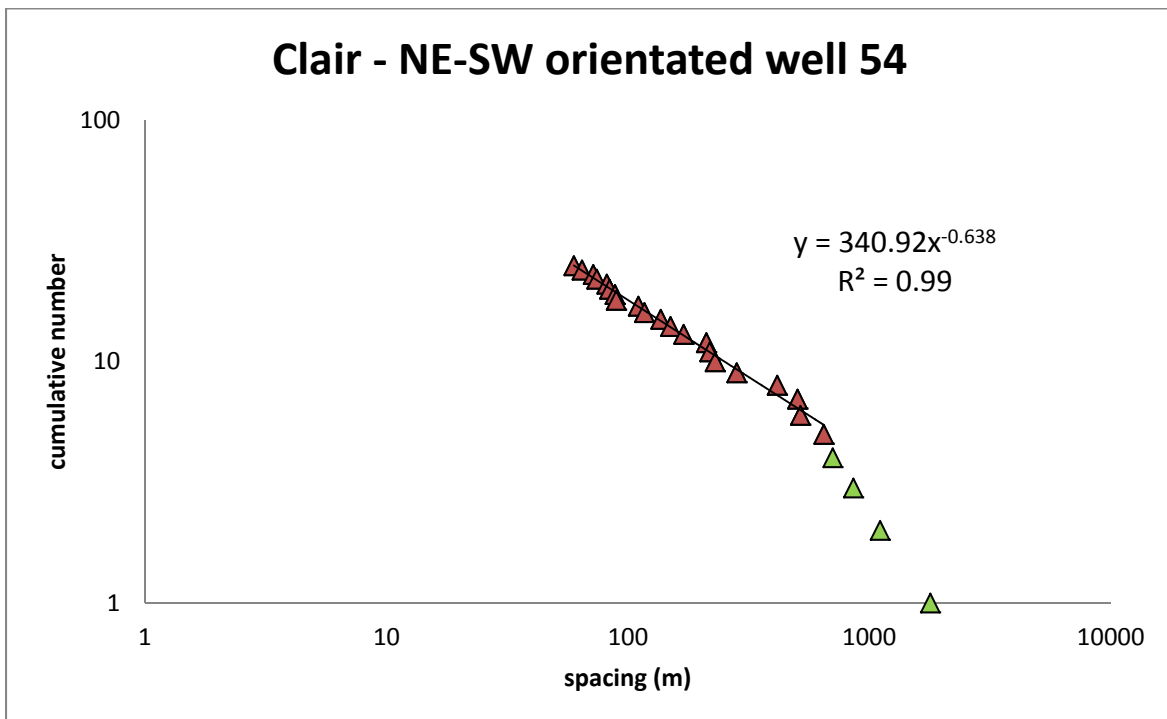
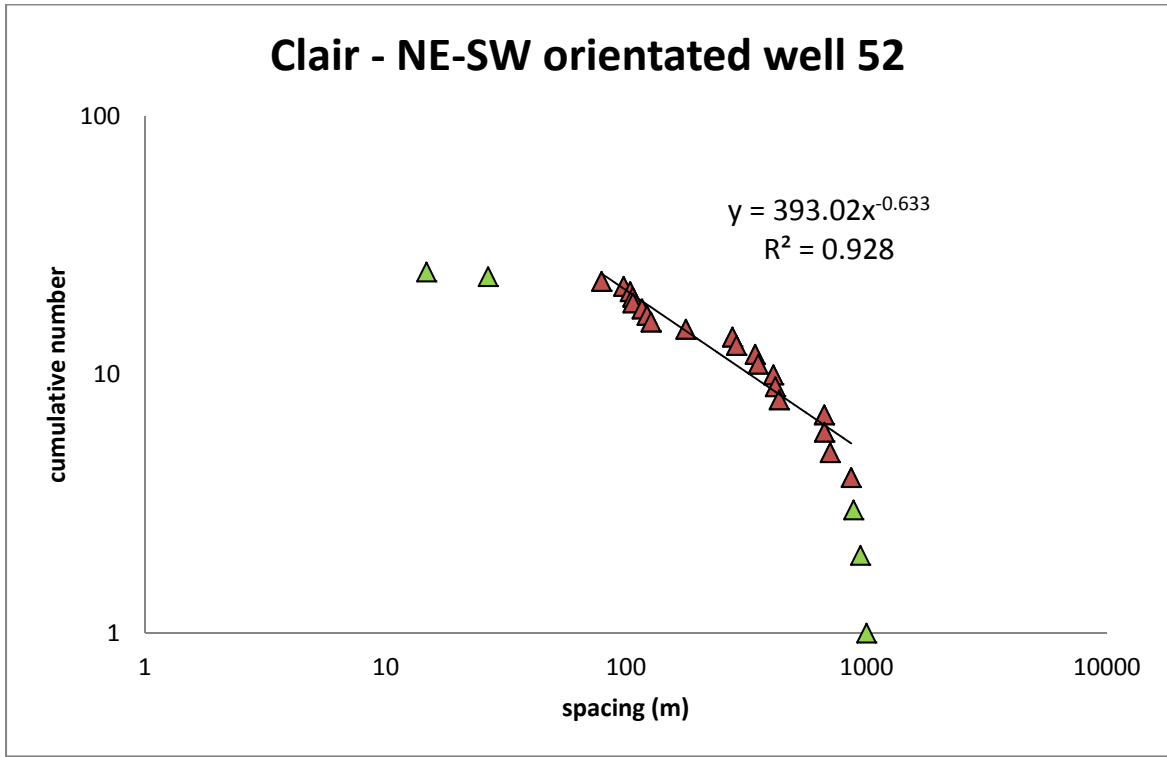


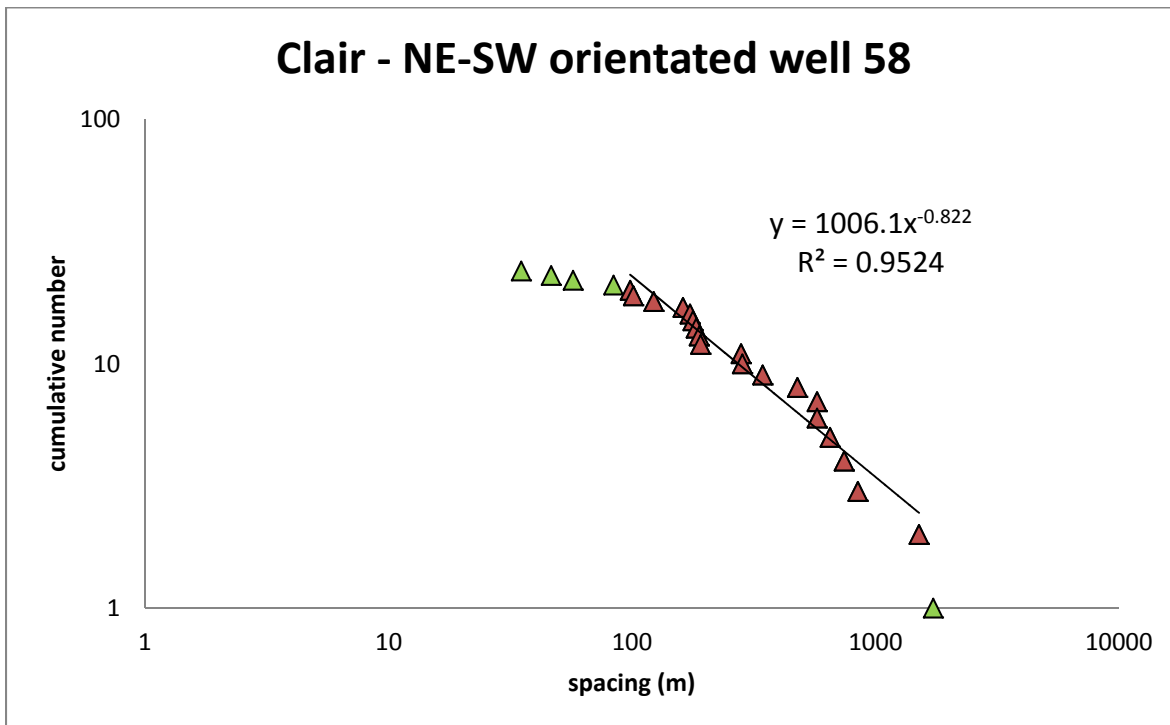
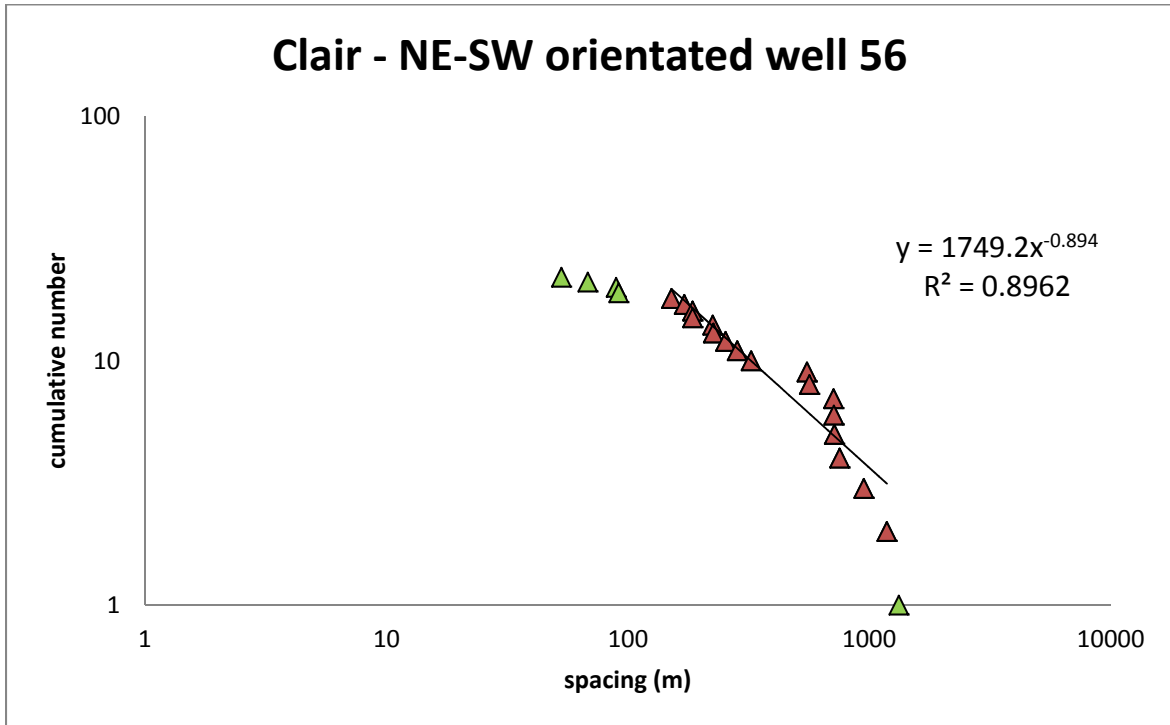


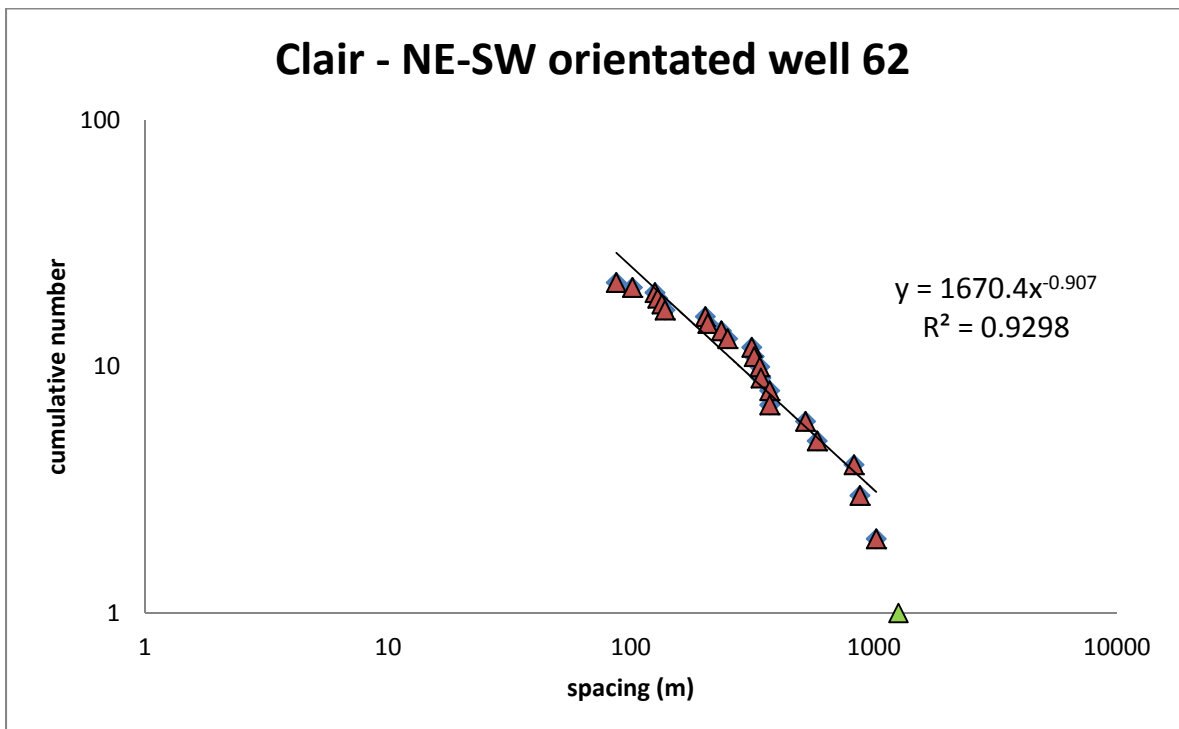
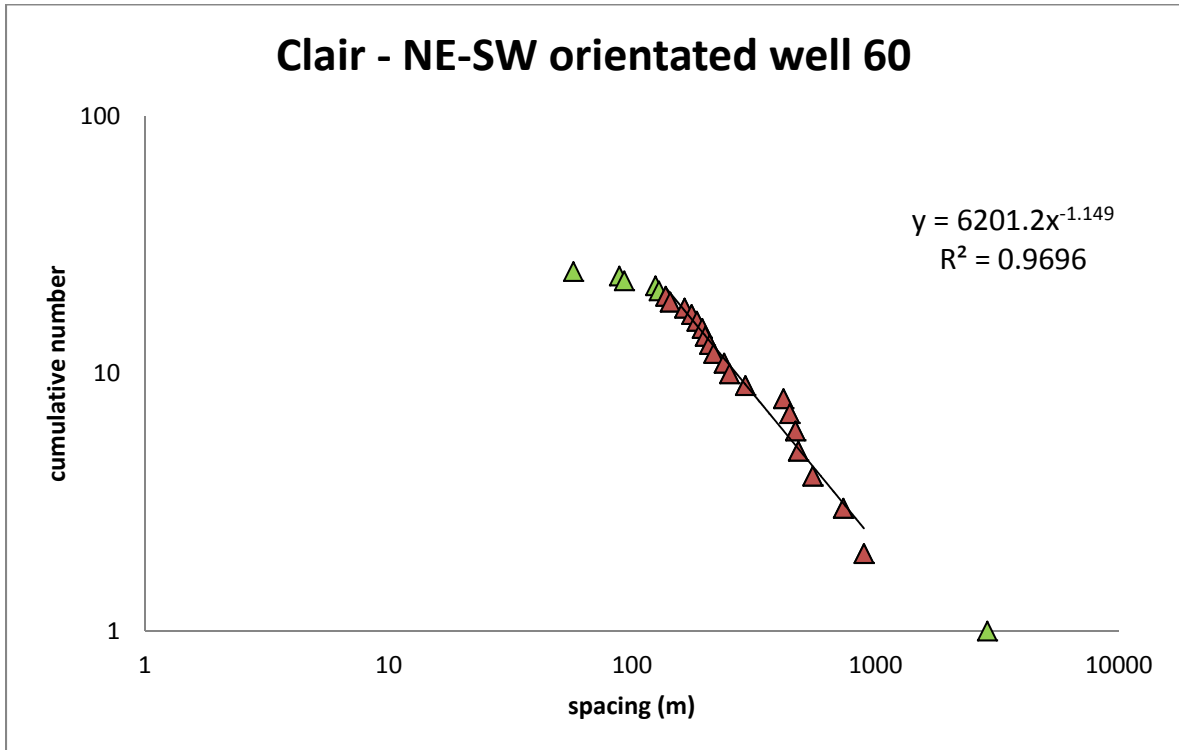


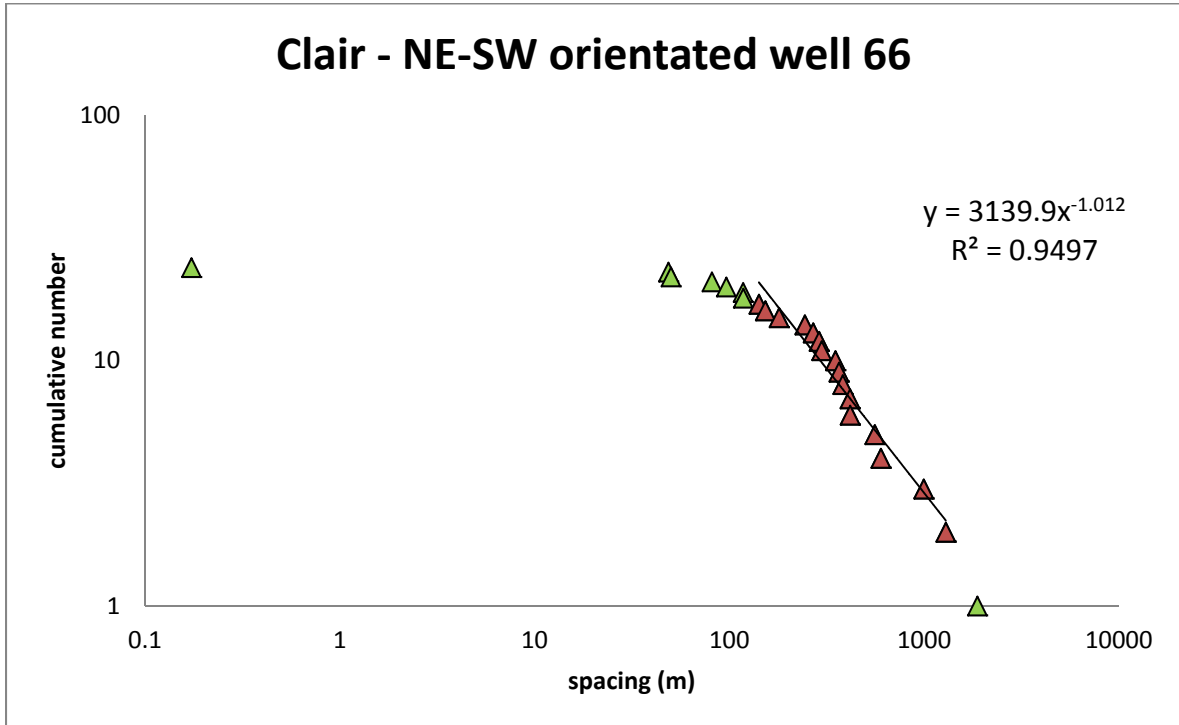
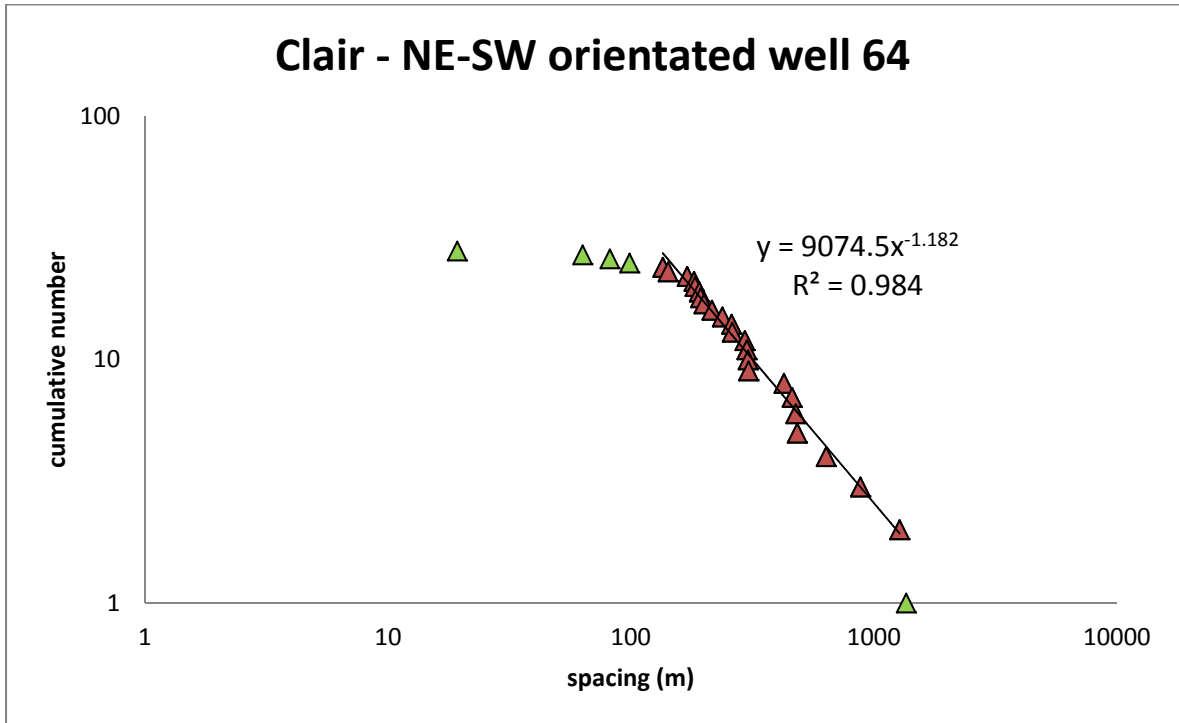






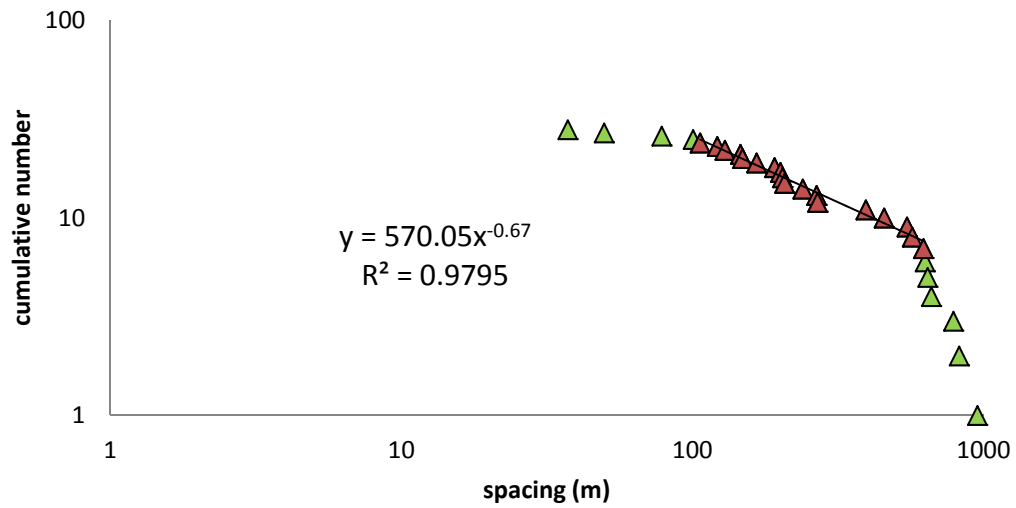




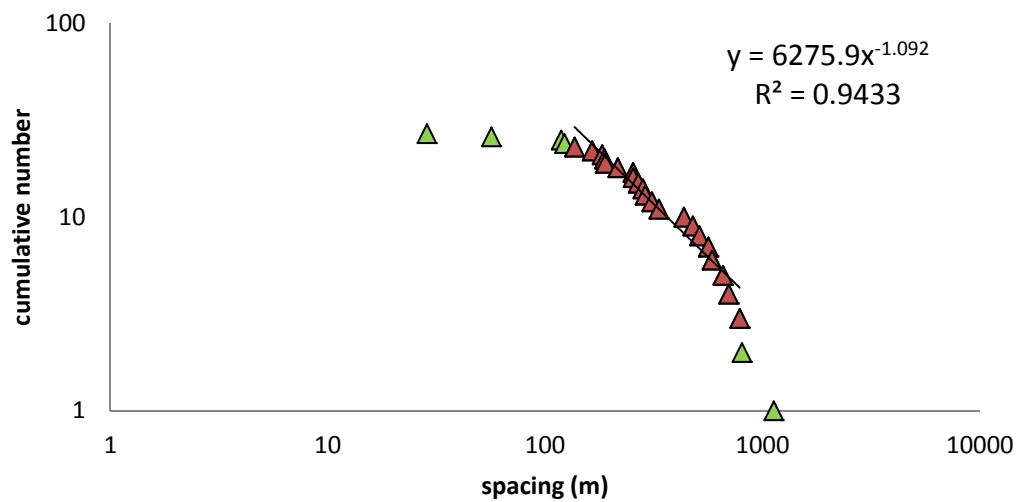


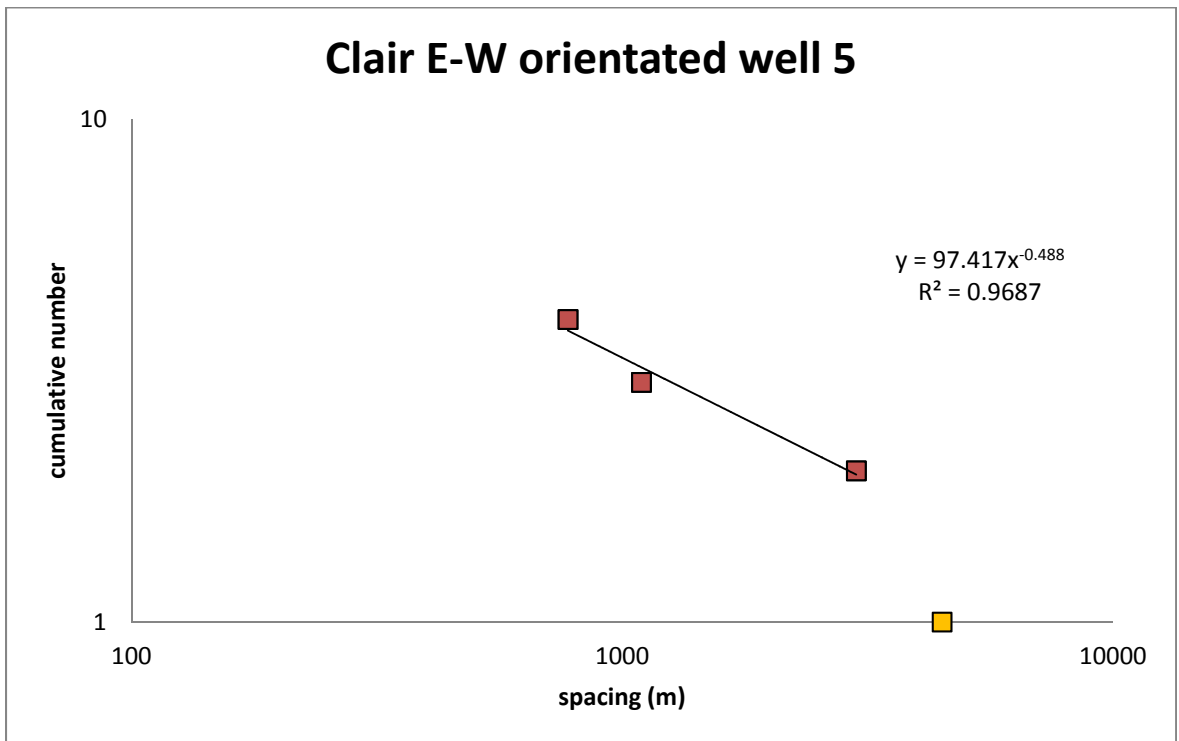
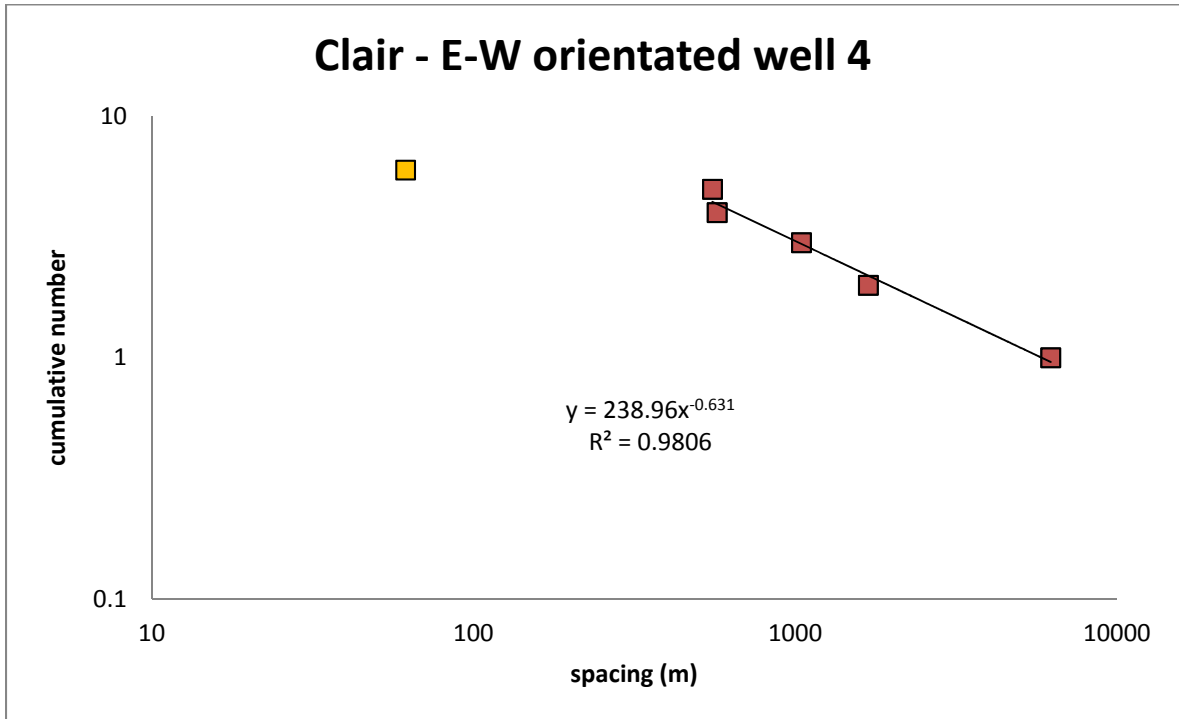


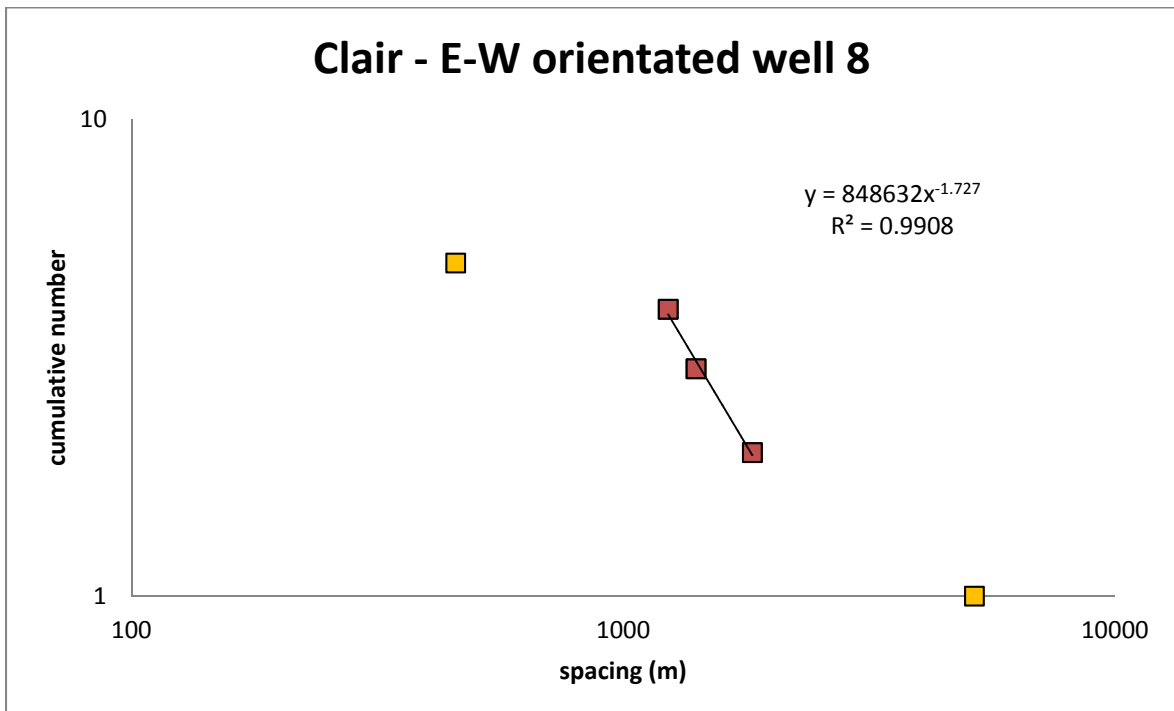
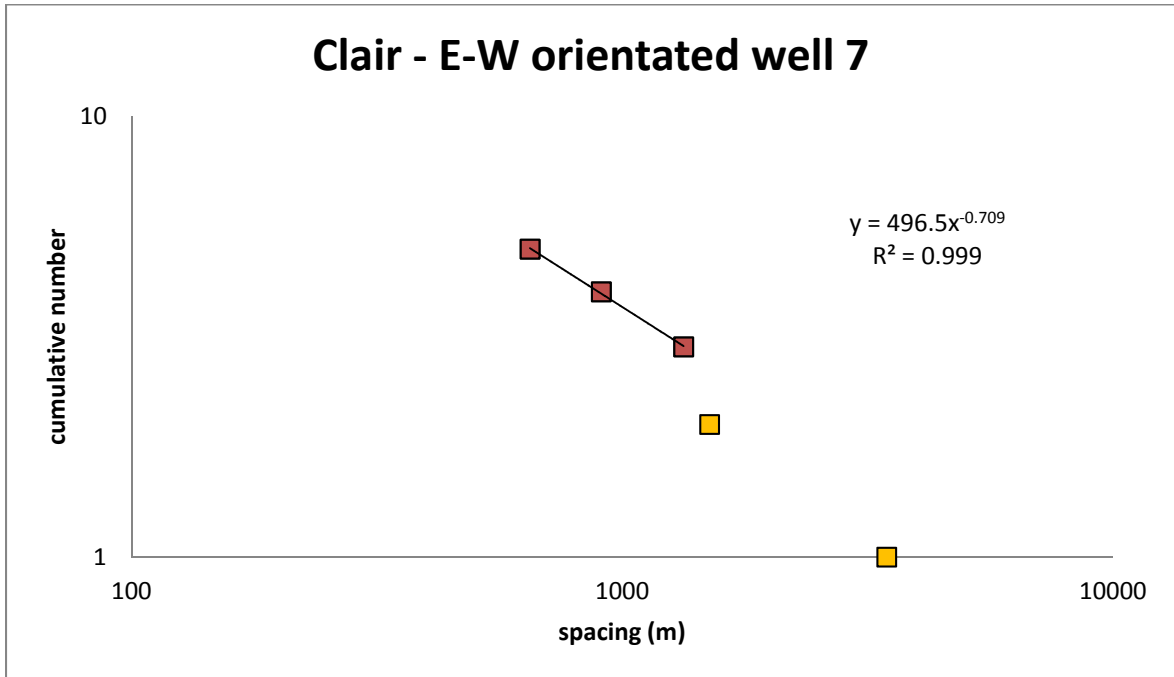
### Clair - NE-SW orientated well 68

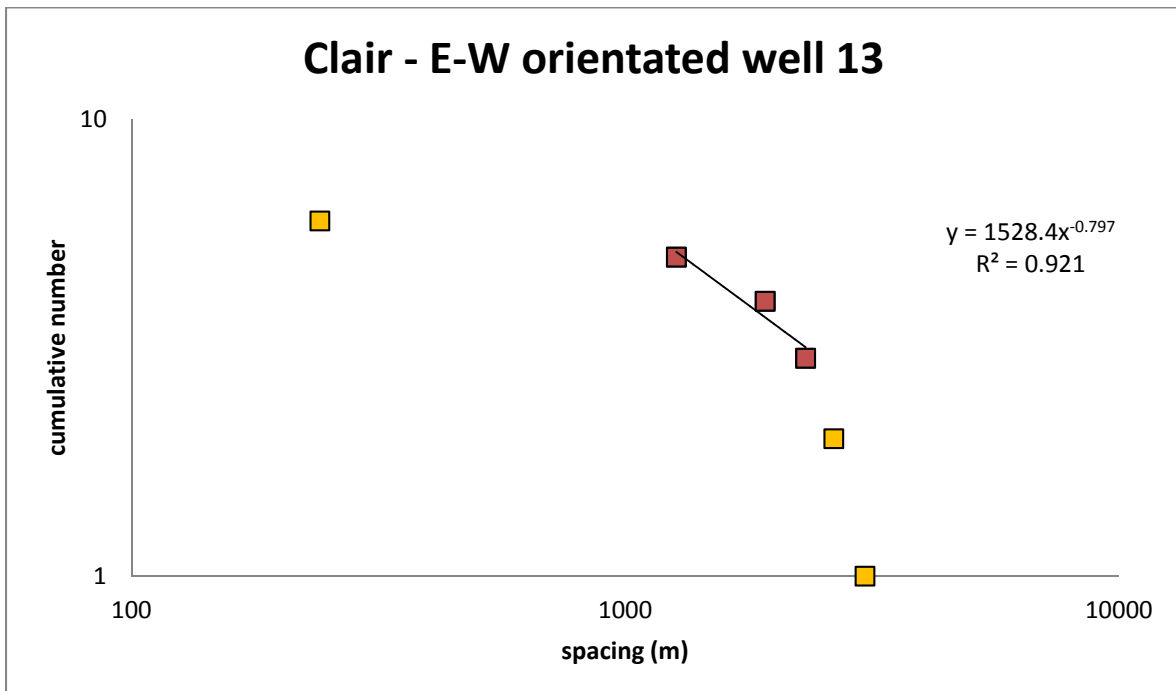
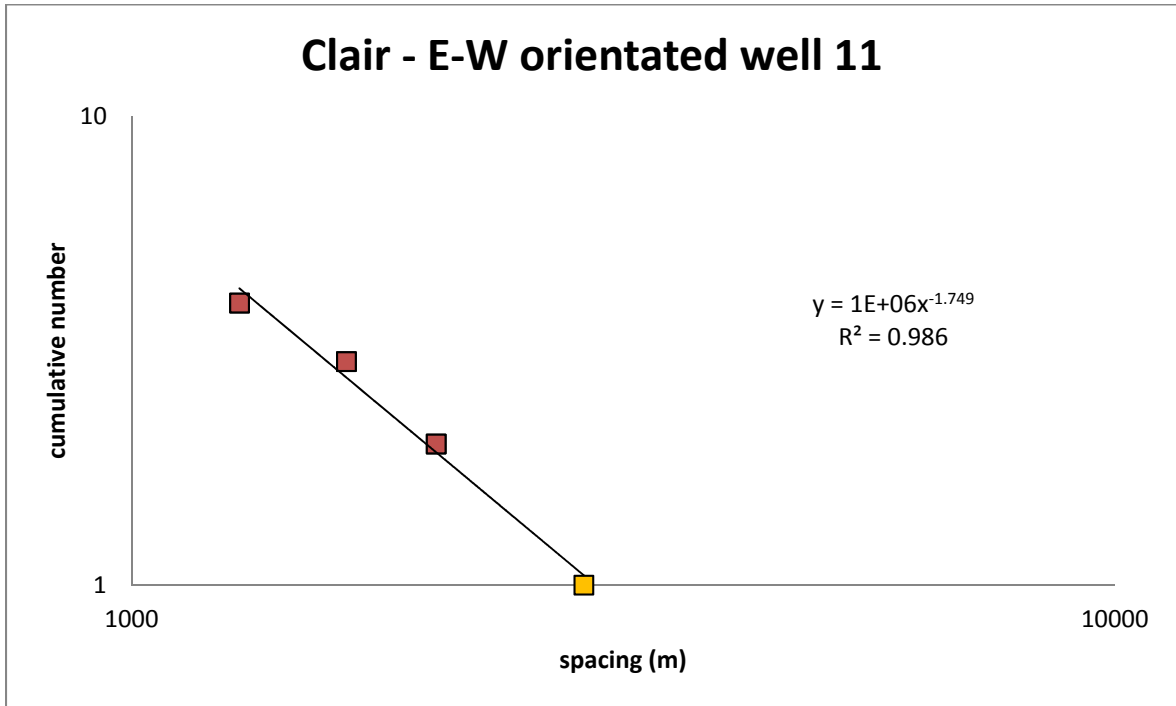


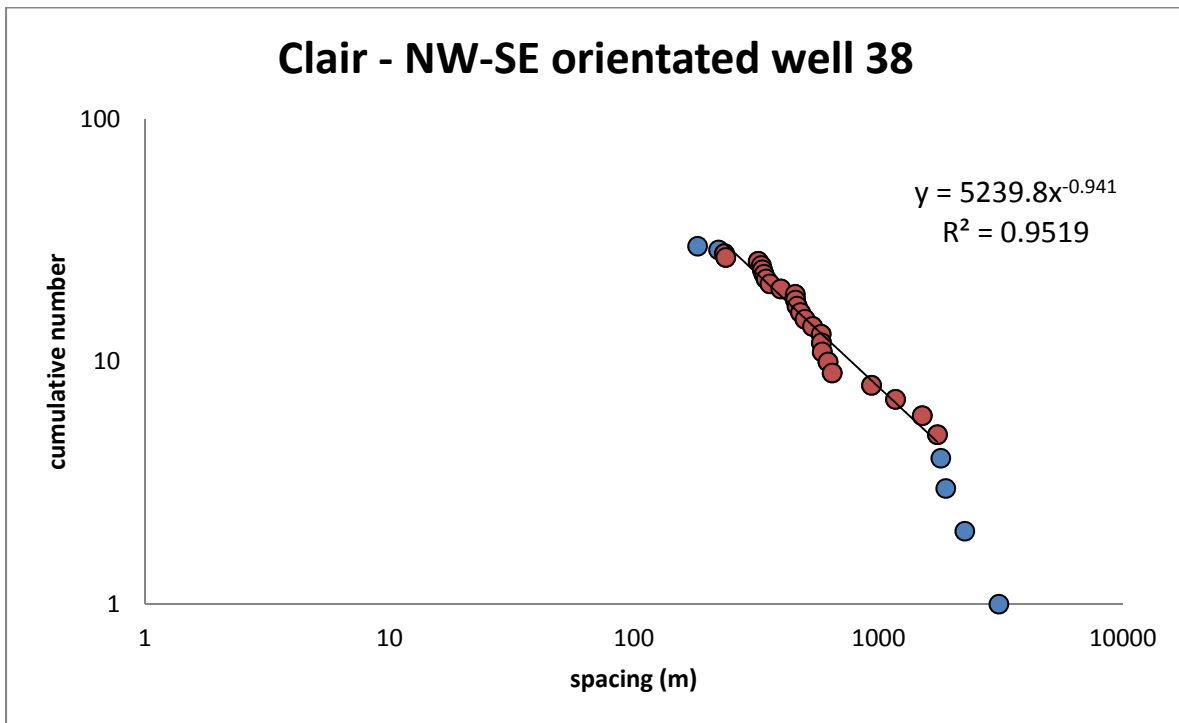
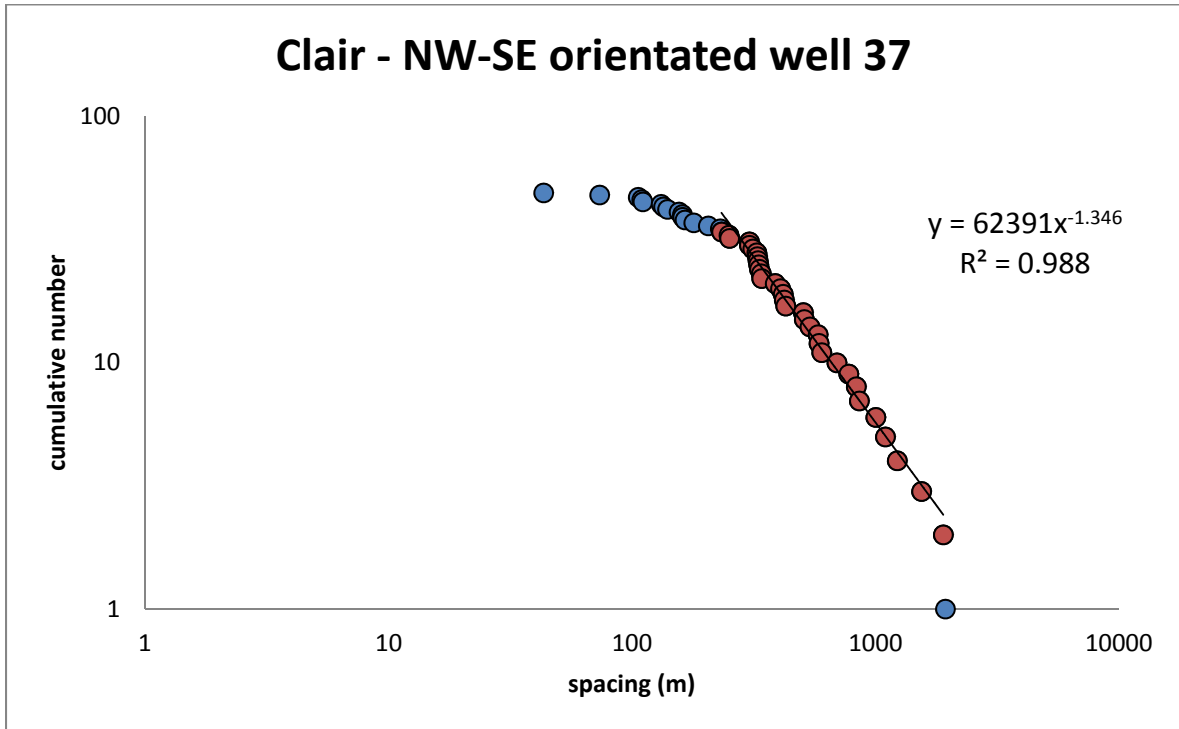
### Clair - NE-SW orientated well 70

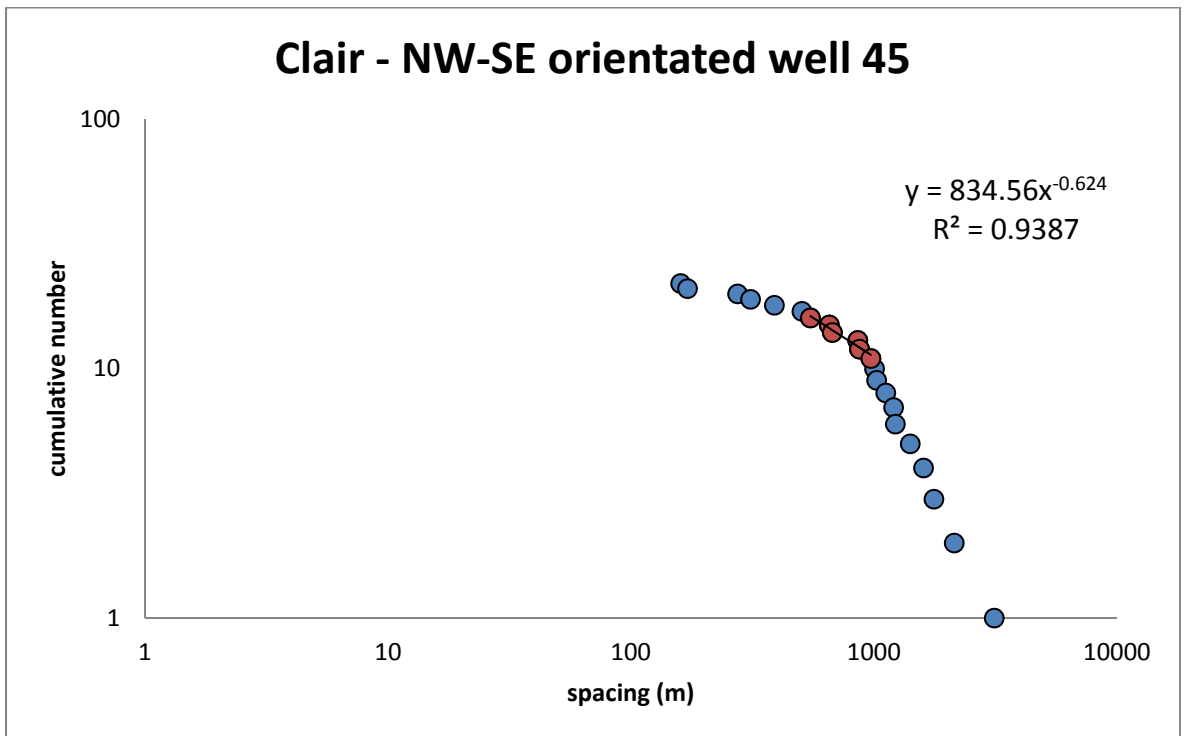
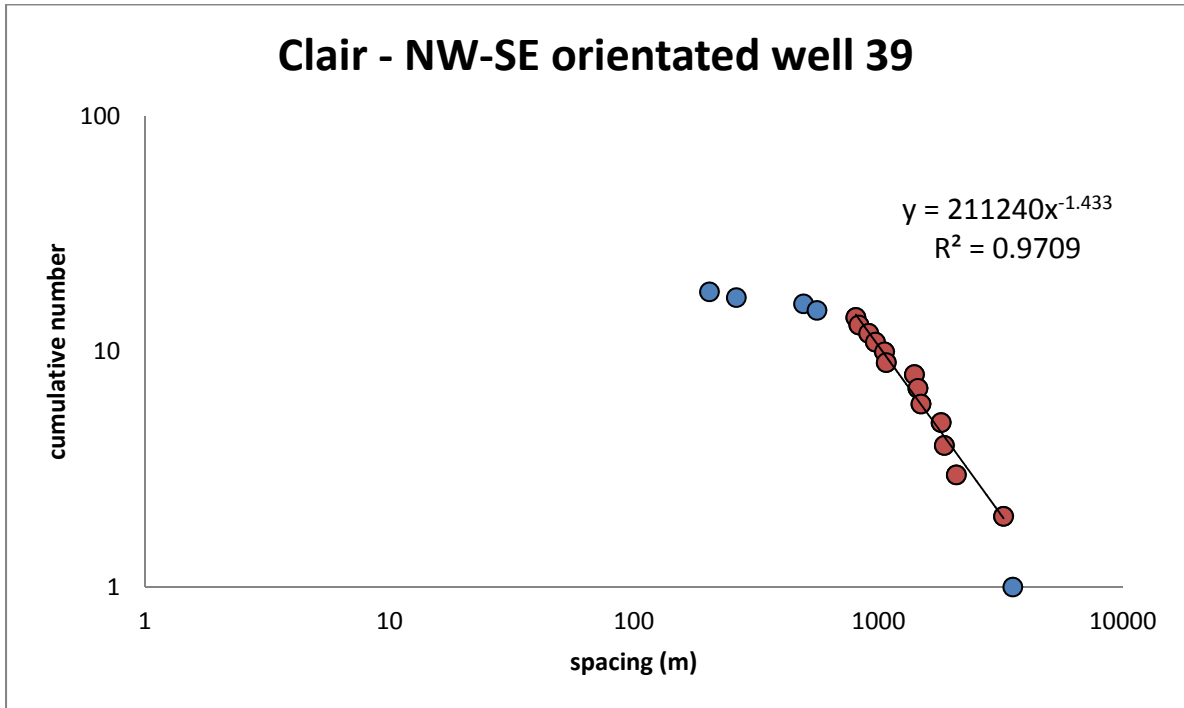





























### III: Basement core logs

#### Log of Drill Core

##### CORE 7-A2

21-0-2560m

##### HORIZONTAL CORE

Description of Core	Depth (m)	Photographs	Fracture Log	Rock Defects	Structural Information	Fracture orientation	Interpretation
Biotite gneiss. Coarse-grained. Quartz (20%), plagioclase (30%), amphibole (30%), epidote (20%), very little pyrite and biotite. Feldspars are fractured. 5cm thick hematite vein with brecciated host rock. Has smaller veins branching off of it. sample 7-a2-1	2140			Fractures filled with hematite. discrete veining mineralised with epidote, hematite & carbonate.	foliation 25° to edge of core picked out by biotite & epidote foliations.		conjugate sets.
	2141			carbonate & hematite filled shear fractures associated with feldspar.	50° dip		
catches rich in quartz (90%) or feldspar (80%) they are coarser grained than the rest of the host.	2142			lots of discrete veins in same orientation as foliation. epidote veins fractures filled with hematite.	foliation 45° to edge of core picked out by epidote & amphibole.		conjugate sets.
Basic gneiss 30% plagioclase, 30% pyroxene, 30%epidote 10% other felds - medium grained. Brecciated bands containing hydrocarbons. Coarse-grained pyrite fractures. 1cm thick veins of coarse-grained quartz. High % of epidote & amphibole. Plagioclase (30%), Quartz (30%), epidote (30%), biotite (10%)	2143			less than 1mm thick. vertical fractures containing pyrite and hydrocarbons. 5mm thick. Some carbonate fill. hematite veins smashed zone infilled with hydrocarbons & hematite.	no obvious foliation. foliation 25° to edge of core		
fine-grained. Pyroxene (70%), epidote (25%), quartz (5%). Quartz is mainly in veins. Granodiorite gneiss. Quartz (40%), plagioclase (30%), Epidote (20%), patches of amphibole & biotite (10%).	2144			closely spaced fractures perpendicular to foliation. some oil staining in lower fractures & hematite & pyrite	foliation 25° to edge of core picked out by feldspar.		conjugate sets.
Quartz (40%), amphibole & biotite (30%), epidote (20%) feldspar (10%). Quartz and Feldspar are segregated from the other minerals.	2145			5.1m 3cm wide shear fracture containing hydrocarbons. Fracture filled with hydrocarbons. Other fractures filled by carbonate hematite & epidote.	vertical. 85° to edge of core.		
brecciated. Patches more concentrated in biotite & hornblende. Granodiorite in composition. Pyrite associated with brecciation. Feldspar (<10%).	2146			heavily fractured. Shows hematite and oil staining. veins filled with epidote & h/i's	fault dips 50° to edge of core sample 7-a2-2		fault/damage zone. Oil staining around the more open fractures.
Quartz (80%), Epidote (10%), Biotite & Hornblende (10%).	2147			fractures under fault mainly contain hydrocarbons.	foliation 45° to edge of core.		
1.45m granodiorite gneiss Pyroxene (30%) Epidote (40%). Plagioclase (20%) quartz (20%) Epidote overgrows other minerals. Later development form the breakdown of feldspar.	2148			fractures perpendicular to foliation. pyrite along open fractures	10° to edge of core. 90° to edge of core.		
21m missing.	2149			steep angled fractures with hematite. shallow fractures contain epidote.	60° to edge of core. 50° to edge of core.		
Granodiorite gneiss. Some mafic bands. Amphibole (20%), Quartz (40%), epidote (20%), plagioclase (20%). mafic band. No pyrite.	2178			fractures containing hematite, carbonate & very little hydrocarbons. open fractures containing hydrocarbons & carbonate. shear fractures.	80° to edge of core. 90° to each other. foliation 70° to edge of core.		diamond shape pattern indicates conjugate sets and possibly quadraxial stresses.
Granodiorite gneiss with mafic bands (medium grained pyroxene and plagioclase). Patches of orthoclase. Very little pyrite. Feldspars concentrate around fractures associated with hematite.	2179			fractures perpendicular to foliation and others filled with hydrocarbons and/or oil stained. larger fracture with oil staining. Has a damage zone. Associated with	foliation 50° to edge of core. 30° to edge of core. 85° to edge of core.		
Granodiorite gneiss. Patchy orthoclase.	2180						

Large fracture is tensile and vertical.			hematite, carbonate & epidote.	10° to edge of core 105° to edge of core all steep (~70°)		a lot of fractures = more connectivity
Grandiorite gneiss (plag, pyroxene, quartz) Patches concentrated in o Brecciated areas contain fractures with hydrocarbons. % of epidote is increasing with depth. Photo.	2181		All fractures are oil stained, except minor ones that are filled with carbonate. fractures containing hydrocarbons are vuggy. Other contain carbonate. fractures have dendritic pattern.	foliation 50° to edge of core. 70° to edge of core parallel to each other.		conjugate sets.
Grandiorite gneiss. Orthoclase (30%). Same grain size as rest of rock. - coarse grained. No orientation to patches of orthoclase.	2182		fractures cut completely across foliation. Vuggy hydrocarbon & carbonate fractures. Main fracture is 2cm wide with small fractures spilling off of it.	vertical. foliation unclear. 85° to edge of core 5° to edge of core.		conjugate sets. carbonate and hydrocarbon fractures are unrelated. tensile fracture.
Grandiorite gneiss with granitic patches. Quartz (30%), plagioclase (50%), biotite (~20%), epidote (~10%)	2183		fracture associated with carbonate & hydrocarbons fractures are not connected. Most are parallel to each other and they are open	no foliation. 60° dip. 70° to edge of contact. 110° to edge of contact.		connectivity lower so no hydrocarbons.
sample 7-32-3 Grandiorite gneiss with lenses of granite at top. Coarse-grained. Epidote still ~10% of the rock.	2184		main fractures are parallel to each other. Contain hematite & carbonate No hydrocarbons.	no obvious foliation 70° to edge of core		
16.35m. More mafic gneiss. With 50% pyroxene, plagioclase (40%) rest orthoclase and accessories	2185		fractures steepen with depth. vuggy areas filled with hematite & carbonate. Shear fracture. No hydrocarbon	no obvious foliation. 60° to edge of core parallel to each other.		
17.30m. Lots of epidote (40%) & carbonate (40%). Rest is quartz & hematite & small traces of pyrite.	2186		shear zone with sinistral sense of movement. discrete fractures with hematite & epidote fill.	15° to edge of core vertical 90° to each other		conjugate sets.
50% granite gneiss, rest grandiorite gneiss. Much more intensely veined. Lenses of granite. Zones of brecciation still missing.	2187		veins of hematite & epidote. diamond pattern to veins.	40° to edge of core 20° to edge of core		2 conjugate sets? quadrinodal stresses.
Grandiorite Gneiss, brecciated at the top. Quartz (30%), plagioclase (50%), biotite (10%), accessories (10%). Lenses of mafic. Feldspar is orthoclase. Epidote associated with mafic (biotite & hornblende).	2246		fractures filled with hematite.	35° to edge of contact. 140° to edge of contact.		conjugate sets.
Granite/grandiorite gneiss with pegmatite lenses. Coarser-grained. Grains average 1cm in diameter. Mafic bands with 50% pyroxene, amphibole & some biotite. mafic and pegmatites seems to be associated.	2247		some large fractures with associated hydrocarbons.	foliation 50° to edge of core. 50° to edge of core. 60° to edge of core 30° to edge of core		
Grandiorite gneiss with quartz rich lenses. 22.35m. 5cm thick brecciated zone with cement of hematite. Below is a Grandiorite gneiss. Coarse-grained. Large quartz grains. Some very thin epidote veins.	2248		shear fracture. smaller more discrete veins of hematite.			
Grandiorite gneiss with mafic bands. Photo. Very coarse grained quartz.	2250		discrete fractures with oil staining fracture at base of brecciated zone. fractures do not exhibit oil staining but may still contain hydrocarbons.	no obvious foliation 50° to edge of core 80° to edge of core 100° to edge of core.		gneiss is brecciated at a result of shearing i.e. Breccia occurs in a fault core.
Quartz concentrated in patches. 1cm grain size, same for biotite.	2251		are between 2 closely spaced fractures is damaged and brecciated.	foliation 70° to edge of core. 10° to edge of core 30° to edge of core 70° to edge of core		
Oil staining stops. Epidote is present again.	2252		Fractures are closed.	random orientations.		less connectivity of fractures.
Grandiorite gneiss. Sticky bands of mafic material and granite. No epidote. Quartz (30%), plagioclase (60%), biotite (10%).	2253		most fractures parallel to foliation. Infilled with hematite.	foliation 70° to edge of core. 60° to edge of core 15° to edge of core		
Banded mafic and granitic gneisses.	2253		fractures have a dendritic pattern.	40° dip or vertical.		



			fractures cut across the bands. 2 main fracture sets.	20° to edge of core (vertical) 160° to edge of core (40° dip)		
Granodiorite gneiss. Quartz (30%), plagioclase (50%), biotite (10%), epidote (10%). No banding. Some small patches of pegmatite.	2254		fractures are branching. They contain hydrocarbons. most smaller fractures are parallel to the foliation	foliation 70° to edge of core. 50° to edge of core 160° to edge of core		
Granite gneiss. 1cm diameter for average grains. Quartz (40%) feldspar (50%), biotite (10%).	2437		2 sets of fractures filled with carbonate & small amounts of epidote.	no obvious foliation 15° to edge of core 70° to edge of core		conjugate sets?
	2438		very few fractures			
Contact at 40° to edge of core - quite sharp. Granite gneiss. Banded. Quartz (50%), biotite/hornblende (40%), feldspar (~10%), epidote (~2%). Stripy appearance. Coarse-grained. Pyrite associated with mafic patches.	2439		large open fractures containing h/c's other minor fractures also contain h/c's minor carbonate veining	45° to edge of contact. conjugate sets at 90° to each other.		fractures tend to cut through the quartz rich areas.
31.15m. blotchy contact. Much more mafic. Fine-grained. Bands between quartz & biotite are coarser-grained quartz & feldspar. Contain quartz veins which follow foliation. Foliation steepens up with depth. Muscovite (~10%) and pyrite.	2440		small fractures	foliation 50° to edge of contact. 90° to each other. foliation 15° to edge of contact		possibly a deformed dyke. conjugate sets
	2441		large fractures (3cm) wide. Contain h/c's & carbonate.			
32.90m. Epidote (80%)	2442		large open fracture (13cm wide). Contains oil stained rock and h/c's associated with pyrite.	90° to edge of core		
sample 7-a2-4	2443		small epidote veins. carbonate shear fracture (1cm wide). fractures contain hematite or carbonate.	50° to edge of core 90° to edge of core 85° to edge of core		
34.70m. 20cm wide quartz rich patch. Coarse-grained. Quartz (60%), feldspar (30%), biotite (10%). 34.90m. Granodiorite gneiss. Medium-grained. Banded.	2444		veins at 90° to each other. open fracture with breccia in it containing hydrocarbons. minor carbonate veining and some with hematite.	no obvious foliation 65° to edge of core 70° to edge of core 145° to edge of core		
Granodiorite gneiss with mafic bands. Small bands of orthoclase which cross cut the foliation at 15°. Patches of epidote & pyrite associated with the mafic bands.	2445		large open fractures containing h/c's & carbonate. Also small veins contain h/c's carbonate.	foliation 30° to edge of core. 60° to edge of core. 125° to edge of core. 15° to edge of core		
	2446					
32m missing	2499		fractures are very clean and parallel to each other. one big open fracture containing h/c's very little veining.	foliation 30° to edge of core. 90° to edge of core. 120° to edge of core.		
	2500					
Granodiorite gneiss. Coarse-grained. With orthoclase (20%), quartz (50%), biotite (10%), plagioclase (10%), accessories (10%). Also where there is hydrocarbons is bubbly and more weathered.	2501		fractures are very clean. Maybe some carbonate mineralisation.	85° to edge of core 120° to edge of core.		

large patches of quartz & feldspar that are very coarse-grained.	2502						
41.85m. Granite gneiss. Coarse-grained. Orthoclase (40%).	2503		no fractures.	foliation 50° to edge of core.			
Stroey granodiorite gneiss, plagioclase instead of orthoclase. Orthoclase is concentrated in patches. <u>Granite/pegmatite gneiss</u> . Very coarse-grained.	2504		fractures are discrete but exhibit oil staining. Some carbonate veins. cut across the foliation.	45° to edge of core. 125° to edge of core. 90° to edge of core. foliation is undulating			
43.10m. Granite gneiss. Coarse-grained. Some streakiness but no obvious foliation. Photo.	2505		ladder fractures. Contain h.c.'s. Well connected. Some are vuggy.	no obvious foliation. 160° to edge of core. conjugates at 70° to edge of core.		closely resemble the dominant fracture type in the Assynt terrane particularly noticeable near shear zones such as Carrap.	
44.15m. <u>Granodiorite gneiss</u> . Coarse-grained.	2506		fractures are conjugate set at 70° to each other. 1cm wide fractures contain carbonate some exhibit hydrocarbon staining.	foliation 55° to edge of core. 120° to edge of core. 45° to edge of core.			
Banded granodiorite & granite gneiss. ~1% epidote.	2507		there are also discrete carbonate veins.	no obvious foliation.			
<u>Granite/pegmatite</u> . Very coarse-grained. Highly veined with hematite, epidote and occasionally hydrocarbons. Photo. Epidote (10%), orthoclase (70%), quartz (20%).	2508		veins cut across grains of orthoclase. Fractures contain carbonates & hydrocarbons. they are open.	no obvious foliation.			
<u>Pegmatite</u> . Much more quartz rich (70%).	2509		tensile fracture with hydrocarbons.				
rock is oil stained.	2510		still highly veined with carbonate.	40° to edge of core.			
Rubby and oil stained. Very coarse-grained. Granodiorite gneiss. Epidote (20%). Granodiorite gneiss with patches of granite gneiss.	2511		large fracture or close knit fracture network. Contain carbonate & hematite. Roughly parallel to each other. pervasive veining - probably quartz.	no obvious foliation.			
Granodiorite gneiss. Fine-grained. <u>Mafic minerals</u> (50%).	2512		one large fracture containing a breccia	no obvious foliation. 85° to edge of core.		tensile fracture.	
<del>2513. Sample missing.</del>	<del>2513</del>	<del></del>	<del></del>	<del></del>	<del></del>	<del></del>	<del></del>
50.50m. Granite gneiss. Very coarse-grained (some grains >2cm). Orthoclase (30%), quartz (40%), epidote (10%), biotite (20%).	2514		densely fractured. Fractures are randomly orientated and most are oil stained. Associated with pyrite.	no obvious foliation.			
51.50m. <u>Banded Granodiorite/gabbro gneiss</u> . Quartz & feldspar are segregated from pyroxene & amphibole. Large individual grains of orthoclase (3cm in diameter). Photo.	2515		parallel fractures. Possible shear zone. Oil stained and also contains carbonate.	foliation 75° to edge of core.			
52.15m. <u>Gabbro gneiss</u> . Fine-grained. Interlayered with granite and granodiorite.	2516		fractures are clean and open.	no obvious foliation. 45° to edge of core. 95° to edge of core.			
53.10m. <u>Granite gneiss/pegmatite</u> . Coarse-grained.	2517		fractures contain hydrocarbons & carbonate. fractures are in patches with random orientations. Cut across grains.				
Red of core. orthoclase (50%), epidote (15%), quartz (20%), biotite (15%) photo. Very coarse-grained. <u>Pegmatite</u> .	2518		fracturing is in random patches. Epidote is concentrated where there are fractures. The majority of fractures are oil stained.	no obvious foliation.			
sample 7-a2-5	2519		Very few clastic filled fractures or veins.				
Pegmatite up to 90% orthoclase. Orthoclase crystals are very fractured and can exceed 10cm in size. Pegmatite also contains large (1.5-2cm) crystals of epidote which tends to occur in patches. Very little quartz (~5%) and it is sparsely distributed. Some fine grained basic material which I assume is pyroxene. There are also crystals of pyrite scattered through it. sample 7a-2-6	2520		Almost no fractures at all.	15° to edge of core. 110° to edge of core.			
	2521		Highly fractured zone. main fracture orientation. shear fractures.				
	2522		Oil is associated with pyrite throughout the fractures.				
	2523						

KEY FOR FRACTURE LOG (fractures in of core)
0
1
2
3
4
5
6 to 10
11 to 15
16 to 20
21 to 25
>25

### Log of Drill Core

CORE 9-2

7825-8090ft

VERTICAL WELL

Description of Core	Depth (m)	Fracture Log	Rock Defects	Structural Information	Interpretation
Laminated quartz sands interbedded with a matrix supported conglomerate of granite gneiss. Sand contains muscovite, feldspar, quartz. Well-sorted, well-rounded.	2386				fluvial environment of deposition.
	2387				
Conglomerate - up to 2cm sized clasts of granitic gneiss material supported by sand. Poorly sorted. 248ft missing	2463				
Very coarse grained granite. Orthoclase (30%), quartz (40%), biotite (30%).	2463.6		carbonate veining, can be diffuse and patchy	fabric dips 65° 85° dip. 50° dip.	Granite sheet - just like what is seen at the Laxford Front?
Bands of coarser-grained pegmatite.	2464.6		no meso-scale fracturing	fabric dips 30°	
Coarse grained granite gneiss. Pretty consistent through rest of core.					
	2465.6		tesile fracture. Filled with carbonate.	65° dip.	
sample 9-2-1					
	2466.6				
	2467.6				

KEY FOR FRACTURE LOG (fractures/m of core)	
3	
4	
5	
6 to 12	

### Log of Drill Core

CORE 7/1

1683-1811m

SPOT CORE

Description of Core	Depth (m)	Fracture Log	Rock Defects	Structural Information	Interpretation
Top 15cm. Grey granodiorite gneiss. Coarse-grained. Quartz(50%), feldspar - orth & plag (35%), biotite(10%), epidote (<5%) & calcite (<5%). Quartz is fractured, as is the orthoclase feldspar. No obvious fabric. Some lenses of iron staining. 50-65cm. Brecciated. Still Granodiorite Gneiss. Vuggy.	1683		epidote veins. calcite veins  small fractures around the clasts.  calcite veining (1mm thick)	85° dp. 5° dip. 85° dp.  random orientations	I think the fractures are a result of the coring process.
Clasts up to 1.5cm diameter. Poorly sorted. Clasts are angular. Lots of pyrite mineralisation - it goes around the granodiorite casts. Also calcite mineralisation (5cm thick veins) Iron staining.					
1-1.25m. Granodiorite. 1.5cm grains of plagioclase & quartz. Quartz & plagioclase seem to cluster together. <5% biotite. 55m missing	1684		Epidote forms fabric	25° dp.	The core is highly weathered. The fabric gets more obvious with depth. Very top of basement?
	1739				
2-2.25m. Granodiorite gneiss. Quartz (50%), plagioclase (50%) Calcite mineralisation. This section is very rubbly.	1739.8		Calcite in veins  branching veins of calcite.	80°, 65° or 0° dip.	
More epidote.					
69m missing	1808.8				fractures are conjugate to each other.
3-3.25m. Granodiorite Gneiss. Medium-grained. Patchy epidote and biotite (10%). Quartz and feldspar make up the other 90%.	1808.8		veils with hematite calcite veins	88° dp. 15°	
3.5-3.85m. Granodiorite Gneiss. Banded - some of the bands are richer in orthoclase than others. Coarse-grained. Quartz (40%), epidote (30%), feldspar (20%) & biotite (10%).			gran preferred orientation - gives fabric. no obvious veins.	fabric dips 10°	
4.1-4.25m. Brecciated. Quartz (80%). The rock is fractured. fractures associated with oil staining. Epidote concentrated in same orientation as fractures.	1809.8		diamond shape fracture pattern	random orientation	quadrifacial fracturing?
4.5-4.75m. Rubbly texture. Granodiorite gneiss. Medium-grained. Quartz & Feldspar (90%), biotites & epidote (10%).			tensile fractures filled with calcite fractures with oil staining	random orientations.	
	1810.8				

KEY FOR FRACTURE LOG (fractures/m of core)	
2	
3	
4	
5	

### Log of Drill Core

#### CORE 8-2

1854.5-1861.65m








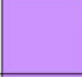


Description of Core	Depth (m)	Fracture Log	Rock Defects	Structural Information	Interpretation
Banded Granite gneiss with patches of quartz. Bands of granodiorite composition are 3cm thick. Coarse-grained. Orthoclase (30%), Quartz (45%), biotite (15%), epidote (5%), accessories (5%). % of biotite increases with depth.	1854.5		fractures offset veins of hematite. Fractures contain calcite	fabric dips 45° at 90° to veins 70° dip 30° dip	Quite obvious fluid flow through the whole core but no evidence of hydrocarbons.
	1855.5				Is connectivity not high enough or were the fractures sealed during hydrocarbon migration?
Granodiorite/mafic gneiss. Varies between fine and coarse-grained gneiss across the core.	1856.5		calcite in fractures no veining	no obvious fabric.	
	1857.5		shear fracture with calcite. others contain hematite	no obvious fabric. 60° dip 20° dip	
Granite Gneiss. Coarse-grained. Small patches of epidote. Quartz (50%), orthoclase (30%), biotite (20%).	1858.5		fractures in 2 sets. Filled with either calcite or hematite	40° dip 50° dip	fractures are conjugates to each other.
20cm thick band of pegmatite Granodiorite Gneiss. Coarse-grained. Quartz (50%), orthoclase (20%), amphibole (20%), biotite (10%)	1859.5		veins of epidote & hematite they cut straight across each other.	no obvious fabric 85° dip (ep) 15° dip (hem)	
Granite Gneiss. Coarse-grained. orthoclase (40%), Quartz (50%), biotite (10%). Some patches of > 80% epidote.	1860.5		hematite veins tensile calcite veins	55° dip	form fracture conjugate sets to each other (90°).
Granodiorite gneiss. Rich in epidote. Probably contains chlorite. Bands of more granitic gneiss (no epidote)	1861.5		calcite veining small open veins hematite staining along cracks		Epidote has come in later. Greenschist facies deformation shown by chlorite?

KEY FOR FRACTURE LOG (fractures/m of core)	
11	
12	
13	
14	
15	
16	
17	
18	
19	

### Log of Drill Core

CORE 8-8

2484-2500m

Description of Core	Depth (m)	Photographs	Fracture Log	Rock Defects	Structural Information	Interpretation
Basal conglomerate consisting of clasts of granite, epidote, basalt, granodiorite. It is supported by a microbreccia to a mud matrix. Clasts vary in size from 1mm to >20cm. Very poorly sorted. Occasionally interbedded with a fine quartz sandstone which is laminated. Epidote is mainly associated with the mafic clasts. Clasts: granite (60%); granodiorite (25%); mafic (15%).	2484			clean open fracture some epidote veins	45° dip	Pulses of conglomerate = pulses of high energy. Loose rubble falling off of the ridge.
				clean open fracture	horizontal	
	2485			carbonate veins along the edges of bigger clasts (>5cm)		
Top of Basement Banded granodiorite gneiss and basalts.	2486				fabric dips 50°	
	2487			Epidote catclaste in shear fractures is preferentially developed in the granodiorite gneiss bands		The top 2.2m of this core is referred to as the basal conglomerate. Below this the rock shows no signs of clasts and hence I believe that this marks the boundary at the top of the basement sequence.
Graded contact into granitic gneisses. Bands of coarse-grained orthoclase. There is less quartz (50% -> 25%). Quartz is concentrated near the orthoclase.	2488					
	2489			Intense branching veins associated with epidote	fabric dips 55° 60° average dip.	
Granodiorite gneiss.	2490			zones of veining carbonate veins epidote veins	70° dip 60° dip 10° dip	
	2491			fabric dips 55° epidote veins shear fracture	65° dip	
Granite gneiss. Large orthoclase crystals (1.5cm) Banded granodiorite & granite	2492			fabric dips 40° small epidote veins few carbonate veins large epidote veins (1-5cm)	85° dip	
	2493			fewer veins		





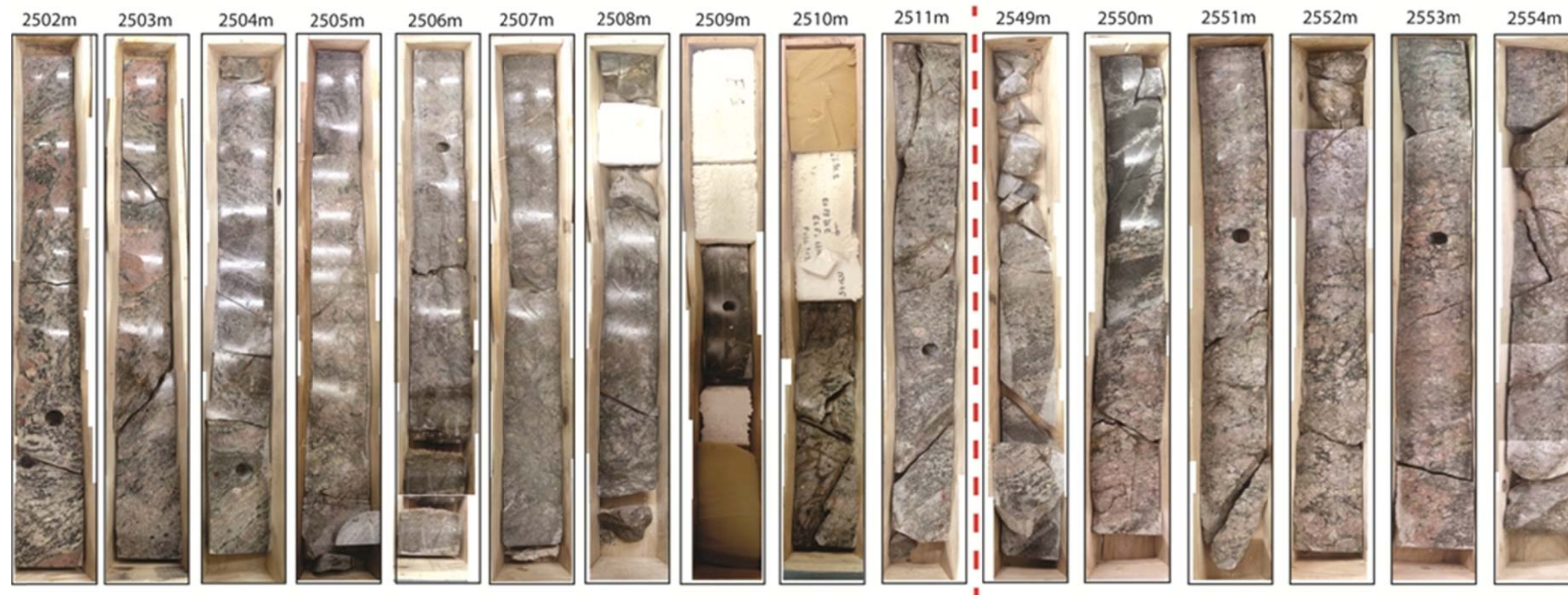
V: Photo-logs from core 206/7a-2 and photographs from 206/12-1

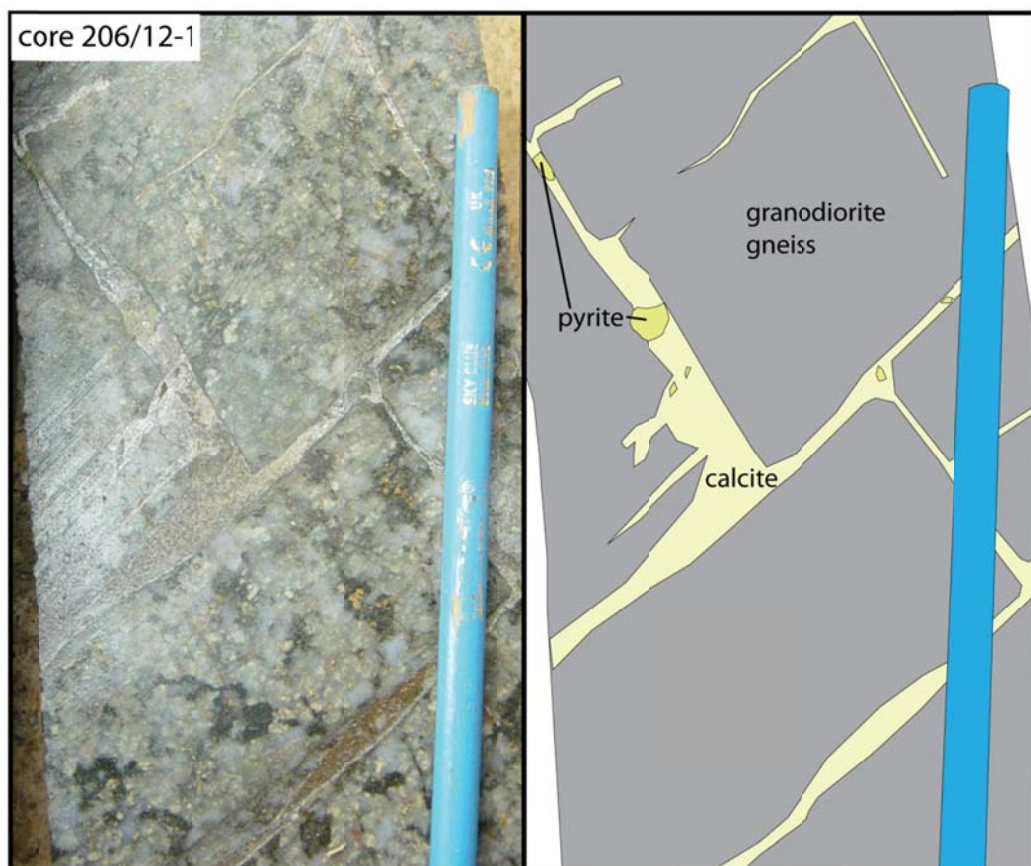
## CORE 206/7A/-2





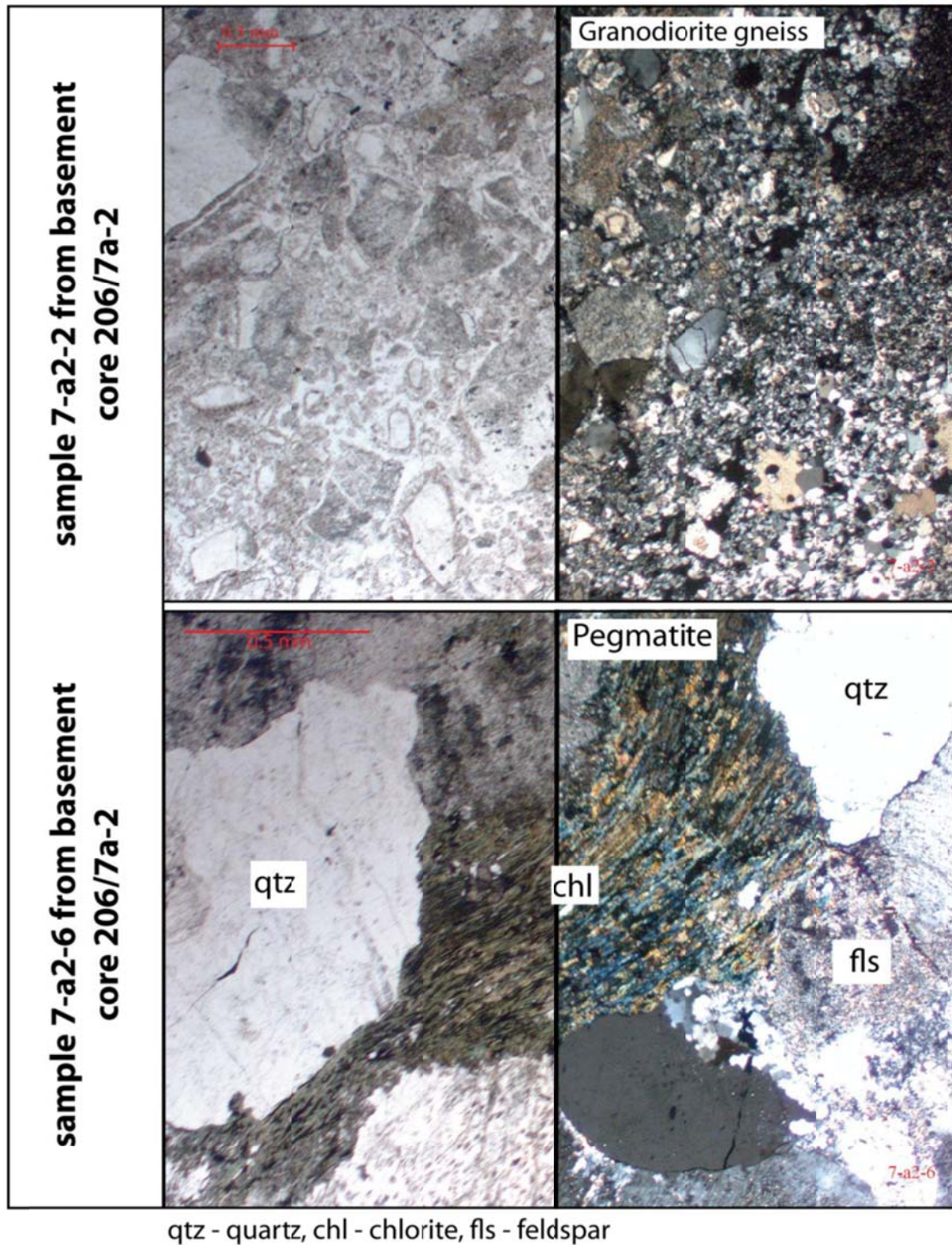
## CORE 206/7A/-2



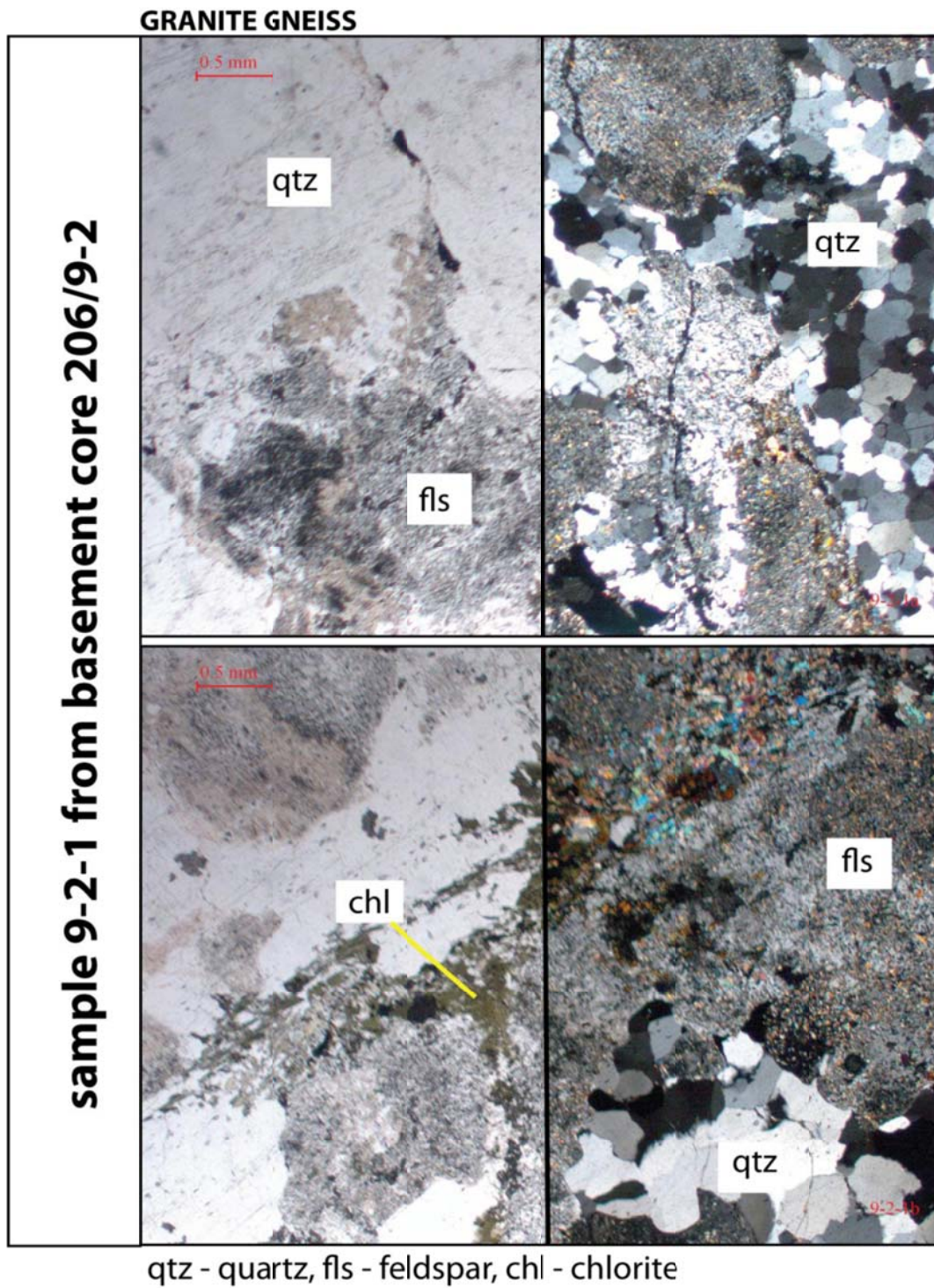


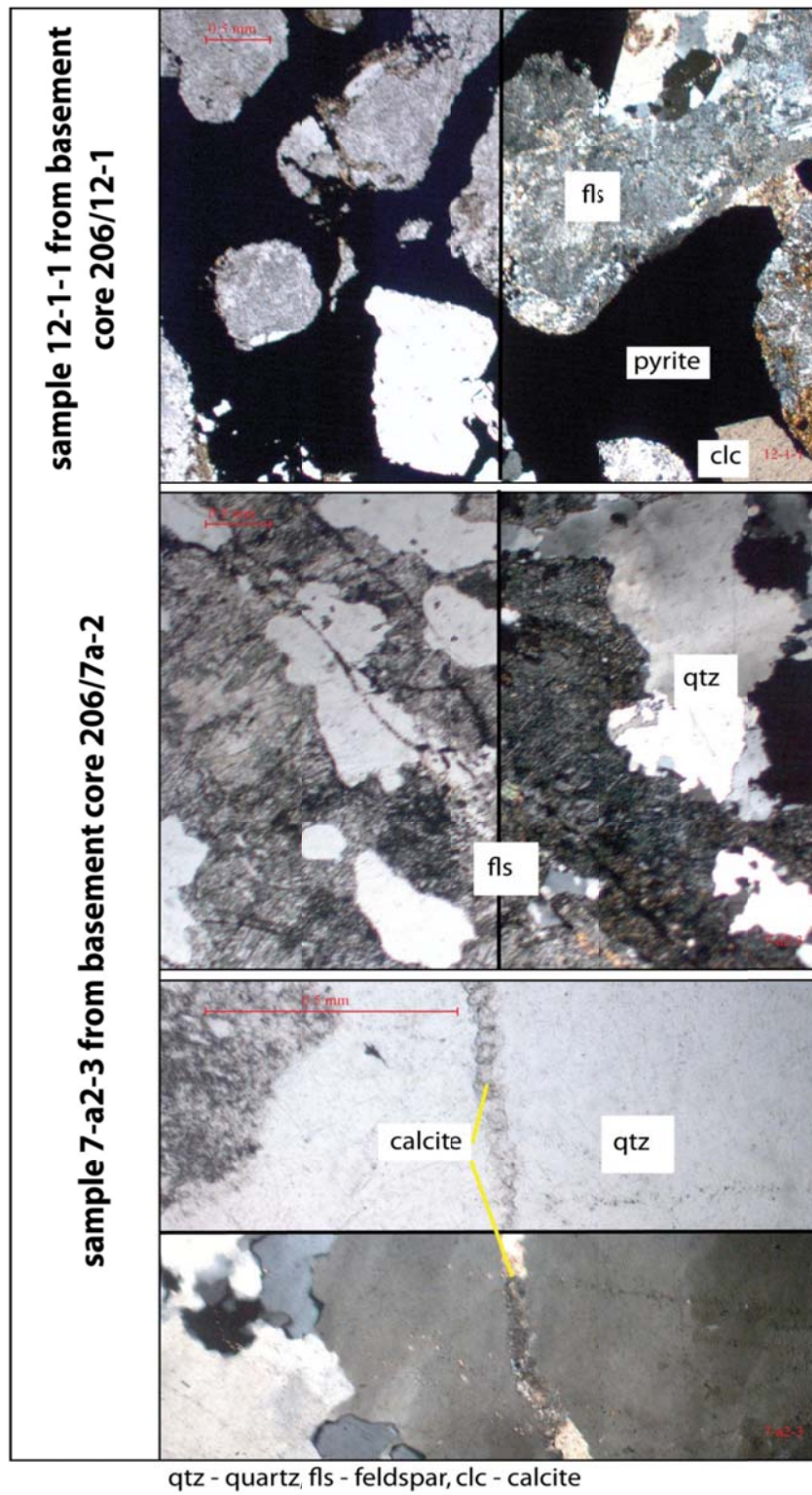


## VI: Thin section photographs





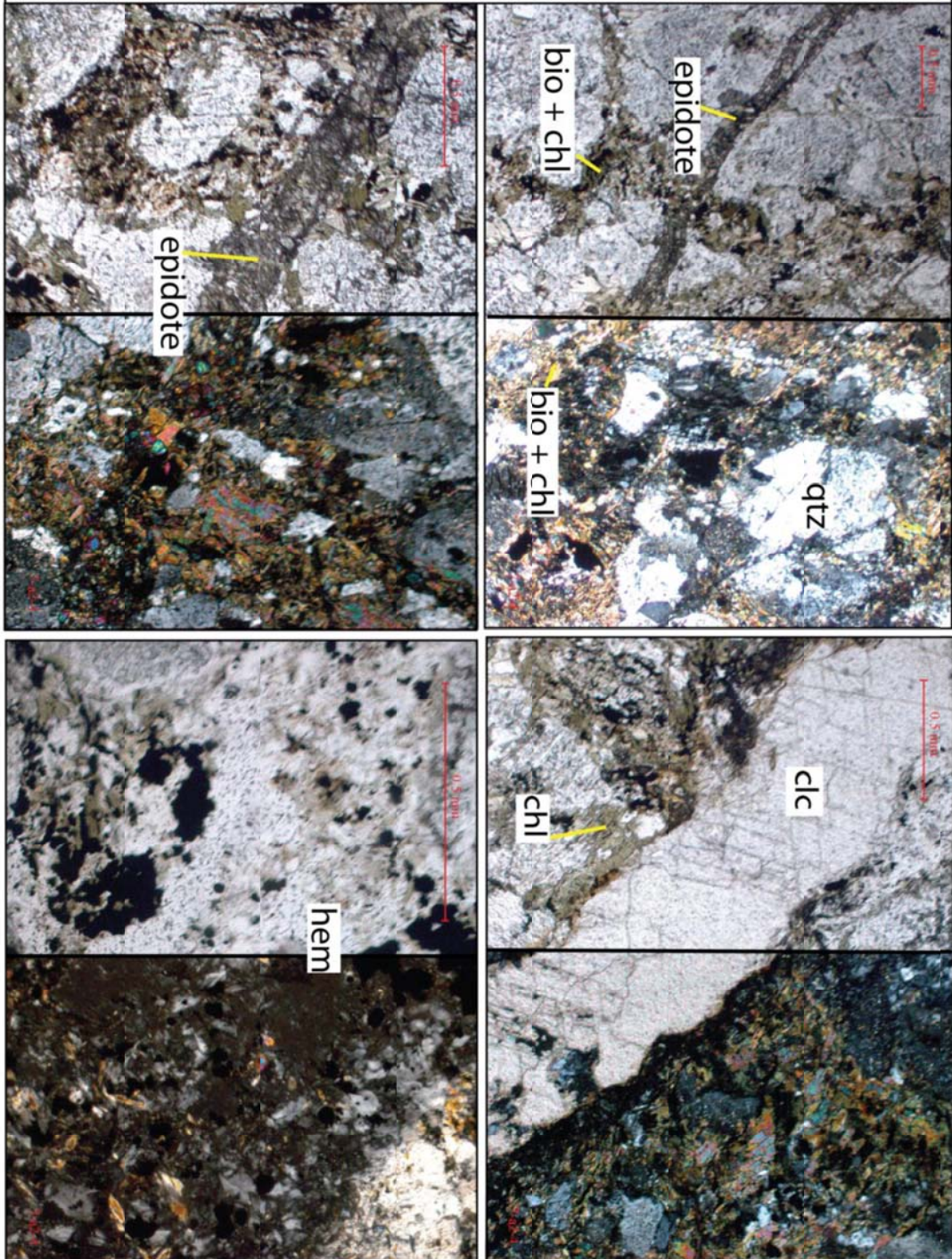




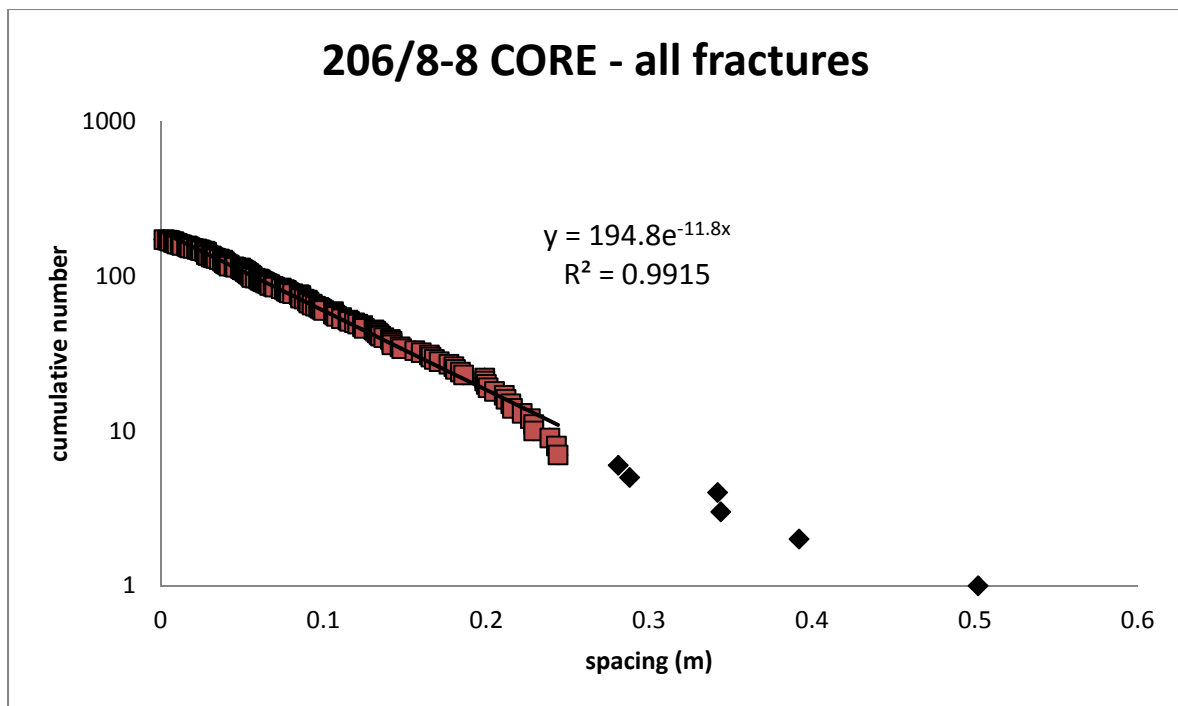
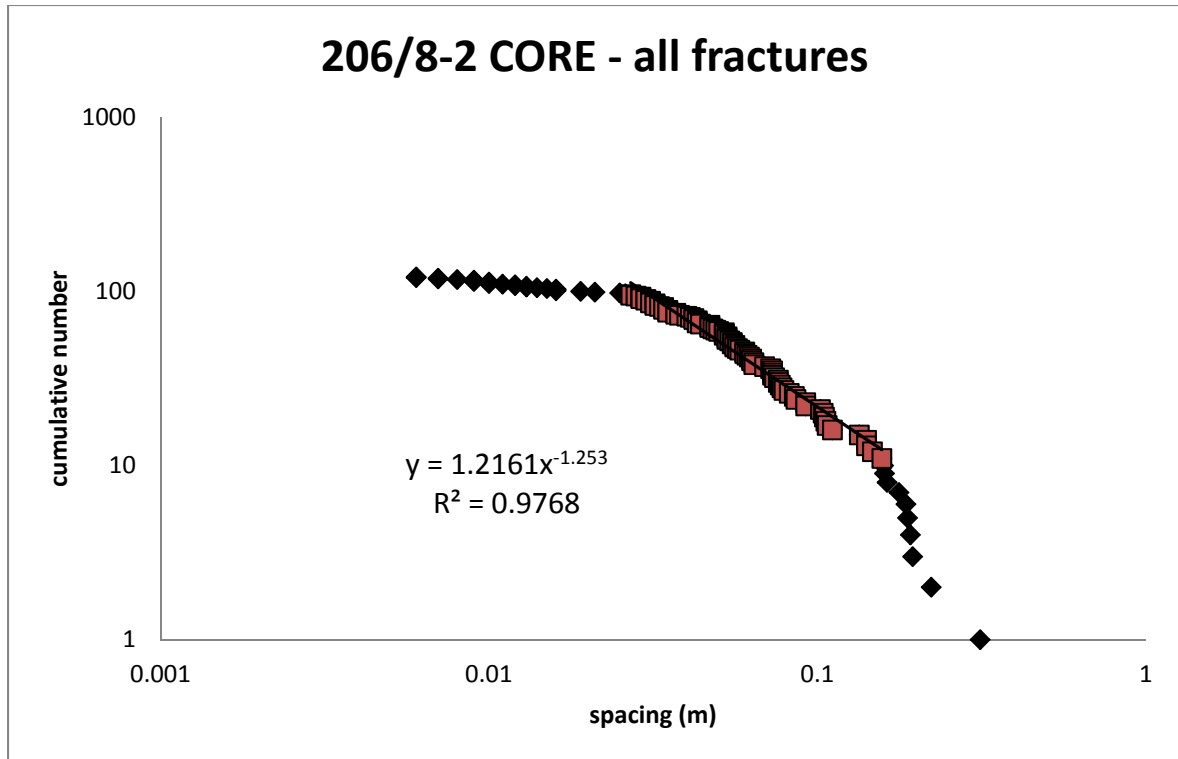


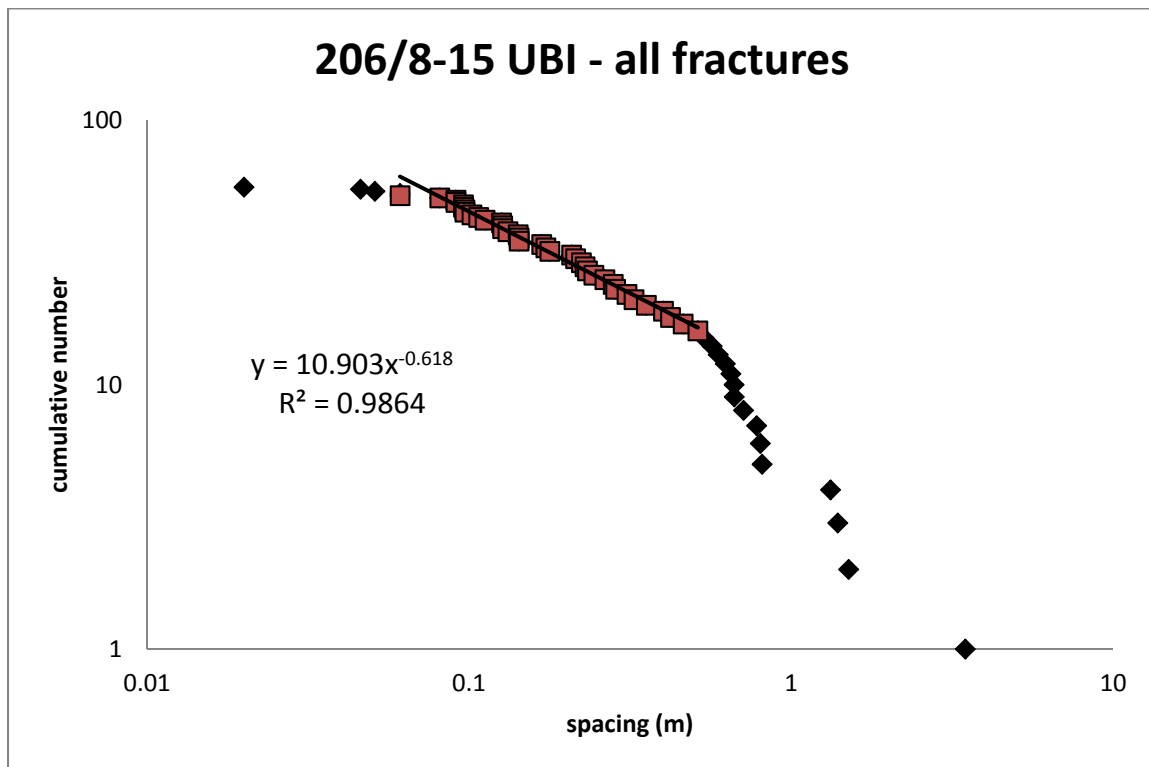
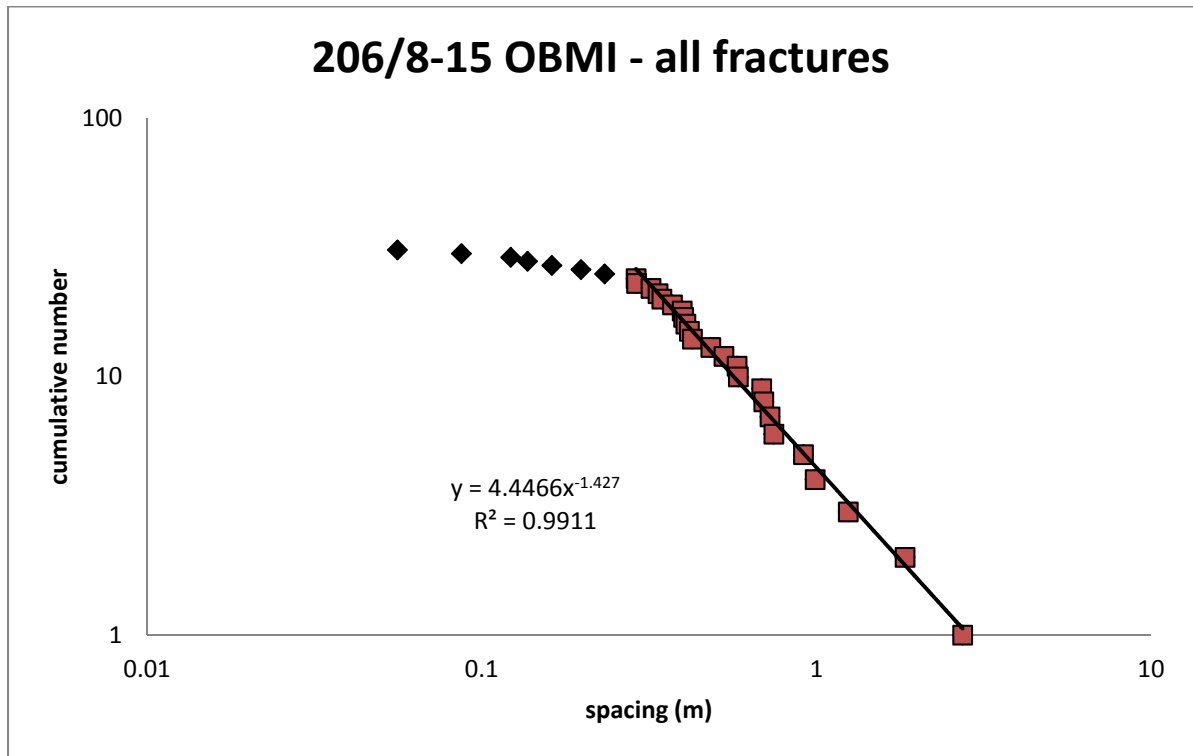
**sample 7-a2-4 from basement core 206/7a-2**

qtz - quartz, clc - calcite, hem - hematite, bio - biotite, chl - chlorite

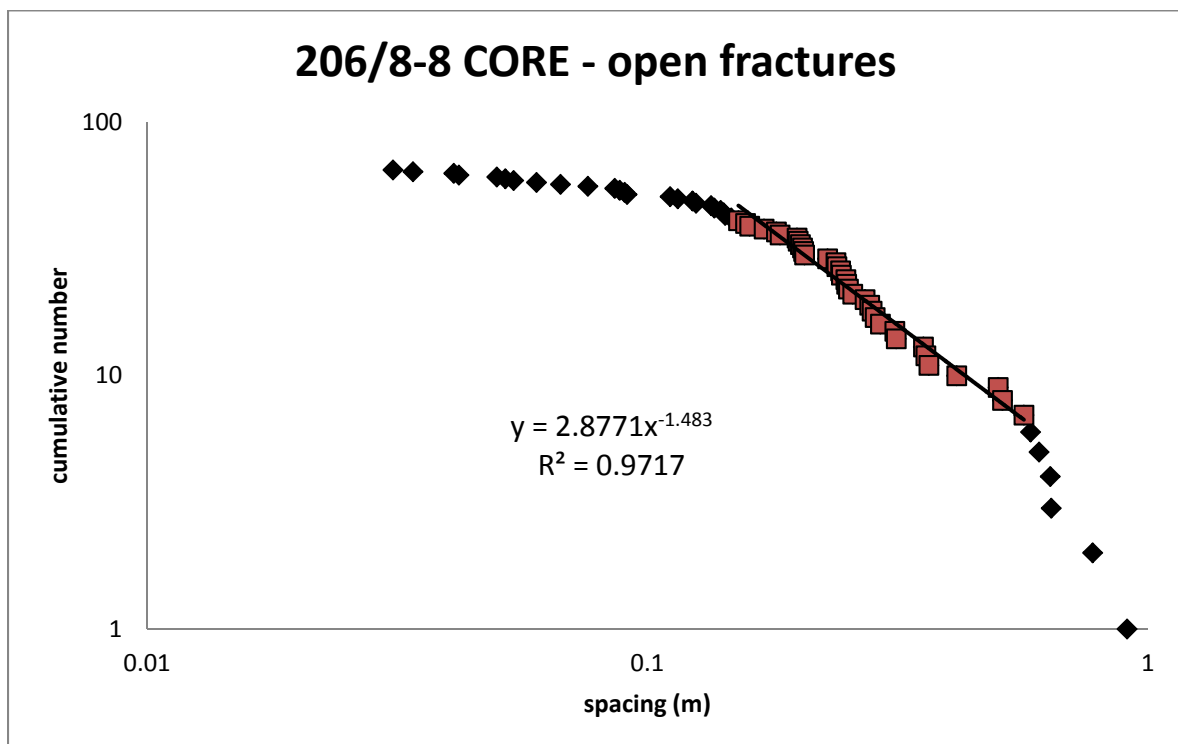
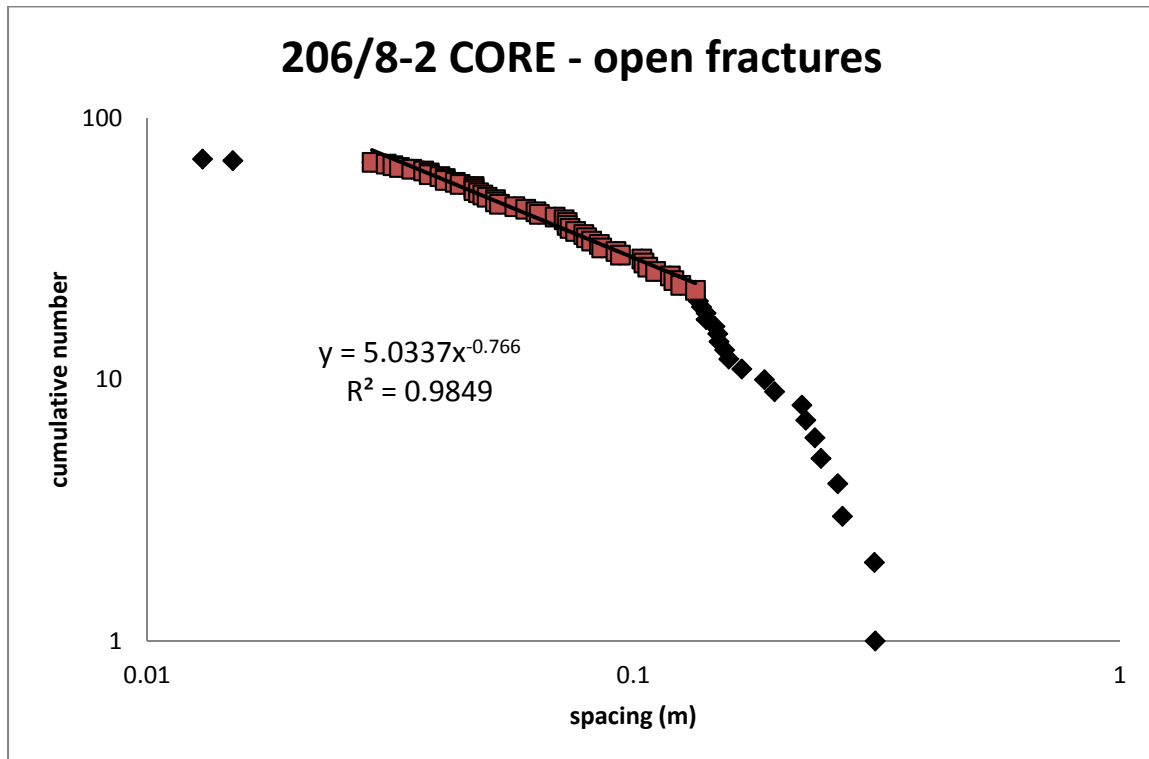


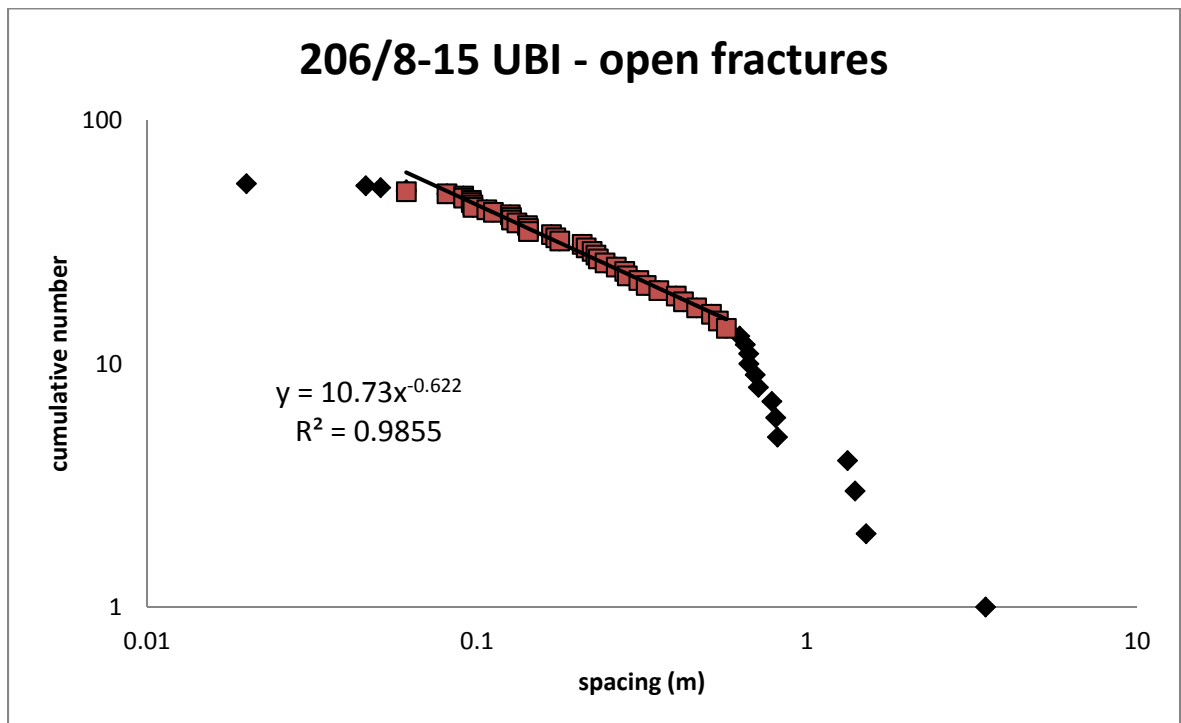
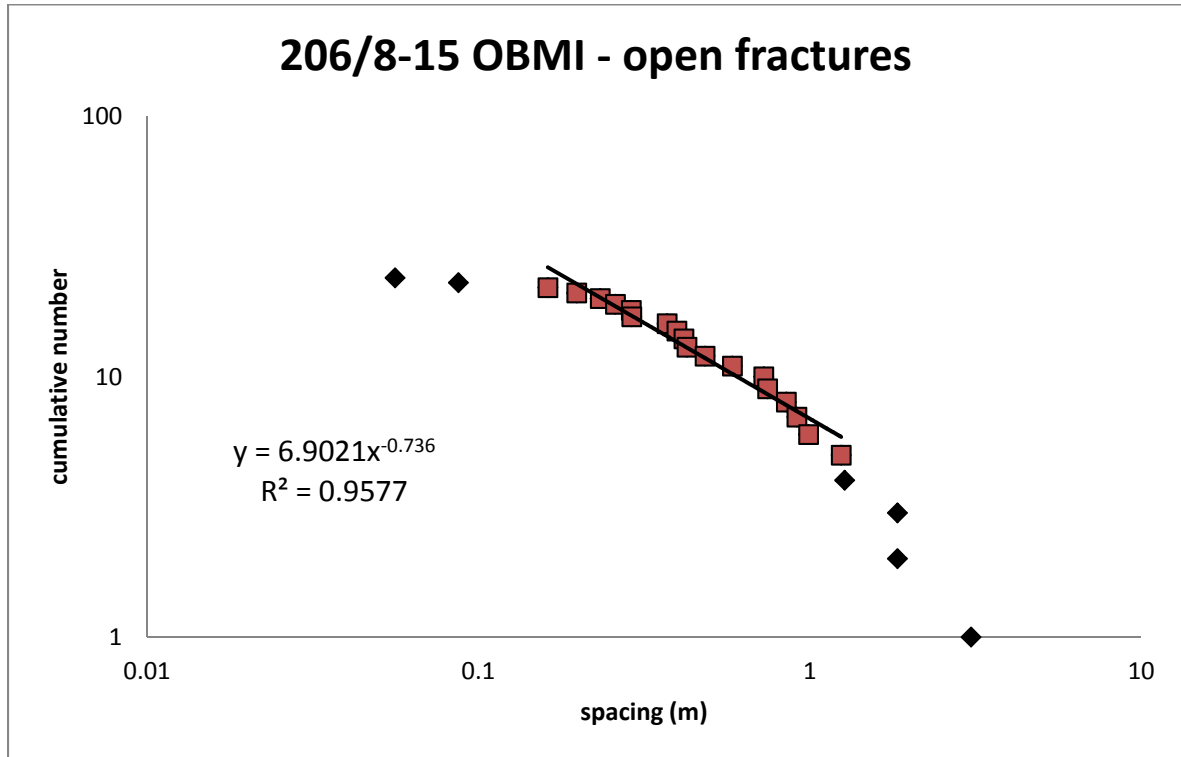
## VII: 1-dimensional fracture spacing population distribution plots for basement core samples

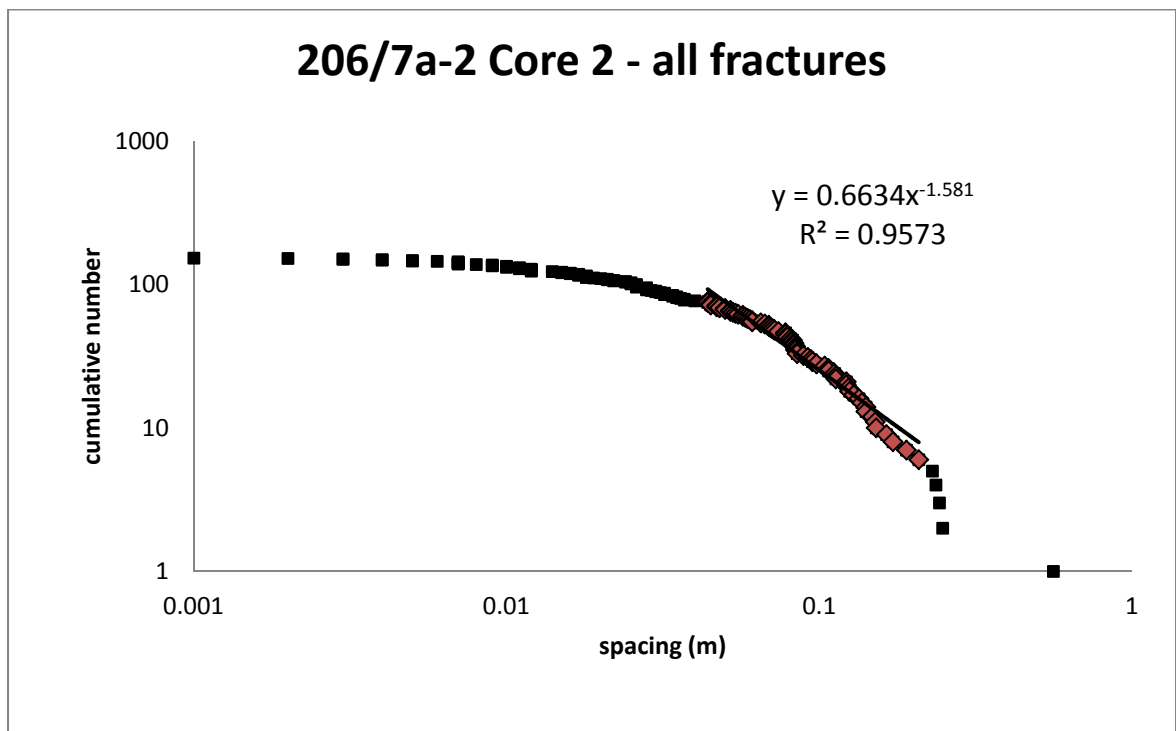
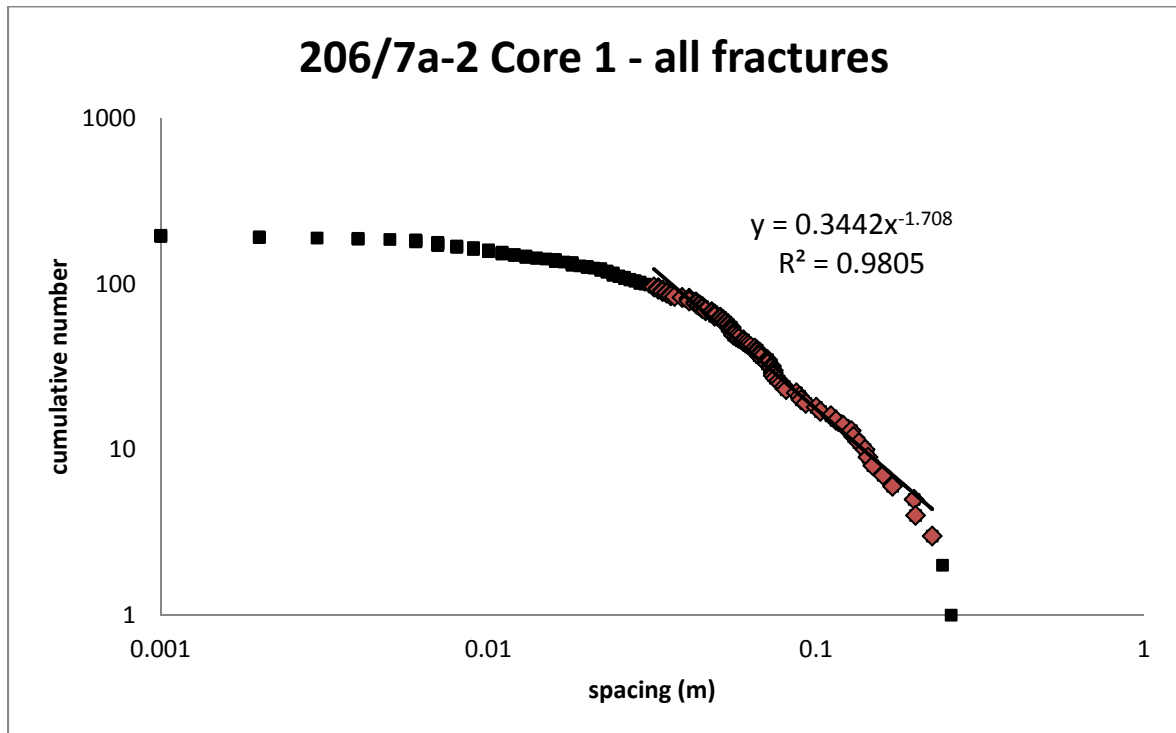


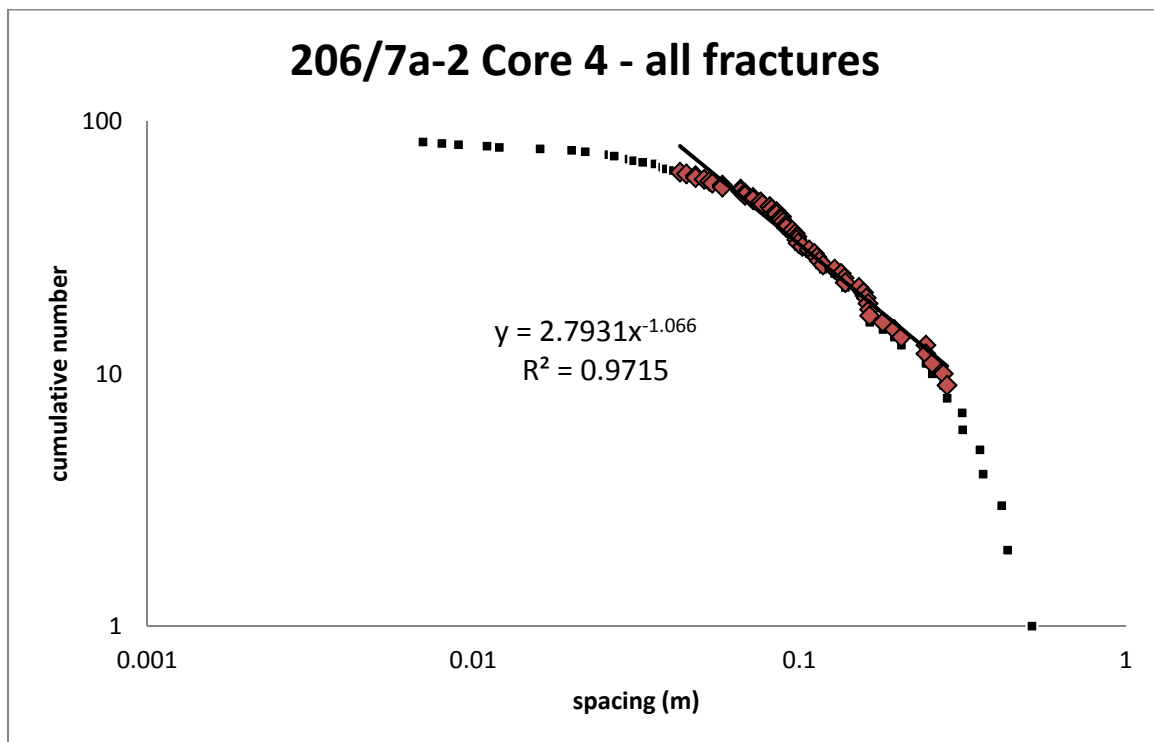
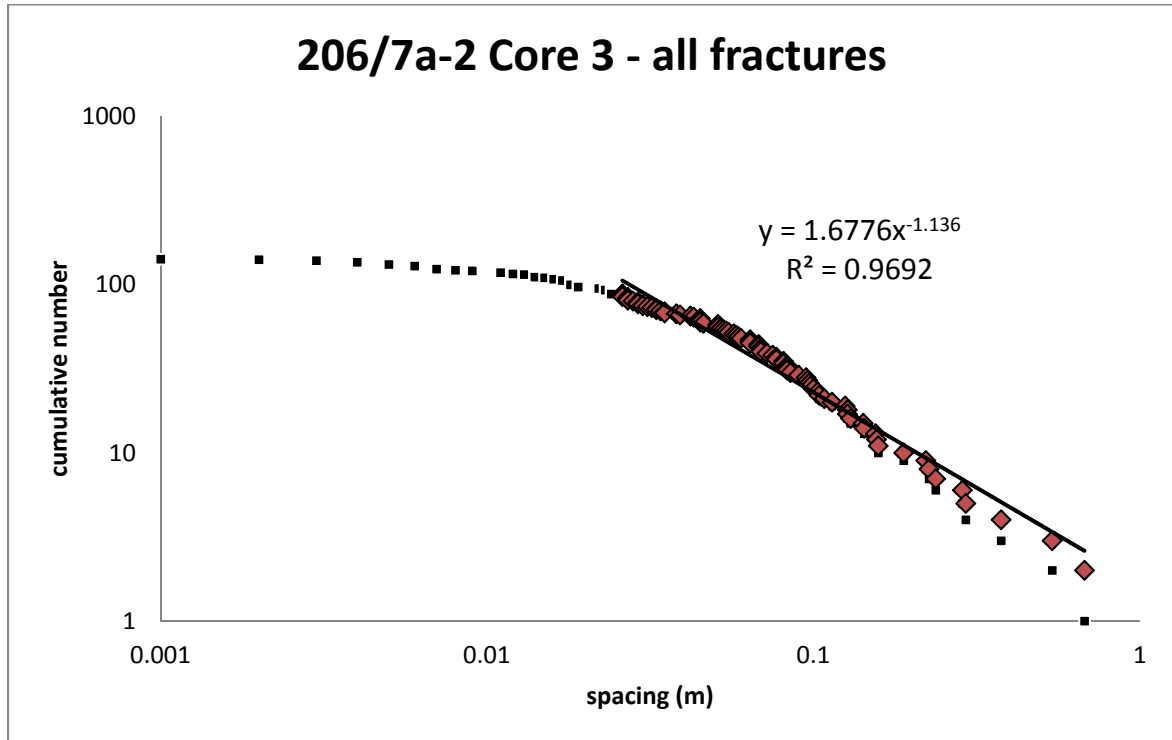


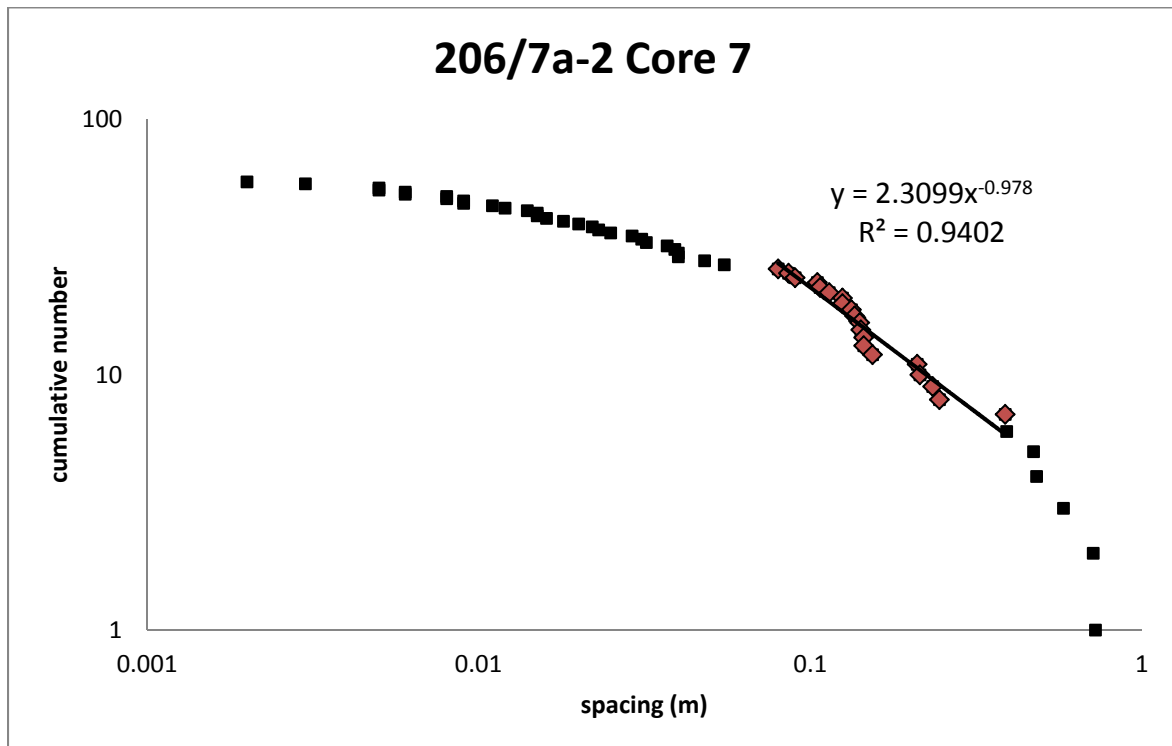
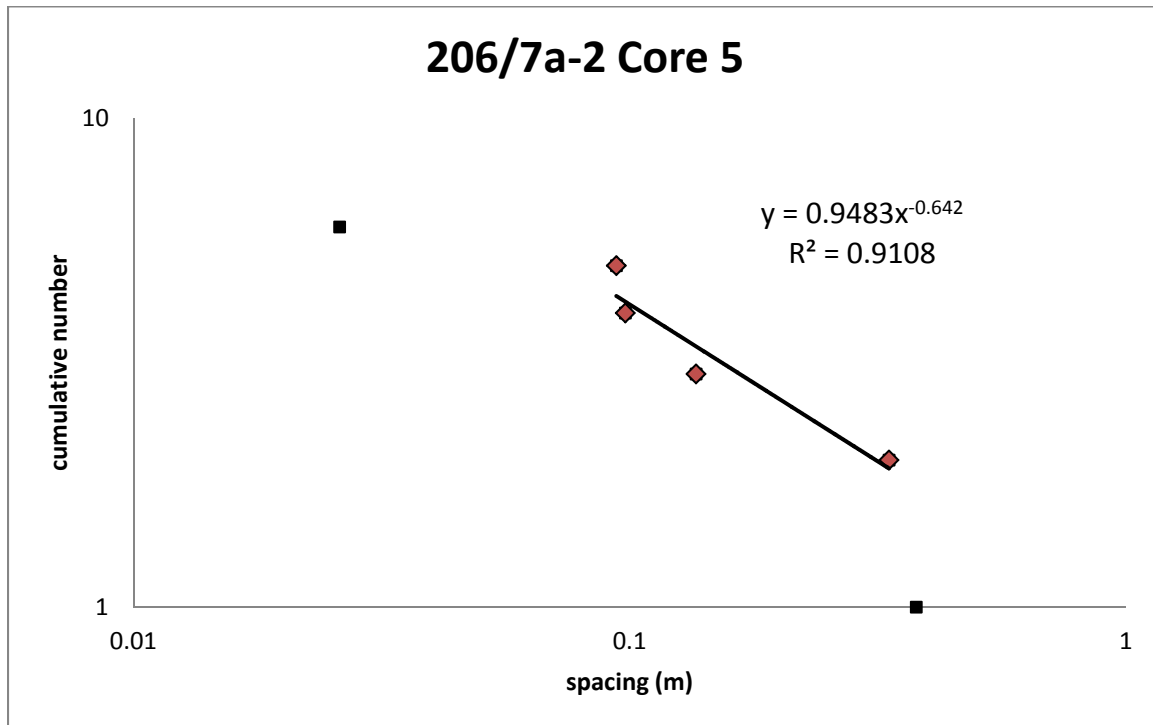


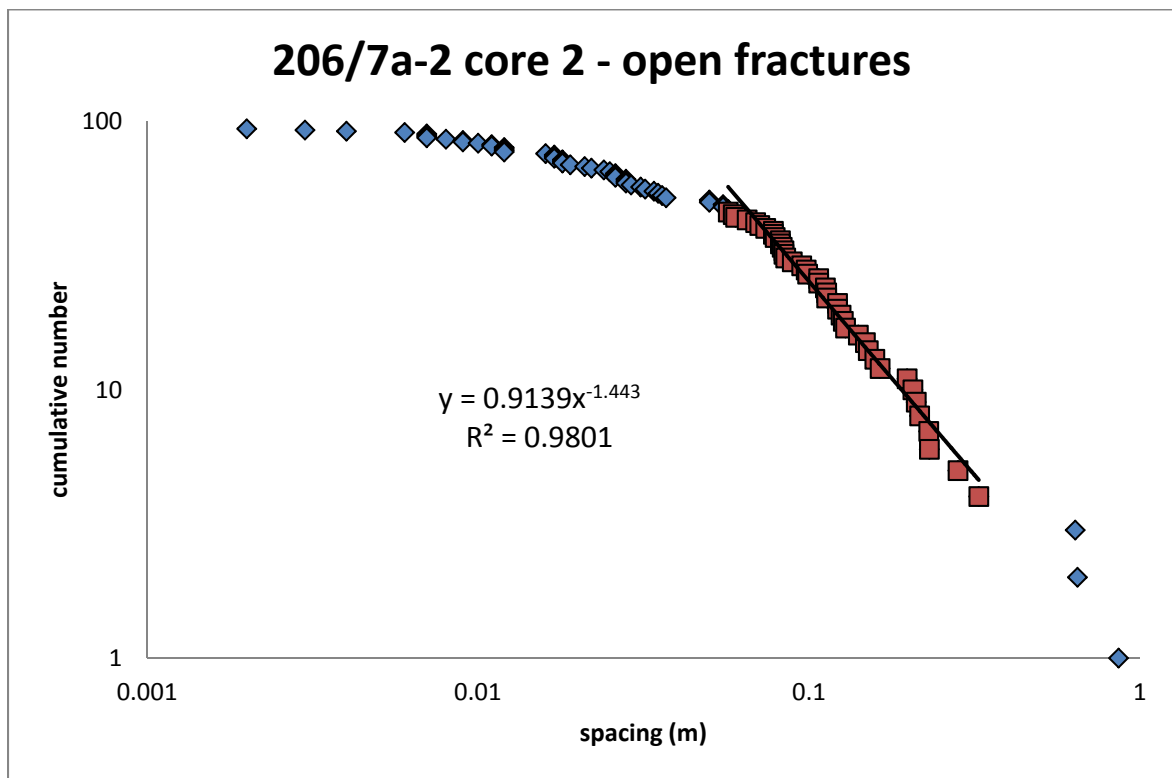
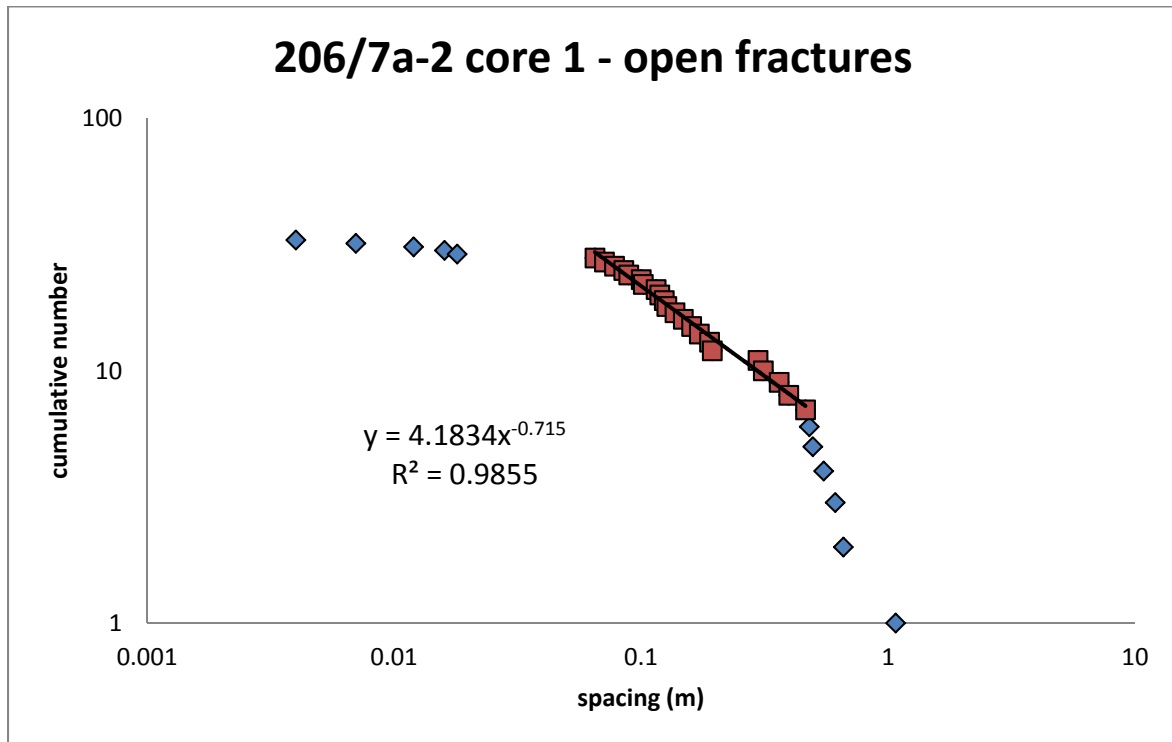


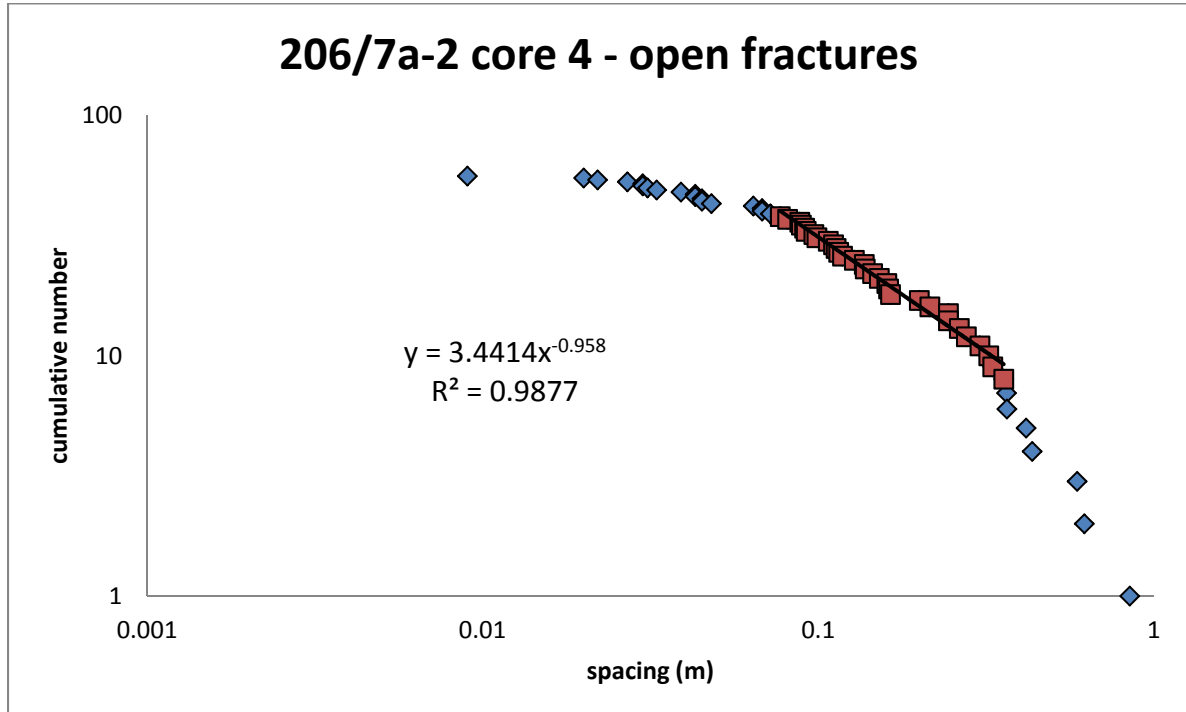
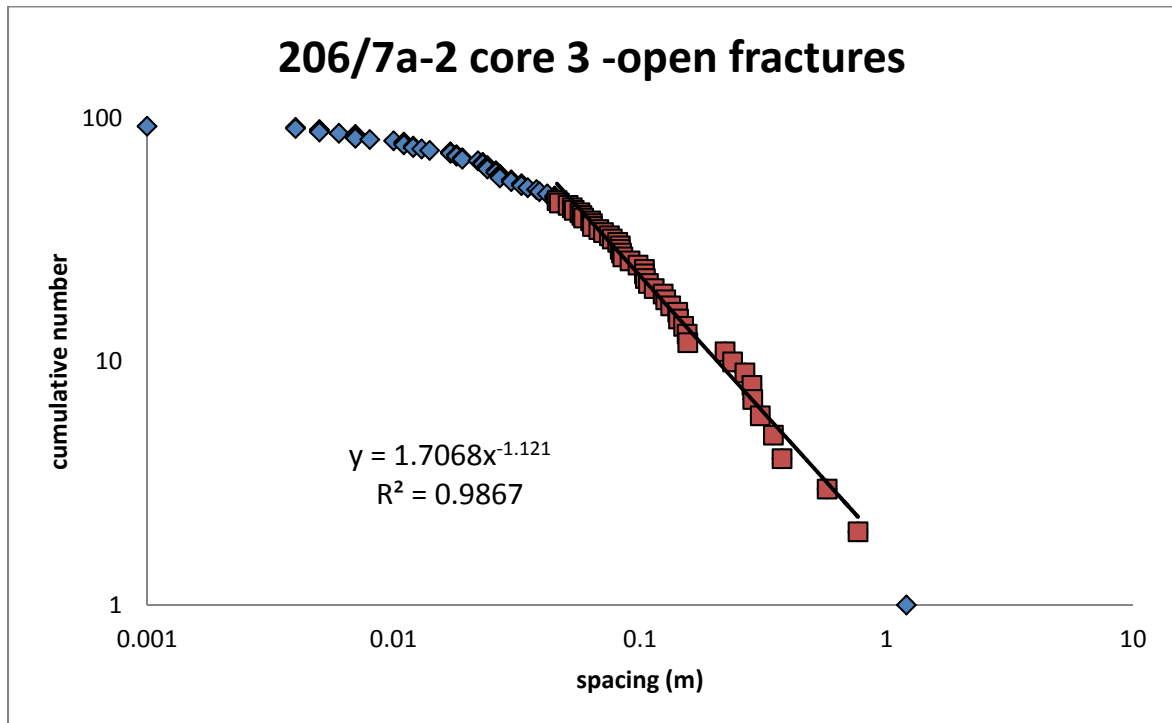


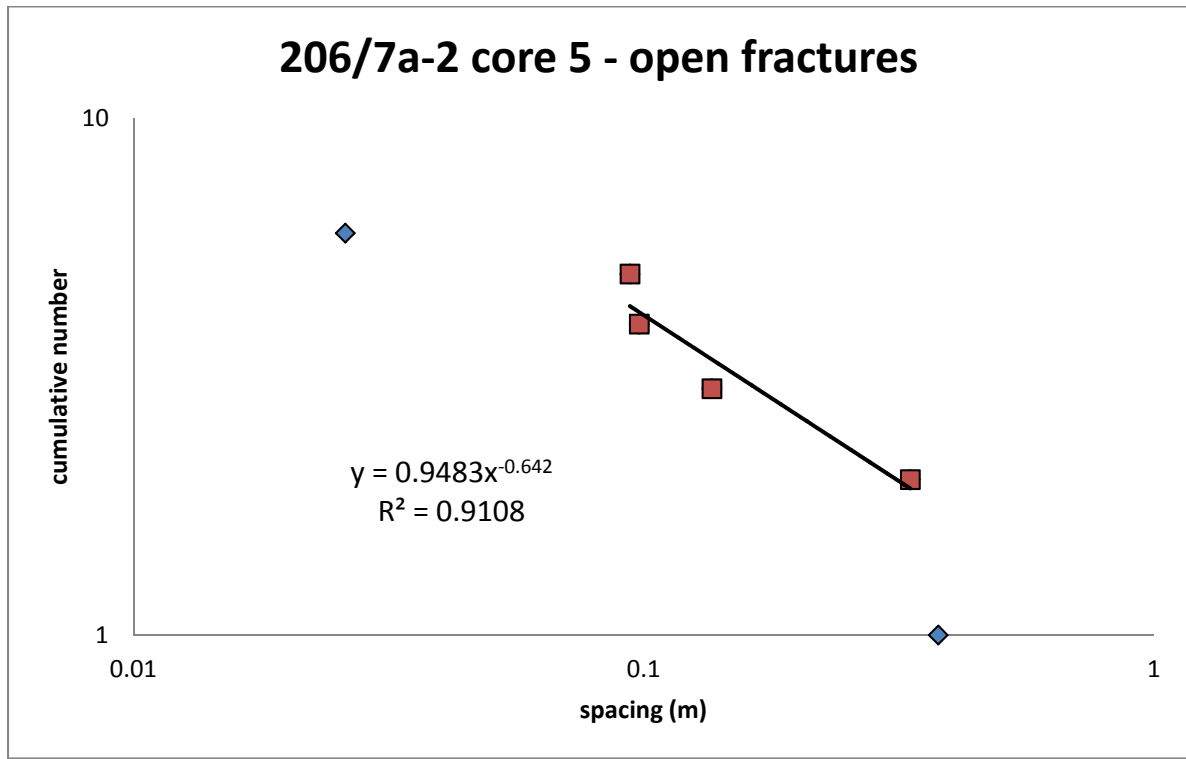










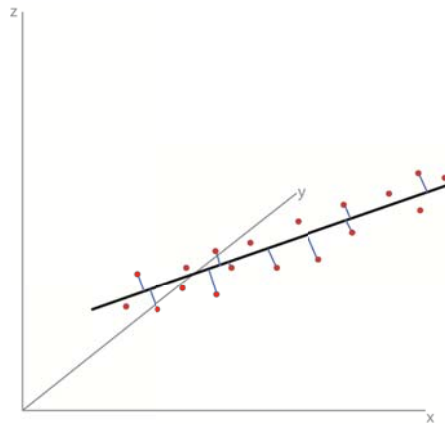




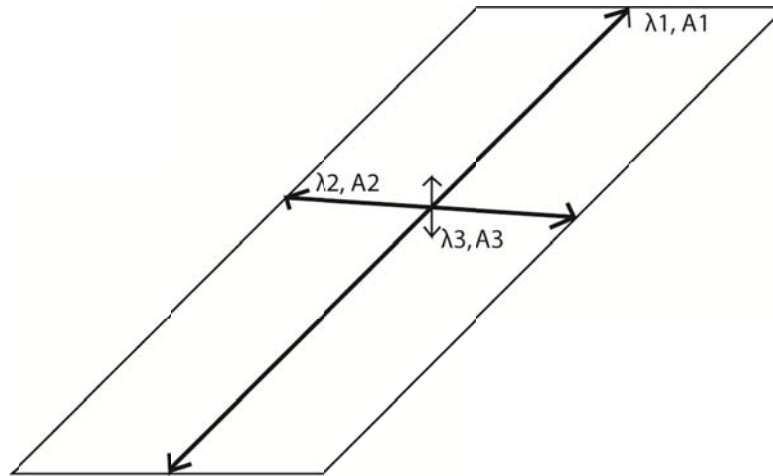
## **APPENDIX D**

### **I: Work-flow for converting RiScan® polyline picks into best-fit fracture planes**

Data points are collected from polyline interpretation of fracture planes from TLS outcrop point cloud datasets. Each data point has an x, y and z value which is plotted on a 3-dimensional graph. An orthogonal regression is plotted through the data points to minimise error away from the fracture plane.



The resulting x, y and z values are then entered into a matrix and the eigenvectors and eigenvalues for each fracture plane are determined. Eigenvectors ( $\lambda_1$ ,  $\lambda_2$  and  $\lambda_3$ ) determine the orientation of the resulting fracture plane and eigen-values (A1, A2 and A3) determine the size of the three fracture plane axes.



To ensure each interpreted fracture plane represents real fractures (as closely as possible),  $A_3$  should be very small,  $A_1$  should be long and  $A_2$  should be  $>10\text{cm}$  (follow the rule  $A_1 < A_2 < A_3$ ). Any data points creating fracture planes that do not meet this requirement are rejected. This is because data points that define an intermediate eigen-value that is  $<10\text{cm}$  are considered an unreliable fit to a plane due to the resolution of the terrestrial laser scan equipment ( $\sim 4\text{cm}$ ). By rejecting fractures that do not meet this eigen-value criteria ensures that the fracture planes used in the TLS models represent real fracture planes (both in orientation and size) as accurately as possible.

## II: Workflow for fracture presence analysis using S-Grids in Paradigm GoCad® 2009.2

### Creating the S-grids

1. Import outcrop surface: Objects/right-click on PointsSet/import from/DXF/ select outcrop surface file (should be saved as .DXF file) and click ok
  - a. The imported points can then be used to create an outcrop surface by: right-click on point object/merge all parts/surface (top toolbar)/new/from pointsSet/name/ select outcrop pointsSet and click ok
2. Import fracture surfaces: File/Import objects/Cultural Data/DXF/ select fracture .DXF file and click ok

3. Create voxel that encompasses the outcrop surface: Voxel (top toolbar)/new/from objects box/select outcrop surface and click ok (at this point you can set how many cells the s-grid will have by changing the nu, nv and nw values).
4. Create s-grid: sgrid (top toolbar)/from voxel/select voxel and click ok
5. Create region: sgrid selected on top toolbar/region/create/ object: sgrid/ region: name it and click ok
6. Initialize region: sgrid selected on top toolbar/region/ create/ initialize from surfaces/ stratigraphic grid: sgrid/ region name: newly created region/ surface: select all fracture surfaces/ click including intersecting cells and click ok (this process takes a while) – you should be left with all the fractures displayed as cubes which you can then paint with the properties you create in the next steps.
7. Create property: sgrid (top toolbar)/property/create property/property name:presence and click ok – then right click on newly created property/ initialize to constant/select region/make constant 5 and click ok (this makes the region visible, and the same colour, on the s-grid)
8. Steps 5-7 should be conducted for both the fractures and the outcrop surface.
9. Steps 3-7 should be conducted at, at least 3 different s-grid resolutions – this is achieved by varying the number of cells in each s-grid (Step 3)

#### **Fracture presence analysis: 2- dimensions**

10. View the s-grid square on (e.g. many of the analysis conducted in this thesis are completed from the west) and with the outcrop surface property turned on (the region should be off) count the number of coloured cells in each slice across the s-grid i.e. if you have 50 x 50 x 50 cells then you will have 50 slices through the TLS s-grid model.
  - a. For slices with large number of coloured cells, screenshots can be taken and image software such as UTHSCSA ImageTool used to semi-automatically count the coloured cells.
11. The same process should also be used to count the number of coloured cells for fractures (a cell will be coloured if it has been intersected by a fracture).

12. The number of cells intersected by fractures is then divided by the number of cells intersected by outcrop to determine the proportion of outcrop that is fractured.
13. To make this analysis fill the entire 2-dimensional slice the proportion of fractures in each outcrop slice is multiplied by the total number of cells in the slice.
14. These calculations should be completed for all resolutions of S-grid and the results plotted on a graph of cell size (length) versus number (fracture/outcrop\*total number of cells in slice). A trend line should then be plotted between the data points and the slope of this trend line is your fractal dimension which describes how much of each outcrop is filled by fractures.

#### **Fracture presence analysis: 3-dimensions**

15. Fracture presence can also be determined in 3-dimensions by determining the number of cells containing outcrop (right click on the sgrid region/ total number of cells in region/ the number will be displayed in bottom left hand corner of the screen) and the total number of cells containing fractures and using the calculation (fractures/outcrop \* total number of cells in volume) and following step 14.

#### **Fracture intersection analysis**

16. Fracture intersection analysis uses intersection curves between fractures and then follows steps 5-15 (at step 6 region should be initialised from curves not surfaces).
17. Intersection curves are created by surface (top toolbar)/ tools/ cut by surfaces/ cut all surfaces by each other (this takes a while) then curves (top toolbar)/ new/from surfaces/borders/one/number it and click ok/ use cross to select line where one fracture meets another. This can be a time consuming process but there is no automatic way to select surface intersections.
18. The resulting curves are then used from step 5 to conduct a fracture intersection analysis.



## References

---

- AGUILERA, R. 1995. *Naturally fractured reservoirs*, Tulsa, Okla, PennWell Books. 521 p.
- AHLGREN, S. & HOLMLUND, J. 2002. Outcrop scans give new view. *AAPG explorer*, 22-23.
- ALEKSANDROWSKI, P. 1985. Graphical determination of principal stress directions for slickenside lineation populations: an attempt to modify arthaud's method. *Journal of Structural Geology*, 7, 73-82.
- ALLEN, P. A. & MANGE-RAJETZKY, M. A. 1992. Devonian-Carboniferous sedimentary evolution of the Clair area, offshore north-western UK: impact of changing provenance. *Marine and Petroleum Geology*, 9, 29-52.
- ANDERSON, E. M. 1951. *The dynamics of faulting and dyke formation with applications to Britain*, Edinburgh, Oliver & Boyd. 206 p.
- ANDERSON, J. L., OSBORNE, R. H. & PALMER, D. F. 1983. Cataclastic rocks of the San Gabriel fault--an expression of deformation at deeper crustal levels in the San Andreas fault zone. *Tectonophysics*, 98, 209-240, 247-251.
- ANDERSSON, J. E., EKMAN, L., NORDQVIST, R. & WINBERG, A. 1991. Hydraulic testing and modelling of a low-angle fracture zone at Finnsjön, Sweden. *Journal of Hydrology*, 126, 45-77.
- ANGELIER, J. 1979. Determination of the mean principal directions of stresses for a given fault population. *Tectonophysics*, 56, T17-T26.
- ATKINSON, B. K. 1987. *Introduction to fracture mechanics and its geophysical applications*, Academic Press Limited. p. 1-26
- ATTFIELD, P. 1987. The Structural History of the Canisp Shear Zone. In: PARK, R. G. & TARNEY, J. (eds.) *Evolution of the Lewisian and comparable Precambrian high-grade terranes*. Geological Society, London, Special Publication, 165-173.
- BALLANTYNE, C. K., SCHNABEL, C. & XU, S. 2009. Readvance of the last British-Irish Ice Sheet during Greenland Interstade 1 (GI-1): the Wester Ross Readvance, NW Scotland. *Quaternary Science Reviews*, 28, 783-789.
- BAMFORD, D., NUNN, K., PRODEHL, C. & JACOB, B. 1978. LISPB – IV. Crustal structure of Northern Britain. *Geophysical Journal of the Royal Astronomical Society*, 54, 43-60.

- BARNICOAT, A. C. 1987. The causes of high-grade metamorphism of the Scourie complex, NW Scotland. *In: PARK, R. G. & TARNEY, J. (eds.) Evolution of the Lewisian and comparable Precambrian high-grade terranes*. Geological Society, London, Special Publication, v. 27, 73-79.
- BARR, D., HOLSWORTH, R. E. & ROBERTS, A. M. 1986. Caledonian ductile thrusting in a Precambrian metamorphic complex: The Moine of northwestern Scotland. *Geological Society of America Bulletin*, 97, 754-764.
- BARR, D., SAVORY, K. E., FOWLER, S. R., ARMAN, K. & MCGARRITY, J. P. 2007. Pre-development fracture modelling in the Clair field, west of Shetland. *In: LONERGAN, L., JOLLY, R. J. H., RAWNSLEY, K. & SANDERSON, D. J. (eds.) Fractured Reservoirs*. London: Geological Special Publication, v. 270, 205-225.
- BARTHOLOMEW, I. D., PETERS, J. M. & POWELL, C. M. 1993. Regional structural evolution of the North Sea: oblique slip and the reactivation of basement lineaments. Geological Society, London, v. 4, 1109-1122.
- BARTON, C. C. & LA POINTE, P. R. 1995a. *Fractals in petroleum geology and earth processes*, New York ; London, Plenum Press, 342 p.
- BARTON, C. C. & LA POINTE, P. R. 1995b. *Fractals in the earth sciences*, New York, Plenum Press, 265 p.
- BARTON, N. 1978. International society for rock mechanics commission on standardization of laboratory and field tests. *International Journal of Rock Mechanics and Mining Science* 15, 319-368.
- BATCHELOR, T., GUTMANIS, J. & ELLIS, F. 2010. Hydrocarbon production from fractured basement formations. Geoscience Limited, 1-40.
- BEACH, A. 1973. The Mineralogy of High Temperature Shear Zones at Scourie, N. W. Scotland. *J. Petrology*, 14, 231-248.
- BEACH, A. 1980. Retrogressive metamorphic processes in shear zones with special reference to the Lewisian complex. *Journal of Structural Geology*, 2, 257-263.
- BEACOM, L., HOLDSWORTH, R. E., MCCAFFREY, K. J. W. & ANDERSON, T. 2001. A quantitative study of the influence of pre-existing compositional and fabric heterogeneities upon fracture zone development during basement reactivation. *In: HOLDSWORTH, R. E., STRACHAN, R. A.,*

- MAGLOUGHLIN, J. F. & KNIPE, R. J. (eds.) *The nature and tectonic significance of fault zone weakening*. Geological Society Special Publication, v. 186, 195-211.
- BEACOM, L. E. 1999. *The Kinematic Evolution of Reactivated and Non-Reactivated Faults in Basement Rocks, NW Scotland*. Ph.D., Queen's University of Belfast.
- BEACOM, L. E., ANDERSON, T. B. & HOLDSWORTH, R. E. 1999. Using basement-hosted clastic dykes as syn-rifting palaeostress indicators: an example from the basal Stoer Group, northwest Scotland. *Geological Magazine*, 136, 301-310.
- BELL, B. R. & JOLLEY, D. W. 1997. Application of palynological data to the chronology of the Palaeogene lava fields of the British Province: implications for magmatic stratigraphy. *Journal of the Geological Society*, 154, 701-708.
- BELLIAN, J. A., KERANS, C. & JENNETTE, D. C. 2005. Digital Outcrop Models: Applications of Terrestrial Scanning Lidar Technology in Stratigraphic Modeling. *Journal of Sedimentary Research* 75, 166-176.
- BERGBAUER, S. & KING, R. 2009. Clair Ridge - End - of - Appraise Fracture Uncertainty Statement. BP, internal presentation.
- BERTHÉ, D., CHOUKROUNE, P. & JEGOUZO, P. 1979. Orthogneiss, mylonite and non coaxial deformation of granites: the example of the South Armorican Shear Zone. *Journal of Structural Geology*, 1, 31-42.
- BIKERMAN, M., BOWES, D. R. & VAN BREEMEN, O. 1975. Rb-Sr whole rock isotopic studies of Lewisian metasediments and gneisses in the Loch Maree region, Ross-shire. *Journal of the Geological Society*, 131, 237-254.
- BINNS, P. E., MCQUILLIN, R. & KENOLTY, N. 1974. *The geology of the Sea of Hebrides*, London, H. M. Stationary Office, No 73/14.
- BLINKINSOP, T. G. & TRELOAR, P. J. 1995. Geometry, classification and kinematics of S-C and S-C' fabrics in the Mushandike area, Zimbabwe. *Journal of Structural Geology*, 17, 397-408.
- BLUNDELL, D. J., HURICH, C. A. & SMITHSON, S. B. 1985. A model for the MOIST seismic reflection profile, N Scotland. *Journal of the Geological Society*, 142, 245-258.
- BONNET, E., BOUR, O., ODLING, N., DAVY, P., MAIN, I., COWIE, P. & BERKOWITZ, B. 2001. Scaling of fracture systems in geological media. *Reviews of Geophysics*, 39, 347-384.



- BONS, P. D. 2000. The formation of veins and their microstructures. *In*: JESSELL, M. W. & URAI, J. L. (eds.) *Stress, strain and structure. A volume in honour of W D Means*. Journal of the Virtual Explorer, v 2.
- BORGOS, H. G., COWIE, P. A. & DAWERS, N. H. 2000. Practicalities of extrapolating one-dimensional fault and fracture size-frequency distributions to higher-dimensional samples. *J. Geophys. Res.*, 105, 28377-28391.
- BOULTON, G. S., PEACOCK, J. D. & SUTHERLAND, D. G. 2002. Quaternary. *In*: TREWIN, N. H. (ed.) *The Geology of Scotland*. London: Geological Society, 409-430.
- BOUR, O., DAVY, P., DARCEL, C. & ODLING, N. 2002. A statistical scaling model for fracture network geometry, with validation on a multiscale mapping of a joint network (Hornelen Basin, Norway). *J. Geophys. Res.*, 107, 2113.
- BOWES, D. R. & GHALY, T. S. 1964. Age relations of Lewisian basic rocks, south of Gairloch, Ross-shire. *Geological Magazine*, 101, 150-160.
- BRADWELL, T., STOKER, M. & KRABBENDAM, M. 2008a. Megagrooves and streamlined bedrock in NW Scotland: The role of ice streams in landscape evolution. *Geomorphology*, 97, 135-156.
- BRADWELL, T., STOKER, M. & LARTER, R. 2007. Geomorphological signature and flow dynamics of The Minch palaeo-ice stream, northwest Scotland. *Journal of Quaternary Science*, 22, 609-617.
- BRADWELL, T., STOKER, M. S., GOLLEDGE, N. R., WILSON, C. K., MERRITT, J. W., LONG, D., EVEREST, J. D., HESTVIK, O. B., STEVENSON, A. G., HUBBARD, A. L., FINLAYSON, A. G. & MATHERS, H. E. 2008b. The northern sector of the last British Ice Sheet: Maximum extent and demise. *Earth-Science Reviews*, 88, 207-226.
- BRODIE, J. & WHITE, N. 1994. Sedimentary basin inversion caused by igneous underplating: Northwest European continental shelf. *Geology*, 22, 147-150.
- BRUHN, R. L., YONKEE, W. A. & PARRY, W. T. 1990. Structural and fluid-chemical properties of seismogenic normal faults. *Tectonophysics*, 175, 139-157.
- BUCHAN, K. L., MERTANEN, S., PARK, R. G., PESONEN, L. J., ELMING, S. A., ABRAHAMSEN, N. & BYLUND, G. 2000. Comparing the drift of Laurentia and Baltica in the Proterozoic: the importance of key palaeomagnetic poles. *Tectonophysics*, 319, 167-198.

- BUTLER, R. W. H. 1982. A structural analysis of the Moine Thrust Zone between Loch Eriboll and Foinaven, NW Scotland. *Journal of Structural Geology*, 4, 19-29.
- BUTLER, R. W. H. 1984. Structural evolution of the Moine thrust belt between Loch More and Glendhu, Sutherland. *Scottish Journal of Geology*, 20, 161-179.
- BUTLER, R. W. H. 2010. The role of thrust tectonic models in understanding structural evolution in NW Scotland. *Geological Society, London, Special Publications*, 335, 293-320.
- BUTLER, R. W. H., HOLDSWORTH, R. E. & LLOYD, G. E. 1997. The role of basement reactivation in continental deformation. *Journal of the Geological Society*, 154, 69-71.
- BYERLEE, J. 1993. Model for episodic flow of high-pressure water in fault zones before earthquakes. *Geology*, 21, 303-306.
- CAINE, J. S., EVANS, J. P. & FORSTER, C. B. 1996. Fault zone architecture and permeability structure. *Geology*, 24, 1025-1028.
- CARTER, K. E. & DWORKIN, S. I. 1990. Channelized fluid flow through shear zones during fluid-enhanced dynamic recrystallization, Northern Apennines, Italy. *Geology*, 18, 720-723.
- CARTER, N. & LINES, L. 2001. Fault imaging using edge detection and coherency measures on Hibernia 3-D seismic data. *The Leading Edge*, 20, 64-69.
- CARTWRIGHT, I. & BARNICOAT, A. C. 1987. Petrology of Scourian supracrustal rocks and orthogneisses from Stoer, NW Scotland: implications for the geological evolution of the Lewisian complex. In: PARK, R. G. & TARNEY, J. (eds.) *Evolution of the Lewisian and comparable Precambrian high-grade terrains*. Oxford: Geological Society by Blackwell Scientific, v 27, 93-107.
- CHESTER, F. M., EVANS, J. P. & BIEGEL, R. L. 1993. Internal Structure and Weakening Mechanisms of the San Andreas Fault. *J. Geophys. Res.*, 98, 771-786.
- CHESTER, F. M. & LOGAN, J. M. 1987. Composite planar fabric of gouge from the Punchbowl Fault, California. *Journal of Structural Geology*, 9, 621-634, IN5-IN6.
- CHILDS, C., WALSH, J. J. & WATTERSON, J. 1990. A method for estimation of the density of fault displacements below the limits of seismic resolution in reservoir formations. In: Buller, A. T., Berg, O., Hejelmeland, J., Kleppe, O., Torsaeter, O. & Aasen, J. O., *North Sea oil and gas reservoirs II*. Kluwer Academic Publishers, 309-318.

- CHOPRA, S. & MARFURT, K. J. Year. Seismic Attributes for Fault/Fracture Characterization. *In: Let it Flow - CSPG CSEG Convention*, 2007.
- CHRISTENSEN, K., OLAMI, Z. & BAK, P. 1992. Deterministic 1/f noise in nonconservative models of self-organized criticality. *Physical Review Letters*, 68, 2417.
- CLIFFORD, P. J., O'DONOVAN, A. R., SAVORY, K. E., SMITH, G. & BARR, D. Year. Clair Field - Managing Uncertainty in the Development of a Waterflooded Fractured Reservoir. *In: Offshore Europe*, 2005 Aberdeen. Society of Petroleum Engineers.
- COBBOLD, P. R., MEISLING, K. E. & MOUNT, V. S. 2001. Reactivation of an Obliquely Rifted Margin, Campos and Santos Basins, Southeastern Brazil. *AAPG Bulletin*, 85, 1925-1944.
- CONEY, D., FYFE, T. B., RETAIL, P. & SMITH, P. J. 1993. *Clair appraisal: the benefits of a co-operative approach*, Geological Society, London, Petroleum Geology Conference Series, v4, 1409-1420.
- CONEY, P. J., JONES, D. L. & MONGER, J. W. H. 1980. Cordilleran suspect terranes. *Nature*, 288, 329-333.
- CONWAY, A. 2010. Current understanding of faulting in the Clair Field. Personal Communication.
- CONWAY, A., COLE, A., LARSON, H. & KWIATKOWSKI, A. 2008. NSBU GGRE Conference. internal presentation.
- CORFU, F., HEAMAN, L. M. & ROGERS, G. 1994. Polymetamorphic evolution of the Lewisian complex, NW Scotland, as recorded by U-Pb isotopic compositions of zircon, titanite and rutile. *Contributions to Mineralogy and Petrology*, 117, 215-228.
- COUZENS, T. 2008. *Greater Clair Tectono-stratigraphy*, internal report.
- COWARD, M. P. 1985. The thrust structures of southern Assynt, Moine thrust zone. *Geological Magazine*, 122, 595-607.
- COWARD, M. P. 1990a. The Precambrian, Caledonian and Variscan framework to NW Europe. *Geological Society, London, Special Publications*, 55, 1-34.
- COWARD, M. P. 1990b. Shear zones at the Laxford front, NW Scotland and their significance in the interpretation of lower crustal structure. *Journal of the Geological Society*, 147, 279-286.

- COWARD, M. P. & PARK, R. G. 1987. The role of mid-crustal shear zones in the Early Proterozoic evolution of the Lewisian. *In: PARK, R. G. & TARNEY, J. (eds.) Evolution of the Lewisian and comparable high-grade terranes*. Geological Society, London, Special Publication, v 27, 127-138.
- CRESSWELL, D. & PARK, R. G. 1973. The metamorphic history of the Lewisian rocks of the Torridon area in relation to that of the remainder of the Laxfordian belt. *In: PARK, R. G. & TARNEY, J. (eds.) The early Precambrian rocks of Scotland and related rocks of Greenland*. University of Keele, pp 200.
- DALY, M. C., CHOROWICZ, J. & FAIRHEAD, J. D. 1989. Rift basin in Africa: the influence of reactivated steep basement shear zones. *In: COOPER, M. A. & WILLIAMS, G. D. (eds.) Inversion Tectonics*. Geological Society, London, Special Publications, v 44, 309-334.
- DALZIEL, I. W. D. & SOPER, N. J. 2001. Neoproterozoic Extension on the Scottish Promontory of Laurentia: Paleogeographic and Tectonic Implications. *The Journal of Geology*, 109, 299-317.
- DAVENPORT, C. A., RINGROSE, P. S., BECKER, A., HANCOCK, P. & FENTON, C. 1989. *Geological investigations of late and post glacial earthquake activity in Scotland*. *In: Gregersen, S. and Basham, P. Earthquakes at North-Atlantic Passive Margins: Neo-tectonics and Post-Glacial rebound*. Proceedings of the NATO advances research workshop, Vordingborg, Denmark, 1988, May 9-13, 175-194.
- DAVIES, F. B. 1976. Early Scourian structures in the Scourie-Laxford region and their bearing on the evolution of the Laxford Front. *Journal of the Geological Society*, 132, 543-554.
- DAVIES, J. H. F. L., HEAMAN, L. M., DUFRANE, S. A. & MUEHLENBACHS, K. 2009. Geochronology and isotope geochemistry of the Scourie dykes, Scotland *6th International Dyke Conference*. Varanasi, India.
- DAVIES, R., CLOKE, I., CARTWRIGHT, J., ROBINSON, A. & FERRERO, C. 2004. Post-breakup compression of a passive margin and its impact on hydrocarbon prospectivity: An example from the Tertiary of the Faeroe-Shetland Basin, United Kingdom. *AAPG Bulletin*, 88, 1-20.
- DAVIS, G. H. & REYNOLDS, S. J. 1996. *Structural Geology of Rocks and Regions*, Canada, John Wiley & Sons, Inc, p 864.
- DEAN, K., MCLACHLAN, K. & CHAMBERS, A. 1999. Rifting and the development of the Faeroe-Shetland Basin. *In: FLEET, A. J. & BOLDY, S. A. R. (eds.) Petroleum Geology of Northwest Europe: Proceedings of the 5th Conference*. London: the Geological society, v 5, 533-544.

- DENNIS, A. J. & SECOR, D. T. 1987. A model for the development of crenulations in shear zones with applications from the southern appalachian piedmont. *Journal of Structural Geology*, 9, 809-817.
- DEWEY, J. F. & STRACHAN, R. A. 2003. Changing Silurian-Devonian relative plate motion in the Caledonides: sinistral transpression to sinistral transtension. *Journal of the Geological Society*, 160, 219-229.
- DOCKRILL, B. & SHIPTON, Z. K. 2010. Structural controls on leakage from a natural CO<sub>2</sub> geologic storage site: Central Utah, U.S.A. *Journal of Structural Geology*, 32, 1768-1782.
- DORE, A. G., LUNDIN, E. R., FICHLER, C. & OLESEN, O. 1997. Patterns of basement structure and reactivation along the NE Atlantic margin. *Journal of the Geological Society*, 154, 85-92.
- DU HUNG, N. & VAN, L., H. 2003. Petroleum Geology of Cuu Long Basin - Offshore Vietnam. *AAPG International Conference Barcelona, Spain: APPG Search and Discovery*, No 10062.
- DUNNING, F. W. 1985. Geological structure of Great Britain, Ireland and surrounding seas. *Geological Society of London Mapchart*.
- DURNEY, D. W. & RAMSAY, J. G. 1973. Incremental strains measured by syntectonic crystal growths. In: DE JONG, K. A. & SCHOLTEN, R. (eds.) *Gravity and tectonics*. New York: Wiley p 72-95.
- EINSTEIN, H. H. & BAECHER, G. B. 1983. Probabilistic and statistical methods in engineering geology. *Rock Mechanics and Rock Engineering*, 16, 39-72.
- ELDHOLM, O. & GRUE, K. 1994. North Atlantic volcanic margins: Dimensions and production rates. *J. Geophys. Res.*, 99, 2955-2968.
- ELLIOTT, D. & JOHNSON, M. R. W. 1980. Structural evolution in the northern part of the Moine thrust belt, NW Scotland *Transactions of the Royal Society of Edinburgh: Earth Sciences*, 71, 69-96.
- ELLIS, D., JOLLEY, D. W., PASSEY, S. R. & BELL, B. R. 2009. Transfer Zones: The application of new geological information from the Faroe Islands applied to the offshore exploration of intra basalt and sub-basalt strata. In: ZISKA, H. & VARMING, T. (eds.) *Faroe Islands Exploration Conference: Proceedings of the 2nd Conference*. Annales Societatis Scientarum Faroensis Supplement, poster presentation.

- ENFIELD, M. A. & COWARD, M. P. 1987. The Structure of the West Orkney Basin, northern Scotland. *Journal of the Geological Society*, 144, 871-884.
- ETHERIDGE, M. A., WALL, V. J. & VERNON, R. H. 1983. The role of the fluid phase during regional metamorphism and deformation. *Journal of Metamorphic Geology*, 1, 205-226.
- EVANS, C. R. 1965a. Geochronology of the Lewisian Basement Near Lochinver, Sutherland. *Nature*, 207, 54-56.
- EVANS, C. R. 1965b. Geochronology of the Lewisian Basement Near Lochinver, Sutherland. *Nature*, 207, 54-56.
- EVANS, C. R. & LAMBERT, R. S. J. 1974. The Lewisian of Lochinver, Sutherland; the type area for the Inverian metamorphism. *Journal of the Geological Society*, 130, 125-150.
- EVANS, C. R. & TARNEY, J. 1964. Isotopic Ages of Assynt Dykes. *Nature*, 204, 638-641.
- FALT, U., GUERIN, G., RETAIL, P. & EVANS, M. 1992. Clair Discovery: Evaluation of Natural Fracturation in a Horizontal Well Drilled in the Basement and Producing From Overlying Sediments. *European Petroleum Conference Cannes, France*, 11-21.
- FINDLAY, A. & SELBY, D. 2011. *Re-Os isotope dating of bitumen and pyrite from Clair basement core samples*, personal communication.
- FINLAY, A. J. & SELBY, D. 2011. Constraining basin models for the Faroe-Shetland Basin using Re-Os geochronology. *West of Shetlands Conference*. London: PESGB, abstract.
- FLEISCHMANN, K. H. & NEMCOK, M. 1991. Paleostress inversion of fault-slip data using the shear stress solution of Means (1989). *Tectonophysics*, 196, 195-202.
- FLOYD, P. A., WINCHESTER, J. A. & PARK, R. G. 1989. Geochemistry and tectonic setting of Lewisian clastic metasediments from the Early Proterozoic Loch Maree Group of Gairloch, NW Scotland. *Precambrian Research*, 45, 203-214.
- FORSTER, C. B. & EVANS, J. P. 1991. Hydrogeology of thrust faults and crystalline thrust sheets: Results of combined field and modeling studies. *Geophys. Res. Lett.*, 18, 979-982.
- FRIEND, C., KINNY, P. & KINNY, P. 2001. A reappraisal of the Lewisian Gneiss Complex: geochronological evidence for its tectonic assembly from disparate terranes in the Proterozoic. *Contributions to Mineralogy and Petrology*, 142, 198-218.
- FRIEND, C., KINNY, P. & LOVE, G. 2007. Timing of magmatism and metamorphism in the Gruinard Bay area of the Lewisian Gneiss Complex: comparison with the Assynt Terrane and

implications for terrane accretion—reply. *Contributions to Mineralogy and Petrology*, 153, 489-492.

GILLESPIE, P. A., HOWARD, C. B., WALSH, J. J. & WATTERSON, J. 1993. Measurement and characterisation of spatial distributions of fractures. *Tectonophysics*, 226, 113-141.

GONTIJO-PASCUTTI, A., BEZERRA, F. H. R., TERRA, E. L. & ALMEIDA, J. C. H. 2010. Brittle reactivation of mylonitic fabric and the origin of the Cenozoic Rio Santana Graben, southeastern Brazil. *Journal of South American Earth Sciences*, 29, 522-536.

GOODENOUGH, K. M., PARK, R. G., KRABBENDAM, M., MYERS, J. S., WHEELER, J., LOUGHLIN, S. C., CROWLEY, Q. G., FRIEND, C. R. L., BEACH, A., KINNY, P. D. & GRAHAM, R. H. 2010. The Laxford Shear Zone: an end-Archean terrane boundary? *In*: LAW, R. D., BUTLER, R. W. H., HOLDSWORTH, R. E., KRABBENDAM, M. & STRACHAN, R. A. (eds.) *Continental Tectonics and Mountain Building: The Legacy of Peach and Horne*. London: Geological Society, Special Publications, v 335, 103-120.

GUDMUNDSSON, A., SIMMENES, T. H., LARSEN, B. & PHILIPP, S. L. 2009. Effects of internal structure and local stresses on fracture propagation, deflection, and arrest in fault zones. *Journal of Structural Geology*, v32, No 11, 1643-1655.

HADIZADEH, J. & RUTTER, E. 1983. The low temperature brittle-ductile transition in a quartzite and the occurrence of cataclastic flow in nature. *Geologische Rundschau*, 72, 493-509.

HALL, A. M. 1991. Pre-Quaternary landscape evolution in the Scottish Highlands. *Transactions of the Royal Society of Edinburgh: Earth Sciences*, 82, 1-26.

HALL, J. 1978. 'LUST'--a seismic refraction survey of the Lewisian basement complex in NW Scotland. *Journal of the Geological Society*, 135, 555-563.

HALL, J. 1987. Physical properties of Lewisian rocks: implications for deep crustal structure. *In*: PARK, R. G. & TARNEY, J. (eds.) *Evolution of the Lewisian complex and comparable Precambrian high-grade terranes*. Geological Society, London, Special Publication, v 27, 185-192.

HANCOCK, P. L. 1985. Brittle microtectonics - Principles and Practice *Journal of Structural Geology*, 7, 437-457.

HART, G. 2008. Depletion plan ConocoPhillips summary view. Personal Communication.

- HAY, S. J., HALL, J., SIMMONS, G. & RUSSELL, M. J. 1988. Sealed microcracks in the Lewisian of NW Scotland: a record of 2 billion years of fluid circulation. *Journal of the Geological Society*, 145, 819-830.
- HERZOG, H. J. 2001. Peer Reviewed: What Future for Carbon Capture and Sequestration? *Environmental Science & Technology*, 35, 148A-153A.
- HESTHAMMER, J., JOHANSEN, T. E. S. & WATTS, L. 2000. Spatial relationships within fault damage zones in sandstone. *Marine and Petroleum Geology*, 17, 873-893.
- HINZ, K., ELDHOM, O., BLOCK, M. & SKOGSEID, J. Year. Evolution of North Atlantic volcanic continental margins. In: PARKER, J. R., ed. *Petroleum Geology of NW Europe: Proceedings of the 4th Conference*, 1993. 901-914.
- HITCHEN, K., STOKER, M. S., EVANS, D. & BEDDOE-STEPHENS, B. 1995. Permo-Triassic sedimentary and volcanic rocks in basins to the north and west of Scotland. *Geological Society, London, Special Publications*, 91, 87-102.
- HOLDSWORTH, R. E. 2001. *The nature and tectonic significance of fault zone weakening*, Bath, Geological Society, p 344.
- HOLDSWORTH, R. E., BUTLER, C. A. & ROBERTS, A. M. 1997. The recognition of reactivation during continental deformation. *Journal of the Geological Society*, 154, 73-78.
- HOLLAND, J. G. 1966. Geochemical studies in the Lewisian. *Unpublished PhD thesis*. Oxford University.
- HUANG, Q. & ANGELIER, J. 1989. Fracture spacing and its relation to bed thickness. *Geological Magazine*, 126, 335-362.
- HUDSON, J. A. & PRIEST, S. D. 1979. Discontinuities and rock mass geometry. *International Journal of Rock Mechanics and Mining Sciences & Geomechanics Abstracts*, 16, 339-362.
- IMBER, J., HOLDSWORTH, R. E., BUTLER, C. A. & LLOYD, G. E. 1997. Fault-zone weakening processes along the reactivated Outer Hebrides Fault Zone, Scotland. *Journal of the Geological Society*, 154, 105-109.
- JENSEN, L. N. 1984. Quartz microfabric of the Laxfordian Canisp Shear Zone, NW Scotland. *Journal of Structural Geology*, 6, 293-302.



- JOHNSON, Y. A., PARK, R. G. & WINCHESTER, J. A. 1987. Geochemistry, Petrogenesis and Tectonic Significance of the Early Proterozoic Loch Maree Group Amphibolites of the Lewisian Complex, NW Scotland. *Geological Society, London, Special Publications*, 33, 255-269.
- JOHNSTON, D., MCCAFFREY, K. J. W. & LORIGA, M. A. 1994. *A manual describing recording, analysis and prediction of vein and related fracture distributions*, Raw materials programme, p 200.
- JOLLY, R. J. H. & SANDERSON, D. J. 1997. A Mohr circle construction for the opening of a pre-existing fracture. *Journal of Structural Geology*, 19, 887-892.
- JONES, R. 2011. Fitting criteria for polylines into fracture surfaces. *personal communication*.
- JONES, R. R., HOLDSWORTH, R. E., MCCAFFREY, K. J. W., CLEGG, P. & TAVARNELLI, E. 2005. Scale dependence, strain compatibility and heterogeneity of three-dimensional deformation during mountain building: a discussion. *Journal of Structural Geology*, 27, 1190-1204.
- JONES, R. R., MCCAFFREY, K. J. W., CLEGG, P., WILSON, R. W., HOLLIMAN, N. S., HOLDSWORTH, R. E., IMBER, J. & WAGGOTT, S. 2008a. Integration of regional to outcrop digital data: 3D visualisation of multi-scale geological models. *Computers & Geosciences*, 1-15.
- JONES, R. R., WAWRZYNIEC, T. F., HOLLIMAN, N. S., MCCAFFREY, K. J. W., IMBER, J. & HOLDSWORTH, R. E. 2008b. Describing the dimensionality of geospatial data in the earth sciences--Recommendations for nomenclature. *Geosphere*, 4, 354-359.
- JONES, R. W. & MILTON, N. J. 1994. Sequence development during uplift: Palaeogene stratigraphy and relative sea-level history of the Outer Moray Firth, UK North Sea. *Marine and Petroleum Geology*, 11, 157-165.
- KALSBECK, F., AUSTRHEIM, H., BRIDGWATER, D., HANSEN, B. T., PEDERSEN, S. & TAYLOR, P. N. 1993. Geochronology of Archaean and Proterozoic events in the Ammassalik area, South-East Greenland, and comparisons with the Lewisian of Scotland and the Nagssugtoqidian of West Greenland. *Precambrian Research*, 62, 239-270.
- KAVEN, J. O., MAERTEN, F. & POLLARD, D. D. 2011. Mechanical analysis of fault slip data: Implications for paleostress analysis. *Journal of Structural Geology*, 33, 78-91.
- KINNY, P. D. & FRIEND, C. R. L. 1997. U-Pb isotopic evidence for the accretion of different crustal blocks to form the Lewisian Complex of northwest Scotland. *Contributions to Mineralogy and Petrology*, 129, 326-340.

- KINNY, P. D., FRIEND, C. R. L. & LOVE, G. J. 2005. Proposal for a terrane-based nomenclature for the Lewisian Gneiss Complex of NW Scotland. *Journal of the Geological Society*, 162, 175-186.
- KNOTT, S. D., BEACH, A., BROCKBANK, P. J., LAWSON BROWN, J., MCCALLUM, J. E. & WELBON, A. I. 1996. Spatial and mechanical controls on normal fault populations. *Journal of Structural Geology*, 18, 359-372.
- KNOTT, S. D., BURCHELL, M. T., JOLLEY, E. J. & FRASER, A. J. Year. Mesozoic to Cenozoic plate reconstructions of the North Atlantic and hydrocarbon plays of the Atlantic margins. In: PARKER, J. R., ed. *Petroleum Geology of NW Europe: Proceedings of the 4th Conference*, 1993. 953-974.
- KOKKALAS, S., JONES, R. R., MCCAFFREY, K. J. W. & CLEGG, P. 2007. Quantitative fault analysis at Arkitsa, Central Greece, using terrestrial laser-scanning (LiDAR). *Bulletin of the Geological Society of Greece*, 37.
- KRABBENDAM, M. & LESLIE, A. G. 2010. Lateral variations and linkages in thrust geometry: the Traligill Transverse Zone, Assynt Culmination, Moine Thrust Belt, NW Scotland. *Geological Society, London, Special Publications*, 335, 335-357.
- KRABBENDAM, M., PRAVE, T. & CHEER, D. 2008. A fluvial origin for the Neoproterozoic Morar Group, NW Scotland; implications for Torridon–Morar Group correlation and the Grenville Orogen foreland basin. *Journal of the Geological Society*, 165, 379-394.
- KROHE, A. 1990. Local variations in quartz [c]-axis orientations in non-coaxial regimes and their significance for the mechanics of S-C fabrics. *Journal of Structural Geology*, 12, 995-1004.
- LADEIRA, F. L. & PRICE, N. J. 1981. Relationship between fracture spacing and bed thickness. *Journal of Structural Geology*, 3, 179-183.
- LAMBERT, R. S. J. & HOLLAND, J. G. 1972. A geochronological study of the Lewisian from Loch Laxford to Durness, Sutherland, N. W. Scotland. *Journal of the Geological Society*, 128, 3-19.
- LEE, M. J. & HWANG, Y. J. 1993. Tectonic evolution and structural styles of the East Shetland Basin. *Geological Society, London, Petroleum Geology Conference series*, 4, 1137-1149.
- LIEBOVITCH, L. S. & TOTH, T. 1989. A fast algorithm to determine fractal dimensions by box counting. *Physics Letters A*, 141, 386-390.
- LISTER, G. S. & SNOKE, A. W. 1984. S-C Mylonites. *Journal of Structural Geology*, 6, 617-638.

- LIU, X. & GALLOWAY, W. E. 1997. Quantitative determination of Tertiary sediment supply to the North Sea Basin. *AAPG Bulletin*, 81, 1482-1509.
- LONG, J. C. S. & BILLAUX, D. M. 1987. From field data to fracture network modeling: An example incorporating spatial structure. *Water Resour. Res.*, 23, 1201-1216.
- LOVE, G. J., KINNY, P. D. & FRIEND, C. R. L. 2004. Timing of magmatism and metamorphism in the Gruinard Bay area of the Lewisian Gneiss Complex: comparisons with the Assynt Terrane and implications for terrane accretion. *Contributions to Mineralogy and Petrology*, 146, 620-636.
- MAIN, I., IRVING, D., MUSSON, R. & READING†, A. 1999. Constraints on the frequency–magnitude relation and maximum magnitudes in the UK from observed seismicity and glacio-isostatic recovery rates. *Geophysical Journal International*, 137, 535-550.
- MÄKEL, G. H. 2007. The modelling of fractured reservoirs: constraints and potential for fracture network geometry and hydraulics analysis. *Geological Society, London, Special Publications*, 292, 375-403.
- MANDELBROT, B. B. 1982. *The fractal geometry of nature*, San Francisco, W.H. Freeman.
- MANZOCCHI, T., RINGROSE, P. S. & UNDERHILL, J. R. 1998. Flow through fault systems in high-porosity sandstones. *Geological Society, London, Special Publications*, 127, 65-82.
- MANZOCCHI, T., WALSH, J. J. & BAILEY, W. R. 2009. Population scaling biases in map samples of power-law fault systems. *Journal of Structural Geology*, 31, 1612-1626.
- MARETT, R. 1996. Aggregate properties of fracture populations. *Journal of Structural Geology*, 18, 169-178.
- MARETT, R. & ALLMENDINGER, R. W. 1991. Estimates of strain due to brittle faulting: sampling of fault populations. *Journal of Structural Geology*, 13, 735-738.
- MCBRIDE, J. H. & ENGLAND, R. W. 1994. Deep seismic reflection structure of the Caledonian orogenic front west of Shetland. *Journal of the Geological Society*, 151, 9-16.
- MCCAFFREY, K. J. W., FEELY, M., HENNESSY, R. & THOMPSON, J. 2008. Visualization of folding in marble outcrops, Connemara, western Ireland: An application of virtual outcrop technology. *Geosphere*, 4, 588-599.

- MCCAFFREY, K. J. W., SLEIGHT, J. M., PUGLIESE, L. & HOLDSWORTH, R. E. 2003. Fracture formation and evolution in crystalline rocks: Insights from attribute analysis. *Geological Society Special Publications*, 214, 109-124.
- MCKIE, T. 1990. Tidal and storm influenced sedimentation from a Cambrian transgressive passive margin sequence. *Journal of the Geological Society*, 147, 785-794.
- MCKIE, T. & GARDEN, I. R. 1996. Hierarchical stratigraphic cycles in the non-marine Clair Group (Devonian) UKCS. In: HOWELL, J. A. & AITKEN, J. F. (eds.) *High Resolution Sequence Stratigraphy: Innovations and Applications*. London: Geological Society Special Publications, v 104, 139-157.
- MILODOWSKI, A. E., METCALFE, R., BAILEY, D. E. & NADEN, J. 1998. A pilot study of the history of fracturing and mineralisation in the Clair Field, West Shetland Basin. British Geological Survey. Technical survey WG/98/18C, Mineralogy and Petrology Series, p 64.
- MOLINA, J. M., RUIZ-ORTIZ, P. A. & VERA, J. A. 1995. Neptunian dykes and associated features in southern Spain: mechanics of formation and tectonic implications. *Sedimentology*, 42, 957-969.
- MONDT & JAAP, C. 1993. Use of dip and azimuth horizon attributes in 3D seismic interpretation. *SPE formation evaluation*, 8, 253-257.
- MOORBATH, S. 1969. Evidence for the age of deposition of the Torridonian sediments of north-west Scotland. *Scottish Journal of Geology*, 5, 154-170.
- MOORBATH, S., STEWART, A. D., LAWSON, D. E. & WILLIAMS, G. E. 1967. Geochronological studies on the Torridonian sediments of north-west Scotland. *Scottish Journal of Geology*, 3, 389-412.
- MOY, D. J. & IMBER, J. 2009. A critical analysis of the structure and tectonic significance of rift-oblique lineaments ('transfer zones') in the Mesozoic-Cenozoic succession of the Faroe-Shetland Basin, NE Atlantic margin. *Journal of the Geological Society*, 166, 831-844.
- MUSSON, R. M. W. 1996. The seismicity of the British Isles. *Annali de Geofisica*, v 39, 463-469.
- MYERS, J. S. 1987. The East Greenland Nagssugtoqidian mobile belt compared with the Lewisian Complex. In: PARK, R. G. & TARNEY, J. (eds.) *Evolution of the Lewisian and comparable Precambrian high-grade terranes*. Geological Society, London, Special Publication, v27, 235-246.

- MYHRE, P. I., CORFU, F. & BERGH, S. 2011. Palaeoproterozoic (2.0–1.95 Ga) pre-orogenic supracrustal sequences in the West Troms Basement Complex, North Norway. *Precambrian Research*, 186, 89-100.
- NARR, W. & SUPPE, J. 1991. Joint spacing in sedimentary rocks. *Journal of Structural Geology*, 13, 1037-1048.
- NEEDHAM, T., YIELDING, G. & FOX, R. 1996. Fault population description and prediction using examples from the offshore U.K. *Journal of Structural Geology*, 18, 155-167.
- NELSON, R. A. 1982. An approach to evaluating fractured reservoirs. *Journal of Petroleum Technology*, 34, 2167-2170.
- NELSON, R. A. 1985. *Geological analysis of naturally fractured reservoirs* Houston, Gulf Publishing Company p 332.
- NEUZIL, C. & TRACY, J. 1981. Flow through fractures *Water resources research*, 17, 191-199.
- NGUYEN, H. A. & LE, X. L. Year. Combination of underground CO<sub>2</sub> storage and increased oil recovery in Su Tu Den - SW fractured basement reservoir. *In: Proceedings of the international symposium Hanoi geoengineering, 2010 Hanoi, Vietnam abstract.*
- NICHOLS, G. J. 2005. Sedimentary evolution of the Lower Clair Group, Devonian, West of Shetland: climate and sediment supply controls on fluvial, aeolian and lacustrine deposition. *Geological Society, London, Petroleum Geology Conference series*, 6, 957-967.
- NICHOLSON, P. G. 1993. A Basin Reappraisal of the Proterozoic Torridon Group, Northwest Scotland. *In: FROSTICK, L. E. & STEEL, R. J. (eds.) Tectonic Controls and Signatures in Sedimentary Successions.* International Association of Sedimentologists. Oxford Press, UK.
- NICOL, A., WATTERSON, J., WALSH, J. J. & CHILDS, C. 1996. The shapes, major axis orientations and displacement patterns of fault surfaces. *Journal of Structural Geology*, 18, 235-248.
- NIETO-SAMANIEGO, A. F. & ALANIZ-ALVAREZ, S. A. 1995. Influence of the structural framework on the origin of multiple fault patterns. *Journal of Structural Geology*, 17, 1571-1577.
- NIETO-SAMANIEGO, A. F. & ALANIZ-ALVAREZ, S. A. 1997. Origin and tectonic interpretation of multiple fault patterns. *Tectonophysics*, 270, 197-206.
- O'HARA, M. J. 1961. Zoned Ultrabasic and Basic Gneiss Masses in the Early Lewisian Metamorphic Complex at Scourie, Sutherland. *J. Petrology*, 2, 248-276.

- ODLING, N. E., GILLESPIE, P., BOURGINE, B., CASTAING, C., CHILES, J. P., CHRISTENSEN, N. P., FILLION, E., GENTER, A., OLSEN, C., THRANE, L., TRICE, R., AARSETH, E., WALSH, J. J. & WATTERSON, J. 1999. Variations in fracture system geometry and their implications for fluid flow in fractures hydrocarbon reservoirs. *Petroleum Geoscience*, 5, 373-384.
- ODLING, N. E. & RODEN, J. E. 1997. Contaminant transport in fractured rocks with significant matrix permeability, using natural fracture geometries. *Journal of Contaminant Hydrology*, 27, 263-283.
- OGILVIE, S. 2011. Well planning in the Clair Field. *Tectonic Studies Group, AGM*. Durham University, abstract.
- ORTEGA, O. J., MARRETT, R. A. & LAUBACH, S. E. 2006. A scale-independent approach to fracture intensity and average spacing measurement. *AAPG Bulletin*, 90, 193-208.
- PARK, R. G. 1964. The structural history of the Lewisian rocks of Gairloch, Wester Ross, Scotland. *Quarterly Journal of the Geological Society*, 120, 397-426.
- PARK, R. G. 1966. Nature and origin of Lewisian basic rocks at Gairloch, Ross-shire. *Scottish Journal of Geology*, 2, 179-199.
- PARK, R. G. 1970. Observations on Lewisian Chronology. *Scottish Journal of Geology*, 6, 379-399.
- PARK, R. G. 1994. Early Proterozoic tectonic overview of the northern British Isles and neighbouring terrains in Laurentia and Baltica. *Precambrian Research*, 68, 65-79.
- PARK, R. G. 2005. The Lewisian terrane model: a review. *Scottish Journal of Geology*, 41, 105-118.
- PARK, R. G. 2009. Lewisian of the Scottish Mainland. In: MENDUM, J. R., BARBER, A. J., BUTLER, R. W. H., FLINN, D., GOODENOUGH, K. M., KRABBENDAM, M., PARK, R. G. & STEWART, A. D. (eds.) *Lewisian, Torridonian and Moine Rocks of Scotland*. The Geological Conservation Review Series, v 147, p 639.
- PARK, R. G., CLIFF, R. A., FETTES, D. J. & STEWART, A. D. 1994. Precambrian rocks in North-West Scotland west of the Moine Thrust. In: GIBBONS, W. & HARRIS, A. L. (eds.) *A revised correlation of Precambrian rocks in the British Isles*. Geological Society, London, Special Report No 2, 6-22.
- PARK, R. G., CRANE, A. & NIAMATULLAH, M. 1987. Early Proterozoic structure and kinematic evolution of the southern mainland Lewisian. In: PARK, R. G. & TARNEY, J. (eds.) *Evolution of*

- the Lewisian and comparable Precambrian high-grade terranes*. Geological Society, London, Special Publication, v27, 73-79.
- PARK, R. G. & CRESSWELL, D. 1973. The dykes of the Laxfordian belts. *In*: PARK, R. G. & TARNEY, J. (eds.) *The Early Precambrian of Scotland and related rocks of Greenland*. Newcastle, Staffordshire: Dept. of Geology, University of Keele, p 200.
- PARK, R. G., KINNY, P. D., FRIEND, C. R. L. & LOVE, G. J. 2005. Discussion on a terrane-based nomenclature for the Lewisian Gneiss Complex of NW Scotland *Journal*, Vol. 162, 2005, pp. 175-186. *Journal of the Geological Society*, 162, 893-895.
- PARK, R. G., STEWART, A. D. & WRIGHT, D. T. 2002. The Hebridean Terrane. *In*: TREWIN, N. H. (ed.) *The Geology Scotland*. London: The Geological Society, p 576.
- PARK, R. G. & TARNEY, J. 1987. The Lewisian complex: a typical Precambrian high-grade terrane? *In*: PARK, R. G. & TARNEY, J. (eds.) *Evolution of the Lewisian and comparable Precambrian high-grade terranes*. Geological Society, London, Special Publication, v 27, 13-25.
- PARK, R. G., TARNEY, J. & CONNELLY, J. N. 2001. The Loch Maree Group: Palaeoproterozoic subduction–accretion complex in the Lewisian of NW Scotland. *Precambrian Research*, 105, 205-226.
- PASSCHIER, C. W. 1991. Geometric constraints on the development of shear bands in rocks. *Geol Mijnb*, 70, 203-211.
- PASSCHIER, C. W. & TROUW, R. A. J. 2005. *Microtectonics*, Berlin, Springer-Verlag, p 366.
- PEACH, B. N., GEIKIE, A. & TEALL, J. J. H. 1907. *The geological structure of the North-West Highlands of Scotland*, Glasgow, Printed for His Majesty's Stationery Office by James Hedderwick & Sons, p 825.
- PEACOCK, D. C. P. & SANDERSON, D. J. 1992. Effects of layering and anisotropy on fault geometry. *Journal of the Geological Society*, 149, 793-802.
- PICKERING, G., BULL, J. M. & SANDERSON, D. J. 1995. Sampling power-law distributions. *Tectonophysics*, 248, 1-20.
- PICKERING, G., BULL, J. M., SANDERSON, D. J. & HARRISON, P. V. 1994. Fractal fault displacements: A case study from the Moray Firth, Scotland. *In*: KRUHL, J. A. (ed.) *Fractals and dynamic systems in geosciences*. Berlin: Springer-Verlag 105-120.

- PIK, R. & MARTY, B. 2009. Helium isotopic signature of modern and fossil fluids associated with the Corinth rift fault zone (Greece): Implication for fault connectivity in the lower crust. *Chemical Geology*, 266, 67-75.
- POLLARD, D. D., SALTZER, S. D. & RUBIN, A. M. 1993. Stress inversion methods: are they based on faulty assumptions? *Journal of Structural Geology*, 15, 1045-1054.
- PRICE, N. J. & COSGROVE, J. W. 1991. *Analysis of geological structures*, Cambridge University Press, p 520.
- PRIEST, S. D. & HUDSON, J. A. 1976. Discontinuity spacings in rock. *International Journal of Rock Mechanics and Mining Science & Geomechanics Abstracts*, 13, 135-148.
- PRIEST, S. D. & HUDSON, J. A. 1981. Estimation of discontinuity spacing and trace length using scanline surveys. *International Journal of Rock Mechanics and Mining Sciences & Geomechanics Abstracts*, 18, 183-197.
- RAINBIRD, R. H., HAMILTON, M. A. & YOUNG, G. M. 2001. Detrital zircon geochronology and provenance of the Torridonian, NW Scotland. *Journal of the Geological Society*, 158, 15-27.
- RAMSAY, J. G. 1997. The geometry of a deformed unconformity in the Caledonides of NW Scotland. In: SENGUPTA, S. (ed.) *Evolution of Geological Structures*. London: Chapman & Hall, p 500.
- READ, H. H. 1926. *The Geology of Strath Oykeil and Lower Loch Shin*, His Majesty's Stationery Offices, p 220.
- RICHTER, D. 1966. On the New Red Sandstone Neptunian Dykes of the Tor Bay Area (Devonshire). *Proceedings of the Geologists' Association*, 77, 173-186.
- RIEDEL, W. 1929. Zur Mechanik geologischer Brucherscheinungen *Centralbl. f. Mineral. Geol. u. Pal.*, 1929 B, 354-368.
- RINGROSE, P. S. 1989. Recent fault movement and palaeoseismicity in western Scotland. *Tectonophysics*, 163, 305-314.
- RITCHIE, J. D. & DARBYSHIRE, D. P. F. 1984. Rb–Sr dates on Precambrian rocks from marine exploration wells in and around the West Shetland Basin. *Scottish Journal of Geology*, 20, 31-36.



- ROBERTS, A. M. & HOLDSWORTH, R. E. 1999. Linking onshore and offshore structures: Mesozoic extension in the Scottish Highlands. *Journal of the Geological Society*, 156, 1061-1064.
- RODGERS, G., CROUGH, T. E., BLUCK, B. J. & KWOK, Y. Y. 1990. Provenance ages of the Torridonian sandstone of NW Scotland using single grain U-Pb zircon analysis *Geological Society of Australia ICOG abstracts*, 7, 84.
- RODGERS, S. F. 2000. Stress related flow - are we looking the right way? *Dialog*, p 1-3.
- ROLLIN, K. E. 1994. Geophysical correlation of Precambrian rocks of northern Britain. In: GIBBONS, W. & HARRIS, A. L. (eds.) *A revised correlation of Precambrian rocks in the British Isles*. London: Geological Society Special Publication, p 200
- ROLLINSON, H. R. 2006. Archaean Crustal Evolution. In: BROWN, M. & RUSHMER, T. (eds.) *Evolution of the continental crust*. Cambridge: Cambridge University Press.
- ROLLINSON, H. R. 2007. *Early Earth Systems: A geochemical approach*, Oxford, Blackwell Publishing, 173-230.
- ROLLINSON, H. R. & FOWLER, M. B. 1987. The magmatic evolution of the Scourian complex at Gruinard Bay. In: PARK, R. G. & TARNEY, J. (eds.) *Evolution of the Lewisian and comparable Precambrian high-grade terrains*. London: Geological Society, Special Publication, v27, 57-71.
- ROULEAU, A. & GALE, J. E. 1985. Statistical characterization of the fracture system in the Stripa granite, Sweden. *International Journal of Rock Mechanics and Mining Sciences & Geomechanics Abstracts*, 22, 353-367.
- SAGI, D. 2010. Terrestrial Laser Scan fracture modelling in GOCAD, *In prep*.
- SALAH, M. G. & ALSHARHAN, A. S. 1998. The PreCambrian Basement: A Major Reservoir in the the Rifted Basin, Gulf of Suez. *Journal of Petroleum Science and Engineering*, 19, 201-222.
- SAMPLE, J. C. 2010. Stable isotope constraints on vein formation and fluid evolution along a recent thrust fault in the Cascadia accretionary wedge. *Earth and Planetary Science Letters*, 293, 300-312.
- SANDERSON, D. & MCCAFFREY, K. J. W. 2011. Reconstructed box counting for full 2- and 3-dimensional fracture modelling. *In prep*.
- SASSEN, D. S. 2008. Coherency attribute algorithm for polarimetric ground penetrating radar (GPR). *SEG Technical Program Expanded Abstracts*, 27, 1172-1176.

- SAUNDERS, A. D., FITTON, J. G., KERR, A. C., NORRY, M. J. & KENT, R. W. 1997. *The North Atlantic Igneous Province*, Washington, DC, ETATS-UNIS, American Geophysical Union, p 438.
- SAUNDERS, A. D., JONES, S. M., MORGAN, L. A., PIERCE, K. L., WIDDOWSON, M. & XU, Y. G. 2007. Regional uplift associated with continental large igneous provinces: The roles of mantle plumes and the lithosphere. *Chemical Geology*, 241, 282-318.
- SCHROEDER, M. 1991. *Fractals, Chaos, Power-laws: Minutes from a Infinite Paradise*, New York, Freeman, p 448.
- SCOTCHMAN, I. C., CARR, A. D. & PARNELL, J. Year. Hydrocarbon generation modelling along the UK North Eastern Atlantic Margin. *In: AAPG Hedberg Conference "Hydrocarbon Habitat of Volcanic Rifted Passive Margins"*, September 8-11, 2002 Stavanger, Norway.
- SCOTCHMAN, I. C., CARR, A. D. & PARNELL, J. 2006. Hydrocarbon generation modelling in a multiple rifted and volcanic basin: a case study in the Foinaven Sub-basin, FaroeShetland Basin, UK Atlantic margin. *Scottish Journal of Geology*, 42, 1-19.
- SCOTCHMAN, I. C., GRIFFITH, C. E., HOLMES, A. J. & JONES, D. M. 1998. The Jurassic petroleum system north and west of Britain: a geochemical oil-source correlation study. *Organic Geochemistry*, 29, 671-700.
- SEN, Z. & KAZI, A. 1984. Discontinuity spacing and RQD estimates from finite length scanlines. *International Journal of Rock Mechanics and Mining Sciences & Geomechanics Abstracts*, 21, 203-212.
- SHERATON, J. W., SKINNER, A. C. & TARNEY, J. 1973a. The Geochemistry of the Scourian Gneisses of the Assynt District. *In: PARK, R. G. & TARNEY, J. (eds.) The Early Precambrian of Scotland and related rocks of Greenland*. Newcastle, Staffordshire: Dept. of Geology, University of Keele, p 200.
- SHERATON, J. W., TARNEY, J., WHEATLEY, T. J. & E, W. A. 1973b. The structural history of the Assynt district. *In: PARK, R. G. & TARNEY, J. (eds.) The early Precambrian rocks of Scotland and related rocks of Greenland*. University of Keele, p 200.
- SIBSON, R. H. 1974. Frictional constraints on thrust, wrench and normal faults. *Nature*, 249, 542-544.
- SIBSON, R. H. 1977. Fault rocks and fault mechanisms. *Journal of the Geological Society*, 133, 191-213.

- SIBSON, R. H. 1983. Continental fault structure and the shallow earthquake source. *Journal of the Geological Society*, 140, 741-767.
- SIBSON, R. H. 1985. A note on fault reactivation. *Journal of Structural Geology*, 7, 751-754.
- SIBSON, R. H. 1986. Brecciation processes in fault zones - Inferences from earthquake rupturing. *Pure and Applied Geophysics*, 124, 159-175.
- SIBSON, R. H. 1990. Conditions for fault-valve behaviour. *Geological Society, London, Special Publications*, 54, 15-28.
- SIBSON, R. H., MOORES, J. M. M. & RANKIN, A. H. 1975. Seismic pumping--a hydrothermal fluid transport mechanism. *Journal of the Geological Society*, 131, 653-659.
- SLEIGHT, J. M. 2001. *Fracture characteristics from two Reactivated Basement Fault Zones: Examples from Norway and Shetland*. Unpublished Ph.D., University of Durham.
- SMITH, P. J. & BOTT, M. H. P. 1975. Structure of the Crust Beneath the Caledonian Foreland and Caledonian Belt of the North Scottish Shelf Region. *Geophysical Journal of the Royal Astronomical Society*, 40, 187-205.
- SMITH, R. L., STEARN, J. E. F. & PIPER, J. D. A. 1983. Palaeomagnetic studies of the Torridonian sediments, NW Scotland. *Scottish Journal of Geology*, 19, 29-45.
- SMYTHE, D. K., SOWERBUTTS, W. T. C., BACON, M. & MCQUILLIN, R. 1972. Deep Sedimentary Basin below Northern Syke and the Little Minch. *nature physical science*, 236, 87-89.
- SOPER, N. J. & ENGLAND, R. W. 1995. Vendian and Riphean rifting in NW Scotland. *Journal of the Geological Society*, 152, 11-14.
- SPERNER, B. & ZWEIGEL, P. 2010. A plea for more caution in fault-slip analysis. *Tectonophysics*, 482, 29-41.
- STEARNS, D. W. & FRIEDMAN, M. 1972. Reservoirs in fractured rock. *Stratigraphic oil and gas fields: Classification, Exploration methods and Case Histories*. Tulsa: AAPG Memoir p 270.
- STEEL, R. J. 1974. Cornstone (Fossil Caliche): Its Origin, Stratigraphic, and Sedimentological Importance in the New Red Sandstone, Western Scotland. *The Journal of Geology*, 82, 351-369.
- STEIN, A. M. 1988. Basement controls upon basin development in the Caledonian foreland, NW Scotland. *Basin Research*, 1, 107-119.
- STEIN, A. M. 1992. Basin development and petroleum potential in The Minches and Sea of the Hebrides Basins. *Geological Society, London, Special Publications*, 62, 17-20.

- STEWART, A. D. 1988a. The Sleat and Torridon Groups. *In: WINCHESTER, J. A. (ed.) Later Proterozoic stratigraphy of the northern Atlantic regions*. Glasgow Blackie, p 31-47.
- STEWART, A. D. 1988b. The Stoer Group, Scotland. *In: WINCHESTER, J. A. (ed.) Later Proterozoic stratigraphy of the northern Atlantic regions*. Glasgow: Blackie, 17-30.
- STEWART, A. D. 1991a. Geochemistry, provenance and palaeoclimate of the Sleat and Torridon groups in Skye. *Scottish Journal of Geology*, 27, 81-95.
- STEWART, A. D. 1991b. Torridonian. *In: CRAIG, G. Y. (ed.) The Geology of Scotland (3rd edition)*. London: Geological Society, p 65-74.
- STEWART, A. D. 1993. Late Proterozoic and Late Palaeozoic movement on the Coigach fault in NW Scotland. *Scottish Journal of Geology*, 29, 21-28.
- STEWART, A. D. & GEOLOGICAL SOCIETY OF LONDON. 2002. *The later Proterozoic Torridonian rocks of Scotland : their sedimentology, geochemistry and origin*. London, Geological Society, p 130.
- STEWART, A. D. & IRVING, E. 1974. Palaeomagnetism of Precambrian Sedimentary Rocks from NW Scotland and the Apparent Polar Wandering Path of Laurentia. *Geophysical Journal of the Royal Astronomical Society*, 37, 51-72.
- STEWART, I. S., FIRTH, C. R., RUST, D. J., COLLINS, P. E. F. & FIRTH, J. A. 2001. Postglacial fault movement and palaeoseismicity in western Scotland: A reappraisal of the Kinloch Hourn fault, Kintail. *Journal of Seismology*, 5, 307-328.
- STOKER, M. S., HITCHEN, K. & GRAHAM, C. C. 1993. The Geology of the Hebrides and West Shetland Shelves, and Adjacent Deep-water Areas. *British Geological Survey, UK Offshore Regional Report*, p 159.
- STRACHAN, R. A., SMITH, M., HARRIS, A. L. & FETTES, D. J. 2002. The Northern Highland and Grampian terranes. *In: TREWIN, N. H. (ed.) The Geology of Scotland*. London: The Geological Society, 81-147
- SURVEY, B. G. 1998. *Summer Isles. Scotland Sheet 101W. Solid and Drift Geology. 1:50,000*. BGS (NERC).
- SUTTON, J. 1963. Long-Term Cycles in the Evolution of the Continents. *Nature*, 198, 731-735.

- SUTTON, J. & WATSON, J. 1950. The pre-Torridonian metamorphic history of the Loch Torridon and Scourie areas in the North-West Highlands, and its bearing on the chronological classification of the Lewisian. *Quarterly Journal of the Geological Society*, 106, 241-307.
- SWAN, A. R. H. & SANDILANDS, M. 1995. Introduction to geological data analysis. *International Journal of Rock Mechanics and Mining Sciences and Geomechanics Abstracts*, 32, 387A-387A.
- SWETT, K. 1981. Cambro-Ordovician strata in Ny Friesland, Spitsbergen and their palaeotectonic significance. *Geological Magazine*, 118, 225-250.
- SWETT, K. & SMIT, D. E. 1972. Paleogeography and Depositional Environments of the Cambro-Ordovician Shallow-Marine Facies of the North Atlantic. *Geological Society of America Bulletin*, 83, 3223-3248.
- TARNEY, J. 1963. Assynt dykes and their metamorphism. *Nature*, 199, 672-674.
- TARNEY, J. 1973. The Scourie dyke suite and the nature of the Inverian event in Assynt. In: PARK, R. G. & TARNEY, J. (eds.) *The early Precambrian rocks of Scotland and related rocks in Greenland*. University of Keele, p 200.
- TARNEY, J. & WEAVER, B. L. 1987. Geochemistry of the Scourian complex: petrogenesis and tectonic models. In: PARK, R. G. & TARNEY, J. (eds.) *Evolution of the Lewisian and comparable Precambrian high-grade terrains*. Oxford: Geological Society by Blackwell Scientific, v27, 45-56.
- THOMSON, K., UNDERHILL, J. R., GREEN, P. F., BRAY, R. J. & GIBSON, H. J. 1999. Evidence from apatite fission track analysis for the post-Devonian burial and exhumation history of the northern Highlands, Scotland. *Marine and Petroleum Geology*, 16, 27-39.
- TORSVIK, T. H. & STURT, B. A. 1987. On the origin and stability of remanence and the magnetic fabric of the Torridonian Red Beds, NW Scotland. *Scottish Journal of Geology*, 23, 23-38.
- TRINKS, I., CLEGG, P., MCCAFFREY, K. J. W., JONES, R., HOBBS, R., HOLDSWORTH, R. E., HOLLIMAN, N. S., IMBER, J., WAGGOTT, S. & WILSON, R. W. 2005. Mapping and analysing virtual outcrops. *Visual Geosciences*, 1-7.
- TUCKER, M. E. & WRIGHT, V. P. 1990. *Carbonate Sedimentology*, Blackwell Scientific Publications, p 496.
- TURCOTTE, D. L. 1989. Fractals in geology and geophysics. *Pure and Applied Geophysics*, 131, 171-196.

- TURCOTTE, D. L. 1992. Fractals, Chaos, Self-organized critically and tectonics. *Terra Nova*, 4, 4-12.
- TURNBULL, M. J. M., WHITHOUSE, M. J. & MOORBATH, S. 1996. New isotopic age determinations for the Torridonian, NW Scotland. *Journal of the Geological Society*, 153, 955-964.
- TWISS, R. J. & MOORES, E. M. 2007. *Structural Geology*, New York, W.H. Freeman and Company, p 736.
- VAN BREEMEN, O., AFTALION, M. & JOHNSON, M. R. W. 1979. Age of the Loch Borrolan complex, Assynt, and late movements along the Moine Thrust Zone. *Journal of the Geological Society*, 136, 489-495.
- VERNON, R., HOLDSWORTH, R. E., SELBY, D., FINDLAY, A. & FARREL, T. 2011. The age, geological character and structural setting of quartz-pyrite veins in the Assynt Terrane, Lewisian Complex, NW Scotland. *In prep.*
- VERNON, R. H., WILLIAMS, V. A. & D'ARCY, W. F. 1983. Grain-size reduction and foliation development in a deformed granitoid Batholith. *Tectonophysics*, 92, 123-145.
- VIGNES-ADLER, M., LE PAGE, A. & ADLER, P. M. 1991. Fractal analysis of fracturing in two African regions, from satellite imagery to ground scale. *Tectonophysics*, 196, 69-86.
- WALLACE, R. 1984. Patterns and timing of late Quaternary faulting in the Great Basin Province and relation to some regional tectonic features. *J. Geophys. Res.*, 89, 5763-5769.
- WALSH, J., WATTERSON, J. & YIELDING, G. 1991. The importance of small-scale faulting in regional extension. *Nature*, 351, 391-393.
- WALSH, J. J. & WATTERSON, J. 1993. Fractal analysis of fracture patterns using the standard box-counting technique: valid and invalid methodologies. *Journal of Structural Geology*, 15, 1509-1512.
- WARRINGTON, G., AUDLEY-CHARLES, M. G., ELLIOTT, R. E., EVANS, W. B., IVIMEY-COOK, H. C., KENT, P. G., ROBINSON, P. L., SHOTTON, F. W. & TAYLOR, F. M. 1980. *A correlation of Triassic rocks in the British Isles: Special Report*, p 78.
- WATTS, A. B. 1971. Geophysical investigations on the continental shelf and slope north of Scotland. *Scottish Journal of Geology*, 7, 189-218.

- WEAVER, B. L. & TARNEY, J. 1980. Rare earth geochemistry of Lewisian granulite-facies gneisses, northwest Scotland: Implications for the petrogenesis of the Archaean lower continental crust. *Earth and Planetary Science Letters*, 51, 279-296.
- WHEELER, J., PARK, R. G., ROLLINSON, H. R. & BEACH, A. 2010. The Lewisian Complex: insights into deep crustal evolution. *Geological Society, London, Special Publications*, 335, 51-79.
- WHEELER, J., WINDLEY, B. F. & DAVIES, F. B. 1987. Internal evolution of the major Precambrian shear belt at Torridon, NW Scotland. *Geological Society, London, Special Publications*, 27, 153-163.
- WHITEHOUSE, M. J. 1989. Sm-Nd evidence for diachronous crustal accretion in the Lewisian complex of northwest Scotland. *Tectonophysics*, 161, 245-256.
- WHITEHOUSE, M. J., BRIDGWATER, D. & PARK, R. G. 1997. Detrital zircon ages from the Loch Maree Group, Lewisian Complex, NW Scotland: confirmation of a Palaeoproterozoic Laurentia&#x2014;Fennoscandia connection. *Terra Nova*, 9, 260-263.
- WIBBERLEY, C. A. J., YIELDING, G. & DI TORO, G. 2008. Recent advances in the understanding of fault zone internal structure: a review. *Geological Society, London, Special Publications*, 299, 5-33.
- WILKINSON, M., MCCAFFREY, K. J. W., ROBERTS, G., COWIE, P. A., PHILLIPS, R. J., MICHETTI, A. M., VITTORI, E., GUERRIERI, L., BLUMETTI, A. M., BUBECK, A., YATES, A. & SILEO, G. 2010. Partitioned postseismic deformation associated with the 2009 Mw 6.3 L'Aquila earthquake surface rupture measured using a terrestrial laser scanner. *Geophys. Res. Lett.*, 37, L10309.
- WILSON, R. W., HOLDSWORTH, R. E., WILD, L. E., MCCAFFREY, K. J. W., ENGLAND, R. W., IMBER, J. & STRACHAN, R. A. 2010. Basement-influenced rifting and basin development: a reappraisal of post-Caledonian faulting patterns from the North Coast Transfer Zone, Scotland. *Geological Society, London, Special Publications*, 335, 795-826.
- WINSLOW, M. 1983. Clastic dike swarms and the structural evolution of the foreland fold and thrust belt of the southern Andes. *Geological Society of America Bulletin*, 94, 1073-1080.
- WITT, A. J., FOWLER, S. R., KJELSTADLI, R. M., DRAPER, L. F., BARR, D. & MCGARRITY, J. P. 2010. Managing the start-up of a fractured oil reservoir: development of the Clair field, West of Shetland. *Geological Society, London, Petroleum Geology Conference series*, 7, 299-313.

- WOODCOCK, N. H. & MORT, K. 2008. Classification of fault breccias and related fault rocks. *Geological Magazine*, 145, 435-440.
- WOODCOCK, N. H. & NAYLOR, M. A. 1983. Randomness testing in three-dimensional orientation data. *Journal of Structural Geology*, 5, 539-548.
- WRIGHT, D. T. & KNIGHT, I. 1995. A revised chronostratigraphy for the lower Durness Group. *Scottish Journal of Geology*, 31, 11-22.
- WYLDE, J. J., WILLIAMS, G. D. M. & COUSINS, R. E. 2005. Unlocking the Potential: A North Sea Heavy Oil Success Story. *SPE International Thermal Operations and Heavy Oil Symposium*. Calgary, abstract.
- YIELDING, G., NEEDHAM, T. & JONES, H. 1996. Sampling of fault populations using sub-surface data: a review. *Journal of Structural Geology*, 18, 135-146.
- ZIEGLER, P. A. 1982. *Geological Atlas of Western and Central Europe*, The Hague, p 239.